CODEN: JASI

0001-4966

The Journal of the Acoustical Society of America

Vol. 108, No. 1 July 2000

(Continued)

THE JOURNAL OF THE ACOUSTICAL SOCIETY OF AMERICA VOL. 108, NO. 1, JULY 2000

CONTENTS—*Continued from preceding page*

(Continued)

THE JOURNAL OF THE ACOUSTICAL SOCIETY OF AMERICA VOL. 108, NO. 1, JULY 2000

CONTENTS—*Continued from preceding page*

ACOUSTICAL NEWS—USA

Elaine Moran
Acoustical Society of America, Suite 1NO1, 2 Huntington Quadrangle, Melville, NY 11747-4502

Editor's Note: *Readers of this Journal are asked to submit news items on awards, appointments, and other activities about themselves or their colleagues. Deadline dates for news items and notices are 2 months prior to publication.*

New Fellows of the Acoustical Society of America

Mohsen Badiey—For contributions to the understanding of the effect of sediment properties on shallow water propagation.

Mendel Kleiner—For contributions to acoustical measurements, computer modeling and auralization.

Robin S. Langley—For contributions to understanding complex vibratory systems.

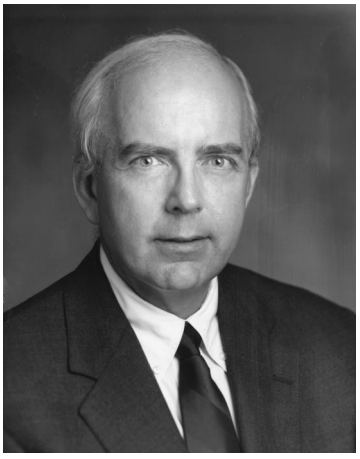

Paul J. Vidmar—For contributions to the understanding of ocean bottom acoustics.

 0001-4966/2000/108(1)/1/4/$17.00

UTD/Callier Center Advanced Hearing Research Center Dedicated

The Callier Center opened the doors of its new Advanced Hearing Research Center (AHRC) on the Callier Campus in Dallas, Texas, during a dedication of the new facility on Friday, March 24, 2000. The new facility extends Callier's research programs focused on hearing and hearing loss, with the goal of embellishing service programs to the community. ASA member Ross Roeser is Director of the Callier Center.

The newly constructed 12 500 square foot facility provides additional laboratory, office, and clinical space for the assessment and treatment of hearing loss, as well as classrooms for undergraduate and graduate students studying communication and its disorders. Students will also have the opportunity to become more actively involved with patients in the clinical services areas. The new facility provides research laboratories for the application of studies on both children and adults with cochlear implants and hearing aids, and the designs allows Callier researchers to test their findings in real-time situations with patients.

USA Meetings Calendar

Listed below is a summary of meetings related to acoustics to be held in the U.S. in the near future. The month/year notation refers to the issue in which a complete meeting announcement appeared.

2000

13–16 July — ClarinetFest 2000, Norman, OK [Dr. Keith Koons, Music Dept., Univ. of Central Florida, P.O. Box 161354, Orlando, FL 32816-1354; Tel.: 407-823-5116; Email: kkoons@pegasus.cc.ucf.edu].

27–28 July — First International AutoSEA Users Conference, San Diego, CA [Vibro-Acoustic Sciences, Attn: Ali Behnam, 12555 High Bluff Dr., Suite 310, San Diego, CA 92130; Tel.: 858-350-0057; Fax: 858-350-8328; Email: info@vasci.com; WWW: www.vasci.com/company/events/asuc/].

2–4 August — 2000 Ultrasonic Transducer Engineering Conference, University Park, PA [K. Kirk Shung, NIH Resource on Medical Ultrasonic Transducer Technology, Pennsylvania State Univ., 231 Hallowell Bldg., University Park, PA 16802; Tel.: 814-865-1407; Fax: 814-863-0490; Email: kksbio@engr.psu.edu].

21–23 Sept. — Eighth Annual Conference on the Management of the Tinnitus Patient, Iowa City, IA [Richard Tyler, Tel.: 391-356-2471; Email: tyler@uiowa.edu; WWW: www.medicine.uiowa.edu/otolaryngology/news/news].

22–25 Oct. — IEEE Ultrasonics Symposium, San Juan, Puerto Rico [R. Almar, 896 Buttonwood Ln., Altamonte Springs, FL 32714; Fax: 407-290-5181; WWW: www.uffcsymp2000.org].

4–8 Dec. — Joint Meeting: 140th Meeting of the Acoustical Society of America/NoiseCon 2000, Newport Beach, CA [Acoustical Society of America, Suite 1NO1, 2 Huntington Quadrangle, Melville, NY 11747-4502; Tel.: 516-576-2360; Fax: 516-576-2377; Email: asa@aip.org; WWW: asa.aip.org]. Deadline for receipt of abstracts: 28 July 2000.

2001

22–25 March — ''New Frontiers in the Amelioration of Hearing Loss,'' St. Louis, MO [Sarah Uffman, CID Department of Research, 4560 Clayton Ave., St. Louis, MO 63110; Tel.: 314-977-0278; Fax: 314-977-0030; Email: suffman@cid.wustl.edu].

30 April–3 May — 2001 SAE Noise & Vibration Conference & Exposition, Traverse City, MI [Patti Kreh, SAE Int'l., 755 W. Big Beaver Rd., Suite 1600, Troy, MI 48084; Tel.: 248-273-2474; Fax: 248-273-2494; Email: pkreh@sae.org]. Deadline for submitting abstracts: 14 July 2000.

4–8 June — 141st Meeting of the Acoustical Society of America, Chicago, IL [Acoustical Society of America, Suite 1NO1, 2 Huntington Quadrangle, Melville, NY 11747-4502; Tel.: 516-576-2360; Fax: 516-576-2377; Email: asa@aip.org; WWW: asa.aip.org].

7–10 Oct. — 2001 IEEE International Ultrasonics Symposium Joint with World Congress on Ultrasonics, Atlanta, GA [W. O'Brien, Electrical and Computer Engineering, Univ. of Illinois, 405 N. Mathews, Urbana, IL 61801; Fax: 217-244-0105; WWW: www.ieee-uffc.org/2001].

Revision List

New Associates

Adrian, Marcus E., MacKey Mitchell Associates, 800 St. Louis Union Station, Suite 200, St. Louis, MO 63135

Aizawa, Naomi, 746 South Front Street, Philadelphia, PA 19147

Baumann, Uwe, ENT/Audiology, Univ. of Munich, Marchionini Str. 15, Muenchen 81377, Germany

Becker-Schweitzer, Joerg, Roland Str. 20, Aachen 52070, Germany

Burnham, Denis K., Univ. of Western Sydney, Macarthur Auditory Research Center, FASS 4B, P.O. Box 555, Campbelltown, Sydney NSW 2560, Australia

Cormack, Robert, 40 Harbor View Drive, Sugarland, TX 77479

Delaney, Kevin J., AETC, Inc., 8910 University Center Lane, Suite 900, San Diego, CA 92122-1012

DiPerna, Daniel T., Naval Surface Warfare Center, Code 722, 9500 MacArthur Boulevard, West Bethesda, MD 20817

Doron, Eyal, Remon Medical Tech., Ltd., 7 Halamish Str., P.O. Box 3533, Caesarea Industrial Park 38900, Israel

Drennan, Ward R., MRC Inst. of Hearing Research, Glasgow Royal Inf., Queen Elizabeth Building, 16 Alexandra Parada, Glasgow G31 2ER, U.K.

Evangelista, Gianpaolo, EPFL, Lab. de Communications Audiovisuelles, IN-R Ecublens, CH-1015 Lausanne, Switzerland

Fedorov, Vladimir E., Inst. for Dynamics of Geospheres, Russian Academy of Sciences, Lehniskyprosa 38, No. 6, B334, Moscow 117334, Russia

Gahler, Mark R., 8721 Susquehanne Street, Lorton, VA 22079

Han, Sang-Kyu, Naval Postgraduate School, Undersea Warfare Academic Group, 589 Dyer Road, Room 200A, Monterey, CA 93943-5143

Hicks, Lori A., 8201 Mardi Gras, Lubbock, TX 79424

Ji, Zhenlin, Center for Automotive Research, Ohio State University, 930 Kinnear Road, Columbus, OH 43212

Karlow, Edwin A., Physics Dept., La Sierra Univ., 4700 Pierce Street, Riverside, CA 92515

Kessissoglou, Nicole J., Mechanical Engineering, James Cook University, Townsville QLD 4811, Australia

Krantz, Richard J., Physics Dept., Metropolitan State College of Denver, Campus Box 69, Denver, CO 80217

Kuczaj, Stan A., Psychology Dept., Univ. of Southern Mississippi, 231B OMH, Hattiesburg, MS 39406-5025

Macaulay, Gavin J., Fisheries Acoustics, National Inst. of Water and Atmospheric Research, 301 Evans Bay Parada, Wellington, New Zealand

Makarewicz, Rufin, H. Mickiewicz Univ., Acoustics, Umultowska 85, Poznan 61-614, Poland

Marash, Alex I., 1600 Van Epps Street, Atlanta, GA 30316

Maxwell, Suzanne L., 22606 Oak Knoll Drive, Chugiak, AK 99567

Melchert, Willi S., P.O. Box 51394, Jeddah 21543, Saudi Arabia

Merdes, Daniel W., Applied Research Lab., Pennsylvania State Univ., P.O. Box 30, State College, PA 16804-0030

Morgan III, Julian H., 4588 Lemans Drive, Orlando, FL 32808-1914

Ng, Charles T. K., ATA Sound Ltd., R & D, Suite 205, 8900 Nelson Way, Seu Discovery Park, BC V5A 4W4, Canada

Osgood, Boyd, 12825 SW 20th Court, Beaverton, OR 97008-5154

O'Toole, Russell L., 17246 Longbow Drive, Lockport, IL 60441

Page, Sarah J., DERA Bincleaves, Newton's Road, Weymouth, Dorset DT4 8UR, U.K.

Potter, Timothy J., 851 Oakwood Boulevard, Apt. 24, Dearborn, MI 48124-2346

Prame, Eric S., Speech, Music and Hearing, Royal Inst. of Technology, Drottning Kristinas V. 31, Stockholm SE100-44, Sweden

Reuter, Eric L., 132 Parker Street, Maynard, MA 01754

Sanchez-Dehesa, Jose, Fisica Teorica de la Materia Condensada, Univ. Autonoma de Madrid, Facultad de Ciencias (C-5), Madris 28049, Spain

Schneider, Robert M., 206 Heavens Way, Yorktown, VA 23693-2616

Stewart, Gerald T., Unit 2, 22 Leighton Place, Hornsby NSW 2077, Australia
Suppappola, Seth B., 1197 West Kelly Lane, Tempe, AZ 85284-3771
Takagi, Shigeru, 4-31, Iwaya-Machi, Nagaski 852-8052, Japan
Thompson, Brian C., 3308 Ashwood Drive, Cincinnati, OH 45213
Trask, Thomas J., Special Technologies Group, Newcomb & Boyd, One Northside 75, Atlanta, GA 30318-7761
Weinstein, Jonathan, 3572 Summer Drive, Wantagh, NY 11793
Wilkinson, Emily R., Audio Engineering and Acoustics, AuSim, Inc., 4962 West El Camino Real, Los Altos, CA 94022-1410
Wong, Alex, ATA Sound Ltd., Suite 205, 8900 Nelson Way, Bunaby, BC V5A 4W9, Canada
Yoda, Minami, Woodruff School of Mechanical Engineering, Georgia Inst. of Technology, Atlanta, GA 30332-0405
Yoo, Young-Joo, K. H. Technology Co., Ltd., R & D Team, C.P.O. Box 3519, Seoul 100-635, South Korea
Young, Thomas M., Meyer Sound Laboratories, 2832 San Pablo Avenue, Berkeley, CA 94702
Zahui, Marcellin, 3131 South Woodfield Boulevard, #220, Sault Ste. Marie, MI 49783
Zannin, Paulo H. T., Rue Oyapock 49, ap. 1202, Curitiba, Parana, 80050-450, Brazil
Zhu, Quing, Electrical & Systems Eng. 0157, Univ. of Connecticut, 260 Glenbrok Road, Storrs, CT 06269

New Students

Aanerud, Marian E. M., 2409 4th Avenue, North, #13, Moorhead, MN 56560
Adams, Carla L., 221 North Dithridge, #4, Pittsburgh, PA 15213-1442
Adams, Stephanie A., David L. Adams Associates, Inc., 1701 Boulder Street, Denver, CO 80211
Akeel, Umair, Ohio Wesleyan Univ., HWCC Box 1638, Delaware, OH 43015
Backfish, Michael R., Indiana State Univ., Box 2309N28, Terre Haute, IN 47804
Bauer, Adam Q., 923 Sundown Drive, Kirksville, MO 63501
Baynes, Charlie E., 57-58 Main Road, Longdenville, Chaguanas, Trinidad
Beaujean, Pierre-Philippe, 3681 Turtle Run Boulevard, Apt. 1118, Coral Springs, FL 33073
Beckers, Gabriel J. L., Inst. of Evolutionary and Ecological Sciences, Leiden University, Behavioural Biology, Kaiserstraat 63, Leiden 2311GP, The Netherlands
Biskie, Joel A., 301 Bluff Street, Port Byron, IL 61275-9787
Bruton, Frank L., Salisbury State Univ., Box 1133, Salisbury, MD 21801-6867
Buysman, John J., 1500 St. Olaf Avenue, Coon Rapids, MN 55051
Chen, Larissa, 192 Foster Street, #3A, New Haven, CT 06511
Chigoy, Brett J., 1609 Johnston Street, Lafayette, LA 70503
Corrigan, Joseph J., 75 Ardmore Avenue, Apt. 3-O, Ardmore, PA 19003
Devitt, Nicole M., P.O. Box 491, St. Mary's City, MD 20686
Draeger, Adam G., Univ. of Wisconsin, 124 McGregor, Platteville, WI 53818
Drexel, Michael V., 2327 Wavetree Lane, NW, Acworth, GA 30101-6211
Dunlap, Andrew L., 6617 Pond View Road, Clarkston, MI 48348
Dvelis, Jason M., 12 King Philip Road, Pawtucket, RI 02861
Dzikowicz, Ben R., Physics Dept., Washington State Univ., Pullman, WA 99164-2814
Eames, Cheryl L., 1311 North Merslacy Road, Apt. No 12, Bloomington, IL 61704
Eaton, Cortney A., 15210 Amberly Drive, #923, Tampa, FL 33647
Eldredge, Mark R., 555 West Main Street, Platteville, WI 53186
Emadi, Gulam, 813 Hinman Avenue, Apt. 3, Evanston, IL 60202
Federman, Jeremy, 26 Morse Street, South Portland, ME 04106-2730
Felix, James A., P.O. Box 652, Bethany, WV 26032
Finfer, Daniel C., 118 West Fowler, West Lafayette, IN 47906
Fitzsimmons, Patrick M., 2109 Fountain Hill Drive, Timonium, MD 21093
Frank, Scott D., Dept. of Mathematical Sciences, Rensselaer Polytechnic Inst., 110 8th Street, Amos Eaton 301, Troy, NY 12180
Freeman, John J., 405 Latimer Road, Raleigh, NC 27609
Ghosh, Satrajit S., Dept. of Cognitive and Neural Systems, Boston University, 677 Beacon Street, Boston, MA 02215
Girardin, Kathryn D., 386 Smithfield Road, Norridgwock, ME 04957
Gorton, Andrew J., 4532 North Claremont, Apt. 6, Chicago, IL 60625
Grassi, Massimo, Via Callegari 31, Padova 35133, Italy
Griffo, George F., 612 Borrie Avenue, Brielle, NJ 08730
Harris, Dave A., 2700 Jefferson Avenue, Unit 8, Cincinnati, OH 45219
Hartman, Matthew J., 109 East Louisiana, Ruston, LA 71270
Hataier, Jennifer L., 294 Manor Lane, Jamesport, NY 11947-0389
Heesch, David A., P.O. Box 1195, Clyde, NC 28721
Hill, Spencer C., 6851 Alvarado Road, Unit 17, San Diego, CA 92120
Hill, Steven R., 4001 Sul Road, #312, San Angelo, TX 76904
Hollingshead, Tom M., 3248 Bethel Boulevard, Zion, IL 60099
Hughes, Gregory M., P4 Regency Place, Lawrence, KS 66049
Hunter, Tyrone, 900 West Market Street, Greensboro, NC 27401
Johns, Athena C. M., Univ. of the Pacific, Casa Jackson No. 314, Stockton, CA 95211
Johnson, Ben A., 111 Pickwick Lane, Oak Ridge, TN 37830
Johnson, Elizabeth K., Psychology Dept., Johns Hopkins University, Ames Hall, 3400 North Charles Street, Baltimore, MD 21218
Johnson, Krista L., 1711 Washington Street, Evanston, IL 60202
Johnson, Matthew K., Bethel College, 3900 Bethel Drive, No. 992, Saint Paul, MN 55112-6999
Kluetz, Erik M., 1500 St. Olaf Avenue, Northfield, MN 55057
Kochetov, Alexei, Linguistics Dept., Univ. of Toronto, 130 St. George St., Room 6076, Toronto, ON M5S 3H1, Canada
Koski, Jason M., Michigan Technological Univ., 411 East McNair Hall, Houghton, MI 49931
Krein, Michael D., 833 West Buena Avenue, Apt. 1501, Chicago, IL 60613
Largen, Daniel F., 13140 Thomas Avenue South, Burnsville, MN 55337
Lemieux, Daniel A., 656 East Holmes Hall, East Lansing, MI 48825
Libbey, Bradley W., Mechanical Engineering, Georgia Inst. of Technology, Graduate Box 268, Atlanta, GA 30332-0405
Lockhart, Daniel B., 830 Lincoln Avenue, Steamboat Springs, CO 80487
Ma, Wei-Li D., Biology Dept., Boston University, 7 Water Street, Woods Hole, MA 02540
Maki, Garret M., 714 East Simpson Street, Lafayette, CO 80026
Mallebrera, Manuel M., Nybrovej 304 F60, Lyngby 2800, Denmark
Marks, Daniel T., Drew University, P.O. Box 802, CM650 Drew, Madison, NJ 07940
Mason, Russell D., Inst. of Sound Recording, Univ. of Surrey, School of Performing Arts, Guildford, Surrey GU2 5XH, U.K.
McAlister, Geoffrey I., 1500 St. Olaf Avenue, Northfield, MN 55057
Militello, Alex G., 8031 Summerview Drive, Fayetteville, NY 13066-9688
Mize, Lauren E., Box 2011, 2000 North Parkway, Memphis, TN 38112-1690
Moramli, Saifulrizal, 336344 Gatech Station, Atlanta, GA 30332-1075
Murphy, Benjamin D., 1202 Main, Carthage, IL 62321
Nelson, Paul H., 424 1/2 North 2nd Street, River Falls, WI 54022
Noel, Benjamin E., 3801 Clinton Parkway, #P3, Lawrence, KS 66047
Olgin, John G., 3526 Okeefe, El Paso, TX 79902
Onsuwan, Chutamanee, Linguistics Dept., Univ. of Michigan, 1076 Frieze Building, Ann Arbor, MI 48109-1285
Ortiz, Jeanette A., P.O. Box 8287, Northfield, IL 60093
Palmer, Bradley D., 2193 Adam Street, Conway, AR 72032
Pieleanu, Ioana N., 276 Hanover Street, Apt. 2R, Boston, MA 02113
Quick, Scott S., 435 Greenland Avenue, Oconomowoc, WI 53066
Rayess, Nassif E., Mechanical Engineering, Wayne State University, 505 Anthony Wayne Drive, Detroit, MI 48202
Riebau, Rhianna A., 223C Garden Ridge Road, Catonsville, MD 21228
Russell, Kendra L., Virginia Military Institute, VMI Box 1394, Lexington, VA 24450
Russo, Peter L., 3500 Greyston Drive, #173, Austin, TX 78731
Sarwono, Joko J. S., 24 Crescent Avenue, Manchester M8 5UD, U.K.
Sawin, Sven E., 2232 Cram Place, #2, Ann Arbor, MI 48105
Scales, E. Steven, Georgia Inst. of Technology, 325659 Georgia Tech Station, Atlanta, GA 30332-1070
Schmitt, John C., Univ. of Wisconsin, 327 Porter Hall, Platteville, WI 53818
Scholtz, Nicole O., 106 Central Street, Wellesley Hill, MA 02481-8281
Shaklee, Joel B., 300 East Pitkin, Fort Collins, CO 80524
Singer, Nancy E., 8325 33rd Avenue North, Crystal, MN 55427-1817
Smith, Dana M., 920 36th Street, Boulder, CO 80303
Smith, Kelly A., 6090 Shade Road, Greenville, OH 45331
Smith, Michael A., 1125 Wareman Avenue, Pittsburgh, PA 15226-2239

Sottile, Albert J., P.O. Box 8731, Greensboro, NC 27419-8731
Sousa Lima, Renata S., Rue Bambui 131, Beo Horizonte, Minas Gerais, 30210-490, Brazil
Stapleton, Gabriel T., 129 Private Road, 3035, Ironton, OH 45638
Stucky, Julie K., 105 Botsford, Muncie, IN 47306
Tabelin, Jason B., Virginia Tech, 327 Barringer Hall, Blacksburg, VA 24060-0001
Terry, Tiffini G., 900 Whirlpool Drive, Apt. 8304, Oxford, MS 38655
Thomas, Charles R., 34 Gardner Street, Apt. #33, Allston, MA 02134
Tincoff, Ruth J., Psychology, Johns Hopkins Univ., 3400 North Charles Street, Baltimore, MD 21218
Toop, Katie E., Box 1928, 3900 Bethel Drive, Saint Paul, MN 55112-6999
Torng, Pao-chuan, 112 Ells Avenue, Champaign, IL 61820
Turri, Albert F., 6403-B Jamesville Drive, Tampa, FL 33617
Vacca, Giacomo, Dept. of Applied Physics, Stanford University, Stanford, CA 94305
Valente, Daniel P., 34004 West 14 Mile Road, West Bloomfield, MI 48322
Voix, Jeremie J., Genie Mecanique, Univ. du Quebec, 1100 Notre-Dame Quest, Montreal, PQ H3C 1K3, Canada
Von-Paumgartten, Luiz, 1720 Wells Branch Parkway, #3104, Austin, TX 78728
Wagner, James L., 1124 27th Avenue, Apt. 15, Moorhead, MN 56560
Wallenfang, Monica J., 750 West Hampton Drive, Indianapolis, IN 46208
Walsh, Caey P., 225 NW 16th Street, Corvallis, OR 97330
Wang, Peng, Blk. 932-9-193, Jurong West Street 91, Singapore 640932
Waxman, Jacob E., 53 Glenwood Avenue, Newton, MA 02459
Werner, Carl S., P.O. Box 3270, Palmer, AK 99645
Woll, Brandon S., P.O. Box 2737, West Point, NY 10997
Yu, GongQiang, Blk. 312, #06-233 Clementi Ave. 4, 120312 Singapore
Zelinger, Richard S., 1308 6th Street, Greeley, CO 80631

Students to Associates

S. M. Beckman, B. R. Blankenship, M. A. Brantley, I. M. Hallaj, L. G. Huettel, J. Kang, K. R. Lohr, T. Norris, D. Phillips, M. M. Rose, S. T. Roweis, B. C. Seep, D. J. Sinder, B. J. Sperry, M. Tabain, M. Turgeon, K. E. Wage, U. Yasutaka

Associates to Students

J. R. Motta da Silva, C. D. Weltzin

Reinstated

E. L. Goshorn, F. C. Schafer, J. J. Welsh, H. J. Whitehouse—*Members*
R. D. Shilling—*Associate*

Resigned

I. K. Bjorno, M. P. de Vries, D. A. Driscoll, D. Schmidt, G. A. Winbow, K. H. Wycoff—*Members*
G. L. Lamb, Jr., F. Trampler—*Associate*
T. J. Rosario—*Student*

Deceased

G. Chertock, V. A. Fromkin, T. Itow, A. M. Liberman, J. B. C. Purcell, W. F. Snyder, C. F. Wiebusch—*Fellows*
W. W. Denner, K. Green—*Members*

Fellows	838
Members	2822
Associates	2923
Students	982
	7565

BOOK REVIEWS

P. L. Marston
Physics Department, Washington State University, Pullman, Washington 99164

These reviews of books and other forms of information express the opinions of the individual reviewers and are not necessarily endorsed by the Editorial Board of this Journal.

Editorial Policy: *If there is a negative review, the author of the book will be given a chance to respond to the review in this section of the Journal and the reviewer will be allowed to respond to the author's comments. [See ''Book Reviews Editor's Note,'' J. Acoust. Soc. Am.* ***81****, 1651 (May 1987).]*

Nonlinear Wave Processes in Acoustics

Konstantin A. Naugolnykh and Lev A. Ostrovsky

Cambridge University Press, Cambridge, UK, 1998.
x+298 pp. Price: $74.95 hardback and $30.95 paperback.

The area of acoustics concerned with nonlinear wave propagation is traditionally called nonlinear acoustics. Several books on this subject are available [Zarembo and Krasil'nikov (1966), Beyer (1974), Rudenko and Soluyan (1975), Hamilton and Blackstock (1998)]. The book by Naugolnykh and Ostrovsky provides yet another perspective on nonlinear acoustics, and it is written by two leading experts who have worked in this field for almost 40 years. Perhaps the more novel feature of their book, which is reflected in the title, is that nonlinear acoustics is considered as a branch of nonlinear wave physics. Such an approach appears to be very fruitful, as it permits the application to acoustics of many concepts and results obtained in other areas of nonlinear wave physics (e.g., nonlinear optics).

The book consists of seven chapters. Chapter 1, entitled ''Nonlinearity, dissipation and dispersion in acoustics,'' describes several models illustrating the combined effects of these three phenomena on acoustic waves in various media. Westervelt, simple-wave, and Burgers equations are developed for nonlinear propagation in gases, liquids, and isotropic solids. Besides these results (which can be found in all books on nonlinear acoustics), the authors consider media with internal structure having dimensions small compared with a wavelength, such as liquids with gas bubbles and isotropic solids with empty spherical cavities. It is shown how these microinhomogeneities introduce not only additional losses, but also dispersion and a substantial increase in nonlinearity. The chapter concludes with discussion of ''anomalous'' nonlinearities in elastic solids, which are modeled with stress–strain relations not described by a simple power law. Such nonlinearities are associated with dislocations, grains, and microcracks in the medium. Recent developments in this area are very interesting, and it is unfortunate that only a brief survey of these results is presented.

In Chapter 2, entitled ''Simple waves and shocks in acoustics,'' evolution of nonlinear plane waves is considered when effects of dissipation and dispersion are much weaker than that of nonlinearity. In this case, initially smooth acoustic perturbations transform eventually to weak shock waves. The chapter presents classical results for shock formation and describes the corresponding evolution of the frequency spectrum within the framework of the simple-wave and Burgers equations. Results for propagation of intense noise are also presented. In our opinion, the most interesting part of this chapter is Section 6, where propagation in media with anomalous nonlinearity is considered. Models are presented for media with two different stress–strain relations. The first, based on a modified Burgers equation, describes propagation in cubically nonlinear media. The second model describes waveform evolution in media with a bimodular constitutive law, for which compression and tension are characterized by different elastic moduli. It is shown that the nonquadratic character of the nonlinearity results in many new features connected with shock formation. In the next section, generation and amplification of sound by a distributed supersonic source (e.g., a laser beam) is modeled with solutions of a forced simple-wave equation. Nonlinear effects in standing waves are then discussed, and the chapter concludes with general results for energy and momentum associated with plane waves of finite amplitude.

The next chapter, entitled ''Nonlinear geometrical acoustics,'' is an area in which both authors have considerable experience. An augmented Burgers equation for propagation in ray tubes is developed and applied to spherical and cylindrical waves, and in particular to explosion waveforms. Finite-amplitude propagation in stratified media is considered, and two situations are described. In the first, a plane wave propagates in a direction normal to the inhomogeneous layers, in which case the ray paths are parallel straight lines. Examples cited by the authors include propagation in an isothermal atmosphere and in the solar chromosphere. In the more general case of off-normal propagation, the ray paths are curved. Solutions are developed for a monopole in a linearly stratified medium and a point source in an exponential atmosphere. The chapter concludes with an analysis of self-refraction based primarily on Whitham's approach. One of the interesting effects considered is the formation of discontinuities in the wave front as rays intersect when the propagation speed varies along a single shock front. The phenomenon is referred to as a wave front fracture, secondary shock, or shock–shock.

Chapter 4, entitled ''Nonlinear sound beams,'' begins with the KZK equation and several of its asymptotic solutions. A simple modeling procedure is considered in which nonlinearity and diffraction are taken into account in nonoverlapping spatial regions. This approach was useful for understanding basic nonlinear effects in sound beams before numerical solutions and more recent asymptotic results become available. As reviewed in this chapter, the approach predicts broadening of far field beam patterns due to shock formation. For focused beams it explains why weak nonlinearity increases the peak pressure in the focal region (because of higher harmonic generation) and shock formation causes it to decrease (because of increased absorption). Reflection of nonlinear waves from caustics is also discussed. Unfortunately, none of the results presented in this chapter was obtained within the past two decades, during which time many new developments were reported in both theory and experiment.

The next chapter is entitled ''Sound–sound interaction (nondispersive medium),'' where problems involving multiple-frequency wave interaction in quadratically nonlinear media are considered. The simple-wave equation is used to investigate examples of collinear interaction of a weak wave with sound of finite amplitude. Parametric arrays are described using the classical models of Westervelt and Berktay, in which the primary beams are modeled by simple collimated plane waves, and several experiments are reviewed. In the last section, the parametric receiving array is described and its application to nonlinear acoustic tomography is considered.

Classical nonlinear acoustics is restricted to nondispersive or weakly dispersive media. In Chapter 6, entitled ''Nonlinear acoustic waves in dispersive media,'' the effects of dispersion and nonlinearity are of the same order. Several interesting models are offered for wave interactions in the presence of dispersion. The first model describes nonlinear wave propagation in a medium with frequency-selective absorption. In media with negligible dispersion, all harmonics interact resonantly and the initial signal energy does not couple preferentially with a specific spectral component but is instead distributed over a wide frequency band. Selective absorption of unwanted harmonics permits reduction of the number of spectral components participating in the nonlinear interaction, which in turn offers a means of controlling the nonlinear wave processes. Parametric amplification and generation in waveguides and resonators is investigated using a coupled set of equations for three-wave interactions. The analogous problem has been well-studied in nonlinear optics. Bubbly liquids are considered next. At low frequencies, waves in a bubbly liquid are described by the Korteweg–de Vries–Burgers equation, which admits solutions for solitons. When the

 0001-4966/2000/108(1)/14/2/$17.00

acoustic frequency is close to the resonance frequency of the bubbles, the dispersion is large and a different model is required. Both situations are discussed. Another dispersive system that allows the formation of solitons is compressional waves in a thin solid rod, propagation of which is described by the Korteweg–de Vries (KdV) equation. The final example considered is a granular medium, and a simple model is proposed for a one-dimensional chain formed by contacting elastic spheres of the same radius. It is shown that when the chain is statically precompressed, the KdV equation is obtained in the long wavelength approximation. When the chain is not precompressed, nonlinear effects are large even at low wave amplitudes. Solitary wave solutions exist in this case as well. Experiments related to most of the aforementioned models are mentioned.

The last chapter, entitled ''Self-action and stimulated scattering of sound,'' is devoted to effects of nonlinearity higher than quadratic order (several such cases are considered in the previous chapters). Quadratic nonlinearity is considered to be negligible in this chapter, although in most practical situations this is not the case. However, under certain conditions the cubic nonlinearity can indeed be more pronounced. Attention is devoted to self-action and stimulated scattering of sound, which are nonlinear effects normally associated with media described by cubic nonlinearity. Equations modeling self-focusing of acoustic beams due to heating caused by absorption are derived and then analyzed using approaches developed in nonlinear optics. Self-action phenomena in modulated waves are also considered by analogy with the corresponding cubic nonlinear effects in optics. The analysis is based on a nonlinear Schrödinger equation. Stability of harmonic waves and the possibility of dark solitons are discussed. The four-wave interaction that produces nonlinear wave front reversal is described, as well as various physical realizations of this phenomenon. Self-action effects associated with bubbly liquids are covered. The last section describes phase locking of nonlinear oscillations.

The style throughout most of the book presumes the reader is already familiar with the foundations of nonlinear acoustics and basic concepts of wave physics, and many equations are presented without intermediate steps. We would not recommend this book to those who wish to learn the elementary principles of nonlinear acoustics, detailed derivation of the main equations, and applications. Although any such text is constrained by limits on length, we feel it useful to note a number of topics that are not considered, such as wave interaction in anisotropic solids, nonlinear surface acoustic waves, radiation pressure, acoustic streaming, and interaction of acoustic waves with other types of waves.

This book is nevertheless an excellent complement to the existing books on nonlinear acoustics. The authors present in a clear and interesting fashion the properties of nonlinear acoustic waves and their dependence on the basic effects of dissipation, dispersion, reflection, refraction, and diffraction. This monograph by K. Naugolnykh and L. Ostrovsky should be very useful not only for acousticians, but also for researchers in different fields of wave physics.

OLEG A. SAPOZHNIKOV
Department of Acoustics
Faculty of Physics
Moscow State University
Moscow 119899, Russia

MARK F. HAMILTON
Department of Mechanical Engineering
The University of Texas at Austin
Austin, Texas 78712-1063

Applied Audiology for Children (3rd ed.)

D. M. C. Dale

Jackmur Publications CYF, London N12 7LE, England.
xi+224 pp. Price: unknown.

I have a history with this book. A publisher sent me a manuscript version seeking my opinion as to whether they should publish it. I said that it should not be published without extensive revision because its organization makes no sense and because it abounds with errors. Presumably, that publisher returned it to the author with my comments, because I got it again. The organization was still confusing and it still contained many of the same errors. Again, I recommended extensive revision and correction.

Now it has appeared for review, but from a different publisher. Who is this publisher? It is one unfamiliar to me, but I know that it has the same address as the author. I assume, therefore, that he published it himself. Of course, he can do that if he wishes. I assume, also, that he found that easier than making the corrections; the errors are still there.

All of the above is rather unfortunate. There is a great deal of useful, practical information in this book—if you can find it. Also, Professor Dale has made important contributions to pediatric audiology and to the education of the deaf. A native New Zealander, he has been principal of the Auckland School for Deaf Children and he was the first president of the New Zealand Residential Child Care Association. He earned his Ph.D. at Manchester University (in England). He became Senior Lecturer in Audiology and Education of the Deaf at the University of London. This recitation is to inform the reader that he should know what he is talking about. He fails to demonstrate that in this book.

I take issue with a number of things in the text. For example, in the preface, he informs us that ''In line with modern text-book publishing policy, references have been used rather sparingly.'' Oh? Does current policy discourage the use of references? I have authored, co-authored, and edited 13 books. This is certainly news to me. More to the point, the book suffers from its lack of references.

The organization of the book utterly confounds me. The first—the very first—chapter is ''Sound Amplification.'' Why would one begin an audiology text book with a chapter on hearing aids and then follow it with chapters on hearing measurement and the acoustics of speech? I don't get it. Why, given that the first chapter is called ''Sound Amplification,'' is ''Ear Moulds'' the ninth chapter? What would cause one to end such a book with a chapter on screening? I'm afraid that I just don't get it. Of course, one could choose to read the chapters in any sequence.

The book also contains just plain errors. Space and sense prohibit recounting all of them here, but here are some examples. He explains frequency in terms of c.p.s. and adds Hz as a kind of afterthought. Didn't we abandon that notation quite a number of years ago? On page 4, he tells us that SPL stands for speech perception level. When did SPL no longer signify sound pressure level? He tells us that hearing aids contain tubes, what (being British) he calls valves. Where can one buy an aid without transistors or printed circuits? For that matter, the accompanying figure shows a body aid. Are they still available in any number? Speaking of figures, most of them (but not all of them) have no captions. They are collected in an attachment at the end of the book. That is a bit annoying, but so be it; but then why caption some and not all? Similarly, the reference list does not correspond to the text. I was interested in finding his reference number 159. There is no 159 on the reference list. Proofreading and copy editing might have been in order.

Enough. Call me crabby and I suppose I am. However, in good conscience, I could not and would not recommend this book to my students or to yours. That is unfortunate. Professor Dale had hidden some good stuff under all this confusion, but it isn't worth the effort. Sorry. The late Cuban author Reinaldo Arenas had said that ''One must, somehow, struggle ceaselessly against things that are ill done.''

SANFORD E. GERBER
Department of Communication Disorders
Eastern Washington University
Cheney, Washington 99004

 0001-4966/2000/108(1)/16/1/$17.00

REVIEWS OF ACOUSTICAL PATENTS

Lloyd Rice
11222 Flatiron Drive, Lafayette, Colorado 80026

The purpose of these acoustical patent reviews is to provide enough information for a Journal reader to decide whether to seek more information from the patent itself. Any opinions expressed here are those of reviewers as individuals and are not legal opinions. Printed copies of United States Patents may be ordered at $3.00 each from the Commissioner of Patents and Trademarks, Washington, DC 20231.

Reviewers for this issue:

GEORGE L. AUGSPURGER, *Perception, Incorporated, Box 39536, Los Angeles, California 90039*
DAVID PREVES, *Songbird Medical, Inc., 5 Cedar Brook Drive, Cranbury, New Jersey 08512*
KEVIN P. SHEPHERD, *M.S. 463, NASA Langley Research Center, Hampton, Virginia 23681*
ERIC E. UNGAR, *Acentech, Incorporated, 33 Moulton Street, Cambridge, Massachusetts 02138*

5,805,708

43.38.Ja SPEAKER SYSTEM FOR COMPUTER

Tommyca Freadman, Goshen, New York
8 September 1998 (Class 381/159); filed 22 October 1996

The goal is to provide greatly improved sound quality from a laptop computer. ''By providing multiple sound emitting ports and by localizing the speaker in a specific desired position relative to an upper and lower surface of the computer case in the preferred embodiments of the present invention, it is possible to back-fire and front-fire the sound to prevent cancellation of sound waves ... [producing] relatively huge sound as compared to the single or two-speaker front firing system of the prior art.'' Well, that says it all.—GLA

5,929,393

43.38.Ja SPEAKER CABINET WITH SOUNDING BOARD

Charles W. Jeter, Jr., Haynesville, Louisiana
27 July 1999 (Class 181/199); filed 12 July 1996

Resilient membrane **14** covers an opening in ''sounding board'' **13**, which is spaced close to rear panel **4**. A bass slot **10** is included, ''... for air

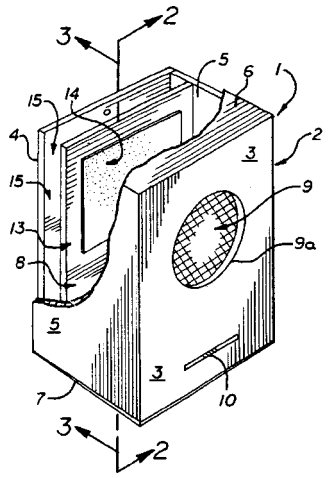

circulation into and from the enclosure interior and facilitating the attenuated sound produced by the vinyl sheet on the sounding board.''—GLA

5,991,421

43.38.Ja RADIALLY EXPANDING MULTIPLE FLAT-SURFACED WAVEGUIDE DEVICE

Alexander Farone, assignor to Single Source Technology and Developments, Incorporated
23 November 1999 (Class 381/338); filed 10 November 1997

The inventor has rediscovered and patented the morning glory horn. A novel feature of the invention is that throat flare geometry is partly determined by driver cone mass.—GLA

5,939,656

43.38.Lc MUSIC SOUND CORRECTING APPARATUS AND MUSIC SOUND CORRECTING METHOD CAPABLE OF ACHIEVING SIMILAR AUDIBILITIES EVEN BY SPEAKER/HEADPHONE

Masayuki Suda, assignor to Kabushiki Kaisha Kawai Gakki Seisakusho
17 August 1999 (Class 84/630); filed in Japan 25 November 1997

A fair amount of work has been done in developing circuits that make headphones sound more like loudspeakers. A composer working with a synthesizer, for example, would like to be able to go back and forth between loudspeakers and headphones without being distracted by discrepancies in timbre and localization. In most electronic musical instruments and personal stereo systems the loudspeakers are automatically disconnected when headphones are plugged in. It seems obvious that headphone/speaker equalization could be automatically selected at the same time, but the inventor seems to be the first to have realized this.—GLA

5,937,071

43.38.Vk SOUND FIELD EXPANDING APPARATUS WITH IMPROVED TONE CONTROL SYSTEM

Tatsuya Kishii and Masao Noro, assignors to Yamaha Corporation
10 August 1999 (Class 381/98); filed in Japan 30 September 1996

A symmetrical sound field expansion circuit incorporates adjustable bass and treble compensation. Circuit values allow practical implementation in an LSI chip.—GLA

 0001-4966/2000/108(1)/17/7/$17.00

5,945,643

43.40.Tm VIBRATION DAMPENING MATERIAL AND PROCESS

Donald J. Casser, Milwaukee, Wisconsin
31 August 1999 (Class 181/290); filed 16 June 1995

This patent describes a wide variety of laminated panels with reportedly good damping performance. It discusses arrangements that include well-known free-layer and constrained-layer configurations, as well as layers consisting of fiber-reinforced materials and the use of perforations to reduce weight. It also suggests some appropriate specific materials and processes for the construction of laminates.—EEU

5,984,043

43.40.Tm MAGNETIZED FLAT DAMPING COMPONENT AND ADHESIVE, ESPECIALLY FOR USE IN SOUND-DEADENING MATS

Thomas Ruhe *et al.*, assignors to M. Faist GmbH & Company KG
16 November 1999 (Class 181/206); filed in Germany 11 April 1995

This patent relates to layers used for acoustical isolation or for damping of sheet metal structural components, such as are used in the automotive industry. Layers of insulating or damping material are typically furnished with adhesive layers for affixing these materials to the sheet metal components. In arrangements according to this patent, magnetizable particles are integrated into the adhesive layer, thus facilitating installation, improving adhesion, and making efficient use of the mass they add.—EEU

5,945,603

43.40.Yq VIBRATION DETECTOR ADAPTED FOR USE IN A VIBRATION MEASURING DEVICE

David Shih, Tainan, Taiwan
31 August 1999 (Class 73/652); filed 24 June 1998

This patent pertains to vibration sensors used for monitoring multiple items of equipment in industrial plants. A sensor is typically attached to steel or iron surfaces by means of a magnet, which must be unscrewed from the sensor and replaced by a rod probe if one wants to measure the vibrations of a nonmagnetic structure. To eliminate this tedious replacement process, the magnet at the base of the sensor is kept in place; when a probe is needed, it is attached to the sensor via a magnet built into the probe's attachment end.—EEU

5,979,242

43.40.Yq MULTI-LEVEL VIBRATION TEST SYSTEM HAVING CONTROLLABLE VIBRATION ATTRIBUTES

Gregg K. Hobbs, assignor to Hobbs Engineering Corporation
9 November 1999 (Class 73/663); filed 20 April 1998

The vibration test system described in this patent consists in concept of an array of resiliently interconnected platforms. Each platform may be provided with a rotary inertial shaker and with adjustable dynamic absorbers. The intent is to select and/or adjust the interconnections, shakers, and dynamic absorbers so that the test item, which is mounted on one of the platforms, is subjected to vibrations with prescribed amplitudes and frequencies.—EEU

5,934,959

43.50.Gf MARINE MUFFLER

Frederick R. Inman, Sr. and Frederick R. Inman, Jr., assignors to Inman Marine Corporation
10 August 1999 (Class 440/89); filed 10 November 1997

A muffler for application to marine internal combustion engines is composed of three concentric chambers, the outer one containing sound absorbing material such as stainless steel wool. The volume of the outer two chambers is greater than that of the innermost chamber. Exhaust gas flows from the inner chamber through louvered openings into the second chamber,

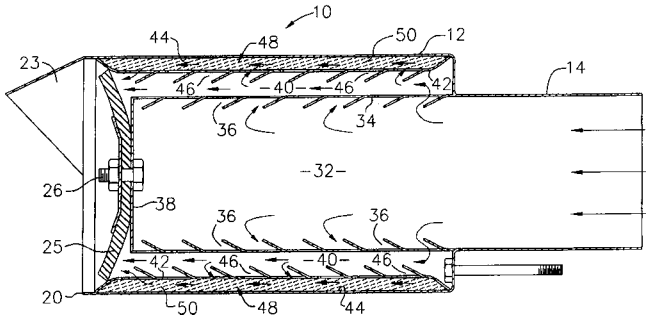

where a portion of the flow enters the third, outermost chamber. A flapper valve **25** is designed to prevent air and water from entering the muffler under low or no exhaust pressure conditions. This arrangement yields at least a 5 dB reduction under engine idle conditions.—KPS

5,952,624

43.50.Gf NOISE ATTENUATOR

Jerry Brian Hornback and Jose Eduardo Lapore, assignors to Arvin Industries, Incorporated
14 September 1999 (Class 181/255); filed 30 April 1997

A muffler for an internal combustion engine is described in which the inlet tube **30** is terminated by a cross-shaped ''acoustic reflector'' consisting of two curved strips **38**. The presence of these strips yields an average noise

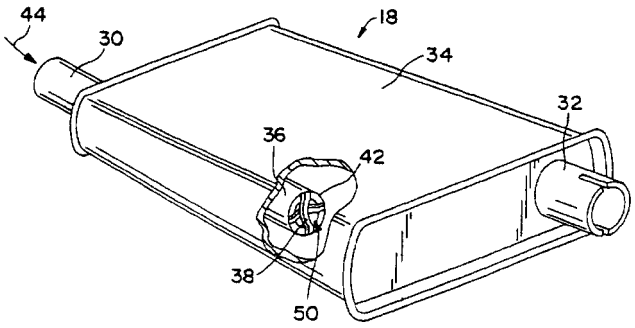

reduction of 5.5 dB from about 1 to 10 kHz with an increase in backpressure of less than 5 percent.—KPS

5,960,912

43.50.Gf VIBRATION DAMPER FOR A DRUM BRAKE

Yukio Nishizawa and Hironobu Saka, assignors to Sumitomo Electric Industries, Limited
5 October 1999 (Class 188/1.11E); filed in Japan 7 June 1996

A method to reduce the vibration of the drum of a drum brake, which is the main cause of break squeals, is described in which a piezoelectric sensor, magnetic sensor, or accelerometer is used to detect the vibration and a magnetic or piezoelectric actuator is used to reduce the vibration using a feedback controller. Various geometrical arrangements are described, as is the control circuit.—KPS

5,965,853

43.50.Gf SOUND ABSORBING AIRCRAFT TRANSPARENCY AND METHOD OF MAKING SAME

William W. Hornsey, assignor to PPG Industries Ohio, Incorporated
12 October 1999 (Class 181/289); filed 7 November 1997

A double paned aircraft window with an air gap is described. The outboard pane consists of a two-ply acrylic construction. The inner pane is a multilayer laminate with vibration damping characteristics consisting of a substrate layer to which a damping layer is adhered. The patent gives extensive details of material selection and design construction.—KPS

5,964,266

43.50.Lj TIRE FOR MOTOR-VEHICLE WHEELS PROVIDED WITH A TREAD PRODUCING A LOW ROLLING NOISE

Maurizio Boiocchi and Gianfranco Colombo, assignors to Pirelli Coordinamento Pneumatici, S.p.A.
12 October 1999 (Class 152/209.2); filed in Italy 31 May 1993

A tire tread pattern consisting of rows of raised shaped blocks is presented in which the number of such blocks gradually increases from the center of the tire tread toward the outer edges. Thus the stiffness increases from the edge to the center yielding lower rolling noise.—KPS

5,927,944

43.50.Nm FAN WITH BLADES HAVING INTEGRAL ROTATING VENTURI

Christian L. Belady, assignor to Hewlett-Packard Company
27 July 1999 (Class 415/220); filed 30 May 1997

An annular ring attached to the tips of the blades of an axial fan is described. The figure shows a cross sectional view which illustrates the

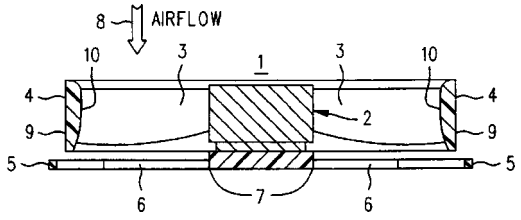

manner in which this ring creates a venturi effect which is aimed at reducing vortices shed from the tip region of the blades.—KPS

5,929,396

43.50.Nm NOISE REDUCING DIFFUSER

Elias A. Awad, Palos Verdes, California
27 July 1999 (Class 181/211); filed 29 July 1997

The diffuser described in this patent is based on the premise that a sound wave will suffer distortion if it travels through a pipe that has a diameter that is less than one-fourth of the sound's wavelength. The idea of this patent is to direct the sound wave created downstream from a source, such as a gas nozzle, into a pipe of sufficiently small diameter so that much of the longitudinal component of the sound will be converted to radial components, which will be dissipated by repeated impingement on the pipe's wall. As stated in the patent, the diffuser should be placed no further than one-quarter wavelength from the source, and the mouth of the diffuser should be slightly larger than the noise-producing nozzle, so that it is the nozzle that controls the flow.—EEU

5,943,856

43.50.Nm TURBOFAN ENGINE WITH REDUCED NOISE

Robert W. Lillibridge *et al.*, assignors to Burbank Aeronautical Corporation II
31 August 1999 (Class 60/262); filed 29 August 1995

A hush kit designed for the Pratt and Whitney JT3D family of engines commonly found on Boeing 707 and Douglas DC-8 is described. Both the by-pass air and the engine exhaust flow through a common nozzle which contains a multi-lobed mixer and a thrust reverser. Modifications to the engine inlet include changes to the separation distance between the inlet guide vanes and the fan blades, and the incorporation of an acoustically treated inlet centerbody.—KPS

5,947,412

43.50.Nm JET ENGINE NOISE SUPPRESSOR ASSEMBLY

Charles H. Berman, assignor to Titan Corporation
7 September 1999 (Class 244/1N); filed 10 January 1997

A noise suppression system to reduce noise from jet engine exhausts is described in which numerous L-shaped conduits **38**, **54**, and **66** are designed to enhance mixing between the hot engine core flow and the fan flow and/or ambient flow. Each conduit contains a valve (**46**, **58**, **70**) which is open

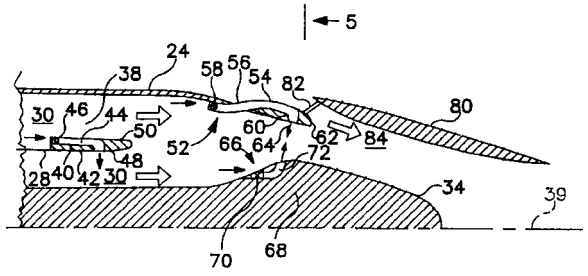

during take-off when noise reduction is desired. A conically shaped ejector shroud **80** enables ambient air flow to be combined with the engine flow at **64.** Various other geometric arrangements are shown including those for engines not having a center body plug **34**.—KPS

5,952,621

43.50.Nm SOUND ATTENUATION SYSTEM AND RELATED METHOD

Alan R. D. Curtis *et al.*, assignors to GTE Internetworking Incorporated
14 September 1999 (Class 181/213); filed 15 April 1998

A method to reduce noise radiation from fan tones in the by-pass duct of a jet engine is described. The wall of the duct contains multiple circumferential cavities each covered with a wire mesh screen and located downstream of the engine fan. The dimensions of the cavities are selected to yield desired values of acoustic impedance in order to achieve two objectives. One or more cavities are designed to attenuate noise propagating downstream from the noise source. The remaining cavities are designed to produce a reflected sound wave which is out of phase with the sound propagating upstream of the source, thus achieving attenuation via destructive interference.—KPS

5,961,067

43.50.Nm METHOD FOR REDUCING TURBOPROP NOISE

Edward J. Hall and Joseph P. Meade, assignors to Allison Engine Company
5 October 1999 (Class 244/1N); filed 10 September 1996

A reduction in propeller noise is achieved by reducing the interaction between the propeller and a bubble of partially stagnated air in front of the engine inlet. This is achieved either by appropriate spacing between the propeller trailing edge and the inlet duct or by modifying the scavenge duct to allow greater volume flow. A 2 dB(A) reduction in the average interior noise under cruise conditions is noted.—KPS

5,961,289

43.50.Nm COOLING AXIAL FLOW FAN WITH REDUCED NOISE LEVELS CAUSED BY SWEPT LAMINAR AND/OR ASYMMETRICALLY STAGGERED BLADES

Dieter Lohmann, assignor to Deutsche Forshungsanstalt fur Luft- und Raumfahrt e.V.
5 October 1999 (Class 416/189); filed 22 November 1995

An axial cooling fan for a vehicle engine is described in which the tips of the fan blades are attached to a surrounding ring. The focus of the patent is the optimization of the blade shape for both aerodynamic and acoustic efficiency. The resultant blade shape is distinguished by a strong forward sweep near the hub followed by a strong rearward sweep toward the tip. Detailed descriptions of the blade geometry are given.—KPS

5,961,290

43.50.Nm HELICOPTER BLADE AEROFOIL

Makoto Aoki *et al.*, assignors to Advanced Technology Institute of Commuter-Helicopter Limited
5 October 1999 (Class 416/223R); filed in Japan 14 February 1997

Blade coordinates for a helicopter rotor are given in which the leading edge radius and the camber line are optimized for maximum lift coefficient from zero to approximately 90% of the blade radius. The tip region is designed to have a large drag divergence mach number. Reductions of several dB relative to a conventional symmetric airfoil such as NACA0010 are noted. Detailed blade coordinates are given for airfoils having a thickness to chord ratio of 8%–12%.—KPS

5,966,452

43.50.Nm SOUND REDUCTION METHOD AND SYSTEM FOR JET ENGINES

Elwood G. Norris, assignor to American Technology Corporation
12 October 1999 (Class 381/71.1); filed 7 March 1997

A method to reduce jet noise from the exhaust of an aircraft engine is composed of a pressure sensor in the exhaust duct, a controller circuit, and an electrically conductive rod placed near the exit of the duct. The electrical signal to the rod serves to excite the gas plasma thus generating an interference wave to cancel the noise in the jet exhaust.—KPS

5,966,525

43.50.Nm ACOUSTICALLY IMPROVED GAS TURBINE BLADE ARRAY

Robert J. Manzi, Jr. *et al.*, assignors to United Technologies Corporation
12 October 1999 (Class 395/500.29); filed 9 April 1997

Multiple pure tone noise or ''buzzsaw'' noise generated by the fan of a turbofan aircraft engine is caused in large part by blade-to-blade differences. Such differences arise due to manufacturing and installation tolerances and result in spectral components at the shaft rotation speed and its harmonics. A procedure is described which, based on the measured blade differences, seeks to circumferentially arrange the blades so that the acoustic energy is concentrated in the lowest harmonics which are more easily attenuated by the engine nacelle.—KPS

5,975,238

43.55.Dt PLATE RESONATOR

Helmut Fuchs *et al.*, assignors to Fraunhofer Gesellschaft zur Foerderung der angewandten Forschung e. V.
2 November 1999 (Class 181/295); filed in Germany 24 February 1995

The subject of this patent is an acoustic absorber that can be tuned to absorb low-frequency sound, as may be desirable in small rooms with little absorption. The absorber described in this patent consists in essence of a thin flexible plate that is fastened atop a thicker plate, which is soft and highly damped. In some embodiments the back surface of the thicker plate is fastened to a heavy plate, which may be mounted to a wall or ceiling of a room. In other embodiments the back surface of the thicker plate is covered by a second light plate; such configurations are used in arrangements in which sound can impinge on both sides of the composite plate structure. Tuning is achieved by appropriate selection of materials and dimension.—EEU

5,987,146

43.66.Ts EAR CANAL MICROPHONE

Vincent Pluvinage *et al.*, assignors to ReSound Corporation
16 November 1999 (Class 381/328); filed 3 April 1997

An open ear canal hearing aid system intended for mild hearing losses is described. Tubes are placed in the open ear canal for picking up ambient sounds and delivering processed sounds. If the microphone and receiver are located in the tubes, electrical connections are made via wires inside the tubes to the input and output of an amplifier that provides appropriate gain and frequency shaping. Alternately, the microphone and/or receiver may be located remotely with the sound processor amplifier. Feedback caused by the open ear fitting may be controlled by selectively lowering gain or by using a cancellation circuit in the sound processor.—DAP

6,009,311

43.66.Ts METHOD AND APPARATUS FOR REDUCING AUDIO INTERFERENCE FROM CELLULAR TELEPHONE TRANSMISSIONS

Mead C. Killion and Norman P. Matzen, assignors to Etymotic Research
28 December 1999 (Class 455/63); filed 21 February 1996

Switched digital cellular telephone signals in close proximity to a hearing aid are often induced into the hearing aid wiring and demodulated by nonlinearities in the hearing aid circuitry. The modulation lies in the audio frequency band and often creates a buzzing sound, often loud enough to make the hearing aid unusable. This invention describes transmission of an unused frequency rather than switching the carrier off. Alternately, a second antenna is added to the digital cellular telephone that transmits a low-power signal to fill in the ''gaps'' in the temporally modulating carrier signal. The result in both cases is a carrier signal presented to the hearing aid with little or no temporal fluctuations.—DAP

5,961,443

43.70.Dn THERAPEUTIC DEVICE TO AMELIORATE STUTTERING

Michael Pierre Rastatter *et al.*, assignors to East Carolina University
5 October 1999 (Class 600/23); filed 31 July 1996

It is well known that stuttering effects are reduced while a delayed copy of the speech is played back to the subject. In order to provide such feedback during normal living situations, this patent describes an in-the-ear

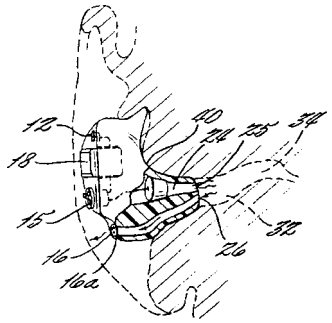

device which plays back the user's speech signal, picked up by an attached microphone and delayed within the device by a short memory storage loop.—DLR

5,953,696

43.72.Ar DETECTING TRANSIENTS TO EMPHASIZE FORMANT PEAKS

Masayuki Nishiguchi and Jun Matsumoto, assignors to Sony Corporation
14 September 1999 (Class 704/209); filed in Japan 10 March 1994

This speech synthesizer is intended for use with a multiband encoder (MBE) vocoding system. It enhances the MBE spectral data by emphasizing and smoothing the formant peaks and deepening the formant troughs. These modifications are done during voiced intervals and on a frequency-specific basis. The changes are said to reduce nasal-sounding and fricative-sounding distortions.—DLR

5,960,391

43.72.Ar SIGNAL EXTRACTION SYSTEM, SYSTEM AND METHOD FOR SPEECH RESTORATION, LEARNING METHOD FOR NEURAL NETWORK MODEL, CONSTRUCTING METHOD OF NEURAL NETWORK MODEL, AND SIGNAL PROCESSING SYSTEM

Masahiko Tateishi and Shinichi Tamura, assignors to Denso Corporation
28 September 1999 (Class 704/232); filed in Japan 13 December 1995

This patent describes a recurrent neural network said to be able to separate speech and noise components from a composite signal. Different versions of the network are available to accept inputs and produce outputs in

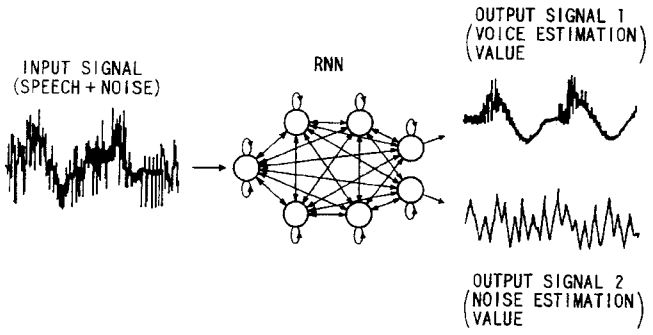

various forms; as PCM samples, as FFT coefficients, or as filtered frequency bands. The patent text includes formulas and descriptions for generating the network coefficients.—DLR

5,963,901

43.72.Ar METHOD AND DEVICE FOR VOICE ACTIVITY DETECTION AND A COMMUNICATION DEVICE

Antti Vaehaetalo *et al.*, assignors to Nokia Mobile Phones Limited
5 October 1999 (Class 704/233); filed in Finland 12 December 1995

This voice presence detector consists of a filter bank analyzer followed by signal-to-noise (SNR) analysis of each band. Suggested input processing would consist of overlapping trapezoidal windows followed by a 128-point FFT. The power spectrum is divided into eight equal-width bands. The ratio of power to reference gives an SNR value for each band. These are averaged by band and by time, resulting in an overall SNR value which is compared to a threshold for the final voice presence decision. When no voice is present, band power measures are used to update the reference noise levels.—DLR

5,970,441

43.72.Ar DETECTION OF PERIODICITY INFORMATION FROM AN AUDIO SIGNAL

Fisseha Mekuria, assignor to Telefonaktienbolaget LM Ericsson
19 October 1999 (Class 704/207); filed 25 August 1997

The stated goal of this pitch detector is high-quality pitch extraction from clean speech or from speech containing either correlated or uncorrelated noise. This result is achieved by low-pass and nonlinear filtering of the signal, followed by threshold detection of the signal peaks. A suggested nonlinear filter consists of the square of positive signal values or zero for negative values. The threshold value is adapted by adjustment of a scaling factor.—DLR

5,970,447

43.72.Ar DETECTION OF TONAL SIGNALS

Mark A. Ireton, assignor to Advanced Micro Devices, Incorporated
19 October 1999 (Class 704/233); filed 20 January 1998

The device described here is a speech presence detector based on zero-crossing counts (ZCR). The ZCR signal is smoothed and differentiated.

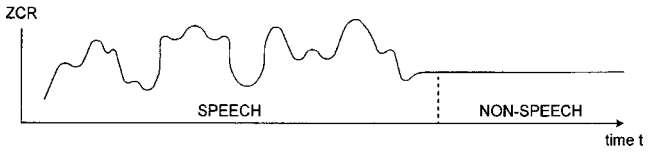

The energy in the resulting signal over a fixed time period is again smoothed and compared to a threshold to indicate speech presence.—DLR

5,953,381

43.72.Dv NOISE CANCELER UTILIZING ORTHOGONAL TRANSFORM

Yuriko Tsukahara, assignor to Kabushiki Kaisha Toshiba
14 September 1999 (Class 375/346); filed in Japan 29 August 1996

This noise reduction system performs a 64-point FFT on the input speech signal and then divides the coefficients into three frequency groups. The mean spectral amplitude in each group is computed and compared to a group-specific threshold. Various group-specific adjustments are then performed on the coefficients, depending on whether the group average was above threshold. Various embodiments of the disclosure involve different adjustment strategies. The adjusted coefficients are then inverse transformed to produce the final output.—DLR

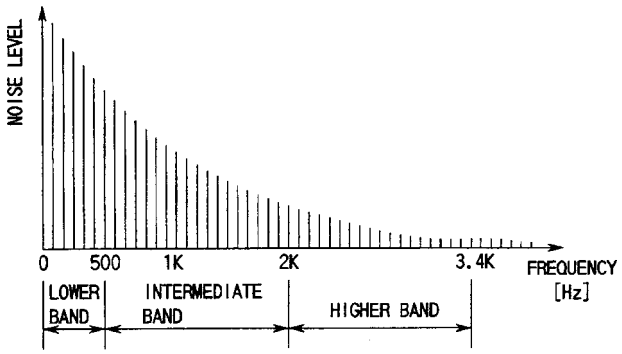

5,963,895

43.72.Gy TRANSMISSION SYSTEM WITH SPEECH ENCODER WITH IMPROVED PITCH DETECTION

Rakesh Taori *et al.*, assignors to U.S. Philips Corporation
5 October 1999 (Class 704/207); filed in European Patent Office 10 May 1995

This patent describes a vocoder which includes a novel pitch detector. Similar to a traditional autocorrelation pitch detector, this one instead performs a cross-correlation with a reference signal. The reference **44** is initially extracted from the speech signal using one of several positive peak functions, as in example **42**. The reference is then adapted as the correlation proceeds.—DLR

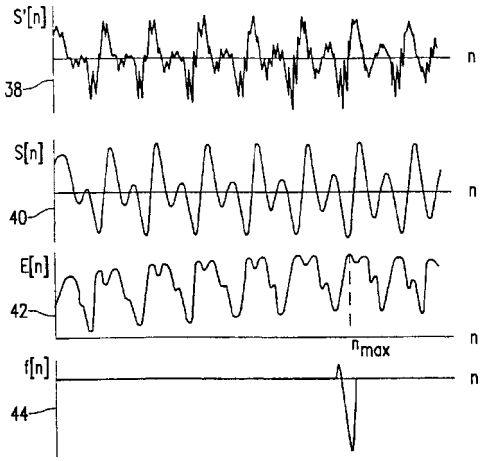

5,949,961

43.72.Ja WORD SYLLABIFICATION IN SPEECH SYNTHESIS SYSTEM

Richard A. Sharman, assignor to International Business Machines Corporation
7 September 1999 (Class 395/2.69); filed 19 July 1995

This patent presents a method for word syllabification based on probabilities of occurrence of candidate syllables and syllable sequences. Several alternate strategies are available, including bottom up (checking individual candidate probabilities first), top down (sequence probabilities first), and some combined techniques.—DLR

5,950,152

43.72.Ja METHOD OF CHANGING A PITCH OF A VCV PHONEME-CHAIN WAVEFORM AND APPARATUS OF SYNTHESIZING A SOUND FROM A SERIES OF VCV PHONEME-CHAIN WAVEFORMS

Yasuhiko Arai *et al.*, assignors to Matsushita Electric Industrial Company, Limited
7 September 1999 (Class 704/207); filed in Japan 20 September 1996

Speech pitch alteration of vowel sounds has become a highly developed technology, allowing rate adjustments by as much as halving or doubling. Unfortunately, the techniques often cause major distortions in the

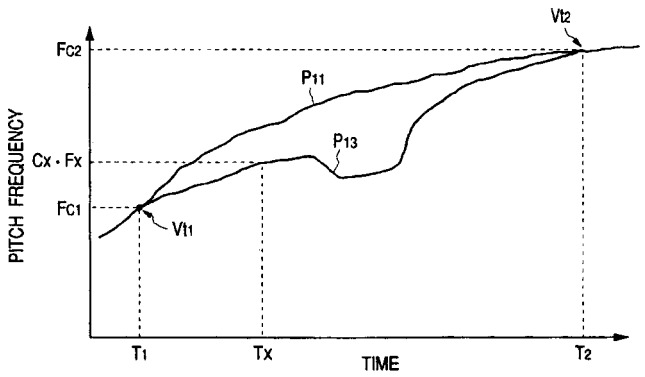

regions closely surrounding the consonants. This patent presents a method based on analyses of VCV (vowel–consonant–vowel) patterns to predict the appropriate pitch profile during the consonant transition periods.—DLR

5,970,453

43.72.Ja METHOD AND SYSTEM FOR SYNTHESIZING SPEECH

Richard Anthony Sharman, assignor to International Business Machines Corporation
19 October 1999 (Class 704/260); filed in the United Kingdom 7 January 1995

This speech synthesizer constructs phonemes from units much smaller than the typical diphone or demisyllable units. Human speech is analyzed to determine a sequence of waveform fragments, also described as fenones, to represent each phoneme in each applicable context. One waveform segment is extracted per pitch period of the input speech signal. The fenone waveforms are clustered by spectral similarity to reduce storage requirements.—DLR

5,946,655

43.72.Ne METHOD OF RECOGNIZING A SEQUENCE OF WORDS AND DEVICE FOR CARRYING OUT THE METHOD

Volker Steinbiss *et al.*, assignors to U.S. Philips Corporation
31 August 1999 (Class 704/251); filed in Germany 14 April 1994

This discrete word recognizer uses a strategy of normalizing the word scores during the scanning of a word candidate tree. This allows scores from the present tree to be compared with scores from other candidate trees before a correction has been applied, which occurs at the completion of a tree scan.—DLR

5,949,886

43.72.Ne SETTING A MICROPHONE VOLUME LEVEL

Ralph J. Nevins, Somerville, Massachusetts and Nancy Gardner, Cambridge, Massachusetts
7 September 1999 (Class 381/57); filed 26 October 1995

Speech recognition systems have typically been quite sensitive to microphone volume level settings and yet, the known algorithms to adjust the mic gain are notoriously variable in performance. Known mic gain control methods are usually acoustically based, and rarely take into account the recognition performance as a function of the gain setting. This patent describes a feedback-loop method of gain control setting which considers the recognition results of at least three gain settings and tunes the gain using a type of optimum search strategy.—DLR

5,950,159

43.72.Ne WORD SPOTTING USING BOTH FILLER AND PHONE RECOGNITION

Katherine Mary Knill, assignor to Hewlett-Packard Company
7 September 1999 (Class 704/251); filed in European Patent Office 1 April 1996

The word-spotting method described in this patent is intended for use in a personal computer with standard equipment such as a sound card and is thus designed to be simple and efficient. The speech input is first segmented and the segments classified as phones using standard hidden Markov models. Keywords are then sought in the phone sequence using approximate string searching techniques.—DLR

5,953,701

43.72.Ne SPEECH RECOGNITION MODELS COMBINING GENDER-DEPENDENT AND GENDER-INDEPENDENT PHONE STATES AND USING PHONETIC-CONTEXT-DEPENDENCE

Chalapathy Venkata Neti and Salim Estephan Roukos, assignors to International Business Machines Corporation
14 September 1999 (Class 704/254); filed 22 January 1998

This speech recognition system incorporates a strategy to improve the gender limitations of typical recognizers. During training, the speaker gender is used to construct both gender-specific and gender-independent models for each speech segment. A score is maintained for each type of model and used during recognition to modify the segment matching strategy.—DLR

5,960,397

43.72.Ne SYSTEM AND METHOD OF RECOGNIZING AN ACOUSTIC ENVIRONMENT TO ADAPT A SET OF BASED RECOGNITION MODELS TO THE CURRENT ACOUSTIC ENVIRONMENT FOR SUBSEQUENT SPEECH RECOGNITION

Mazin G. Rahim, assignor to AT&T Corporation
28 September 1999 (Class 704/244); filed 27 May 1997

This speech recognition training method offers a way to adapt the speaker models to various background environments. Training utterances which represent a variety of backgrounds are processed using a starting reference model to produce sets of projections from the model. The projections are used to generate new models and the process repeated to proliferate models until the desired accuracy is achieved.—DLR

The wave bivector formalism associated with circumferential leaky waves

Frédéric Padilla,[a] Bernard Poirée,[b] Maryline Talmant,[a] and Gérard Quentin[a]
Groupe de Physique de Solides-CNRS UMR 7588, Tour 23, Université Paris 7-Denis Diderot, 2 place Jussieu, 75251 Paris, France

(Received 18 July 1999; accepted for publication 31 March 2000)

It is shown that the circumferential internal waves propagating around an elastic cylinder can be locally seen as plane evanescent waves, at any observation point inside the surrounding fluid. This is done by direct calculation of the associated complex bivector. The exact anatomy of the wave is detailed and the phase propagation paths are found to be curved, as expected. The transition to the plane interface is achieved. Polarization ellipses associated with the acoustic displacement vector are described. The additional low evanescence assumption leads to conventional ray interpretation with identification of the ray tube divergence coefficients, and the wavefront is found to be the involute of a circle. © *2000 Acoustical Society of America.* [S0001-4966(00)03007-1]

PACS numbers: 43.20.Fn [DEC]

INTRODUCTION

When an acoustic field is incident on a solid elastic cylinder immersed in a fluid, in the high-frequency approximation, two types of phenomena occur: The geometrical effects (incident, reflected, and transmitted fields) and the circumferential waves which propagate around the cylinder and radiate in the surrounding fluid. Among these circumferential waves is the circumferential Rayleigh wave, so called because its trace velocity and attenuation along the interface tend toward that of the well-known surface wave on a flat interface in the limit of very high frequency.

Numerous theoretical works about circumferential waves have been previously published.[1,2] In order to express the pressure in the fluid as a sum of geometrical and circumferential waves, the Sommerfeld–Watson transformation is employed. It consists of an integral representation of the scattered pressure and an evaluation of each contribution (geometrical and circumferential) with the integration contour method. The circumferential Rayleigh wave is described as a radiating wave along the path on the cylinder. For an observation point located in the fluid, the wave radiated by the circumferential Rayleigh wave is described as a homogeneous one. In order to do that, approximations are made on the distance between the observation point and the cylinder, and on the complex angle associated with each mode. However, it is known that the wave radiated in the fluid by the generalized Rayleigh wave which propagates on a plane fluid–solid interface is an evanescent wave.[3–5] As a consequence, with the classical description of the circumferential Rayleigh wave, the limit from cylindric to plane interface may not be reached completely: the evanescent characteristic of the wave in the fluid is not described in the case of a cylindrical interface. Problems also occur because the Descartes–Snell laws are not satisfied.

The primary objective of this paper is to propose a complete description of the circumferential Rayleigh wave. It is shown that the radiated wave is actually heterogeneous, i.e., is locally tangent to a plane evanescent plane wave. With this description, there is no discontinuity between the wave on the cylindrical surface and the wave in the fluid. Moreover, the limit from the cylinder to the plane interface is obtained. Finally, the movement of fluid particles caused by the propagation of the wave shall be described with the polarization ellipses associated with the acoustic displacement vector. These results are obtained by way of calculations without any approximation on the distance between the observation point and the cylinder as well as on the complex angle associated with each mode.

In order to demonstrate the evanescent characteristic of the wave radiated in the fluid, it is convenient to describe this wave with the formalism of the evanescent plane waves. These waves may be described by a complex wave vector $\mathbf{K}' + i\mathbf{K}''$, where $\mathbf{K}'$ is the propagation vector and $\mathbf{K}''$ is the attenuation vector. These waves are characterized by two different directions of propagation and attenuation. In the classification of inhomogeneous plane waves,[6–9] the harmonic evanescent plane waves are such that the propagation direction $\mathbf{K}'$ is orthogonal to the damping direction $\mathbf{K}''$.[10,11] Like the more usual homogeneous plane waves, bulk evanescent plane waves are solutions of the acoustic wave propagation equation in unbounded elastic media.[12] This formalism is also the natural framework for analysis of the propagation in dissipative bodies, solid or fluid.[13] However, in usual acoustic problems, the contribution of these waves is neglected because the contribution of the nonevanescent field is dominant. The evanescent plane-wave formalism exhibits fully its interest in guided modes problems, where the evanescent plane-wave contribution becomes essential, for example in ducts below the cutoff frequency or on solid–fluid interfaces beyond the critical angles. In particular, the complex wave bivector is an efficient tool to define Rayleigh,[3–5]

[a]Present address: Laboratoire d'Imagerie Paramétrique-CNRS UMR 7623, Université Paris 6-Pierre et Marie Curie, 15 rue de l'Ecole de Médecine, 75006 Paris, France.
[b]Present address: DGA/SPAé/ST/CE, 26 Bd. Victor, 00460 Armées, France.

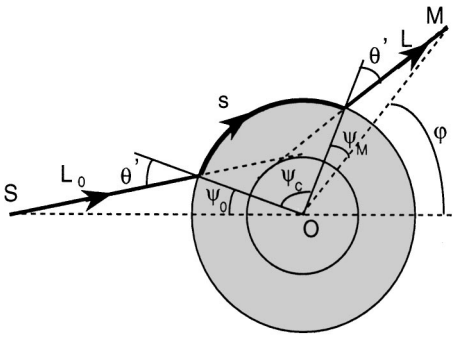

FIG. 1. The propagation path of the wave from the source S to the observation point M. L_0 is the length of the straight line from the source to the cylinder, s is the length of the curved propagation path along the cylinder, and L is the length of the straight line from the cylinder to the observer. The angle θ' is the excitation and the emergence angle of the wave.

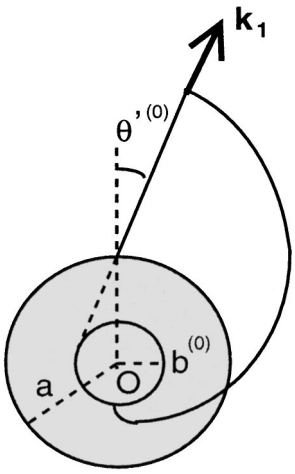

FIG. 2. The wave described in the zero-order approximation. The wavefronts are the involutes of the circle of radius $b^{(0)}$, and the straight rays are tangent to this circle. The wave propagates with the wave vector $k_1 = \omega/c_1$.

Stoneley,[14,15] or plate waves.[16,17] A wave propagating along a solid–fluid interface may actually be decomposed as a set of three evanescent plane waves: one with longitudinal polarization in the fluid, one with longitudinal, and one with shear polarization in the solid.

With the study of scattering by a cylinder, it shall be demonstrated that the evanescent plane-wave formalism also leads to very interesting results when curved surfaces are involved. Curved wavefronts may actually be seen as locally plane, and this property allows us to demonstrate that the circumferential Rayleigh wave scattered by the cylinder is locally an evanescent plane wave in the fluid. More generally, the purpose of this paper is to point out that the wave bivector formalism may also be used for the description of the whole group of internal or leaky waves propagating around a solid cylinder, which contains the Rayleigh and the Whispering Gallery waves.[18]

The structure of this paper is the following: In Sec. I. we describe the radiated pressure in the fluid. The case of geometrical acoustics is studied in Sec. II where all the quantities are real. Analytical and geometrical descriptions of the wavefronts and of the rays are given. In Sec. III, the pressure is interpreted without approximation on the complex angles. A direct calculation of the wave bivector is made. The exact anatomy of the wave is detailed and the phase propagation paths are found to be curved, as expected. The transition to the plane interface is achieved. Finally, a calculation of the radiated pressure with a first-order approximation on the complex angles is presented.

I. PRESSURE IN THE FLUID

We assume that a cylindrical wave, emanating from an infinite line source located at point S with polar coordinates $(r_0, \varphi = \pi)$ in the ambient fluid, is incident upon a solid elastic cylinder of radius a. The problem is reduced to a two-dimensional one in the plane of the right cross section of the cylinder (Fig. 1). The Sommerfeld–Watson transformation applied to the normal mode series leads to both a qualitative and quantitative understanding, displaying the propagation of circumferential waves around the solid cylinder, in addition to the refraction effects.[1,2]

With a frequency sufficiently high to neglect the background integral, the total pressure at an observation point M of polar coordinates (r, φ) located inside the ambient fluid is written as the sum of two contributions: the geometrical part, taking into account the incident, reflected, and transmitted waves inside the cylinder, and the contribution of circumferential waves, falling into two different groups: the external or creeping waves with grazing excitation angle and the internal or leaky waves with small excitation angles. The geometrical part is calculated using the saddle-point method and the contribution of circumferential waves arises as a sum of residues from complex zeroes $v(x_1) = v' + iv''$ of the characteristic equation $D(v, x_1) = 0$, resulting from satisfying the boundary conditions at the cylinder surface $r = a$. The dimensionless quantity $x_1 = k_1 a$, where k_1 is the wave number of the bulk wave in the fluid, is usually called the frequency. Solutions of this equation are the complex azimuthal wave numbers $v(x_1)$ of the circumferential waves when $r = a$.

The rest of this paper concerns leaky waves, for which the roots $v(x_1)$ of the characteristic equation are lower than the frequency x_1. The residue contribution p to the total pressure at point M of the first clockwise circumnavigation of such a wave is written as

$$p(r,\varphi) = \frac{\pi}{4} P_0 E(x_1, v) H_v^{(1)}(k_1 r_0) \frac{H_v^{(2)}(x_1)}{H_v^{(1)}(x_1)} \times H_v^{(1)}(k_1 r) \cdot \exp i(v(\pi - \varphi) - \omega t), \quad (1)$$

where P_0 is a constant and the quantity $E(x_1, v)$ is usually called the launching coefficient. The Hankel functions are replaced by asymptotic expansions. Because of the relative position of the index v and the frequency $k_1 a$, Debye expansion of Hankel function $H_v^{(1)}(k_1 r)$ for large $k_1 a$ is adequate for any observation point outside the cylinder $r > a$. The frequency is assumed to reach a value high enough such for the first term of the expansion to give an accurate evaluation of the cylinder function,

$$H_v^{(1)}(k_1 r) = \sqrt{\frac{2}{\pi}} \exp\left(-i\frac{\pi}{4}\right) \frac{1}{[k_1^2 r^2 - v^2]^{1/4}} \cdot \exp i\left[\sqrt{k_1^2 r^2 - v^2} - v \arccos\left(\frac{v}{k_1 r}\right)\right]. \quad (2)$$

By introducing asymptotic expansions and the complex angle $\theta = \theta' + i\theta''$ defined by,

$$v = k_1 a \sin\theta, \quad (3)$$

and by replacing $\pi - \varphi$ by $\pi - \varphi = \psi_0 + \psi_c + \psi_M$ (Fig. 1), the pressure p in Eq. (1) becomes

$$p = \frac{P_0}{2} E(x_1, v) \frac{1}{\left[\left(\frac{r}{a}\right)^2 - \sin^2\theta\right]^{1/4}} \frac{1}{\left[\left(\frac{r_0}{a}\right)^2 - \sin^2\theta\right]^{1/4}} \cdot \exp i[x_1(\phi_0 + \phi_c + \phi_M) - \omega t], \quad (4)$$

where,

$$\phi_c = \psi_c \sin\theta,$$
$$\phi_M = \sin\theta\left[\psi_M + \left(\frac{\pi}{2} - \theta\right) - \arccos\left(\frac{a\sin\theta}{r}\right)\right] - \cos\theta + \sqrt{\left(\frac{r}{a}\right)^2 - \sin^2\theta}. \quad (5)$$

The contribution ϕ_0 to the total phase has the same expression as the contribution ϕ_M, with ψ_M and r replaced, respectively, by ψ_0 and r_0.

In the next section, geometrical interpretation of the pressure term Eq. (4) is given. In order to do that, the phase term is developed at different orders of approximation of the parameter θ''/θ'. The imaginary part of the angle θ is actually smaller than the real part.[19] From a mathematical point of view, the developments should be made as functions of the parameter v''/v', because the complex azimuthal wave number is the direct solution of the dispersion equation. However, since θ and v are related by Eq. (3), it is equivalent and more convenient to use the parameter θ''/θ'.

II. ZERO ORDER OF APPROXIMATION OF THE PRESSURE

In this section, the imaginary part of the angle θ is neglected, i.e., the angle is supposed to be $\theta \approx \theta'^{(0)} + 0(\theta'')$. Since all the quantities are real, this is the domain of conventional geometrical acoustics.

The propagation path is then completely interpreted with geometrical arguments. We denote,

$$L_0 = \sqrt{r_0^2 - a^2 \sin^2\theta'^{(0)}} - a\cos\theta'^{(0)},$$
$$s = a\psi_c, \quad (6)$$
$$L = \sqrt{r^2 - a^2 \sin^2\theta'^{(0)}} - a\cos\theta'^{(0)}.$$

The meaning of L_0, s, and L is straightforward from Fig. 1: L_0 is the distance from the source to the cylinder, s is the length of the propagation path around the cylinder, and L is the distance from the cylinder to the observation point. The total phase $x_1\phi = x_1(\phi_0 + \phi_c + \phi_M)$ can be written as $x_1\phi = k_1 L_0 + ks + k_1 L$, where k is the azimuthal wave number. The angle $\theta'^{(0)}$ appears as the excitation and the emergence angle of the wave.

The wavefront equation, which is the loci of constant phase, is explicitly found as

$$\varphi = \frac{\sqrt{r^2 - b^2}}{b} - \arcsin\left[\frac{b}{r}\right] + C, \quad (7)$$

where C is a constant independent of the cylindrical coordinates (r, φ), and $b^{(0)} = a\sin\theta'^{(0)}$. This is exactly the equation of the involute of the circle of radius $b^{(0)}$ (Fig. 2).

It corresponds to straight rays in the fluid. By construction, these rays are normal to the wavefront and are tangent to the inner circle of radius $b^{(0)}$. The local plane wave in the fluid is homogeneous. Its phase velocity matches the bulk wave velocity in the fluid. Visualization works[20–22] show off the resulting spiral wavefronts in the ambient fluid consistent with the ray interpretation.[1,2,23] The amplitude term $[(r/a)^2 - \sin^2\theta]^{-1/4}$ of the pressure is equal to the ray tube divergence coefficient as reported in Ref. 24.

The limit of this description is clear: The attenuation caused by radiation during propagation around the cylinder is not considered. In previous works,[1,2] a first-order approximation is made along the cylinder surface, and a zero-order approximation is made in the fluid, which gives rise to a problem of continuity. It is shown in the next section that a more general result may be obtained when no approximation is made about the complex angles.

III. COMPLETE DESCRIPTION OF THE PRESSURE

The analysis is now done with the complete angle θ. Only the assumption of high-frequency domain is needed. The description of the wave is based upon the determination of the complex wave vector associated with the radiated wave in the fluid.

A. Complex wave vector

The wave vector is calculated as the gradient of the phase. Also, the terms in Eq. (4) independent of the observation position do not contribute to the expression of the local wave bivector and we call p_0 the product of these terms: the harmonic time factor, the launching coefficient, the ratio of Hankel functions with argument independent of the position, the Hankel function $H_v^{(1)}(k_1 r_0)$ related to the source which can also be rejected at infinity. The only terms under consideration are the Hankel function related to the observer and the exponential function. The pressure term is also written,

$$p = p_0 A(r) \exp i\eta, \quad (8)$$

with

$$\eta = \sqrt{k_1^2 r^2 - v^2} + v\left[\pi - \varphi - \arccos\left(\frac{v}{k_1 r}\right)\right],$$
$$A(r) = [k_1^2 r^2 - v^2]^{-1/4}, \quad (9)$$

and p_0 is a term regrouping the constant factors and the terms related to the source.

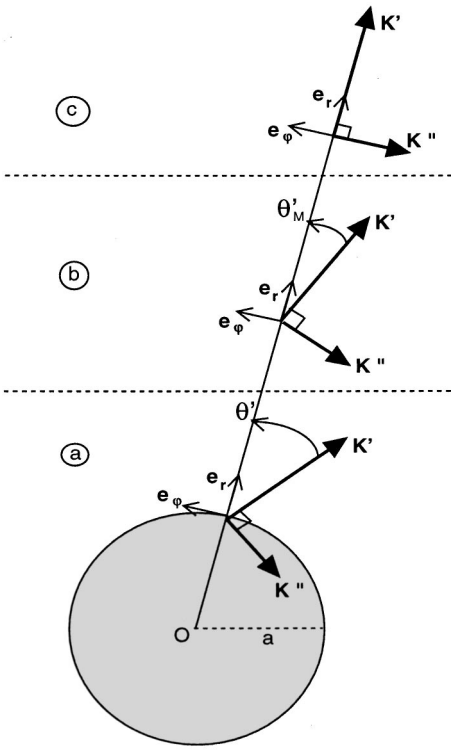

FIG. 3. The wave vector at different observation points. *a*: On the cylinder surface, *b*: in the fluid, *c*: infinite distance of observation.

The local complex bivector $(\mathbf{K}',\mathbf{K}'')$ is calculated using $\mathbf{K}=\text{grad}\,\eta$. Deriving the vector $\mathbf{K}$, attention is focused on the separation between real and imaginary parts and the ability to geometrically interpret the result. This is obtained by introducing the complex angle $\theta_M=\theta'_M+i\,\theta''_M$, relative to the observation point and defined as: $\sin\theta_M=(a/r)(v/x_1)$ [Fig. 3(b)]. This yields the following expression:

$$\mathbf{K}=k_1\cosh(\theta''_M)\mathbf{l}+ik_1\sinh(\theta''_M)\mathbf{h}, \tag{10}$$

where $\mathbf{l}$ and $\mathbf{h}$ are, respectively, the propagation and damping directions, expressed in the local $(\mathbf{e_r},\mathbf{e}_\phi)$ coordinate system attached to the observation point

$$\mathbf{l}_{(\mathbf{e_r},\mathbf{e}_\phi)}=\begin{pmatrix}\cos\theta'_M\\ -\sin\theta'_M\end{pmatrix},\quad\text{and}\quad \mathbf{h}_{(\mathbf{e_r},\mathbf{e}_\phi)}=\begin{pmatrix}-\sin\theta'_M\\ -\cos\theta'_M\end{pmatrix}. \tag{11}$$

From this expression, it is straightforward to deduce: $\mathbf{K}\cdot\mathbf{K}=k_1^2$ and $\mathbf{K}'\cdot\mathbf{K}''=0$. These two properties prove that the wave radiated in any point M by any internal circumferential leaky wave is locally tangential to a plane evanescent wave, with curves of constant phase orthogonal to equiamplitude.

The direction of the propagation vector $\mathbf{K}'$ is given by the real part of the angle θ_M, which is a function of the radial distance, for a given wave and a given frequency x_1, as illustrated in Fig. 3. On the cylinder surface $r=a$, the projection of the bivector on the azimuthal direction is $(-v',-v'')$ as expected, and the propagation direction is given by the real part of the angle $\theta_M(r=a)=\arcsin(v/x_1)$, which is the angle between the propagation direction $\mathbf{K}'$ and the radial direction $\mathbf{e_r}$. This angle θ' is a quantity intrinsic to the internal wave and the frequency considered. It is directly related by relation (3) to the solution v of the characteristic equation $D(v,x_1)=0$ in the first quadrant of the v complex plane. As the radial distance increases, the angle θ'_M decreases until the vector $\mathbf{K}'$ becomes collinear to the radial direction for an infinite distance of observation. Because the phase path is defined as the tangent of the propagation vector $\mathbf{K}'$, its concavity is governed by the real part of the complex angle θ_M. It is positive for all radial distances and lies between zero for infinite distance of observation and θ' on the cylinder surface. The subsequent qualitative phase path is illustrated in Fig. 4. The phase velocity of the evanescent wave is lower than the velocity c_1 of the homogeneous bulk wave in the fluid, and is equal to $c_1/\cosh\theta''_M$.

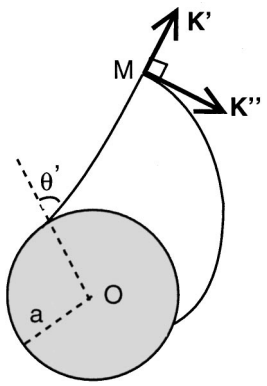

FIG. 4. The complete description of the wave. The wave vector is complex. The rays are curved and the wavefronts are not involutes of circle anymore. At point *M*, the wavefront is locally represented by the bivector $(\mathbf{K}',\mathbf{K}'')$.

B. Limit of the plane interface

The above expression of the wave bivector (10) is consistent with the limit of zero curvature. In order to demonstrate this, the discussion is restrained here to the Rayleigh circumferential wave which takes its name from its asymptotic behavior in the low wavelength limit. By solving the characteristic equation in the limit of infinite frequency, its reduced azimuthal wave number on the cylinder surface $v_R/(k_1a)$ is found[25] to reach asymptotically the value $k_R^-/(k_1)$, where k_R^- is the wave number along the interface of the well-known surface wave propagating on the boundary of a flat elastic half-space. Let us consider the limit of infinite cylinder radius a, letting the observation point such that the ratio r/a tends toward unity. In that case, the complex angle θ_M is such that $\sin\theta_M$ tends toward $k_R^-/(k_1)$. Equation (10) expressed in Cartesian coordinates, with the unitary vector $\mathbf{e_x}$ directed along the interface and the orthogonal vector $\mathbf{e_y}$ directed toward the fluid, gives

$$\mathbf{K}_{(\mathbf{e_x},\mathbf{e_y})}=\begin{pmatrix}k_R'^-\\ \text{Re}\,\sqrt{k_1^2-k_R^{-2}}\end{pmatrix}+i\begin{pmatrix}k_R''^-\\ \text{Im}\,\sqrt{k_1^2-k_R^{-2}}\end{pmatrix}, \tag{12}$$

where Re and Im are written for real and imaginary part. The limit found is exactly the coordinates of the wave bivector of the Rayleigh surface wave on the flat interface with a phase velocity, again different from the sound velocity in the fluid.[3] An illustration of this passage from cylinder to plane interface is proposed in Fig. 5.

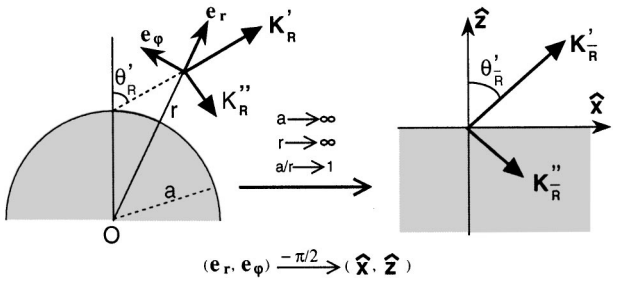

FIG. 5. The Rayleigh wave from the cylinder to the plane interface. The limit of the plane interface is obtained when $a \to +\infty$, $r \to +\infty$, and $a/r \to 1$. Then, a rotation of $-\pi/2$ is applied to transform the vectors $(\mathbf{e}_r, \mathbf{e}_\varphi)$ into $(\mathbf{e}_x, \mathbf{e}_y)$.

C. Polarization ellipses

From the description of evanescent plane waves, information can also be obtained on the displacement of fluid particles caused by the propagation of the waves in the fluid.

By definition, the extremity of the polarization vector is the path covered by particles over time. For an evanescent plane wave, polarization is an oriented ellipse.[12,26] Some polarization ellipses have been drawn in Fig. 6. A few comments have to be made about this figure. First, along a wavefront and at a given time, all the displacement vectors have the same orientation in the cylindrical coordinates system centered at the center *O* of the cylinder. Second, the effects caused by evanescence and ray tube divergence coefficient on the amplitude are opposed along a wavefront. If we follow a wavefront from the cylinder to infinity, there is a loss of amplitude by geometrical divergence as we move far from the cylinder. However, the evanescence vector is always locally tangent to the wavefront, and it is oriented on the opposite direction from the one of our path as seen in Fig. 4. Therefore the amplitude decreases by evanescence as we move along a wavefront from infinity to the cylinder. The effects of divergence and evanescence are also opposed along a wavefront.

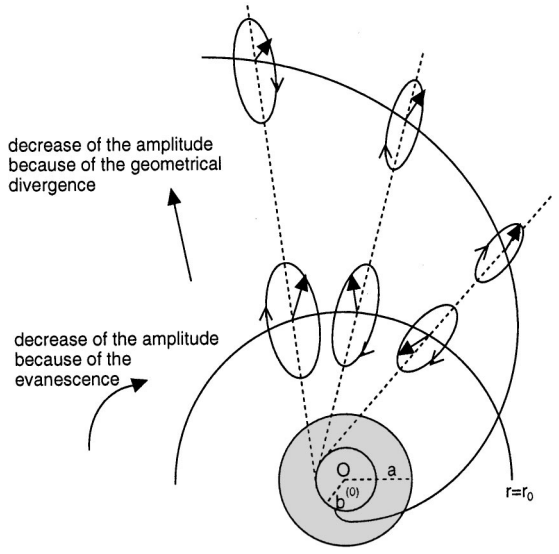

FIG. 6. Polarization ellipses for the acoustic displacement vector.

D. First-order approximation of the pressure

The evident advantage of the evanescent description is that it takes into account azimuthal attenuation by radiation during propagation around the cylinder, and it also gives a complete description of the wave in the fluid.

The evanescent properties have been described by calculating the wave vector in the high-frequency approximation, without any approximation on the angle θ.

A first-order expansion as a function of the parameter θ''/θ' would have been sufficient to show off the evanescent character of the wave in the fluid. With a first-order approximation, the complex wave bivector is given by

$$\mathbf{K}'^{(1)}_{(\mathbf{e}_r,\mathbf{e}_\phi)} = \mathbf{K}'^{(0)}_{(\mathbf{e}_r,\mathbf{e}_\phi)} = k_1 \begin{pmatrix} \cos\theta'_M \\ -\sin\theta'_M \end{pmatrix}, \tag{13}$$

and

$$\mathbf{K}''^{(1)}_{(\mathbf{e}_r,\mathbf{e}_\phi)} = k_1 \begin{pmatrix} -\frac{1}{2}\left(\frac{a}{r}\right)^2 \theta'' \sin 2\theta' \left[1-\left(\frac{a}{r}\sin\theta'\right)^2\right]^{-1/2} \\ -\frac{a}{r}\theta'' \cos\theta' \end{pmatrix}. \tag{14}$$

The evanescent characteristic of the radiated wave is obtained from the last equations because $\mathbf{K}'^{(1)} \cdot \mathbf{K}''^{(1)} = 0$. The decrease of amplitude by evanescence is described because the wave vector is complex. As the propagation vector $\mathbf{K}'^{(1)}$ is the same with the zero-order and with the first-order approximations, it may be shown that the rays and the wavefronts are the same as the ones in the zero-order approximation, i.e., straight rays and involute of circle for the wavefronts. Nevertheless, the first-order approximation is incomplete because the wave radiated in the fluid is described like a locally evanescent plane wave which propagates with the phase velocity c_1. A complete description has demonstrated that the phase velocity of the radiated wave was lower than c_1.

In summary, the first-order approximation gives an incomplete description of the radiated wave. This is why the complete description was preferably emphasized in this paper.

IV. CONCLUSION

It has been demonstrated that the wave radiated by any circumferential internal wave propagating around solid cylinder immersed in water can be locally seen as a plane evanescent wave. As a proof, a direct calculation of the wave bivector has been achieved. Evidence of corresponding curved rays has been displayed. Let us recall that no approximation on the radiation coefficient or on the distance of observation has been used. However, as usual, the high-frequency assumption is required in order to achieve analytical derivations.

The evanescent plane-wave description satisfies the boundary condition between the wave in the fluid and the wave on the cylinder surface, i.e., the complex Snell–Descartes laws. Moreover, it allows us to achieve the transition to the plane interface, and to describe the polarization ellipses associated with the acoustic displacement vector.

Because of the low-radiation coefficient of the circumferential wave, experimental demonstration of the exact anatomy of the radiated pressure can not be achieved. The usual geometrical picture is a well-adapted tool even if it does not describe the intrinsic evanescent properties of the wave. Nevertheless, it is not excluded that precise flying times measurements will, in the future, enlight the difference in celerity between the radiated wave and the homogeneous plane wave in the fluid.

Finally, similar results should be obtained for the second group of circumferential waves: the creeping or Franz waves. The Franz waves, which are analogous to the waves propagating on rigid cylinders, belong to the group of external waves. In electromagnetism, Choudhary and Felsen[27] had considered diffraction of a plane evanescent wave by a perfectly conducting cylinder, which is the counterpart of acoustically rigid scatters. From the calculation of the phase expression under some approximation specific to the case of creeping waves, the phase propagation paths have been derived and found to be curved. This confirms the results derived from our analytical analysis.

[1] G. V. Frisk and H. Überall, ''Creeping waves and lateral waves in acoustic scattering by large elastic cylinders,'' J. Acoust. Soc. Am. **59**, 46–54 (1976).

[2] A. Derem, ''Théorie de la matrice S et transformation de Sommerfeld-Watson dans la diffusion acoustique'' (in French), *La diffusion Acoustique*, edited by N. Gespa (CEDOCAR, Paris, 1987), pp. 189–277.

[3] G. Quentin, A. Derem, and B. Poirée, ''The formalism of evanescent plane waves and its importance in the study of the generalized Rayleigh wave,'' J. Acoust. **3**, 321–336 (1990).

[4] O. Leroy, G. Quentin, and J.-M. Claeys, ''Energy conservation for inhomogeneous plane wave,'' J. Acoust. Soc. Am. **84**, 374–378 (1988).

[5] F. Padilla, M. de Billy, and G. Quentin, ''Theoretical and experimental studies of surface waves on plane solid-fluid interfaces when the fluid sound velocity is located between the shear and the longitudinal ones in the solid,'' J. Acoust. Soc. Am. **106**, 666–673 (1999).

[6] M. Hayes, ''Inhomogeneous plane waves,'' Arch. Ration. Mech. Anal. **8**, 41–79 (1984).

[7] G. Caviglia, A. Morro, and E. Pagani, ''Inhomogeneous waves in viscoelastic media,'' Wave Motion **12**, 143–159 (1990).

[8] M. Deschamps and Chevée, ''Reflection-refraction of a heterogeneous plane wave by a solid layer,'' Wave Motion **15**, 61–75 (1992).

[9] K. Van den Abeele and O. Leroy, ''On the influence of frequency and width of an ultrasonic bounded beam in the investigation of materials: Study in terms of inhomogeneous plane waves,'' J. Acoust. Soc. Am. **93**, 2688–2699 (1993).

[10] L. B. Felsen, ''Evanescent waves,'' J. Opt. Soc. Am. **66**, 751–760 (1976).

[11] M. Deschamps, ''Reflection and refraction of the evanescent plane wave on plane interfaces,'' J. Acoust. Soc. Am. **96**, 2841–2848 (1994).

[12] B. Poirée, ''Les ondes planes évanescentes dans les fluides parfaits et les solides élastiques'' (in French), J. Acoust. **2**, 205–216 (1989).

[13] G. Caviglia and A. Morro, *Inhomogeneous Waves in Solids and Fluids* (World Scientific, London, 1992).

[14] N. Favretto-Anrès, ''Theoretical study of the Stoneley-Scholte wave at the interface between an ideal fluid and a viscoelastic solid,'' Acust. Acta Acust. **82**, 829–838 (1996).

[15] B. Poirée and F. Luppé, ''Evanescent plane waves and the Scholte-Stoneley interface wave,'' J. Acoust. **4**, 575–588 (1991).

[16] O. Poncelet and M. Deschamps, ''Lamb waves generated by complex harmonic inhomogeneous plane waves,'' J. Acoust. Soc. Am. **102**, 292–300 (1997).

[17] F. Luppé, G. Chatelets, and G. Maze, ''Diffraction of Lamb waves at the end section of a plate,'' J. Acoust. Soc. Am. **87**, 1807–1809 (1990).

[18] L. M. Brekhovskikh, ''Surface waves confined to the curvature of the boundary in solids,'' Sov. Phys. Acoust. **13**, 462–472 (1968).

[19] M. Talmant, J.-M. Conoir, and J.-L. Rousselot, ''High frequency scattering by shells,'' Acta Acust. (China) **3**, 509–515 (1995).

[20] W. G. Neubauer, ''Pulsed circumferential waves on aluminium cylinders in water,'' J. Acoust. Soc. Am. **45**, 1134–1144 (1969).

[21] W. G. Neubauer and L. R. Dragonette, ''Observation of waves radiated from circular cylinders caused by an incident pulse,'' J. Acoust. Soc. Am. **48**, 1135–1149 (1970).

[22] Z. Wu, G. Zhou, and S. Feng, ''Visualization of the sound scattering by a cylinder,'' Acta Acust. **18**, 81–90 (1993).

[23] P. L. Marston, ''GTD for backscattering from elastic spheres and cylinders in water and the coupling of surface elastic waves with the acoustic field,'' J. Acoust. Soc. Am. **83**, 25–37 (1988).

[24] L. B. Felsen, J. M. Ho, and I. T. Lu, ''Three-dimensional Green's function for fluid-loaded thin elastic cylindrical shell: Alternative representations and ray acoustic forms,'' J. Acoust. Soc. Am. **87**, 554–569 (1990).

[25] G. V. Frisk, J. W. Dickey, and H. Überall, ''Surface wave modes on elastic cylinders,'' J. Acoust. Soc. Am. **58**, 996–1008 (1975).

[26] Ph. Boulanger and M. Hayes, *Bivectors and Waves in Mechanics and Optics* (Chapman & Hall, London, 1993).

[27] S. Choudhary and L. B. Felsen, ''Asymptotic theory for inhomogeneous waves,'' IEEE Trans. Antennas Propag. **21**, 827–842 (1973).

A fast method for acoustic imaging of multiple three-dimensional objects

Y. X. You,[a] G. P. Miao, and Y. Z. Liu
School of Naval Architecture and Ocean Engineering, Shanghai Jiaotong University, Shanghai 200030, People's Republic of China

(Received 16 December 1999; accepted for publication 14 April 2000)

This paper is concerned with the inverse problem for imaging multiple three-dimensional objects using the information of the far-field pattern of the scattered wave. A spatially dependent function, which has noticeably different values inside and outside the obstacle, is derived. A numerical method based on the characterization is developed to obtain a visualization of the obstacle. The most remarkable advantage of this method is that it does not need any prior knowledge about the geometry and physical properties of the scatterer, and requires only the information of the far-field measurements for a finite number of directions of incidence and observation distributed over a limited range. Furthermore, the scheme is very simple and fast since it avoids the use of the iterative procedure and requires only the solution of a linear system. Some numerical examples with synthetic far-field data are given showing the practicality and efficiency of this scheme. © *2000 Acoustical Society of America.* [S0001-4966(00)05007-4]

PACS numbers: 43.20.Fn [ANN]

INTRODUCTION

For numerous applications in medicine, geophysics, and material science, the inverse problem of recovering the shape of the obstacle from its far-field effects on a known acoustic wave has received considerable attention in recent years.[1–3] Inverse problems of this type are both nonlinear and improperly posed. The difficulties make the designing of robust inversion algorithms especially challenging. The earliest methods for approximately solving the inverse problem are various linear approximate methods which only involve the special case where the Born or physical optics approximation is valid.[4–7] Nevertheless there are very interesting applications where high or low frequency approximation is not available, one has to work with frequencies in the resonance region.

There have been a number of methods developed for solving the inverse problem for frequencies in the resonance region during the last two decades, which explicitly considered the nonlinear and ill-posed nature of the problem. Roughly speaking, these methods may be categorized as two separate groups. The first class of such works consists of an iterative procedure that at each step requires the solution of the forward problem.[8–13] However, to date, numerical experiments based on such algorithms have only been performed in two dimensions. The second class consists of a nonlinear optimization procedure which is achieved by separating the inverse problem into two parts: one is responsible for the ''best-fit'' to the far-field pattern, while the other accounts for best-fit to the boundary condition.[14–22] Such schemes are particularly attractive since they do not require the solution of the direct problem and have successfully been used to numerically solve the three-dimensional inverse problem.[15,18–22] The main advantage of these methods mentioned previously is that they can yield not only the size and orientation of the obstacle but also more complicated features such as inlets or bumps. However, all of these methods are relied on knowing the type of boundary conditions satisfied by the total field on the surface of the obstacle in advance. It is also assumed in all of these algorithms that the obstacle is simply connected and starlike with respect to the origin in order that the surface of the scattering domain can be represented in a simple parametric form. A further drawback of such schemes is that they are often very time consuming and suffer from possible local minima.

A new group of schemes has recently been developed to avoid all these difficulties. The idea is based on the observation that in many practical situations it is important to determine only the support of the obstacle (e.g., the number of components and their rough sizes and orientations) instead of the fine details of the shape of the scatterer. The so-called simple method[23,24] is the most noticeable one in these schemes, in which a spatially dependent function which blows up on the obstacle surface is used as a reliable indicator of the support of the scattering domain. A rigorous mathematical analysis of the simple approach was provided by Kirsch[25] who proposed a modification of the original version. The simple method has recently been applied to the numerical implementation of the three-dimensional inverse problem.[26] Potthast[27] presented a similar but different procedure for generating the spatially dependent function which becomes unbounded on the boundary of the scatterer. More recently, Norris[28] derived a new function that is finite inside the obstacle but unbounded outside the scatterer. The main attractive features of these methods are that they do not require any assumptions about the connectivity and the surface boundary conditions of the obstacle. In addition, these approaches are very simple and fast since they do not require both the use of a large optimization scheme and the solution of the forward problem in the inversion procedure. However, in the theoretical analysis of these methods, only the full-aperture problem with several incoming plane waves is considered. Nevertheless, in many applications of practical importance, one must consider the case where the incident

[a]Electronic mail: gpmiao@mail.sjtu.edu.cn

waves come from directions covering a limited range and the far-field patterns are measured at observation points distributed over a limited aperture.

The purpose of the paper is devoted to a presentation of a fast method for imaging multiple three-dimensional obstacles, which may be viewed as a further development of the simple method mentioned above. In contrast to the original version of the simple scheme, the present approach requires only the limited-aperture knowledge of the far-field measurements for a finite number of directions of incidence and observation distributed over a limited range instead of the full-aperture information of the far-field patterns for all incident and observation directions. In the next section, the mathematical details of such method are analyzed and its basic outline described. In the final section, a scheme used to numerically implement the approach is proposed, and some numerical examples are given illustrating some behaviors of this scheme.

I. THEORY ANALYSIS FOR A FAST METHOD

Let D be the open complement of an unbounded simply connected domain D^+ in R^3 with smooth boundary ∂D. Note that D may consist of several disconnected parts. Assume that the incident wave is given by $u^i(x;d) = e^{ikx\cdot d}$, where $x \in R^3$, $k>0$ is the wavenumber in the surrounding medium D^+ and d is a fixed unit vector which describes the direction of the incident wave. The field u^i leads to a scattered field u^s. Let $u=u^i+u^s$ denote the total field in D^+. Throughout this paper the time-harmonic factor $e^{i\omega t}$, where ω is the angular frequency, has been suppressed. Then the direct scattering problem of a time-harmonic acoustic wave by the obstacle D consists in finding a total field u which solves the Helmholtz equation

$$\Delta u + k^2 u = 0 \quad \text{in } D^+, \tag{1}$$

and the scattered field u^s is required to satisfy the Sommerfeld radiation condition at infinity

$$\lim_{r\to\infty} r\left(\frac{\partial u^s}{\partial r} - iku^s\right) = 0, \quad r=|x| \tag{2}$$

uniformly in all directions $\hat{x}=x/|x|$. Here, and in what follows, the hat on the top of a vector indicates the corresponding unit directional vector. Moreover, the total field u satisfies some unknown boundary condition on ∂D:

$$B(u) = 0 \quad \text{on } \partial D, \tag{3}$$

which may be any of the following:

Dirichlet boundary condition:

$$u = 0 \quad \text{on } \partial D; \tag{4}$$

Neumann boundary condition:

$$\frac{\partial u}{\partial n} = 0 \quad \text{on } \partial D; \tag{5}$$

Impedance boundary condition:

$$\frac{\partial u}{\partial n} + i\lambda u = 0 \quad \text{on } \partial D, \tag{6}$$

where λ is a real constant and n is the unit outward normal to ∂D.

The Sommerfeld radiation condition (2) implies that u^s has the asymptotic behavior

$$u^s(x) = \frac{e^{ikr}}{r} F(\hat{x};d) + O(r^{-2}), \quad r\to\infty \tag{7}$$

so that when $r\to\infty$ the leading term of the expansion in inverse powers of r is given by a spherical wave e^{ikr}/r coming out from the origin modulated by the ''far-field pattern'' F.

Let $\Lambda=\{d_l | d_l \in \partial B, l=1,2,\ldots,M\}$ be the set of directions of the incident waves and $\Omega=\{\hat{x}_l | \hat{x}_l \in \partial B, l=1,2,\ldots,N\}$ be the set of directions where the far-field patterns F are measured, where ∂B is the unit sphere in R^3. Then the inverse problem under consideration is to image the unknown obstacle D from the only knowledge of the far-field pattern $F(\hat{x};d)$ for $\hat{x}\in\Omega$ and $d\in\Lambda$.

Now, let us begin the analysis for solving the inverse problem. Applying Green's theorem to the exterior of the scatterer, we obtain

$$H_D(x)u(x) = u^i(x) + \frac{ik}{4\pi}\int_{\partial D}\left[u(y)\frac{\partial h_0^{(1)}(k|x-y|)}{\partial n} - h_0^{(1)}(k|x-y|)\frac{\partial u(y)}{\partial n}\right] d\sigma(y), \tag{8}$$

where $h_0^{(1)}$ is a spherical Hankel function of the first kind, the Heaviside function H_D equals 1 for $x\in D^+$, and 0 for $x\in D$. Let x tend to infinity, by the asymptotic behavior of the Hankel $h_0^{(1)}$ and with the aid of Eq. (8), we have

$$F(\hat{x};d) = \frac{1}{4\pi}\int_{\partial D}\left[u(y)\frac{\partial e^{-ik\hat{x}\cdot y}}{\partial n} - \frac{\partial u(y)}{\partial n}e^{-ik\hat{x}\cdot y}\right] d\sigma(y). \tag{9}$$

We introduce the function

$$v(y) = \sum_{l=1}^{N} g_l e^{-ik\hat{x}_l\cdot y}, \tag{10}$$

where the g_l, $1\leqslant l\leqslant N$, are the complex constants. Note that $v(y)$ is a solution of the Helmholtz equation for $y\in R^3$. Functions of the form (10) are called the discrete Herglotz wave functions. Then using (9) and (10), we get

$$\sum_{l=1}^{N} g_l F(\hat{x}_l;d) = \frac{1}{4\pi}\int_{\partial D}\left[u(y)\frac{\partial v(y)}{\partial n} - \frac{\partial u(y)}{\partial n}v(y)\right] d\sigma(y). \tag{11}$$

Let y_0 be a given point in D, and assume that the g_l, $1\leqslant l\leqslant N$, can be chosen so that v satisfies

$$\Delta v + k^2 v = 0 \quad \text{in } D, \tag{12}$$

$$B(v(y)) = -B(h_0^{(1)}(k|y-y_0|)) \quad \text{on } \partial D. \tag{13}$$

Note that a unique solution of (12)–(13) exists, provided that k^2 is not a Dirichlet or Neumann eigenvalue for D.

Let us write $u^s(x;d)$ and $u^i(x;d)$ to indicate the dependence of these fields on the incident direction d. Then using (8) and (13), we can easily obtain

$$\frac{ik}{4\pi}\int_{\partial D}\left[u(y)\frac{\partial v(y)}{\partial n}-\frac{\partial u(y)}{\partial n}v(y)\right]d\sigma(y)=u^i(y_0;d) \tag{14}$$

for the Dirichlet or Neumann boundary condition and

$$\begin{aligned}
&\frac{ik}{4\pi}\int_{\partial D}\left[u(y)\frac{\partial h_0^{(1)}(k|x-y_0|)}{\partial n}\right.\\
&\left.-h_0^{(1)}(k|x-y_0|)\frac{\partial u(y)}{\partial n}\right]d\sigma(y)\\
&=\frac{ik}{4\pi}\int_{\partial D}u(y)\left[\frac{\partial h_0^{(1)}(k|x-y_0|)}{\partial n}\right.\\
&\left.+i\lambda h_0^{(1)}(k|x-y_0|)\right]d\sigma(y)\\
&=-\frac{ik}{4\pi}\int_{\partial D}u(y)\left[\frac{\partial v(y)}{\partial n}+i\lambda v(y)\right]d\sigma(y)\\
&=-\frac{ik}{4\pi}\int_{\partial D}\left[u(y)\frac{\partial v(y)}{\partial n}-v(y)\frac{\partial u(y)}{\partial n}\right]d\sigma(y)\\
&=-u^i(y_0;d)
\end{aligned} \tag{15}$$

for the impedance boundary condition.

From (11), (14), and (15), we conclude that

$$ik\sum_{l=1}^{N}g_l F(\hat{x}_l;d)=u^i(y_0;d),\quad d\in\partial B. \tag{16}$$

The above simple analysis means that if there exist g_l, $1\leqslant l\leqslant N$, such that $v(y)$ defined by (10) solves the boundary value problem (12)–(13), then Eq. (16) has an exact solution. Unfortunately, an exact solution to (16), in general, may not exist, for there may usually not exist a solution for the boundary problem (12)–(13) such that it is a discrete Herglotz wave function. However, we will hereinafter show that an approximate solution to (16) can always be found within an arbitrary prescribed error in the maximum norm.

Now, we address the above problem. In order to simplify our presentation, we restrict ourselves to the case with the Dirichlet boundary condition. To accomplish this, let us introduce the linear space $V=\mathrm{Span}\{e^{-iky\cdot\hat{x}_l}|\hat{x}_l\in\partial B, l=1,2,\ldots\}\subset L^2(\partial D)$. Then, if k^2 is not a Dirichlet eigenvalue for D, the linear space V is complete in $L^2(\partial D)$ for any countable dense set $\{\hat{x}_l|\hat{x}_l\in\partial B, l=1,2,\ldots\}$ in ∂B.[3] This implies that, for any $\varepsilon>0$, we can find g_l, $1\leqslant l\leqslant N$, such that

$$\left\|\sum_{l=1}^{N}g_l e^{-ikx\cdot\hat{x}_l}+h_0^{(1)}(k|x-y_0|)\right\|_{L^2(\partial D)}<\varepsilon. \tag{17}$$

Hence, from (10), we obtain

$$\|v(x)+h_0^{(1)}(k|x-y_0|)\|_{L^2(\partial D)}<\varepsilon. \tag{18}$$

Now, let us define U^s by

$$U^s=\sum_{l=1}^{N}g_l u^s(x;-\hat{x}_l). \tag{19}$$

Then, from (4) and (18), we have

$$\|U^s(x))-h_0^{(1)}(k|x-y_0|)\|_{L^2(\partial D)}<\varepsilon. \tag{20}$$

Notice that $h_0^{(1)}(k|x-y_0|)$ and U^s are the radiating solutions of the Helmholtz equation having the far-field pattern $(1/ik)e^{-ik\hat{x}\cdot y_0}$ and $U_\infty=\Sigma_{l=1}^{N}g_l F(\hat{x};-\hat{x}_l)$, respectively. Hence, the fact that the far-field pattern of the radiating solution of the direct scattering problem continuously depends on the boundary data yields that there exists a positive constant C, independent of ε, such that

$$\max_{\hat{x}\in\partial B}\left|ik\sum_{l=1}^{N}g_l F(\hat{x};-\hat{x}_l)-e^{-ik\hat{x}\cdot y_0}\right|<C\varepsilon. \tag{21}$$

Now, the reciprocity principle implies that

$$\max_{d\in\partial B}\left|ik\sum_{l=1}^{N}g_l F(\hat{x}_l;d)-u^i(y_0;d)\right|<C\varepsilon. \tag{22}$$

It should be noted that, for the Neumann or impedance boundary condition, the relations (18) and (22) are also valid, provided k^2 is not a Neumann eigenvalue for D. We can further find from (18) that $\|v\|_{L^2(\partial D)}$ is unbounded as y_0 tends to ∂D, and hence it follows from (10) that $|\tilde{g}|$ is also unbounded as y_0 approaches ∂D, where $\tilde{g}=(g_1,g_2,\ldots,g_N)^T$ and $|\tilde{g}|=\sqrt{\Sigma_{n=1}^{N}|g_n|^2}$, the superscript T denotes transposition.

The above results lead to an extremely simple method for imaging the obstacle D, whose general procedure can be described as follows:

(i) Choose a grid S such that the unknown obstacle is contained in the grid.

(ii) Find the vector function $\tilde{g}$ from Eq. (16) for each point y_0 on grid S.

(iii) Determine the boundary ∂D of the obstacle by choosing those points $y_0\in S$ where $|\tilde{g}|$ achieves its maximum (approaching ∂D from inside D).

In practice, the far-field data is usually obtained for a discrete set of incident waves from directions covering a limited range. We assume that such data is available for incoming plane waves with directions which are in the set Λ, and Eq. (16) also holds for each of these incident directions. This observation reveals that the vector function $|\tilde{g}|$ can be approximately determined by

$$ik\sum_{l=1}^{N}g_l(y_0)F(\hat{x}_l;d_m)=u^i(y_0;d_m),\quad m=1,2,\ldots,M. \tag{23}$$

Let $g_l=g_l(y_0)$, $\tilde{u}_m=u^i(y_0;d_m)$, and $A=(A_{ml})_{M\times N}$ for $m=1,\ldots,M$ and $n=1,\ldots,N$, where $A_{ml}=ikF(x_l;d_m)$. Let $\tilde{g}(y_0)=(g_1,g_2,\ldots,g_N)^T$, $B(y_0)=(\tilde{u}_1,\tilde{u}_2,\ldots,\tilde{u}_M)^T$. Then the above equations can be written as

$$A\tilde{g}(y_0)=B(y_0). \tag{24}$$

Equation (24) is a linear system of M equations in N unknowns, so that to determine the unknowns we require $M \geqslant N$. As the number of incident and scattering directions increases, the condition number of the matrix A grows rapidly. Therefore, the linear system (24) is ill-conditioned and needs to be regularized. One possibility for this is Tikhonov regularization,[29] where instead of (24), the regularization linear system

$$(\alpha^2 I + A^* A)\tilde{g}_\alpha(y_0) = A^* B(y_0) \tag{25}$$

with a positive ''regularization parameter'' α is solved, where A^* denotes the adjoint of A and $\tilde{g}_\alpha(y_0)$ is the known regularization solution of the linear system (24).

Let $\{(\sigma_n, u_n, v_n) | n = 1,2,\ldots,N\}$ be the singular system of the matrix A, where u_n and v_n are the left and right singular vectors, respectively, of A, and σ_n are the singular values of A, which are non-negative and appear in nonincreasing order:

$$\sigma_1 \geqslant \sigma_2 \geqslant \cdots \geqslant \sigma_N \geqslant 0. \tag{26}$$

It is well known that the solution to (25) can be expressed in terms of the singular system of A as

$$\tilde{g}_\alpha(y_0) = \sum_{n=1}^{N} \frac{\sigma_n u_n^T B(y_0)}{\sigma_n^2 + \alpha^2} v_n . \tag{27}$$

II. NUMERICAL RESULTS

In the section, we shall further present an effective numerical implementation of the algorithm described in the previous section and give some numerical results to illustrate properties of this algorithm.

The data for the inverse problem is far-field pattern $F(\hat{x}; d)$ for $\hat{x} \in \Omega$ and $d \in \Lambda$, which is generated by approximately solving the direct scattering problem using a least squares method.[18,19,30] Here we wish to emphasize that the inversion algorithm developed in this paper has no connection to the solution of the direct scattering problem.

Let us define the following three sets of incident and observation directions:

$$\Omega_1 = \left\{ \hat{x}(\theta,\phi) \,\middle|\, \theta = \frac{\pi i}{7}, \phi = \frac{\pi j}{4}, i = 1,2,\ldots,6, j = 1,2,\ldots,8 \right\},$$
$$\Lambda_1 = \{ d \,|\, d = -\hat{x}, \hat{x} \in \Omega_1 \}, \tag{28}$$

$$\Omega_2 = \left\{ \hat{x}(\theta,\phi) \,\middle|\, \theta = \frac{\pi i}{12}, \phi = \frac{\pi j}{4}, i = 1,2,\ldots,6, j = 1,2,\ldots,8 \right\},$$
$$\Lambda_2 = \{ d \,|\, d = -\hat{x}, \hat{x} \in \Omega_2 \}, \tag{29}$$

$$\Omega_3 = \left\{ \hat{x}(\theta,\phi) \,\middle|\, \theta = \frac{\pi i}{12}, \phi = \frac{\pi j}{7}, i = 1,2,\ldots,6, j = 0,1,\ldots,7 \right\},$$
$$\Lambda_3 = \{ d \,|\, d = -\hat{x}, \hat{x} \in \Omega_3 \}, \tag{30}$$

where $\hat{x}(\theta,\phi) = (\sin\theta\cos\phi, \sin\theta\sin\phi, \cos\theta)$.

Three different types of data are used in the computations: (1) Type I—the full aperture case: the incident range is Λ_1, and the view range is Ω_1; (2) Type II—the upper half of the unit sphere: the incident range is Λ_2, and the view range is Ω_2; (3) Type III—the upper quarter of the unit sphere: the incident range is Λ_3, and the view range is Ω_3. Notice that, in each of these types, the incident waves illuminate the obstacle from 64 different directions uniformly distributed over the incident range Λ and the far-field pattern $F(\hat{x}; d)$ is measured in 64 different directions equidistantly spaced in the scattering range Ω. In addition, the far-field pattern is measured on the same side as the incoming waves. Obviously, this is a realistic case if the far-field data are obtained in an experiment.

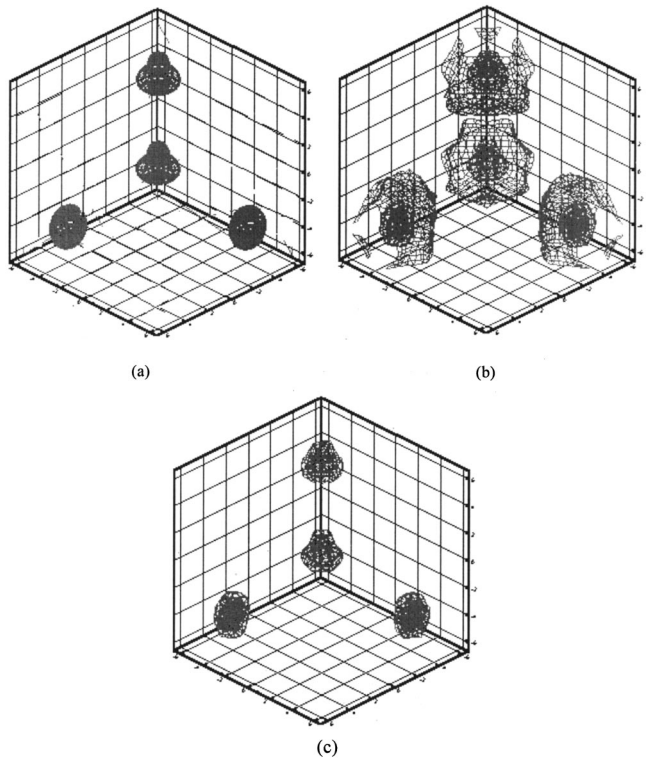

FIG. 1. Reconstructions for four pseudo-Apollos. (a) Original; (b) 3D contour plot of $|\hat{g}_\alpha(y_0)|$ when $\lambda = 1.1$; (c) 3D contour plot of $|\hat{g}_\alpha(y_0)|$ when $\lambda = 1.85$.

In all the examples, we have taken the wavenumber $k = 1$. When we consider the impedance boundary condition, we choose $\lambda = k$. For the Tikhonov regularization, the regularization parameter α is selected by trial and error. In our experiments, we have taken $\alpha = 10^{-6}, 10^{-8}, 10^{-10}$, respectively, for the three different types of data mentioned above. When we consider the reconstructions of simply connected obstacles, S has been taken as a uniform $32 \times 32 \times 32$ grid of the cube $[-3,3]^3$ in R^3, while for reconstructions of disconnected obstacles, S has been chosen as a uniform $32 \times 32 \times 32$ grid of the cube $[-6,6]^3$ in R^3.

The analysis outlined previously shows that the norm of $\tilde{g}_\alpha$ is large as y_0 approaches ∂D from inside D. Computationally we find that the norm of $\tilde{g}_\alpha$ is also large outside D, but it is small inside D. We define the function $|\hat{g}_\alpha(y_0)|$ by

$$|\hat{g}_\alpha(y_0)| = \frac{\log|\tilde{g}_{\max}|}{\log|\tilde{g}_\alpha(y_0)|}, \tag{31}$$

where $|\tilde{g}_{\max}| = \max_{y_0 \in S} |\tilde{g}_\alpha(y_0)|$. The new function $|\hat{g}_\alpha(y_0)|$ is large inside D but small outside D, and hence whose local

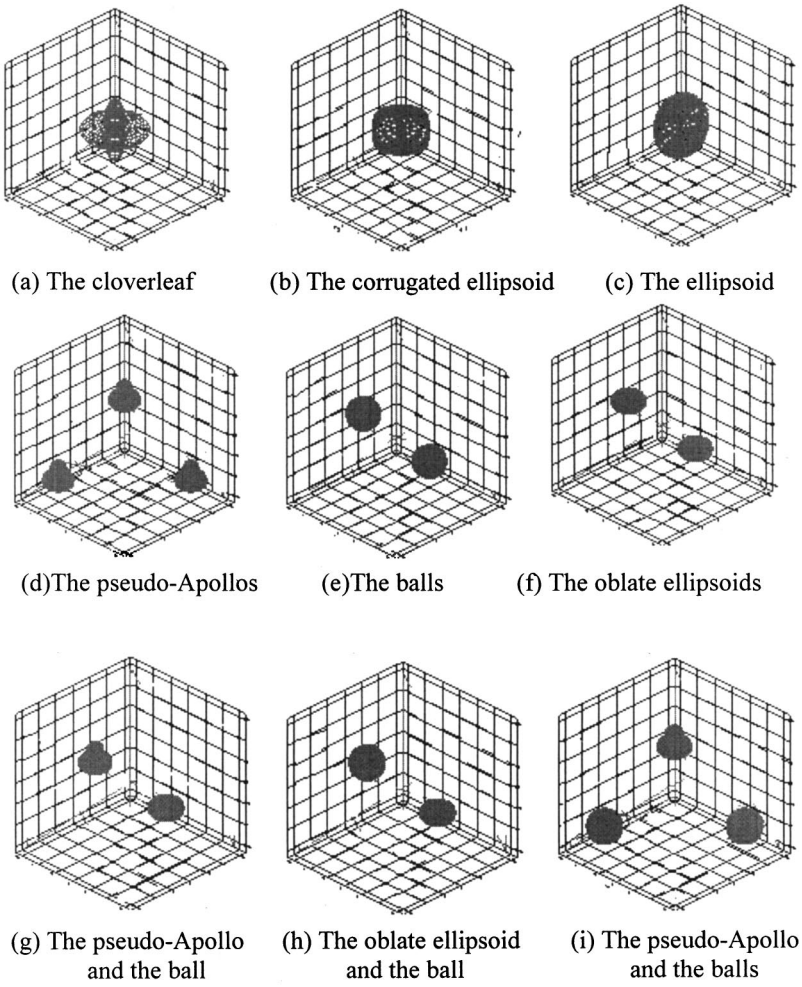

FIG. 2. The obstacles used in the numerical experiments.

extrema are located inside of the obstacle. Motivated by this observation, we use those points on the grid S where $|\hat{g}_\alpha(y_0)|$ arrives at its local extrema as a visualization of the obstacle. This can be achieved by drawing the 3D contour plot of $|\hat{g}_\alpha(y_0)|$ as a function of y_0 on S.

We start by illustrating some properties of the 3D contour plot for a disconnected scatterer with type I data, which is given by two pseudo-Apollos and two ellipsoids with Dirichlet boundary condition shown in Fig. 1(a). In Fig. 1(b) we draw the 3D contour plot of $|\hat{g}_\alpha(y_0)|$ where the contour level (denoted by γ) has been taken as $\gamma=1.1$. We can see from this picture that the number of components of the scatterer and their sizes and orientations are clearly visible, but the precise shape of the surface of each component is also ambiguous. In order to gain sufficient resolution to identify the boundary, we set a filter to keep all (almost all) local extrema in the picture. The procedure may be achieved by such a way, that is, if $|\hat{g}_\alpha(y_0)|<\gamma_0$, then the point y_0 is removed from the contour plot, where the level γ_0 is determined by trial and error in the present paper. Figure 1(c) shows a result with filtering. The result reveals that the use of such filter technique yields a reasonably good image of the disconnected obstacle. This procedure can be summarized in four points:

(1) Compute the singular system $\{(\sigma_n,u_n,v_n)|n=1,2,\ldots,N\}$ of the matrix A.
(2) Choose a searching grid S and find a regularization solution $\tilde{g}_\alpha(y_0)$ from (27) for each $y_0\in S$.
(3) Determine the function $\hat{g}_\alpha(y_0)$ from (31) and draw the 3D contour plot of $\hat{g}_\alpha(y_0)$ as a function of y_0 on S.
(4) Investigate the 3D contour plot and set a filter such that most of the local extrema are remained in the picture.

Now, we further give some numerical examples to illustrate some performance of the above algorithm. The obstacles used in the numerical experiments are shown in Fig. 2, where the ball has radius $\rho=1.5$, and we direct readers to Refs. 15 and 21 for the parametric representations of the other obstacle surfaces.

We first consider the numerical experiments for simply connected obstacles. In Fig. 3, we illustrate the reconstructions for three simply connected obstacles which are the sound soft cloverleaf, the sound hard corrugated ellipsoid, and the sound impedance ellipsoid, respectively. The results reveal that no matter how the total field satisfies a type of boundary condition on the surface of these scatterers, the algorithm can yield a reasonably good image of the obstacle. And the results further show that a satisfactory reconstruction can also be obtained even when the incident and observation apertures are as small as the upper quarter of the unit sphere. However, a less accurate reconstruction is obtained for smaller incident and observation apertures. Physically

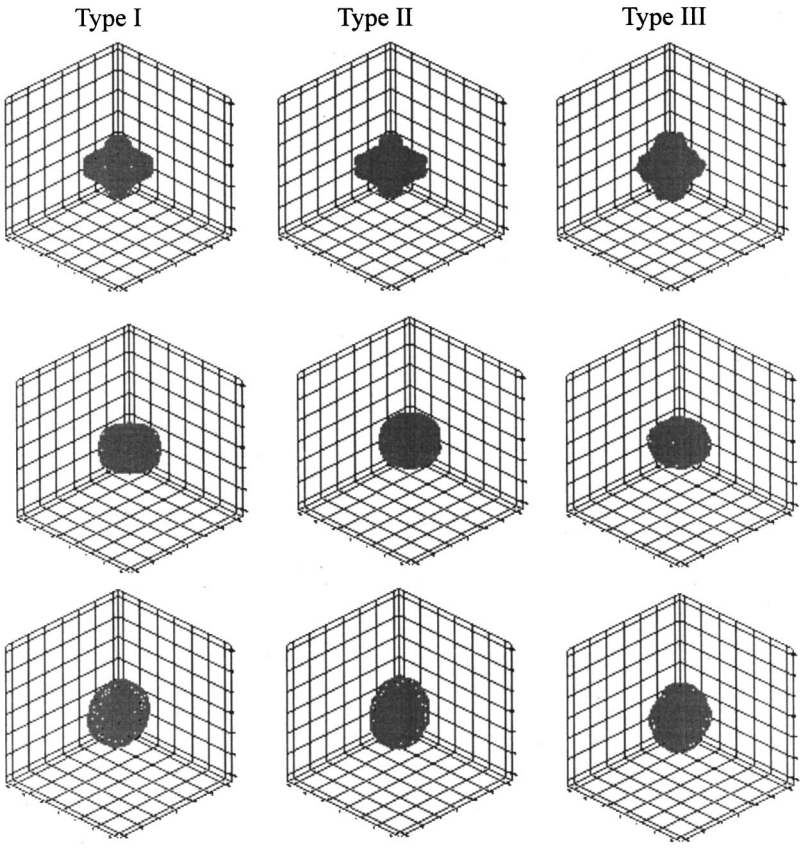

FIG. 3. Reconstructions of simply connected obstacles. Top row: reconstruction of a sound soft cloverleaf; middle row: reconstruction of a sound hard corrugated ellipsoid; lower row: reconstruction of a sound impedance ellipsoid.

this is explained by the fact that the information available from the shadow region decreases if the incident and observation apertures decrease. On the other hand, we find that as the incident and observation apertures decrease, the singular values of the matrix A decrease rapidly. This observation reveals that for small incident and observation apertures the linear system (24) becomes severely ill-conditioned so that the use of a regularization procedure such as Tikhonov regularization to solve (24) becomes insufficient to cure the ill-posedness.

In the next examples we consider the reconstructions of disconnected obstacles. In order to state these results economically, we restrict ourselves to type I numerical experiments. We perform two types of numerical experiments: (1) the total field only satisfies one of the boundary conditions (4)–(6) on the boundary of each component; (2) the total field may satisfy different boundary conditions on each boundary. The disconnected obstacles used in type1 are: (a) three disjoint sound soft pseudo-Apollos; (b) two disjoint sound hard balls; (c) two disjoint sound impedance oblate ellipsoids. Reconstructions for these disconnected obstacles are shown in Fig. 4. The disconnected obstacles used in type 2 are: (a) a sound soft pseudo-Apollo and a sound hard oblate ellipsoid; (b) a sound hard ball and a sound impedance oblate ellipsoid; (c) a sound soft pseudo-Apollo, a sound hard ball, and a sound impedance one. Figure 5 shows the reconstructions for these disconnected obstacles. In all these examples, we succeed in determining both the number of components of these disconnected obstacles and a reasonably satisfactory shape of each component no matter how the total field satisfies a type of boundary condition on each boundary.

III. SUMMARY

A numerical method is presented for solving the inverse problem of reconstructing the shape of multiple three-dimensional objects from the limited aperture far-field data, which is based on using the 3D contour plot of a spatially dependent function which has noticeable different values in-

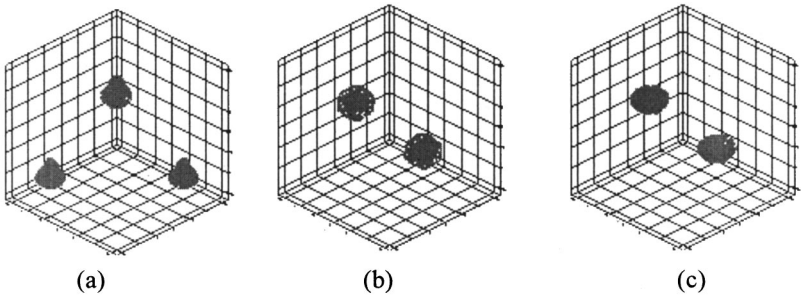

FIG. 4. Reconstructions of multiple obstacles with the same boundary conditions. (a): reconstruction of three sound soft acorns; (b): reconstruction of two sound hard balls; (c): reconstruction of two sound impedance oblate ellipsoid.

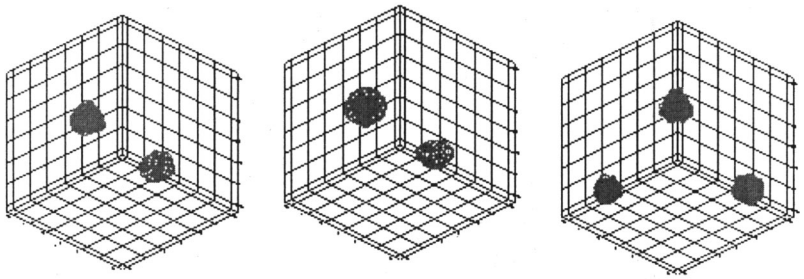

FIG. 5. Reconstructions of multiple obstacles with the different boundary conditions. (a): reconstruction of a sound soft pseudo-Apollo and a sound hard oblate ellipsoid; (b): reconstruction of a sound hard ball and a sound impedance oblate ellipsoid; (c): reconstruction of a sound soft pseudo-Apollo, a sound hard ball (left) and a sound impedance ball (right).

side and outside the obstacle as a visualization of the obstacle. The approach has several features which are of importance for diverse areas of technology and engineering. The first feature is that it is very simple and rapid since it only requires the solution of a linear system. In particular, each solution computation of the linear system is independent of any other solution, and hence the solution computation of the linear system can be carried out in parallel trivially. The second feature is that it does not require any prior information about the geometry of the scatterers (e.g., the number of components and a rough idea of each component), nor does it presuppose knowledge of the surface boundary conditions of each component. The final feature is that it requires only the information of the far-field pattern for a finite number of directions of incidence and observation distributed over a limited range. This scheme has been shown to be efficient and robust by reconstructing a number of scatterers having a variety of shapes and boundary conditions. These numerical results reveal that this method can handle reconstructions of disconnected obstacles without difficulty even if the total field satisfies different boundary conditions on the surface of each component. Furthermore, a reasonably good reconstruction is possible even when the incident and observation apertures are as small as the upper quarter of the unit sphere.

ACKNOWLEDGMENT

This work was supported by the National Natural science Foundation of China.

[1] M. Bertero and E. R. Pike, *Inverse Problems in Scattering and Imaging* (Hilger, New York, 1984).
[2] *Inverse Problems: An Interdisciplinary Study*, edited by P. C. Sabatie (Academic, London, 1987).
[3] D. Colton and R. Kress, *Inverse Acoustic and Electromagnetic Scattering Theory* (Springer, Berlin, 1992).
[4] N. N. Bojarski, ''A survey of the physical optics inverse scattering identity,'' IEEE Trans. Antennas Propag. **AP-30**, 980–989 (1982).
[5] A. Charalambopoulos and G. Dassios, ''Inverse scattering via low-frequency moments,'' J. Math. Phys. **3**, 4206–4216 (1992).
[6] Y. Amaoudov, G. Dassios, and V. Georgiev, ''High-frequency asymptotic in inverse scattering by ellipsoids,'' Math. Mech. Appl. Sci. **16**, 1–12 (1993).
[7] R. J. Lucas, ''An inverse problem in low-frequency scattering by a rigid ellipsoid,'' J. Acoust. Soc. Am. **95**, 2330–2333 (1994).
[8] A. Roger, ''Newton-Kantorovich algorithm applied to an electromagnetic inverse problem,'' IEEE Trans. Antennas Propag. **AP-29**, 232–238 (1981).
[9] A. Boström, ''The null-field approach in series form—The direct and inverse problems,'' J. Acoust. Soc. Am. **79**, 1223–1229 (1986).
[10] A. Kirsch, ''The domain derivative and two applications in inverse scattering theory,'' Inverse Probl. **9**, 81–96 (1993).
[11] L. Monch, ''A Newton method for solving the inverse scattering problem for a sound-hard obstacle,'' Inverse Probl. **12**, 309–323 (1996).
[12] T. Scotti and A. Wirgin, ''Shape reconstruction of an impenetrable scattering body via the Raleigh hypothesis,'' Inverse Probl. **12**, 1027–1055 (1996).
[13] L. S. Couchman, ''Inverse Neumann obstacle problem,'' J. Acoust. Soc. Am. **104**, 2615–2621 (1998).
[14] D. Colton and P. Monk, ''A novel method for solving inverse scattering problem for time-harmonic acoustic waves in the resonance region II,'' SIAM (Soc. Ind. Appl. Math.) J. Appl. Math. **46**, 506–523 (1986).
[15] D. Colton and P. Monk, ''The numerical solution of the three-dimensional inverse scattering problem for time harmonic acoustic waves,'' SIAM (Soc. Ind. Appl. Math.) J. Sci. Stat. Comput. **8**(3), 278–291 (1987).
[16] A. Kirsch and R. Kress, ''An optimization method in inverse acoustic scattering problem,'' in *Boundary Elements IX, Fluid Flow and Potential Applications*, edited by C.A. Brebbia *et al.* (Springer, Berlin, 1987), Vol. 3, pp. 3–18.
[17] T. S. Angell, R. E. Kleinman, B. Kok, and G. F. Roach, ''Target reconstruction from scattered far field data,'' Ann. Telecommun. **44**, 456–463 (1989).
[18] D. S. Jones and X. Q. Mao, ''The inverse problem in hard acoustic scattering,'' Inverse Probl. **5**, 731–748 (1989).
[19] D. S. Jones and X. Q. Mao, ''A method for solving the inverse problem in soft acoustic scattering problem,'' IMA J. Appl. Math. **44**, 127–143 (1990).
[20] R. Kress and A. Zinn, ''On the numerical solution of the three-dimensional inverse obstacle scattering problem,'' J. Comput. Appl. Math. **42**, 49–61 (1992).
[21] L. Misici and F. Zirilli, ''Three-dimensional inverse obstacle scattering for time harmonic acoustic waves: A numerical method,'' SIAM (Soc. Ind. Appl. Math.) J. Sci. Stat. Comput. **15**(3), 1174–1189 (1994).
[22] T. S. Angell, W. C. Jiang, and R. E. Kleinman, ''A distributed source method for inverse acoustic scattering,'' Inverse Probl. **2**, 531–544 (1997).
[23] D. Colton and A. Kirsch, ''A simple method for solving inverse scattering problems in the resonance region,'' Inverse Probl. **12**, 383–393 (1996).
[24] D. Colton, M. Piana, and R. Potthast, ''A simple method using Morozov's discrepancy principle for solving inverse scattering problems,'' Inverse Probl. **13**, 1477–1493 (1997).
[25] A Kirsch, ''Characterization of the shape the scattering obstacle by the spectral data of the far field operator,'' Inverse Probl. **14**, 1489–1512 (1998).
[26] D. Colton, K. Giebermann, and P. Monk, ''A regularized sampling method for solving three dimensional inverse scattering problems,'' http://www.wissrech.iam.uni-bonn.de/people/gieberma.html.
[27] R. Potthast, ''A fast new method to solve inverse scattering problems,'' Inverse Probl. **12**, 731–742 (1996).
[28] A. N. Norris, ''A direct inverse scattering method for imaging obstacle with unknown surface conditions,'' IMA J. Appl. Math. **61**, 267–290 (1998).
[29] C. W. Groetsch, *The Theory of Tikhonov Regularization for Fredholm Equations of the First Kind* (Pitman, Boston, 1984).
[30] P. M. Van den Berg and J. T. Fokkema, ''The Rayleigh hypothesis in the theory of diffraction by a cylindrical obstacle,'' IEEE Trans. Antennas Propag. **AP-27**, 577–583 (1979).

Exact solutions to one-dimensional acoustic fields with temperature gradient and mean flow

B. Karthik, B. Manoj Kumar, and R. I. Sujith
Department of Aerospace Engineering, Indian Institute of Technology, Madras 600036, India

(Received 1 March 1998; accepted for publication 17 March 2000)

An exact solution for one-dimensional acoustic fields in ducts in the presence of an axial mean temperature gradient and mean flow is presented in this paper. The analysis is valid for mean Mach numbers such that the square of the mean Mach number is much less than one. The one-dimensional wave equation for ducts with axial mean temperature gradient and mean flow is derived. By appropriate transformations, the wave equation is reduced to an analytically solvable hypergeometric differential equation for the case of a linear mean temperature profile. The developed solution is applied to investigate the dependence of sound propagation in a duct on factors such as temperature gradient and mean flow. The results obtained using the analytical solution compare very well with the numerical results. The developed solution is also compared with an existing analytical solution. © *2000 Acoustical Society of America.*
[S0001-4966(00)05206-1]

PACS numbers: 43.20.Mv, 43.50.Yw [DEC]

NOMENCLATURE

a, b, c	arguments of hypergeometric function
C_1, C_2	constants of integration in Eqs. (17)
F	hypergeometric function
i	$\sqrt{-1}$, imaginary number
k	wave number in Eq. (19)
m	steady mass flow rate (kg/m^2/s)
M	Mach number
p	pressure (Pa)
P	acoustic pressure (Pa)
R	specific gas constant (J/kg/K)
s	transformation variable in Eq. (15)
t	time (s)
T	temperature (K)
u	velocity (m/s)
U	acoustic velocity (m/s)
x	axial distance (m)
κ	temperature gradient (K/m)
ρ	density (kg/m^3)
ψ	digamma function
ω	angular frequency (rad/sec)

Superscripts

$'$	oscillating quantity
$-$	time-averaged quantity
$*$	complex conjugate

INTRODUCTION

This paper describes exact analytical solutions for sound propagation in ducts in the presence of mean flow and mean temperature gradient. The behavior of one-dimensional acoustic fields in ducts is a problem of considerable scientific and practical interest. For instance, there is a need to develop an understanding of the manner in which a mean axial temperature gradient (caused, for example, by heat transfer to or from the walls) in the presence of mean flow affects the propagation of sound waves and the stability of small amplitude disturbances in a duct. Such understanding will improve existing capabilities for controlling combustion instabilities in propulsion and power generating systems, designing pulse combustors and automotive mufflers, analyzing the behavior of resonating thermal systems, and measuring impedances of high temperature systems (e.g., flames). These results can also be used to analyze the propagation of sound waves in catalytic converters.

The behavior of one-dimensional waves in ducts with an axial temperature gradient is described by the solutions of a second order wave equation with variable coefficients by Cummings[1] and Peat.[2] Cummings[1] has developed an approximate, semianalytical solution for ducts with axial mean temperature gradients in the absence of mean flow which is valid at sufficiently high frequencies. He used a slight variation of the Wentzel–Kramers–Brillouin (WKB) method to obtain the approximate solution of the wave equation with variable coefficients. Peat[2] and Munjal and Prasad[3] have developed exact solutions for ducts with small temperature gradients, in the presence of mean flow. Kapur *et al.*[4] obtained numerical solutions for sound propagation in ducts with axial temperature gradients, in the absence of mean flow, by integrating the wave equation using a Runge–Kutta method. The same approach was followed by Zinn and co-workers (Salikuddin and Zinn;[5] Baum *et al.*;[6] Meyer *et al.*;[7] Zinn and Narayanasami;[8] Matta and Zinn[9]), who developed the impedance tube technique for high temperature systems, in the presence of mean flow. Sujith *et al.*[10–12] have found exact solutions for acoustic waves in ducts which are valid even in the presence of large temperature gradients, in the absence of

mean flow. Cherng and Na[13] have developed an analytical method for the determination of the required shape of a duct for a prescribed sound pressure level distribution in the presence of an unsteady isentropic flow. Munjal and Doige[14] have adapted the two-microphone method for sound propagation in the presence of mean flow and acoustic damping.

While the numerical solutions are accurate, they often do not provide adequate insight and feel for the physics of the problem. Analytical solutions can also be used to benchmark numerical results. Hence it is desirable to obtain analytical solutions. The analytical solutions currently in use, developed by Peat,[2] are applicable only for the case of small temperature gradients. Large temperature gradients exist in pulse combustor tail pipes and also in impedance tube experiments involving high temperature flames (Salikuddin and Zinn;[5] Baum *et al.*;[6] Meyer *et al.*;[7] Zinn and Narayanasami;[8] Matta and Zinn[9]). Therefore, in this investigation, an attempt was made to obtain an analytical solution for sound propagation in ducts with mean flow and arbitrarily large mean temperature gradients.

A derivation of the exact solution that describes the behavior of one-dimensional oscillations in a duct with a mean temperature gradient and mean flow is outlined in this paper. First, the one-dimensional wave equation for a constant area duct with an arbitrary axial temperature gradient and mean flow is derived for a perfect, inviscid and non-heat-conducting gas. Next, assuming periodic solutions, the derived wave equation is reduced to a second order wave equation with variable coefficients. Using appropriate transformations, this second order wave equation is then reduced to a hypergeometric equation for the case of a linear mean temperature profile. The analysis is valid for mean Mach numbers such that the square of the mean Mach number is much less than one.

I. DERIVATION OF THE WAVE EQUATION AND ITS SOLUTION

The derivation of the wave equation for a constant area duct with a mean temperature gradient and mean flow is presented in this section. Assuming a perfect, inviscid and non-heat-conducting gas, the one-dimensional momentum, energy (Culick[15]) and state equations can be expressed in the following form:

Momentum:

$$\rho \frac{\partial u}{\partial t} + \rho u \frac{\partial u}{\partial x} + \frac{\partial p}{\partial x} = 0, \tag{1}$$

Energy:

$$\frac{\partial p}{\partial t} + u \frac{\partial p}{\partial x} + \gamma p \frac{\partial u}{\partial x} = 0, \tag{2}$$

State:

$$p = \rho R T. \tag{3}$$

Expressing each of the dependent variables as the sums of steady and time dependent, small amplitude solutions,

$$\begin{aligned} \rho(x,t) &= \overline{\rho}(x) + \rho'(x,t), \\ p(x,t) &= \overline{p}(x) + p'(x,t), \\ u(x,t) &= \overline{u}(x) + u'(x,t), \end{aligned} \tag{4}$$

and substituting these expressions into the conservation equations yield the systems of steady equations and wave equations. Assuming that the square of the mean flow Mach number is smaller than 0.1 (which means $M<0.3$ or $\overline{u} = 100$ m/s at ambient temperature), the solution of the steady momentum equation shows that the mean pressure, $\overline{p}$, is constant in the duct (see Appendix A for proof).

The first order acoustic momentum and energy equations can then be reduced to

$$\overline{\rho}\frac{\partial u'}{\partial t} + \overline{\rho} u' \frac{d\overline{u}}{dx} + \overline{\rho u}\frac{\partial u'}{\partial x} + \frac{\partial p'}{\partial x} = 0, \tag{5}$$

$$\frac{\partial p'}{\partial t} + \overline{u}\frac{\partial p'}{\partial x} + \gamma \overline{p}\frac{\partial u'}{\partial x} + \gamma p' \frac{d\overline{u}}{dx} = 0. \tag{6}$$

The justification for neglecting the term $\rho' \overline{u}(d\overline{u}/dx)$ is given in Appendix B.

Assuming that the solution has a harmonic time dependence [i.e., $p'(x,t) = P(x)e^{i\omega t}$ and $u'(x,t) = U(x)e^{i\omega t}$], Eqs. (5) and (6) reduce to

$$\left[i\omega + \frac{d\overline{u}}{dx} \right] U + \frac{1}{\overline{\rho}}\frac{dP}{dx} + \overline{u}\frac{dU}{dx} = 0, \tag{7}$$

$$\left[i\omega + \gamma \frac{d\overline{u}}{dx} \right] P + \overline{u}\frac{dP}{dx} + \gamma \overline{p}\frac{dU}{dx} = 0. \tag{8}$$

Combining Eqs. (7) and (8) by eliminating U and its derivative yields the following second order ordinary differential equation with variable coefficients:

$$\begin{aligned} &\left[\frac{\overline{u}^2}{\gamma \overline{p}} - \frac{1}{\overline{\rho}} \right] \frac{d^2P}{dx^2} + \left[\left(\frac{3}{\gamma} + 1 \right) \frac{\overline{u}}{\overline{p}} \frac{d\overline{u}}{dx} + \frac{1}{\overline{\rho}^2} \frac{\partial \overline{\rho}}{\partial x} + \frac{2\overline{u}\omega}{\gamma \overline{p}} i \right] \frac{dP}{dx} \\ &+ \left[\left(\frac{2}{\gamma} + 1 \right) \frac{\omega}{\overline{p}} \frac{d\overline{u}}{dx} + \frac{2}{\overline{p}} \left(\frac{d\overline{u}}{dx} \right)^2 - \frac{\omega^2}{\gamma \overline{p}} \right] P = 0. \end{aligned} \tag{9}$$

The steady state equation of continuity can be represented as

$$m = \overline{\rho u} \quad (\text{constant}). \tag{10}$$

Using Eq. (10) and the equation of state, i.e., Eq. (3), Eq. (9) becomes

$$\begin{aligned} &\left[\frac{m^2 R^2 \overline{T}^2}{\gamma \overline{p}^3} - \frac{R\overline{T}}{\overline{p}} \right] \frac{d^2P}{dx^2} + \left[\left(\frac{3}{\gamma} + 1 \right) \frac{m^2 R^2 \overline{T}}{\overline{p}^3} \frac{d\overline{T}}{dx} - \frac{R}{\overline{p}} \frac{d\overline{T}}{dx} \right. \\ &\left. + \frac{2mR\overline{T}\omega}{\gamma \overline{p}^2} i \right] \frac{dP}{dx} + \left[\left(\frac{2}{\gamma} + 1 \right) \frac{mR\omega}{\overline{p}^2} \frac{d\overline{T}}{dx} \right. \\ &\left. + \frac{2m^2R^2}{\overline{p}^3} \left(\frac{d\overline{T}}{dx} \right)^2 - \frac{\omega^2}{\gamma \overline{p}} \right] P = 0. \end{aligned} \tag{11}$$

Equation (11) has variable coefficients. Therefore, exact solutions of this equation for a general mean temperature

profile $\overline{T}(x)$ cannot be obtained. Assuming that the mean temperature profile is known, Eq. (11) is transformed from the x space to the $\overline{T}(x)$ space, yielding the following differential equation:

$$\left[\frac{m^2R^2\overline{T}^2}{\gamma\overline{p}^3}-\frac{R\overline{T}}{\overline{p}}\right]\left[\left(\frac{d\overline{T}}{dx}\right)^2\frac{d^2P}{d\overline{T}^2}+\frac{d^2\overline{T}}{dx^2}\frac{dP}{d\overline{T}}\right]$$
$$+\left[\left(\frac{3}{\gamma}+1\right)\frac{m^2R^2\overline{T}}{\overline{p}^3}\frac{d\overline{T}}{dx}-\frac{R}{\overline{p}}\frac{d\overline{T}}{dx}+\frac{2mR\overline{T}\omega}{\gamma\overline{p}^2}i\right]$$
$$\times\left(\frac{d\overline{T}}{dx}\right)\frac{dP}{d\overline{T}}+\left[\left(\frac{2}{\gamma}+1\right)\frac{mR\omega}{\overline{p}^2}\frac{d\overline{T}}{dx}\right.$$
$$\left.+\frac{2m^2R^2}{\overline{p}^3}\left(\frac{d\overline{T}}{dx}\right)^2-\frac{\omega^2}{\gamma\overline{p}}\right]P=0. \tag{12}$$

In order to solve Eq. (12), the temperature profile, $\overline{T}(x)$, whose shape depends on the physics of the problem, must be known. However, the equation reduces to a standard differential equation only for a linear temperature distribution.

A linear mean temperature distribution is given by the expression

$$\overline{T}=T_0+\kappa x, \tag{13}$$

where T_0 and κ are constants that describe the temperature at $x=0$ and the mean temperature gradient, respectively. Using Eq. (13), Eq. (12) reduces to the following form:

$$\left[\frac{m^2R^2\overline{T}^2}{\gamma\overline{p}^3}-\frac{R\overline{T}}{\overline{p}}\right]\frac{d^2P}{d\overline{T}^2}+\left[\left(\frac{3}{\gamma}+1\right)\frac{m^2R^2\overline{T}}{\overline{p}^3}-\frac{R}{\overline{p}}\right.$$
$$\left.+\frac{2mR\overline{T}\omega}{\gamma\overline{p}^2\kappa}i\right]\frac{dP}{d\overline{T}}+\left[\left(\frac{2}{\gamma}+1\right)\frac{mR\omega}{\overline{p}^2\kappa}+\frac{2m^2R^2}{\overline{p}^3}\right.$$
$$\left.-\frac{\omega^2}{\gamma\overline{p}\kappa^2}\right]P=0. \tag{14}$$

To further simplify the preceding equation, a new independent variable s is introduced such that

$$s=\frac{m^2R}{\gamma\overline{p}^2}\overline{T}, \tag{15}$$

where $s=M^2$, M being the local Mach number.

Transforming Eq. (14) from the $\overline{T}$ to s space yields the following ordinary differential equation:

$$s(1-s)\frac{d^2P}{ds^2}+\left(1-s\left((3+\gamma)+\frac{2\omega\overline{p}}{m\kappa R}i\right)\right)\frac{dP}{ds}$$
$$+\left(\left(2\gamma-\frac{\omega^2\overline{p}^2}{\kappa^2m^2R^2}\right)+(2+\gamma)\frac{\omega\overline{p}}{\kappa mR}i\right)P=0. \tag{16}$$

The preceding equation is a hypergeometric differential equation whose solution is given by (Humi and Miller;[16] Abramowitz and Stegun;[17] Lebedev[18])

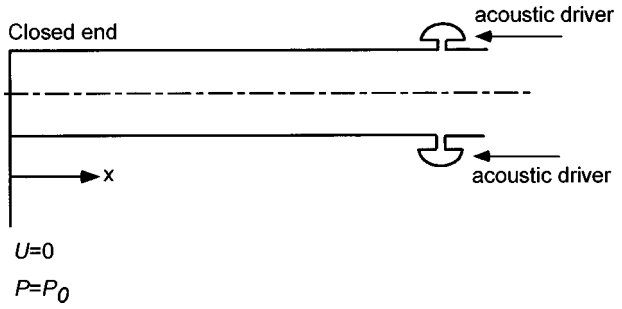

FIG. 1. Coordinate system with the imposed boundary condition.

$$P=C_1F(a,b;c,s)+C_2[F(a,b;c,s)\ln s$$
$$+\sum_{n=1}^{n=\infty}\frac{(a)_n(b)_n}{(c)_nn!}s^n[\psi(a+n)-\psi(a)+\psi(b+n)$$
$$-\psi(b)-2\psi(n+1)-2\psi(1)]], \tag{17}$$

where C_1 and C_2 are arbitrary constants.

Using Eqs. (7), (8) and (10), the expression for the acoustic velocity becomes

$$U=\frac{1}{\left(\frac{mR\kappa}{\overline{p}}+i\omega\right)}\left[s\left(\frac{\gamma R\kappa}{\overline{p}}+i\omega\right)P\right.$$
$$\left.+\frac{sR\kappa}{\overline{p}}\left(\frac{m^2Rs}{\gamma\overline{p}}-1\right)\frac{dP}{ds}\right]. \tag{18}$$

Here the variables a, b, c are given by the following relations:

$$c=1,$$
$$a+b+1=3+\gamma+\frac{2\omega\overline{p}}{\kappa mR}i, \tag{19}$$
$$ab=2\gamma+\frac{\omega^2\overline{p}^2}{\kappa^2m^2R^2}+(2+\gamma)\frac{\omega\overline{p}}{\kappa mR}i,$$

where

$$F(a,b;c,s)=\sum_{n=1}^{n=\infty}\frac{(a)_n(b)_n}{(c)_nn!}s^n,$$
$$(a)_n=(a)(a+1)(a+2),\ldots,(a+n-2)(a+n-1),$$
$$\psi(z)=\frac{d}{dz}\ln(\Gamma(z)),$$
$$\psi(z+n)=\psi(z+1)+\sum_{n=1}^{n=i-1}\frac{1}{z+n},$$
$$\psi(z)=\psi(z+1)+\frac{1}{z},$$
$$\psi(n+1)=\psi(1)+\sum_{n=2}^{n=n}n^{-1},$$

$\psi(1)=-v$, which is the Euler's constant (0.577 215 664).

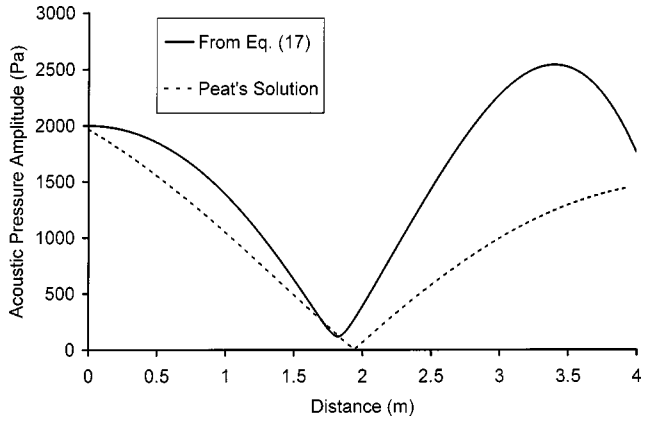

FIG. 2. Comparison of the analytical solution derived in this study and Peat's solutions of the acoustic pressure amplitude distribution in a duct closed at one end and open at the other end. Circular frequency, $\omega = 500$ rad/s, $\overline{u} = 15$ m/s, $\overline{T} = 1100 - 200x$ K.

A. Reduced general solutions

In this section it has been shown that under various simplifying conditions the general solution derived above reduces to established results.

In the absence of mean flow (i.e., $\overline{u} = 0 \Rightarrow m = 0$), Eq. (14) reduces to Eq. (10) of Sujith *et al.*[10]

$$\frac{d^2p}{d\overline{T}^2} + \left[\frac{1}{\overline{T}}\right]\frac{dp}{d\overline{T}} + \left[\frac{\omega^2/\kappa^2}{\gamma R\overline{T}}\right]p = 0. \tag{20}$$

In the absence of temperature gradient (i.e., $d\overline{T}/dx = 0 \Rightarrow \overline{\rho}$ = constant), Eq. (11) reduces to Eq. (3) of Prasad and Crocker,[19]

$$[1 - M^2]\frac{d^2p}{dx^2} - 2kM\omega i\frac{dp}{dx} + k^2p = 0, \tag{21}$$

where $k^2 = \omega^2/\gamma R\overline{T}$.

In the absence of a temperature gradient and of mean flow, Eq. (11) reduces to the classical Helmholtz equation,

$$\frac{d^2p}{dx^2} + k^2p = 0. \tag{22}$$

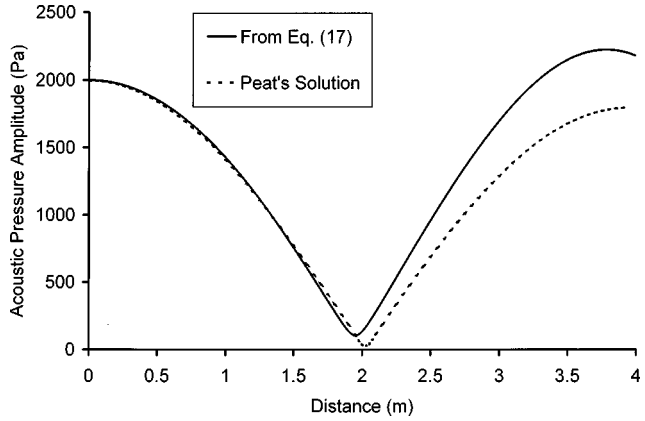

FIG. 3. Comparison of analytical solution derived in this study and Peat's solutions of the acoustic pressure amplitude distribution in a duct closed at one end and open at the other end. Circular frequency, $\omega = 500$ rad/s, $\overline{u} = 15$ m/s, $\overline{T} = 1100 - 100x$ K.

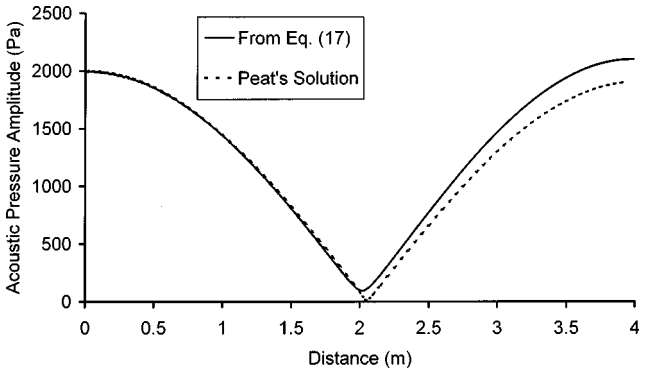

FIG. 4. Comparison of the analytical solution derived in this study and Peat's solutions of the acoustic pressure amplitude distribution in a duct closed at one end and open at the other end. Circular frequency, $\omega = 500$ rad/s, $\overline{u} = 15$ m/s, $\overline{T} = 1100 - 50x$ K.

II. ACOUSTIC BEHAVIOR OF A DUCT

In this section, the developed solution is applied to investigate sound propagation in a duct in the presence of mean flow and mean temperature gradient. The problem solved is a duct with an acoustically closed end and a linear temperature gradient and mean flow in which a standing wave pattern of a given frequency and amplitude is established using an acoustic driver at the other end. This is a scenario encountered while determining the admittances of burning solid propellant samples. The propellant sample is kept at the closed end of the impedance tube, and ignited. The propellant burns to give gaseous products. The flow of these gases will lead to the establishment of a mean flow in the duct. If the propellant burning rate does not respond to the acoustic oscillations, there will be no acoustic velocity fluctuations, i.e., the sample surface will behave like a hard termination. An acoustically hard termination can also be obtained by using a sintered plate, which will allow the passage of a mean flow, but would not allow acoustic oscillations.

The duct coordinate system is shown in Fig. 1. At the closed end of the duct the acoustic velocity $U = 0$, and the acoustic pressure $P = P_0$. Using these conditions, the value of the constants C_1 and C_2 found in Eq. (17) can be determined. In the calculations presented here P_0 was chosen as 2000 Pascals.

The effect of temperature gradient and mean flow upon the distributions of the amplitudes of the acoustic pressure and velocity is investigated. Using the relationships

$$|P|^2 = PP^*, \quad |U|^2 = UU^*,$$

where P^* and U^* are complex conjugates of P and U, respectively, the amplitude distributions for different values of κ are calculated.

To check the validity of the results, the same problem was solved numerically by integrating the original conservation equations using a fourth order Runge–Kutta scheme. The results were virtually identical; the difference between the results is too small to be observed on a plot.

The derived solution was compared with Peat's solution[2] for different axial mean temperature distributions. The axial mean temperature profiles were chosen as $\overline{T}$

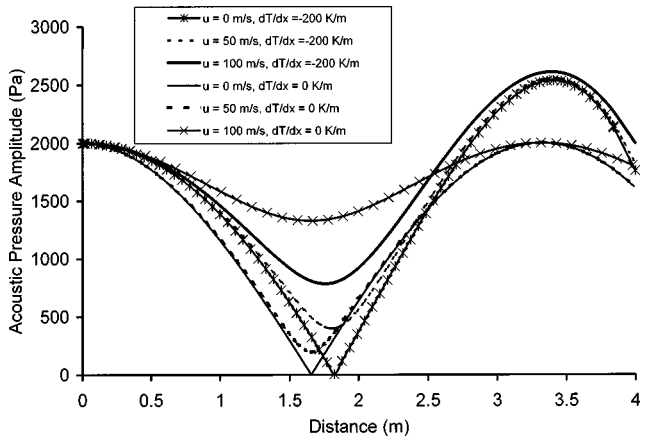

FIG. 5. The comparison of acoustic pressure amplitude with axial distance in a duct closed at one end and open at the other, for different mean velocities for a duct with a constant mean temperature of 700 K and for a duct with a mean temperature variation of $\overline{T}=1100-200x$ K. Circular frequency, $\omega=500$ rad/s.

$=1100-200x$, $\overline{T}=1100-100x$ and $\overline{T}=1100-50x$. The mean velocity at $x=0$ was chosen as 15 m/s. The circular frequency of the oscillations was 500 radians/s. The acoustic pressure amplitude distributions obtained using the analytical solution and the Peat's solution are compared in Figs. 2–4. Examination of these figures shows that Peat's solution and the derived solution match well for low temperature gradients. As the temperature gradient is increased, the derived solution deviates from Peat's solution.[2] It should be noted that the criteria given by Peat[2] are those for a mean temperature profile of the form $T_0=T_m(1-T_rx/a)$, $T_r\leqslant 0.1$. It can also be noted from these figures that the wavelength increases as the temperature in the duct increases.

The effect of temperature gradient with respect to zero temperature gradient is shown in Fig. 5 for different values of mean velocities. The solution used to calculate the variation of acoustic pressure amplitude for zero temperature gradient is from Prasad and Crocker.[19] Calculation for the zero temperature gradient was done for an average temperature of 700 K. Neglecting temperature gradient gives erroneous results, as can be observed in the figure. The location of the acoustic pressure minimas cannot be predicted correctly if the temperature gradient is not taken into account. It may also be seen that the values of the pressure maximas are not constant in the presence of a mean temperature gradient, whereas in the absence of a mean temperature gradient, the pressure maximas are constant.

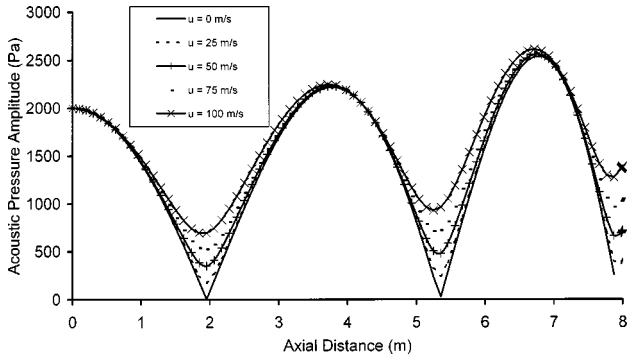

FIG. 6. The variation of acoustic pressure amplitude with axial distance in a duct closed at one end and open at the other, for different mean velocities. Circular frequency, $\omega=500$ rad/s, $\overline{T}=1100-100x$ K.

In pulse combustors, or impedance tube experiments to investigate the impedance of flames or propellant burning surfaces, temperature gradients of the order of -200 K/m are common. The solution derived in this investigation is valid for such arbitrarily large temperature gradients.

The axial variation of acoustic pressure amplitudes for different mean velocities for a mean temperature distribution of $\overline{T}=1100-100x$ is shown in Fig. 6. The circular frequency chosen was 500 radians/s as before. As expected, the minimums go up with the increase in mean velocity, indicating damping caused by mean flow. Table I shows the values of the acoustic pressure minimums and the standing wave ratio (SWR) as a function of the mean velocity at $x=0$ for temperature distributions of $\overline{T}=1100-100x$, $\overline{T}=1100-200x$ and for a constant temperature. It can be seen that there is a significant effect of mean flow on the acoustic pressure minimum and the standing wave ratios. Neglecting the effects of mean flow can therefore lead to significant errors in admittance determination, which is dependent on the standing wave ratio.

III. CONCLUSIONS

Exact solutions describing the behavior of one-dimensional acoustic waves in ducts in the presence of an axial temperature gradient and mean flow were obtained by applying suitable transformations to the wave equation. The analysis takes into account the presence of a mean flow but the solutions are valid only when the square of mean Mach numbers is very much smaller than one. This would correspond to Mach numbers less than 0.3 or velocities less than 100 m/s at ambient temperature. Solutions were obtained for

TABLE I. Acoustic pressure minimums and the standing wave ratio (SWR) as a function of the mean velocity at $x=0$.

	Temperature distribution					
	$\overline{T}=700$		$\overline{T}=1100-100x$		$\overline{T}=1100-200x$	
Mean velocity (m/s)	Acoustic pressure minimum (Pa)	SWR	Acoustic pressure minimum (Pa)	SWR	Acoustic pressure minimum (Pa)	SWR
0	0	0	0	0	0	0
50	194.3	0.10	348.6	0.17	399.2	0.2
100	1327.0	0.66	688.8	0.34	785.1	0.39

a duct with a linear mean temperature profile. The solution was applied to determine the effect of different mean flow velocities and mean temperature gradients on the acoustic oscillations in a duct. This solution is compared with an existing analytical solution. The developed solution is valid for arbitrarily large mean temperature gradients.

The solution obtained in this analysis is in terms of hypergeometric functions and is easy to evaluate. These closed form expressions presented herein can be used also as benchmarks for checking the results obtained from computer programs that are intended for applications for systems with axial mean temperature gradients and mean flow.

ACKNOWLEDGMENT

The authors wish to acknowledge Dr. B. T. Zinn, Regent's Professor at the Georgia Institute of Technology, for introducing them to this problem.

APPENDIX A

The one-dimensional momentum equation can be written as below,

$$\overline{\rho u}\frac{d\overline{u}}{dx}+\frac{d\overline{p}}{dx}=0. \tag{A1}$$

The steady state continuity equation is

$$\overline{\rho u}=\text{constant}. \tag{A2}$$

Combining (A1) and (A2), the momentum equation can be written as

$$\frac{d(\overline{\rho}\overline{u}^2+\overline{p})}{dx}=0\Rightarrow\overline{\rho}\overline{u}^2+\overline{p}=\text{constant}. \tag{A3}$$

Hence $\overline{p}(1+\gamma M^2)=\text{constant}$. Therefore, when $M\ll 1$, $\overline{p}\approx\text{constant}$.

APPENDIX B

The term under consideration, i.e., $\rho'\overline{u}(d\overline{u}/dx)$, is compared with another term in the momentum equation $(\partial p'/\partial x)$. Nondimensionalizing ρ' by $\rho'_{\max}$, $\overline{u}$ with $\overline{u}_{\max}$, x by λ and p' by $p'_{\max}$, the former term becomes $(\rho'_{\max}\overline{u}^2_{\max}/\lambda)\tilde{\rho}'\tilde{u}(d\tilde{u}/d\tilde{x})$, and the latter becomes $(P'_{\max}/\lambda)\times(\partial\tilde{p}'/\partial\tilde{x})$, where $\sim$ denotes the nondimensional quantity.

Considering the ratio of the orders of magnitude,

$$\frac{\rho'_{\max}\overline{u}^2_{\max}}{\lambda}\Bigg/\frac{p'_{\max}}{\lambda}=\frac{\rho'_{\max}}{p'_{\max}}\overline{u}^2_{\max}=\frac{1}{c^2}\overline{u}^2_{\max}=M^2_{\max}.$$

$M^2_{\max}$ was assumed to be much less than 1. Hence the term in the numerator is much smaller than that term in the denominator and was neglected.

[1] A. Cummings, ''Ducts with axial temperature gradients: An approximate solution for sound transmission and generation,'' J. Sound Vib. **51**, 55–67 (1977).
[2] K. S. Peat, ''The transfer matrix of a uniform duct with a linear temperature gradient,'' J. Sound Vib. **123**, 43–53 (1988).
[3] M. L. Munjal and M. G. Prasad, ''On plane-wave propagation in a uniform pipe in the presence of a mean flow and a temperature gradient,'' J. Acoust. Soc. Am. **80**, 1501–1506 (1986).
[4] A. Kapur, A. Cummings, and P. Mungur, ''Sound propagation in a combustion can with axial temperature and density gradients,'' J. Sound Vib. **25**, 129–138 (1972).
[5] M. Salikuddin and B. T. Zinn, ''Adaptation of impedance tube technique for the measurement of combustion process admittances,'' J. Sound Vib. **68**, 119–132 (1980).
[6] J. D. Baum, B. R. Daniel, and B. T. Zinn, ''Determination of solid propellant admittance by the impedance tube technique,'' AIAA Paper No. 80-0281 (1980).
[7] L. Meyer, B. R. Daniel, and B. T. Zinn, ''Acoustic radiation from axisymmetric ducts: A comparison of theory and experiment,'' AIAA Paper No. 80-0097 (1981).
[8] B. T. Zinn and L. Narayanasami, ''Application of impedance tube technique in the measurement of driving provided by solid propellants during combustion instabilities,'' Acta Astron. **9**, 303–315 (1982).
[9] L. M. Matta and B. T. Zinn, ''Theoretical study of flow turning losses in the presence of temperature gradients,'' AIAA Paper No. 94-0099 (1994).
[10] R. I. Sujith, G. A. Waldherr, and B. T. Zinn, ''An exact solution for one-dimensional acoustic fields in ducts with an axial temperature gradient,'' J. Sound Vib. **184**, 389–402 (1995).
[11] B. Manoj Kumar and R. I. Sujith, ''Exact solution for one-dimensional acoustic fields in ducts with a quadratic mean temperature profile,'' J. Acoust. Soc. Am. **101**, 3798–3799 (1997).
[12] B. Manoj Kumar and R. I. Sujith, ''Exact solution for one-dimensional acoustic fields in ducts with polynomial temperature profiles,'' Trans. ASME, J. Vib. Acoust. **120**, 965–969 (1998).
[13] G. Cherng and T. Y. Na, ''Unsteady isentropic flow through ducts with prescribed sound pressure level distribution,'' Trans. ASME, J. Vib. Acoust. **117**, 279–284 (1995).
[14] M. L. Munjal and A. G. Doige, ''The two microphone method incorporating the effects of mean flow and acoustic damping,'' J. Sound Vib. **137**, 135–138 (1990).
[15] F. E. C. Culick, ''Acoustic oscillations in solid propellant rocket chambers,'' Astronautica Acta **12**(2), 113–126 (1966).
[16] M. Humi and W. Miller, *Second Course in Ordinary Differential Equations for Scientists and Engineers* (Springer-Verlag, New York, 1988).
[17] M. Abramowitz and I. A. Stegun, *Handbook of Mathematical Functions with Formulas, Graphs, and Mathematical Tables* (Wiley, New York, 1972).
[18] N. Lebedeu, *Special Functions and Their Applications* (Dover, New York, 1972).
[19] M. G. Prasad and M. J. Crocker, ''Evaluation of four-pole parameters for a straight pipe with a mean flow and a linear temperature gradient,'' J. Acoust. Soc. Am. **69**, 916–921 (1981).

A rapid technique to determine the internal area function of finite-length ducts using maximum length sequence analysis

M. H. F. de Salis[a] and D. J. Oldham
Acoustics Research Unit, School of Architecture and Building Engineering, University of Liverpool, P.O. Box 147, Liverpool L69 3BX, United Kingdom

(Received 15 July 1999; accepted for publication 23 March 2000)

This paper describes a rapid technique for reconstruction of the internal area function of a duct using blockage-induced eigenvalue shifts determined from eigenfrequencies measured under two sets of duct termination boundary conditions. A single broad band maximum length sequence (MLS) measurement of short duration is utilized to obtain the transfer function of the duct, which in turn can be utilized to determine its eigenvalue shifts and subsequently its internal area function using an inverse perturbation technique. The reconstruction results display the same order of accuracy as those obtained previously using swept sine measurements of extended duration. An expression for the determination of the area function is presented utilizing resonant frequency information alone, thus rendering duct length determination unnecessary. A computational routine further simplifies the process such that the accuracy of the technique could be ascertained for a range of configurations including longer ducts and ducts that initially have nonuniform internal cross section over their length. Development of a relationship between obstacle length and wavelength of the lowest eigenfrequency required for successful reconstruction is also described. This is an important result for longer ducts where measurement of lower eigenfrequencies may present problems using standard measurement equipment.
[S0001-4966(00)00907-3]

PACS numbers: 43.20.Mv, 43.20.Ks [DEC]

INTRODUCTION

In situations where monitoring of the internal state of a duct or pipe is important, yet untenable using conventional visual techniques, a nonintrusive acoustical method for determination of the internal area function may be of interest. Wu and Fricke[1] have developed a means of monitoring the internal area function of a duct or pipe using acoustic measurements. The internal or blockage area function of the duct was determined using the blockage-induced eigenfrequency shifts measured in both a closed–closed and closed–open duct with excellent accuracy for small blockage perturbations. The technique built upon earlier work undertaken by Domis,[2] who had introduced the idea of a blockage detection technique using eigenfrequency shifts analysis with a view to application in nuclear cooling systems. Wu and Fricke[3] went on to develop Domis' work using blockage-induced eigenfrequency shifts in a closed–closed duct pipe to size an obstacle located close to one of the longitudinal terminations of the duct. The process used by Wu and Fricke[1] incorporated perturbation theory adapted from Bellman[4] and was similar to techniques developed by Schroeder[5] and Mermelstein[6] for use in the sizing of vocal tracts. The new technique, however, proved to be more applicable to the work in larger ducts and pipes[1] than to vocal tracts. This was due in part to the large amount of eigenfrequency shift information available below the cut-on frequency of the duct and also partly to do with difficulties experienced in accurately determining the glottis condition for use in the reconstruction of the vocal tract, as noted by Sondhi.[7]

However, Wu and Fricke's technique[1] was limited in practicality in two major areas. First, the measurement needed to be repeated four times, twice for the blockage-perturbed duct and twice for the unblocked duct to obtain the required two sets of eigenfrequency shifts. Second, the method of obtaining the duct eigenfrequency shifts using swept sine analysis was slow and laborious.

This paper addresses the problem of the extended process involved with the acquisition of the duct eigenfrequencies from which the blockage-induced eigenvalue shifts and subsequently the blockage reconstruction are processed. The following sections describe the use of maximum length sequence or MLS analysis[8,9] to obtain the impulse response of the duct system from a rapid broadband measurement. The frequency-transfer function of the duct may then be processed and the eigenfrequencies and subsequently the eigenvalues rapidly acquired. Using this technique, the eigenvalues of the blockage-perturbed and the unblocked duct may be rapidly acquired for the two sets of termination boundary conditions and the blockage reconstruction completed.

The transfer functions for the relatively short-duration broadband MLS measurements are of fairly coarse resolution when compared to those that can be obtained from a very slow swept sine analysis. In spite of this, the reconstructions are shown to be of high accuracy compared to those obtained using the exact eigenvalue shift solutions calculated from the theory. An expression is then developed that eliminates the need for duct-length evaluation by using the resonant frequency and the temperature-corrected speed of sound in air to build up the required reconstructed area function. The new technique using MLS analysis and a computational process-

[a]Electronic mail: m.de-salis@liv.ac.uk

ing routine for the measured frequency spectra allows rapid application of the technique to a number of different duct configurations, such as longer ducts of larger cross section and ducts that are initially nonuniform in cross section. Reconstructions excluding the lowest-order eigenvalue shifts are presented and used to establish that these are not necessarily the most important shifts for the reconstruction process. This is contrary to the previous findings of Wu and Fricke[1] and is an important result for the implementation of the technique in practice.

I. THEORY

The requirement for the reconstruction method used by Wu and Fricke[1] is to obtain the shifts in duct eigenvalue due to the introduction of a blockage under two sets of standard termination boundary conditions, namely the duct with closed–open and closed–closed terminations. Using an expression for the perturbed eigenfunction and eigenvalue described in Bellman[4] and substituting it into the classic Webster's horn equation for a one-dimensional lossless tract, Wu and Fricke obtained a solution for the blockage area function $A_b(x)$ as a function of the blockage-induced eigenvalue shifts in the closed–open and the closed–closed duct,[1]

$$\frac{A_b(x)}{A_0(x)}=\left[1-\exp\left(1-\sum_{n=1}\left[\frac{L}{n\pi}\right]^2\delta_n \times\cos\left(\frac{2n\pi x}{L}\right)-\sum_{n=1}\left[\frac{2L_e}{(2n-1)\pi}\right]^2\chi_n \times\cos\left(\frac{(2n-1)\pi x}{L_e}\right)-a_0\right)\right], \tag{1}$$

where $A_b(x)$ is the blockage cross-sectional area function within the duct, $A_0(x)$ is the unblocked area of the duct, δ_n is the nth order eigenvalue shift of the closed–closed duct due to blockage perturbation, χ_n is the nth order eigenvalue shift of the closed–open duct due to blockage perturbation, L is the geometric duct length for the closed–closed duct, L_e is the end-corrected duct length for the closed–open duct, and a_0 is a dc component proportional to the size of the blockage and inversely proportional to the length of the duct.

The closed–closed duct eigenvalue shift due to blockage perturbation δ_n and the corresponding closed–open shift χ_n are expressed as

$$\delta_n=\frac{4\pi^2(f_{\mathrm{nccp}}^2-f_{\mathrm{ncc}}^2)}{c^2}, \tag{2}$$

and

$$\chi_n=\frac{4\pi^2(f_{\mathrm{ncop}}^2-f_{\mathrm{nco}}^2)}{c^2}, \tag{3}$$

where f_{nccp} and f_{ncop} are the blockage-perturbed closed–closed and closed–open duct resonant frequencies and f_{ncc} and f_{nco} are the unperturbed closed–closed and closed–open duct resonant frequencies, respectively. The two sets of eigenvalue shifts are required to obtain the complete expansion of the unique blockage area function in Eq. (1). Blockage functions that are asymmetrical about the longitudinal midpoint of the duct may be obtained using the closed–open shifts χ_n alone, while symmetrical functions may be obtained using the closed–closed shifts δ_n alone. Wu[10] has proposed a technique using closed–open shifts χ_n alone, thus eliminating the need to determine a second set of eigenfrequencies. However, application of this technique is limited to blockage area functions with no symmetry about the midpoint of the duct due to nonuniqueness of the solution using a single set of eigenfrequencies. Reconstructions have been successfully achieved by the authors using eigenfrequency and antiresonant frequency shifts measured under one set of boundary conditions, i.e., in the closed–open duct alone.[11]

Wu and Fricke[1] found mode-order identification to be difficult above the initial transverse modal cut-on frequency of the duct, so only shifts in longitudinal mode eigenfrequencies below the cut-on frequency were used in the reconstructions. The accuracy of the method was found to increase with the number of eigenvalue shifts incorporated from the fundamental inclusive up to the cut-on limit. To give an idea of the limitations imposed by the cut-on frequency limit, it was noted that when the wavelength of the Nth duct eigenfrequency was equal to twice the blockage length then the first N eigenfrequency shifts would be required to give an accurate reconstruction of the blockage. This roughly limits the method to blockages larger than the diameter or longest cross dimension of the duct. In addition to this, the lower-order eigenvalue shifts were deemed to be the most crucial to the success of the reconstruction. The perturbation theory used to derive Eq. (1) was found to be valid for blockage area to duct area ratios $b\leqslant 0.5$.[1]

To get an idea of the maximum possible accuracy using Wu and Fricke's analysis,[1] a numerical analysis may be performed on a hypothetical duct internal area function $A(x)=A_0-A_b(x)$. Rearranging Eq. (1), the nth-order blockage-induced eigenvalue shift for a duct of uniform cross-sectional area $A_0(x)$ over its length L and with imposed blockage area function $Ab(x)$ may be expressed for the closed–closed duct as follows:

$$\delta_n=-\left[\frac{n\pi}{L}\right]^2\int_0^L \ln A(x)\cos\left(\frac{2n\pi x}{L}\right)dx, \tag{4}$$

and for the closed-open duct

$$\chi_n=-\left[\frac{(2n-1)\pi}{2L}\right]^2\int_0^L \ln A(x) \times\cos\left(\frac{(2n-1)\pi x}{L}\right)dx, \tag{5}$$

where $A(x)=A_0(x)-A_b(x)$.

Inserting these solutions back into Eq. (1) gives the reconstructed blockage area function $A_b(x)$. Using the first 23 eigenfrequency and subsequent eigenvalue shifts which were available to Wu and Fricke[1] below the cut-on frequency of the 2-m-long 0.1-m-diameter duct gives the reconstructed blockage area function for a typical blockage as shown in Fig. 1. This reconstruction from the prediction of the exact solutions shows the highest degree of accuracy possible using the available eigenfrequency shifts. The results attained by Wu and Fricke using high-frequency resolution swept

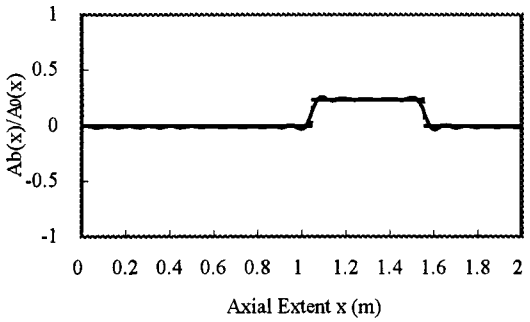

FIG. 1. Reconstruction of simulated blockage area function $Ab(x)/A(x)$ from Eq. (1) using first 23 eigenvalue shifts δn and χn theoretically evaluated from Eqs. (5) and (6). Reconstructed ———, actual ---.

sine analysis were in fact of similar accuracy to this for such a simple single obstacle, although a greater error was apparent towards the ends of the reconstruction.

II. EXPERIMENTAL ACQUISITION OF THE DUCT-TRANSFER FUNCTION USING MAXIMUM LENGTH SEQUENCE ANALYSIS

The reconstruction process of Wu and Fricke[1] displayed an excellent degree of accuracy, yet in practical terms the extended duration of the frequency sweep measurement used in this and other work[3,12] represents a limitation to the practical application of the process. However, the reconstruction could be achieved in a fraction of the time using a broadband excitation technique to obtain a simultaneous measurement across the frequency range to reveal the eigenfrequencies of the duct system. Applying broadband maximum length sequence (MLS) to a small cavity has been shown to generate a frequency response with a similar degree of accuracy and noise immunity to a swept sine analysis many thousands of time its duration.[13] Thus, MLS analysis could be used to enable a rapid reconstruction of the internal area function of a duct using the theory developed by Wu and Fricke[1] and limited only by the resolution of the digitally processed frequency spectrum.

Using MLS, the system impulse response is achieved via a process equivalent to a cross-correlation of the undistorted pseudorandom digital input signal with its distorted form recorded at a measurement point within the system. The equivalent process is achieved in a fraction of the CPU time taken for a full cross-correlation by applying a fast Hadamard transform (FHT) algorithm[14] to the distorted measured signal. Once the impulse response is processed, any extraneous noise is spread across the impulse response time history. A significant fraction of the extraneous noise may

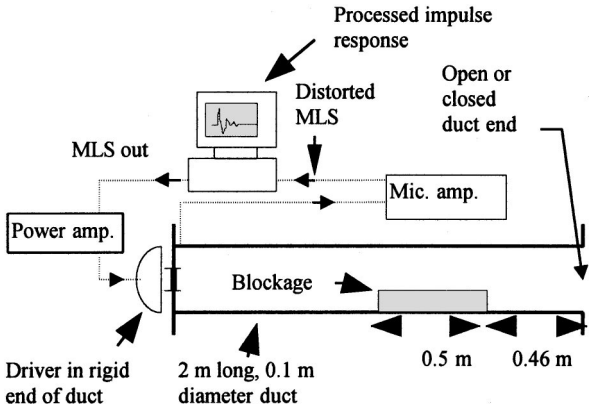

FIG. 2. Test rig for closed–open end duct with blockage of area ratio $A_b(x)=0.23$.

then be windowed out on Fourier analysis, providing the true response has fallen to a negligible value at the furthest extent of the window function.

Figure 2 shows the experimental setup used in this work with a duct of 2-m length and 0.1-m diameter and cross-modal cut-on frequency of approximately 1900 Hz. The measurements took place in the Acoustics Research Unit open laboratory space with no concessions made to insulating against background noise emanating from nearby transportation and industrial sources. The excitation signal applied was a 16 384-point maximum length sequence of 2-Khz bandwidth and 8-Khz sampling rate. Figure 3 shows a 16 384-point impulse response computed from the distorted maximum length sequence measured within the unblocked closed–open duct over a period of 4 s or two sequences within the duct. The first sequence ensures a steady noise level within the duct, while the fast Hadamard transform is applied to the second sequence recorded at the microphone. The windowed portion of the time history in Fig. 3 avoids signal truncation of the impulse response while eliminating a large proportion of the background noise which is evenly spread over the time history. A fast Fourier transform of 8192 points is applied to the window yielding the spectra of 1-Hz frequency resolution shown in Fig. 4. While the measurement is rapid with no application of ensemble averaging, the modal peaks of the duct system are clearly defined above the relatively low residual noise level. The noise immunity of the process may be increased further by using a longer MLS and windowing more of the noise out.

Figure 4 shows the measured transfer function for the closed–open duct unblocked and blockage-perturbed, clearly showing the blockage-induced shifts in the eigenfrequencies.

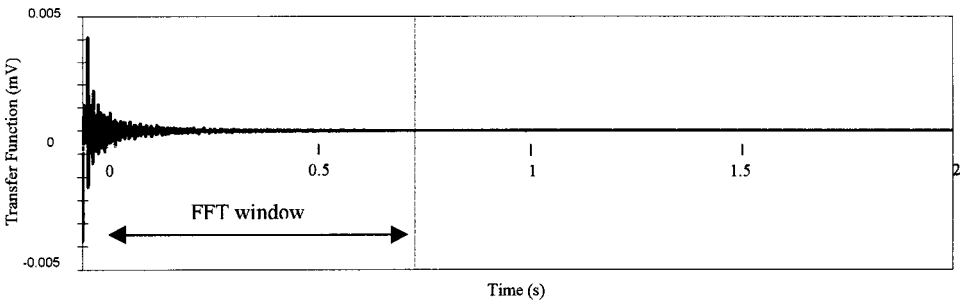

FIG. 3. Impulse response time history determined from distorted maximum length sequence measured at microphone in Fig. 2 and showing extent of FFT window.

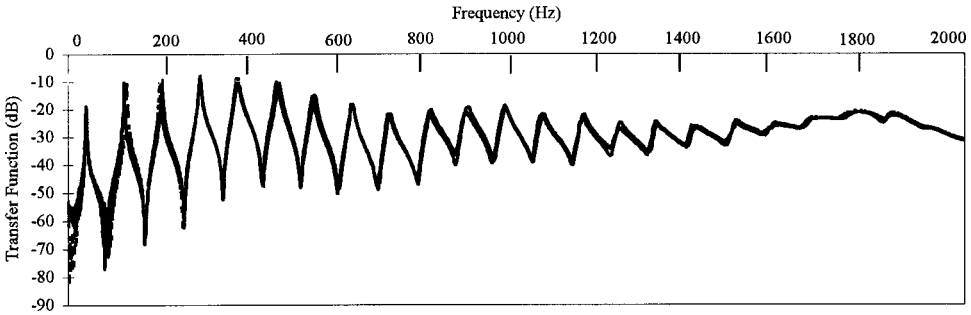

FIG. 4. Measured transfer function in closed–open 2-m-long, 0.1-m-diameter duct unblocked and with blockage shown in Fig. 2. Unblocked ———, blockage ---.

With processing of the eigenfrequencies and subsequent eigenvalues of Fig. 4 in combination with those for the unblocked and the partially blocked closed–closed duct, Eq. (1) may then be applied to the blockage-induced eigenvalue shifts to reconstruct the duct blockage area function.

III. PROCESSING OF RESULTS

To achieve the reconstruction in Eq. (1) as described by Wu and Fricke[1] requires

(a) The closed–closed and closed–open eigenfrequency shifts of the unblocked and the blockage-perturbed duct, and subsequently the associated eigenvalue shifts, δ_n and ν_n from Eq. (2) and Eq. (3), respectively.
(b) The length of the duct L.
(c) The limit of planar propagation, i.e., the cut-on frequency of the duct f_c to ensure only longitudinal modes are selected.

As previously noted, determination of the longitudinal eigenfrequencies requires location of the maxima within the frequency response measured within the duct. Wu and Fricke[1,3,12] among others,[2] achieved this using a swept sine approach and noting the positions of the peaks from the recorded pressure data within the cavity. A more automated approach was sought for the current work and the MLS-generated frequency-transfer functions were processed in a computational numerical analysis package.[15] The frequency spectrum was initially low-pass filtered at a frequency of 4/5 the initial cross-modal cut-on frequency, which for the 0.1-m-diameter duct used was approximately 1900 Hz. This low-pass filtration helped avoid cross-modal interference and problems with insufficient peak definition at higher frequencies noted at the higher end of the spectra in Fig. 4. This allowed selection of the first 15 eigenfrequencies or peaks in Fig. 4 for the 2-m-length 0.1-m-diameter duct in comparison to the 23 selected by Wu and Fricke using a nonautomated process.[1] The spectrum was also high-pass filtered to avoid spurious peaks at low frequency. These were found to occur due to system noise which will have been significant in the light of the weak response of the transducers in these regions. The low-frequency limits were calculated from the spacing of the higher-order frequency modes to prevent loss of the lowest eigenfrequencies, thus eliminating the need for duct-length measurement which ties in with work described in later sections. On the assumption that the fourth- and fifth-picked resonant frequencies are valid and nonspurious, the difference between the two gives a close approximation to the lowest resonant frequency using the following approximations:

closed–open

$$f_{1co} \approx (f_{5co} - f_{4co})/2, \tag{6}$$

closed–closed

$$f_{1co} \approx (f_{5cc} - f_{4cc}). \tag{7}$$

IV. BLOCKAGE AREA FUNCTION RECONSTRUCTION

Once the eigenfrequencies had been selected for the closed–open and closed–closed blockage-perturbed and unblocked ducts, the required eigenvalue shifts were processed using Eqs. (2) and (3) and the blockage area function reconstruction completed using Eq. (1).

A. Eigenvalue shifts

The first 15 eigenvalue shifts due to the blockage perturbation in Fig. 1 are shown in Fig. 5. These shifts amount to the odd and even components of the blockage reconstruction expansion when substituted into Eq. (1). There is a contrast with the simple periodic pattern of constant amplitude reported in Wu and Fricke's early work,[3] where the blockage to be sized was placed at the end of a closed–closed duct. In this case, as the eigenfrequency order increased and the acoustic wave subsequently decreased in wavelength, the shifts would form a simple periodic pattern with increasing mode order of constant amplitude due to interaction with the blockage.

The pattern of eigenvalue shifts is not so simple in the case of the arbitrarily positioned blockage. The position of the obstacle on the modal pressure distributions of increasing order does not vary simply (unless of course the obstacle is

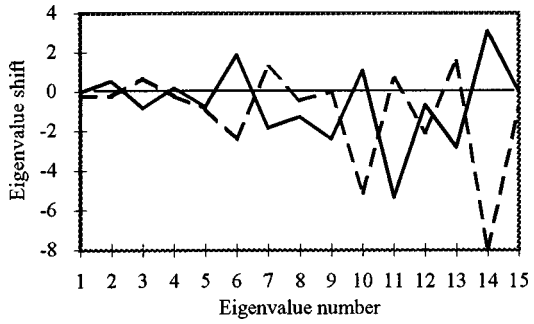

FIG. 5. First 15 eigenvalue shifts for obstacle in Fig. 2 in closed–open and in closed–closed condition 2-m long, 0.1-m-diameter duct. Closed–open ———, closed–closed ---.

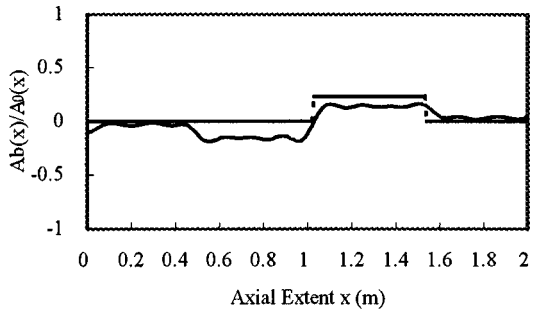

FIG. 6. Single blockage from Fig. 2 in 2-m-long 0.1-m-diameter duct reconstructed using closed–open set of eigenvalue shifts in Eq. (1). Reconstructed ———, actual ---.

at the end of the duct). Thus, more advanced analysis is required to obtain information about the size and position of the obstacle.

B. Blockage reconstruction

Figure 6 shows the blockage reconstruction using only the closed–open eigenvalue shifts in Fig. 5 in the reconstruction of Eq. (1). The problem with nonuniqueness of the area function when obtained from measurements under single sets of termination condition is clearly shown. Comparison with the actual blockage area function reveals a half-size image of the obstacle positioned asymmetrically about the midpoint of the duct as noted by Wu and Fricke.[1] In the case of the detection of a blockage or blockages with a symmetry about the axial midpoint of the duct, the two components would cancel and the blockage would not be detectable. In addition, such a perturbation with no degree of symmetry about the axial midpoint of the duct could have been caused by a dilation at the position of the image.

Wu[10] suggested that such a single boundary condition reconstruction could be used alone as a detection mechanism if the blockages in the pipe were known to be constrictions, and as such any negative area image arising in the reconstruction could be defaulted to zero. However, Wu did not consider the case of blockages with any degree of symmetry about the axial midpoint of the duct which will have caused cancellation and could easily result in a situation in which a blockage goes undetected.

The blockage area function reconstruction shown in Fig. 7 is obtained only from the closed–closed duct eigenvalue shifts shown in Fig. 5. The reconstruction blockage is half

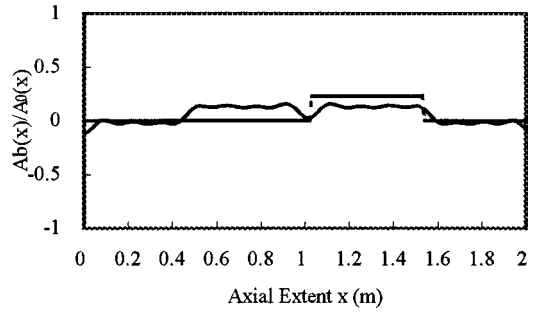

FIG. 7. Single blockage in 2-m-long 0.1-m-diameter duct reconstructed using closed–closed set of eigenvalue shifts in Eq. (1). Reconstructed ———, actual ---.

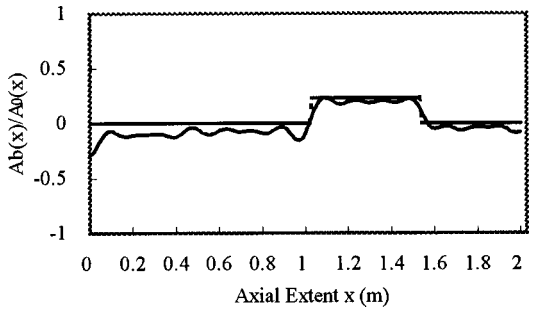

FIG. 8. Single blockage from Fig. 2 reconstructed with no added dc component using closed–open and closed–closed eigenvalue shifts in Eq. (1). Reconstructed ———, actual ---.

the size of the actual blockage and has a symmetric image about the midpoint of the duct. The area function could in this case have easily been caused by two slimmer blockages symmetrically positioned about the midpoint of the duct. In addition to this, any function displaying a degree of asymmetry would experience partial or full cancellation in the reconstruction process.

The complete area function obtained using the two sets of eigenvalue shifts shown in Fig. 5 less the dc component a_0 in Eq. (1) is shown in Fig. 8. The position of the blockage is clear, as is the negative dc shift over the duct length. Using a regression analysis, Wu and Fricke[1] found the dc component a_0 to equal the product of the blockage area ratio $A_b(x)/A_0(x)$ and the blockage length L_b divided by the duct length L, i.e.,

$$a_0 = A_b(x)/A_0(x)\left(\frac{L_b}{L}\right). \tag{8}$$

In the present work, it was found that addition of the term $(-a_0)$ within the exponential brackets in Eq. (1) was equivalent to adding the dc term separately; thus, Eq. (1) may be written as

$$A_b(x)/A_0(x) = 1 - \exp(-E-F) + a_0, \tag{9}$$

where E and F denote the cosine series terms.

Thus, a_0 can be added as a separate term over the length of the duct after the initial reconstruction analysis. The dc shift could therefore in practice be added later after estimating the position of the zero area line in Fig. 8, approximating the size of the blockage and calculating a_0 using Eq. (8).

The final reconstruction including the dc shift is given in Fig. 9. The results are comparable to those obtained by Wu and Fricke,[1] but may be obtained with greater rapidity. Each one of the four required measurements took 4 s. Post processing in MATLAB[15] for a five-column matrix of frequencies at 1-Hz resolution and cutoff approximately 2000 Hz on a 90-MHz 32 MB RAM PC took around 30 s. The accuracy is slightly inferior to that obtained by Wu and Fricke,[1] their reconstructions displaying a degree of accuracy similar to the simulated reconstruction in Fig. 1, although distortion towards the edges of the reconstruction was also apparent in their work. The resolution of the frequency sweep in Wu and Fricke[1] is not given, although it may be deduced from the accuracy of the results in comparison to Fig. 1 that the resolution of the frequency spectra used was finer than 1 Hz. To

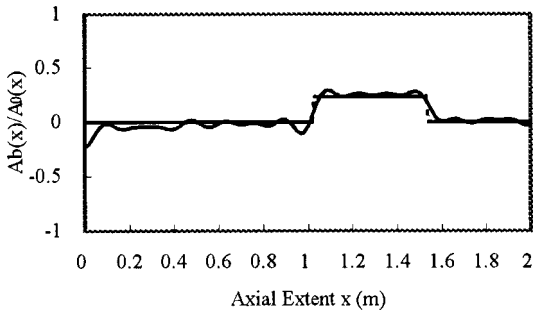

FIG. 9. Single blockage from Fig. 2 reconstructed with added dc component using closed–open and closed–closed eigenvalue shifts in Eq. (1). Reconstructed ———, actual ---.

achieve such good frequency resolution, however, will have required an extended measurement duration. Figure 9 shows that a good result may be obtained using a relatively coarse resolution, i.e., 1 Hz.

C. Blockage area function reconstruction—no measured duct length

The distribution $\Phi_n(x)$ over the duct length at resonance may be accurately determined for the unblocked duct using the actual measured resonant frequencies within the duct rather than the duct length. The eigenfunction may then be gauged using the speed of sound c in air.

Thus, Eq. (1) may also be written as follows:

$$A_b(x)/A_0(x) = \left(1 - \exp\left[-\sum_{a=1}\left[\frac{c}{2\pi f_{\mathrm{nco}}}\right]^2 \delta_n \times \cos\left(\frac{4\pi f_{\mathrm{nco}}}{c}\right) - \sum_{n=l}\left[\frac{c}{2\pi f_{\mathrm{ncc}}}\right]^2 \chi_n \times \cos\left(\frac{4\pi f_{n,\mathrm{cc}}}{c}\right) - a_0\right]\right), \tag{10}$$

where f_{no} is the resonant frequency of the unblocked closed–open duct and f_{nc} is the resonant frequency of the unblocked closed–closed duct.

The method is exactly equivalent to the measured length method using Eq. (1), but no geometric length measurement or end correction is required as this is taken into account in the case of the closed–open condition.

To obtain an accurate value for the speed of sound in air, a temperature-dependent expression can be used. The expression used in Wu and Fricke's[3] assessment of the closed –closed duct length is as follows:

$$c = 331.45\sqrt{(1 + T/373.16)}. \tag{11}$$

Equation (11) was used by Wu and Fricke[3] to ascertain the geometric length of the duct from a single eigen- or resonant frequency who noted that the length estimated from the eigenfrequencies varied with mode order due to errors in assumptions about the frequency independence of the boundary conditions. With this in mind, the expression for the geometric duct length had to be corrected by including damping terms for use in their blockage-sizing calculations.

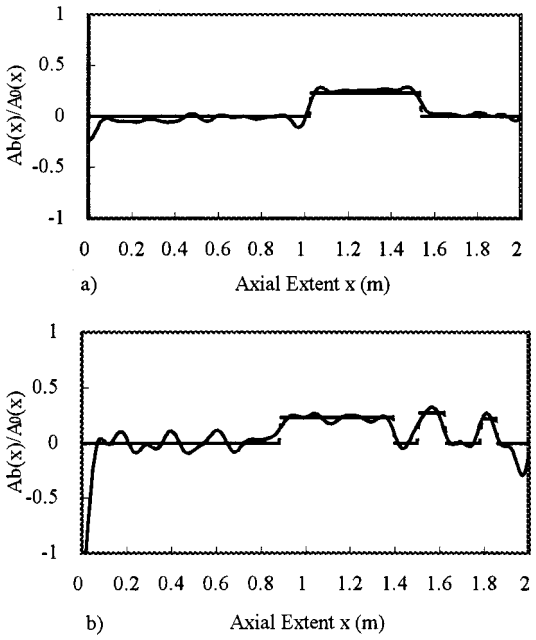

FIG. 10. Reconstruction of blockages using Eq. (10). (a) Single blockage from Fig. 2; (b) multiple blockages. Reconstructed ———, actual ---.

However, this length estimation error becomes obsolete when using the resonant frequencies directly in Eq. (10) and the reconstruction may be achieved requiring only the transfer-function measurement and a simple temperature measurement.

Figure 10 shows reconstructions of blockage area functions obtained using Eq. (10). Figure 10(a) shows the blockage function in Fig. 9 reconstructed using Eq. (10). Figure 10(b) shows the technique applied to multiple blockages. Wu and Fricke experienced the same problems with distortion at the driver end of the duct, positioned at $x=0$ in the figure, and in the case of multiple blockages the accuracy is comparable to that obtained by Wu and Fricke. However, this was also apparent using Eq. (1), and the two techniques show almost identical degrees of accuracy.

In light of these results, the remainder of the paper will use the reconstruction expansion as a function of the resonant frequency approach from Eq. (10). To achieve this, the following values must be input:

(a) An approximate value of the largest duct diameter or cross dimension to determine the cut-on frequency limits.
(b) Air temperature.
(c) The matrix of transfer functions for the two duct states, blocked and unblocked, for each of the two sets of duct end boundary conditions.

The need for an accurate geometric measurement of the duct length is avoided, which makes the procedure simpler to carry out and also universal for ducts of different length. However, the cross dimensions of the largest duct section must always be input to ensure that measurements are limited to planar propagation throughout, thus avoiding cross-modal activity and interference.

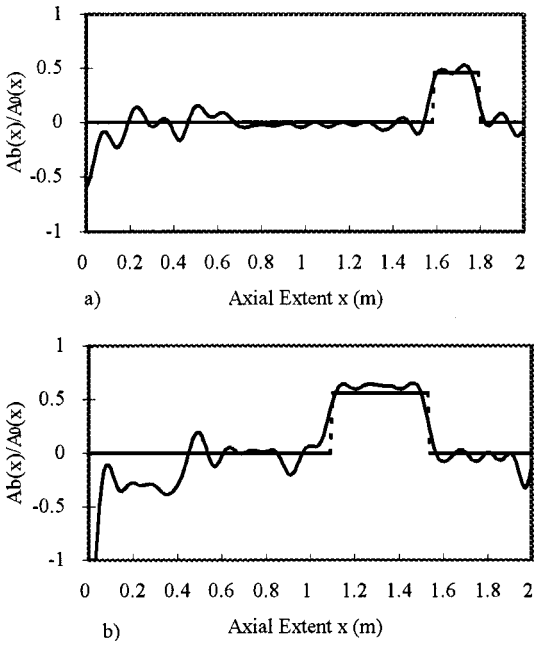

FIG. 11. Reconstruction of large blockage using Eq. (10). (a) $Ab(x)/A(x) = 0.48$, (b) $Ab(x)/A(x) = 0.56$. Reconstructed ———, actual ---.

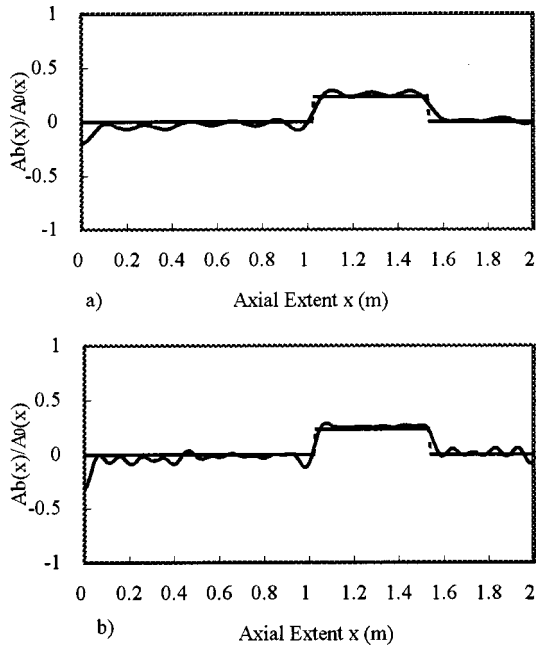

FIG. 12. Reconstruction of blockage in Fig. 2. (a) Using first 12 eigenvalue shifts, (b) using first 23 eigenvalue shifts. Reconstructed ———, actual ---.

D. Larger obstacles

Wu and Fricke[1,3] found difficulties with reconstructions of obstacles with comparatively large cross-sectional area ratios. Wu and Fricke[3] found that for obstacles of cross-section area ratio above about 0.5, a regression analysis was needed to realize the size of the obstacle in the end of the duct, the applied perturbation analysis results proving inaccurate within this region. This is to be expected as the perturbation analysis used is generally valid only for small perturbations,[4–6] and will not hold up when the obstacle substantially distorts the sound field.

The difficulties are illustrated in the reconstructions shown in Fig. 11. In each case the actual obstruction is picked out quite successfully, yet the error at the driver end of the duct is larger than previously experienced.

E. Number of eigenvalue shifts utilized

Wu and Fricke[1] looked at the effect of increasing or decreasing the number of eigenvalue shifts, from shift order 1 inclusive, used in the analysis. In each case the effect of an increased number of eigenvalue shifts was shown to sharpen the image of the blockage. This was to be expected, as the resulting higher-order Fourier components allow the representation of steeper gradients and sharper changes in area. Figure 12(a) shows that using only the first 12 closed–closed and closed–open eigenvalue shifts gives a good representation of the blockage. Figure 12(b) shows the reconstruction using the first 23 eigenvalue shifts as used by Wu and Fricke.[1] The inclusion of an increased number of eigenvalue shifts sharpens up the reconstruction to some degree, although increases in accuracy are minimal compared to the reconstruction using the first 15 eigenvalue shifts in Fig. 9.

F. Longer ducts of larger cross section

In the development of a practical blockage detection method in pipes and ducts, the test sections may well be of greater axial extent than the test ducts employed to date, and of greater cross section. The main problem envisaged with the implementation of the perturbation analyses in longer ducts was the low-frequency measurement required when determining the fundamental modes. Wu and Fricke[1] reported that the fundamental frequency shifts were the most important for the reconstruction, and thus any measurement problem at very low frequencies due to lack of source power or microphone sensitivity could invalidate the technique.

The reconstructions for a 3.88-m-long 0.2-m-diameter duct are shown in Figs. 13(a) and 13(b). The obstacle in Fig. 13(a) shows a fairly accurate reconstruction with a slight error at the nondriver end. However, if the process were to be employed only for the monitoring of constrictions the results would be excellent, as only positive perturbations shown in the reconstruction would be of importance. Figure 13(b) shows an obstacle placed almost centrally within the duct. In this case the eigenfrequency and therefore the eigenvalue shifts will be close to zero for all the closed–open modes. For this example the unique solution may thus be obtained from the single set of boundary conditions, i.e., closed–closed. Investigations were limited to centrally positioned obstacles in Wu and Fricke's previous two-dimensional blockage reconstruction work[12] due to difficulties in implementing the open end required to obtain the second set of boundary conditions in the 2D cavity.

G. Blockage area reconstruction in nonuniform tracts

In many types of ducting systems, constrictions and or expansions will occur naturally within the unperturbed tract. Figure 14(b) shows the reconstructed area function of the

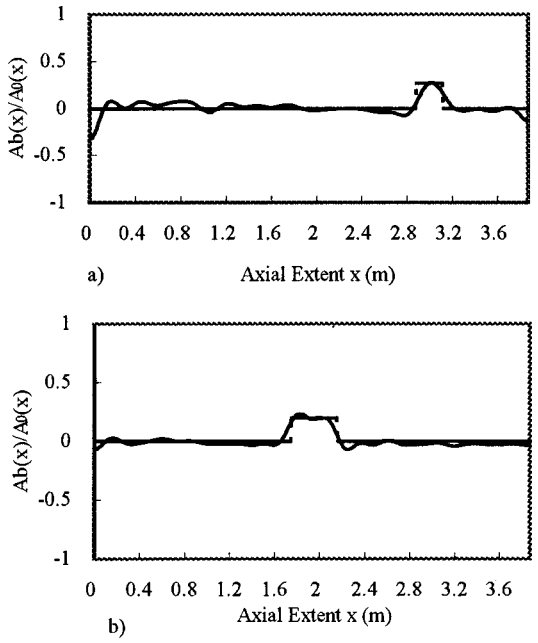

FIG. 13. Single blockages in 3.88-m-long, 0.2-m-diameter duct reconstructed using Eq. (10). Reconstructed ———, actual ---.

third blockage in Fig. 14(a) from the blockage-induced eigenfrequency shifts from the initially nonuniform tract containing two blockages. The result is favorable but shows an error fluctuation at a position symmetrical about the midpoint of the tract.

It must be noted, however, that unlike in the duct of uniform cross-sectional area, the resonant pressure distribution corresponding to the initially nonuniform tract is difficult to predict exactly. This compromises the simple blockage/ acoustic field interaction governing the perturbation theory used to develop the reconstruction process.[4] However, for ducts that are initially fairly uniform in cross section, the eigenfunctions of the wholly uniform cross-section duct make for a good approximation. This has been shown for the reconstructions in vocal tracts,[5,6] where the tract was never initially uniform but the degree of nonuniformity was always minor.

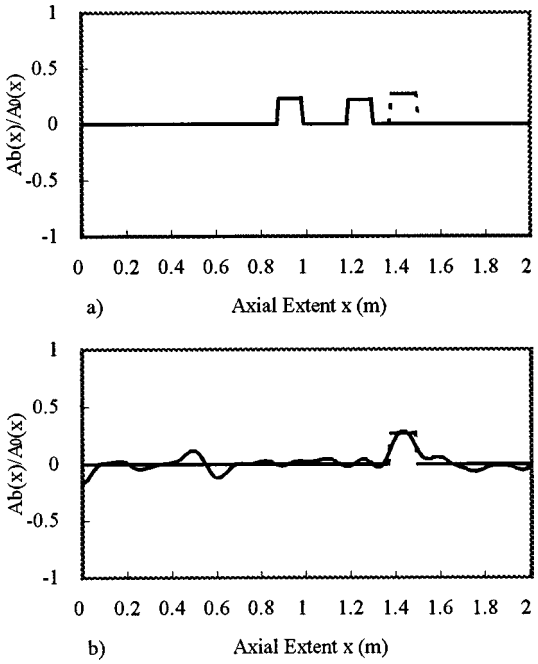

FIG. 14. Reconstruction of blockage in initially nonuniform tract. from blockage-induced eigenvalue shifts. (a) Initial blockage function and blockage to be added; (b) reconstruction of added blockage. Reconstructed ———, actual ---.

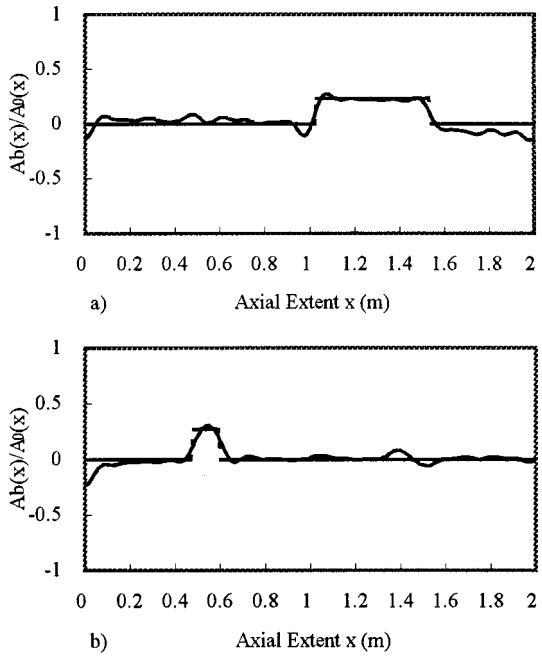

FIG. 15. Reconstructions less initial closed–open eigenvalue shift. (a) Fig. 2, (b) smaller blockage less than 1/20th wavelength of fundamental. Reconstructed ———, actual ---.

H. Effect of excluding lower-frequency shifts

Wu and Fricke[1] reported that the inclusion of the fundamental eigenfrequency shifts was paramount to the success of the reconstruction process. This is shown in Fig. 15(a), where the reconstruction less the first-order closed–open shift shows a low-frequency error over the duct length when compared to Fig. 9. However, Fig. 15(b) shows no such error due to exclusion of the lowest eigenvalue shift. In fact, in this case the lowest frequency has not shifted and therefore adds nothing to the reconstruction. Further reconstructions for obstacles placed at different positions in both 2-m- and 4-m-length ducts have shown that obstacles of less than 1:20th of the wavelength of a particular eigenfrequency will not cause a significant enough shift in the eigenvalue to warrant inclusion of the shift in the reconstruction in Eq. (1) or (10).

These results are reassuring, as one of the problems envisaged with reconstructions in longer ducts was attempting to excite the duct and gain meaningful measurements at the fundamental frequencies which, say for a 20-m duct would be approximately 4 Hz. However, it is apparent that for obstacles of limited extent relative to duct length the lower eigenvalue shifts are not essential, and in fact may be sources of error.

V. CONCLUSION

A rapid technique for reconstructing the internal area function of a duct has been developed using eigenvalue shifts determined using maximum length sequence analysis under two sets of boundary conditions. In conjunction with an automated computational processing routine, the results were obtained in a fraction of the time and with a fraction of the labor required for earlier work using swept sine analysis.[1] With validation of this technique, a new expression for the blockage reconstruction expressing the Fourier expansion as a function of eigenfrequencies has been developed and tested. This eliminates the need for measurement of the duct length required in Wu and Fricke's work[1] and thus further simplifies application of the technique.

Using the new rapid technique has allowed the authors to test application of the eigenvalue shift method in a variety of duct configurations. The work has confirmed Wu and Fricke's findings,[1,3] that obstacles approaching half the cross-sectional area of the duct and above became difficult to reconstruct as the perturbation analysis becomes invalid for such large perturbations. It was also found, as Wu and Fricke noted,[1] that while increasing the number of eigenvalue shifts in the reconstruction generally improved accuracy the increase in accuracy was minimal above the first 18 eigenfrequency shifts used.

Further work has proved the technique successful for longer ducts where lower-frequency excitation and measurement were required. The technique also showed a degree of success for blockage-perturbed ducts with initially nonuniform cross-sectional area functions. It was found that contrary to previous reports,[1] the fundamental eigenfrequency shifts were not necessarily of paramount importance for the area function reconstruction within the duct, and that the low limit of frequency shifts required was dependent on the size of the blockage to be reconstructed.

ACKNOWLEDGMENTS

The authors would like to thank the Engineering and Physical Sciences Research Council of the United Kingdom for their support of this work.

[1] Q. Wu and F. Fricke, ''Determination of blocking locations and cross-sectional area in a duct by eigenfrequency shifts,'' J. Acoust. Soc. Am. **87**, 67–75 (1990).

[2] M. Antonopoulos-Domis, ''Frequency dependence of acoustic resonances on blockage position in a fast reactor subassembly wrapper,'' J. Sound Vib. **72**(4), 443–450 (1980).

[3] Q. Wu and F. Fricke, ''Estimation of blockage dimensions in a duct using measured eigenfrequency shifts,'' J. Sound Vib. **133**(2), 289–301 (1989).

[4] R. Bellman, *Perturbation Techniques in Mathematics, Physics and Engineering* (Holt, Rinehart, and Winston, New York, 1968), pp. 25–26.

[5] M. R. Schroeder, ''Determination of the geometry of the human vocal tract by acoustic measurements,'' J. Acoust. Soc. Am. Suppl. 1 **41**, S1089–S1100 (1967).

[6] P. Mermelstein, ''Determination of the vocal-tract shape from measured formant frequencies,'' J. Acoust. Soc. Am. **41**, 1283–1294 (1967).

[7] M. M. Sondhi and B. Gopinath, ''Determination of vocal-tract shape from impulse response at the lips,'' J. Acoust. Soc. Am. **49**(2), 1867–1873 (1971).

[8] D. D. Rife and R. Vanderkooy, ''Transfer function measurement with maximum-length sequences,'' J. Audio Eng. Soc. **37**(6), 419–444 (1989).

[9] MLSSA Users Manual (DRA Associates, 1995).

[10] W. Qunli, ''Reconstruction of blockage in a duct from single spectrum,'' Appl. Acoust. **41**(3), 229–236 (1994).

[11] M. H. F. de Salis and D. J. Oldham, ''Determination of the blockage area function of a finite duct from a single pressure response measurement,'' J. Sound Vib. **221**(1), 180–186 (1999).

[12] Q. Wu and F. Fricke, ''Determination of the size of an object and its location in a rectangular cavity by eigenfrequency shifts: First order approximation,'' J. Acoust. Soc. Am. **144**, 131–147 (1991).

[13] W. T. Chu, ''Architectural acoustic measurements using periodic pseudo-random sequences,'' J. Acoust. Soc. Am. **66**, 475–478 (1984).

[14] J. Borish and B. Angell, ''An efficient algorithm for measuring the impulse response using pseudorandom noise,'' J. Audio Eng. Soc. **31**, 478–487 (1983).

[15] MATLAB High Performance Numeric Computation and Visualization Software—Users Guide (The Maths Works, Inc., Natick, 1992).

Simulation of stress waves in attenuating drill strings, including piezoelectric sources and sensors

José M. Carcione[a] and Flavio Poletto
Istituto Nazionale di Oceanografia e di Geofisica Sperimentale (OGS), Borgo Grotta Gigante 42c, 34010 Sgonico, Trieste, Italy

(Received 10 February 1999; accepted for publication 4 April 2000)

A key element in drill steering and prediction of lithology ahead-of-the-bit is the transmission of while-drilling information from the bottom of the well to the rig operator and the geophysicists. Mud-pulse telemetry, based on pressure pulses along the drilling mud and extensional waves through the drill string, is the most used technique. The last method, properly designed, could transmit data rates up to 100 bits per second, against the 1 or 2 bits per second achieved with pressure pulses. In this work, a time-domain algorithm is developed for the propagation of one-dimensional axial, torsional, and flexural stress waves, including transducer sources and sensors. In addition, the equations include relaxation mechanisms simulating the viscoelastic behavior of the steel, dielectric losses, and any other losses, such as those produced by the presence of the drilling mud, the casing, and the formation. Moreover, the algorithm simulates the passbands and stopbands due to the presence of the coupling joints and pulse distortion and delay due to nonuniform cross-section areas. Acoustic and electric pulses, generated at one location in the string, can be propagated and detected at any other location by piezoelectric and acoustic sensors, such as PCB accelerometers, clamp-on ammeters, force, and strain transducers. [S0001-4966(00)02907-6]

PACS numbers: 43.20.Mv, 43.40.Cw, 43.38.Fx, 43.20.Hq [DEC]

INTRODUCTION

Systems for transmitting information in a borehole involve electromagnetic radiation through the drill string and formations, the use of an insulated conducting cable, pressure pulses through the mud column, and acoustic wave propagation along the drill string. The most obvious technique, i.e., electrical transmission, would require stopping the drilling process every 10 m (a drill pipe segment) to add new electrical junctions. The only successful method is the transmission of pressure pulses, but this technique has a low transmission rate of about 2 bits per second. On the other hand, acoustic telemetry based on extensional waves along the drill string is a promising technique that, at present, is able to transmit 10 codified bits per second over a range of 1 km.[1,2] Several patents have been presented on devices based on this telemetry technique, for instance, those issued by Hixon,[3] Cox and Chaney,[4] and Sharp and Smither.[5]

An important application of the acoustic telemetry method is the Seisbit® technology, which uses the extensional wave generated at the drill bit (the pilot signal detected at the rig) to obtain RVSP seismograms.[6,7] Improvement of the method requires the understanding of signal transmission and attenuation of the main types of waves (extensional, torsional, and flexural) through the drill-string waveguide. At the frequencies used in hydrocarbon drilling, i.e., from 1 Hz to 2 kHz, longitudinal and torsional waves are nondispersive in a uniform pipe. However, in real drill strings, the propagation is affected by the presence of coupling joints, a nonuniform cross-sectional area, attenuation, and drilling noise. The quasiperiodic structure of this waveguide generates a classical pattern of passbands and stop bands.[3] For instance, extensional waves in a typical drill string have the first passband from 0 to 226 Hz and the first stop band from 226 to 280 Hz.[1] The ranges for torsional waves are 0 to 130 Hz and 130 to 176 Hz, respectively. Deviations from a perfect periodic structure and a variable cross section modify the location of these bands. In addition, other attenuation mechanisms act on the extensional waves. These include viscous dissipation into the drilling mud, conversion from extensional to torsional and flexural waves, and contact with the formation and well casing.

Besides waves from an acoustic source, such as the drill bit, it is important to transmit while-drilling information from piezoelectric transducer sources, located, for instance, in the bottom-hole assembly, to the drill rig on the surface. Both acoustic and electromagnetic energy can be transmitted through the waveguide if a constitutive equation based on piezoelectric coupling is assumed. In general, the signal wavelength is far greater than the 4.5-in diameter of the drill string, and the phenomenon can be accurately described by the one-dimensional wave equation.

In the present work, we develop a time-domain algorithm for the propagation of extensional, torsional, and flexural stress waves coupled with the electrostatic field equations, in order to include transducer sources and sensors. In addition, the equations include relaxation mechanisms simulating the viscoelastic behavior of the steel, dielectric losses, and any other losses, such as those produced by the presence of the drilling mud, the casing, and the formation. Moreover, the method, based on the one-dimensional (1D) wave equation, considers the presence of the coupling joints and nonuniform cross-section areas.

[a]Electronic mail: jcarcione@ogs.trieste.it

I. EXTENSIONAL WAVES

The analysis of wave propagation for a ferroelectric ceramic, classified as hexagonal crystal *6mm*, is performed in the Appendix. Propagation along the symmetry axis (direction of poling) implies the existence of coupled acoustic and electromagnetic waves and one stiffened acoustic wave, with elastic and electromagnetic polarizations directed along the symmetry axis. If we assume that the wavelength of the pulse propagating through the drill string is at least five times larger than the diameter of the string, the problem is one dimensional. In this case, the stiffened acoustic wave is the extensional wave propagating along the drill string.

Moreover, following Drumheller,[9] we consider the presence of piezoelectric sources and sensors, and attenuation due to the viscoelastic properties of the steel, the presence of drilling mud, and other factors, like leaky modes.

A. The constitutive equations

Using the results obtained in the Appendix for a ferroelectric medium, the electric field E (E_3) denotes the axial component. The acoustic constitutive equation relates the axial (z)-component of the stress tensor, denoted by T_P (T_3), with the axial component of the strain tensor, denoted by S (S_3). The constitutive equations of the transducers, including electromagnetic losses, are

$$T_P = cS - eE, \quad D = eS + \epsilon * \partial_t E, \tag{1}$$

where D (D_3) is the electric displacement (nonzero in this case, since there are conduction currents), c (c_{33}) is the plane wave modulus, e (e_{z3}) is the piezoelectric coupling, and $\epsilon(t)$ (ϵ_{zz}) is the dielectric relaxation function (the symbol $*$ denotes time convolution).

The dielectric relaxation function includes one Debye mechanism, which is mathematically equivalent to a Zener model. Then

$$\epsilon = \epsilon^0[1-(1-\alpha^2)\exp(-t\omega_1\alpha)]h(t), \quad \alpha = \sqrt{\epsilon^\infty/\epsilon^0}, \tag{2}$$

where ϵ^0 is the static permittivity, ϵ_∞ is the optical permittivity, ω_1 is the center frequency of the Debye peak, and h is the Heaviside function. Moreover, we should consider Ohm's law, relating the conduction current J_c to the electric field E,

$$J_c = \sigma E, \tag{3}$$

where σ is the conductivity. We have neglected ferromagnetic relaxation, damping due to the piezoelectric coupling, and out-of-phase conduction currents.

The constitutive equation of the drill string can be written as

$$T_A = Y * \partial_t S, \quad Y = Y_1 + Y_2, \tag{4}$$

where the acoustic relaxation function Y_1 can be described by a Zener model, representing the string material, and a Maxwell model, representing additional dissipation factors, such as energy loss by radiation into the fluids which surround the drill string. The Zener relaxation function is

$$Y_1 = Y_0[1-(1-\nu^2)\exp(-t\omega_0\nu)]h(t), \quad \nu = \sqrt{\frac{Y_U}{Y_0}}, \tag{5}$$

where Y_0 is the relaxed Young's modulus, Y_U is the unrelaxed Zener modulus, and ω_0 is the center frequency of the relaxation peak. The Maxwell relaxation function is simply

$$Y_2 = \eta Y_0[\exp(-t/\tau)-1]h(t), \tag{6}$$

where τ is the relaxation time and η is a dimensionless parameter. The unrelaxed or instantaneous contribution (i.e., when $t\to 0$ or $\omega\to\infty$) of the Maxwell relaxation function is zero, while the relaxed contribution (when $t\to\infty$ or $\omega\to 0$) is $-\eta Y_0$, so the relaxed modulus is $(1-\eta)Y_0$.[9]

The transducer, described by the constitutive equations (1), is assembled in parallel to the metal part of the drill pipe, described by the constitutive equation (4). If the ratio of the transducer area to the total area is denoted by Θ, the total stress acting on this cross section is

$$T = (1-\Theta)T_A + \Theta T_P = (1-\Theta)Y*S + \Theta cS - \Theta eE, \tag{7}$$

since the parallel configuration implies that the strain is equal in both materials. Note that the system has an effective piezoelectric constant Θe.

B. The wave equation

The wave propagation problem is solved by introducing the balance of linear momentum and Maxwell's equations. Consider a small element PQ of length δz and let the cross-sectional area of the rod be $a(z)$. Continuity of particle velocity and force holds for a rod whose cross-sectional dimensions are small compared to the length of the rod (the stress can be double-valued or discontinuous). If the force on the face passing through P is F, the stress on the other face will be $F+(\partial_z F)\delta z$, and if v is the particle velocity of the element, Newton's second law implies

$$\rho a\,\delta z\,\partial_t v = \delta z\,\partial_z F. \tag{8}$$

On the other hand, the total force acting on the cross section of the drill string is

$$F = aT. \tag{9}$$

Introducing an acoustic source f, such as the drill bit, Eq. (8) can be rewritten as

$$\rho\partial_t v = a^{-1}\partial_z(aT) + f. \tag{10}$$

The material density $\rho(z)$ is given by

$$\rho = (1-\Theta)\rho_1 + \Theta\rho_2, \tag{11}$$

where ρ_1 is the density of the drill string and ρ_2 is the density of the transducer.

Time convolutions in the constitutive equation (7) can be avoided by introducing memory variables.[10] We obtain

$$T = [(1-\Theta)Y_U + \Theta c]S + (1-\Theta)Y_0(\zeta_1 - \eta\zeta_2) - \Theta eE, \tag{12}$$

where the memory variables ζ_1 and ζ_2 satisfy

$$\partial_t\zeta_1 = -\omega_0\nu[\zeta_1 - (1-\nu^2)S] \tag{13}$$

and

$$\partial_t\zeta_2 = \frac{1}{\tau}(S-\zeta_2). \tag{14}$$

Since $\partial_t S=\partial_z v$, and redefining $\partial_t \zeta_l \rightarrow \zeta_l$, Eqs. (12)–(14) become

$$\begin{aligned}
\partial_t T &= [(1-\Theta)Y_U+\Theta c]\partial_z v \\
&\quad +(1-\Theta)Y_0(\zeta_1-\eta\zeta_2)-\Theta e\partial_t E, \\
\partial_t \zeta_1 &= -\omega_0\nu[\zeta_1-(1-\nu^2)\partial_z v], \\
\partial_t \zeta_2 &= \frac{1}{\tau}(\partial_z v-\zeta_2),
\end{aligned} \tag{15}$$

where we have used Eq. (9).

On the other hand, the radial-component of the electromagnetic equation in the transducer is,[11]

$$0=\sigma E+\partial_t D+J \tag{16}$$

[the generalized version of Eq. (A8i)], where J (J_r) is the electric current source.

Since part of the cross-sectional area consists of metal, we assume an effective piezoelectric coupling Θe. Taking this into account and introducing the hidden variable ξ,[12] substitution of Eq. (1) into Eq. (16) yields

$$0=\sigma_e E+\epsilon^\infty \partial_t E+\Theta e\partial_z v+\epsilon^0\xi+J, \tag{17}$$

where

$$\sigma_e=\sigma+\omega_1\alpha(1-\alpha^2)\epsilon^0,$$

with ξ obeying the following first-order equation:

$$\partial_t \xi=-\omega_1\alpha[\xi+\omega_1\alpha(1-\alpha^2)E]. \tag{18}$$

Time-differentiation of Eq. (17) gives

$$\sigma_e\mathcal{E}+\epsilon^\infty\partial_t\mathcal{E}+\Theta e\partial_z\partial_t v+\epsilon^0\psi+\mathcal{J}=0, \tag{19}$$

where $\mathcal{E}=\partial_t E$, $\psi=\partial_t\xi$, and $\mathcal{J}=\partial_t J$. Equation (10) implies $\partial_t v=[a^{-1}\partial_z aT+f]/\rho$. Substituting this expression into Eq. (19) we obtain

$$\sigma_e\mathcal{E}+\epsilon^\infty\partial_t\mathcal{E}+\Theta e\partial_z\left\{\frac{1}{\rho}[a^{-1}\partial_z aT+f]\right\}+\epsilon^0\psi+\mathcal{J}=0, \tag{20}$$

which, together with the time derivative of (18),

$$\partial_t\psi=-\omega_1\alpha[\psi+\omega_1\alpha(1-\alpha^2)\mathcal{E}], \tag{21}$$

forms the electromagnetic equations.

C. Plane wave solution

Let us assume a harmonic wave with a phase factor $\exp(i\omega t)$, where ω is the angular frequency. Then, the constitutive equations (1) and (4) can be written as

$$\begin{aligned}
T_P &= cS-eE, \\
D &= eS+\tilde{\epsilon}E, \\
T_A &= \tilde{Y}S,
\end{aligned} \tag{22}$$

where

$$\tilde{Y}=\nu Y_0\frac{\omega_0+i\omega\nu}{\omega_0\nu+i\omega}-\frac{\eta Y_0}{1+i\omega\tau} \tag{23}$$

and

$$\tilde{\epsilon}=\alpha\epsilon_0\frac{\omega_1+i\omega\alpha}{\omega_1\alpha+i\omega}. \tag{24}$$

Now, assume a plane wave with a particle velocity having an spatial phase factor $\exp(-i\omega sz)$, where s is the complex slowness (this quantity is complex in the lossy case; the real and imaginary parts are related to the wave number and the attenuation, respectively). For any field variable, we have $\partial_z\rightarrow -i\omega s$. It is easy to show that the dispersion equation is

$$s^2\left[(1-\Theta)\tilde{Y}+\Theta c+\frac{(\Theta e)^2}{\epsilon^*}\right]=\rho, \tag{25}$$

where

$$\epsilon^*=\tilde{\epsilon}-\frac{i}{\omega}\sigma. \tag{26}$$

The physical phase velocity and attenuation factor are given by

$$V_p=[\mathrm{Re}(s)]^{-1} \tag{27}$$

and

$$\overline{\alpha}=-\omega\,\mathrm{Im}(s), \tag{28}$$

respectively.

D. Wave equation in matrix form

Equations (20) and (21), together with Eqs. (10) and (15), form the wave equation in the quasistatic case. Note that $\partial_t E$ must be replaced by the variable $\mathcal{E}$ in Eq. (15). These equations govern solutions that travel at velocities comparable to acoustic velocities.

The quasistatic differential equations can be written in matrix form as

$$\partial_t\mathbf{w}=\mathbf{M}\mathbf{w}+\mathbf{s}, \tag{29}$$

where

$$\mathbf{w}=[v,T,\zeta_1,\zeta_2,\mathcal{E},\psi]^\top \tag{30}$$

is the unknown vector,

$$\mathbf{s}=[f/\rho,0,0,0,-[\mathcal{J}+\Theta e\partial_z(\rho^{-1}f)]/\epsilon^\infty,0]^\top \tag{31}$$

is the source vector, and $\mathbf{M}$ is the propagation matrix, given by

$$\mathbf{M}=\begin{pmatrix}
0 & M_{12} & 0 & 0 & 0 & 0 \\
M_{21} & 0 & M_{23} & M_{24} & M_{25} & 0 \\
M_{31} & 0 & M_{33} & 0 & 0 & 0 \\
M_{41} & 0 & 0 & M_{44} & 0 & 0 \\
0 & M_{52} & 0 & 0 & M_{55} & M_{56} \\
0 & 0 & 0 & 0 & M_{65} & M_{66}
\end{pmatrix}, \tag{32}$$

where

$$\begin{aligned}
&M_{12}=(\rho a)^{-1}\partial_z a, \\
&M_{21}=[(1-\Theta)Y_U+\Theta c]\partial_z, \quad M_{23}=(1-\Theta)Y_0, \\
&M_{24}=-(1-\Theta)\eta Y_0, \quad M_{25}=-e\Theta, \\
&M_{31}=\omega_0\nu(1-\nu^2)\partial_z, \quad M_{33}=-\omega_0\nu,
\end{aligned} \tag{33}$$

$$M_{41}=\tau^{-1}\partial_z, \quad M_{44}=-\tau^{-1},$$

$$M_{52}=-\frac{\Theta e}{\epsilon^{\infty}}\partial_z(\rho a)^{-1}\partial_z a, \quad M_{55}=-\sigma_e/\epsilon^{\infty},$$

$$M_{56}=-\epsilon^0/\epsilon^{\infty}, \quad M_{65}=-\omega_1^2\alpha^2(1-\alpha^2), \quad M_{66}=-\omega_1\alpha.$$

II. TORSIONAL WAVES

The constitutive equation for torsional waves in a ferroelectric ceramic is similar to that of the extensional waves, given in Eq. (1). For torsional vibrations, E denotes the azimuthal component E_ϕ of the electric field, T_P is the ϕz-component of the piezoelectric stress tensor, S is the ϕz-component of the strain tensor, D is the azimuthal component (D_ϕ) of the electric displacement, c is the rigidity modulus c_{44}, e is the piezoelectric coupling (e_{x5}), and $\epsilon(t)$ is the dielectric relaxation function $\epsilon_{11}(t)$. As before, the acoustic relaxation function $c_{44}(t)$ of the drill string (Y for extensional waves) can be described by a parallel connection between a Zener model and a Maxwell model, representing additional dissipation factors. Similarly, a Debye mechanism represents the dielectric relaxation function.

The wave propagation problem is solved by introducing the balance of angular momentum[13,14] and Maxwell's equations. Let ϕ denote the relative angular displacement of two cross sections, so that $\partial_z\phi$ is the twist of the cylinder. The torsional couple is equal to the radius of gyration R_T multiplied by the force aT, i.e., $C=aR_TT$, where T is the ϕz-component of the total stress tensor. The moment of the kinetic reactions about the axial axis $\rho aR_T^2\partial_{tt}\phi$ balances the angular moment $\partial_z C$. Then, the equation of motion is

$$\rho aR_T^2\partial_{tt}\phi=\partial_z(aR_TT). \tag{34}$$

Note that the radius of gyration is defined by

$$R_T^2=a^{-1}\int d^2da \tag{35}$$

(Ref 15), where d is the distance to the axis of rotation. For a hollow cylinder, the radius of gyration, with respect to the axial axis z, is

$$R_T=\frac{1}{\sqrt{2}}(r_1^2+r_2^2)^{1/2}, \tag{36}$$

where r_1 and r_2 are the inner and outer radii, respectively. Defining $\Omega=\partial_t\phi$ and the polar moment of inertia per unit mass,

$$I=aR_T^2=\frac{\pi}{2}(r_2^4-r_1^4), \tag{37}$$

Eq. (34) becomes

$$\rho\partial_t\Omega=I^{-1}\partial_z(I\hat{T})+f_T, \tag{38}$$

where $\hat{T}=T/R_T$ (it is assumed that the ϕ-displacement is equal to $R_T\phi$), and we have introduced the external torque f_T. The time derivative of the constitutive equation is

$$R_T\partial_t\hat{T}=[(1-\Theta)Y_U+\Theta c]\partial_zR_T\Omega + (1-\Theta)Y_0(\zeta_1-\eta\zeta_2)-\Theta e\mathcal{E}, \tag{39}$$

where, for simplicity, we use the same notation as for the extensional waves. Here, Y_0 and Y_U denote the relaxed and unrelaxed limits of the drill-string relaxation function c_{44}, and ζ_1 is the corresponding hidden variable, with v replaced by $R_T\Omega$ in Eq. (15). The same argument holds for the parameters of the Maxwell model.

In matrix notation, the equation describing torsional oscillations, coupled with the quasistatic electromagnetic field, has the form (26), where

$$\mathbf{w}=[\Omega,\hat{T},\zeta_1,\zeta_2,\mathcal{E},\psi]^{\top} \tag{40}$$

is the unknown vector,

$$\mathbf{s}=[f_T/\rho,0,0,0,-[\mathcal{J}+\Theta e\partial_z(R_T\rho^{-1}f_T)]/\epsilon^{\infty},0]^{\top} \tag{41}$$

is the source vector, and $\mathbf{M}$ is the propagation matrix, whose components have the same expression (33), except for

$$\begin{aligned}
&M_{12}=(I\rho)^{-1}\partial_zI, \quad M_{21}=[(1-\Theta)Y_U+\Theta c]R_T^{-1}\partial_zR_T,\\
&M_{23}=(1-\Theta)R_T^{-1}Y_0, \quad M_{24}=-(1-\Theta)R_T^{-1}\eta Y_0,\\
&M_{25}=-\Theta R_T^{-1}e,\\
&M_{31}=\omega_0\nu(1-\nu^2)\partial_zR_T,\\
&M_{41}=\tau^{-1}\partial_zR_T,\\
&M_{52}=-\frac{\Theta e}{\epsilon^{\infty}}\partial_zR_T(\rho I)^{-1}\partial_zI.
\end{aligned} \tag{42}$$

It can be shown that the dispersion relation has the form (25).

III. FLEXURAL WAVES

In the simplest theory of flexural vibrations it is assumed that the motion of each element of the pipe is purely one of translation in a direction perpendicular to the axis of the pipe. We assume that the wavelength is much larger than the diameter of the drill string. Therefore, effects such as rotary inertia are neglected.[13,14] Following Kolsky,[14] the equation of motion for flexural vibrations of bars is

$$\rho a\partial_{tt}w=-\partial_z\mathcal{F}+f_F, \tag{43}$$

where w is the displacement in the plane of bending [e.g., if (x,z) is the bending plane, w points in the x-direction], f_F is the external force, and $\mathcal{F}$ is the shearing force. This is given by

$$\mathcal{F}=-\partial_zM=\partial_z(aR_F^2Y_U\partial_{zz}w), \tag{44}$$

where M is the bending moment, Y_U is the unrelaxed Young modulus, and R_F is the radius of gyration of the cross section about an axis through its centroid at right angles to the plane of bending. For the (x,z)-plane $R_F^2=a^{-1}\int x^2da$, which for a hollow cylinder is

$$R_F=\tfrac{1}{2}(r_1^2+r_2^2)^{1/2}. \tag{45}$$

Coupling with the axial force F implies additional terms in Eqs. (43) and (10). Chin[16] (pp. 225, 257, and 271). Including these interactions and since $F=aT$, Eqs. (10) and (43) become

$$a\rho\partial_tv=\partial_zF+aY_UR_F^2\partial_z[(\partial_{zzz}w)(\partial_zw)]+af \tag{46}$$

and

$$\rho a \partial_{tt} w = -\partial_z(\mathcal{F} + F\partial_z w) + f_F, \tag{47}$$

with F given by Eq. (9). Coupling with the axial motion allows the inclusion of losses and piezoelectric effects.

On the other hand, assuming a large bending radius, Drumheller[17] obtains the following coupled differential equations:

$$\rho a \partial_t v = \partial_z F - \frac{\mathcal{F}}{r_b} + af \tag{48}$$

and

$$\rho a \partial_{tt} w = -\partial_z \mathcal{F} - \frac{F}{r_b} + f_F, \tag{49}$$

where r_b is the radius of curvature of the string (bending radius). Assuming no loss for simplicity, the stress is[17]

$$T = [(1-\Theta)Y_U + \Theta c]\left(S + \frac{w}{r_b}\right) + \Theta e E, \tag{50}$$

where $Y_U = Y_0$.

Let $\hat{x}(z)$ denote the reference line of the string. The condition $\hat{x}(z) = 0$ defines a straight string. For large bending radius,

$$\partial_{zz}\hat{x} = \frac{1}{r_b(z)}. \tag{51}$$

Since $\partial_z(F\partial_z w)$ in Eq. (47) is equal to $\partial_z F \partial_z w + F\partial_{zz} w$, Eqs. (47) and (49) are equivalent if $\partial_z F \partial_z w$ can be neglected and $\partial_{zz} w \approx \partial_{zz}\hat{x} = 1/r_b$. Similarly, Eq. (46) is equivalent to Eq. (48) if $(\partial_{zzzz} w)(\partial_z w)$ can be neglected and $\partial_{zz} w \approx 1/r_b$. However, note that the presence of a radius of curvature implies the action of a lateral force f_F in Eq. (47), otherwise there is no coupling between the flexural and axial motions when solving the problem with Eqs. (46) and (47).

Moreover, the drill string is prestressed by its weight, but in order to avoid collapse, it is lifted at the surface, where it is in tension. Since it must contact the formation in order to drill, it is in compression at the bit. Hence, the static axial load changes from tension at the surface to compression at the bit, with the point of zero stress close to the drill collar. Assuming $z = 0$ at the bit and that the distance to the neutral point is z_N, the force per unit area of drill string is

$$N = a\rho g(z - z_N), \tag{52}$$

where g is the acceleration of gravity. In terms of the *weight-on-bit* (WOB), the force is $N = a\rho g z - \mathrm{WOB}$[16] (p. 145). The axial force satisfies $N < 0$ for the segments in tension, and $N > 0$ for the segments in compression. The transition $N = 0$ defines the neutral point of the drill string. When modeling gravity effects, the force N should be added to the axial force F in Eqs. (47)–(49).

Plane wave analysis

Let us consider a uniform drill string subject to the variable axial force N and assume that there is no coupling with the extensional wave. Substitution of Eq. (44) into (47) with $F = 0$ yields

$$\rho a \partial_{tt} w + a R_F^2 Y \partial_{zzzz} w + \partial_z(N\partial_z w) = 0, \tag{53}$$

where we assume that there are no external forces. A plane wave ansatz $\exp i(kx - \omega t)$, where k is the complex wave number, gives the following dispersion equation:[16]

$$\rho a \omega^2 = a R_F^2 Y k^4 - Nk^2 + ik\partial_z N. \tag{54}$$

Using Eq. (52) and $\partial_z N = a\rho g$, we get

$$\rho\omega^2 = R_F^2 Y k^4 - \rho g(z - z_N)k^2 + ik\rho g. \tag{55}$$

Equation (55) has four solutions, with phase velocity and attenuation factor given by

$$V_p = \omega[\mathrm{Re}(k)]^{-1}, \quad \overline{\alpha} = -\mathrm{Im}(k), \tag{56}$$

respectively. The group velocity is equal to the derivative of the angular frequency with respect to the real part of k. It gives

$$V_g = \left[\mathrm{Re}\left(\frac{\partial k}{\partial \omega}\right)\right]^{-1}. \tag{57}$$

From Eq. (55) we obtain

$$\frac{\partial k}{\partial \omega} = 2\rho\omega[4R_F^2 Y k^3 - 2k\rho g(z - z_N) + i\rho g]^{-1}. \tag{58}$$

IV. THE ALGORITHMS

Previous algorithms for computing drill-string axial motion use the method of characteristics and low-order finite differencing,[18] and frequency-domain techniques.[19] Here, drill-string axial, torsional, and lateral vibrations are computed with a fourth-order Runge-Kutta technique. The method calculates the field at time $(n+1)dt$, where dt is the time step, as

$$\mathbf{w}^{n+1} = \mathbf{w}^n + \frac{dt}{6}(\Delta_1 + 2\Delta_2 + 2\Delta_3 + \Delta_4), \tag{59}$$

where

$$\Delta_1 = \mathbf{M}\mathbf{w}^n + \mathbf{s}^n,$$

$$\Delta_2 = \mathbf{M}\left(\mathbf{w}^n + \frac{dt}{2}\Delta_1\right) + \mathbf{s}^{n+1/2},$$

$$\Delta_3 = \mathbf{M}\left(\mathbf{w}^n + \frac{dt}{2}\Delta_2\right) + \mathbf{s}^{n+1/2},$$

$$\Delta_4 = \mathbf{M}(\mathbf{w}^n + dt\,\Delta_3) + \mathbf{s}^{n+1}.$$

The spatial derivatives are calculated with the Fourier and Chebyshev methods by using the fast Fourier transform (FFT).[20,21] These approximations are infinitely accurate for band-limited periodic functions with cutoff spatial wave numbers which are smaller than the cutoff wave numbers of the mesh. When using the Chebyshev method, nonperiodic boundary conditions can be implemented at the end of the pipes, and the grid points can be distributed in accordance with the structure and geometry of the drill string. We consider the following coordinate transformation from the computational to the physical domain:

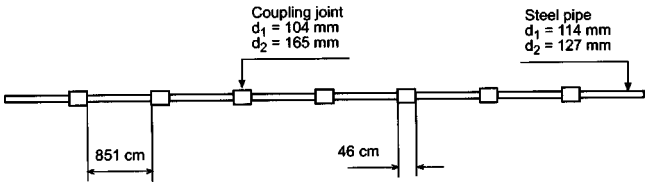

FIG. 1. Regular drill string consisting of pipes and tool joints.

$$z_j = z_{\max}\left[\frac{q(\zeta_j)-q(-1)}{q(1)-q(-1)}\right], \quad j=0,\ldots,n_z-1, \tag{60}$$

mapping the interval $[-1,1]$ onto the interval $[0,z_{\max}]$, where $\zeta_j=\cos[\pi j/(n_z-1)]$ are the Gauss-Lobatto collocation points. The function

$$q=q(\zeta,\boldsymbol{\alpha}) \tag{61}$$

is a family of transformations, where $\boldsymbol{\alpha}$ is a vector of parameters defining the mapping. The spatial derivative of a field variable in the physical domain is then given by

$$\frac{\partial u}{\partial z}=\frac{\partial u}{\partial \zeta}\frac{\partial \zeta}{\partial z}=\left[\frac{q(1)-q(-1)}{z_{\max}}\right]\frac{\partial \zeta}{\partial q}\frac{\partial u}{\partial \zeta}. \tag{62}$$

For instance, in the second example we use the following symmetric mapping function:

$$q(\zeta)=\frac{\arcsin(\gamma\zeta)}{\arcsin(\gamma)}, \tag{63}$$

satisfying $q(1)=1$ and $q(-1)=-1$. Here $\boldsymbol{\alpha}=\gamma$, and

$$\frac{\partial \zeta}{\partial q}=\frac{\arcsin(\gamma)}{\gamma}\sqrt{1-\gamma^2\zeta^2}. \tag{64}$$

This mapping stretches the mesh at the boundaries. When $\gamma\to 0$, we obtain the Gauss-Lobatto collocation points, and $\gamma\to 1$ gives equally distributed points as in the Fourier differential operator. Using this mapping, the spatial derivative (62) can be rewritten as

$$\frac{\partial u}{\partial z}=\frac{1}{\gamma dz}\arcsin\left[\gamma\sin\left(\frac{\pi}{n}\right)\right]\sqrt{1-\gamma^2\zeta^2}\frac{\partial u}{\partial \zeta}, \tag{65}$$

where n_z is the number of grid points, and dz is the maximum grid spacing.

Free surface boundary conditions at the end of the pipes are implemented by the technique described in Ref. 21.

V. EXAMPLES

A. Propagation of extensional stress waves along an attenuating drill string with periodic coupling joints

A drill string with the characteristics shown in Fig. 1 is used to simulate acoustic transmission through nine pipe elements separated by ten tool joints. In particular, this problem has been solved by Drumheller[18] with a different numerical algorithm, based on the method of finite differences. The Young modulus of the pipe and coupling joints is $Y_U=Y_0=206$ GPa, and the material density is $\rho=7850$ kg/m^3. We consider $n_z=3465$ and a uniform grid spacing $dz=23$ cm. The source time history is

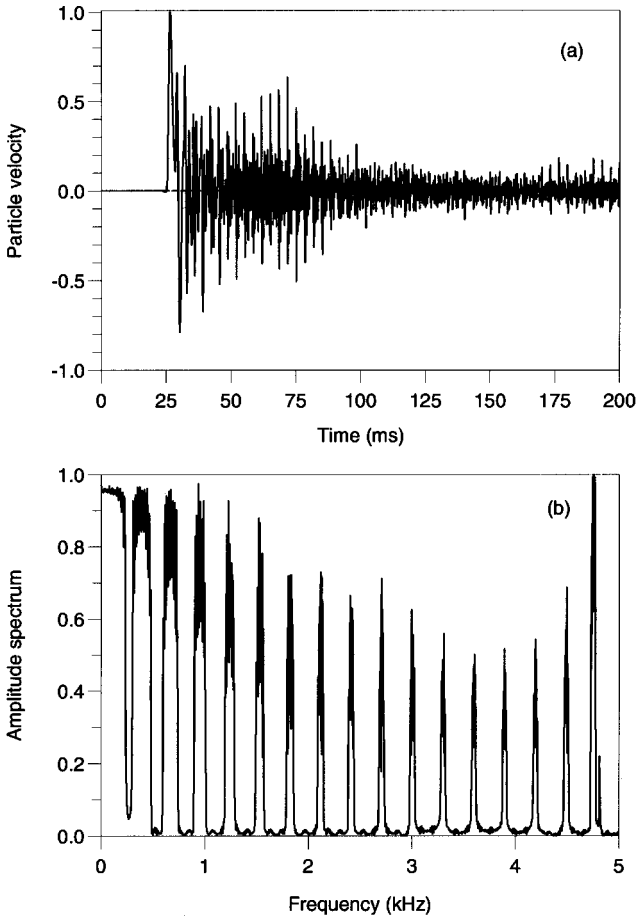

FIG. 2. Time history (a) and Fourier transform (b) of the sinc extensional pulse propagated along ten tool joints (see Fig. 1).

$$f(t)=\mathrm{sinc}[2\pi f_c(t-t_0)],$$

which corresponds to a gate function in the frequency domain. The source frequency is 5.568 kHz, which is half the maximum frequency ''supported'' by the mesh, i.e., $f_{\max}=V_{p\,\min}/(2dz)$, where $V_{p\,\min}$ is the minimum phase velocity. Frequencies beyond this limit are aliased. The source is located at grid point 1499 and the receiver at grid point 2050. The first tool joint starts at grid point 1599, with each joint modeled by two grid points and each pipe element by 37 grid points. The spatial derivatives are computed with the Fourier method, and absorbing regions of length 18 grid points are implemented at the two ends of the drill string to avoid wraparound effects. The wave field is computed by using a time step of 1 μs, with the time history resampled every 40 μs.

Figure 2 shows the time history (a) and its Fourier transform (b), where the characteristic passbands can be appreciated.[1,8] The transform was made using a sampling interval of 40 μs and 5544 points.

The following numerical experiment considers the band-limited time function

$$f(t)=\exp\left[-\tfrac{1}{2}f_c^2(t-t_0)^2\right]\cos[\pi f_c(t-t_0)], \tag{66}$$

where f_c is the cutoff frequency and $t_0=3/f_c$.

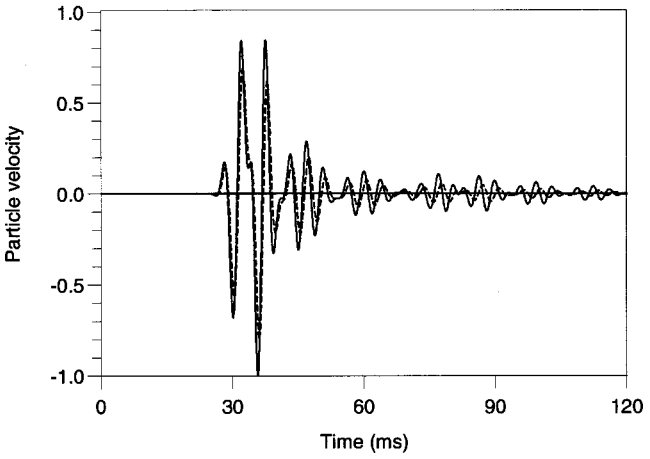

FIG. 3. Time history for extensional waves corresponding to the model illustrated in Fig. 1, showing the case without loss (continuous line) and with loss (broken line).

Attenuation can be easily parameterized as a function of the minimum quality factor Q of the relaxation peak and the central frequency f_0 of this peak. We have

$$Q=\frac{2\nu}{\nu^2-1} \quad \text{and} \quad f_0=\frac{\omega_0}{2\pi}.$$

We assume $f_c=500\,\text{Hz}$, $Q=200$, $f_0=f_c/2$, and Maxwell's parameters $\eta=0.02$ and $\tau=200\,\mu\text{s}$, which are used to model the radiated energy into the fluids surrounding the drill string. Figure 3 compares the time histories corresponding to the lossless (continuous line) and lossy (broken line) cases. As expected, the attenuation is more pronounced for the coda waves.

B. Transmission of extensional pulses between ferroelectric ceramics

In this example we consider the propagation of stress waves between two piezoelectric transducers joined by a hollow cylinder made of brass. The model and configuration, shown in Fig. 4, correspond to a laboratory experiment conducted by Drumheller.[9] The Young modulus of the cylinder is $Y_U=Y_0=108.13\,\text{GPa}$, and its material density is $\rho=8456\,\text{Kg/m}^3$. Intrinsic loss in the brass is described by the Zener model with $Q=180$ and $f_0=20\,\text{KHz}$.

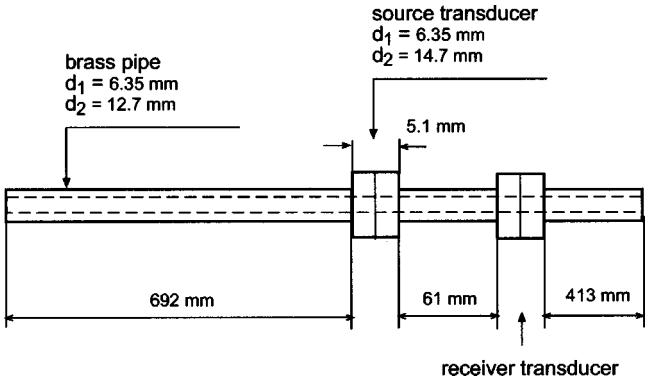

FIG. 4. Geometry of the experiment corresponding to the ferroelectric transducers (not in scale). Both ends of the brass pipe satisfy free surface boundary conditions.

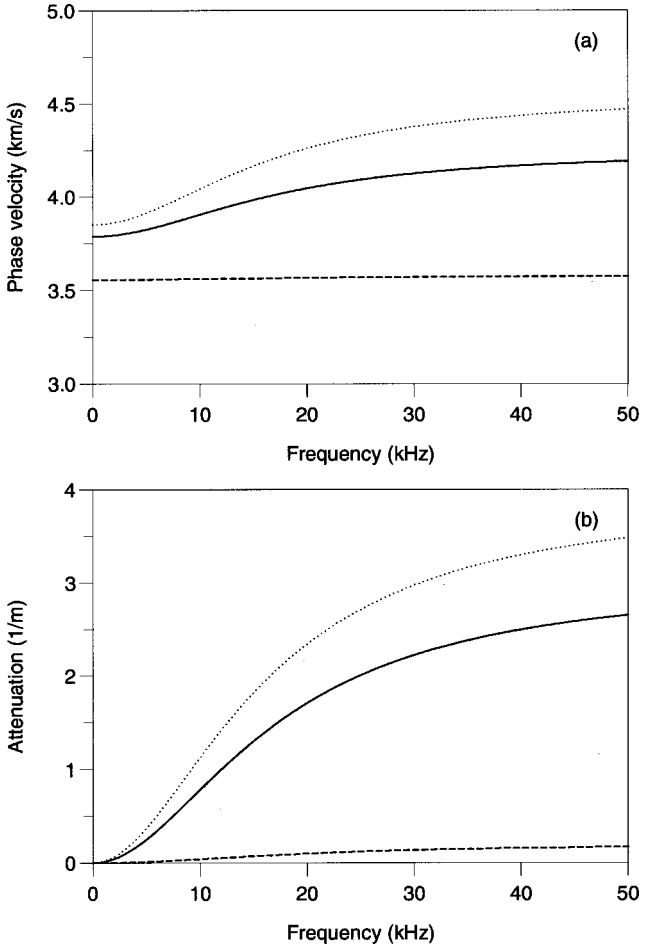

FIG. 5. Phase velocity (a) and attenuation factor (b) of a wave propagating in an assemble brass/ferroelectric ceramic (continuous line), where the proportion of ceramic is $\Theta=0.8$. The broken line corresponds to the pure brass material (i.e., $\Theta=0$) and the dashed line to the pure ceramic material (i.e., $\Theta=1$).

As in the acoustic case, dielectric loss is parameterized by the minimum quality factor Q_e and the central frequency f_1 of the relaxation peak. We have

$$Q_e=\frac{2\alpha}{\alpha^2-1} \quad \text{and} \quad f_1=\frac{\omega_1}{2\pi}.$$

The source transducer is made of lead titanate-zirconate (PZT-5H ceramic) whose properties[9,11] are $c=48.24\,\text{GPa}$, $\rho=7489\,\text{kg/m}^3$, $e=23.3\,\text{C/m}^2$, $\epsilon^0=1470\,\epsilon_0$, $Q_e=50$, $f_1=20\,\text{kHz}$, and $\sigma=1.5\,\text{mS/m}$. On the other hand, the receiver transducer (also PZT-5H ceramic) has acoustic properties $c=111\,\text{GPa}$, $\rho=7485.3\,\text{kg/m}^3$, and similar electric properties to the source transducer. These data are in agreement with Table IV of Ref. 9. Figure 5 shows the phase velocity (27) (a) and attenuation factor (28) (b) as a function of frequency for the receiver transducer. The continuous line corresponds to a wave propagating in an assemble of brass/ferroelectric ceramic, where the proportion of ceramic is $\Theta=0.8$, while the broken line corresponds to the pure brass material (i.e., $\Theta=0$) and the dashed line to the pure ceramic material (i.e., $\Theta=1$).

We consider $n_z=694$ and a uniform grid spacing $dz=1.745\,\text{mm}$. The source transducer is located between grid

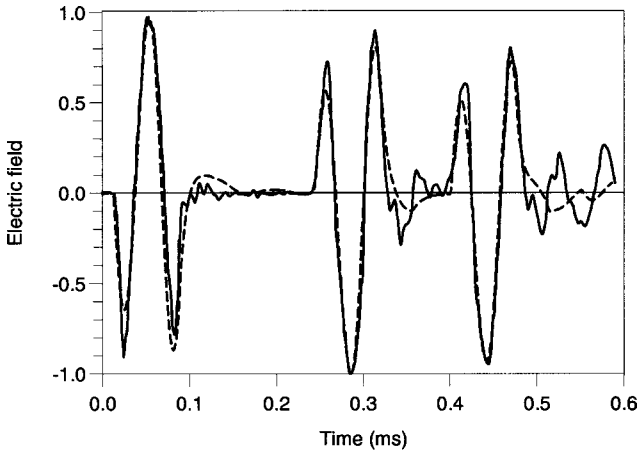

FIG. 6. Time history of an extensional pulse propagated between two piezoelectric transducers (see Fig. 4) (broken line) compared to the experimental results obtained by Drumheller (Ref. 9) (continuous line).

points 407 and 410, and the electric current is applied to grid point 408. The time history of the source, $\mathcal{J}(t)$, is given in Fig. 9 of Drumheller.[9] The receiver transducer is located between grid points 446 and 449, and the signal is recorded at grid point 447. The spatial derivatives are computed with the Chebyshev method, using the mapping function (63) with $\gamma=0.999$. Free surface boundary conditions are satisfied by the two ends of the brass cylinder. The wave field is computed by using a time step of 0.1 μs, with the time history resampled every 1.6 μs.

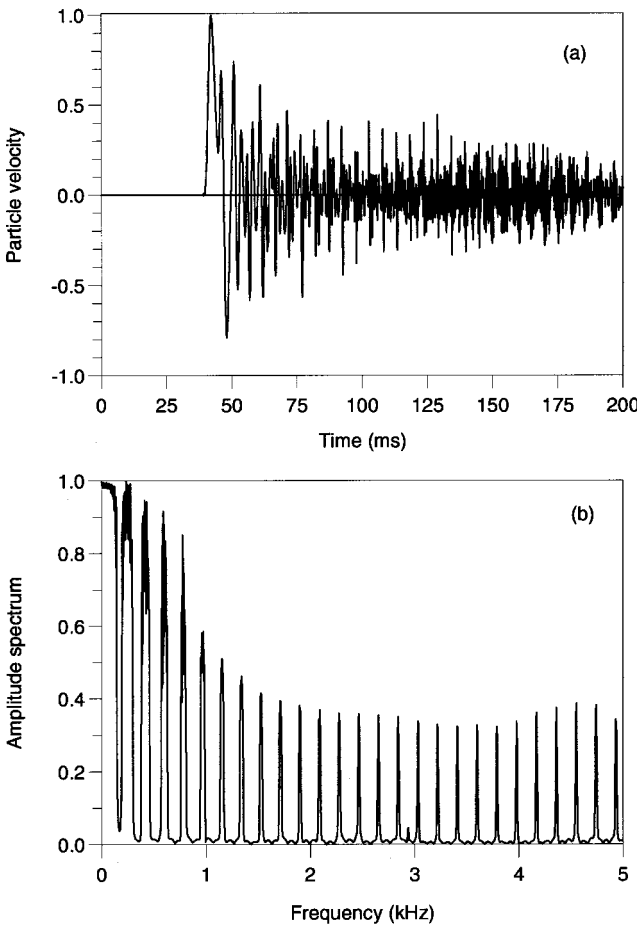

FIG. 7. Time history (a) and Fourier transform (b) of the sinc torsional pulse propagated along ten tool joints (see Fig. 1).

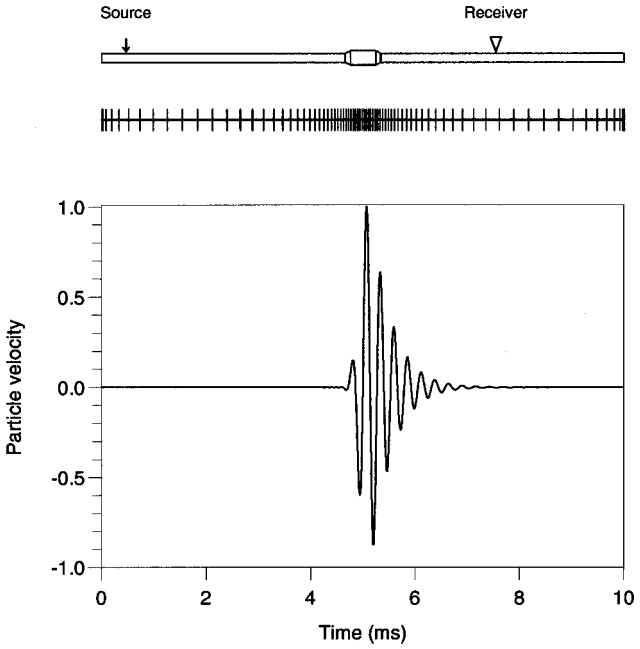

FIG. 8. Section of drill string, numerical mesh, and time history of the angular velocity Ω for torsional waves propagating from source to receiver.

The time history of the electric field at the receiver transducer is illustrated in Fig. 6 (broken line) and compared to the experimental results (continuous line). The first pulse is the direct signal traveling from source to receiver. The second and third pulses are the reflections off the right and left boundaries, respectively.

C. Transmission of torsional stress waves

The drill string shown in Fig. 1 is used to simulate transmission of torsional waves. The rigidity modulus of the pipe and coupling joints is $Y_U=Y_0=82.4\,\mathrm{GPa}$. The same mesh and modeling parameters of the previous example are used here. Figure 7 shows the time history (a) (Ω) and its Fourier transform (b). As before, the transform was made using a sampling interval of 40 μs and 5544 points.

The following simulation uses the Chebyshev differential operator and a mapping transformation to model in detail the geometrical features of the coupling joints, while using a coarse distribution of grid points for modeling the pipes (see Fig. 8). For simplicity, we consider propagation through one coupling joint. The Gauss-Lobatto collocation points are redistributed by using the following mapping function:

$$q(\zeta)=\frac{2}{\pi}\arctan[\varepsilon\tan(\varphi)],\quad \varphi=\frac{\pi\zeta}{2},\tag{67}$$

with $\varepsilon=0.2$, satisfying $q(1)=1$ and $q(-1)=-1$, and

$$\frac{\partial\zeta}{\partial q}=\frac{1}{\varepsilon}[\cos^2(\varphi)+\varepsilon^2\sin^2(\varphi)].\tag{68}$$

Equation (67) is a particular case of the transformation used in Ref. 21. Using this mapping, the spatial derivative (62) can be rewritten as

$$\frac{\partial u}{\partial z}=\frac{2}{\varepsilon z_{\max}}[\cos^2(\varphi)+\varepsilon^2\sin^2(\varphi)]\frac{\partial u}{\partial \zeta}, \tag{69}$$

where $z_{\max}$ is the length of the string.

We consider $n_z=309$, a string length $z_{\max}=20.5$ m, and a source time-history with dominant frequency $f_d=4$ kHz. The diameters of the pipes and joint are those illustrated in Fig. 1, but with a linear transition from grid point 144 (10.02 m) to 147 (10.08 m) (from pipe to joint) and from point 163 (10.42 m) to 166 (10.48 m) (from joint to pipe). Figure 8 shows the string and the numerical mesh, where one grid point every four is represented. The source is located at grid point 20 (0.95 m) and the receiver at grid point 260 (15.46 m). At the two ends of the string, nonreflecting boundary conditions based on the method of characteristics are imposed[21] and, in addition, absorbing strips of length 18 are implemented to avoid any spurious reflection. The time-history, computed with a time step of 1 μs and resampled to 10 μs, is shown in Fig. 8. A set of coupling joints can be modeled by a general transformation based on functions of the type given in Eq. (67).

D. Propagation of flexural waves

The simulation of flexural waves requires a careful analysis of the dispersion equation. In order to avoid aliasing, the source spectrum must be band-limited, with the minimum frequency strictly greater than zero. This will be illustrated in the following analysis. According to the sampling theorem the maximum frequency allowed by the mesh is

$$f_{\max}=\frac{V_{p\,\min}}{2dz},$$

where $V_{p\,\min}$ is the minimum phase velocity obtained from Eq. (56),

$$V_{p\,\min}=2\pi f_{\min}[\mathrm{Re}(k(f_{\min}))]^{-1},$$

with $f_{\min}$ the minimum frequency of the spectrum. Then, the minimum allowable dz is

$$dz_{\min}=\frac{\pi f_{\min}[\mathrm{Re}(k(f_{\min}))]^{-1}}{f_{\max}}.$$

Neglecting gravity forces ($N=0$) and coupling with the axial force ($F=0$) we obtain

$$dz_{\min}=\frac{\sqrt{\pi R_F c_0 f_{\min}}}{\sqrt{2}f_{\max}},$$

where $c_0=\sqrt{Y/\rho}$.

Let us consider the example illustrated in Fig. 1 with $N=F=0$. The perturbation is initiated by the flexural force f_F, with a time history whose frequency spectrum is a Butterworth filter having a minimum frequency of 50 Hz and a maximum frequency of 570 Hz (computed for the pipe section), corresponding to a grid spacing $dz=23$ cm. The wavelet and its Fourier transform are illustrated in Figs. 9(a) and 9(b), respectively.

The dispersion equation (55),

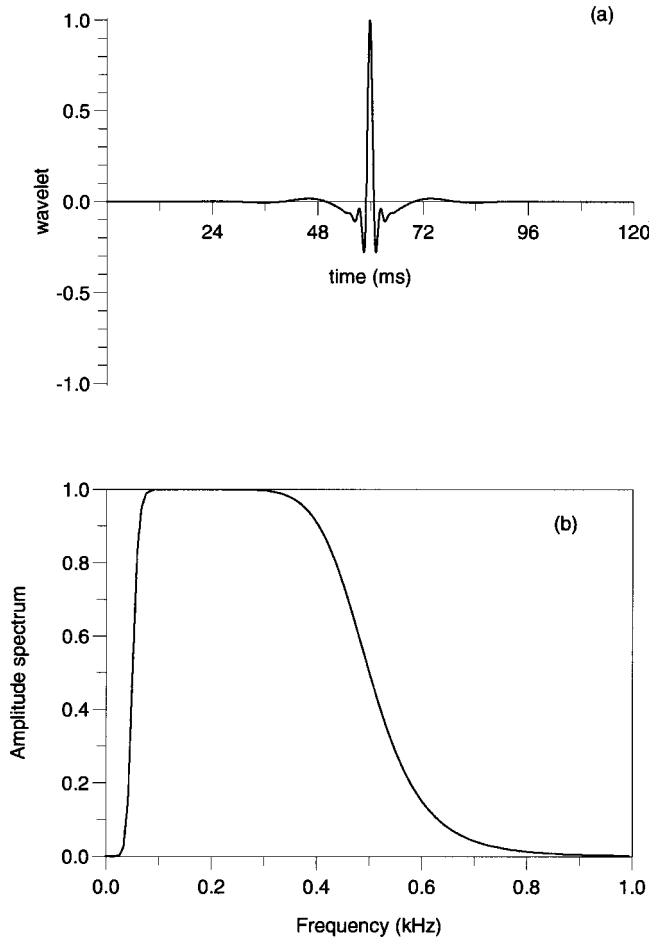

FIG. 9. Time history (a) and Fourier transform (b) of the Butterworth wavelet used to simulate flexural waves.

$$\omega^2=c_0^2R_F^2k^4,$$

has the solutions

$$k=\pm\sqrt{\frac{\omega}{c_0R_F}},\quad\text{and}\quad k=\pm i\sqrt{\frac{\omega}{c_0R_F}}, \tag{70}$$

which correspond to a propagating mode and a static mode, respectively. The phase velocity of the propagating modes is given by

$$V_p=\sqrt{2\pi R_F c_0 f},\quad\text{and}\quad V_{p\,\max}/V_{p\,\min}=\sqrt{f_{\max}/f_{\min}}.$$

In principle, the minimum and maximum velocities propagating in the drill string are 262 and 914 m/s (pipes), and 280 and 978 m/s (joints), respectively. The wavelength is

$$\lambda=\sqrt{2\pi R_F c_0/f},$$

which yields minimum and maximum wavelengths for the pipe section of 1.5 and 5.24 m, respectively. These values are much larger than the radius of gyration of the pipes (0.043 m), a necessary condition for the validity of the theory.[14] On the other hand, the group velocity is twice the phase velocity.[14]

The same mesh and modeling parameters of the first example are used here, and due to less stringent conditions concerning algorithm stability, the wave field is computed with a time step of 10 μs.

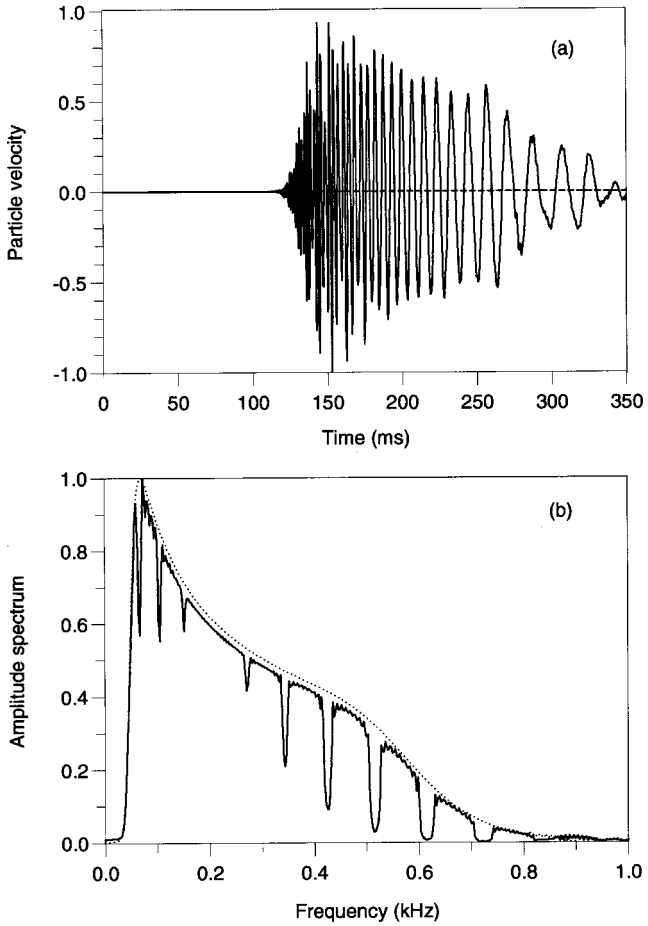

FIG. 10. Time history (a) and Fourier transform (b) of the flexural wave propagated along ten tool joints (see Fig. 1). The dotted line is the amplitude spectrum of the flexural wave in the absence of coupling joints.

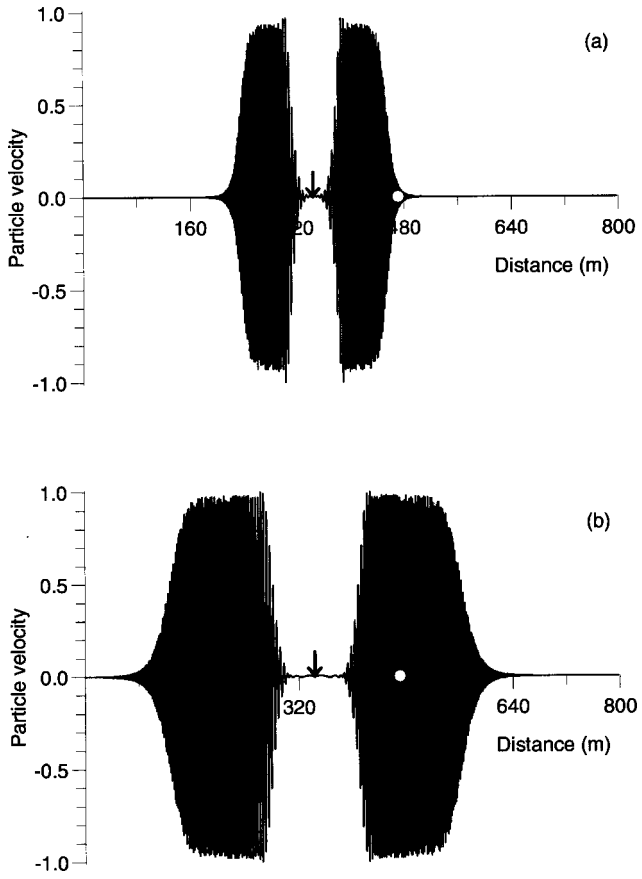

FIG. 11. Snapshots of the flexural wave at 120 (a) and 180 ms (b) in the absence of tool joints. The arrow indicates the source and the white dot the receiver.

Figure 10 shows the particle velocity $\dot{w}$ (a) and its Fourier transform (b). The dotted line is the amplitude spectrum of the flexural wave in the absence of coupling joints. The transform was made using a sampling interval of 400 μs and 924 points. Since source and receiver are 126.73 m apart, since the maximum group velocity is approximately 1828 m/s (pipes), and since the source delay is approximately 50 ms, the first break arrives at nearly 120 ms, as can be verified in Fig. 10(a). Moreover, high-frequency energy (short wavelengths) arrives earlier than low-frequency energy, in agreement with the prediction of the dispersion equation. The spectrum indicates that high-frequency energy has been lost. Actually, the energy has been distributed between the propagation and static modes, and the $\sqrt{\omega}$ dependence of the static-mode attenuation factor [see Eq. (70)] explains the dissipation of the high-frequency components. On the other hand, Fig. 10(b) reveals the presence of stopbands. Snapshots of the particle velocity at 120 (a) and 180 ms (b) are shown in Fig. 11, where the arrow and white dot indicate the source and receiver locations, respectively. As can be appreciated, the high-frequency energy precedes the low-frequency energy, and the width of the signal increases with time due to the velocity dispersion effect.

In the last example, we consider coupling between the axial and the flexural motions, corresponding to the drill string of the first example (Fig. 1), where the source is an axial force. The problem is solved by using the equations obtained by Drumheller[9] [see Eqs. (48) and (49), respectively]. The radius of curvature of the drill string, r_b, is constant and equal to 120 times the radius of gyration of the pipes. Figure 12 shows the wave field, where the (a) corresponds to the flexural particle velocity $\dot{w}$ and (b) to the extensional particle velocity v. The lateral motion represents a substantial loss of energy from the axial motion. This example is only intended to provide an idea of eventual capabilities of the modeling algorithm. An extensive analysis of coupling and energy exchange will be carried out in a future work.

VI. CONCLUSIONS

We presented the basic theory and algorithm for simulating the different vibrations' modes propagating in drill strings. A set of examples illustrates the versatility of the numerical algorithm: simulation of stopbands in axial and torsional wave propagation, generation of stress waves by piezoelectric transducers, mode attenuation, use of an adaptive mesh for modeling the shape of the coupling joints, flexural mode dispersion and dissipation, and coupling to the axial mode.

The modeling is the basis for further research on acoustic telemetry, such as in the Seisbit® method: in particular, simulation of coupled axial, torsional, and lateral vibrations, inclusion of nonlinear back-interaction of lateral bending on

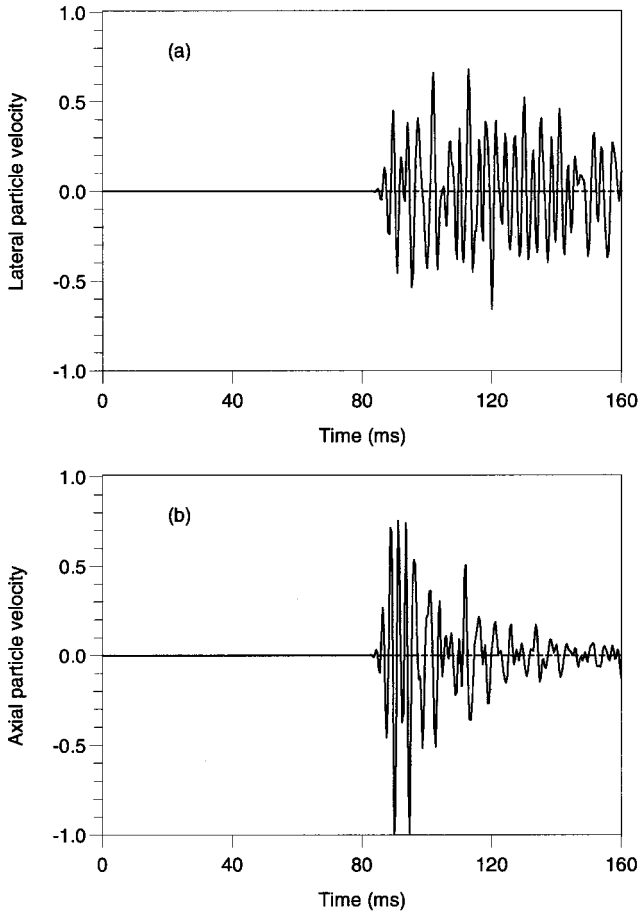

FIG. 12. Flexural (a) and extensional (b) particle velocities $\dot{w}$ and v caused by an axial force, corresponding to the model illustrated in Fig. 1.

the axial torsional waves; modeling of boundary conditions, such as rock-bit interaction, allowing the simulation of bit-bounce, rate-of-penetration, stick-slip oscillations, and torque reversals; modeling dual bending modes; focusing of lateral vibrations at the neutral point, etc. Moreover, the algorithm can be implemented in a more complex context, where the whole drill string/drive system is simulated.[22]

ACKNOWLEDGMENTS

Thanks to Fabio Cavallini and Géza Seriani for important technical comments.

APPENDIX: WAVE PROPAGATION IN A PIEZOELECTRIC SOLID

Let us assume for simplicity a lossless piezoelectric medium. Such a medium is characterized by the constitutive equations (Ref. 11, p. 274),

$$\mathbf{T}=\mathbf{c}:\mathbf{S}-\mathbf{e}\cdot\mathbf{E}, \tag{A1}$$

$$\mathbf{D}=\mathbf{e}:\mathbf{S}+\boldsymbol{\epsilon}\cdot\mathbf{E}, \tag{A2}$$

where $\mathbf{T}$ is the 6×1 stress vector, $\mathbf{S}$ is the 6×1 strain vector, $\mathbf{D}$ is the 3×1 electric displacement vector, and $\mathbf{E}$ is the 3×1 electric field vector; the dot and the double dot denote the scalar and double scalar products, as defined by Auld.[11] Let us assume a medium classified as hexagonal *6mm*, with its symmetry axis coinciding with the z-direction. The stiffness, dielectric, and piezoelectric matrices are given by

$$\mathbf{c}=\begin{pmatrix} c_{11} & c_{12} & c_{13} & 0 & 0 & 0 \\ c_{12} & c_{11} & c_{13} & 0 & 0 & 0 \\ c_{13} & c_{13} & c_{33} & 0 & 0 & 0 \\ 0 & 0 & 0 & c_{44} & 0 & 0 \\ 0 & 0 & 0 & 0 & c_{44} & 0 \\ 0 & 0 & 0 & 0 & 0 & c_{66} \end{pmatrix}, \tag{A3}$$

where $c_{66}=c_{11}-2c_{12}$,

$$\boldsymbol{\epsilon}=\begin{pmatrix} \epsilon_{xx} & 0 & 0 \\ 0 & \epsilon_{xx} & 0 \\ 0 & 0 & \epsilon_{zz} \end{pmatrix}, \tag{A4}$$

and

$$\mathbf{e}=\begin{pmatrix} 0 & 0 & 0 & 0 & e_{x5} & 0 \\ 0 & 0 & 0 & e_{x5} & 0 & 0 \\ e_{z1} & e_{z1} & e_{z3} & 0 & 0 & 0 \end{pmatrix}, \tag{A5}$$

respectively.

In the absence of sources and conduction currents, Newton's and Maxwell's equations can be written in compact form as

$$\nabla\cdot\mathbf{T}=\rho\partial_{tt}\mathbf{u}, \quad -\nabla\times\mathbf{E}=\mu\partial_t\mathbf{H}, \quad \nabla\times\mathbf{H}=\partial_t\mathbf{D}, \tag{A6}$$

where $\mathbf{u}$ is the elastic displacement vector, $\mathbf{H}$ is the magnetic field vector, ρ is the density, μ is the magnetic permeability, and

$$\nabla\cdot=\begin{pmatrix} \partial_x & 0 & 0 & 0 & \partial_z & \partial_y \\ 0 & \partial_y & 0 & \partial_z & 0 & \partial_x \\ 0 & 0 & \partial_z & \partial_y & \partial_x & 0 \end{pmatrix},$$
$$\nabla\times=\begin{pmatrix} 0 & -\partial_z & \partial_y \\ \partial_z & 0 & -\partial_x \\ -\partial_y & \partial_x & 0 \end{pmatrix}. \tag{A7}$$

Assume that a uniform z-propagating plane wave exists in the medium. Then, $\partial_x=\partial_y=0$ and substitution of the constitutive equations (A1) and (A2) into the dynamical equations (A6) yields

$$\begin{aligned} &c_{44}\partial_{zz}u_1-e_{x5}\partial_zE_1=\rho\partial_{tt}u_1, \quad \text{(a)}\\ &c_{44}\partial_{zz}u_2-e_{x5}\partial_zE_2=\rho\partial_{tt}u_2, \quad \text{(b)}\\ &c_{33}\partial_{zz}u_3-e_{z3}\partial_zE_3=\rho\partial_{tt}u_3, \quad \text{(c)}\\ &\partial_zE_2=\mu\partial_tH_1, \quad \text{(d)}\\ &-\partial_zE_1=\mu\partial_tH_2, \quad \text{(e)}\\ &0=\mu\partial_tH_3, \quad \text{(f)}\\ &-\partial_zH_2=e_{x5}\partial_{zt}u_1+\epsilon_{xx}\partial_tE_1, \quad \text{(g)}\\ &\partial_zH_1=e_{x5}\partial_{zt}u_2+\epsilon_{xx}\partial_tE_2, \quad \text{(h)}\\ &0=e_{z3}\partial_{zt}u_3+\epsilon_{zz}\partial_tE_3. \quad \text{(i)} \end{aligned} \tag{A8}$$

Assume a phase factor $\exp(i\omega t)$, where ω is the angular frequency, and a spatial phase factor $\exp(-i\omega sz)$, where s is the

slowness in the z-direction. For any field variable, we have

$$\partial_t \rightarrow i\omega \quad \text{and} \quad \partial_z \rightarrow -i\omega s.$$

Using these relations and eliminating the magnetic field components, Eqs. (A8) become

$$\begin{aligned}
&(c_{44}s^2-\rho)v_1+e_{x5}sE_1=0, \quad \text{(a)}\\
&(c_{44}s^2-\rho)v_2+e_{x5}sE_2=0, \quad \text{(b)}\\
&(c_{33}s^2-\rho)v_3+e_{z3}sE_3=0, \quad \text{(c)}\\
&\mu e_{x5}sv_1+E_1(s^2-\mu\epsilon_{xx})=0, \quad \text{(g)}\\
&\mu e_{x5}sv_2+E_2(s^2-\mu\epsilon_{xx})=0, \quad \text{(h)}\\
&-se_{z3}v_3+\epsilon_{zz}E_3=0, \quad \text{(i)}
\end{aligned} \tag{A9}$$

where $\mathbf{v}=\partial_t\mathbf{u}$ is the particle velocity vector. Equations (A9a)(b) and (A9f)(h) give the dispersion equation for the *quasiacoustic* and *quasielectromagnetic* waves,

$$(s^2-\mu\epsilon_{x5})(s^2c_{44}-\rho)-\mu e_{x5}^2s^2=0, \tag{A10}$$

with **v** and **E** polarized in the plane perpendicular to the symmetry (poling) axis. On the other hand, Eqs. (A9c) and (A9i) yield the dispersion relation of the piezoelectrically *stiffened acoustic wave*,

$$s^2\left(c_{33}+\frac{e_{z3}^2}{\epsilon_{zz}}\right)=\rho, \tag{A11}$$

with **v** and **E** polarized along the symmetry (poling) axis. From Eqs. (A8f) and (A8i), this wave mode satisfies $\partial_t H_3=0$ and $\partial_t D_3=0$, and H_3 and D_3 are both zero, except for time-independent fields that are not of interest. That the electric field has zero curl implies that it can be represented as the gradient of a scalar potential even though it is time-varying, not static. This is called a *quasistatic field*.[11]

[1] D. S. Drumheller, ''Attenuation of sound waves in drill strings,'' J. Acoust. Soc. Am. **94**(4), 2387–2396 (1993).
[2] D. S. Drumheller and S. D. Knudsen, ''The propagation of sound waves in drill strings,'' J. Acoust. Soc. Am. **97**(4), 2116–2125 (1995).
[3] E. L. Hixon, US Patent 3,252,225 (1966).
[4] W. H. Cox and P. E. Chaney, ''Telemetry system,'' US Patent No. 4,293,936 (1981).
[5] H. E. Sharp and M. A. Smither, ''Borehole acoustic telemetry system with phase shifted signals,'' US Patent 4,562,559 (1985).
[6] F. Miranda, L. Aleotti, F. Abramo, F. Poletto, A. Craglietto, S. Persoglia, and F. Rocca, ''Impact of seismic while drilling technique on exploration wells,'' First Break **14**, 55–68 (1996).
[7] L. Aleotti, F. Poletto, F. Miranda, P. Corubolo, F. Abramo, and A. Craglietto, ''Seismic while-drilling technology: Use and analysis of the drill-bit seismic source in a cross-hole survey,'' Geophys. Prospect. **47**, 25–39 (1999).
[8] T. G. Barnes and B. R. Kirkwood, ''Passbands for acoustic transmission in an idealized drill string,'' J. Acoust. Soc. Am. **51**, 1606–1608 (1972).
[9] D. S. Drumheller, ''Extensional stress waves in one-dimensional elastic waveguides,'' J. Acoust. Soc. Am. **92**(6), 3389–3402 (1992).
[10] J. M. Carcione, D. Kosloff, and R. Kosloff, ''Wave propagation simulation in a linear viscoelastic medium,'' Geophys. J. R. Astron. Soc. **95**, 597–611 (1988).
[11] B. A. Auld, *Acoustic Fields and Waves in Solids* (Krieger, Malabar, Florida, 1990).
[12] J. M. Carcione, ''Ground penetrating radar: Wave theory and numerical simulation in lossy anisotropic media,'' Geophysics **61**, 1664–1677 (1996).
[13] A. E. H. Love, *A Treatise on the Mathematical Theory of Elasticity* (Cambridge University Press, Cambridge, 1952).
[14] H. Kolsky, *Stress Waves in Solids* (Clarendon, Oxford, 1953).
[15] P. M. Morse and K. U. Ingard, *Theoretical Acoustics* (Princeton University Press, Princeton, NJ, 1986).
[16] W. C. Chin, *Wave Propagation in Petroleum Engineering* (Gulf, □□, 1994).
[17] D. S. Drumheller, ''Coupled extensional and bending motion in elastic waveguides,'' Wave Motion **17**, 319–327 (1993).
[18] D. S. Drumheller, ''Acoustic properties of drill strings,'' J. Acoust. Soc. Am. **85**(3), 1048–1064 (1989).
[19] N. J. C. Lous, S. W. Rienstra, and I. J. B. F. Adan, ''Sound transmission through a periodic cascade with application to drill pipes,'' J. Acoust. Soc. Am. **103**(5), 2302–2311 (1998).
[20] D. Kosloff, M. Reshef, and D. Loewenthal, ''Elastic wave calculations by the Fourier method,'' Bull. Seismol. Soc. Am. **74**, 875–891 (1984).
[21] J. M. Carcione, ''A 2D Chebyshev differential operator for the elastic wave equation,'' Comput. Methods Appl. Mech. Eng. **130**, 33–45 (1996).
[22] J. D. Jansen and L. van den Steen, ''Active damping of self-excited torsional vibrations in oil well drill strings,'' J. Sound Vib. **179**(4), 647–668 (1995).

Calculation of B/A for n-alkane liquids using the Tait equation

Bruce Hartmann, Gilbert F. Lee, and Edward Balizer
Polymer Science Group, Naval Surface Warfare Center, 9500 MacArthur Boulevard, West Bethesda, Maryland 20817-5700

(Received 30 June 1999; accepted for publication 14 March 2000)

The B/A parameter of acoustic nonlinearity was calculated for a series of n-alkane liquids using the Tait PVT equation of state supplemented with specific heat data. The calculations of sound speed, sound speed derivatives, the two components of B/A, and the value of B/A itself were compared with experimental data taken from the literature and with earlier calculations using a different equation of state. In addition, a comparison of the results with Ballou's rule (linear relation of B/A and reciprocal sound speed) was made. It is concluded that B/A can be calculated from the Tait equation of state with about the same accuracy as direct measurements of sound speed versus pressure and temperature, though the the temperature derivatives of the sound speed are calculated with much lower accuracy than pressure derivatives. The calculations made using the Tait equation are about the same accuracy as calculations made using our equation of state. Also, Ballou's rule does not hold for these liquids. [S0001-4966(00)05606-X]

PACS numbers: 43.25.Ba [MFH]

INTRODUCTION

The nonlinearity parameter B/A for a liquid, as a function of pressure, P, and absolute temperature, T, can be expressed as[1]

$$\frac{B}{A}=2\rho c\left(\frac{\partial c}{\partial P}\right)_T+\frac{2cT\alpha}{C_P}\left(\frac{\partial c}{\partial T}\right)_P=\left(\frac{B}{A}\right)'+\left(\frac{B}{A}\right)'' \tag{1}$$

in terms of the liquid density ρ, sound speed c, thermal expansion coefficient α, and specific heat at constant pressure C_P. Sound speed can be expressed as

$$c=\sqrt{B_S V}=\sqrt{(C_P/C_V)B_T V}=\sqrt{\gamma B_T V}, \tag{2}$$

where $V=1/\rho$ is the specific volume, B_S is the adiabatic bulk modulus, B_T is the isothermal bulk modulus, and C_P and C_V are the specific heat capacities at constant pressure and constant volume, respectively. The ratio of specific heats is given by the standard thermodynamic relation

$$\frac{C_P}{C_V}=\gamma=\frac{C_P}{C_P-TV\alpha^2 B_T}, \tag{3}$$

where thermal expansion coefficient and isothermal bulk modulus are defined as

$$\alpha=\frac{1}{V}\left(\frac{\partial V}{\partial T}\right)_P \tag{4}$$

and

$$B_T=-V\left(\frac{\partial P}{\partial V}\right)_T, \tag{5}$$

respectively.

From the equations presented, it can be seen that all the required information to calculate B/A can be obtained from a PVT equation of state except C_P. Experimental values will be used here. Note that only the heat capacity at zero pressure is required since $C_P(T,P)$ can be calculated from $C_P(T,0)$ using the thermodynamic relation

$$\left(\frac{\partial C_P}{\partial P}\right)_T=-T\left(\frac{\partial^2 V}{\partial T^2}\right)_P, \tag{6}$$

where the required integration can be carried out knowing the equation of state.

This method of calculating B/A from an equation of state and C_P has been demonstrated using our equation of state and compared with experimental data for a series of n-alkane liquids and molten polyethylene.[2] In this paper, the same procedure is followed using the Tait equation. The Tait equation has a long history of use in simple liquids and polymers, both in the molten and solid states. The main goal of this article is to compare and contrast the two equations in the, very demanding, application of nonlinear acoustics and to gain some insight into the strengths and weaknesses of the equation of state method in general.

The next section of the paper will present all the equations needed to calculate B/A from the Tait equation and specific heat data. Following this, comparisons will be made with experimental data of the PVT properties, sound speed, sound speed derivatives, and B/A for a series of six n-alkane liquids and molten polyethylene. The results calculated with the Tait equation are also compared with the results calculated with our equation of state. Finally, calculated and experimental results are compared with Ballou's rule. The conclusions from this work are presented in the final section.

I. THEORETICAL DEVELOPMENT

Tait[3] proposed an empirical equation for the volume isotherm of seawater of the form

$$\frac{dV}{dP}=-\frac{K}{B(T)+P}, \tag{7}$$

where V is specific volume and K and $B(T)$ are constants. In applying this result to liquids in general, the equation is usually integrated from zero pressure to an arbitrary pressure with the result that

$$V(T,P)-V(T,0)=-K\ln(1+P/B(T)). \tag{8}$$

Dividing through by $V(T,0)$ and rearranging yields the final form

$$V(T,P)=V(T,0)[1-C\ln(1+P/B(T))], \tag{9}$$

where $C=K/V(T,0)$ and its temperature dependence is neglected. Sometimes C is assumed to be a universal constant for all liquids but will be allowed to vary in this work. It is generally assumed that the zero pressure volume isobar is of the form

$$V(T,0)=V_0\exp(\alpha_0 T), \tag{10}$$

where V_0 and α_0 are constants for each liquid, and that the function $B(T)$ is of the form

$$B(T)=B_0\exp(-B_1 T), \tag{11}$$

where B_0 and B_1 are constants for each liquid. The combination of Eqs. (9)–(11) is referred to as the Tait equation. There are five adjustable parameters that describe each liquid using the Tait equation: C, V_0, α_0, B_0, and B_1.

Evaluating Eqs. (4) and (5) using the Tait equation gives

$$\alpha=\alpha_0-\frac{CB_1PV(T,0)/V(T,P)}{B(T)+P} \tag{12}$$

for the thermal expansion coefficient and

$$B_T(T,P)=\frac{B(T)+P}{C}\frac{V(T,P)}{V(T,0)} \tag{13}$$

for the isothermal bulk modulus.

The last input required for the calculation of sound speed is the specific heat. First, evaluate the pressure derivative of the specific heat using Eq. (6). The result is

$$\left(\frac{\partial C_P}{\partial P}\right)_T=-\alpha_0^2TV(T,P)+\frac{2\alpha_0CB_1TV(T,0)P}{B(T)+P}+\frac{CB_1^2TB(T)V(T,0)P}{(B(T)+P)^2}. \tag{14}$$

Integrating this result gives

$$C_P(T,P)=C_P(T,0)+TV(T,0)\left[-\alpha_0^2TV(T,0)[(1+CP)-(B(T)+P)\overline{V}(T,0)]+2\alpha_0B_1TV(T,0)[CP-B(T)\overline{V}(T,P)]+B_1^2TB(T)V(T,0)\times\left[\overline{V}(T,P)-\frac{CP}{B(T)+P}\right]\right], \tag{15}$$

where the reduced volume variable is defined as

$$\overline{V}(T,P)=1-\frac{V(T,P)}{V(T,0)}. \tag{16}$$

Here C_P along the zero pressure isotherm will be taken from experimental results expressed as a power series in absolute temperature

$$C_P(T,0)=N_0+N_1T+N_2T^2+N_3T^3. \tag{17}$$

The pressure derivative of the sound speed can be calculated using the above equations and for $(B/A)'$ we find

$$\left(\frac{B}{A}\right)'=\frac{2Tc(T,P)}{1-C\ln(1+P/B(T))}\left[\frac{CPB_1^2B(T)}{(B(T)+P)^2}+\frac{2\alpha_0B_1CP}{B(T)+P}-\alpha_0^2\left(1-\ln\left(1+\frac{P}{B(T)}\right)\right)\right]. \tag{18}$$

This is the dominant term in B/A, typically representing 90% of the total.

The $(B/A)''$ term involves the temperature derivative of the sound speed. From Eqs. (1) and (2), it follows that

$$\left(\frac{B}{A}\right)''=\frac{T\alpha}{C_P}\left[\gamma B_T\left(\frac{\partial V}{\partial T}\right)_P-\gamma V\left(\frac{\partial B}{\partial T}\right)_P+B_TV\left(\frac{\partial\gamma}{\partial T}\right)_P\right], \tag{19}$$

where

$$\left(\frac{\partial V}{\partial T}\right)_P=\alpha_0V(T,P)-\frac{V(T,0)CB_1P}{B(T)+P}, \tag{20}$$

$$\left(\frac{\partial B_T}{\partial T}\right)_P=-\frac{B_1B(T)}{C}\frac{V(T,P)}{V(T,0)}-B_1P, \tag{21}$$

and

$$\left(\frac{\partial\gamma}{\partial T}\right)_P=\frac{1}{C_P-TV\alpha^2B_T}\left(\frac{\partial C_P}{\partial T}\right)_P-\frac{C_P}{(C_P-TV\alpha^2B_T)^2}\left[\left(\frac{\partial C_P}{\partial T}\right)_P-T\left(\alpha^2B_T\left(\frac{\partial V}{\partial T}\right)_P+2\alpha VB_T\left(\frac{\partial\alpha}{\partial T}\right)_P+V\alpha^2\left(\frac{\partial B_T}{\partial T}\right)_P\right)\right]. \tag{22}$$

The temperature derivatives of volume and bulk modulus are given in Eqs. (20) and (21), and the temperature derivative of the thermal expansion coefficient is given by

$$\left(\frac{\partial\alpha}{\partial T}\right)_P=-\frac{CB_1^2P}{(B(T)+P)^2}\frac{V(T,0)}{V(T,P)}\left[B(T)+CP\frac{V(T,0)}{V(T,P)}\right], \tag{23}$$

and the only remaining quantity to determine is the temperature derivative of the specific heat.

Differentiating Eq. (15) yields

$$\left(\frac{\partial C_P}{\partial T}\right)_P=(N_1+2N_2T+3N_3T^2)+F1+F2+F3, \tag{24}$$

where the term in parentheses comes from Eq. (17) and

$$F_1=(\alpha_0^2+\alpha_0^3T)V(T,0)[(B(T)+P)\overline{V}(T,P)-(1+C)P]+\alpha_0^2B_1TV(T,0)[CP-\overline{V}(T,P)B(T)], \tag{25}$$

TABLE I. Tait parameters for *n*-alkanes.

n	*C*	V_0 (cm^3/g)	α_0 (1/K)	B_0 (MPa)	B_1 (1/K)	ΔV_{av} (cm^3/g)
5	0.095 125	0.999 32	1.6110*e*-3	506.79	8.4329*e*-3	0.0036
7	0.088 289	0.968 25	1.4117*e*-3	738.01	8.4624*e*-3	0.0049
8	0.090 147	0.968 16	1.3057*e*-3	872.39	8.4123*e*-3	0.0017
9	0.086 023	0.977 20	1.2039*e*-3	844.13	8.1520*e*-3	0.0013
12	0.084 311	0.980 28	1.0498*e*-3	752.32	7.2031*e*-3	0.0009
16	0.084 516	0.977 78	9.4975*e*-4	579.37	5.9494*e*-3	0.0005
∞	0.088 730	0.917 81	7.7982*e*-4	582.54	4.5184*e*-3	0.0003

$$F_2 = 2\alpha_0 B_1 V(T,0)\Bigg[(1+\alpha_0 T)(CP-\overline{V}(T,P))B(T) + B_1 T B(T)\left(\overline{V}(T,P)-\frac{CP}{B(T)+P}\right)\Bigg], \tag{26}$$

$$F_3 = B_1^2 V(T,0)B(T)(1+\alpha_0 T)\left[\overline{V}(T,P)-\frac{CP}{B(T)+P}\right] - B_1^3 T V(T,0)B(T)\left[\overline{V}(T,P)-\frac{2CP}{B(T)+P} + \frac{CPB(T)}{[B(T)+P]^2}\right]. \tag{27}$$

II. COMPARISON WITH EXPERIMENT

The first step is to determine the Tait equation parameters for the *n*-alkanes by fitting to experimental PVT data. Each liquid will be identified by the number, *n*, of carbon atoms in the chain. Data for $n=7$, 8, 9, 12, and 16 was taken from Boelhouwer[4] and for $n=5$ from Belinskii and Ikramov.[5] For molten polyethylene, data was taken from Olabisi and Simha.[6] Fitting was carried out with a nonlinear least squares fit routine. The resulting parameters are listed in Table I along with the average value of the volume fit. An example of the fit is shown in Fig. 1 for *n*-heptane, the liquid for which there is the most experimental data (63 data points) and which has the worst fit (an average of 0.5% difference between measured and calculated volumes). Looking at the average volume difference listed in Table I, the Tait equation gives progressively better overall fits as the chain length increases (*n*-pentane is the only exception), being 0.03% for molten polyethylene. Looking in detail at the individual errors, there are as many positive as negative. There is no trend with temperature but the fit is generally better at high pressure than at low pressure. The *C* values in Table I are reasonably close to the universal value[6,7] of 0.0894 often assumed for both organic liquids and molten polymers.

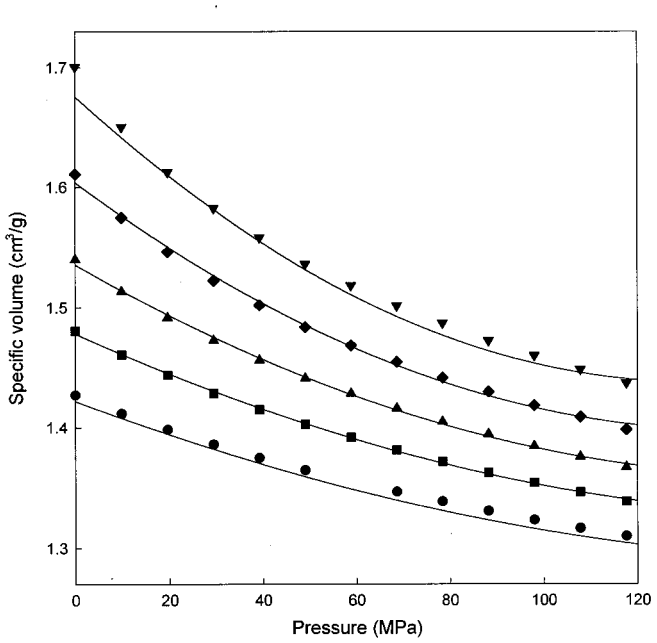

FIG. 1. Volume isotherms for *n*-heptane (experimental values: ● 273 K, ■ 303 K, ▲ 333 K, ◆ 363 K, ▼ 393 K. Tait equation: solid lines).

TABLE II. Coefficients of heat capacity polynomial $C_p(T,0)=N_0+N_1T+N_2T^2+N_3T^3$.[a]

n	N_0	N_1	10^3N_2	10^6N_3	Temperature range (K)
5	43.994	−0.140 67	0.547 51	−0.405 91	150–300
7	56.582	−0.144 90	0.578 13	−0.416 67	240–370
8	147.031	−1.051 89	3.831 23	−4.272 69	220–300
9	207.014	−1.576 03	5.523 39	−6.041 31	225–315
12	438.377	−3.599 983	11.982 37	−12.842 61	270–320
16	1368.915	−11.963 75	37.751 52	−39.160 98	295–320
∞	4.1788	0.010 476	0	0	420–630

[a]Units of cal/mol K for *T* in K. Taken from Ref. 8, except $n=\infty$ from Ref. 9.

The same quantities were calculated earlier using our equation of state,[2] which is of the form

$$\overline{PV^5} = \overline{T}^{3/2} - \ln \overline{V}, \tag{28}$$

where $\overline{P}=P/P_0$, $\overline{V}=V/V_0$, and $\overline{T}=T/T_0$, and P_0, V_0, and T_0 are the reducing parameters for the liquid. As can be seen, the form of this equation is quite different from the Tait equation. For the liquids presented here, the Tait equation fits the data slightly better than our equation except for $n=5$ and 7, though the better fit is achieved through the use of five adjustable parameters while our equation uses only three adjustable parameters. Both equations agree with experiment more closely as *n* increases and as *P* increases.

Experimental values of $C_P(T,0)$ for the *n*-alkanes were taken from published values.[8] They are given in the form of cubic polynomials in temperature. It is important to use these polynomials only over their stated range of validity. Extrapolating outside this range can lead to significant errors, and it is this temperature range that limits the range over which B/A can be calculated. In addition, C_P values for molten polyethylene, linear in temperature, were also taken from the literature.[9] The temperature coefficients are collected in Table II.

Having all the needed input parameters, the sound speed of the *n*-alkane liquids can now be calculated. Values at room temperature and zero pressure are listed in the first column of Table III. Experimental values taken from Boelhouwer[10] are also listed. These experimental values are said to be accurate to within 1%. The calculated values agree with the experimental values from 2% to 5%. The values

TABLE III. *n*-alkane parameters at 20 °C and $P=0$.

n	c (m/s)	$\partial c/\partial T$ (m/s K)	$\partial c/\partial P$ (m/s MPa)	ρ (g/cm^3)	α (10^{-4}/K)	C_p (cal/g K)
			Calculated using Tait equation			
5	974	−4.66	8.62	0.624	16.1	⋯
7	1185	−6.07	7.14	0.683	14.1	⋯
8	1260	−6.44	5.99	0.705	13.1	⋯
9	1285	−6.21	6.03	0.719	12.0	⋯
12	1353	−5.52	5.55	0.750	10.5	⋯
16	1379	−4.33	5.32	0.774	9.5	⋯
∞	1555	−3.71	3.93	0.867	7.8	⋯
			Experimental			
5	1030	−4.50	7.21	0.626	16.0	0.550
7	1153	−4.35	6.87	0.683	12.4	0.533
8	1193	−4.20	6.51	0.702	11.5	0.529
9	1227	−4.09	6.22	0.718	10.8	0.527
12	1298	−3.93	5.59	0.749	9.7	0.525
16	1357	−3.72	5.05	0.773	8.9	0.528

TABLE IV. Nonlinearity parameters at 20 °C and $P=0$.

n	$(B/A)'$	$(B/A)''$	B/A
	Calculated from Tait equation		
5	10.48	−1.87	8.61
7	11.56	−2.68	8.88
8	10.64	−2.81	7.82
9	11.15	−2.56	8.59
12	11.27	−2.10	9.17
16	11.37	−1.51	9.86
∞	10.60	−1.22	9.38
	Experimental		
5	9.30	−1.89	7.41
7	10.82	−1.63	9.19
8	10.90	−1.53	9.37
9	10.96	−1.44	9.52
12	10.87	−1.32	9.55
16	10.59	−1.19	9.40

calculated with the Tait equation are slightly better than the values calculated using our equation (our highest difference is 7%). All of the calculated Tait values are higher than the experimental values except for $n=5$ while the calculated sound speeds with our equation are all lower than the experimental. The major source of the difference between experimental and calculated in either case is in the calculation of the bulk modulus since the density and specific heat are known to 1%. This finding is in agreement with the general observation that derivatives (such as bulk modulus) are an order of magnitude more uncertain than the undifferentiated value (such as volume).

Sound speed isotherms for *n*-heptane are plotted in Fig. 2 for high and low temperatures. Sound speeds along other isotherms are intermediate between these two. At 253 °K, the average difference between calculated and experimental is 8% while at 353 °K the difference is 2%. In all cases, the calculated values are higher than the experimental values.

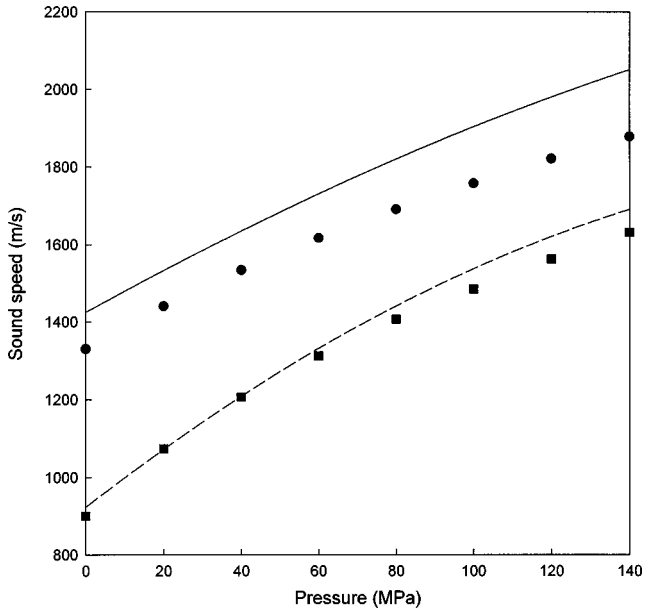

FIG. 2. Sound speed isotherms for *n*-heptane (experimental values: ● 253 K, ■ 353 K. Tait equation: solid line 253 K, dashed line 353 K).

Also, it can be seen that values at low pressure are closer to experimental values than those at high pressure, contrary to the volume fits that were more accurate at high pressure.

Temperature and pressure derivatives of sound speed at room temperature and zero pressure are listed in Table III. Experimental values were calculated using a standard cubic spline routine. The results were checked using a moving five-point least-square fit to a quadratic with very good agreement. Being the derivative of measured data, these results are not as accurate as the sound speed data from which they were calculated. The calculated pressure derivatives agree with experimental values to about 5%, except for *n*-pentane. Half of the calculated values are higher than the experimental values and half are lower. The calculated temperature derivatives are much further from the experimental values, an average of 40%. In this case, all the calculated values are lower than the experimental values. Once again, *n*-pentane is an exception. Fortunately, the temperature derivative appears in $(B/A)''$ which only contributes about 10% to the total value. A similar situation occurred with our equation, namely that the temperature derivatives were in overall poor agreement with experiment.

For completeness, the other parameters needed to calculate B/A, density, thermal expansion coefficient, and specific heat are also listed in Table III at room temperature and zero pressure. As expected, the calculated density is in very good agreement with experiment, an average of 0.2% different. All the calculated values are higher than experimental except for *n*-pentane. Calculated thermal expansion coefficients compare with experimental values to within an average of about 11%, except for *n*-pentane which is within 0.6%. Since the thermal expansion coefficient depends on the temperature derivative of the volume (or density), it is expected to be less accurate.

Using the parameters from Table III, B/A and its components, $(B/A)'$ and $(B/A)''$, were calculated and are listed in Table IV. Calculated values of $(B/A)'$ agree with experimental values to within an average of 6% while calculated $(B/A)''$ values are more than 50% greater than experimental values. Since $(B/A)''$ is smaller than $(B/A)'$, the final values of B/A are dominated by the accuracy of $(B/A)'$ and the

values of B/A agree with experiment to an average of 9%. This is almost identical to the agreement found earlier with our equation of state,[2] though in that case all the calculated values were greater than experimental values while for the Tait equation the calculated values are generally lower than experimental. The fact that similar problems were observed with the two very different equations of state suggest some fundamental problem in the calculation of the temperature derivatives of the sound speed. The overall difference of 9% between experimental and calculation is estimated to be comparable to the accuracy of the experimental measurement, based on stated experimental accuracy of B/A measurements in liquids and the variation between experimental values reported by different workers on the same liquid (water being the most studied liquid). Thus, we conclude that the calculated values are about as accurate as measured values.

A Monte Carlo procedure[11] was used to estimate the error in B/A due to errors in the Tait parameters. The first step was to determine the errors expected for the Tait parameters. It was assumed that the volume measurements for *n*-heptane have a normal distribution of random errors with mean zero and standard deviation 0.0005 cm^3/g for given values of pressure and temperature. Random errors were then added to the measured volumes and the Tait parameters determined using a nonlinear least-squares algorithm. After 20 000 simulations, the standard deviations of the five Tait parameters were found to be $\sigma(V_0)=1.10e\text{-}3\ cm^3/g$, $\sigma(\alpha_0)=3.30e\text{-}6\ K^{-1}$, $\sigma(C)=6.24e\text{-}4$, $\sigma(B_0)=19.9\ MPa$, and $\sigma(B_1)=7.00e\text{-}5\ K^{-1}$. Assuming that these values are representative, 100 000 Monte Carlo simulations were run calculating B/A from the Tait parameters with random error added to them. For the temperature range from 253 to 293 K and the pressure range from 0 to 100 MPa, the error in B/A averages 1.5%. In addition, a simulation was also done allowing error in the Tait parameters and the heat capacity measurement. The error in B/A was unchanged from the value with error only in the Tait parameters. Since this error is less than the difference between calculated and experimental values of B/A, it is concluded that the major source of the difference is more likely due to failure of the Tait equation rather than the accuracy with which the parameters are determined.

Ballou's rule is an empirical observation that B/A is a linearly increasing function of $1/c$.[12] While only roughly true, the rule is useful in correlating data for different liquids of widely varying properties. Some justifications of this rule have been presented.[13,14] A plot of Ballou's rule is shown in Fig. 3 along with the experimental data that was used to establish the rule. As can be seen, the liquid metals as a group have low B/A and low $1/c$ while various organic liquids are clustered around higher B/A values with higher $1/c$ values. Also shown in Fig. 3 are the results for the *n*-alkane liquids studied here. The scatter in the experimental and calculated data is well within the scatter of the various organic liquids used for Ballou's rule, though the data could best be described as having an essentially constant B/A. Thus, Ballou's rule does not apply within this class of liquid, though the class as a whole crudely falls on the overall curve for a range of liquids of very different types.

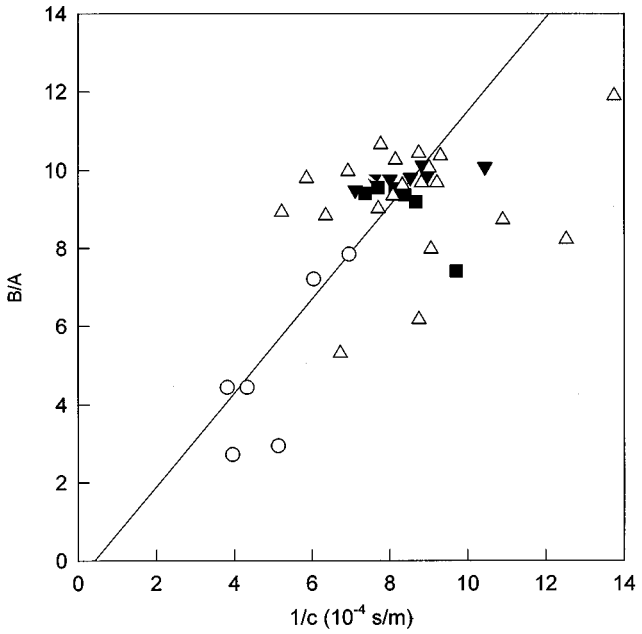

FIG. 3. B/A versus reciprocal sound speed. (Ballou's rule: solid line. Liquid metals, experimental values: ○. Various organic liquids, experimental values: △. *n*-alkane liquids, experimental values: ■. *n*-alkane liquids, calculated from Tait equation: ▼.)

III. CONCLUSIONS

Using the Tait equation of state supplemented with experimental heat capacity, the acoustic parameter of nonlinearity B/A was calculated and compared with experimental data and with the results of a previous calculation using a different equation of state. The comparison was made for a series of six normal alkane liquids and molten polyethylene.

A number of specific conclusions were reached:

(1) B/A can be calculated from the Tait equation of state with an accuracy of better than 10%, about the same accuracy as determinations from directly measuring sound speed as a function of pressure and temperature.
(2) $(B/A)''$ is calculated with poor accuracy but $(B/A)'$ is calculated reasonably accurately.
(3) The above conclusions apply equally well to the Tait equation and to our equation, perhaps indicating a fundamental limitation in the calculation of temperature dependence of sound speed.
(4) Ballou's rule is not followed within this class of liquid, but the class as a whole is in crude agreement with the rule.

ACKNOWLEDGMENT

This work was supported by the Carderock Division, Naval Surface Warfare Center's In-House Laboratory Independent Research Program, sponsored by the Office of Naval Research.

[1] R. T. Beyer, ''Parameter of nonlinearity in fluids,'' J. Acoust. Soc. Am. **32**, 719–721 (1960).
[2] B. Hartmann and E. Balizer, ''Calculated B/A parameters for *n*-alkane liquids,'' J. Acoust. Soc. Am. **82**, 614–620 (1987).
[3] P. G. Tait, ''Report on some of the physical properties of fresh water and

of sea-water,'' Phys. Chem. **2**, 1 (1888); ''Physics and Chemistry of the Voyage of H. M. S. Challenger,'' Vol. II, Part IV, 1888 Scientific Papers, Volume LXI.
[4] J. W. M. Boelhouwer, ''PVT relations of five liquid *n*-alkanes,'' Physica **34**, 1021–1028 (1960).
[5] B. A. Belinskii and Sh. Kh. Ikramov, ''Comprehensive investigation of the acoustical parameters, viscosity, and density of *n*-pentane over a wide pressure interval,'' Sov. Phys. Acoust. **18**, 300–303 (1973).
[6] O. Olabisi and R. Simha, ''Pressure-volume-temperature studies of amorphous and crystallizable polymers. I. Experimental,'' Macromolecules **8**, 206–210 (1975).
[7] G. A. Neece and D. R. Squire, ''On the Tait and related empirical equations of state,'' J. Phys. Chem. **72**, 128–136 (1968).
[8] J. F. Messerly, G. B. Guthrie, S. S. Todd, and H. L. Finke, ''Low-temperature thermal data for *n*-pentane, *n*-heptadecane, and *n*-octadecane,'' J. Chem. Eng. Data **12**, 338–346 (1967).
[9] V. Bares and B. Wunderlich, ''Heat capacity of molten polymers,'' J. Polym. Sci. **2**, 861–873 (1973).
[10] J. W. M. Boelhouwer, ''Sound velocities in and adiabatic compressibilities of liquid alkanes at various temperatures and pressures,'' Physica **34**, 484–492 (1967).
[11] K. Binder and D. W. Heermann, *Monte Carlo Simulation in Statistical Physics*, 2nd ed. (Springer-Verlag, Berlin, 1992).
[12] A. B. Coppens, R. T. Beyer, M. B. Seiden, J. Donohue, F. Guepin, R. H. Hodson, and C. Townsend, ''Parameter of nonlinearity in fluids. II,'' J. Acoust. Soc. Am. **38**, 797–804 (1965).
[13] B. Hartmann, ''Potential energy effects on the sound speed in liquids,'' J. Acoust. Soc. Am. **65**, 1392–1396 (1979).
[14] B. Frank and J. D. N. Cheeke, ''On the Mie potential and the acoustic nonlinearity parameter B/A,'' J. Acoust. Soc. Am. **101**, 1184–1186 (1997).

The scaling of the wall pressure fluctuations in polymer-modified turbulent boundary layer flow

Timothy A. Brungart, Wayne J. Holmberg, Arnold A. Fontaine, Steven Deutsch, and Howard L. Petrie

The Pennsylvania State University, Applied Research Laboratory, P. O. Box 30, State College, Pennsylvania 16804-0030

(Received 15 June 1998; revised 6 June 1999; accepted 20 April 2000)

Wall pressure fluctuations and integrated skin friction were measured beneath a turbulent boundary layer that was modified by adding drag-reducing polymer to the pure water flow. The measurements were performed on an axisymmetric model, equipped with an isolated cylindrical drag balance section, and placed in the test section of the 0.3048-m-diam water tunnel at ARL Penn State. Data were acquired at a free-stream velocity of 10.7 m/s with pure water and with polymer added to the water at concentrations of 1, 5, 10, and 20 weight parts per million. Nondimensionalization of the wall pressure fluctuation frequency spectra with traditional outer, inner, and mixed flow variables failed to adequately collapse the data. The mean square wall pressure fluctuations were found to scale linearly with the wall shear stress. Polymer addition had little effect on the characteristic time scale of the flow. These properties were used to develop a novel form of the nondimensional wall pressure fluctuation spectrum that provided the best collapse of the measured data.
 [S0001-4966(00)05107-9]

PACS numbers: 43.28.Ra, 43.50.Nm [LCS]

INTRODUCTION

Wall pressure fluctuations induced by the turbulent boundary layer have been studied extensively over the past four decades because of their importance as a source of noise and vibration in engineering applications ranging from sonar systems to automobiles to aircraft. Keith *et al.*[1] have shown that outer flow variable scaling [i.e., $\Phi(\omega)U_0/(\rho^2U_0^4\delta^*)$ vs $\omega\delta^*/U_0$] is effective at providing reasonable collapse of lower-frequency (i.e., $\omega\delta^*/U_0 \lesssim 1$) equilibrium turbulent boundary layer wall pressure spectra. Here $\Phi(\omega)$ is the pressure spectrum, U_0 is the free-stream velocity, ρ is the fluid density, and δ^* is the boundary layer displacement thickness. Mixed flow variable scaling [i.e., $\Phi(\omega)U_0/(\tau^2\delta^*)$ vs $\omega\delta^*/U_0$] has also been shown[1] to collapse the lower-frequency wall pressure fluctuations reasonably well, while inner flow variable scaling [i.e., $\Phi(\omega)u_\tau^2/(\tau^2\nu)$ vs $\omega\nu/u_\tau^2$] provides effective collapse at high frequencies [i.e., $\omega\nu/u_\tau^2 \gtrsim 0.1$]. The symbol τ represents the wall shear stress, u_τ is the friction velocity [$u_\tau=(\tau/\rho)^{1/2}$], and ν is the fluid kinematic viscosity. While the outer variable scaling nondimensionalizes the point pressure spectral amplitude on the free-stream dynamic head (i.e., ρU_0^2), the mixed and inner variable scaling use τ.

The drag-reducing characteristics of high-molecular-weight polymers have also been studied extensively since the discovery of the phenomenon by Toms[2] in 1948. Because of polymer's ability to reduce turbulent shear stress and the dependence of the boundary layer wall pressure spectral amplitude on the shear stress, polymer has the potential to suppress noise and vibration caused by boundary layer unsteady pressures. Compared to its effect on drag reduction, however, polymer effects on turbulent boundary layer wall pressure fluctuations have received little attention. Barker[3] showed that drag-reducing polymer additives do indeed reduce wall pressure fluctuations, but was unable to effectively collapse his data. Work from the former Soviet Union[4,5] has also showed that polymer-induced drag reduction is associated with a reduction in wall pressure fluctuations but specific scaling relationships have remained elusive. The dependence of the turbulence-induced wall pressure fluctuations on the wall shear stress indicates that nondimensionalization of the pressure spectral amplitude by the free-stream dynamic head alone is not generally appropriate. The objective of this work is to develop a scaling relationship for turbulent boundary layer wall pressure fluctuations that are modified by adding drag-reducing polymer to the pure water flow.

I. EXPERIMENTAL ARRANGEMENT AND METHODOLOGY

Experiments were conducted in the cylindrical test section of the 0.3048-m-diam water tunnel at ARL Penn State. Figure 1 shows the 89-mm-diam, 632-mm-long axisymmetric model, which has been used in previous drag reduction studies.[6,7] The model was mounted to a 200-mm-long sting held in the center of the cylindrical section of the water tunnel by two 127-mm-long struts. The struts were inclined at 45 degrees to the vertical, and were bolted to the tunnel wall. Identical dummy struts were mounted opposite the support struts to preserve flow symmetry. A steel wire, 0.35 mm in diameter, was placed 46 mm from the nose in an effort to trip the boundary layer and ensure a fully turbulent boundary layer at the balance and location of the pressure transducer. Laser doppler velocimeter (LDV) velocity profiles measured[7] at three locations on the balance section indicated that the boundary layers were fully developed. Deutsch and Castano[6] and Fontaine and Deutsch[7] provide a detailed description of the model and its boundary layer characteristics.

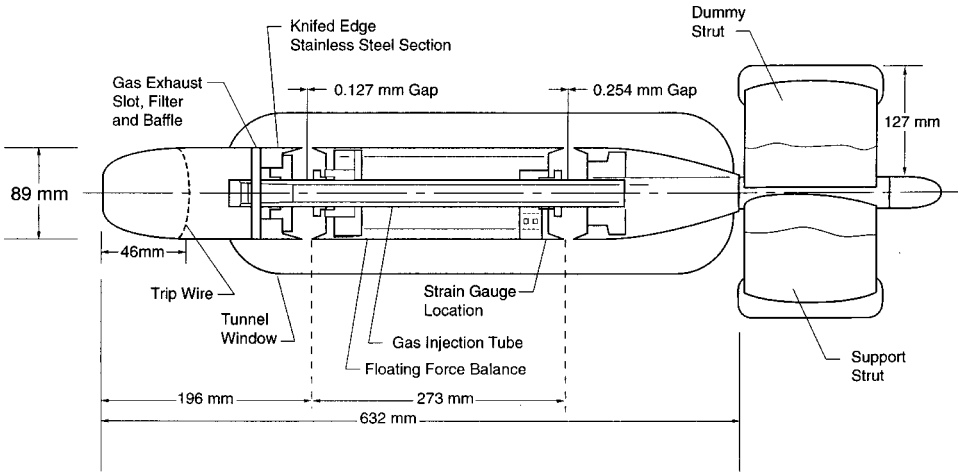

FIG. 1. Schematic of the string-mounted axisymmetric model.

Integrated skin friction was measured along an isolated cylindrical section by incorporating a strain gauged shear member as a force sensor. The balance is 273 mm long with upstream and downstream nominal gaps of 0.127 and 0.254 mm, respectively. The upstream edge of the balance is located 196 mm from the nose of the body. The balance was dry calibrated using a radially centered pully and incremental weights, and showed excellent linearity ($R^2=0.99999$) over the entire range of anticipated loads. Force as a function of tunnel velocity was consistent throughout the experiments. The force data were digitized at a sampling frequency of 1 kHz for 2 s of run time.

The turbulent boundary layer wall pressure fluctuations were measured with a 0.254-cm-diam, PCB model 105 A, piezoelectric sensor placed at the axial center of the balance and mounted flush with the model surface. The pressure transducer's sensitivity was measured in air with a pulse tube calibrator and found to be in good agreement with the factory specified value. The unsteady pressure signal was low-pass filtered at 20 kHz and sampled at 51.2 kHz with a record length of 2048 points. This provides a measurement bandwidth of 25 Hz. Typically 128 averages were taken at each test condition, which corresponds to a theoretical spectral estimate, with a 95% confidence interval, of $\pm 17.7\%$, assuming a Gaussian process.

A polymer ocean tunnel environment was obtained by injecting concentrated solutions of polyethylene oxide (polyox) into the tunnel during operation. The tunnel was then idled at approximately 5 m/s for several minutes to provide uniform mixing of the injected solution at concentrations of 1, 5, 10, and 20 weight parts per million (wppm). Most measurements were performed at a velocity of 10.7 m/s. The selection of the most appropriate velocity at which to perform the wall pressure fluctuation measurements involved a compromise between pressure transducer signal-to-noise ratio and spatial resolution. Wall pressure spectra were acquired at a given tunnel velocity numerous times after polymer injection to monitor polymer shear degradation so that these effects could be avoided.

Surveys of the boundary layer streamwise velocity component were conducted at the location of the wall pressure sensor for the 10.7 m/s test velocity and all polymer concentrations. The surveys were performed using a fringe mode LDV with a 5-W argon ion laser. One beam was frequency shifted at an effective shift of 2 MHz. Doppler signals were processed with a TSI IFA Model 655 correlator processor. The boundary layer velocity profiles were integrated to obtain the displacement thicknesses and these values were used to scale the wall pressure fluctuation spectra.

II. EXPERIMENTAL RESULTS

Spectra of the turbulent boundary layer wall pressure fluctuations showed good repeatability over the course of the experiments. Unfortunately, the measured unsteady pressure signal exceeded the tunnel background noise only at frequencies between 225 Hz and 6 kHz. At frequencies below 225 Hz, tunnel noise contaminated the wall pressure fluctuation signal, whereas at frequencies above 6 kHz, bubble-related noise dominated. These frequency restrictions were not known *a priori* and data were acquired up to 20 kHz resulting in the 25-Hz measurement bandwidth.

The wall pressure fluctuation frequency spectrum, nondimensionalized with inner flow variables, is shown in Fig. 2(a) to compare favorably with the results of Keith and Bennett.[8] At a 4.6-m/s test velocity, the ratio of the transducer diameter, $d_{\text{transducer}}$, to a viscous length scale, ν/u_τ, denoted by $d^+=d_{\text{transducer}}u_\tau/\nu$, for the two data sets are similar, and the nondimensionalized spectra are in reasonable agreement. When nondimensionalized with mixed flow variables, the current data agree with the results of Keith and Bennett[8] at lower frequencies, where transducer spatial averaging effects are minimal. At higher frequencies, the current levels lie below those reported by Keith and Bennett due to our higher ratio of $d_{\text{transducer}}/\delta^*$ ($d_{\text{transducer}}/\delta^*=3.05$ vs 0.89). The current spectrum and the spectrum measured by Keith and Bennett,[8] nondimensionalized with mixed flow variables, are compared in Fig. 2(b).

The effect of a polyox ocean environment on the turbulent boundary layer wall pressure fluctuations is shown in Fig. 3. Interpretation of the results are complicated by the fact that ν/u_τ becomes larger and hence d^+ becomes smaller as τ decreases and, therefore, the sensor response suffers less attenuation due to spatial averaging. Corcos[9] developed a correlation for the effect of spatial averaging on sensor response, however, his assumption of uniform sensor spatial

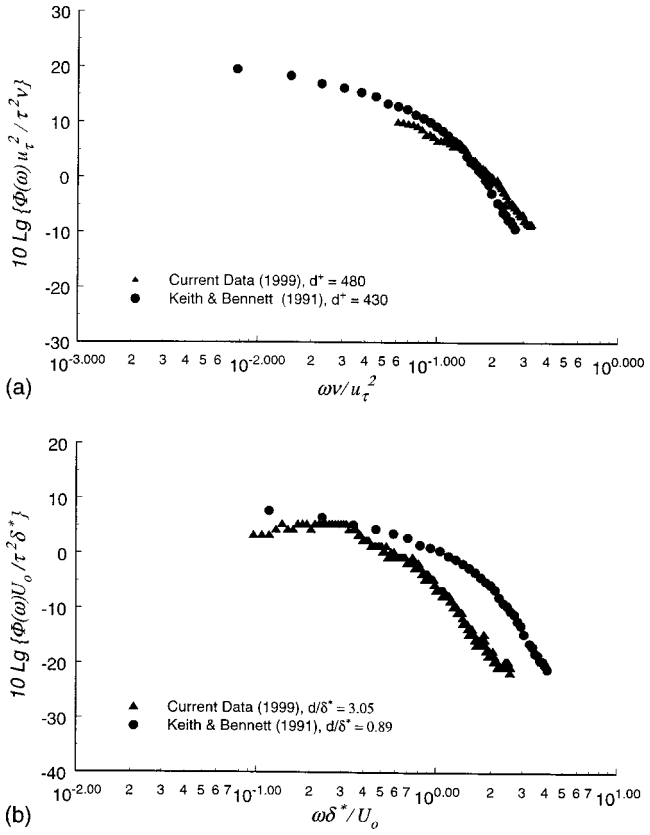

FIG. 2. Comparison of the current pure water wall pressure fluctuation spectrum to the spectrum measured by Keith and Bennett (Ref. 8): (a) inner flow variables and (b) mixed flow variables.

response places the correction into question at high frequencies, where the current sensors are most attenuated. Since any correction for changing sensor resolution with polymer concentrations is itself subject to question, none were applied to the data.

The data in Fig. 3 show that polymer addition to a pure water boundary layer is effective at reducing the wall pressure fluctuations over the entire measurable frequency range. At the highest concentration used, 20 wppm, reductions of approximately 6–8 dB were achieved. Figures 4–6 show the data of Fig. 3 nondimensionalized with traditional outer, inner, and mixed flow variables, respectively. The values of δ^* and τ used for nondimensionalization were obtained from the LDV-measured velocity profiles and drag balance data, respectively. It is apparent that the mixed flow variable scaling is most effective at collapsing the spectra, albeit to a limited degree.

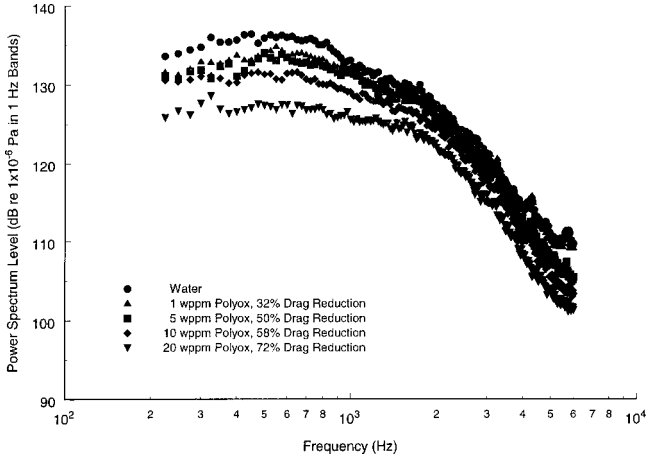

FIG. 3. The effect of a polyox ocean environment on the turbulent boundary layer wall pressure fluctuations.

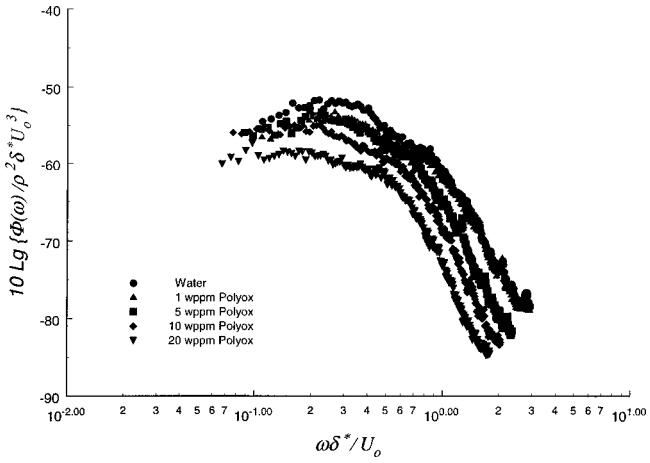

FIG. 4. The measured wall pressure fluctuation frequency spectra, nondimensionalized with outer flow variables.

Farabee and Casarella[10] identify four regions in the turbulent boundary layer as dominating the wall pressure fluctuations over four specific frequency ranges. The low-frequency range, defined by $\omega\delta/u_\tau \leqslant 5$, is dominated by sources associated with the large-scale structures induced by the unsteady potential flow observed above the boundary layer. It dominates frequencies below approximately 40 Hz for the pure water boundary layer under study. A mid-frequency range is presumed dominated by structures in the outer region of the boundary layer (i.e., $5 \leqslant \omega\delta/u_\tau \leqslant 100$). It extends from approximately 40 to 850 Hz for the pure water boundary layer spectrum shown in Fig. 3. Flow structures in the boundary layer log region supposedly dominate the Fig. 3 pure water spectrum from 850 Hz to 8 kHz. Frequencies above approximately 8 kHz arise from structures closer to the wall, in the boundary layer buffer region.

Since the flow structures that dominate the Fig. 3 pure water spectrum are located in the outer part of the boundary

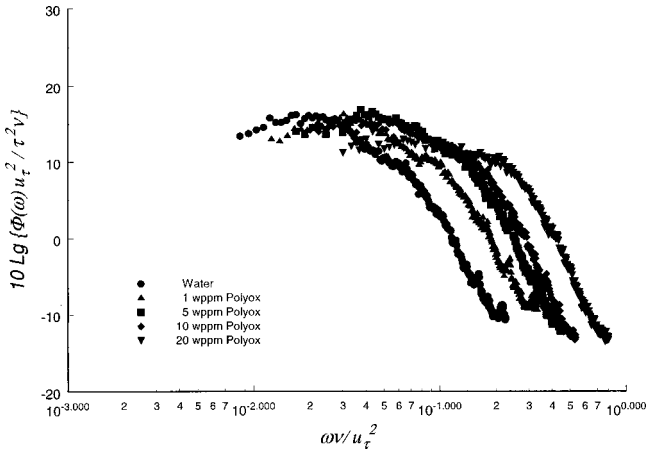

FIG. 5. The measured wall pressure fluctuation frequency spectra, nondimensionalized with inner flow variables.

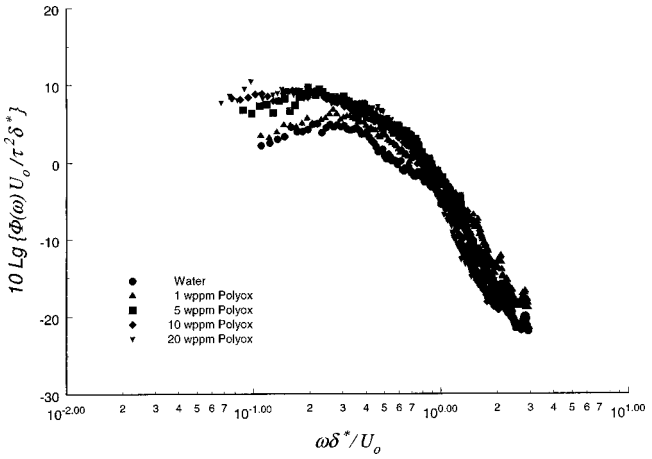

FIG. 6. The measured wall pressure fluctuation frequency spectra, nondimensionalized with mixed flow variables.

layer log region and inner part of the wake, it is reasonable that mixed flow variable scaling provides the most effective collapse of the data. The particular mixed flow variable scaling used in Fig. 6, however, nondimensionalizes $\Phi(\omega)$ with the inner flow amplitude scale τ^2 and ω with the outer flow time scale δ^*/U_0. The mean square wall pressure fluctuations shown in Fig. 3, normalized with the pure water value and plotted against the shear stress, also normalized with the pure water value, are shown in Fig. 7. The mean square wall pressure levels were obtained by integrating the corresponding Fig. 3 spectra from 225 Hz to 6 kHz and appear to scale on the wall shear stress in a near-linear fashion. The slope of the line shown is approximately 0.012 ρU_0^2. Figure 3 shows that the polymer and its associated shear stress reduction appear to have little impact on the characteristic time scale of the flow (i.e., the curves appear to be offset in amplitude but not in frequency). The inner and outer flow time scales, ν/u_τ^2 and δ^*/U_0, respectively, for the Fig. 3 spectra vary substantially and are summarized in Table I. This suggests that the polymer spectral data can be best collapsed by nondimensionalizing the frequency with the mixed flow time scale δ^*/u_τ and nondimensionalizing the mean square wall pressure amplitude with the (mixed) product of the free-stream

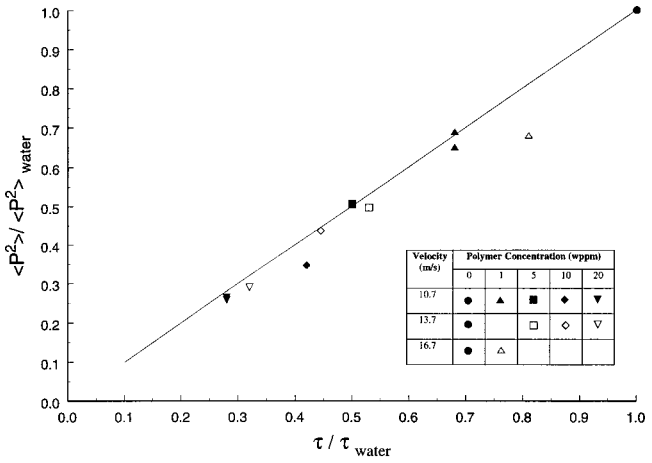

FIG. 7. Plot of the mean square wall pressure fluctuations, normalized with the pure water value, versus the wall shear stress, normalized with the pure water value.

TABLE I. Time scales for the 10.7 m/s pure water and polymer-modified turbulent boundary layer.

Polymer concentration (wppm)	δ^* (m)	u_τ (m/s)	δ^*/U_0 (s)	ν/u_t^2 (s)	δ^*/τ (s)
0	8.31×10^{-4}	0.41	7.76×10^{-5}	5.98×10^{-6}	2.03×10^{-3}
1	8.24×10^{-4}	0.34	7.70×10^{-5}	8.80×10^{-6}	2.44×10^{-3}
5	6.67×10^{-4}	0.29	6.23×10^{-5}	1.20×10^{-5}	2.30×10^{-3}
10	5.80×10^{-4}	0.27	5.41×10^{-5}	1.42×10^{-5}	2.18×10^{-3}
20	5.08×10^{-4}	0.22	4.74×10^{-5}	2.13×10^{-5}	2.34×10^{-3}

dynamic head and wall shear stress, $\rho U_\infty^2 \tau$. The value of δ^*/u_τ changes little compared to how ν/u_τ^2 and δ^*/U_0 change over the range of conditions corresponding to the Fig. 3 spectra, and is also given in Table I. Figure 8 shows that the spectra collapse reasonably well across the entire measurable frequency range when nondimensionalized in this fashion. Farabee and Beckley[11] independently identified a variant of this scaling relationship as providing the best collapse of their point pressure spectra data measured in a fully developed turbulent pipe flow containing drag-reducing polymer additives at concentrations ranging from 1 to 10 wppm. Like the current scaling relationship, Farabee and Beckley[11] used $\rho U_\infty^2 \tau$ to nondimensionalize $\Phi(\omega)$ but used the time scale U_0/D to nondimensionalize the frequency where D is the pipe diameter. Note that at a constant speed, U_0/D is a constant, independent of polymer concentration, as is δ^*/u_τ, approximately, for the current data.

III. SUMMARY AND CONCLUSIONS

Wall pressure fluctuations were measured beneath a turbulent boundary layer that was modified by adding drag-reducing polymer to the pure water flow. Skin friction measurements were performed at the same location at corresponding test conditions. Nondimensionalization of the wall pressure fluctuation frequency spectra with traditional outer, inner, and mixed flow variables failed to adequately collapse the data. The mean square wall pressure fluctuations were found to scale linearly with the wall shear stress. Polymer addition had little effect on the characteristic time scale

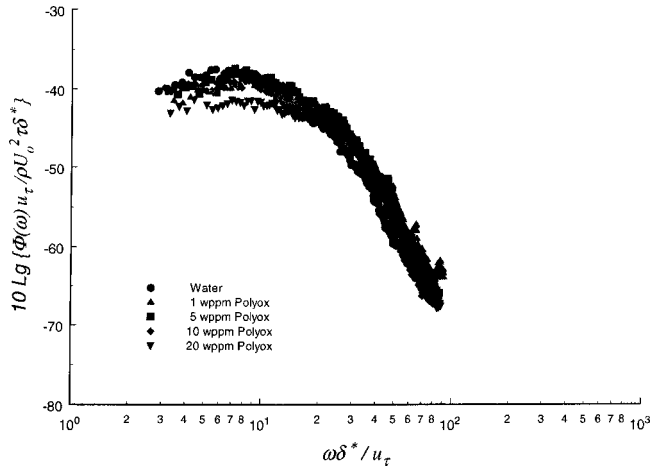

FIG. 8. The wall pressure fluctuation frequency spectra nondimensionalized with the variables providing the best collapse of the data.

of the flow. These properties were used to develop a nondimensional wall pressure fluctuation spectrum that took the form of

$$\frac{\Phi(\omega)u_\tau}{\rho U_0^2 \tau \delta^*} \text{ vs } \frac{\omega \delta^*}{u_\tau}.$$

This nondimensionalization provided the best collapse of the data across the entire measurable frequency range.

[1] W. L. Keith, D. A. Hurdis, and B. M. Abraham, ''A comparison of turbulent boundary layer wall pressure spectra,'' J. Fluids Eng. **114**, 338–347 (1992).

[2] B. A. Toms, ''Some observations on the flow of linear polymer solutions through straight tubes at large Reynolds numbers,'' in *Proceedings First International Congress on Rheology* (North-Holland, Amsterdam, 1948), Vol. II, pp. 135–141.

[3] S. J. Baker, ''Radiated noise from turbulent boundary layers in dilute polymer solutions,'' Phys. Fluids **16**, 1387–1394 (1973).

[4] I. F. Kadykov and L. M. Lyamshev, ''Influence of polymer additives on the pressure fluctuations in a boundary layer,'' Sov. Phys. Acoust. **16**, 59–63 (1970).

[5] E. M. Greshilov, A. V. Evtushenko, and L. M. Lyamshev, ''Hydrodynamic noise and Toms effect,'' Sov. Phys. Acoust. **21**, 247–251 (1975).

[6] S. Deutsch and J. Castano, ''Microbubble skin friction reduction on an axisymmetry body,'' Phys. Fluids **29**, 3590–3597 (1986).

[7] A. A. Fontaine and S. Deutsch, ''The influence of the type of gas on the reduction of skin friction drag by microbubble injection,'' Exp. Fluids **13**, 128–136 (1992).

[8] W. L. Keith and J. C. Bennett, ''Low frequency measurements of the wall shear stress and wall pressure in a turbulent boundary layer,'' AIAA J. **29**, 526–530 (1991).

[9] G. M. Corcos, ''Resolution of pressure in turbulence,'' J. Acoust. Soc. Am. **35**, 192–199 (1963).

[10] T. M. Farabee and M. J. Casarella, ''Structural features of wall pressure fluctuations beneath turbulent boundary layers,'' Phys. Fluids A **3**, 2410–2420 (1991).

[11] T. M. Farabee and J. J. Beckley, Jr., private communication on the hydroacoustics of turbulent boundary layers, 24 February 1998.

Coupled mode perturbation theory of range dependence

C. T. Tindle, L. M. O'Driscoll, and C. J. Higham
Physics Department, University of Auckland, Bag 92019, Auckland, New Zealand

(Received 12 July 1998; revised 17 February 2000; accepted 28 March 2000)

The conventional coupled mode solution is combined with perturbation theory to give a fast, accurate range-dependent normal mode solution for deep water acoustic propagation. Perturbation theory is used to calculate the new normal modes at each range step. The new modes are obtained as a linear combination of the modes for the previous step without requiring a numerical solution of the depth-separated wave equation. The process may be repeated for many steps and yields normal modes and eigenvalues which are sufficiently accurate for solution of practical problems in deep water. The method is applied to long-range propagation through oceanic fronts. © *2000 Acoustical Society of America.* [S0001-4966(00)01607-6]

PACS numbers: 43.30.Bp [SAC-B]

INTRODUCTION

It is somewhat surprising that there appears to be no reference in the underwater acoustics literature to a combination of perturbation theory and coupled modes. These are both important mathematical techniques which rely on small incremental changes to solve differential equations and they complement each other in their application to underwater acoustics. The use of perturbation theory to determine the normal modes for coupled mode calculations in deep water greatly improves the speed of such calculations without significant loss of accuracy.

The normal mode method for the solution of problems in underwater sound propagation is exact in a horizontally layered environment and a number of versatile computer codes have been developed.[1–3] However, real cases always have some range dependence and there are a number of ways in which normal mode theory has been extended to apply to range-dependent problems. The simplest extension is to use the adiabatic approximation[4] which assumes that there is no interchange of energy between modes and that each mode function adjusts itself to the sound speed profile at each range. The adiabatic approximation is useful if the range dependence is very slight. Unfortunately, its accuracy in any particular case can only be determined by comparison with some other solution.

Early work on range-dependent normal modes was done by Hawker and Rutherford[5] who used an approximate separation of the wave equation to develop mode coupling coefficients to describe the redistribution of energy as the normal modes propagate in range. Later, Thompson[6] expanded the normal modes in terms of harmonic oscillator functions and solved the wave equation for the range-dependent harmonic oscillator coefficients.

The most successful extension of normal mode theory to range-dependent problems is the coupled mode theory introduced by Evans.[7] The environment is divided into a number of range-independent sections to give a stepwise approximation to the range-dependent problem. The stepwise problem is solved exactly in each section and solutions are matched at the step boundaries. For sufficiently small steps the solution becomes independent of the number of steps and is then assumed to be an exact numerical solution of the range-dependent problem. The coupled mode method is computation intensive and somewhat impractical for routine solution of range-dependent problems. Nevertheless, it is important for providing a reference solution to benchmark problems.[8]

In the present work we will show that a combination of coupled mode theory and perturbation theory is able to substantially improve the efficiency of a coupled mode calculation by removing the need to solve the depth-separated wave equation for the normal modes at each range step. Instead, the normal modes are found by applying perturbation theory to the modes of the previous step. This procedure gives normal modes and wave numbers of good accuracy and allows fast coupled mode calculations.

The coupled mode perturbation theory will be verified by studying the effect of normal mode propagation through schematic oceanic fronts representative of the boundary between different water masses. This allows us to study both the accuracy of the perturbation approximation and the details of the mode coupling process. It is found that the effect of mode coupling depends on whether phase or amplitude changes are more important. For slow range dependence the phase change for each range step can be quite large. The mode coupling then takes place with essentially random phase and there is no systematic change of mode amplitudes. In contrast, for rapid range dependence, the phase change in each range step is small and mode coupling can accumulate to give large changes in mode amplitudes.

In Secs. I and II we briefly outline normal mode theory and coupled mode theory to establish notation. In Sec. III we use perturbation theory to obtain theoretical expressions for the approximate normal modes and eigenvalues for use in the coupled mode expressions. In Sec. IV we introduce our schematic examples of oceanic fronts. In Sec. V we verify that perturbation theory gives accurate mode functions and eigenvalues. We then use the approximate modes and standard coupled mode theory to look at mode coupling in long-range propagation and show that our coupled mode perturbation theory allows practical calculation of long-distance propagation in deep water. Our results also give a physical interpretation of why the adiabatic approximation works for very

slow range dependence. Discussion and conclusions are given in Sec. VI.

I. NORMAL MODE SOLUTION

The normal mode solution to underwater sound propagation in a range-independent situation is well known.[9] The environment is assumed to be stratified into layers. The speed of sound $c(z)$ is assumed to be a function of depth z but independent of range. The density $\rho(z)$ increases with depth but is constant in each layer. For simplicity we assume all layers are fluid.

The acoustic pressure at range r and depth z due to a harmonic source of angular frequency ω at $r=0$ and depth z_s can be written

$$p(r,z)=i\pi\rho^{-1}(z_s)\sum_n U_n(z_s)U_n(z)H_0^{(1)}(k_n r). \tag{1}$$

Equation (1) is normalized to give unit pressure at unit distance. The normal modes $U_n(z)$ are solutions of

$$d^2U_n/dz^2+[\omega^2/c^2(z)-k_n^2]U_n=0. \tag{2}$$

The parameter k_n is the normal mode eigenvalue and corresponds to the wave number for horizontal propagation. In writing Eq. (1) the contribution of the branch line integral has been ignored because it decays rapidly with range in most circumstances.[9]

The normal mode functions must also satisfy boundary conditions. At the surface the pressure vanishes and this requires

$$U_n(0)=0. \tag{3}$$

The normal mode functions must vanish at great depth in order to represent finite energy so we have

$$[U_n(z)]_{z\to\infty}\to 0. \tag{4}$$

Continuity of pressure and displacement at any horizontal interface (say $z=h$) require

$$U_n(h^-)=U_n(h^+), \tag{5}$$

$$\rho^{-1}(h^-)[dU_n/dz]_{z=h^-}=\rho^{-1}(h^+)[dU_n/dz]_{z=h^+}. \tag{6}$$

With these boundary conditions the normal modes are orthogonal with weight function $\rho^{-1}(z)$ and satisfy

$$\int_0^\infty \rho^{-1}(z)U_m(z)U_n(z)\,dz=\delta_{mn}. \tag{7}$$

For practical calculations the Hankel function may be replaced by its asymptotic form and the pressure field may be written as

$$p(r,z)=(2\pi/r)^{1/2}e^{i\pi/4}\rho^{-1}(z_s)\times\sum_n U_n(z_s)U_n(z)(k_n)^{-1/2}\exp(ik_n r). \tag{8}$$

Equation (8) is the usual normal mode expansion of the acoustic field in a range-independent environment. The normal mode theory may be extended to a range-dependent environment using coupled modes.

II. RANGE DEPENDENCE AND COUPLED MODES

In the coupled mode[7] approach to range-dependent problems in underwater acoustics the range-dependent environment is replaced by a series of short, range-independent sections. The acoustic field is computed by expanding the field at the end of one section in terms of the normal modes of the next section. By stepping in range the full field solution is obtained.

A full discussion of the way in which the field can be matched at the end of each range section is given in Ref. 10. The original coupled modes formulation of Evans[7] includes forward and backward propagation and both pressure and particle velocity matching at each range boundary. The range step is reduced until the solution converges. No approximations are involved and after convergence the solution is regarded as exact. Porter *et al.*[10] showed that back propagation is negligible in the exact solution and discussed a number of approximate solutions including the ''approximate single-scatter'' solution which will be used here.

If the ith range sections runs from $r=r_{i-1}$ to $r=r_i$ the field in the ith section can be written

$$p^{(i)}(r,z)=r^{-1/2}\sum_n A_n^{(i)}U_n^{(i)}(z)\exp[ik_n^{(i)}(r-r_{i-1})]. \tag{9}$$

The superscript (i) refers to values in the ith section. In the first range section the values of the $A_n^{(1)}$ are found using Eq. (8).

For coupled modes, the $A_n^{(i)}$ values in subsequent sections are found by matching fields at the end of each range step. At the end of the ith section the field is expanded in terms of the modes of the $(i+1)$th section.

In the approximate single-scatter formulation the mode coefficients are the average of those found by matching the pressure and particle velocity separately. The result may be written

$$A_m^{(i+1)}=\sum_n A_n^{(i)}\exp[ik_n^{(i)}(r_i-r_{i-1})]\times\frac{1}{2}\left[\int_0^\infty\frac{U_m^{(i+1)}(z)U_n^{(i)}(z)\,dz}{\rho^{(i+1)}(z)}+\frac{k_n^{(i)}}{k_m^{(i+1)}}\int_0^\infty\frac{U_m^{(i+1)}(z)U_n^{(i)}(z)\,dz}{\rho^{(i)}(z)}\right]. \tag{10}$$

For deep water propagation involving no bottom interaction the factor $k_n^{(i)}/k_m^{(i+1)}$ is close to unity and the density profile $\rho(z)$ is independent of range. Therefore, for simplicity and convenience we replace Eq. (10) with

$$A_m^{(i+1)}=\sum_n A_n^{(i)}\exp[ik_n^{(i)}(r_i-r_{i-1})]\times\int_0^\infty\frac{U_m^{(i+1)}(z)U_n^{(i)}(z)\,dz}{\rho(z)}. \tag{11}$$

The integrals in Eqs. (10) and (11) are easily evaluated numerically if the normal modes are known at closely spaced depths. The process may then be repeated to determine the field at all ranges.

Since the objective is to obtain a solution valid for continuous range dependence the solution must be independent of the precise choice of range steps. Therefore, to complete the coupled mode solution the number of range steps is increased until the solution becomes stable in the sense that the use of more sections give no significant change in the field.

Coupled mode theory is computation intensive because, not only must the full set of normal modes be calculated at each range step, but also the number of steps must be increased until the solution converges. Even though highly efficent fast normal mode codes exist, the coupled mode approach is largely impractical for the solution of realistic range-dependent problems.

Perturbation theory offers the opportunity to greatly improve the efficiency of the coupled mode solution by removing the need for numerical solution of the depth-separated wave equation at each range step.

There is a sense in which coupled mode theory and perturbation theory belong naturally together. Coupled mode theory assumes the range-dependent problem can be approximated as a series of small range-independent steps. Perturbation theory makes this same small step assumption and so it is natural to use perturbation theory to calculate the new normal modes for each range step. The smaller the steps the better the approximation in both cases.

III. PERTURBATION THEORY

If a set of normal modes is known for some particular sound speed profile, perturbation theory provides a method of obtaining the set of normal modes for a slightly different profile.

To derive the relevant equations it is convenient to define a function $q(z)$ as follows:

$$q(z)=[\omega/c(z)]^2. \tag{12}$$

Suppose we have a set of normal modes $U_n(z)$ with eigenvalues k_n for some particular sound speed profile $c(z)$. If the sound speed profile changes to $c(z)+\Delta c(z)$, the parameter $q(z)$ changes to $q(z)+\Delta q(z)$ and we can assume the eigenvalues change to $k_n+\Delta k_n$ and the normal modes change to $U_n+\Delta U_n$.

Since the normal modes U_n form a complete set we can expand ΔU_n as follows:

$$\Delta U_n(z)=\sum_m a_{nm}U_m(z). \tag{13}$$

In the Appendix [Eqs. (A8) and (A9)] we show that Δk_n and a_{nm} are given by

$$\Delta k_n=\frac{1}{2k_n}\int_0^\infty \frac{\Delta q(z)U_n^2(z)\,dz}{\rho(z)}, \tag{14}$$

$$a_{nm}=\frac{1}{(k_n^2-k_m^2)}\int_0^\infty \frac{\Delta q(z)U_n(z)U_m(z)\,dz}{\rho(z)}, \tag{15}$$

where Eq. (15) applies for $n\neq m$. The a_{nn} are found by requiring the perturbed modes to satisfy the normalization integral of Eq. (7) and the result is

$$a_{nn}=-\frac{1}{2}\sum_{m\neq n} a_{nm}^2. \tag{16}$$

If the normal mode functions are saved numerically as a function of depth, it is simple to evaluate expressions (13)–(16) numerically and to determine the perturbed eigenvalues and normal modes. These perturbed normal modes are readily incorporated into the standard coupled mode formalism.

A. Perturbation theory and coupled modes

If we take the normal modes and eigenvalues and the function $\Delta q(z)$ in Eqs. (14)–(16) to be those appropriate to the end of the ith range step, perturbation theory then gives the following values for the wave numbers and normal modes of the $(i+1)$th step:

$$k_n^{(i+1)}=k_n^{(i)}+\Delta k_n^{(i)}, \tag{17}$$

$$U_n^{(i+1)}=U_n^{(i)}+\sum_m a_{nm}^{(i)}U_m^{(i)}. \tag{18}$$

For the applications considered later the density function $\rho(z)$ is constant and independent of range. In this case substitution of Eq. (18) into Eq. (11) and use of the orthogonality condition (7) yields

$$A_n^{(i+1)}=A_n^{(i)}\exp[ik_n^{(i)}(r_i-r_{i-1})]$$
$$+\sum_m a_{nm}^{(i)}A_m^{(i)}\exp[ik_m^{(i)}(r_i-r_{i-1})]. \tag{19}$$

We have therefore determined the normal mode amplitudes in the $(i+1)$th range step from those in the ith range step without numerically solving the depth-separated wave equation. This is a considerable saving of computational effort. The values from Eqs. (17) and (18) may be substituted into the appropriate form of Eq. (9) and the process repeated to find the acoustic field at any desired range.

Equation (19) is important in that, when combined with Eq. (15), it shows explicitly how mode coupling arises.

The coupling coefficients $a_{nm}^{(i)}$ for $n\neq m$ are given by Eq. (15), which shows that coupling takes place at depths where $\Delta q(z)$ is nonzero. The strongest coupling will occur between nearby modes for two reasons. First, the term $k_m^2-k_n^2$ is smallest when m is close to n and, second, if n and m are far apart, the product $U_n(z)U_m(z)$ will oscillate rapidly and the integral will be small.

While the coupling coefficients $a_{nm}^{(i)}$ assess the mode coupling due to a change in the sound speed profile, the other factors in the summation in Eq. (19) are also important. The factor $A_m^{(i)}$ shows that the coupling of energy from mode m into mode n depends on the amplitude of mode m, as expected. The factor $\exp[ik_m^{(i)}(r_i-r_{i-1})]$ shows that phase is important in mode coupling and will be discussed in detail later.

IV. PROPAGATION AND OCEANIC FRONTS

In large sections of the world's oceans the sound speed profile $c(z,r)$ changes very slowly as a function of range. In

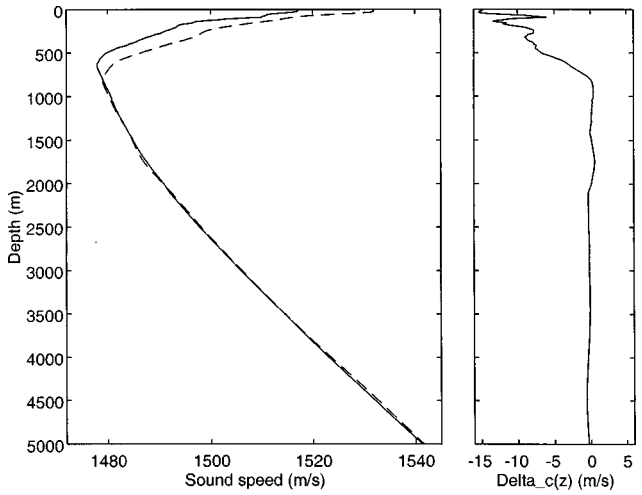

FIG. 1. Sound speed profiles at source (– – –) and receiver (———) for the SLICE89 experiment. The right-hand figure shows the difference in the two profiles.

many cases the range dependence can be neglected and much successful early analysis of underwater sound propagation in the deep ocean was done under this assumption.

An oceanic front is a boundary between identifiable water masses. From the point of view of ocean acoustics, a water mass is identified by its sound speed profile and an oceanic front can be regarded as a region in which the sound speed profile changes rapidly with range.

In order to study the accuracy of the perturbed normal modes and propagation through an oceanic front we will consider a transition between two different sound speed profiles. The two profiles are shown in Fig. 1. They are the profiles at the source and receiver in the SLICE89 experiment.[11] It is convenient to refer to these as the source and receiver profiles even though our later graphs of propagation loss refer to a moving receiver.

The second part of Fig. 1 shows the difference between the two sound speed profiles. The difference is a complicated function of depth and should provide a good test of perturbation theory.

As test cases we will consider fronts which we will identify as ''slow,'' ''moderate,'' and ''fast.'' For these three cases the transition between sound speed profiles occurs over 1000, 100, or 10 km, respectively.

The three fronts are shown schematically in Fig. 2. In all cases we will consider propagation for a range of 1000 km

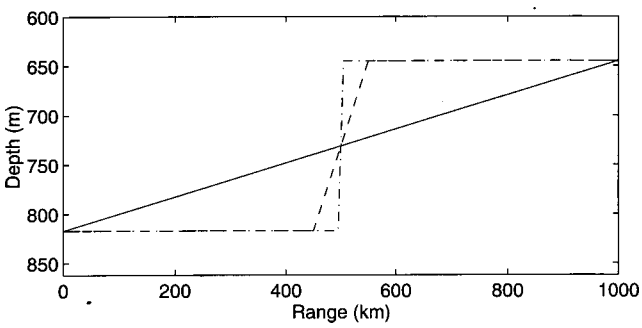

FIG. 2. The depth of the sound speed minimum as a function of range for the slow (———), moderate (— — —) and fast (·–·–·) fronts.

and the figure shows the depth of the sound speed minimum in each case. For the slow front there is a steady linear change between the two profiles. The depth of the sound speed minimum changes linearly over the whole range from 817 m at the source to 645 m at the receiver.

The moderate front occurs over the range 450–550 km. In the range 0–450 km the sound speed profile is constant and equal to the source profile of Fig. 1. The profile then changes linearly into the receiver profile over the range 450–550 km and so the depth of the sound speed minimum rises linearly over this range as indicated in Fig. 2. From 550 to 1000 km the profile is constant and equal to the receiver profile of Fig. 1.

The fast front is similar to the moderate front but occurs very rapidly over the range 495–505 km as illustrated in Fig. 2.

The perturbed normal mode approach described above is applied to a given situation by first dividing the range-dependent environment into range steps. In each step the sound speed profile is constant. By taking a large number of range steps the actual range-dependent profile can be closely approximated. For our schematic fronts we begin by taking 100 range steps while the sound speed profile is varying. For the moderate and fast fronts there are large range-independent sections before and after the fronts and we use the exact normal modes in these sections. The exact normal modes may be found using any suitable normal mode code.

The acoustic field is calculated as follows. The exact normal modes at the source are used to find the field in the first range step using Eq. (8). The perturbed normal modes are then found for the next range steps using Eqs. (14)–(18) and their amplitudes are found from Eq. (19). The field in the next range step is calculated using Eq. (9) and the whole process is repeated for the entire range. Apart from the source field and the normal modes at the beginning of the range-independent sections following the moderate and fast fronts, perturbed mode functions and eigenvalues are used throughout.

V. RESULTS

The sound speed profile at the source was shown in Fig. 1. A 100-Hz harmonic source is placed near the sound speed minimum at 804 m. The mode amplitudes at the source are shown in Fig. 3 as a function of mode number. There are 114 trapped modes in the source profile and, as expected, mode 1 is strongly excited by a source near the minimum. The mode amplitudes oscillate as a function of mode number because as mode number increases steadily, each mode gets an extra node as a function of depth and so there is a systematic pattern of nodes and antinodes at the source depth.

A. Normal modes

Representative modes (4, 21, 48, 80) at the source and receiver are shown in Fig. 4. The source and receiver sound speed profiles are shown again as the slowly varying dashed and solid curves, respectively. The rapidly oscillating curves are the representative modes in the corresponding profiles. The sound speed minimum is shallower at the receiver and

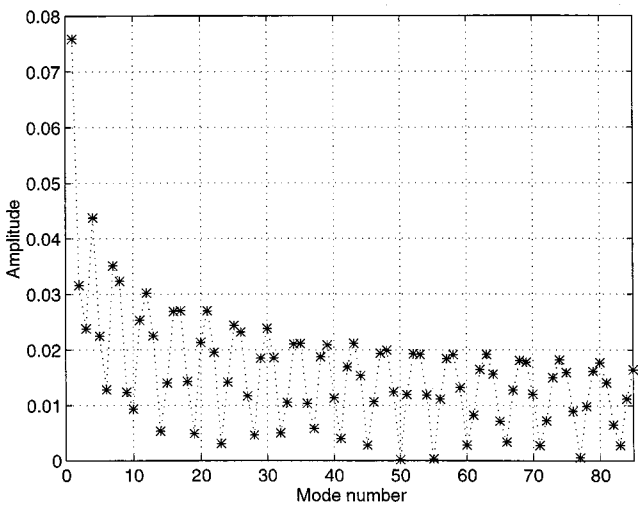

FIG. 3. Mode amplitudes at the source.

so the normal modes move upwards between source and receiver. The modes are plotted at their phase speeds. Since the receiver is at a higher latitude and in colder water than the source, the sound speed minimum moves toward the surface and the value of the sound speed at the minimum and the phase speeds of the modes are lower at the receiver.

The modes calculated using perturbation theory are also shown in Fig. 4 as the dot–dash curves, and in most places they agree within the line width with the solid lines of the exact modes. The separate curves are just visible for the uppermost oscillation of mode 21. The perturbed modes were calculated using 100 steps to approximate the range dependence, i.e., they were obtained by starting with the exact modes at the source and perturbing them 100 times using Eqs. (14)–(18).

Figure 4 shows that the perturbed mode functions give an excellent approximation to the exact mode functions. If smaller steps are taken, the approximations are even better.

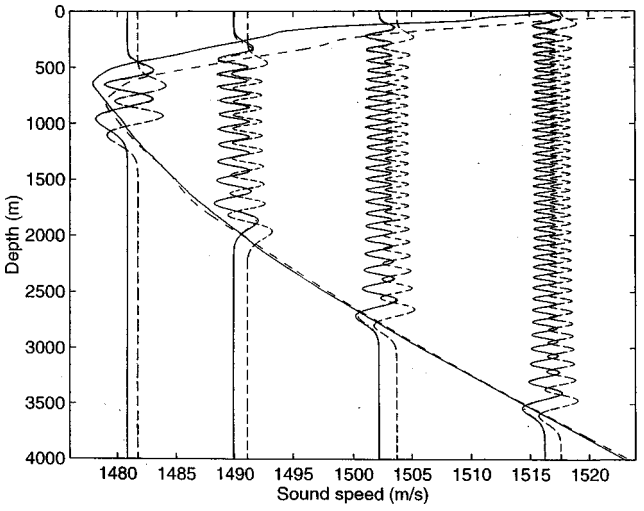

FIG. 4. Exact modes 4, 21, 48, and 80 as a function of depth at the source (dashed curves) and receiver (solid curves). The modes are shown at their phase speeds in the corresponding sound speed profiles. The dash–dot curves are the approximate mode functions at the receiver for the coupled perturbed modes.

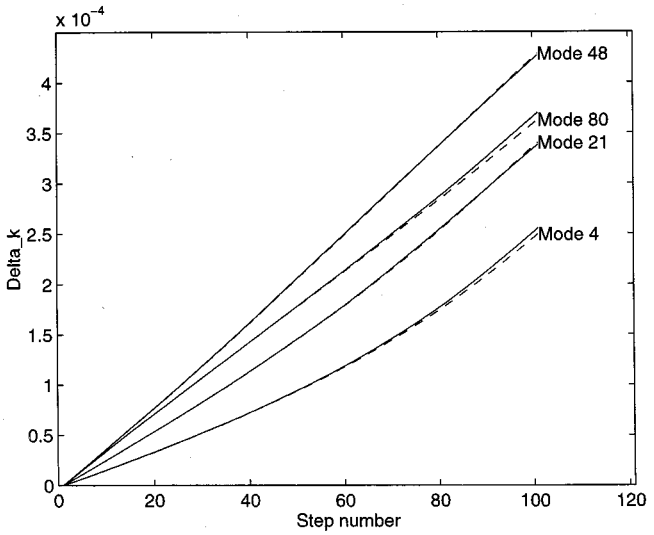

FIG. 5. Change in wave numbers for exact (———) and approximate (---) modes as a function of step number.

B. Wave numbers

The change in wave numbers as a function of step number are compared for the representative modes in Fig. 5. Other modes have similar behavior. The solid lines show the change in the exact wave numbers as a function of step number. The dashed lines show the approximate values obtained by starting with the exact values at the source and then applying perturbation theory 100 times. The perturbed values provide a good approximation and are obtained much more rapidly than by repeated solution of the normal mode wave equation.

As with the mode functions, the accuracy of the perturbation approximation to the wave numbers can be improved by taking smaller steps.

C. Mode amplitudes

As propagation proceeds through the front there is coupling of energy between modes. The resulting mode amplitudes as a function of step number are shown in Fig. 6 for the representative modes. The solid lines are the exact mode amplitudes found from conventional coupled mode theory using the exact modes at each step. The dashed curves are the mode amplitudes obtained using coupled perturbed modes, i.e., the coupled mode theory is as before but uses the approximate modes obtained from perturbation theory.

Figure 6(a) is for the slow front in which the mode coupling takes place over a range of 1000 km. There are small oscillations but no substantial change of mode amplitudes. The propagation is effectively adiabatic, as might be expected from such a slow change with range.

We can understand this near adiabatic propagation by considering Eq. (19). First, we note that with very slow range dependence the coupling coefficients $a_{nm}^{(i)}$ are all small because they are all proportional to Δq through Eq. (15). Second, we note that with slow range dependence large steps can be taken for a given Δq and the phase of each term in Eq. (19) may go through many cycles of 2π. For Fig. 6(a) the range step is 10 km and the phase term is about 4000 rad.

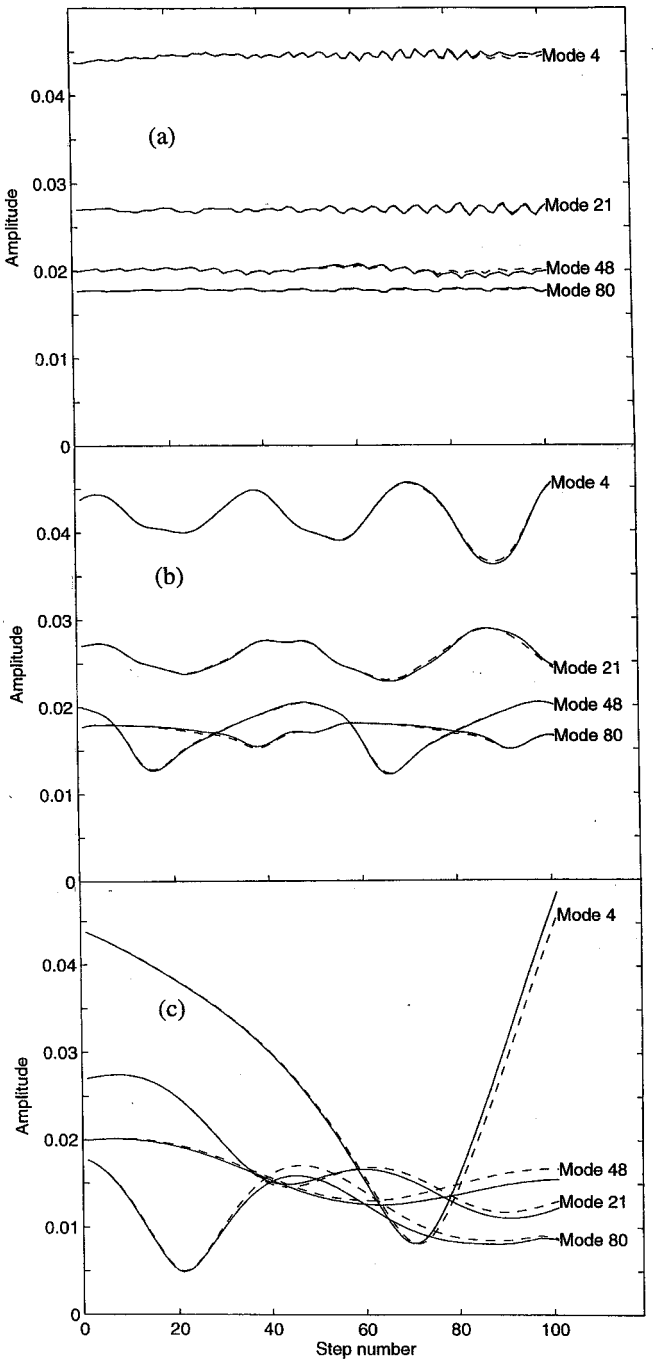

FIG. 6. Exact (———) and approximate (---) mode amplitudes as a function of step number for (a) slow, (b) moderate, and (c) fast fronts.

Therefore, for large range steps, the terms with $n \neq m$ of the summation will effectively have random phase in Eq. (19). These terms will cancel each other out to give $A_n^{(i+1)} \approx A_n^{(i)} \exp[ik_n^{(i)}(r_i - r_{i-1})]$ and negligible change of mode amplitude. This is identical to the adiabatic approximation.

In contrast, for small range steps, the phase terms in Eq. (19) will be small and the terms with $n \neq m$ can add over successive steps to give a large change in the mode amplitude. This is exactly what happens in Figs. 6(b) and 6(c). The range steps are 1 km and 100 m, respectively, and there are substantial changes of mode amplitudes with range. Mode coupling is therefore strong when the sound speed profile changes rapidly with range, as expected physically.

The dashed curves in Fig. 6 show that the coupled perturbed modes give an excellent approximation to the range dependence of the mode amplitudes. As noted above for the mode functions and wave numbers the accuracy of the mode amplitudes can be improved by taking smaller range steps.

D. Propagation loss

At the source and receiver there are 114 and 81 modes, respectively, with turning points within the water column. Therefore, as propagation proceeds, the highest modes are no longer trapped in the sense that they correspond to rays which are reflected from the surface and are attenuated by scattering from surface waves. Such modes are neglected in the calculation of the propagation loss. However, we include 130 modes in the mode coupling calculations in order to give a better approximation to the complete set and to give a better approximation to the perturbed mode functions.

In order to assess the usefulness of our coupled perturbed mode calculations we compute the transmission loss to a range of 1000 km in each of the three cases of Fig. 2. The results are shown in Fig. 7. For clarity we show only the results for the range 950–1000 km. The solid curves are the results obtained using coupled mode theory as described in Eqs. (9)–(11) with exact modes at each step. The dashed curves are obtained using coupled perturbed modes, i.e., the coupling is found from standard coupled mode theory but uses the approximate perturbed modes.

For Figs. 7(b) and 7(c) the coupled perturbed modes give a good approximation to the transmission loss. For the perturbation calculation the exact modes were used twice, once at the source and once at the end of the front. The exact and approximate results agree well and are within 0.2 dB on the peaks. The accuracy of the coupled perturbed mode calculation can be improved by taking smaller range steps for the range-dependent section.

For Fig. 7(a) the coupled perturbed modes apparently give a poor approximation. The poor agreement results from taking too large a range step as can be understood as follows. Figure 5 shows that after 100 range steps the wave numbers are slightly in error. Normal mode calculations are very sensitive to wave number errors because of the $\exp(ik_n r)$ terms in Eqs. (8) and (9). The maximum wave number error in Fig. 5 is about 8×10^{-6} for mode 80 at the 100th step. If we take $\pi/60$ as the maximum tolerable phase error, then the wave number error in Fig. 5 will limit the maximum step size to 5 km. If 2-km range steps are taken, the curves in Fig. 7(a) agree within 0.1 dB.

The phase errors are not important for the moderate and fast fronts results in Figs. 7(b) and 7(c) because the step sizes are 1 km and 100 m, respectively.

We have already noted that the accuracy of the coupled perturbed mode calculation can be improved by taking smaller range steps. Another obvious way to improve the accuracy of the coupled perturbed mode calculation is to insert the exact modes whenever the error in the wave numbers is likely to lead to significant phase errors. Figure 8 shows the propagation loss result for the slow front after inserting the exact wave numbers and mode functions after every tenth step. Figure 8 can be compared with Fig. 7(a)

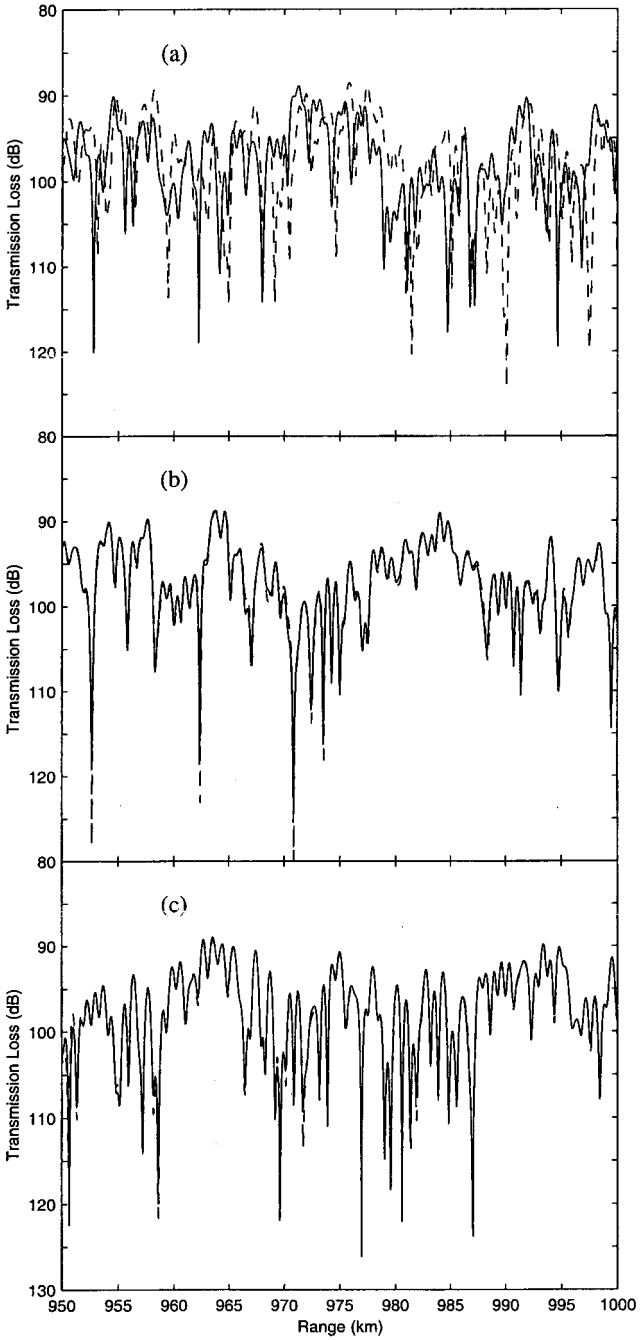

FIG. 7. Exact (———) and approximate (---) transmission loss as a function of range (last 50 km only) for (a) slow, (b) moderate, and (c) fast fronts.

and shows that, apart from the deep nulls, the coupled perturbed mode calculation agrees with the full coupled mode result within a fraction of a dB.

VI. DISCUSSION AND CONCLUSION

The results presented above were all obtained by dividing the range-dependent part of each test situation into 100 steps. If smaller steps are taken, the accuracy of the coupled perturbed mode solution improves and the errors in the wave numbers, the normal mode functions, the mode amplitudes, and the propagation loss are all reduced.

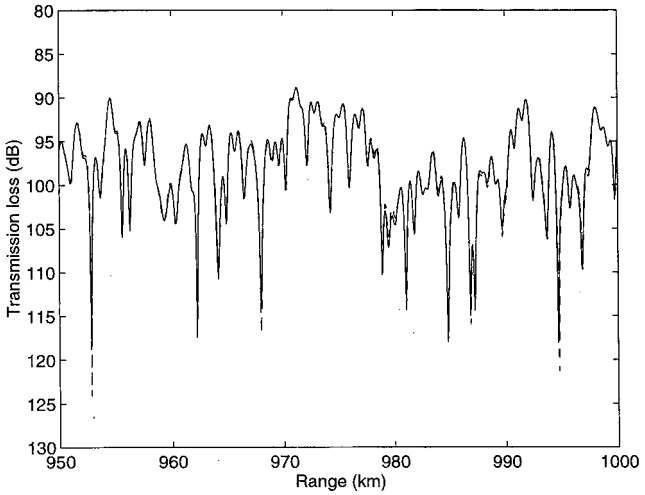

FIG. 8. Transmission loss as a function of range (last 50 km only) for a slow front. The solid line is the exact result and the dashed line is the coupled perturbed mode result using the exact mode functions at every tenth step, i.e., every 100 km.

The accuracy of the solution may also be improved by occasionally inserting the exact wave numbers and mode functions as demonstrated in Fig. 8.

The question of whether it is better to take smaller steps or to insert the exact values more often is an interesting one which is beyond the scope of the present work. However, we note that a practical way to resolve this question in any particular case would be to compute the exact functions every 50 steps or so and determine the maximum error in the wave number. The wave number error multiplied by the step length gives an estimate of the error in the phase terms of Eq. (9). If the error is acceptable, the calculation can proceed as before, if not, the exact values should be found at some smaller number of steps until the error is acceptable.

Of course, a coupled mode calculation is not complete until it converges in the sense that use of a smaller step size gives the same solution. This convergence would also be necessary in the coupled perturbed mode approach but would not be a problem as the whole calculation is considerably faster.

We note again that, to our knowledge, the combination of coupled modes and perturbation theory has not appeared in the underwater acoustics literature. This is surprising because our results show that coupled mode theory and perturbation theory complement each other well. Coupled modes require small range steps and the smaller the range step the more accurate the perturbation calculation. The results presented show that the coupled perturbed modes are capable of giving an accurate description of propagation in a range-dependent situation. The method is significantly faster than the conventional coupled mode approach because it removes the need to numerically solve the wave equation for the normal modes at each step.

Our examination of representative ocean fronts shows that for sufficiently slow range dependence the effects of mode coupling are negligible and propagation is adiabatic. This does not mean the mode coupling terms are small, but rather that they combine with random phase and cancel each

other out. In contrast, for fast range dependence the phase terms are small and there can be very rapid coupling of energy between modes.

ACKNOWLEDGMENT

We are grateful to John Colosi for supplying numerical sound speed profile data from the SLICE89 experiment.

APPENDIX

Combining Eqs. (2) and (12), the depth-separated wave equation for the normal modes becomes

$$d^2U_n/dz^2+[q(z)-k_n^2]U_n=0. \tag{A1}$$

To apply perturbation theory we assume that if $q(z)$ changes by $\Delta q(z)$, there will be corresponding changes ΔU_n and Δk_n in U_n and k_n, respectively. The new values must satisfy the depth-separated wave equation so we have

$$d^2(U_n+\Delta U_n)/dz^2 + [q(z)+\Delta q(z)-(k_n+\Delta k_n)^2](U_n+\Delta U_n)=0. \tag{A2}$$

Subtracting Eq. (A1) from Eq. (A2) and neglecting the second-order terms gives

$$d^2(\Delta U_n)/dz^2+[q(z)-k_n^2]\Delta U_n+[\Delta q(z)-2k_n\Delta k_n]U_n=0. \tag{A3}$$

Since the U_n form a complete set we can expand ΔU_n in terms of them as in Eq. (13). To evaluate the first term of Eq. (A3) we write

$$d^2(\Delta U_n)/dz^2=\sum_m a_{nm}d^2U_m/dz^2, \tag{A4}$$

and then use Eq. (A1) to obtain

$$d^2(\Delta U_n)/dz^2=-\sum_m a_{nm}[q(z)-k_m^2]U_m. \tag{A5}$$

Substitution of Eqs. (13) and (A5) into Eq. (A3) gives

$$-\sum_m a_{nm}[q(z)-k_m^2]U_m+[q(z)-k_n^2]\sum_m a_{nm}U_m + [\Delta q(z)-2k_n\Delta k_n]U_n=0. \tag{A6}$$

The terms in $q(z)$ cancel and we obtain

$$\sum_{m\neq n} a_{nm}[k_m^2-k_n^2]U_m+[\Delta q(z)-2k_n\Delta k_n]U_n=0. \tag{A7}$$

Multiplying Eq. (A7) by $U_n/\rho(z)$, integrating over $(0,\infty)$, using the orthogonality integral of Eq. (7), and rearranging gives

$$\Delta k_n=\frac{1}{2k_n}\int_0^\infty \frac{\Delta q(z)U_n^2(z)\,dz}{\rho(z)}. \tag{A8}$$

Finally, multiplying Eq. (A7) by $U_m/\rho(z)$, with $m\neq n$, integrating over $(0,\infty)$, using the orthogonality integral of Eq. (7), and rearranging gives

$$a_{nm}=\frac{1}{(k_n^2-k_m^2)}\int_0^\infty \frac{\Delta q(z)U_n(z)U_m(z)\,dz}{\rho(z)}. \tag{A9}$$

[1] F. B. Jensen and M. C. Ferla, ''SNAP: The SCLANTCEN normal-mode acoustic propagation model,'' Rep. SM-121 (SACLANT Undersea Research Centre, La Spezia, Italy, 1979).

[2] M. B. Porter, ''The KRAKEN normal mode program,'' Rep. SM-245 (SACLANT Undersea Research Centre, La Spezia, Italy, 1991).

[3] E. K. Westwood, C. T. Tindle, and N. R. Chapman, ''A normal mode model for acousto-elastic ocean environments,'' J. Acoust. Soc. Am. **100**, 3631–3645 (1996).

[4] A. D. Pierce, ''Extension of the method of normal modes to sound propagation in an almost-stratified medium,'' J. Acoust. Soc. Am. **37**, 19–27 (1965).

[5] S. R. Rutherford and K. E. Hawker, ''Consistent coupled mode theory of sound propagation for a class of nonseparable problems,'' J. Acoust. Soc. Am. **70**, 554–564 (1981).

[6] I. J. Thompson, ''Mixing of normal modes in a range-dependent model ocean,'' J. Acoust. Soc. Am. **69**, 1280–1289 (1981).

[7] R. B. Evans, ''A coupled mode solution for acoustic propagation in a waveguide with stepwise depth variations of a penetrable bottom,'' J. Acoust. Soc. Am. **74**, 188–195 (1983).

[8] F. B. Jensen and C. M. Ferla, ''Numerical solutions of range-dependent benchmark problems in ocean acoustics,'' J. Acoust. Soc. Am. **87**, 1499–1510 (1990).

[9] F. B. Jensen, W. A. Kuperman, M. B. Porter, and H. Schmidt, *Computational Ocean Acoustics* (A.I.P., New York, 1994).

[10] M. B. Porter, F. B. Jensen, and C. M. Ferla, ''The problem of energy conservation in one-way models,'' J. Acoust. Soc. Am. **89**, 1058–1067 (1991).

[11] T. F. Duda, S. M. Flatte, J. A. Colosi, B. D. Cornuelle, J. A. Hildebrand, W. S. Hodgkiss, P. F. Worcester, B. M. Howe, J. A. Mercer, and R. C. Spindel, ''Measured wavefront fluctuations in 1000-km pulse propagation in the Pacific Ocean,'' J. Acoust. Soc. Am. **92**, 939–955 (1992).

Manifestation of ray stochastic behavior in a modal structure of the wave field

A. L. Virovlyansky
Institute of Applied Physics, Russian Academy of Science, 46 Ul'yanov Street, 603600 Nizhny Novgorod, Russia

(Received 9 December 1998; accepted for publication 28 March 2000)

A ray-based mathematical formalism is described to analyze modal structure variations in a range-dependent wave guide. In the scope of this formalism mode amplitudes are expressed through parameters of ray trajectories. Therefore, the approach under consideration provides a convenient tool to study how chaotic ray motion manifests itself in an irregular range dependence of the modal structure. The phenomenon of nonlinear ray-medium resonance playing a crucial role in the emergence of ray chaos has been interpreted from the viewpoint of normal modes. It has been shown that in terms of modes the coexistence of regular and chaotic rays means the presence of regular and irregular constituents of mode amplitudes. An analog to incoherent summation of rays has been proposed to evaluate mode intensities (squared mode amplitudes) smoothed over the mode number. Numerical calculations have shown that it gives correct results for smoothed mode intensities at surprisingly long ranges. © *2000 Acoustical Society of America.*
[S0001-4966(00)01707-0]

PACS numbers: 43.30.Dr, 43.30.Bp, 43.30.Re [SAC-B]

INTRODUCTION

In the past decade it was realized that the phenomenon of ray chaos, an analog to the dynamical chaos in classical mechanics,[1,2] should play a great role in the long-range sound propagation through a range-dependent ocean.[3–8] It is quite clear that extreme sensitivity of chaotic rays to initial conditions and small variations of environmental parameters poses severe restrictions on ray theory applications to different direct and inverse problems such as, for example, that of ocean-acoustic tomography.[6,9] Furthermore, it is natural to expect that, under environmental conditions leading to ray chaos, the structure of the full-wave-theory solution should also be very complicated despite some smoothing due to diffractive effects. The problem of understanding how chaotic motion of ray trajectories reveals itself in the resulting wave picture is called the problem of *wave* chaos. It has the well-known prototype in quantum theory called the problem of *quantum* chaos.[10] The problems of quantum and wave chaos become equivalent, at least from the formal viewpoint, when the wave theory is considered in the limit of small-angle propagation. In this case the wave field obeys the parabolic equation[11,12] having exactly the same form as the Shrödinger equation.

The objective of the present study is examining one important aspect of the wave chaos problem, namely, the complicated range variations of the field modal structure in a range-dependent multimode wave guide. Our analysis is performed in the scope of parabolic equation approximation. The main reason for making this choice is the great simplification in numerical calculating the wave field which comes with use of this approximation. On the other hand, as it has been demonstrated in Ref. 8, such models of small-angle propagation retain many important features typical of sound propagation through the real ocean. In the present paper numerical solution to the parabolic equation governing the wave field have been obtained with the UMPE code.[13]

The problem of modal structure range variations is addressed here on the basis of a ray approach formulated in Refs. 14–17. For simplicity we restrict our attention to a two-dimensional cw field. The idea of our approach consists in projecting the ray theory solution to the parabolic equation onto normal modes and evaluating the corresponding integral using the stationary phase technique. It has been shown that each mode is formed by contribution from a finite number of rays which we call the eigenrays for this mode. This approach yields an expression for the mode amplitude through parameters of ray trajectories and, thus, establishes a relationship between the ray and mode representations of the wave field in a range-dependent wave guide. In the case of weak inhomogeneities this result reduces to relations obtained in Refs. 18–20.

The explicit expressions relating ray trajectories to mode amplitudes provide a convenient tool for studying how some features of ray chaos exhibit themselves in mode amplitude range variations. In this article we consider a wave guide with periodic range dependence. This model, being rather artificial from the viewpoint of underwater acoustics, nevertheless has an important advantage which makes it a good starting point for a ray-based analysis of an irregular modal structure. The point is that the properties of ray chaos in periodic wave guides are known comparatively well because they are identical to extensively studied properties of chaotic dynamics of a nonlinear oscillator driven by an external periodic force.[1,2,21–23]

We discuss how typical features of the ray chaos, such as exponential growth (with range) of eigenrays contributing to the field point and coexistence of chaotic and regular ray trajectories (the presence of stable islands in the chaotic sea on the phase plane[1,2,5]), manifest themselves in the mode amplitude range dependence. It has been shown that the phe-

nomenon of nonlinear ray-medium resonance playing a crucial role in the emergence of ray chaos has its analog for modes which we call the mode-medium resonance.[16] According to the heuristic criterion proposed by Chirikov,[21–23] chaos is a result of an overlap of different resonances. In terms of normal modes it corresponds to overlapping different mode-medium resonances leading to complicated and irregular range variations of the modal structure.

The article is organized as follows. In Sec. I we give a description of a ray-based technique of evaluating the mode amplitude. In more detail this topic is discussed in Ref. 16. The subject of Sec. II is a brief discussion of a nonlinear ray-medium resonance and manifestation of this phenomenon in the modal structure. It has been shown that the known analytic relations for ray trajectories involved in an isolated resonance in the scope of our formalism can be used for analysis of mode-medium resonance. We argue that under condition of ray chaos mode amplitudes should exhibit an irregular range dependence. At the same time, due to coexistence of stochastic and regular ray trajectories, the mode amplitude as a function of range should typically consist of two constituents: regular and irregular ones. In Sec. II these ideas are supported by numerical calculations performed for a simple model of an acoustic wave guide with periodic range dependence. It has been demonstrated numerically that number of eigenrays contributing to the given mode does grow exponentially with range. Comparison with the result of numerical solution of a parabolic equation has shown that the applicability of the ray approach fails at comparatively short ranges due to a fast growing number of caustics. Some calculations have been carried out to illustrate the existence of regular and irregular constituents of mode amplitude. The most unexpected and encouraging result obtained in this section is the fact that the mode intensity smoothed over the mode number can be properly predicted in the scope of our approximate approach at such long ranges where the number of contributing eigenrays and caustics is so great that the ray approach cannot be applied for evaluation of amplitudes of individual modes.

I. RAY APPROACH FOR MODAL STRUCTURE ANALYSIS

A. Ray representation of the wave field in the parabolic equation approximation

Let us consider the cw field at a carrier frequency f in a 2-D wave guide medium. It is assumed that the sound speed C does not depend on time t and is a function of both horizontal coordinate x and vertical coordinate z. In the limit of small-angle propagation the complex amplitude of the wave field $u(x,z)$ (the time factor $e^{-i2\pi ft}$ is omitted throughout) obeys the parabolic equation[11–13]

$$ik\frac{\partial u}{\partial x}=-\frac{1}{2}\frac{\partial^2 u}{\partial z^2}+k^2U(x,z)u, \tag{1}$$

with

$$U(x,z)=\frac{1}{2}\left(1-\frac{C_0^2}{C^2(x,z)}\right). \tag{2}$$

Here C_0 is a reference phase speed, and $k=2\pi f/C_0$ is the wave number in the reference medium with $C=C_0$. Equation (1) coincides with the Schrödinger equation. The x variable plays the role of time and k^{-1} plays the role of the Planck constant.

The corresponding Hamiltonian, $H=p^2/2+U(x,z)$, is a function of coordinate z, momentum p, and timelike variable x. Solutions to the Hamilton equations

$$\frac{dz}{dx}=\frac{\partial H}{\partial p},\quad \frac{dp}{dx}=-\frac{\partial H}{\partial z}, \tag{3}$$

define the ray trajectories which we denote as

$$z=z(x,p_0,z_0),\quad p=p(x,p_0,z_0), \tag{4}$$

where z_0 and p_0 are initial values of the coordinate and the momentum at $x=0$, respectively. Note that $p=\tan\theta$, where θ is a current ray grazing angle.

The ray eikonal, which is an analog to the mechanical action, is given by the relation[24,25]

$$S=\int (p\,dz-H\,dx), \tag{5}$$

where the integral runs over the ray trajectory.

In the scope of the geometrical optics approximation (or the semiclassical approximation as it is called in quantum theory) the solution of Eq. (1) is represented in the form[1,24]

$$u(x,z)=\sum_\nu A^\nu(x,z)e^{ikS^\nu(x,z)-i(\pi/2)\mu^\nu}, \tag{6}$$

where each term describes a contribution to the total wave field from an *eigenray*, that is, a ray which passes through the point (x,z). The sum goes over all the eigenrays contributing at a particular receiver position. In the above formula the superscript ν numbers the eigenrays, A^ν and S^ν are the amplitude and the eikonal of the νth eigenray, respectively, and μ^ν is the Maslov index, or the integral number of times that the νth ray passes through caustics (at caustics the ray amplitude A^ν goes to infinity and the semiclassical approximation fails).

The explicit expression for the ray amplitude depends on the source exciting the wave field, or, in other words, on the initial conditions to Eq. (1) at $x=0$. We consider two important examples of such initial conditions. Since we are going to analyze the contribution from an individual eigenray, we shall omit the superscript ν in the remaining part of this subsection.

1. The point source

The starting wave field,

$$u(0,z)=\delta(z-z_0), \tag{7}$$

and the desired solution represents the Green's function of Eq. (1). In this case all the rays escape from the same point z_0 determined by the source position and each ray is ''labeled'' by its initial momentum p_0.

The quasiclassical expression for the Green's function is known (see, for example, Ref. 26) and the ray amplitude can be presented in the form

$$A=\sqrt{\frac{k}{2\pi i|\partial z/\partial p_0|}}. \tag{8}$$

It should be pointed out that the eigenrays are determined by the relation

$$z=z(x,p_0,z_0), \tag{9}$$

which formally coincides with the first equality in (4) but is considered here as an equation in p_0. On the other hand, this equation can be treated as a definition of p_0 as a function of x and z. Substituting the function $p_0=p_0(x,z)$ into Eq. (8) (after evaluating the derivative) determines the ray amplitude as a function of x and z.

2. Quasi-plane wave source

The initial wave field is determined by the function

$$u(0,z)=a(z)e^{iks(z)}, \tag{10}$$

where $a(z)$ and $s(z)$ are two functions slowly varying with z: their characteristic scales are much greater than the wavelength, $2\pi/k$. At the same time we assume that, due to large k, the phase of (10) is a rapidly oscillating function. This type of source excites a quasi-plane wave.

The detailed description of the semiclassical solution to Eq. (1) with the initial conditions (10) is given in Ref. 27. In this case different rays start from different points z_0. The trajectory leaving the point z_0 has the initial momentum

$$p_0=\overline{p}(z_0), \quad \overline{p}(z)=\frac{\partial s(z)}{\partial z}. \tag{11}$$

So, in this example (as opposed to the previous one), each ray is labeled by its initial coordinate z_0. The eigenrays are defined by the equation

$$z=z_s(x,z_0), \quad z_s(x,z_0)=z(x,z_0,\overline{p}(z_0)). \tag{12}$$

Solving Eq. (12) for z_0 one finds the starting points of the rays crossing the given observation point z at the given distance x. The initial momenta of these eigenrays are then found from Eq. (11).

The function $u(x,z)$ is represented by the sum (6) with

$$A=\frac{a(z_0)}{\sqrt{\partial z_s/\partial z_0}}\,e^{iks(z_0)}. \tag{13}$$

The values of z_0 and, hence, of A, in accordance with the above remark, can be considered as functions of x and z.

B. Action-angle variables

The analysis of quasi-periodic behavior of ray trajectories, which is typical of wave guide propagation, can be simplified by introducing the so-called action-angle variables.[25] The corresponding procedure is briefly described in this subsection.

In many propagation models the potential $U(x,z)$ can be regarded as a sum of range-dependent and range-independent components, i.e., $U(x,z)=U_0(z)+\varepsilon V(x,z)$.

In the range-independent wave guide ($\varepsilon=0$) with the Hamiltonian $H_0=p^2/2+U_0(z)$, the conservation law $H_0(p,z)=E$ holds true along the ray trajectory with the constant E being an analog to the mechanical energy. The explicit expression for the momentum p as a function of E and z is $p(E,z)=\pm\sqrt{2[E-U_0(z)]}$.

All the trajectories are periodic curves. The coordinates of their upper and lower turning points ($z_{\max}$ and $z_{\min}$, respectively) are functions of the ''energy,'' E, and determined by the equation $U_0(z)=E$. For simplicity we shall assume that the potential $U_0(z)$ is smooth, has the only minimum, and its walls tend to infinity as $z\to\pm\infty$.

An important characteristic of ray trajectories, which are widely used in both classical mechanics and ray theory, is the so-called action variable I related to E by[25]

$$I=\frac{1}{2\pi}\oint dz\,p(E,z)=\frac{1}{\pi}\int_{z_{\min}}^{z_{\max}}dz\,\sqrt{2[E-U_0(z)]}, \tag{14}$$

where the integration goes over the period of the ray trajectory. Equation (14) defines the function $E(I)$. Now the turning point coordinates, $z_{\min}$ and $z_{\max}$, can also be regarded as functions of I.

The canonical transformation from our (p,z) variables to the action-angle variables (I,θ) is given by the pair of equations[25]

$$p=\frac{\partial G(z,I)}{\partial z}, \quad \theta=\frac{\partial G(z,I)}{\partial I} \tag{15}$$

with the generating function

$$G(z,I)=\int^{z}dz\,\sqrt{2[E(I)-U_0(z)]}. \tag{16}$$

Note, that p and z are periodic functions of the angle variable θ, i.e., $p(I,0)=p(I,\theta+2\pi)$ and $z(I,\theta)=z(I,\theta+2\pi)$.

In the range-dependent environment ($\varepsilon\neq0$) we define the action-angle variables using *the same* relations [given in Eqs. (15) and (16)] as in the unperturbed wave guide. The Hamilton equations in the new variables take the form[1]

$$\frac{dI}{dx}=-\varepsilon\frac{\partial V}{\partial\theta}, \quad \frac{d\theta}{dx}=\omega(I)+\varepsilon\frac{\partial V}{\partial I}, \tag{17}$$

where $\omega(I)=dH_0(I)/dI$ is the spatial frequency of the trajectory oscillations along the x axis in the unperturbed wave guide.

C. Normal mode representation of the wave field

We define the normal mode representation of the wave field $u(x,z)$ in a range-dependent environment as an expansion into a sum of eigenfunctions of the unperturbed Sturm–Liouville eigenvalue problem[12,24]

$$-\frac{1}{2}\frac{d^2\varphi_m}{dz^2}+k^2U_0(z)\varphi_m=k^2E_m\varphi_m \tag{18}$$

with appropriate boundary conditions.

The eigenfunctions, $\varphi_m(z)$, represent normal modes of unperturbed wave guide. They are orthogonal and we normalize them in such a way that

$$\int_{-\infty}^{\infty} dz\, \varphi_m(z)\varphi_n(z) = \delta_{mn}. \tag{19}$$

In the Wentzel–Kramers–Brillouin (WKB) approximation the mth eigenvalue E_m is given by the relation $E_m = E(I_m)$, where

$$kI_m = m + \tfrac{1}{2}, \quad m = 0,1,..., \tag{20}$$

and the mth eigenfunction $\varphi_m(z)$ between its turning points can be represented as follows:[12,28]

$$\varphi_m(z) = \varphi_m^+(z) + \varphi_m^-(z), \tag{21}$$

where

$$\varphi_m^{\pm}(z) = Q_m(z) e^{\pm i(kS_0(z,I_m) - \pi/4)}, \tag{22}$$

$$S_0(z,I) = \int_{z_{\min}}^{z} dz\, \sqrt{2[E(I) - U_0(z)]}, \tag{23}$$

$$Q_m(z) = \frac{1}{\sqrt{D(I_m)}\sqrt[4]{2[E_m - U_0(z)]}}, \tag{24}$$

$$D(I) = \frac{2\pi}{\omega(I)} = 2\int_{z_{\min}}^{z_{\max}} \frac{dz}{\sqrt{2[E(I) - U_0(z)]}}. \tag{25}$$

The quantity I_m can be identified as an action variable corresponding to the mth mode.

The modes form a complete set, which means that we can represent an arbitrary function as a sum of normal modes. Thus, we write the wave field as

$$u(x,z) = \sum_m c_m(x)\varphi_m(z). \tag{26}$$

In terms of modal decomposition (26) the problem of field evaluation reduces to evaluation of complex mode amplitudes $c_m(x)$. By projecting the wave field $u(x,z)$, taken in the geometrical optics approximation (6), onto normal modes of an unperturbed wave guide, these amplitudes can be expressed through solutions of rays equations. The corresponding procedure, which consists in evaluation of the integral

$$c_m(x) = \int dz\, u(x,z)\varphi_m(z) \tag{27}$$

using the stationary phase technique, has been considered in Ref. 16. Here we present only the final expressions for $c_m(x)$.

It turns out that the amplitude of the mth mode at the given range x is formed by contributions from the rays with action variables equal to that of the given mode, i.e., with

$$I = I_m. \tag{28}$$

In what follows we shall call such rays the eigenrays for the given modes or simply eigenrays referring to the geometrical optics eigenrays passing through the observation point as the standard eigenrays. Equation (28) singles out the eigenrays for the mth mode in exactly the same manner as do Eqs. (9) and (12) relative to standard eigenrays.

Let us discuss this point. First of all, note that we can consider the action variable satisfying Eqs. (17) as a function of range, and initial values of the momentum p_0 and the coordinate z_0, i.e.,

$$I = I(x,p_0,z_0). \tag{29}$$

For the point source given in Eq. (7) the value of z_0 is the same for all the rays and substitution of Eq. (29) into Eq. (28) yields the equation in p_0 analogous to Eq. (9), defining the initial momenta of the eigenrays for the mth mode.

The amplitude of the mth mode is given by the sum

$$c_m = \sum_n \frac{1}{\sqrt{2\pi i |\partial I/\partial p_0|_{p_0 = p_{0n}}}} e^{ik\Phi_n + i\alpha_n}, \tag{30}$$

where each term represents a contribution from an eigenray with an initial momentum p_{0n} (an index n numbers contributing eigenrays). The explicit expressions for the phase terms are (since the subsequent formulas describe characteristics of a single eigenray, the subscript n is omitted)

$$\Phi = S - \sigma S_0(z,I_m) \tag{31}$$

and

$$\alpha = \left(\operatorname{sgn}\left(\frac{\partial p/\partial p_0}{\partial z/\partial p_0}\right) - \operatorname{sgn}(p) - 2\mu\right)\frac{\pi}{4}. \tag{32}$$

Here z is the coordinate and p is the momentum of the eigenray at a range x, and S and μ are its eikonal and Maslov index, respectively. The function $\operatorname{sgn}(x)$ gives the sign of its argument.

An analog to Eq. (30) for the quasi-plane wave source (10) is given by

$$c_m = \sum_n \frac{a(z_{0n})}{\sqrt{k|\partial I/\partial z_0|_{z_0 = z_{0n}}}} e^{iks(z_{0n}) + ik\Phi_n + i\alpha_n}, \tag{33}$$

where z_{0n} is an initial coordinate of the nth eigenray. The expressions for the phase terms Φ and α are again determined by Eqs. (31) and (32) except the partial derivatives in Eq. (32) should be evaluated with respect to z_0.

Equations (30) and (33) reduce the mode amplitude evaluation to a procedure quite analogous to that generally used when evaluating the field amplitude at the given point. It includes solving the Hamilton (ray) equations, finding the eigenrays, and calculating ray eikonals and some derivatives with respect to initial values of ray parameters.

The two following important points concerning Eqs. (30) and (33) should be emphasized. First, these equations have been derived *without* assuming the perturbation εV to be small. Only applicability of geometrical optics approximation has been required. Second, although we have considered the two particular types of the starting field, the results can be easily modified for treating an arbitrary source. This issue is discussed in Ref. 16.

II. MODE-MEDIUM RESONANCE

Having the comparatively simple expressions relating the mode amplitudes to rays, we can now discuss how the complicated ray trajectory dynamics reveals itself in the

mode amplitude variations. In so doing, we restrict our attention to a wave guide with a weak (ε is now considered as a small parameter) periodic range dependence with a spatial period $2\pi/\Omega_0$. Since the perturbation $V(x,z(I,\theta))$ is periodic in x and θ, it can be represented in the form of the Fourier series

$$V=\frac{1}{2}\sum_{l,q} V_{l,q}(I)e^{i(l\theta-q\Omega_0 x)}+\text{c.c.}, \tag{34}$$

where the symbol c.c. denotes complex conjugation.

A group of ray trajectories are captured in a ray-medium resonance if their action variables are close to I_0 satisfying the condition

$$l\omega(I_0)=q\Omega_0, \tag{35}$$

with l and q being two integers. For an analytical treatment of such rays it is convenient to introduce the new canonical variables $\Delta I=I-I_0$ and $\psi=\theta-\omega_0 x$. For small enough ε these variables satisfy the following approximate equations,

$$\Delta\dot{I}=\varepsilon l V_0\sin(l\psi+\psi_0), \quad \dot{\psi}=\omega'\Delta I, \tag{36}$$

where $\omega'=d\omega(I)/dI$ at $I=I_0$, V_0 is an absolute value of the resonant term in the sum (34), and ψ_0 is a constant depending on the phase of this term. For a more detailed description of the corresponding formalism see, for example, Refs. 1 and 2.

Equations (36) formally coincide with the Hamilton equations for the nonlinear pendulum in classical mechanics and the variables ΔI and ψ are analogs to the momentum and coordinate of the pendulum, respectively. It is clear that the values of ΔI corresponding to the finite motion belong to the interval $-\Delta I_{\max}<\Delta I<\Delta I_{\max}$, where

$$\Delta I_{\max}=2\sqrt{\varepsilon V_0/|\omega'|}. \tag{37}$$

From the viewpoint of rays, the above equation defines the width of the resonance in terms of action. Each trapped ray oscillates with some spatial frequency. The width of the resonance in terms of spatial frequency can be approximately estimated as

$$\Delta\omega=|\omega'|\Delta I_{\max}/2=\sqrt{\varepsilon V_0|\omega'|}. \tag{38}$$

Rays with the action variable ΔI exceeding $\Delta I_{\max}$ are not captured into the resonance.

Nonlinear ray medium resonance plays an important role in the emergence of ray chaos. If there are at least two nonlinear resonances centered at spatial frequencies ω and $\omega+\delta\omega$, a chaotic motion of ray trajectories is possible. It takes place when the Chirikov's criterion,[21–23]

$$\frac{\Delta\omega}{\delta\omega}>1, \tag{39}$$

is met, i.e., when the resonances overlap leading to the stochastic instability of the system.

The trajectories of two stochastic rays with close initial conditions diverge exponentially[1–5] and the number of eigenrays contributing at a given field point grows exponentially with range.[7]

The ray approach for mode amplitude evaluation, discussed in the preceding subsection, provides a convenient way to interpret the ray-medium resonance and related phenomena from the viewpoint of normal modes.

Let us consider the case when only one mode is excited at $x=0$, i.e., $u(0,z)=\varphi_m(z)$. According to Eqs. (21) and (22), this starting field represents a superposition of two terms defined in Eq. (10). Each term can be associated with a congruence of rays taking off from the part of the initial cross section $x=0$ laying between the mode turning points. The initial momenta of these rays are defined in Eq. (11), where $s(z)$ must be replaced with $S_0(z,I_m)-\pi/4$ for one of the congruences and with $-S_0(z,I_m)+\pi/4$ for another. So there will be two rays, leaving each point with the initial momenta equal in absolute value and opposite in sign.

Initial values of the action variable I are equal to I_m for *all* the rays belonging to *both* congruences, while the initial values of the angle variable θ cover the whole interval from 0 to 2π.

A situation which we call *mode-medium resonance* occurs when the value of I_m satisfies Eq. (35). In this case the above rays are trapped into the resonance and if the latter is isolated, Eqs. (17) simplify to Eqs. (36) with $I_0=I_m$. Combining these equations with the results on ray-mode relations presented in the preceding subsection allows one to make some conclusions and estimations concerning the dependence of modal structure on range.

For example, it is clear that due to the resonance, at ranges of order of $1/\Delta\omega$, there will appear a bundle of rays with the action variables ΔI in the interval $|\Delta I|<\Delta I_{\max}$. This means [see Eqs. (28) and (33)] that starting with such ranges, the mth mode is split into a group of M modes with

$$M=\Delta I_{\max}/k=\Delta I_{\max}=2\sqrt{\varepsilon V_0/\omega'}/k. \tag{40}$$

In the case of overlapping resonances, it is natural to expect a further broadening of a group of modes. Moreover, as we already know, the overlapping of resonances causes the emergence of ray chaos with exponential proliferation of standard eigenrays.[7] It is almost obvious that under chaotic conditions the number of eigenrays contributing to the given mode also grows exponentially with range, giving rise to a very complicated range dependence of mode amplitudes.

III. NUMERICAL RESULTS

A. Models

To demonstrate an application of the above ray approach to analysis of modal structure variations with range, we consider a simple wave guide with the two components of potential given by

$$U_0(z)=\begin{cases} Lz, & z\geqslant 0,\\ \infty, & z<0,\end{cases} \quad \varepsilon V(x,z)=Lz\sum_{j=1}^{J}\varepsilon_j\sin\Omega_j x. \tag{41}$$

It can be easily shown that this potential can be treated by means of the relations from Sec. I derived for a smooth function $U_0(z)$. Only two minor revisions are necessary: (1) the constant $\frac{1}{2}$ on the right-hand side of Eq. (20) must be changed to $-\frac{1}{4}$ (the lowest mode number is now 1) and (2) the constant phase shift $-\pi/4$ in Eq. (22) and all subsequent formulas must be replaced by $-\pi/2$.

Using the explicit expressions for the main characteristics of unperturbed ray trajectories,

$$E(I)=\left(\frac{I}{a}\right)^{2/3}, \quad a=\frac{2\sqrt{2}}{3\pi L},$$

$$S_0(z,I)=\pi[I-(I-a^{2/3}zL)^{3/2}],$$

$$D(I)=3\pi a^{2/3}I^{1/3},$$

we readily obtain the relations connecting (p,z) variables to action-angle variables (I,θ):

$$z=\frac{E(I)}{L}\left[1-\left(2n+1-\frac{\theta}{\pi}\right)^2\right],$$

$$\theta\in(2\pi n,2\pi(n+1)), \quad n=0,1,...,$$

$$p=\sqrt{2E(I)}\left(2n+1-\frac{\theta}{\pi}\right),$$

$$\theta\in(2\pi n,2\pi(n+1)), \quad n=0,1,... .$$

The perturbation in terms of action-angle variables for $J=1$ takes the form

$$V=\frac{\varepsilon_1}{2i}\left(\frac{I}{a}\right)^{2/3}\sum_{q=-\infty}^{\infty} b_q(e^{i(q\theta+\Omega x)}-e^{i(q\theta-\Omega x)}), \tag{42}$$

with

$$b_q=\begin{cases}\frac{2}{3}, & q=0,\\ -2\pi^{-2}q^{-2}, & q\neq 0.\end{cases}$$

It is obvious that for $J>1$ we should add similar sums for each nonzero ε_j.

The half-width of a mode-medium resonance in terms of the number of trapped modes, given in Eq. (40), for the present environmental model with $J=1$ translates into

$$M=2\sqrt{\varepsilon_1}m. \tag{43}$$

From the viewpoint of underwater acoustics, Eqs. (41) present a strongly idealized model of an acoustic wave guide with a pressure release surface at $z=0$ and a range-dependent sound speed profile

$$C(x,z)=\frac{C_0}{\sqrt{1-2Lz(1+\Sigma_{j=1}^{J}\varepsilon_j\sin\Omega_j x)}}, \tag{44}$$

$0<z<z_{\text{bot}}$. The selected values of the constants defining the unperturbed potential $U_0(z)$ are $C_0=1500$ m/s and $L=4.35\times10^{-5}$ 1/m. It is assumed that the carrier frequency $f=250$ Hz. The unperturbed sound speed profile is shown in Fig. 1 by the solid line. It is assumed that the bottom is located at a so large depth, z_{bot}, that it does not affect the modes which we are going to consider.

Below we consider two particular models of a range-dependent wave guide. A spatial period of the jth harmonic, $2\pi/\Omega_j$, is denoted as $\mathcal{D}_j$.

Model 1. This peturbation consists of two harmonics $(J=2)$ with parameters listed as follows

ε_1	$\mathcal{D}_1$	ε_2	$\mathcal{D}_2$
0.03	13.149	0.03	16.346

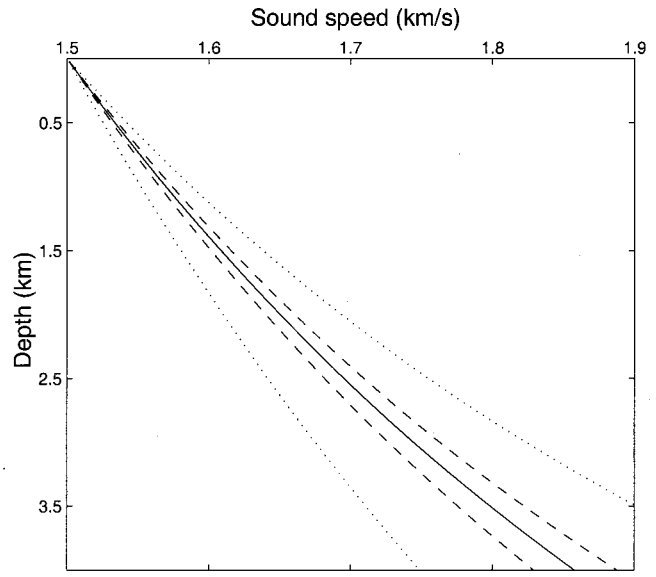

FIG. 1. Unperturbed sound speed profile (solid line) and maximum deviations from this profile due to perturbations in model 1 (dashed lines) and in model 2 (dotted lines).

The values of $\mathcal{D}_j$'s are expressed in km. They satisfy the relation $\mathcal{D}_1:\mathcal{D}_2=4:5$.

Model 2. In this model perturbation includes seven harmonics $(J=7)$ with the parameters

ε_1	ε_2	ε_3	ε_4	ε_5	ε_6	ε_7
0.03	0.03	0.03	0.03	0.03	0.07	0.07

$\mathcal{D}_1$	$\mathcal{D}_2$	$\mathcal{D}_3$	$\mathcal{D}_4$	$\mathcal{D}_5$	$\mathcal{D}_6$	$\mathcal{D}_7$
7.4	8.222	9.867	12.333	14.8	16.444	24.667

Here the values of $\mathcal{D}_j$'s are again expressed in km. They are related as $\mathcal{D}_1:\mathcal{D}_2:\mathcal{D}_3:\mathcal{D}_4:\mathcal{D}_5:\mathcal{D}_6:\mathcal{D}_7=9:10:12:15:18:20:30$.

Note that in both models the potential remains a linear function of depth at any range. Dashed and dotted curves in Fig. 1 show the limits within which the sound speed profile varies with range.

The parameters of both models have been chosen to ensure an overlapping of resonances centered at frequencies Ω_j and their integer multiples, and, hence, to ensure the emergence of ray chaos. In model 1 the chaos is expected to be ''weaker'' than that in model 2 because the perturbation in model 1 is weaker and the resonances overlap only slightly.

B. Poincaré map

Each model describes a range-dependent environment with a period $\mathcal{D}_{\text{LCM}}$ being the least common multiple of corresponding $\mathcal{D}_j$'s. The latter have been chosen to make the value of $\mathcal{D}_{\text{LCM}}$ not very large in order to simplify numerical evaluation of the Poincaré map[1–3]

$$(p_{n+1},z_{n+1})=\hat{T}(p_n,z_n),$$

where a symbol $\hat{T}$ denotes transformation of the momentum and coordinate of the ray trajectory taken at a range $n\mathcal{D}_{\text{LCM}}$ to that at a range $(n+1)\mathcal{D}_{\text{LCM}}$. The idea to choose the peri-

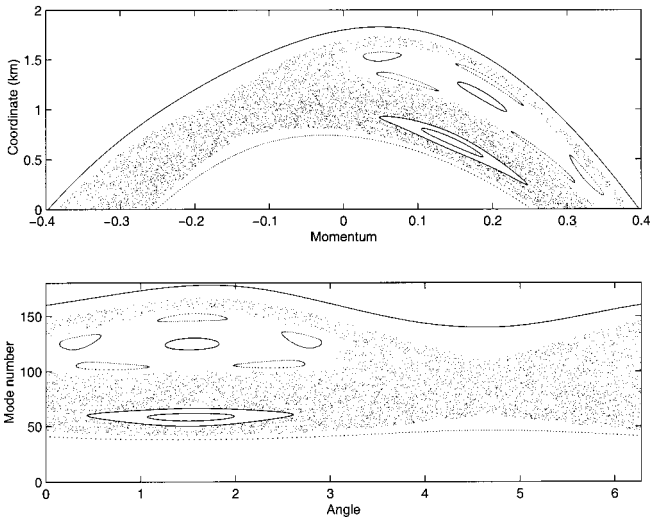

FIG. 2. Phase portrait of model 1 in terms of momentum-coordinate (upper panel) and action-angle (lower panel) variables. Using the quantization rule the action variable is expressed through the mode number formally considered as a continuous parameter.

ods of a multi-frequency perturbation being integer multiples of some fixed value has been used in Ref. 29. It allows one to construct rather realistic models whose chaotic properties can be studied with the Poincaré map.

The upper panel in Fig. 2 shows a phase portrait of model 1 in terms of momentum-coordinate variables. This is a set of dots depicting points (p_n, z_n) calculated for several rays at ranges up to 10 000 km. It demonstrates a picture typical of dynamical chaos: chaotic sea (parts of the phase plane filled with chaotically distributed dots) with stable islands (the areas where dots form regular curves). A phase portrait of model 2 is shown in Fig. 3 (upper panel). Here the chaotic sea occupies more space compared to model 1, confirming our conjecture that in model 2 ray chaos is more ''strong.''

The same phase portraits in terms of action-angle variables are shown in the lower panels of Figs. 2 and 3. Since we are going to use these results to make some conclusions

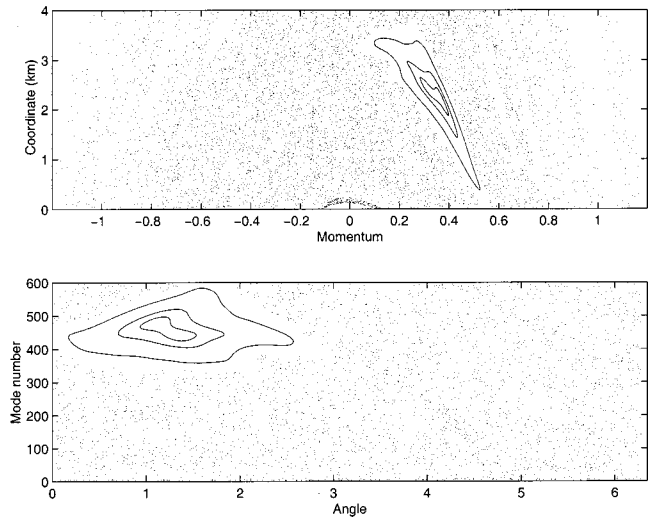

FIG. 3. As in Fig. 2, but for model 2.

concerning field modal structures, the values of action variable I are expressed via mode number m, i.e., instead of (θ, I) phase plane we consider (θ, m) plane. A linear transformation from I to m has been performed (formally considering m as a continuous variable) on the basis of Eq. (20) slightly modified in accordance with a remark made after Eqs. (41).

The phase portraits demonstrate that the mode amplitude as a function of range is, generally, composed of two constituents: a chaotic one and a regular one. Indeed, eigenrays contributing to the given mode satisfy Eq. (28) and, so, points corresponding to them on the phase plane (m, θ) are lying on a horizontal line $m = \text{const}$. Typically, a part of such a line belongs to a chaotic sea while other parts can cross stable islands. It means that the mode amplitude can be formed by contributions partially from chaotic rays, and partially from regular ones.

Below this phenomenon is examined further. However, before doing this we present numerical evidence that the ray approach considered in Sec. I provides a rather good prediction of mode amplitudes at comparatively short ranges and discuss the role of caustics in breaking down this approach.

C. Eigenrays, caustics, and mode amplitudes

In numerical simulation we will restrict our attention to the case when the starting field represents a single eigenfunction, i.e., $u(0,z) = \varphi_{m_0}(z)$. All the numerical results for both models presented shortly have been obtained for $m_0 = 60$. Initial parameters of rays corresponding to such a field have already been described in Sec. II. However, an additional remark should be made. The WKB approximation to our $\varphi_{m_0}(z)$ remains valid at the upper turning point $z_{\min} = 0$ but it fails at the lower turning point at $z_{\max} = 940$ m. To avoid this difficulty we simply ignore the part of the starting field in the vicinity of $z_{\max}$ by accounting only the eigenrays starting from the points z_0 belonging to the interval $0 < z_0 < z_{\max} - \Delta l$, where Δl is a small offset.

The eigenrays contributing to the mth mode are defined to be roots of the equation in z_0

$$I(x, p_0, z_0) = I_m, \tag{45}$$

where

$$p_0 = \pm \sqrt{2[E(I_{m_0}) - U_0(z_0)]}.$$

Figures 4 and 5 show the dependences of action variable at the three fixed ranges on initial ray coordinate z_0 for model 1 and 2, respectively. Here we again express the action variable via the mode number m. So, the values of z_0 satisfying Eq. (45) for three chosen ranges correspond to intersections of the curves presented in Figs. 4 and 5 with the horizontal straight line $m = \text{const}$. It is clearly seen that the shapes of the curves become more and more complicated with range and the number of eigenrays contributing to the given mode grows for both models.

This situation is very similar to that for standard eigenrays discussed in Ref. 7, where ''the exponential proliferation of eigenrays'' has been demonstrated numerically. In our case the number of eigenrays also increases exponen-

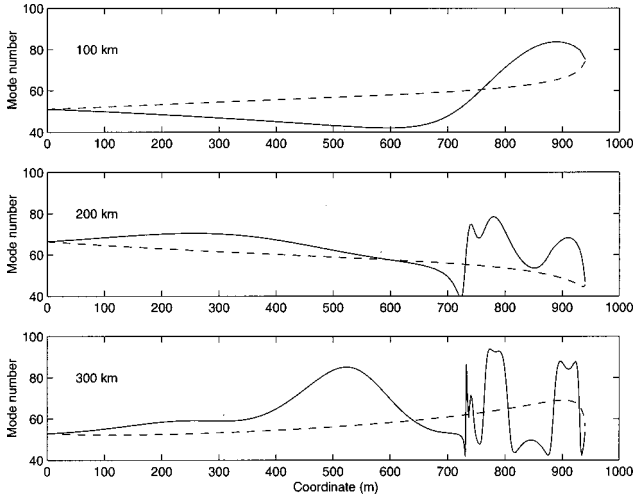

FIG. 4. Action variable versus starting depth at 100 km (upper panel), 200 km (middle panel), and 300 km (lower panel) ranges for model 1. The solid (dashed) curves correspond to rays starting upwards (downwards). Action variable is again expressed through an equivalent mode number.

tially with range. Figure 6 shows the number of eigenrays contributing to the 60th mode for both models with exponential fits. The fact that the eigenray proliferation in model 2 is much more rapid is consistent with our expectation that the chaos in this model is ''stronger.''

There is one more feature common for standard geometrical optics and our approach. In standard ray theory the predicted intensity is infinite at caustics which are curves in the (z,r) plane where the cross section of a ray tube vanishes. In the scope of our approach the contribution from the eigenray can also be infinite. It occurs when the derivative in the denominators in Eq. (30) or (33) vanishes. In this case we can say that the ray passes through a caustic in the (I,r) plane. In the reminder of this article we shall use the term caustic in this sense, i.e., we shall always mean caustics in the (I,r) plane.

The extrema of curves like those shown in Figs. 4 and 5 determine starting depths of rays passing through caustics at a given distance. Contributions from eigenrays with initial values of z_0 close to such depths cannot be evaluated using

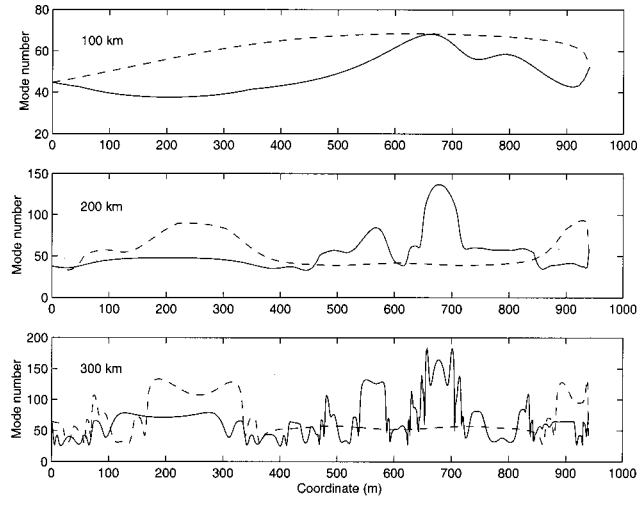

FIG. 5. As in Fig. 4, but for model 2.

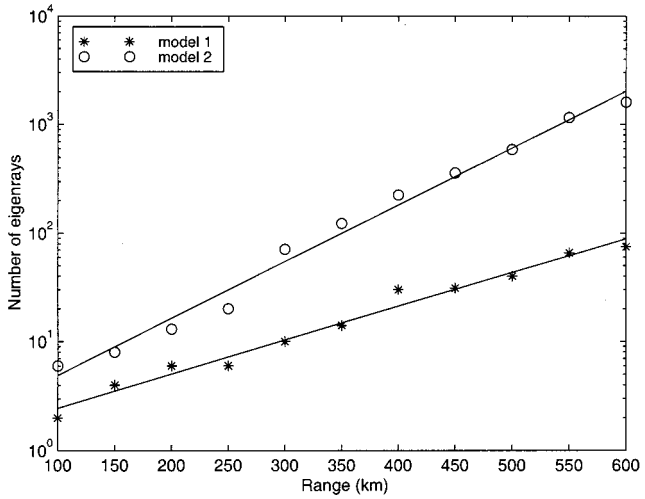

FIG. 6. Number of eigenrays contributing to mode 60 as a function of range.

our ray approach. It is clear that the same problem exists for any source. By analogy with standard geometrical optics,[30] Eqs. (30) and (33) can be modified to obtain relations for the ray amplitude (expressing the amplitude in the vicinity of a caustic via the Airy function) which does not break down at a caustic. However, we do not consider this subject here.

It seems almost obvious that, under conditions of ray chaos, the number of caustics should grow exponentially with range, and mode amplitude predictions made on the basis of Eq. (30) or (33) can be accurate only at short ranges. For our models the limiting ranges can be estimated as 100–200 km. It is seen from Figs. 7 and 8 where the mode amplitudes at 100- and 200-km ranges given by Eq. (33) are shown along with the absolute values of their deviations from the mode amplitudes obtained by numerical solution of the parabolic equation (1) using the UMPE code.[13] These deviations (marked by circles) we consider as errors of approximate results provided by the ray approach (asterisks).

In the upper panel of Fig. 7 it is seen that the errors are

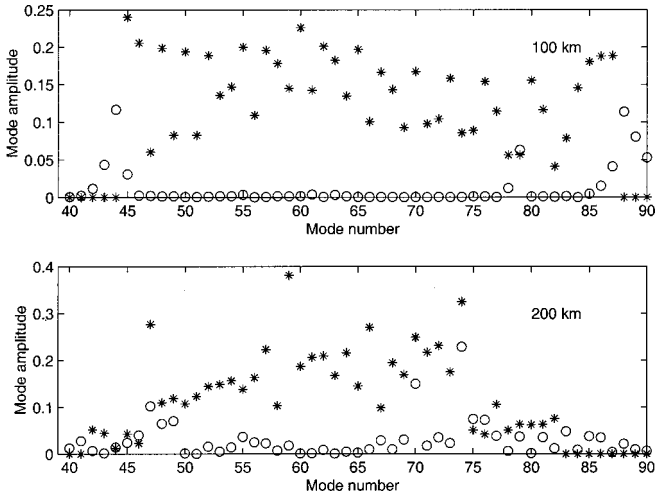

FIG. 7. Model 1. Comparison of mode amplitudes, $|c_m|$, predicted with our ray approach at 100 km (upper panel) and 200 km (lower panel) ranges to the result of numerical solution of the parabolic equation using the UMPE code. Asterisks: Ray approach predictions. Circles: Absolute values of differences between the ray approach predictions and the results computed with the UMPE code.

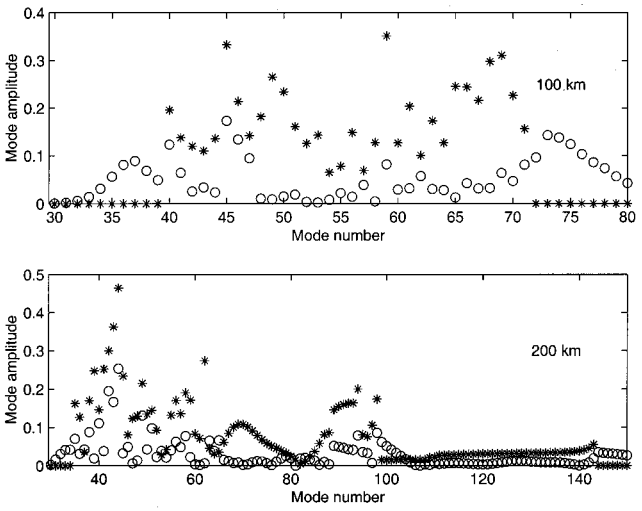

FIG. 8. As in Fig. 7, but for model 2.

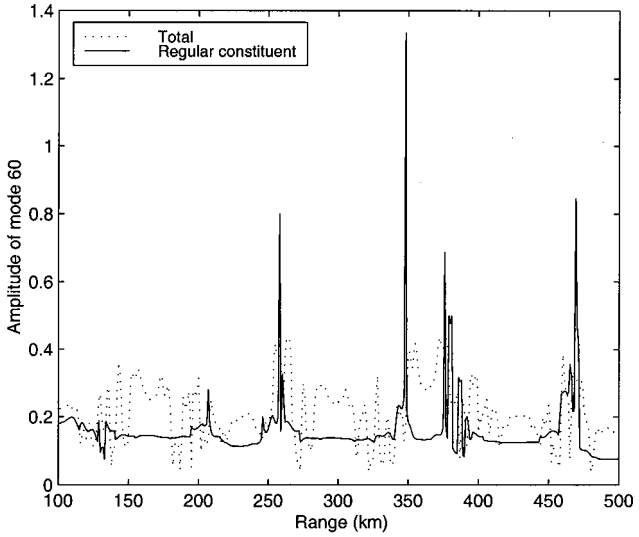

FIG. 9. Absolute value of the total amplitude of the 60th mode, $|c_{60}(x)|$, calculated with the UMPE code and that of its regular constituent, $|c^r_{60}(x)|$, evaluated using the ray approach versus range.

most pronounced for the modes with numbers 44, 79, 88, and for some neighboring modes. Looking at the upper panel of Fig. 4 we can easily understand what is ''wrong'' with these modes. (*i*) The extrema of the curves presented in this plot correspond to modes 44 and 88, which means that the corresponding eigenrays pass through caustics. (*ii*) The starting depths of eigenrays contributing to mode 79 are close to the lower turning point (where the WKB approximation fails) of the 60th mode forming the starting field. In the same manner one can interpret the most pronounced errors shown at the three other plots in Figs. 7 and 8.

D. Regular and chaotic constituents of the mode amplitude

Our numerical calculations for model 1 have shown that the ray trajectories corresponding to the initial field $u(0,z) = \varphi_{60}(z)$ and starting downwards from depths in the range of 162–923 m are regular. The points depicting such rays on the phase portrait constructed using the Poincaré map belong to the lower stable island in the lower panel of Fig. 2. The remaining trajectories should be chaotic. This prediction is consistent with the result presented in Fig. 4: while the solid line representing the action variables of the rays starting upwards becomes more and more complicated with range, the majority of the dashed line representing the rays starting downwards remains smooth. As it has already been mentioned in Sec. III B we expect that

$$c_m(x) = c^r_m(x) + c^c_m(x), \tag{46}$$

where the first (second) term on the right-hand side is formed by contributions from the regular (chaotic) eigenrays. It would be natural to presume that the regular constituent, $c^r_m(x)$, can be predicted with Eq. (33) (by retaining in this sum only the contributions from regular eigenrays) at much larger ranges than the total mode amplitude $c_m(x)$. To support this idea we have calculated the function $c^r_{60}(x)$ at ranges from 100 to 500 km. It is easy to see that the straight line $m_0 = 60$ will cross the above-mentioned stable island in Fig. 2. So, we can expect a significant contribution from regular eigenrays to the 60th mode.

The result is shown in Fig. 9. At the range intervals where the function $|c^r_{60}(x)|$ is almost constant the regular constituent at any particular distance is formed by a contribution from only one eigenray. These ''smooth'' parts of the curve are interspersed with sharp peaks formed by several eigenrays passing near caustics.

Comparing the two curves shown in Fig. 9, we see that even far from caustics the regular costitutent plays an important role in forming the total mode amplitude. Although the remaining (chaotic) constituent is formed by contributions from numerous eigenrays (see Fig. 6), the values of their contributions are, typically, small and, besides, they weaken each other due to interference.

It should be pointed out that we have not offered a rigorous definition of the regular constituent. The latter has been introduced only on the basis of the approximate ray approach. That is why we cannot check the accuracy of our prediction of this constituent as it has been done in the preceding subsection for the total mode amplitudes. Nevertheless, we can demonstrate that the function $c_{60}(x)$ numerically calculated with the UMPE code does have the component close to $c^r_{60}(x)$, given by Eq. (33). It is seen from Fig. 10 where the values of the correlation coefficient

$$K_m = \frac{\left|\int c_m(x)(c^r_{60}(x))^* \, dx\right|}{\sqrt{\left(\int |c_m(x)|^2 \, dx\right)\left(\int |c_{60}(x)|^2 \, dx\right)}}$$

are presented for $m = 60-79$. Here the integration is carried out over the range interval from 100 to 500 km and the asterisk denotes complex conjugation. This figure confirms that, indeed, the component $c^r_{60}(x)$ presents in the range dependence of the 60th mode with a considerably larger weight than in the range dependencies of the amplitudes of neighboring modes.

Note that the above considerations, in some cases, may be too simplistic. They are based on the assumption that every point inside a stable island corresponds to a regular ray

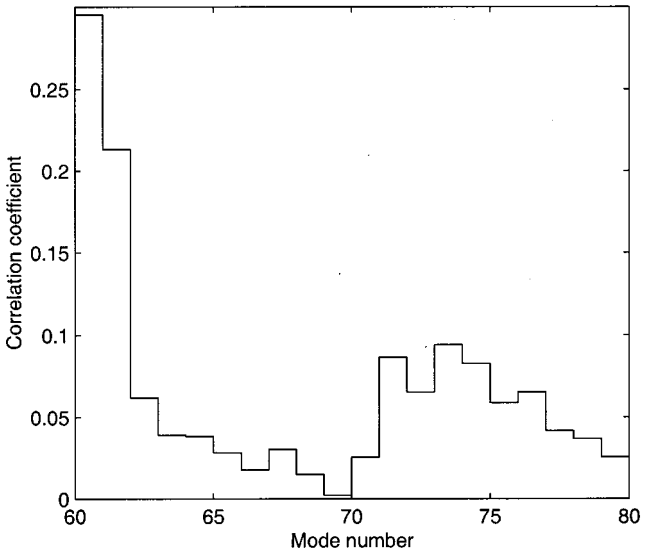

FIG. 10. Correlation between the regular constituent of the 60th mode predicted by the ray approach and total amplitudes of modes 60÷80 computed with the UMPE code.

trajectory. However, in reality it is not so. Inside almost any stable island there are chaotic areas which may be tiny.[1,29] (So the statement made at the very beginning of this subsection may be true of the majority but not of all rays starting from the depths 162–923 m, as well as not all the remaining rays may be chaotic.) The notion of regular constituent has a good sense only when the influence of such areas is insignificant.

E. Incoherent summation of eigenrays with smoothing over the mode number

In this subsection we focus on an approximate evaluation of the mode intensity $|c_m|^2$ by incoherent summation of eigenrays. Proceeding from Eq. (33) and neglecting products of different terms forming c_m we get

$$|c_m|^2=\sum_n \frac{|Q_{m_0}(z_n)|^2}{k|\partial I/\partial z_0|_{z_0=z_{0n}}} \tag{47}$$

with the function $Q_m(z)$ [see Eq. (24)] substituted for $a(z)$. When calculating the field intensity in standard geometrical optics, a similar procedure is often used for two reasons:[12] it has some computational advantages and gives a smooth transmission loss result which is less sensitive to small variations of environmental parameters than that obtained by coherent summation. Probably, the same advantages remain valid for Eq. (47). On the other hand, due to ignoring some terms on the right-hand side, this relation can hardly provide a good approximation to the mode intensity and, in addition, the problem with caustics persists.

Nevertheless, it can be expected that Eq. (47), applied to calculation of the mode intensity *smoothed* over the mode number, will give a much more accurate result because it is clear that smoothing would considerably diminish the neglected terms. Moreover, as we shall see below, Eq. (47) after smoothing gives a simple formula without singularities at caustics.

The coordinates z_{0n}'s in Eqs. (33) and (47) are different roots of the equation $z_0=Z_0(I,x)$, where $Z_0(I,x)$ is a many-valued function representing the starting depth of the ray which at the range x has the action variable equal to I. Once again, we shall label the mode by the value of the corresponding action variable related to the mode number via Eq. (20). Then the summation over the mode number m can be approximately replaced with the integration over the action variable I according to

$$\sum_{m=m_1-\delta m}^{m_1+\delta m} \cdots = k\int_{k(m_1-\delta m)}^{k(m_1+\delta m)} \cdots dI.$$

A sum of several mode intensities defined in Eq. (47) can be approximated as

$$\sum_{m=m_1-\delta m}^{m_1+\delta m} |c_m|^2 \simeq \sum_n |Q_{m_0}(z_{0n})|^2 \Delta z_{0n}, \tag{48}$$

where

$$\Delta z_{0n}=k\int_{k(m_1-\delta m)}^{k(m_1+\delta m)} \left|\frac{\partial z_0}{\partial I}\right| dI$$

is the interval of starting depths surrounding the point z_{0n}. The interval Δz_{0n} corresponds to a bunch of ray trajectories close to that starting from z_n and having the action variables at the range x within the interval $k(m_1-\delta m)<I<k(m_1+\delta m)$. It is assumed that the variation of $Q_m(z)$ at the interval Δz_{0n} is negligible.

On the basis of these relations the following procedure to calculate averaged mode intensities can be proposed. The interval of depths between turning points of the m_0th mode we sample by a large number of points spaced ζ apart ($\zeta \ll z_{\max}-z_{\min}$). Consider a fan of rays starting from these points and sampling the two families of rays defined in Sec. II. There are two rays launching from each sample point z_n with the initial momenta $\pm p_n$, where $p_n=\sqrt{2[E_{m_0}-U_0(z_n)]}$. Taking into account the explicit expression for $Q_m(z)$ we associate the mth mode at the range x with the intensity

$$|\widetilde{c_m}|^2=\frac{\zeta}{D_{m_0}}\sum_{n,\beta}\frac{\Delta_{mn}^{\beta}}{\sqrt{2[E_{m_0}-U_0(z_n)]}}, \tag{49}$$

where

$$\Delta_{mn}^{\beta}=\begin{cases}1, & \text{if } (m-\frac{1}{2})/k<I(x,\beta p_n,z_n)<(m+\frac{1}{2})/k\\ 0, & \text{otherwise,}\end{cases}$$

and the summation runs over the indices n and $\beta=\pm 1$ representing numbers of sample points and signs of initial momenta, respectively. To avoid a singularity on the right-hand side of Eq. (49), the neighborhood of the turning point of the m_0th mode should be excluded from the sampled interval of depths, as it has been done in Sec. III C.

It is clear that $|\widetilde{c_m}|^2$, generally, gives a poor approximation to $|c_m|^2$. However, according to Eq. (48) we can hope that, after averaging over a large enough number of modes,

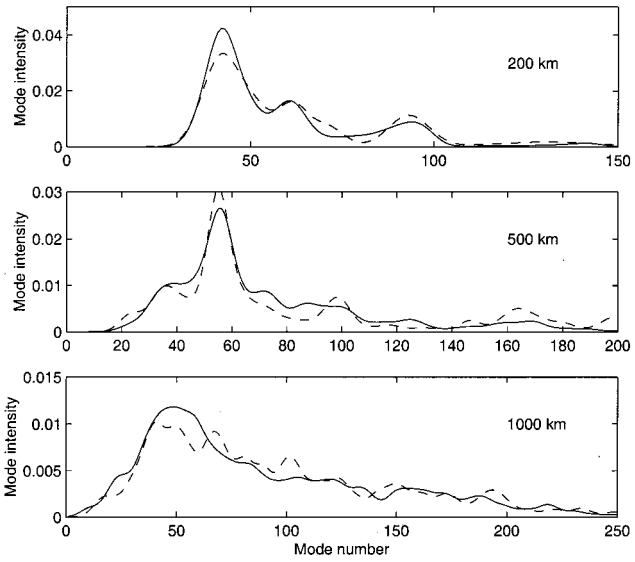

FIG. 11. Mode intensity smoothed over mode number with the smoothing scale $\Delta m = 5$ at 200 km (upper panel), 500 km (middle panel), and 1000 km (lower panel) ranges. Solid line: Incoherent summation of eigenrays. Dashed line: Result of computations carried out with the UMPE code.

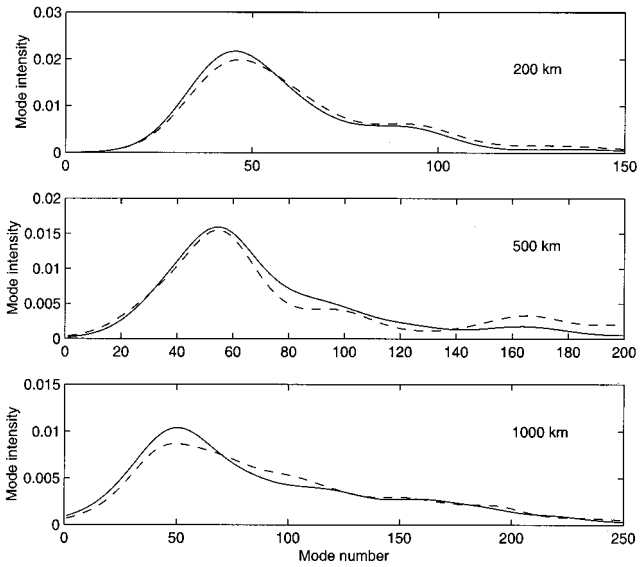

FIG. 12. As in Fig. 11, but for the smoothing scale $\Delta m = 15$.

Eq. (49) will yield a much better prediction of the smoothed mode intensity. The smoothing can be carried out using the relation

$$\overline{|c_m|^2} = T^{-1} \sum_{m'} e^{-(m-m')^2/\Delta m^2} |\widetilde{c_{m'}}|^2,$$

$$T = \sum_{m'} e^{-(m-m')^2/\Delta m^2}, \tag{50}$$

where the sum goes over all excited modes, and $\Delta m \gg 1$ is a smoothing scale.

Since this procedure practically consists only in evaluation of fan of ray trajectories, it can be very easily implemented numerically. Here we face neither the problem with caustics nor the problem of looking for roots of Eq. (45).

On the other hand, the above method is somewhat heuristic and studying its applicability requires further investigations. In the present paper we only present numerical evidence that for our model the predictions made on the basis of Eqs. (49) and (50) remain valid at unexpectedly long ranges.

The mode intensities smoothed with two different smoothing scales Δm at three different ranges in model 2 are shown in Figs. 11 and 12. The results of ray calculations (solid curves) are compared to the results obtained with the UMPE code (dashed curves). The latter have been computed by replacing $|c_{m'}|^2$'s in Eq. (50) with the exact mode intensities found from a numerical solution of Eq. (1). These two results remain surprisingly close, even at 500- and 1000-km ranges where each mode is formed by a very large number of eigenrays (see Fig. 6) and caustics are so numerous that Eq. (33), which has been our starting point when deriving Eqs. (48) and (49), cannot be used. Note that the results presented in Figs. 11 and 12 have been computed using only 3000 sample rays. This is much less than the number of eigenrays contributing to an individual mode at 1000-km range, which can be estimated by extrapolating the corresponding straight line in Fig. 6.

IV. CONCLUSION

The ray formalism, discussed in Sec. I clarifying the ray-mode relations in a range-dependent wave guide, at the same time provides a convenient tool for establishing the bridge between ray chaos and wave chaos. The parabolic equation approximation has been used here only for computational reasons. An analogous ray formalism for the modal structure analysis can be readily obtained proceeding from the Helmholtz equation.

The fact that the mode amplitude is expressed through parameters of ray trajectories allows one to make some conclusions concerning the irregular modal structure on the basis of known properties of the ray chaos. To illustrate this statement we have turned our attention to wave guides with periodic range dependence because the properties of ray chaos in such wave guides are known comparatively well. The ray-based approach has permitted us to elucidate how the ray-medium resonance, playing such an important role in the emergence of the ray chaos, reveals itself in modal structure variations. It has been shown that there is an analog to this phenomenon for modes which we call the mode-medium resonance.

''Exponential proliferation'' of standard eigenrays[7] also has its counterpart in terms of normal modes. It has been shown numerically that the number of eigenrays contributing to the given mode grows exponentially with range.

Another characteristic feature of the ray chaos is the coexistence of regular and chaotic rays. In terms of normal modes this fact means that the mode amplitude consists of two constituents: a regular one formed by contributions from regular rays, and an irregular one formed by chaotic rays.

It has been demonstrated numerically that caustics which are a real scourge for the standard geometrical optics, play a similar negative role in the ray approach under con-

sideration in this paper. Due to fast growing of the number of caustics with range, the validity region of our approach is restricted to rather short ranges.

On the other hand, the numerical calculation has demonstrated that ray-based predictions of mode intensities smoothed over mode number remain valid at such long ranges where this method can no longer be used for evaluation of amplitudes of individual modes. This fact looks very encouraging. It gives us hope that in wave guides with more realistic range dependences some smoothed characteristics of the modal structure may also be predicted at long ranges in the scope of a simple ray approach.

ACKNOWLEDGMENTS

This work was done at the Courant Institute of Mathematical Sciences. I thank Professor G. Zaslavsky for the benefit of our discussions on problems of quantum and wave chaos. I am grateful to Professor F. D. Tappert for his offer to use the UMPE code and to Professor K. B. Smith for the indications which helped to modify the code. The work was supported by the U. S. Navy Grant No. N00014-97-1-0426.

[1] S. S. Abdullaev and G. M. Zaslavskii, ''Classical nonlinear dynamics and chaos of rays in wave propagation problems in inhomogeneous media,'' Usp. Fiz. Nauk **161**(8), 1–43 (1991).
[2] S. S. Abdullaev, *Chaos and Dynamics of Rays in Waveguide Media*, edited by G. Zaslavsky (Gordon and Breach Science, New York, 1993).
[3] D. R. Palmer, M. G. Brown, F. D. Tappert, and H. F. Bezdek, ''Classical chaos in nonseparable wave propagation problems,'' Geophys. Res. Lett. **15**, 569–572 (1988).
[4] M. G. Brown, F. D. Tappert, and G. Goni, ''An investigation of sound ray dynamics in the ocean volume using an area preserving mapping,'' Wave Motion **14**, 93–99 (1991).
[5] K. B. Smith, M. G. Brown, and F. D. Tappert, ''Ray chaos in underwater acoustics,'' J. Acoust. Soc. Am. **91**, 1939–1949 (1992).
[6] K. B. Smith, M. G. Brown, and F. D. Tappert, ''Acoustic ray chaos induced by mesoscale ocean structure,'' J. Acoust. Soc. Am. **91**, 1950–1959 (1992).
[7] F. D. Tappert and X. Tang, ''Ray chaos and eigenrays,'' J. Acoust. Soc. Am. **99**, 185–195 (1996).
[8] J. Simmen, S. M. Flatte, and G.-Y. Wang, ''Wavefront folding, chaos, and diffraction for sound propagation through ocean internal waves,'' J. Acoust. Soc. Am. **102**, 239–255 (1997).
[9] W. Munk and C. Wunsch, ''Ocean acoustic tomography: A scheme for large scale monitoring,'' Deep-Sea Res., Part A **26**, 123–161 (1979).
[10] *Quantum Chaos: Between Order and Disorder: A Selection of Papers*, edited by G. Casati and B. V. Chirikov (Cambridge U. P., New York, 1995).
[11] F. D. Tappert, ''The parabolic approximation method,'' in *Wave Propagation and Underwater Acoustics*, edited by J. B. Keller and J. S. Papadakis (Springer-Verlag, Berlin, 1977), pp. 224–284.
[12] F. B. Jensen, W. A. Kuperman, M. B. Porter, and H. Schmidt, *Computational Ocean Acoustics* (AIP, Woodbury, NY, 1994).
[13] K. B. Smith and F. D. Tappert, UMPE: *The University of Miami parabolic equation model, Version 1.1*, Marine Physical Laboratory Technical Memorandum 432 (Scripps Inst. of Oceanography, San Diego, 1994).
[14] G. P. Berman and G. M. Zaslavsky, ''Condition of stochasicity in quantum nonlinear systems,'' Physica A **97**, 367–382 (1979).
[15] G. M. Zaslavsky, *Chaos in Dynamical Systems* (Harwood Academic, New York, 1985).
[16] A. L. Virovlyansky and G. M. Zaslavsky, ''Wave chaos in terms of normal modes,'' Phys. Rev. E **59**, 1656–1668 (1999).
[17] A. L. Virovlyanskii and O. V. Lebedev, ''Modal structure of the wavefield in a range-dependent Pekeris waveguide,'' Acoust. Phys. **44**(4), 384–388 (1998).
[18] A. L. Virovlyansky, V. V. Kurin, N. V. Pronchatov-Rubtsov, and S. I. Simdyankin, ''Fresnel zones for modes,'' J. Acoust. Soc. Am. **101**, 163–173 (1997).
[19] A. L. Virovlyanskii and A. G. Kosterin, ''Method of smooth perturbations for the description of the fields in multimode waveguides,'' Sov. Phys. Acoust. **33**(4), 351–354 (1987).
[20] A. L. Virovlyansky, A. G. Kosterin, and A. N. Malakhov, ''Fresnel zones for modes and analysis of field fluctuations in random multimode waveguides,'' Waves Random Media **1**, 409–418 (1991).
[21] B. V. Chirikov, ''A universal instability of many-dimensional oscillator systems,'' Phys. Rep. **52**(5), 263–379 (1979).
[22] G. M. Zaslavsky and B. V. Chirikov, ''Stochastic instability of non-linear oscillations,'' Sov. Phys. Usp. **14**(5), 549–672 (1972).
[23] A. G. Lichtenberg and M. A. Lieberman, *Regular and Stochastic Motion* (Springer Verlag, New York, 1983).
[24] L. D. Landau and E. M. Lifshits, *Quantum Mechanics* (Nauka, Moscow, 1974).
[25] L. D. Landau and E. M. Lifshits, *Mechanics* (Nauka, Moscow, 1973).
[26] M. C. Gutzwiller, ''Phase-integral approximation in momentum space and the bound states of an atom,'' J. Math. Phys. **8**, 1979 (1967).
[27] V. P. Maslov and M. V. Fedoriuk, *Semi-classical Approximation in Quantum Mechanics* (Reidel, Boston, 1981).
[28] L. M. Brekhovskikh and Yu. Lysanov, *Fundamentals of Ocean Acoustics* (Springer-Verlag, Berlin, 1991).
[29] G. M. Zaslavsky, *Physics of Chaos in Hamiltonian Systems* (Imperial College, London, 1988).
[30] L. M. Brekhovskikh, *Waves in Layered Media* (Academic, New York, 1980).

Acoustically derived ice-fracture velocity in central Arctic pack ice

Catherine Stamoulis[a] and Ira Dyer
Massachusetts Institute of Technology, Department of Ocean Engineering, Cambridge, Massachusetts 02139

(Received 16 September 1998; accepted for publication 20 March 2000)

Sounds radiated by fractures in Arctic ice (called acoustic events) are used to estimate fracture velocity. Both speed and orientation are obtained by measuring Doppler shifts induced by source motion. Data from the SIMI experiment of 1994 in the central Arctic are used in the frequency window 10 to 350 Hz. The estimation procedure assumes that each fracture propagates unilaterally, i.e., unidirectionally. Results for a population of 186 events show fracture propagation speed to be mostly subsonic, in the range 100 to 1100 m/s, significantly lower than the Rayleigh wave speed (1700 m/s for sea ice) assumed in previous studies. The wide range of speeds observed indicates either the presence of distinct multiple fractures in each event, or of a single mechanism at different stages in its propagation. © *2000 Acoustical Society of America.* [S0001-4966(00)00707-4]

PACS numbers: 43.30.Ma, 43.30.Nb [DLB]

INTRODUCTION

Ice activity is the predominant contributor to underwater ambient noise in the Arctic ocean. Fracture propagation in Arctic sea ice remains only partially understood, and is difficult to observe through direct *in situ* measurements. Characteristics of the ambient noise and its generating mechanisms can, however, be studied through the analysis of individual transients in the noise time series, termed events. The focus of this paper is the estimation of fracture speed and orientation (strike angle) which, together with fault dimensions, characterize crack or fault propagation. Distinct fracture mechanisms, identified from the analysis of the event horizontal radiation patterns are discussed in detail in Ref. 1.

The data analyzed were collected during the SIMI experiment of 1994 in the central Arctic. A horizontal array of 24 hydrophones, suspended 60 m below the ice, was used. The maximum aperture of the array was approximately 700 m. A 1-h data segment from day J98 (Julian day 98), between local times 2300:03 and 2359:54 was analyzed, in a frequency window from 10 to 350 Hz.

Events were detected through the use of a square-law detector.[2] For a detection to be accepted, the event signal was constrained to be evident in at least 5 of the 24 channels. A total of 186 events in the 1-h segment, of sufficient clarity for velocity analysis, was detected in the ambient noise data and is reported here. The location of each event was determined by an error-minimization ray-tracing procedure. The analyzed events were located in an area approximately 1.2 km^2, shown in Fig. 1.

Events of different durations and signature types were detected. Conclusive results have not been published on the connection between signature types and ice mechanisms,[3,2] but here we examine fracture propagation parameters as a function of event signature. Two categories are distinguished, namely single- and multiple-signal component events, termed simple and compound, respectively.[2] Four basic signatures are identified, shown in Fig. 2, and both simple events and individual components of compound events are classified accordingly. We use the same signature nomenclature as Chen.[3] Type I is called a pop or burst, types II and III are damped sinusoids, the former a complicated pop usually consisting of two type I pops, and the latter a longer sinusoid. The fourth signature type is a series of pulses, usually of random separation. Type IV events are different from compound events in that the separation between pulses is about an order of magnitude smaller than the separation between signal components in compound events. The signature statistics are summarized in Tables I and II. The predominant types are III and IV; see Tables I and II.

Several researchers have studied ice fracture as a source which radiates acoustic energy in the water. In regard to fracture-speed estimation and identification of event-generating mechanisms, the most pertinent work is that of Farmer and Xie, who investigated crack propagation in landfast and shorefast ice.[4,5] From the frequency components of the detected events, they deduced that more than one scale is associated with the fracture process and that the event source moves with the developing crack. They also suggested that although the horizontal and vertical scales are the two primary scales associated with a crack, finer scale features may also contribute to noise signals.

I. SOURCE SPEED AND ORIENTATION PHYSICS

Faulting (series of fractures) is one of the dominant ice motion processes in the Arctic. Parameters that characterize fault propagation in the ice include source speed and orientation (strike angle). Source motion affects the radiated sound field. Thus, prior to the estimation of the event radiation characteristics, source speed and orientation must be determined in order to appropriately correct the recorded peak-event pressures for Doppler effects. The estimation approach presented here assumes that fracture propagation is unilateral.

[a]Electronic mail: caterina@mit.edu

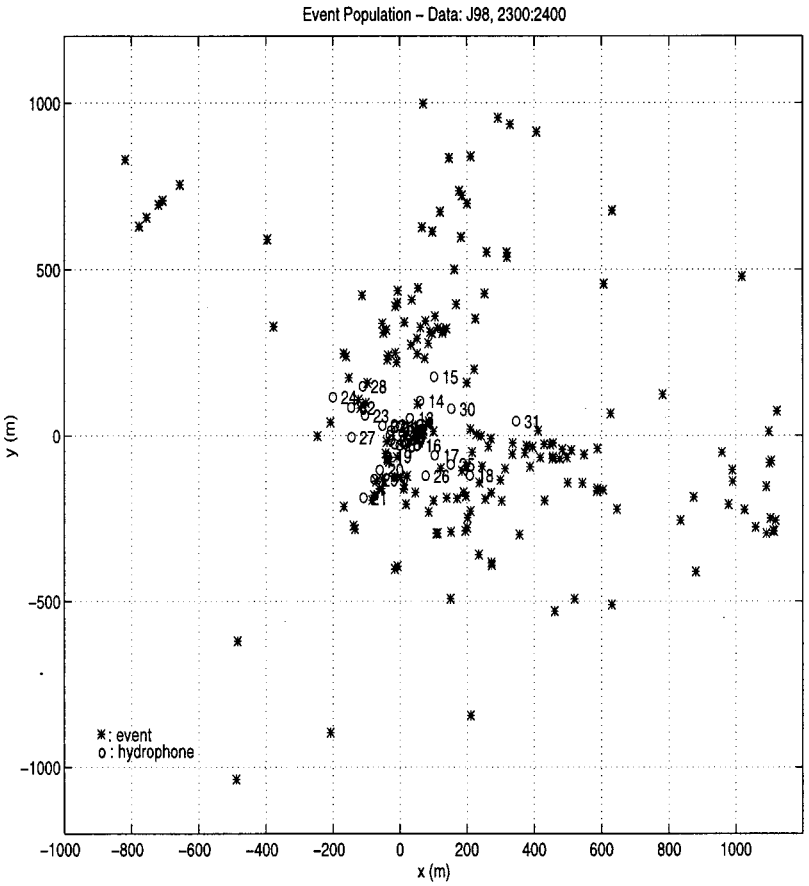

FIG. 1. Event population of 186 detected in a 1-h data segment. The locations of the hydrophones are shown in the plot.

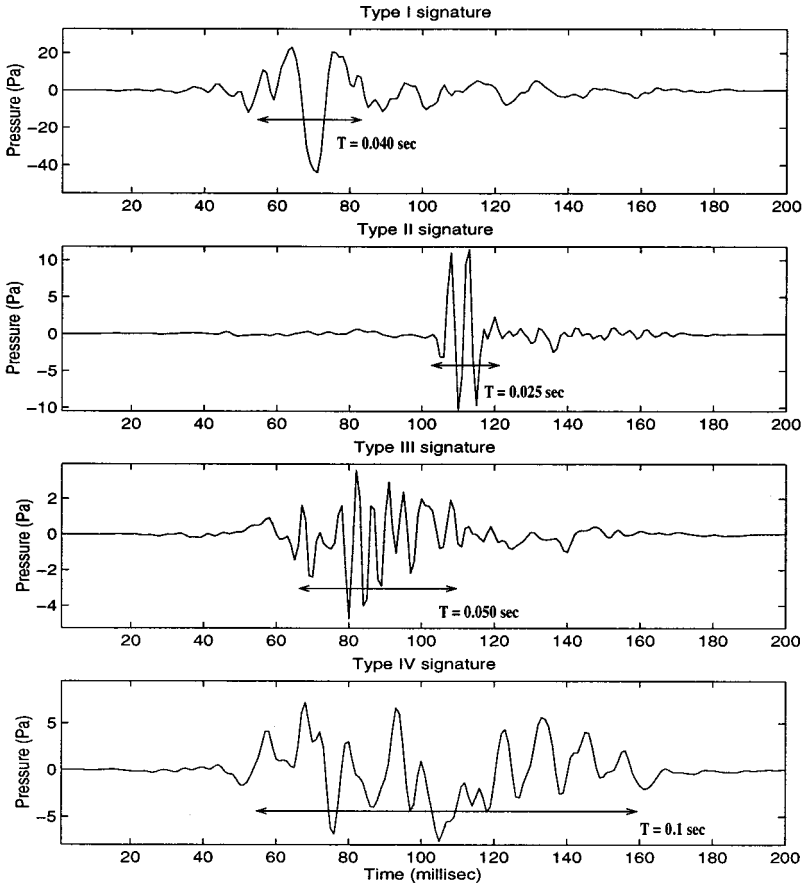

FIG. 2. Event signature types.

TABLE I. Distribution of event population with signature type.

Signature type	Event population No. of events	%
Type I	23	12
Type II	25	13
Type III	63	34
Type IV	75	41

Consider a fracture, propagating at a vertical angle θ_s in the ice and cutting through the entire ice sheet, as shown in Fig. 3, where ϕ_i is the horizontal angle of receiver i, measured from the x axis, ϕ_s is the horizontal angle between the propagation direction of the source and the x-axis, $\mathbf{V}$ is the velocity of the source and $\mathbf{V}\cos(\theta_s)$ is the component of velocity in the $x-y$ plane. The ice thickness is on average 3 m and thus much smaller than the wavelength of the event sources analyzed here. We assume that the fracture propagates in the $x-y$ plane, and vertically cuts through the entire ice thickness. The dip angle θ_s is small and thus neglected.[2] This assumption is supported by observations of pack ice fractures. Consequently, the unknown variables are the propagation speed $|\mathbf{V}|$ and the source orientation ϕ_s. We first estimate the orientation angle, then the source speed, and finally the intrinsic source frequency, using Eq. (1) of Sec. III.

To estimate the parameters of interest, analysis of acoustic events in the frequency domain is convenient. In particular, the peak-event frequency, bandwidth, and Doppler shift, estimated from the event spectrum, are needed in the calculation of source speed, direction of propagation, and intrinsic source frequency. The analysis is performed channel by channel, for frequencies between 10 and 350 Hz. (The low cutoff frequency was established based on the spectrum of cable strum,[2] which often dominates the spectra for frequencies <10 Hz. The upper cutoff frequency is set by limits imposed by the data acquisition system).

II. ESTIMATION OF EVENT SPECTRUM

Standard fast Fourier transforms (FFT) of the event temporal signals are used to obtain their spectra. Corrections are made to account for transmission loss,[2] sensitivity of the hydrophones (155 dB re 1 V/1 μPa) and for the input gain setting of the data acquisition system (20 dB). The bandwidth

TABLE II. Statistics of event signatures.

Signature type	Simple events Duration (s)	No. of events	% of category
Type I	0.015–0.040	14	7
Type II	0.020–0.045	15	8
Type III	0.050–0.065	47	25
Type IV	0.08–0.12	40	22
Comp. type I	0.065–0.12	9	5
Comp. type II	0.060–0.12	10	5
Comp. type III	0.080–0.12	16	9
Comp. type IV	0.12–0.2	35	19

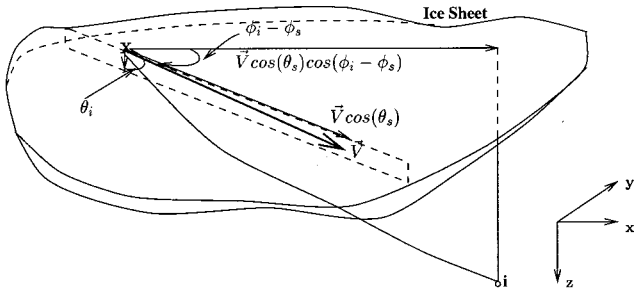

FIG. 3. Propagating fracture in the ice.

of an event is defined as the frequency range within the half-power (or -3 dB) points, at which the pressure is reduced from its peak value by $1/\sqrt{2}$.

A second parameter estimated from an event spectrum is the frequency range for which the signal-to-noise ratio (SNR) is above a particular threshold (we use 5 dB in this study). The latter is necessary to determine which portion(s) of the event spectrum will be used in a cross-correlation procedure for determination of the Doppler shift. This is very important, particularly for a compound event, the spectrum of which is characterized by multiple peaks, separated by segments of the spectrum in which SNR may be less than 5 dB (typically 1–3 dB). SNR can be estimated by comparing the event spectrum and the ambient noise spectrum measured just prior to the event.

The spectrum of a typical narrow-band event (bandwidth 1 octave or less), is shown in Fig. 4, in which the event and noise spectra are compared. There is one dominant energy band in the event. In contrast, the presence of several distinct spectral peaks of comparable amplitude, as shown in Fig. 5, suggests that there is more than one dominant energy band in the event and, consequently, more than one scale associated with the generating process in the ice. As previously mentioned, such spectra are characteristic of compound events. In this particular channel, the low-frequency band of the event, 12 to 32 Hz, is about 1 octave wide. The high-frequency band, 90 to 350 Hz, and on average between 100 and 300 Hz for all channels detecting this event, is about 1 $\frac{1}{2}$ octaves wide. In general, we observed that these well-separated event frequency bands are each of the order of 1 octave wide.

For simple events, peak frequency is directly measured from their spectra in each channel, and then averaged (after Doppler corrections[2]) over all channels. For compound events, we use the frequency of the highest spectral energy band (energy is proportional to the product of the squared peak pressure and bandwidth). The statistics of peak-event frequency, in the low-(below 100 Hz) and the mid- (100 to 350 Hz) frequency ranges, are summarized in Table III. We observed 77 low-frequency and 109 mid-frequency events. Although type I and II events, both simple and compound, are almost equally distributed in the two ranges, simple and compound type III and IV events occur predominantly in the mid-frequency range. For compound events, signature type and peak frequency appear uncorrelated.

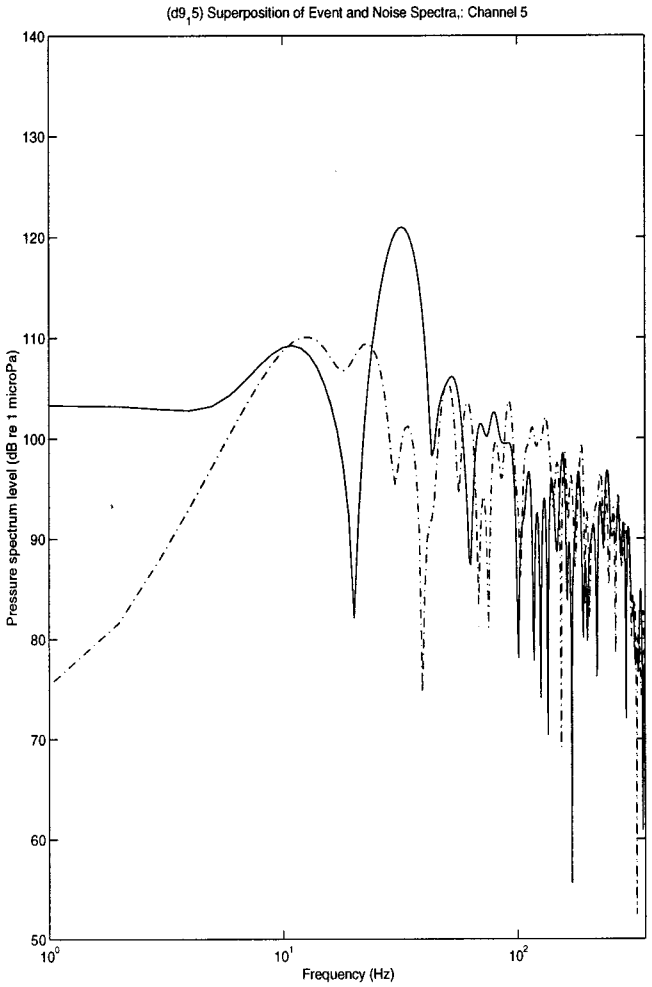

FIG. 4. Spectrum of narrow-band event. The peak frequency of the event is 38 Hz and its bandwidth is approximately 10 Hz. The maximum SNR is about 17 dB.

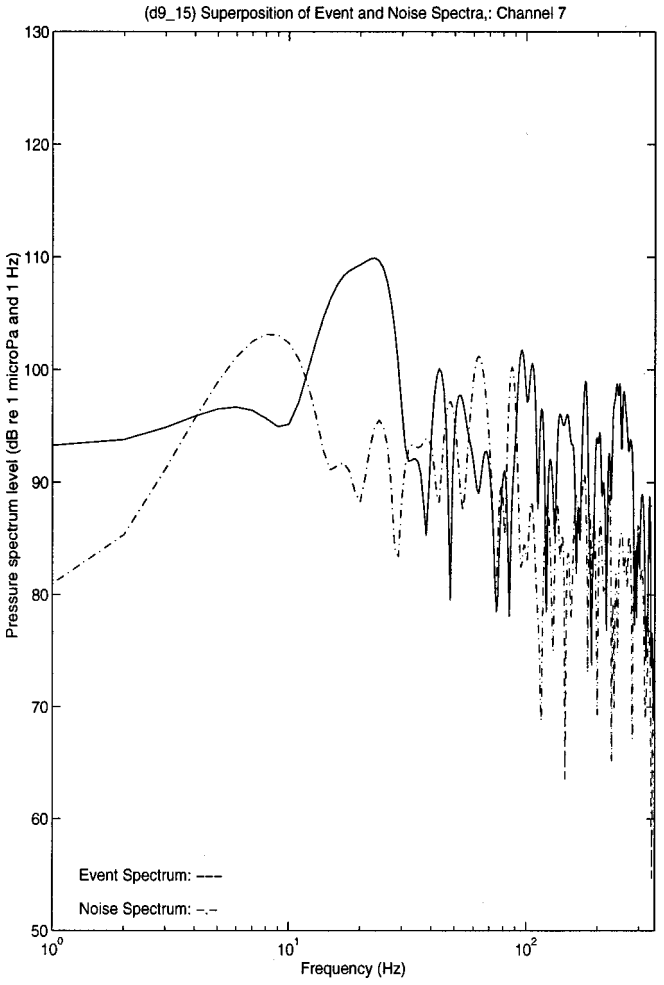

FIG. 5. Compound event spectrum. In the frequency ranges 12–32 Hz and 90–350 Hz, SNR is >5 dB.

III. ESTIMATION OF DOPPLER SHIFT

Ice fractures are moving sound sources. Thus, the peak frequencies of the events observed in each channel are not equal to the intrinsic source frequency; they are shifted according to the speed and orientation of the source relative to the hydrophone receiver. Consider two coordinate systems, one fixed and the other moving at constant speed relative to the first. Transformation from the first to the second system is Galilean. Doppler shifts result from this change in coordinates, since frequency is not Galilean invariant.[6] The received frequency ω_i is related to the intrinsic frequency of the source ω_0 by

$$\omega_i = \omega_0 + \mathbf{V}\cdot\hat{R}\frac{\omega_i}{c} \Leftrightarrow \omega_i = \frac{\omega_0 c}{c - \mathbf{V}\cdot\hat{R}} \quad i = 1,2,...,24, \qquad (1)$$

where $\mathbf{V}$ is the velocity of the moving source with respect to the stationary receiver, c is the sound speed, and $\hat{R}_i = \mathbf{R}/|\mathbf{R}|$ is the unit vector in the direction of receiver i. $\mathbf{R}$ is the vector from the point at which the sound ray was emitted into the water at the source location, to the reception point $(x_i, y_i, z = 60)$ and $|\mathbf{R}|$ is the distance between source and receiver. The difference $\Delta\omega_i = \omega_i - \omega_0$ is the Doppler shift. The source frequency ω_0 is not known and thus the true Doppler shift $\Delta\omega_i$ can only be estimated. The peak-event frequency at each hydrophone is measured and so is the relative Doppler shift $\Delta\omega_{i,j} = \omega_i - \omega_j$, between any two received peak frequencies i and j. It is reflected in the event spectrum at each hydrophone and can be determined through spectrum cross-correlation. The frequency resolution is 1 Hz, and thus this is also the minimum measurable Doppler shift. The Doppler effect is shown in Fig. 6, in which the event spectra measured in two channels are superimposed. The difference in pressure levels (about 12 dB at their respective peaks) is due to different Doppler shifts and the horizontal directivity of the source. Although a Doppler shift can be roughly estimated by comparing the peak-event frequencies, cross-

TABLE III. Statistics of low- and midfrequency events.

Signature type	No. of events ($f_{peak} < 100$ Hz)	No. of events ($f_{peak} > 100$ Hz)
I	8	6
II	9	6
III	12	35
IV	17	23
Compound I	5	4
Compound II	7	3
Compound III	6	10
Compound IV	13	22

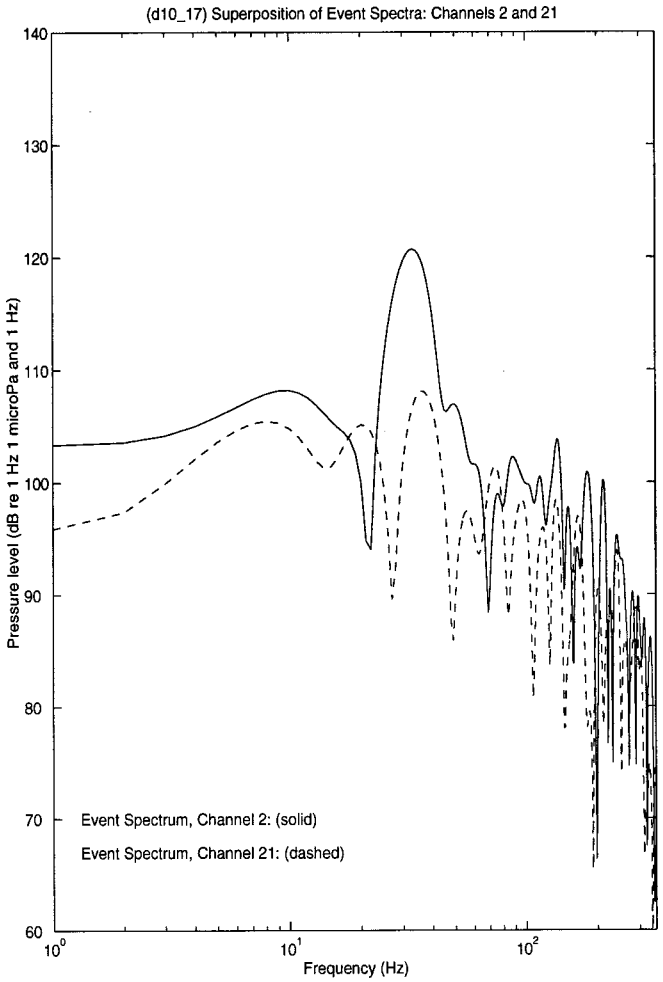

FIG. 6. Superimposed event spectra at two channels. Their refractive distance from the event is 530 and 672 m, respectively. The distance between hydrophones is 244 m.

correlation of the spectra is a more appropriate procedure, since it yields an estimate of the shift of the broader event spectrum instead of the shift in peak frequency only. The frequency shift at the absolute maximum cross-correlation coefficient is the Doppler shift sought. Figure 7 shows an example of the error in Doppler shift resulting from the use of peak-event frequencies in the estimation, relative to the Doppler shift obtained by spectrum cross-correlation.

In the above plot, channel 1 has been used as the reference channel, i.e., its spectrum has been cross-correlated with the event spectrum in all other hydrophones and its peak frequency has been compared to the corresponding peak frequencies, in the two Doppler shift estimation procedures, respectively. The relative error is between 0 and 3 Hz for hydrophones which are close to hydrophone 1 and between 4 and 18 Hz for distant hydrophones.

Note that we use only the event's more energetic frequency band, because cross-correlation outside this band does not provide as much useful information in Doppler shift estimation, and its inclusion would reduce the spectral cross-correlation coefficient and consequently its accuracy.

For compound events, two or more values of Doppler shift are obtained, corresponding to the two or more frequency bands in the event spectrum, in which the SNR is $\geqslant 5$ dB. The Doppler shift used in the estimation of source speed is that for the band of higher spectral energy. Doppler shifts for the analyzed events range between 1 and 90 Hz, with low Doppler shift values observed for both low- and mid-frequency events.

IV. ESTIMATION OF PROPAGATION DIRECTION

Equation (1) can be rewritten as

$$\omega_i = \frac{\omega_0 c}{c - |\mathbf{V}| \cos(\phi_i - \phi_s) \cos(\theta_i)}. \tag{2}$$

$\mathbf{V} \cdot \hat{R}_i$ in Eq. (1) is the magnitude of the component of velocity $\mathbf{V}$ in the direction $\hat{R}_i$ of receiver i and θ_i is the launch angle. Assuming propagation of the source in the horizontal plane of ice, this velocity component is $\mathbf{V}\cos(\phi_i - \phi_s)$ and its projection in the slant direction of the receiver is $\mathbf{V}\cos(\phi_i$

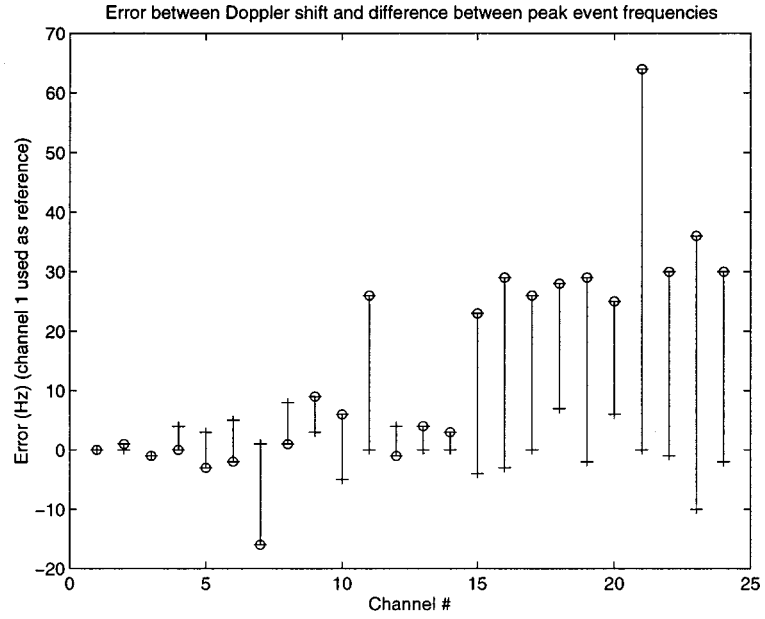

FIG. 7. Relative error in Doppler shift, computed as the difference between the estimates obtained through spectrum cross-correlation and comparison of peak-event frequencies. Symbols used: (+) for Doppler shift values when spectrum cross-correlation is used; (○) for corresponding values when the estimated peak-event frequencies are used.

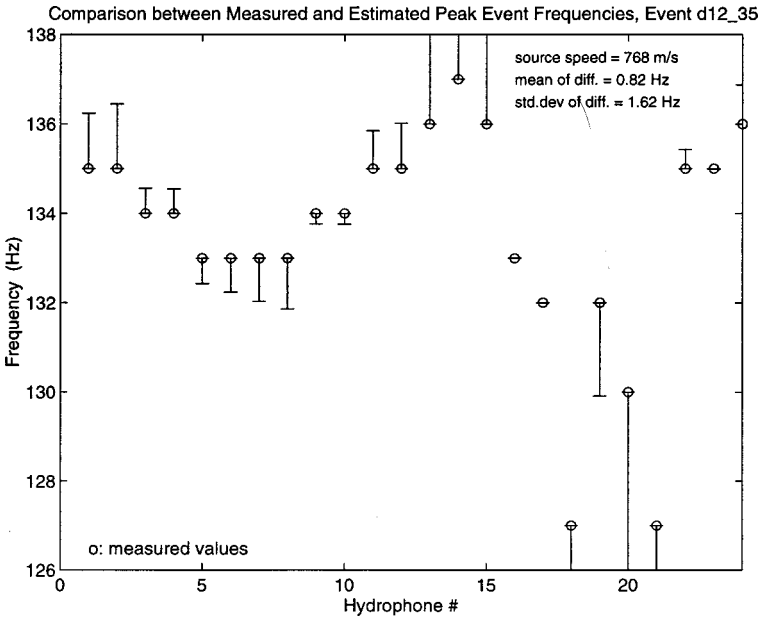

FIG. 8. Comparison between estimated and measured peak-event frequencies. Error bar indicates their difference for each hydrophone. The mean absolute difference of the two sets of values is 0.82 Hz and the standard deviation is 1.62 Hz.

$-\phi_s)\cos\phi_i$. The three unknowns are the source orientation ϕ_s, speed $|\mathbf{V}|$, and frequency ω_0. Given the observed frequencies and horizontal angles for three hydrophones, source orientation ϕ_s, speed V, and intrinsic frequency ω_0 can be calculated uniquely. Since it is not known *a priori* which combination of hydrophones will give the most accurate estimate of the parameters sought, all combinations of hydrophones (i,j,k), $i,j,k,=1,...,24$ are used in the procedure. Least-squares fits are then used to obtain the best estimates, first of the direction of propagation, then of source speed, and finally of the intrinsic source frequency. For hydrophones *i, j, k*, the source orientation is given by

$$\phi_s=\tan^{-1}\left[\frac{\omega_j\Delta\omega_{ki}\cos\phi_j\cos\theta_j-\omega_i\Delta\omega_{kj}\cos\phi_i\cos\theta_i-\omega_k\Delta\omega_{ji}\cos\phi_k\cos\theta_k}{-\omega_j\Delta\omega_{ki}\sin\phi_j\cos\theta_j+\omega_i\Delta\omega_{kj}\sin\phi_i\cos\theta_i+\omega_k\Delta\omega_{ji}\sin\phi_k\cos\theta_k}\right], \tag{3}$$

in which the Doppler shift $\Delta\omega_{ij}$, estimated from spectral cross-correlation, is used. Equation (3) is an exact expression for ϕ_s. Theoretically, all *i, j, k* combinations should yield the same value; in reality, this is not the case.[2]

V. ESTIMATION OF FRACTURE PROPAGATION SPEED

Once the source orientation ϕ_s has been estimated from data recorded in any two channels, the propagation speed V can be obtained with the use of

$$|\mathbf{V}|=\frac{(\omega_j-\omega_i)c}{\omega_j\cos(\phi_j-\phi_s)\cos\theta_j-\omega_i\cos(\phi_i-\phi_s)\cos\theta_i}. \tag{4}$$

All combinations *i, j* are used in the estimation and a least-squares fit then results in the speed estimate. Once both $|\mathbf{V}|$ and ϕ_s are known, the intrinsic source frequency ω_0 is obtained from Eq. (1).

To assess the error in Doppler shift and consequently speed, orientation, and intrinsic source frequency estimates, the expected peak-event frequencies are calculated, using the parameter values in Eq. (1), and are compared to the measured values. The difference between estimates and measurements is shown in Fig. 8, for a single event.

For the analyzed population of 186 events, the mean error (averaged over the number of hydrophones) between estimated and measured peak frequencies is in the range 0.15 to 3.7 Hz.

In the source-speed estimation procedure, two upper bounds are used, v_R and α, the latter being the compressional wave speed in sea ice. Use of these bounds prevents divergence of the speed estimates. It is physically possible for tensile and shear fractures to propagate at α, depending on their fracture length (above or below a critical length).[7,11]

The distribution of source speed for 186 events, having reasonable Doppler shift accuracy, is shown in Fig. 9, and the statistics of source speed for different types of signatures are summarized in Table IV. A preponderance (69% or 135 of the total number of events) has speeds in the range 100–1100 m/s. Only 28 events have estimated speeds below this range and 23 above. The upper bound of this range (1100 m/s) is $0.65v_R$, where v_R is the Rayleigh wave speed. This result is not surprising; even in the case of earthquakes, typical propagation speeds are approximately 0.6 to 0.8 of either

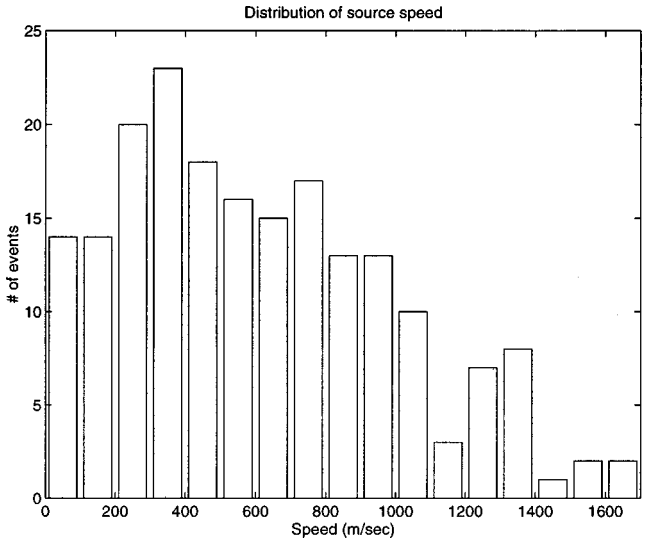

FIG. 9. Distribution of source speed, for all signature types.

β or v_R, where β is the shear wave speed. Values as low as 0.2β have also been recorded during earthquake precursory fault motion.[8]

We examine the distribution of source speed with peak frequency and signature type in detail, beginning with Fig. 10. Previously, researchers have assumed that source speed and peak frequency are proportional.[9] However, it was shown recently[2] that source speed is proportional to the corner frequency of the displacement spectrum of the event signal (i.e., the spectrum of the second integral of pressure) not the peak-event frequency. Corner frequency is defined as the frequency at the intersection of the low- and high-frequency trends in the spectrum. The latter is commonly used to estimate fault dimensions, the estimation of which for Arctic ice faults is discussed in detail in Refs. 2 and 10. Figure 11 shows the lack of proportionality with peak-event frequency, although on average there is some agreement of the data with a best-fit regression line (not shown here). However, the corner frequency regression line has a much smaller standard error.[2]

Type I and III events are associated with the fastest speeds, and type IV with the slowest. For type I and III events only, we obtained two sets of source-speed estimates, under the theoretical upper-bound assumptions. Under the v_R speed-bound assumption, for type I events, source speed is in the range 500–1500 m/s, and for type III events, it is in the range 400–1440 m/s, and is uncorrelated with peak frequency. Under the α speed-bound assumption for both type I and III, the second set of estimates, not shown here, is in the range 1726–3182 m/s. It is shown in Ref. 1 that shear fracture is accompanied by the formation of tensile cracks. Thus, both shear and normal stresses exist at the crack-tip field. The shear components are limited by the v_R bound (due to in plane shear) and the normal components are limited by the α bound. Thus, the two fracture-speed estimates under the two bounds reflect the occurrence of such fractures. For type II events, there is a wide range of speed estimates; the highest event density occurs between 300 and 400 m/s. This event sample is, however, too small to reach firm conclusions on the connection between speed and event type II. Finally, for type IV events, there are no estimated speeds above 1000 m/s. The highest event concentration is in the range 8–400 m/s.

TABLE IV. Statistics of estimated source speed as a function of signature type.

Signature type	Mean speed (m/s)	σ (m/s)
I	1030	309
II	620	366
III	922	297
IV	350	239
Comp. I	858	235
Comp. II	357	158
Comp. III	465	432
Comp. IV	373	268

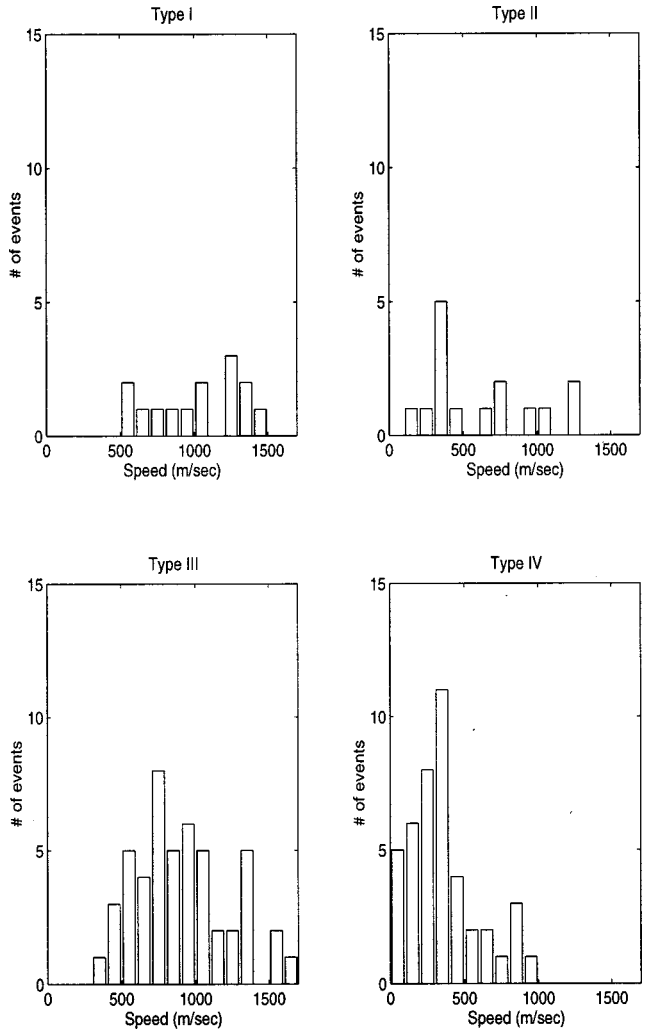

FIG. 10. Distribution of source speed, for simple events.

Thus, the results for all four simple event types indicate that there is some correlation between source speed and signature. Source motion is typically associated with fracture propagation. The variation in speed and its lack of linear peak-frequency dependence indicates that this process possibly radiates sound at different stages in its formation, consisting of distinct frequency content.

The distribution of source speed for compound event

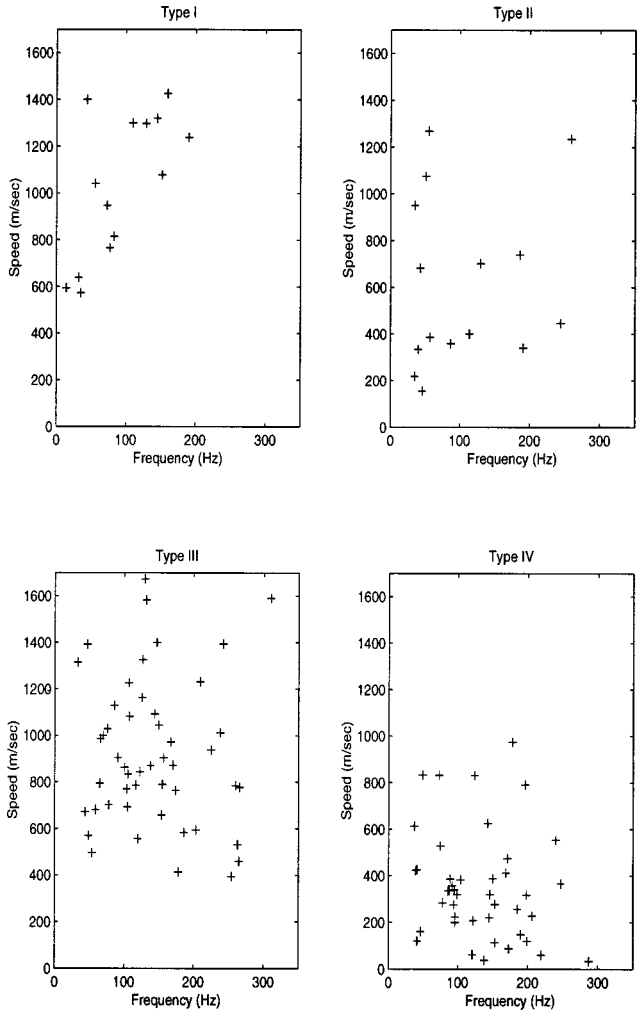

FIG. 11. Source speed versus peak frequency, for simple events.

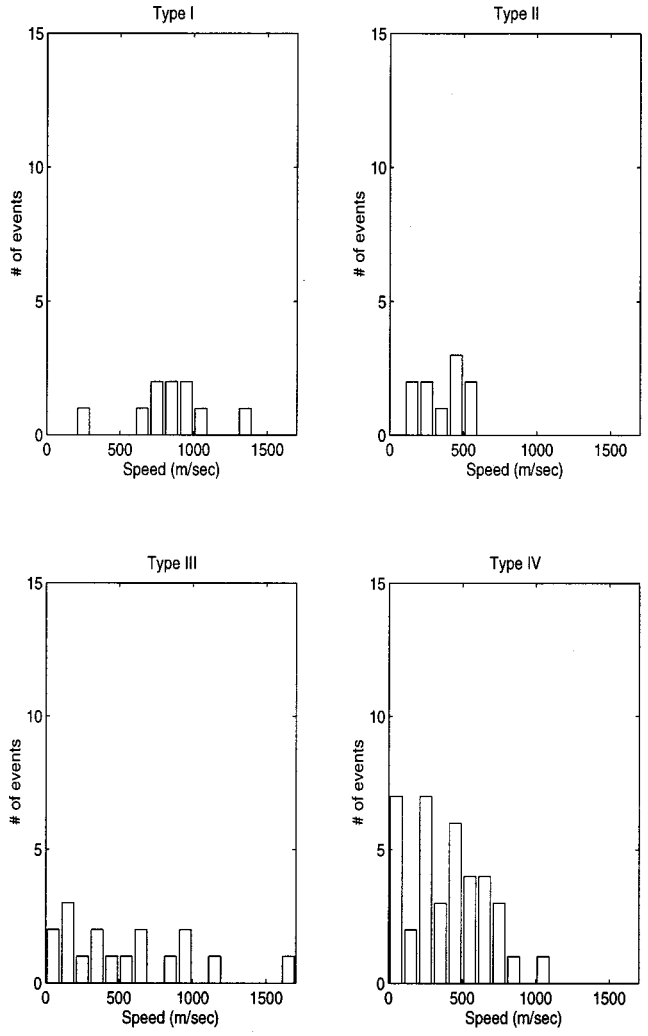

FIG. 12. Distribution of source speed, for compound events.

types is shown in Fig. 12, and a variation of this parameter as a function of peak event frequency is shown in Fig. 13. The sample of type I and II events is too small to reach any meaningful conclusions. For type III events, however, the sample is large and shows a wide spread of speed estimates and no concentration in a particular range. For type IV events, also well sampled, source speeds are concentrated in the range 5–800 m/s. There is no clear correlation between individual signature types and source speed for compound events. The spread of the source-speed data in each of the plots in Fig. 13 again indicates no apparent direct relationship between compound event signatures and peak frequency. For type III and IV events, this spread is more pronounced.

VI. SUMMARY AND CONCLUSIONS

Speed and orientation of ice fractures were obtained for 186 events, each yielding a good speed estimate. We estimated Doppler shifts associated with source motion, which fell in the range between 1 and 90 Hz. From estimated frequency shifts and peak-event frequencies we also calculated source speed and orientation (strike angle), two of the parameters that characterize fracture propagation.

In previous studies of event physics, the Rayleigh wave speed, approximately 1700 m/s for sea ice, has been assumed as the source speed, particularly in cases when fracture is the most plausible event-generating mechanism. The Doppler shift measurements reported here lead to more competent estimates of source speed, resulting in negation of the Rayleigh wave speed assumption for fractures in sea ice. For 76% of 186 events, the speed is significantly lower, in the range 100–1100 m/s. Note that a large majority of the estimated speeds is subsonic. For 17% of the events, predominantly type I and III, the estimated fracture speed is between 1000 and 1698 m/s, some fraction of which is supersonic. Also, speed estimates lower than 100 m/s were obtained for 7% of the events, the majority of which has type IV signatures. Events for which the estimated speed is above 100 m/s are attributed to fracture processes; thus, a possible explanation for the low velocity estimates is that the medium may undergo a rapid transition from velocity weakening to velocity strengthening.[7] Also, there are other sound-radiating mechanisms in the Arctic, such as floe unloading,[9] a post-fracture process that does not involve source motion. Events for which the estimated speed is small may have been induced by such nearly stationary processes. Indeed, we confirm this hypothesis in Ref. 1 via analysis of radiation from

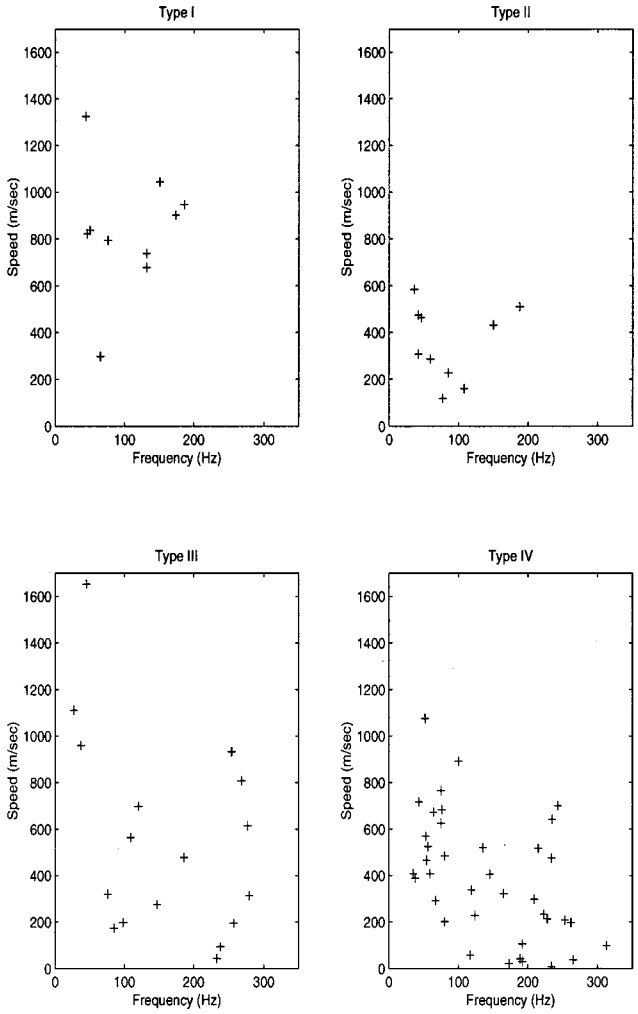

FIG. 13. Source speed versus peak frequency, for compound events.

such events. Finally, the wide range of speed estimates indicates either multiple distinct fracture mechanisms or one or two mechanisms at different stages in their formation. These indications gain support through our work in Ref. 1.

ACKNOWLEDGMENTS

The data were collected during the SIMI experiment in 1994, and we thank the MIT and WHOI teams for their efforts. Financial support for this work was provided in part by ONR.

[1] C. Stamoulis and I. Dyer, ''Sound Radiation from Ice-Induced Acoustic Events'' (unpublished).
[2] C. Stamoulis, ''Analysis of Ice-Induced Acoustic Events in the Central Arctic,'' Ph.D. thesis, Massachusetts Institute of Technology, 1997.
[3] C. F. Chen, ''Analysis of Marginal Ice Zone Noise Events,'' Ph.D. thesis, Massachusetts Institute of Technology, 1990.
[4] Y. Xie and D. M. Farmer, ''The Sound of Ice Breakup and Floe Interaction,'' J. Acoust. Soc. Am. **91**, 1423–1428 (1992).
[5] Y. Xie and D. M. Farmer, ''The Sound Generated by Propagating Cracks in Sea Ice,'' J. Acoust. Soc. Am. **85**, 1480–1500 (1989).
[6] A. D. Pierce, *Acoustics: An Introduction to its Physical Principles and Applications* (Acoustical Society of America, New York, 1991).
[7] H. Scholz, *The Mechanics of Earthquake and Faulting* (Cambridge University Press, Cambridge, 1992).
[8] K. Kasahara, *Earthquake Source Mechanics*, Cambridge Earth Science Series (Cambridge University Press, Cambridge, 1981).
[9] C. F. Chen, S. Merz, and I. Dyer, ''Analysis of Marginal Ice Zone Events'' (1990) (unpublished).
[10] C. Stamoulis and I. Dyer, ''Particle Motion and Scaling Relationships of Faults in Arctic Sea Ice'' (unpublished).
[11] K. Aki and P. G. Richards, *Quantitative Seismology, Theory and Models* (Freeman, San Francisco, 1980), Vols. I and II.

Tomography of dispersive media

Fabian E. Ernst and Gérard C. Herman
Department of Applied Analysis, Faculty of Information Technology and Systems, Delft University of Technology, Mekelweg 4, NL-2628 CD Delft, The Netherlands

(Received 19 March 1999; revised 24 February 2000; accepted 28 March 2000)

When waves propagate through layered structures, the phase velocity is frequency dependent (dispersive). If one wants to reconstruct the velocity variations in this medium, conventional traveltime-based tomographic methods cannot be used, since each frequency component has a different traveltime. A tomographic method is presented for reconstructing the phase velocity of guided waves in laterally varying media. The dispersive character of guided waves is explicitly accounted for by using a phase-based error criterium instead of ''picked'' traveltimes. Phase velocity and source waveform can be reconstructed to within a few percent, and the algorithm is shown to be robust in the presence of interference noise. When applied to seismic field data, the reconstructed phase velocity field correlates well with the topography of the area. © *2000 Acoustical Society of America.* [S0001-4966(00)01807-5]

PACS numbers: 43.30.Pc, 43.60.Pt, 43.20.Ks, 43.40.Ph [SAC-B]

INTRODUCTION

Dispersive waves are encountered in many fields of science, e.g., seismology, geophysics, and underwater acoustics. The essential characteristic of dispersive waves is that different frequencies have different propagation properties. Often, this arises when waves propagate in a layered structure. Certain combinations of layer parameters give rise to resonance effects, leading to propagation of guided-wave modes. Since different frequency bands are influenced in different ways by the layering, the phase velocity of the guided waves is dispersive.

If the structure is known, computation of the propagation parameters is a well-defined, albeit sometimes computationally intensive, task. However, in most field situations, the structure is only approximately known. One is then interested in reconstructing the structure from observed wave fields, which are either generated artificially (acoustical sources in geophysics and underwater acoustics) or naturally (earthquakes). In this case we have an inverse problem of having to reconstruct a medium from waves propagating through it: a *tomographic* problem.

In this paper, we discuss a tomographic method for the reconstruction of a laterally varying, dispersive medium from scalar guided waves. Although the derivation of the method is based on wave propagation in layered media, only the propagation parameters (in this case the phase velocities) are reconstructed. Techniques to invert for the layer parameters from the dispersion of the phase velocity have been discussed in, for instance, global seismology[1] and the geotechnical literature.[2]

Tomographic problems have received a significant amount of attention. Current solution methods can be divided into two main classes:

(i) *Waveform inversion methods* try to find model parameters such that an optimal fit is obtained directly between data computed with those parameters and the observed data. This approach is especially popular in seismology,[3,4] but is also used in geophysics.[5] Waveform inversion methods have the advantage that the data are readily available. The relation between the error criterium and the parameter set, however, might be very nonlinear. This may lead to an abundance of local minima, making the problem unsuitable for gradient-based iterative solution strategies.

(ii) On the other hand, certain *properties* of the observed data may be used and compared to the same properties of modeled data. This concept is used in *traveltime inversion methods* which optimize the fit between the traveltimes of actual and simulated data, used in various underwater acoustics,[6,7] geophysical,[8] and other applications. In that case, only measurements of the kinematic aspects of the wave field are needed. The advantage of traveltime inversion is that the relation between traveltime and slowness is less nonlinear. The traveltime has to be extracted in some way from the actual data, which is a nonlinear procedure. The accuracy of a traveltime inversion method is often limited when traveltimes have to be picked manually. Moreover, for dispersive waves no unique traveltime exists, since each frequency band propagates with a different velocity.

The observed wave field at a certain location can be expressed in terms of its kinematic behavior (arrival time) and dynamic behavior (amplitude). The kinematic aspects are, from a practical point of view, the most reliable sources of information. We therefore develop a tomographic method based on a generalization of traveltimes.[9] This enables not only reconstruction of lateral variations, but also of dispersion. Generalized traveltime inversion has the basic characteristics of traveltime inversion, in the sense that it is only slightly nonlinear in the slowness. This makes it suitable for iterative solution algorithms, thus avoiding the need for global optimization methods. On the other hand, no hand-picked traveltimes are needed; it is sufficient to assume that the direct guided wave can be separated sufficiently well from other waves present in the data by means of time windowing.

In the seismic situation, the direct guided wave usually has a very large amplitude compared to other wave types, enabling us to distinguish it clearly from other wavetypes. If different guided modes are present in the data, they become separated in time for sufficient distances from the source due to differences in propagation velocities. Generalized traveltimes have already been applied successfully to velocity model estimation for (nondispersive) cross-borehole tomography.[10,11]

The tomographic method discussed in this paper has been developed in order to estimate the phase velocity of seismic waves propagating near the surface of the earth. Within the context of seismic exploration, these waves are considered as ''coherent noise.'' Once the phase velocity of these waves is known, guided waves and scattered guided waves can be modeled and removed from the seismic data.[12] Although this research has originated in geophysics, application is not restricted to a seismic context, but can also be used for reconstruction of dispersive velocities in, for instance, global seismology and underwater acoustics.

We first briefly review the forward problem of guided-wave propagation in laterally varying layered media in Sec. I. In this paper, we assume that the observed direct guided wave can be described with sufficient accuracy by adiabatic local normal mode theory, and we apply the tomography algorithm to a single mode. Provided each mode can be extracted separately from the data, this also allows for independent reconstruction of the phase velocity for multiple modes. We use high-frequency asymptotics to derive an efficient forward modeling scheme. Generalized traveltimes, and their extension to dispersive velocity models, are discussed in Sec. II. We also investigate the null space of the resulting error norm (this is related to uniqueness issues), as well as its sensitivity to (additive) noise, such as interfering events. In Sec. IV, we discuss the estimation of the effective source waveform once the phase slowness field is reconstructed. To find an optimal model, we have to discretize the model space of the phase slowness. The parametrization in the spatial and frequency dimensions is discussed in Sec. V. The method is applied to numerically simulated data in Sec. VI to assess the effect of noise on the reconstruction, and compare the results of our reconstruction with actual dispersion curves and source waveforms. Finally, we apply the method in Sec. VII to a representative seismic field data set.

I. WAVE PROPAGATION IN LATERALLY VARYING, LAYERED MEDIA

We assume that the background medium, the propagation characteristics of which we want to reconstruct, consists of a vertical stack of layers over a halfspace. The properties of these layers (acoustic velocity c, density ρ, and layer thickness h) may vary in lateral (horizontal) directions, however, we assume that the lateral variations occur on a length scale which is large compared to the dominant wavelength. This fairly general model is suitable to model wave propagation for a wide class of problems. The (frequency domain) scalar Helmholtz equation for the acoustic pressure p due to a nonimpulsive point source is given by

$$\rho(\mathbf{x})\nabla\frac{1}{\rho(\mathbf{x})}\nabla p(\mathbf{x},\omega,\mathbf{s})+\frac{\omega^2}{c^2(\mathbf{x})}p(\mathbf{x},\omega,\mathbf{s}) = -W_s(\omega)\,\delta(\mathbf{x}-\mathbf{s}), \tag{1}$$

where $\mathbf{x}=(x,y,z)^T$ denotes the spatial coordinates, $\mathbf{s}$ is the source location, ω is the angular frequency, and W_s is the source waveform. This equation is supplemented by radiation conditions at large distances from the source, and continuity conditions at interfaces between layers.

For the laterally invariant case, it is well known that the solution for the pressure can be expressed in terms of a sum of guided modes and an integral representing the radiating field. In case of lateral variations, it is usually no longer possible to write the expression for the pressure in closed form. We therefore use an approximate solution based on local normal modes.[13] Propagation of normal modes and energy exchange between modes can then be described by a system of mode-coupling equations.[14,15] If lateral variations are weak and gradual, the local-normal-mode approach can be simplified even further by neglecting coupling between different modes: the *adiabatic assumption*. This implies that no energy is exchanged between modes. The propagation of guided modes can be computed very efficiently using high-frequency asymptotics. Equations for amplitudes and traveltimes can be derived using perturbation theory.[16] The high-frequency asymptotic approximation is also accurate to first order in ω^{-1}, just as the adiabatic guided-wave approximation.

Under the assumption that the modes can be separated in time (which is usually the case in seismic situations, and which also holds for multiple-mode propagation sufficiently far from the source), we restrict ourselves in the remainder of this paper to the reconstruction of the phase slowness for a single mode.

Using both the adiabatic local normal mode approximation and high-frequency asymptotics, the solution of the Helmholtz equation (1) for a single laterally propagating guided mode can be written as[12]

$$p(\mathbf{x},\omega,\mathbf{s}) = W_s(\omega)\,\phi(z,\omega,\mathbf{x_h})A(\mathbf{x_h},\omega,\mathbf{s_h}) \times\exp(-i\omega\tau(\mathbf{x_h},\omega,\mathbf{s_h}))\phi(s_z,\omega,\mathbf{s_h}), \tag{2}$$

where a subscript h denotes horizontal (lateral) coordinates and (subscript) z denotes the vertical coordinate. The equations for the modal functions ϕ, traveltimes τ, and amplitudes A are given by

$$\rho(z,\mathbf{x_h})\frac{d}{dz}\frac{1}{\rho(z,\mathbf{x_h})}\frac{d\phi(z,\mathbf{x_h})}{dz} +\left(\frac{\omega^2}{c^2(\mathbf{x})}-\frac{\omega^2}{c_{\mathrm{ph}}^2(\omega,\mathbf{x_h})}\right)\phi(z,\omega,\mathbf{x_h})=0, \tag{3}$$

$$(\nabla_{\mathbf{h}}\tau(\mathbf{x_h},\omega,\mathbf{s_h}))^2=c_{\mathrm{ph}}^{-2}(\omega,\mathbf{x_h}), \tag{4}$$

$$2\nabla_{\mathbf{h}}A(\mathbf{x_h},\omega,\mathbf{s_h})\cdot\nabla_{\mathbf{h}}\tau(\mathbf{x_h},\omega,\mathbf{s_h}) +A(\mathbf{x_h},\omega,\mathbf{s_h})\Delta_h\tau(\mathbf{x_h},\omega,\mathbf{s_h})=0. \tag{5}$$

This expression can be interpreted as follows: the kinematic aspects of guided-wave propagation follow from the travel-

times τ, which can be found by ray tracing in the phase velocity field c_{ph}. The geometrical spreading is accounted for in the amplitudes A. The local structure of the medium follows from the local modal amplitudes ϕ. Initial conditions for Eqs. (4) and (5), taking the presence of the point source into account, can be derived using matched asymptotic expansions.[12]

II. GENERALIZED TRAVELTIME INVERSION

A. Generalized traveltimes

Traveltime tomographic methods are based on associating a traveltime (either manually or automatically) with a certain event (in this case the arrival of the direct guided wave), and subsequently estimating model parameters to optimize the fit between ''picked'' and computed traveltimes. Due to the dispersive nature of guided waves, no single traveltime can be associated with the direct guided wave. Each frequency travels with a different phase velocity. The traveltime of a certain event then also varies with frequency, leading to a dispersive $\tau(\omega)$. This has consequences for the (nonlinear) derivation of traveltimes from given data.

To overcome this problem, we use generalized traveltimes, based on the work of Herman.[9] In the present paper, generalized traveltimes are defined slightly different, i.e., by

$$\tau_{sr}^{GT}(d,\omega) = t_{sr,\min} - \frac{d}{d\omega}\Phi\left\{\sum_i \exp(-(\alpha+j\omega)(t_i - t_{sr,\min}))\tilde{d}_{sr}(t_i)\right\} \tag{6}$$

with i such that $t_{sr,\min} < t_i < t_{sr,\max}$. Here α is a real positive damping constant which can be used to avoid zeros in the complex frequency plane, and $t_{sr,\min}$ and $t_{sr,\max}$ denote the start and end of a time window surrounding the arrival of the direct guided wave. The sample times are denoted by t_i, and $\tilde{d}$ is a windowed and tapered version of the input time data d (usually the pressure, or the vertical velocity at the surface). Here $\Phi(z)$ denotes the argument of a complex number z, defined by

$$\Phi(z) = \Im \log(z), \tag{7}$$

where $\Im$ denotes the imaginary part.

With this definition of generalized traveltimes, dispersive waves can be handled, since the generalized traveltimes can be frequency dependent. Moreover, this no longer requires picking of a traveltime, but makes only delineation necessary of a time window around the arrival of the direct guided wave. It can, for instance, be handled by specifying a minimum and maximum value for velocities to extract the direct wave from the data. Since the direct guided wave in the seismic situation is usually the direct surface wave (''ground roll''), it can be distinguished rather well in the data due to its high amplitude.

Unwrapping the phase of the wave field may lead to various problems (see also Ref. 17 for a discussion on problems related to phase unwrapping). The most fundamental of these problems is that the position of the unwrapped phase curve can be determined only modulo an integer number of multiples of 2π, since low frequencies are often missing in data (due to instrument and source limitations, the finite cutoff frequency of guided waves or other causes). Additional information is therefore required to uniquely define the phase. For application to nondispersive waves, this additional information is available by requiring that the phase is linear with frequency, i.e., the linearly extrapolated phase curve should cross the origin. However, for dispersive waves such information is not available. Consequently, despite the fact that the *variation with frequency* of the phase can be computed, the phase itself is only defined up to a constant. (This is the reason why we have redefined the generalized traveltimes from Ref. 9.) Whereas the original generalized traveltimes reduce for $\alpha=0$ to phase traveltimes, the ones used in this paper reduce to group traveltimes.

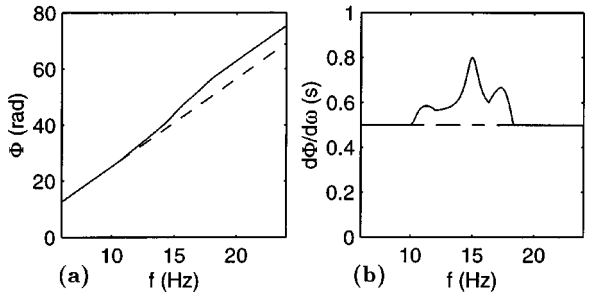

FIG. 1. (a) Dashed line: unwrapped phase for a single nondispersive event; solid line: unwrapped phase for the same event combined with an interfering event in the same time window. The phase is not only distorted in the bandwidth of the interference (from 10 to 18 Hz), but has also an error of 2π for higher frequencies. (b) Dashed line: derivative of the unwrapped phase (group traveltime) for a single nondispersive event; solid line: derivative of unwrapped phase for the same event combined with an interfering event in the same time window. Contrary to (a), the derivative of the phase is only distorted in the bandwidth of the interfering signal (10–18 Hz), and not for other frequencies. Moreover, if approximate bounds on the group traveltimes are known, evidently noisy data can be discarded.

The new definition has two important advantages: First of all, the quantity τ^{GT} is uniquely defined, and the error norm has, for weak lateral variations and a suitable parametrization, a well-defined minimum. The problem of nonuniqueness has now been shifted to the null space of the error norm; this is discussed in Sec. III B. This null space can be characterized by one additional parameter. However, estimation of this additional parameter can be carried out *after* constructing the optimal parametrization from the error norm.

As a second advantage, noisy data can be identified more quickly and taken care of. Noise, which is always present in seismic data, together with interfering other events, may lead to distortions of the phase. During phase unwrapping, certain types of noise, especially those leading to small spectral amplitudes, may accumulate in an additional error in the phase of 2π.[17] This is illustrated in Fig. 1(a), where we have plotted the unwrapped phase for two situations: noise-free data of a single broadband event, and the same event together with a strong smallband (between 10 and 18 Hz) interfering event. From the figure it is clear that unwrapping the phase in the interference case results in an error in the phase of 2π for higher frequencies, *also at frequencies which are noise-free*. This problem is again related to the phase ambiguity of 2π. Of course, the phase is also

distorted in the bandwidth of the interfering events. When carrying out the same test for the derivative of the phase with respect to frequency [see Fig. 1(b)], the derivative is only distorted in the bandwidth of the interfering event, and not for the noise-free frequencies. Moreover, the distortion stands out clearly from the nondistorted region. Usually certain upper and lower bounds on the velocity are known. These bounds provide us with estimates on minimum and maximum traveltimes, allowing us to filter out noisy data points with generalized traveltimes outside a specified range. For noisy data an error criterium based on $d\Phi/d\omega$ is therefore more robust than an error criterium based on Φ itself.

B. Computation of the generalized traveltimes

There are various methods to compute the derivative of the phase of a time series. The most straightforward method would be to take the Fourier transform, unwrap the phase (with an arbitrary initial value at the lowest frequency), and subsequently differentiate numerically. However, this procedure might become numerically unstable if we have small frequency increments. A numerically more robust method can be derived by differentiating equation (7) and recalling the differentiation property of the Fourier transform (denoted by $\mathcal{F}$):

$$\frac{d\Phi}{d\omega} = \Im \frac{-i\mathcal{F}\{t\exp(-\alpha t)d_{sr}(t)\}}{\mathcal{F}\{\exp(-\alpha t)d_{sr}(t)\}} = -\Re \frac{\mathcal{F}\{t\exp(-\alpha t)d_{sr}(t)\}}{\mathcal{F}\{\exp(-\alpha t)d_{sr}(t)\}}, \tag{8}$$

where $\Re$ denotes the real part of a complex number.

The derivative of the phase with respect to frequency can therefore be computed as a quotient of two Fourier transforms. Note that at frequencies where the spectral magnitude of the data is zero, the derivative of the phase is not defined. This may especially be the case for noisy data and data where interfering events are present. This problem can be avoided by taking an appropriate nonzero value of the damping coefficient α, in order to shift zeroes of the spectrum into the complex frequency plane. Alternatively, the phase might be (arbitrarily) defined by means of some interpolation mechanism. However, near these zeroes, the phase should be treated with care.[17] This is discussed further in the next section.

III. ERROR CRITERIUM

A. Error criterium based on generalized traveltimes

In our approach, the optimal phase slowness model is defined as the model which minimizes the following regularized weighed least-squares norm:

$$\min E = \sum_s \sum_r \sum_\omega w_{sr\omega}^2 |\tau_{sr}^{GT}(d_{sr}^{\text{real}},\omega) - \tau_{sr}^{GT}(d_{sr}^{\text{synth}}(\mathbf{p}),\omega)|^2 + \sigma^2 \|\mathbf{p}-\mathbf{p}_{a\ priori}\|^2, \tag{9}$$

where τ^{GT} are the generalized traveltimes, defined by Eq. (6), d^{real} and d^{synth} denote real and synthetic (numerically simulated) data, and $\mathbf{p}$ is the vector of discretized slownesses. This discretization is discussed further in Sec. V. The summation is over all sources, receivers, and frequencies of interest.

It is well known for tomographic problems[8] that a certain amount of regularization is necessary. This regularization is carried out here by including an additional term with *a priori* information $\mathbf{p}_{a\ priori}$ on the slowness field. This *a priori* information might, for instance, be the outcome of a preliminary estimate of a laterally invariant, dispersive medium. The constant σ is used to balance the misfit and *a priori* terms.

If the signal level is approximately constant in a certain bandwidth, frequencies with a relatively high spectral magnitude have a relatively small error in the generalized traveltime. At frequencies where the spectral magnitude is zero, the generalized traveltimes are undefined. In order to circumvent this problem and to reduce noise effects, weighing of the error with relative spectral magnitude is used. We therefore take the weights $w_{sr\omega}$ in expression (9) as

$$w_{sr\omega} = \frac{|d_{sr}^{\text{real}}(\omega)|}{\max_\omega |d_{sr}^{\text{real}}(\omega)|}. \tag{10}$$

The removal of potentially strong sources of noise is especially important because the minimization procedure is based on a least-squares norm, which is known to be sensitive to outliers. Removal of these outliers increases the accuracy of our minimization algorithm.

The minimization of error norm (9) with respect to the parameter vector $\mathbf{p}$ is carried out using a preconditioned nonlinear conjugate-gradient (Fletcher–Reeves) algorithm.[18]

It can be shown that when using error criterium (9), the parameter vector completely determines the *group slowness*, but to obtain the *phase slowness* a nontrivial null-space component has to be estimated.

B. The null space of the error norm

We now analyze the null space of the error norm, i.e., variations in the phase slowness field which do not influence the error. A nontrivial null space would indicate nonuniqueness of the reconstructed phase slowness field. This analysis is mainly directed towards the frequency-dependent part (dispersion) of the phase slowness field. To this extent, we first consider laterally invariant media, and take $\alpha=0$ for simplicity.

The phase of a wave, transmitted through a laterally invariant medium, is given by

$$\Phi(\omega) = -\omega p_{\text{ph}}(\omega)\|\mathbf{r_h}-\mathbf{s_h}\|. \tag{11}$$

Since the error criterium is based on the derivative of the phase, the null space consists of those phase slowness variations p_N for which

$$\frac{d\Phi}{d\omega} = -\frac{d}{d\omega}\omega p_N(\omega)\|\mathbf{r_h}-\mathbf{s_h}\| = 0. \tag{12}$$

Thus, the null space of the error norm consists of phase slowness variations

$$p_N(\omega)=\frac{p_1}{\omega}, \quad p_1 \in R. \tag{13}$$

Although the group slowness might be completely reconstructed with our error norm, the phase slowness has an ambiguity inversely proportional to frequency. For nondispersive media, this ambiguity can be resolved because then p_{ph} is independent of ω (i.e., $p_1=0$). However, for dispersive media and guided waves with a cutoff frequency $\omega_c>0$ (thus prohibiting us from analyzing the behavior for zero frequency), another method has to be used to find p_1.

In general, information on the null space has to be derived from *a priori* information. Here, the null-space parameter p_1 is derived in the following way: We assume that the vertical velocity of the wave motion, given by

$$v_z=-\frac{1}{i\omega\rho}\frac{\partial p}{\partial z}, \tag{14}$$

is the quantity measured at the receiver. (If the pressure is measured, a similar analysis can be carried out.) Consider the backpropagated wave field (the wave field after deconvolution by the Green's function) $\hat{v}_z$, defined as

$$\hat{v}_z(\mathbf{r},\omega,\mathbf{s})=v_z(\mathbf{r},\omega,\mathbf{s})\exp(i\omega\tau(\mathbf{r_h},\omega,\mathbf{s_h}))A^{-1}(\mathbf{r_h},\omega,\mathbf{s_h}), \tag{15}$$

which is in the case of noise-free data identical to [see Eqs. (2) and (14)]

$$\hat{v}_z(\mathbf{r},\omega,\mathbf{s})=-\frac{W_s(\omega)}{i\omega\rho}\phi(s_z,\omega,\mathbf{s_h})\frac{d\phi}{dz}(r_z,\omega,\mathbf{r_h}) \times\exp(-ip_1\|\mathbf{r_h}-\mathbf{s_h}\|), \tag{16}$$

where τ and A are the traveltime and amplitude of the phase slowness field with the optimal group slowness field and taking the null-space parameter $p_1=0$. The main effect of this slowness component is a small time shift of the wave field and a slight distortion of the wave field. The only offset-dependent factor (which is different for each receiver) is the one containing p_1. We take the null-space parameter such that

$$P=\sum_s \frac{\Sigma_\omega\|\Sigma_r\hat{v}_z(\mathbf{r},\omega,\mathbf{s})\|^2}{\Sigma_\omega\Sigma_r\|\hat{v}_z(\mathbf{r},\omega,\mathbf{s})\|^2} \tag{17}$$

is maximized, i.e., maximizing the sum of the *semblance*[19] of the backpropagated and stacked traces for each shot record. The use of semblance allows us to account for variations in the source strength.

For the case of laterally varying media, also spatial resolution issues become important. For nondispersive media, these have been well discussed in the literature.[20] For dispersive media, the spatial resolution issues are similar. However, for dispersive media we also need to consider the uniqueness in the frequency dimension. The above analysis now leads to a null space which is now no longer parametrized by a scalar p_1, but by a laterally varying function $p_1(x,y)$. The null space is no longer linear, since lateral variations of p_1 lead to changes in the ray paths. Despite the fact that, in principle, the same methodology can be applied, the optimization problem for p_1 now becomes much more difficult. For practical purposes we therefore assume that p_1 does not depend on the spatial coordinates, i.e., all lateral variations are already accounted for in the group slowness. It is then sufficient to take the null space as one-dimensional, meaning that we only have to find a single parameter p_1.

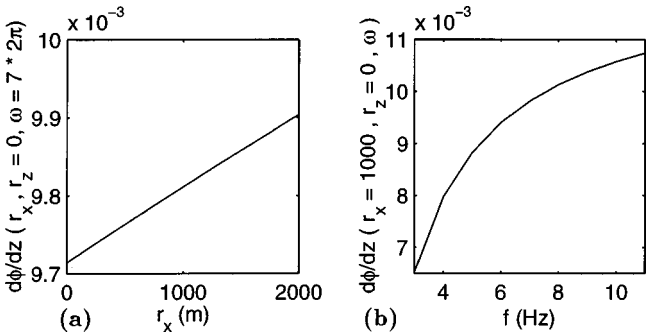

FIG. 2. The value of the (real-valued) modal function $d\phi/dz$ at the surface at the receiver locations in a medium with a linearly varying velocity in the upper layer (for a description of the geometry, see Sec. VI). (a) The modal function at 7 Hz for each receiver. The *lateral variations* are on the order of 2.5%. This makes it feasible to combine the effects of the source waveform and the modal functions in an effective source waveform. (b) The modal function at receiver 41 ($x=1000$) for all relevant frequencies. It is clear that the *dispersive effect* of the modal function is much stronger than the lateral variation for this type of background medium, and should be taken into account during estimation of the effective source waveform.

IV. SOURCE ESTIMATION

For some application, it is not only the velocity field one is interested in, but also the direct guided wave has to be computed. In order to be able to compute the direct wave it is necessary to know the source waveform, as can be inferred from expressions (2). Apart from that, also the modal functions ϕ are as yet unknown.

If we are able to extract the direct wave field from the data, which is an underlying assumption of this tomographic method, and the background medium is known as well, we can use a deconvolution approach, where the deconvolution operator is the Green's function: Once the background medium is known, propagation effects can be removed from the observed direct wave. Physically, this deconvolution operation with the lateral propagation operator amounts to backpropagating the wave field from the receiver to the source. The backpropagated wave field (15) is, in the case of noise-free data and for the correct phase slowness model, given by [see Eqs. (2) and (14)]

$$\hat{v}_z(\mathbf{r},\omega,\mathbf{s})=-\frac{W_s(\omega)}{i\omega\rho}\phi(s_z,\omega,\mathbf{s_h})\frac{d\phi}{dz}(r_z,\omega,\mathbf{r}). \tag{18}$$

If no lateral variations occur, and all receivers are at the same depth, it is theoretically impossible to separate the effects of the source waveform from the effect of the modal functions. For the case of lateral variations, it is still not possible to discern between source waveform and the modal function at the source, although the modal function at the receiver varies. However, due to the fact that lateral variations are assumed to be gradual, the variations in the modal functions at the receiver locations are also gradual. This is illustrated in Fig. 2, where the modal function at the receivers has been plotted for the background model and acquisition geometry

used in Sec. VI. It can be seen that lateral variations are on the order of 2.5%, making it feasible to combine the effects of source waveform and modal functions into an effective source waveform.

In practical situations, the variations from shot to shot in the source waveform, and the frequency dependence of source and receiver response, dominate the differences between receivers. Since the lateral variations are hard to discern, especially for noisy data, and only the *combination* of source waveform and modal functions occur in the expressions for the direct wave field, we define the effective guided wave source waveform as follows:

$$W_s^{\text{eff}}(\omega) := \frac{1}{N_r} \sum_r \hat{v}_z(\mathbf{r},\omega,\mathbf{s}), \tag{19}$$

where N_r denotes the number of receivers used in the estimation procedure for this shot. This method of averaging the backpropagated traces is the guided-wave equivalent of the method employed by Hokstad *et al.*[21]

The combination of the source wavelet and modal functions in expression (2) is then for forward modeling purposes in an unknown background model replaced by the effective source wavelet of (19), resulting in the following expression for the direct wave:

$$v_z(\mathbf{r},\omega,\mathbf{s}) = W_s^{\text{eff}}(\omega) A(\mathbf{r},\omega,\mathbf{s}) \exp(-i\omega\tau(\mathbf{r},\omega,\mathbf{s})). \tag{20}$$

The averaging of the backpropagated field may be carried out in the frequency domain as well as in the time domain. While the whole analysis is carried out in the frequency domain, it may be advantageous to do the averaging in the time domain to be able to exercise control over the length of the source waveform. Furthermore, time-domain averaging was found to be more robust in the presence of residual slowness errors.

Finally, observation of the backpropagated field before averaging can give us an indication of the quality of the background model estimation. Similar results for various receiver distances from the source indicate a good quality of the estimate, whereas trends in the backpropagated results indicate residual errors in the slowness field or in the null-space parameter.

V. PARAMETRIZATION OF THE SLOWNESS AND THE SOURCE

As discussed previously, the parameter governing wave propagation along the surface is the phase slowness. Since this slowness is dispersive, it is a function of three independent variables: the lateral coordinates x and y, and the frequency ω.

In order to reconstruct the slowness numerically, it has to be parametrized into a finite number of parameters. To ensure enough smoothness to be able to do dynamic ray tracing, continuity up to the second spatial derivatives is needed. We therefore parametrize in the lateral dimensions by bicubic splines, which is a conventional way to handle smooth lateral variations. A general formulation for the phase slowness, including the null-space term, becomes

$$p_{\text{ph}}(x,y,\omega) = \sum_{i=-1}^{I+1} \sum_{j=-1}^{J+1} \sum_{k=1}^{K} p_{ijk} N_i(x) N_j(y) g_k(\omega) + \frac{p_1}{\omega}. \tag{21}$$

Here N denotes a cubic spline, and g relates to the parameterization in the frequency dimension.

To avoid distortions due to trends in the phase of the source, the parametrization of the background model might be extended by a parameter τ_s for each source, representing the trend in the phase (time delay of the source). For $\alpha=0$ and a time window completely surrounding the direct wave, the generalized traveltimes as defined by Eq. (6) are then given by

$$\tau_{sr}^{GT}(d,\omega) = \frac{d}{d\omega}\omega \int_{\Gamma_{sr}} \left\{ \sum_{i=-1}^{I+1} \sum_{j=-1}^{J+1} \sum_{k=1}^{K} p_{ijk} N_i(x(\sigma)) \times N_j(y(\sigma)) g_k(\omega) + \frac{p_1}{\omega} \right\} d\sigma + \tau_s, \tag{22}$$

which can be approximated under the assumption that dispersion of the phase slowness dominates the variation with frequency of the ray path by

$$\tau_{sr}^{GT}(d,\omega) \sim \sum_{i=-1}^{I+1} \sum_{j=-1}^{J+1} \sum_{k=1}^{K} p_{ijk} \frac{d}{d\omega}\omega g_k(\omega) \int_{\Gamma_{sr}} N_i(x(\sigma)) \times N_j(y(\sigma))\, d\sigma + \tau_s, \tag{23}$$

where we see that the null-space parameter p_1 is indeed not contained in the generalized traveltimes. From Eq. (23) it follows that the parametrization of the group traveltimes in the frequency dimension is governed by $f_k(\omega)$, defined by

$$f_k(\omega) = \frac{d}{d\omega}\omega g_k(\omega). \tag{24}$$

Whereas the parametrization in the spatial dimensions is handled in a conventional way by using cubic splines, the parametrization in the frequency dimension (f and g) is not obvious. The actual frequency dependence of the phase slowness is governed by the dispersion relation. This dispersion relation relates the frequency dependence of the phase slowness in a nonlinear way to the frequency and the actual medium parameters (such as layer thicknesses, velocities, and densities). In principle these medium parameters might be inverted for through the dispersion relation.[1,2] However, for our application we are mainly interested in the phase slowness itself, and not in the layer structure. Although the reconstructed dispersion relation should be consistent with an actual dispersion relation resulting from a certain layer structure, we assume here that such an inversion is, in principle, possible, but it is not carried out.

This leaves us some freedom in the choice of parametrization in the frequency dimension. Our definition of generalized traveltimes [Eq. (6)] requires differentiability of the phase with respect to frequency, thus also requiring differentiability of the phase slowness. We have tested various continuous parametrizations,[22] and found a parametrization for f_k in terms of parabolic splines to be optimal in terms of accuracy, stability of the numerical scheme, and computa-

tional effort. The functions g_k then follow from Eq. (24), where the integration constant is taken to be zero.

Note that a group slowness (strictly speaking, a group slowness along the ray path) can be defined as

$$p_g(x,y,\omega)=\sum_{i=-1}^{I+1}\sum_{j=-1}^{J+1}\sum_{k=1}^{K} p_{ijk}N_i(x)N_j(y)f_k(\omega). \quad (25)$$

Hence, the parameter vector **p** completely determines the group slowness.

Finally, we remark that the general parametrization (21) also allows reconstruction of background models which do not vary in one or both spatial dimensions, or which are nondispersive, by making appropriate choices for the parametrization of lateral variation and dispersion.

The main effort for the minimization of error norm (9) lies in the computation of the gradient: the derivative of the generalized traveltimes with respect to the model parameters. For $\alpha=0$, we use expression (23) for the generalized traveltimes and the stationarity of the ray path with respect to the model parameters[23] to arrive at

$$\frac{\partial \tau_{sr}^{GT}(\omega)}{\partial p_{ijk}}=\int_{\Gamma_{sr}} N_i(x(\sigma))N_j(y(\sigma))f_k(\omega)\,d\sigma \quad (26)$$

and

$$\frac{\partial \tau_{sr}^{GT}(\omega)}{\partial \tau_{s'}}=\delta_{ss'}. \quad (27)$$

VI. APPLICATION TO NUMERICALLY SIMULATED DATA

A. Introduction

To test our algorithm, we have applied it to a numerically simulated data set containing all features of interest. The use of numerically simulated data allows us to compare the reconstruction with the actual numerical values. The computation of the data is discussed in Sec. VI B.

We have first applied our algorithm to the data as is (without noise or other distortions) in Sec. VI C. We can then compare the fit between actual dispersion curves (satisfying the local dispersion relation) and the reconstructed dispersion curves, as well as assess the quality of the estimated effective source waveform. Moreover, the smoothness of the error surface is checked.

Subsequently, the effect of interfering events is assessed in Sec. VI D. As already discussed in Sec. II A, interfering events can have a dramatic effect on the group traveltimes.

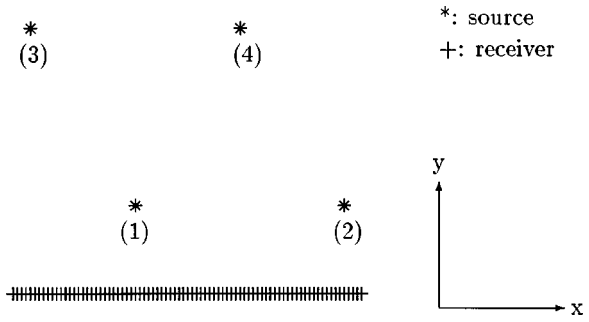

FIG. 3. Acquisition geometry used for the tests on numerically simulated data. Sources are at 250 m and at 750 m distance from the receiver line. The receiver line consists of 81 detectors, the spacing is 25 m.

To this extent, we added a simulated deep reflection to the data, leading to a distortion near the apex (the top of the hyperbola) of certain shots. Again, dispersion curves were reconstructed. As a form of quality control, the estimated direct guided wave is subtracted from the original data in order to see how the interfering event, which is the relevant signal for geophysical applications, is affected.

B. Description of the geometry and data simulation

The acquisition geometry consists of four sources and a line of 81 receivers. The spacing between the receivers is 25 m. For an overview of the source and receiver locations, see Fig. 3.

The background model we use here consists of a layer with a thickness of 50 m, in which the velocity varies from 260 m/s in the northeastern corner to 240 m/s in the southwestern corner. Beneath this layer is a half-space with a velocity of 350 m/s.

The direct guided wave is computed based on the actual dispersion relation and modal structure [Eq. (2)]. The source has been taken as a zero-phase waveform with a 3–11-Hz frequency bandwidth.

C. Application to noise-free data

The generalized traveltime tomography has first been carried out on the synthetic dataset without noise. This allows us to compare the reconstructed results with the actual numerical values, thus giving us an estimate of the accuracy of the reconstruction.

In Fig. 4 we have plotted the dispersion curves at two locations on the receiver line: at $x=700$ m and at $x=1900$ m. The solid line denotes the actual local dispersion

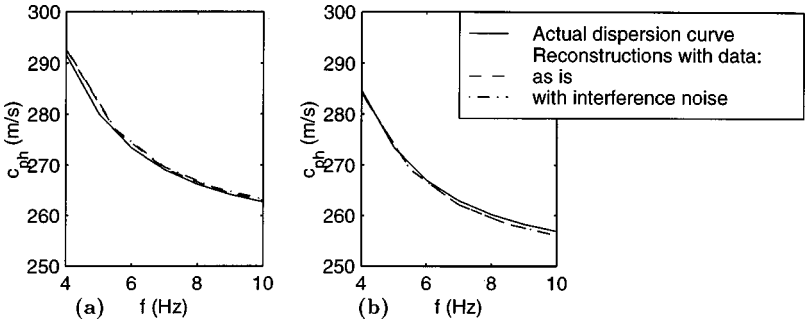

FIG. 4. Dispersion curves of the resulting phase velocity field after application of our tomographic algorithm to synthetic data. (a) Dispersion curves at receiver 29 ($x=700$ m); (b) dispersion curves at receiver 77 ($x=1900$ m). The slowness is parametrized in lateral directions by one cell, and in the frequency dimension by a parabolic profile. The reconstruction for all situations is accurate to within 1–2 m/s (less than 1%).

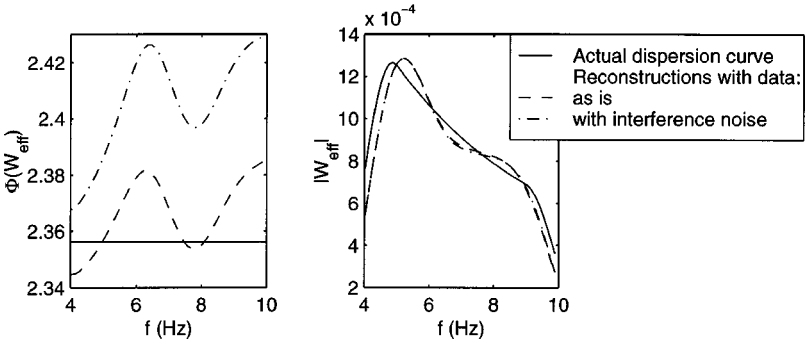

FIG. 5. Phase (left) and amplitude (right) of the effective source waveform [Eq. (19)] after application of our algorithm to synthetic data. The phases are reconstructed well. The reconstructed amplitudes are similar for both situations, indicating that the process of averaging and tapering during computation of the effective source waveform is the main cause for the distortion.

curve in the actual medium, computed through the dispersion relation. The dashed line is the reconstructed result. Both dispersion curves agree to within 1 m/s (leading to a relative error of less than 0.5%). In Fig. 5, amplitude and phase of the effective source waveform for shot 3, as defined by Eq. (19), are shown. Both the phase (which is related to the kinematic behavior) and the amplitude are reconstructed well. The errors in the amplitude are mainly due to the averaging and tapering in the time domain during computation of the effective source waveform.

In order to check the resolution of the reconstruction, we varied two arbitrarily chosen slowness parameters, $p_{1,0,3}$ and $p_{-1,1,2}$ (related to the high-frequency behavior in the southeastern corner, and the low-frequency behavior in the northwestern corner, respectively) by 10% around the reconstructed solution. The resulting error surface is depicted in Fig. 6. It can clearly be seen that the surface has a well-defined, unique minimum, making generalized traveltime inversion very amenable to iterative solution strategies. The contour lines correspond to rms errors of the generalized traveltimes in steps of 0.5 ms, where the innermost contour corresponds to a rms error of 14.75 ms (which indicates an error in the traveltimes of less than 1%).

D. Effects of interfering events

We now direct our attention towards the effect of additive noise. As we have seen in Sec. II A (Fig. 1), interfering events can have a detrimental effect on the generalized traveltimes. To assess the effects of this type of noise—which is, in practical cases, of more interest than random noise—we have simulated a deep reflection from a point scatterer. The parameters were chosen such that the scattered field arrives at approximately the same time as the direct guided wave near the apex. The bandwidth of the scattered field was 3–24 Hz. An example of a shot record for the data containing the direct guided wave and a simulated deep reflection is shown in Fig. 7(a). This type of coherent interference is expected to be the main source for errors in our tomographic reconstruction of the phase velocity when applied to real seismic data.

Again we have applied the slowness reconstruction algorithm to the data set obtained in this way. The reconstructed dispersion curves at receivers 29 and 77 are denoted by the dash–dotted line in Fig. 4. The actual dispersion curve is denoted by the solid line. In comparison with the reconstructed dispersion curve for the noise-free case, denoted by the dashed line, the dispersion curve is hardly affected by the additional additive noise; the velocities are still accurate within 2 m/s (less than 1%). The source waveform for shot 3 is plotted in Fig. 5 (dash–dotted line). The actual source waveform is given by the solid line. Again, the amplitude and phase of the source waveform are reconstructed well, comparable to the results for the noise-free case.

We also subtracted the modeled data adaptively (by allowing small time shifts and amplitude corrections) from the original data to check the overall quality of the tomographic algorithm. The remainder of the wave field after subtraction is shown in Fig. 7(b). The deep reflection has hardly been

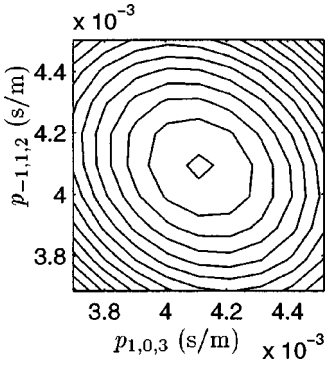

FIG. 6. Contour lines of the error surface for variations of ±10% of two parameters of the slowness. Contour lines are in steps of 0.5 ms, the inner line corresponding to 14.75 ms. The error surface is very smooth with a clear global minimum. This indicates the suitability of this norm for iterative solution strategies.

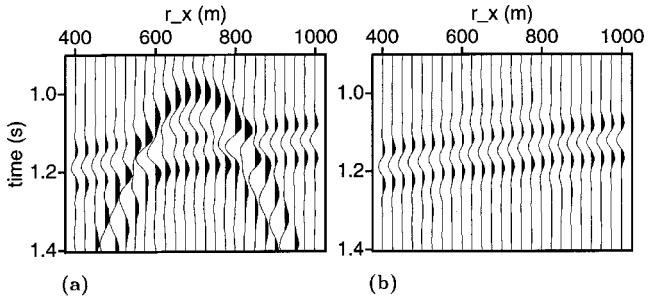

FIG. 7. (a) Part of shot 3 of the synthetic data where a deep reflection has been added. The reflection has a bandwidth of 3–24 Hz, which partially coincides with the bandwidth of the direct wave. This type of noise is of practical importance in our application. (b) The shot record of (a) after estimating the phase slowness field and source waveform, and adaptive subtraction of the direct guided wave. The direct wave can almost be completely removed (indicating that the phase slowness field and source waveform are correct). The deep reflection, however, is hardly affected, resulting in an improvement of the interfering event-to-guided wave ratio in the indicated time-window of 12.6 dB.

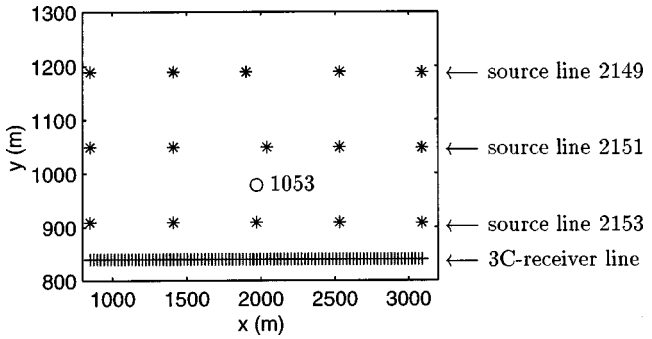

FIG. 8. Geometry for the field data tests. There is one single-station receiver line, denoted by ''+.'' The sources used in the tomography algorithm have been denoted by ''*.'' The shot labeled ''1053'' is used in Fig. 13.

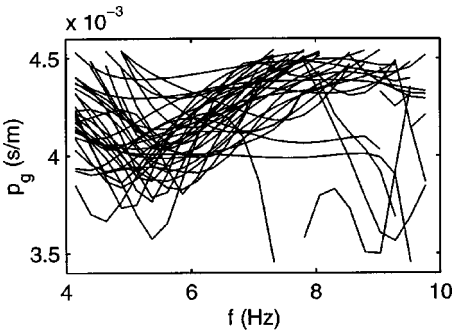

FIG. 9. Generalized traveltimes (divided by offset in order to enable comparisons for different receivers) for a shot in the middle of line 2151 of the PanCanadian data set. Each curve represents the signal of one receiver. The variation with frequency of the generalized traveltimes indicates dispersion. The fact that the curves are not on top of each other suggests lateral variations, whereas outliers could indicate near-field variations and other distortions.

affected, while the direct guided wave has been removed almost completely. The improvement in terms of signal-to-guided-wave ratio around the apex (in the time window from 0.9 to 1.4 s, from $x=400$ m to $x=1000$ m) is 12.6 dB. This is especially important for practical application to 3D seismic data, since the apex of the direct guided wave (which is a hyperbolic event in this case) cannot readily be removed with conventional methods like filtering in the frequency wave number domain.

VII. APPLICATION TO SEISMIC FIELD DATA

A. Introduction

In this section, we apply the method to representative 3D seismic field data, provided by PanCanadian Petroleum. Due to the geometry of sources and receivers, lateral variations of the background model can be reconstructed. This data set is rather complex due to the large amount of lateral variation in the background model and the large amount of attenuation, leading to small amplitudes at later times. Application of our algorithm to this data set serves as an example of how our method should be applied to field data sets.

The acquisition geometry consists of sources on a 70 m×70 m grid. (See Fig. 8.) We use the single-geophone receiver line in the southern part of the area, which has a receiver spacing of 23.3 m (one-third of the grid spacing). The typical frequency range of the guided waves is between 4 and 10 Hz, with a dominant frequency of approximately 7 Hz. We have restricted ourselves to application of our method to the area to the north of the receiver line. Since the record length is 2.5 s, and typical guided-wave velocities are about 250 m/s, there are three source lines (2153, 2151, and 2149, resp.), with distances of 70, 210, and 350 m from the receiver line, where shots have a significant number of traces (recordings) containing the direct guided wave (''ground roll''). Shots from these lines have been used in the background model estimation.

B. Background model estimation

The background model is estimated from the direct guided wave (''ground roll''). In order to extract the direct guided wave from the data, minimum and maximum group velocities have been estimated as $c_{g,\min}=220$ m/s and $c_{g,\max}=300$ m/s. These velocities are used to define a time window as follows:

$$t_{sr,\min}=\|\mathbf{r_h}-\mathbf{s_h}\|/300-0.2 \text{ s}, \tag{28}$$

$$t_{sr,\max}=\|\mathbf{r_h}-\mathbf{s_h}\|/220+0.3 \text{ s}. \tag{29}$$

Everything outside this time window is muted in the background model estimation step.

The near subsurface is usually characterized by a large amount of attenuation. This attenuation is so far not considered in our guided-wave propagation model. Commonly, attenuation of the wave field is described by a quality factor Q.[19] Defining a new constant β as $\beta=(2Qc_{\text{ph}})^{-1}$, the loss due to attenuation can be approximated (using the expression for a homogeneous medium) by

$$L_{sr}=\exp(-\beta\omega\|\mathbf{s_H}-\mathbf{r_H}\|). \tag{30}$$

An estimation for β is computed by fitting the amplitudes of the modeled data to those of the observed data in a least-squares sense. The loss factor is then incorporated in the forward modeling of the direct wave. Of course this procedure can be refined,[24] but this is not considered necessary for our purposes. For this data set, we have first estimated the attenuation coefficient as $\beta=3.99\times10^{-5}$ s/m, which corresponds to a quality factor $Q\sim45$ (using a phase velocity of 280 m/s). This attenuation coefficient is used throughout this section in all Green's function computations.

Since the background model is assumed to vary smoothly, a representative subset of the available shots has been taken for computational purposes. For each receiver line, 5 regularly spaced shots have been used, resulting in a total number of 15 shots for the tomography algorithm. The reconstruction has been carried out in the frequency band from 4 to 10 Hz, and weighing with spectral magnitude has been applied. Figure 9 shows the generalized traveltimes (which have been divided by offset for scaling purposes). Each line corresponds to the signal recorded at one receiver. Only those recordings and frequencies used in the tomography algorithm are shown. We see that the generalized traveltimes of the PanCanadian data set are noisy, since the

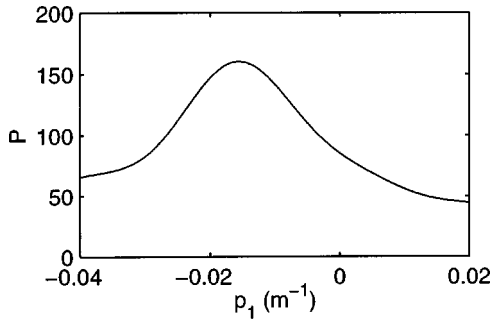

FIG. 10. Semblance of the backpropagated and stacked traces as function of the integration parameter p_1 [defined in Eq. (17)]. A clear maximum at $p_1 = -1.56\times10^{-2}$ can be discerned. This value is used to integrate from group slowness to phase slowness.

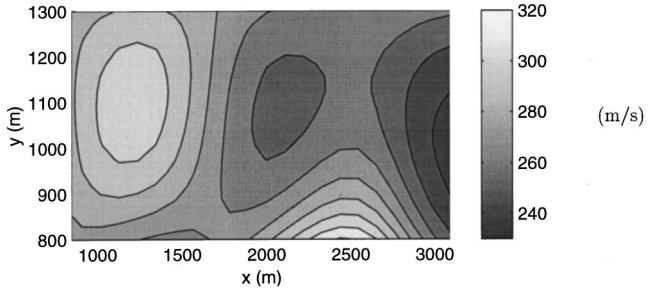

FIG. 11. Reconstructed phase slowness model (in m/s) at the dominant frequency (7 Hz). Dark shades denote low velocities, lighter shades high velocities. The velocity increases in western to northwestern direction. Lateral variations are on the order of 15% to 20%, and distinct low- and high-velocity regions can be discerned.

curves are spread out over a wide range. This might indicate lateral variation, but also near-field heterogeneities or the presence of interfering events.

A stepwise reconstruction of the background model is now carried out. First, an invariant dispersive background model is reconstructed. The display of the generalized traveltimes indicates a clear presence of dispersion. We use a parabolic representation of the dispersion curve. Reconstruction of an invariant dispersive model results in a dispersion curve where group velocities range from 257 m/s at 4 Hz to 233 m/s at 10 Hz. Using the invariant model as a starting model and as *a priori* information in the regularized inversion [Eq. (9)], a laterally varying model is reconstructed. From numerical tests we found that taking $\sigma^2 = 10^{4.5}$ provides a good trade-off between data fit and smoothness of the background model. Since source and receiver lines are parallel, the average ray direction is north–south, and therefore we expect better resolution in the east–west direction than in the north-south direction. Various numerical tests on this data set showed that taking four cells in the east–west direction was enough to handle inline lateral variations. Since we have only three source lines, we only use one cell in the north–south direction. Because no explicit boundary conditions are imposed, we have four degrees of freedom (cubic profile) in the crossline direction, and seven degrees of freedom (cubic profile in each cell) in the inline direction.

Now that the group slowness has been reconstructed using generalized traveltime inversion, the parameter p_1 has to be found to be able to integrate from group slowness to phase slowness. The total semblance [Eq. (17)] of the backpropagated and stacked traces has a clear maximum at $p_1 = -1.56\times10^{-2}$ (see also Fig. 10).

The reconstructed phase slowness is a function of three parameters: the lateral coordinates x and y, and frequency ω. Dispersion is approximately 20% over the frequency band of interest. The phase velocity is around 40 m/s higher than the group velocity. In Fig. 11, the phase slowness has been plotted for the dominant frequency of 7 Hz. The velocity generally increases in the western to northwestern direction. Lateral variations are on the order of 25%, and distinct low- and high-velocity regions can be discerned.

In Fig. 12, the terrain elevation of the area of interest is shown. Since at each source and receiver location elevation data is available, the topography can be resolved in much greater detail than the background model phase velocity. To compare quantities on the same scale, we have filtered the elevation data to have a similar spatial bandwidth for both phase velocity and elevation. Comparing Figs. 11 and 12, an interesting similarity between phase velocity and elevation is visible: Both variables decrease toward the east, with a local maximum in the southeastern part near the receiver line, and a local minimum in the middle. This correlation between phase velocity and terrain elevation can be expected, and might be caused by a variety of reasons: A near-surface geology consisting of a layer of varying thickness over a more or less horizontal layer structure, density variations, or other variations in shallow subsurface conditions. These results indicate that it might be possible to reconstruct specific geologic features using guided-wave tomography. In any case, the positive correlation between phase velocity and elevation increases the confidence in the reconstructed background model, since the elevation data have not been used during the phase velocity estimation.

C. Source estimation and direct wave modeling

Once the optimal estimate for the phase slowness has been found, the source waveforms can be found (for each shot record separately) by averaging the backpropagated traces [Eq. (19)]. Note that this can also be done for shots not

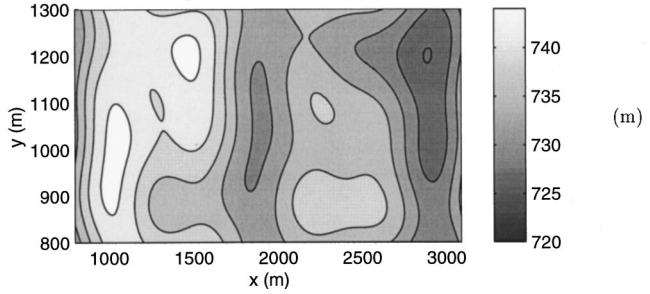

FIG. 12. Terrain elevation (in meters above sea-level) in the area of interest. In order to make a good comparison with the phase velocity field of Fig. 11, the topography has been filtered to obtain a comparable spatial bandwidth as the phase velocity model, using maximum wavenumbers of $k_x = 2\times10^{-3}\ \mathrm{m}^{-1}$ (x direction) and $k_y = 5\times10^{-3}\ \mathrm{m}^{-1}$ (y direction), respectively. A clear similarity between the reconstructed phase velocity of Fig. 11 and the elevation can be discerned. Since the topography information is not used in the phase velocity estimation procedure, this increases the confidence in the reconstruction.

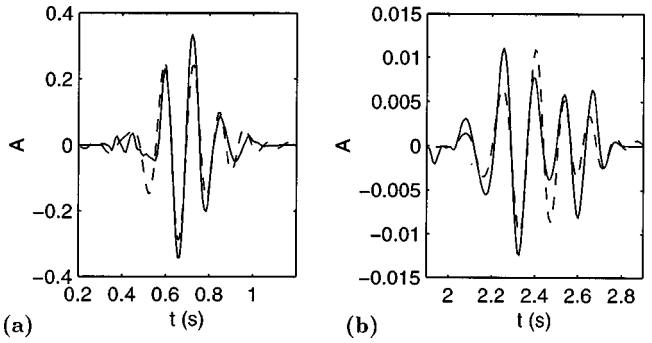

FIG. 13. Observed (solid) and modeled (dashed) signal at two receivers at distances from the source of (a) 146.5 m and (b) 577.0 m, respectively. The dispersion becomes clear from the spreading of the waveform. The correlation between observed and modeled data is 0.922 and 0.871, respectively.

used in the tomography algorithm. Subsequently, the direct wave can be computed using the estimated source waveform, the reconstructed phase slowness model, and the estimated attenuation factor [Eqs. (20) and (30)]. In Fig. 13, we have displayed modeled and observed traces at different offsets. The dispersive character is illustrated by the spreading of the waveform for larger offsets. Note also the good correlation (above 0.85) between the observed and modeled traces. The differences are mainly caused by interfering waves due to higher modes.

VIII. SUMMARY AND CONCLUSION

In this paper, we have discussed a tomographic algorithm for the reconstruction of a dispersive, laterally varying velocity field. This method can be used to reconstruct the phase velocity of a single guided mode in a laterally varying, layered medium. In contrast to conventional traveltime-based methods, dispersion is explicitly accounted for.

The kinematic behavior of the wave field is the most reliable source of information. Therefore reconstruction of the kinematic aspects forms the basis of our reconstruction algorithm. To simulate the kinematic aspects of guided-wave propagation, the only parameter we need to reconstruct is the phase slowness. The reconstruction of the phase slowness from the direct guided wave is a tomographic problem, since the slowness field is reconstructed from waves propagating through it. To define an optimal model, a traveltime norm is used, minimizing the difference between traveltimes of observed and modeled data. To handle the dispersion of the traveltimes for guided waves, we use generalized traveltimes which are based on the phase of the wave field. For reasons of robustness and uniqueness, these generalized traveltimes are taken as group traveltimes instead of phase traveltimes. This introduces a nontrivial null space into the error norm: the group slowness can be reconstructed, but the phase slowness has an ambiguity inversely proportional to frequency. This ambiguity can be resolved by choosing the null-space parameter such as to maximize the semblance of the backpropagated wave field (i.e., the traces deconvolved with the Green's function).

Once the slowness is estimated, an effective source waveform can be defined by averaging the backpropagated traces. This effective source waveform comprises the actual source waveform, as well as the modal functions at source and receiver locations. This is not a major drawback, since for weak lateral variations the shot-to-shot variations dominate variations in the receiver response.

The error norm is minimized by a conjugate–gradient method. Since the generalized traveltimes are nearly linear in the slowness parameters, the error surface is smooth, making the problem amenable to an iterative solution strategy.

We have tested the method on synthetic (numerically simulated) data, and found that we were able to estimate the slowness, also for noisy data, to approximately 1% accuracy. The algorithm was shown to be robust in the presence of additive noise (in the form of interfering events). For the latter example, the estimated wave field was subtracted from the original data, resulting in a large improvement of signal-to-noise ratio (the ''signal'' being the interfering event whereas the ''noise'' was the direct guided wave).

We have also applied our tomography algorithm to a seismic field data set. This data set, a 3D data set provided by PanCanadian, has a complex near-surface structure with significant lateral variation. Due to the 3D data acquisition geometry, a complete near-surface phase velocity model can be estimated. We have found this phase velocity field to be strongly varying. Furthermore, it correlates well with the terrain elevation. This increases the confidence in the reconstructed background model, since the topography data is independent information, not used in the inversion. This indicates that the background model reconstructed for 3D data sets such as the PanCanadian data set might thus also be used to obtain information about the near-surface geology.

This algorithm has primarily been developed to be able to model direct and scattered guided seismic waves in near-surface layers of the earth. The phase slowness and source waveform as estimated by our algorithm are sufficient to completely model propagation of these waves.[12] However, the reconstructed dispersion curves might also be used for other purposes, for example to invert the dispersion relation for the layer parameters. This is, for instance, of interest in global seismology[1] and geotechnical applications.[2]

ACKNOWLEDGMENTS

This research has been supported financially by the Dutch Technology Foundation STW and Shell Research. The seismic data have been provided by PanCanadian Petroleum.

[1] J. Dorman and M. Ewing, ''Numerical inversion of seismic surface wave dispersion data and crust-mantle structure in the New York-Pennsylvanian area,'' J. Geophys. Res. **67**, 5227–5241 (1962).
[2] D. Yuan and S. Nazarian, ''Automated surface wave method: inversion technique,'' Geotech. Eng. **119**, 1112–1126 (1993).
[3] J. H. Woodhouse and A. M. Dziewonski, ''Mapping the upper mantle: Three-dimensional modelling of earth structure by inversion of seismic waveforms,'' J. Geophys. Res. **89**, 5953–5986 (1984).
[4] R. Snieder, ''Large scale waveform inversions of surface waves for lateral heterogeneity—I: Theory and numerical examples,'' J. Geophys. Res. **93**, 12055–12065 (1988).
[5] K. Hsu and C. Esmersoy, ''Parametric estimation of phase and group slownesses from sonic logging waveforms,'' Geophysics **57**, 978–985 (1992).
[6] E. C. Shang, ''Ocean acoustic tomography based on adiabatic mode theory,'' J. Acoust. Soc. Am. **85**, 1531–1537 (1989).

[7] W. H. Munk, *Ocean Acoustic Tomography* (Cambridge U.P., Cambridge, 1995).
[8] N. D. Bregman, R. C. Bailey, and C. H. Chapman, ''Crosshole seismic tomography,'' Geophysics **54**, 200–215 (1989).
[9] G. C. Herman, ''Generalization of traveltime inversion,'' Geophysics **57**, 9–14 (1992).
[10] W. J. F. van Geloven and G. C. Herman, ''Crosswell tomography using generalized traveltime inversion,'' in *Expanded Abstracts SEG 65th Ann. Mtg.*, Houston, 1995, edited by J. R. Sumner, Soc. Expl. Geophys.
[11] J. C. M. Goudswaard, A. P. E. ten Kroode, R. K. Snieder, and A. R. Verdel, ''Detection of lateral velocity contrasts by crosswell traveltime tomography,'' Geophysics **63**, 523–533 (1998).
[12] F. E. Ernst and G. C. Herman, ''Removal of guided waves from seismic data in laterally varying media,'' Wave Motion **28**, 173–189 (1998).
[13] A. D. Pierce, ''Extension of the method of normal modes to sound propagation in an almost stratified medium,'' J. Acoust. Soc. Am. **37**, 19–27 (1965).
[14] B. L. N. Kennett, ''Guided wave propagation in laterally varying media —I. Theoretical development,'' Geophys. J. R. Astron. Soc. **79**, 235–255 (1984).
[15] Y. Desaubies, C. S. Chiu, and J. H. Miller, ''Acoustic mode propagation in a range-dependent ocean,'' J. Acoust. Soc. Am. **80**, 1148–1160 (1986).
[16] H. Weinberg and R. Burridge, ''Horizontal ray theory for ocean acoustics,'' J. Acoust. Soc. Am. **55**, 63–79 (1974).
[17] E. Poggiagliolmi, A. J. Berkhout, and M. M. Boone, ''Phase unwrapping, possibilities and limitations,'' Geophys. Prospecting **30**, 281–291 (1982).
[18] J. M. Ortega and W. C. Rheinboldt, *Iterative Solution of Nonlinear Equations in Several Variables* (Academic, New York, 1970).
[19] R. E. Sheriff and L. P. Geldart, *Exploration Seismology* (Cambridge U.P., Cambridge, 1995).
[20] J. W. Rector and J. K. Washbourne, ''Characterization of resolution and uniqueness in cross-well direct-arrival tomography using the Fourier slice theorem,'' Geophysics **59**, 1642–1649 (1994).
[21] K. Hokstad, M. Landro, and R. Mittet, ''Estimation of effective source signatures from marine VSP data,'' Geophys. Prospecting **44**, 179–196 (1996).
[22] F. E. Ernst and G. C. Herman, ''A generalized traveltime method for estimating a laterally varying dispersive velocity field,'' in *Theoretical and Computational Acoustics '97*, Singapore, 1998, edited by Y. C. Teng, E. C. Shang, Y. H. Pao, M. H. Schultz, and A. D. Pierce (World Scientific, Singapore, 2000), pp. 91–101.
[23] R. K. Snieder and M. Sambridge, ''Ray perturbation theory for traveltimes and ray-paths in 3-D heterogeneous media,'' Geophys. J. Int. **109**, 294–322 (1992).
[24] A. Ribodetti and J. Virieux, ''Asymptotic theory for imaging the attenuation factor *Q*,'' Geophysics **63**, 1767–1778 (1998).

Experimental study of the liquid flow near a single sonoluminescent bubble

Tanguy Verraes, Françoise Lepoint-Mullie, and Thierry Lepoint
Institut Meurice, 1, Avenue E. Gryzon, 1070, Bruxelles, Belgium

Michael S. Longuet-Higgins
Institute for Nonlinear Science, University of California, San Diego, La Jolla, California 92093-0402

(Received 20 October 1999; accepted for publication 3 April 2000)

Tracers (sulphur particles produced *in situ* by a bubble itself, fuchsin spots and dust) were used to probe the liquid flows in the neighborhood of single sonoluminescent bubbles maintained in levitation in a resonant acoustic setup. The flows caused by the bubble were distinguished clearly from the streamings (mean Lagrangian velocity: ~ 20 μm/s) associated with resonant cells in the absence of a bubble. The liquid flow due to the presence of the bubble formed around it over a few mm. The radial component of the Lagrangian velocities (maximum value measured: ~ 260 μm/s) of this flow evolved as r^{-1}, with r as the distance from the bubble, while the tangential component remained approximately constant (~ 20 μm/s). In the Appendix by M. S. Longuet-Higgins, a simplified model of microstreaming involving a spherical bubble in translational and radial oscillation gives a qualitative description of the experiments. A fairly good agreement was observed between the experiments and the modeling, which involved a dipole flow enclosed in a Stokeslet. © *2000 Acoustical Society of America.* [S0001-4966(00)03207-0]

PACS numbers: 43.35.Sx [HEB]

INTRODUCTION

This paper deals with the microstreaming activity of a single levitating bubble driven acoustically in the sonoluminescing mode. The reasons for the choice of this particular mode are developed below.

From a general point of view, microstreaming (Coakley and Nyborg, 1978) is a *rectified* component of an oscillating fluid motion which arises especially near a solid, or near other boundaries such as the surface of a gas bubble in a liquid (see, for example, Davison and Riley, 1971; Longuet-Higgins, 1998; see also Wu and Du, 1997). The presence of a sharp boundary induces an additional oscillatory component of the field of velocity in a thin boundary layer, whose thickness L_m is of the order $(2\mu/\rho\omega)^{1/2}$, where μ, ρ and ω are the shear viscosity, the density and the radian frequency of the oscillation, respectively. Also, there is *microstreaming*, an additional steady or rectified component of the velocity which extends much further into the fluid, in fact, as far as radial distance r (with respect to the bubble), which may be large when compared to both L_m and the equilibrium radius of the bubble. Therein lies its usefulness as a diagnostic tool since the bubble itself may be too small to observe directly.

The type of streaming referred to should not be confused with the *acoustic streaming* in the body of a fluid. This streaming arises from the spatial attenuation of a sound wave (Lighthill, 1978; see also Nyborg, 1953; Starritt *et al.*, 1989).

Microstreaming is known to be significant in heat and mass transfers towards the environment. As emphasized by Eller (1969), rectified diffusion is enhanced by microstreaming because of the convection of the dissolved gas. Considerable attention is paid to microstreaming in biological systems (for a review see Leighton, 1994). Moreover, in sonochemistry streaming around a bubble enhances reactant transport, (perhaps) the erosion of solids (Elder *et al.*, 1954) and electrodeposition (Yaeger and Hovorka, 1953), etc.

Apart from theoretical investigations into microstreaming associated with the presence of rigid bodies in a sound field (Nyborg, 1958, 1965; Stuart, 1966; Riley, 1967; Wang and Lee, 1990; and associated references), there are two groups of studies on bubbles, i.e., isolated bubbles far from, or close to, boundaries. The latter case was studied by Nyborg (1958) and Elder (1959). One of the most advanced theoretical investigations associated with a bubble distant from a boundary was carried out by Longuet-Higgins (1998) and looks into the case of an isolated bubble in transverse and radial nonlinear oscillation in a viscous, incompressible liquid. The inertia of the internal gas was neglected. In order to obtain analytical solutions, Longuet-Higgins limited his analysis to the case where the oscillatory radial and translational motion displacements were small compared to the bubble radius.

In the present paper we report experimental measurements of the flow of liquid around a single acoustically driven bubble. As defined by Gaitan *et al.* (1992), such a system may exist in four modes (dancing, shuttlecock, stable nonluminescent and stable luminescent). We focused our attention on single sonoluminescent bubbles even though we noted microstreaming in the shuttlecock and stable nonsonoluminescing modes (to a lesser extent, however). The reasons for this choice are (*i*) single bubble sonoluminescence (SL) is extensively studied, so that this work is a supplement to current data. (*ii*) A single sonoluminescent bubbles offers the best opportunity for modeling microstreaming when compared to the shuttlecock system, which is the other mode involving significant chemical activity. (*iii*) Another objective was to increase our knowledge of a recent

analysis of the ''SL/sonochemistry (SC)/bubble dynamics'' correlation in the case of single bubbles (Lepoint *et al.*, 1999). (*iv*) Finally, in relation to this latter study, it appears necessary to understand the reason(s) why *filaments* of colored chemical species are observed in single bubble sonochemistry experiments. Indeed most models describe spherical bubbles with purely radial oscillations. Chemical particles released by such a purely radially oscillating bubble would be expected to evolve as a halo. In the single bubble sonochemistry experiment so evoked, an air bubble driven in the SL regime (for example) is trapped at the antinode of a resonant cell containing an aqueous solution of CCl_4, KI and starch. The chemical sequence consists of the intracavity decomposition of CCl_4 into $Cl(\cdot)$ radicals which are transferred to the surrounding liquid and oxidize I^- into iodine. A single weak blue thread originates at the bubble so indicating that iodine complexes with starch. This filament forms in a direction that is likely to change (upwards or downwards) during the experiment. The origin of this change remains undetermined. The time taken for a filament to form over a few mm is $\sim$1 min. This picture is very similar to what is illustrated in Fig. 4 of the present paper (the production of colloidal sulphur by a single sonoluminescing bubble).

In this investigation we used three types of tracers: (*i*) chemical tracers released by a bubble itself (sulphur particles arising from the intracavity decomposition of CS_2 dissolved in an air/water solution), (*ii*) dust particles in suspension and (*iii*) fuchsin spots introduced into a resonant cell by means of a syringe. The motion of both the streaks in the colloidal sulphur and the small dust particles in suspension led to the determination of the field of Lagrangian velocities for particles in the vicinity ($\sim$3 mm) of a sonoluminescent bubble. This work was carried out with a home-made cell (cell 2). Moreover, in home-made cell 1 we investigated the behavior of the liquid by following the drift motion of fuchsin spots released in the neighborhood of a bubble. We extract the main quantitative results in the discussion.

A simplified model giving a qualitative explanation of the experimental observations is reported in the Appendix, which has been developed by M. S. Longuet-Higgins. This model takes into consideration a velocity field such as the one obtained in a preceding theoretical analysis (i.e., a dipole+a viscous Stokeslet flow) and a cloud of suspended particles simulating the dye spots sinking at a vertical velocity relative to the neighboring fluid.

I. EXPERIMENT

The experimental setup using fuchsin as a tracer involved home-made cell 1 (volume: 30 ml; the distance between the two PZT transducers glued laterally and face to face: 37 mm; resonance frequency: 43.1 kHz) driven by a Biosonic GPUS 100 W generator (applied voltage: $18<V<21$ V). The *Oy* axis defined in Fig. 1 was the line of sight of a CCD camera with an additional lens. The time between two consecutive injections of fuchsin by means of a syringe was $\sim$10 min. Home-made cell 2 was also employed (frequency: 42.8 kHz; with dust and/or sulphur particles as tracers) with a Leica MS5 stereomicroscope. The field of observation is specified in the text, and the sketches are associated with photographs obtained via videotapes. In the case of the direct photographic record, the field of observation was 4×2.7 mm^2. The cells placed in a room at $T=24\pm2$ °C were illuminated by cold light. Each experiment was carried out at ambient pressure. In the second set of experiments the line of sight was the *Oz* axis (top view experiments). In all the experiments the amount of O_2 associated with dissolved air was 2 to 3 mg/L (Consort Z-800 oxymeter). In determining the field of Lagrangian velocities, the real distances from the TV screen were obtained by using as a reference either the diameter of the cell or the external diameter of the syringe used for the dye injection. The fuchsin solution had a concentration of 5.74×10^{-3} M, a specific mass of 1001.2 kg/m^3, and a dynamic viscosity (μ measured by running a solution through a capillary—Cannon-Fenkse viscosimeter—or by a rotative viscometer—Viscolab® FP10 with a drum MS-23 DIN from Physica) equal to 0.95×10^{-3} $k\mathrm{g\,m^{-1}\,s^{-1}}$. The diameter of the syringe needle was 0.46 ± 0.01 mm (injected volume ~0.05 μL). The CS_2 solution was prepared by adding 3.8 ml of a saturated aqueous Cs_2 solution (kept in a vacuum) to 26.2 ml of degassed demineralized water.

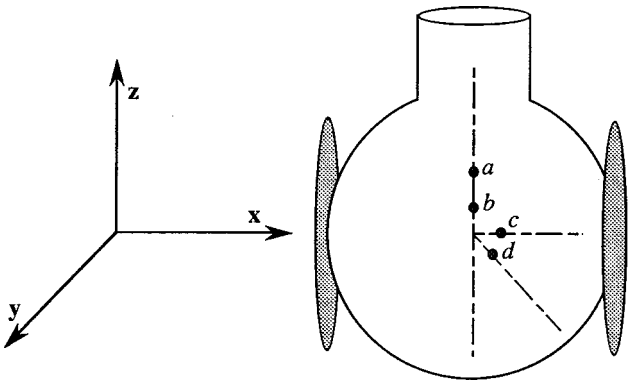

FIG. 1. Representation of the various sites where fuchsin spots were released (cell 1). The spots were injected as closely as possible to the vertical *Oxz* plane intersecting a levitating bubble. The line of site is the *Oy* axis.

II. RESULTS

In all the descriptions below a levitating bubble is considered as the (0,0,0) point of a Cartesian referential system (Fig. 1).

A. Fuchsin as tracer

Two experiments were carried out on cell 1 in order to determine the intrinsic response of the liquid in the cell when ultrasound was applied (global streaming due to thermal gradients and/or acoustic streaming). In the first case (without either a bubble or ultrasound) a spot of fuchsin was released near the center of the resonant cell. The spot fell vertically, without any observable deviation in relation to the *Oz* axis [mean fall velocity over five experiments: 180 μm/s ($\pm15\%$)]. In the second case (without a bubble), the ultrasound field was applied at such an intensity that if a bubble were introduced, it would luminesce. When a spot of dye was released, it fell and drifted slightly but systematically in the same direction, so that the lateral difference in relation to

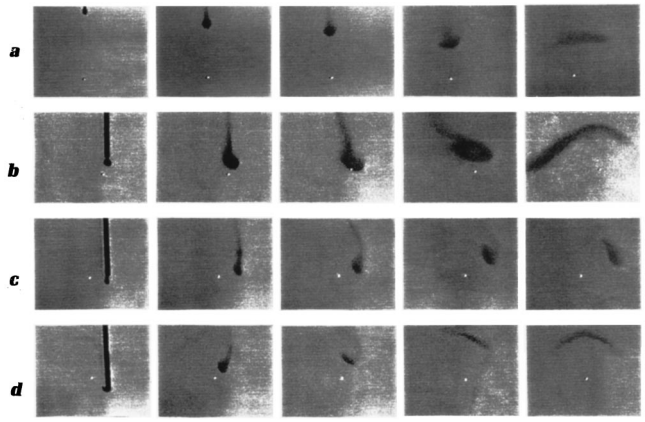

FIG. 2. (a) Sketch of the trace left by fuchsin when released 6 mm above a bubble on the vertical *Oz* axis; (b) same as (a), but the dye was released about 1 mm; (c) same as (a), but with the dye released 1.5 mm from the bubble on the *Ox* axis; (d) same as (a), but with the fuchsin spot released 2 mm from the bubble on an axis forming an angle of ~135° to the *Oz* axis (cell 1; line of sight: *Oy* axis).

the *Oz* axis was between 5 to 10 mm at the bottom of the cell. The mean fall velocity over five experiments was 110 μ m/s (±30%). These fall velocities were determined over 15 mm.

Several injections of dye were carried out at various positions around a sonoluminescing bubble [denoted *a, b, c* and *d*] as indicated in Fig. 1, with these positions as close as possible to the vertical *Oxz* plane. The response of these ''sonoluminescing bubble/fuchsine spots'' systems is outlined in Fig. 2. In Fig. 2(a), a fuchsin spot released ~6 mm above a bubble fell to a distance of ~3 mm above it. It then spread so as to generate a cap maintained in levitation. In Fig. 2(b), a drop of fuchsin solution was released 1 mm directly above a bubble. The dye was repelled upwards at a mean velocity of ~50 μm/s estimated over 45 s of observation. Its upward progression was stopped when it reached a vertical distance of 3.5 mm from the bubble and, again, a cap formed. In Fig. 2(c) the fuchsin spot—released at 1.5 mm to the side of the bubble and along the *Ox* axis—was repelled upward and laterally. However, we noted that with an injection at a distance greater than 3 mm along the *Ox* axis, the fuchsin spots came under the effects of gravity without being disturbed by the presence of the luminescing body. In Fig. 2(d), a fuchsin spot was injected 2 mm from the bubble at the level of the *Oxz* plane on an axis forming an angle of about 135 degrees to the *Oz* axis. As shown in Fig. 2(d), the dye was ''sucked up.'' With too remote injections (distances >3 mm from the bubble), the fuchsin drop came under the effects of gravity.

In an alternative experiment we reversed the injection sequence. A fuchsin spot was first released and reached the central zone of the cell within 10 s or so. A small air bubble injected at the top of the reactor was trapped in the spot. We did not record any significant difference when using the usual injection procedure. The dye was immediately repelled upwards (Fig. 3).

Qualitatively, with cell 2 we observed the same results as those described above. However, we noted that, in the presence of a bubble, the direction of repulsion was different

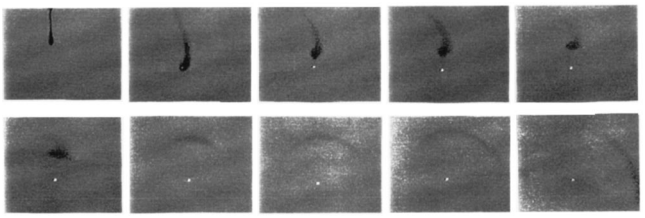

FIG. 3. Drift motion of a dye spot within which a sonoluminescing bubble was enclosed (cell 1; line of sight: *Oy* axis).

from what was observed in cell 1. The dye was repelled backwards and the cap formed at ~2 mm. This was confirmed with sulphur particles and dust as tracers. We attributed the differences in cell response to manual glass blowing and the imperfect adhesion of the PZT, which might well have induced a nonrepeatable distribution of the sound field.

B. Sulphur particles and dust as tracers

In Weissler's reaction studied by Lepoint *et al.* (1999), the contrast between the ''starch–iodine'' complex and the solution is not strong enough for visualization via a stereomicroscope. Arguing that volatile compounds present in a bubble are pyrolyzed during its violent collapse (Suslick, 1988; Henglein, 1993) and that CS_2 (vapor pressure: 370 mm Hg at 24 °C) is known to undergo reactions in the presence of O_2 and air, we investigated the behavior of a bubble levitating in a 4.8×10^{-3} M CS_2 aqueous solution.

We observed single bubble sonochemistry for the non-luminescing shuttlecock, and the stable non-luminescing and stable luminescing modes. Figure 4 shows the cloud of sulphur particles associated with a luminescing bubble (the oblong spot was caused by the translational motion of the bubble over ~200 μm during exposure; frequency of motion: 4 Hz). The sulphur cloud formed towards the rear of cell 2 and in the close vicinity of the *Oxy* plane. A typical observation (recording the top view) was as follows. The field of observation was 3.2×2.5 mm^2. Without a bubble (but with the acoustic field activated) the flow of dust naturally in suspension in the liquid was directed more or less towards the *Oxy* plane, as indicated in Fig. 5(a). The mean velocity of the dust was ~20±8 μm/s over a distance of 1.5 mm in the case of the particles remaining in the focal zone.

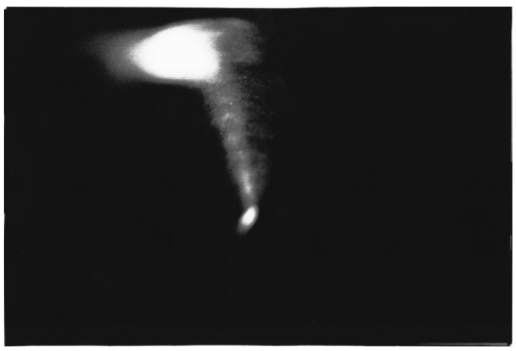

FIG. 4. Development of a cloud of sulphur particles (intracavity decomposition of CS_2). The distance of translation is ~200 μm, and the frequency of to and fro motion is 4 Hz). The field of observation was 4 mm×2.7 mm; (cell 2; line of sight: *Oz* axis).

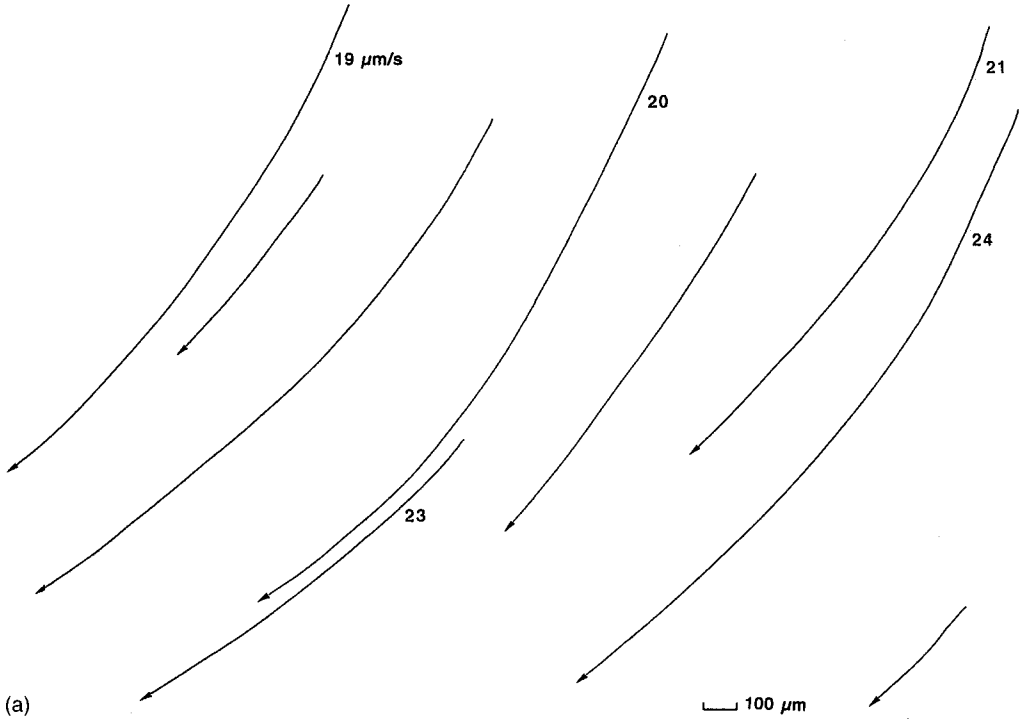

FIG. 5. (a) Liquid flows (with dust as tracers) in cell 2 without bubbles but with ultrasound. Arrows represent velocity vectors (μm/s). The zone of observation was 3.2 mm$\times$2.5 mm (line of sight: *Oz* axis). (b) Tracer flows (dust and sulphur particles) with a sonoluminescing bubble. Arrows represents Lagrangian velocitiy vectors (μm/s). The same conditions of observation as in (a).

When a bubble was introduced at the top of the reactor in order to limit disturbances in the field of observation, it was trapped at the center of the cell. A cloud of sulphur formed almost instantaneously and the dust flow changed immediately in both direction and velocity, following the flow of the sulphur particles. Figure 5(b) gives the field of Lagrangian velocities for chemical and dust particles. These measurements were carried out each 100 μm. In the case of the sulphur cloud, we followed the motion of the streaks on a TV screen; these can be seen in Fig. 4.

III. DISCUSSION

The first point to be emphasized is that the flow caused by a bubble in its neighborhood (over a few mm) can be distinguished unambiguously from the streamings intrinsic to the cells, i.e., global and/or acoustic streamings, the latter resulting from sound wave attenuation. From experiments it appears that global streaming due to thermal gradients is negligible. Indeed in the ''no bubble/no ultrasound'' experiments the fall of the fuchsin spots obeyed Rybczynski–Hadamard's law [Eq. (1)] (Levich, 1962) and was not therefore impeded by side flows:

$$v=\frac{2g(\rho-\rho_w)\alpha^2}{3\mu_w}\,\frac{\mu_w+\mu}{2\mu_w+3\mu}. \tag{1}$$

In this equation, v represents the fall velocity, g is the gravity constant, α is the radius of the drop, and ρ and μ are the density and viscosity, respectively. The subscript w denotes quantities related to water. Strictly speaking, Rybczynski–Hadamard's law describes the fall of a liquid drop in a liquid medium, when the fluids are immiscible. The short time of the experiments makes the diffusion of a fuchsin spot in water negligible, so that in a first approximation, Eq. (1) can be extended to our situation. Assuming a spherical spot ($\alpha=2.285\times10^{-4}$ m) with ρ and μ determined as indicated in Sec. I, we can in fact check that for an injected volume (0.05 ml) of fuchsin, the theoretical value of v was 165 μm/s. An experimental value of v determined over 15 mm was 180($\pm$30) μm/s (see the first part of Sec. II A).

The second point concerns acoustic streaming. In the case of cell 1 and under the effect of an acoustic field, we compared the velocity vectors associated with the fall of dye spots in both the presence (50 μm/s) and the absence of a bubble (100 μm/s). The measurements were carried out over 2 mm and therefore exhibited some difference from the values obtained over 15 mm. We found that the mean velocity due to acoustic streaming was $\sim$56 μm/s, with the vector oriented at $\sim$160 degrees in relation to the *Oz* axis.

Third, from data obtained with fuchsin as a tracer we deduced the radial and tangential components (with respect to the *Oz* axis) as a function of the distance from a bubble (Fig. 6). The radial component evolves as r^{-1}, while the tangential component appears to be approximately constant (at least in the zone investigated).

Concerning the dye repelling mechanism, the possibility may be excluded that the momentum carried by diverging shock waves (rapidly transformed into an acoustic wave) released on collapse in the liquid (Holzfuss *et al.*, 1998; Wang *et al.*, 1999) is high enough to induce the motion of the dye spots. If this were the case, one would expect (*i*) the fuchsin spot released in zones *c* and *d* (see Fig. 1) to be displaced laterally or towards the southeastern sector of Figs. 2(c) and 2(d), respectively; and (*ii*) the fuchsin spot enclosing a

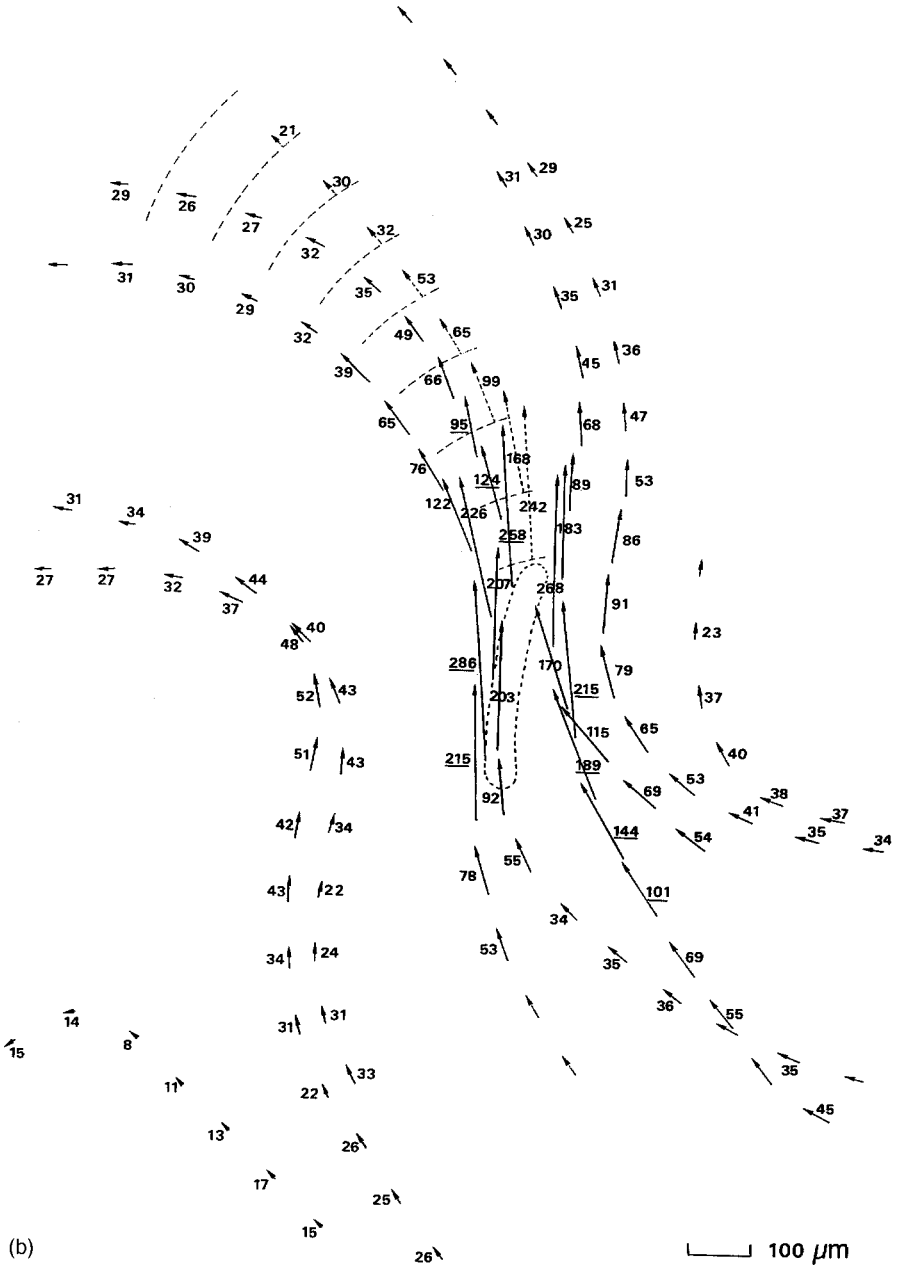

FIG. 5. (*Continued.*)

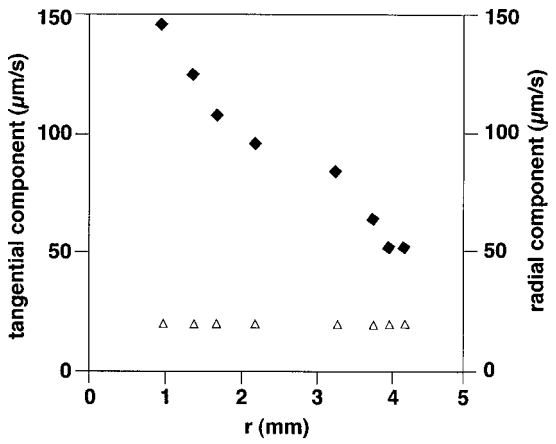

FIG. 6. Evolution of the radial (squares) and tangential (triangles) components of the mean velocity vector (the case of cell 1; line of sight: *Oy* axis).

sonoluminescent bubble (Fig. 3) to spread in the form of a halo. The experimental data in Figs. 2(c), 2(d), and 3 invalidate this hypothesis.

The experimental observations associated with the motion of fuchsin spots, dust and sulphur particles can be understood qualitatively by assuming that a dipolar flow forms around a bubble. In the Appendix to the paper a simplified model describes typical experiments with fuchsin spots. This model by Longuet-Higgins is based on a recent description of the Lagrangian streamfunction associated with a spherical bubble undergoing small radial and translational oscillations simultaneously (Longuet-Higgins, 1998). In the Appendix the effect of gravity is superimposed on the radial and tangential velocities corresponding to this Lagrangian streamfunction [first part of Eqs. (A1) and (A2)]. In these equations the terms in $(a/r)^3$ and (a/r) represent a dipole and a viscous ''Stokeslet'' flow (a is the radius of the bubble), respectively.

The pattern observed in Fig. 5(b) can be understood as the combination of the flow due to the streaming intrinsic to cell 2 [Fig. 5(a)] and the radial velocity vectors associated with an idealized dipolar flow represented schematically in Fig. A1 (in connection with the Appendix). Since the radial component of flow velocity decreases with increasing distance from a bubble, the resulting vector, which involves the streaming intrinsic to cells, tilts progressively.

It must be noted that the model developed in the Appendix applies to a zone which surrounds a bubble and which is well beyond the oscillatory boundary layer of thickness (L_m). In the case of a bubble of mean radius 10 μm, which is likely to be encountered in levitation experiments, $L_m \sim 3$ μm $[(2\mu/\rho\omega)^{1/2}$ with $\rho = 10^3$ kg m^{-3}; $\mu = 10^{-3}$ kg m^{-1} s^{-1}, acoustic frequency: 43×10^3 s$^{-1}]$. The shear stress accompanying the existence of this layer can be estimated via Eq. (2) of Coakley and Nyborg (1978):

$$\xi = \frac{\mu\omega\Delta'^2}{R_0 L_m}, \tag{2}$$

where Δ' and R_0 are the amplitudes of the radial displacement and the equilibrium radius of the bubble. Assuming $R_0 \sim 5\mu$m and $\Delta' = 10R_0$, $\xi \sim 36\times10^3$ Nm^{-2} and the velocity gradient is as high as 36×10^6 s^{-1}. These results can be compared with values calculated by Coakley and Nyborg in the typical case of a 5-μm radius bubble with wall amplitude$=0.5$ μm in a 1-MHz acoustic field, i.e., $\xi \sim 560$ Nm^{-2} and a velocity gradient of 5.5×10^5 s^{-1}.

Any quantitative analysis of the radial (u_r) and tangential (u_θ) velocities [such as given in their dimensional form in Eqs. (3) and (4)] in the zone described by Longuet-Higgins' (1998) model is strictly confined to small-amplitude radial and lateral displacements. [Equations (3) and (4) represent the (appropriate) Lagrangian microstreaming velocities. It will be noted that the corresponding Eulerian mean flow, also given in Longuet-Higgins (1998), is fully consistent with the field equations for the Eulerian mean flow at large distances r, as given by Davison and Riley (1971). In this respect the flow differs from the form suggested by Wu and Du (1997) equation (28), which is inconsistent with Davison and Riley's equations.] We have

$$u_r = \varepsilon\varepsilon' a\omega \sin\phi \left[-\frac{a}{r} + \frac{1}{2}\frac{a^3}{r^3} + \frac{1}{2}\frac{a^6}{r^6} \right] \cos\theta, \tag{3}$$

$$u_\theta = \varepsilon\varepsilon' a\omega \sin\phi \left[\frac{1}{2}\frac{a}{r} + \frac{1}{4}\frac{a^3}{r^3} + \frac{a^6}{r^6} \right] \sin\theta. \tag{4}$$

In this set of equations r is the distance to the center of the bubble and $a = R_0$, the mean bubble radius; ω is the characteristic frequency of oscillation (i.e., the acoustic frequency); $\varepsilon = \Delta/a$ and $\varepsilon' = \Delta'/a$, where Δ and Δ' are the lateral and radial displacement, respectively; ϕ is the phase difference between the radial and transverse oscillations, and θ the polar angle. The axisymmetric function [ψ in Longuet-Higgins' (1998) paper] with which u_r and u_θ are associated was developed in a series expansion in powers of ε and ε' in order to couple the radial and transverse oscillations. For ε and $\varepsilon' \ll 1$ it was possible to stop the expansion to the second-order terms (in $\varepsilon^2, \varepsilon\varepsilon', \varepsilon'^2$). As emphasized by Longuet-Higgins, ε' cannot be of the order of 1 or higher.

Some future theoretical developments are thus necessary for the large-scale radial and lateral displacements encountered in sonoluminescence experiments such as in this paper. In this sense, the determination of the Lagrangian velocities [Fig. 5(b)] is of prime importance. Indeed, any further theoretical modeling will have to be consistent with these data.

IV. CONCLUSION

In conclusion, (1) the experiments reported in this paper show the general character of both single bubble sonochemistry and the properties of streaming in the neighborhood of a single levitating bubble. This streaming causes anisotropy in the spatial distribution of tracers either present in the solution, or released by the bubble itself.

(2) Our observations show that the streaming produced beyond the oscillatory boundary layer (the only streaming which can be observed with our technique) does not arise from the momentum carried by the diverging shock/pressure wave which is known to be released on violent collapse.

(3) The present observations indicate that the streaming around a levitating bubble is dipolar. As a matter of fact, Longuet-Higgins's modeling (a dipole+a viscous ''Stokeslet'' flow) accounts very well for the experimental observation, at least qualitatively. This consistency between theory and experiment suggests that an actual bubble in levitation exhibits radial and translational oscillations simultaneously.

(4) Further theoretical developments appear to be necessary in order to describe quantitatively the streaming associated with single bubbles in levitation. Indeed both sonoluminescing and stable nonluminescing bubbles are known to exhibit large radial displacements ($\varepsilon > 1$) which cannot be described quantitatively within the framework of the current theory. In this sense the determination of the Lagrangian velocity field for the particles of a liquid is of prime importance because any further theoretical developments will have to be consistent with it.

(5) The last point concerns the possible consequences of the coupling of radial and translational oscillations. As mentioned by Prosperetti (1997) and Longuet-Higgins (1997), the coupling between these two modes of oscillation could lead a bubble to collapse inwards asymmetrically. Recent results obtained by Lauterborn's group via the visualization of the collapse of laser-generated bubbles tends to show that ''pure symmetric collapses do not exist.'' Up to now, the implication of an asymmetric collapse in the process of SL remained undetermined. However, the question arises of determining the extent to which asymmetry in bubble collapse affects the development of the extreme conditions associated with SL.

APPENDIX: A SIMPLIFIED MODEL FLOW

Some of the dye pattern seen by Verraes *et al.* (experiments with fuchsin) can be understood qualitatively on the basis of a simplified model as follows.

Imagine the dye to be replaced by a cloud of suspended particles, each sinking, independently of the others, with a vertical velocity $-\gamma$ relative to the neighboring fluid. Thus if

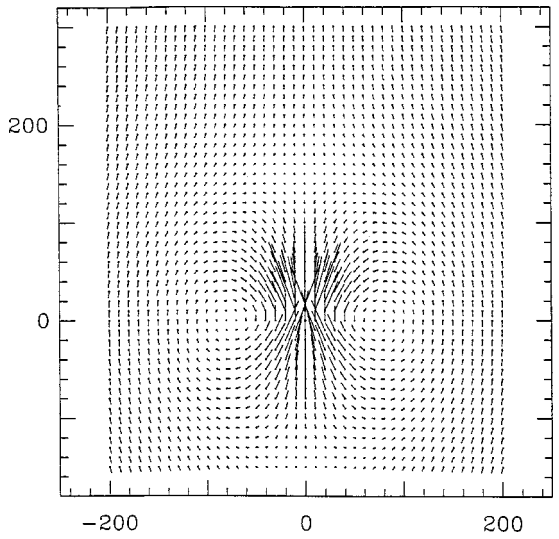

FIG. A1. Representation of the velocity field given by Eqs. (A1) and (A2). The vertical and horizontal axes represent distances expressed in reduced values with respect to a (the mean radius of a bubble).

u denoted the streaming velocity due to the oscillating bubble, each particle of dye will behave as if it were in a velocity field $u+(0,0,-\gamma)$, in rectangular coordinates (x,y,z). Of course γ is in reality by no means independent of the form of the cloud of dye and of the local dye concentration. Nevertheless, the model may serve to gain some insights into the development of the dye cloud as a whole.

In Fig. A1 we have assumed the velocity field to be given by

$$u_r=\left[-\frac{a}{r}+\frac{1}{2}\frac{a^3}{r^3}+\frac{1}{2}\frac{a^6}{r^6}\right]\cos\theta-\gamma\cos\theta, \tag{A1}$$

$$u_\theta=-\left[\frac{1}{2}\frac{a}{r}+\frac{1}{4}\frac{a^3}{r^3}+\frac{a^6}{r^6}\right]\sin\theta+\gamma\sin\theta \tag{A2}$$

in spherical coordinates, a being the mean radius of the sphere and γ being a constant taken as $\frac{1}{150}$. The first group in Eqs. (A1) and (A2) represents the bubble's streaming velocity, and the last terms represent the sinking velocity of each particle of dye. In Fig. A1 the velocity vectors are drawn at each point of a grid in a vertical plane through the origin. Close to the origin, where r/a lies between 1 and 10, say, there is a strong upwards drift. However, at distances such that $10<r/a<100$, say, the flow has essentially the form of a Stokeslet, and the streamlines are approximately toruses. Beyond this radius, at $r/a=\gamma,\theta=0$, there is a stagnation point at which the Stokeslet is just balanced by the sinking velocity γ. There is a similar stagnation point when $\theta=\pi$. Within a radius a/γ approximately, the fluid recirculates. Outside this critical radius the flow is always downwards, by passing the circulating region.

How does this flow affect the boundary of an initially spherical blob of dye? In Fig. A2 we show the time-history of a spherical boundary, released at a point $r/a=400$, $\theta=0$, vertically above the stagnation point. As it falls it becomes compressed vertically and stretched horizontally (preserving the total volume). On approaching the stagnation point the blob is stretched and thinned into an almost spherical cap, centered on the origin.

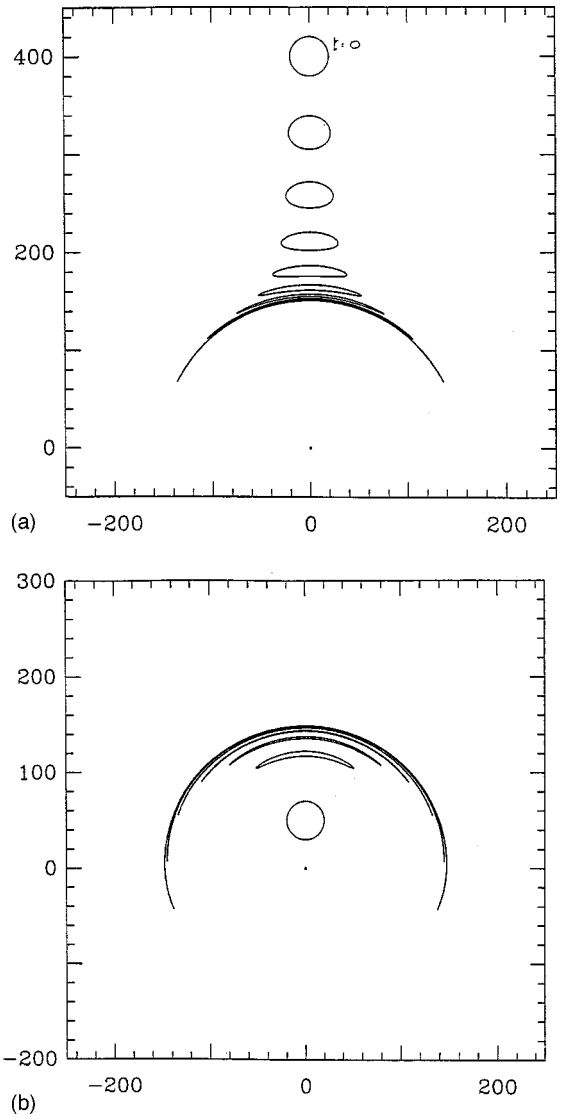

FIG. A2. (a) The case of the time-history of an initially spherical blob of dye (radius=20a) released at $y/a=400$ and $\theta=0$. This situation is similar to the experiments in Fig. 2(a). (b) The same as in (a), but in the case of an initially spherical boundary released below the critical radius ($y/a=150$). This situation corresponds to the experiments in Fig. 2(b).

It will be noted that we have ignored the molecular diffusion of the dye. Moreover, as the dye streak thins out, its relative sinking velocity will decrease, so that the streak will tend to lie somewhat outside the sphere. Eventually, on the outskirts of the Stokeslet flow, it may even be carried upwards.

Figure A2(b) shows a similar sequence when the spherical blob is initially inside the critical radius. In this case the blob starts by *rising*. On approaching the stagnation point from below, the blob is stretched horizontally into a spherical cap as previously.

Figure A3 illustrates three cases when the initial position of the blob is at a point below the bubble and to the side, at an angle of 135° to the vertical. In Fig. A3(a) the initial position is at the point $x/a=150$, $y/a=-150$, which is out-

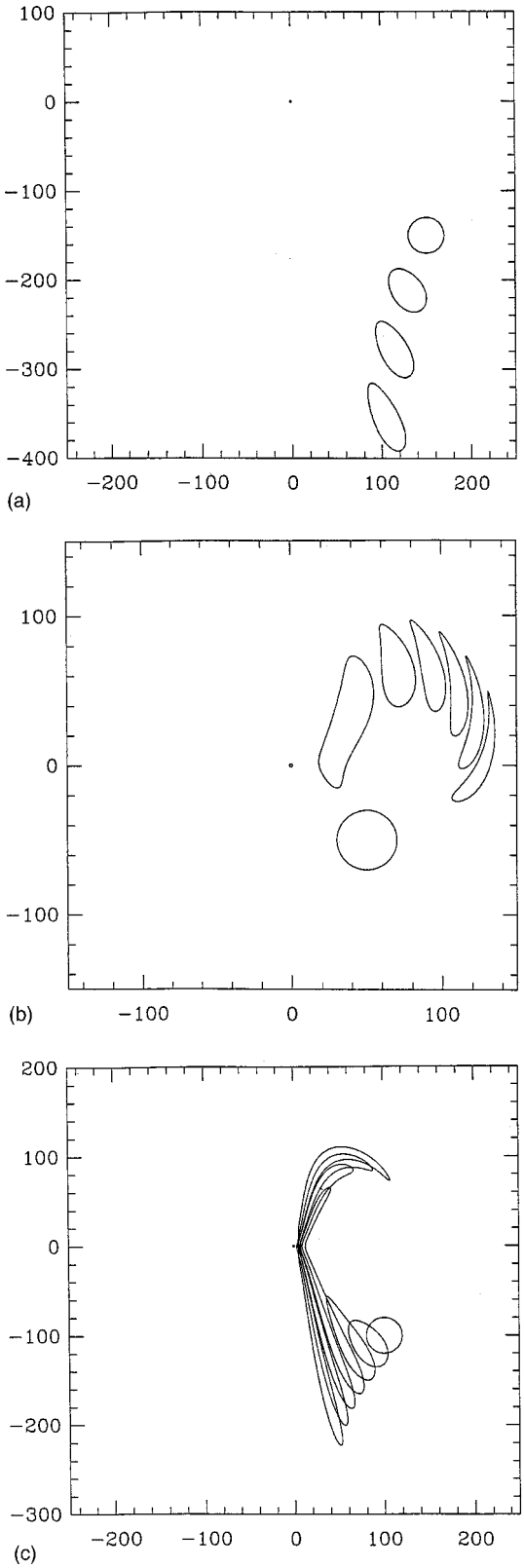

FIG. A3. The case of a blob situated initially at a point below a bubble and at an angle of 135 degrees to the vertical. (a) Initial position of the blob: $x/a=150$; $y/a=-150$. (b) Same as (a) but $x/a=50$; $y/a=-50$. This situation corresponds to the experiments in Fig. 2(c). (c) Same as (a), but with $x/a=100$; $y/a=-100$.

side the critical radius. The blob always falls. At the same time it is drawn towards the axis and undergoes moderate distortion. (There is distortion in the azimuthal direction also, but this is not shown.)

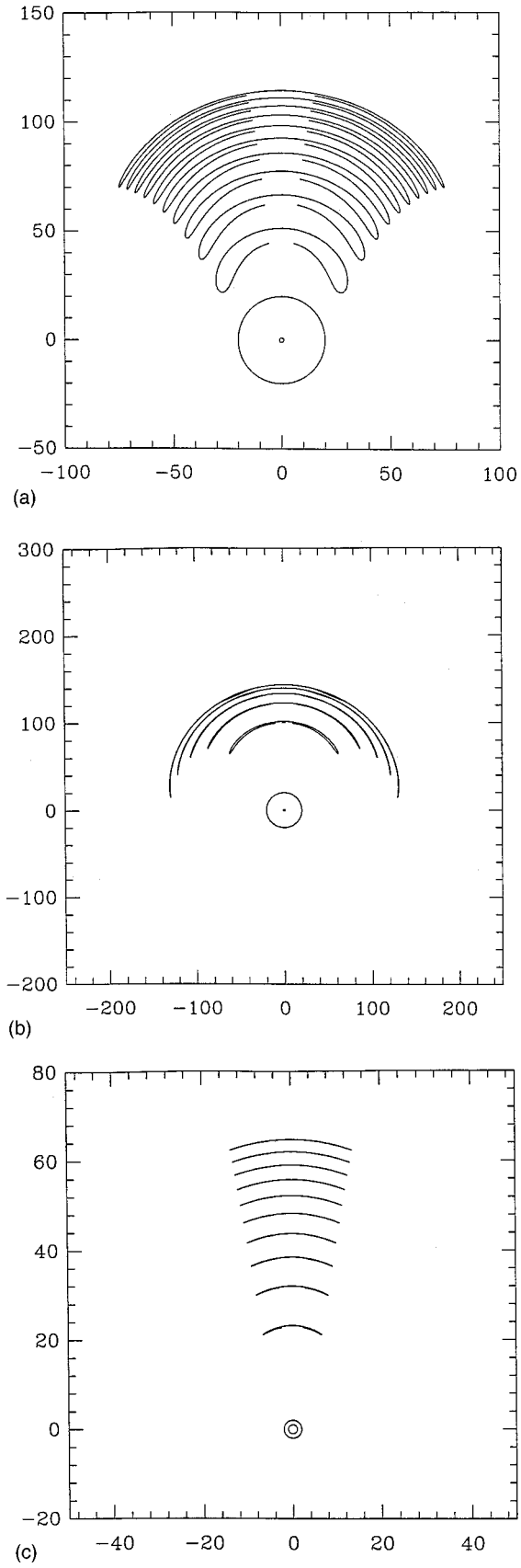

FIG. A4. (a) The theoretical case associated with a blob of dye (radius = $20a$) surrounding a bubble. (b) Same as (a), but the sequence is extended in time. These graphs are related to the experiments in Fig. 3. (c) Same as (a), but with a blob of radius=$2a$.

Figure A3(b) shows a corresponding sequence when the blob is initially at $x/a=50$, $y/a=-50$, *inside* the critical radius. The blob first rises towards the bubble, then passes it and moves to the side. Some of the dyed fluid eventually approaches the critical radius. Other parts of the blob recirculate.

Figure A3(c) is an example when $x/a=100$, $y/a=-100$, so that the blob of dye initially straddles the critical radius. The part of the blob outside the boundary falls as in Fig. A3(a); the part inside the boundary moves upwards, then outwards, as in Fig. A3(b). Note that those particles initially near the critical radius are carried towards the lower stagnation point on the axis of symmetry, where they may be diverted either downwards or else upwards towards the origin.

Finally we show in Fig. A4 what happens when the blob of dye initially surrounds the bubble. In Fig. A4(a) the initial radius of the blob is $20a$ (as in all the previous diagrams). The dye in the blob is swept upwards past the bubble into a roughly spherical cap, becoming thinner as it rises and spreads out. The same sequence is extended in time in Fig. A4(b).

The last sequence, in Fig. A4(c), illustrates what happens if the dye is at first rather close to the bubble; the initial radius of the blob is now only $2a$. The blob rises past the bubble as in Figs. A4(a) and A4(b), but now the ascending region is narrower; the angle of the enclosing cone has been reduced. If the initial radius of the cone is reduced still further, so as to represent dyed fluid generated by a chemical reaction at the bubble surface, then the rising dye is confined to a narrow streak along the axis of symmetry until it encounters the stagnation point, then it spreads outwards as before.

Coakley, W. T., and Nyborg, W. L. (**1978**). *Ultrasound: Its Applications in Medicine and Biology*, edited by F. J. Fry (Elsevier, New York), Part 1, pp. 77–159.

Davison, B. J., and Riley, N. (**1971**). ''Cavitation microstreaming,'' J. Sound Vib. **15**, 217–233.

Elder, A. I., Kolb, J., and Nyborg, W. L. (**1954**). ''Small-scale acoustic streaming effects in liquids,'' J. Acoust. Soc. Am. **26**, 933A.

Elder, A. I. (**1959**). ''Cavitation microstreaming,'' J. Acoust. Soc. Am. **31**, 54–164.

Eller, A. I. (**1969**). ''Growth of bubbles by rectified diffusion,'' J. Acoust. Soc. Am. **46**, 1246–1250.

Gaitan, D. F., Crum, L. A., Roy, R. A., and Church, C. C. (**1992**). ''Sonoluminescence and bubble dynamics of a single, stable, cavitation bubble,'' J. Acoust. Soc. Am. **91**, 3166–3183.

Henglein, A. (**1993**). ''Contributions to various aspects of cavitation chemistry,'' in *Advances in Sonochemistry*, edited by T. J. Mason (JAI, London), Vol. 3, pp. 17–83.

Holzfuss, J., Rüggeberg, M., and Billo, A. (**1998**). ''Shock wave emissions of a sonoluminescing bubble,'' Phys. Rev. Lett. **81**, 5434–5437.

Leighton, T. J. (**1994**). *The Acoustic Bubble* (Academic, London).

Lepoint, T., Lepoint-Mullie, F., and Henglein, A. (**1999**). ''Single bubble sonochemistry,'' in *Sonochemistry and Sonoluminescence*, edited by L. A. Crum, T. J. Mason, J. L. Reisse, and K. S. Suslick (Kluwer Academic, Dordrecht), pp. 285–290.

Levich, V. G. (**1962**). *Physicochemical Hydrodynamics* (Prentice-Hall, New York), p. 401.

Lighthill, J. (**1978**). ''Acoustic streaming,'' J. Sound Vib. **61**, 391–418.

Longuet-Higgins, M. S. (**1997**). ''Particle drift near an oscillating bubble,'' Proc. R. Soc. London, Ser. A **453**, 1551–1568.

Longuet-Higgins, M. S. (**1998**). ''Viscous streaming from an oscillating spherical bubble,'' Proc. R. Soc. London, Ser. A **454**, 725–742.

Nyborg, W. L. (**1953**). ''Acoustic streaming due to attenuating plane waves,'' J. Acoust. Soc. Am. **25**, 68–75.

Nyborg, W. L. (**1958**). ''Acoustic streaming near a boundary,'' J. Acoust. Soc. Am. **30**, 329–339.

Nyborg, W. L. (**1965**). ''Acoustic streaming,'' in *Physical Acoustics*, edited by W. P. Mason (Academic, New York), Vol. II B, Chap. 11.

Prosperetti, A. (**1997**). ''A new mechanism for sonoluminescence,'' J. Acoust. Soc. Am. **101**, 2003–2007.

Riley, N. (**1967**). ''Oscillatory viscous flow: review and extension,'' J. Inst. Math. Appl. **3**, 419–434.

Starritt, H. C., Duck, F. A., and Humphrey, V. F. (**1989**). ''An experimental investigating of streaming in pulsed diagnostic ultrasound beams,'' Ultrasound Med. Biol. **15**, 363–373.

Stuart, J. T. (**1966**). ''Double boundary layers in oscillatory viscous flow,'' J. Fluid Mech. **24**, 673–687.

Suslick, K. S. (ed.) (**1988**). ''Homogeneous sonochemistry,'' in *Ultrasound: Its Chemical, Physical and Biological Effects* (VCH, New York), pp. 123–163.

Wang, T. G., and Lee, C. P. (**1990**). ''Outer acoustic streaming,'' J. Acoust. Soc. Am. **88**, 2367–2375.

Wang, Z. Q., Pecha, R., Gompf, B., and Eisenmeger, W. (**1999**). ''Single bubble sonoluminescence: Investigations of the emitted pressure wave with a fiber optic probe hydrophone,'' Phys. Rev. E **59**, 1777–1780.

Wu, J., and Du, G. (**1997**). ''Streaming generated by a bubble in an ultrasound field,'' J. Acoust. Soc. Am. **101**, 1899–1907.

Yaeger, E., and Hovorka, F. (**1953**). ''Ultrasonic waves and electrochemistry. I. A survey of the electrochemical applications of ultrasonic waves,'' J. Acoust. Soc. Am. **25**, 443–455.

Attenuation and dispersion of sound in dilute suspensions of spherical particles

S. Temkin
Department of Mechanical and Aerospace Engineering, Rutgers University, 98 Brett Road, Piscataway, New Jersey 08854-8058

(Received 25 June 1999; accepted for publication 21 March 2000)

This paper considers sound propagation in dilute suspensions of constant-mass particles that can translate and pulsate under the effects of a small amplitude sound wave. A new theory for sound attenuation and dispersion is developed on the basis of the changes of the suspension's compressibility produced by the relative motions between host fluid and particles. The approach, used earlier to treat propagation in rigid-particle suspensions, decouples the propagation problem from the more difficult problem of obtaining accurate descriptions for the fluid-particle interactions. In this work the role of the pulsational motion is included in the theoretical framework. The resulting theory is thus applicable to aerosols, bubbly liquids, emulsions, and hydrosols composed of elastic particles, and includes, as a special limit, rigid-particle suspensions. The results are expressed in terms of three complex quantities that describe, respectively, the particles' translational velocity, temperature, and pressure, relative to their counterparts in the fluid. Theoretical results for these quantities, applicable in wide frequency ranges, are available from previous studies [Temkin and Leung, J. Sound Vib. **49**, 75–92 (1976), Temkin, J. Fluid. Mech. **380**, 1–38 (1999)]. Together with the compressibility theory presented here, they provide a more general description of propagation in dilute suspensions than presently available. In the case of aerosols and hydrosols, the theory produces known results for the attenuation and the sound speed. For bubbly liquids and emulsions the new results presented here differ from those available in the literature. The differences are traced to the neglect in the existing theories of the acoustic pressure disturbance produced by the pulsations of the particles.
[S0001-4966(00)00507-5]

PACS numbers: 43.35.Bf [HEB]

LIST OF SYMBOLS

$b,\ b_i$	Nondimensional external and internal wave numbers
b_T	Nondimensional external wave number based on the isothermal sound speed
$c_s(0)$	Suspension's equilibrium isentropic sound speed
c_w	Wood's sound speed
$c_s(\omega)$	Suspension's frequency-dependent adiabatic sound speed
$c_{vf},\ c_{vp}$	Specific heats at constant volume
$c_{sf},\ c_{sp}$	Isentropic sound speeds in fluid and particle materials
$c_{Tf},\ c_{Tp}$	Isothermal sound speeds in fluid and particle materials
$c_{pf},\ c_{pp}$	Specific heats at constant pressure
e	Suspension's internal energy per unit mass
$e_f,\ e_f$	Internal energies, per unit mass, of fluid and of particles
$\dot{e}_{tr}$	Translational energy dissipation rate
$h=2\rho_p c_{pp}/3\rho_f c_{pf}$	Heat capacity ratio
m_p	Mass of one particle
p	Pressure
p'	Imposed pressure fluctuation
p_f	Fluid's thermodynamic pressure
$q=(1+i)z$	Complex frequency variable
$u_f,\ u_p$	Velocities of fluid and particulate phases
$\dot{w}$	Compression work rate per unit mass of suspension
$y=\sqrt{\omega a^2/2\nu_f}$	Ratio of particle radius to fluid's viscous penetration depth
$z=\sqrt{\omega a^2/2\kappa_f}$	Ratio of particle radius to fluid's thermal penetration depth
$z_p=\sqrt{\omega a^2/2\kappa_p}$	Ratio of particle radius to particle's thermal penetration depth
C_m	Particle mass loading
E_0	Acoustic energy density in unattenuated wave
$K_s(\omega)$	Suspension's frequency-dependent adiabatic compressibility
K_{sf}	Isentropic compressibility of fluid phase
$K_s(0)$	Equilibrium compressibility of the suspension
$N_s=\rho_f c_{sf}^2/\rho_p c_{sp}^2$	Ratio of internal to external isentropic compressibilities
N_T	Ratio of internal to external isothermal compressibilities
$\dot{Q}_p$	Heat transfer rate to a particle
$T_f,\ T_p$	Fluid and particle temperatures
U_f	Dilute-suspension fluid velocity in a sound wave

U_{f0}	Velocity amplitude in unattenuated wave
$V=u_p/U_f$	Particle to fluid complex velocity ratio
α_{tr}, α_{th}	Translational and thermal amplitude-attenuation coefficients
$\bar{\alpha}=\alpha c_s(0)/\omega$	Nondimensional attenuation based on $c_s(0)$
$\hat{\alpha}=\alpha c_{sf}/\omega$	Nondimensional attenuation based on c_{sf}
$\hat{\alpha}_{ac}=\alpha_{ac}c_{sf}/\omega$	Nondimensional acoustic radiation attenuation coefficient
$\hat{\alpha}_{tr}=\alpha_{tr}c_{sf}/\omega$	Nondimensional translational attenuation coefficient
$\hat{\alpha}_{th}=\alpha_{th}c_{sf}/\omega$	Nondimensional thermal attenuation coefficient
β_f, β_p	Coefficients of thermal expansion
$\hat{\beta}=c_{sf}^2/c_s^2(0)-c_{sf}^2/c_s^2(\omega)$	Dispersion coefficient
$\hat{\beta}_{pul}=\hat{\beta}_{ac}+\hat{\beta}_{th}$	Pulsational dispersion coefficient
$\hat{\beta}_{ac}$, $\hat{\beta}_{th}$	Acoustic radiation and thermal dispersion coefficients
$\hat{\beta}_{tr}$	Translational dispersion coefficients
γ_f, γ_p	Specific heat ratios
$\delta=\rho_{f0}/\rho_{p0}$	Material density ratio
$\delta_{\nu f}=\sqrt{2\nu_f/\omega}$	Fluid's viscous wave penetration depth
$\delta_{\kappa f}=\sqrt{2\kappa_f/\omega}$	Fluid's thermal penetration depth
$\delta_{\nu f}=\sqrt{2\nu_f/\omega}$	Particle's viscous penetration depth
$\delta_{\kappa p}=\sqrt{2\kappa_p/\omega}$	Particle's thermal penetration depth
$\delta\tau$	Element of suspension volume
$\delta\tau_f$, $\delta\tau_p$	Volumes of fluid and particles in a volume element of suspension
θ_f'	Temperature fluctuation of disturbance produced by particle
ϕ_m	Concentration of particles by mass
ϕ_v	Concentration of particles by volume
κ	Polytropic index
κ_f, κ_p	Thermal diffusivities
μ_f, μ_p	Dynamic viscosities
ν_f, ν_p	Kinematic viscosities
$\rho=\sigma_f+\sigma_p$	Average suspension density
ρ_f, ρ_p	Material densities
ρ_{f0}, ρ_{p0}	Ambient material densities
ρ_0	Equilibrium suspension density
σ_f, σ_p	Densities of fluid and particulate *phases*
ω	Circular frequency
ω_{T0}	Resonance frequency for pulsational motion
$\Pi=p_p'/P_f'$	Particle-to-fluid complex pressure ratio
$T=T_p'/\Theta_f'$	Particle-to-fluid complex temperature ratio
Θ_f'	Temperature fluctuation in background wave
$\Omega=\omega/\omega_{T0}$	Nondimensional frequency

INTRODUCTION

The propagation of small amplitude acoustic waves in fluids that contain particles is an old and much studied subject, both from the fundamental and applied points of view. The studies date back to the nineteenth century when Tyndall[1] studied the effects of fogs on sound propagation. Since then a considerable body of knowledge has been gained thanks to the many studies that have considered the subject in depth. Further, in some instances, theoretical formulations exist that have received experimental corroboration. These include the important case first addressed theoretically, namely dilute suspensions of rigid particles or droplets in gases (see, for example, Ref. 2, and references cited therein). In other cases, success has not been so clear, for example, in the case of bubbly liquids existing theories predict attenuation coefficients near resonance that differ from those obtained experimentally. Some of these differences may be due to bubble interaction effects which are accentuated in the resonance region, but as shown by Sangani,[3] the inclusion of interactions in the theory does not significantly produce better agreement with experiments. Further, the differences exist for very small volume concentrations, so that it is at least possible that other effects are responsible for them.

At a more fundamental level, however, the existing theories have been developed for specific types of suspensions, e.g., aerosols or bubbly liquids, and for limited frequency regions within each type, and thus a theory applicable to more general suspensions in less restrictive frequency ranges is still lacking. For example, the well-known attenuation theory of Epstein and Carhart[4] describes well the attenuation of sound in aerosols in a wide frequency range, but does not include dispersion. Both effects are well described by the particulate relaxation theory developed by this author and Dobbins[5] on the basis of a two phase fluid-dynamic model for an aerosol, but the theory is based on the simplest models for the force on and the heat transfer to a particle and is therefore only applicable to aerosols. More complete particle force and heat transfer models have been incorporated in the two phase theories since then, and this has produced results that are applicable in a wider frequency range in some suspensions.[6–9] Such models include the effects of unsteadiness on the viscous force on a particle but leave out those produced by fluid compressibility. Also, the effects of heat transfer appear in these works only in the lowest frequency-approximation limit.

The two-phase approach is based on model conservation equations for the particulate and the host-fluid phases, complemented by suitable phase-interaction terms which couple the motions and temperatures of the two phases. Wavelike solutions are easily obtained from the linear approximation to those equations, which yield both the attenuation and the speed of propagation. However, the results are usually given in terms of a complex dispersion relation that usually requires numerical computation, making it difficult to interpret them. Furthermore, these conservation equations

are based for specific suspensions, e.g., dusty gases,[10] bubbly liquids,[11–14] hydrosols,[15] but these do not exist for general types of suspensions. Fortunately, the two-phase model is not needed for acoustic motions, because, for them, one is usually interested in the propagation constants in the vicinity of an equilibrium condition.

Sound propagation in suspensions has also been investigated by means of the Kramers–Kronig relations.[16–19] These are based on causality requirements and connect the attenuation to the speed, so that if one of these quantities is known, the other can be determined from them. The method produces the sound speed, provided the attenuation is known independently, but can be cumbersome for attenuations that depends on the frequency in a complicated manner, as seems to be the case for most suspensions.

Another method that has been used to obtain the propagation constants in liquid suspensions is based on the idea, apparently first expressed by Wood[20] and by Herzfeld,[21] that the compressibility of a suspension is given by the sum of the compressibilities of the particles and fluid, weighed in proportion to the volume occupied by each phase. Although this has been demonstrated only for isothermal suspensions,[22] and has been used with some success in them,[23,24] it has also been used in situations where thermal effects are important, e.g., bubbly liquids and emulsions, both at zero and finite frequencies. In the first case, the method produces a sound speed, known as Wood's speed. At finite frequencies, it results in a propagation constant whose real part contains a low-frequency sound speed, commonly taken to be given by Wood's formula, and whose imaginary part is related to the attenuation computed from the scattering theory of Carstensen and Foldy[25] for bubbly liquids, and from the dissipation theory of Epstein and Carhart,[4] Isakovich,[26] and Allegra and Hawley[27] for emulsions (see, for example, Refs. 28–29). Although the method produces plausible theoretical results, its validity remains uncertain, mainly because of the *ad hoc* procedure used in defining the compressibility.

Nevertheless, provided a compressibility can be defined from first principles, the compressibility approach can produce correct results that throw further light on the propagation of acoustic waves in a suspension. Recently,[30] the author developed such a theory for *rigid-particle* suspensions which shows that a first-principles approach, based on the relative temperature and translational velocity between particles and fluid, is possible.

The present work uses a similar approach to study propagation in dilute suspensions of compressible particles. Here a dynamic compressibility is obtained by taking into account both translational and pulsational motions of the particles in the wave, such as might exist in bubbly liquids and in emulsions. The results obtained here include, as a special limiting case, the rigid-particle results obtained earlier. Although limited to constant-mass particles, the theory provides a fairly general, and mathematically simple theory for the attenuation coefficient and the phase velocity of plane sound in suspensions. Results for these quantities are given in terms of three complex ratios which quantify the departures of the suspension's compressibility from its known equilibrium value. These ratios are the particle-to-fluid translational velocity, temperature, and pressure, and are known from earlier work for single spherical particles. Thus the translational velocity ratio is obtained from the work of Temkin and Leung,[31] whereas the pressure and temperature ratios are provided by the author's recent work on compressible particles.[32]

Use of these ratios in the theory developed here results in explicit forms for the attenuation and the sound speed for the basic suspension types mentioned earlier. The theory is first reduced for the case of small attenuation and dispersion, applicable to very dilute suspensions, in which case the results we obtain for the attenuation are equal to previously known results that were obtained using a different formulation based on energy dissipation. On the other hand, the results obtained for the phase velocity agree with previously known results for aerosols, but differ from those existing for bubbly liquids and emulsions, owing to the neglect in those theories of the acoustic pressure disturbance produced in the liquid by the pulsating particle.

When large attenuations exist, as is the case with bubbly liquids having even modest concentrations, the more complete results are used to obtain the attenuation and the sound speed. For the attenuation, it is shown that in the vicinity of resonance, the propagation is dominated by the effects of acoustic radiation from the particle, and not by thermal dissipation as it has been assumed before. Thus we find that the attenuation and sound speed in the resonance region very closely follow the results predicted by the isothermal model of Kennard.[33] Below that frequency region, thermal effects are dominant, but the attenuation there is very small compared to that at resonance. We compare our attenuation results to those obtained experimentally by Silberman,[34] and find significant differences at most frequencies. For the sound speed, we compare our low-frequency, or equilibrium, speed to the results obtained sometime ago by Karplus,[35] and find good agreement. At finite frequencies, there seem to be no suitable experimental data that can be used to provide an independent comparison of the theory in the resonance region. This includes the recent results of Cheyne *et al.*,[36] whose data cover the resonance region but as explained in Sec. V, their procedures do not allow an independent verification of any theory. Nevertheless, if we follow the same procedure as used by them to compare their results to the theory of Commander and Prosperetti,[37] we find a good agreement with the theory developed here.

I. BASIC CONSIDERATIONS

For the sake of completeness, we first repeat here the basic definition of a suspension compressibility that was given earlier.[30] As is well known, a continuous medium can sustain acoustic waves if its density changes when forces are applied at the boundaries enclosing them. Such changes can be quantified by the medium's adiabatic compressibility, K_s, defined by

$$K_s = -\frac{1}{\delta\tau}\frac{d(\delta\tau)}{dp}. \tag{1}$$

Here $\delta\tau$ is an element of volume in the medium, and dp is the external pressure change producing the deformation of the element. The subscript s in K_s is used to indicate that this quantity should be computed while holding the entropy of the element constant. If K_s is known, we can obtain the linearized isentropic speed for the medium by means of $c_s^2 = 1/\rho_0 K_s$, where ρ_0 is the ambient medium density.

Although seemingly simple, this approach presents difficulties because some of the quantities appearing in it cannot always be defined in suspensions. An important exception occurs at frequencies so low that equilibrium exists in the medium, in which case thermodynamic arguments make it possible to obtain it for suspensions of particles in gases or in liquids. Indeed, for suspensions of constant-mass particles, we have shown[38] that the sound speed at very low frequencies in aerosols, bubbly liquids, emulsions, and hydrosols, is given by

$$\frac{c_{sf}^2}{c_s^2(0)} = \frac{1-\phi_v}{1-\phi_m}[\gamma_f(1-\phi_v)+\gamma_p\phi_v N_s] - (\gamma_f-1)\frac{(1-\phi_v+\phi_v\beta_p/\beta_f)^2}{1+\phi_m(c_{pp}/c_{pf}-1)}. \tag{2a}$$

Here, ϕ_v is the particle volume concentration, $\phi_m = (\rho_p/\rho_f)\phi_v/(1-\phi_v)$ is the mass concentration of particles, N_s is the ratio of particle to fluid isentropic compressibilities given by $N_s = \rho_f c_{sf}^2/\rho_p c_{sp}^2$, where c_{sf} and c_{sp} are the isentropic sound speeds in the fluid and particle materials, γ_f and γ_p are the corresponding specific heat ratios, β_f and β_p are the coefficients of thermal expansion, and c_{pf} and c_{pp} are the fluid and particle specific heats at constant pressure.

Another sound speed in suspensions that can be obtained from purely thermodynamic arguments is the frozen speed, denoted by $c_s(\infty)$. That speed can be defined in a high-frequency limit where the particles are essentially at rest, or frozen. It was also computed in Ref. 38, but the value given there is incorrect as it was calculated by considering a constant suspension volume instead of a constant suspension mass. The correct value is that given earlier by Chu[39] and is given by

$$\frac{c_{sf}^2}{c_s^2(\infty)} = \frac{(1-\phi_v)^2}{1-\phi_m}, \tag{2b}$$

where ϕ_m is the concentration, by mass, of the particles in the suspension.

To obtain the equilibrium compressibility of the suspension, we note that the density of a homogeneous suspension can be written as

$$\rho = \rho_f(1-\phi_v)/(1-\phi_m). \tag{3}$$

Hence, the suspension's equilibrium compressibility, $K_s(0)$, applicable when $\omega \to 0$, is given by

$$\frac{K_s(0)}{K_{sf}} = \gamma_f(1-\phi_v+\gamma_p\phi_v N_s/\gamma_f) - (\gamma_f-1)\frac{(1-\phi_v+\phi_v\beta_p/\beta_f)^2}{1+\phi_v(\rho_p c_{pp}/\rho_f c_{pf}-1)}, \tag{4}$$

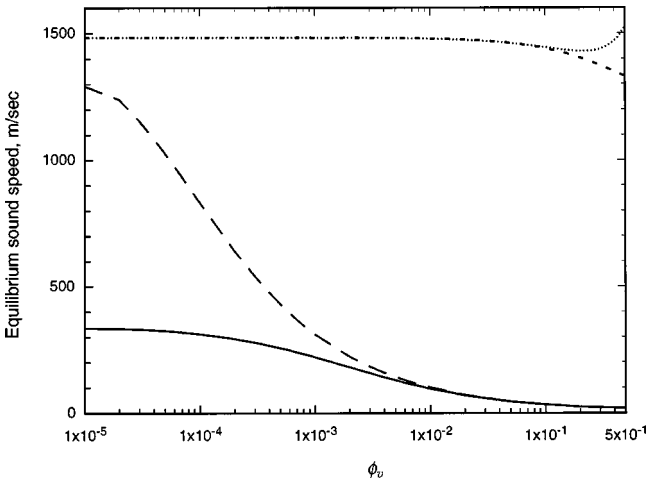

FIG. 1. Equilibrium sound speed for typical examples of basic suspension types. —— water droplets in air; — — — air bubbles in water; - - - toluene droplets in water; · · · · alumina particles in water.

where K_{sf} is the adiabatic compressibility of the fluid material. For small volume concentrations, this becomes

$$K_s(0)/K_{sf} = 1-\phi_v+\phi_v[\gamma_p N_s+(\gamma_f-1)\times(\rho_p c_{pp}/\rho_f c_{pf}-2\beta_p/\beta_f)], \tag{5}$$

showing that, generally, the zero-frequency compressibility of a suspension is not given by the sum of particle and fluid compressibilities. The only exception occurs when *both* γ_p and γ_f are unity. It should be noted that the term $\gamma_p\phi_v N_s$ in Eq. (4) can be of order one for some suspensions even if ϕ_v is small. Thus in bubbly liquids, $N_s = O(10^4)$, making $\gamma_p\phi_v N_s$ fairly large for small concentrations.

From the acoustic perspective, a suspension in equilibrium is an ideal medium, characterized by two independent quantities such as the sound speed, given by Eq. (2a), and the density, given by Eq. (3). Because the sound speed at finite frequencies is sometimes referred to its equilibrium value, it is useful to first get an idea of the typical values of $c_s(0)$. For a given particle-fluid combination, the speed depends only on the volume concentration of particles, as shown in Fig. 1, where $c_s(0)$ is plotted as a function of ϕ_v for typical examples of the four basic types of suspensions to which Eq. (2a) applies. It is seen that when the concentration is small, only aerosols and bubbly liquids display significant sound speed variations. Low-frequency sound waves in dilute emulsions and hydrosols essentially travel with a speed that is equal to that in the fluid alone. However, for volume concentrations that are of the order of 0.1 or larger, some changes occur in these suspensions as well. Thus at volume fractions of the order of 0.1 or larger, the second term in Eq. (2a), which mainly reflects thermal effects, begins to make a significant contribution to those changes. At even larger concentrations than those shown in the figure, $c_s(0)$ approaches c_{sp}, the sound speed in the particle material.

But in work on liquid suspensions, the low-frequency sound speed in liquid suspensions is often estimated on the basis of Wood's equation. If c_w denotes that speed, that equation may be expressed as

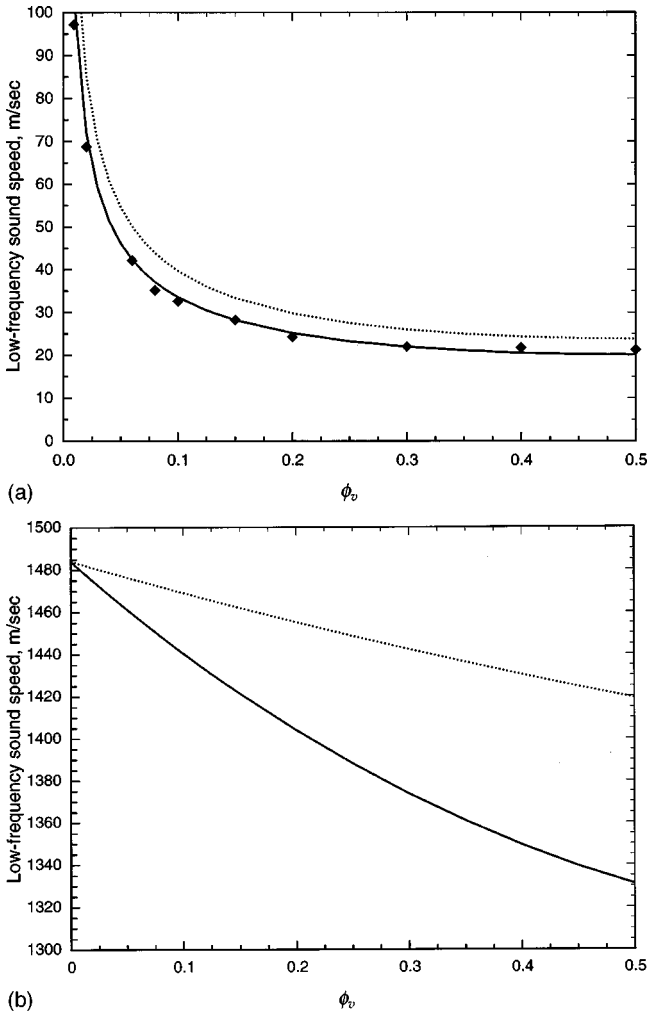

FIG. 2. (a) Comparison of Eqs. (2) and (6) for air bubbles in water with experimental data. —— $c_s(0)$, Eq. (2a); · · · · · c_w, Eq. (6); ♦ Karplus (1961), 250 Hz. (b) Comparison of Eqs. (2a) and (6) for an emulsion of toluene droplets in water —— $c_s(0)$, Eq. (2a); · · · · · c_w, Eq. (6).

$$\frac{c_{sf}^2}{c_w^2}=\frac{1-\phi_v}{1-\phi_m}(1-\phi_v+\phi_v N_s), \tag{6}$$

a result that can be obtained from Eq. (2a) by putting both γ_p and γ_f equal to 1. As this step shows, and as discussed earlier,[38] Wood's equation applies only to isothermal suspensions, and leaves out, entirely, thermal effects. Because these are important for bubbly liquids, we reconsider briefly the numerical differences between the two results. These were discussed earlier, but that work did not include comparison with experimental work, as the author was not aware of measurements that could be used for that purpose. However, a paper by Kieffer[40] contains experimental data obtained by Karplus[35] in bubbly liquids at low frequencies that cover a wide range of volume concentrations. A more recent, but more limited, set of experiments appears in an unpublished thesis by Micaelli.[41] In Fig. 2(a) we show Karplus data together with the speeds predicted by Eqs. (2a) and (6). It is seen that Eq. (2a) agrees well with the experimental data, and that Wood's speed overestimates them at all volume concentrations shown in the figure. This agreement demonstrates the validity of Eq. (2a), at least for the volume concentrations shown in the figure.

Thermal effects are also important for aerosols and emulsions, but there seem to be no equivalent measurements of the low-frequency sound speed in them. However, for aerosols Eq. (2a) agrees with the limiting expression that is obtained from fluid-dynamic results derived for them.[5,10,38,42–44] Thus the agreement between experiments and theory in the case of bubbly liquids, and between two different theoretical results in the case of aerosols, seems to provide sufficient support for the use of Eq. (2a) in other cases where no independent results exist. In Fig. 2(b) we show the low-frequency sound speed as calculated by the two results for a suspension of toluene droplets in water. It is seen there that the differences between Wood's equation and Eq. (2a) are significant. This is important because of the role this speed plays at finite frequencies.

Finite frequencies

As the frequency increases above $\omega=0$, changes occur owing to nonequilibrium effects, for example, nonuniform velocity, pressure, and temperature. These preclude the use of Eq. (4) at finite frequencies. Nevertheless, if the departures from equilibrium are small, it is possible to define a dynamic compressibility through Eq. (1) by considering the changes produced by those mechanisms that are active outside equilibrium. If we assume *a priori* that each such mechanism contributes separately to the changes, we can express the departures of the frequency-dependent compressibility from its equilibrium value as

$$K_s(\omega)/K_s(0)-1=[K_s(\omega)/K_s(0)-1]_1 +[K_s(\omega)/K_s(0)-1]_2+\cdots, \tag{7}$$

where the subscript s is used to represent adiabatic conditions in the suspension as a whole. We specialize this equation for monochromatic waves of small amplitude, in which case $K_s\rightarrow\tilde{K}_s(\omega)$, where the tilde is used to represent a complex value and $\tilde{K}_s(\omega)=[\rho_0\tilde{c}_s^2(\omega)]^{-1}$, where $\tilde{c}_s(\omega)$ is a complex sound speed. Because the main reason for a complex compressibility is attenuation, it is preferable to work with a complex wave number: $\tilde{k}=\omega/\tilde{c}_s(\omega)$. Thus $\tilde{k}=\omega/c_s(\omega)+i\alpha(\omega)$, where $\alpha(\omega)$ is the amplitude-attenuation coefficient, and $c_s(\omega)$ is real and represents the phase velocity. In terms of this, the compressibility becomes $K_s(\omega)/K_s(0)=c_s^2(0)/c_s^2(\omega)-\bar{\alpha}^2+2i\bar{\alpha}c_s(0)/c_s(\omega)$, where $\bar{\alpha}=\alpha c_s(0)/\omega$, and where, for simplicity, we have omitted the tilde on $\tilde{K}_s(\omega)$.

The quantity $\bar{\alpha}$ defined above is a nondimensional amplitude-attenuation coefficient given by $\bar{\alpha}=\alpha\lambda/2\pi$, where the wavelength λ refers to nondispersive waves traveling in a medium having a sound speed given by $c_s(0)$. For very dilute suspensions, it is customary to use the wavelength in the fluid without particles to scale the attenuation. This is given by $\hat{\alpha}=\alpha c_{sf}/\omega$. In strongly dispersive media, however, it may be more useful to scale the attenuation with the effective wavelength $2\pi c_s(\omega)/\omega$. This introduces yet another nondimensional attenuation coefficient, i.e., $\alpha c_s(\omega)/\omega$. The equations may be written in terms of any of

these three attenuations, and for simplicity we write them in terms of $\overline{\alpha}$, noting that the other attenuations can easily be obtained from it. Thus remembering that α must be positive in order for the amplitude of the waves to decay as they travel, we obtain

$$\frac{c_s^2(0)}{c_s^2(\omega)}-\overline{\alpha}^2=1+\Re[K_s(\omega)/K_s(0)-1]_1 +\Re[K_s(\omega)/K_s(0)-1]_2+\cdots, \tag{8}$$

$$2\overline{\alpha}\frac{c_s(0)}{c_s(\omega)}=|\Im\{K_s(\omega)\}/K_s(0)|_1+|\Im\{K_s(\omega)\}/K_s(0)|_2 +\cdots, \tag{9}$$

where the symbols $\Re$ and $\Im$ are used to represent real and imaginary parts.

Equations (8) and (9) are equal to those given recently by the author[30] in relation to a suspension of rigid particles. In that work we identified viscosity and heat conductivity as the effects contributing to the changes of compressibility through their action on the translational motions and on the temperature oscillations. A more fundamental description can be made in terms of the various motions that the particles can execute.

II. PARTICLE MOTIONS

We now consider small fluid particles immersed in a different fluid. It is known from basic fluid kinematics that the most general motion of a sufficiently small *material element* can be represented as the sum of a *uniform* translation, a *rigid-body* rotation, and a *stretching* motion that can be split into a *uniform expansion* (or contraction), and a *deformation* of the element without a change of volume (see, for example, Ref. 45). Although the theorem does not apply to particles of finite size, we may expect that it remains approximately valid when the particles are very small when compared to other relevant scales for the motion wavelength in the acoustic case. If so, the motion of a particle can be characterized by a uniform translational motion where each point of the particle has a velocity $\mathbf{u}_p$, a rigid-body rotation with angular velocity Ω_p, a uniform expansion with a volume-rate change dv_p/dt, and a change of area, dA_p/dt, without a change of volume.

Each of these motions can produce a change in the suspension compressibility because it may affect the volume of a suspension. Ultimately, each of these contributions can be related to an energy-dissipation mechanism, but it is advantageous to cast the problem in terms of the various particle motions that can exist.

In what follows we ignore shape oscillations as well as particle rotation, so that the only remaining particle motions are the rigid-body *translation* and the uniform expansion/contraction, or *pulsational*, motion. Thus the equations for the sound speed and the attenuation given above can be expressed as

$$\frac{c_s^2(0)}{c_s^2(\omega)}-\overline{\alpha}^2=1+\Re[K_s(\omega)/K_s(0)-1]_{tr} +\Re[K_s(\omega)/K_s(0)-1]_{pul}+\cdots, \tag{10}$$

$$2\overline{\alpha}\frac{c_s(0)}{c_s(\omega)}=|\Im\{K_s(\omega)\}/K_s(0)|_{tr}+|\Im\{K_s(\omega)\}/K_s(0)|_{pul} +\cdots. \tag{11}$$

It is possible to include, at this stage, shape oscillations and particle rotations, which, like mass evaporation and condensation, would make additional contributions. However, for particles whose radius is smaller than the wavelength, shape oscillations are negligible. Particle rotations, on the other hand, do not exist in a strictly plane wave in dilute suspensions because of the symmetry of the motion around a sphere. This would be different in concentrated suspensions, but these are not considered here.

We return now to Eqs. (10) and (11). If the right hand sides of these equations are known and are denoted respectively by $X(\omega)$ and $Y(\omega)$, the solution of these equations can be expressed as

$$\frac{c_s^2(0)}{c_s^2(\omega)}=\frac{1}{2}X+\frac{1}{2}(X^2+Y^2)^{1/2} \tag{12a}$$

and

$$\overline{\alpha}=\tfrac{1}{2}Y[\tfrac{1}{2}X+\tfrac{1}{2}(X^2+Y^2)^{1/2}]^{-1/2}. \tag{12b}$$

These may be simplified considerably when *both* the dispersion and the attenuation effects are small. Here we may neglect $\overline{\alpha}^2$ compared to unity in Eq. (10), and set $c_s(\omega)=c_s(0)$ in Eq. (11), thus obtaining

$$\frac{c_s^2(0)}{c_s^2(\omega)}=X(\omega) \tag{13a}$$

and

$$\overline{\alpha}=\tfrac{1}{2}Y(\omega). \tag{13b}$$

III. COMPRESSIBILITY CHANGES

The departing point in the calculation of the compressibility is Eq. (1). To use this equation we first consider a small volume element $\delta\tau$ having *n equal* particles which are allowed to pulsate, thereby changing their volume. The mass of the particles in the volume element is δM_p, and that of the fluids is δM_f. The volume element is chosen so that it always contains the same particles and the same fluid, that is, $\delta M=\delta M_p+\delta M_f$ is a constant. The corresponding volume, $\delta\tau=\delta\tau_f+\delta\tau_p$, is, however, variable. We may obtain δM_p and δM_f in various ways, for example, in terms of the particulate and fluid phase densities, σ_p and σ_f, defined by $\sigma_p=\phi_v\overline{\rho_p}$, where $\overline{\rho_p}(t)=v_p^{-1}\int_{v_p}\rho_p(\mathbf{x},t)dV$ is the average density within one particle. Thus $\delta M_f=\sigma_f\delta\tau_f$. Similarly, for the fluid mass, we obtain $\sigma_f=(1-\phi_v)\overline{\rho_f}$, where $\overline{\rho_f}(t)=(\delta\tau_f)^{-1}\int_{\delta\tau_f}\rho_f(\mathbf{x},t)dV$ is the average fluid density in the element, so that $\delta M_f=\sigma_f\delta\tau_f$. Thus the density of the suspension element is

$$\rho=(1-\phi_v)\overline{\rho_f}+\phi_v\overline{\rho_p}. \tag{14}$$

This is known as the effective density in a suspension, and may also be written in terms of the mass fraction. Thus

$$\frac{1}{\rho}=\frac{1-\phi_m}{\overline{\rho_f}}+\frac{\phi_m}{\overline{\rho_p}}. \tag{15}$$

A. Translational motions

The contribution to the suspension compressibility arising from the translational motion was evaluated recently for dilute suspensions of rigid particles[30] and is given by

$$\left(\frac{K_s(\omega)}{K_s(0)}-1\right)_{tr}=\frac{C_m}{1+C_m}(V-1), \tag{16}$$

where C_m is the mass loading, given by $C_m=\sigma_p/\sigma_{f0}$, $\delta=\rho_{f0}/\rho_{p0}$, $V=u_p/U_f$, where u_p is the complex translational velocity of a particle in a sound wave, evaluated in the absence of other particles, and U_f is the complex velocity of the fluid in the sound wave, evaluated in isentropic conditions and without particles. This equation derives from simple considerations of the relative motion between particles and fluid and shows that whenever the velocity ratio differs from unity, the compressibility of the suspension will differ from its equilibrium value.

Because the translational motion is controlled, to a large extent, by viscosity, the attenuation resulting from Eq. (16) is often referred to as a viscous attenuation. However, fluid inertia and compressibility also affect the results and it is preferable to refer to this as the translational attenuation.

B. Pulsational motion

Let us now consider the contributions due to the pulsational motions. This may be expressed in terms of the pulsational velocity of the particle's surface, and this can, in turn, be expressed in terms of the pressure and temperature in the particle. To save space we consider the changes in terms of the latter quantities directly.

When the frequency of oscillation is finite, the changes of pressure and temperature in a particle are different from those of the fluid at some distance from it. That is, the suspension element is generally not in equilibrium. However, the volume element, $\delta\tau$, has been defined in such a manner so that it contains the *same* fluid and particles during the pulsations. Then, the *total* mass contained in $\delta\tau$ is conserved so that the Lagrangian rate of change of the total mass in $\delta\tau$ is zero, or $d(\rho\delta\tau)/dt=0$. Thus

$$\frac{1}{\delta\tau}\frac{d(\delta\tau)}{dt}=-\frac{1}{\rho}\frac{d\rho}{dt}. \tag{17}$$

Since ρ is well defined in terms of the particle and fluid density averages and of the mass fraction, which is constant during the pulsations owing to our choice of volume element, the right hand side of Eq. (17) can be easily obtained from Eq. (15). Thus taking the derivative and linearizing the result, we obtain

$$\frac{d\rho'}{dt}=\left[\frac{1-\phi_m}{\rho_{f0}}\frac{d\overline{\rho_f'}}{dt}+\frac{\phi_m}{\rho_{p0}}\frac{d\overline{\rho_p'}}{dt}\right]\rho_0^2, \tag{18}$$

where $\overline{\rho_f'}$ and $\overline{\rho_p'}$ are the fluctuations of the average densities in the suspension element, and where ρ_0 is the ambient suspension density.

We now calculate the derivatives of the density fluctuations, keeping in mind that they are to be obtained for adiabatic conditions for the suspension as a whole. Since the heat transfer rate to the suspension element can be written as $\dot{Q}=\dot{Q}_f+\dot{Q}_p$, where $\dot{Q}_f$ and $\dot{Q}_p$ are the heat transfer rates to the fluid and to the particles in the element, we see that in adiabatic conditions for the suspension, $\dot{Q}_f=-\dot{Q}_p$, that is, heat transfer occurs between the particles and the fluid. Thus both derivatives appearing above must be calculated taking this heat transfer rate into account.

Consider first $d\overline{\rho_f'}/dt$. To obtain its value we first use the fluid's equation of state, $\rho_f=\rho_f(T_f,p_f)$. This is used to obtain the linearized local fluctuation of the fluid density as $\rho_f'=p_f'/c_{Tf}^2-\beta_f T_f'$, where both the isothermal sound speed, c_{Tf}, and the coefficient of thermal expansion, β_f, are evaluated at ambient conditions. Averaging this density fluctuation over the volume occupied by the fluid, we obtain

$$\overline{\rho_f'}=\frac{1}{c_{Tf}^2}\overline{p_f'}-\beta_f\overline{T_f'}, \tag{19}$$

where $\overline{T_f}$ and $\overline{p_f}$ are average values of the fluid temperature and pressure in the element. It should be noted that if no heat transfer occurs between fluid and particles, or if no particles are present in the fluid, the above fluctuations are related by the isentropic acoustic relations. Thus for example, in a fluid *without* particles, the isentropic relation between the pressure fluctuation P_f' and the temperature fluctuation Θ_f' is

$$P_f'=\frac{\rho_{f0}c_{pf}}{\beta_f T_0}\Theta_f'. \tag{20}$$

When particles are present, the heat transfer between fluid and particles renders this expression invalid, essentially because the temperature of the fluid is affected by the transfer. We show in Appendix A that for small departures from equilibrium, the average pressure and temperature fluctuations in a suspension element are related by

$$\overline{p_f'}-\frac{\rho_{f0}c_{pf}}{\beta_f T_0}\overline{T_f'}=\frac{\phi_v}{1-\phi_v}\left[\frac{\rho_{p0}c_{pp}}{\beta_f T_0}\overline{T_p'}-\frac{\beta_p}{\beta_f}\overline{p_p'}\right]. \tag{21}$$

This reduces to Eq. (20) only when $\phi_v=0$.

Consider now $d\overline{\rho_p'}/dt$. This may be expressed in terms of the averages of the temperature and pressure fluctuation within a particle, $\overline{T_p'}$ and $\overline{p_p'}$, respectively. Thus proceeding as with the fluid density, we obtain

$$\overline{\rho_p'}=\frac{1}{c_{Tp}^2}\overline{p_p'}-\beta_p\overline{T_p'}. \tag{22}$$

Substituting these expressions into Eq. (18), and remembering that the oscillations are monochromatic, so that $d/dt=-i\omega$, we obtain

$$\frac{\rho'}{\rho_0}=\frac{1-\phi_v}{\rho_{f0}c_{Tf}^2}\overline{p_f'}-\beta_f(1-\phi_v)\overline{T_f'}+\frac{\phi_v}{\rho_{p0}c_{Tp}^2}\overline{p_p'}-\phi_v\beta_p\overline{T_p'}. \tag{23}$$

Now, for monochromatic oscillations, the definition of the compressibility gives

$$\tilde{K}_s=\frac{1}{\rho_0}\frac{\rho'}{p'}. \tag{24}$$

Hence, using the thermodynamic relation $\beta^2c_{Tp}^2T_0=c_p(\gamma-1)/\gamma$, applicable to both fluids, we obtain

$$\frac{K_s(\omega)}{K_{sf}}=(1-\phi_v)\frac{\overline{p_f'}}{p'}\left[\gamma_f-\frac{\rho_{f0}c_{pf}}{\beta_fT_0}(\gamma_f-1)\frac{\overline{T_f'}}{\overline{p_f'}}\right]+\phi_v\left[\gamma_pN_s\frac{\overline{p_p'}}{p'}-\frac{\beta_p}{\beta_f}(\gamma_f-1)\frac{\rho_{f0}c_{pf}}{\beta_fT_0}\frac{\overline{T_p'}}{p'}\right], \tag{25}$$

where $K_{sf}=1/\rho_{f0}c_{sf}^2$ is the isentropic compressibility of the fluid. To simplify this result, it is advantageous to introduce the nondimensional complex ratios

$$\Pi=\frac{\overline{p_p'}}{P_f'} \tag{26a}$$

and

$$T=\frac{\overline{T_p'}}{\Theta_f'}. \tag{26b}$$

In terms of these, and using Eq. (21), we may write Eq. (25) as

$$\frac{K_s(\omega)}{K_{sf}}=\left[1-\phi_v+(\gamma_f-1)\phi_v\left(\frac{\rho_{p0}c_{pp}}{\rho_{f0}c_{pf}}T-\frac{\beta_p}{\beta_f}\Pi\right)\right]\frac{\overline{p_f'}}{p'}+\phi_v\left[\gamma_pN_s\Pi-\frac{\beta_p}{\beta_f}(\gamma_f-1)T\right]\frac{P_f'}{p'}. \tag{27}$$

In addition to the average pressure fluctuation in the particle, $\overline{p_p'}$, Eq. (27) contains three other pressure fluctuations: the pressure fluctuation in the fluid without particles, P_f'; the pressure fluctuation in the fluid in the suspension element, $\overline{p_f'}$; and the imposed pressure fluctuation, p'. For finite volume concentrations, the first of these would differ from the second because of particle interactions. However, for sufficiently dilute suspensions we may neglect those interactions so that $\overline{p_f'}\approx P_f'$.

Now consider the applied pressure fluctuation p'. For sufficiently dilute suspensions we may also take it to be equal to P_f', and this is done below. But for future reference it is noted that the value of p' is determined by the motion of the boundary enclosing the suspension. Hence, in suspensions that are not dilute, we could adjust the motion of that part so that the applied pressure equals the pressure that would exist in a dilute suspension. This artifice may be useful for the study of finite-concentration suspension, as shown in our study of finite mass concentrations in aerosols.[44] For the present investigation, however, the dilute approximation $p'\approx P_f'$ is used. Thus using the two approximate results for $\overline{p_f'}$ and p', Eq. (27) gives

$$(K_s/K_{sf}-1)_{pul}=-\phi_v+\phi_v\{[\gamma_pN_s-(\beta_p/\beta_f)(\gamma_f-1)]\Pi+(\gamma_f-1)[\rho_{p0}c_{pp}/\rho_{f0}c_{pf}-\beta_p/\beta_f]T\}. \tag{28}$$

This expresses the changes in the compressibility of a fluid that arise from the particles' pulsations in terms of the pressure and temperature ratios. Expressing Eq. (28) in terms of $K_s(\omega)/K_s(0)$, and adding the contribution due to the translational motion of the particles, we obtain

$$\frac{K_s(\omega)}{K_s(0)}=1+\phi_v\frac{K_{sf}}{K_s(0)}\left\{\frac{\rho_{p0}}{\rho_{f0}}(V-1)+\left[\gamma_pN_s-\frac{\beta_p}{\beta_f}(\gamma_f-1)\right]\times(\Pi-1)+(\gamma_f-1)\left(\frac{\rho_{p0}c_{pp}}{\rho_{f0}c_{pf}}-\frac{\beta_p}{\beta_f}\right)(T-1)\right\}, \tag{29}$$

where the value of $K_{sf}/K_s(0)$ applicable to small concentrations is given by Eq. (5).

Equation (29) gives the compressibility of a dilute suspension of constant-mass particles in and out equilibrium, in terms of three complex ratios which, in fact, measure the departures from equilibrium. These are the translational velocity ratio, u_p/U_f, the pressure ratio $\overline{p_p'}/P_f'$, and the temperature ratio T_p'/Θ_f'. It is noted that the solution decouples the propagation problem from that of determining these ratios for a single sphere in a fluid as a function of the frequency. The latter requires the solutions of two separate, linear boundary-value problems, one for the translational velocity, and another for the radial velocity of a fluid sphere in a sound wave. Both problems have been solved previously, as discussed below.

But even in its present form, Eq. (29) shows in a clear and succinct manner the importance of these ratios in determining the dynamic response of a suspension to small amplitude oscillatory changes. Thus in the limit of low frequencies these ratios are equal to unity, and Eq. (29) reduces to $K_s=K_s(0)$, so that the attenuation coefficient is zero and the sound speed is $c_s(0)$. At finite frequencies, these ratios are complex, in which case there is attenuation and dispersion.

Equation (29) also shows that the compressibility depends on certain property ratios. These appear as factors in the various terms of Eq. (29), indicating which effects are important in specific suspensions. Table I gives the values of these ratios for particular combinations that apply to aerosols, bubbly liquids, emulsions, and hydrosols. It is noted that in some cases these ratios have either large or small values, making it possible to obtain simpler forms, but that in the case of emulsions, the ratios are of order one, so that it is usually necessary to retain all terms in Eq. (29).

IV. PARTICLE-FLUID RATIOS

Before obtaining the attenuation and the dispersion, we consider the complex particle-fluid ratios for the translational velocity, the temperature, and the pressure of a particle in a suspension that is sustaining a sound wave. The ratios are known from first principles in special cases that relate to single spherical particles in fluids of infinite extent, and we limit the discussion below to this case. Because the transla-

TABLE I. Property ratios for some suspensions at 1 atm and 15 °C.

	Air bubbles in water	Alumina particles in water	Silica particles in water	Toluene drops in water	Water drops in air
c_{sp}/c_{sf}	0.230	4.043	2.763	0.926	4.357
ρ_f/ρ_p	8.16×10^{2}	0.370	0.454	1.15	1.23×10^{-3}
N_s	1.55×10^{4}	1.97×10^{-2}	5.95×10^{-2}	1.34	6.46×10^{-5}
c_{pp}/c_{pf}	0.241	5.42×10^{-2}	0.20	0.395	4.136
β_p/β_f	2.32×10^{1}	1.73×10^{-4}	2.1	6.93	4.31×10^{-2}
κ_p/κ_f	1.45×10^{2}	1.97×10^{3}	3.93	0.788	6.91×10^{-3}

tional and pulsational motions are, by assumption, decoupled, the translational velocity ratio may be calculated on the assumption that the particles are not pulsating. However, a general result that applies to particles made of an arbitrary material and in a wide frequency range does not exist. Nevertheless, we assume that, in all cases, the particles translate in a sound wave as though they are rigid. In the case of bubbles, the assumption is warranted because contaminants collect on the surface of their surface making them behave as rigid,[45] as far as the translational motion is concerned. In addition, because of their small inertia relative to that of the surrounding liquid, the translational motion of the bubbles makes only an insignificant contribution to the total dissipation because the corresponding term in Eq. (29) is of the order of 10^{-3} relative to the others. In the case of droplets in liquids, however, neither of the above supporting reasons exist, thus making the assumption questionable. Thus at low frequencies the force on a drop translating in another liquid differs from that on a rigid sphere by a factor equal to[45] $(1+2\mu_f/3\mu_p)/(1+\mu_f/\mu_p)$, where μ_f and μ_p are the viscosities of the host and particle fluids, respectively. However, if the two viscosities are comparable, this ratio is of the order of one and, therefore, no significant error is introduced by the use of a rigid particle result. At higher frequencies, the differences are probably smaller because of the shorter penetration of shear waves into the droplet. Finally, in the case of liquid droplet aerosols, the above ratio is essentially equal to one. Thus we take the translational velocity in all cases to be equal to the velocity which rigid, spherical particles would acquire in the sound wave. This was obtained some time ago by Temkin and Leung,[31] and may be expressed as

$$V=-3\delta\frac{F+iG}{H+iI}e^{-ib}, \tag{30}$$

where F, G, H, and I are real functions of the nondimensional frequency variables $y=\sqrt{\omega a^2/2\nu_f}$, accounting for viscous effects, and $b=\omega a/c_{sf}$, accounting for compressibility effects in the exterior fluid. In these relations a is the particle radius and ν_f is the kinematic viscosity of that fluid. This result includes both viscous and added mass forces, and both of these forces include the effects of compressibility. Explicit forms for these functions that include typographical corrections are given elsewhere.[46,47] Equation (30) reduces to well-known expressions that apply to specific types of particles in limited portions of the frequency spectrum. The equation has been discussed at length in our previous work (see Sec. III of Ref. 46), and the discussion need not be repeated here. It is important to point out, however, that $V\to1$ at very low frequencies and zero at high frequencies (see Fig. 1 of Ref. 46). The last limit does not occur if compressibility effects are ignored.

Consider now the pulsational motion. Here the quantity of interest is the radial velocity of the surface of the particle, or equivalently, the temperature and pressure ratios. These have also been obtained in a variety of situations, using several simplifying assumptions that limit the results to portions of the frequency spectrum. For example, in the case of gas bubbles in liquids, these quantities have been obtained under the assumptions that the gas in the bubble obeys adiabatic, isothermal, or polytropic relations. A more general result that applies to both droplets and bubbles was obtained recently by the author,[32] on the assumption that $b<1$, so that only the radial mode is excited. The result for the temperature may also be expressed as the ratio of complex quantities, viz.,

$$T=\frac{X+iY}{U+iV}, \tag{31}$$

where the functions X, Y, U, and V are real functions of several nondimensional variables and are given in Appendix A of that work, and for convenience, are also given in Appendix B of this work. The result includes, as a limiting case, the temperature oscillations of rigid particles, in which case the result is of wider applicability than that given earlier.[30] However, this limiting case does not generally apply to all liquid suspensions because the compressibility of liquids is generally so small that the compressibility ratio, N_s, is of the order of one for some hydrosols.

For nonrigid particles, the pressure fluctuation ratio is also needed and this is obtained from the temperature by means of

$$\Pi=\frac{3(1-ib)+3i(\gamma_f-1)(q-b)(b/q)^2+i(\gamma_f-1)b^2[(\kappa_f/\kappa_p)(q-b)G(q_i)+i\beta_p/\beta_f]T}{\gamma_p b^2N_s+(1-ib)b_i^2G(b_i)}, \tag{32}$$

where $q=(1+i)z$, with $z=\sqrt{\omega a^2/2\kappa_f}$, and κ_f is the thermal diffusivity of the fluid, $q_i=(1+i)z_p$, with $z_p=\sqrt{\omega a^2/2\kappa_p}$, and κ_p is the thermal diffusivity of the fluid, $b_i=\omega a/c_{sp}$, and $G(w)=\tanh(w)/[w-\tanh(w)]$. This result for the pressure follows from Eq. 3.36 of Ref. 32. In Fig. 3(a) and (b) we show the temperature and pressure ratios for the four types of suspension treated here. In all cases, the diameter of the particle is 100 μm.

V. ATTENUATION AND DISPERSION

Outside equilibrium, sound waves experience attenuation and dispersion, which can be computed by means of Eqs. (8) and (9). To compare our results to existing ones, which give the sound speed and the attenuation in terms of the sound speed in the fluid alone, we express them in terms of that speed. To do this, we use the value of $K_s(0)/K_{sf}$ given by Eq. (5), applicable to small volume concentrations. Thus the equations for the phase velocity and the attenuation become

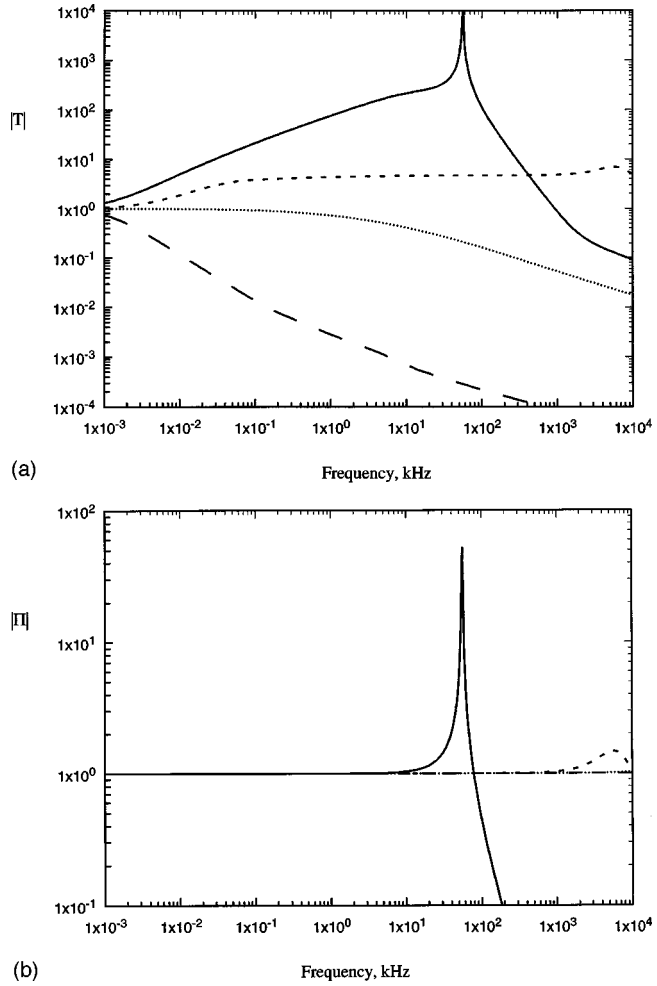

FIG. 3. (a) Amplitude of the temperature ratio for several types of particles having a diameter equal to 100 μm. — — — water droplet in air; · · · · alumina particle in water; - - - toluene droplet in water; —— air bubble in water. (b) Amplitude of the pressure ratio for several types of particles having a diameter equal to 100 μm. — — — water droplet in air; · · · · alumina particle in water; - - - toluene droplet in water; —— air bubble in water.

$$\frac{c_{sf}^2}{c_s^2(\omega)}-\hat{\alpha}^2=\frac{c_{sf}^2}{c_s^2(0)}+\phi_v\left(1+\frac{\phi_v}{\delta}\right)\left\{\frac{1}{\delta}[\Re\{V\}-1]+(\gamma_f-1)\left(\frac{\rho_{p0}c_{pp}}{\rho_{f0}c_{pf}}-\frac{\beta_p}{\beta_f}\right)[\Re\{T\}-1]\right\}+\phi_v\left(1+\frac{\phi_v}{\delta}\right)\left(\gamma_pN_s-(\gamma_f-1)\frac{\beta_p}{\beta_f}\right)\times[\Re\{\Pi\}-1], \tag{33}$$

$$2\hat{\alpha}\frac{c_{sf}}{c_s(\omega)}=\phi_v\left(1+\frac{\phi_v}{\delta}\right)\times\left\{\frac{1}{\delta}|\Im\{V\}|+\left|(\gamma_f-1)\left(\frac{\rho_{p0}c_{pp}}{\rho_{f0}c_{pf}}-\frac{\beta_p}{\beta_f}\right)\Im\{T\}+\left(\gamma_pN_s-(\gamma_f-1)\frac{\beta_p}{\beta_f}\right)\Im\{\Pi\}\right|\right\}, \tag{34}$$

where

$$\frac{c_{sf}^2}{c_s^2(0)}=1+\phi_v/\delta+\phi_v[\gamma_pN_s+(\gamma_f-1)\times(\rho_{p0}c_{pp}/\rho_{f0}c_{pf}-2\beta_p/\beta_f)-2] \tag{35}$$

is the low concentration limit of Eq. (2a), applicable to suspensions of compressible particles.

These equations represent the desired results. They describe sound propagation in dilute suspensions and show that, for a given value of the volume concentration, the attenuation, and sound speed depends strongly on the ratios of the material properties of the fluids inside and outside the particle, and that their variations with frequency are determined by the particle velocity, temperature, and pressure, relative to their counterparts in the fluid, as expressed by the particle-fluid ratios, V, T and Π. Although the expressions for these ratios are algebraically involved, their use in Eqs. (33) and (34) provide the solution to the problem of sound propagation in dilute suspensions of constant-mass particles in a very wide frequency range. This frequency range is only limited by the assumptions made in deriving the particle-to-fluid ratios. Of these, the most restrictive is that used in the pulsational theory, which assumes that $b=(\omega a/c_{sf})<1$. This thus sets the frequency limit for a given particle radius and host fluid. In addition, the results ignore all particle–particle interactions. Because in this paper two different kinds of particle motions are included in three types of suspensions, it is not possible to use a single value of the concentration that will insure that interactions are absent. However, since the ratio of particle diameter to interparticle distance is of the order of $\phi_v^{1/3}$, we require that this quantity be small compared to unity. Thus an upper value of the concentration may thus be taken to be not much larger than 0.01.

Because of the generality claimed for the theory, it is important to compare them to existing results, which, as stated earlier, have been derived for specific types of suspensions. The comparison is thus done best by considering, separately, aerosols hydrosols, emulsions, and bubbly liq-

uids. The comparisons are simpler for suspensions so dilute that ϕ_v/δ and $\phi_v N_s$ are both small compared to unity, and this case is considered first.

A. Small attenuation and dispersion

Before we consider specific suspensions in detail, we note that when the attenuation and the dispersion are small at all frequencies, the solution to the above equations is given by Eqs. (13a) and (13b), which may be expressed as

$$\frac{c_{sf}^2}{c_s^2(\omega)} = \frac{c_{sf}^2}{c_s^2(0)} + \phi_v \left\{ \frac{\Re\{V\}-1}{\delta} + (\gamma_f - 1)\left(\frac{\rho_{p0} c_{pp}}{\rho_{f0} c_{pf}} - \frac{\beta_p}{\beta_f} \right)[\Re\{T\}-1] + \left(\gamma_p N_s - (\gamma_f - 1)\frac{\beta_p}{\beta_f} \right)[\Re\{\Pi\}-1] \right\}, \tag{36}$$

$$\hat{\alpha} = \frac{1}{2}\phi_v \left\{ \frac{1}{\delta}|\Im\{V\}| + \left| (\gamma_f - 1)\left(\frac{\rho_{p0} c_{pp}}{\rho_{f0} c_{pf}} - \frac{\beta_p}{\beta_f} \right)\Im\{T\} + \left(\gamma_p N_s - (\gamma_f - 1)\frac{\beta_p}{\beta_f} \right)\Im\{\Pi\} \right| \right\}. \tag{37}$$

We note that the contributions produced by the various mechanisms can, in this case, be separated.

1. Attenuation

Because the effects are separable, we may define translational and pulsational attenuation coefficients by means of

$$\hat{\alpha}_{tr} = \frac{1}{2}\frac{\phi_v}{\delta}|\Im\{V\}|, \tag{38}$$

$$\hat{\alpha}_{pul} = \frac{1}{2}\phi_v \left| (\gamma_f - 1)\left(\frac{\rho_{p0} c_{pp}}{\rho_{f0} c_{pf}} - \frac{\beta_p}{\beta_f} \right)\Im\{T\} + \left(\gamma_p N_s - (\gamma_f - 1)\frac{\beta_p}{\beta_f} \right)\Im\{\Pi\} \right|. \tag{39}$$

As Eq. (32) shows, T and Π are related to one another, which means that the two terms inside the absolute sign in Eq. (39) are coupled.

a. Rigid particles. In the case of particles that are nearly rigid in comparison with the exterior fluid, e.g., droplets in air, both β_p/β_f and N_s are negligible, and Eq. (39) gives an attenuation that is due to thermal effects only. Thus

$$\hat{\alpha}_{th} = \frac{1}{2}\phi_v(\gamma_f - 1)\frac{\rho_{p0} c_{pp}}{\rho_{f0} c_{pf}}|\Im\{T\}|. \tag{40}$$

These forms are useful for comparison with existing results for them. Consider the translational attenuation first. This is given by Eq. (38) and was earlier found to agree with dissipation-based results, applicable to specific types of suspensions and frequency ranges.[30] We now show that this agreement applies in general. Thus when the particle are executing harmonic translational oscillations without a change of volume, the force on one of them is $-i\omega m_p u_p$. The average energy spent by this force to produce a relative particle displacement $(u_p - U_f)$ per unit time is $\langle \dot{e}_{tr} \rangle = \frac{1}{2}\omega m_p \Im\{u_p U_f^*\}$, where the asterisk represents a complex conjugate. Multiplying this by the number of particles per unit volume, and using the energy-based definition of the attenuation, $\hat{\alpha}_{tr} = n|\langle \dot{e}_{tr} \rangle|/2\omega E_0$, where $E_0 = \frac{1}{2}\rho_{f0} U_{f0}^2$ is the energy density in the incident wave, produces Eq. (38). Thus regardless of the type of suspension, the dissipation, and the compressibility calculations lead to the same analytical result for the translational attenuation. Specific results applicable to special cases were discussed earlier and need not be considered here. It should nevertheless be pointed out that those results were found to agree with other theories as well as with experimental results applicable to them.

Similar agreement is found for the attenuation due to thermal effects. This is given by Eq. (40) and is identical to the dissipation based result obtained earlier for this case.[30]

b. Nonrigid particles. We now consider the pulsational attenuation for particles whose compressibility is not negligible in comparison to that of the host fluid. This includes some hydrosols, emulsions, and bubbly liquids. Now, the pulsation attenuation is given by Eq. (39), and includes two dissipative mechanisms: thermal dissipation and dissipation due to acoustic radiation. However, because the particle temperature and pressure are not independent of one another, it is not usually possible to use that equation to obtain separate attenuation coefficients, as is possible when energy methods are used. Nevertheless, a comparison between the sum of the existing thermal and acoustic attenuations and Eq. (39) is possible. These energy dissipation thermal and acoustic coefficients were obtained recently.[32] The first was obtained to various degrees of accuracy, but the form given below, which ignores dissipation in the exterior fluid is sufficient. This is obtained from Eq. 7.4 of that work by omitting the second term on the right hand side of that equation. Thus

$$\hat{\alpha}_{th} = \tfrac{3}{2}\phi_v(\gamma_f - 1)(\beta_p/\beta_f)|\Re\{iT\Pi^*\}|. \tag{41}$$

Similarly, the attenuation due to acoustic radiation, called acoustic for simplicity, was found to be given by

$$\hat{\alpha}_{ac} = \frac{3\phi_v}{2b}|\Pi - 1|^2. \tag{42}$$

This equation corrects the typographical omission of the factor b in Eq. (7.2) of Ref. 32.

2. Hydrosols

To illustrate these ideas we first show in Fig. 4(a) the dissipation based attenuation coefficients for a hydrosol composed of 100 μm glass particles in water and having a volume concentration equal to 10^{-3}. The density ratio for this case is 0.85, which is sufficiently different from unity so as to produce a translational attenuation that overwhelms the thermal effects. At higher frequencies, the particles' translational motion essentially ceases, but, nevertheless, a significant amount of attenuation is produced by them via scattering. Next is the acoustic attenuation produced by the radial pulsations of the particle. This is negligible at most frequencies, but if the particles' compressibility is not negligible, it becomes of the same order of magnitude as the translational scattering at high frequencies. Finally, two results are shown for the thermal attenuation. The first is based on Eq. (44) and

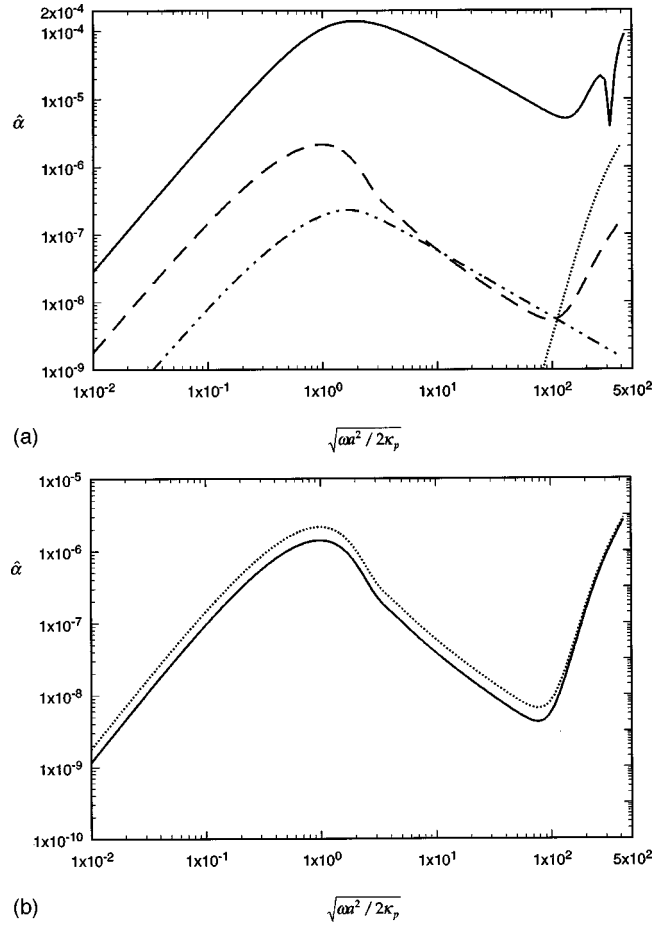

FIG. 4. (a) Nondimensional attenuations for 100 μm silica particles in water. $\phi_v = 10^{-3}$. —— Translational; — — — Thermal; –·–·–·– Thermal, rigid particles; · · · · Acoustic. (b) Comparison of present results for the pulsational attenuation with the dissipation results obtained from dissipation theory for a hydrosol composed of 100 μm silica particles in water. $\phi_v = 10^{-3}$. —— Dissipation theory; · · · · Compressibility theory.

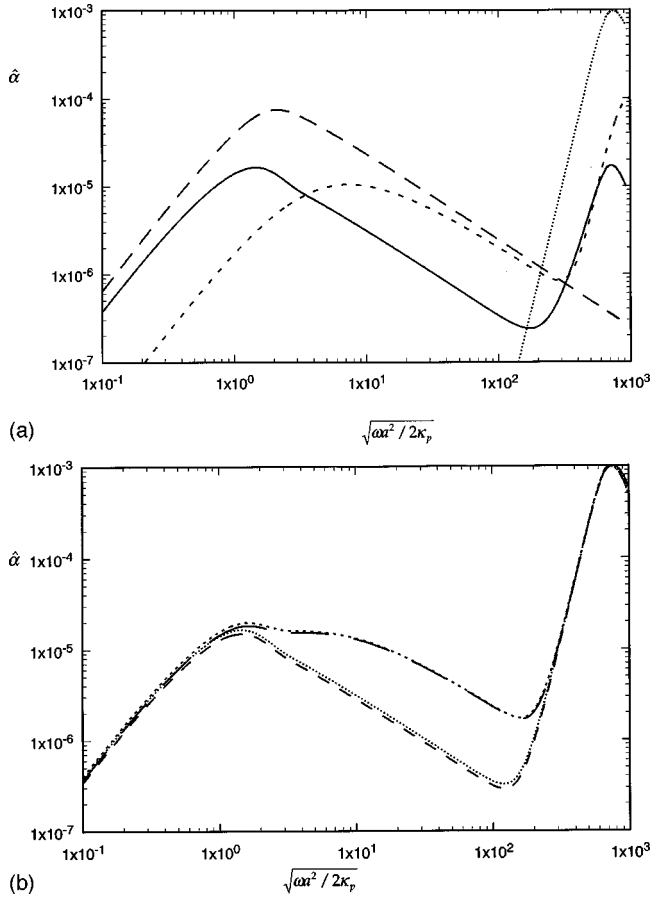

FIG. 5. (a) Nondimensional attenuations for 100 μm toluene droplets in water. $\phi_v = 10^{-3}$. —— Thermal; — — — Thermal, Isakovich; - - - Translational; · · · · Acoustic. (b) Comparison of present results for the pulsational attenuation with the dissipation results obtained from dissipation theory for an emulsion of 100 μm toluene droplets in water. $\phi_v = 10^{-3}$. · · · · Dissipation; ———— Compressibility; – – – Total attenuation via dissipation; - - - Total attenuation via compressibility.

includes the effects of the pulsational motion. The second is based on Eq. (40) and disregards them. It is seen the pulsational thermal attenuation is significantly larger than the rigid particle value at low frequencies, and that at moderately large frequencies both attenuations are comparable, owing to the particle's temperature being, then, essentially constant. However, at the high-frequency limit shown in the figure, the pulsational thermal attenuation is seen to increase in amplitude owing to thermal effects associated with the radial resonance. These features are not general; other particle-fluid combinations produce different relative magnitudes of the various effects.

In Fig. 4(b) we show the sum of the thermal and acoustic dissipation-based attenuations as well as the pulsational attenuation, $\hat{\alpha}_{pul}$, as given by Eq. (39) for the above hydrosol. It is seen that the two computations agree fairly well throughout the frequency range shown in the figure.

3. Emulsions

Figure 5(a) and (b) show the corresponding results for an emulsion of 100 μm toluene particles in water, having a volume concentration equal to 10^{-3}. The attenuations are shown as a function of $z_p = \sqrt{\omega a^2/2\kappa_p}$. Also shown in Fig. 5(a) is the thermal attenuation predicted by the theories of Isakovich,[26] and of Allegra and Hawley.[27] As noted earlier,[32] our attenuation differs from theirs in two important aspects. First, those theories do not seem to include acoustic radiation as a dissipation mechanism. Second, their thermal attenuation does not include the effects of pressure variations within the particles, a neglect that results in a larger thermal dissipation than it actually exists. This can be seen by setting $\Pi = 1$ in both Eqs. (41) and (42). This eliminates the pressure disturbance and produces the results of Allegra and Hawley and of Isakovich.

Figure 5(b) shows a comparison between the dissipation and compressibility attenuations, and it can be seen there that the two theoretical results are nearly equal. This agreement, like that observed previously for rigid particles, and above for elastic particles is important because of the different methods used in the derivations of the two sets of results. Incidentally, the agreement occurs for concentrations as large as 0.1 m and implies that the complete equations are not needed for emulsions.

4. Bubbly liquids

We now consider the pulsational attenuation in bubbly liquids. A comparison of the present results with the

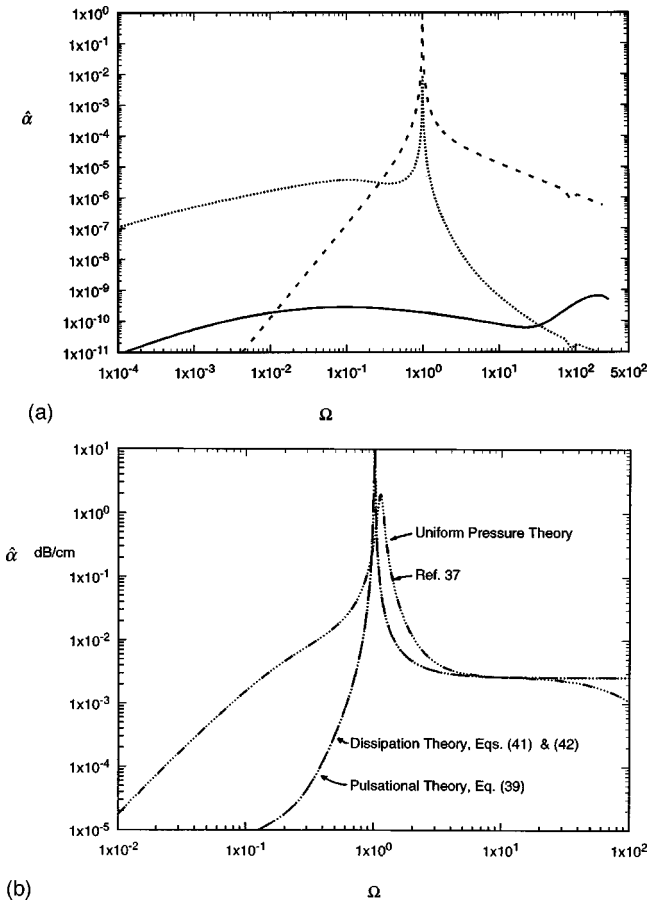

FIG. 6. (a) Nondimensional attenuations for 100 μm air bubbles in water. $\phi_v = 10^{-6}$. —— Translational; — — — Acoustical; · · · · Thermal. (b) Comparison of present results for the pulsational attenuation in dB/cm with corresponding result obtained from dissipation theory and from the existing theories for a bubbly liquid consisting of 100 μm diameter air bubbles in water. $\phi_v = 10^{-6}$. ——— Dissipation ($\hat{\alpha}_{th} + \hat{\alpha}_{ac}$); — — — Ref. 37; · · · · Pulsational; · · · · Uniform pressure.

dissipation-based attenuation is possible only when the attenuation is small, as this is assumed in the dissipation theory. To do this we consider a very dilute suspension of air bubbles in water. In Fig. 6(a) we show the separate dissipation results, and in Fig. 6(b) we show $\hat{\alpha}_{th} + \hat{\alpha}_{ac}$ as computed from the dissipation theory and the current result for $\hat{\alpha}_{pul}$, Eq. (39), for a bubbly liquid of 100 μm air bubbles in water having a volume concentration equal to 10^{-6}. As the figure shows, the two results are in agreement at all frequencies including the resonance region. As in the previous cases, this agreement between different theories is important.

Also shown in Fig. 6(b) are the results of two other theories. One of those is the dilute theory currently in use, as represented, for example, by Commander and Prosperetti.[37] That theory has been derived by several authors, and in essence is the isothermal theory first derived by Kennard,[33] modified so as to include thermal dissipation. This is done via a thermal damping coefficient[48] which overestimates, by a significant amount, the actual thermal damping.[32] Also, that theory uses Wood's equation as the low-frequency sound speed in bubbly liquids, which as shown in Fig. 2(a) and elsewhere,[38] leaves out thermal effects. The second additional theory is that derived form the present results, Eq. (39), by setting $\Pi = 1$. Because the pressure is, then, everywhere equal to P_f', we have named this theory the *uniform pressure theory*. It is seen that these two theories agree with one another, and produce a dilute attenuation coefficient that differs, considerably, from the present results in the region below resonance. As in the case of emulsions, the differences are due to the neglect in those theories of the acoustic pressure disturbance produced by the pulsating particle.

The comparison also shows some differences in the resonance region, but the most salient one relates to the frequency at which resonance occurs. In the existing theory, i.e., that frequency depends on various quantities, some of which are themselves functions of the frequency. Thus in the absence of surface tension effects, the resonance frequency used in those theories may be expressed as

$$\omega_0 = \frac{c_{Tp}}{a}\sqrt{3\kappa/\delta}. \tag{43}$$

Here $\kappa = \kappa(\omega)$ is Prosperetti's polytropic index (Eq. 3.23 of Ref. 48), a quantity that varies from unity at low frequencies to γ_p at high frequencies. Our theory, on the other hand, shows that resonance always occurs at a frequency given by

$$\omega_{T0} = \frac{c_{Tp}}{a}\sqrt{3/\delta}. \tag{44}$$

This value follows from our general results, and corresponds to that which is obtained when propagation in the *liquid* is nearly isothermal, even though the bubbles temperature varies. Thus Prosperetti's resonance frequency is always larger than that predicted by Eq. (44), by a factor equal to $\sqrt{\kappa}$.

5. Dispersion

Let us now consider the changes in the sound speed that occurs as the frequency of the sound waves is changed in a suspension. This may be done directly in terms of $c_s(\omega)$, or, if the suspension is very dilute, in terms of

$$\hat{\beta} = \frac{c_{sf}^2}{c_s^2(0)} - \frac{c_{sf}^2}{c_s^2(\omega)}. \tag{45}$$

This quantity is useful for dilute suspensions because, for them, it is given by separate contributions due to translational and pulsational effects. Thus $\hat{\beta} = \hat{\beta}_{tr} + \hat{\beta}_{pul}$, where

$$\hat{\beta}_{tr} = \phi_v \frac{1 - \Re\{V\}}{\delta}, \tag{46}$$

$$\hat{\beta}_{pul} = \phi_v \left\{ (\gamma_f - 1)\left(\frac{\rho_{p0} c_{pp}}{\rho_{f0} c_{pf}} - \frac{\beta_p}{\beta_f}\right)[1 - \Re\{T\}] + \left(\gamma_p N_s - (\gamma_f - 1)\frac{\beta_p}{\beta_f}\right)[1 - \Re\{\Pi\}] \right\}. \tag{47}$$

The last of these may also be subdivided into thermal and acoustic coefficients, but the form above is needed later, and also makes it clear which effects and physical properties dominates the speed changes for a given suspension. Thus if $\beta_p \ll \beta_f$ and $N_s \ll 1$, the particles may be regarded as rigid, in which case Eq. (47) reduces to

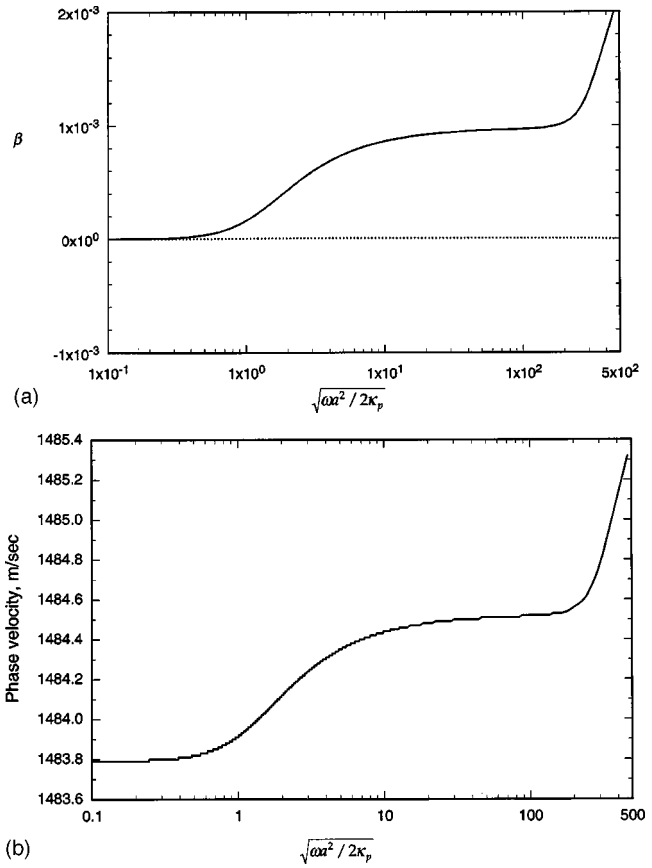

FIG. 7. (a) Dispersion coefficient for a hydrosol consisting of 100 μm diameter silica particles in water. $\phi_v = 10^{-3}$. —— Translational; · · · · Pulsational. (b) Phase velocity in a hydrosol consisting of 100 μm diameter silica particles in water. $\phi_v = 10^{-3}$. Translational effects only.

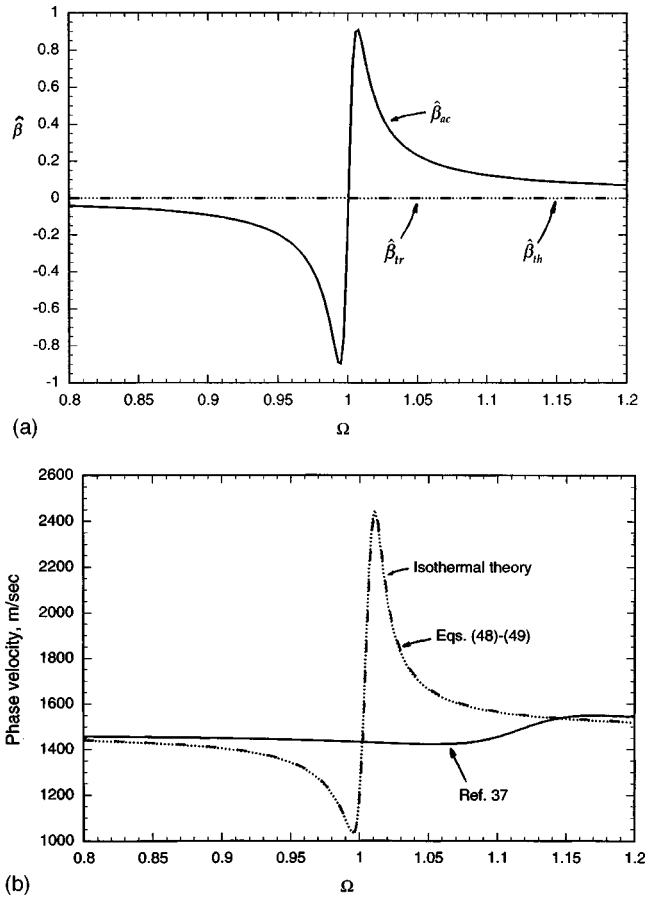

FIG. 8. (a) Dispersion coefficients for a bubbly liquid consisting of 100 μm diameter air bubbles in water. $\phi_v = 10^{-6}$. —— Acoustical; — — — Translational; · · · · Thermal. (b) Phase velocity in a bubbly liquid consisting of 100 μm diameter air bubbles in water. $\phi_v = 10^{-6}$. —— Ref. 37; — — — Present results, Eqs. (48)–(49); · · · · Isothermal results, Eqs. (50)–(51).

$$\hat{\beta}_{pul} \to \phi_v(\gamma_f - 1)\frac{\rho_{p0}c_{pp}}{\rho_{f0}c_{pf}}[1 - \Re\{T\}],$$
$$\beta_p \ll \beta_f \quad \text{and} \quad N_s \ll 1. \tag{48}$$

This quantity, together with Eq. (46), prescribes sound dispersion in dilute suspensions of rigid particles. This case was treated earlier,[30] and the result given by Eq. (48) is equal to the thermal dispersion, $\hat{\beta}_{th}$, given there. For nonrigid particles, Eqs. (46) and (47) apply. This includes all liquid suspensions, and is particularly important for bubbly liquids and the emulsions. Below, we reduce the present results for the three types of liquid suspensions and compare them to the theories currently in use.

a. Hydrosols. We again consider a hydrosol consisting of 100 μm diameter silica particles in water, and having a volume concentration equal to 0.001. As shown in Fig. 7(a), the pulsational dispersion contribution is negligible for this case, even though they include thermal effects. But even the translational effects are rather small. This is shown in Fig. 7(b) where we show the changes of the phase velocity produced by the translational effects alone. It should be noted that for the selected case, the frequency corresponding to the highest value of z_p shown in the figure is about 12 MHz.

b. Bubbly liquids. In the case of bubbly liquids, the translational contribution is negligible, owing to the very large value of the fluid to particle density ratio. Hence, the dispersion is largely due to the pulsational contribution, which is, itself, dominated by the acoustic component, given by the second term in Eq. (46). This is shown in Fig. 8(a) where we show the dispersion coefficient for a very dilute suspension of 100 μm diameter air bubbles in water versus $\Omega = \omega/\omega_{T0}$. In the graph we show the various contributions to the dispersion coefficient β. Also shown there is the sum of all the contributions.

In Fig. 8(b) we show that phase velocity, $c_s(\omega)$, as a function of the nondimensional frequency ratio $\Omega = \omega/\omega_{T0}$, as predicted by Eq. (47) and by the existing theories as given by Commander and Prosperetti.[37] It is seen that significant differences also exist here, and the reasons are the same as in the case of the attenuation. We shall return to these issues later, when we discuss propagation in bubbly liquids having larger volume concentrations than considered in this section.

c. Emulsions. In Fig. 9(a) we show the dispersion coefficient $\hat{\beta}$ for an emulsion of 100 μm diameter Toluene droplets in water. It is seen that, except for the region near resonance, the changes are generally very small. At low frequencies, the thermal and translational contributions have similar, but opposite, values, with the acoustic contribution becoming dominant at higher frequencies.

These results are new and are quite different from those

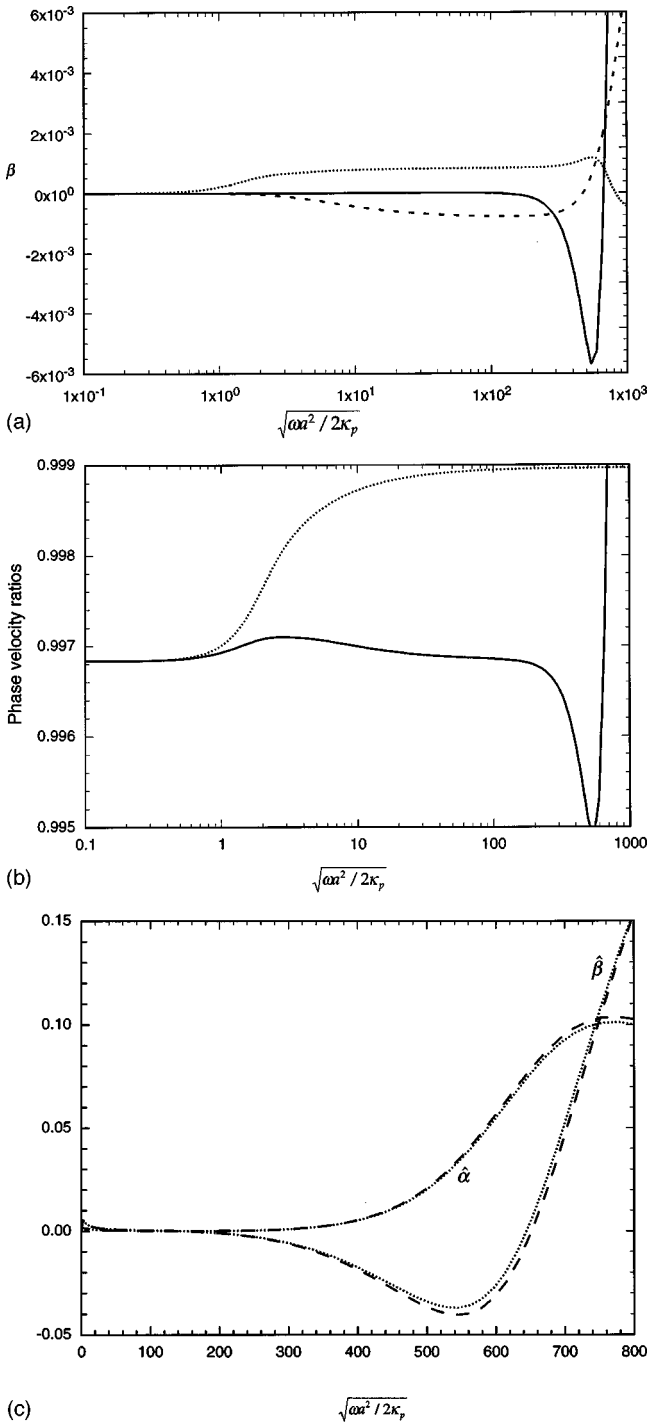

FIG. 9. (a) Dispersion coefficient for an emulsion consisting of 100 μm diameter toluene droplets in water. $\phi_v = 10^{-2}$. — — — Translational; —— Acoustical; · · · · Thermal. (b) Phase velocity ratio $c_s(\omega)/c_{sf}$ in an emulsion of 100 μm diameter toluene droplets in water. $\phi_v = 10^{-2}$. —— Complete theory; · · · · Uniform pressure theory. (c) Attenuation and dispersion in an emulsion of 100 μm diameter toluene droplets in water. — — — Eqs. (33)–(34); · · · · Eqs. (36)–(37). $\phi_v = 0.1$.

currently in use. These have been obtained on the basis of a model based on the theories of Isakovich[26] and Allegra and Hawley[27] (see, for example, Refs. 29 and 49). Essentially, these models also use a complex compressibility to connect the frequency sound speed to the attenuation, as our starting equation does, but the result ignores some important effects. First, the effects considered by them are the same as those included in the Allegra and Hawley and Isakovich formulations. As described earlier[32] and above, these theories leave out the pressure disturbance produced by the particle in the fluid. Hence, what has been called here the acoustic contribution is completely absent in those theories. Second, the thermal effects are overestimated, owing to the neglect of the pressure disturbance. Third, the translational contribution used in those theories contains an incorrect dependence on the density ratio as discussed elsewhere.[30,46] This tends to decrease the effects of the relative velocity between particle and fluid. Lastly, the zero frequency sound speed used in all of these theories is that given by Wood, which, as stated in the Introduction, does not apply to emulsions.

An idea of the effects of these omissions may be obtained from Fig. 9(b), where we plot two results for the phase velocity ratio, $c_s(\omega)/c_{sf}$. The first of these is based on our current results, but takes the pressure to be uniform everywhere and neglects the translational contribution. It, however, uses our zero frequency speed, Eq. (2), instead of Wood's equation. The second result is our complete theory without translational effects. Except for the zero frequency speed, the first result is essentially equal to that predicted by the existing theories. It is clear that the omissions of the effects mentioned above produce significant differences between the existing and current results. However, in spite of these, McClements and Povey's experiments show good agreement with their theory. We have no explanation for this agreement but would like to point out that the attenuation and the speed of sound are not independent quantities. This is a direct consequence of the causality requirement, as expressed by the Kramers–Kronig relations (see, for example, Refs. 50 and 51). Thus once the attenuation is specified over the complete frequency range, the sound speed is prescribed by those relations, and this is in fact implied by our results. As the derivation of those relations makes it clear, there is no freedom to separately define either the phase velocity or the attenuation; both quantities must satisfy the theory. But in the existing theories, the propagation constant is obtained by adding a phase velocity that obeys Wood's equation at zero frequencies to a complex part that is related to the Allegra and Hawley and Isakovich result. In the author's opinion, this procedure necessarily leads to results that cannot represent the effects present during the propagation.

In anticipation of the next section, we point out here that the dilute equations considered in this section agree, in the case of emulsions and hydrosols, with the more complete equations for volume concentrations as large as 0.1. This is shown in Fig. 9(c) where the attenuation and dispersion coefficients predicted by both the dilute and complete equations are shown as a function of the frequency. Essentially, this agreement implies that we require the complete equations only for bubbly liquids that do not have exceedingly small concentrations, as those considered above.

B. finite attenuation and dispersion

We now consider the complete set of equations, Eqs. (33) and (34). For aerosols and hydrosols this set reduces to previously known results and need not be considered here. Also, except for aerosols having finite mass concentrations,

the complete set of equations is not required for them. This is also true for emulsions and hydrosols because the attenuation is generally small in them. Thus we need the complete set of equations only to discuss propagation in bubbly liquids. Here the effects of resonance are highly pronounced and it is usually not possible to neglect the square of the attenuation coefficient in Eq. (33). However, certain other simplifications are possible. First, the translational effects are generally negligible, owing to that large value of the density ratio δ applicable to bubbly liquids. Second, since N_s is of the order of 10^4, and $\gamma_f - 1$ is small, we may neglect the second term inside the pressure-ratio term on the right hand side of Eqs. (33) and (34). Further simplification is possible at frequencies that are not very small. At these, the temperature terms in Eqs. (33) and (34) may be neglected. Hence, Eqs. (33) and (34) reduce to

$$\frac{c_{sf}^2}{c_s^2(\omega)} - \hat{\alpha}^2 = 1 + \phi_v \gamma_p N_s \Re\{\Pi\}, \tag{49}$$

$$2\hat{\alpha}\frac{c_{sf}}{c_s(\omega)} = \phi_v \gamma_p N_s |\Im\{\Pi\}|. \tag{50}$$

It should be added that, although the temperature does not explicitly appear in this simplified set of equations, the complex pressure ratio, Π, appearing in them, is generally affected by it.

1. Isothermal conditions

While no ordinary suspension remains at constant temperature during the passage of a sound wave, propagation in liquids is nearly isothermal because $\gamma_f \approx 1$ for them. For the purpose of comparison with actual cases, where temperature changes occur, it is of some interest to consider a hypothetical case in which the suspension as *a whole* remains at constant temperature. The results for this case may be obtained from the nonisothermal results, Eqs. (49)–(50), by taking $\gamma_f = \gamma_p = 1$. Thus denoting all variables with the subscript T to denote isothermal conditions, we have

$$\frac{c_{Tf}^2}{c_T^2(\omega)} - \hat{\alpha}_T^2 = 1 + \phi_v N_T \Re\{\Pi_T\}, \tag{51}$$

$$2\hat{\alpha}_T\frac{c_{Tf}}{c_T(\omega)} = \phi_v N_T |\Im\{\Pi_T\}|. \tag{52}$$

Now, the value of Π_T for a small spherical bubble of equilibrium radius a is easily computed from first principles, or from Eq. (32), and is given by

$$\Pi_T = \frac{1 - ib_T}{1 - \Omega^2 - ib_T}, \tag{53}$$

where $b_T = \omega a / c_{Tf}$. Substituting this in the above set we obtain

$$\frac{c_{Tf}^2}{c_T^2(\omega)} - \hat{\alpha}_T^2 = 1 + \phi_v N_T \frac{1 - \Omega^2 + b_T^2}{(1-\Omega^2)^2 + b_T^2}, \tag{54}$$

$$2\hat{\alpha}_T\frac{c_{Tf}}{c_T(\omega)} = \phi_v N_T \frac{b_T \Omega^2}{(1-\Omega^2)^2 + b_T^2}. \tag{55}$$

These equations have the same structure as those available in the literature. As far as this author knows, the first derivation of these results was given by Kennard[33] in a war report released in 1950. In fact, the right hand side of Eqs. (54) and (55) can be expressed in a manner identical to that in Kennard's set. Similar equations were derived later by Carstensen and Foldy[25] on the basis of scattering theory; by van Wijngaarden[28] on the basis of a fluid dynamic model similar to that used by Kennard, and in equivalent manners by other authors (for example, Refs. 14, 37, and 52). A similar set was derived by this author[16] on the basis of the Kramers–Kronig relations. Also, the resonant theory of Gaunaurd and Uberall[53] produces, when reduced numerically, results which are similar to those produced by this set.

2. Comparison to existing theories

Consider first the attenuation. In Fig. 10(a) we show $\hat{\alpha}$ as a function of $\Omega = \omega/\omega_{T0}$, as predicted by various theories for a bubbly liquid having a volume concentration equal to 10^{-2}. It is seen that the isothermal and the present theories agree fairly well in the resonance region and beyond. Below resonance the two sets diverge owing to thermal effects not included in the isothermal theory. On the other hand, the existing theories predict a much larger attenuation below resonance. This is due to their using a thermal damping coefficient that significantly overestimates thermal dissipation in that frequency region. In the resonance region closer agreement is obtained, and this is due to the fact that acoustic radiation is, there, the dominant dissipative mechanism. However, we see again that the existing theory produces an attenuation peak at a higher frequency than predicted by the present results.

Similar results are found for the phase velocity, $c_s(\omega)$. In Fig. 10(b) we show this quantity as predicted by the three theories used above. Here, the differences between existing and current results occur immediately above resonance, where $c_s(\omega)$ changes most rapidly. The differences depend on bubble size and seem to decrease as the size is increased.

Figure 11 shows the attenuation for a range of volume concentrations, as predicted by the present theory. We see that both the amplitude and the width of the attenuation peak change, but that the frequency of the maximum attenuation values remain fixed. This is as it should be because all the curves were based on the same pressure and temperature ratios. Hence, the differences in the various curves are not produced by different bubble responses, but by the different properties of the bubbly liquid that result from increased gas concentration.

Let us now consider some implications of these attenuation results. For this purpose, we choose the effective wavelength, $2\pi c_s(\omega)/\omega$ as the reference distance. For a 100 μm air bubble this distance is about 2.5 mm or smaller in the resonance region. Now, the decay in that distance is given by $\exp[-2\pi\hat{\alpha}c_s(\omega)/\omega]$. From Fig. 11 it is seen the value of the product $\hat{\alpha}\cdot c_s(\omega)/\omega$ in that region is larger than 10 for a volume concentration equal to 10^{-2}, implying that in a distance comparable to the effective wavelength the amplitude of the wave becomes negligible. In the opinion of the author,

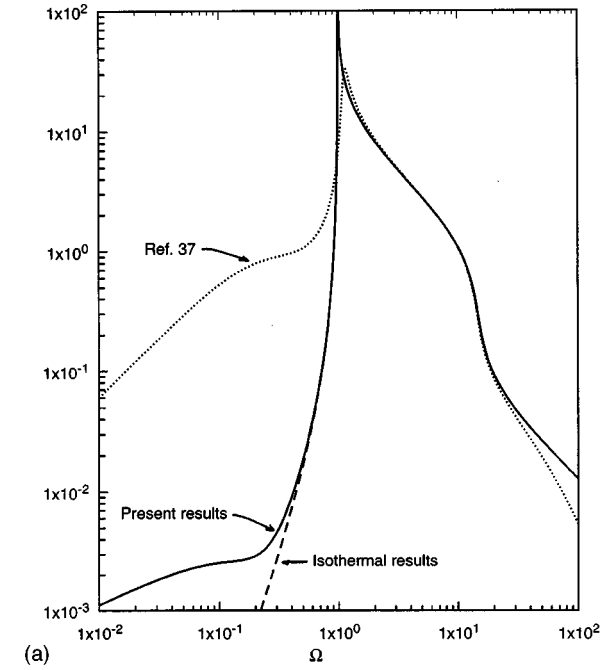

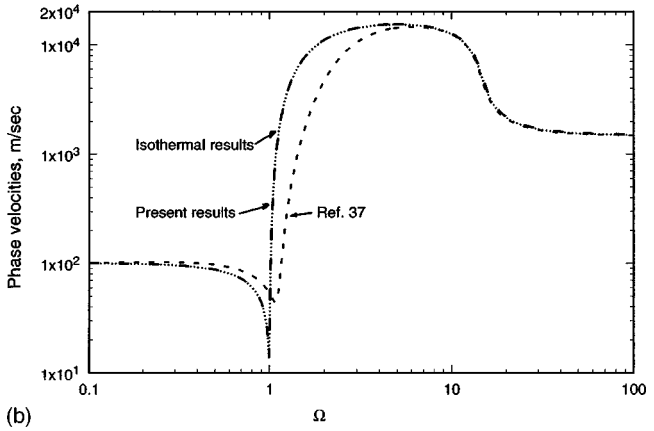

FIG. 10. (a) Attenuation for 100 μm diameter air bubbles in water. —— Complete results, Eqs. (33)–(34); — — — Isothermal results, Eqs. (53)–(54); · · · · Ref. 37. $\phi_v = 0.01$. (b) Variations of $c_s(\omega)$ and $c_T(\omega)$ with frequency for a bubbly liquid consisting of 100 μm air bubbles in water. $\phi_v = 0.01$. — — — $c_s(\omega)$ from, Eqs. (33)–(34); · · · · $c_T(\omega)$ from, Eqs. (53)–(54); - - - Ref. 37.

it is not possible to accurately measure such decays directly, that is, by measuring the amplitude of the wave as a function of position in a propagating wave.

C. Comparison with experimental results

1. Attenuation

With these comments in mind we consider the experimental measurements of attenuation that were reported in the fifties by Silberman.[34] These measurements are regarded as the most accurate, particularly with regard to size control[3,37] and have also been chosen because of the wide range of frequencies covered by them.[12,54] Commander and Prosperetti[37] have shown that if account is made of the polydispersity of the suspensions used by Silberman, good agreement is obtained between some features of their theory and the data. This agreement does not include the amplitude of the attenuation, which is not affected by size averaging.

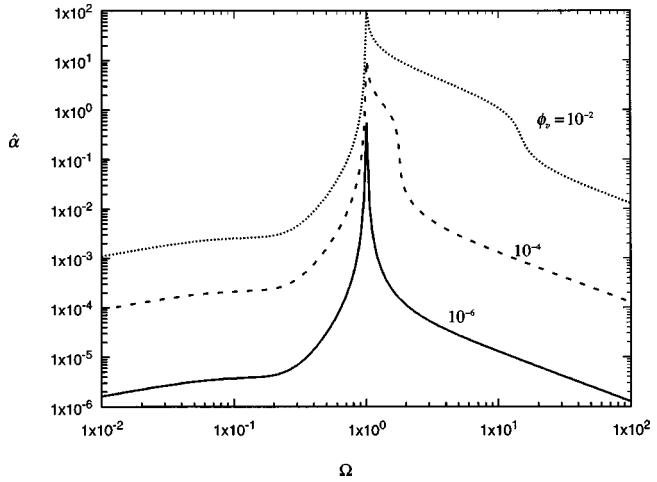

FIG. 11. Attenuation in a bubbly liquid having different dilute concentrations. Bubble diameter is 100 μm.

Similar differences were observed by Sangani,[3] and by Drumheller and Bedford[12] in their more detailed analyses. On the other hand, Ruggles *et al.*[54] report excellent agreement with their two-phase theory, but the theory involves several empirical quantities that are probably responsible for the good agreement.

We now compare Silberman data to the theory developed here. His attenuation data were obtained for a range of volume concentrations, and we have selected two such data sets for comparison. In Figs. 12 and 13 we show his data for $\phi_v = 3.77 \times 10^{-4}$, and 0.01, respectively. These correspond to Figs. 9 and 5 of Silberman's original paper. In each case, the data were given for several bubble sizes, and we have

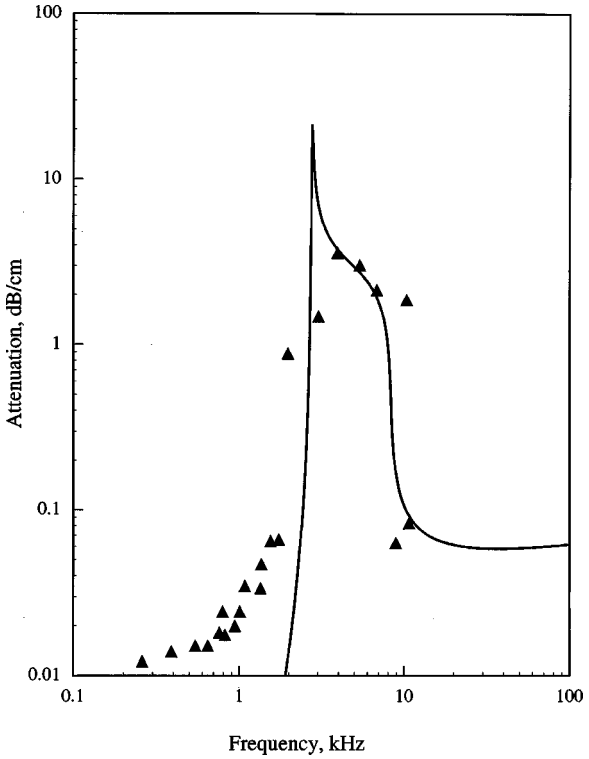

FIG. 12. Comparison between the predicted attenuation with Silberman's Fig. 9 data. $\phi_v = 3.8 \times 10^{-4}$, $a = 0.2$ cm.

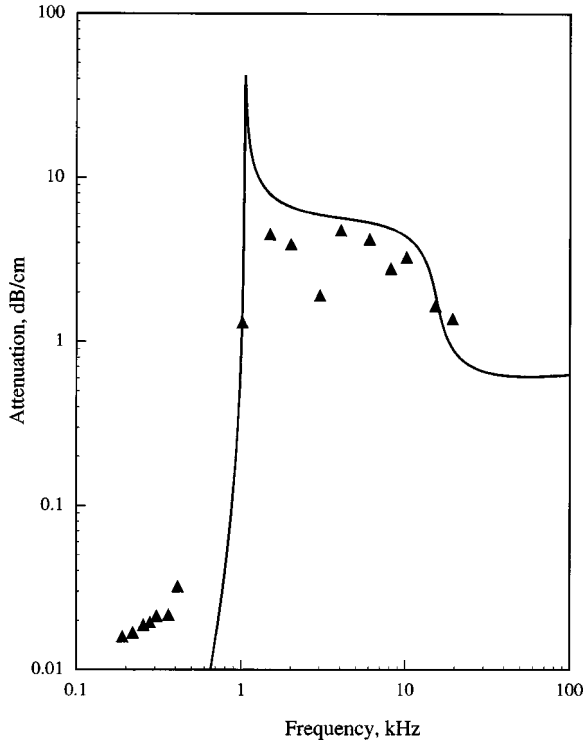

FIG. 13. Comparison between the predicted attenuation with Silberman's Fig. 5 data. $\phi_v = 0.01$, $a = 0.528$ cm.

selected only one of those sizes for each set to reduce our monodisperse theory. The selected sizes are the most representative of each experimental set, so that for them the suspension may be regarded as monodisperse. The data are presented in the manner given by Silberman, that is, the attenuation coefficient is given in dB/cm as a function of the frequency in kHz. The comparison includes some data points not displayed by Sangani in his Fig. 18. Most of these apply to the low-frequency range, but some occur at high frequencies. We consider the two frequency ranges separately.

In the resonance region and beyond we observe a rough agreement between theory and experiments. However, the actual differences between experimental measurements and theory remain rather large, and are hidden by the logarithmic presentation. It should be noted that Silberman used the direct decay method to measure the attenuation in the high-attenuation region [see his Eq. (7) and accompanying paragraph]. Given the difficulties described above in making accurate decay measurements in the resonance region, we cannot expect a better agreement than that shown in the figure.

Consider now the low-frequency region. Here the above limitations do not apply because the attenuation is small. Nevertheless, the disagreement between theory and experiments seems stronger, while, as shown by Commander and Prosperetti,[37] agreement with their theory is nearly perfect. But that agreement relies on a thermal damping coefficient that overestimates the actual damping in that frequency region by about two orders of magnitude.[32] It must therefore be concluded that the agreement reported by these authors is fortuitous.

2. Phase velocity

As pointed out earlier, the phase velocity and the attenuation coefficient are related by means of the K–K equations. Thus experimental verification of a propagation theory only requires measurements of either quantity. However, given the experimental difficulties associated with the measurements of the attenuation, sound speed data can be useful.

But measuring this quantity in the resonance region has also proven to be difficult, as shown by Silberman's data. It is true that Fox *et al.*[55] were able to cover that region, but their data have a rather large spread of bubble sizes. Recently, however, Cheyne *et al.*[36] reported phase velocity measurements in a bubbly liquid having a well-controlled bubble size and volume concentration. Their measurements were made in a nonintrusive manner and extend from about 185 Hz to about 13 000 Hz, a range that included the resonance region for the bubble size used. Although the data are presented in a log–log scale, their Fig. 4 shows excellent agreement with the existing theories, as represented by Commander and Prosperetti.[37]

As we have shown in Fig. 10(b), the numerical differences between the speeds predicted by our present results, by the isothermal results, and by Commander and Prosperetti's results are generally not large. An important exception occurs in the resonance region, where the Commander and Prosperetti's theory predicts a less pronounced minimum speed than ours, as well as a smaller value beyond this minimum point. In addition, the minima points in the two theoretical sets occur at different values of the frequency. That minimum value is very important because it nearly corresponds to the resonance frequency of a bubble in a liquid. Given the excellent agreement obtained by Cheyne *et al.*, it would appear that the resonance frequency for a bubble is given by Prosperetti's result, Eq. (43), rather than by our Eq. (44). However, in order to compare their measurements with the theory, Cheyne *et al.* determined the bubble size from the maximum of the existing attenuation, making the reasonable assumption that maximum attenuation occurs at resonance. This measurement thus fixes the resonance frequency, but in order to compare the results of either an attenuation or a speed to the theory, the bubble size present *during* the measurements should also be determined. Had this been done independently, such a measurement would have been sufficient to provide a test of both Eq. (43) as well as of the complete attenuation and dispersion theory of Commander and Prosperetti. Instead, Cheyne *et al.* took Eq. (43) as correct and used it to determine the particle size, stating that *prior*, high-speed camera measurements produced sizes that agreed with those obtained by this procedure. These remarks are not in any manner a criticism of the experimental measurements; they are meant only to indicate that while the procedure may support the overall trend predicted by the existing theory for the phase velocity, it does not provide an independent verification of it.

Similar conclusions apply if we compare our theory to the measurements of Cheyne *et al.* using their procedure to determine the bubble size to reduce our theory, but use the resonance frequency predicted by Eq. (43), instead of that predicted by Eq. (44). Thus using their measured resonance

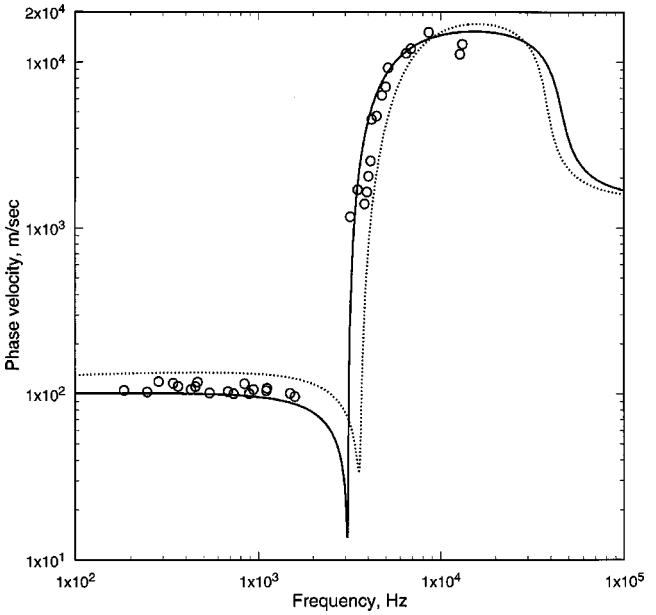

FIG. 14. Comparison between the predicted and measured phase velocity in a bubbly liquid. $\phi_v = 0.01$. The bubble diameter was 900 μm (see text). —— Eqs. (33)–(34); · · · · Ref. 37; ○: Cheyne *et al.*

frequency (3100 Hz) we obtain $a \approx 900$ instead of 1100 mm as obtained by them. In Fig. 14 we show the results of the comparison. Although the agreement is seen to be good, the comparison is not independent of the theory and cannot, therefore, be used to support its details.

In a large sense, then, the comparisons with existing experimental measurements of sound attenuation and dispersion in bubbly liquids near the resonance region have not resulted in an unequivocal support of either the existing theory or of the new theory presented here. The present theory has the theoretical advantage that it is more general and that some of its aspects are corroborated by different types of arguments. For example, the attenuation for very dilute suspensions derived from this theory agrees from that obtained from energy dissipation arguments. From an experimental point of view, however, it would appear that in the vicinity of resonance, the simple theoretical set given by Eqs. (54) and (55) is adequate to treat bubbly suspensions having volume concentrations as large as 0.01. The reason for this view is that in that region, the isothermal set agrees with the far more complete new result presented here, Eqs. (49) and (50). That complete set includes thermal dissipation, but as demonstrated before, in a wide region near resonance thermal dissipation is negligible compared to the dissipation produced by acoustic radiation.

Incidentally, both the isothermal set and the more complete set predict that the linear resonance frequency of a bubble is given by Eq. (44), although the assumption of isothermal bubble behavior is not made in the complete theory. While other theoretical reasons exist that support this result, it is clear, however, that an independent experimental verification would be highly desirable. This would require a knowledge of the resonance frequency of a gas bubble of known size. Assuming that the size can be accurately measured, it remains to measure the resonance frequency in a simple manner that does not relay on either the attenuation or the dispersion. One possible type of measurement that does not depend on either one of those quantities is to observe the phase angle of the pressure disturbance emitted by a driven bubble. Near resonance, the radiated pressure is far from being negligible and it ought to be possible to measure it at some convenient angle with respect to the incoming beam. As the resonant frequency is crossed, the phase angle of the nondimensional radiated pressure, given by our quantity $\Pi - 1$, changes rapidly by an amount nearly equal to π radians; a change that should be relatively easy to detect. Of course, this method may prove to be as difficult to carry out as any other, and that better methods can be found to determine the linear value of the resonant frequency. This basic quantity is important both in the acoustic propagation problem, and in the bubble interior problem, where it plays a more important role.

VI. CONCLUSIONS

A new theory has been presented that describes sound propagation in dilute suspension of nonevaporating particles in fluids. The theory is more general than previously existing theories and applies to aerosols, bubbly liquids, emulsions, and hydrosols. The theory provides a unified frame in which the dispersive effects are cast in terms of certain particle ratios that describe the relative motions between host fluid and particles. The accuracy and limitations of the theory are determined by those of these ratios; those used here are the most general presently available. The general results presented here reduce to known theories for the attenuation and dispersion for specific suspensions where first-principle results exist, and compares well with existing measurements in aerosols,[56,57] and in an acceptable manner with the attenuation measurements of Allegra and Hawley in emulsions, as reported earlier.[32] In the case of bubbly liquids, the theory is in rough agreement with the experimental results of Silberman in the resonance region, but differs strongly from them in the low frequency region. For the sound speed, comparison with the experimental data of Cheyne *et al.* is inconclusive because the size of the bubbles present during their experiments was not measured separately. However, comparison of our sound speed in the limit of low frequency, where bubble size is immaterial, to the experimental results of Karplus shows a good agreement, clearly supporting that theoretical result.

APPENDIX A: DERIVATION OF EQ. (21)

We consider a small volume element in the suspension, subject to an external pressure p. The pressures, temperatures, densities in the fluid and in the particles have averages values determined in Sec. IV. These can be used to obtain expressions for the internal energy of the suspension, as the sum of the internal energy of the fluid and of the particles. Thus the change of energy, per unit mass, of a volume element $\delta\tau$ consisting of the same particles and fluid is

$$de = (1-\phi_m)\overline{de_f} + \phi_m \overline{de_p}, \tag{A1}$$

where $\overline{e_f}$ and $\overline{e_p}$ are, respectively, the internal energy of the fluid per unit mass of fluid, and per unit mass of particles. Now, because the deformation is adiabatic, the first law of thermodynamics gives

$$\frac{de}{dt}=(1-\phi_m)\frac{d\overline{e_f}}{dt}+\phi_m\frac{d\overline{e_p}}{dt}=\dot{w}, \tag{A2}$$

where $\dot{w}$ is the rate at which work is done on the suspension element, per unit mass, and is given by $\dot{w}=-p[d(\delta\tau)/dt]/\delta M$.

We now linearize Eq. (A2). The work rate becomes $\dot{w}=(p_0/\rho_0^2)(d\rho'/dt)$, or

$$\dot{w}=p_0\left[\frac{1-\phi_m}{\rho_{f0}^2}\frac{d\overline{\rho_f'}}{dt}+\frac{\phi_m}{\rho_{p0}^2}\frac{d\overline{\rho_p'}}{dt}\right]. \tag{A3}$$

The linearized changes of the fluid's and particles' internal energy can be expressed as

$$\begin{aligned} de_f'&=c_{vf}\,dT_f'+\frac{1}{\rho_{f0}^2}(p_0-T_0\rho_{f0}c_{Tf}^2)d\rho_f',\\ de_p'&=c_{vp}dT_p'+\frac{1}{\rho_{p0}^2}(p_0-T_0\rho_{p0}c_{Tp}^2)d\rho_p'. \end{aligned} \tag{A4}$$

Substituting these quantities into Eq. (A2) yields, after some algebra,

$$\begin{aligned} &(1-\phi_m)\frac{T_0\beta_f c_{Tf}^2}{\rho_{f0}}\frac{d\rho_f'}{dt}+\phi_m\frac{T_0\beta_p c_{Tp}^2}{\rho_{p0}}\frac{d\rho_p'}{dt}\\ &\quad=(1-\phi_m)c_{vf}\frac{dT_f'}{dt}+\phi_m c_{vp}\frac{dT_p'}{dt}. \end{aligned} \tag{A5}$$

The changes of density may be expressed in terms of the changes of pressure and temperature by means of $d\rho'=-\rho_0\beta dT'+dp'/c_T^2$, applicable to both fluid and particles. This gives

$$\begin{aligned} &(1-\phi_m)\frac{T_0\beta_f}{\rho_{f0}}\frac{d\overline{p_f'}}{dt}+\phi_m\frac{T_0\beta_{p0}}{\rho_{p0}}\frac{d\overline{p_f'}}{dt}\\ &\quad=(1-\phi_m)c_{pf}\frac{d\overline{T_f'}}{dt}+\phi_m c_{pp}\frac{d\overline{T_p'}}{dt}, \end{aligned} \tag{A6}$$

where use was made of the identity $c_{vf}+T_0\beta_f^2c_{Tf}^2=c_{pf}$. Finally, expressing the ratio $\phi_m/(1-\phi_m)$, which defines the mass loading, as $\rho_{p0}\phi_v/\rho_{f0}(1-\phi_m)$, and rearranging yields Eq. (21).

APPENDIX B: THE FUNCTIONS *X*, *Y*, *U*, AND *V* APPEARING IN EQ. (31)

Let

$$J=b_i^2G(b_i),\quad \Gamma_R=\Re\{G(q_i)\},\quad \text{and}\quad \Gamma_I=\Im\{G(q_i)\}.$$

Then,

$$\begin{aligned} X=&-6Jb(b+z)z^2+6(2+z)(J+3\gamma_pN_sb^2)z^2\\ &-3J[(\gamma_f-1)b^2(z-b)+2z^2]\\ &-3b[bJ+2(\beta_p/\beta_f)z^2][bz(\gamma_f-1)-2z^2], \end{aligned}$$

$$\begin{aligned} Y=&-6(J+\gamma_pN_sb^2)(b+z)z^2-6Jb(2+z)z^2\\ &-3Jb[bz(\gamma_f-1)-2z^2]\\ &+3[(\gamma_f-1)b^2(z-b)+2z^2][bJ+2(\beta_p/\beta_f)z^2], \end{aligned}$$

$$\begin{aligned} U=&2b^2(\gamma_f-1)Jz^2\{-\beta_p/\beta_f+(\kappa_f/\kappa_p)[\Gamma_I(b-z)-\Gamma_Rz]\}\\ &+2b^2(\gamma_f-1)z^2(\kappa_f/\kappa_p)[\Gamma_R(z-b)-\Gamma_Iz]\\ &\times[bJ+2(\beta_p/\beta_f)z^2]-4(J+\gamma_pb^2N_s)z^2z_p^2[z\Gamma_R\\ &-(1+z)\Gamma_I]-2Jbz^2\{3hz^2+2z_p^2[\Gamma_R(1+z)+z\Gamma_I]\}, \end{aligned}$$

$$\begin{aligned} V=&2b^2(\gamma_f-1)Jz^2(\kappa_f/\kappa_p)[\Gamma_R(z-b)-\Gamma_Iz]\\ &-2b^2(\gamma_f-1)z^2\{-\beta_p/\beta_f+(\kappa_f/\kappa_p)[\Gamma_I(b-z)-\Gamma_Rz]\}\\ &\times[bJ+2(\beta_p/\beta_f)z^2]+4bJz^2z_p^2[z\Gamma_R-(1+z)\Gamma_I]\\ &-2(J+\gamma_pb^2N_s)z^2\{3hz^2+2z_p^2[\Gamma_R(1+z)+z\Gamma_I]\}. \end{aligned}$$

[1] J. Tyndall, *Sound*, 3rd ed. (Appleton, New York, 1875).
[2] N. A. Gumerov, A. I. Ivanadev, and N. I. Nigmatulin, ''Sound waves in monodisperse gas-particle or vapour droplet mixtures,'' J. Fluid Mech. **193**, 53–74 (1988).
[3] A. S. Sangani, ''A pairwise interaction theory for determining the linear acoustic properties of dilute bubbly liquids,'' J. Fluid Mech. **232**, 221–284 (1991).
[4] P. S. Epstein and R. R. Carhart, ''The absorption of sound in suspensions and emulsions. I. Water fog in air,'' J. Acoust. Soc. Am. **25**, 553–565 (1953).
[5] S. Temkin and R. A. Dobbins, ''Attenuation and dispersion of sound by particulate relaxation processes,'' J. Acoust. Soc. Am. **40**, 317–324 (1966).
[6] A. H. Harker and J. A. G. Temple, ''Velocity and attenuation of ultrasound in suspensions of particles in fluids,'' J. Phys. D **21**, 1576–1588 (1988).
[7] C. M. Atkinson and H. K. Kytömaa, ''Acoustic wave speed and attenuation in suspensions,'' Int. J. Multiphase Flow **18**, 577–592 (1992).
[8] J. M. Evans and K. Attenborough, ''Coupled phase theory for sound propagation in emulsions,'' J. Acoust. Soc. Am. **102**, 278–282 (1997).
[9] C. Verdier and M. Piau, ''Acoustic wave propagation in two phase viscoelastic fluids: The case of polymer emulsions,'' J. Acoust. Soc. Am. **101**, 1868–1876 (1997).
[10] F. E. Marble, ''Dynamics of a gas containing small solid particles.'' Proc. AGARD Combustion Propulsion Colloq., 57th (1963), pp. 175–215.
[11] L. van Wijngaarden, ''On the equations of motion for mixtures of liquids and gas bubbles,'' J. Fluid Mech. **33**, 465–474 (1968).
[12] D. S. Drumheller and A. Bedford, ''A theory of bubbly liquids,'' J. Acoust. Soc. Am. **66**, 197–208 (1979).
[13] A. Biesheuvel and L. van Wijngaarden, ''Two-phase equations for a dilute dispersion of gas bubbles in a liquid,'' J. Fluid Mech. **148**, 301–318 (1984).
[14] M. J. Miksis and L. Ting, ''Effective equations of multiphase flows—Waves in a bubbly liquid,'' Adv. Appl. Mech. **28**, 141–261 (1992).
[15] D. A. Drew, ''Mathematical modeling of two-phase flow,'' Annu. Rev. Fluid Mech. **15**, 261–291 (1983).
[16] S. Temkin, ''Attenuation and dispersion of sound in bubbly liquids via the Kramers–Kronig relations'' J. Fluid Mech. **211**, 61–72 (1990).
[17] A. Onuki, ''Sound propagation in phase-separating fluids,'' Phys. Rev. A **43**, 6740–6755 (1991).
[18] Z. Ye, ''Acoustic dispersion and attenuation in many spherical scatterer systems and the Kramers–Kronig relations,'' J. Acoust. Soc. Am. **101**, 3299–3305 (1997).
[19] J. L. Leander, ''Comments on Acoustic dispersion and attenuation in many spherical scatterer systems and the Kramers-Kronig relations,'' J. Acoust. Soc. Am. **101**, 3299–3305 (1997), J. Acoust. Soc. Am. **104**, 1111–1115 (1998).
[20] A. B. Wood, *A Textbook of Sound* (Bell and Sons, London, 1941), pp. 361–362.
[21] K. F. Herzfeld, ''Propagation of sound in suspensions,'' Philos. Mag. **9**, 741–751, 752–768 (1930).

[22] P. L. Chambre, ''Speed of a plane wave in a gross mixture,'' J. Acoust. Soc. Am. **26**, 329–331 (1954).
[23] R. J. Urick, ''A sound velocity method for determining the compressibility of finely divided substances,'' J. Appl. Phys. **18**, 983–987 (1947).
[24] R. J. Urick and W. S. Ament, ''The propagation of sound in composite media,'' J. Acoust. Soc. Am. **21**, 115–119 (1948).
[25] E. L. Carstensen and L. L. Foldy, ''Propagation of sound through a liquid containing bubbles,'' J. Acoust. Soc. Am. **19**, 481–501 (1947).
[26] M. A. Isakovich, ''On the propagation of sound in emulsions,'' Zh. Eksp. Teor. Fiz. **18**, 907–912 (1948).
[27] J. R. Allegra and S. A. Hawley, ''Attenuation of sound in suspensions and emulsions: Theory and experiments,'' J. Acoust. Soc. Am. **51**, 1545–1564 (1971).
[28] L. van Wijngaarden, ''One dimensional flow of liquids containing small gas bubbles.'' Annu. Rev. Fluid Mech. **4**, 369–396 (1972).
[29] D. J. McClements and M. J. W. Povey, ''Scattering of ultrasound by emulsions,'' J. Phys. D Appl. Phys. **22**, 38–47 (1989).
[30] S. Temkin, ''Sound propagation in dilute suspensions of rigid particles,'' J. Acoust. Soc. Am. **103**, 838–849 (1998).
[31] S. Temkin and C. M. Leung, ''On the velocity of a rigid sphere in a sound wave,'' J. Sound Vib. **49**, 75–92 (1976).
[32] S. Temkin, ''Radial pulsations of a fluid particle in a sound wave,'' J. Fluid Mech. **380**, 1–38 (1999).
[33] E. H. Kennard, ''Radial motion of water surrounding a sphere of gas in relation to pressure waves,'' in *Underwater Explosion Research, A Compendium of British and American Reports, Vol. II: The Gas Globe*, Office of Naval Research, U.S. Department of the Navy (1950).
[34] E. Silberman, ''Sound velocity and attenuation in bubbly mixtures measured in standing wave tubes,'' J. Acoust. Soc. Am. **29**, 925–933 (1957).
[35] H. B. Karplus, ''The velocity of sound in liquids containing gas bubbles.'' Res. Develop/Rep. ARF-4132-12, Atomic Energy Commission (1961).
[36] S. A. Cheyne, C. T. Stebbings, and R. Roy, ''Phase velocity measurements in bubbly liquids using a fiber optic laser interferometer,'' J. Acoust. Soc. Am. **97**, 1621–1624 (1995).
[37] K. W. Commander and A. Prosperetti, ''Linear pressure waves in bubbly liquids: Comparison between theory and experiments,'' J. Acoust. Soc. Am. **85**, 732–746 (1989).
[38] S. Temkin, ''Sound speeds in suspensions in thermodynamic equilibrium,'' Phys. Fluids A **4**, 2399–2409 (1992).
[39] B. T. Chu, ''Thermodynamics of a dusty gas and its application to some aspects of wave propagation in the gas,'' Report No. DA-4761/1. Division of Engineering, Brown University, Providence, RI (1960).
[40] S. Kieffer, ''Sound speed in liquid-gas mixtures: Water–air and water–steam,'' J. Geophys. Res. **82**, 2895–2904 (1977).
[41] J.-C. Micaelli, ''Propagation d'ondes dans le écoulements diphasiques a bulles a deux constituants,'' Étude théorique et expérimentale. These. Université de Grenoble (1982).
[42] G. Rudinger, ''Some effects of finite particle volume on the dynamics of gas-particle mixtures,'' Amer. Inst. Aero. Astro. J. **3**, 1217–1222 (1965).
[43] F. E. Marble, ''Dynamics of dusty gases,'' Annu. Rev. Fluid Mech. **2**, 397–446 (1970).
[44] S. Temkin, ''Particle force and heat transfer in a dusty gas sustaining an acoustic wave,'' Phys. Fluids **5**, 1296–1304 (1993).
[45] G. K. Batchelor, *An Introduction to Fluid Dynamics* (Cambridge University Press, Cambridge, 1967).
[46] S. Temkin, ''Viscous attenuation of sound in dilute suspensions of rigid particles,'' J. Acoust. Soc. Am. **100**, 825–831 (1996).
[47] S. Temkin, *Elements of Acoustics* (Wiley, New York, 1981).
[48] A. Prosperetti, ''The thermal behavior of oscillating gas bubbles in liquids,'' J. Fluid Mech. **222**, 587–616 (1991).
[49] Y. Fukumoto and T. Izuyama, ''Thermal attenuation and dispersion of sound in a periodic emulsion,'' Phys. Rev. A **46**, 4905–4921 (1992).
[50] L. D. Landau and E. M. Lifshitz, *Fluid Mechanics* (Pergamon, New York, 1959).
[51] A. B. Bhatia, *Ultrasonic Absorption* (Dover, New York, 1967), p. 91.
[52] R. E. Caflisch, M. Miksis, C. Papanicolaou, and L. Ting, ''Effective equations for wave propagation in bubbly liquids,'' J. Fluid Mech. **153**, 259–273 (1985).
[53] G. C. Gaunaurd and H. Überall, ''Resonance theory of bubbly liquids,'' J. Acoust. Soc. Am. **69**, 362–370 (1981).
[54] A. E. Ruggles, R. T. Lahey, Jr., D. A. Drew, and H. A. Scarton, ''The relationship between standing waves, pressure pulse propagation, and critical flow rate in two-phase mixtures,'' J. Heat Transfer **111**, 467–473 (1989).
[55] F. E. Fox, S. R. Curley, and G. Larson, ''Phase velocity and absorption measurements in water containing air bubbles,'' J. Acoust. Soc. Am. **27**, 534–539 (1955).
[56] S. Temkin and R. A. Dobbins, ''Measurements of the attenuation and dispersion of sound by an aerosol,'' J. Acoust. Soc. Am. **40**, 1016–1024 (1966).
[57] S. N. Foner and B. H. Nall, ''Attenuation of sound by rigid spheres: Measurements of the viscous and thermal components of attenuation and comparison with theory,'' J. Acoust. Soc. Am. **57**, 59–66 (1975).

Acoustic imaging of objects buried in soil

Catherine H. Frazier[a)]
Bioacoustics Research Laboratory and Department of Electrical and Computer Engineering, University of Illinois at Urbana-Champaign, Urbana, Illinois 61801

Nail Çadallı[b)] and David C. Munson, Jr.[c)]
Coordinated Science Laboratory and Department of Electrical and Computer Engineering, University of Illinois at Urbana-Champaign, Urbana, Illinois 61801

William D. O'Brien, Jr.[d)]
Bioacoustics Research Laboratory and Department of Electrical and Computer Engineering, University of Illinois at Urbana-Champaign, Urbana, Illinois 61801

(Received 17 May 1999; accepted for publication 13 March 2000)

In this study, we demonstrate an acoustic system for high-resolution imaging of objects buried in soil. Our goal is to image cultural artifacts in order to assess in a rapid manner the historical significance of a potential construction site. We describe the imaging system and present preliminary images produced from data collected from a soil phantom. A mathematical model and associated computer software are developed in order to simulate the signals acquired by the system. We have built the imaging system, which incorporates a single element source transducer and a receiver array. The source and receiver array are moved together along a linear path to collect data. Using this system, we have obtained *B*-mode images of several targets by using delay-and-sum beamforming, and we have also applied synthetic aperture theory to this problem. © *2000 Acoustical Society of America.* [S0001-4966(00)00207-1]

PACS numbers: 43.35.Pt [HEB]

INTRODUCTION

Once a cultural or archeological resource site is identified, it must be assessed in order to determine its significance and eligibility for National Registry of Historic Places (Executive Order 11593). Current methods for this assessment involve scattered small-scale digs at the site, which are expensive and imprecise. The cost of complete assessments is prohibitive; therefore, there is an urgent need to significantly reduce the cost of data recovery, especially for the many sites having lower probabilities of containing significant cultural or archeological resources. This study proposes an acoustic system for high-resolution imaging of buried artifacts, within this context.

In addition to finding cultural artifacts, a system designed to image buried objects could be adapted to detect land mines. However, a system built for detecting artifacts can look straight down, while a system for finding land mines must have side-looking capability. There is currently a world-wide effort to reduce the harm caused to local populations by unexploded ordnance. Acoustic and electromagnetic systems have been proposed to meet this purpose. Land mines can be metallic or plastic, and they range in size. A small anti-personnel mine can be as small as 50 mm. Electromagnetic systems have detection/identification problems due to the air/ground interface, which reflects much of the incident energy, and other objects such as rocks and ammunition shells or other metal fragments, which are difficult to distinguish from mines.[1,2] In practice, up to one thousand metal fragments are found for every one mine.[3] Despite this, land mines may be easier to detect than cultural artifacts because land mines are often larger than artifacts and they have greater reflectivity due to larger impedance mismatch with soil.

An acoustic system has potential advantages over existing imaging modalities. Current technologies in seismic exploration and borehole techniques are not designed to meet the resolution requirements for imaging cultural artifacts or land mines. In 1990, a study showed that, using acoustic techniques for subsurface imaging, resolution could be improved from tens of meters achievable in petroleum and mineral exploration to on the order of 1 meter using geophysical tomography (boreholes) for applications such as finding buried waste or abandoned mines.[4] However, finding cultural artifacts will require resolution on the order of 5 cm.

Ground penetrating radar (GPR) has had some success in identifying underground structures; however, the success is site specific, depending on the moisture content of the soil.[5] In Ref. 6, a comparison was made between GPR and the seismic reflection method for shallow geological surveys to a depth of 50 m. They showed that GPR was effective in dry soil, but that water attenuated the electromagnetic energy. Conversely, acoustic energy propagated better in a saturated medium than in dry soil. Thus, an acoustic system would complement a GPR system.

At the same time our system was being developed, Smith *et al.*[7] developed an acoustic system for localizing reflections from a buried object on a natural beach. They used a shaped pulse, as does our system, rather than impulse excitation. The center frequency of their transmitted pulse was

[a)]Electronic mail: hillsley@brl.uiuc.edu
[b)]Electronic mail: cadalli@dsp.csl.uiuc.edu
[c)]Electronic mail: d-munson@uiuc.edu
[d)]Electronic mail: wdo@uiuc.edu

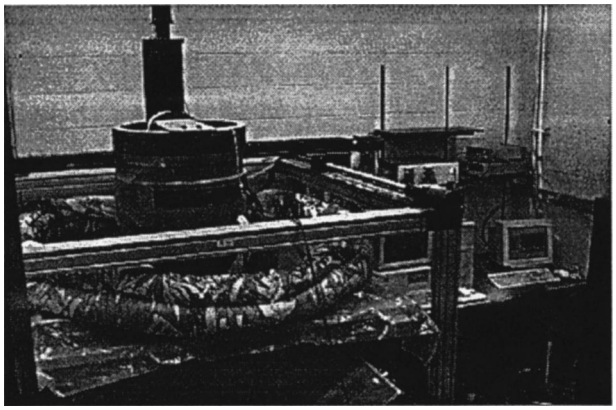

FIG. 1. Experimental system.

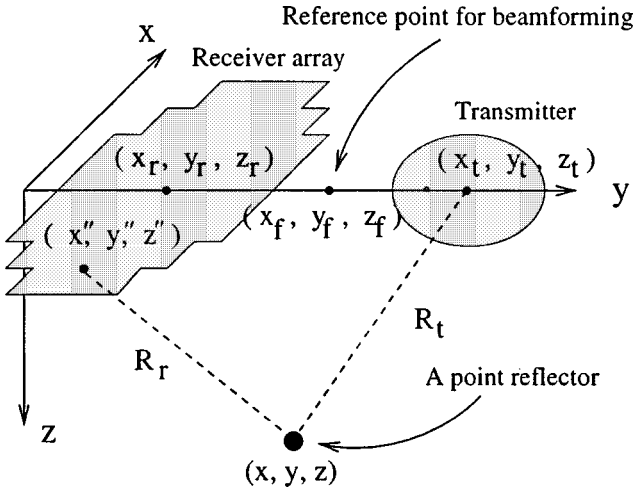

FIG. 2. Array of transducers and associated coordinate system. Surface of the array is in the *x*-*y* plane. Array motion is in the *y* direction.

100 Hz, and they considered propagating distances up to 10 m. Our system is intended to be used up to a maximum depth of 1 m and to detect smaller objects; therefore, we propagate a much higher frequency pulse. The main disadvantage in Smith's system is that it requires subtracting a background image, with no targets present, making it an impractical system for use in a situation where data are not taken before targets are placed.

In this paper, we present a system that demonstrates the feasibility of acoustically imaging small objects buried in dry homogeneous soil. This paper is organized as follows: In the next section we describe the experimental system. The characteristics of the soil used in our tests are presented in Sec. II. Section III introduces the data model. Section IV explains the methods we used for image reconstruction and presents images reconstructed from both simulated and real data. Further research directions are listed in Sec. V.

I. EXPERIMENTAL SYSTEM

Our imaging system has been constructed and is in operation at the U.S. Army Construction Engineering Research Laboratory (CERL) in Champaign, Illinois, where the data are collected in a controlled volume of soil. A picture of the system is shown in Fig. 1. The soil is contained in a cubic wooden box of 1.2 m per side. The box has a false bottom, with only the top 60 cm filled with soil. The system incorporates a torpedo transducer array from the Applied Research Laboratory at Pennsylvania State University. The torpedo head, which contains the receiver array, is suspended above the box by a metal frame that surrounds the box. The source is to the right of the torpedo head. Sitting on top of the box of soil is a child's pool filled with 3 cm depth of water. The water is used to couple the sound energy between the transducers and the sand since the transducers are designed for underwater applications. To the right of the frame are two computers. The left computer is used to control the motion of the receiver array along three translational axes. The right computer controls the data acquisition, including communication with the motion control computer.

The source transducer is a single element that is well approximated as a point source. In future versions of the system, we hope to use a transmitter array to provide focusing of the transmit beam to increase the energy coupled into a localized volume of soil, thereby improving signal-to-noise ratio. In the torpedo head, a 52-element sonar array (8×8, 3.56 cm^2 close-packed elements with 3 elements in each corner missing) serves as the receive array, and allows for beamforming on receive. The receiver array and the corresponding coordinate system are depicted in Fig. 2. The *z* axis represents the depth into the soil and the *x*-*y* plane represents the soil surface. The *y* and *z* dimensions are called azimuth and range, respectively. The detailed geometry of the transmitter and the receiver is shown in Fig. 3. Due to the size of the torpedo and the source, the smallest possible center-to-center spacing of the source and receive array is 33 cm.

A block diagram of the system is shown in Fig. 4. Movement of the array is accomplished by a motion control system with three translational axes. Only the two horizontal axes, with positional accuracy of 3 μm, were used for the scans. Position control is achieved through a PC-based control card using LabView software to create the interface. The motion control program allows manual positioning or automatic control by the data acquisition computer, which uses the serial port to send position coordinates to the motion control computer.

The data acquisition computer uses an Hewlett Packard

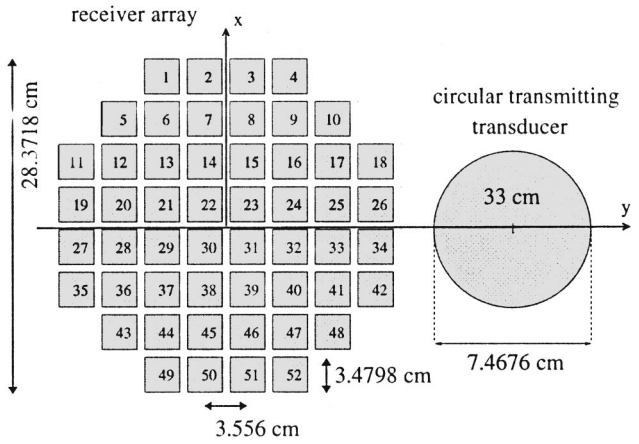

FIG. 3. Geometry of the transmitter and receiving array; view from the top. Origin is at the center of the receiver array.

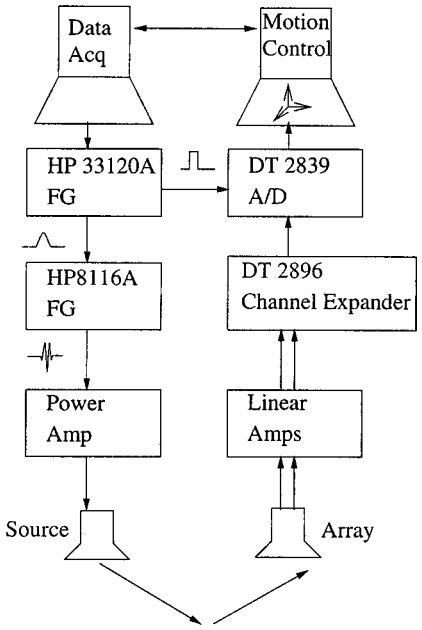

FIG. 4. Block diagram of imaging system.

Interface Bus (HPIB) interface card to communicate with the HP33120A function/arbitrary waveform generator to set up initial parameters for the excitation signal. The excitation signal is generated by the function/arbitrary waveform generator modifying the signal (AM modulation) from an HP8116A pulse/function generator. The resulting signal is a cosine-weighted pulse of 6 cycles at 6 kHz which is plotted in Fig. 5. The choice of center frequency was influenced by the operational requirements of the acoustic transducers and by resolution considerations. Achievable resolution is determined in part by the medium. Propagation speed determines the wavelength for a given frequency. With a higher frequency, better resolution can be achieved; however, higher frequencies suffer from large attenuation resulting in poor signal-to-noise ratio. The signal was amplified by either a 3000-W amplifier (Industrial Test Equipment Co.) or a 1000-W amplifier with variable output impedance capability (Instruments, Inc. Model L10).

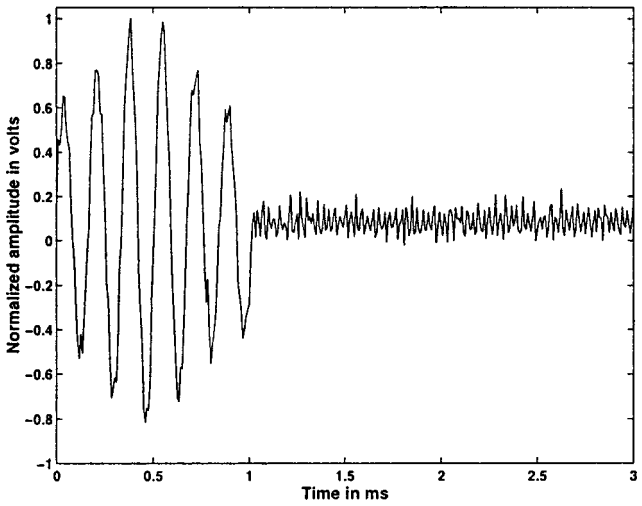

FIG. 5. Transmitted signal.

Signals from the 52 elements were captured individually so that processing could be done off-line. Received signals were averaged 64 times. A separate transmit pulse was used for each signal captured, so that at each position of the source and receiver array, 3328(52×64) pulses were transmitted. Before the received signal was digitized, it was amplified by an in-line linear amplifier with a gain of 330.

The synchronization signal from the HP33120A was used to trigger data collection by the Data Translation A/D board (DT 2839, 12 bit, 1 MHz). The DT 2839 has 8 channels, so we used a DT 2896 channel expander (Data Translation) to allow us to capture the 52 channels individually.

II. SOIL PROPERTIES

The soil was gathered from the University of Illinois Sand Farm in Mason County, Illinois. Physical characterization of the soil was performed by University of Illinois Professor Robert Darmody, a certified soil classifier by the Illinois Soil Classifiers Association. The sand content was 94%, most of which was evenly divided between the medium (250–500 μm) and fine (100–250 μm) sand subclasses. Because of the low clay content, the soil was nonplastic. Organic carbon content was low, as was the soil moisture.

Acoustic properties of soil are described by the Biot theory for sound propagation in a porous medium.[8,9] The theory predicts the propagation of two compressional waves and a shear wave in the porous medium. The first compressional wave is characterized by particle motion in phase with the fluid motion. The second compressional wave is characterized by particle motion out of phase with the fluid motion. The first wave is often referred to as the fast compressional wave because it generally has a higher speed than the wave of the second type, or slow compressional wave. Also, the slow compressional wave generally has much higher attenuation than the fast compressional wave. The velocity of the shear wave is determined by the shear modulus of the solid. For materials such as clays, silts or muds, the velocity may be much slower than either compressional wave. The attenuation of the shear wave may be larger or smaller than the attenuation of the fast wave. In our experiments, the Biot fast wave was the only wave detected, which was a result of the high attenuation of the slow wave, and more importantly, the coupling conditions, which led to the preferential coupling of energy into the fast wave.

The wave speed and attenuation of the propagated wave were determined using the experimental system described above. The source and receiver were positioned above a steel plate buried at a depth of 12 cm. The 6 kHz center frequency pulses described previously were transmitted and received at the 52 elements. The array was then moved an additional 2 cm away from the source and the data collection was repeated. Data were collected for a total of five positions of the array in increments of 2 cm. This data collection differs from the data collection for images, where the relative positions of the source and receiver remained fixed.

The total distance traveled by the pulse was calculated using geometric acoustics. It was assumed that the speed of sound was constant in the first 12 cm of sand, so the sound traveled over a linear path from the source to the plate and

from the plate to the receiver element. The sound speed was measured by correlating the signal received by each element with the signal received by the same element after the array had been moved to a different position. The difference in pulse travel distance was then divided by the difference in time of arrival. Results showed that the speed of sound in the sand was 166 ± 27 m/s.

Attenuation was measured by first finding the log power spectrum of the received signals. The first position of the array was used as a reference for comparison with the four other positions. The log decrements for the four positions were calculated and fitted to a line for each of the 52 elements, so that the slopes of the lines give 52 estimates of the attenuation per cm at a particular frequency. The average slope, where the average was taken over the 52 estimates, was then taken to be the attenuation in dB/cm at that frequency. Finally a line was fit to the data for the range of frequencies. The results showed that for our sand, the attenuation was approximately 0.65 (dB/cm)/kHz in the frequency range from 500 Hz to 2 kHz. We did not receive a useful signal above 2 kHz so we could not extend attenuation measurements to higher frequencies. A larger soil characterization study performed in the Bioacoustics Research Laboratory measured speed of sound and attenuation of the fast compressional wave over the range of frequencies, 1–10 kHz, for six soil types as a function of four soil moistures and two soil compactions using through transmission methods.[10] The study showed that speed of sound and attenuation for all samples varied over small ranges, 100–300 m/s and 0.1–1 dB/cm kHz, respectively.

Our results are in general agreement with the results for unconsolidated sand by Hickey and Sabatier.[11] They measured a phase velocity of 143 m/s for the slow wave and 240 m/s for the fast wave. The slow wave attenuation was measured to be 3.0 dB/cm at 1 kHz and the fast wave attenuation was measured to be 0.87 dB/cm at 1 kHz. In their experiments, both phase velocity and attenuation of the slow wave increased with frequency.

III. DATA ACQUISITION MODEL

We have developed a mathematical model and associated computer software to simulate the signals acquired by the experimental system. Our simulator serves as a convenient platform for the development of image reconstruction algorithms. In our model, the medium (soil) is assumed to consist of densely spaced point scatterers, which are placed on a three-dimensional grid, representing the object(s) and the soil background. Each scatterer is assigned a reflection coefficient $\Gamma_0(x,y,z)$, with magnitude $m(x,y,z)$ and phase $\theta(x,y,z)$.

In considering the returned signal, let us first deal with the case of one scatterer. The received response from a particular reflector is a delayed version of the transmitted signal scaled by the reflection coefficient of the scatterer and by a factor which is dependent on the range function and which is due to the attenuation of the medium and the radial expansion of the spherical wave.[12] The transmitted signal is $\mathrm{Re}\{s(t)e^{j2\pi f_0 t}\}$ where $s(t)$ is a baseband pulse and f_0 is the carrier frequency.

Receiving element surfaces are considered to be decomposed into a collection of point receivers. Since the transmitting element is approximately omnidirectional, such a decomposition is not necessary for that element. For a particular scatterer, the signal received at a transducer is the sum of the signals received by those point receivers on the surface of the transducer. This model accounts for the curvature of the wavefront incident on the transducer and eliminates the need for the knowledge of the receiving transducer beam pattern. In reference to Fig. 2, let us denote the coordinates of a point scatterer by the vector $\mathbf{v}=(x,y,z)$. Similarly, we denote the center locations of the transmitter and the receiver array by $\mathbf{v}_t=(x_t,y_t,z_t)$ and $\mathbf{v}_r=(x_r,y_r,z_r)$, respectively. Notice that for the case when the transmitter and the receiver array are in the x-y plane and move along the y axis, we have $\mathbf{v}_t=(0,y_t,0)$ and $\mathbf{v}_r=(0,y_r,0)$. The signal received by the ith receiver, when the transmitter is at $\mathbf{v}_t$ and the center of the receiver array is at $\mathbf{v}_r$, is

$$\tilde{g}_i(t_1,\mathbf{v}_t,\mathbf{v},\mathbf{v}_r)=\int\int w_i(x'',y'';\mathbf{v}_r)m(x,y,z)\times\mathrm{Re}\left\{s\left(t-\frac{R(\mathbf{\Lambda})}{c}\right)e^{j[2\pi f_0(t-R(\Delta)/c+\theta(x,y,z)]}\right\}\times\frac{e^{-gaR(\mathbf{\Lambda})}}{R_t(\mathbf{v}_t,\mathbf{v})R_r(\mathbf{v}'',\mathbf{v})}dx''dy''. \quad (1)$$

Here $\mathbf{v}''=(x'',y'',z'')$ is the coordinate of the simple receiver on the surface of the ith receiver transducer. If the receiver array is in the x-y plane, $z''=0$. This surface is represented by the window function $w_i(x'',y'';\mathbf{v}_r)$, the location of which depends on the position of the array center, $\mathbf{v}_r$. Vector $\Lambda=[\mathbf{v}\mathbf{v}_t\mathbf{v}''\mathbf{v}_r]$ is defined for notational simplicity. The attenuation coefficient of the medium (in units of m^{-1}) is α and c is the speed of sound in soil. The range function $R(\Lambda)$ is the sum of $R_t(\mathbf{v}_t,\mathbf{v})$, which is the distance from the transmitter to a particular scatterer, and $R_r(\mathbf{v}'',\mathbf{v})$, which is the distance from the scatterer to the infinitesimal receiver surface on a particular receiver transducer. R_t and R_r are given as

$$R_t(\mathbf{v}_t,\mathbf{v})=\sqrt{(x-x_t)^2+(y-y_t)^2+(z-z_t)^2},$$
$$R_r(\mathbf{v}'',\mathbf{v})=\sqrt{(x-x'')^2+(y-y'')^2+(z-z'')^2}. \quad (2)$$

The integrand in Eq. (1) is a delayed version of the transmitted signal reflected from a scatterer at $\mathbf{v}$. It is scaled by the magnitude of the reflectivity and phase shifted by the phase of the reflectivity. The fractional term in the integrand is the attenuation term. The numerator of this term represents the attenuation due to the medium and the denominator accounts for the attenuation due to the spherical expansion of the acoustic wave. The return wave is incident onto a point receiver at the coordinate $\mathbf{v}''$. The limits of the integration are determined by $w_i(x'',y'';\mathbf{v}_r)$. Hence, the integration is over the surface of the ith receiver transducer.

After quadrature demodulation, we have the complex baseband representation of the received signal as

$$\overline{g_i}(t,\mathbf{v}_t,\mathbf{v},\mathbf{v}_r)=\int\int w_i(x'',y'';\mathbf{v}_r)\Gamma_0(x,y,z)\times\frac{e^{-\alpha R(\Lambda)}}{R_t(\mathbf{v}_t,\mathbf{v})R_r(\mathbf{v}'',\mathbf{v})}\cdot s\left(t-\frac{R(\Lambda)}{c}\right)\times e^{-jkR(\Lambda)}dx''dy'', \quad (3)$$

where $k=2\pi f_0/c$ is the wavenumber. The term due to attenuation can be eliminated approximately by using time gain compensation (TGC) on the received data.[13] The total received signal for the ith transducer of the receiver array, for a fixed array position is the sum of responses from all scatterers in the medium:

$$\hat{g}_i(t,\mathbf{v}_t,\mathbf{v}_r)=\int_0^\infty\int_{-\infty}^{\infty}\int_{-\infty}^{\infty}\overline{g_i}(t,\mathbf{v}_t,\mathbf{v},\mathbf{v}_r)dxdydz. \quad (4)$$

In computer implementation of this model, it is not possible to account for a continuum of scatterers or a semi-infinite medium. Therefore we assume a finite size, three-dimensional, discrete grid of point scatterers in order to simulate objects and the background soil.

IV. IMAGE RECONSTRUCTION

By translating the receiver array across the surface of the medium, it is possible to obtain sufficient data to form an image of the soil subsurface. The data acquisition system is moved along a straight line, and at regular spatial intervals the system emits the tapered sinusoidal pulse and collects returns. We mainly have explored two methods of forming images from the collected data, as explained below. Reconstructed images represent the *y*-*z* plane at a fixed *x* value according to our coordinate convention in Fig. 2.

A. Beamforming and experimental results

At each position of the data acquisition system, a single beam can be formed by focusing the array broadside, so that a conventional *B*-mode image may be formed with data from multiple positions. Alternatively, since the signals have been recorded separately, several beams can be formed for each source/receiver array position by synthesizing several elements centered at positions between the source and the receiver. To synthesize an element between the source and receiver, the 52 signals are first delayed to simulate a signal transmitted from a synthesized position, and then are delayed to simulate a focused receiver at the synthesized position. Creating multiple beams at each position of the source and receiver could provide for some averaging to increase signal-to-noise ratio, although this was not done in our study.

Focusing of the 52 individual received signals is accomplished off-line through delay-and-sum beamforming, using dynamic focusing so that multiple depths in the image are in focus. The lateral resolution is not constant as a function of depth, due to the fixed size of the array. As stated earlier, the coordinates (x'',y'',z'') in Fig. 2 are used to designate the position of a simple receiver on the ith receiver. For this discussion, we will use the coordinates $(x_i,y_i,0)$, where (x_i,y_i) is the center of the ith receiver element. The subscript i varies from 1 to 52 and is used to enumerate the elements. The center of the array lies on the x axis so that half of the elements are in the region where $x>0$ and half are in the region where $x<0$. The source is centered at position $(0,y_t,0)$, and the synthetic element is centered at $(0,y_f,0)$. In our case, the synthetic element is both transmitter and receiver. The reason for using such synthesized elements in delay computation rather than using one of the receive elements as a reference for the others is to utilize the shortest path length traveled by the transmitted signal for a particular depth so as to reduce the effect of attenuation.

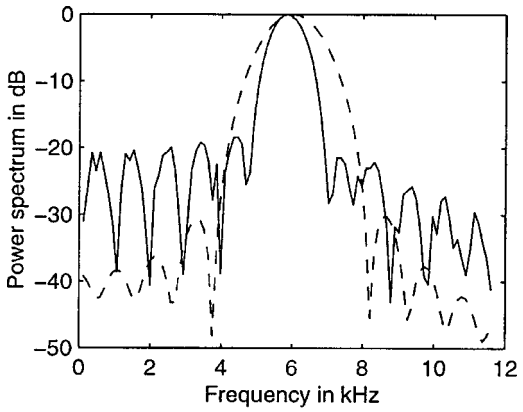

FIG. 6. Log spectra of simulated (dashed) and actual (solid) transmitted signals.

For a desired focal point, $(0,y_f,z_f)$, where the focal point is always directly below the synthetic element, the beamforming is accomplished as follows:

$$t_t=(z_f-\sqrt{(y_t-y_f)^2+z_f^2})/c, \quad (5)$$

$$t_{ri}=(z_f-\sqrt{x_i^2+(y_f-y_i)^2+z_f^2})/c, \quad (6)$$

$$g(t)=\sum_{i=1}^{52}s_i(t-t_t-t_{ri}). \quad (7)$$

The delay, t_t, is the same for each element. It compensates for the difference in travel time from the actual source to the focal point and from the synthetic source to the focal point. The delay, t_{ri}, is different for each element. It compensates for the difference in travel times from the focal point to the actual receivers and from the focal point to the synthetic receiver. The $g(t)$ are envelope-detected using the Hilbert Transform and displayed side-by-side to form an image.

Data were collected using a variety of targets. In each case, the source and receiver array were moved in 0.5-cm steps. The information about the targets was contained in frequencies below 1500 Hz rather than near 6 kHz, which was the center frequency of our transmit pulse. The received signal contained a strong signal at 6 kHz; however, this was most likely reverberation within the pool. The high received signal strength at frequencies below 1500 Hz can be explained as follows. In the transmitted signal, the energy at frequencies below 2 kHz is 20 dB below the center frequency, as shown in Fig. 6. The attenuation in the soil was measured to be 0.65 (dB/cm)/kHz for the frequencies be-

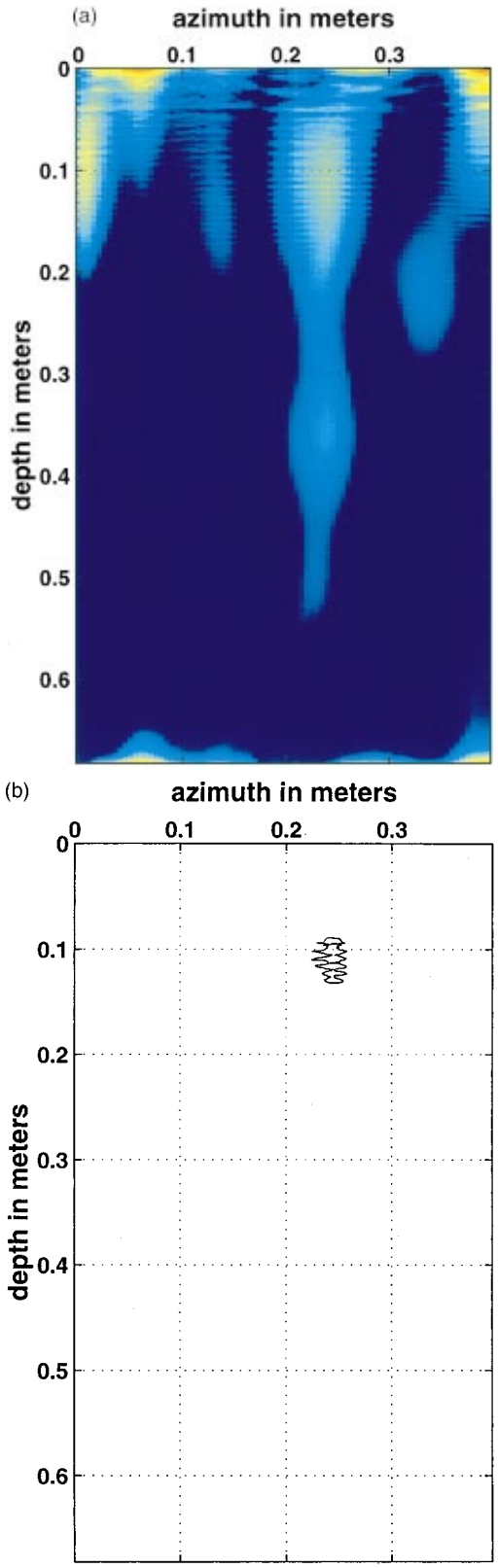

FIG. 7. (a) Image of air-filled furnace pipe. The axis of the pipe is perpendicular to the page. The reflection due to the pipe is centered at approximately 0.24 meters in azimuth and 0.12 meters in depth. (b) Contour plot showing the location of the target in the image.

tween 500 Hz and 2 kHz. The pulse typically must travel 40 cm from the source to the target to the receiver element. In this distance, the 6 kHz signal would be attenuated 156 dB, assuming that the attenuation measurement can be extended to this high frequency. The 500 Hz signal would be attenuated just 13 dB. Therefore, low frequencies should be more prominent in the received signal.

The delay and sum imaging algorithm was modified so that the DC bias of the signal received at each element was removed before any further calculations. The second step in processing the data was to filter the signals such that only frequencies below 1500 Hz were kept, because the SNR is poor at high frequencies.

A reconstructed image of a single target is shown in Fig. 7. Part (b) of the figure shows the location of the target in the image. The target was an air-filled aluminum furnace pipe (7.5-cm diameter, 90-cm length) buried at a depth of 8.5 cm. The pipe appears as the bright spot centered between 0.2 and 0.3 m in azimuth and between 0.1 and 0.2 m in depth. The bright spots in the corners are due to reflections from the sides of the box. The bright spot beneath the pipe, between 0.3 and 0.4 m in depth is due to a multiple reflection. The image was formed by synthesizing an element 8 cm from the center of the array.

A reconstructed image with multiple targets is shown in Fig. 8. Part (b) of the figure shows the location of the five targets in the image. The image shows resolution targets buried at approximately 9-cm depth. The resolution targets were 5 bars with center-to-center spacings of 3.7, 6.2, 8.8, and 10.1 cm. Each bar was $1.2\times7.5\times60$ cm with the longest dimension perpendicular to the scan, and the smallest dimension parallel to the scan. The total width of the target cluster was 30 cm. The data were focused by forming a synthesized element at a position 2.5 cm from the center of the array. The first bar appears at the left of the image (between 0 and 0.1 meters in azimuth) and is less bright than the others. Two bars appear between 0.1 and 0.2 m in azimuth. The second bar appears small and is difficult to distinguish. The third bar is centered at approximately 0.15 meters in azimuth and 0.15 meters in depth. The remaining bars are those with the largest separations and are bright targets in the image. One is centered at approximately 0.24 m in azimuth and 0.14 m in depth. The other is centered at approximately 0.38 m in azimuth and 0.1 m in depth. The predicted axial resolution is 16 cm at best, as calculated from the pulse duration and the speed of sound in the soil.

Figure 9 shows a second image with multiple targets. The soil contained three buried objects: two bottles, and a metal bar, $70\times10\times1$ cm. The bar was buried 6 cm deep so that the lateral dimension was 1 cm and the axial dimension was 10 cm. The bottles were buried end to end so that at the position where the source and array passed over them, they behaved as an air-filled glass tube, 7 cm in diameter and 30-cm long. They were buried 11.5-cm deep. Part (b) of the figure shows the locations of the bar and bottles in the image. The bar appears on the left, and the bottles appear on the right. The image was formed by synthesizing a single element at the position of the receiver array. In this image, the metal bar appears as the bright spot centered at approximately 0.14 m in azimuth and 0.15 m in depth. The spot immediately to the right of it is a side lobe. The spots below the metal bar are due to multiple reflections. The bottles

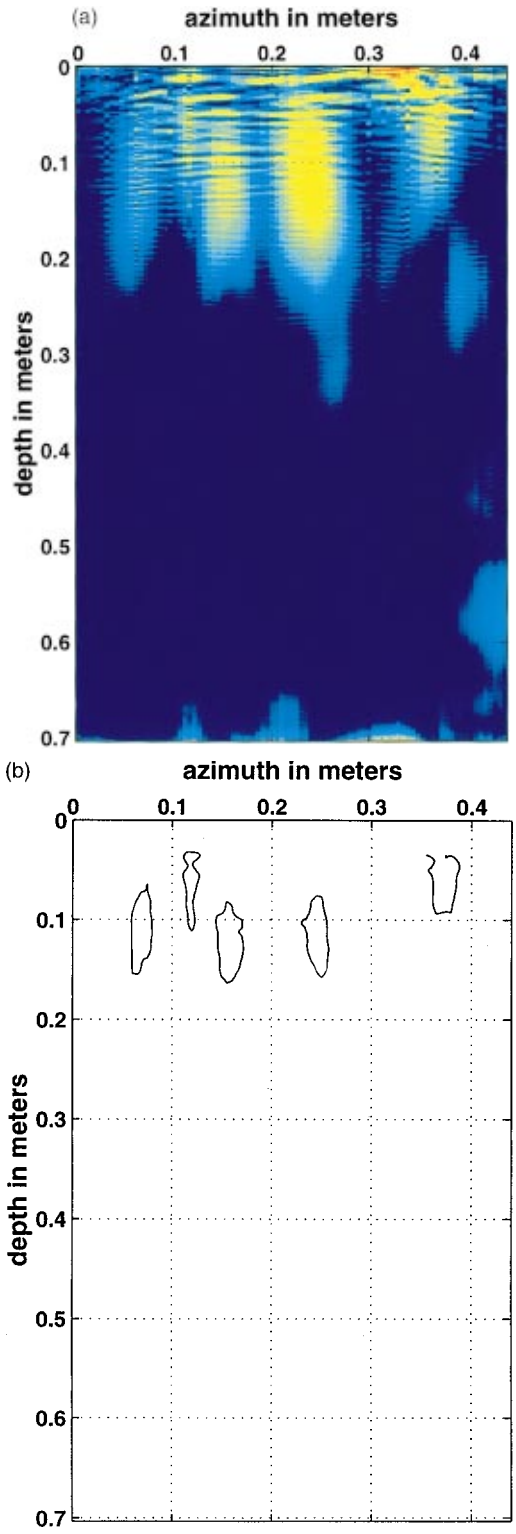

FIG. 8. (a) Image of resolution target. The resolution target consists of 5 parallel metal bars with increasing center-to-center separation (3.7, 6.2, 8.8, and 10.1 cm). It is difficult to distinguish the second and third bars in the image. In the image, the reflections due to the bars are centered at (0.05, 0.15), (0.11, 0.05), (0.15, 0.15), (0.24, 0.14) and (0.38, 0.1), where the first coordinate is the azimuth, the second coordinate is the depth, and both coordinates are given in meters. (b) Contour plot showing the locations of the metal bars in the image.

appear as a spot located approximately 0.38 meters in azimuth and 0.15 meters in depth. We conclude from this image that solid targets give a stronger reflection than do air-filled targets.

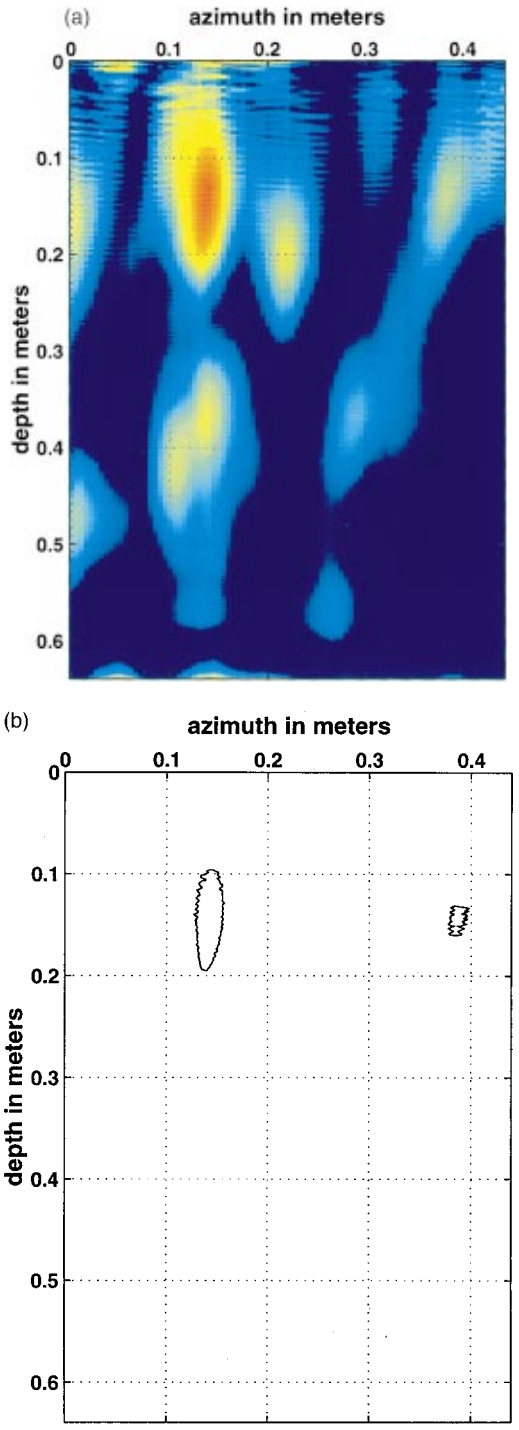

FIG. 9. (a) *B*-mode reconstructed image of metal bar and bottles using real data. The reflection due to the metal bar is centered at 0.14 meters in azimuth and 0.16 meters in depth. The reflection due to the bottles is centered at 0.38 meters in azimuth and 0.13 meters in depth. (b) Contour plot showing the locations of the targets in the image.

B. Synthetic aperture approach and simulation results

Given N transducers, a linear receiver array could provide far higher resolution than a rectangular array if synthetic aperture processing were used. Suppose data were collected from a linear array moved in a direction normal to its orientation. This corresponds to a linear array with its longer dimension being along the x axis as depicted in Fig. 10. High resolution in the direction of travel could then be obtained by

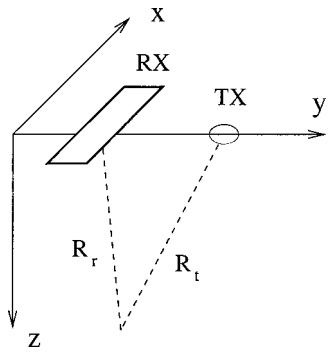

FIG. 10. Linear array and off-center transmitter.

using algorithms similar to those employed in synthetic aperture radar (SAR) or synthetic aperture sonar. High resolution along the dimension of the array would be obtained by using the beamforming approaches described above. A difference between subsurface imaging and SAR is that in the former we have attenuation of the signal due to the medium. We have developed a SAR-type reconstruction algorithm for the acoustic imaging scenario using a modification of the correlation algorithm described in Refs. 14 and 15. The main steps and the necessary modifications are explained briefly in the following.

By passing the returned signal through a quadrature demodulator, the carrier can be suppressed and the complex baseband signal can be obtained for each of the receivers in the linear array. The linear array then can be focused to a fixed depth, or can be dynamically focused to various depths by using beamforming. This results in a single waveform for each location of the data acquisition system. Let us denote the signal obtained after focusing as

$$\overline{g}(t,y_a)=\int_{-\infty}^{\infty}\int_{-\infty}^{\infty}\Gamma_0(y,z)w_a(y-y_a)w_r(z)\times s\left(t-\frac{R_t+R_r}{c}\right)e^{jk(R_t+R_r)}dy\,dz, \tag{8}$$

where y_a is the azimuth coordinate at which the returns are collected by the linear receiver array. $w_a(y)$ and $w_r(z)$ are window functions representing the area illuminated by the transmitted acoustic beam in the azimuth and range directions, respectively. First-order Taylor approximations of R_r and R_t,

$$R_r=\sqrt{(y-y_a)^2+z^2}\approx z+\frac{(y-y_a)^2}{2z}, \tag{9}$$

$$R_t=\sqrt{(y-y_a-d)^2+z^2}\approx z+\frac{(y-y_a-d)^2}{2z}, \tag{10}$$

are valid if the conditions $z\gg y-y_a$ and $z\gg y-y_a-d$ hold. Here, d is the distance between the transmitter and receiver. We assume that the transmitted signal varies slowly enough that $s(t-(R_t+R_r)/c)\approx s(t-2z/c)$. Assigning $\Gamma(y,z)=\Gamma_0(y,z)e^{-j2kz}$ and making the change of variables, $y\to\nu$, and $z\to\xi$, and $t=2z/c$, we can write

$$g(y_a,z)=\int\overline{\Gamma}(y_a,\xi)w_r(\xi)s\left(\frac{2}{c}(z-\xi)\right)d\xi \tag{11}$$

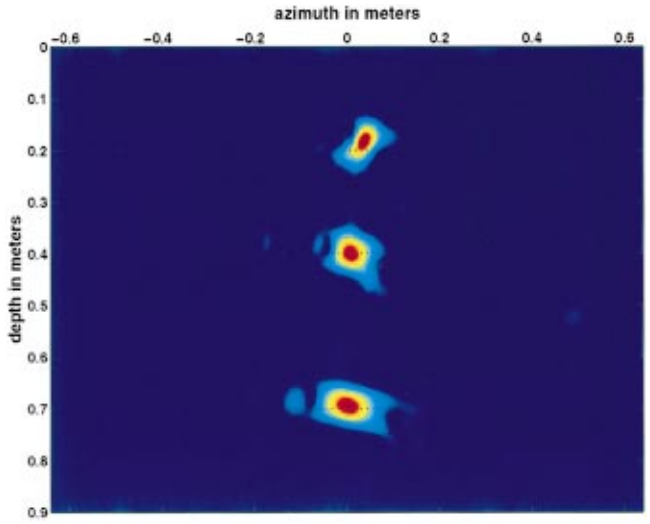

FIG. 11. SAR-type reconstruction of three point objects from simulated data.

$$\overline{\Gamma}(y_a,\xi)=\int\Gamma(\nu,\xi)w_a(\nu-y_a)\exp\left(-jk\frac{(\nu-y_a)^2}{2\xi}\right)\times\exp\left(-jk\frac{(\nu-y_a-d)^2}{2\xi}\right)d\nu. \tag{12}$$

In the so-called range processing step, the received signal in Eq. (11) is correlated with the transmitted signal to find a matched-filter estimate for $\overline{\Gamma}(y_a,z)$. Then this estimate is used to solve for $\overline{\Gamma}(y_a,z)$ by correlating the estimate of $\overline{\Gamma}(y_a,z)$ with the filter corresponding to the exponential terms in Eq. (12). This step is called azimuth processing. With the above formulation, range processing is the same as in the standard correlation-based SAR algorithm in Ref. 14. But in the standard algorithm, since it has been derived for a radar scenario, there is only one signal received by the single antenna located on the radar platform. Also, for the case of a single antenna, the transmitter-to-reflector and reflector-to-receiver distances are the same in the radar case. Notice that the attenuation term in Eq. (1) is not incorporated in Eq. (8). This is because we apply time-gain compensation to the received signal to compensate approximately for the effect of attenuation.

The above SAR-type algorithm was applied to simulated data consisting of three point targets and background soil scatterers. A linear array of 8 receivers, corresponding to the center of the experimental receiver array, were used. The point targets were positioned at $x=y=0$ and at depths 0.1 m, 0.4 m, 0.7 m. The grid for the background soil scatterers extended from $x=-0.2$ m to $x=0.2$ m, from $y=-0.49$ m to $y=0.49$ m, and from $z=0.01$ m to $z=0.9$ m. The resulting image is shown in Fig. 11. As mentioned, we used time-gain compensation to nearly eliminate the effect of attenuation. Without the compensation, only the scatterer at $z=0.1$ could be seen. Note that the point objects are not reconstructed at their correct locations in depth. This effect is most noticeable for the object closest to the surface. The reason for this is that our Taylor approximations for the transmitter-reflector-receiver distances are not valid for close objects. In a SAR

scenario, these approximations generally are valid because the range distance in radar imaging is typically very large. Note also that we approximated two distance functions in our case to take into account the off-center transmitter. If the standard monostatic SAR algorithm had been applied without that modification, the point target images in Fig. 11 would have been shifted in the azimuth direction, too. The clouds around the images of point objects are due to the soil scatterers.

In a SAR reconstruction, resolution in the range direction increases as the bandwidth of the transmitted signal increases. Azimuth resolution depends on the distance covered by the data acquisition system during illumination of a target by the transmitted acoustic beam. Collecting more data in the azimuth dimension provides for an increase in resolution in the azimuth direction. In our experimental system, the length of the scan is limited by the size of the box, which presented a complication to successfully applying SAR-type imaging. In addition, it may be necessary to apply autofocus techniques[16] to successfully form images from experimental data.

V. CONCLUSIONS AND FURTHER RESEARCH

An acoustic approach was described for imaging objects buried in soil, with the primary purpose of detecting and imaging cultural artifacts. An experimental system was designed and implemented. Also, a mathematical model and associated computer software were developed in order to simulate the signals acquired by the actual system. Subsurface images were reconstructed from real and simulated data by using delay-and-sum beamforming and by the application of synthetic aperture theory.

We have shown that our acoustic system can successfully detect objects buried in soil. Targets spaced 5 cm apart can be resolved as separate objects. Targets with a cross section as small as 1.2 cm by 7.5 cm can be seen as long as they have sufficient length.

The images clearly show targets; however, there is also much clutter which needs to be identified and removed. *B*-mode images could be improved by modifying the processing. First, apodization weights could be applied to the receiver array elements to reduce sidelobes. This modification should remove effects such as those due to the sides of the box in the image of the pipe. Second, we could form small images at each position of the source and receiver and then average the images from different transducer positions to create the final image with an improved signal-to-noise ratio. As discussed previously, we could create these small images by synthesizing multiple elements between the source and receiver.

The system itself could be improved to produce data with better signal-to-noise ratio. Currently we use a point source and array receiver. The source and receiver were chosen because of their availability and their ability to transmit high powered, shaped pulses and to receive small signals. With a focused source, we could transmit more energy to the region of interest, rather than spreading the energy over a wide area. In addition, if we could put the source and receiver closer together, we could increase the depth of penetration by reducing the total distance the sound must travel from source to target to receiver at a given depth. Our source had been designed to give the best performance between 6 kHz and 10 kHz. We actually used received signal components at a lower frequency, so another improvement would be to use a source with an optimal response at 2 kHz or even below. Also, work has already begun on developing transducers better matched to the impedance of soil.

We must be able to see smaller targets in order to use the system to detect cultural artifacts. Currently we can detect objects with small cross-sectional area and significant length. By moving the source and receiver in two dimensions rather than along a linear path, we would be more likely to detect small objects.

Finally, the system must be moved from the laboratory to the outdoors, where the actual use of the system will occur. Besides testing the equipment in a more realistic environment with a nonhomogeneous soil sample, this would allow us to collect data over a longer scan, making synthetic aperture approaches more appropriate. Wave-number–domain SAR algorithms, which are expected to give more accurate results for near-field sources, can then be tested.[17,18] In order to bring the system outside, a new mechanism for holding the transducers will be necessary as well as a new means of coupling the acoustic energy to the soil. Most likely, the transducers will be mounted on a vehicle. One possibility is to mount multiple transducers on a cylinder which is then rotated across the soil surface. Water coupling, using the child's pool, could be used in initial outdoor tests, but this would limit the total length of the scan. A final system will not have its transducer impedance matched to water, so coupling through a thin layer of air should be possible, although further investigation will be necessary. Coupling through air will change the boundary conditions, resulting in more energy coupled into the slow Biot wave.

This research was supported by the U.S. Army Construction Engineering Research Laboratory under Contract DACA88-96 K 0002.

[1] L. J. Carter, G. H. Bryant, M. LeFevre, and W. C. Wong, ''Moisture and land mine detection,'' in *Proceedings of the EUREL International Conference on the Detection of Abandoned Land Mines: A Humanitarian Imperative Seeking a Technical Solution*, Edinburgh, UK, Edinburgh International Conference Centre, Oct. 7–9, 1996, pp. 83–87.

[2] A. Langman and M. R. Inggs, ''A stepped frequency cw polarimetric radar for mine detection,'' in *Proceedings of the EUREL International Conference on the Detection of Abandoned Land Mines: A Humanitarian Imperative Seeking a Technical Solution* (Ref. 1), pp. 109–113.

[3] R. J. Chignell, ''Ground penetrating radar: A sensor for mine detection,'' in *Proceedings of the EUREL International Conference on the Detection of Abandoned Land Mines: A Humanitarian Imperative Seeking a Technical Solution* (Ref. 1), pp. 103–108.

[4] A. J. Witten and W. C. King, ''Acoustic imaging of subsurface features,'' J. Env. Eng. **116**, 166–181 (1990).

[5] L. Peters, Jr., J. J. Daniels, and J. D. Young, ''Ground penetrating radar as a subsurface environmental sensing tool,'' Proc. IEEE **82**, 1802–1822 (1994).

[6] D. M. McCann, P. D. Jackson, and P. J. Fenning, ''Comparison of seismic and ground probing radar methods in geological surveying,'' IEE Proc. F, Radar Signal Process. **135**, 380–390 (1988).

[7] E. Smith, P. S. Wilson, F. W. Bacon, J. F. Manning, J. A. Behrens, and T. G. Muir, ''Measurement and localization of interface wave reflections from a buried target,'' J. Acoust. Soc. Am. **103**, 2333–2343 (1998).

[8] M. A. Biot, ''Theory of propagation of elastic waves in a fluid saturated porous solid. I. low-frequency range,'' J. Acoust. Soc. Am. **28**, 168–178 (1956).
[9] M. A. Biot, ''Theory of propagation of elastic waves in a fluid saturated porous solid. II. high-frequency range,'' J. Acoust. Soc. Am. **28**, 179–191 (1956).
[10] W. D. O'Brien, Jr. and R. G. Darmody, ''Acoustic characterization of soil,'' Soil Sci. Soc. Am. J. (submitted).
[11] C. Hickey and J. Sabatier, ''Measurements of two types of dilatational waves in an air-filled unconsolidated sand,'' J. Acoust. Soc. Am. **102**, 128–136 (1997).
[12] A. D. Pierce, *Acoustics: An Introduction to Its Physical Principles and Applications* (McGraw-Hill, New York, 1981).
[13] K. K. Shung, M. B. Smith, and B. M. W. Tsui, *Principles of Medical Imaging* (Academic, San Diego, 1992).
[14] D. C. Munson, Jr. and R. L. Visentin, ''A signal processing view of strip-mapping synthetic aperture radar,'' IEEE Trans. Acoust., Speech, Signal Process. **37**, 2131–2147 (1989).
[15] J. C. Curlander and R. N. McDonough, *Synthetic Aperture Radar*, Wiley Series in Remote Sensing (Wiley, New York, 1991).
[16] C. V. Jakowatz, Jr., D. E. Wahl, P. H. Eichel, D. C. Ghiglia, and P. A. Thompson, *Spotlight-Mode Synthetic Aperture Radar: A Signal Processing Approach* (Kluwer Academic, Boston, 1996).
[17] C. Cafforio, C. Prati, and F. Rocca, ''SAR data focusing using seismic migration techniques,'' IEEE Trans. Aerosp. Electron. Syst. **27**, 194–207 (1991).
[18] M. Soumekh, ''A system model and inversion for synthetic aperture radar imaging,'' IEEE Trans. Image Process. **1**, 64–76 (1992).

Transient interaction of parallel thin-walled cylindrical piezoelectric ceramic radiators

Artashes E. Babaev, Viktor G. Savin, and Andrei A. Leiko
Institute of Mechanics, National Academy of Sciences, Ukraine

(Received 25 July 1997; revised 19 April 1999; revised 6 March 2000; accepted 15 March 2000)

This paper includes formulation of the multiconnected transient problem for an underwater transducer system of two thin-walled cylindrical piezoelectric ceramic radiators, description of an analytical method of solution, and investigation of fundamental regularities of transient processes. All these points take into account the interaction of reflectors. Radiators with continuous and sectioned electrodes are considered during excitation with different electrical impulses. An experimental test of selected mathematical models has been done. © *2000 Acoustical Society of America.* [S0001-4966(00)05106-7]

PACS numbers: 43.38.Ar, 43.38.Fx [SLE]

INTRODUCTION

Lately there has appeared a tendency to excite ultrasonic piezoelectric[1] devices by short-time or complicated-shape electrical or mechanical impulses. Correct determination of the resulting dynamic processes requires the choice and test of applicability of basic mathematical models and the development of effective methods of solution of transient transduction problems. Systems of two or more piezoelectric ceramic transducers make the task more complicated because it is necessary to satisfy conditions on each boundary surface. There are practically no investigations of transient processes in multiconnected regions with boundaries which do not belong to one family of coordinate surfaces in the area of continuous media mechanics. This article investigates the transient operation of two thin-walled cylindrical piezoelectric ceramic transducers excited by electrical impulses and situated in fluid.

References 2–5 are very close to the topic of the current paper. References 2 and 3 describe scattering of harmonic waves by periodically vibrating surfaces using a nonlinear model of the medium. Interaction of a plane wave with plane and cylindrical surfaces and of a cylindrical wave with a cylindrical surface were considered. Approximate and exact solutions of the problem of scattering of an harmonic spherical wave from a continuous elastic cylinder are obtained in Refs. 4 and 5.

I. MATHEMATICAL MODELS

The system of two cylindrical piezoelectric transducers with fluids filling the inner volumes and external infinite space is considered here. The transducers are radially polarized and are excited by transient electrical impulses. The electrodes have two arbitrarily oriented cuts each in the axial direction on the outer and inner surfaces of the cylinders. The above electrode configuration makes it possible to excite multiple modes of vibration of transducers when different electrical impulses are supplied to each pair of electrode sections. The transducers are excited in pulsating vibrations when the electrodes are continuous (without cuts).

We assume that the piezoelectric ceramic cylinders are infinitely long (plane problem) and thin-walled (Fig. 1).

The mathematical modeling of the investigated transient process has been done using classical theories: the theory of thin electroelastic shells based on Kirchhoff–Love hypotheses[6] and the theory of acoustic approximation.[7]

We introduce the polar coordinates r_1, θ_1 and r_2, θ_2 with centers on the axes of cylinders. The mean radii of the cylinders and cylinder thicknesses are designated as R_k and h_k $(k=1,2)$ and the distance between points O_1 and O_2 is designated as l (Fig. 1).

We designate the normal and tangential components of the displacement vector of the shell number k as $w^{(k)}$ and $u^{(k)}$ $(k=1,2)$, the intensity of electrical field being excited in the shell as $E^{(k)}$, the hydrodynamic load as $q^{(k)}$, the waves' potential of acoustic media filling the external infinite space as $\varphi^{(0)}$ and inner volumes as $\varphi^{(i)}$ $(i=1,2)$, the pressure arising in acoustic media as $p^{(i)}$ $(i=0,1,2)$, the physical parameters of the corresponding piezoelectric ceramic shells (the modulus of elasticity, piezoelectric moduli; density and permittivity) as $C_{11}^{(k)}$, $e_{13}^{(k)}$, $d_{33}^{(k)}$, $\gamma^{(k)}$, $\varepsilon_{33}^{(k)}$ $(k=1,2)$, the parameters of fluids (sonic velocity and density) as c_i, ρ_i $(i=0,1,2)$, and the time as t. We introduce the dimensionless parameters. The quantities $u^{(k)}$, $w^{(k)}$, l, h_k, R_k, r_k are divided by the radius R_1 $(R_1=1)$; $q^{(k)}$, $p^{(i)}$ are divided by $\rho_0 c_0^2$; $E^{(k)}$ is divided by $1/d_{33}$; t is divided by R_1/c_0; and $\varphi^{(i)}$ is divided by $R_1 c_0$.

Taking into account the assumptions made, the initial system of equations describing combined motions of electroelastic radiators and media contacting them has the form

$$(1+\varepsilon^{(k)})\frac{\partial^2 u^{(k)}}{\partial\theta_k^2}+\frac{\partial w^{(k)}}{\partial\theta_k}-\varepsilon^{(k)}\frac{\partial^3 w^{(k)}}{\partial\theta_k^3}-a^{(k)}\frac{\partial E^{(k)}}{\partial\theta_k}=b^{(k)}\frac{\partial^2 u^{(k)}}{\partial t^2},$$

$$-\frac{\partial u^{(k)}}{\partial\theta_k}+\varepsilon^{(k)}\frac{\partial^3 u^{(k)}}{\partial\theta_k^3}-w^{(k)}-\varepsilon^{(k)}\frac{\partial^4 w^{(k)}}{\partial\theta_k^4}+a^{(k)}E^{(k)}=b^{(k)}\frac{\partial^2 w^{(k)}}{\partial t^2}-d^{(k)}q^{(k)}, \quad (1)$$

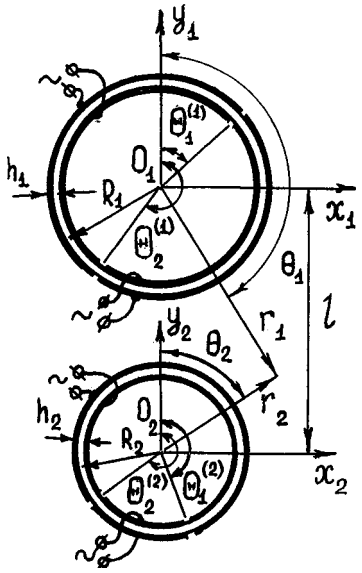

FIG. 1. A schematic representation of the two multimode cylindrical piezoelectric radiators.

$$\Delta_k \varphi^{(0)} = \alpha_0^2 \frac{\partial^2 \varphi^{(0)}}{\partial t^2}, \tag{2}$$

$$\Delta_k \varphi^{(k)} = \alpha_k^2 \frac{\partial^2 \varphi^{(k)}}{\partial t^2}, \tag{3}$$

$$q^{(k)} = [-\mu_0 p^{(0)} + \mu_k p^{(k)}]_{r_k = R_k}, \tag{4}$$

$$p^{(i)} = -\mu_i \frac{\partial \varphi^{(i)}}{\partial t}, \tag{5}$$

where $\Delta_k = (\partial^2/\partial r_k^2) + (1/r_k)(\partial/\partial r_k) + (1/r_k^2)(\partial^2/\partial \theta_k^2)$ is the Laplace operator in the polar coordinate system r_k, θ_k; $\varepsilon^{(k)}$, $a^{(k)}$, $b^{(k)}$, $d^{(k)}$, α_i, and μ_i are the constants,

$$\varepsilon^{(k)} = \frac{h_k^2}{12 R_k^2}\left(1 + \frac{e_{13}^{(k)^2}}{C_{11}^{(k)} \varepsilon_{33}^{(k)}}\right), \quad a^{(k)} = \frac{R_k e_{13}^{(k)}}{R_1 C_{11}^{(k)} d_{33}^{(1)}},$$

$$b^{(k)} = \frac{R_k^2 c_0^2 \gamma^{(k)}}{R_1^2 C_{11}^{(k)}}, \quad d^{(k)} = \frac{R_k^2 \rho_0 c_0^2}{R_1 h_k C_{11}^{(k)}}, \quad \alpha_i = \frac{c_0}{c_i}, \quad \mu_i = \frac{\rho_i}{\rho_0}.$$

Let's assume that electrodes of the shell number k have two cuts along the line where $\theta_k = \Theta_j^{(k)}$ $(j=1,2)$, $r_k = R_k \pm h_k/2$, and each couple of electrodes is supplied with the corresponding electrical impulses. In this case the intensity of electrical field $E^{(k)}$ $(k=1,2)$ is expressed by the formula

$$E^{(k)} = \left\{ \frac{Q_1^{(k)}(t)}{h_k} H(\theta_k - \Theta_1^{(k)}) H(\Theta_2^{(k)} - \theta_k) + \frac{Q_2^{(k)}(t)}{h_k} [H(\theta_k - \Theta_2^{(k)}) + H(\Theta_1^{(k)} - \theta_k)] \right\} H(t), \tag{6}$$

where $Q_j^{(k)}(t)$ are the functions defining the electrical impulses profiles and H is the Heaviside function.

In the case of continuous electrodes,

$$E^{(k)} = \frac{Q^{(k)}(t)}{h_k} H(t). \tag{7}$$

The boundary conditions on the external and internal surfaces of the shells assure their contact with acoustical media without tearing off

$$\frac{\partial w^{(k)}}{\partial t} = \left.\frac{\partial \varphi^{(0)}}{\partial r_k}\right|_{r_k = R_k}, \quad \frac{\partial w^{(k)}}{\partial t} = \left.\frac{\partial \varphi^{(k)}}{\partial r_k}\right|_{r_k = R_k} \quad (k=1,2). \tag{8}$$

Then evaluating at $r_k = R_k$ is a good approximation for thin-walled cylinders, rather than at $r_k = R_k \pm h_k/2$.

The initial conditions are homogeneous, i.e., considered hydroelectroelastic system is in state of rest till the moment $t=0$. At this point the electrical impulses begin to excite the piezoelectric transducers.

We would like to note that the assumptions described above were applied by other authors to the problems of transient hydroelasticity of the shells.[8,9]

II. METHOD OF SOLUTION

The Laplace transformation in time was used to solve the problem. In the transform space the unknowns are sought in the form of a series of characteristic modes of vibrations (Fourier series),

$$\varphi^{(0)L} = \sum_{k=1}^{2} \sum_{n=0}^{\infty} \varphi_{nk1}^{(0)L}(s, r_k) \cos n\theta_k + \varphi_{nk2}^{(0)L}(s, r_k) \sin n\theta_k, \tag{9}$$

$$\varphi^{(k)L} = \sum_{n=0}^{\infty} \varphi_{n1}^{(k)L}(s, r_k) \cos n\theta_k + \varphi_{n2}^{(k)L}(s, r_k) \sin n\theta_k, \tag{10}$$

$$w^{(k)L} = \sum_{n=0}^{\infty} w_{n1}^{(k)L}(s) \cos n\theta_k + w_{n2}^{(k)L}(s) \sin n\theta_k, \tag{11}$$

$$u^{(k)L} = \sum_{n=0}^{\infty} u_{nl}^{(k)L}(s) \sin n\theta_k + u_{n2}^{(k)L}(s) \cos n\theta_k \quad (k=1,2), \tag{12}$$

where the functions transformed according to Laplace are marked by the L index, and s is the parameter of transformation. It should be noted that according to (9) the field in the acoustical medium described by the potential $\varphi^{(0)}$ is represented as a superposition of waves radiated by each piezoelectric transducer $(k=1,2)$.

The transformed form of electrical field intensity $E^{(k)L}$ could be expanded in the same way as (9)–(12),

$$E^{(k)L}(s) = \sum_{n=0}^{\infty} E_{n1}^{(k)L}(s) \cos n\theta_k + E_{n2}^{(k)L}(s) \sin n\theta_k, \tag{13}$$

where

$$E_{nj}^{(k)L}(s)=\sigma_{nj1}^{(k)}Q_1^{(k)L}(s)+\sigma_{nj2}^{(k)}Q_2^{(k)L}(s) \quad (j=1,2),$$

$$\sigma_{n1i}^{(k)}=\begin{cases}\dfrac{2\pi\delta_{2i}-(-1)^i[\Theta_2^{(k)}-\Theta_1^{(k)}]}{2\pi h_k} & (n=0)\\ -(-1)^i\dfrac{\sin n\Theta_2^{(k)}-\sin n\Theta_1^{(k)}}{\pi n h_k} & (n>0)\end{cases},$$

$$\sigma_{n2i}^{(k)}=-(-1)^i\,\frac{\cos n\Theta_1^{(k)}-\cos n\Theta_2^{(k)}}{\pi n h_k}.$$

$i=1,2$, δ_{2i} is the symbol of Kroneker.

The modes $\varphi_{nki}^{(0)L}$, $\varphi_{ni}^{(k)L}$ satisfy the modified Bessel equations after substitution of the series (9), (10) in the wave equations (2), (3) transformed according to Laplace. As a result, the general solution can be written in the form[4] (note that pressure in the external space approaches zero if $r_k\to\infty$ and pressure in the inner volumes is limited if $r_k\to 0$. Also $\varphi^{(0)L}$ is forbidden to approach infinity if $r_k\to\infty$, and $\varphi^{(k)L}$ is forbidden to approach infinity if $r_k\to 0$):

$$\varphi^{(0)L}=\sum_{k=1}^{2}\sum_{n=0}^{\infty}\left\{A_{n1}^{(k)L}(s)\frac{1}{s}e^{s\alpha_0R_k}K_n(s\alpha_0r_k)\cos n\theta_k + A_{n2}^{(k)L}(s)\frac{1}{s}e^{s\alpha_0R_k}K_n(s\alpha_0r_k)\sin n\theta_k\right\}, \tag{14}$$

$$\varphi^{(k)L}=\sum_{n=0}^{\infty}\left\{B_{n1}^{(k)L}(s)\frac{1}{s}e^{-s\alpha_kR_k}I_n(s\alpha_kr_k)\cos n\theta_k + B_{n2}^{(k)L}(s)\frac{1}{s}e^{-s\alpha_kR_k}I_n(s\alpha_kr_k)\sin n\theta_k\right\}. \tag{15}$$

In formulas (14) and (15), l_n and K_n are the modified Bessel functions of the first and the second kind, $A_{ni}^{(k)L}(s)$ and $B_{ni}^{(k)L}(s)$ are unknown functions dependent on the transformation parameter s. They will be determined from the boundary conditions.

The summation theorem[10] is used for the function K_n for representation of the potential $\varphi^{(0)L}$ using the variables of each polar coordinate system,

$$K_n(zr_j)e^{in\theta_j}=\sum_{m=-\infty}^{\infty}(-1)^mK_{n-m}(zR_{ij})\times I_m(zr_i)e^{i(n-m)\theta_{ij}+in\theta_i}, \tag{16}$$

where R_{ij} and θ_{ij} are the coordinates of the center O_i of polar system r_i, θ_i in the system r_j, θ_j. It should be noted that the reduction formula is correct if $r_i<R_{ij}$. For Fig. 1: $\theta_{12}=\pi$, $\theta_{21}=0$, $R_{12}=R_{21}=l$. Taking in account the reexpansion (16), the function $\varphi^{(0)L}$ is expressed using variables r_1, θ_1 $(r_1<l)$,

$$\begin{aligned}\varphi^{(0)L}=\sum_{n=0}^{\infty}&\left\{A_{n1}^{(1)L}(s)\frac{1}{s}e^{s\alpha_0R_1}K_n(s\alpha_0r_1)\right.\\&+\sum_{m=0}^{\infty}A_{m1}^{(2)L}(s)v_n(-1)^n\frac{1}{s}e^{s\alpha_0R_2}I_n(s\alpha_0r_1)\\&\left.\times[K_{m-n}(s\alpha_0l)+K_{n+m}(s\alpha_0l)]\right\}\cos n\theta_1\\&+\sum_{n=1}^{\infty}\left\{A_{n2}^{(1)L}(s)\frac{1}{s}e^{s\alpha_0R_1}K_n(s\alpha_0r_1)\right.\\&+\sum_{m=1}^{\infty}A_{m2}^{(2)L}(s)(-1)^n\frac{1}{s}e^{s\alpha_0R_2}I_n(s\alpha_0r_1)\\&\left.\times[K_{m-n}(s\alpha_0l)-K_{m+n}(s\alpha_0l)]\right\}\sin n\theta_1,\end{aligned} \tag{17}$$

and using variables r_2, θ_2 $(r_2<l)$,

$$\begin{aligned}\varphi^{(0)L}=\sum_{n=0}^{\infty}&\left\{\sum_{m=0}^{\infty}A_{m1}^{(1)L}(s)v_n(-1)^m\frac{1}{s}e^{s\alpha_0R_1}I_n(s\alpha_0r_2)\right.\\&\times[K_{m-n}(s\alpha_0l)+K_{m+n}(s\alpha_0l)]\\&\left.+A_{n1}^{(2)L}(s)\frac{1}{s}e^{s\alpha_0R_2}K_n(s\alpha_0r_2)\right\}\cos n\theta_2\\&+\sum_{n=1}^{\infty}\left\{\sum_{m=1}^{\infty}A_{m2}^{(1)L}(s)(-1)^m\frac{1}{s}e^{s\alpha_0R_1}I_n(s\alpha_0r_2)\right.\\&\times[K_{m-n}(s\alpha_0l)-K_{m+n}(s\alpha_0l)]\\&\left.+A_{n2}^{(2)L}(s)\frac{1}{s}e^{s\alpha_0R_2}K_n(s\alpha_0r_2)\right\}\sin n\theta_2,\end{aligned} \tag{18}$$

where $v_0=1/2$, $v_n=1$ $(n>0)$.

Using the correlation of (17), (18) and (4), (5) we will obtain the following expansion in Fourier series of the hydrodynamic loads $q^{(k)L}$ $(k=1,2)$ acting on the piezoelectric transducers:

$$q^{(k)L}=\sum_{n=0}^{\infty}q_{n1}^{(k)L}(s)\cos n\theta_k+q_{n2}^{(k)L}(s)\sin n\,\theta_k. \tag{19}$$

The components $q_{ni}^{(k)L}$ $(i=1,2)$ of those series are described as follows:

$$\begin{aligned}q_{ni}^{(1)L}(s)=A_{ni}^{(1)L}(s)g_{0n}^L(s,\alpha_0R_1)+&\sum_{m=0}^{\infty}A_{mi}^{(2)L}(s)\\&\times e^{-s\alpha_0(l-R_1-R_2)}v_n(-1)^nf_{0n}^L(s,\alpha_0R_1)\\&\times[g_{0m-n}^L(s,\alpha_0l)-(-1)^ig_{0m+n}^L(s,\alpha_0l)]\\&-\mu_1B_{ni}^{(1)L}(s)f_{0n}^L(s,\alpha_0R_1),\end{aligned} \tag{20}$$

$$q_{ni}^{(2)L}(s)=\sum_{m=0}^{\infty}A_{mi}^{(1)L}(s)e^{-s\alpha_0(l-R_1-R_2)}v_n(-1)^m \times f_{0n}^{L}(s,\alpha_0R_2)[g_{0m-n}^{L}(s,\alpha_0l)-(-1)^i \times g_{0m+n}^{L}(s,\alpha_0l)]+A_{ni}^{(2)L}(s)g_{0n}^{L}(s,\alpha_0R_2) -\mu_2B_{ni}^{(2)L}(s)f_{0n}^{L}(s,\alpha_0R_2). \quad (21)$$

We use the following designations:

$$f_{jn}^{L}(s,z)=\frac{1}{s^j}e^{-sz}I_n(sz);\quad g_{jn}^{L}(s,z)=\frac{1}{s^j}e^{sz}K_n(sz). \quad (22)$$

Substituting the series (11), (12), (19) in the motion equations of electroelastic shells (1) transformed according to Laplace and solving them as regards to the normal components of displacements with number n, one finds the following dependence for $w_{ni}^{(k)L}$ $(i=1,2;\ k=1,2)$:

$$w_{ni}^{(k)L}=\kappa_1^{(k)}\frac{s^2+\beta_{n1}^{(k)}}{s^4+\lambda_{n1}^{(k)}s^2+\lambda_{n2}^{(k)}}q_{ni}^{(k)L}(s) +\kappa_2^{(k)}\frac{s^2+\beta_{n2}^{(k)}}{s^4+\lambda_{n1}^{(k)}s^2+\lambda_{n2}^{(k)}} \times[\sigma_{ni1}^{(k)}Q_1^{(k)L}(s)+\sigma_{ni2}^{(k)}Q_2^{(k)L}(s)], \quad (23)$$

where

$$\lambda_{n1}^{(k)}=\frac{(1+n^2)(1+n^2\varepsilon^{(k)})}{b^{(k)}},\quad \lambda_{n2}^{(k)}=\frac{n^2(n^2-1)^2\varepsilon^{(k)}}{b^{(k)^2}},$$

$$\beta_{n1}^{(k)}=\frac{n^2(1+\varepsilon^{(k)})}{b^{(k)}},\quad \beta_{n2}^{(k)}=\frac{n^2(1-n^2)\varepsilon^{(k)}}{b^{(k)}},$$

$$\kappa_1^{(k)}=\frac{\rho_0R_1}{\gamma_kh_k},\quad \kappa_2^{(k)}=\frac{R_1e_{13}^{(k)}}{R_kd_{33}^{(1)}\gamma_kc_0^2}.$$

Using the boundary conditions (8) and formulas (14), (15), (17), (18), and (23) we obtain two independent infinite systems of equations as regards to unknowns $A_{ni}^{(k)L}(s)$, $B_{ni}^{(k)L}(s)$ according to the cos-components $(i=1)$ and sin-components $(i=2)$ of Fourier series,

$$A_{ni}^{(1)L}(s)F_{nij}^{(1)L}(s)+B_{ni}^{(1)L}(s)G_{nij}^{(1)L}(s) =M_{nij}^{(1)L}(s)+\sum_{m=0}^{\infty}A_{mi}^{(2)L}(s)e^{-s\alpha_0(l-R_1-R_2)}N_{nmij}^{(1)L}(s), \quad (24)$$

$$A_{ni}^{(2)L}(s)F_{nij}^{(2)L}(s)+B_{ni}^{(2)L}(s)G_{nij}^{(2)L}(s) =M_{nij}^{(2)L}(s)+\sum_{m=0}^{\infty}A_{mi}^{(1)L}(s)e^{-s\alpha_0(l-R_1-R_2)}N_{nmij}^{(2)L}(s) \quad (j=1,2). \quad (25)$$

The elements of those systems are the functions dependent on the parameter of Laplace transformation s,

$$F_{ni1}^{(k)L}(s)=\left(\kappa_1^{(k)}-\frac{n}{R_k}\right)g_{1n}^{L}(s,\alpha_0R_k) +\left(\kappa_1^{(k)}\beta_{n1}^{(k)}-\lambda_{n1}^{(k)}\frac{n}{R_k}\right)g_{3n}^{L}(s,\alpha_0,R_k) -\lambda_{n2}^{(k)}\frac{n}{R_k}g_{5n}^{L}(s,\alpha_0R_k)+\alpha_0g_{0n+1}^{L}(s,\alpha_0,R_k) +\lambda_{n1}^{(k)}\alpha_0g_{2n+1}^{L}(s,\alpha_0R_k) +\lambda_{n2}^{(k)}\alpha_0g_{4n+1}^{L}(s,\alpha_0R_k);\quad (i=1,2),$$

$$F_{ni2}^{(k)L}(s)=\kappa_1^{(k)}[g_{1n}^{L}(s,\alpha_0R_k)+\beta_{n1}^{(k)}g_{3n}^{L}(s,\alpha_0R_k)],$$

$$G_{ni1}^{(k)L}(s)=-\mu_k\kappa_1^{(k)}[f_{1n}^{L}(s,\alpha_kR_k)+\beta_{n1}^{(k)}f_{3n}^{L}(s,\alpha_kR_k)],$$

$$M_{nij}^{(k)L}(s)=-\kappa_2^{(k)}\left\{\sigma_{ni1}^{(k)}\left(\frac{1}{s}+\beta_{n2}^{(k)}\frac{1}{s^3}\right)Q_1^{(k)L}(s) -\sigma_{ni2}^{(k)}\left(\frac{1}{s}+\beta_{n2}^{(k)}\frac{1}{s^3}\right)Q_2^{(k)L}(s)\right\}\quad (j=1,2),$$

$$N_{nmij}^{(k)L}(s)=V_{nmi}^{(k)L}(s)W_{nj}^{(k)L}(s), \quad (26)$$

$$V_{nmi}^{(k)L}(s)=(-1)^{n(2-k)+m(k-1)}v_n[g_{0m-n}^{L}(s,\alpha_0l) -(-1)^ig_{0m+n}^{L}(s,\alpha_0l)],$$

$$W_{n1}^{(k)L}(s)=\left(\frac{n}{R_k}-\kappa_1^{(k)}\right)f_{1n}^{L}(s,\alpha_0R_k) +\left(\lambda_{n1}^{(k)}\frac{n}{R_k}-\kappa_1^{(k)}\beta_{n1}^{(k)}\right)f_{3n}^{L}(s,\alpha_0R_k) +\lambda_{n2}^{(k)}\frac{n}{R_k}f_{5n}^{L}(s,\alpha_0R_k)+\alpha_0f_{0n+1}^{L}(s,\alpha_0R_k) +\lambda_{n1}^{(k)}\alpha_0f_{2n+1}^{L}(s,\alpha_0R_k) +\lambda_{n2}^{(k)}\alpha_0f_{4n+1}^{L}(s,\alpha_0R_k),$$

$$W_{n2}^{(k)L}(s)=-\kappa_1^{(k)}[f_{1n}^{L}(s,\alpha_0R_k)+\beta_{n1}^{(k)}f_{3n}^{L}(s,\alpha_0R_k)].$$

The evidence of the regularity of infinite systems (24), (25) in the considered case is impossible because the range of parameter s is unlimited. The traditional method used for substantiation of infinite systems' convergence in similar stationary problems of continuous medium mechanics is based on usage of the asymptotical formulas of Bessel functions, where order is considerably bigger than argument.[10–12] Such a method is not applicable for the current problem also because the range of parameter s is unlimited. The necessity exists to open in evident form the function determinations with order equal to the quantity of retained characteristic modes of vibration if we accomplish the reduction of infinite systems (without analytical approval of that procedure). The formulas describing the sought quantities become complicated (contain repeated product of Bessel functions) and bulky. The inversion of those formulas will cause principal and apparently practically insuperable mathematical difficulties. Taking into account the influence of multiple reflected and radiated waves fronts the approximation or numerical

methods for obtaining the reliable results is nondesirable in this case.

In accordance with the approach method, we assume that boundary conditions (8) will be satisfied in the space of the originals through exact inversion of Eqs. (24) and (25). As a result, the solution of two independent, $(i=1,2)$ infinite systems of the Volterra equations of the first kind with lagging arguments is done for determination of the unknowns $A_{ni}^{(k)}(t)$, $B_{ni}^{(k)}(t)$,

$$\int_0^t A_{ni}^{(1)}(\tau)F_{nij}^{(1)}(t-\tau)d\tau+\int_0^t B_{ni}^{(1)}(\tau)G_{nij}^{(1)}(t-\tau)d\tau$$

$$=M_{nij}^{(1)}(t)+\sum_{m=0}^{\infty}\int_{\alpha_0(l-R_1-R_2)}^{t}A_{mi}^{(2)}[\tau-\alpha_0(l-R_1-R_2)]$$

$$\times N_{nmij}^{(1)}(t-\tau)d\tau H[t-\alpha_0(l-R_1-R_2)], \tag{27}$$

$$\int_0^t A_{ni}^{(2)}(\tau)F_{nij}^{(2)}(t-\tau)d\tau+\int_0^t B_{ni}^{(2)}(\tau)G_{nij}^{(2)}(t-\tau)d\tau$$

$$=M_{nij}^{(2)}(t)+\sum_{m=0}^{\infty}\int_{\alpha_0(l-R_1-R_2)}^{t}A_{mi}^{(1)}[\tau-\alpha_0(l-R_1-R_2)]$$

$$\times N_{nmij}^{(2)}(t-\tau)d\tau H[t-\alpha_0(l-R_1-R_2)]. \tag{28}$$

According to (26), functions $F_{nij}^{(k)L}$ and $V_{nmi}^{(k)L}$ are linear combinations of functions g_{1n}^{L}, g_{3n}^{L}, g_{5n}^{L}, g_{0n+1}^{L}, g_{2n+1}^{L}, g_{4n+1}^{L}, g_{0m-n}^{L}, g_{0m+n}^{L} and functions $G_{nij}^{(k)L}$ and $W_{ni}^{(k)L}$ are linear combinations of the functions f_{1n}^{L}, f_{3n}^{L}, f_{5n}^{L}, f_{0n+1}^{L}, f_{2n+1}^{L}, f_{4n+1}^{L} (22). The originals $g_{0n}(t,z)$ and $f_{0n}(t,z)$ are obtained from operational calculus tables,[13]

$$g_{0n}(t,z)=\frac{ch\left[n\ \mathrm{arch}\dfrac{z+t}{z}\right]}{\sqrt{2tz+t^2}},$$

$$f_{0n}(t,z)=\begin{cases}\dfrac{\cos\left[n\arccos\dfrac{z-t}{z}\right]}{\pi\sqrt{2tz-t^2}} & (0<t<2z),\\ 0 \quad (2z\leqslant t)\end{cases} \tag{29}$$

while $g_{\xi n}$, $f_{\xi n}$ $(\xi>0)$ are obtained as a result of the evident form of the integration of $g_{\xi-1n}$, $f_{\xi-1n}$,

$$g_{\xi n}(t,z)=\int_0^t g_{\xi-1n}(\tau,z)d\tau, \qquad f_{\xi n}(t,z)=\int_0^t f_{\xi-1n}(\tau,z)d\tau, \tag{30}$$

for example,

$$g_{10}(t,z)=\mathrm{arch}\frac{z+t}{z},$$

$$g_{1n}(t,z)=\frac{1}{n}sh\left(n\ \mathrm{arch}\frac{z+t}{z}\right) \quad (n>0),$$

$$f_{10}(t,z)=\begin{cases}\dfrac{1}{\pi}\arccos\dfrac{z+t}{z} & (0<t<2z),\\ 1 \quad (2z\leqslant t)\end{cases}$$

$$f_{1n}(t,z)=\begin{cases}\dfrac{1}{n\pi}\sin\left(n\arccos\dfrac{z-t}{z}\right) & (0<t<2z)\\ 0 \quad (2z<t)\end{cases} \qquad (n>0).$$

The above described formulas are mentioned in the monograph.[14] The functions $N_{nmij}^{(k)}(t)$ are described by the Duhamel integral,

$$N_{nmij}^{(k)}(t)=\int_0^t V_{nmi}^{(k)}(t-\tau)W_{nj}^{(k)}(\tau)d\tau. \tag{31}$$

The functions $M_{ni}^{(k)L}$ are transformed similarly to $N_{nmij}^{(k)L}$.

In the following paragraph we will prove that two infinite systems $(i=1,2)$ of the integral equations (27), (28) may be solved using the reduction method.

The systems (27), (28) were solved by parceling out of time interval and calculating the integrals on each stage using the method of the quadrature formulas.[15] The shift in the arguments of unknowns being the components of the infinite series, allows us to solve the equations corresponding to the boundary conditions on the surfaces of each piezoelectric transducer and to each characteristic form of vibrations n independently. During the initial stage of transient process $[t<\alpha_0(l-R_1-R_2)]$, the m-series equal zero and the unknowns $A_{ni}^{(1)}(t)$, $B_{ni}^{(1)}(t)$ are obtained from Eqs. (27) while unknowns $A_{ni}^{(2)}(t)$, $B_{ni}^{(2)}(t)$ are taken from Eqs. (28). The previously obtained values $A_{ni}^{(1)}(t)$ and $A_{ni}^{(2)}(t)$ (using the time lag) are used in time range $t>\alpha_0(l-R_1-R_2)$ to calculate the infinite series in Eqs. (27) and (28).

After the systems' solution we determine the physical characteristics of the considered transient processes. Thus we invert exactly the functions $p^{(j)L}$ $(j=0,k)$, taking into account the formulas (5), (14), and (15) to calculate the pressure in acoustical media on external and inner surfaces of piezoelectric transducers with number k $(k=1,2)$. The unknown quantities can be written in the form

$$P^{(j)}(t,R_k,\theta_k)=\sum_{n=0}^{\infty}p_{n1}^{(j)}(t,R_k)\cos n\theta_k + p_{n2}^{(j)}(t,R_k)\sin n\theta_k. \tag{32}$$

The components of the expansion into Fourier series $p_{ni}^{(j)}$ $(j=0,1,2)$ are described by the integrals

$$p_{ni}^{(0)}(t,R_1)=-\int_0^t A_{ni}^{(1)}(\tau)g_{0n}(t-\tau,\alpha_0R_1)d\tau$$

$$-\sum_{m=0}^{\infty}\int_{\alpha_0(l-R_1-R_2)}^{t}A_{mi}^{(2)}[\tau-\alpha_0(l-R_1-R_2)]$$

$$\times U_{nmi}^{(1)}(t-\tau)d\tau H[t-\alpha_0(l-R_1-R_2)],$$

$$p_{ni}^{(0)}(t,R_2)=\sum_{m=0}^{\infty}\int_{\alpha_0(l-R_1-R_2)}^{t}A_{mi}^{(1)}[\tau-\alpha_0(l-R_2-R_1)]$$

$$\times U_{nmi}^{(2)}(t-\tau)d\tau H[t-\alpha_0(l-R_1-R_2)]$$

$$-\int_0^t A_{ni}^{(2)}(\tau)g_{0n}(t-\tau,\alpha_0R_2)d\tau,$$

$$p_{ni}^{(k)}(r,R_k)=-\mu_k\int_0^t B_{ni}^{(k)}(\tau)f_{0n}(t-\tau,\alpha_k R_k)d\tau$$

$$(k=1,2), \tag{33}$$

where

$$U_{nmi}^{(k)}(t)=\int_0^t f_{0n}(\tau,\alpha_0 R_k)V_{nmi}^{(k)}(t-\tau)d\tau. \tag{34}$$

In the expressions (33), the functions $A_{ni}^{(k)}$, $B_{ni}^{(k)}$ are known [they are determined as a result of the equation system (27) and (28) solution]. The functions g_{0n}, f_{0n} are described in (29). $V_{nmi}^{(k)}$ is expressed using g_{0m-n} and g_{0m+n} (26). The integrals (33) and (34) were calculated using the quadrature formulas method.

The loads on the shells $q^{(k)}$, the displacements $w^{(k)}$, $u^{(k)}$, and other physical values are calculated in the same way.

The control of the precision of obtained results was done by varying the step of dividing the time interval on segments and the number of the characteristic forms of vibration.

III. SUBSTANTIATION OF APPLICABILITY OF THE REDUCTION METHOD

We will show that the reduction method is applicable to solve the infinite system of integral equations (27) and (28) and will simplify the calculations by consideration of the case where inside volumes of shells do not contain the acoustical media. The equations corresponding to $j=2$ should be excluded and the equality should be read $B_{ni}^{(k)L}=0$ in the system of Eqs. (24) and (25).

We introduce the new unknowns,

$$X_{ni}^{(k)L}(s)=F_{ni1}^{(k)L}(s)A_{ni}^{(k)L}(s) \quad (k=1,2). \tag{35}$$

Their usage allows us to reduce the mentioned system to canonical form,

$$X_{ni}^{(1)L}(s)=M_{ni1}^{(1)L}(s)+\sum_{m=0}^{\infty}X_{ni}^{(2)L}(s)e^{-s\alpha_0(l-R_1-R_2)}Z_{nmi1}^{(1)L}(s), \tag{36}$$

$$X_{ni}^{(2)L}(s)=M_{ni1}^{(2)L}(s)+\sum_{m=0}^{\infty}X_{ni}^{(1)L}(s)e^{-s\alpha_0(l-R_1-R_2)}Z_{nmi1}^{(2)L}(s), \tag{37}$$

where

$$Z_{nmi1}^{(1)L}(s)=\frac{N_{nmi1}^{(1)L}(s)}{F_{mi1}^{(2)L}(s)}, \quad Z_{nmi1}^{(2)L}(s)=\frac{N_{nmi1}^{(2)L}(s)}{F_{mi1}^{(1)L}(s)}. \tag{38}$$

Accomplishing the inversion of Eqs. (36) and (37), we get the following system of Volterra equations relative to unknowns $X_{ni}^{(k)}$:

$$X_{ni}^{(1)}(t)=M_{ni1}^{(1)}(t)+\sum_{m=0}^{\infty}\int_{\alpha_0(l-R_1-R_2)}^{i}X_{mi}^{(2)}[\tau-\alpha_0(l-R_1-R_2)]Z_{nmi1}^{(1)}(t-\tau)d\tau H[t-\alpha_0(l-R_1-R_2)],$$

$$X_{ni}^{(2)}(t)=M_{ni1}^{(2)}(t)+\sum_{m=0}^{\infty}\int_{\alpha_0(l-R_1-R_2)}^{t}X_{mi}^{(1)}[\tau-\alpha_0(l-R_1-R_2)]Z_{nmi1}^{(2)}(t-\tau)d\tau H[t-\alpha_0(l-R_1-R_2)]. \tag{39}$$

The numerical values of functions $Z_{nmi1}^{(k)}$ can be found as the result of solving the integral equations. It can be shown in particular case for the function $Z_{nm11}^{(1)}$. We transport the formula (38) to the form

$$Z_{nm11}^{(1)L}(s)\tilde{F}_{m11}^{(2)L}(s)=\tilde{N}_{m11}^{(1)L}(s), \tag{40}$$

where

$$\tilde{F}_{m11}^{(2)L}(s)=\frac{1}{s^m}F_{m11}^{(2)L}(s), \quad \tilde{N}_{nm11}^{(1)L}(s)=\frac{1}{s^m}N_{nm11}^{(1)L}(s),$$

and the function $F_{m11}^{(2)L}$ is expressed by K_n, K_{n-1} according to the recurrent formulas. Inverting the equality (40) we obtain the integral equation for the unknown $Z_{nm11}^{(1)}(t)$,

$$\int_0^t Z_{nm11}^{(1)}(\tau)\tilde{F}_{m11}^{(2)}(t-\tau)d\tau=\tilde{N}_{nm11}^{(1)}(t). \tag{41}$$

The functions $\tilde{F}_{m11}^{(2)}$, $\tilde{N}_{nm11}^{(1)}$ are obtained analytically,

$$\tilde{F}_{m11}^{(2)}(t)=\int_0^t\left\{\left[\left(\kappa_1^{(2)}+\frac{m}{R_2}\right)+\left(\kappa_1^{(2)}\beta_{m1}^{(2)}+\lambda_{m1}^{(2)}\frac{m}{R_2}\right)\frac{(t-\tau)^2}{2!}+\lambda_{m2}^{(2)}\frac{(t-\tau)^4}{4!}\right]\tilde{g}_m(\tau,\alpha_0R_2)\right\}d\tau+\alpha_0\left\{\tilde{g}_{m-1}(t-\alpha_0R_2)+\int_0^t\left[\lambda_{n1}^{(2)}\frac{(t-\tau)}{1!}+\lambda_{n2}^{(2)}\frac{(t-\tau)^3}{3!}\right]\tilde{g}_{m-1}(t,\alpha_0R_2)d\tau\right\},$$

$$N_{nm11}^{(1)}(t)=(-1)^n\left\{\int_0^t\left[\left(\frac{n}{R_1}-\kappa_1^{(1)}\right)+\left(\lambda_{n1}^{(1)}\frac{n}{R_1}-\kappa_1^{(1)}\beta_{n1}^{(1)}\right)\frac{(t-\tau)^2}{2!}+\lambda_{n2}^{(1)}\frac{n}{R_1}\frac{(t-\tau)^4}{4!}\right]\times\Phi_{nm}^{(1)}(\tau)d\tau+\alpha_0\frac{d}{dt}\Phi_{nm}^{(2)}(t)+\alpha_0\int_0^t\left[\lambda_{n1}^{(1)}+\lambda_{n2}^{(1)}\frac{(t-\tau)^2}{2!}\right]\Phi_{nm}^{(2)}(\tau)d\tau\right\},$$

$$\Phi_{nm}^{(1)}(t)=v_n\left\{\int_0^{\chi(t)}\tilde{f}_n(\tau,\alpha_0R_1)\tilde{g}_{m-n}(t-\tau,\alpha_0l)d\tau+\frac{d^{2n}}{dt^{2n}}\int_0^{\chi(t)}\tilde{f}_n(\tau,\alpha_0R_1)\tilde{g}_{m+n}(t-\tau,\alpha_0l)d\tau\right\},$$

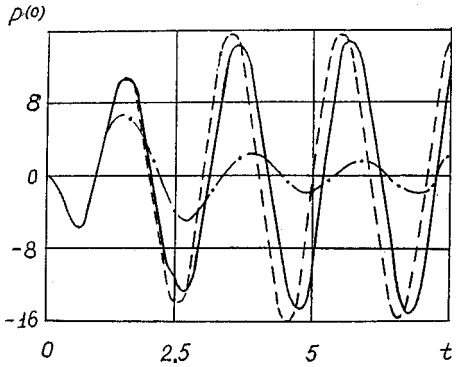

FIG. 2. Acoustic pressures in the points: $r_1=R_1$, $\theta_1=0$ (——), $\pi/2$ $(3\pi/2)$ (- - - -), π (-·-·-·) where $l=3$. The piezoelectric radiators have continuous electrodes and are excited by electrical impulses $Q_k^{(1)}(t)=\sin\omega t$ $(k=1,2)$ where $\omega=3.05$ (the natural radial, resonance frequency of the shells).

$$\Phi_{nm}^{(2)}(t)=v_n\left\{\int_0^{\chi(t)}\tilde{f}_{n+1}(\tau,\alpha_0R_1)\tilde{g}_{m-n}(t-\tau,\alpha_0 l)\,d\tau + \frac{d^{2n}}{dt^{2n}}\int_0^{\chi(t)}\tilde{f}_{n+1}(\tau,\alpha_0R_1) \times\tilde{g}_{m+n}(t-\tau,\alpha_0 l)\,d\tau\right\},$$

$$\chi(t)=\begin{cases} t & (0<t<2\alpha_0R_1)\\ 2\alpha_0R_1 & (2\alpha_0R_1<t)\end{cases},$$

using the calculation tables[13] for the functions

$$\tilde{g}_m^L(s,z)=e^{sz}K_m(sz)/s^m,\quad \tilde{f}_m^L(s,z)=e^{-sz}I_m(sz)/s^m,$$

$$\tilde{g}_m(t,z)=\frac{\sqrt{\pi}(2zt+t^2)^{m-1/2}}{2^m\Gamma(m-\frac{1}{2})z^m},$$

$$\tilde{f}_m(t,z)=\begin{cases}\dfrac{(2zt-t^2)^{m-1/2}}{\sqrt{\pi}2^m\Gamma(m-\frac{1}{2})z^m} & (0<t<2z)\\ 0 & (2z\leqslant t)\end{cases}$$

(Γ is the Gamma function).

We can show that double series $\Sigma_{m=0}^{\infty}\cdot\Sigma_{n=0}^{\infty}|Z_{nm11}^{(1)}|$ are convergent for the finite values t.

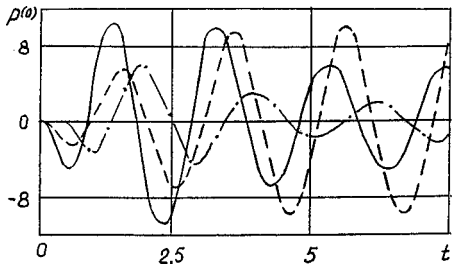

FIG. 3. Acoustic pressures in the points: $r_1=R_1$, $\theta_1=0$ (——), $\pi/2$ $(3\pi/2)$ (- - - -), π (-·-·-·) where $l=3$. The piezoelectric radiators have a longitudinal orientation of electrodes $(\Theta_k^{(1)}=\pi/2,\ \Theta_k^{(2)}=3\pi/2)$ and they are excited by electrical impulses $Q_k^{(2)}(t)=\sin\omega t$ $(\omega=3.05)$, $Q_k^{(1)}(t)=0$ (the electrodes are short-circuited in the region $\pi/2<\theta_k<3\pi/2$).

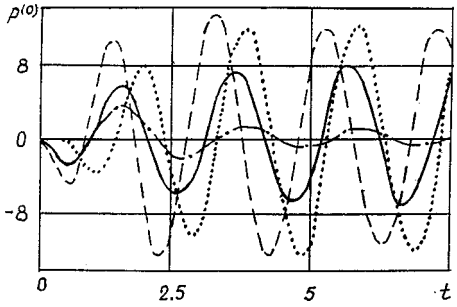

FIG. 4. Acoustic pressures in the points: $r_1=R_1$, $\theta_1=0$ (——), $\pi/2$ (- - - -), π (-·-·-·), $3\pi/2$ (····) where $l=3$. The piezoelectric radiators have a transversal orientation of electrodes $(\Theta_k^{(1)}=0,\ \Theta_k^{(2)}=\pi)$ and they are excited by electrical impulses $Q_k^{(1)}(t)=\sin\omega t$ $(\omega=3.05)$, $Q_k^{(2)}(t)=0$ (the electrodes are short-circuited in the region $\pi<\theta_k<2\pi$).

We apply the mean-value theorem to the integral in Eq. (41) where $\tilde{F}_{m11}^{(2)}>0$ if $t>0$,

$$Z_{nm11}^{(1)}(\varsigma t)=\frac{\tilde{N}_{nm11}^{(1)}(t)}{\int_0^t\tilde{F}_{m11}^{(2)}(\tau)\,d\tau}\qquad(0<\varsigma<1).$$

We use the following correlation:

$$\sum_{n=0}^{\infty}\Phi_{nm}^{(1)}(t)=\frac{\sqrt{\pi}[2\alpha_0(l-R_1)t+t^2]^{m-1/2}}{2^m[\alpha_0(l-R_1)]^m\Gamma(m+\frac{1}{2})}.\tag{42}$$

It is obtained as the result of multiplication of expansion (16) (theorem of summation) by $e^{s\alpha_0(l-R_1)}/s^m$ and its inversion where $\theta_i=\pi$, $r_i=R_1$, $\theta_j=0$, $r_j=l-R_1$.

We can show that $\Phi_{nm}^{(1)}>0$ and $\Phi_{nm}^{(2)}>0$, where $t>0$. Taking into account the equality (42) we can get the following estimation of the double series under consideration:

$$\sum_{m=0}^{\infty}\sum_{n=0}^{\infty}|Z_{nm11}^{(1)}|<C\sum_{m=0}^{\infty}m^6\left[\frac{2\alpha_0(l-R_1)t+t^2}{\alpha_0(l-R_1)}\right]^{m-6}\times\left[\frac{\alpha_0R_2}{2\alpha_0R_2t+t^2}\right]^m.\tag{43}$$

C is a constant.

The resulting single m-series converges according to the D'Alembert indication if

$$\frac{[2\alpha_0(l-R_1)t+t^2]\alpha_0R_2}{\alpha_0(l-R_1)[2\alpha_0R_2t+t^2]}<1,$$

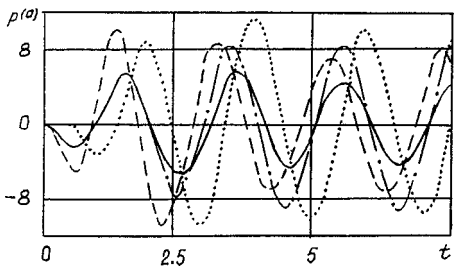

FIG. 5. Acoustic pressures in the points: $r_1=R_1$, $\theta_1=0$ (——), $\pi/2$ (- - - -), π (-·-·-·), $3\pi/2$ (····) where $l=4$. The piezoelectric radiators have a transversal orientation of electrodes $(\Theta_k^{(1)}=0,\ \Theta_k^{(2)}=\pi)$ and they are excited by electrical impulses $Q_k^{(1)}(t)=\sin\omega t$ $(\omega=3.05)$, $Q_k^{(2)}(t)=0$.

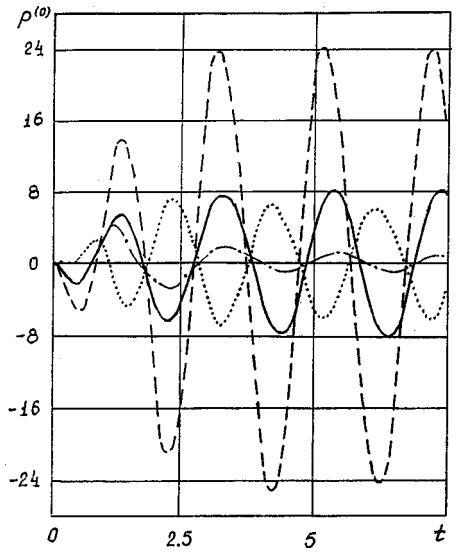

FIG. 6. Acoustic pressures in the points: $r_1=R_1$, $\theta_1=0$ (——), $\pi/2$ (- - - -), π (-·-·-), $3\pi/2$ (····) where $l=3$. The piezoelectric radiators have a transversal orientation of electrodes ($\Theta_k^{(1)}=0$, $\Theta_k^{(2)}=\pi$) and they are excited by electrical impulses $Q_k^{(1)}(t)=\sin\omega t$, $Q_k^{(2)}(t)=-\sin[\omega(t-T_0)]\times H(t-T_0)$ ($\omega=3.05$, $T_0=0.4$).

on condition that $l-(R_1+R_2)>0$ (the cylindrical surfaces are neither intersected nor contacted). The similar estimation is valid for the functions $Z_{nm21}^{(1)}$, $Z_{nmi1}^{(2)}$ $(i=1,2)$.

Considering the infinite system of integral equations (39) the solutions of this system on the time interval $0<t<\alpha_0(l-R_1-R_2)$ are in accord with solutions of the problems of radiation for single shells. The values $X_{ni}^{(k)}(t)$ $(i,k=1,2)$ obtained for that time interval are limited and are decreasing with the increase of n. The functions $X_{ni}^{(k)}$ with lag in argument are being used for the calculation of the infinite series when $t>\alpha_0(l-R_1-R_2)$ in Eqs. (39). Taking into account the limitation of $X_{ni}^{(k)}$ and summation of $Z_{nmi1}^{(k)}$ in n and m we can conclude that the infinite series in (39) converge. The solution is limited and is decreasing with the increase of n where t is finite. Consequently the reduction method is applicable for the solution of the infinite system of integral equations (39) and equivalent system (27) and (28).

IV. NUMERICAL RESULTS

The accuracy of performed calculations was controlled by means of comparison of the numerical results. These results were obtained by varying the number of modes of vibration and the duration of integrals' division steps of t. The results were considered acceptable where the difference of the extreme values of the sought physical characteristics was less than 4%.

The calculations were done for two identical cylindrical piezoelectric radiators made of the material TsTBS-3,[16] the physical parameters of which are as follows:

$$C_{11}^{(k)}=15.1\cdot 10^{10}\,\frac{N}{m^2},\quad e_{13}^{(k)}=-7.9\,\frac{C}{m^2},$$

$$d_{33}^{(k)}=2.86\cdot 10^{-10}\,\frac{C}{N},\quad \gamma^{(k)}=7.21\cdot 10^{3}\frac{kg}{m^3},$$

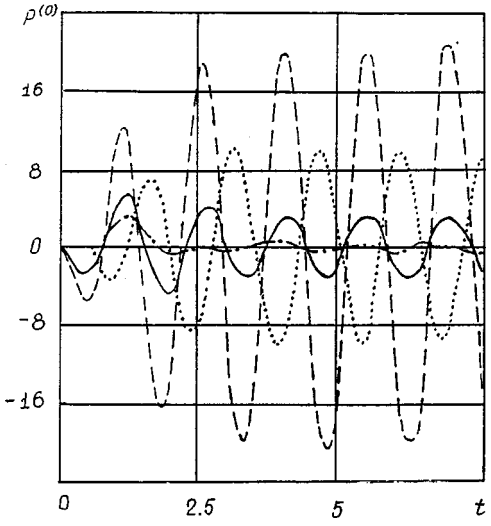

FIG. 7. Acoustic pressures in the points: $r_1=R_1$, $\theta_1=0$ (——), $\pi/2$ (- - - -), π (-·-·-), $3\pi/2$ (····) where $l=2.7$. The piezoelectric radiators have a transversal orientation of electrodes sections ($\Theta_k^{(1)}=0$, $\Theta_k^{(2)}=\pi$) and they are excited by electrical impulses $Q_k^{(1)}(t)=\sin\omega t$, where $\omega=4.32$ (the fundamental circumferential mode resonance frequency of the shells), $Q_k^{(2)}(t)=0$.

$$\varepsilon_{33}^{(k)}=1280\cdot\varepsilon_0$$

$$\left(\varepsilon_0=8.84\cdot 10^{-12}\,\frac{F}{m}\right.$$

$$\left.-\text{dielectric permittivity of vacuum}\right),$$

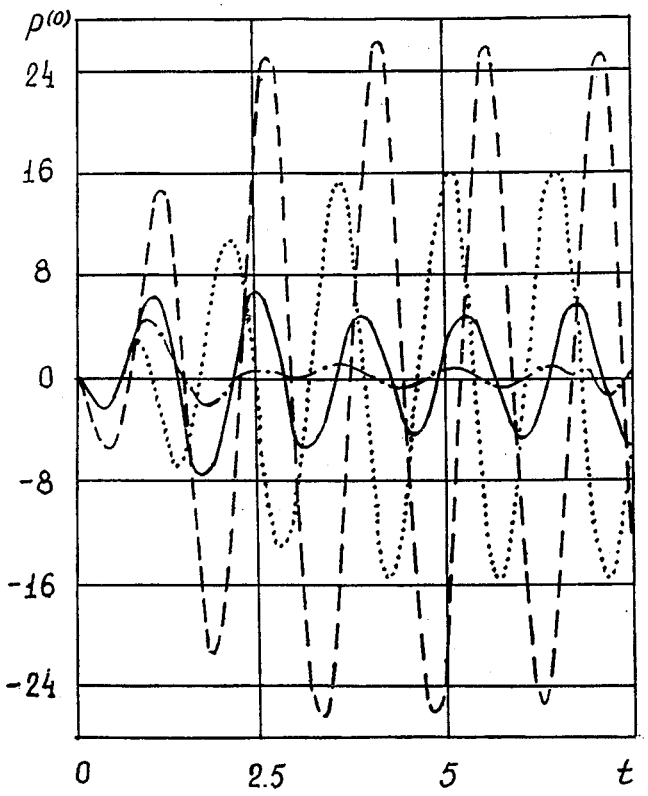

FIG. 8. Acoustic pressures in the points: $r_1=R_1$, $\theta_1=0$ (——), $\pi/2$ (- - - -), π (-·-·-), $3\pi/2$ (····) where $l=2.7$. The piezoelectric radiators have a transversal orientation of electrodes sections ($\Theta_k^{(1)}=0$, $\Theta_k^{(2)}=\pi$) and they are excited by electrical impulses $Q_k^{(1)}(t)=\sin\omega t$ and $Q_k^{(2)}(t)=-\sin[\omega(t-T_0)]H(t-T_0)$ ($\omega=4.32$, $T_0=0.4$).

with the relative geometrical dimensions: $h_k/R_k=1/25$, $R_k=1$ $(k=1,2)$. The radiators were dipped in water and their interior was evacuated.

Figures 2–8 show graphic curves of the acoustic pressures $p^{(0)}$ in the typical points of contact of the first $(k=1)$ cylinder with fluid: $r_1=R_1$, $\theta_1=0;\pi/2;\pi;3\pi/2$. The piezoelectric transducers were excited with transient electrical impulses of sinusoidal form. The variants were chosen where the electrodes didn't have any cuts (one-mode radiations) and where the electrodes had cuts at $\Theta_k^{(1)}=\pi/2$; $\Theta_k^{(2)}=3\pi/2$ and $\Theta_k^{(1)}=0$; $\Theta_k^{(2)}=\pi$ (multimodes' radiations with longitudinal and transversal orientation of electrodes sections). The graphic curves presented in Figs. 2–6 were obtained for the following initial findings: continuous electrodes, $Q_k^{(1)}(t)=\sin\omega t$ ($\omega=3.05$ is the shells' radial resonance frequency), $l=3$ (Fig. 2); $\Theta_k^{(1)}=\pi/2$, $\Theta_k^{(2)}=3\pi/2$ (longitudinal orientation of the electrodes sections), $Q_k^{(2)}(t)=\sin 3.05t$, $Q_k^{(1)}(t)=0$ (the electrodes are short-circuited in the region $\pi/2<\theta_k<3\pi/2$), $l=3$ (Fig. 3); $\Theta_k^{(1)}=0$, $\Theta_k^{(2)}=\pi$ (transversal orientation of the electrodes sections), $Q_k^{(1)}(t)=\sin 3.05t$, $Q_k^{(2)}=0$ (the electrodes are short-circuited in the region $\pi<\theta_k<2\pi$), $l=3$ (Fig. 4); and $l=4$ (Fig. 5); $\Theta_k^{(1)}=0$, $\Theta_k^{(2)}=\pi$, $Q_k^{(1)}(t)=\sin 3.05t$, $Q_k^{(2)}(t)=-\sin[3.05(t-T_0)]H(t-T_0)$, here $T_0=0.4$, $l=3$ (Fig. 6). Figures 7 and 8 correspond to the cases where $l=2{,}7$, $\Theta_k^{(1)}=0$, $\Theta_k^{(2)}=\pi$, $Q_k^{(1)}(t)=\sin\omega t$ ($\omega=4.32$ is the shell's fundamental circumferential mode resonance frequency), $Q_k^{(2)}(t)=0$ (Fig. 7) and $Q_k^{(2)}(t)=-\sin[4.32(t-0.4)]H(t-0.4)$ (Fig. 8).

The calculations show that interaction between piezoelectric transducers may cause essential redistribution of the pressures on their surfaces and may require solving the transient hydroelectroelasticity multiconnected problems. For instance, using single-mode radiation (Fig. 2) we can significantly reduce the pressure in the nearby points of contact of the shells with the fluid $r_k=R_k$, $\theta_1=\pi$ and $\theta_2=0$ by choosing the distance between the axes of the cylinders $(l=3)$. The reason is that the effects of the radiated and reflected waves for $l=3$ in the above-mentioned points are nearly antiphase and tend to cancel each other in the case where superposition exists. If electrodes are longitudinally oriented, the amplitudes $p^{(0)}$ are decreasing in the points $r_k=R_k$, $\theta_k=0;\pi$ and are increasing in the points $r_k=R_k$, $\theta_k=\pi/2$ (Fig. 3) when t is increasing in the considered time interval. The system of transducers with transversal orientation of electrodes with a short-circuited section in region $\pi<\theta_k<2\pi$ where $l=3$ creates comparatively high and close values of pressures where $\theta_k=\pi/2$ and $\theta_k=3\pi/2$ (Fig. 4). The directivity of the system appreciably deteriorates in the case of $l=4$ (Fig. 5). It should be noted that for the variants of electrodes' disposition, according to Figs. 4 and 5 excitation of acoustic medium in the epicentrum of short-circuited sections ($\theta_k=3\pi/2$) begins with lag in time $t\approx 0.4$. The amplitudes of pressure may be significantly increased in the points $r_k=R_k$, $\theta_k=\pi/2$, with more than three times smaller values of $p^{(0)}$ in other points $r_k=R_k$, $\theta_k=0;\pi;3\pi/2$ supplying the sections $0<\theta_k<\pi$ of each piezoelectric transducer with sinusoidal electrical signal $Q_k^{(1)}(t)=\sin 3.05t$ and supplying the sections $\pi<\theta_k<2\pi$ with the same signal, which is antiphased and lagged in time $Q_k^{(2)}(t)=-\sin 3.05(t-0.4)H(t-0.4)$ electrical signal (Fig. 6). Thus the described regime of work of the considered hydroelectroelastic system allows one to create one-directional radiation ($\theta_k=\pi/2$).

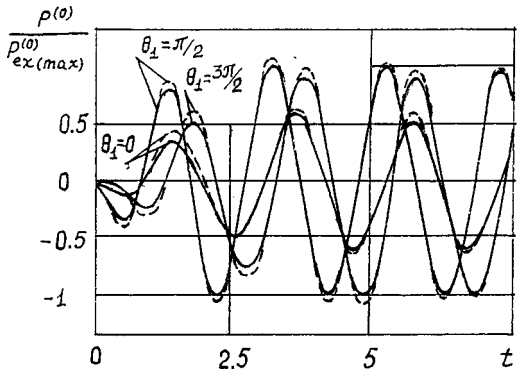

FIG. 9. Comparison of the acoustic pressures obtained as a result of experiment (——) and calculation (- - - -).

We can receive small pressure in the closest ($r_k=R_k$, $\theta_1=\pi$, $\theta_2=0$) and farthest ($r_k=R_k$, $\theta_1=0$, $\theta_2=\pi$) points of the shell's surfaces in the case of excitation of piezoelectric transducers where the frequency of oscillating vibrations is $\omega=4.32$ and the distance between the axis of cylinders is $l=2.7$ (Figs. 7 and 8). Though the excess of the pressures in the points $r_k=R_k$, $\theta_k=\pi/2$ where each of the piezoelectric transducers is being excited with two electrical signals $[Q_k^{(1)}(t)=\sin\omega t$, $Q_k^{(2)}(t)=-\sin[\omega(t-T_0)]H(t-T_0)$, $\omega=4.32$, $T_0=0.4]$ is not so considerable as for $\omega=3.05$ (Fig. 8).

V. EXPERIMENTAL TESTING OF THE APPLICABILITY OF THE USED MATHEMATICAL MODELS

The applicability of the formulations of multiconnected transient problems of hydroelectroelasticity has been tested experimentally in the limits of the chosen mathematical models.

When executing the experiment we used two identical multimodes radial-polarized cylindrical piezoelectric ceramic radiators made of the material TsTBS-3 which has the following relative geometrical dimensions: $h_k/R_k=0.09$, $R_k/L_k=0.18$, where h_k is the thickness, R_k is the radius, and L_k is the height of each cylinder $(k=1,2)$. The ends of the transducers were closed by circular metallic plates which ensured hermetic sealing of the inner volumes upon their immersion into the water. The experiment was done in the basin with the length of 8 m, the width of 4 m, and the depth of 4 m. The walls of the basin were covered with a soundproofed rubber layer. The distance between the axis of the piezoelectric ceramic cylinders was $l=3R_k$. The electrodes on the surfaces had cuts along lines $\theta_k=0$, $\theta_k=\pi$, $r_k=R_k\pm h_k/2$ (Fig. 1). The electrodes' sections $0<\theta_k<\pi$ of each piezoelectric transducer were supplied with the transient electrical signal produced by the generator. The sections $\pi<\theta_k<2\pi$ were short-circuited (transversal radiation). The regime of excitation of the considered hydroelectroelastic

system by the sinusoidal impulse $Q_k^{(1)}(t)=\sin \omega t$ on the shells' radial resonance frequency was investigated.

The measurements of the pressure arising in the water $P_{ex}^{(0)}$ were accomplished. The registration of $P_{ex}^{(0)}$ was made using the small hydrophones (piezoelectric ceramic spheres with diameter 0,007 m) set on equal distance from the ends of one of the cylinders ($k=1$) close to the points of its external surface $\theta_1=0;\pi/2;\pi$. The apparatus used during the experiment allowed us to determine the values of hydrodynamic pressures with a mean-square error of no more than 4%.

Considering that the heights of the cylinders L_k are significantly greater than their radii R_k, we supposed that the shells were infinitely long.

The results of the accomplished measurements and calculations are presented by the solid and dashed lines in Fig. 9. While the graphs were being constructed the hydrodynamic pressures were being divided by the maximum value of $P_{ex}^{(0)}$, where $\theta_1=\pi/2$, alongside the time being divided by R_1/c_0.

On the whole, the comparison of the experimental and theoretical results suggests that the coincide rather well.

The experimental test of the calculations' accuracy was accomplished for relatively thick-walled cylinders ($h_k/R_k=0.09$), where the probable difficulty caused by shell theory can appear. The necessity of this test was caused by the fact that the geometric parameters used here are characteristic for real hydroradiators where excitation of the transducers on the relative low frequency exists (the natural radial resonance frequency). However, the considered regime is the most popular one in hydroacoustics and its reseach is a point of great interest.

So, we can draw the conclusion, which is based on the calculations and experiments performed, that the initial mathematical models (the theory of thin-walled piezoelectric ceramic shells based on the Kirchhoff–Love hypotheses and the acoustical theory) are applicable with sufficiently high accuracy for description of transient processes in the multiconnected hydroelectroelastic systems.

[1] W. P. Mason, *Piezoelectrical Crystals and their Application in Ultrasonics* (Van Nostrand, New York, 1950), p. 40.
[2] J. C. Piquette, ''Non-linear scattering of acoustic wave by vibrating obstacles,'' NRL Memorandum Report 5077, 1 June 1983, p. 159.
[3] J. C. Piquette and A. L. Van Buren, ''Nonlinear scattering of acoustic waves by vibrating surfaces,'' J. Acoust. Soc. Am. **76**, 880–889 (1984).
[4] J. C. Piquette, ''Spherical wave scattering by an elastic solid cylinder of infinite length,'' J. Acoust. Soc. Am. **79**, 1248–1259 (1986).
[5] J. C. Piquette, ''Spherical wave scattering by an elastic solid cylinder—A numerical comparison of an approximate theory with the exact theory,'' J. Acoust. Soc. Am. **82**, 699–702 (1987).
[6] V. T. Grinchenko, A. F. Ulitko, and N. A. Shul'ga, ''Mechanics of coupled fields in structural elements,'' in *Electroelasticity* (Naukova Dumka, Kiev, 1989), Vol. 5, p. 280 (in Russian).
[7] L. I. Sedov, *Continuum Mechanics* (Nauka, Moscow, 1970), Vol. 1, p. 492, Vol. 2, p. 568 (in Russian).
[8] H. Huang, ''Transient response of two fluid-coupled spherical elastic shells to an incident pressure pulse,'' J. Acoust. Soc. Am. **65**, 881–887 (1979).
[9] H. Huang, ''Transient response of two fluid-coupled cylindrical elastic shells to an incident pressure pulse,'' Amer. Soc. Mech. Eng. **E46**, 513–518 (1979).
[10] A. N. Guz', V. D. Kubenko, and A. E. Babaev, *Hydroelasticity of Shell Systems* (Vyscha shkola, Kiev, 1984), p. 208 (in Russian).
[11] A. N. Guz' and V. T. Golovchan, *Diffraction of Elastic Waves in Multiply Connected Bodies* (Naukova Dumka, Kiev, 1972), p. 254 (in Russian).
[12] A. N. Guz', V. D. Kubenko, and M. A. Cherevko, *Diffraction of Elastic Waves* (Naukova Dumka, Kiev, 1978), p. 308 (in Russian).
[13] V. A. Ditkin and A. P. Prudnikov, *Handbook on Operational Calculus* (Vysshaya Shkola, Moscow, 1965), p. 467 (in Russian).
[14] A. E. Babaev, *Nonsteady Waves in Continua Mediums with a System of Reflecting Surface* (Naukova Dumka, Kiev, 1990), p. 176 (in Russian).
[15] A. F. Verlan and V. S. Sithikov, *Integral Equations* (Naukova Dumka, Kiev, 1986), p. 544 (in Russian).
[16] *Piezoelectric Ceramic Transducers*, edited by S. I. Pugachev (Sudostroenie, Leningrad, 1984), p. 256.

Determination of the dynamic elastic moduli and internal friction using thin resonant bars

Qiushuang Guo and David A. Brown
Acoustics Research Laboratory, Department of Electrical and Computer Engineering, University of Massachusetts, Dartmouth, North Dartmouth, Massachusetts 02747

(Received 5 September 1998; accepted for publication 13 March 2000)

Analysis of the data from the resonant-bar technique for determining wave speed and internal friction is presented. Internal friction has been included in the longitudinal and torsional wave equations and the analytical solution has been obtained. In determining the acoustical constants of lossy materials, a broad frequency spectrum is used that includes many resonances and not just data at or near the individual resonances. Corrections due to the mass, length, stiffness, and damping of the transducers are also presented. The theoretical solutions are compared with the measured magnitude and phase response data for torsional, longitudinal, and flexural measurements and are shown to be in good agreement. © *2000 Acoustical Society of America.* [S0001-4966(00)04506-9]

PACS numbers: 43.40.At, 43.40.Cw [CBB]

INTRODUCTION

The accurate measurement of the elastic constants and internal friction coefficients is important in the fields of science and engineering research as well as in product design and quality control. Several resonant bar approaches have been previously undertaken.[1–5] The resonant bar technique is often used as it is relatively easy to perform and has the advantage of having high signal-to-noise ratio. The main idea is that the elastic constants can be calculated from the resonant modes of the bar which can be measured at high precision. Barone and Giacomini showed that three modes (torsional, longitudinal, and flexural) can be measured electrodynamically on the same apparatus to obtain both the Young's and shear elastic moduli. The damping can be obtained by measuring the quality factor (Q) which is a measure of the stored energy to the dissipated energy per cycle of the system. Many researchers including Rudnick, Garrett, and Brown *et al.* have made significant improvements to and extensions of this technique over many years.[6–12]

Figure 1 shows the typical setup of the experiment. The length of the sample bar is about 30 cm. Two copper coils are epoxied at the two ends of the bar and used as exciting and receiving transducers which in turn are placed in the magnetic field of two magnets. The exciting voltage, which is proportional to the exciting force or torque on the bar, is the input, and the induced voltage at receiving transducer is the output. The spectrum analyzer is used to determine the system or bar response. The simplest model that can be used for the system is the lossless free-free bar model which is treated in introductory texts in acoustics. This method can often be used to obtain accuracy better than 10% and in samples with only moderate damping. However, since there are transducers at the ends of the bar that are epoxied to the bar, the effects of the mass and stiffness have to be considered to increase the accuracy of the measurement. Two approaches have been used. Garrett used Rayleigh's method and demonstrated that the mass effects can be treated as an effective length correction for each mode.[6] Another approach, derived by Danielson and documented by Meisel based on the Hamilton's energy method, accounted for the resonant frequency shift due to the mass and stiffness perturbation as presented at a point a distance in from the end of the bar.[11]

In this paper, two new methods are presented to model the system and obtain improved accuracy. The first one is a forced-free uniform bar model that includes internal friction. The second model includes the mass and stiffness correction of the transducers and epoxy (Fig. 2) on the forced-free bar. The bar is modeled as having three parts of finite length each having different acoustical properties. The middle section of the bar is the same as the ''bare'' bar, while the two ends have different acoustic constants due to the transducers and epoxy.[12] The difference in acoustical constants determined from the models shows the error if no correction effects are considered in determining the acoustic constants. We start by including the internal friction in the wave equations and then obtain the analytical solutions for the longitudinal and torsional waves. From fitting the solution with experiment data, the wave speed and the internal friction coefficient are determined. A broad spectrum is used to get the best fit, whereas most previous treatments rely only on the data at or near the resonant frequency. The dispersion in the material is also obtained.

I. LONGITUDINAL WAVE EQUATION AND SOLUTION

A. Solution of the longitudinal wave equation without consideration of the mass and stiffness corrections

In the first treatment the bar is considered as an unperturbed uniform bar; however, the coupling between the axial motion and the radial motion and internal damping of the material are included. An element that is not at the axis of the bar has speed both in the axial direction and in the radial direction. Thus the coupled motion affects the determination of Young's modulus.[13] The wave equation becomes

 0001-4966/2000/108(1)/167/8/$17.00

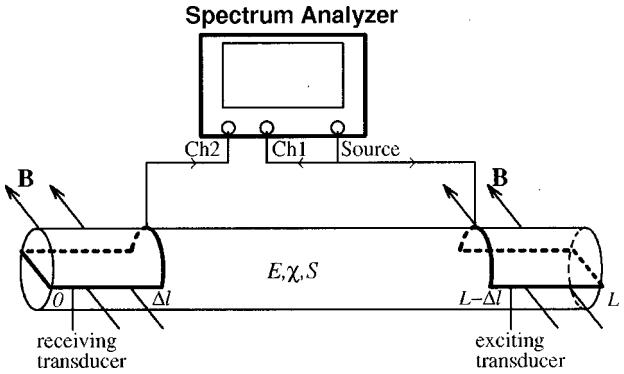

FIG. 1. Illustration of the bar, transducer coil and the magnetic field direction for torsional modes. The forces on the two sides of the bar are equal but in opposite vertical direction.

$$\frac{\partial^2 u}{\partial t^2} - c_L^2 \frac{\partial^2 u}{\partial z^2} - \nu^2 K_P^2 \frac{\partial^4 u}{\partial z^2 \partial t^2} - \chi \frac{\partial^3 u}{\partial z^2 \partial t} = 0, \tag{1}$$

where $u = u(z,t)$ is the displacement of a ''disc'' element at z, z is the axis of the bar, ν is Poisson's ratio, $K_P = \sqrt{I_P/S}$ is the polar radius of gyration, I_P is the polar moment of inertia of the bar's cross section, $I_P = \int\int (x^2+y^2)dxdy$, and the speed $c_L = \sqrt{E/\rho}$. Here, E, ρ, S are Young's modulus, density, and cross sectional area of the bar, respectively. The $\chi = \gamma/\rho(\mathrm{m}^2/\mathrm{s})$ represents the internal friction property and $\gamma(\mathrm{N\cdot s/m}^2)$ is the internal frictional stress when the time derivative of strain in the bar is unity $(1/s)$. The internal damping χ (γ) is proportional to the imaginary part of the complex moduli and will be discussed in Sec. IV.

The first two terms of the wave equation (1) are the same as those of the lossless linear wave equation. The third term represents coupled motion and the fourth term is due to internal friction. The solution of the wave equation is

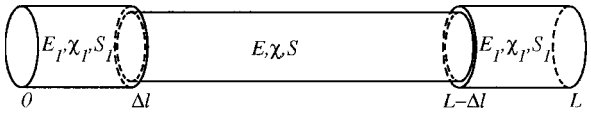

FIG. 2. Illustration of the model used to include the effects of the mass, elasticity and internal friction of the transducer and the epoxy. The greater cross-sectional area is to account for the mass correction.

$$u = [\bar{A}e^{-(\alpha_0 + jk_0)z} + \bar{B}e^{(\alpha_0 + jk_0)z}]e^{j\omega t}, \tag{2}$$

where $\bar{A}$ and $\bar{B}$ are complex constants determined by boundary condition and α_0 and k_0 can be determined from

$$k_0 = \omega\left(\frac{\Delta}{2\delta} + \frac{1}{2\sqrt{\delta}}\right)^{1/2} \tag{3}$$

and

$$\alpha_0 = \frac{\chi\omega^3}{2k_0\delta} = \frac{\chi\omega^2}{[2\delta(\Delta+\sqrt{\delta})]^{1/2}}, \tag{4}$$

where

$$\Delta = c_L^2 - \omega^2\nu^2K_P^2 > 0 \quad \text{and} \quad \delta = \Delta^2 + \chi^2\omega^2. \tag{5}$$

For the case when there is no friction, i.e., $\chi = 0$, we have the familiar result $\alpha_0 = 0$ and

$$k_0 = \left(\frac{\omega^2}{c_L^2 - \nu^2K_P^2\omega^2}\right)^{1/2}.$$

If we do not include the effects of the transducer mass and substitute the wave solution (2) into the boundary condition,

$$F_{\mathrm{ext}}|_{z=0} = 0, \quad F_{\mathrm{ext}}|_{z=L} = F_0e^{j\omega t}, \tag{6}$$

we arrive at the result,

$$\bar{A} = \bar{B} = \frac{F_0}{\rho S(\alpha_0 + jk_0)(c_L^2 - \nu^2K_P^2\omega^2 + j\chi\omega)[e^{(\alpha_0+jk_0)L} - e^{-(\alpha_0+jk_0)L}]}. \tag{7}$$

The frequency response is obtained,

$$H_0^L = \frac{(\partial u/\partial t)|_{z=0}}{f|_{z=L}} = \frac{j\omega\cdot 2\bar{A}}{F_0} = \frac{j\cdot 2\omega}{\rho S(\alpha_0 + jk_0)(\Delta + j\chi\omega)[e^{(\alpha_0+jk_0)L} - e^{-(\alpha_0+jk_0)L}]}, \tag{8}$$

where the magnitude of the response is

$$|H_0^L| = \frac{\omega}{\rho S(\alpha_0^2+k_0^2)^{1/2}\delta^{1/2}[\sin^2(k_0L)\cosh^2(\alpha_0L) + \cos^2(k_0L)\sinh^2(\alpha_0L)]^{1/2}}, \tag{9}$$

and the phase of the response is

$$\angle H_0^L = \frac{\pi}{2} - \arctan\left(\frac{k_0}{\alpha_0}\right) - \arctan\left(\frac{\chi\omega}{\Delta}\right) - \arctan\left(\frac{\sin(k_0L)\cosh(\alpha_0L)}{\cos(k_0L)\sinh(\alpha_0L)}\right). \tag{10}$$

Equations (9) and (10) can be compared with the measurements to determine acoustical properties of wave speed and internal friction coefficient.

B. Solution of the longitudinal wave equation with transducer mass and stiffness correction

Since the transducers and epoxy will affect the response of the bar, we consider the bar as having three parts (Fig. 2).

The two parts at the ends are of the same length as the transducers and by symmetry have the same acoustic constants which are different from those of the ends or middle of the bar. The solutions at the receiving end, bare bar, and exciting end are

$$u_{\mathrm{I}}=\overline{A}_1[e^{-(\alpha_1+jk_1)z}+e^{(\alpha_1+jk_1)z}]e^{j\omega t}, \quad \text{for } 0\leqslant z\leqslant \Delta l, \tag{11}$$

$$u_{\mathrm{II}}=[\overline{A}_2e^{-(\alpha_0+jk_0)z}+\overline{B}_2e^{(\alpha_0+jk_0)z}]e^{j\omega t}, \quad \text{for } \Delta l\leqslant z\leqslant L-\Delta l, \tag{12}$$

$$u_{\mathrm{III}}=[\overline{A}_3e^{-(\alpha_1+jk_1)z}+\overline{B}_3e^{(\alpha_1+jk_1)z}]e^{j\omega t}, \quad \text{for } L-\Delta l\leqslant z\leqslant L, \tag{13}$$

where α_0 and k_0 are the same as before (for part II of the bar) and α_1 and k_1 are the corresponding quantities at part I and part III of the bar. Here Δl is the length of a transducer. We have the same boundary conditions as Eq. (6) at the two bar ends. At $z=\Delta l$ and $z=L-\Delta l$, displacement and force are equal, such that,

$$u_{\mathrm{I}}|_{z=\Delta l}=u_{\mathrm{II}}|_{z=\Delta l}, \quad u_{\mathrm{II}}|_{z=L-\Delta l}=u_{\mathrm{III}}|_{z=L-\Delta l}, \tag{14}$$

$$E_1S_1\left.\frac{\partial u_{\mathrm{I}}}{\partial z}\right|_{z=\Delta l}+\rho_1S_1\nu_1^2K_{P1}^2\left.\frac{\partial^3u_{\mathrm{I}}}{\partial t^2\partial z}\right|_{z=\Delta l}+\rho_1S_1\chi_1\left.\frac{\partial^2u_{\mathrm{I}}}{\partial t\partial z}\right|_{z=\Delta l}=ES\left.\frac{\partial u_{\mathrm{II}}}{\partial z}\right|_{z=\Delta l}+\rho S\nu^2K_P^2\left.\frac{\partial^3u_{\mathrm{II}}}{\partial t^2\partial z}\right|_{z=\Delta l}+\rho S\chi\left.\frac{\partial^2u_{\mathrm{II}}}{\partial t\partial z}\right|_{z=\Delta l}, \tag{15}$$

$$ES\left.\frac{\partial u_{\mathrm{II}}}{\partial z}\right|_{z=L-\Delta l}+\rho S\nu^2K_P^2\left.\frac{\partial^3u_{\mathrm{II}}}{\partial t^2\partial z}\right|_{z=L-\Delta l}+\rho S\chi\left.\frac{\partial^2u_{\mathrm{II}}}{\partial t\partial z}\right|_{z=L-\Delta l}=E_1S_1\left.\frac{\partial u_{\mathrm{III}}}{\partial z}\right|_{z=L-\Delta l}+\rho_1S_1\nu_1^2K_{P1}^2\left.\frac{\partial^3u_{\mathrm{III}}}{\partial t^2\partial z}\right|_{z=L-\Delta l}+\rho_1S_1\chi_1\left.\frac{\partial^2u_{\mathrm{III}}}{\partial t\partial z}\right|_{z=L-\Delta l}, \tag{16}$$

where E_1, ρ_1, S_1 are the corresponding properties in parts I and III and E, ρ, S are the properties in part II. Thus the frequency response can be obtained,

$$H_m^L=\frac{j\cdot\omega(\Delta+j\chi\omega)(\alpha_0+jk_0)}{\rho S[\overline{K}^2W_2+\overline{K}_1^2W_1+2\overline{K}\overline{K}_1W_{12}+j(\overline{K}^2V_2+\overline{K}_1^2V_1+2\overline{K}\overline{K}_1V_{12})]}. \tag{17}$$

Here we have the rather tedious substitution that

$$W_1=\left(\frac{\rho_1S_1}{\rho S}\right)^2(cs\cdot sh\cdot cs_1^2\cdot sh_1^2-cs\cdot sh\cdot sn_1^2\cdot ch_1^2-2\cdot sn\cdot ch\cdot sn_1\cdot cs_1\cdot sh_1\cdot ch_1), \tag{18}$$

$$W_2=cs\cdot sh\cdot cs_1^2\cdot ch_1^2-cs\cdot sh\cdot sn_1^2\cdot sh_1^2-2\cdot sn\cdot ch\cdot sn_1\cdot cs_1\cdot sh_1\cdot ch_1, \tag{19}$$

$$W_{12}=\frac{\rho_1S_1}{\rho S}(cs\cdot ch\cdot cs_1^2\cdot sh_1\cdot ch_1-cs\cdot ch\cdot sn_1^2\cdot sh_1\cdot ch_1-sn\cdot sh\cdot sn_1\cdot cs_1\cdot sh_1^2-sn\cdot sh\cdot sn_1\cdot cs_1\cdot ch_1^2), \tag{20}$$

$$V_1=\left(\frac{\rho_1S_1}{\rho S}\right)^2(sn\cdot ch\cdot cs_1^2\cdot sh_1^2-sn\cdot ch\cdot sn_1^2\cdot ch_1^2+2\cdot cs\cdot sh\cdot sn_1\cdot cs_1\cdot sh_1\cdot ch_1), \tag{21}$$

$$V_2=sn\cdot ch\cdot cs_1^2\cdot ch_1^2-sn\cdot ch\cdot sn_1^2\cdot sh_1^2+2\cdot cs\cdot sh\cdot sn_1\cdot cs_1\cdot sh_1\cdot ch_1, \tag{22}$$

$$V_{12}=\frac{\rho_1S_1}{\rho S}(sn\cdot sh\cdot cs_1^2\cdot sh_1\cdot ch_1-sn\cdot sh\cdot sn_1^2\cdot sh_1\cdot ch_1+cs\cdot ch\cdot sn_1\cdot cs_1\cdot sh_1^2+cs\cdot ch\cdot sn_1\cdot cs_1\cdot ch_1^2), \tag{23}$$

$$\overline{K}=(\alpha_0\Delta-k_0\chi\omega)+j(k_0\Delta+\alpha_0\chi\omega)\equiv p+jq, \tag{24}$$

$$\overline{K}_1=(\alpha_1\Delta_1-k_1\chi_1\omega)+j(k_1\Delta_1+\alpha_1\chi_1\omega)\equiv p_1+jq_1, \tag{25}$$

and where $l'=L-2\Delta l$, which is the length of the ''bare'' part of the bar. In this result we rely on the following notation for hyperbolic sinusoidal functions for simplicity,

$$sn=\sin(k_0l'), \quad cs=\cos(k_0l'),$$
$$sh=\sinh(\alpha_0l'), \quad ch=\cosh(\alpha_0l'), \tag{26}$$
$$sn_1=\sin(k_1\Delta l), \quad cs_1=\cos(k_1\Delta l),$$
$$sh_1=\sinh(\alpha_1\Delta l), \quad ch_1=\cosh(\alpha_1\Delta l). \tag{27}$$

II. TORSIONAL WAVE EQUATION AND SOLUTION

A. Solution of the torsional wave equation without consideration of transducer mass and length corrections

The torsional wave equation has the same form as the longitudinal wave equation and is identical if we make the following transformation:

$$u\rightarrow\psi, \quad c_L^2\rightarrow\frac{J}{I_P}c_T^2, \quad \nu^2K_P^2\rightarrow\mu^2, \quad \chi\rightarrow\chi_T, \tag{28}$$

where ψ is angular displacement, the shear speed $c_T=\sqrt{G/\rho}$, G is the shear modulus, χ_T is the internal friction constant for shear strain, and

$$\mu^2=\frac{\int\int\Phi^2dxdy}{I_P},$$

$$J=\int\int\left(x^2+y^2+x\frac{\partial\Phi}{\partial y}-y\frac{\partial\Phi}{\partial x}\right)dxdy. \tag{29}$$

Here, Φ is the Saint Venant warping function which describes the relation between the strains of the bar in three dimensions. For a cylindrical symmetric bar, $\Phi=0$, thus $J=I_P$. Often it is desirable to choose a cylindrical sample for experimental investigation for these and other reasons. The magnitude of the warping function Φ for bars of various shapes can be found in Ref. 13. The solution of the torsional wave equation is of the same form as that of the longitudinal wave equation with the substitution of α_0, α_1, k_0, k_1 by α_{T0}, α_{T1}, k_{T0}, k_{T1}, which can be determined from results similar to Eqs. (3) and (4).

B. Solution of the torsional wave equation with transducer mass and length correction

There is a difference between the torsional wave and the longitudinal wave vibrations due to the effect of the transducer length at the sides of the bar. In the longitudinal wave system, the force is generated primarily in the end of the traditionally used exciting coil and received primarily in the end of the receiving coil. The coils can then be treated as simple masses. On the other hand, in the torsional wave system, the excitation torque is produced through the length of the coil so the excitation is distributed along the length of the bar spanned by the coil sides. The received signal is picked up along the receiving transducer length. Because the angular velocity is different along the bar, the received signal is proportional to the integral of the speed along the length. When the length correction is included, the wave equation at the exciting transducer becomes

$$\frac{\partial^2\psi_{\mathrm{III}}}{\partial t^2}-c_{T1}^2\frac{J_1}{I_{P1}}\frac{\partial^2\psi_{\mathrm{III}}}{\partial z^2}-\mu_1^2\frac{\partial^4\psi_{\mathrm{III}}}{\partial z^2\partial t^2}-\chi_{T1}\frac{\partial^3\psi_{\mathrm{III}}}{\partial z^2\partial t}=M_0e^{j\omega t}. \tag{30}$$

The solution is

$$\psi_{\mathrm{III}}=[\overline{A}_3e^{-(\alpha_{T1}+jk_{T1})z}+\overline{B}_3e^{(\alpha_{T1}+jk_{T1})z}]e^{j\omega t}-\frac{M_0}{\omega^2}e^{j\omega t}, \tag{31}$$

which is the combination of the wave solution of the bar and the common vibration of the bar excited by the torque when there is no wave, i.e., the sum of the homogenous and inhomogeneous solutions. From the boundary conditions, the solution at the receiving transducer can be derived as

$$\psi_1=\overline{A}_1[e^{-(\alpha_{T1}+jk_{T1})z}+e^{(\alpha_{T1}+jk_{T1})z}]e^{j\omega t}, \tag{32}$$

with

$$\overline{A}_1=\frac{-M_0(R_N+j\cdot I_N)}{2\omega^2(R_D+j\cdot I_D)}\cdot\left(\frac{S_1\rho_1}{S\rho}\right), \tag{33}$$

$$R_N=(p_T\cdot p_{T1}-q_T\cdot q_{T1})\cdot cs_{T1}\cdot sh_{T1}-(p_T\cdot q_{T1}+p_{T1}\cdot q_T)\cdot sn_{T1}\cdot ch_{T1}, \tag{34}$$

$$I_N=(p_T\cdot p_{T1}-q_T\cdot q_{T1})\cdot sn_{T1}\cdot ch_{T1}+(p_T\cdot q_{T1}+p_{T1}\cdot q_T)\cdot cs_{T1}\cdot sh_{T1}, \tag{35}$$

$$R_D=(p_T^2-q_T^2)W_{T2}+(p_{T1}^2-q_{T1}^2)W_{T1}+2(p_T\cdot p_{T1}-q_T\cdot q_{T1})W_{T12}-2p_T\cdot q_T\cdot V_{T2}-2p_{T1}\cdot q_{T1}\cdot V_{T1}-2(p_{T1}\cdot q_T+p_T\cdot q_{T1})V_{T12}, \tag{36}$$

$$I_D=(p_T^2-q_T^2)V_{T2}+(p_{T1}^2-q_{T1}^2)V_{T1}+2(p_T\cdot p_{T1}-q_T\cdot q_{T1})V_{T12}+2p_T\cdot q_T\cdot W_{T2}+2p_{T1}\cdot q_{T1}\cdot W_{T1}+2(p_{T1}\cdot q_T+p_T\cdot q_{T1})W_{T12}, \tag{37}$$

where W_{T1}, W_{T2}, W_{T12}, V_{T1}, V_{T2}, V_{T12}, p_T, p_{T1}, q_T, q_{T1} can be calculated from the equations similar to (18)–(25) with the corresponding constant substitution in (28). Also, sn_T, cs_T, h_T, ch_T and sn_{T1}, cs_{T1}, sh_{T1}, ch_{T1} can be calculated from equations similar to (26) and (27) with the substitution of α_0, k_0, α_1, k_1 by α_{T0}, k_{T0}, α_{T1}, k_{T1}. At the receiving end, the output voltage induced in the magnetic field is obtained by the integral of signal along the transducer. The output voltage is

$$v_{\mathrm{out}}\propto\omega\int_0^{\Delta l}\overline{A}_1[e^{-(\alpha_{T1}+jk_{T1})z}+e^{(\alpha_{T1}+jk_{T1})z}]dz=2\overline{A}_1\omega\frac{cs_{T1}\cdot sh_{T1}+j\cdot sn_{T1}\cdot ch_{T1}}{\alpha_{T1}+j\cdot k_{T1}}. \tag{38}$$

Therefore, the frequency response of the system is

$$H_{m,l}^T(\omega)=\frac{v_{\mathrm{out}}}{M_0}\propto\frac{(R_N+j\cdot I_N)(cs_{T1}\cdot sh_{T1}+j\cdot sn_{T1}\cdot ch_{T1})}{\omega(R_D+j\cdot I_D)(\alpha_{T1}+j\cdot k_{T1})}. \tag{39}$$

The magnitude of the response is

$$|H_{m,l}^T(\omega)|=\frac{(R_N^2+I_N^2)^{1/2}(cs_{T1}^2\cdot sh_{T1}^2+sn_{T1}^2\cdot ch_{T1}^2)^{1/2}}{\omega(R_D^2+I_D^2)^{1/2}(\alpha_{T1}^2+k_{T1}^2)^{1/2}}, \tag{40}$$

and the phase of the response is

$$\angle H_{m,l}^T(\omega)=\arctan\left(\frac{I_N}{R_N}\right)+\arctan\left(\frac{sn_{T1}\cdot ch_{T1}}{cs_{T1}\cdot sh_{T1}}\right)-\arctan\left(\frac{I_D}{R_D}\right)-\arctan\left(\frac{k_{T1}}{\alpha_{T1}}\right). \tag{41}$$

To compare the measured data with the theoretical model, we must include the contributions from the preamplifier used at the receiving end. We also have to consider the fact that the frequency response changes when the number of rounds of coils changes. At the exciting end, the exciting force is proportional to the electrical current,

$$F_0\propto I\propto U_{\mathrm{in}}, \tag{42}$$

where U_{in} is the electrical voltage drop over a resistor in the exciting circuit. At the receiving end, the speed of the trans-

ducer V is proportional to the induced voltage difference over the two ends of the transducer,

$$V \propto U_{\text{out}}. \tag{43}$$

The measured frequency response H_{meas} is defined by

$$H_{\text{meas}} = U_{\text{out}}/U_{\text{in}}. \tag{44}$$

It is proportional to the theoretical frequency response H_{theor}.

$$H_{\text{meas}} \propto \frac{V}{F_0} = H_{\text{theor}}, \tag{45}$$

where H_{theor} may be expressed by Eq. (8) or (39). The relation between the measured and the theoretical frequency response is therefore

$$H_{\text{meas}} = C' \cdot H_{\text{theor}}, \tag{46}$$

where C' is a complex number representing the effects of transducers and the preamplifier and the supports. Equation (40) can be changed to the form in decibels as

$$\begin{aligned} 20\log|H_{\text{meas}}| &= 20\log|H_{\text{theor}}| + 20\log|C'| \\ &= 20\log|H_{\text{theor}}| + \text{gain}. \end{aligned} \tag{47}$$

The relation between the measured and the theoretical phase of the response is

$$\angle H_{\text{meas}} = \angle H_{\text{theor}} + \angle C' = \angle H_{\text{theor}} + \text{shift}. \tag{48}$$

Equations (47) and (48) will be used to do the curve fitting for the magnitude of the response and the phase of the response of the torsional bar system, respectively. $|H_{\text{theor}}|$ and $\angle H_{\text{theor}}$ will be replaced by (40) and (41). The shear modulus and the internal friction coefficient can be obtained from the curve fitting. The *gain* and phase *shift* can be determined by fitting the measured data but this is not related to the acoustic properties of the materials and will not be reported.

III. FITTING MEASURED DATA

We obtained our best data for torsional modes as these are strongly excited with the chosen conventional electrodynamic transduction configuration used by most researchers.[6] The existing transducer configuration does not produce optimum results for longitudinal data due to asymmetry and weak coupling, although improvements to this are forthcoming. The material of the bar under the subject investigation is the E-CAST F-28 epoxy resin with 215 hardener (ECP), a material that has been used in the prototyping of fiber optic hydrophones. The length of the bar is 0.2952 ± 0.0005 and the diameter of the bar is 0.0125 ± 0.0005 m. The length of one transducer (exciting or receiving) is 0.0365 ± 0.0005 m. The mass density of the material is 1.162×10^3 kg/m^3. The mass of the bar without transducers is 42.10 ± 0.05 g. The mass of a transducer (including epoxy) is 0.83 ± 0.05 g.

Four theoretical equations have been fit to the data. These include: the torsional equation similar to Eq. (8) representing no mass and length correction, the torsional equation similar to Eq. (17) representing the mass correction but with no length correction, the Eq. (39) with $m=0$ representing length correction but no mass correction, and the equation (39) representing both the mass and length corrections. The last result, i.e., the equation with mass and length corrections, gives the best fit, especially at high frequency. The mass of the transducers is assumed to be uniformly distributed over a short length of the bar and can be represented as an effective mass. An effective mass of about 60% of the transducer mass provides the best fit. This is because the rectangular transducer coils are modeled as uniformly distributed mass, while the uniformly distributed mass appears more rigid to torsional excitation. The fit is obtained by making the standard deviation from the measured magnitude of the response to be a minimum. The torsional wave speed and internal friction coefficient and gain factors are the fitting parameters. It is assumed that the transducers and the epoxy do not affect the inherent acoustic constants of the bar but only the system. The parameters $\alpha_{T1} = \alpha_{T0}$ and $k_{T1} = k_{T0}$ are used in the fit. The dispersion effects of the material are also included, i.e., the wave speed and internal friction coefficient dependency on frequency. A piecewise fit method is used where each piece covers a particular frequency range that either includes a peak or a valley in the magnitude of the response. Eight pieces are chosen for the frequency range of the measurement. This method allows one to obtain the frequency dependence of the moduli and damping and the dispersion properties of the wave speed assuming the correctness of our model.

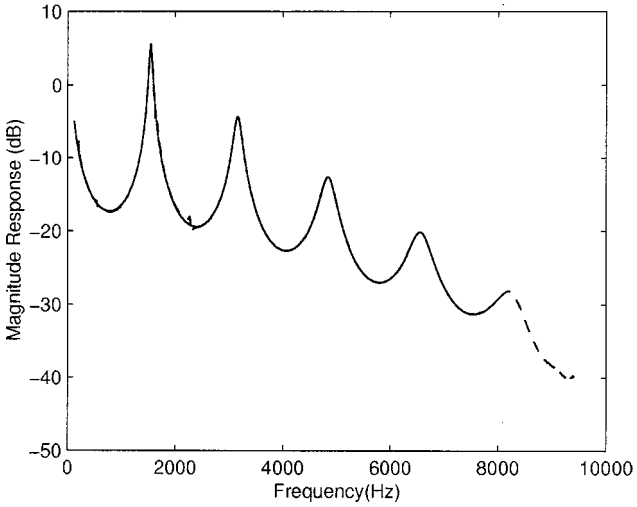

FIG. 3. Theoretical (solid line) and measured (dashed line) frequency response (magnitude) for the sample of E-CAST F-28 epoxy resin with 215 hardner (ECP). A piecewise fit is used by dividing the frequency band into eight intervals and obtaining an optimum fit for each interval.

The data of the magnitude and phase of the theoretical fits are shown in Figs. 3 and 4. Figures 5 and 6 show the frequency dependence of wave speed and internal friction coefficient for the parameters that we have determined. The error in wave speed appears to be approximately ± 1 m/s. The error in the internal friction coefficient is ± 0.01 m^2/s. It is observed that a good fit can be obtained up to 8100 Hz, which coincides with the length of one transducer coil which is approximately equal to 1/4 of the acoustical wavelength. Above this frequency, the theoretical model cannot accurately describe the system.

The mass of the transducer wire and the mass and damp-

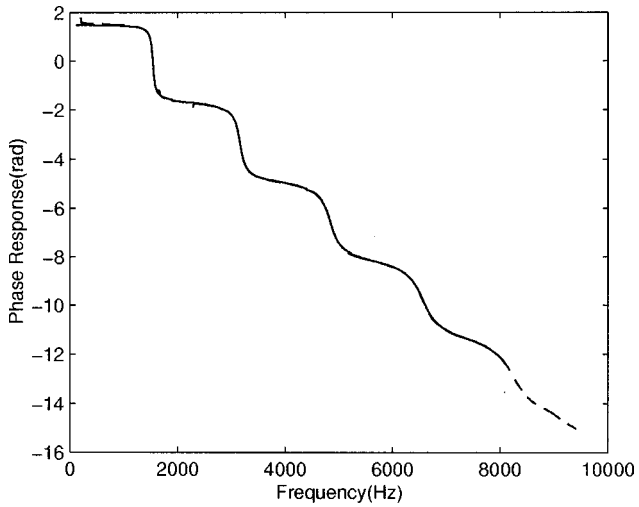

FIG. 4. Theoretical (solid line) and measured (dashed one) phase of the frequency response for the E-CAST F-28 sample.

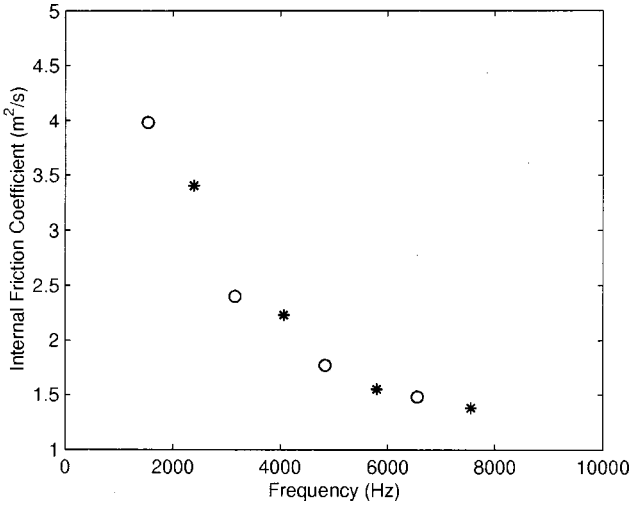

FIG. 6. Internal friction coefficient as a function of frequency. The circles are points derived from fitting the data near resonance while the stars are points derived from fitting the data between resonance peaks or in the valleys where the signal-to-noise ratio is lowest.

ing of the epoxy have an important impact on the determination of wave speed and internal friction coefficient. This was accounted for by treating the bar ends with an effective mass and damping coefficient. At the first peak corresponding to a frequency of 1537 Hz, the value of the wave speed obtained from this model is 943 m/s, 35 m/s more than that if the transducer mass and length are not considered. This corresponds to an error of 7.4% of the value of shear modulus. The internal friction coefficient obtained from the corrected equation is 14.1% greater than from the noncorrected equation. As the frequency increases, the difference between the acoustic constants obtained from the two equations becomes smaller. For example, the percentage differences become 0.8% and 0.7%, respectively, at the fourth peak (6552 Hz).

By calculating all the coefficients of the solutions for three parts of the bar as in Eqs. (11), (12), and (13), the amplitude distribution and phase distribution along the bar can be plotted. Figure 7 shows the distribution when the bar is excited at the frequency 4064 Hz, which corresponds to the second valley in the magnitude response. Figure 8 is the distribution when the frequency is 4832 Hz, corresponding to the third peak in the magnitude response. The effects of the internal friction can be displayed from the facts that the amplitude distribution is not symmetric and the phase distribution is something between those of an ideal traveling wave and a standing wave. The internal friction can also be shown from the fact that there is no zero amplitude position along the bar.

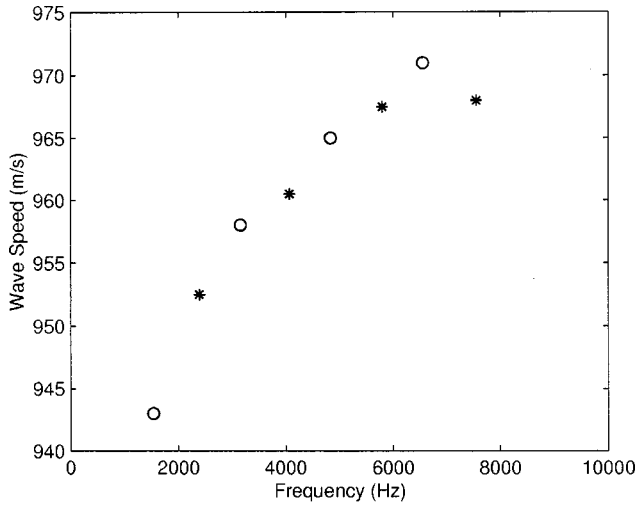

FIG. 5. Wave speed as a function of frequency. The circles are points derived from fitting the data near resonance while the stars are points derived from fitting the data between resonance peaks or in the valleys where the signal-to-noise ratio is lowest.

IV. DISCUSSION AND SUMMARY

The longitudinal and torsional wave equations have been solved by considering the effects of the coupled motion and

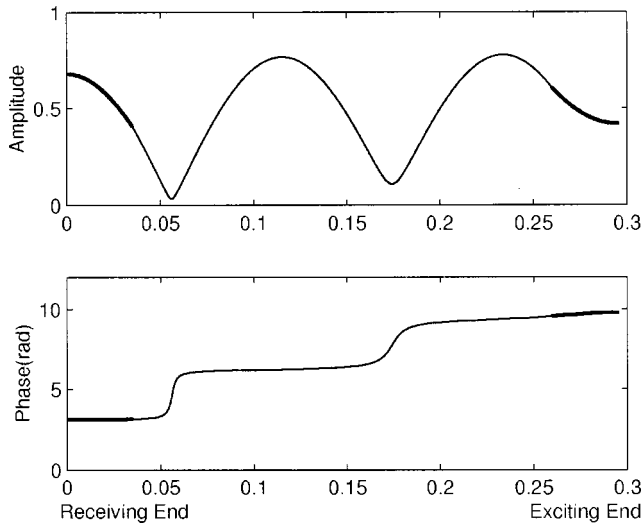

FIG. 7. Amplitude (absolute value) and phase distribution along the length of the bar. The frequency of excitation is 4088 Hz and corresponds to a frequency between the second and third resonance. The thick lines represent the end parts of the bar that have transducer loading. The wave speed is 960 m/s and the internal friction coefficient is 2.23 m^2/s. The horizontal axis has dimensions of meters.

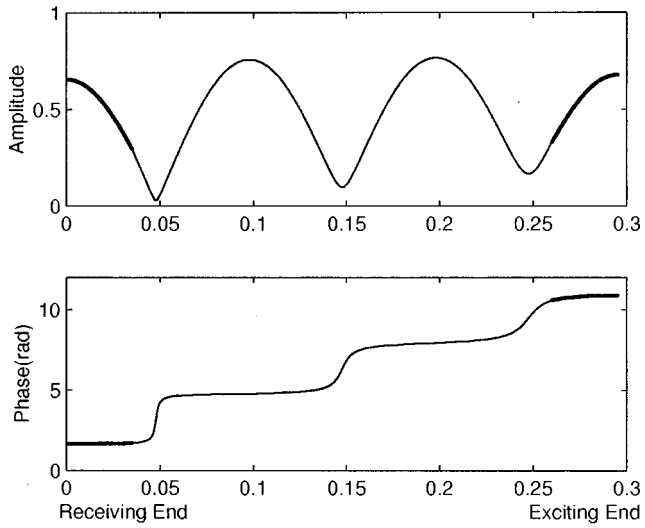

FIG. 8. Amplitude (absolute value) and phase distribution along the length of the bar for a frequency of excitation of 4832 Hz which corresponds to the third resonance peak. The thick lines represent the end parts of the bar that have transducer loading. The wave speed is 9650 m/s and the internal friction coefficient is 1.76 m^2/s. The horizontal axis has dimensions of meters.

internal friction. Solutions with mass and length corrections have also been obtained. The admittance frequency response has been derived and fitted to the experimental data. The minimum standard deviation from the measured magnitude of the response and a piecewise fit method are applied to get the best agreement. The following conclusions are reached.

The model including the mass and length correction fits the data much better than the model without mass and length corrections. While the transducers are needed to do the measurement, they also affect the system characteristics. In this case, the mass and length of the transducer change the admittance frequency response and should be included in the calculation for accurate results. This is a motivation to investigate alternative transduction techniques and/or improved models. The wave speed and shear modulus are also determined for the case when the corrections are included and these results are higher than the values obtained when no corrections are considered. The corrections become less important as frequency increases. Table I provides the wave speeds and the internal friction coefficients as obtained from previous methods[6] and from the models from this paper.

The internal friction does not affect the determination of the shear modulus significantly. Internal friction makes the effective length of the bar slightly longer than that of the bare bar for this sample; as illustrated in Table I, however, the correction is less than 0.2%. The value of the internal friction coefficient is on the order of 1 m^2/s, which means that if the time derivative of shear strain of the bar of cross area 1 m^2 is unity (s^{-1}), the internal shear friction force will be on the order of 10^3 N. By comparison, the elastic shear force is on the order of 10^9 N if the shear strain is unity.

TABLE I. Comparison of the wave speeds and internal friction coefficients obtained from different models under study. c_0^f is the wave speed from free-free bar model without correction. c_m^f is the wave speed from free-free bar model with mass correction (Ref. 6) c_0 and χ_0 are the wave speed and internal friction coefficient from the curve fitting method without corrections. $c_{m,l}$ is the wave speed and internal friction coefficient from the curve fitting method with mass and length corrections.

Mode number	Frequency (Hz)	c_0^f (m/s)	c_m^f (m/s)	c_0 (m/s)	$c_{m,l}$ (m/s)	χ_0 (m^2/s)	$\chi_{m,l}$ (m^2/s)
1	1537	907	978	908	943	3.42	3.98
2	3153	931	1004	931	958	2.22	2.40
3	4832	951	1026	952	965	1.75	1.77
4	6552	967	1043	967	971	1.47	1.48

The internal friction coefficient introduced here is related to the complex modulus and loss tangent and hence the quality factor Q. The complex modulus is

$$\overline{E} = E + j \cdot E' = E + j\omega \cdot \gamma = \rho(c_L^2 + j\omega \cdot \chi). \tag{49}$$

The loss tangent is

$$\tan \delta = 1/Q = E'/E = \omega\gamma/E = \omega\chi/c_L^2. \tag{50}$$

In a nondispersive media, γ and χ are independent of frequency but the complex modulus and loss tangent are dependent on frequency. For this sample and in the frequency range of 50 to 8100 Hz, the loss tangent increases with increasing frequency, but the internal friction coefficient decreases.

This system appears to provide an accurate way to obtain the frequency dependence of the material's dynamic moduli and internal friction coefficient and the dispersion. It is observed that the wave speed increases with frequency up to 7100 Hz. On the other hand, the internal friction coefficient decreases with frequency. The internal friction is very important at high frequencies because the time derivative of strain is high. It is worth considering whether the internal friction should be described by fractional order derivatives and this would need further study.[14–16]

It is evident from Figs. 7 and 8 that at the end of the receiving transducer, the amplitude of the angular displacement is always a relative maximum. This is reasonable since it is nearly a free end. At the exciting end, the amplitude is a maximum when the frequency corresponds to a peak in the magnitude of the response (Fig. 8). The amplitude at the exciting end becomes much smaller when the frequency corresponds to a minimum in the response as illustrated in Fig. 7.

The mode shape is different from the case in which the internal friction is not considered. There is not a true ''node,'' i.e., every mass element oscillates with nonzero amplitude. This is especially evident for higher modes. The amplitude distribution along the bar is not symmetric even if the bar is symmetric about the center. Near the exciting transducer, the maximum amplitude is larger and the maximum amplitude becomes smaller near the receiving end. The phase distribution is not a ''stair'' function with step π, which is the case when the dissipation factor is not present. Near the exciting end, the phase is more like that of a traveling wave since there is little reflection wave due to internal damping. Near the receiving transducer, the phase is more like that of a standing wave since there is a strong reflection wave.

The frequency responses of the longitudinal and flexural wave response, as well as improvements in the transducer design, are the subject of ongoing research.

ACKNOWLEDGMENTS

This work was supported in part by the Electrical Engineering Doctoral Program and the Strategic Envirotechnology Partnership (STEP) through the Advanced Technology and Manufacturing Center at the University of Massachusetts, Dartmouth.

[1] ASTM C623-71, 1971 (reapproved in 1989), ''Standard test method for Young's modulus, shear modulus, and Poisson's ratio for glass and glass-ceramics by resonance'' (1971).
[2] A. Barone and A. Giacomini, ''Experiments on some electrodynamic ultrasonic vibrators,'' Acustica **4**, 182–184 (1954).
[3] S. Spinner, T. W. Riechard, and W. E. Tefft, ''A comparison of experimental and theoretical relations between the Young's modulus and flexural and longitudinal resonance frequencies of uniform bars,'' J. Res. Natl. Bur. Stand., Sec. A **64**, 147–155 (1960).
[4] S. Spinner and R. C. Valore, Jr., ''Comparison of theoretical and empirical relations between the shear modulus and torsional resonance frequencies for bars of rectangular cross section,'' J. Res. Natl. Bur. Stand., Sec. A **60**, 459–464 (1958).
[5] I. Rudnick, ''Acoustics goofs or irreproducible effects in acoustics,'' J. Acoust. Soc. Am. Suppl. 1 **83**, S38 (1988).
[6] S. L. Garrett, ''Resonant acoustic determination of elastic moduli,'' J. Acoust. Soc. Am. **88**, 210–221 (1990).
[7] D. A. Brown and S. L. Garrett, ''Resonant acoustic determination of complex elastic moduli,'' NASA Technology 2001 Conference, San Jose, CA (1991).
[8] B. H. Tan, ''Resonant acoustic determination of complex elastic moduli,'' Master's Thesis, Naval Postgraduate School, Monterey, CA, DTIC AD-A245 050, 1991.
[9] D. A. Brown, B. H. Tan, and S. L. Garrett, ''Nondestructive dynamic complex moduli measurements using a Michelson fiber interferometer and a resonant bar technique,'' SPIE Conference Proceedings, Sept. 19–21 (1990), Vol. 1370.
[10] D. L. Bartlett, ''Determination of the complex elastic moduli of materials using a 'free-free' bar technique,'' Master's Thesis, Naval Postgraduate School, Monterey, CA, 1994.
[11] J. E. Meissel, ''Acoustic spectroscopic determination of dynamic materials properties from a 'free-free' bar resonant based technique,'' Master's Thesis, Naval Postgraduate School, Monterey, CA, 1994.
[12] Q. Guo and D. A. Brown, ''Effects of transducer mass on resonance frequency and quality factor of free-free bar,'' J. Acoust. Soc. Am. **101**, 3062 (A) (1997).
[13] A. E. H. Love, *A Treatise on the Mathematical Theory of Elasticity*, 4th ed. (Dover, New York, 1944).
[14] R. L. Bagley, ''The thermorheologically complex material,'' Int. J. Eng. Sci. **29**, 797–806 (1991).
[15] T. F. Nonnenmacher, ''Fractional relaxation equations for viscoelasticity and related phenomena,'' Lect. Notes Phys. **381**, 309–332 (1991).
[16] R. S. Rutman, ''On physical interpretations of fractional integration and differentiation,'' Theor. Math. Phys. **105**, 1509–1519 (1995).

A strip-element method for analyzing wave scattering by a crack in an immersed axisymmetric laminated composite cylinder

Z. C. Xi, G. R. Liu,[a] K. Y. Lam, and H. M. Shang
Department of Mechanical and Production Engineering, National University of Singapore, 10 Kent Ridge Crescent, Singapore 119260

(Received 20 May 1999; revised 18 January 2000; accepted 22 January 2000)

A strip-element method is presented for analyzing wave scattering by a crack in a laminated composite cylinder immersed in a fluid. In this approach, two-nodal-line and three-nodal-line axisymmetric strip elements are employed to model the fluid and laminated cylinder, respectively. Governing equations for the fluid and solid elements in the frequency domain are derived with a variational method and the Hamilton principle. The associated characteristic equations in the wave-number domain are obtained through Fourier transform techniques. Responses of the fluid-loaded cylinder to a line load are found by a modal-analysis method and inverse Fourier transform techniques. Numerical results are presented for cracked laminated composite cylinders submerged in water. Water is found to have strong influence on the scattered wave fields in a cracked laminated composite cylinder. © *2000 Acoustical Society of America.* [S0001-4966(00)05004-9]

PACS numbers: 43.40.Ey, 43.20.Tb [CBB]

INTRODUCTION

As fiber-reinforced composite materials are being widely used in the aircraft and aerospace industry, detection of cracks in composite structures is of practical importance. A common method of evaluating composite cracks is the ultrasonic technique which identifies crack-induced scattered wave field. In this technique, a fluid (usually water) is generally used as a coupling medium between an ultrasonic wave generator and composite materials. Composite materials have a low density. The presence of the fluid alters the scattering wave field, which accordingly affects the sensitivity in detecting cracks in composites. It is therefore important to account for the interaction of the fluid and composite structure in interpreting ultrasonic test data.

The literature on ultrasonic waves and anisotropic media interaction was well reviewed by Nayfeh (1995). Thus, the only work surveyed here is the interaction of ultrasonic waves and fluid-loaded anisotropic media. Three types of structures have been used in studies on the interaction of ultrasonic waves and fluid-loaded anisotropic media: anisotropic half space, plate, and cylinder. The study of ultrasonic wave interaction with fluid-loaded anisotropic media began with fluid-coupled anisotropic half spaces. Atalar (1983) conducted a theoretical analysis of wave propagation in special kinds of anisotropic half spaces immersed in a fluid. Arikan *et al.* (1989) extended this analysis to a general anisotropic half space. Braga and Herrmann (1989) studied an immersed laminated isotropic half space by a propagator matrix method. Gracewski and Bogy (1986) conducted analytical investigation of the time-harmonic elastic wave scattering by an interface crack in a layered half space submerged in water. Variations of stress intensity factors at crack tips with incident angles were discussed for plane waves in water incident on an iron layer–iron half space. Nayfeh (1991) employed an analytical method to obtain reflection and transmission coefficients from a liquid–monoclinic half space, and discussed their dependence on propagation direction and incident angles. Liu *et al.* (1992) studied a line-focus acoustic microscope and anisotropic-layer/substrate configurations using a combined finite-element and boundary-element method. Nayfeh and Chimenti (1988a, 1988b) investigated, both theoretically and experimentally, reflections from single specially and generally orthotropic plates submerged in a fluid. In their analyses, the Cremer correspondence principle was found to be valid only when the ratio of fluid to solid density is small. Furthermore, Chimenti and Nayfeh (1990) extended their work on the single orthotropic plate to cross-ply laminated composite plates using a transfer matrix approach. Nayfeh and Taylor (1988) investigated surface wave characteristics of multilayered media that are in contact with fluid on one side while their other side is free or in contact with another solid substrate. Dayal and Kinra (1989) examined both analytically and experimentally the wave speed and attenuation for a symmetric cross-ply composite laminate as well. Mal *et al.* (1989) performed theoretical and experimental studies on bounded plates. Liu *et al.* (1996) carried out stress wave analysis of composite laminates excited by underwater explosion shocks. More recently, Liu *et al.* (1999a) utilized a strip-element method (SEM) to treat wave scattering by a crack in an immersed laminated composite plate. Compared with the voluminous references on fluid-coupled anisotropic half spaces and plates, very few studies have been reported on the interaction of ultrasonic waves with fluid-loaded anisotropic cylinders because of the complexity of the problem. Dayal (1994) derived dispersion equations of composite cylinders submerged in a fluid. Using the finite-element method and an effective modulus theory,

[a]Electronic mail: mpeliugr@nus.edu.sg

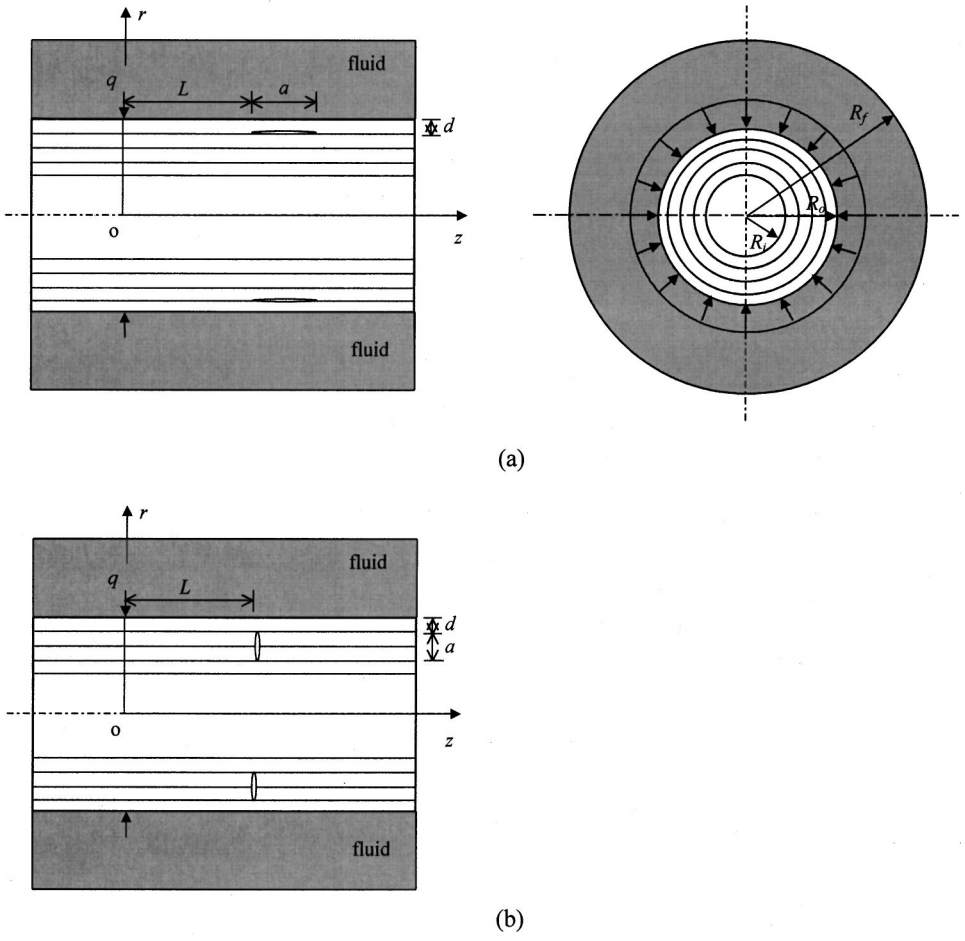

FIG. 1. Geometry of an immersed laminated composite cylinder containing (a) an axial or (b) radial crack.

McCoy and Sun (1997) analyzed thick-section hollow composite cylinders subjected to underwater blasts. However, these references were limited to composite cylinders without cracks.

In this paper, an SEM is formulated for analyzing the ultrasonic wave scattered by a crack in an axisymmetric laminated composite cylinder that is submerged in a fluid and subjected to harmonic excitation of line source. The present method is based on the numerical–analytical method proposed by Huang and Dong (1984) for perfect composite cylinders in air and the SEMs proposed by Liu and Achenbach (1994, 1995) and by Liu *et al.* (1999b) for cracked laminated composite plates and cylinders. In this method, two-nodal-line axisymmetric fluid strip elements and three-nodal-line axisymmetric solid strip elements are used to model the fluid and cylinder, respectively. A set of governing equations for the fluid and solid elements in the frequency domain is derived using a variational approach and the Hamilton principle. The associated characteristic equations in the wave-number domain are obtained by the application of Fourier transform techniques. Responses of the fluid-loaded composite cylinder subjected to a line load are obtained using a modal-analysis technique and inverse Fourier transform techniques. Numerical examples are given for immersed composite cylinders with either a radial or an axial crack. The effects of the fluid on the scattered wave field from fluid-loaded cracked composite cylinders are discussed.

I. PROBLEM

Consider an immersed laminated composite cylinder containing either an axial or radial crack, whose geometries are shown in Fig. 1, where R_i and R_o are, respectively, the inner and outer radii of the cylinder, and R_f is the outer radius of the fluid. The fluid is assumed to be irrotational, inviscid, and acoustic. The fluid–cylinder coupling effect occurs at the fluid–cylinder interface and decays with the increase of the distance away from the cylinder. It has little influence on the fluid remote from the fluid–cylinder interface. For large R_f, the acoustic pressure on the outer surface of the fluid can be assumed to be zero. The cylinder is made of an arbitrary number of linearly elastic shell-like laminae. The bonding between plies is perfect except in the region of the crack. Deformations of the cylinder are assumed to be small. Let z and r denote the axial and radial coordinates, respectively. The crack is assumed to be annular, with a designating the size of the crack, and d and L defining the location of the crack. The axial crack is located either within one of the layers or along an interface between the layers. The radial crack corresponding to $d=0$ refers to the outer surface-breaking crack. The outer surface of the cylinder is subjected to a transverse line load of magnitude $q = q_0 \exp(i\omega t)$ that is uniformly distributed along the circumferential direction and located at $z=0$, where ω is the circular frequency of excitation and t is time. It is of interest to

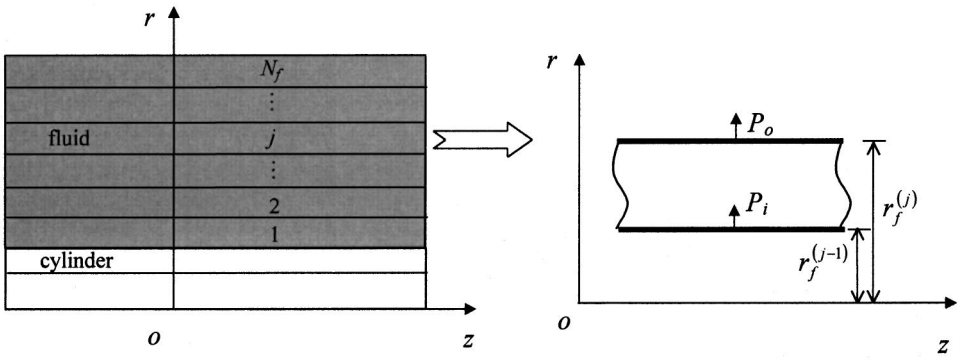

FIG. 2. Fluid strip element mesh and the jth isolated fluid strip element.

find the wave scattered by the crack in the cylinder. As both the geometry and load do not vary in the circumferential direction, the problem is axisymmetric.

II. THEORY

A. Axisymmetric fluid strip element

In this analysis, the pressure $p(z,r,t)$ in the acoustic fluid is selected as an unknown. It follows from the dynamic equilibrium and continuity equations of the fluid that

$$\frac{\partial^2 p}{\partial z^2}+\frac{\partial^2 p}{\partial r^2}+\frac{1}{r}\frac{\partial p}{\partial r}-\frac{1}{c^2}\frac{\partial^2 p}{\partial t^2}=0, \tag{1}$$

where c is the speed of sound in the fluid and t is time.

A two-nodal-line axisymmetric fluid strip element, shown in Fig. 2, is used in discretizing the fluid. It is assumed that the fluid is divided into N_f axisymmetric fluid strip elements in the radial direction. Letting $r_f^{(j-1)}$ and $r_f^{(j)}$ represent, respectively, the inner and outer radii of the jth fluid element, the pressure within the fluid element is approximated as

$$p(z,r,t)=\mathbf{N}_f(r)\mathbf{P}^e(z)\exp(i\omega t), \tag{2}$$

where $\mathbf{P}^e=[P_i P_o]^T$ is the vector of unknown pressure amplitudes of the fluid element on the nodal lines. The shape function matrix of the fluid element is given by $\mathbf{N}_f(r)=[(1-\hat{r}_f)\,\hat{r}_f]$, in which $\hat{r}_f=(r-r_f^{j-1})/(r_f^{(j)}-r_f^{(j-1)})$ and $r_f^{(j-1)}\leqslant r\leqslant r_f^{(j)}$.

An equivalent functional expression for Eq. (1) is given by

$$J=\pi\int_{r_f^{(j-1)}}^{r_f^{(j)}}\left(\frac{\partial p}{\partial z}\frac{\partial p}{\partial z}+\frac{\partial p}{\partial r}\frac{\partial p}{\partial r}+\frac{2p}{c^2}\frac{\partial^2 p}{\partial t^2}\right)r\,dr-2\pi R_o p\frac{\partial p}{\partial r}. \tag{3}$$

Substituting Eq. (2) into Eq. (3) and performing variational manipulation of J with respect to $\mathbf{P}^e$, the following governing equation for the fluid strip element is derived:

$$-\mathbf{A}^e_{2\,f}\frac{d^2\mathbf{P}^e}{dz^2}+\left(\mathbf{A}^e_{uf}-\frac{\omega^2}{c^2}\mathbf{M}^e_f\right)\mathbf{P}^e=\mathbf{E}^e, \tag{4}$$

where

$$\mathbf{A}^e_{0f}=\int_{r_f^{(j-1)}}^{r_f^{(j)}}\frac{\partial\mathbf{N}_f^T}{\partial r}\frac{\partial\mathbf{N}_f}{\partial r}r\,dr,\quad \mathbf{A}^e_{2\,f}=\int_{r_f^{(j-1)}}^{r_f^{(j)}}\mathbf{N}_f^T\mathbf{N}_f r\,dr, \tag{5}$$

$$\mathbf{M}^e_f=\int_{r_f^{(j-1)}}^{r_f^{(j)}}\mathbf{N}_f^T\mathbf{N}_f r\,dr,\quad \mathbf{E}^e=R_o\mathbf{N}_f^T\frac{\partial p}{\partial r}. \tag{6}$$

The governing equation for the fluid can be derived by assembling elements at the nodal lines

$$-\mathbf{A}_{2\,f}\frac{d^2\mathbf{P}}{dz^2}+\left(\mathbf{A}_{0f}-\frac{\omega^2}{c^2}\mathbf{M}_f\right)\mathbf{P}=\rho_f\omega^2 R_o\mathbf{B}^T\mathbf{U}, \tag{7}$$

where

$$\mathbf{B}^T=\begin{bmatrix}0&\cdots&0&1\\0&\cdots&0&0\\\vdots&\ddots&\vdots&\vdots\\0&\cdots&0&0\end{bmatrix}_{N_f\times N}. \tag{8}$$

Note that the following conditions have been used in deriving Eq. (7):

$$\left(\frac{\partial p}{\partial r}\right)_1^i=-\rho_f\frac{\partial^2\hat{w}}{\partial t^2}, \tag{9}$$

$$p_j^o=p_{j+1}^i,\quad \left(\frac{\partial p}{\partial r}\right)_j^o=\left(\frac{\partial p}{\partial r}\right)_{j+1}^i\quad \text{for } 1<j<N_f-1, \tag{10}$$

$$p_{N_f}^o=p, \tag{11}$$

where the subscripts denote the element numbers, the superscripts denote the inner and outer surfaces of the element, ρ_f denotes the density of the fluid, and $\hat{w}$ denotes the radial displacement on the outer surface of the cylinder due to the pressure $p(z,r,t)$. Details of the process of assembling elements are available in Zienkiewicz and Taylor (1989). The quantity $\hat{w}$ may be expressed as $\hat{w}=\mathbf{nNU}$, where $\mathbf{n}=[0\ 1]$, and $\mathbf{N}$ and $\mathbf{U}$ are, respectively, the shape function matrix and vector of unknown displacement amplitudes of a solid strip element on nodal lines, which will be introduced in the next section. Equations (9) and (11) are the boundary conditions on the outer surface of the fluid and the fluid–cylinder interface; and Eq. (10) is the continuity conditions on the nodal lines of the fluid element.

B. Axisymmetric solid strip element

The strain–displacement relations of the cylinder are given by

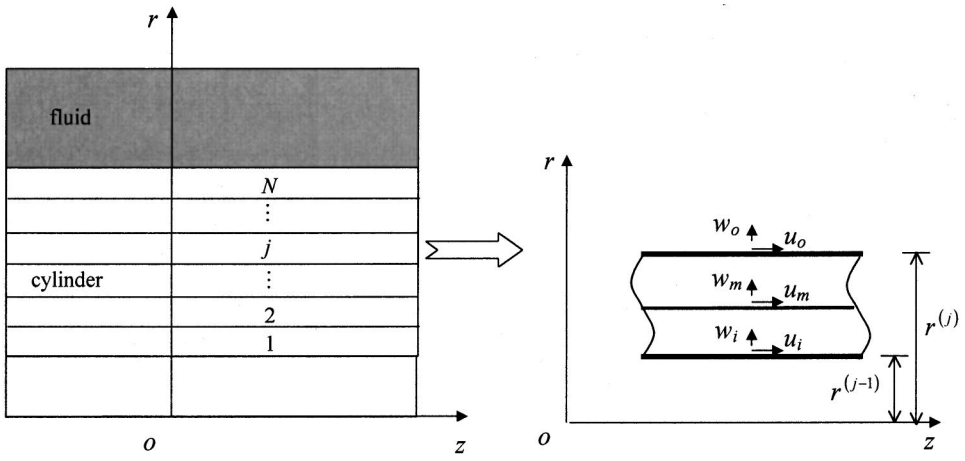

FIG. 3. Cylinder strip element mesh and the jth isolated solid strip element.

$$\varepsilon = \mathbf{L}\mathbf{u}, \tag{12}$$

where $\varepsilon = [\varepsilon_z\ \varepsilon_\theta\ \varepsilon_r\ \gamma_{rz}]^T$ is the vector of strains and $\mathbf{u} = [u\ w]^T$ is the vector of displacements. Here, u and w are the displacement components in the axial and radial directions, respectively. The operator matrix $\mathbf{L}$ is given by

$$\mathbf{L} = \begin{bmatrix} \dfrac{\partial}{\partial z} & 0 & 0 & \dfrac{\partial}{\partial r} \\ 0 & \dfrac{1}{r} & \dfrac{\partial}{\partial r} & \dfrac{\partial}{\partial z} \end{bmatrix}^T = \mathbf{L}_1\frac{\partial}{\partial z} + \mathbf{L}_2\frac{\partial}{\partial r} + \mathbf{L}_3\frac{1}{r}, \tag{13}$$

where the matrices $\mathbf{L}_1$, $\mathbf{L}_2$, and $\mathbf{L}_3$ can be obtained by inspection from Eq. (13).

A lamina under consideration is transversely isotropic, so that the stresses are related to strains by

$$\sigma = \overline{\mathbf{Q}}\varepsilon, \tag{14}$$

where $\sigma = [\sigma_z\ \sigma_\theta\ \sigma_r\ \tau_{rz}]^T$ is the vector of stresses and

$$\overline{\mathbf{Q}} = \begin{bmatrix} \overline{Q}_{11} & \overline{Q}_{12} & \overline{Q}_{13} & 0 \\ \overline{Q}_{12} & \overline{Q}_{22} & \overline{Q}_{23} & 0 \\ \overline{Q}_{13} & \overline{Q}_{23} & \overline{Q}_{33} & 0 \\ 0 & 0 & 0 & \overline{Q}_{55} \end{bmatrix}, \tag{15}$$

is the matrix of the off-principal-axis stiffness coefficients of the lamina whose expressions in terms of engineering constants are given by Vinson and Sierakowski (1987).

Laminated composite shells are heterogeneous along the thickness direction. In order to achieve high precision, a three-nodal-line element, shown in Fig. 3, is used in discretizing the cylinder. It is assumed that the cylinder is divided into N axisymmetric solid strip elements in the radial direction. For the cylinder with an axial crack, the meshing ensures that one nodal line goes through the axial crack. For the cylinder with a radial crack, the meshing ensures that two nodal lines go through the two tips of the radial crack. If $r^{(j-1)}$ and $r^{(j)}$ represent, respectively, the inner and outer radii of the jth solid element, then the displacements within the solid element are approximated as

$$\mathbf{u} = \mathbf{N}(r)\mathbf{U}^e(z)\exp(i\omega t), \tag{16}$$

where $\mathbf{U}^e = [u_i\ w_t\ u_m\ w_m\ u_o\ w_o]^T$ is the vector of the unknown displacement amplitudes of the solid element on the nodal lines. The shape function matrix of the solid element is given by $\mathbf{N}(r) = [(1-3\hat{r}+2\hat{r}^2)\mathbf{I}\ 4(\hat{r}-\hat{r}^2)\mathbf{I}\ (-\hat{r}+2\hat{r}^2)\mathbf{I}]$ in which $\hat{r} = (r-r^{(j-1)})/(r^{(j)}-r^{(j-1)})$, $r^{(j-1)} \leqslant r \leqslant r^{(j)}$, and $\mathbf{I}$ is a 2×2 identity matrix.

The governing equation for the axisymmetric solid strip element follows from the Hamilton variational principle, which takes the following form:

$$\int_{t_0}^{t_1} \delta(V-T)\,dt = 0, \tag{17}$$

where t_0 and t_1 are arbitrary time instants, and V and T are the potential energy and kinetic energy of the element, respectively. The potential energy of the element in the absence of body forces is given by

$$V = \pi\int_{r^{(j-1)}}^{r^{(j)}} \varepsilon^T\sigma r\,dr - 2\pi R_o\mathbf{p}\mathbf{u}, \tag{18}$$

where $\mathbf{p}$ is the vector of the external nodal forces and $\mathbf{u}$ is the vector of the displacements at the loaded position. Substitution of Eqs. (12) through (14) into Eq. (18) gives

$$\begin{aligned} V = \pi\int_{r^{(j-1)}}^{r^{(j)}} \Bigg(& \frac{\partial\mathbf{u}^T}{\partial z}\mathbf{D}_{11}\frac{\partial\mathbf{u}}{\partial z} + \frac{\partial\mathbf{u}^T}{\partial z}\mathbf{D}_{12}\frac{\partial\mathbf{u}}{\partial r} + \frac{1}{r}\frac{\partial\mathbf{u}^T}{\partial z}\mathbf{D}_{13}\mathbf{u} \\ & + \frac{\partial\mathbf{u}^T}{\partial r}\mathbf{D}_{12}^T\frac{\partial\mathbf{u}}{\partial z} + \frac{\partial\mathbf{u}^T}{\partial r}\mathbf{D}_{22}\frac{\partial\mathbf{u}}{\partial r} + \frac{1}{r}\frac{\partial\mathbf{u}^T}{\partial r}\mathbf{D}_{23}\mathbf{u} \\ & + \frac{1}{r}\mathbf{u}^T\mathbf{D}_{13}^T\frac{\partial\mathbf{u}}{\partial z} + \frac{1}{r}\mathbf{u}^T\mathbf{D}_{23}^T\frac{\partial\mathbf{u}}{\partial r} + \frac{1}{r^2}\mathbf{u}^T\mathbf{D}_{33}\mathbf{u}\Bigg) r\,dr \\ & - 2\pi R_o\mathbf{u}^T\mathbf{p}, \end{aligned} \tag{19}$$

where

$$\begin{aligned} & \mathbf{D}_{11} = \mathbf{L}_1^T\overline{\mathbf{Q}}\mathbf{L}_1 \quad \mathbf{D}_{12} = \mathbf{L}_1^T\overline{\mathbf{Q}}\mathbf{L}_2 \quad \mathbf{D}_{13} = \mathbf{L}_1^T\overline{\mathbf{Q}}\mathbf{L}_3 \\ & \mathbf{D}_{22} = \mathbf{L}_2^T\overline{\mathbf{Q}}\mathbf{L}_2 \quad \mathbf{D}_{23} = \mathbf{L}_2^T\overline{\mathbf{Q}}\mathbf{L}_3 \quad \mathbf{D}_{33} = \mathbf{L}_3^T\overline{\mathbf{Q}}\mathbf{L}_3. \end{aligned} \tag{20}$$

The kinetic energy of the element is expressed in terms of the displacement vector as

$$T=\pi\int_{r^{(j-1)}}^{r^{(j)}}\frac{\partial\mathbf{u}^T}{\partial t}\frac{\partial\mathbf{u}}{\partial t}\rho r\,dr, \tag{21}$$

where ρ is the mass density of the material of the element.

Substituting Eqs. (19) and (21) into Eq. (17), using Eqs. (2) and (16), and then taking variation with respect to $\mathbf{U}^e$ leads to the following governing equation for the solid strip element:

$$-\mathbf{A}_2^e\frac{d^2\mathbf{U}^e}{dz^2}+\mathbf{A}_1^e\frac{d\mathbf{U}^e}{dz}+(\mathbf{A}_0^e-\omega^2\mathbf{M}^e)\mathbf{U}^e=\mathbf{F}^e, \tag{22}$$

where

$$\mathbf{A}_0^e=\int_{r^{(j-1)}}^{r^{(j)}}\left(\frac{\partial\mathbf{N}^T}{\partial r}\mathbf{D}_{22}\frac{\partial\mathbf{N}}{\partial r}+\frac{1}{r}\frac{\partial\mathbf{N}^T}{\partial r}\mathbf{D}_{23}\mathbf{N}+\frac{1}{r}\mathbf{N}^T\mathbf{D}_{23}^T\frac{\partial\mathbf{N}}{\partial r}+\frac{1}{r^2}\mathbf{N}^T\mathbf{D}_{33}\mathbf{N}\right)r\,dr, \tag{23}$$

$$\mathbf{A}_1^e=\int_{r^{(j-1)}}^{r^{(j)}}\left(-\mathbf{N}^T\mathbf{D}_{12}\frac{\partial\mathbf{N}^T}{\partial r}-\frac{1}{r}\mathbf{N}^T\mathbf{D}_{13}\mathbf{N}+\frac{\partial\mathbf{N}^T}{\partial r}\mathbf{D}_{12}^T\mathbf{N}+\frac{1}{r}\mathbf{N}^T\mathbf{D}_{13}^T\mathbf{N}\right)r\,dr, \tag{24}$$

$$\mathbf{A}_2^e=\int_{r^{(j-1)}}^{r^{(j)}}\mathbf{N}^T\mathbf{D}_{11}\mathbf{N}r\,dr,$$
$$\mathbf{M}^e=\int_{r^{(j-1)}}^{r^{(j)}}\mathbf{N}^T\mathbf{N}\rho r\,dr,\quad \mathbf{F}^e=R_o\mathbf{N}^T\mathbf{p}. \tag{25}$$

The governing equation for the cylinder can be derived by assembling elements at the nodal lines

$$-\mathbf{A}_2\frac{d^2\mathbf{U}}{dz^2}+\mathbf{A}_1\frac{d\mathbf{U}}{dz}+(\mathbf{A}_0-\omega^2\mathbf{M})\mathbf{U}=R_o\mathbf{B}\mathbf{P}+R_0\mathbf{q}_0, \tag{26}$$

where

$$q_0=[0\ \cdots\ 0\ q_0]^T. \tag{27}$$

The coupling matrix $\mathbf{B}$ in Eq. (26) is the same as that in Eq. (8), through which the acoustic pressure of the fluid influences the displacements of the laminated cylinder. Note that the following interface and boundary conditions have been used during the process of assembling elements at the nodal lines:

$$\mathbf{p}_1^i=0, \tag{28}$$

$$\mathbf{p}_j^o=\mathbf{p}_{j+1}^i\mathbf{U}_j^o=\mathbf{U}_{j+1}^i\quad \text{for } 1<j<N-1, \tag{29}$$

$$\mathbf{p}_N^o=[0(p+q)]^T, \tag{30}$$

where the subscripts denote the element numbers, and the superscripts denote the inner and outer surfaces of the element.

As can be seen from Eqs. (7) and (26), the original partial differential equations for both the fluid and cylinder have been simplified to ordinary differential equations through the strip-element idealization. As a result, computational effort is grossly reduced using SEM.

C. Particular solution

The particular solutions of Eqs. (7) and (26) can be found by a modal-analysis method. To this end, the following Fourier transforms of the pressure and displacement amplitude vectors with respect to the axial coordinate z are introduced:

$$\tilde{\mathbf{P}}(k)=\int_{-\infty}^{\infty}\mathbf{P}(z)e^{ikz}\,dz,\quad \tilde{\mathbf{U}}(k)=\int_{-\infty}^{\infty}\mathbf{U}(z)e^{ikz}\,dz, \tag{31}$$

where k is the wave number. The application of Eq. (31) to Eqs. (7) and (26) leads to the characteristic equations of the fluid and cylinder in the wave-number domain

$$\left[k^2\mathbf{A}_{2\,f}+\mathbf{A}_{0f}-\frac{\omega^2}{c^2}\mathbf{M}_f\right]\tilde{\mathbf{P}}=\rho_f\omega^2R_o\mathbf{B}^T\tilde{\mathbf{U}}, \tag{32}$$

$$[k^2\mathbf{A}_2+ik\mathbf{A}_1+\mathbf{A}_0-\omega^2\mathbf{M}]\tilde{\mathbf{U}}=R_o\mathbf{B}\tilde{\mathbf{P}}+R_o\mathbf{q}_0. \tag{33}$$

These two equations can be rewritten in a more compact form, as follows:

$$[\mathbf{A}-k\mathbf{B}]\mathbf{d}=\mathbf{p}, \tag{34}$$

where

$$\mathbf{A}=\begin{bmatrix}\mathbf{0} & \mathbf{0} & \mathbf{I} & \mathbf{0}\\ \mathbf{0} & \mathbf{0} & \mathbf{0} & \mathbf{I}\\ \omega^2\mathbf{M}-\mathbf{A}_0 & R_o\mathbf{B} & -i\mathbf{A}_1 & \mathbf{0}\\ \rho_f\omega^2R_o\mathbf{B}^T & \frac{\omega^2}{c^2}\mathbf{M}_f-\mathbf{A}_{0f} & \mathbf{0} & \mathbf{0}\end{bmatrix}, \tag{35}$$

$$\mathbf{B}=\begin{bmatrix}\mathbf{I} & 0 & 0 & 0\\ 0 & \mathbf{I} & 0 & 0\\ 0 & 0 & \mathbf{A}_2 & 0\\ 0 & 0 & 0 & \mathbf{A}_{2\,f}\end{bmatrix},\quad \mathbf{p}=\begin{Bmatrix}\mathbf{0}\\ \mathbf{0}\\ -\mathbf{q}_0R_o\\ \mathbf{0}\end{Bmatrix},\quad \mathbf{d}=\begin{Bmatrix}\tilde{\mathbf{U}}\\ \tilde{\mathbf{P}}\\ k\tilde{\mathbf{U}}\\ k\tilde{\mathbf{P}}\end{Bmatrix}. \tag{36}$$

Equation (34) is called the characteristic equation of the fluid-loaded cylinder in the wave-number domain. By means of a modal-analysis technique (Liu and Achenbach 1995), the associated eigenvector can be written as

$$\mathbf{d}=\sum_{m=1}^{2(M+M_f)}\frac{\varphi_m^L\mathbf{P}\varphi_m^R}{(k-k_m)B_m}, \tag{37}$$

where $M=3(2N+1)$ and $M_f=N_f+1$ are the number of degrees of freedom of the solid and fluid strip elements, respectively, and $B_m=\varphi_m^L\mathbf{B}\varphi_m^R$. Here, the eigenvalues and the left and right eigenvectors k_m, φ_m^L, and φ_m^R are obtained from the characteristic equations

$$[\mathbf{A}-k_m\mathbf{B}]\varphi_m^R=\mathbf{0},\quad \varphi_m^L[\mathbf{A}-k_m\mathbf{B}]=\mathbf{0}. \tag{38}$$

If the eigenvectors φ_m^L and φ_m^R are written in a partition form as

$$\varphi_m^L=[\varphi_{m1}^L\varphi_{m2}^L\varphi_{m3}^L\varphi_{m4}^L]\varphi_m^R=[\varphi_{m1}^R\varphi_{m2}^R\varphi_{m3}^R\varphi_{m4}^R]^T, \tag{39}$$

where φ_{m1}^L, φ_{m3}^L, φ_{m1}^R, and φ_{m3}^R have the dimension of M, while φ_{m2}^L, φ_{m4}^L, φ_{m2}^R, and φ_{m4}^R have the dimension of M_f, then we have

$$\tilde{\mathbf{U}}_p = -\sum_{m=1}^{2(M+M_f)} \frac{\varphi_{m3}^L \mathbf{q}_0 R_o \varphi_{m1}^R}{(k-k_m)B_m}, \tag{40}$$

$$\tilde{\mathbf{P}}_p = -\sum_{m=1}^{2(M+M_f)} \frac{\varphi_{m3}^L \mathbf{q}_0 R_o \varphi_{m2}^R}{(k-k_m)B_m}. \tag{41}$$

By applying the inverse Fourier transformation to Eqs. (40) and (41), the displacement in the spatial domain can be found

$$\mathbf{U}_p = -\frac{1}{2\pi}\int_{-\infty}^{\infty} \sum_{m=1}^{2(M+M_f)} \frac{\varphi_{m3}^L \mathbf{q}_0 R_o \varphi_{m1}^R}{(k-k_m)B_m} e^{-ikz}\, dk, \tag{42}$$

$$\mathbf{P}_p = -\frac{1}{2\pi}\int_{-\infty}^{\infty} \sum_{m=1}^{2(M+M_f)} \frac{\varphi_{m3}^L \mathbf{q}_0 R_o \varphi_{m2}^R}{(k-k_m)B_m} e^{-ikz}\, dk. \tag{43}$$

Notice that φ_{m3}^L, φ_{m1}^R, φ_{m2}^R, $\mathbf{q}_0$, and B_m are independent of k. The integrals in Eqs. (42) and (43) are analytic functions of k, except at $2(M+M_f)$ poles ($k=k_m$) in the complex k plane. Hence, the integrations in Eqs. (42) and (43) may be analytically evaluated by employing the Cauchy's theorem

$$\mathbf{U}_p = \begin{cases} -i\displaystyle\sum_{m=1}^{M+M_f} \frac{\varphi_{m3}^{+L}\mathbf{q}_0 R_o \varphi_{m1}^{+R}}{B_m^+} e^{-ik_m^+ z} & \text{for } z \geqslant 0 \\ i\displaystyle\sum_{m=1}^{M+M_f} \frac{\varphi_{m3}^{-L}\mathbf{q}_0 R_o \varphi_{m1}^{-R}}{B_m^-} e^{-ik_m^- z} & \text{for } z < 0 \end{cases}, \tag{44}$$

$$\mathbf{P}_p = \begin{cases} -i\displaystyle\sum_{m=1}^{M+M_f} \frac{\varphi_{m3}^{+L}\mathbf{q}_0 R_o \varphi_{m2}^{+R}}{B_m^+} e^{-ik_m^+ z} & \text{for } z \geqslant 0 \\ i\displaystyle\sum_{m=1}^{M+M_f} \frac{\varphi_{m3}^{-L}\mathbf{q}_0 R_o \varphi_{m2}^{-R}}{B_m^-} e^{-ik_m^- z} & \text{for } z < 0 \end{cases}. \tag{45}$$

D. General solution

The complementary solution of the associated homogeneous equation of Eq. (26) can be expressed by superposition of the right eigenvectors φ_m^R

$$\mathbf{U}_c = \sum_{m=1}^{2M} C_m \varphi_m^R \exp(ik_m z) = \mathbf{G}(z)\mathbf{C}, \tag{46}$$

where the subscript c denotes the complementary solution and the coefficient vector $\mathbf{C}$ is to be specified. The addition of the particular and complementary solutions in Eqs. (44) and (46) yields the general solution of Eq. (26) in the form

$$\mathbf{U} = \mathbf{U}_c + \mathbf{U}_p = \mathbf{G}(z)\mathbf{C} + \mathbf{U}_p. \tag{47}$$

Thus, the coefficient vector $\mathbf{C}$ can be expressed in terms of particular and general solutions at radial boundaries

$$\mathbf{C} = \mathbf{G}_b^{-1}(\mathbf{U}_b - \mathbf{U}_{pb}), \tag{48}$$

where the subscript b denotes boundaries. Substitution of Eq. (47) into Eq. (48) gives

$$\mathbf{U} = \mathbf{G}(z)\mathbf{G}_b^{-1}(\mathbf{U}_b - \mathbf{U}_{pb}) + \mathbf{U}_p. \tag{49}$$

The stress boundary conditions at the tips of the crack are given by

$$\mathbf{R}_b = \mathbf{K}\mathbf{U}_b + \mathbf{S}_p, \tag{50}$$

where

$$\mathbf{R}_b = \begin{Bmatrix} \mathbf{R}_b^L \\ \mathbf{R}_b^R \end{Bmatrix}, \quad \mathbf{U}_b = \begin{Bmatrix} \mathbf{U}_b^L \\ \mathbf{U}_b^R \end{Bmatrix}, \tag{51}$$

$$\mathbf{K} = \begin{bmatrix} \mathbf{R}_1 & \mathbf{0} \\ \mathbf{0} & \mathbf{R}_1 \end{bmatrix} + \begin{bmatrix} \mathbf{R}_2 \partial \mathbf{G}^L/\partial z \mathbf{G}_b^{-1} \\ \mathbf{R}_2 \partial \mathbf{G}^R/\partial z \mathbf{G}_b^{-1} \end{bmatrix}, \tag{52}$$

$$\mathbf{S}_p = \begin{bmatrix} \mathbf{R}_2 & \mathbf{0} \\ \mathbf{0} & \mathbf{R}_2 \end{bmatrix} \begin{Bmatrix} \partial \mathbf{U}_p^L/\partial z \\ \partial \mathbf{U}_p^R/\partial z \end{Bmatrix} - \begin{bmatrix} \mathbf{R}_2 \partial \mathbf{G}^L/\partial z \mathbf{G}_b^{-1} \\ \mathbf{R}_2 \partial \mathbf{G}^R/\partial z \mathbf{G}_b^{-1} \end{bmatrix} \begin{Bmatrix} \mathbf{U}_p^L \\ \mathbf{U}_p^R \end{Bmatrix}, \tag{53}$$

are the external traction and displacement vectors on the radial boundaries, the stiffness matrix, and the equivalent external force acting on the radial boundaries, respectively. In Eqs. (52) and (53), the superscripts L and R represent the left- and the right-hand side of the crack tip.

III. NUMERICAL RESULTS AND DISCUSSION

In this section, the following dimensionless parameters are used:

$$\overline{z} = z/(R_o - R_i), \quad \overline{L} = L/(R_o - R_i), \quad \overline{a} = a/(R_o - R_i),$$
$$\overline{d} = d/(R_o - R_i),$$
$$\overline{R} = R_i/(R_o - R_i), \quad \overline{R}_f = (R_f - R_o)/(R_o - R_i),$$
$$\overline{w} = Q_{44} w/R_i q_0, \quad \overline{\omega} = \omega(R_o - R_i)/c_s,$$
$$c_s = \sqrt{Q_{44}/\rho},$$

where Q_{44} and ρ are the material constant and mass density of the reference material C0. In a laminate code, a lamina numbering increases from the inner to the outer surface. Letters C and G represent carbon/epoxy and glass/epoxy, respectively. Numbers following the letters indicate the angle of the fiber orientation with respect to the z axis. The subscript s implies that the lay-up of the structure is symmetrical about the middle surface. It should be noted that the difference between a cylinder and a circular cylindrical shell lies in the thickness. Hence, the present analysis also applies to a laminated composite circular cylindrical shell. In order to examine wave scattering from both the fluid-coupled cylinder and shell, two values of inner radius-to-thickness ratio, namely, $\overline{R}=1$ and $\overline{R}=20$, are adopted. The first ratio is for the cylinder, while the second ratio is for the shell. The material properties used in the calculations are are taken from Takahashi and Chou (1987). The fluid is taken as water of $\rho_f = 1.0\ \text{g/cm}^3$ and $c = 1.48\times 10^3\ \text{m/s}$. In view of the large domain of the fluid in the ultrasonics, $\overline{R}_f = 20$ is used. Numerical examples are given for $(\text{C90/G0})_s$, $(\text{C0/G90})_s$, and $(\text{C90/G0/G90})_s$ laminated composite cylinders and circular cylindrical shells submerged in fluid.

Figures 4 and 5 illustrate, respectively, the distributions of the radial displacement on the outer surface of an immersed $(\text{C90/G0})_s$ cylinder and shell containing an outer surface-breaking crack of $\overline{a}=1/4$, $\overline{L}=4$, and $\overline{d}=0$. For the sake of comparison, results for the corresponding dry cases are also plotted in the same figures (dotted lines). From these figures, it is obvious that the distribution patterns of the dis-

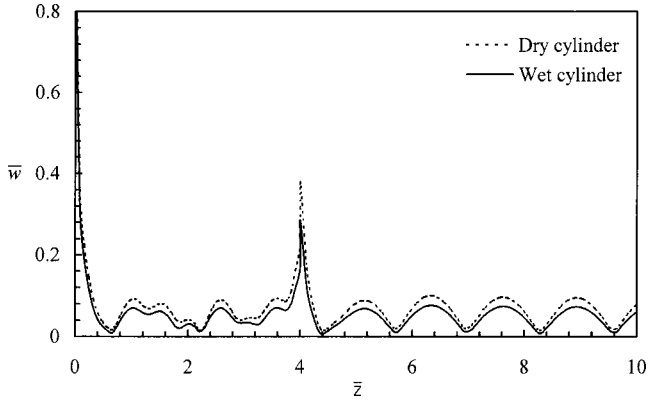

FIG. 4. Distribution of the radial displacement on the outer surface of an immersed $(C90/G0)_s$ cylinder with an outer surface-breaking crack ($\overline{\omega}=3.14$, $\overline{R}=1$).

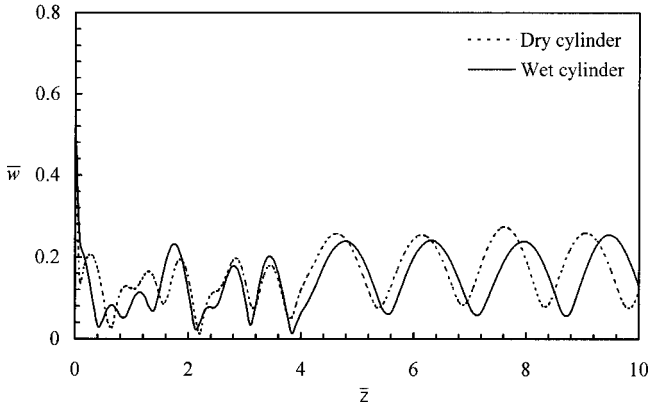

FIG. 6. Distribution of the radial displacement on the outer surface of an immersed $(C0/G90)_s$ cylinder with an interior radial crack ($\overline{\omega}=6.28$, $\overline{R}=1$).

placement of the cylinder and shell are not altered by the presence of the fluid. However, the magnitudes of the displacement of the cylinder and shell are reduced significantly as the presence of the fluid increases the equivalent structural mass.

Figures 6 and 7 illustrate, respectively, the distributions of the radial displacement on the outer surface of an immersed $(C0/G90)_s$ cylinder and shell containing an interior radial crack of $\overline{a}=1/2$, $\overline{L}=4$, and $\overline{d}=1/4$. Again, these figures show that the presence of the fluid does not change the distribution patterns of the displacement response. However, the noticeable different effects of the fluid on the cylinder and on the shell can be observed in Figs. 6 and 7. The presence of the fluid results in shifting the cylinder displacement between the loaded position and crack to the left, and shifting the displacement beyond the crack to the right (Fig. 6). The magnitudes of the displacement at the right-hand region of the crack are also reduced by the presence of the fluid. The trend at the left-hand region of the crack is somewhat less conspicuous. The displacement is increased at some positions and then is reduced at the other positions. This is probably due to the cylinder being thicker and the inside crack is at a distance from the outer surface. From Fig. 7, the presence of the fluid seems to have little effect on the wave field of the shell, both in the trend and magnitude, for the dimensionless frequency $\overline{\omega}=1.57$. However, when the frequencies of $\overline{\omega}=3.14$ and $\overline{\omega}=6.28$ are used, the presence of the fluid can reduce considerably the displacement magnitudes of the shell. Here, the purposes for presenting the result for the dimensionless frequency $\overline{\omega}=1.57$ are twofold. These findings clearly indicate that the fluid effect is dependent on the frequency used; for the particular specimen configuration used in this paper, the choice of $\overline{\omega}=1.57$ is best for crack detection.

Figures 8 and 9 illustrate, respectively, the distributions of the radial displacements on the outer surface of an immersed $(C90/G0/G90)_s$ cylinder and shell containing an axial crack of $\overline{a}=1$, $\overline{L}=4$, and $\overline{d}=1/3$. Figure 8 shows clearly that the addition of the fluid on the responses of the cylinder is pronounced. The displacements beyond the crack shifts to the right and the severity of shifting is much more than that for the interior radial crack. In addition, its values increase due to the effect of the fluid. Meanwhile, more apparent displacement distributions in the region of the crack make it easier to identify the extension of the crack. In contrast, the displacement field between the loading position and the crack does not shift, but its change is less dramatic than that for the corresponding dry cylinder. Figure 9 shows similar trends as Fig. 7 in that the presence of fluid does not

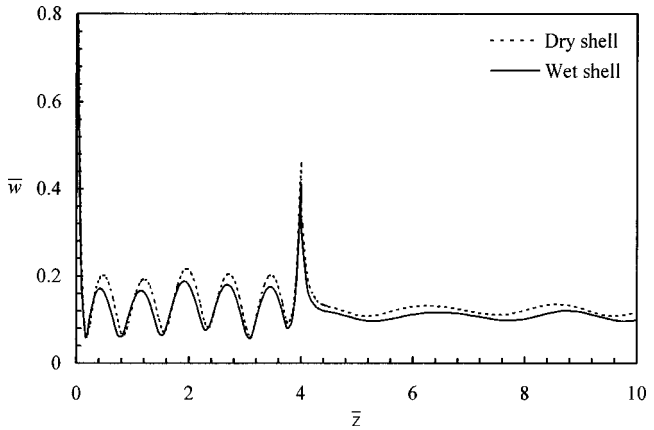

FIG. 5. Distribution of the radial displacement on the outer surface of an immersed $(C90/G0)_s$ shell with an outer surface-breaking crack ($\overline{\omega}=3.14$, $\overline{R}=20$).

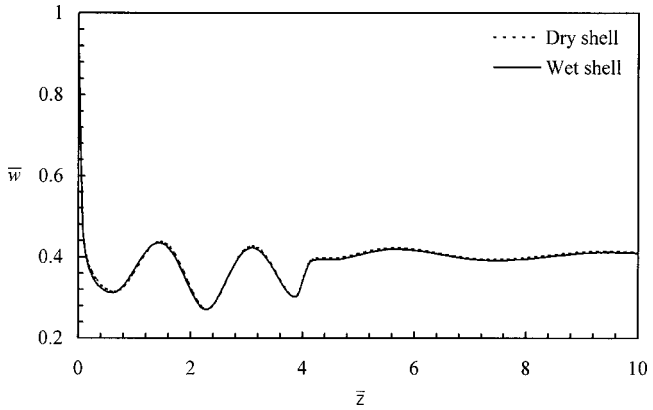

FIG. 7. Distribution of the radial displacement on the outer surface of an immersed $(C0/G90)_s$ shell with an interior radial crack ($\overline{\omega}=1.57$, $\overline{R}=20$).

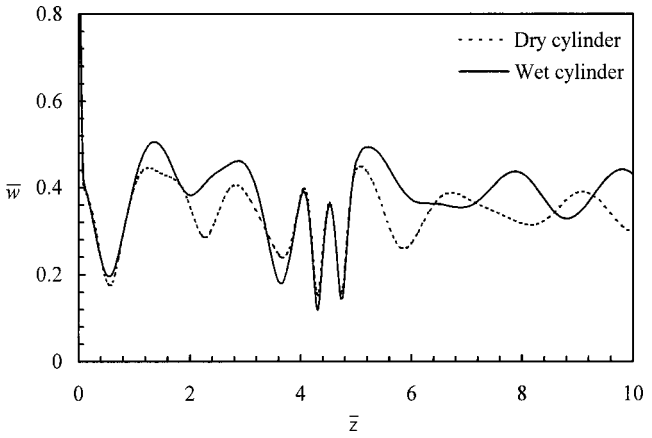

FIG. 8. Distribution of the radial displacement on the outer surface of an immersed $(C0/G90/G0)_s$ cylinder with an axial crack ($\bar{\omega}=3.14$, $\bar{R}=1$).

change the distribution patterns of the shell displacement, but reduces the magnitudes of the displacement.

IV. CONCLUSIONS

An SEM has been presented for analyzing wave scattering by a crack in an immersed composite cylinder. Numerical examples are given for immersed cracked composite cylinders and circular cylindrical shells. The numerical results indicate that the presence of the fluid has little influence on the displacement distribution patterns of both the cylinder and shell, that it can reduce significantly the displacement magnitudes of the shell, and that its effects on the cylinder displacement values depend upon the thickness of the cylinder, and the position and direction of the crack.

The use of SEM not only reduces the spatial dimensions of the problem by one, but also makes it easier to deal with composite cylinders made of an arbitrary number of anisotropic layers, of arbitrary lay-ups, and of any types of materials. The crack within the cylinder can be either radial or axial. The resulting coupled characteristic equations with the fluid pressure and cylinder displacement amplitudes as unknowns are solved simultaneously rather than staggeringly so that the results obtained have high precision. Compared to the finite-element method, the number and bandwidth of the SEM governing equations are smaller. In addition, the SEM can model infinite problems accurately with ease.

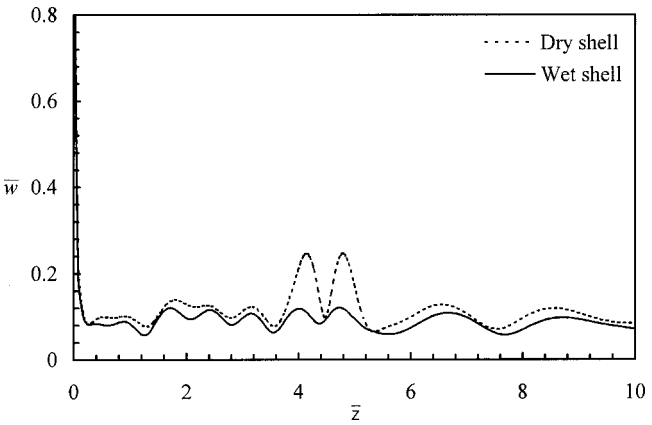

FIG. 9. Distribution of the radial displacement on the outer surface of an immersed $(C0/G90/G0)_s$ shell with an axial crack ($\bar{\omega}=3.14$, $\bar{R}=20$).

Atalar, A. (**1983**). ''Reflection of ultrasonic waves at a liquid–cubic–solid interface,'' J. Acoust. Soc. Am. **73**, 435–440.

Arikan, O., Teletar, E., and Atalar, A. (**1989**). ''Reflection coefficient null of acoustic waves at a liquid–anisotropic–solid interface,'' J. Acoust. Soc. Am. **85**, 1–10.

Braga, A. M. B., and Herrmann, G. (**1989**). ''Wave propagation in submerged layered composites,'' in *Elastic Wave Propagation*, edited by M. F. McCarthy and M. A. Hayes (Elsevier, Amsterdam).

Chimenti, D. E., and Nayfeh, A. H. (**1990**). ''Ultrasonic reflection and guided wave propagation in biaxially laminated composite plates,'' J. Acoust. Soc. Am. **87**, 1409–1415.

Dayal, V. (**1994**). ''Longitudinal waves in fluid loaded composite cylinders,'' in *Progress in Noise Control for Industry Proceedings-National Conference on Noise Control Engineering* (Institute of Noise Control Engineering, Poughkeepsie, NY).

Dayal, V., and Kinra, V. K. (**1989**). ''Leaky Lamb waves in an anisotropic plate: An exact solution and experiments,'' J. Acoust. Soc. Am. **85**, 2268–2276.

Gracewski, S. M., and Bogy, D. B. (**1986**). ''Elastic wave scattering from an interface crack in a layered half space submerged in water. I. Applied tractions at the liquid–solid interface. II. Incident plane waves and bounded beams,'' ASME J. Appl. Mech. **53**, 326–338.

Huang, K. H., and Dong, S. B. (**1984**). ''Propagating waves and edge vibrations in anisotropic composite cylinders,'' J. Sound Vib. **96**, 363–379.

Liu, G. R., and Achenbach, J. D. (**1994**). ''A strip element method for stress analysis of anisotropic linearly elastic solids,'' ASME J. Appl. Mech. **61**, 270–277.

Liu, G. R., and Achenbach, J. D. (**1995**). ''Strip element method to analyze wave scattering by cracks in anisotropic laminated plates,'' ASME J. Appl. Mech. **62**, 607–613.

Liu, G. R., Achenbach, J. D., Kim, J. O., and Li, Z. L. (**1992**). ''A combined finite element method/boundary element method technique for $V(z)$ curves of anisotropic–layer/substrate configurations,'' J. Acoust. Soc. Am. **92**, 2734–2740.

Liu, G. R., Lam, K. Y., and Chan, E. S. (**1996**). ''Stress waves in composite laminates excited by transverse plane shock waves,'' Shock Vib. **3**, 419–433.

Liu, G. R., Wang, X. J., and Xi, Z. C. (**1999a**). ''An exact solution for wave propagation in composite laminates submerged in a fluid,'' Int. J. Mech. Sci. (submitted).

Liu, G. R., Xi, Z. C., Lam, K. Y., and Shang, H. M. (**1999b**). ''A strip element method for analyzing wave scattering by a crack in an immersed composite laminate,'' ASME J. Appl. Mech. **66**, 898–903.

Mal, A. K., Xu, P. C., and Bar-Cohen, Y. (**1989**). ''Analysis of leaky Lamb waves in bounded plates,'' Int. J. Eng. Sci. **27**, 779–791.

McCoy, R. W., and Sun, C. T. (**1997**). ''Fluid–structure interaction analysis of a thick-section composite cylinder subjected to underwater blasting loading,'' Compos. Struct. **37**, 45–55.

Nayfeh, A. H. (**1991**). ''Elastic wave reflection from liquid–anisotropic substrate interfaces,'' Wave Motion **14**, 55–67.

Nayfeh, A. H. (**1995**). *Wave Propagation in Layered Anisotropic Media with Applications to Composites* (Elsevier, Amsterdam).

Nayfeh, A. H., and Chimenti, D. E. (**1988a**). ''Propagation of guided waves in fluid-coupled plates of fiber-reinforced composite,'' J. Acoust. Soc. Am. **83**, 1736–1743.

Nayfeh, A. H., and Chimenti, D. E. (**1988b**). ''Ultrasonic wave reflection from liquid coupled orthotropic plates with application to fibrous composites,'' J. Appl. Mech. **55**, 863–870.

Nayfeh, A. H., and Taylor, T. W. (**1988**). ''Surface wave characteristics of fluid-loaded multilayered media,'' J. Acoust. Soc. Am. **84**, 2187–2191.

Takahashi, K., and Chou, T.-W. (**1987**). ''Non-linear deformation and failure behavior of carbon/glass hybrid laminates,'' J. Compos. Mater. **21**, 396–407.

Vinson, J. R., and Sierakowski, R. L. (**1987**). *The Behavior of Structures Composed of Composite Materials* (Martinus Nijhoff, Dordrecht).

Xi, Z. C., Liu, G. R., Lam, K. Y., and Shang, H. M. (**1999**). ''A strip element method for analyzing wave scattering by a crack in an axisymmetric cross-ply composite cylinder,'' ASME J. Appl. Mech. (in press).

Xi, Z. C., Yam, L. H., and Leung, T. P. (**1997a**). ''Free vibration of a partially fluid-filled cross-ply laminated composite circular cylindrical shell,'' J. Acoust. Soc. Am. **101**, 909–917.
Xi, Z. C., Yam, L. H., and Leung, T. P. (**1997b**). ''Free vibration of a laminated composite circular cylindrical shell partially filled with fluid,'' Composites, Part B **28B**, 359–375.
Zienkiewicz, O. C., and Taylor, R. L. (**1989**). *The Finite Element Method*, 4th ed. (McGraw-Hill, London).

Dissipation in solids: Thermal oscillations of atoms

Cem E. Çelik and Adnan Akay[a)]
Mechanical Engineering Department, Carnegie Mellon University, Pittsburgh, Pennsylvania 15213

(Received 24 May 1999; revised 13 April 2000; accepted 15 April 2000)

Dissipation in solids describes conversion of kinetic energy to thermal energy. Heat capacity of a solid relates to the kinetic energy of the oscillations of its atoms with the assumption that they are in thermal equilibrium. Previous studies investigated criteria related to thermal relaxation, the process by which thermal equilibrium is established. They examined conditions for irreversible distribution of energy among the modes of a nonlinear periodic structure that represents atoms in a solid. These studies all point to the chaotic behavior of a freely vibrating nonlinear lattice as the kernel of the problem in addressing thermal relaxation. This paper extends the results of previous studies on thermalization to modeling of dissipation as energy absorption that takes place during forced vibration of particles in a nonlinear lattice. Results show that dissipation and chaotic behavior of the particles develop simultaneously. Such behavior develops when the forcing frequency falls within a resonance band. The results also support the argument that for a real solid, both in terms of size and complexity, resonance bands overlap significantly broadening the frequency range within which dissipation takes place. © *2000 Acoustical Society of America.*
[S0001-4966(00)04707-X]

PACS numbers: 43.40.Ga, 43.25.Ts, 43.25.Dc [DEC]

INTRODUCTION

The concept of dissipation in solids often refers to conversion of kinetic energy to heat. For example, during passage of a sound wave, or during friction between two surfaces, some of the energy associated with sound wave, or moving surfaces, dissipates as heat. Common forms of dissipation—material damping, contact damping, and the like, play an important role in the response of dynamic systems of any length scale. However, despite its ubiquity and significance in dynamic systems, dissipation in solids is often treated as a strictly empirical phenomenon with little success in describing it based on first principles. Several primary obstacles impede attempts to quantify dissipation and they involve modeling heat capacity. Heat capacity of a solid describes the increase in its internal energy per unit temperature. It follows that an increase of internal energy in response to an external excitation constitutes dissipation. Internal energy of a solid is proportional to the average kinetic energy of oscillations of its atoms. Thus, quantifying dissipation relies on accurate prediction of the oscillatory response of atoms in a solid. However, a comprehensive understanding of the dynamic behavior of atoms, the focus of this paper, has long constituted a significant impediment to accurate quantification of heat capacity. Additional difficulties include lack of precise descriptions of potentials between atoms and the computational requirements to simulate a solid of practical dimensions. Traditionally, dynamic behavior of atoms in a solid is investigated by simulating them as particles in a lattice. Difficulties relate to determining the effects caused by weak nonlinearities that represent the potentials between the atoms. As discussed below, previous studies show that only a subset of all possible responses of a lattice describes heat capacity. The present model considers the forced-vibration response of a lattice and shows that the specific conditions under which the response of a freely vibrating lattice qualifies as heat also apply to modeling of dissipation.

Qualitative relationships between thermal energy and vibrations of atoms in a solid exist in terms of average kinetic energy of atoms. However, such relationships involving energy of atoms and temperature in a solid assume that the vibrations of atoms are in statistical (thermal) equilibrium, or ''thermalized,'' such that all states of atoms have equal probability of having equal energy. As a result, investigations of thermalization process in a lattice look for conditions leading to energy equipartitioning among its modes of vibration.

In studies of freely vibrating nonlinear lattices, thermal equilibrium has been traditionally associated with ergodicity, which describes the trajectory of a particle's response in a lattice. However, more recent studies make a distinction between equipartitioning of energy and ergodicity (*viz.*, Ref. 1). The discovery of the Toda lattice validated this distinction since the Toda lattice is integrable, thus not ergodic, yet exhibits energy sharing.[2] Increasingly, deterministic models of lattice dynamics point to chaos, instead of ergodicity, as an indicator of thermalization and the means of energy equipartitioning, suggesting that, above absolute-zero temperature, atoms in a solid display chaotic oscillations.[3,4]

When modeling dissipation in solids, in addition to the requirement that absorbed energy is equipartitioned, absorption must also be irreversible. Results in this paper suggest that such irreversible energy absorption by a lattice occurs only when the lattice oscillations are thermal or chaotic. Thus, chaos also acts as an indicator of dissipation in a solid. Otherwise, energy absorbed by the system is coherent and periodically returns to the external source. Thus, chaotic behavior insures both equipartitioning and irreversibility of energy absorbed by a lattice.

This paper extends the results of previous studies on

a)Electronic mail: akay@cmu.edu

thermalization in freely vibrating lattices to modeling dissipation as forced vibration of a nonlinear lattice. It treats dissipation as energy absorbed by a one-dimensional lattice of oscillators excited by a harmonic force representing a sound wave, or friction, in a solid. Unlike mechanical vibration problems involving linear periodic structures, the nonlinear lattice used here does not have an explicit dissipation mechanism in the classical sense. Thus, increase in energy of oscillators represents the absorbed energy by the lattice. Numerical solutions of the equations of motion reveal the conditions under which chaos occurs and a lattice absorbs energy. Results show that dissipation coincides with chaotic behavior of the particles in a lattice. Such behavior develops when the force frequency falls within a resonance band. The results also support the argument that for a real solid, both in terms of size and complexity, resonance bands become contiguous and dissipation takes place throughout a wide spectrum of frequencies. The treatment of dissipation presented in this paper closely relates to the concepts connected with the thermalization process in freely vibrating nonlinear lattices. The review given in the next section provides the background related to the behavior of particles in such lattices to assist in interpreting numerical results given in this paper and elsewhere.

I. BACKGROUND: MODELING THERMAL VIBRATIONS

One-dimensional lattices, or chains, are frequently used to investigate the thermalization process; that is, to examine equipartitioning of energy during free vibration of atoms in solids. In such studies initial conditions provide the energy to the system, often in terms of energy associated with a single mode of the corresponding linear system, to investigate its irreversible distribution to other modes. Most of these studies use its Hamiltonian H to describe the dynamic behavior of a lattice of oscillators connected to each other with nonlinear springs. Nonlinearity in a system virtually assures that its Hamiltonian is nonintegrable. Of particular interest to the studies of equipartitioning is the case of weakly nonlinear lattices for which Hamiltonians are said to be *nearly* integrable and expressed as $H=H_0+\mu H_1$, where μH_1 represents the weak nonlinearity that modifies the Hamiltonian, H_0, of the corresponding linear, integrable system.

Perturbation and direct numerical methods comprise the common approaches to solve weakly nonlinear lattice equations. Perturbation techniques, once commonly used in solving nearly integrable Hamiltonian systems, can describe only a subset of the solution space but not those essential to the characterization of thermalization or equipartitioning of energy (*viz.*, Ref. 3), namely the chaotic behavior of a lattice. A theorem first proposed by Kolmogorov[5] and a decade later solved by Arnol'd[6] and Moser,[7] highlights the shortcomings of perturbation techniques by showing the existence of a larger space of solutions for nearly integrable Hamiltonians than those predicted earlier. Thus, only numerical methods offer the possibility of describing the complete solution space including chaotic response that characterizes thermalization. Secondary references provide further details of the Kolmogorov–Arnol'd–Moser (KAM) theorem (*viz.*, Refs. 2 and 8).

Before describing the complete solution space of weakly nonlinear systems uncovered by the KAM theorem, it is useful to review the solution space of corresponding linear integrable systems. An integrable system, for example a lattice of harmonic oscillators, with n degrees of freedom and the same number of basic (natural) frequencies ω_i $(i=1,n)$, exhibits two distinct types of motion that depend on its natural frequency distribution. For resonantly coupled frequencies in which frequencies rationally depend on each other such that $\Sigma l_i\omega_i=0$ (l_i are integers), the system is said to have internal resonances. In such cases, motion of the system is periodic and energy sharing can take place among its modes under certain initial conditions.[1,9] Such linearly dependent, or commensurate, frequencies occur except when n equals 2^N (N is an integer) or is a prime number as shown by Hemmer,[10] cited in Ford.[9] If the frequencies of the system are linearly independent, or are incommensurate, in which case $\Sigma l_i\omega_i=0$ has no solution except for $l_i=0$, the trajectory is everywhere dense on a torus and is usually (topologically) ergodic.[2] The spectrum of the motion includes the sums of frequencies and the motion is said to be conditionally periodic or quasiperiodic. Systems with such nonresonant (diophantine) conditions, in general, do not share energy among their modes.[9] Considering a system with only two degrees of freedom makes it possible to visualize the trajectories of motion of the two different systems described above. For such a system a set of nested tori constitute its energy surfaces on which the trajectories lie. The trajectories of the resonant systems meet, whereas for the nonresonant systems they never meet, and display an ergodic behavior.

A weak nonlinearity influences the two types of solutions described above, periodic and quasiperiodic orbits that lie on nested tori, very differently. A weak nonlinearity slightly perturbs the tori with quasiperiodic motion with incommensurate frequencies, but most of these, sometimes called the KAM tori, survive the perturbation and continue to exist, albeit with deformed shapes. (Perturbation techniques can show existence of these perturbed tori, thus lending support for the use of such solution methods.) On the other hand, weak nonlinearities in the system destroy the resonant tori and replace them by elliptic and hyperbolic orbits.[11] Motion on these pathologically distributed, destroyed tori can be chaotic, a result that cannot be obtained by perturbation analysis (*viz.*, Ref. 3). The solution space of these destroyed KAM tori, which corresponds to the internal resonant conditions of a lattice, represents the conditions for equipartitioning or thermalization of vibrations in a lattice.[2,3,8]

Nonlinearity also modifies the conditions for internal resonance and, hence, the conditions under which energy sharing takes place among its modes. When considered in the spectral domain, nonlinearity relaxes the resonance conditions for a harmonic system as $\Sigma l_i\omega_i\cong 0$ and makes equipartitioning easier to achieve. In nonlinear systems, as shown later, resonances occur within a band around each basic frequency ω_i. Widths of these resonance bands increase with increasing nonlinearity, but decrease with increasing frequency.[2] Numerical results suggest that, in weakly coupled oscillatory systems, energy sharing can take place only if there is a resonance, and that resonances will occur

provided $\Sigma l_i \omega_i \leq \mu$ for certain values of l_i determined by the coupling between the oscillators. No energy sharing can take place if $\Sigma l_i \omega_i \gg \mu$.[1] Nonlinearity also brings resonance bands closer together by increasing their widths. As the resonance bands begin to overlap, propensity for energy equipartitioning also increases. Chirikov's resonance-overlap theorem describes this phenomenon, suggesting that when resonances overlap, they destroy all regular motion between them.[12] Computations later in this paper show the significance of these resonance regions to energy absorption. As discussed above, the destroyed tori in the phase space and the corresponding spectrum of the destroyed regular motion show a chaotic behavior.

A. Free vibrations, energy sharing, and ergodicity

Much of the work of the past 50 years to reconcile statistical mechanics and classical mechanics originated from the work of Fermi, Pasta, and Ulam (FPU),[13] who made the first attempt to test ergodicity in a nonlinear chain of oscillators with numerical simulations. In their classic and oftencited work, FPU numerically integrated equations of motion that describe the free vibration of a weakly nonlinear chain subject to a specific initial condition assigned to a particular mode. With this experiment they intended to show that response of the lattice would reach a steady state with energy spread over many of its modes. FPU examples did not show this result and, in fact, demonstrated recurrence: initial energy did spread over a few of the modes but then reorganized itself back in the original distribution. This result contradicted an earlier theorem by Fermi[14] based on Poincaré's theorem,[15] explained elsewhere; *viz.*, Ref. 3. FPU results also called into question the conventional understanding that no matter how small, any nonlinearity would lead to equipartitioning.

The seemingly paradoxical results of FPU led to many subsequent studies, each of which provided a partial explanation, until the implications of KAM theorem became better recognized. Among those investigations that followed FPU to explore the relationship between weak nonlinearity and ergodicity, some recognized the need to dissociate energy equipartitioning from ergodicity (*viz.*, Ref. 1) and identified the development of chaos as the path to thermalization. Most of these studies found that development of chaos requires a certain threshold of energy. Below such a threshold, motion may behave nearly periodic; above it, motion becomes decidedly chaotic. The threshold for chaotic response also depends on the strength of nonlinearity. Low-energy initial conditions or weak nonlinearity in the chain prevents it from reaching equipartitioning (*viz.*, Refs. 16 and 17). In some cases recurrence may follow an initial equipartitioning of energy.[18] As exposed by KAM, recurrence represents the quasiperiodic regime, whereas irreversible equipartitioning that defines thermal vibrations takes place in the chaotic regime.[3]

The studies cited above describe the progress on the thermalization process among the modes of a freely vibrating nonlinear lattice of particles. However, Chirikov's approximate resonance overlap criterion notwithstanding, criteria for the onset of chaos in such systems are not yet established.

B. Forced vibrations and energy dissipation

The characteristics described above that govern equipartitioning among freely vibrating modes of a lattice also govern the energy exchange between a lattice and an external source. As shown later in this paper, for irreversible absorption of energy from a source, force and lattice spectra must meet certain criteria, otherwise energy exchange becomes reversible. For example, exciting the system with a frequency that falls within a resonance band of a lattice rapidly increases its energy level. In addition, if the excitation takes place in a region where resonances overlap, response will lead to equipartitioning and energy absorption.

Compared with those about equipartitioning in freely vibrating lattices, fewer studies considered dissipation or response of weakly nonlinear lattices excited by external forces. These studies include exploration of resonance overlap and quantum chaos by comparing classical and quantum theories with a Morse oscillator driven by single- and two-frequency excitation.[19–21] A series of studies on friction at the atomic level consider one-dimensional lattices and show the differences in energy absorption as a function of lattice parameters (*viz.*, Refs. 22 and 23).

II. MODELING OF ATOMIC VIBRATIONS

This section describes modeling of irreversible energy absorption by numerically solving the equations of motion of a lattice of particles that represent atoms in a solid. In solids atoms are held in equilibrium with respect to each other by means of electrostatic forces or interatomic potentials, often described as bonds between atoms. Such bonds connecting each atom to its neighbors confine the motion of atoms to oscillations about their respective equilibrium positions.

Vibrations of atoms in a solid may be represented by an idealized one-dimensional lattice with a periodic structure of identical mass-and-spring cells. The model used here consists of an array of masses linked together with nonlinear springs. The spring force, $K(x)$, which depends on the distance between the oscillators, represents the forces due to the interatomic potentials between atoms in a solid

$$K(x) = 2bD(e^{-b(x-a)} - e^{-2b(x-a)}). \tag{1}$$

The interatomic potential is represented by Morse potential[24]

$$V(x) = D(e^{-2b(x-a)} - 2e^{-b(x-a)}), \tag{2}$$

where the interatomic distance, or lattice constant, a, in our example is equal to $2.48 \cdot 10^{-10}$m. D is the depth of the potential well and constant b is the measure of steepness of the potential, which together determine the equivalent spring constant k for small displacements about the equilibrium point as $k = \partial^2 V / \partial x^2 \approx 2Db^2$.

The chain of particles, each with mass m, has one end fixed and the other free. The particles freely oscillate only along the axis of the chain. The external force, $F(t) = A \cos \omega t$ due to, for example, the interfacial potential between the two surfaces, acts on the free end of the chain. In the case of friction, amplitude A depends on the interfacial distance between the atoms on sliding surfaces, determined by the equilibrium of the normal contact force and the

repulsion–attraction field between the surface atoms. Frequency ω represents the passage of atoms across the free end of the chain determined by the ratio of relative speed to lattice constant of the surfaces.

The equation of motion for each particle in a one-dimensional lattice containing n atoms can be written as

$$m\ddot{x}_i = 2bD(e^{-2b(x_i - x_{i-1} - a)} - e^{-b(x_i - x_{i-1} - a)}) - 2bD(e^{-2b(x_{i+1} - x_i - a)} - e^{-b(x_{i+1} - x_i - a)}), \quad (3)$$

where $i = 1, \ldots, n-1$. The equation describing the motion of the atom at its free end is

$$m\ddot{x}_n = 2bD(e^{-2b(x_n - x_{n-1} - a)} - e^{-b(x_n - x_{n-1} - a)}) + A\cos\omega t. \quad (4)$$

As shown below, a parametric study of the influence of initial conditions and external force parameters points to a correlation between energy absorption of a lattice from an external source and its vibration response. Use of Poincaré maps and spectral analyses also support the earlier conclusions regarding the connection between chaos and equipartition in freely vibrating lattices.[3] Energy calculations discussed below use the actual kinetic and potential energies associated with each oscillator, rather than the approximate form based on summation of modal energies reported in some previous studies.

Results demonstrate how response spectra change with vibration amplitude and show the existence of *resonance bands* around the corresponding harmonic frequencies of a lattice. Results also show that widths of the resonance bands broaden with increased nonlinearity and that a lattice absorbs energy more readily when excited within these bands. Energy exchange among nonlinear modes is enhanced when resonance bands broaden and approach neighboring ones leading to the resonance overlap described earlier.[12] The following solutions begin with the calculation of resonance bands of a freely vibrating lattice followed by a demonstration of its energy exchange absorption when excited by an external force. The examples presented in this paper use few oscillators primarily to emphasize the physics of the problem. Some of the previous studies address concerns related to the number of oscillators (*viz.*, Refs. 4, 22, and 23) as discussed later in the paper.

A. Free-vibration response and resonance bands

Increasing initial-condition amplitude, and thus the energy of a 3-degrees of freedom (DOF) lattice, causes transition from a nearly linear behavior to a nonlinear response, as shown in Fig. 1. During transition, the frequency content of the spectrum becomes more dense and the resonance bands broader. As the amplitude increases, the spectrum shifts from containing only natural frequencies of the corresponding harmonic lattice to the analogous free-vibration frequencies of the nonlinear lattice and their integer multiples and combinations. The free-vibration frequencies also decrease with displacement amplitude, resembling a softening spring. The nearly- or quasiperiodic behavior at low-energy initial conditions eventually changes to chaotic behavior at high amplitudes with a corresponding spread of energy to other parts of the spectrum.

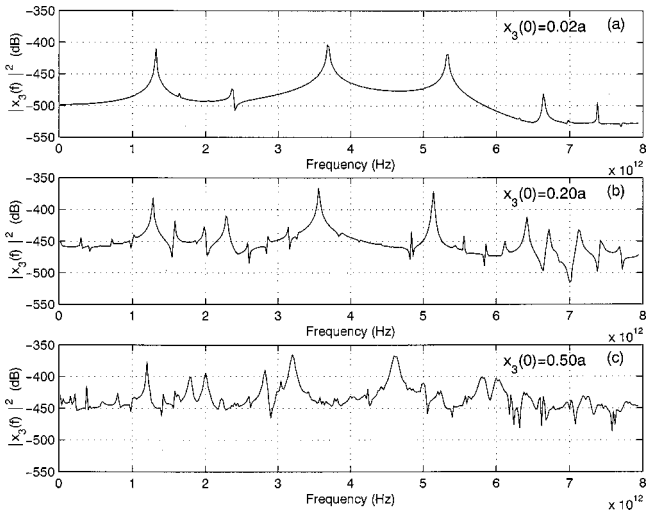

FIG. 1. Effect of initial condition amplitude on the free-vibration response of the system. Power spectrum of x_3 shifts from a nearly linear response (a) to a distribution of energy to other frequencies (b) and (c). (a) $x_3(0) = 0.02a$, (b) $x_3(0) = 0.20a$, (c) $x_3(0) = 0.50a$. In all cases, $x_1(0) = x_2(0) = \dot{x}_1(0) = \dot{x}_2(0) = \dot{x}_3(0) = 0$.

As described above, the initial energy level of a freely vibrating lattice influences its internal resonances, their overlap, and as a result equipartitioning of energy.[1] With increasing energy levels, the free-vibration frequencies change from line frequencies to wider bands of frequencies and the spectrum of lattice vibrations exhibits sums and harmonics of its free-vibration frequencies, thereby increasing the chances for internal resonances.

Coincidence of the harmonics and sums of free-vibration frequencies with other frequencies further broadens the resonance bands. It follows that lattices with larger number of oscillators have a higher probability of such coincidences and therefore a higher propensity to have overlapping frequency bands.

B. Forced vibrations and energy absorption

In the case of a nonlinear lattice excited by an external force, energy equipartitioning also depends on the amplitude of vibrations of the lattice or its energy level. Since the energy level of the lattice depends on the frequency and amplitude of the force that excites it, proximity of excitation frequency to any of the free-vibration frequencies of a lattice critically determines its response amplitude.

Results displayed in Fig. 2 represent the envelop of the maximum vibration amplitudes obtained by a frequency sweep demonstrating the effects force amplitude and frequency have on the response of a lattice. These results show that resonance occurs upon excitation within a band around the free-vibration frequencies of a lattice. The width of the resonance bands and the peak amplitude at each band increase with increasing force amplitude. Increases in each cause the neighboring separatrices in the phase plane to approach each other and manifest themselves as an overlap of resonances in the spectrum.[12,21] The resonance bands about

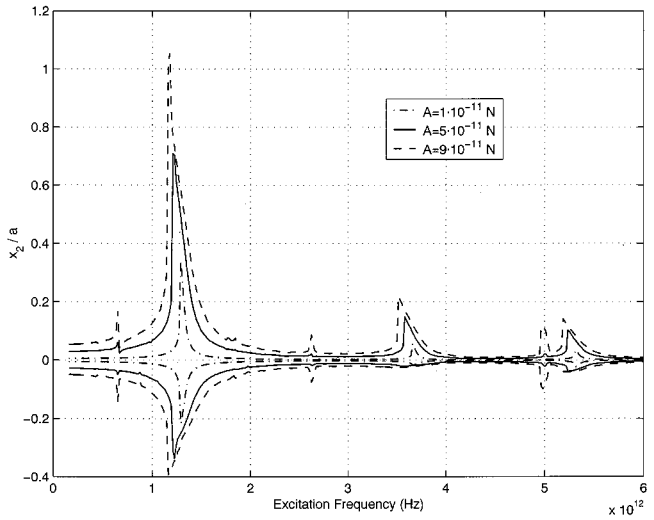

FIG. 2. Envelops of peak vibration amplitudes obtained by a frequency sweep show the influence of external force amplitude on response. With low excitation amplitudes, oscillators have nearly equal amplitudes in both directions about equilibrium. Particularly near resonances, as a result of asymmetric potential between them, oscillators move different distances away (+direction) and toward each other with higher excitation forces.

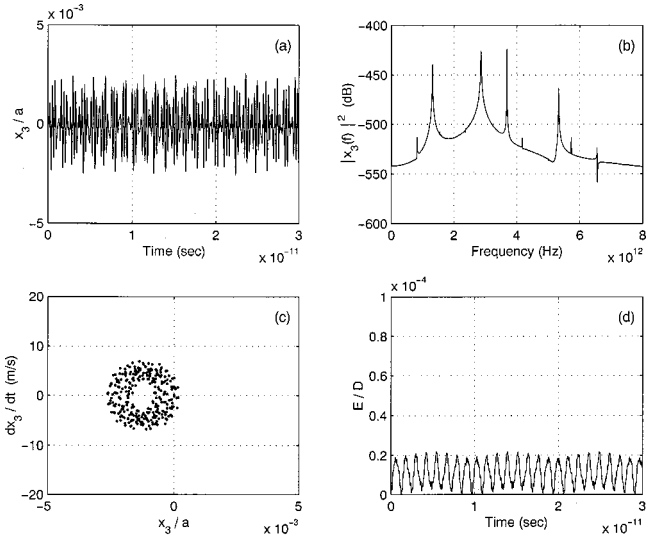

FIG. 3. Response of a 3 DOF system to harmonic excitation when forcing frequency falls outside the resonance band. Nondimensional time history (a), power spectrum (b), and Poincaré map (c) of m_3 support the recurrence demonstrated by the nondimensional energy of the total system in (d). $A=9.0\cdot10^{-11}$ N, $f=2.86\cdot10^{12}$ Hz.

the free-vibration frequencies are called the primary resonance bands. Similar behavior develops around the linear combination of free-vibration frequencies, which are called the secondary resonance bands. Unlike their harmonic counterparts, the amplitudes within resonance bands are bounded due to the amplitude dependence of the nonlinear potential between the particles. The analysis given in the Appendix shows sources of the primary and secondary resonances that are also described in dynamics literature as small denominators or divisors.[3] The significance of excitation within resonance bands to dissipation and equipartitioning will be discussed below.

Oscillations behave nearly linearly when excitation frequency is outside the resonance bands. In such cases, a lattice does not absorb energy, for it never reaches the energy threshold necessary to develop chaos (Fig. 3). As the force frequency approaches a resonance band, beats develop and the energy of the lattice oscillates between a maximum and zero; see Fig. 4. This periodic energy exchange, back and forth between the external source and the array, is analogous to the recurrence seen in free vibrations of a lattice. Corresponding Poincaré maps indicate quasiperiodicity or near-chaos depending on the proximity of force frequency to the resonance band. When the force frequency falls within the resonance band, response amplitude increases with an accompanying net energy absorption by the array, as seen in Fig. 5.

These results reveal that a lattice irreversibly absorbs energy when its oscillation characteristics exhibit chaos. Both the frequency and amplitude of forcing function play a key role in that they can increase the response amplitudes, and thus the energy level of the lattice, pushing it to the chaotic regime. In this context, excitation in a resonance band becomes important.

Lattices also absorb energy when the excitation frequency is a linear combination of its free-vibration frequencies.[1] As demonstrated by Fig. 6, excitation of the lattice at one of its secondary resonance bands displays chaotic behavior with accompanying energy absorption. Secondary resonances appear as small divisors in the analysis given in the Appendix supporting this result.

Results displayed in Figs. 3 and 4 demonstrate that if the excitation frequency falls outside the primary or secondary resonance bands of a lattice, it will not absorb energy in the form of thermal vibrations. This apparent limitation suggests that not all force amplitudes and frequencies may lead to chaos and, consequently, dissipation can occur only in the limited cases where excitation frequency falls within a resonance band. Described differently, a lattice with a finite number of oscillators has a low probability to reach a state of chaos unless the potential between the atoms has a very

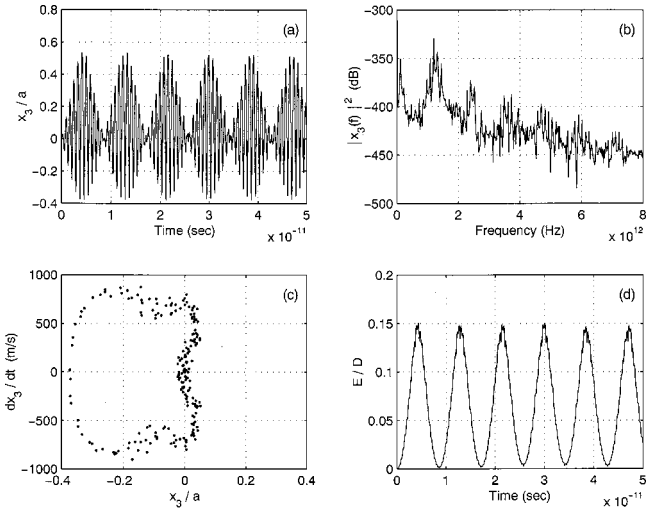

FIG. 4. When the forcing frequency is close to a resonance band, the power spectrum of x_3 shows distribution of energy to other frequencies (b) with corresponding scatter in Poincaré map (c). Total energy of the system (d) exhibits near-recurrence. $A=9.0\cdot10^{-11}$ N, $f=1.32\cdot10^{12}$ Hz.

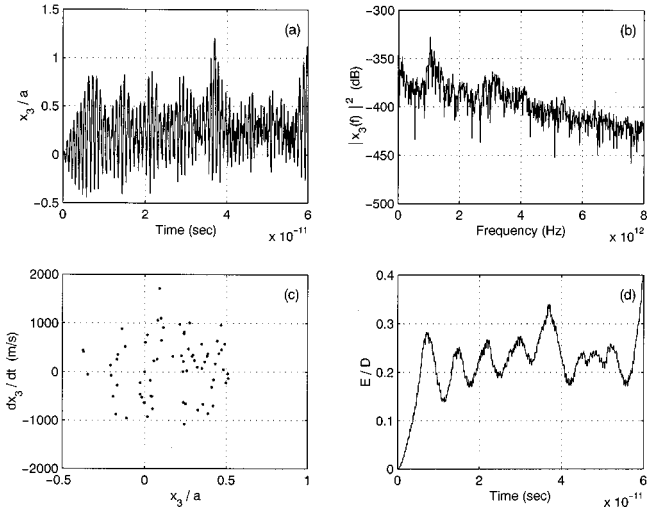

FIG. 5. When the forcing frequency falls within a resonance band, power spectrum (b) and Poincaré map (c) indicate chaotic response with corresponding energy absorption by the system (d). $A=9.0\cdot10^{-11}$ N, $f=1.18\cdot10^{12}$ Hz.

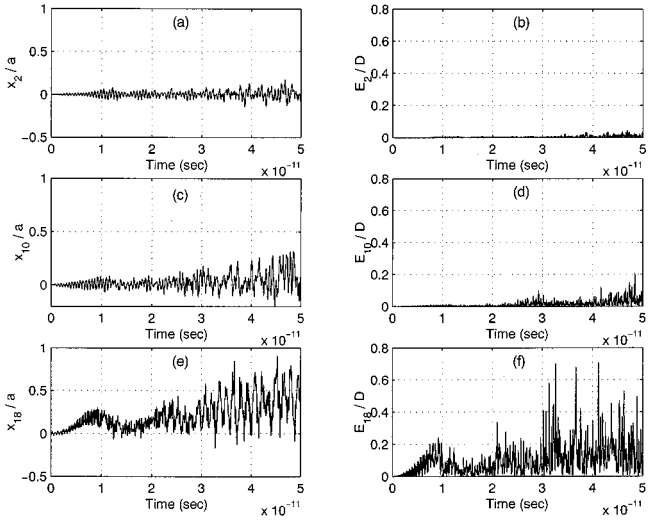

FIG. 7. Displacement and energy of oscillators 2, 10, and 18 of a 20-oscillator lattice when unequal masses are placed at oscillators 6 and 13.

strong nonlinearity. This restriction, however, relaxes as the size of the lattice increases, for the density of resonance bands in the spectrum of a freely vibrating lattice depends on the number of oscillators in a lattice.

Solids have a much more complex structure than an idealized periodic lattice. For example, impurities, or different atoms, in a lattice constitute impedance changes in an otherwise idealized lattice. They cause scattering and redistribution of the energy absorbed from external excitation source. An example displayed in Fig. 7 demonstrates the significantly different average energy levels between impurities, simulated by different masses placed at locations $n=6$ and 13 of a 20-oscillator lattice.

Impurities or nonideal lattice components influence response through two different means. They introduce new wavelengths, and thus new resonant frequencies which are lower than the resonant frequencies of the corresponding ideal lattice. Impurities also introduce impedance changes to an otherwise perfectly periodic structure which trap the energy as it propagates from the excitation point into the lattice, resulting in higher thermal energy near the excitation source.

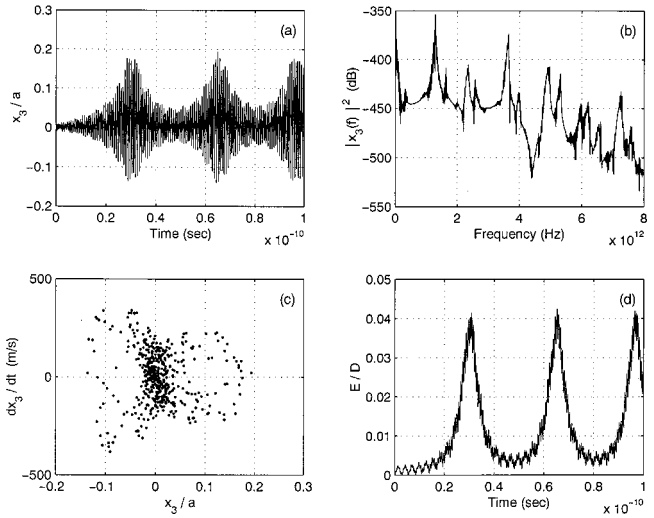

FIG. 6. When the forcing frequency falls within a secondary resonance band, the system again exhibits distribution of energy to other frequencies. $A=9.0\cdot10^{-11}$ N, $f=4.96\cdot10^{12}$ Hz.

III. DISCUSSION

This paper treats dissipation in solids by considering it as energy absorption by a lattice of oscillators that represent atoms in a solid. Because the lattice does not have a phenomenological dissipation mechanism, the irreversible increase in its internal energy becomes the only possible means of energy absorption.

Conditions governing thermalization in a freely vibrating lattice also apply to its irreversible absorption of energy when excited by a force. For example, internal energy of a lattice increases irreversibly when excitation frequency falls within a resonance band. Otherwise, a periodic energy exchange takes place between the force source and lattice as in the case of linear systems. During energy exchange, particles exhibit periodic or quasiperiodic responses, whereas during irreversible energy absorption lattice response displays a chaotic behavior. Thus, as for the case of a thermalization process in a freely vibrating lattice, chaotic response in a lattice also appears as an indicator of irreversible energy absorption, or dissipation.

Studies show that the number of oscillators does not fundamentally affect the nature of lattice dynamics (*viz.*, Ref. 4). However, the strong dependence of dissipation on excitation frequency raises a question concerning the possibility that dissipation may not take place when force frequencies fall outside of resonant bands. The gaps between resonance bands represent the inherent shortcoming of modeling solids with a small number of particles. Lattices that have the same order of complexity and number of oscillators as solids of practical dimensions will very likely not have such gaps. Lattices containing sufficiently large number of atoms possess a more dense, contiguous spectrum with overlapping resonance bands and, therefore, have a higher propensity to

reach a state of energy equipartitioning through chaos. Large nonlinear lattices also have a higher likelihood of having linear combinations of free-vibration frequencies that coincide with the excitation frequency. Increasing the dimension of a lattice from 1 to 3 further increases the likelihood of such coincidences. Impurities, or different atoms, in a lattice cause scattering and alter the energy distribution in the vibration field. Thus, the presence of impurities leads to additional free-vibration frequencies lower than those in an ideal lattice. These additional resonance bands permit forces with lower excitation frequencies to also cause dissipation. Hence, it is safe to extrapolate from the present and previously reported results that even for ideal lattices but with very large number of oscillators, energy will be absorbed during friction or during passage of a sound wave in a solid. Also, because solids are not at absolute-zero temperature, their atoms must already have a chaotic motion representing their thermalized vibrations.

IV. CONCLUSIONS

The underlying issues concerning modeling of dissipation in solids place it at the confluence of nonlinear dynamics, statistical mechanics, and computational mechanics. Notwithstanding the need for computational power required to model dissipation in solids of practical dimensions, definitive criteria for thermalization still elude us. Some issues still remain unsolved regarding whether the numerical results show physical or information chaos. The current descriptions of thermalization and dissipation are somewhat *ad hoc* in that they do not describe molecular dynamics in detail. Furthermore, such models still need accurate descriptions of the potentials between atoms.

The complexities of the dynamic response of a weakly nonlinear lattice outlined earlier requires a better understanding of the mathematical framework founded upon the theorem by KAM, which provides a description of the solution space and conditions to reach chaos for such systems. The mathematical framework upon which numerical solutions are based assumes nonintegrability of the Hamiltonian describing the lattice. Siegel's theorem assures the assumption that a lattice structure that represents a real solid will have a nonintegrable Hamiltonian.[3,25]

APPENDIX: ESTIMATION OF PRIMARY AND SECONDARY RESONANCES

The following analysis of a single-degree-of-freedom nonlinear oscillator driven by a harmonic force reveals the primary and secondary resonances described earlier in the main body of this paper. The following equation governs the motion of an oscillator attached to a rigid wall with a spring force derived from Morse potential:

$$m\ddot{x}=2bD(e^{-2b(x-a)}-e^{-b(x-a)})+A\cos\omega t; \tag{A1}$$

expanding the expression for the spring force in Taylor series yields

$$m\ddot{x}=2bD[-b(x-a)+\tfrac{3}{2}b^2(x-a)^2-\tfrac{7}{6}b^3(x-a)^3+\cdots]+A\cos\omega t. \tag{A2}$$

Substituting for the displacement the nondimensional form $u=(x-a)/a$ simplifies the equation of motion

$$\ddot{u}=\frac{2bD}{m}[-bu+\tfrac{3}{2}ab^2u^2-\tfrac{7}{6}a^2b^3u^3-\cdots]+\frac{A}{ma}\cos\omega t, \tag{A3}$$

and neglecting the nonlinear terms larger than the third order reduces Eq. (A3) to the following form:

$$\ddot{u}+\sigma^2u=\varepsilon u^2-\gamma\varepsilon u^3+F_0\cos\omega t, \tag{A4}$$

where $\varepsilon=3ab^3D/m$, $\gamma=7ab/9$, $F_0=A/ma$, and $\sigma=\sqrt{2b^2D/m}$ represents the natural frequency of the corresponding linear system.

Use of the KBM perturbation method[26] to solve Eq. (A4) requires expansion of u in the form of a power series

$$u=u_0+\varepsilon u_1+\varepsilon^2u_2+\varepsilon^3u_3+\cdots. \tag{A5}$$

Substituting Eq. (A5) into Eq. (A4) and arranging the terms according to powers of ε gives a set of differential equations to be solved recursively

$$\ddot{u}_0+\sigma^2u_0=F_0\cos\omega t, \tag{A6}$$

$$\ddot{u}_1+\sigma^2u_1=u_0^2-\gamma u_0^3, \tag{A7}$$

$$\ddot{u}_2+\sigma^2u_2=2u_0u_1-3\gamma u_0^2u_1, \tag{A8}$$

$$\vdots$$

The solution of Eq. (A6) with zero initial conditions is simply

$$u_0=\frac{F_0}{\sigma^2-\omega^2}[\cos\omega t-\cos\sigma t]. \tag{A9}$$

Recursively solving Eqs. (A6), (A7), and (A8), by neglecting all secular terms and including only the first two terms of the power series, leads to the following expression for u:

$$\begin{aligned}u=&\frac{F_0}{\sigma^2-\omega^2}[\cos\omega t-\cos\sigma t]+\frac{\varepsilon F_0^2}{(\sigma^2-\omega^2)^2}\\&\times\left[\frac{1}{\sigma^2}+\frac{\cos2\omega t}{2(\sigma^2-4\omega^2)}-\frac{\cos2\sigma t}{6\sigma^2}-\frac{\cos(\omega+\sigma)t}{\sigma^2-(\omega+\sigma)^2}\right.\\&\left.-\frac{\cos(\omega-\sigma)t}{\sigma^2-(\omega-\sigma)^2}\right]-\frac{\varepsilon\gamma F_0^3}{4(\sigma^2-\omega^2)^3}\left[\frac{\cos3\sigma t}{8\sigma^2}\right.\\&+\frac{9\cos\omega t}{2(\sigma^2-\omega^2)}+\frac{\cos3\omega t}{2(\sigma^2-9\omega^2)}-\frac{3\cos(2\omega+\sigma)t}{\sigma^2-(2\omega+\sigma)^2}\\&-\frac{3\cos(2\omega-\sigma)t}{\sigma^2-(2\omega-\sigma)^2}+\frac{3\cos(\omega+2\sigma)t}{\sigma^2-(\omega+2\sigma)^2}\\&\left.+\frac{3\cos(\omega-2\sigma)t}{\sigma^2-(\omega-2\sigma)^2}\right].\end{aligned} \tag{A10}$$

A simple inspection of Eqs. (A9) and (A10) shows the primary resonance at $\omega=\sigma$. The secondary resonances occur when the excitation frequency equals to σ, $\sigma/2$, $\sigma/3$, 2σ, or 3σ. A similar analysis for a multi-degree-of-freedom system

would reveal secondary resonances involving linear combinations of the free-vibration frequencies of the system.

[1] J. Ford and J. Waters, ''Computer studies of energy sharing and ergodicity for nonlinear oscillator systems,'' J. Math. Phys. **4**, 1293–1306 (1963).
[2] E. A. Jackson, *Perspectives of Nonlinear Dynamics* (Cambridge University Press, New York, 1994), Vols. 1–2.
[3] J. Ford, ''The Fermi–Pasta–Ulam problem: Paradox turns discovery,'' Phys. Rep. **213**, 271–310 (1992).
[4] G. Benettin, ''Ordered and chaotic motions in dynamical systems with many degrees of freedom,'' in *Molecular-Dynamics Simulation of Statistical-Mechanical Systems*, edited by G. Ciccotti and W. G. Hoover (North-Holland, New York, 1986).
[5] A. N. Kolmogorov, ''Preservation of conditionally periodic movements with small change in the Hamiltonian function,'' Dokl. Akad. Nauk SSSR **98**, 527 (1954).
[6] V. I. Arnold, ''Small denominators and problem of stability of motion in classical and celestial mechanics,'' Russ. Math. Surveys **18**, 85–191 (1963).
[7] J. Moser, ''On invariant curves of area-preserving mappings of an annulus,'' Nachr. Akad. Wiss. Goett. II, Math.-Phys. Kl. **2**, 1–20 (1962).
[8] E. Ott, *Chaos in Dynamical Systems* (Cambridge University Press, New York, 1993).
[9] J. Ford, ''Equipartition of energy for nonlinear systems,'' J. Math. Phys. **2**, 387–393 (1961).
[10] P. Hemmer, ''Dynamic and Stochastic Types of Motion in the Linear Chain,'' Ph.D. thesis, Trondheim, 1959.
[11] R. Z. Sagdeev, D. A. Usikov, and G. M. Zaslavsky, *Nonlinear Physics: From the Pendulum to Turbulence and Chaos* (Harwood Academic, New York, 1988).
[12] B. V. Chirikov, ''A universal instability of many dimensional oscillator model,'' Phys. Rep. **52**, 263–379 (1979).
[13] E. Fermi, *Collected Papers* (University of Chicago Press, Chicago, 1965), Vol. 2.
[14] E. Fermi, ''Beweiss dass ein mechanisches normalsystem in allgmeinen quasi-ergodisch ist,'' Phys. Z. **24**, 261–265 (1923).
[15] H. Poincaré, *Les Methodes Nouvelles de la Mécanique Celeste* (Gauthier-Villars, Paris, Reprinted by Dover, 1957), Vols. 1–3.
[16] N. Saito and H. Hirooka, ''Computer studies of ergodicity in coupled oscillators with anharmonic interactions,'' J. Phys. Soc. Jpn. **23**, 167–171 (1967).
[17] H. Hirooka and N. Saito, ''Computer studies on the approach to thermal equilibrium in coupled anharmonic oscillators. I. Two-dimensional case,'' J. Phys. Soc. Jpn. **25**, 624–630 (1969).
[18] S. D. Stoddard, J. Ford, and J. S. Turner, ''On the integrability of Toda lattice,'' Prog. Theor. Phys. **50**, 1547–1560 (1973).
[19] M. E. Goggin and P. W. Millonni, ''Driven Morse oscillator: Classical chaos, quantum theory and photodissociation,'' Phys. Rev. A **37**, 796–806 (1988).
[20] M. E. Goggin and P. W. Millonni, ''Driven Morse oscillator: Classical chaos and quantum theory for two-frequency excitation,'' Phys. Rev. A **38**, 5174–5181 (1988).
[21] J. H. Kim and H. W. Lee, ''Relativistic chaos in the driven harmonic oscillator,'' Phys. Rev. E **51**, 1579–1581 (1995).
[22] J. B. Sokoloff, ''Fundamental mechanisms for energy dissipation at small solid sliding surfaces,'' Wear **167**, 59–68 (1993).
[23] J. B. Sokoloff, ''Microscopic mechanisms for kinetic friction: Nearly frictionless sliding for small solids,'' Phys. Rev. B **52**, 7205–7214 (1995).
[24] U. Ingard, *Fundamentals of Waves and Oscillations* (Cambridge University Press, New York, 1993).
[25] C. L. Siegel, Ann. Math. **42**, 806 (1941).
[26] L. Meirovitch, *Methods of Analytical Dynamics* (McGraw-Hill, New York, 1988).

Narrowband and broadband active control in an enclosure using the acoustic energy density

John W. Parkins
RTH Systems, 135 Storm Road, Groton, New York 13073

Scott D. Sommerfeldt
Department of Physics, Brigham Young University, N241 ESC, Provo, Utah 84602

Jiri Tichy
Acoustics Department, The Pennsylvania State University, Applied Science Building, North Atherton Street, State College, Pennsylvania 16802

(Received 29 July 1999; accepted for publication 28 March 2000)

An active control system based on the acoustic energy density is investigated. The system is targeted for use in three-dimensional enclosures, such as aircraft cabins and rooms. The acoustic energy density control method senses both the potential and kinetic energy densities, while the most popular control systems of the past have relied on the potential energy density alone. Energy density fields are more uniform than squared pressure fields, and therefore, energy density measurements are less sensitive to sensor location. Experimental results are compared to computer-generated results for control systems based on energy density and squared pressure for a rectangular enclosure measuring $1.5\times2.4\times1.9$ m. Broadband and narrowband frequency pressure fields in the room are controlled experimentally. Pressure-field and mode-amplitude data are presented for the narrowband experiments, while spectra and pressure-field data are presented for the broadband experiment. It is found that the energy density control system has superior performance to the squared pressure control system since the energy density measurement is more capable of observing the modes of a pressure field. Up to 14.4 and 3.8 dB of cancellation are achieved for the energy density control method for the narrowband and broadband experiments presented, respectively. [S0001-4966(00)02007-5]

PACS numbers: 43.50.Ki [MRS]

INTRODUCTION

Most active control systems for use in three-dimensional enclosures employ pressure microphones as error sensors. These control systems typically minimize the sum of the squared pressures at the microphone locations, effectively minimizing the sum of the potential energy densities at these points.[1] However, acoustic energy exists in two states: potential energy in the form of pressure, and kinetic energy in the form of particle velocity. Systems based on minimizing potential energy density are therefore neglecting half the acoustic energy. Reduction of the potential energy density at a point in space may significantly increase both the kinetic energy density at that point as well as the total energy in the enclosure. A control system based on minimizing the sum of the total energy densities at discrete points yields improved global noise reduction, since it attenuates both forms of acoustic energy.

Since the early 1990s, active control systems based on energy density have been investigated. In 1992, Sommerfeldt and Nashif studied the efficacy of a single-axis energy density based system for use in ducts.[2] In 1995, Sommerfeldt *et al.* investigated a three-axis energy density control system, using a single sensor, for use in rectangular enclosures.[3] Park and Sommerfeldt modeled broadband active control in a one-dimensional enclosure in 1995.[4] Recently, Qiu *et al.* presented a theoretical comparison of near-field error sensor control systems which included energy density sensing.[5]

The previous work in energy density-based active control systems is expanded in this paper to include narrowband control using three-axis energy density sensing with multiple sensors/control sources, and broadband control using a single energy density sensor/control source, in a rectangular enclosure. In analyzing the effectiveness of the energy density control strategy, the performance is compared to the more common system based on minimizing the sum of the squared pressures. A computer model is used to predict the results of active cancellation for both strategies for active control, as well as modeling a method whereby the integrated potential energy density over the enclosure volume is minimized. The latter system has been proposed as an optimal control system.[6] Experimental results are presented for the energy density and squared pressure control schemes. Pressure-field as well as mode-amplitude data are presented for both computer-generated and experimental data.

I. THE ACOUSTIC ENERGY DENSITY

The time-averaged total acoustic energy density at a point in space, $\mathbf{x}=(x,y,z)$, is defined as

$$e(\mathbf{x})\equiv U(\mathbf{x})+T(\mathbf{x}), \tag{1}$$

which is the sum of the potential energy density, $U(\mathbf{x})$, and the kinetic energy density, $T(\mathbf{x})$. The potential energy is stored in the form of pressure, while the kinetic energy is manifested as particle velocity. In terms of the acoustic pres-

sure and particle velocity, the total energy density can be written as

$$e(\mathbf{x})=\frac{1}{4\rho c^2}|\hat{p}(\mathbf{x})|^2+\frac{\rho}{4}|\hat{\mathbf{v}}(\mathbf{x})|^2, \tag{2}$$

where $\hat{\mathbf{v}}(\mathbf{x})=(\hat{v}_x(\mathbf{x}),\hat{v}_y(\mathbf{x}),\hat{v}_z(\mathbf{x}))$ is the vector particle velocity, c is the speed of sound, and ρ is the density. Equation (2) can also be written as

$$e(\mathbf{x})=\frac{1}{4\rho c^2}|\hat{p}(\mathbf{x})|^2+\frac{\rho}{4}|\hat{v}_x(\mathbf{x})|^2 + \frac{\rho}{4}|\hat{v}_y(\mathbf{x})|^2+\frac{\rho}{4}|\hat{v}_z(\mathbf{x})|^2. \tag{3}$$

Hence, four scalar acoustic quantities are needed to determine the acoustic energy density at a point in space.

II. MODAL REPRESENTATION OF THE PRESSURE FIELD

The complex pressure $\hat{p}(\mathbf{x})$ in an enclosure can be represented by an infinite sum of the weighted eigenfunctions of the enclosure as

$$\hat{p}(\mathbf{x})=\sum_{N=1}^{\infty}\hat{A}_N\Psi_N(\mathbf{x}). \tag{4}$$

The eigenfunctions or mode functions, $\Psi_N(\mathbf{x})$, for a rigid undamped rectangular room with dimensions $L_x\times L_y\times L_z$ are

$$\Psi_N(\mathbf{x})=\cos k_x x\cos k_y y\cos k_z z, \tag{5}$$

where

$$k_x=\frac{l\pi}{L_x},\quad k_y=\frac{m\pi}{L_y},\quad \text{and}\quad k_z=\frac{n\pi}{L_z}. \tag{6}$$

The mode indices l, m, and n each take on integer values. The resonance frequencies, f_N, of the enclosure are given by

$$f_N=\frac{c}{2\pi}\sqrt{k_x^2+k_y^2+k_z^2}=\frac{ck}{2\pi}, \tag{7}$$

where k is the acoustic wave number. If a point monopole source is added to the enclosure to control the field, the complex pressure can be represented by

$$\hat{p}(\mathbf{x})=\sum_{N=1}(\hat{A}_N+\hat{B}_N\hat{Q}_c)\Psi_N(\mathbf{x}), \tag{8}$$

where $\hat{Q}_c$ is the complex source strength of the monopole. If G monopole sources are used to control the field, the complex pressure field can be written as

$$\hat{p}(\mathbf{x})=\sum_{N=1}^{\infty}\left(\hat{A}_N+\sum_{g=1}^{G}\hat{B}_{N,g}\hat{Q}_{c,g}\right)\Psi_N(\mathbf{x}). \tag{9}$$

Equation (9) can also be written as

$$\hat{p}(\mathbf{x})=\sum_{N=1}^{\infty}\hat{C}_N\Psi_N(\mathbf{x}), \tag{10}$$

where $\hat{C}_N=\hat{A}_N+\Sigma_{g=1}^{G}\hat{B}_{N,g}\hat{Q}_{c,g}$ are the complex modal amplitudes of the resulting pressure field.

III. OPTIMAL CONTROL SOLUTIONS

The performance functions for minimizing the integrated potential energy, squared pressure, and energy density can be expressed as

$$J_{\mathrm{PE}}=\int_V\frac{|\hat{p}(\mathbf{x})|^2}{4\rho c^2}dV, \tag{11a}$$

$$J_{\mathrm{SP}}=\sum_{i=1}^{I}|\hat{p}(\mathbf{x_i})|^2, \tag{11b}$$

$$J_{\mathrm{ED}}=\sum_{i=1}^{I}\frac{1}{4\rho c^2}|\hat{p}(\mathbf{x_i})|^2+\frac{\rho}{4}|\hat{\mathbf{v}}(\mathbf{x}_i)|^2, \tag{11c}$$

where there are I sensors, located at the positions $\mathbf{x}_i$.

Using Eq. (9), and minimizing Eq. (11a) with respect to the G control source strengths, $\hat{Q}_{c,g}$, yields the optimal source strengths for the integrated potential energy density control strategy. These optimal source strengths are given by

$$\hat{\mathbf{Q}}_{c,\mathrm{PE}}=-(\hat{\mathbf{B}}'^H\hat{\mathbf{B}}')^{-1}\hat{\mathbf{B}}'^H\hat{\mathbf{A}}', \tag{12}$$

where

$$\hat{\mathbf{A}}'\equiv[\hat{A}'_1\quad\cdots\quad\hat{A}'_N\quad\cdots\quad\hat{A}'_\infty]^T, \tag{13}$$

$$\hat{\mathbf{B}}'\equiv\begin{bmatrix}\hat{B}'_{1,1}&\cdots&\hat{B}'_{N,1}&\cdots&\hat{B}'_{\infty,1}\\ \vdots&\ddots&\vdots&\ddots&\vdots\\ \hat{B}'_{1,g}&\cdots&\hat{B}'_{N,g}&\cdots&\hat{B}'_{\infty,g}\\ \vdots&\ddots&\vdots&\ddots&\vdots\\ \hat{B}'_{1,G}&\cdots&\hat{B}'_{N,G}&\cdots&\hat{B}'_{\infty,G}\end{bmatrix}, \tag{14}$$

and

$$\hat{\mathbf{Q}}_{c,\mathrm{PE}}\equiv[\hat{Q}_{c,1},\ldots,\hat{Q}_{c,g},\ldots,\hat{Q}_{c,G}]^T. \tag{15}$$

The elements of $\hat{\mathbf{A}}'$ are related to $\hat{A}_N$ by $\hat{A}'_N=\hat{A}_N\sqrt{V\Lambda_N}$, while the elements of $\hat{\mathbf{B}}'$ are related to $\hat{B}_{N,g}$ by $\hat{B}'_{N,g}=\hat{B}_{N,g}\sqrt{V\Lambda_N}$. The Hermitian transpose is indicated by a superscript H. A single solution exists if the number of control sensors is greater than or equal to the number of control sources. For the special case of a single control source, the complex amplitude of the control source is

$$\hat{Q}_{c,\mathrm{PE}}=-\frac{\Sigma_{N=1}^{\infty}\hat{A}_N\hat{B}_N^*\Lambda_N}{\Sigma_{N=1}^{\infty}\hat{B}_N\hat{B}_N^*\Lambda_N}, \tag{16}$$

where

$$\Lambda_N=\frac{1}{\epsilon_l\epsilon_m\epsilon_n} \tag{17}$$

and

$$\epsilon_i=\begin{cases}1, & \text{if } i=0\\ 2, & \text{if } i\neq 0.\end{cases} \tag{18}$$

Minimizing Eq. (11b) with respect to the G control source strengths, $\hat{Q}_{c,g}$, yields the optimal source strengths for a control system based on the squared pressure. These source strengths are given by

$$\hat{\mathbf{Q}}_{c,\mathrm{SP}}=\hat{\mathbf{C}}^{-1}\hat{\mathbf{D}}, \tag{19}$$

where

$$\hat{\mathbf{Q}}_{c,\mathrm{SP}}=\begin{bmatrix}\Re e\{Q_{c,1}\}\\ \Im m\{Q_{c,1}\}\\ \Re e\{Q_{c,2}\}\\ \Im m\{Q_{c,2}\}\\ \vdots\\ \Re e\{Q_{c,G}\}\\ \Im m\{Q_{c,G}\}\end{bmatrix}, \tag{20}$$

$$\hat{\mathbf{D}}=\begin{bmatrix}-\Sigma_{i=1}^{I}\Sigma_{N=1}^{\infty}\Sigma_{M=1}^{\infty}\Re e\{\hat{B}_{N,1}^{*}\hat{A}_M\}\Psi_N(\mathbf{x_i})\Psi_M(\mathbf{x}_i)\\ \vdots\\ -\Sigma_{i=1}^{I}\Sigma_{N=1}^{\infty}\Sigma_{M=1}^{\infty}\Re e\{\hat{B}_{N,G}^{*}\hat{A}_M\}\Psi_N(\mathbf{x_i})\Psi_M(\mathbf{x}_i)\\ -\Sigma_{i=1}^{I}\Sigma_{N=1}^{\infty}\Sigma_{M=1}^{\infty}\Im m\{\hat{B}_{N,1}^{*}\hat{A}_M\}\Psi_N(\mathbf{x_i})\Psi_M(\mathbf{x}_i)\\ \vdots\\ -\Sigma_{i=1}^{I}\Sigma_{N=1}^{\infty}\Sigma_{M=1}^{\infty}\Im m\{\hat{B}_{N,G}^{*}\hat{A}_M\}\Psi_N(\mathbf{x_i})\Psi_M(\mathbf{x}_i)\end{bmatrix}, \tag{21}$$

$$\hat{\mathbf{C}}^{-1}=\begin{bmatrix}c_{11} & c_{12} & \cdots & c_{1(2G-1)} & c_{1(2G)}\\ \vdots & & \ddots & & \vdots\\ c_{G1} & c_{G2} & \cdots & c_{G(2G-1)} & c_{G(2G)}\\ c_{(G+1)1} & c_{(G+1)2} & \cdots & c_{(G+1)(2G-1)} & c_{(G+1)(2G)}\\ \vdots & & \ddots & & \vdots\\ c_{(2G)1} & c_{(2G)2} & \cdots & c_{(2G)(2G-1)} & c_{(2G)(2G)}\end{bmatrix} \tag{22}$$

and

$$c_{p(2q-1)}=\sum_{i=1}^{I}\sum_{N=1}^{\infty}\sum_{M=1}^{\infty}\Re e\{\hat{B}_{N,p}^{*}\hat{B}_{M,q}\}\Psi_N(\mathbf{x}_i)\Psi_M(\mathbf{x}_i),$$

$$c_{p(2q)}=-\sum_{i=1}^{I}\sum_{N=1}^{\infty}\sum_{M=1}^{\infty}\Im m\{\hat{B}_{N,p}^{*}\hat{B}_{M,q}\}\Psi_N(\mathbf{x}_i)\Psi_M(\mathbf{x}_i),$$

$$c_{(G+p)(2q-1)}=\sum_{i=1}^{I}\sum_{N=1}^{\infty}\sum_{M=1}^{\infty}\Im m\{\hat{B}_{N,p}^{*}\hat{B}_{M,q}\}\Psi_N(\mathbf{x}_i)\Psi_M(\mathbf{x}_i),$$

$$c_{(G+p)(2q)}=\sum_{i=1}^{I}\sum_{N=1}^{\infty}\sum_{M=1}^{\infty}\Re e\{\hat{B}_{N,p}^{*}\hat{B}_{M,q}\}\Psi_N(\mathbf{x}_i)\Psi_M(\mathbf{x}_i), \tag{23}$$

where p and q are integers ranging from 1 to G. Again, a single solution exists if the number of control sensors is greater than or equal to the number of control sources. For the special case of a single control source, the complex amplitude of the control source is given by

$$\hat{Q}_{c,\mathrm{SP}}=-\frac{\Sigma_{i=1}^{I}\Sigma_{N=1}^{\infty}\Sigma_{M=1}^{\infty}\hat{A}_N\Psi_N(\mathbf{x}_i)\Psi_M(\mathbf{x}_i)}{\Sigma_{i=1}^{I}\Sigma_{N=1}^{\infty}\Sigma_{M=1}^{\infty}\hat{B}_N\Psi_N(\mathbf{x}_i)\Psi_M(\mathbf{x}_i)}. \tag{24}$$

Minimizing Eq. (11c) with respect to the G control source strengths $\hat{Q}_{c,g}$ yields the same solutions defined in Eqs. (19)–(23), where the function $\Psi_N(\mathbf{x}_i)\Psi_M(\mathbf{x}_i)$ is replaced by $F_{NM}(\mathbf{x}_i)$. These are the optimal source strengths when employing the energy density control. The function $F_{NM}(\mathbf{x}_i)$ is defined by

$$F_{NM}(\mathbf{x}_i)\equiv\Psi_N(\mathbf{x}_i)\Psi_M(\mathbf{x}_i)+\frac{\nabla\Psi_N(\mathbf{x}_i)\nabla\Psi_M(\mathbf{x}_i)}{k^2}. \tag{25}$$

For the special case of a single control source, the complex amplitude of the control source is given by

$$\hat{Q}_{c,\mathrm{ED}}=-\frac{\Sigma_{i=1}^{I}\Sigma_{N=1}^{\infty}\Sigma_{M=1}^{\infty}\hat{A}_N F_{NM}(\mathbf{x}_i)}{\Sigma_{i=1}^{I}\Sigma_{N=1}^{\infty}\Sigma_{M=1}^{\infty}\hat{B}_N F_{NM}(\mathbf{x}_i)}. \tag{26}$$

IV. CONTROL IMPLEMENTATION

The pressure as well as the three components of vector velocity are needed to implement the energy density control, as indicated by Eq. (3). Single-element velocity sensors, such as gradient microphones, do not have the accuracy and response needed in the frequency range of interest. To determine the acoustic velocity along an axis, two pressure microphones can be used.

Euler's equation in one dimension relates the gradient of the pressure to the time derivative of the velocity at a given point through the relation

$$\rho\frac{\partial v_x(x,t)}{\partial t}=-\frac{\partial p(x,t)}{\partial x}, \tag{27}$$

which can be rewritten as

$$v_x(x,t)=-\frac{1}{\rho}\int_{-\infty}^{t}\frac{\partial p(x,\tau)}{\partial x}d\tau. \tag{28}$$

Equation (28) can be approximated as

$$v_x(x,t)\approx-\frac{1}{\rho}\int_{-\infty}^{t}\frac{p_2(\tau)-p_1(\tau)}{\Delta x}d\tau, \tag{29}$$

where $p_2(t)$ and $p_1(t)$ are the pressures measured by two microphones separated by a distance Δx.[7] Hence, the velocity can be estimated by integrating the difference between the outputs of two pressure microphones separated in space. The integration can be performed using analog electronics, but was implemented digitally in the control processor. An inexpensive energy density sensor was developed for this project, and its characteristics are explained in a recently submitted paper.[8] The sensor employs six electret microphones mounted on the surface of a 1-in. (0.0254-m) radius wooden sphere. The errors associated with the energy density sensor were found to be minimal (within ± 1.75 dB) for the frequencies used in the active control experiments presented here.

The energy density control algorithm is a filtered-x LMS-based algorithm and takes the following form:

$$w_i(n+1)=w_i(n)-\mu\rho c v_x(n)r_{vx}(n-i)$$
$$-\mu\rho c v_y(n)r_{vy}(n-i)-\mu\rho c v_z(n)r_{vz}(n-i)$$
$$-\mu p(n)r_p(n-i), \tag{30}$$

where $w_i(n)$ is the ith coefficient of the control filter at discrete time n, μ is a convergence parameter, v indicates the velocity components, r indicates the filtered reference signals, and $p(n)$ is the pressure at time n. For v, the subscripts x, y, and z indicate the direction of the velocity component, and for r, the subscripts indicate the signal being filtered (either pressure or the velocity components). This algorithm is based on updating the coefficients according to the negative gradient of the energy density. As such, it is only necessary to measure the pressure and velocity components and not the energy density itself. The squared pressure-control algorithm is also a filtered-x LMS-based algorithm and takes the form

$$w_i(n+1)=w_i(n)-\mu p(n)r_p(n-i). \tag{31}$$

Equations for multiple channel squared pressure and energy density control can be found in Ref. 9.

A transfer function must be estimated between the source and the pressure measurement as well as from the source to each of the three velocity measurements, for energy density control. For the squared pressure control, only the transfer function from the source to the pressure sensor is needed. The transfer functions were estimated passively and on-line using the techniques presented by Sommerfeldt and Tichy.[10] The control algorithms were implemented using a Spectrum DSP96002 digital signal-processing card.

A schematic of the control system is shown in Fig. 1. In this experimental configuration, three control sensors and three control sources are employed. The noise excitation signal is used as a reference and is filtered by three adaptive filters, $W1(z)-W3(z)$, to control the field produced by the noise source. For the squared pressure system, each sensor outputs a single time-domain pressure signal to the controller. For the energy density system, each sensor outputs six time-domain pressure signals to the controller. Two of these signals are used for each direction to estimate the velocity component, and the average of the six signals is used to estimate the pressure.

V. SQUARED PRESSURE AND ENERGY DENSITY FIELD NODES

The normalized squared pressure and normalized energy density fields for the (l,m,n) mode are described by

$$p_n^2(\mathbf{x})=\cos^2 k_x x \cos^2 k_y y \cos^2 k_z z, \tag{32a}$$

$$e_n(\mathbf{x})=\frac{1}{k^2}(k_x^2\cos^2 k_y y \cos^2 k_z z+k_y^2\cos^2 k_x x \cos^2 k_z z$$
$$+k_z^2\cos^2 k_x x \cos^2 k_y y). \tag{32b}$$

The locations of the nodes of these fields are determined by setting Eqs. (32) to zero. Therefore, the squared pressure field has nodes where $\cos k_x x$, $\cos k_y y$, or $\cos k_z z$ are zero. These nodes are located at

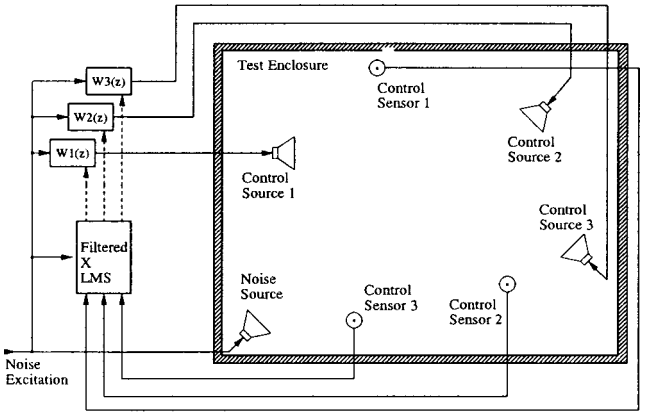

FIG. 1. Schematic of active control system.

$$x=\frac{\pi}{k_x}\left(\frac{2h+1}{2}\right),\quad 0\leqslant x\leqslant L_x,\quad h=0,1,2...,$$
$$y=\frac{\pi}{k_y}\left(\frac{2i+1}{2}\right),\quad 0\leqslant y\leqslant L_y,\quad i=0,1,2..., \tag{33}$$
$$z=\frac{\pi}{k_z}\left(\frac{2j+1}{2}\right),\quad 0\leqslant z\leqslant L_z,\quad j=0,1,2...,$$

which define nodal planes. There are l planes perpendicular to the x axis, m planes perpendicular to the y axis, and n planes perpendicular to the z axis for an (l,m,n) mode. Nodes for the energy density field, on the other hand, exist only when all three terms of Eq. (32b) are zero. This only occurs where the nodal planes of the squared pressure field intersect. Thus, the nodes of the energy density field exist as lines and there are no nodes in the energy density field for axial modes.

A volume velocity source, such as a loudspeaker, can generate a given mode if it is not located on a pressure node. Pressure sensors and energy density sensors can sense a given mode if they are not located on their respective nodes. Energy density sensors are statistically more likely to observe modes compared to pressure sensors, since the energy density field nodes are one-dimensional compared to the two-dimensional squared pressure-field nodes. Pressure fields composed of many modes will also have more regions of minima than energy density fields. A detailed discussion of energy density field nodes is presented in Ref. 11.

VI. THE TEST ENCLOSURE

The enclosure used for all the active control experiments measures $1.5\times2.4\times1.9$ m, and is shown in Fig. 2. Three Bose 101 speakers and one energy density sensor can be seen in this experimental configuration. The noise source speaker is mounted to the ceiling in the upper left corner of the enclosure, while two control source speakers are located on stands on the floor. The energy density sensor (the small light-colored sphere) can be seen on a microphone boom between the control sources. A scanning measurement system comprising slides, motors, cables, and a microphone array is also seen in the photograph.

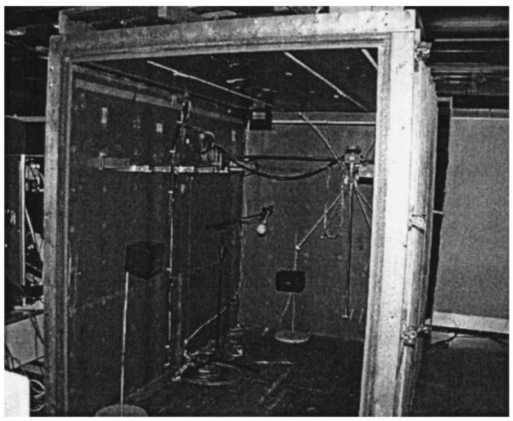

FIG. 2. Interior of enclosure used in active control experiments.

The walls of the enclosure consist of a $3\frac{3}{8}$-in.-thick layer of sand sandwiched between a $\frac{3}{8}$-in. chipboard layer (exterior surface) and a 2-in. particle-board layer (interior surface). Two-by-four bracing separates the particle board from the chipboard, and the sand fills the gap. The floor of the enclosure, which is isolated from the laboratory floor, does not have the sand or chipboard layers. The front wall of the enclosure is mounted on a structure with casters, and clamps into place. The enclosure has a very low transmission coefficient, and is therefore highly reverberant and relatively immune to external noise.

A simple method was used to determine the resonance frequencies of the enclosure. The enclosure was excited by bursts of random noise transmitted through the noise source. Measurements from a microphone located in the opposite corner were collected between excitations, and the spectra were averaged. The measurement therefore averaged energy due to the reverberant decay of the enclosure and not due to the forced signal. The reverberation power spectrum was normalized by the speaker response, and yielded the power spectrum shown in Fig. 3. The peaks in the power spectrum correspond to the resonances of the enclosure and are listed in Table I along with those predicted by theory. The predicted frequencies were calculated from Eq. (7). The difference between the experimental and predicted frequencies are also listed in Table I. All the measured resonances are shifted slightly higher than those predicted, which is likely due to finite vibrations of the walls.

Reverberation times of the enclosure were measured three times at three resonance frequencies: 73.25, 92.25, and 228.5 Hz, by measuring the time-domain energy decay slope. These resonance frequencies correspond to modes (0,1,0), (0, 0,1), and (2,0,0), respectively. The reverberation times are shown in Table II.

VII. COMPUTER MODEL

A computer program written in MATLAB™ was developed for this research to predict the results of active noise control in a rectangular enclosure. The program implements the equations of the previous sections using the approach developed by Nelson and Elliott,[12] with the optimal source strengths defined in Eqs. (12), (19), and (25).

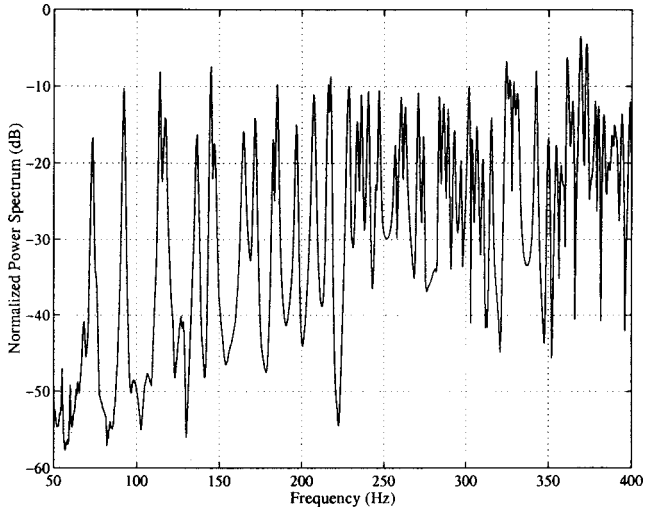

FIG. 3. Enclosure reverberation power spectrum, normalized by excitation speaker response.

The absorption coefficients of the enclosure walls were also required by the computer model. The absorption coefficients, α_*, are related to the mode indices, *l*, *m*, and *n*, and reverberation times, $T_{60,N}$, by the equation

$$\frac{\epsilon_l \alpha_x}{L_x} + \frac{\epsilon_m \alpha_y}{L_y} + \frac{\epsilon_n \alpha_z}{L_z} = \frac{55.28}{cT_{60,N}}. \tag{34}$$

The reverberation times measured for three modes yield three equations. The three equations were solved simultaneously for the absorption coefficients, and were determined to be $\alpha_x = 0.0479$, $\alpha_y = 0.0313$, and $\alpha_z = 0.0730$. Each of these absorption coefficients is an average for a pair of opposing surfaces perpendicular to the indicated axis. The absorption coefficient for the floor and ceiling, $\alpha_z = 0.0730$, was higher than that of the walls because the floor has much less mass than the walls, and therefore a higher transmission coefficient. Wall vibration was also taken into account, to some degree, in the program by modifying the enclosure dimensions as a function of frequency.[9]

It was determined experimentally that the sum of 80 modes accurately described the acoustic fields encountered. The contributions of the higher-order modes were minimal for the excitation frequencies used in the experiments. Thus, 80 modes were used in the numerical simulations. The 80 modes consisted of all mode combinations up to mode (3, 3, 4), consistent with the modal decomposition method described in the following section.

VIII. THE ACOUSTIC MEASUREMENT SYSTEM

The acoustic field measurement system acquires samples of the pressure within the enclosure at regular intervals in space. This is accomplished using an eight-channel microphone array seen in the right half of Fig. 2. The array is moved throughout the enclosure using three stepper motors and slides—one for each axis—controlled by a LABVIEW™ program. The use of the array allows samples to be collected at hard-to-reach locations, such as in the corners of the en-

TABLE I. Predicted and experimental resonance frequencies.

Mode No.	l	m	n	Predicted frequency (Hz)	Experimental frequency (Hz)	Difference frequency (Hz)
1	0	0	0	0	NA	NA
2	0	1	0	71.82	73.25	1.43
3	0	0	1	90.64	92.25	1.61
4	1	0	0	113.50	114.00	0.50
5	0	1	1	115.65	117.25	1.60
6	1	1	0	134.31	136.25	1.94
7	0	2	0	143.63	144.75	1.12
8	1	0	1	145.25	147.00	1.75
9	1	1	1	162.04	164.5	2.46
10	0	2	1	169.85	171.75	1.90
11	0	0	2	181.29	182.75	1.46
12	1	2	0	183.07	185.00	1.93
13	0	1	2	195.50	196.50	1.50
14	1	2	1	204.28	207.00	2.72
15	1	0	2	213.89	216.00	2.11

closure. A ninth microphone is located in a corner of the test enclosure, in order to calculate transfer functions and complex pressures.

Low-resolution scanning samples the field throughout the enclosure, while high-resolution scanning samples the field only in the $z/L_z = 0.21$ plane. There is a total of 576 low-resolution data acquisition points, forming an $8 \times 8 \times 9$ grid, where the grid spacings are $\Delta x = 0.19$ m, $\Delta y = 0.30$ m, and $\Delta z = 0.21$ m. The high-resolution scan consists of 21×19 grid points, where the grid spacings are $\Delta x = 0.071$ m and $\Delta y = 0.119$ m. For single-frequency excitation of the enclosure, both the magnitude and phase of the pressures were recorded. For broadband excitation, the flat-weighted rms pressures were recorded. The low-resolution data were also used to determine the total potential energy in the enclosure using the equation

$$U_{\text{tot}} = \frac{1}{4\rho c^2} \sum_{i=1}^{576} |\hat{p}(\mathbf{x}_i)|^2. \tag{35}$$

The sample intervals are small enough for the low-resolution data that the pressure field data can be decomposed into their complex modal amplitudes. The Nth axial mode spans N half-wavelengths in the enclosure. Therefore, the eighth axial mode in the x and y directions and the ninth axial mode in the z direction can be resolved, according to the Nyquist criterion. To be conservative, the modes were decomposed up to the third mode in the x and y directions, and the fourth mode in the z direction in these experiments. Thus, the worst case spatial sampling was 5.3 points per wavelength in the x and y directions, and 4.5 points per wavelength in the z direction. The highest mode resolved was the (3,3,4) mode, which corresponds to a frequency of over 540 Hz. The contributions of higher modes were low enough that antialiasing filters were not necessary when calculating the modal amplitudes.

TABLE II. Measured reverberation times for individual modes.

Mode No.	l	m	n	Frequency (Hz)	T_{60} (s)
2	0	1	0	73.25	1.67
3	0	0	1	92.25	1.32
18	2	0	0	228.50	1.40

The pressure fields were decomposed using the fact that the homogeneous wave equation within the enclosure forms a proper Sturm–Liouville system, and that the eigenfunctions are orthogonal.[13] The pressure field, defined in Eq. (10), is multiplied by the eigenfunctions and integrated over the enclosure to yield the equation

$$\Upsilon = \int_0^{L_x} \int_0^{L_y} \int_0^{L_z} \sum_{N=1}^{\infty} \hat{C}_N \Psi_N(\mathbf{x}) \Psi_M(\mathbf{x}) dx\, dy\, dz. \tag{36}$$

The integral becomes zero when $M \neq N$, while the integral yields $\hat{C}_N V \Lambda_N$ if $M = N$. Therefore, the complex modal amplitudes can be found using the equation

$$\hat{C}_N = \frac{\Upsilon}{V \Lambda_N}, \tag{37}$$

where V is the enclosure volume. The complex pressure is only measured at discrete points; hence, the complex modal amplitudes are determined by using a discrete form of Eq. (36) to yield

$$\hat{C}_N = \frac{\Delta V}{V \Lambda_N} \sum_{i=1}^{8} \sum_{j=1}^{8} \sum_{k=1}^{9} |\hat{p}(\mathbf{x}_{i,j,k})| (\cos \angle \hat{p}(\mathbf{x}_{i,j,k}) + j \sin \angle \hat{p}(\mathbf{x}_{i,j,k})) \Psi_N(\mathbf{x}_{i,j,k}), \tag{38}$$

where $\Delta V = \Delta x \Delta y \Delta z$, and $\angle \hat{p}(\mathbf{x}_{i,j,k})$ indicates the phase of the complex pressure signal. The complex pressure, $\hat{p}(\mathbf{x})$, is sampled and the eigenfunction, $\Psi_N(\mathbf{x})$, is evaluated at the point $\mathbf{x}_{i,j,k} = (x_i, y_j, z_k)$.

IX. PREDICTED AND EXPERIMENTAL ACTIVE CONTROL RESULTS

Various active control experiments were conducted in the course of this research. One broadband and three narrowband experiments are presented here. Single-frequency excitation was used in the narrowband experiments, while band-limited pink-noise excitation was used in the broadband experiment. The noise source excitation signals along with the dominant modes stimulated are listed in Table III. For the first two experiments, an excitation frequency near a resonance was used. In control configuration three, the room was excited at a frequency between resonances, and many modes were stimulated, while the enclosure was excited with band-limited pink noise in configuration four.

Up to three speakers distributed in the enclosure were used as control sources, while up to three control sensors were employed for each experiment. In each experiment, the same control source/sensor configuration was used for both the squared pressure and energy density control methods. The locations of the control sources and sensors are listed in Table III where the coordinates are normalized by the enclosure dimensions. The enclosure is defined in space by a corner at (0,0,0) and another at (1,1,1). A single loudspeaker serving as the noise source was always located at (0.12, 0.97, 0.97).

TABLE III. Predicted and experimental active control results.

Control configuration				Predicted cancellation (dB)			Experimental cancellation (dB)	
No.	Excitation (mode)	Control sources	Control sensors	PE	SP	ED	SP	ED
1	171.5 Hz (0,2,1)	(0.05, 0.11, 0.04)	(0.34, 0.67, 0.24)	7.9	6.4	7.9	6.7	7.1
2	171.5 Hz (0,2,1)	(0.05, 0.11, 0.04) (0.34, 0.96, 0.04) (0.77, 0.97, 0.43)	(0.34, 0.67, 0.24) (0.68, 0.40, 0.49) (0.14, 0.15, 0.71)	16.1	−6.6	15.8	−2.5	14.4
3	130.0 Hz (many)	(0.05, 0.11, 0.04) (0.34, 0.96, 0.04) (0.77, 0.97, 0.43)	(0.34, 0.67, 0.24) (0.68, 0.40, 0.49) (0.14, 0.15, 0.71)	2.9	−4.8	1.5	−1.2	2.5
4	Pink noise	(0.05, 0.11, 0.04)	(0.32, 0.05, 0.50)	NA	NA	NA	1.8	3.8

The predicted and experimental cancellation results are also listed in Table III. The cancellation is defined as the difference in total potential energy between the uncontrolled and controlled fields, as determined from Eq. (35). Cancellation for the predicted and experimental squared-pressure control (SP) and energy density control (ED) are also listed in Table III. Only the predicted integrated potential energy density control (PE) cancellation is presented, since this control method cannot be implemented experimentally. The predicted integrated potential energy density control results are considered optimal, and are used as a baseline for comparing the other two control methods. Various data relating to these experiments are discussed below.

A. Single-frequency control

For the single-frequency excitation experiments, low-resolution and high-resolution data were collected. The low-resolution data were used to determine the total potential energy in the enclosure, as well as to calculate the complex modal amplitudes, $\hat{C}_N$, of the decomposed pressure fields. For each experiment, the magnitudes of the first 40 modes are plotted for the predicted and experimental results using the equation

$$\text{Magnitude (dB)} = 20 \log|\hat{C}_N|. \tag{39}$$

Predicted results comprise the integrated potential energy density, squared pressure, energy density, and uncontrolled cases. The magnitudes of the experimentally determined complex modal amplitudes are plotted below the predicted results. High-resolution sound-pressure-level data in the $z/L_z = 0.21$ plane are plotted in the figures, following the modal magnitude data for each experiment. The sound-pressure level L_p is found from

$$L_p\,(\text{dB}) = 20 \log(p_{\text{rms}}/p_{\text{ref}}), \tag{40}$$

where p_{rms} is the measured pressure and $p_{\text{ref}} = 20\,\mu\text{Pa}$. Again, predicted results are plotted at the top half of the figure, with the experimental results presented in subfigures below them.

1. 171.5-Hz on-resonance control

Two experiments are presented where 171.5 Hz was the excitation frequency. In general, the experimental results for these two control configurations, seen in Figs. 4–7, are consistent with the predictions. The magnitudes of the complex modal amplitudes match fairly well for the dominant modes, while the predicted and experimental pressure fields have similar contours. The cancellation performance achieved experimentally is also consistent with the predictions, as seen in Table III.

In Figs. 4(a) and 4(e), 6(a) and 6(e), the magnitudes of the modes of the predicted and experimental uncontrolled pressure fields are plotted. The excitation frequency is very close to the resonance frequency of 171.75 Hz, corresponding to the tenth mode (0,2,1). The tenth mode is dominant in the two plots, followed by the ninth mode (1,1,1). The magnitudes of the tenth and ninth modes are consistent between those predicted and measured, though two mode magnitudes vary considerably between the predicted and measured results. The experimental results show the fifth and 20th modes to have substantially higher amplitudes than the prediction, which may be due to finite wall vibration.

It was expected that control configuration 1 would yield only fair cancellation for both the energy density and squared pressure control, since the control source is not in a desirable location. Either the ninth or tenth mode produced by the control source will be out of phase with the modes produced by the noise source, but not both. The control sensor, on the other hand, is located in a desirable position. It can observe both the ninth and tenth modes since it is not located near pressure or energy density nodes for these two modes. The pressure-field nodal planes for the tenth mode are located at $y/L_y = 0.25$, $y/L_y = 0.75$, and $z/L_z = 0.5$, while the pressure field nodal planes for the ninth mode are located at $x/L_x = 0.5$, $y/L_y = 0.5$, and $z/L_z = 0.5$. The energy density nodal lines are located at the intersections of these planes.

The predicted and experimental mode magnitudes for configuration 1 generally follow the same trends for the squared pressure and energy density control methods shown in Fig. 4. The mode magnitudes for the energy density control are also very close to those predicted for the optimal control. The pressure fields shown in Fig. 5 are quite consistent between the predicted and experimental results. The predicted and experimental results for the energy density control method are also very similar to the optimal solution, indicating that the energy density control solution yielded nearly the

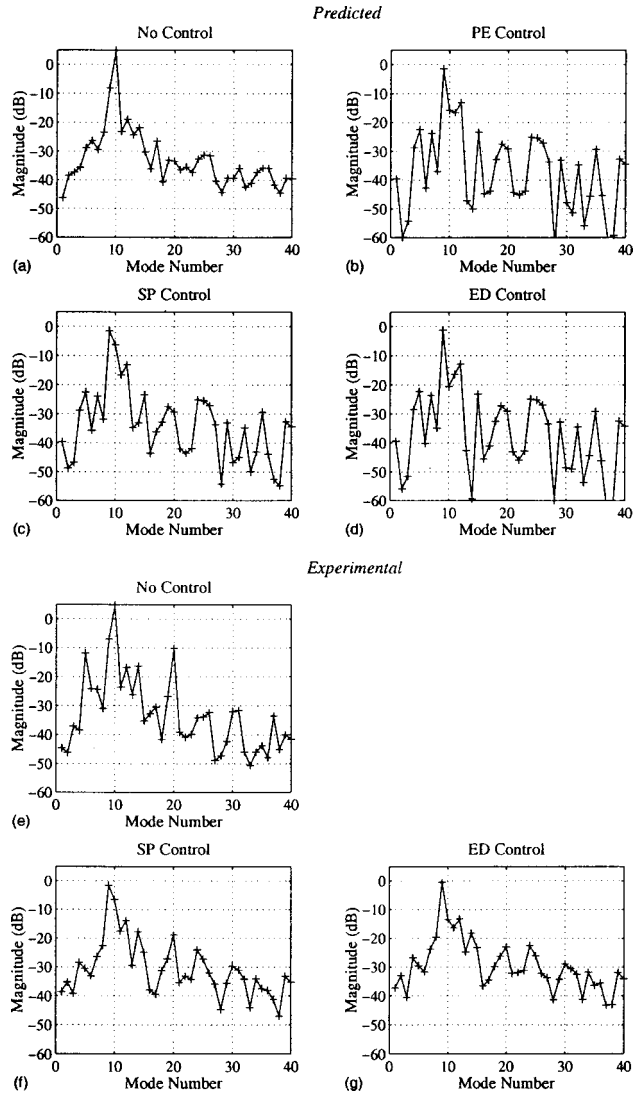

FIG. 4. Control configuration 1. Predicted and experimental mode magnitudes. 171.5 Hz, mode (0,2,1) excitation.

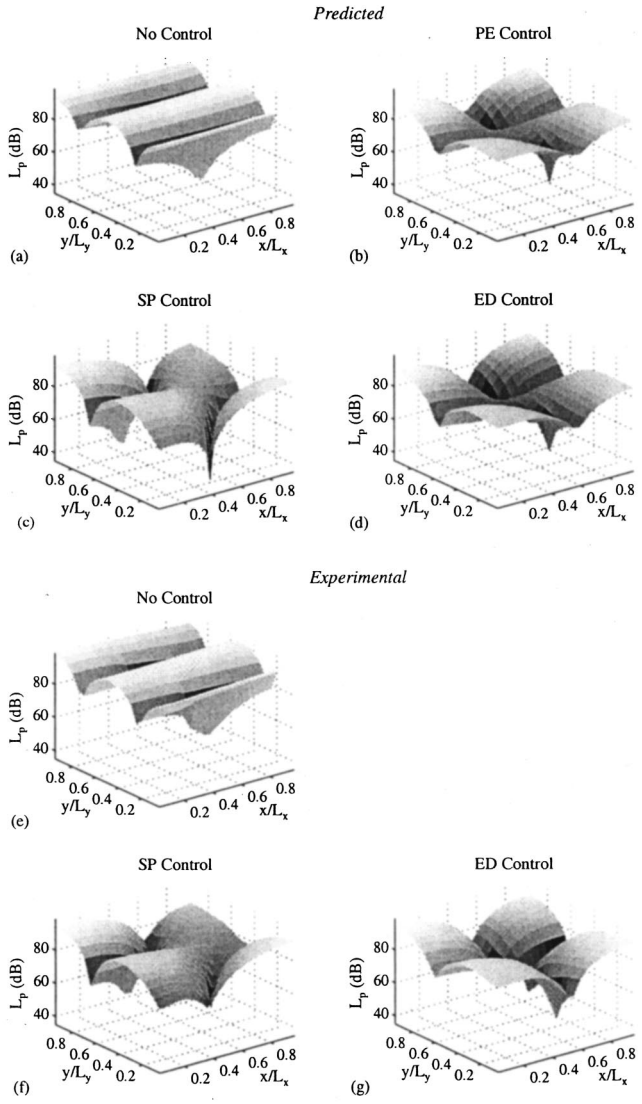

FIG. 5. Control configuration 1. Predicted and experimental sound-pressure distributions for the $z/L_z = 0.21$ plane. 171.5 Hz, mode (0,2,1) excitation.

optimal control. Cancellation predictions, in Table III, are within 0.8 dB for both measured control methods.

Three control sources and three error sensors were used in configuration 2, while the excitation frequency was again 171.75 Hz. The second control sensor is located very close to the ninth and tenth mode pressure-field nodes. Thus, this sensor is not effective at sensing these two modes in the pressure field. The third sensor is located at a good position for both the energy density and pressure fields. The second control source is located at a desirable location since it is able to produce both the tenth and ninth modes out of phase with the noise source. The third source is located near the pressure node $z/L_z = 0.5$, and therefore will tend to produce a field with minimal contribution from the ninth and tenth modes. Therefore, this source will be ineffective at controlling the ninth or tenth modes.

It can be seen in Table III and Figs. 6 and 7 that the squared pressure control increases the total potential energy in the enclosure, while the energy density control achieves significant cancellation. In both the predicted and experimental squared pressure-control mode amplitude results, seen in Figs. 6(c) and 6(f), the ninth and tenth modes have equal amplitude. The magnitude of the ninth mode has significantly increased, causing an increase in the overall potential energy in the enclosure. On the other hand, the ninth and tenth modes have been significantly reduced for the case of energy density control, seen in Figs. 6(d) and 6(g) and there is no dominant mode as a result. The pressure-field contours for the energy density control, seen in Figs. 7(d) and 6(g), are therefore fairly complicated, though there is still some general agreement between the predicted and experimental results. The energy density control results match the optimal control results more closely than the squared pressure results in general for this configuration.

2. Off-resonance control

In configuration 3, three sources and sensors are used to control a field generated by a 130-Hz tone. Controlling fields generated by frequencies between resonances—as in configuration 3—is difficult, due to the control source(s) inability to create the complex pressure field produced by the noise

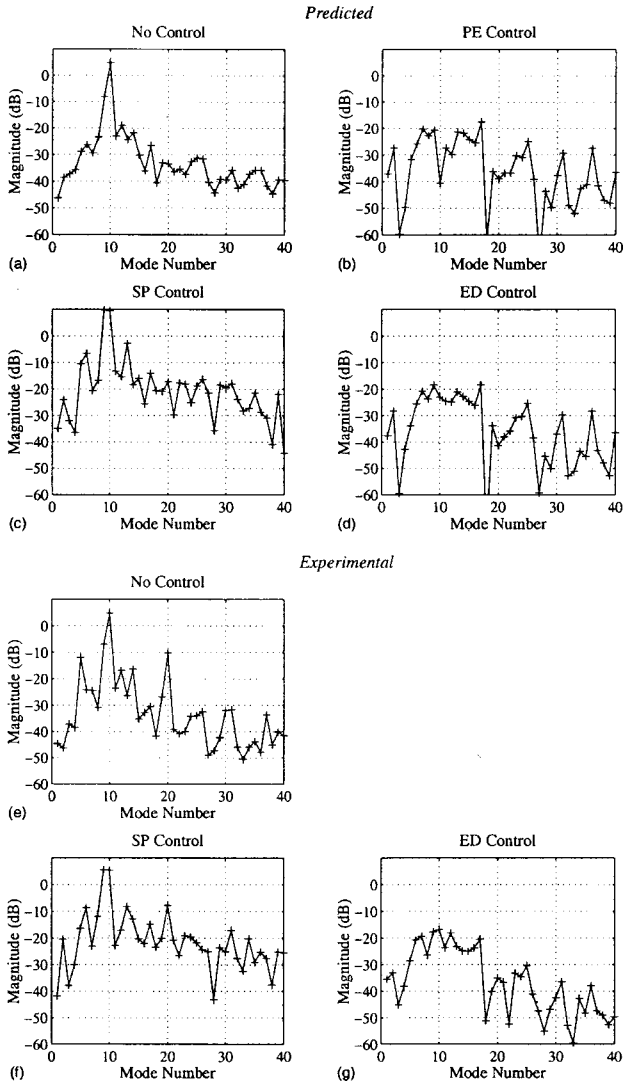

FIG. 6. Control configuration 2. Predicted and experimental mode magnitudes. 171.5 Hz, mode (0,2,1) excitation.

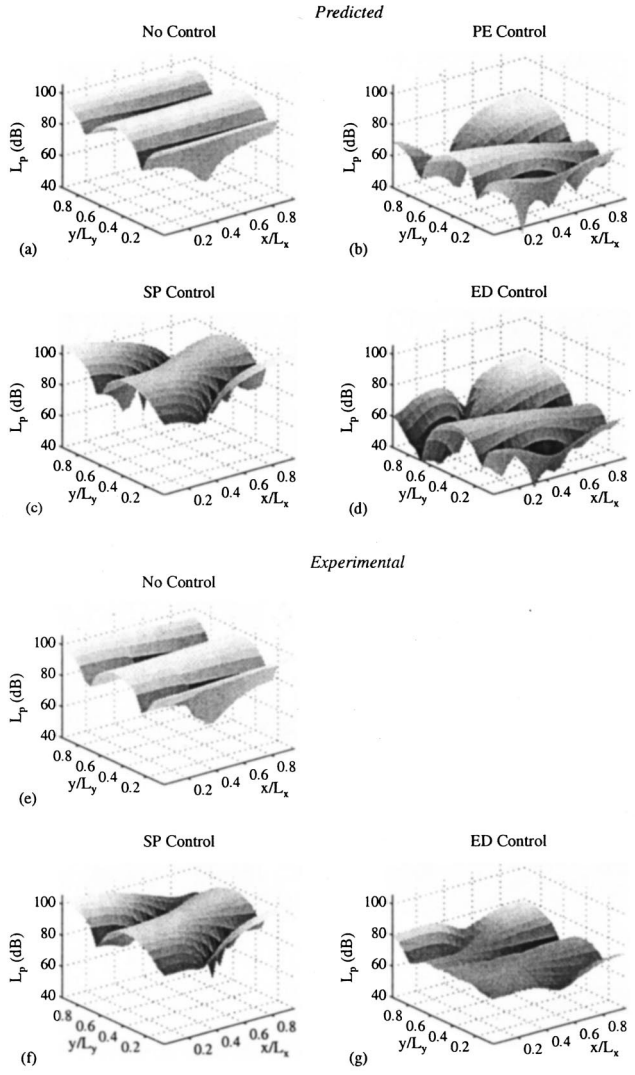

FIG. 7. Control configuration 2. Predicted and experimental sound-pressure distributions for the $z/L_z = 0.21$ plane. 171.5 Hz, mode (0,2,1) excitation.

source. Many modes must be generated with the correct phase relationships when controlling these fields. The excitation frequency is between the fifth mode (0,1,1) frequency at 117.25 Hz and the sixth mode (1,1,0) frequency at 136.25 Hz. Hence, nearby modes are excited by the noise source. The fifth, sixth, eighth, and ninth modes are all within 10 dB of each other, and are the dominant modes seen in Fig. 8(a) for the uncontrolled field.

Though many modes contribute to the fields encountered in this configuration, the results show the same trends. The predicted and experimental cancellation for the squared pressure and energy density control, shown in Table III, both indicate the squared pressure control increasing the total potential energy in the enclosure, while the energy density control reduces the total potential energy. The results for the measured uncontrolled field and the energy density controlled field are consistent with those predicted in Figs. 9(a) 9(d), 9(e), and 9(g), though the measured energy density field is offset in overall magnitude in the pressure-field plot. In this configuration, neither the squared pressure nor the energy density control yields the optimal solution, though the energy density control mode magnitudes more closely resemble the optimal control mode magnitude results. The squared pressure-controlled fields, in Figs. 9(c) and 9(f) and mode magnitude plots, in Figs. 8(c) and 8(f) also show similar trends. Even though this control configuration was relatively complex, due to off-resonance excitation and multiple source/sensors, the computer model was able to predict the results with reasonable accuracy.

B. Broadband control

A single broadband control experiment, configuration 4, is presented here. Pink noise was filtered through a fourth-order 100-Hz Butterworth low-pass filter for excitation of the enclosure. A single control source and a single control sensor were used. The control sensor was positioned closer to the control source than to the noise source, since the control algorithm needs time to filter the reference signal. This delay plus the delay from the control source to the sensor must be less than the delay from the noise source to the sensor, or else the control signal will lag behind the signal to be canceled.[13,14]

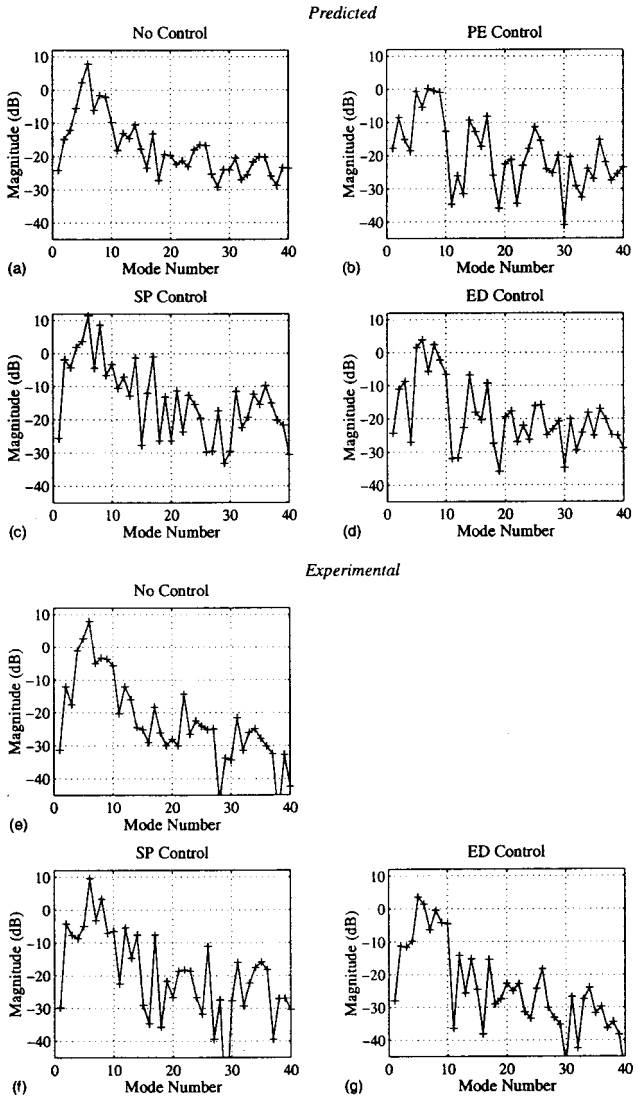

FIG. 8. Control configuration 3. Predicted and experimental mode magnitudes. 130 Hz, off-resonance excitation.

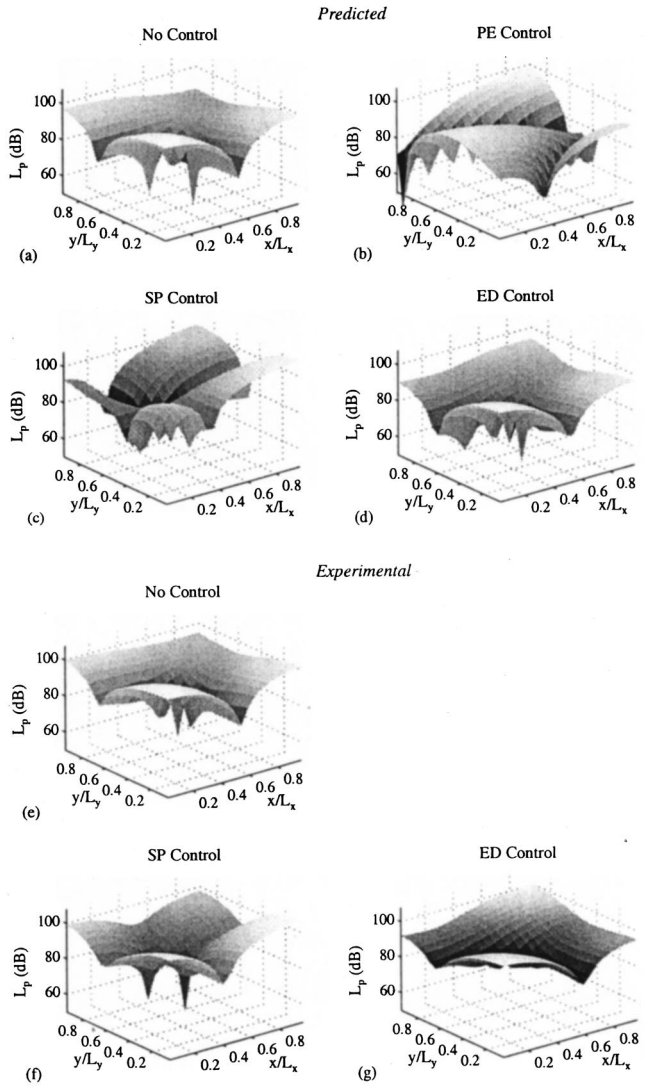

FIG. 9. Control configuration 3. Predicted and experimental sound-pressure distributions for the $z/L_z=0.21$ plane. 130 Hz, off-resonance excitation.

The low-resolution data were used to calculate the total potential energy in the enclosure, by measuring the rms sound-pressure level at each sample point. The sound fields were not decomposed into their modes since complex pressure data, at each point in space, were not measured for the random excitation. (A transfer function would have been required for each point in space to perform modal decomposition, and would have resulted in 576 transfer functions to process for each field.) High-resolution sound-pressure-level data in the $z/L_z=0.21$ plane were collected and are presented in Fig. 10. Power spectra at the control sensor and at a reference microphone in a corner of the enclosure are presented in Figs. 11 and 12 for the uncontrolled and controlled fields. No simulations were run to predict the performance of the broadband control.

The sensor, located at (0.32,0.05,0.50), will not observe modes having a pressure node at $z/L_z=0.50$, when using squared pressure control. These modes are mode three (92.25 Hz), mode five (117.25 Hz), mode eight (147 Hz), mode nine (164.5 Hz), and so on. Hence, the control performance at these frequencies is unpredictable for the squared pressure-control method. The control source, located at (0.05, 0.11, 0.04), is near a corner of the enclosure and is in a generally desirable position.

The pressure field for the energy density control method is lower overall compared to the pressure field for the squared pressure-control method, shown in Fig. 10. This is reflected in the measured reduction in total potential energy, where the energy density control method yielded 3.8 dB of cancellation while the squared pressure-control method yielded 1.8 dB. The shapes of the controlled pressure fields are similar in shape and no longer have the (0,1,0) mode contour of the uncontrolled field.

In Fig. 11, it can be seen that the measurement microphone, which is at the sensor location, is virtually not observing the pressure from the 92.25-Hz energy in the field. This is due to the associated mode of this frequency having a pressure node at the sensor location. The two control methods yield cancellation spectra that are similar, yet with an important difference. Both the squared pressure and energy density control methods reduce the power spectra in the frequency regions around mode two, mode four, and mode five,

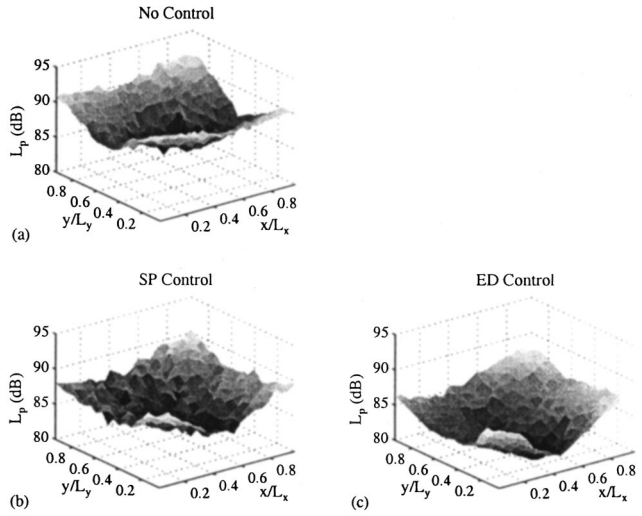

FIG. 10. Control configuration 4. Experimental sound-pressure distributions for the $z/L_z=0.21$ plane. Pink noise excitation.

and both the control methods are ineffective above approximately 125 Hz. On the other hand, there is a dip in the spectrum for the energy density control method at 92.25 Hz not seen in the squared pressure-control plot.

Though the microphone at the sensor did not measure substantial energy at 92.25 Hz, the reference microphone observes all modes in the enclosure, and a peak is seen at this frequency in Fig. 12 for the uncontrolled field. The response is also seen to have increased at 117.25, 147, and 164.5 Hz. In Fig. 12, it is easier to see that the energy density control method is reducing the energy in the enclosure at 92.25 Hz, while the squared pressure-control method is ineffective. Greater cancellation is also achieved at 117.25 Hz and 136.25 Hz for the energy density control method compared to the squared pressure-control method, though the performance is slightly worse around 147 Hz. Due to the greater ability of the error sensor to observe modes, the energy density control method is superior to the squared pressure-control method for this broadband excitation experiment.

X. CONCLUSIONS

The goal of this research was to investigate the efficacy of an active control system based on minimizing the sum of the total energy densities at discrete points in space for reducing the acoustic pressure field in a three-dimensional enclosure. To achieve this end, a numerical model was used to predict, and a physical system was constructed to measure, the performance of this active control system. The optimal solution for the energy density control method was determined for use in a computer program. To gauge its benefits, the total energy density control system was compared to the relatively common active control system based on minimizing the sum of the squared pressures at points in space. The squared pressure-control system was also modeled numerically and implemented physically. Both systems were compared to the predicted results of minimizing the integrated potential energy density, which is considered the optimal control method. A measurement system was also constructed

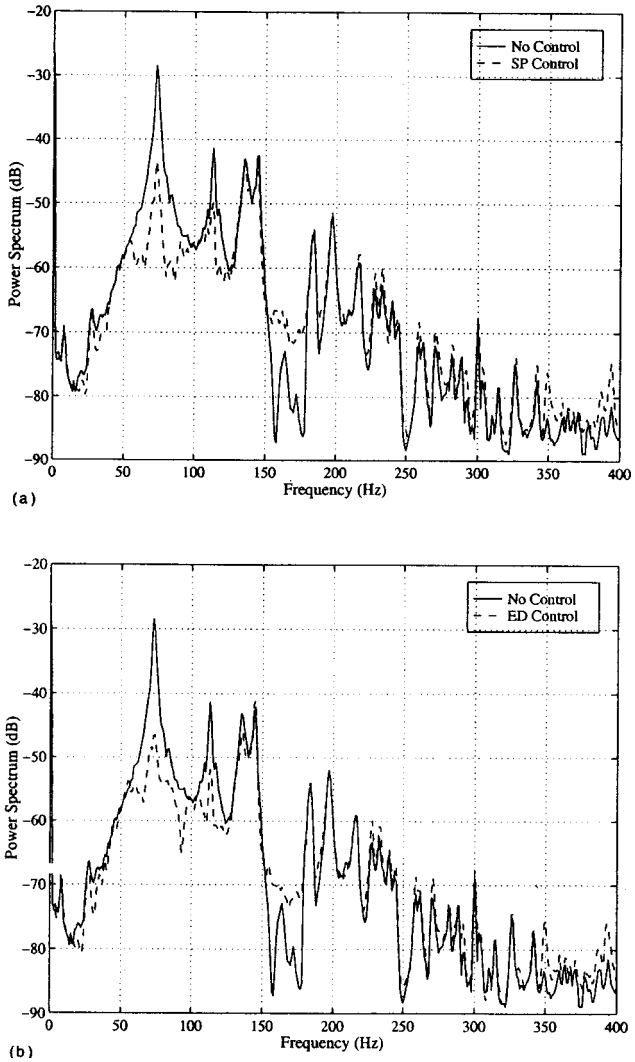

FIG. 11. Control configuration 4. Power spectra (*re* 1 V^2/Hz) measured at control sensor for no control and broadband active control. (a) Squared pressure control. (b) Energy density control.

that could be used to characterize the performance of active control systems in an enclosure through modal decomposition.

Energy density control was superior to the squared pressure control in both narrowband and broadband experiments due to its ability to better sense the acoustic modes. Nodes exist as planes for squared pressure modes, while nodes exist as lines for energy density modes. It is less likely for error sensors to be located at energy density field nodes than squared pressure nodes; hence, fewer sensors are required for the energy density control method to achieve results comparable to that of the squared pressure method. Up to 14.4 and 3.8 dB of cancellation were achieved for the energy density control method for narrowband and broadband experiments, respectively. The close agreement between predicted and experimental results indicates that the energy density sensor, developed in the companion paper,[8] has sufficient accuracy for use in active noise control. The close agreement between predicted and experimental results also shows that an active control system based on the energy density can successfully be constructed.

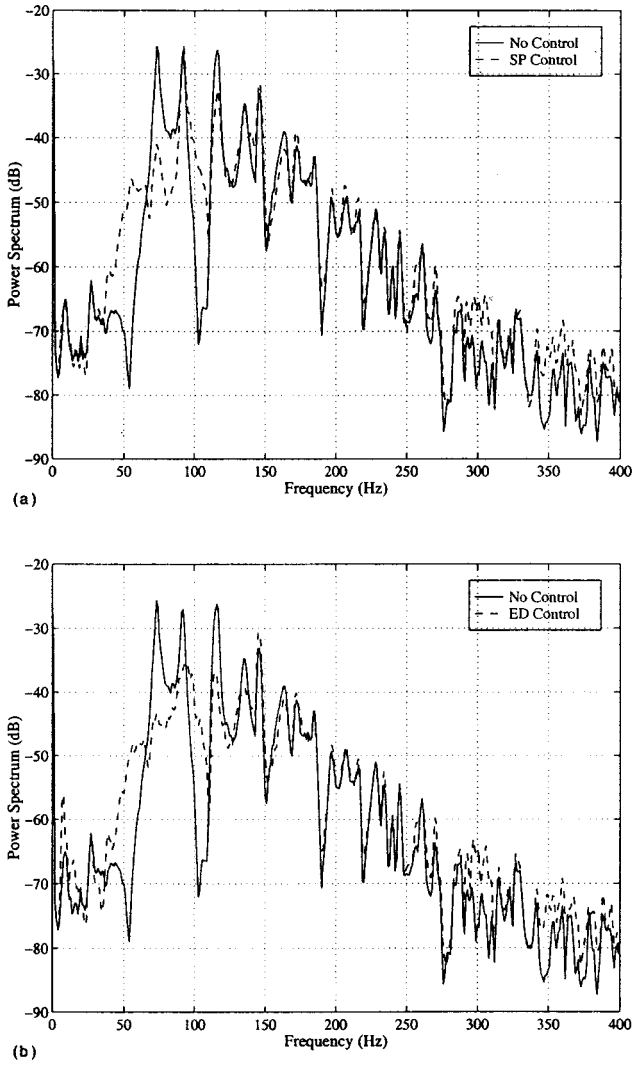

FIG. 12. Control configuration 4. Power spectra (*re* 1 V^2/Hz) measured at reference microphone for no control and broadband active control. (a) Squared pressure control. (b) Energy density control.

The energy density control method used in this research requires the three components of particle velocity as well as the pressure for each error sensor. Thus, a single energy density sensor required four times the signal processing compared to a single pressure sensor. In previous research involving a statistical analysis, it was predicted that an energy-density-based active control system would require approximately one-fourth the number of sensors compared to the squared pressure method (depending on the modal composition of the pressure field) for comparable performance.[11] Thus, the energy density control approach used here is comparable in performance to a squared pressure-control system of similar signal-processing complexity. A benefit of the energy density approach is that compact energy density sensors can be employed, whereas approximately four times the number of pressure sensors must be distributed within the control space, requiring significantly more cabling. In the future, combining the pressure and three velocity measurements into a single energy density measurement might prove to be advantageous. A single channel for processing would then be required per sensor, as in the squared pressure control, instead of four channels.

ACKNOWLEDGMENTS

The authors would like to thank the Applied Research Laboratory at Penn State University and NASA Langley for their support of this research.

[1] S. J. Elliot, P. A. Nelson, I. M. Stothers, and C. C. Boucher, ''In-Flight Experiments on the Active Control of Propeller-Induced Cabin Noise,'' J. Sound Vib. **140**, 219–238 (1990).
[2] S. D. Sommerfeldt and P. J. Nashif, ''Energy Based Control of the Sound Field in Enclosures,'' Second International Congress on Recent Developments in Air and Structure-Borne Sound and Vibration, pp. 361–368 (March, 1992).
[3] S. D. Sommerfeldt, J. W. Parkins, and Y. C. Park, ''Global Active Noise Control in Rectangular Enclosures,'' Proc. ACTIVE 95, pp. 477–488 (1995).
[4] Y. C. Park and S. D. Sommerfeldt, ''Global Attenuation of Broadband Noise Fields Using Energy Density Control,'' J. Acoust. Soc. Am. **101**, 350–359 (1997).
[5] X. Qui, C. H. Hansen, and X. Li, ''A Comparison of Near-Field Acoustic Error Sensing Strategies for the Active Control of Harmonic Free Field Sound Radiation,'' J. Sound Vib. **215**, 81–103 (1998).
[6] P. A. Nelson, A. R. D. Curtis, S. J. Elliot, and A. J. Bullmore, ''The Active Minimization of Harmonic Enclosed Sound Fields,'' J. Sound Vib. **117**, 1–58 (1987).
[7] F. J. Fahy, *Sound Intensity* (Spon, London, 1995), pp. 91–97.
[8] J. W. Parkins, S. D. Sommerfeldt, and J. Tichy, ''Error Analysis of a Practical Energy Density Sensor,'' J. Acoust. Soc. Am. **108**, 211–222 (2000).
[9] J. W. Parkins, ''Active Minimization of Energy Density in a Three-Dimensional Enclosure,'' Ph.D. thesis, Pennsylvania State University, University Park, PA (1998), pp. 101–104.
[10] S. D. Sommerfeldt and J. Tichy, ''Adaptive Control of a Two-Stage Vibration Isolation Mount,'' J. Acoust. Soc. Am. **88**, 938–944 (1990).
[11] J. W. Parkins, J. Tichy, and S. D. Sommerfeldt, ''A Comparison of Two Active Control Methods Through an Investigation of Node Structures,'' Proc. ACTIVE 99, pp. 729–740 (1999).
[12] P. A. Nelson and S. J. Elliott, *Active Control of Sound* (Academic, San Diego, 1993), pp. 314–329.
[13] E. Kreyszig, *Advanced Engineering Mathematics: Sixth Edition* (Wiley, New York, 1988), pp. 225–228.
[14] D. Guicking and M. Bronzel, ''Multichannel Broadband Active Noise Control in Small Enclosures,'' Proc. Inter-Noise 90, Vol. 2, pp. 1255–1258 (1990).

The coherence of reverberant sound fields

Finn Jacobsen and Thibaut Roisin[a)]
Department of Acoustic Technology, Technical University of Denmark, Building 352, Ørsteds Plads, DK-2800 Lyngby, Denmark

(Received 6 December 1999; accepted for publication 21 March 2000)

A new method of measuring spatial correlation functions in reverberant sound fields is presented. It is shown that coherence functions determined with appropriate spectral resolution contain the same information as the corresponding correlation functions, and that measuring such coherence functions is a far more efficient way of obtaining this information. The technique is then used to verify theoretical predictions of the spatial correlation between various components of the particle velocity in a diffuse sound field. Other possible applications of the technique are discussed and illustrated with experimental results obtained in an ordinary room. © *2000 Acoustical Society of America.* [S0001-4966(00)00807-9]

PACS numbers: 43.55.Br, 43.55.Cs [JDQ]

INTRODUCTION

Reverberation rooms are used in a variety of standardized measurements, e.g., in measuring the absorption of materials, the sound power of noise sources, and the transmission loss of partitions. They are also used for testing satellite structures at high sound-pressure levels. All measurements in reverberation rooms are based on the assumption that the sound field is diffuse; therefore, it is of interest to validate the diffuse field theory and to examine the agreement between theoretical predictions and the behavior of sound fields in real rooms.

The diffuse sound field is an idealized concept, and the sound field in any real room differs in fundamental respects from a diffuse field. One possible way of testing the diffuseness of the sound field in a given room might be to compare theoretically predicted spatial correlation functions with measurements. This idea goes back to the middle of the 20th century; the spatial autocorrelation of the sound pressure in a perfectly diffuse sound field was derived by Cook *et al.* as early as in 1955.[1] Cook and his coauthors also made an experimental investigation, using warble tones in a reverberation room equipped with a rotating vane.[1] Since then, many authors have studied pressure correlation functions in diffuse fields, experimentally[2–8] and theoretically.[3,6–13] Spatial correlation functions of other quantities than the sound pressure in a diffuse sound field were derived more than 20 years ago,[10,12] but have never been verified experimentally, although they have found application in various areas, e.g., in active noise control[14,15] and in prediction of the response of a plate to excitation by a diffuse sound field.[16]

The purpose of this paper is (i) to discuss the concept of a diffuse sound field, (ii) to present a new, efficient method of determining spatial correlation functions in a room, (iii) to present experimental results that validate the theoretical predictions in a real room, and (iv) to discuss possible applications.

I. CORRELATION AND COHERENCE IN A DIFFUSE SOUND FIELD

A. A brief review of diffuse-field theory

Many different models of diffuse fields have been described in the literature, including models that make use of concepts such as ergodicity, entropy, and ''mixing.''[1,12,17–20] However, most acousticians would agree on a definition that involves sound coming from all directions. This leads to the concept of a sound field in an unbounded medium generated by distant, uncorrelated sources of random noise evenly distributed over all directions. Since the sources are uncorrelated there would be no interference phenomena in such a sound field, and the field would therefore be completely homogeneous and isotropic. For example, the sound pressure level would be the same at all positions, and temporal correlation functions between linear quantities measured at two points would depend only on the distance between the two points. The time-averaged sound intensity would be zero at all positions. An approximation to this ''perfectly diffuse sound field'' might be generated by a number of loudspeakers driven with uncorrelated noise in a large anechoic room, as in the experimental investigations described in Refs. 3 and 7. The sound field in a reverberation room driven with noise from one source is quite different, of course.

A more realistic model of the sound field in a reverberation room above the Schroeder frequency[21] describes the sound field as composed of plane waves with random phases arriving from all directions.[12,22] This is a pure-tone model, and therefore the various plane waves interfere. The result is a sound field in which the sound-pressure level depends on the position, although the probability of the level being in a certain interval is the same at all positions. Temporal correlation functions between linear quantities measured at two positions depend on the positions, although the probability of a given correlation function being in a certain interval depends only on the distance between the two points. The time-averaged sound intensity assumes a finite value at all positions.[23,24] Since infinitely many plane waves with completely random phases are assumed, this model is also idealized, but it gives a good approximation to the sound field in

[a)]Present address: Les Entreprises Louis De Waele, Avenue Jean Dubrucq 175, B-1080, Bruxelles, Belgium.

a reverberation room driven with a pure tone with a frequency above the Schroeder frequency. With averaging over an ensemble of realizations, the perfectly diffuse field described above is obtained. An approximation to ensemble averaging is obtained if the room is equipped with a rotating diffuser.[12,17]

The second model can be extended to excitation with a band of noise.[25,26] If a reverberation room is driven with a pure tone whose frequency is shifted slightly, the phases and amplitudes of the plane waves that compose the sound field are changed, which means that the entire interference pattern is changed. The longer the reverberation time of the room, the faster the sound field will change as a function of the frequency.[27] It now follows that excitation with a band of noise corresponds to averaging over the band. As a result the sound field becomes more uniform,[25,26] temporal cor-relation functions between linear quantities measured at pairs of positions tend to depend less on the particular positions,[9] and the sound intensity is reduced.[24] The effect of this spectral averaging depends not only on the bandwidth of the excitation (or the analysis) but also on the damping of the room; the longer the reverberation time, the more efficient the averaging. It is apparent that there are many similarities between the sound field in a room driven with noise and the perfectly diffuse sound field, but there are also important differences. It can also be concluded that diffuseness at low frequencies requires a large room, and that long reverberation times (within the limits determined by the requirement of sufficient modal overlap[21]) are favorable.

B. Space-time correlation in a pure-tone "diffuse" sound field

The theory has been described elsewhere,[10,12,28] so only the results will be presented here. Using the second model described above (the sum of plane waves with random phases and amplitudes), it can be shown that the normalized space-time correlation of two pressure signals separated in distance by r and in time by τ is

$$\rho_{pp}(r,\tau)=\frac{\sin(\omega_o r/c)}{\omega_o r/c}\cos(\omega_o \tau), \tag{1}$$

where ω_o is the radian frequency and c is the speed of sound, as already shown in the middle of the 1950s by Cook *et al.*[1] The corresponding correlation function between the pressure and a component of the particle velocity is

$$\rho_{pu_r}(r,\tau)=\sqrt{3}\,\frac{\sin(\omega_o r/c)-(\omega_o r/c)\cos(\omega_o r/c)}{(\omega_o r/c)^2}\sin(\omega_o \tau). \tag{2}$$

The space-time correlation between two particle velocity components in the direction of the line that joins the two points is

$$\rho_{u_r u_r}(r,\tau)=3\frac{(\omega_o r/c)^2\sin(\omega_o r/c)+(2\omega_o r/c)\cos(\omega_o r/c)-2\sin(\omega_o r/c)}{(\omega_o r/c)^3}\cos(\omega_o \tau), \tag{3}$$

and the space-time correlation of two parallel particle velocity components perpendicular to the line that joins the two points is

$$\rho_{u_y u_y}(x,\tau)=3\frac{\sin(\omega_o x/c)-(\omega_o x/c)\cos(\omega_o x/c)}{(\omega_o x/c)^3}\cos(\omega_o \tau). \tag{4}$$

Equation (1) has been verified experimentally by many authors.[1–5,7,8]

C. Space-time correlation in a perfectly diffuse sound field

The perfectly diffuse sound field is not a pure-tone field. In the perfectly diffuse sound field, the normalized temporal correlation functions between pressure and particle velocity signals measured at any pair of positions equal the expressions given by Eqs. (1), (2), (3), and (4) multiplied by a factor of $\sin(\tau\Delta\omega/2)/(\tau\Delta\omega/2)$, provided that $\Delta\omega \ll \omega_o$, where $\Delta\omega$ is the bandwidth of the analysis. (If the bandwidth is wider a correction described in Ref. 13 can be applied.) Conversely, at a given fixed time the corresponding spatial correlation functions equal the expressions given by Eqs. (1), (2), (3), and (4) with $\tau=0$.

D. Coherence in a perfectly diffuse sound field

By definition, the coherence of two signals is the squared modulus of the cross spectrum normalized with the two autospectra,[29]

$$\gamma_{xy}^2(\omega)=\frac{|S_{xy}(\omega)|^2}{S_{xx}(\omega)S_{yy}(\omega)}. \tag{5}$$

However, the coherence is also related to the normalized cross-correlation function. It can be shown that, provided that $\Delta\omega \ll \omega_o$, the coherence estimated with finite spectral resolution is identical with the squared envelope of the normalized cross-correlation at zero time delay, that is,

$$\gamma_{xy}^2(\omega_o,\Delta\omega)=\rho_{xy}^2(0,\omega_o,\Delta\omega)+\hat{\rho}_{xy}^2(0,\omega_o,\Delta\omega), \tag{6}$$

where $\rho_{xy}(\tau,\omega_o,\Delta\omega)$ is the normalized cross-correlation of the bandpass-filtered signals $x(t,\omega_o,\Delta\omega)$ and $y(t,\omega_o,\Delta\omega)$, and $\hat{\rho}_{xy}(\tau,\omega_o,\Delta\omega)$ is the Hilbert transform of $\rho_{xy}(\tau,\omega_o,\Delta\omega)$.[30] From this equation, in combination with the foregoing, it now follows that the coherence functions between pressure and particle velocity signals measured at any pair of positions in an ideal diffuse sound field are

$$\gamma^2_{pp}(\omega,r)=\left(\frac{\sin(\omega r/c)}{\omega r/c}\right)^2, \tag{7}$$

$$\gamma^2_{pu_r}(\omega,r)=3\left(\frac{\sin(\omega r/c)-(\omega r/c)\cos(\omega r/c)}{(\omega r/c)^2}\right)^2, \tag{8}$$

$$\gamma^2_{u_ru_r}(\omega,r)=9\left(\frac{(\omega r/c)^2\sin(\omega r/c)+(2\omega r/c)\cos(\omega r/c)-2\sin(\omega r/c)}{(\omega r/c)^3}\right)^2, \tag{9}$$

$$\gamma^2_{u_yu_y}(\omega,x)=9\left(\frac{\sin(\omega x/c)-(\omega x/c)\cos(\omega x/c)}{(\omega x/c)^3}\right)^2. \tag{10}$$

Equation (7) was shown by Piersol in 1978.[31]

E. Coherence in a reverberation room

The sound field in a real room excited by a source of noise is not composed of infinitely many incoherent sound waves arriving from all direction. In a room without devices such as rotating diffusers, driven by a single source, it is much more realistic to describe the sound field as composed of a large but finite number of coherent waves. Such a system is linear and time invariant, from which it follows that all linear quantities are fully coherent, that is, all coherence functions between pressure and particle velocity signals recorded in the room equal unity.[32] In practice, however, coherence functions are estimated using fast Fourier transform (FFT) analyzers with a finite spectral resolution, and under certain conditions the estimated functions approach the functions given by Eqs. (7), (8), (9), and (10). The experimental technique described in the next section is based on this observation.

It takes a *very* fine spectral resolution (a bandwidth of less than $1/T_{60}$, where T_{60} is the reverberation time of the room) to show that the entire sound field is actually fully coherent. By contrast, if the room is driven with pseudorandom noise synchronized to the FFT analysis, the measured coherence is unity, irrespective of the spectral resolution.[32]

II. COHERENCE VERSUS CORRELATION

The experimental techniques described in the literature, e.g., in Refs. 5 and 7, are based on measurement of correlation functions in different frequency bands. Alternatively, one might measure the corresponding coherence functions, using an appropriate spectral resolution. It follows from Eq. (6) that a coherence function determined with finite spectral resolution contains the same information as many correlation functions. That the spectral resolution is important can be explained as follows. Since the autocorrelation function of a random signal of a finite bandwidth decays to insignificance for a time shift that is inversely proportional to the bandwidth, it follows that the sound waves in a reverberation room *seem* to be practically uncorrelated, i.e., their correlation coefficient is much less than unity, if the time delay between the various waves exceeds the decay time of the autocorrelation, and this will be the case if the bandwidth of the analysis exceeds c/l, where l is a characteristic dimension of the room. Because the sound waves in a reverberation room are reflected many times before they die out, the sound waves that compose the field are essentially uncorrelated even with a somewhat finer spectral resolution. The spectral resolution must not be too fine, though, because in the limit of $\Delta\omega\rightarrow 0$ the estimated coherence will approach the true value, unity, just as estimated normalized correlation functions will approach sinusoids with an amplitude of unity, irrespective of the properties of the sound field. Expressed in simple terms, the waves that compose the sound field *seem* to be generated by independent sources since the analysis is based on short signal segments, and therefore the measured coherence functions will approach the expressions given by Eqs. (7), (8), (9), and (10), provided that the number of waves is sufficient and their directions are sufficiently random. The purpose of the test is to examine whether this is the case.

The advantage of the proposed technique is that many correlation functions are, in effect, determined at the same time.

III. EXPERIMENTAL RESULTS IN A REVERBERATION ROOM

To test the validity of the foregoing considerations and Eqs. (7), (8), (9), and (10), some experiments have been carried out in a large (245 m^3) reverberation room with a reverberation time of about 5 s. Two sound-intensity probes of type Brüel & Kjær 3545 (''*p-p* probes'' based on the finite difference principle) were used to measure the sound pressure and components of the particle velocity. It is prob-

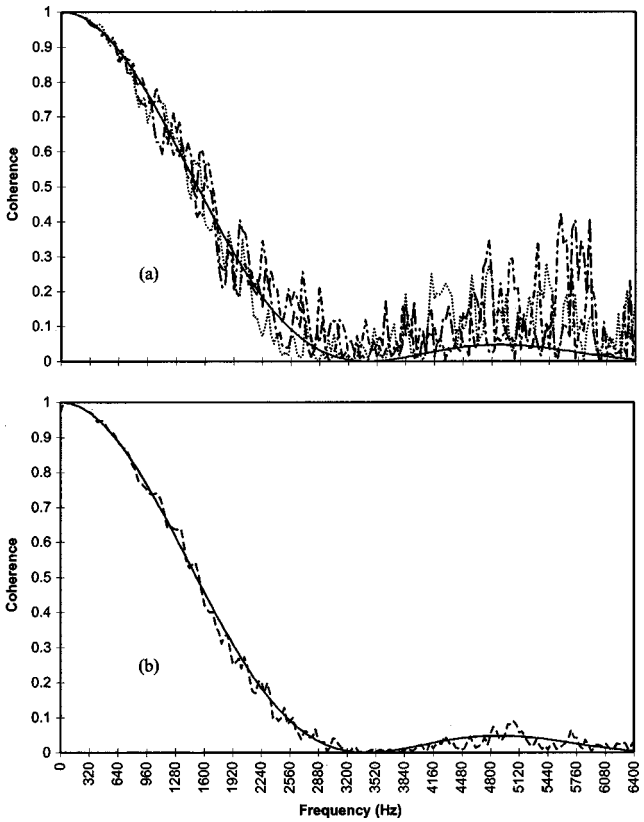

FIG. 1. Coherence between two pressure signals at positions 5 cm apart in a reverberation room, measured with a spectral resolution of 32 Hz. ———, theoretical prediction [Eq. (7)]. (a) Measurements at three pairs of positions; (b) ---, measurement in which the cross and auto spectra have been averaged over ten pairs of positions.

ably advantageous to use a *p-p* sound intensity probe with the microphones in the ''face-to-face'' configuration separated by a solid spacer also in measuring pressure coherence functions, because this ensures that the distance between the acoustic centers of the microphones is almost independent of the frequency and the nature of the sound field.[33,34] A single pressure microphone of type Brüel & Kjær 4192 was used in combination with one of the intensity probes in measuring the pressure-particle velocity coherence. The coherence functions were determined with a dual-channel FFT analyzer of type Brüel & Kjær 2035. The room was driven with random noise generated by the analyzer.

Figure 1(a) shows the result of measuring the coherence between two pressure signals recorded a distance of 5 cm from each other in the room with a spectral resolution of 32 Hz. Measurements at three different pairs of positions are shown. There are similarities between the measured coherence functions and the theoretical prediction [Eq. (7)], but it is also apparent that the measured functions deviate erratically from the prediction and from each other. However, with averaging of the cross and auto spectra over ten pairs of positions chosen at random,

$$\gamma_{xy}^2(\omega,r)=\frac{|\langle S_{xy}(\omega,r)\rangle|^2}{\langle S_{xx}(\omega)\rangle\langle S_{yy}(\omega)\rangle}, \tag{11}$$

where $\langle\ \rangle$ indicates the averaging, the agreement between predicted and measured coherence becomes very good, as

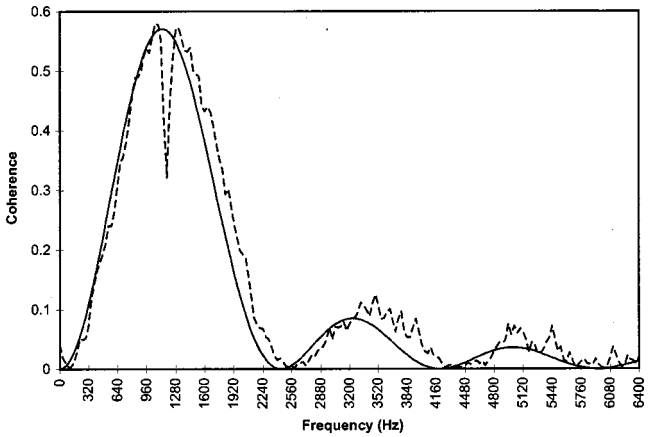

FIG. 2. Coherence between the pressure and a component of the particle velocity at a position 10 cm away in a reverberation room, measured with a spectral resolution of 32 Hz. ———, theoretical prediction [Eq. (8)]; ---, measurement in which the cross and auto spectra have been averaged over ten pairs of positions.

can be seen in Fig. 1(b). In practice the spectral averaging process was simply stopped after a suitable number of spectra had been averaged, the probe was moved to another position, and the averaging was continued.

To measure the corresponding coherence functions between pressure and particle velocity components and between various components of the particle velocity directly with the analyzer would require a multichannel analyzer. Such a device was not available. Instead, signals proportional to the pressure gradients were determined from the two pressure signals from each intensity probe using analog subtracting circuits.

In Fig. 2 a comparison of the coherence between sound pressure and particle velocity and the theoretical prediction is shown. It is worth noting that the acoustic center of the half-inch microphone used in measuring the pressure is about 5 mm in front of the microphone.[35] If this is taken into account the agreement is almost perfect, except for the inexplicable trough in the experimental curve at 1.1 kHz.

Figures 3(a) and 3(b) show the results of similar measurements of the coherence between two components of the particle velocity in the direction of the line that joins the two points and perpendicular to the line, respectively. Again, there is very good agreement with the diffuse field prediction, except at very low frequencies where phase and amplitude mismatch may have affected the estimates of the particle velocity.

Finally, a few additional measurements with the reverberation room driven with pseudorandom noise synchronized to the FFT records were carried out. In the absence of transducer noise and nonlinearities, all coherence functions should equal unity,[32] and without spatial averaging the measured coherence function between two pressure signals recorded a distance of 5 cm from each other was indeed close to unity, as shown in Fig. 4. Since driving the room with pseudorandom noise in effect corresponds to driving it with many pure tones that are analyzed separately, the pure-tone ''diffuse''-field theory applies. Therefore we can expect Eqs. (1), (2), (3), and (4) to describe the spatial correlation, and

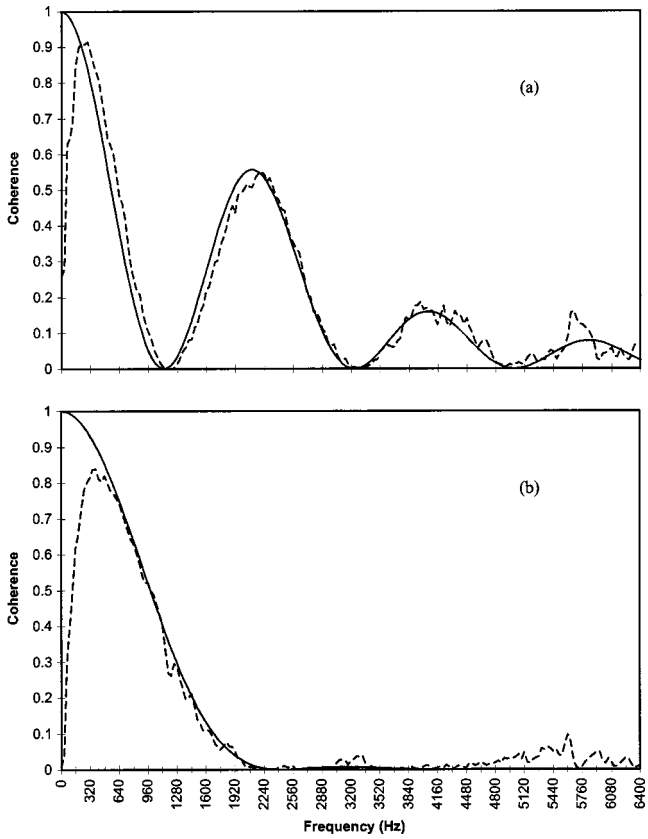

FIG. 3. Coherence between two components of the particle velocity at positions 10 cm from each other in a reverberation room, measured with a spectral resolution of 32 Hz. (a) Components in the same direction. ———, theoretical prediction [Eq. (9)]; ---, measurement in which the cross and auto spectra have been averaged over ten pairs of positions. (b) Perpendicular components. ———, theoretical prediction [Eq. (10)]; ---, measurement in which the cross and auto spectra have been averaged over ten pairs of positions.

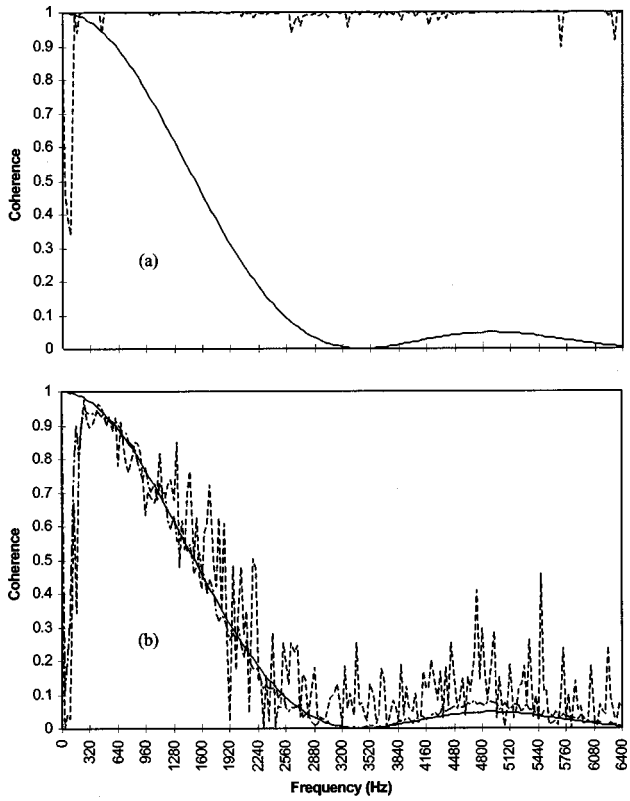

FIG. 4. Coherence between two pressure signals at positions 5 cm apart in a reverberation room driven with synchronized pseudorandom noise generated by the FFT analyzer, measured with a spectral resolution of 32 Hz. ———, theoretical prediction [Eq. (7)]. (a) ---, measurement at one position. (b) ---, measurement with averaging of the cross and auto spectra over ten pairs of positions; — – —, measurement with continuous averaging over many positions.

Eqs. (7), (8), (9), and (10) to describe the spatial coherence. However, without the inherent frequency averaging of a normal FFT analysis, much more spatial averaging is needed, which can be seen by comparing the erratically fluctuating curve in Fig. 4 with Fig. 1(b). In both cases averaging over ten pairs of positions was carried out. With continuous averaging over many positions and directions, carried out by moving the intensity probe slowly around far from the source, the agreement with the theoretical prediction becomes very good.

IV. EXPERIMENTAL RESULTS IN AN ORDINARY ROOM

Further experimental results were determined in an ordinary room of about 180 m^3 with a reverberation time of about 0.5 s. One would not expect the sound field in this room to be particularly diffuse, and the lack of diffuseness is confirmed by the relatively large deviations between the measured and theoretical pressure coherence functions shown in Fig. 5(a). However, with averaging over many positions and directions the agreement between prediction and measurement becomes almost perfect, as can be seen in Fig. 5(b).

Instead of moving the intensity probe around in the room, one might move the source that generates the sound field, and with sufficient averaging one should expect the measured pressure coherence to approach Eq. (7). This is confirmed by the result presented in Fig. 6.

Even in the direct field close to the source where the sound field is far from being diffuse, one can, with appropriate spatial averaging, measure pressure coherence functions that approach the theoretical functions of a perfectly diffuse sound field (although some systematic deviations can be seen), as demonstrated by Fig. 7(b). However, as can be seen in Fig. 7(a), without spatial averaging the measured pressure coherence at any position and in any direction close to the source is completely different from the theoretical value for a diffuse sound field.

V. DISCUSSION

There are strong similarities between the sound field in a reverberation room and a perfectly diffuse field, but there is also a significant difference that reveals itself by the influence of the spectral resolution on the estimated coherence functions: In the limit of very fine spectral resolution, it becomes apparent that the sound field in a room unlike the diffuse field is perfectly coherent. However, estimated with a

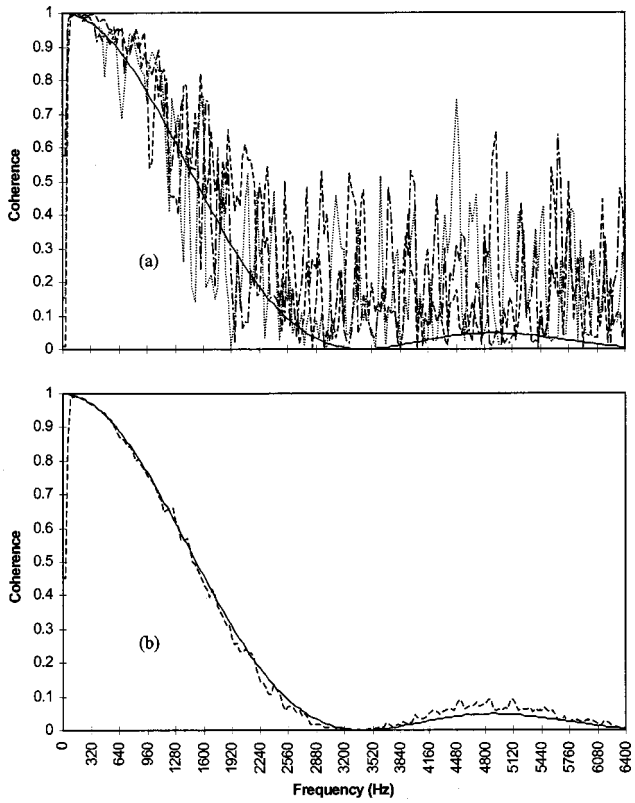

FIG. 5. Coherence between two pressure signals at positions 5 cm apart in an ordinary room, measured with a spectral resolution of 32 Hz. ———, theoretical prediction [Eq. (7)]. (a) Measurements at three pairs of positions; (b) --- , measurement in which the cross and auto spectra have been averaged continuously over many positions.

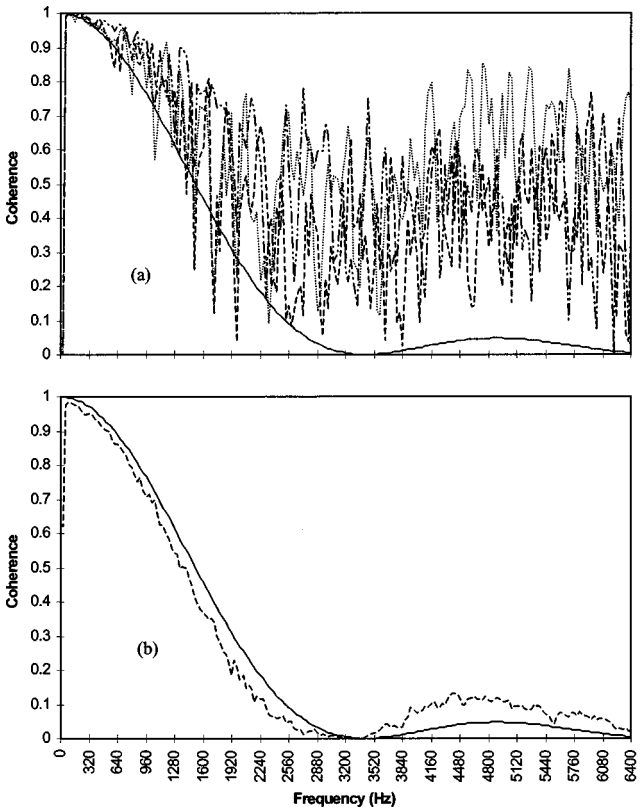

FIG. 7. Coherence between two pressure signals at positions 5 cm apart in an ordinary room, measured with a spectral resolution of 32 Hz. ———, theoretical prediction [Eq. (7)]. (a) Measurements at three pairs of positions one meter from the source; (b) ---, measurement in which the cross and auto spectra have been averaged continuously over many directions at positions 1 m from the source.

less fine resolution the coherence functions approach those predicted by the diffuse-field theory. The longer the reverberation time of the room the less averaging over frequency is needed, and the finer the spectral resolution can be. Another difference is the influence of spatial averaging. Without spatial averaging, the agreement between measurements and predictions for the perfectly diffuse sound field is no more than tolerable even in a large reverberation room with a long reverberation time, but with averaging over just a few points the agreement becomes almost perfect. However, the amount of averaging that is required depends on the quality and size of the room. It is apparent from the results obtained in the ordinary room that with sufficient spatial averaging one can ''prove'' that almost any sound field is diffuse. A rotating diffuser (as used in Refs. 1, 2, and 8) would reduce the amount of spatial averaging required. Exciting the room with several loudspeakers driven with independent noise signals (as in Ref. 7) or moving the source around during the measurement would have a similar effect. The better the agreement between theory and measurement *with the same amount of spatial averaging*, the more diffuse is the sound field, and the more one would expect other predictions from the diffuse-field theory to be valid.

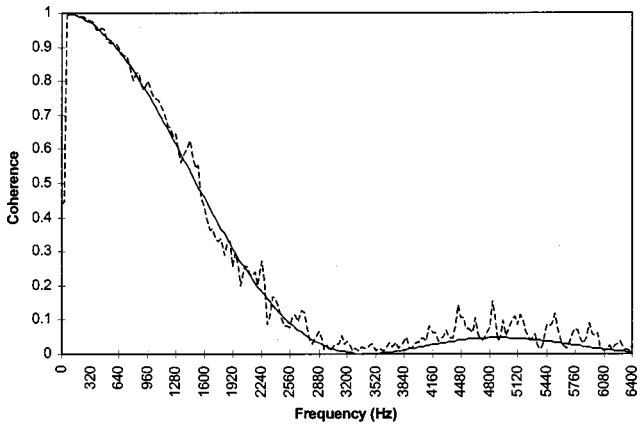

FIG. 6. Coherence between two pressure signals at positions 5 cm apart in an ordinary room, measured with a spectral resolution of 32 Hz. ———, theoretical prediction [Eq. (7)]; ---, measurement in which the source has been moved continuously over many positions.

It is more difficult to measure particle velocity than sound pressure or even sound intensity, because not only phase but also amplitude mismatch between the two pressure microphones gives rise to errors, in particular at low frequencies. This cautions against using measures based on particle velocity, and since Eqs. (2) and (3) have been derived by differentiating Eq. (1) once and twice,[12] there is no reason to expect these functions or the corresponding coherence functions to be more sensitive to deviations from diffuseness.

Applications of the theoretical correlation functions in a diffuse sound field were mentioned in the Introduction. Pos-

sible applications of the experimental technique include evaluating the quality of reverberation rooms. However, it is clear from the results presented here that a comparison of results obtained in different rooms would not make sense unless the same averaging procedure was used.

VI. CONCLUSIONS

Spatial coherence functions in a reverberant sound field have been examined experimentally. The theoretical coherence functions between pressure and particle velocity components in a perfectly diffuse sound field have been shown to give very good predictions of the corresponding functions in a large reverberation room, provided that the analysis is carried out with a spectral resolution of the order of c/l, where l is a characteristic dimension, and provided that a certain amount of spatial averaging is carried out. Since these coherence functions are closely related to the corresponding spatial correlation function, the results verify the spatial correlation functions of reverberant fields derived more than 20 years ago. However, it is important to note that a measured coherence function in perfect agreement with predictions for a diffuse sound field by no means proves that the sound field is diffuse.

The measurement technique described in this paper is far more efficient than measuring correlation coefficients at different distances in a number of frequency bands. Measuring coherence has the advantage that many correlation functions, in effect, are determined at the same time.

[1] R. K. Cook, R. V. Waterhouse, R. D. Berendt, S. Edelman, and M. C. Thompson, Jr., ''Measurement of correlation coefficients in reverberant sound fields,'' J. Acoust. Soc. Am. **27**, 1071–1077 (1955).

[2] C. G. Balachandran, ''Random sound field in reverberation chambers,'' J. Acoust. Soc. Am. **31**, 1319–1321 (1955).

[3] P. Dämmig, ''Zur Messung der diffusität von Schallfeldern durch Korrelation,'' Acustica **7**, 387–398 (1957).

[4] H. Kuttruff, ''Raumakustische Korrelationsmessungen mit einfachen Mitteln,'' Acustica **13**, 120–122 (1963).

[5] M. Koyasu and M. Yamashita, ''Evaluation of the degree of diffuseness in reverberation chambers by spatial correlation techniques,'' J. Acoust. Soc. Jpn. **27**, 132–143 (1971). (In Japanese with an English summary.)

[6] G. C. J. Bart, ''Spatial crosscorrelation in anisotropic sound fields,'' Acustica **28**, 45–49 (1973).

[7] K. Bodlund, ''A new quantity for comparative measurements concerning the diffusion of stationary sound fields,'' J. Sound Vib. **44**, 191–207 (1976).

[8] W. T. Chu, ''Comments on the coherent and incoherent nature of a reverberant sound field,'' J. Acoust. Soc. Am. **69**, 1710–1715 (1981).

[9] C. T. Morrow, ''Point-to-point correlation of sound pressures in reverberation chambers,'' J. Sound Vib. **16**, 29–42 (1971).

[10] K. Kuno and K. Ikegaya, ''A statistical consideration on models for sound fields composed of random plane and spherical wave elements,'' J. Acoust. Soc. Jpn. **30**, 65–75 (1974). (In Japanese with an English summary.)

[11] C. F. Chien and W. W. Soroka, ''Spatial cross-correlation of acoustic pressures in steady and decaying reverberant sound fields,'' J. Sound Vib. **48**, 235–242 (1976).

[12] F. Jacobsen, ''The diffuse sound field,'' The Acoustic Laboratory, Technical University of Denmark, Report No. 27 (1979).

[13] H. Nélisse and J. Nicolas, ''Characterization of a diffuse field in a reverberant room,'' J. Acoust. Soc. Am. **101**, 3517–3524 (1997).

[14] S. J. Elliott and J. García-Bonito, ''Active cancellation of pressure and pressure gradient in a diffuse sound field,'' J. Sound Vib. **186**, 696–704 (1995).

[15] J. García-Bonito and S. J. Elliott, ''Active cancellation of acoustic pressure and particle velocity in the near field of a source,'' J. Sound Vib. **221**, 85–116 (1999).

[16] J.-P. Coyette and C. Lecomte, ''The numerical treatment of a coupled elastic structure subjected to random excitations,'' in *Proceedings of the ISMA 21st International Conference on Noise and Vibration Engineering* (Leuven, Belgium, 1996).

[17] T. J. Schultz, ''Diffusion in reverberation rooms,'' J. Sound Vib. **16**, 17–28 (1971).

[18] R. H. Lyon, ''Needed: A new definition of diffusion,'' J. Acoust. Soc. Am. **56**, 1300–1302 (1974).

[19] H. Kuttruff, *Room Acoustics*, 3rd ed. (Applied Science, London, 1991), see Chap. V.

[20] J.-D. Polack, ''Modifying chambers to play billiards; the foundation of reverberation theory,'' Acustica **76**, 257–272 (1992).

[21] M. Schröder, ''Die statistischen Parameter der Frequenzkurven von grossen Räumen,'' Acustica **4**, 594–600 (1962).

[22] A. D. Pierce, *Acoustics: An Introduction to Its Physical Principles and Applications* (Acoustical Society of America, New York, 1989).

[23] K. J. Ebeling in *Physical Acoustics*, edited by W. P. Mason and R. N. Thurston (Academic Press, Orlando, 1984), Vol. XVII. See Chap. 4, ''Statistical properties of random wave fields.''

[24] F. Jacobsen, ''Active and reactive sound intensity in a reverberant sound field,'' J. Acoust. Soc. Am. **143**, 231–240 (1990).

[25] D. Lubman, ''Fluctuations of sound with position in a reverberant room,'' J. Acoust. Soc. Am. **44**, 1419–1502 (1968).

[26] M. R. Schroeder, ''Effect of frequency and space averaging on the transmission responses of multimode media,'' J. Acoust. Soc. Am. **46**, 277–283 (1969).

[27] M. R. Schroeder, ''Frequency-correlation functions of frequency responses in rooms,'' J. Acoust. Soc. Am. **34**, 1819–1823 (1962).

[28] S. V. Dotsenko and V. I. Il'ichev, ''Correlation description of random sound fields,'' Sov. Phys. Acoust. **33**, 275–278 (1987).

[29] J. S. Bendat and A. G. Piersol, *Engineering Applications of Correlation and Spectral Analysis*, 2nd ed. (Wiley, New York, 1993).

[30] F. Jacobsen, ''Active and reactive, coherent and incoherent sound fields,'' J. Sound Vib. **130**, 493–507 (1989).

[31] A. G. Piersol, ''Use of coherence and phase data between two receivers in evaluation of noise environments,'' J. Sound Vib. **56**, 215–228 (1978).

[32] F. Jacobsen and T. G. Nielsen, ''Spatial correlation and coherence in a reverberant sound field,'' J. Sound Vib. **118**, 175–180 (1987).

[33] E. Frederiksen and M. Piil, ''Characteristics of microphone pairs and probes for sound intensity measurements,'' Brüel & Kjær, Nærum, Denmark, Report BA0077-11 (1987).

[34] V. Cutanda, P. M. Juhl, and F. Jacobsen, ''A numerical investigation of the performance of sound intensity probes at high frequencies,'' in *Proceedings of the Fourth International Congress on Sound and Vibration* (Institute of Acoustics and Vibration, St. Petersburg, Russia, 1996), pp. 1897–1904.

[35] P. Juhl, ''A numerical investigation of standard condenser microphones,'' J. Sound Vib. **177**, 433–446 (1994).

Error analysis of a practical energy density sensor

John W. Parkins
RTH Systems, 135 Storm Road, Groton, New York 13073

Scott D. Sommerfeldt
Department of Physics, Brigham Young University, N241 ESC, Provo, Utah 84602

Jiri Tichy
Acoustics Department, The Pennsylvania State University, Applied Science Building, North Atherton Street, State College, Pennsylvania 16802

(Received 22 July 1999; revised 13 March 2000; accepted 15 March 2000)

The investigation of an active control system based on acoustic energy density has led to the analysis and development of an inexpensive three-axes energy density sensor. The energy density sensor comprises six electret microphones mounted on the surface of a 0.025-m (1 in.) radius sphere. The bias errors for the potential, kinetic, and total energy density as well as the magnitude of intensity of a spherical sensor are compared to a sensor comprising six microphones suspended in space. Analytical, computer-modeled, and experimental data are presented for both sensor configurations in the case of traveling and standing wave fields, for an arbitrary incidence angle. It is shown that the energy density measurement is the most nearly accurate measurement of the four for the conditions presented. Experimentally, it is found that the spherical energy density sensor is within ± 1.75 dB compared to reference measurements in the 110–400 Hz frequency range in a reverberant enclosure. The diffraction effects from the hard sphere enable the sensor to be made more compact by a factor of $\frac{2}{3}$ compared to the sensor with suspended microphones. © *2000 Acoustical Society of America.* [S0001-4966(00)04906-7]

PACS numbers: 43.58.Fm, 43.50.Ki [SLE]

INTRODUCTION

Research in active noise control (ANC) systems has led scientists to investigate the performance of various cost functions such as structural intensity,[1] wave number amplitude,[2] volume velocity,[3] and, most commonly, potential energy density.[4] (The cost function of an ANC system is the function that is minimized as a result of the ANC algorithm.) Sommerfeldt and Nashif, in 1992, proposed using the sum of the acoustic energy densities at discrete points in space as a cost function for controlling acoustic fields in ducts.[5] Nashif constructed a single-axis energy density sensor using instrumentation microphones, and conducted ANC experiments in ducts with promising results.[6] This research led to the development of an ANC system for use in three-dimensional acoustic fields using the total energy density as a cost function.[7–9] In the course of this work on controlling three-dimensional acoustic fields, it was necessary to develop and characterize the performance of a three-axes energy density sensor.

Multiple sensors were needed for the ANC system, which was targeted for use in commercial applications such as aircraft cabins. Therefore, high-precision instrumentation microphones were prohibitively expensive for use in the sensor. Electret microphones manufactured by Lectret Corp. (model 1270A) costing $15 each were chosen for the sensor microphones. Calibration was also an issue since the use of digital calibration filters for each microphone in the sensor was computationally expensive for a controller. Therefore, it was necessary to understand the effects of microphones mismatched in sensitivity and phase, consistent with inexpensive electret microphones, on the calculation of the acoustic quantities in question. The sensors would be used in reverberant fields, therefore the performance of a sensor in a standing wave field was of particular interest.

Since the error analysis of the total energy density measurement requires investigating the errors in the particle velocity and pressure estimates, the errors in potential and kinetic energy density as well as intensity require little additional work, and are useful for gaining insights into the total energy density measurement. All four measurements are functions of the acoustic pressure and/or particle velocity. In this paper, the measurement errors in potential, kinetic, and total energy density as well as intensity are investigated for two sensor configurations. One configuration has the microphones suspended at points in space (referred to as a two-point sensor), while the other has microphones mounted on the surface of a hard sphere (referred to as a spherical sensor).

It is convenient to first study the bias errors (or offset errors) of a single-axis sensor which can be analyzed in greater detail due to its relative simplicity. The bias error equations for a single-axis sensor are investigated, while those of a three-axes sensor are beyond the scope of this work. The understanding gained from the study of the single-axis sensor yields insights into the error mechanisms in a three-axes sensor. Ultimately, the measurement errors of a three-axes energy density sensor are determined for some special cases through computer simulation and experimental measurement.

The bias errors of the spherical sensor are determined for the case of a one-dimensional standing wave field with

arbitrary reflection coefficient and incident angle, when the measurement microphones have a sensitivity and phase mismatch. The bias errors in potential energy density, kinetic energy density, total energy density, and intensity are reported and compared to those of the two-point sensor. Analysis of the two-point sensor yields insights into the performance of the spherical sensor. It will be shown that an inexpensive yet robust spherical energy density sensor can be fabricated with sufficient accuracy for use in practical active control systems.

I. BACKGROUND

A sensor that is capable of measuring the total acoustic energy density is a vector-field sensor, since the particle velocity vector must be determined. Typically, vector-field probes, such as intensity sensors, comprise two small microphones separated by a known distance. The acoustic pressure and velocity are estimated by using finite sum and finite difference approximations, respectively. The measurement errors associated with the two-point sensor have been studied at length, especially as they relate to the intensity measurement.[10] Much less effort has been dedicated to understanding the errors of a total energy density measurement.

Early work concerning the measurement of the total energy density of an airborne acoustic field was conducted by Wolff and Massa in 1933.[11] Using three pressure gradient microphones and a single pressure microphone, the three orthogonal vector components of the particle velocity and the pressure at a point in space were measured. From these four measured quantities, the total energy density was calculated. Wolff and Massa determined, through experimentation, that the squared pressure field in an enclosure had greater spatial variation compared to the total energy density field. Wolff and Massa found that ''Practically, the use of three pressure gradient microphones with their axes mutually perpendicular plus a pressure microphone obtains the effect of averaging the readings of four pressure microphones placed at random distances from each other and several wave-lengths apart....'' [11] In other words, Wolff and Massa's energy density sensor had the advantage of using a single localized instrument comprising four sensors to achieve the same results as four randomly distributed sensors. Wolff and Massa's research indicates that a control system based on a total energy density measurement would be less sensitive to placement of the error sensor than one based on the squared pressure.

Cook and Schade, in 1974, investigated a configuration for an energy density sensor and its use for measurements in a reverberant chamber.[12] They investigated the spatial variances of one-, two-, and three-dimensional potential and total energy density fields. The variance of the total energy density field in a reverberant enclosure was estimated to be one-half that of the squared pressure field. Cook and Schade constructed a three-dimensional energy density sensor using three pairs of microphones. The performance limitations of the energy density sensor were not disclosed.

Elko, in 1991, investigated the diffraction effects of a spherical probe on intensity, potential energy density, and kinetic energy density measurements.[13] Elko investigated a single-axis vector-field sensor consisting of two microphones embedded on the surface of a hard sphere. Elko demonstrated that diffraction from the hard sphere causes beneficial biases which offset systematic biases for the finite sum and finite difference approximations in the pressure and velocity measurements, respectively, for most incidence angles. Elko derived these results for perfectly matched microphones, with regard to sensitivity and phase, in a traveling plane wave field with variable angles of incidence. No investigation was made into the accuracy of a total energy density measurement, or how the sensor would perform in a standing wave field.

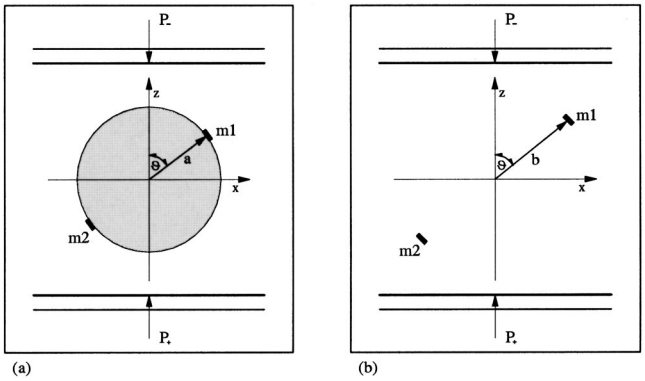

FIG. 1. Plane waves P_+ and P_- incident on (a) a spherical sensor and (b) a two-point sensor.

II. PROBLEM FORMULATION

The geometric configurations of a single-axis spherical sensor and two-point sensor are depicted in Fig. 1. The single-axis spherical sensor consists of two microphones, $m1$ and $m2$, embedded on the surface of a hard sphere with diameter $2a$. The two-point sensor consists of two microphones separated in space by a distance $2b$. The sensors are both centered at the origin. Two plane waves, P_+ and P_-, are incident on the sensors from opposite directions producing a standing wave. The angle of incidence for the wave traveling in the negative z-direction is θ. The complex reflection coefficient of the standing wave is defined by

$$\hat{R} = \frac{\hat{P}_-}{\hat{P}_+} = \eta e^{j\xi}, \tag{1}$$

where $\hat{P}_+$ and $\hat{P}_-$ are the complex amplitudes of the plane waves at the origin when there is no obstacle. (''Hat'' accents above variables and constants indicate complex quantities.) Microphone $m1$ is chosen to have a phase mismatch δ_p, and sensitivity mismatch δ_m, with respect to microphone $m2$ given by

$$\frac{\hat{P}_{m1}}{\hat{P}_{m2}} = \delta_m e^{j\delta_p}, \tag{2}$$

when the microphones are co-located in a pressure field. The variables $\hat{P}_{m1}$ and $\hat{P}_{m2}$ represent the complex pressures at the two microphone locations. The sensitivity mismatch in decibels is

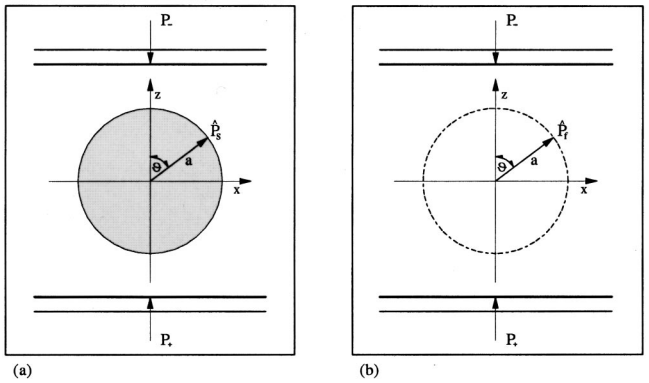

FIG. 2. Plane waves P_+ and P_- incident on (a) a hard-sphere obstacle and (b) no obstacle.

$$\delta_{m,\mathrm{dB}} = 20 \log \delta_m . \tag{3}$$

Since two microphones are used, only the component along the microphone axis (which will be referred to as the θ-component) of the acoustical measures can be resolved. The θ-components of the potential energy density, kinetic energy density, total energy density, and intensity are defined by

$$U_\theta = \frac{|\hat{P}_c|^2}{12\rho c^2}, \tag{4a}$$

$$T_\theta = \frac{\rho |\hat{V}_\theta|^2}{4}, \tag{4b}$$

$$e_\theta = \frac{|\hat{P}_c|^2}{12\rho c^2} + \frac{\rho |\hat{V}_\theta|^2}{4}, \tag{4c}$$

$$I_\theta = \tfrac{1}{2}\Re e\{\hat{P}_c \hat{V}_\theta^*\}, \tag{4d}$$

where $\hat{P}_c$ is the complex pressure, and $\hat{V}_\theta$ is the complex velocity in the θ-direction at the origin. The phase speed and density of air are given by c and ρ, respectively. The equations including the contributions from all three orthogonal axes for these measures are defined by

$$U_t = \frac{|\hat{P}_c|^2}{4\rho c^2} = U_i + U_j + U_k , \tag{5a}$$

$$T_t = \frac{\rho |\hat{\mathbf{V}}_t|^2}{4} = T_i + T_j + T_k , \tag{5b}$$

$$e_t = \frac{|\hat{P}_c|^2}{4\rho c^2} + \frac{\rho |\hat{\mathbf{V}}_t|^2}{4} = e_i + e_j + e_k , \tag{5c}$$

$$\mathbf{I}_t = \tfrac{1}{2}\Re e\{(\hat{P}_c \hat{V}_i^*, \hat{P}_c \hat{V}_j^*, \hat{P}_c \hat{V}_k^*)\} = (I_i, I_j, I_k), \tag{5d}$$

where

$$\hat{\mathbf{V}}_t = (\hat{V}_i, \hat{V}_j, \hat{V}_k) \tag{6}$$

is the complex particle velocity vector at the origin. The complex conjugate operation is indicated by ''$*$,'' while the real part is indicated by ''$\Re e$.'' The three orthogonal axes are represented by subscripts i, j, and k. Using the finite sum and finite difference approximations, the estimated pressure and velocity at the origin are

$$\hat{P}_{ec} = \frac{\hat{P}_{m2} + \hat{P}_{m1}}{2}, \tag{7}$$

$$\hat{V}_{e\theta} = \frac{\hat{P}_{m2} - \hat{P}_{m1}}{j\rho c 2kd}, \tag{8}$$

where d is a constant related to the microphone separation distance.[14]

To determine the bias errors, approximations for the acoustical measures using the finite sum and difference equations are compared to the true values at the origin. The expressions for the four biases are defined by

$$U_{b,\mathrm{dB}} = 10 \log U_{\mathrm{bias}} = 10 \log \left| \frac{\hat{P}_{ec}}{\hat{P}_c} \right|^2 , \tag{9a}$$

$$T_{b,\mathrm{dB}} = 10 \log T_{\mathrm{bias}} = 10 \log \left| \frac{\hat{V}_{e\theta}}{\hat{V}_\theta} \right|^2 , \tag{9b}$$

$$e_{b,\mathrm{dB}} = 10 \log e_{\mathrm{bias}} = 10 \log \left(\frac{e_{e\theta}}{e_\theta} \right), \tag{9c}$$

$$I_{b,\mathrm{dB}} = 10 \log I_{\mathrm{bias}} = 10 \log \left(\frac{I_{e\theta}}{I_\theta} \right). \tag{9d}$$

The true acoustical values at the origin are given by

$$\hat{P}_c = \hat{P}_+ (1 + \hat{R}), \tag{10a}$$

$$\hat{V}_\theta = \hat{P}_+ \frac{(1 - \hat{R})\cos\theta}{\rho c}, \tag{10b}$$

$$e_\theta = \frac{|\hat{P}_+|^2}{12\rho c^2} (|1 + \hat{R}|^2 + 3|1 - \hat{R}|^2 \cos^2\theta), \tag{10c}$$

$$I_\theta = \frac{|\hat{P}_+|^2 (1 - |\hat{R}|^2)\cos\theta}{2\rho c}. \tag{10d}$$

The normalized complex pressure in the field at point (x,y,z) is given by

$$\hat{P}(z) = (e^{-jkz} + \hat{R} e^{jkz}), \tag{11}$$

for a standing wave. There is no loss in generality of Eqs. (10a)–(10d) by assuming $z = 0$ for the standing wave situation since the reflection coefficient, $\hat{R}$, is complex.

III. SCATTERING EFFECTS FROM A HARD SPHERE

The pressure on the surface of the sphere, due to scattering, must be determined to calculate the bias errors of the spherical sensor. The geometry of the problem is depicted in Fig. 2. Two plane waves, P_+ and P_-, form a standing wave with reflection coefficient $\hat{R}$. The hard sphere is centered at the origin. From the equation of scattering of a single plane wave by a sphere,[15] it can be shown that the complex pressure on the surface of a sphere in a standing wave field is given by

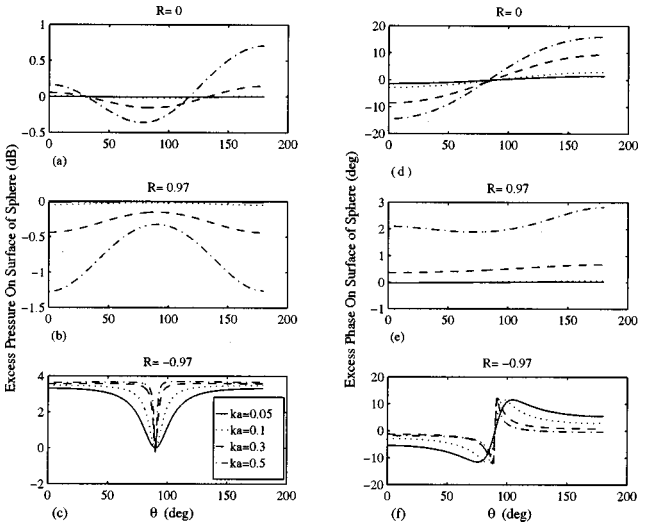

FIG. 3. Excess pressure magnitude and phase on the surface of a hard sphere for various reflection coefficients and values of *ka*.

$$\hat{P}_s(ka,\theta,\hat{R},\hat{P}_+) = \frac{\hat{P}_+}{j(ka)^2}\sum_{n=0}^{\infty}\frac{j^n(2n+1)(\hat{R}+(-1)^n)P_n(\cos\theta)}{h_n^{(2)'}(ka)}, \quad (12)$$

where $P_n(\cos\theta)$ is a Legendre function of order n, and $h_n^{(2)'}$ is the derivative of the spherical Hankel function of the second kind of order n. The $e^{j\omega t}$ convention is used here for the complex representation. The pressure on this same surface with the sphere removed, shown in Fig. 2(b), is given by

$$\hat{P}_f(ka,\theta,\hat{R},\hat{P}_+) = \hat{P}_+ e^{-jka\cos\theta} + \hat{P}_+\hat{R}e^{jka\cos\theta}. \quad (13)$$

The complex excess pressure is defined by

$$\hat{P}_{\text{ex}} = \frac{\hat{P}_s}{\hat{P}_f}, \quad (14)$$

and is plotted in Fig. 3 for three values of real reflection coefficient, R, and four values of ka. To numerically calculate the excess pressure and phase, the first 13 terms in the infinite series of Eq. (12) were used. In Fig. 3(a)–(c), the magnitude of the excess pressures on the surface of a sphere are plotted for $R=0$ (the plane wave case), and $R=\pm 0.97$ (the standing wave cases). Reflection coefficients of ± 0.97 are consistent with the absorption characteristics of an enclosure used by the authors for ANC experiments. When $R=0.97$ the pressure field has a maximum at the sensor location, while when $R=-0.97$ the pressure field has a minimum at the sensor location. Figure 3(d)–(f) show the corresponding phases of the excess pressures on the surface of the sphere. The effects of the sphere are obviously more substantial as ka increases.

For the plane wave case in Fig. 3(a) and (d), there is increased pressure where the plane wave first contacts the sphere at $\theta=180$ deg. The scattering effects on the phase shown in Fig. 3(d) are substantial. The authors have determined that the excess phase varies linearly with ka, indicating a time delay. This time delay yields an effective increase in the acoustic path from one microphone to the other, to be discussed later in this paper. When $R=0.97$ the sensor is at a pressure maximum and a velocity minimum. Here, the sphere has a minimal effect on the pressure field. Both the magnitude and phase of the excess pressure in Fig. 3(b) and (e) are small and relatively uniform. The most significant effect on the magnitude of the excess pressure is seen in Fig. 3(c). In this case, the standing wave field produces a velocity maximum at the location of the sensor. The high velocity of air impinging on the sphere causes a substantial pressure increase, since the pressure without an obstacle present is very small. This also causes the phase to be significantly affected, as seen in Fig. 3(f). Ultimately, the effects of the sphere will cause the bias estimates from finite sum and finite difference for the pressure and velocity estimations to generally improve. This will be seen in plots later in this paper.

The hard sphere effectively changes the acoustic separation of the two microphones embedded on the sphere. The acoustic wave no longer has a direct path from one microphone to the other, but has to travel the contour of the sphere. For a single plane wave propagating in the positive z-direction, the reflection coefficient $R=0$, and the pressure on the surface of the sphere becomes

$$\hat{P}_s(ka,\theta,\hat{R}=0,\hat{P}_+) = \frac{\hat{P}_+}{(ka)^2}\sum_{n=0}^{\infty}(-j)^n(2n+1)P_n(\cos\theta) \times\left\{\frac{(ka)^{n+2}}{1\cdot 3\cdot 5\cdots(2n-1)(n+1)}\right\}. \quad (15)$$

The small ka approximation of Eq. (15) is given by[15]

$$\hat{P}_s(ka,\theta,\hat{R}=0,\hat{P}_+) \approx \hat{P}_+(1-j\tfrac{3}{2}ka\cos\theta). \quad (16)$$

Using the finite difference equation Eq. (8) and Eq. (16), the approximate velocity calculated at low frequency for the spherical sensor using $d=a$ would be

$$\hat{V}_{e\theta} \approx \frac{\hat{P}_+ 3ka\cos\theta}{\rho c 2ka}. \quad (17)$$

The constant d is related to the microphone separation distance. (Its exact value will be developed in the next section.) The approximate velocity at low frequency for the two-point sensor under these conditions where $d=b$ is

$$\hat{V}_{e\theta} = \frac{\hat{P}_+ 2\sin(kb\cos\theta)}{\rho c 2kb} \approx \frac{\hat{P}_+ 2kb\cos\theta}{\rho c 2kb}, \quad (18)$$

using Eqs. (8) and (11). The expressions for the velocity calculated for the spherical sensor and the two-point sensor differ only by the factors $3/a$ and $2/b$, respectively. Therefore, the effective separation of the microphones on the sphere is $\frac{3}{2}$ that of the two-point sensor. For subsequent discussion and comparisons, the microphone separation, b, of the two-point sensor will be assumed to be $\frac{3}{2}$ the microphone separation, a, of the spherical sensor. Thus $ka=\frac{2}{3}kb$.

IV. NUMERICALLY CALCULATED BIAS ERRORS

A. Reflection coefficient and microphone mismatch parameters

The bias error equations become quite complex, especially for the case of the spherical sensor which requires an infinite sum. In order to plot the errors, specific values of the reflection coefficient are chosen. Reflection coefficients of materials are typically not available; however, absorption coefficients are. The absorption coefficient, α, of a material is defined as the energy absorbed by the material divided by the energy incident, which can be written as

$$\alpha = \frac{|\hat{P}_+|^2 - |\hat{P}_-|^2}{|\hat{P}_+|^2}. \tag{19}$$

From Eq. (1), $|\hat{P}_-|^2 = |\hat{R}\hat{P}_+|^2$, and for a purely real reflection coefficient

$$\alpha = 1 - R^2. \tag{20}$$

The walls of the ANC test enclosure consist of sand sandwiched between wood layers, and the absorption coefficient of the walls was estimated to be 0.06. This is equivalent to a reflection coefficient of 0.97. The sensor is located at a pressure maximum if the reflection coefficient is 0.97, while the sensor is located at a pressure minimum if the reflection coefficient is -0.97. The pressure maxima and minima are of interest since the finite sum and difference approximations are particularly subject to error there. A plane wave propagation in the positive z-direction occurs for a reflection coefficient of 0, and is also of interest. Hence, reflection coefficients of ± 0.97 and 0 are used when plotting bias errors.

Specific values of microphone magnitude and phase mismatch are also introduced to plot the bias errors. Measurements of the microphones have shown that they exhibit a first-order roll-off near the 3-dB low-frequency cutoff frequency. The low-frequency cutoff frequency of the microphones varied between 4 and 40 Hz. The microphones also exhibit a second order roll-off near 20 kHz. As an approximation, the response of the microphones was modeled as the first-order high-pass transfer function

$$H(j2\pi f) = \frac{j2\pi f}{j2\pi f + 2\pi f_p}, \tag{21}$$

near the low-frequency cutoff frequency, f_p, since the high-frequency break frequency is almost two orders of magnitude greater than f_p. From Eq. (21) the phase response, in degrees, would be

$$\angle H(j2\pi f) = 90 - \frac{180}{\pi}\tan^{-1}\frac{f}{f_p}. \tag{22}$$

From Eq. (22), a low-frequency cutoff frequency variation of 4 to 40 Hz between microphones causes a maximum phase variation of approximately 16 deg at 100 Hz between the microphones. This phase variation is much too high for determining acoustic vector quantities with any degree of accuracy. Therefore, the microphone pairs were selected to have less than 1 deg phase mismatch at 100 Hz. Assuming that the microphones would be calibrated with regard to sensitivity by using a simple trim potentiometer, there will still be some sensitivity drift even over short periods of time. It was observed that the microphones varied ± 0.25 dB in the laboratory. Hence, phase mismatches of ± 1 deg, and sensitivity mismatches of ± 0.25 dB, are used for the microphone pairs when plotting bias errors.

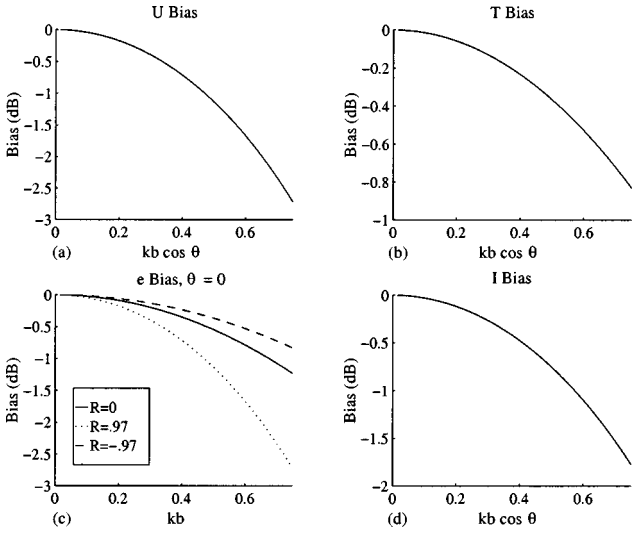

FIG. 4. Bias errors of a two-point sensor with perfectly matched microphones for (a) potential energy density, (b) kinetic energy density, (c) total energy density, and (d) magnitude of intensity measurements.

B. Bias errors of sensors with matched microphones

For the two-point sensor, the bias errors can be calculated using Eqs. (4) and (7)–(10). The normalized complex pressures at the microphones can be found using Eq. (11), where $z = b\cos\theta$ and are given by

$$\hat{P}_{m1} = \delta_m e^{j\delta_p}(e^{-jkb\cos\theta} + \hat{R}e^{jkb\cos\theta}), \tag{23a}$$

$$\hat{P}_{m2} = (e^{jk\cos\theta} + \hat{R}e^{-jkb\cos\theta}). \tag{23b}$$

For matched microphones, $\delta_m = 1$ and $\delta_p = 0$. In Fig. 4, the bias errors are plotted for the two-point sensor with matched microphones. The potential and kinetic energy density as well as the intensity bias errors are not a function of the reflection coefficient. The total energy density bias error is dependent on the real reflection coefficient, R, and angle of incidence, θ, and must be plotted for specific values of each. For different reflection coefficients, the relative contributions of the kinetic and potential energy density change in the total energy density measurement. This is also true for different angles of incidence.

In determining the bias errors for the spherical sensor, only the first 13 terms of Eq. (12) are used, since including more terms does not change the results noticeably. The normalized complex pressures at the two microphones in this case are

$$\hat{P}_{m1} = \delta_m e^{j\delta_p}\frac{\hat{P}_s(kd,\theta,\hat{R},\hat{P}_+)}{\hat{P}_+}, \tag{24a}$$

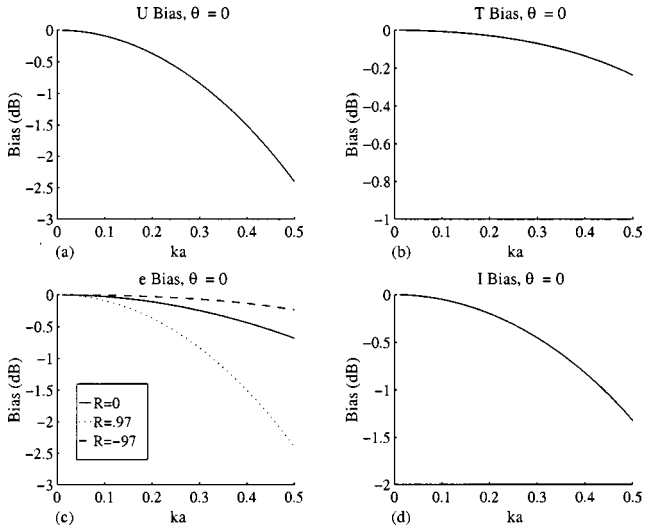

FIG. 5. Bias errors of a spherical sensor with perfectly matched microphones for (a) potential energy density, (b) kinetic energy density, (c) total energy density, and (d) magnitude of intensity measurements.

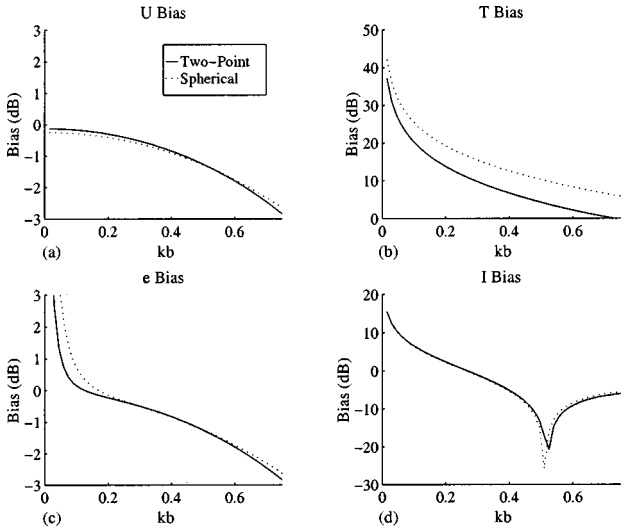

FIG. 6. Bias errors of a spherical sensor and two-point sensor for microphones having a 1-deg phase and 0.25-dB sensitivity mismatch. Sensors are in a standing wave field with reflection coefficient $R=0.97$ and incident angle $\theta=0$. (a) Potential energy density bias, (b) kinetic energy density bias, (c) total energy density bias, (d) magnitude of intensity bias.

$$\hat{P}_{m2}=\frac{\hat{P}_s(kd,\theta+\pi,\hat{R},\hat{P}_+)}{\hat{P}_+}, \tag{24b}$$

where $d=\frac{3}{2}a$. Again, the bias errors can be calculated using Eq. (4) and Eqs. (7)–(10). In Fig. 5, the bias errors are plotted for the spherical sensor with matched microphones.

As Elko noted in his work, there is a general improvement in the bias errors due to the diffraction of the hard sphere.[13] The smallest improvement in the total energy density bias occurs when $R=0.97$. Earlier it was seen that the diffraction effects due to the sphere were minimal for this reflection coefficient compared to $R=-0.97$ and $R=0$. The diffraction of the sphere also causes all the bias errors to be a function of ka and θ separately, so that specific angles of θ must be chosen for plotting. The errors of the two-point sensor increase as $\cos\theta$ approaches unity, so the angle chosen for plotting the bias errors was 0, in order to yield the greatest errors.

C. Bias errors of sensors with mismatched microphones

For matched microphones the bias errors are relatively small. If a sensitivity and phase mismatch are allowed in the microphones, a dramatic effect is seen on the bias errors. The spherical sensor and two-point sensor bias errors are plotted in Fig. 6, for the case of 1 deg phase and 0.25-dB sensitivity mismatch in a standing wave field where $R=0.97$, and the angle of incidence is 0.

As compared to Figs. 4 and 5, the errors in general have significantly increased. There is no longer an improvement in bias errors due to spherical scattering, and generally the errors are dominated by the sensitivity and phase mismatch of the microphones. An important point in comparing the spherical and two-point sensors is that the bias errors show the same trends.

V. TWO-POINT SENSOR BIAS EQUATIONS

The bias error equations for the spherical sensor are intractable due to the infinite series involved. Since the bias error plots for the two-point sensor and the spherical sensor follow the same trends, insight into the bias errors can be gained by studying the bias error equations for the two-point sensor alone. In the case of the two-point sensor, the estimated pressure and velocity using the finite sum and finite difference equations, respectively, are

$$\hat{P}_{ec}=e^{j(\delta p/2)}[(\delta_m+1)(\cos A+\hat{R}\cos B)+j(\delta_m-1)(\sin A+\hat{R}\sin B)], \tag{25a}$$

$$\hat{V}_{e\theta}=\frac{je^{j(\delta p/2)}}{\rho c 2kd}[(\delta_m-1)(\cos A+\hat{R}\cos B)+j(\delta_m+1)(\sin A+\hat{R}\sin B)], \tag{25b}$$

where

$$A=\frac{\delta_p}{2}-kd\cos\theta \quad \text{and} \quad B=\frac{\delta_p}{2}+kd\cos\theta.$$

It follows from Eqs. (7)–(10) that the bias equations are then

$$U_{\text{bias}}=\frac{2\eta(\delta_m^2\cos(\xi+\sigma)+2\delta_m\cos\xi\cos\delta_p+\cos(\xi-\sigma))}{4(1+\eta^2+2\eta\cos\xi)}+\frac{2\delta_m(\cos(\delta_p-\sigma)+\eta^2\cos(\delta_p+\sigma))+(1+\delta_m^2)(1+\eta^2)}{4(1+\eta^2+2\eta\cos\xi)}, \tag{26a}$$

$$T_{\text{bias}}=\frac{2\eta(\delta_m^2\cos(\xi+\sigma)-2\delta_m\cos\xi\cos\delta_p+\cos(\xi-\sigma))}{\sigma^2(1+\eta^2-2\eta\cos\xi)}-\frac{2\delta_m(\cos(\delta_p-\sigma)+\eta^2\cos(\delta_p+\sigma))-(1+\delta_m^2)(1+\eta^2)}{\sigma^2(1+\eta^2-2\eta\cos\xi)}, \tag{26b}$$

$$e_{\text{bias}}=\frac{U_{\text{bias}}|1+\hat{R}|^2+3T_{\text{bias}}|1-\hat{R}|^2\cos^2\theta}{|1+\hat{R}|^2+3|1-\hat{R}|^2\cos^2\theta}, \tag{26c}$$

$$I_{\text{bias}}=\frac{\delta_m(\sin(\delta_p-\sigma)+\eta^2\sin(\delta_p+\sigma)+2\eta\cos\xi\sin\delta_p)}{\sigma(\eta^2-1)}, \tag{26d}$$

where $\sigma=2kd\cos\theta$; ξ and η are defined in Eq. (1). A bias greater than unity indicates an estimate which is high, while a bias between zero and unity indicates an estimate which is low. Negative biases for the velocity or intensity indicate that the vector is 180 deg out of phase. Biases substantially deviating from unity indicate large errors.

The expression for the intensity bias in Eq. (26d) is relatively simple, and clearly indicates the potential for large errors. When the microphones are not phase matched, bias errors increase as σ approaches zero, such as at low frequency and/or an angle of incidence approaching 90 deg. Bias errors also become very large when the numerator of Eq. (26d) approaches zero for finite σ. For $|\sigma|\ll 1$ (in radians) and $|\delta_p|\ll 1$ (in radians), Eq. (26d) can be approximated as

$$I_{\text{bias}}\approx\frac{\delta_m(\sigma(\eta^2-1)+\delta_p|1+\hat{R}|^2)}{\sigma(\eta^2-1)}. \tag{27}$$

The numerator of Eq. (27) becomes zero when

$$\sigma=\frac{\delta_p|1+\hat{R}|^2}{(1-\eta^2)}. \tag{28}$$

Therefore, a finite intensity can yield an intensity estimate of zero, and result in infinite error. The value of σ where this occurs is proportional to δ_p, and therefore the phase mismatch should be kept as small as possible.

The kinetic energy density bias, in Eq. (26b), is a function of $1/\sigma^2$ and the error becomes large for finite phase mismatch as σ approaches zero. For $|\sigma|\ll 1$, the measurement error for the kinetic energy density will be substantially greater than the intensity error, since the intensity bias is a function of $1/\sigma$. The bias errors in kinetic energy density will be greatest when the sensor is at a velocity minimum, when phase mismatches are present in the microphones. The pressures at the two microphones will be large, but very nearly the same in magnitude and phase. Small changes in the microphone phase due to microphone phase mismatch therefore yield a relatively large pressure difference and estimated velocity. At pressure minima, the magnitude of the pressure is low, but the phase gradient is large. Small phase mismatches in the microphones, therefore, have much less of an effect on the estimated velocity in this case.

The expression for the potential energy density in Eq. (26a) is not a function of $1/\sigma$, and therefore does not have the very large errors for small σ as in the intensity and kinetic energy density estimates. For $|\sigma|\ll 1$ rad, and $|\delta_p|\ll 1$, Eq. (26a) can be approximated as

$$U_{\text{bias}}\approx\frac{(1+\delta_m)^2|1+\hat{R}|^2+2\sigma\eta(1-\delta_m^2)\sin\xi+2\sigma\delta_m\delta_p(1-\eta^2)}{4|1+\hat{R}|^2}. \tag{29}$$

When the value of R is not close to -1, the first term in the numerator of Eq. (29) dominates the expression, and Eq. (29) reduces to

$$U_{\text{bias}}\approx\frac{(1+\delta_m)^2}{4}. \tag{30}$$

If $|\delta_{m,\text{dB}}|<1$ dB, then

$$U_{\text{bias}}\approx\sqrt{\delta_m} \tag{31}$$

and

$$U_{b,\text{dB}}\approx\tfrac{1}{2}\delta_{m,\text{dB}}. \tag{32}$$

Hence, the potential energy density bias in decibels for small microphone mismatches and small σ is equal to one-half the sensitivity mismatch in decibels.

The equation for the total energy density bias, Eq. (26c), illustrates that the error is a function of the potential and kinetic energy density bias. The error is high for the kinetic energy density when the sensor is located at a velocity minimum, but the kinetic energy density is quite small compared to the potential energy density. The potential energy density error is relatively small here and dominates the total energy density calculation. Thus the potential energy density mitigates the error due to the kinetic energy density calculation. In general, the errors for the kinetic energy density and potential energy density will not both be high at the same locations, and the errors are reduced for the total energy density calculation.

VI. NUMERICALLY CALCULATED BIAS ERRORS FOR A SPHERICAL SENSOR

A. Results of a single-axis, two-microphone sensor

The bias errors of the spherical sensor were shown to be consistent with the bias errors of the two-point sensor, as illustrated in the previous sections. The spherical sensor also provides a very convenient way of mounting the microphones that is more compact than the two-point sensor by a factor of $\frac{2}{3}$. For these reasons, the spherical sensor is the more attractive sensor and will be studied further in this paper. In this section, the bias errors of the spherical sensor are calcu-

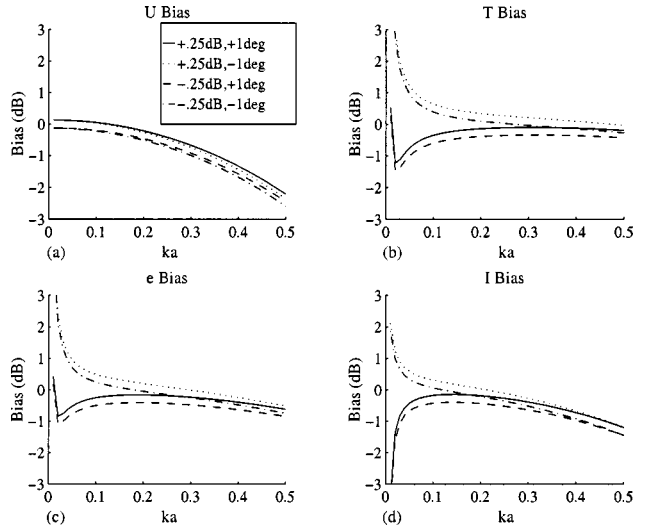

FIG. 7. Bias errors of a spherical sensor with sensitivity and phase mismatched microphones. $R=0$, $\theta=0$. (a) Potential energy density bias, (b) kinetic energy density bias, (c) total energy density bias, (d) magnitude of intensity bias.

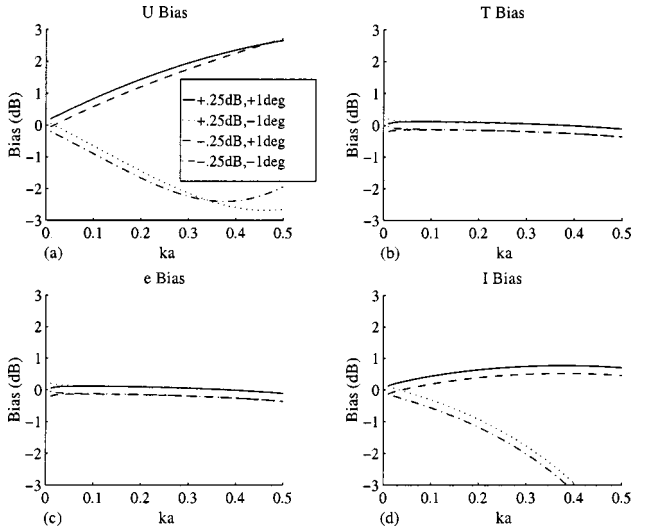

FIG. 9. Bias errors of a spherical sensor with sensitivity and phase mismatched microphones. $R=-0.97$, $\theta=0$. (a) Potential energy density bias, (b) kinetic energy density bias, (c) total energy density bias, (d) magnitude of intensity bias.

lated numerically and plotted for specific parameter values. The bias errors were determined using Eqs. (7)–(10), Eqs. (24), and the first 13 terms of the infinite series in Eq. (12).

The following three figures, Figs. 7–9, show the bias errors for the spherical sensor for reflection coefficients of 0 and ± 97. Four plots are overlaid for each subplot for microphones having a sensitivity mismatch of ± 0.25 dB, with a phase mismatch of ± 1 deg. Figure 7 shows the bias errors for the spherical sensor in a plane wave field, while Figs. 8 and 9 show the bias errors for the spherical sensor in standing wave fields producing a pressure maximum and a pressure minimum at the sensor location, respectively.

The angle of incidence is chosen to be zero for all cases, since this generally yields poor estimations in the total energy density measurement. Earlier, it was shown that the intensity bias error has a singularity for angles of incidence approaching 90 deg. The velocity is zero, but the estimated velocity is finite due to the microphone mismatch. The kinetic energy density and intensity errors are therefore very large. Since the θ-component of the velocity is very small, in this case, the velocity contribution to the total energy density is insignificant. The pressure estimate is very accurate in this case; therefore the total energy density error is low.

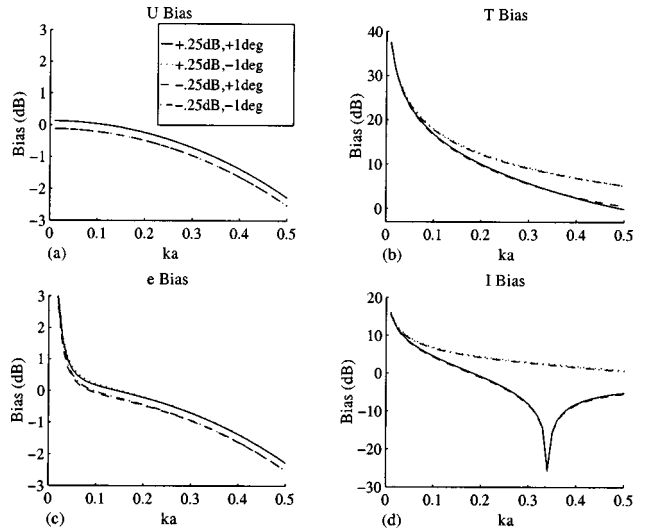

FIG. 8. Bias errors of a spherical sensor with sensitivity and phase mismatched microphones. $R=0.97$, $\theta=0$. (a) Potential energy density bias, (b) kinetic energy density bias, (c) total energy density bias, (d) magnitude of intensity bias.

The plots for the spherical sensor bias errors are consistent with the analysis conducted on the two-point sensor bias equations in the previous section. In each figure, the potential energy density bias plots show the bias error approaching $\frac{1}{2}\delta_{m,\mathrm{dB}}$ (or ± 0.125 dB) for small ka. The kinetic energy density bias error, on the other hand, becomes asymptotically large as ka approaches zero due to its dependence on $1/\sigma^2$. It is difficult to see this in Fig. 9(b) since the error diverges very close the y-axis. The intensity error is similar to the kinetic energy density for very small ka, but the error is not as severe due to its dependence on $1/\sigma$ instead of $1/\sigma^2$. The intensity error also has the singularity indicated by Eq. (28) and seen in Fig. 8(d). The total energy density bias error appears as a combination of the potential and kinetic energy density errors. In all three figures, the potential and kinetic energy densities exhibit larger errors when the sensor is located at a respective minima. When one measurement exhibits large errors, the other does not. The quantity producing the larger error does not contribute to the total energy density as much as the quantity that has smaller errors. Therefore, the total energy density measurement has smaller errors than both. This is true except at low frequencies, where the kinetic energy density approximation swamps out the mitigating effects of the potential energy density approximation. The total energy density bias errors are within ± 1 dB for $.03<ka<.3$ for all the plots. This analysis indicates that the total energy density has the smallest bias errors of all four measurements, except for very small values of ka, when finite sum and difference approximations are used.

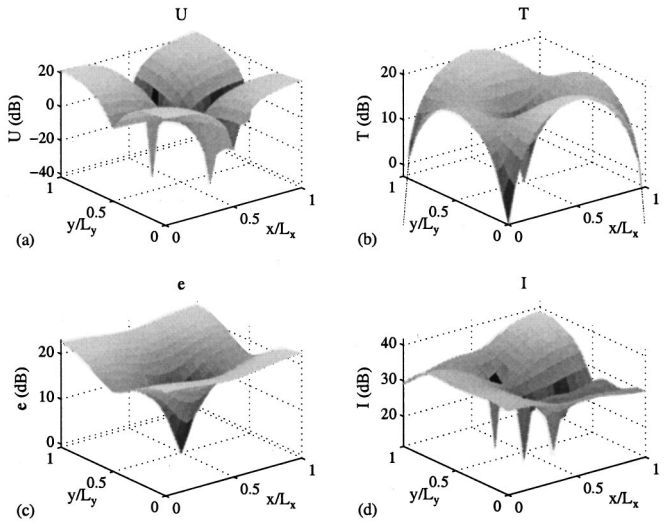

FIG. 10. Predicted (a) potential energy density, (b) kinetic energy density, (c) total energy density, and (d) magnitude of intensity, in the $z/L_z=0.4$ plane for 135.8 Hz, mode (1, 1, 0) excitation.

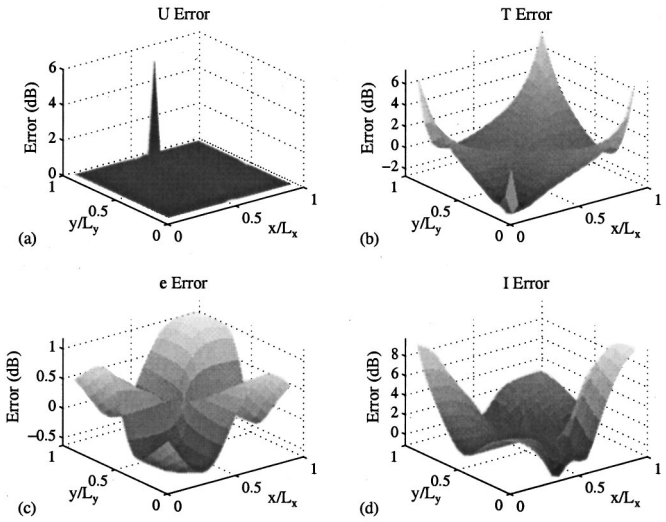

FIG. 11. Predicted spherical sensor error for microphones with a 0.25-dB sensitivity and 1-deg mismatch. (a) Potential energy density bias, (b) kinetic energy density bias, (c) total energy density bias, and (d) magnitude of intensity bias, in the $z/L_z=0.4$ plane for 135.8 Hz, mode (1, 1, 0) excitation.

B. Results of a three-axes, six-microphone sensor

The bias errors for a three-axis spherical sensor in a three-dimensional pressure field were predicted with a simulation. The sensor employs six microphones oriented along three orthogonal axes. A simulation program generates the pressure and velocity fields within a rectangular enclosure due to a point monopole source. The enclosure's dimensions are $1.5\times2.4\times1.9$ m, having one corner at the origin and the other at (1.5, 2.4, 1.9). The source was located at the normalized point in space (0.12, 0.97, 0.97), where normalized coordinates are defined as $(x/L_x, y/L_y, z/L_z)$. The absorption coefficients used for the walls were $\alpha_x=0.0479$, $\alpha_y=0.0313$, and $\alpha_z=0.0730$. These parameters are consistent with an enclosure used by the authors for ANC experiments. Since the errors in measurements are mostly due to the microphone mismatches, the diffraction effects of the sphere were not modeled. The sphere used in the simulation had a radius of 1 in (0.0254 m), consistent with the size of the sensor ultimately constructed. One microphone from each axis pair was offset in sensitivity by 0.25 dB and 1 deg in phase. Thus each microphone pair had a sensitivity and phase mismatch. The excitation frequency of the enclosure was chosen to be 135.8 Hz, corresponding to the sixth mode, with mode indices (1, 1, 0). An on-resonance frequency was chosen due to the variety of pressure and phase gradients created by on-resonance excitation.

The potential, kinetic, and total energy density, as well as the magnitude of the intensity, were calculated in the $z/L_z=0.21$ plane; these plots are shown in Fig. 10. The reference value for each of the quantities was chosen to be unity when calculating magnitudes of the fields in units of decibels. The complex pressures were then calculated numerically for each of the six microphones on the sensor. One microphone in each of the axis pairs was offset in sensitivity and phase. The estimated acoustic fields were then determined using Eqs. (4)–(10), where $d=\frac{3}{2}a$. These fields were compared to the actual predicted fields yielding errors as a function of space in the $z/L_z=0.21$ plane. The error plots are shown in Fig. 11.

It can be seen in Fig. 11 that the smallest errors occur for the total energy density estimation. The error surface is smooth with no singularities or large gradients. The potential energy density estimation has small errors except in one region where it has a sharp peak located at a pressure node. The kinetic energy density estimation has higher errors than the potential energy density estimation, and again the largest errors are at most of the nodes. In this case, the velocity nodes are in the corners and center of the enclosure. As expected, the intensity errors are large since the enclosure is lightly damped. The intensity errors are highest in general where the velocity estimation is poor. As in the two-dimensional sensor analysis, the pressure dominates the total energy density when the velocity error is high, while the velocity dominates the total energy density when the pressure error is high. In the corners of the enclosure, the total energy density estimate improves as the velocity contribution is decreased. The total energy density estimate ensures no singularities in the error. The results of the three-axes spherical sensor are consistent with the analysis for the two-axes sensor. Overall, the magnitudes of the errors in the total energy density estimate are less than 1 dB, which is expected to be low enough for use in an active control system.

VII. EXPERIMENTALLY MEASURED BIAS ERRORS FOR A SPHERICAL SENSOR

The previous analyses indicate the magnitude of the errors associated with a spherical sensor when measuring vector field acoustic quantities. A spherical vector-field sensor was constructed and then tested in a three-dimensional rectangular enclosure consistent with the previous computer simulations. A photograph of two sensors is shown in Fig. 12. A two-inch-diameter wooden ball purchased from a craft store was used as the hard sphere for housing the microphones. Three microphone pairs were mounted along the

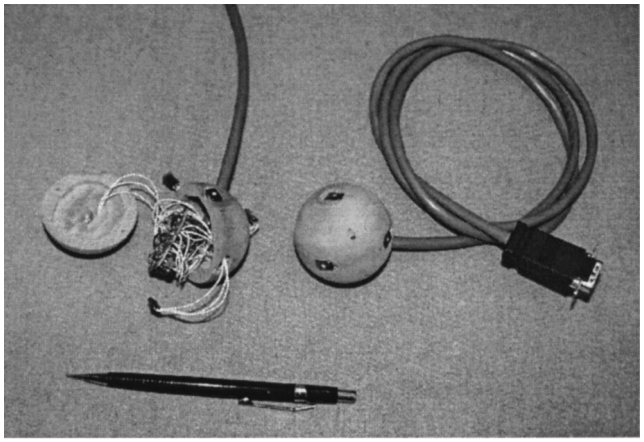

FIG. 12. Two energy density sensors. Sensor diameter is 2 in.

three orthogonal axes. Each pair was used to estimate the acoustic velocity along its axis as well as the average acoustic pressure. The wooden sphere was cut in two and hollowed to make room for bias and gain circuits, while the surface was routed to allow the microphones to be flush-mounted. A cable with a connector termination provides power and signal connections. The sensor on the left is open, revealing the electronic circuit board inside. The total cost of a sensor was approximately $100, $90 of which was for the microphones.

Two sensor locations were chosen for the experiments. One location was in the center of the enclosure at a normalized location of (0.50, 0.50, 0.50), while the other was chosen to be off-center at a normalized location of (0.32, 0.62, 0.64). The sensor was placed in the center of the enclosure due to the many maxima and minima located there, while it was placed off-center to be located in a more random position. Three speakers were placed in close proximity to each other, in a corner of the enclosure to achieve high enough sound pressure levels off-resonance for accurate measurements. A white noise signal was used as the excitation.

A B&K 4135 $\frac{1}{4}$-in diameter matched-microphone pair was used as a two-point sensor to determine the reference measurements. Measurements were taken with the microphone pair aligned with the *x*-, *y*-, and *z*-axes to yield the three orthogonal components of potential, kinetic and total energy density, as well as intensity. A HP 35665A dynamic signal analyzer was used to measure the acoustic quantities along a single axis using the following formulas:

$$U_\theta = \frac{G_1 + G_2 + 2\,\mathrm{Re}\{G_{12}\}}{48\rho c^2}, \tag{33a}$$

$$T_\theta = \frac{G_1 + G_2 - 2\,\mathrm{Re}\{G_{12}\}}{32\rho d^2 \omega^2}, \tag{33b}$$

$$e_\theta = U_\theta + T_\theta, \tag{33c}$$

$$I_\theta = \frac{-1}{\rho 4 d \omega}\,\mathrm{Im}\{G_{12}\}, \tag{33d}$$

where $d=b$, one-half the microphone spacing.[10] The autospectral densities of microphones $m1$ and $m2$ are G_1 and G_2, respectively, while G_{12} is the microphone cross-spectral

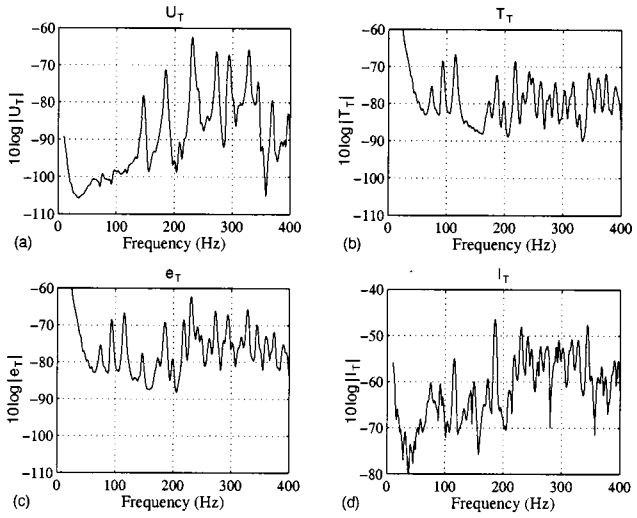

FIG. 13. Two-point sensor experimental measurements. Sensor located at (0.50, 0.50, 0.50). (a) Potential energy density, (b) kinetic energy density, (c) total energy density, (d) intensity.

density. These formulas can be derived from Eqs. (4), (7), and (8) for stationary signals. The three orthogonal components of the acoustic quantities were postprocessed in the software MATLAB™ to yield the complete measurements using Eqs. (5). The acoustic quantities for the spherical sensor were determined the same way, except $d=\frac{3}{2}a$ was used. The two-point sensor microphone spacing was equal to the spacing of the spherical sensor microphones in the experiments, thus $b=a=1$ in.$(0.0254\,\mathrm{m})$.

The acoustic quantities determined using the B&K setup for the sensor located in the center of the enclosure and off-center are plotted in Figs. 13 and 14, respectively. The reference measurements show many fewer peaks in the potential energy density measurement when the sensor is located in the center of the enclosure compared to off-center, since the nodal surfaces of many acoustic modes pass through the center of the enclosure. There are also many velocity minima at the center of the enclosure, and the kinetic energy density

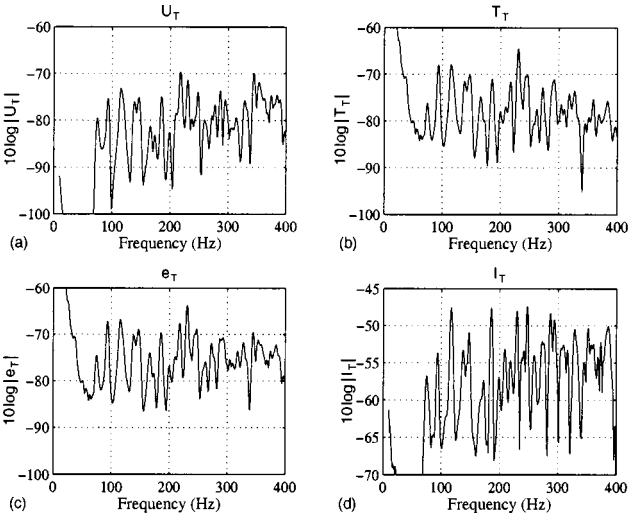

FIG. 14. Two-point sensor experimental measurements. Sensor located at (0.32, 0.62, 0.64). (a) Potential energy density, (b) kinetic energy density, (c) total energy density, (d) intensity.

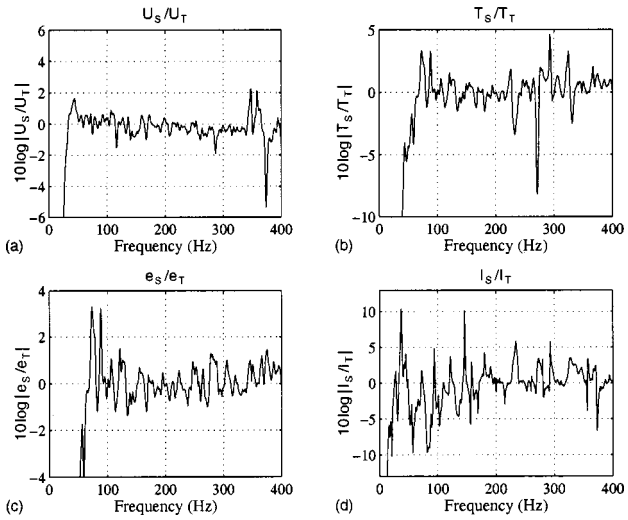

FIG. 15. Difference between two-point sensor measurements and spherical sensor measurements in (a) potential energy density, (b) kinetic energy density, (c) total energy density, and (d) intensity. Sensors located at (0.50, 0.50, 0.50).

measurements show many fewer peaks at that location as well, compared to the off-center location. The total energy density plots have peaks where the potential or kinetic energy density have peaks.

The differences between the spherical sensor measurements and the two-point sensor measurements are shown in Figs. 15 and 16. The differences are due to the sensitivity and phase mismatch of the spherical vector-field sensor, diffraction due to the sphere, and experimental error. The experimental error is mainly due to the inability to remove and replace the sensors so that they are located in exactly the same point in space.

The total energy density estimate using the spherical sensor is within ± 1.75 dB of the measurement made using the matched-microphone B&K setup in the frequency region $110 < f < 400$ Hz. All the other estimates produce errors

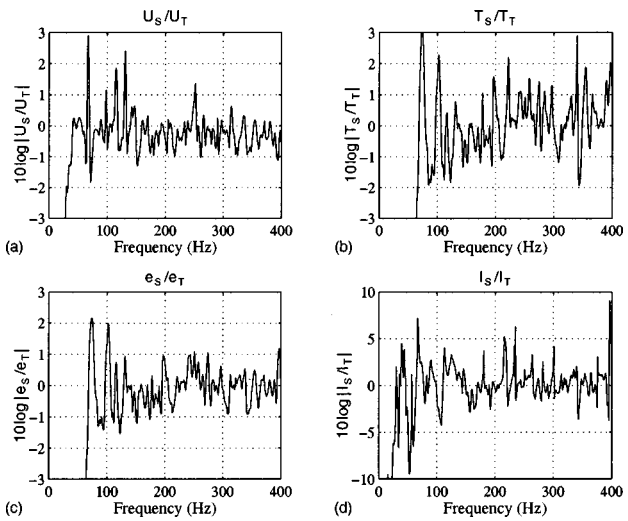

FIG. 16. Difference between two-point sensor measurements and spherical sensor measurements in (a) potential energy density, (b) kinetic energy density, (c) total energy density, and (d) intensity. Sensors located at (0.32, 0.62, 0.64).

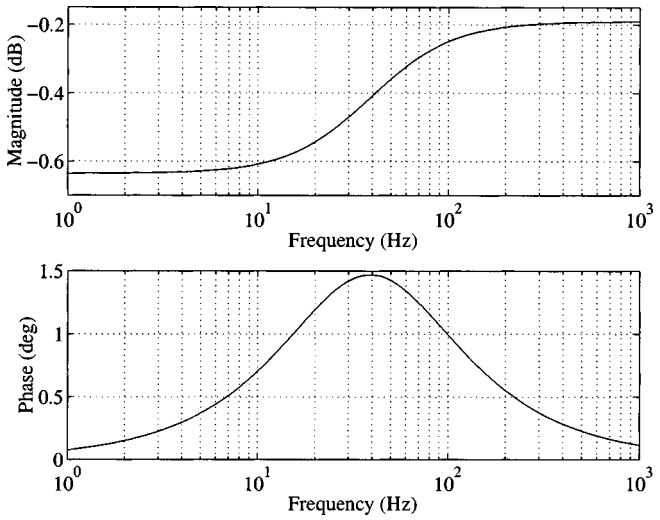

FIG. 17. Bode plot of transfer function between two microphones having a sensitivity mismatch of 0.25 dB and phase mismatch of 1 deg at 100 Hz.

larger than the total energy density estimate in this frequency region. Under 110 Hz the errors for the total energy density increase due to the $1/\sigma^2$ term in the bias equation. As in the three-dimensional field simulation, the energy density measurement tends to smooth out the largest errors from the potential and kinetic energy density measurements.

The errors at low frequency can be even higher than those predicted by the previous analysis. From Eq. (21), the transfer function between two microphones having sensitivity and phase mismatch is given by

$$H(j2\pi f) = \delta_m \frac{j2\pi f + 2\pi f_{p1}}{j2\pi f + 2\pi f_{p2}}. \tag{34}$$

A Bode plot of this transfer function is shown in Fig. 17, where the cutoff frequencies are $f_{p1} = 38$ and $f_{p2} = 40$ Hz. These cutoff frequencies yield a phase mismatch of 1 deg at 100 Hz. The microphones are also given a -0.25-dB sensitivity mismatch.

The previous analysis assumed a constant sensitivity and phase mismatch as a function of frequency, however Fig. 17 shows this not to be true. The phase error increases as the frequency is reduced below 100 until 40 Hz, but decreases as the frequency is increased above 100 Hz. The sensitivity mismatch can also increase at low frequency, depending on the microphone phase/sensitivity combination. Thus the errors in total energy density can be higher than those expected at frequencies lower than the cutoff frequency, but may improve at higher frequencies. The cutoff frequency for the microphones used is no higher than 40 Hz. So long as the energy density sensor is used to measure fields with frequency content above 40 Hz, the acoustical estimates should be more nearly accurate than those predicted by the simulations.

VIII. SUMMARY

Two configurations of a vector-field sensor were studied in this paper with regard to measurement error. The estimates of potential, kinetic, and total energy density as well as intensity were investigated. The spherical sensor's errors are

similar in magnitude to the two-point sensor's, yet had two beneficial features. The spherical sensor provides a convenient way of mounting and locating the sensor microphones, and the diffraction effects of a spherical sensor cause an increase in the effective separation of the microphones. Thus a spherical sensor can be made smaller by a factor of $\frac{2}{3}$ while maintaining the same accuracy as a two-point sensor.

It was shown that the spherical sensor generally improves the accuracy of the acoustical measurements when the sensor microphones are matched in sensitivity and phase. When the microphones are mismatched, however, the effects of the microphone mismatch dominate the errors, and there is no longer a significant improvement in accuracy due to diffraction effects around the sphere. It was also shown that a vector-field sensor could be constructed with inexpensive electret microphones, where the accuracy of the total energy density error could be kept within ± 1.75 dB for two measurements in the $110 < f < 400$-Hz frequency range. The errors seen in the experimental measurements showed the same trends as those predicted by theory and simulation.

ACKNOWLEDGMENTS

The authors would like to thank the Applied Research Laboratory at Penn State University and NASA Langley for funding this research.

[1] A. E. Schwenk, S. D. Sommerfeldt, and S. I. Hayek, ''Adaptive control of structural intensity associated with bending waves in a beam,'' J. Acoust. Soc. Am. **96**, 2826–2835 (1991).

[2] S. D. Sommerfeldt and B. L. Scott, ''Wavenumber sensors for active control of acoustic radiation,'' in *Proceedings of the 1993 North American Conference on Smart Structures and Materials*, 1993, Vol. 1917, pp. 612–622.

[3] X. Pan, T. J. Sutton, and S. J. Elliott, ''Active control of sound transmission through a double-leaf partition by volume velocity cancellation,'' J. Acoust. Soc. Am. **105**, 2828–2835 (1998).

[4] S. J. Elliot, P. A. Nelson, I. M. Stothers, and C. C. Boucher, ''In-flight experiments on the active control of propeller-induced cabin noise,'' J. Sound Vib. **140**, 219–238 (1990).

[5] S. D. Sommerfeldt and P. J. Nashif, ''Energy based control of the sound field in enclosures,'' *Second International Congress on Recent Developments in Air and Structure-Borne Sound and Vibration*, March, 1992, pp. 361–368.

[6] P. J. Nashif, ''An energy-density-based control strategy for minimizing the sound field in enclosures,'' M.S. thesis, Pennsylvania State University, University Park, PA, 1992.

[7] S. D. Sommerfeldt and J. W. Parkins, ''An evaluation of active noise attenuation in rectangular enclosures,'' *Proc. Inter-Noise 94*, pp. 1351–1356 (1994).

[8] S. D. Sommerfeldt, J. W. Parkins, and Y. C. Park, ''Global active noise control in rectangular enclosures,'' *Proc. ACTIVE 95*, pp. 477–488 (1995).

[9] J. W. Parkins, S. D. Sommerfeldt, and J. Tichy, ''Narrowband and broadband active control in an enclosure using the acoustic energy density,'' J. Acoust. Soc. Am. **108**, 192–203 (2000).

[10] F. J. Fahy, *Sound Intensity* (E. & F.N. Spon, London, 1995), pp. 91–97.

[11] I. Wolff and F. Massa, ''Use of pressure gradient microphones for acoustical measurements,'' J. Acoust. Soc. Am. **4**, 217–234 (1933).

[12] R. K. Cook and P. A. Schade, ''New method for measurement of the total energy density of sound waves,'' *Proc. Inter-Noise 74*, pp. 101–106 (Oct. 1974).

[13] G. W. Elko, ''An acoustic vector-field probe with calculable obstacle bias,'' *Proc. Noise-Con 91*, pp. 525–532 (July 1991).

[14] F. J. Fahy, ''Measurement of the acoustic intensity using the cross-spectra-density of two microphone sensors,'' J. Acoust. Soc. Am. **62**, 1057–1059 (1977).

[15] P. M. Morse and K. U. Ingard, *Theoretical Acoustics* (Princeton University Press Reprint 1986, McGraw-Hill, New York, 1968), pp. 418–421.

Time reversal and the inverse filter

Mickaël Tanter, Jean-Louis Thomas, and Mathias Fink
Laboratoire Ondes et Acoustique, ESPCI, Université Paris VII, U.R.A. C.N.R.S. 1503, 10 rue Vauquelin, 75005 Paris, France

(Received 15 October 1998; revised 7 December 1999; accepted 13 April 2000)

To focus ultrasonic waves in an unknown inhomogeneous medium using a phased array, one has to calculate the optimal set of signals to be applied on the transducers of the array. In the case of time-reversal mirrors, one assumes that a source is available at the focus, providing the Green's function of this point. In this paper, the robustness of this time-reversal method is investigated when loss of information breaks the time-reversal invariance. It arises in dissipative media or when the field radiated by the source is not entirely measured by the limited aperture of a time-reversal mirror. However, in both cases, linearity and reciprocity relations ensure time reversal to achieve a spatiotemporal matched filtering. Nevertheless, though it provides robustness to this method, no constraints are imposed on the field out of the focus and sidelobes may appear. Another approach consists of measuring the Green's functions associated to the focus but also to neighboring points. Thus, the whole information characterizing the medium is known and the inverse source problem can be solved. A matrix formalism of the propagation operator is introduced to compare the time-reversal and inverse filter techniques. Moreover, experiments investigated in various media are presented to illustrate this comparison.
[S0001-4966(00)04507-0]

PACS numbers: 43.60.Pt, 43.60.Gk, 43.80.Vj [JCB]

INTRODUCTION

In most applications of ultrasound, medical therapy, or diagnostic, nondestructive testing, the first step consists of focusing an ultrasound beam deeply inside the medium to be investigated. The variations of speed of sound are usually unknown and the method has to be adaptive. In previous papers, it has been shown how time-reversal invariance of the wave equation can be used to focus ultrasonic waves through heterogeneous lossless media.[1,2] This property means that, for each burst of sound that comes from a source and that can be refracted or scattered, there is a set of waves that precisely retraces all of the possible paths, ultimately converging at the original source. This property ensures that the optimal focusing is achieved by applying the time-reversal process on a closed surface covered with a 2D array of reversible transducers and surrounding the source. This leads to the concept of time-reversal cavity, where the divergent wave issued from a point-like source is sampled, time-reversed, and reemitted from the 2D array. Such a processing acts as an inverse filter of the diffraction transfer function that relates the wave-field propagation from the source to the closed surface. However, this filter is not perfect, because evanescent waves emitted by the source cannot be recorded on the surface and thus cannot be time-reversed. Diffraction acts as a low-pass filter and it leads to the classical diffraction limit that prevents the size of the time-reversed focal spot to be smaller than half the wavelength.

In practice, a time-reversal cavity is difficult to realize[3] and the time-reversal operator is only achieved over a limited area known as a time-reversal mirror (TRM). Its limited angular aperture gives rise to another low-pass filter whose cutoff frequency is lower. In a homogeneous medium, this cutoff frequency only depends on the angular aperture of the array and it results in a diffraction spot whose dimensions are proportional to the product of the wavelength by the array angular aperture. However, in a heterogeneous medium the plane wave decomposition is not so well adapted and it becomes very difficult to predict the behavior of a TRM. It strongly depends on the nature of the heterogeneous medium. For example, on the one hand, Derode *et al.* have shown that, compared to a homogeneous medium, the diffraction spot can be much thinner when a multiply scattering medium of large dimensions is used between a source and the array.[4] On the other hand, Tanter *et al.* have shown the opposite effect, when a strongly diffracting aberrating layer is introduced between the source and the array.[5] In this last case, the time-reversal spot is degraded and becomes three times bigger than in a homogeneous medium. Such experiments emphasize that, as soon as a limited aperture is used, heterogeneities even in a lossless medium can induce either an improvement or a degradation of the quality of the time-reversal focusing in comparison with the same experiment conducted in a homogeneous medium. Finally, in a third case, the time-reversal process has been applied to the focusing through the skull, for which loss of information results from absorption in the bone. In such a medium with dissipation, the wave equation is no longer time-reversal invariant. However, the time-reversal process (TRP) has shown its ability to compensate for the shift of the focus. Hence, when a complete time reversal is not achievable because of loss of information induced either by the limited aperture or the attenuation, one can no more rely on the time-reversal invariance and it becomes very difficult to predict the behavior of a TRM.

So, paradoxically, the argument of time-reversal invariance is perhaps not the best approach to describe a time-

reversal experiment when losses of information are involved. However, time-reversal processing remains a spatiotemporal matched filter as soon as linearity and reciprocity assumptions are justified in the medium (it has already been shown that time-reversal processing carries out a matched filtering in the time domain[6] and we extend this result here to the spatial domain). Note that spatial reciprocity has no direct relationship with time-reversal invariance or reversibility. Indeed, whereas reversibility requires energy conservation, the reciprocity relations hold for an absorbing medium and are a direct consequence of the symmetry between causes and effects. Therefore, linearity and reciprocity provide robustness to the time-reversal focusing. However, as a matched filter maximizes the amplitude of the output at a specified location and time for a given input energy, time-reversal processing only optimizes the pressure amplitude at the focus. On the contrary, as it is based on reversibility, an inverse filter adds others constraints on the field around the focus, and thus imposes the sidelobe level or the width of the main lobe.

In the first part of this paper, a matrix formalism of the propagation operator relating the array transducers to a set of control points located in the medium is introduced. Each Fourier component of this spatiotemporal filter is a complex matrix $\mathbf{H}$. For a given Fourier component, the inverse filter process is then easily described by the matrix inverse diffraction operator $\mathbf{H}^{-1}$. The physical meaning of such an inverse diffraction operator is studied by using the singular value decomposition (SVD) of $\mathbf{H}$. In the same way, time-reversal processing is then described by introducing a time-reversal operator $\mathbf{H}\tilde{\mathbf{H}}$, where $\tilde{\mathbf{H}}$ is the transpose conjugate of $\mathbf{H}$. This time-reversal operator is also described by using the singular value decomposition of $\mathbf{H}$ and finally compared to $\mathbf{H}^{-1}$. A first experiment is conducted in a homogeneous medium and the close similarity of inverse filter processing and time-reversal focusing in that particular case is made evident.

In the second part of the paper, two experiments made in two different heterogeneous media are presented to illustrate these theoretical aspects. The propagation operator $\mathbf{H}$ is experimentally acquired in both media and the behavior of the two operators $\mathbf{H}^{-1}$ and $\mathbf{H}\tilde{\mathbf{H}}$ characterizing both focusing processes is described and compared. In both cases, loss of information occurs in the medium and involves a degradation of time-reversal focusing. In the first experiment, we deal with the ultrasonic focusing through the skull bone for which loss of information results from absorption.[7,8] In the second experiment, achieved in a lossless medium, the loss of information is due to the limited aperture of the array combined with the strongly diffracting behavior of a lossless aberrating layer. The influence of the medium heterogeneities on the spatial frequencies content of the wave field during propagation is studied to describe the total or partial loss of information for the time-reversal process as well as the inverse filter technique. Both experiments illustrate the strong robustness of the time-reversal process. In the first experiment, time-reversal focusing is degraded in comparison with the inverse filter process, but an amplitude compensation of the wave field before applying the time-reversal operation allows recovery of the optimal focusing quality reached by the inverse filter technique. In the second experiment, time reversal is degraded, but the inverse filter technique is not able to give better results, though it uses more information characterizing the medium.

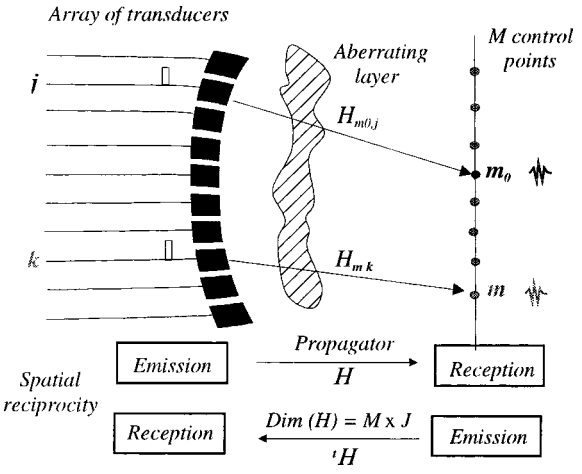

FIG. 1. Source-transducer impulse response.

I. COMPARISON BETWEEN INVERSE FILTER FOCUSING AND TIME-REVERSAL PROCESSING: THEORETICAL APPROACH

A. The propagation operator H

To compare inverse filter focusing and time-reversal processing, we need to define the linear operator relating the elements of the transducer array to a set of control points. The signals applied to the transducer elements are the input of the filter, and the output consists of the signals measured on the control points.

For sake of simplicity, we restrict ourselves to a one-dimensional array of transducers and a spatial sampling of the field, the set of control points, along a line parallel to the array aperture, Fig. 1. We define an impulse response, $h_{mj}(t)$, for each couple (m,j) comprising a control point and a transducer element. This impulse response $h_{mj}(t)$ is the signal received on the mth control point after a temporal Dirac's function is applied on the jth transducer of the array. This response includes all the propagation effects through the medium under investigation as well as the acousto–electric responses of the two elements. As the transformations are supposed to be linear and invariant under a time shift, the $M \times J$ temporal functions $h_{mj}(t)$ for $1 \leqslant m \leqslant M$ and $1 \leqslant j \leqslant J$ can describe any transmit–receive operation for the same arrangement. In the Fourier domain, it gives the transfer matrix representing the propagation of each monochromatic component between the array and the set of control points.

Indeed, let $e_j(t)$, $1 \leqslant j \leqslant J$, J being the input signals on the transducer array. The output signals $f_m(t)$, $1 \leqslant m \leqslant M$, received in the control domain, are given by

$$f_m(t) = \sum_{j=1}^{J} h_{mj}(t) {}_t^{*} e_j(t), \quad 1 \leqslant m \leqslant M, \tag{1}$$

where * is a temporal convolution operator.

A temporal Fourier transform leads to the following relation:

$$F_m(\omega)=\sum_{j=1}^{J}\mathbf{H}_{mj}(\omega)E_j(\omega),\quad 1\leqslant m\leqslant M. \tag{2}$$

Equation (2) leads to the simplified matrix form

$$F(\omega)=\mathbf{H}(\omega)E(\omega), \tag{3}$$

where $E(\omega)=(E_j(\omega))_{1\leqslant j\leqslant J}$ is the column vector of the Fourier transform of the transmitted signals and $F(\omega)=(F_m(\omega))_{1\leqslant m\leqslant M}$ is the column vector of the Fourier transform of the received signals. The transfer matrix $\mathbf{H}(\omega)=(H_{mj}(\omega))_{1\leqslant m\leqslant M,1\leqslant j\leqslant J}$ describes the propagation in the medium from the array to the set of control points and thus, is called the propagation operator.

B. Inverse filter focusing: The inverse diffraction operator H^{-1}

In this case, we try to deal with an inverse diffraction experiment: the aim is to determine the desired field distribution E on a boundary surface (the transducers array) that would give rise after propagation to the field distribution F on another surface (the image plane or control plane). As we want to focus in the image plane, F is chosen to correspond to the optimal focusing obtained in a homogeneous medium. To solve this problem, we have to acquire the direct wave-field propagator $\mathbf{H}$ between the time-reversal mirror and the image plane. Thus, E and F are related by

$$F=\mathbf{H}E\Leftrightarrow E=\mathbf{H}^{-1}F. \tag{4}$$

As is the case in all inverse problems, the inversion of the matrix propagator $\mathbf{H}$ is ill-conditioned.[9] Numerically, the solution to the inversion does not depend continuously on the data, but rather, small errors in these data produce very large errors in the reconstructed results. In order to avoid such a problem, a singular value decomposition is applied to the matrix $\mathbf{H}$ before inversion

$$\mathbf{H}=\mathbf{U}\mathbf{D}\tilde{\mathbf{V}}, \tag{5}$$

where $\dim(\mathbf{H})=M\times J$, $\mathbf{U}$ is an $M\times J$ column-orthogonal matrix, $\mathbf{V}$ is a $J\times J$ orthogonal matrix, $\mathbf{D}$ is a $J\times J$ diagonal matrix ($\mathbf{D}=[\lambda_i\delta_{i,j}]_{ij}$), and $\delta_{i,j}$ is the Kronecker symbol. The inverse of $\mathbf{H}$ is directly related to the inverse of $\mathbf{D}$ with

$$\mathbf{H}^{-1}=\mathbf{V}\mathbf{D}^{-1}\tilde{\mathbf{U}}=\mathbf{V}\left[\frac{1}{\lambda_i}\delta_{i,j}\right]_{i,j}\tilde{\mathbf{U}}. \tag{6}$$

As $\mathbf{H}$ is close to singular, some eigenvalues λ_i become very small and so, sensitive to noise. During inversion, $1/\lambda_i$ tends to infinity and produces very large errors. Indeed, only the main eigenvalues of the decomposition have to be used during inversion. The main idea of the inversion by singular value decomposition is to replace $1/\lambda_i$ by zero, when λ_i becomes very small. This process achieves a regularization of $\mathbf{H}$ before inversion and allows this ill-conditioned problem to become less sensitive to noise. The matrix inversion is only applied to the main eigenvectors of the singular value decomposition of $\mathbf{H}$, giving rise to a noise-filtered approximation $\hat{\mathbf{H}}^{-1}$ of the inverse matrix $\mathbf{H}^{-1}$

$$\hat{\mathbf{H}}^{-1}=\mathbf{V}\hat{\mathbf{D}}^{-1}\tilde{\mathbf{U}}=\mathbf{V}\begin{bmatrix}\frac{1}{\lambda_1} & 0 & & \cdots & & 0\\ 0 & \ddots & & & & \\ & & \frac{1}{\lambda_N} & \ddots & & \vdots\\ \vdots & & \ddots & 0 & & \\ & & & & \ddots & 0\\ 0 & & \cdots & & 0 & 0\end{bmatrix}\tilde{\mathbf{U}}, \tag{7}$$

where N is the number of eigenvalues used in the inversion.

How can we predict this limited number of useful eigenvalues? As explained previously, the irreversible loss of the evanescent waves through propagation sets a bound to the effective spatial information conveyed by the field. In the angular spectrum formalism, it results in a cutoff in the angular spectrum components. In that case, Gabor has shown that the minimum number of parameters necessary to specify the emission field E is associated with the number of eigensolutions of the homogeneous Helmholtz equation.[10] Moreover, the limited aperture of the array decreases this maximal information content that can be conveyed by the field. Hence, due to its limited aperture, the array intercepts only a limited part of the wave field radiated by any point source in the medium. This defines a bundle of plane waves included within a cone relating this point to the array aperture. This bundle of plane waves consists of the angular spectrum components of the field radiated by the array that can be received at the source location. Thus, the finite aperture of the array introduces a sharper cutoff in the angular frequencies of the wave field received at each location in the medium.

From a matrix point of view, the distribution of eigenvalues divides the space into two subspaces: On one hand, the kernel, called the null space of $\mathbf{H}$ which is related to the noise and, on the other hand, the range of $\mathbf{H}$. The rank of $\mathbf{H}$, in other words the number of eigenvalues contained in the range of $\mathbf{H}$, is related to the minimum number of parameters necessary to define the field that can be created by the array in the control plane. Using the plane wave decomposition of the field,[11] this number can be seen in a homogeneous medium as the number of angular spectrum components achievable by the array in the control plane.

Assume we use an array of 100 transducers working at a central frequency of 3.5 MHz ($\lambda=0.42$ mm) in the plane $z=0$. The array aperture D is equal to 41 mm and the array pitch is equal to 0.41 mm (see Fig. 2). A set of 100 control points is located along a line parallel to the array aperture in the plane $z=F=170$ mm. The spatial step δ between two control points is equal to 0.3 mm and all immersed in water, ensuring the medium of insonification is homogeneous. If the control points are assumed to be in the far field, the transducers can be considered as point-like sources and the propagation operator in a homogeneous medium is given by

$$\forall\{m,j\}\in[1,M]\times[1,J],\quad H_{m,j}(\omega)=\frac{1}{d_{mj}}e^{ikd_{mj}}, \tag{8}$$

where d_{mj} is the distance between the mth control point and the jth transducer. The singular value decomposition of this

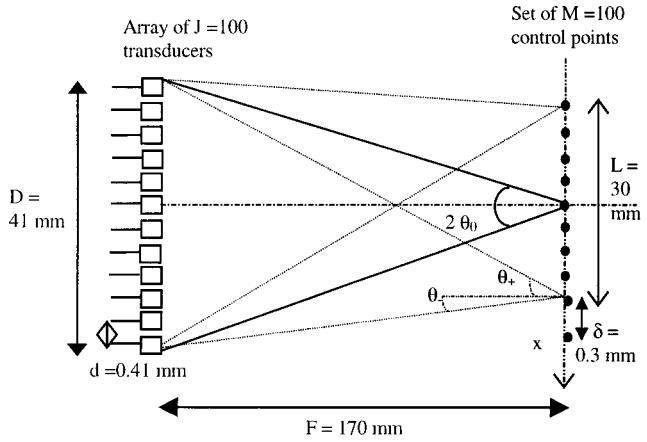

FIG. 2. Theoretical and experimental setup.

matrix has been computed. The number N of useful eigenvalues is found to be equal to 18, as shown in Fig. 3. The transducers and the control points directivity can be taken into account in the computation. In that case, the number of useful eigenvalues remains the same but the useful eigenvalues do not have the same weight anymore.

As explained above, due to the limited aperture of our array, the plane wave decomposition of the field coming from the array and received on each control point consists of a bundle of plane waves included into a cone. For a given control point, this cone is limited between an angle θ_- and θ_+, as seen in Fig. 2, and the spatial frequencies bandwidth B that can be created by the array at the control point location in the control plane is equal to

$$B = f_+ - f_- = \frac{\sin\theta_+ - \sin\theta_-}{\lambda}. \tag{9}$$

This spatial frequency bandwidth varies for each cone associated with one control point. The widest bandwidth is reached for the central control point. In that case, B is equal to

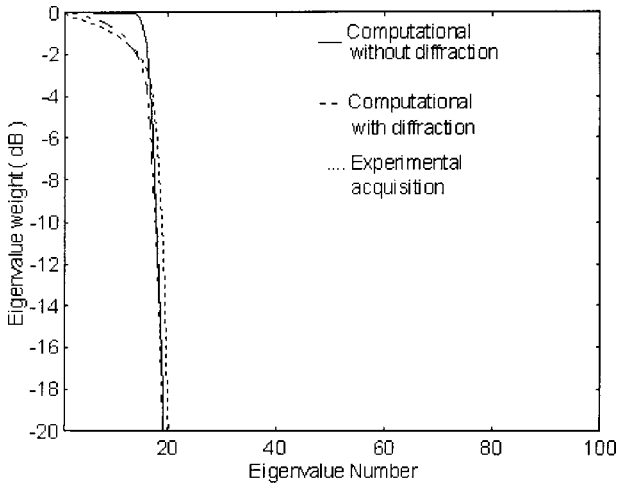

FIG. 3. Computed eigenvalue distribution for the described configuration assuming (a) the control points to be in the far field (solid line), and (b) taking into account the transducer's directivity (dashed dotted line). The number of degrees of freedom is equal to 18. It is compared with the experimental eigenvalue distribution achieved with the same previous setup (dotted line).

$$B_{\max} = f_0 - (-f_0) = 2\frac{\sin\theta_0}{\lambda} = 2\frac{\sin\left(\tan^{-1}\dfrac{D}{2F}\right)}{\lambda}, \tag{10}$$

where θ_0 corresponds to the semiangle defined in Fig. 2.

According to Shannon's sampling theorem, the optimal spatial resolution δ_x in the control plane, obtained locally at the central control point location (it is well-known that the focal spot of a linear array is sharper for a centered focus than for a focus on the edges), is then given by

$$\delta_x = \frac{1}{B_{\max}} = \frac{\lambda}{2\sin\left(\tan^{-1}\dfrac{D}{2F}\right)}. \tag{11}$$

Thus, an overestimation of the number N of spatial degrees of freedom necessary to define the field received in the control plane will correspond to the ratio between the width L of this control plane and the resolution δ_x required to sample the spatial distribution of the field in the control plane

$$N = \frac{L}{\delta_x} = 2\frac{L}{\lambda}\sin\left(\tan^{-1}\frac{D}{2F}\right). \tag{12}$$

This definition of N is valid in the near field of the array. Finally, in the Fraunhofer assumption, when $D/2F \gg 1$, it gives the simple relation

$$N \approx \frac{DL}{\lambda F}. \tag{13}$$

In this case, N can be seen as the number of independent focal spots (lateral resolution $\lambda F/D$) that the array is able to generate in the aperture L of the image plane. This definition of N gives 18 in our numerical case and confirms the number of eigenvalues given by the singular value decomposition of the numerical matrices, Fig. 3.

Moreover, to illustrate these results, the propagation matrix $\mathbf{H}$ has been acquired experimentally. Each term of the matrix is acquired by moving a single transducer on each location of the control points. This single transducer works as a receiver and records successively the signal emitted by each transducer of the array. We keep only the amplitude and phase of the received signal at the central frequency of the transducers. The eigenvalue distribution of the experimental matrix is compared with the numerical case, Fig. 3. One can notice that the rank of the experimental and numerical matrices are in good agreement. Moreover, the far-field assumption made in the numerical case neglecting the transducers directivity is responsible for the lower decreasing of the main eigenvalues in comparison with the experiment. The numerical case, taking into account their directivity, is in total agreement with the experiment.

The N main eigenvectors of the singular value decomposition of $\mathbf{H}$ define all the information that can be conveyed by the field to the control points, and so are kept for the inversion of the matrix. The others are only sensitive to noise, and so will not be taken into account. The inverse propagation matrix $\hat{\mathbf{H}}^{-1}$ is then deduced from Eq. (7). Therefore, according to Eq. (4), it allows us to deduce the field E

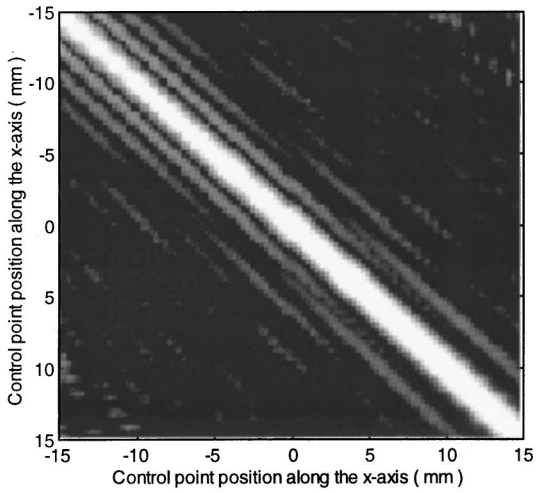

FIG. 4. Amplitude representation of the matrix $\mathbf{H}\hat{\mathbf{H}}^{-1}$ deduced from H experimentally acquired in water.

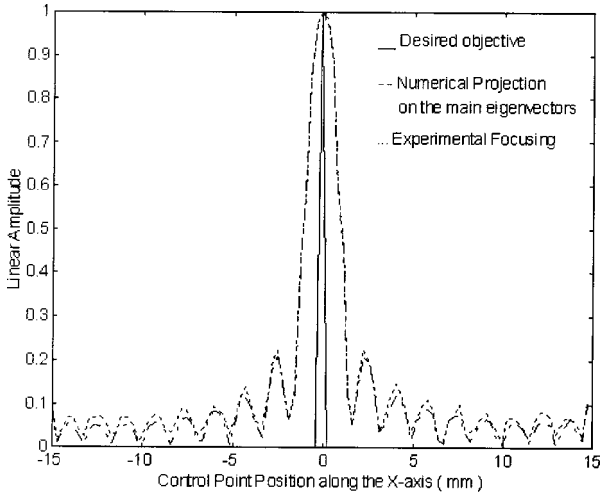

FIG. 5. Spatial distribution in the control plane, on the one hand, of the objective F_{m0}, and on the other hand, of its numerical projection F_{inv} on the 18 main eigenvectors of the SVD of H. Finally, these vectors are compared to the experimental focusing achieved by inverse filter processing.

to be emitted on the array from the field F arising on the control points after propagation in the medium. As we try to deal with a focusing problem, we choose as an objective the ideal focusing pattern F_{m0} on the control point m_0. This ideal focusing pattern is defined by

$$F = F_{m0} = \{\mathbf{0},\ldots,\mathbf{0\,1\,0},\ldots,\mathbf{0}\}. \tag{14}$$

According to Eqs. (4) and (7), the emission vector E_{inv} is directly deduced from F_{m0}

$$E_{\text{inv}} = \hat{\mathbf{H}}^{-1} F_{m0}. \tag{15}$$

This vector, calculated by the inverse filter technique, can now be remitted by the array. It will give rise to the focusing pattern F_{inv} in the control plane defined by

$$F_{\text{inv}} = \mathbf{H}E_{\text{inv}} = \mathbf{H}\hat{\mathbf{H}}^{-1} F_{m0}. \tag{16}$$

This operator $\mathbf{H}\hat{\mathbf{H}}^{-1}$ will be referred to as the inverse focusing operator in the next part of this paper. Due to the limited aperture of the array, $\mathbf{H}\hat{\mathbf{H}}^{-1}$ is not equal to the identity matrix $\mathbf{I_{M\times M}}$, as seen in Fig. 4.

Thus, F_{inv} is not exactly equal to F_{m0}

$$\begin{aligned} F_{\text{inv}} = \mathbf{H}\hat{\mathbf{H}}^{-1} F_{m0} &= \mathbf{U}\mathbf{D}\tilde{\mathbf{V}}\mathbf{V}\hat{\mathbf{D}}^{-1}\tilde{\mathbf{U}} F_{m0} \\ &= \mathbf{U}\mathbf{D}\hat{\mathbf{D}}^{-1}\tilde{\mathbf{U}} F_{m0} \\ &= \mathbf{U}\begin{bmatrix} \mathbf{I}_{N\times N} & 0 & \cdots & 0 \\ 0 & 0 & & \vdots \\ \vdots & & \ddots & \\ 0 & \cdots & & 0 \end{bmatrix}\tilde{\mathbf{U}} F_{m0}. \end{aligned} \tag{17}$$

Equation (17) clearly shows that F_{inv} only corresponds to the projection of the objective vector F_{m0} on the N main eigenvectors of the singular decomposition of $\mathbf{H}$. Figure 5 presents the initial objective F_{m0} of this inverse filter process, its projection F_{inv} on the main eigenvectors of the singular value decomposition of the experimentally acquired matrix $\mathbf{H}$, and finally the experimental focusing obtained by this inverse filter process. Note that the inverse filter is not able to reconstruct F_{m0} because of the limited rank of $\mathbf{H}$ and that we obtain the classical point spread sinc function of the linear array. Moreover, one can notice in Fig. 5 that the experimental focusing obtained by emitting E_{inv}, the solution given by the inverse filter process, is almost equal to the projection of F_{m0} on the N main eigenvectors of the singular value decomposition of $\mathbf{H}$.

C. Time-reversal focusing: The time-reversal operator H^tH^*

Contrary to the inverse filter technique, a time-reversal processing does not require knowledge of the whole propagation operator $\mathbf{H}$. In the case of time-reversal focusing, one uses as inputs the time-reversed version of the set of signals measured by the array elements when one of the control points behaves as an acoustic source.

According to the spatial reciprocity relation, $h_{mj}(t)$ is also the signal measured by the jth transducer element (working as a receiver) when a temporal delta function is applied on the mth control point. Thus, spatial reciprocity implies that the transpose of $\mathbf{H}$, ${}^t\mathbf{H}$ corresponds to the propagation matrix between the control points and the array elements, Fig. 1. In the first step of a time-reversal experiment, one of the control points behaves like a source. Let be this source located at point m_0 in the image plane, defined by the column vector $F_{m0} = {}^t\{0,...,0,1,0,...,0\}$. The wave field E_0 received by the array when F_{m0} is transmitted is

$$E_0 = {}^t\mathbf{H} F_{m0}, \tag{18}$$

where ${}^t\mathbf{H}(\omega) = (h_{jm}(\omega))_{1\leq j\leq J, 1\leq m\leq M}$ is the transfer matrix relating the control points to the transducer elements.

Thus, E_0 can be seen as

$$E_0 = \{\mathbf{H}\}_{m0} = {}^t\mathbf{H} F_{m0}, \tag{19}$$

where $\{\mathbf{H}\}_{m0}$ is the m_0th row of $\mathbf{H}$.

It has been shown[1,3,6] that the TRP achieves a matched filter in the time domain. A matched filter maximizes the ratio between the amplitude of the output and the square root of the energy of the input. In the time domain, it corresponds

to an autocorrelation. The proof of this property requires only that the Green's operator is linear, invariant under a time shift, and satisfies the spatial reciprocity relation. Hence, it holds even if the medium is absorbing. But, this demonstration deals only with the temporal dependency of the signal transmitted and says nothing about their relative amplitudes, i.e., the spatial evolution. We will now show that the TRP also achieves a spatial matched filtering. A spatial filter matched at the location m_0 gives as a solution the column vector E to be emitted by the array generating the maximum amplitude at point m_0 for a given transmitted energy $\|E\|^2$. In others words, E has to maximize

$$J(E)=\frac{\langle \mathbf{H}E|F_{m0}\rangle}{\|E\|}, \tag{20}$$

where $\langle\cdot|\cdot\rangle$ is the usual scalar product for complex vector, $\langle \mathbf{H}E|F_{m0}\rangle$ is the amplitude of the field in the focal plane at point m_0, and $\|E\|$ is the square root of the energy transmitted.

Let $\tilde{\mathbf{H}}$ be the adjoint operator of $\mathbf{H}$. By definition of $\tilde{\mathbf{H}}$,

$$\langle \mathbf{H}E|F_{m0}\rangle=\langle E|\tilde{\mathbf{H}}F_{m0}\rangle, \tag{21}$$

where $\tilde{\mathbf{H}}={}^t\mathbf{H}^*$ and * is the conjugation operation.

Now, if we use the Schwarz's inequality

$$\frac{\langle E|\tilde{\mathbf{H}}F_{m0}\rangle}{\|E\|}\leqslant\|\tilde{\mathbf{H}}F_{m0}\|, \tag{22}$$

and the equality is reached if E is proportional to $\tilde{\mathbf{H}}F_{m0}$, namely $E=k(\omega)\tilde{\mathbf{H}}F_{m0}$, and, as F_{m0} is real

$$E=k(\omega)({}^t\mathbf{H}F_{m0})^*=k(\omega)\{\mathbf{H}\}^*_{m0}. \tag{23}$$

The physical meaning of $({}^t\mathbf{H}F_{m0})^*$ is straightforward; a source located at m_0 would give rise in the array plane to ${}^t\mathbf{H}F_{m0}$ and the conjugation in the Fourier domain corresponds to the time-reversal operation. Hence, the TRP achieves a spatial matched filtering and again, only the spatial reciprocity relation is required. Note, as the TRP is also a temporal matched filter, k is constant. The focusing obtained in the image plane is given by

$$F=\mathbf{H}({}^t\mathbf{H}F_{m0})^*=\mathbf{H}\tilde{\mathbf{H}}F_{m0}, \tag{24}$$

where $\mathbf{H}\tilde{\mathbf{H}}$ is called the time-reversal operator[12,13] and can be compared to the inverse focusing operator defined in Eq. (16) for the inverse filter technique. In spite of time-reversal invariance of the wave equation in lossless media, the time-reversal operator is not the identity matrix $\mathbf{I_{M\times M}}$. In fact, each column m_0 of this matrix corresponds to the directivity pattern obtained in the image plane, by applying the time-reversal process to an initial source located at m_0 in this image plane. As the TRM has a finite aperture, this directivity pattern is a point-spread function and its beamwidth is linked to the ratio aperture/focal length of the mirror. The high spatial angular frequencies of the objective are lost. Thus, $\mathbf{H}\tilde{\mathbf{H}}$ in a homogeneous lossless medium, as well as the inverse filter operator $\mathbf{H}\hat{\mathbf{H}}^{-1}$ in the first subpart, only tends towards the identity matrix (see Fig. 6): The diagonal of this matrix remains spread because of the limited angular aperture of the mirror.

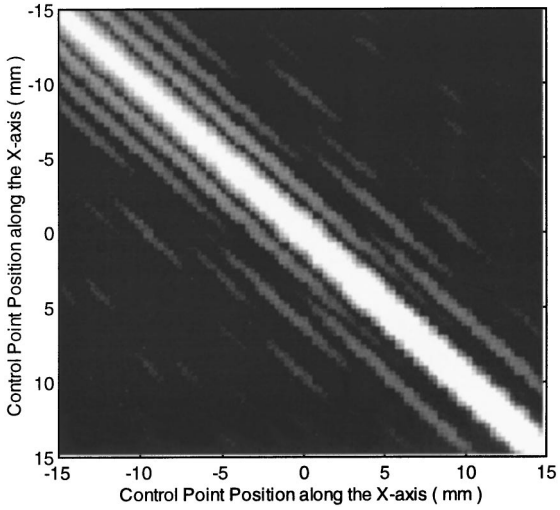

FIG. 6. Amplitude representation of the matrix $\mathbf{H}\tilde{\mathbf{H}}$ deduced from H experimentally acquired in water.

Moreover, according to Eqs. (24) and (5), the time-reversal focusing F_{TR} can be rewritten

$$\begin{aligned} F_{\mathrm{TR}}&=\mathbf{H}\tilde{\mathbf{H}}F_{m0}=\mathbf{U}\mathbf{D}\tilde{\mathbf{V}}\mathbf{V}\tilde{\mathbf{D}}\tilde{\mathbf{U}}F_{m0}\\ &=\mathbf{U}\mathbf{D}\tilde{\mathbf{D}}\tilde{\mathbf{U}}F_{m0}\\ &=\mathbf{U}\begin{bmatrix}\lambda_1^2 & 0 & \cdots & 0\\ 0 & \ddots & & \vdots\\ \vdots & & \ddots & 0\\ 0 & \cdots & 0 & \lambda_M^2\end{bmatrix}\tilde{\mathbf{U}}F_{m0}. \end{aligned} \tag{25}$$

As well as for the inverse filter operator, the focusing F_{TR} obtained by the TRP can be seen as the projection of the desired objective F_{m0}, but now on the whole set of eigenvectors of the SVD of $\mathbf{H}$ weighted by the root of their corresponding eigenvalue. Note that, according to their predominant weight, only the N main eigenvectors have a non-negligible contribution to the construction of F_{TR}.

Thus, F_{TR} is only nearly equal to F_{inv} when the N main eigenvalues of the SVD of $\mathbf{H}$ are equal. A comparison between these two focusing patterns can be made in the case of the propagation through an homogeneous medium. In that case, as seen in Sec. I B, the transducer's directivity introduces a quite slow decrease in the main eigenvalue distribution of $\mathbf{H}$, and F_{TR} is no longer equivalent to F_{inv}. Physically, during a time-reversal experiment, this transducer's directivity introduces on the array aperture an apodization of the wave field coming from the initial source. The time-reversed wave field reemitted by the time-reversal mirror suffers this amplitude modulation a second time and the time-reversal operation no longer achieves an inverse filter.

II. EXPERIMENTAL APPROACH

In the first theoretical part, we have introduced two different operators, $\mathbf{H}\hat{\mathbf{H}}^{-1}$ and $\mathbf{H}\tilde{\mathbf{H}}$, allowing to quantify the optimal focusing quality that can be reached with two differ-

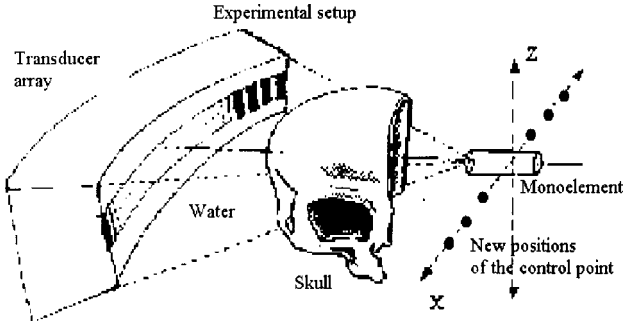

FIG. 7. First experimental setup: A skull is located between the 1D cylindrical array and the image plane.

ent techniques, respectively, the inverse filter technique and the time-reversal processing. We present now two different experiments in order to compare these two processes. Note however that the inverse filter technique requires the acquisition of the whole matrix **H**, as the TRP only requires the knowledge of one single row of this matrix.

In the two experiments presented, time-reversal focusing is not able to achieve the optimal focusing obtained in a homogeneous medium. We compare it to the behavior of the inverse filter process. In both cases, the degradation of time-reversal focusing is due to an information loss in the medium. In the first experiment, this loss is due to absorption, as we try to deal with the problem of ultrasonic focusing through the skull bone. Here, the inverse filter technique gives better results than the time-reversal focusing. However, an improvement of the time-reversal processing[8] can be introduced, allowing to recover the focusing quality obtained by the inverse filter technique. In the second experiment, the loss of information is due to the limited aperture of the array combined with the strong diffraction of a lossless aberrating medium, and we will see that the inverse filter process gives no better results than the TRP.

A. Focusing through the skull

1. Improvement of time-reversal focusing through the skull

In this first experiment, as explained above, time-reversal focusing is no longer as good as the focusing in a homogeneous medium. In that experiment a skull bone is located between the image plane and the TRM. Sound absorption in bone (varying approximately between 0.3 and 2 $\mathrm{dB\,mm^{-1}\,Mhz^{-1}}$) breaks the time-reversal invariance of the wave equation and so degrades the time-reversal focusing. Figure 7 presents the setup of this first experiment. The 1D array is made up of 128 transducers located on a cylindrical surface and working at a central frequency of 1.5 MHz. The radius of curvature of the cylindrical surface is equal to 100 mm. The transducer width and height are, respectively, equal to 1 and 30 mm. The array pitch is equal to 1 mm. The skull is located closed to the array. The control points are disseminated in the medium as stated in the introduction. In our case, we have chosen to place them in a plane called the control plane or image plane. Indeed, we wanted to plot focusing patterns in this plane. The control plane is made of 100 controls points located along a line orthogonal to the axial direction and containing the array geometrical focus. The control points pitch is equal to 0.3 mm and thus, the control points are located between $x=-15$ mm and $x=+15$ mm in the control plane. The matrix propagator is experimentally acquired both in water and through the skull following the procedure explained in the Sec. I: First, a single transducer located at a control point in the image plane acts as an acoustic receiver and stores the signals successively emitted by each transducer of the array. From a Fourier transform analysis, we keep only the phase and amplitude information of this set of signals at the central frequency of the transducers. Thus, it gives a set of M amplitudes and phases that corresponds to a single column of **H**. This set of M amplitudes and phases characterizes the Green's function associated to one control point location. Then, the single transducer is successively moved on the others control points in the image plane in order to record all the columns of **H**. Note that Seip *et al.* proposed to achieve dynamic focusing in ultrasound hyperthermia treatments by acquiring this propagation operator **H** with implantable hydrophone arrays.[14] The amplitude of the whole time-reversal operator $\mathbf{H}\tilde{\mathbf{H}}$ is presented in Fig. 8 when (a) the medium is homogeneous, and (b) when the skull is located between the array and the control points. The amplitude is represented in dB on a grayscale. As explained previously, the m_0th column of the time-reversal operator corresponds to the focusing obtained by time-reversal processing when a single initial acoustic source is available at the position m_0 in the image plane. Thus, one can notice in Fig. 8(c) that the directivity pattern obtained by time-reversal processing through the skull is degraded in comparison with the same experiment in water.

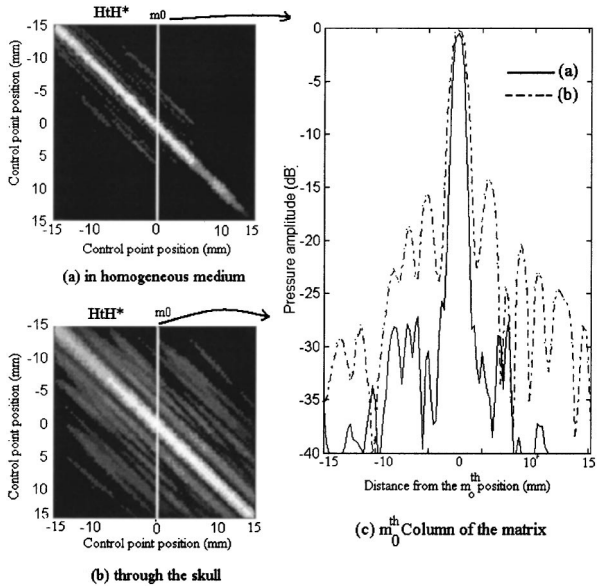

FIG. 8. First experiment in absorbing medium: Matrix H^tH^* (a) in a homogeneous medium, and (b) through the absorbing skull, and the corresponding directivity pattern obtained by time-reversal processing at a position m_0 in the image plane in both cases.

As the TRP achieves a spatial matched filter in spite of the absorption, there is no spatial shift of the focus. The amplitude of the field is always maximized on the initial

source location. However, the TRP imposes no constraint on the other points in the image plane: especially, the focal beam is spread in comparison with the one obtained in a homogeneous medium, and sidelobes appear.

An improvement of the time-reversal process has been proposed in a previous paper to recover an optimal focusing through the skull. It consists of a numerical amplitude compensation of the wavefront received on the mirror.[8] This amplitude compensation allows us to take into account the effects of skull absorption: The amplitude modulation of the wavefront is inverted before applying the time-reversal operation. Thus, this new synthesized field corresponds to the field that would have propagated through a medium with gain. This virtual medium is exactly the same as the real one, except for the acoustic losses that are replaced by gains. Hence, it tends to recreate the inverse of the real medium. However, as we are only able to act on the conditions applied on the boundaries, i.e., the signals emitted by the TRM, this correction is only valid when the losses in the medium are located in a thin layer close to the array. We have extended this method to thin absorbing layers located at some distance of the array by introducing an algorithm of numerical inverse diffraction.[8] In spite of this approximation of a thin absorbing layer, it has been shown that the improvement of time-reversal focusing by amplitude compensation is significant. However, during time-reversal processing only one row of the propagation operator **H** is known and this information is not sufficient when the acoustic losses are not localized in a thin layer, but rather disseminated in the whole medium. On the contrary, when the whole propagation matrix **H** is acquired, all information needed to characterize the medium is known and the emission vector giving the optimal focusing can be deduced from the inversion of **H**. In the next subpart, we compare this optimal solution to the single time-reversal focusing and time-reversal focusing improved by amplitude compensation.

2. Inverse filter process applied to focusing through the skull

We try to compare the solution vector E to be emitted on the array in order to focus at m_0 with the two different methods: Time-reversal processing combined with amplitude compensation and the inverse filter solution $E=\mathbf{H}^{-1}F$. The numerical inversion is realized on a subspace defined by the eigenvectors associated with the most significant eigenvalues. The eigenvalue distribution of the propagation matrix through the skull is presented in Fig. 9.

The inverse filtering solution $E=\mathbf{H}^{-1}F$ obtained with a growing number of eigenvalues is compared with the phase (Fig. 10) and amplitude (Fig. 11) of the solution obtained by time reversal and amplitude compensation. With 11 eigenvalues, the total number of eigenvalues of the range is not used, but with 38 eigenvalues the inverse solution converges towards the time-reversal solution improved by amplitude compensation. In that case, the standard deviation between the phase variations of the two solutions is very small ($\approx\pi/13$), Fig. 10. Moreover, Fig. 11 can be seen as proof that the algorithm of amplitude compensation applied to the TRP gives good results, as there is a very good agreement with

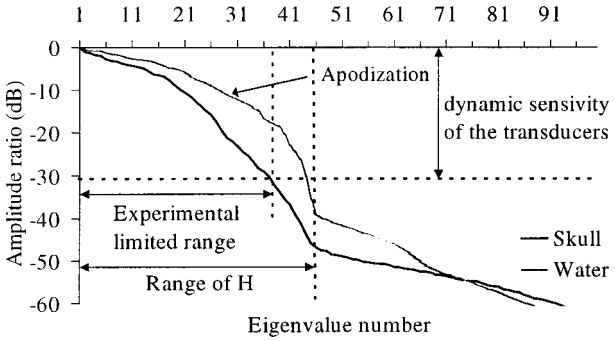

FIG. 9. Eigenvalue ω_i distribution of the matrix propagator H in a homogeneous medium (gray line) and through the skull (black line).

the amplitude modulation of the inverse filtering solution. In the last case, a part of the eigenvalues of the null space is used and the inverse solution becomes irrelevant.

These different solution vectors are then experimentally reemitted by the TRM, and the resulting experimental directivity patterns are compared with the optimal focusing obtained in a homogeneous medium (see Fig. 12). The focusing obtained by improved time-reversal processing and inverse filtering are optimal up to -20 dB. Under this limit, sidelobes are more important for the improved time-reversal focusing than for the focusing obtained by inverse filtering. This difference can be explained by the restricting assumption of very thin absorbing layer made in the case of time reversal and amplitude compensation. In the case of the inverse filtering solution, no particular assumption has been made as the whole matrix characterizing the medium is known.

However, even an inversion of the transfer matrix does

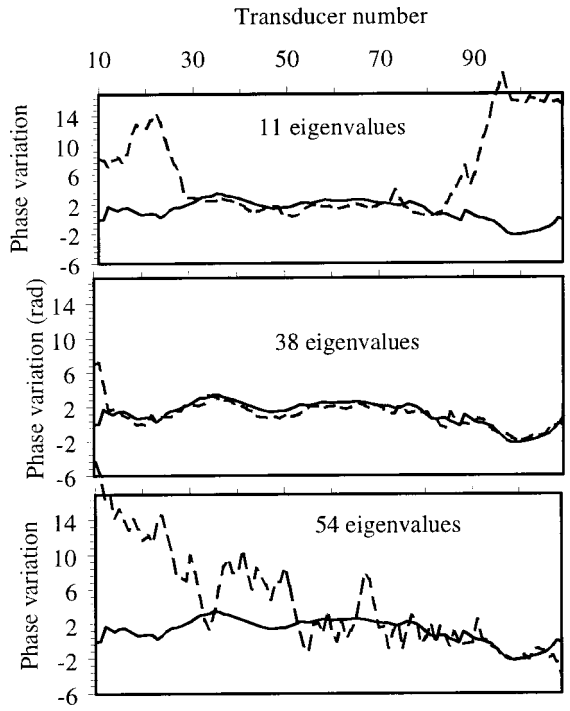

FIG. 10. Phase variation applied on the TRM by time reversal and amplitude compensation (black line) compared with the inverse filtering solution obtained by singular value decomposition of the matrix propagator H (gray line).

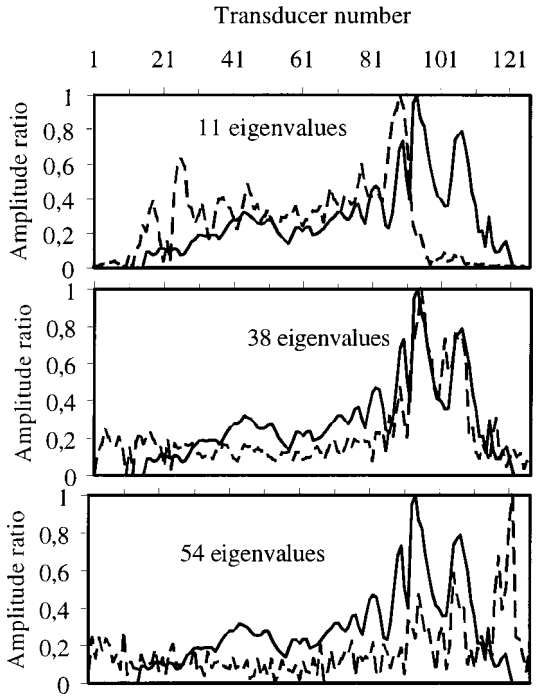

FIG. 11. Amplitude variation applied on the TRM by time reversal and amplitude compensation (black line) compared with the inverse filtering solution obtained by singular value decomposition of the matrix propagator H (gray line).

not yield to the optimal focusing obtained in water. In fact, only the eigenvectors of **H** corresponding to the main eigenvalues can be used in the inversion. This number of useful eigenvalues is limited by the dynamic range of the TRM; see Fig. 9. Therefore, the optimal focusing that can be achieved through the skull while taking into account the dynamic range of the TRM corresponds to the projection of the desired focus pattern F_{m0} on a limited number of eigenvectors of **H**. In our case, this number of eigenvectors is limited to 38 by the dynamic range, Fig. 9. The numerical projection of F_{m0} on these 38 eigenvectors is presented in Fig. 13 and compared to the optimal focusing obtained in water. The

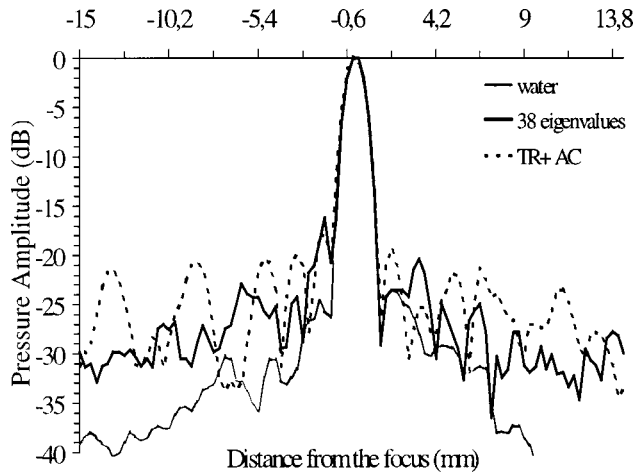

FIG. 12. Experimental directivity patterns obtained in the focal plane. Optimal focusing in water (gray solid line), time-reversal focusing through the skull improved by amplitude compensation (dotted line), and focusing obtained by the inverse filtering process (black solid line).

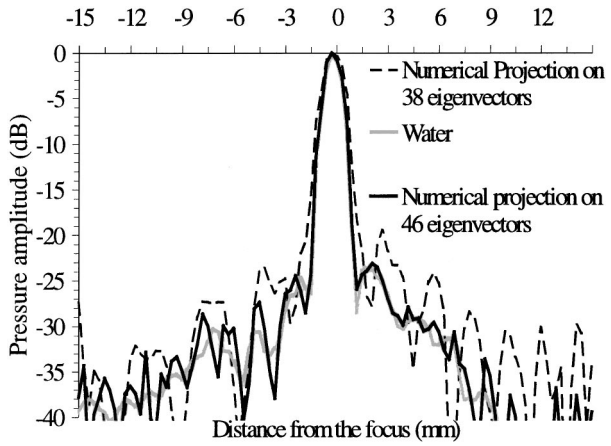

FIG. 13. Desired directivity pattern F_{m0} in the image plane corresponding to the optimal focusing obtained in a homogeneous medium (dotted line), numerical projection of this desired focal vector F_{m0}, on the one hand, on the 38 eigenvectors of H corresponding to the dynamic range of the TRM (dashed line) and on the other hand, on the whole 48 eigenvectors that define the range of H (solid line).

sidelobe level is higher for this numerical projection than for the optimal focusing F_{m0}. On the contrary, one can notice that the numerical projection of F_{m0} on the 48 eigenvectors corresponding to the rank of **H** is able to recover F_{m0}. Thus, according to the dynamic range of the TRM, it is not possible to completely recover the optimal focusing quality of the array through the skull.

So, at this point we have seen that time-reversal focusing is degraded by the acoustic losses in the medium. The propagation through the skull absorbs some angular spectrum components. We have seen that these partially lost angular spectrum components can be recovered by the inverse filter technique or by an amplitude compensation during time-reversal processing. But, such a degradation can also occur in a lossless medium. In that case, as shown below, the loss of information that breaks the time-reversal invariance of the experiment is due to the strong diffraction of some angular spectrum components of the field outside of the array-limited aperture. In that case, we will see that the inverse filter technique as well as time-reversal processing fails to recover these completely lost angular spectrum components and the optimal focusing achieved in a homogeneous medium can no longer be reached.

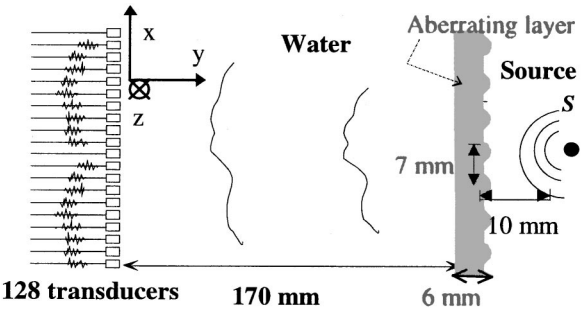

FIG. 14. Second experimental setup: The aberrations are created by the periodic lenticular shape of the lossless phantom.

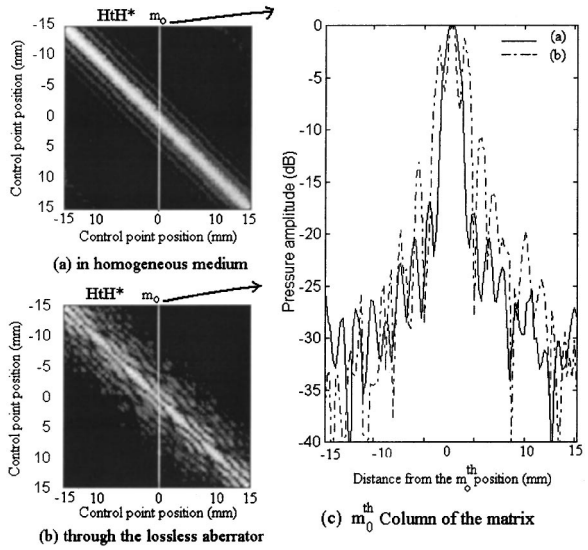

FIG. 15. Second experiment through a lossless aberrator: Time-reversal operator H^tH^* (a) in a homogeneous medium, and (b) through the aberrating layer, and (c) the corresponding directivity patterns obtained at position m_0 in both cases.

B. Focusing through a strongly diffracting lossless aberrator

In this second experiment, a lossless aberrating layer is located between the image plane and the TRM. The experimental setup is presented in Fig. 14. The linear array is made up of 128 transducers working at a frequency of 3.3 MHz. The array pitch is equal to 0.41 mm. The aberrating layer is located 170 mm away from the array. The aberrations are created by the periodic lenticular shape of one side of the phantom. The curvature radius of each lens is equal to 3 mm and the distance between each lens is equal to 7 mm. The control plane is located 10 mm behind the aberrator.

The matrix propagator **H** is experimentally acquired both in water and through the aberrator, as explained in the previous subsection. The amplitude of the associated time-reversal operators $\mathbf{H}\tilde{\mathbf{H}}$ are then compared; see Figs. 15(a) and 15(b). One can notice that time-reversal focusing through the aberrating phantom is no longer optimal, as seen in Fig. 15(c).

Could we find a set of signals to be applied on the array giving a better focusing than the time-reversal process? To answer this question, the inverse filtering technique is applied to focus at position m_0, as explained in the previous

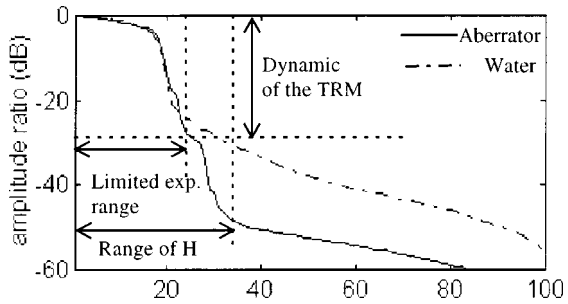

FIG. 16. Eigenvalue ω_i distribution of the matrix propagator in a homogeneous medium (dashed line) and through the aberrating medium (solid line).

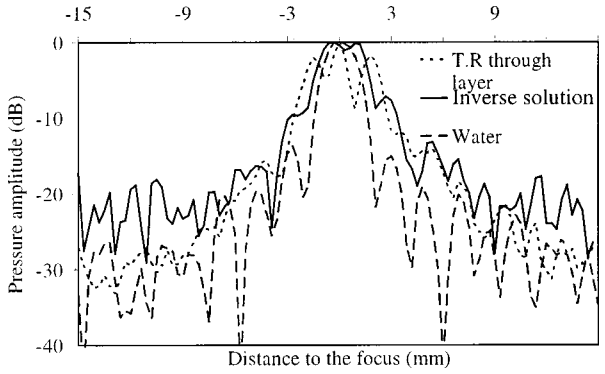

FIG. 17. Experimental directivity patterns obtained in the focal plane. Optimal focusing in water (dashed line), experimental focusing obtained by the inverse filtering process with the 28 main eigenvalues corresponding to the dynamic range of the TRM (solid line) and time-reversal focusing (dotted line).

subsection. The eigenvalues distribution in the singular value decomposition of **H** is represented in Fig. 16 and compared with the eigenvalue distribution in water. Concerning the propagation through the aberrating layer, the range of the **H** is equal to 36 and the number of eigenvalues that correspond to the limited dynamic range of our TRM is equal to 28. Contrary to the skull experiment, one can notice in Fig. 17 that the focusing obtained by inverse filtering processing is not improved in comparison with time-reversal focusing.

Thus, the inverse filter process fails to recover an optimal focusing. However, this failure is not due to the limited dynamic range of the TRM. Indeed, even if we assume this dynamic range to be good enough to take into account the whole eigenvalues in the rank of **H**, the focusing that could be achieved would remain very far from the objective: Fig. 18 presents the comparison between the objective F_{m0} and its numerical projection on the main 36 eigenvectors corresponding to the rank of **H**. It clearly demonstrates that the main limiting factor to good focusing in such a lossless medium is not related to the dynamic range of the TRM. Note that the experimental focusing obtained by inverse filtering presented in Fig. 17 is very similar to the numerical projection on the 36 eigenvectors presented in Fig. 18.

In fact, in the same way as for the time-reversal experi-

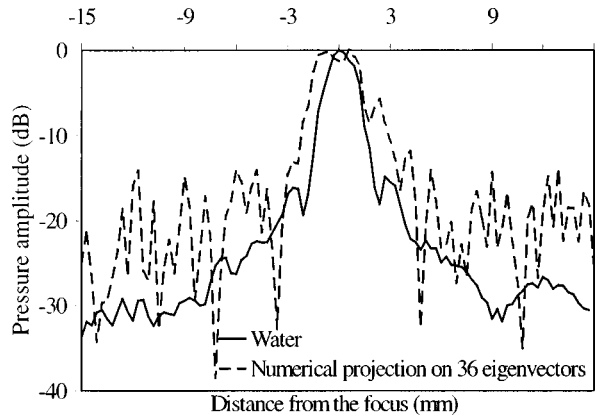

FIG. 18. Desired directivity pattern F in the image plane corresponding to the focusing in water (dashed line) and numerical projection of this desired focal vector F on the main 36 eigenvectors of H that correspond to the rank of H (solid line).

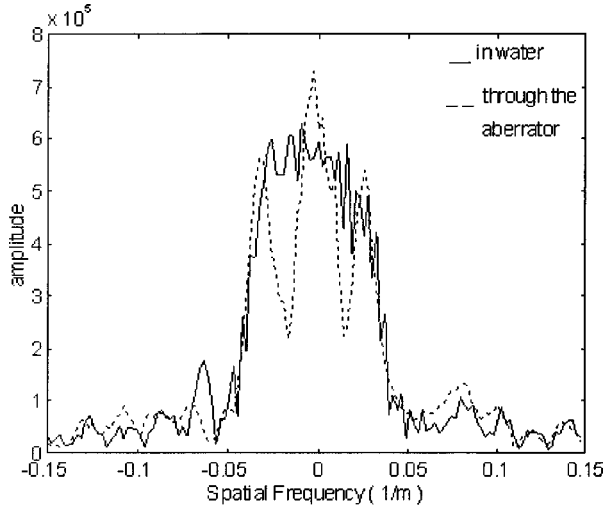

FIG. 19. Spatial frequencies spectrum of the wave field coming from the 50th control point acting as a source and received on the array after propagation in water and through the aberrating layer.

ment, a part of the wave field generated by the acoustic source is diffracted outside the array aperture during the experimental acquisition of **H**. Thus, a lack of information appears for each Green's function corresponding to a single row of the matrix. For this purpose, Fig. 19 presents the spatial frequencies of the wave field received on the array of transducers and coming from the 50th control point acting as a source. As seen previously, this wave field corresponds to a single row of the propagation matrix **H** and its spatial frequencies are easily obtained by calculating the Fourier transform of this vector.

One can notice that the propagation through the aberrating layer destroys a part of the spatial frequencies obtained in the homogeneous case. In particular, due to the periodicity of the lenticular shape of the aberrator, a periodicity appears in the spatial frequencies spectrum of the wave field that propagated through the aberrator: each lens inhibits or enhances selected spatial frequencies; see Fig. 19. A part of the spatial frequencies available in a homogeneous medium is definitively lost when the aberrator is introduced. The experimental configuration (location, size, number of transducers, aberrating medium, etc.) corresponding to this propagation operator is not sufficient and must be modified to reach the desired objective.

The inability of time reversal to recover an optimal focusing through this kind of aberrator has been explained and overcome in a previous paper.[5] A way to overcome this time-reversal failure and recover this loss consists of introducing new boundary conditions between the focal plane and the array. These new boundaries confine the wave field on the array aperture and consequently, time-reversal processing recovers the optimal focusing obtained in water. In that case, the experimental configuration is completely modified, increasing the information content of the new resulting propagation operator **H**.

III. CONCLUSION

The TRP is based on the time-reversal invariance of the wave equation in a lossless medium. In theory, it achieves an inverse wave-field propagator limited only by the evanescent waves. But, in many practical situations, the wave field radiated by the source cannot be completely recorded and this loss of information generates an irreversibility. In particular, this loss in the information content conveyed by the field arises in an absorbing medium. But, another fundamental symmetry of physics, the spatial reciprocity relation, is usually valid. Combined with the linearity and invariance under a time shift of the wave-field propagator, it affords to the TRP its strong robustness. Thus, in these conditions, the TRP is a spatiotemporal matched filter.

However, a matched filter is not always enough. Such a filter maximizes the amplitude of the field at a given time and location but does not constrain the sidelobe level. In particular, to focus through the skull, it has been shown that better results could be obtained if a correction of the amplitude were added to the TRP. This amplitude correction tends to recover a spatial inverse filtering from the time-reversal solution by compensating the spatial frequencies of the field that suffered the most important absorption. This amplitude compensation may be improved since an inversion of the transfer matrix gives even better results.

Moreover, in some nonabsorbing media, time-reversal processing as well as an inversion of the transfer matrix does not yield to the focusing quality obtained in a homogeneous medium. Thus, in a strongly diffracting medium a part of the information content of the propagating field can be diffracted outside the array aperture and is definitively lost for the inversion. Each configuration (aberrations of the propagation medium, location, size, and number of the tranducers and control points) can be described for each monochromatic component by a propagation matrix. The optimal focusing ability in that configuration is then defined as the projection of the desired objective on the main eigenvectors of the singular value decomposition of this matrix.

[1] M. Fink, ''Time-reversed acoustics,'' Phys. Today **20**, 34–40 (1997).
[2] D. R. Jackson and D. R. Dowling, ''Phase conjugation in underwater acoustics,'' J. Acoust. Soc. Am. **89**, 171–181 (1991).
[3] D. Cassereau and M. Fink, ''Time reversal of ultrasonic fields. III. Theory of the closed time-reversal cavity,'' IEEE Trans. Ultrason. Ferroelectr. Freq. Control **39**, 579–593 (1992).
[4] A. Derode, ''Partial coherence of transient ultrasonic fields in anisotropic random media: Application to coherent echo detection,'' J. Acoust. Soc. Am. **101**, 690–704 (1997).
[5] M. Tanter, J.-L. Thomas, and M. Fink, ''Influence of boundary conditions on the time reversal focusing through heterogeneous media,'' Appl. Phys. Lett. **72**(20), 2511–2514 (1998).
[6] C. Dorme and M. Fink, ''Focusing in the transmit–receive mode through inhomogeneous media: The matched filter approach,'' J. Acoust. Soc. Am. **98**, 1155–1161 (1995).
[7] J.-L. Thomas and M. Fink, ''Ultrasonic beam focusing through tissue inhomogeneities with a time reversal mirror: Application to transskull therapy,'' IEEE Trans. Ultrason. Ferroelectr. Freq. Control **43**, 1122–1129 (1996).
[8] M. Tanter, J.-L. Thomas, and M. Fink, ''Focusing and steering through absorbing and aberrating layers: Application to ultrasonic propagation through the skull,'' J. Acoust. Soc. Am. **103**, 2792 (1998).
[9] M. Nieto-Vesperinas, *Scattering and Diffraction in Physical Optics* (Wiley, New York, 1991).
[10] D. Gabor, in *Proceedings of the Symposium on Astronomical Optics*, edited by Z. Kopal (North Holland, Amsterdam, 1956), p. 17.
[11] R. Kahrs Hansen, ''Acoustical imaging using spectral decomposition of the aperture field,'' in *Acoustical Imaging* (Plenum, New York, 1992), Vol. 19, pp. 103–107.

[12] C. Prada and M. Fink, ''Eigenmodes of the time reversal operator: A solution to selective focusing in multiple target media,'' Wave Motion **20**, 151–163 (1994).
[13] C. Prada, S. Manneville, D. Spoliansky, and M. Fink, ''Decomposition of the time reversal operator: Detection and selective focusing on two scatterers,'' J. Acoust. Soc. Am. **99**, 2067-2076 (1996).
[14] R. Seip, P. VanBaren, and E. Ebbini, ''Dynamic focusing in ultrasound hyperthermia using implantable hydrophone arrays,'' IEEE Trans. Ultrason. Ferroelectr. Freq. Control **41**(5), 706–713 (1994).

Complex tone processing in primary auditory cortex of the awake monkey. I. Neural ensemble correlates of roughness

Yonatan I. Fishman[a)]
Department of Neuroscience, Albert Einstein College of Medicine, Rose F. Kennedy Center, Bronx, New York 10461

David H. Reser
Department of Neuroscience, Albert Einstein College of Medicine, Bronx, New York 10461

Joseph C. Arezzo and Mitchell Steinschneider
Departments of Neurology and Neuroscience, Albert Einstein College of Medicine, Bronx, New York 10461

(Received 20 September 1999; accepted for publication 20 April 2000)

Previous physiological studies [e.g., Bieser and Muller-Preuss, Exp. Brain Res. **108**, 273–284 (1996); Schulze and Langner, J. Comp. Physiol. A **181**, 651–663 (1997); Steinschneider *et al.*, J. Acoust. Soc. Am. **104**, 2935–2955 (1998)] have suggested that neural activity in primary auditory cortex (A1) phase-locked to the waveform envelope of complex sounds with low (<300 Hz) periodicities may represent a neural correlate of roughness perception. However, a correspondence between these temporal response patterns and human psychophysical boundaries of roughness has not yet been demonstrated. The present study examined whether the degree of synchronized phase-locked activity of neuronal ensembles in A1 of the awake monkey evoked by complex tones parallels human psychoacoustic data defining the existence region and frequency dependence of roughness. Stimuli consisted of three consecutive harmonics of fundamental frequencies (f_0s) ranging from 25 to 4000 Hz. The center frequency of the complex tones was fixed at the best frequency (BF) of the cortical sites, which ranged from 0.3 to 10 kHz. Neural ensemble activity in the thalamorecipient zone (lower lamina III) and supragranular cortical laminae (upper lamina III and lamina II) was measured using multiunit activity and current source density techniques and the degree of phase-locking to the f_0 was quantified by spectral analysis. In the thalamorecipient zone, the stimulus f_0 at which phase-locking was maximal increased with BF and reached an upper limit between 75 and 150 Hz for BFs greater than about 3 kHz. Estimates of limiting phase-locking rates also increased with BF and approximated psychoacoustic values for the disappearance of roughness. These physiological relationships parallel human perceptual data and therefore support the relevance of phase-locked activity of neuronal ensembles in A1 for the physiological representation of roughness. © *2000 Acoustical Society of America.* [S0001-4966(00)05307-8]

PACS numbers: 43.64.Qh, 43.64.Ri, 43.66.Hg [LHC]

INTRODUCTION

Most sounds in nature have complex frequency spectra. In order to extract biologically meaningful information from such signals, the auditory system has developed a remarkable capacity for analyzing the spectral components of complex sounds. The importance of this frequency analysis is partially reflected in the maintenance of a tonotopic organization throughout the auditory pathway. However, the resolution with which this frequency analysis is performed is limited. Using a variety of methods, psychoacoustic studies in humans and animals have identified a fundamental perceptual unit defining the frequency resolution of the auditory system called the critical bandwidth (CBW). The CBW corresponds to the minimum frequency separation (ΔF) between complex sound components that is required for them to be processed independently by the frequency filters of the auditory system. For frequencies above 500 Hz, the CBW corresponds to 10%–20% of center frequency and thus increases with the frequency of complex sound components (Zwicker *et al.*, 1957).

Components of complex sounds that are separated by less than a CBW cannot be independently perceived (Plomp, 1964; Plomp and Mimpen, 1968). Owing to the partial overlap of their activity patterns on the basilar membrane, these components interact to produce the perception of ''beats'' and ''roughness'' (Plomp and Levelt, 1965; Plomp and Steeneken, 1968; Terhardt, 1974a). These sub-CBW perceptual phenomena are associated with rapid periodic amplitude fluctuations in the envelope of the complex waveform arising from the summation of frequency components. The repetition rate of these amplitude fluctuations corresponds to the ΔF between components. Complex sounds with frequencies separated by less than about 20 Hz give rise to the sensation of beats: loudness fluctuations that are individually discernable by the ear (Terhardt, 1968a,b, 1974a). At larger ΔFs, these individual loudness fluctuations are no longer discernable and instead a buzz or rattlelike sensation is produced, defined as roughness. The presence of beats or roughness is a

a)Electronic mail: yfishman@aecom.yu.edu

major determinant of the perceived dissonance of musical intervals (Plomp and Levelt, 1965; Kameoka and Kuriyagawa, 1969; Terhardt, 1974a,b). In fact, based on their close psychophysical correspondence, it has been argued that sensory dissonance and roughness are equivalent perceptual phenomena (Terhardt, 1974b, 1977, 1978).

The perception of roughness is confined to ΔFs between about 20 and 300 Hz (Plomp and Steeneken, 1968; Terhardt, 1968a,b, 1974a,b). Since roughness is due to interference in the auditory periphery among frequency components separated by less than a CBW, the largest ΔF at which roughness can be detected (just-noticeable roughness) increases with center frequency, in accordance with the frequency dependence of CBW. Roughness is maximal when the ΔF between components is about one-quarter to one-half of the CBW (Plomp and Levelt, 1965; Terhardt, 1974a). Thus, the ΔF corresponding to maximal roughness also increases with center frequency. However, for component frequencies greater than about 2–4 kHz, the largest ΔF at which roughness can be perceived becomes independent of critical bandwidth, remaining at about 250 to 300 Hz (Plomp and Steeneken, 1968; Terhardt, 1968a, 1974a,b). Similarly, for frequencies above 2–4 kHz, the ΔF at which roughness is maximal is largely independent of critical bandwidth, remaining between 75 and 150 Hz. The wide range of reported values of ΔF corresponding to maximal roughness for these higher frequencies may reflect differences in methodological and stimulus characteristics. For example, the ΔF corresponding to maximal roughness for this frequency range is about 75 to 100 Hz for amplitude modulated (AM) tones, i.e., three-component complexes (Terhardt, 1968a, 1974a), whereas it is about 150 Hz for two-tone stimuli (Plomp and Steeneken, 1968).

The neurophysiological basis of roughness remains undetermined. A number of physiological studies have investigated responses to periodic stimuli such as AM tones and click trains at various levels of the auditory pathway, including the auditory cortex (for a review see Langner, 1992). Several of these studies have suggested that activity phase-locked to low ($<$300 Hz) stimulus periodicities in primary auditory cortex (A1) may represent a neural basis for the perception of roughness (Bieser and Muller-Preuss, 1996; Schulze and Langner, 1997; Steinschneider *et al.*, 1998). However, a correlation between these temporal response patterns and psychophysical boundaries of roughness has not been demonstrated. With some exceptions (Goldstein *et al.*, 1959; de Ribaupierre *et al.*, 1972; Steinschneider *et al.*, 1980; Bieser and Muller-Preuss, 1996; Steinschneider *et al.*, 1998), physiological studies of responses to periodic stimuli in A1 have generally reported or implied limiting rates of phase-locking that are considerably lower than psychoacoustic values of ΔF defining the upper limit of roughness perception (e.g., Creutzfeldt *et al.*, 1980; Schreiner and Urbas, 1988; Phillips *et al.*, 1989; Eggermont, 1994a; Gaese and Ostwald, 1995; Eggermont, 1998). These latter studies also report preferred rates of neuronal phase-locking, or best modulation frequencies (BMFs), in A1 that are substantially lower (generally $<$20 Hz) than the highest psychoacoustic values of ΔF corresponding to the perception of maximal roughness. Differences in response measurement techniques, e.g., temporal modulation transfer functions (tMTFs) versus interspike interval (ISI) histograms, may partly account for the discrepancies among the results of these studies. However, the overall low BMFs and limiting rates observed in the majority of these studies may be largely due to the use of anesthetized animals. Anesthetics have been associated with suppression of phase-locked and sustained neuronal responses, and with a decrease in frequency tuning curve bandwidths in auditory cortex (Goldstein *et al.*, 1959; Makela *et al.*, 1990; Karmos *et al.*, 1993; Zurita *et al.*, 1994; Eggermont and Smith, 1995; Schulze and Langner, 1997). The anesthesia-induced decrease in tuning bandwidth may be relevant to temporal encoding of periodic sounds in light of the positive correlation reported between limiting rates of neuronal phase-locking and frequency tuning curve bandwidths in A1 (Eggermont, 1998). Indeed, in an investigation of three auditory areas of the anesthetized cat, failure to observe BMFs and limiting rates comparable to modulation frequencies characteristic of roughness led to the conclusion that roughness is most likely *not* represented by a temporal code in auditory cortex. (Eggermont, 1998). For example, in the case of AM tone stimulation, mean multi-unit BMFs in A1 were 20.6 Hz (tMTFs) and 8.6 Hz (ISI histograms), while limiting rates were 40.3 Hz (tMTFs) and 29.4 Hz (ISI histograms). Accordingly, it was proposed that only rhythm (i.e., stimulus periodicity $<$ 20 Hz) is represented in auditory cortex by phase-locked responses and that roughness may instead be represented by a rate code (Eggermont, 1998).

The aim of this study is to reexamine the hypothesis that roughness is represented by phase-locked neuronal activity in A1. In particular, we investigate whether the magnitude of neuronal ensemble responses phase-locked to the f_0 of harmonic complex tones in A1 of the awake macaque monkey parallels human psychoacoustic data defining the existence region and frequency dependence of roughness.

Macaques have a similar auditory cortical anatomy to that of humans and display psychophysical temporal modulation transfer functions as well as critical band curves that are nearly identical to those of humans (Gourevitch, 1970; Galaburda and Sanides, 1980; Galaburda and Pandya, 1983; Pfingst, 1993; Moody, 1994). Thus, they serve as appropriate animal models for studying spectral and temporal features of complex sound processing in the auditory system. Further, the use of awake animals in the present study circumvents difficulties in the interpretation of results owing to the possible suppression of phase-locked responses in auditory cortex by anesthetics.

In the present study, activity of neuronal populations is recorded using multi-contact electrodes, and measured using auditory evoked potential (AEP), multiunit activity (MUA), and current source density (CSD) techniques. One advantage of these methods is that they allow the simultaneous recording of synchronized firing patterns and synaptic activity of neuronal ensembles across the laminar extent of A1, thereby elucidating sub- and supra-threshold features of lamina-specific cortical events. Synchronous activity of neuronal ensembles has been shown to reliably represent the functional organization of auditory cortex, even in the absence of

changes in single-unit firing rate (deCharms and Merzenich, 1996), and has been proposed as an important mechanism of cortical processing, which may facilitate transmission of information through multiple hierarchical levels (Eggermont, 1994b; Lisman, 1997). Concerted activity of neuronal populations may therefore be more relevant than the isolated firing of single neurons for the encoding of perceptual features, such as roughness. One form of neural synchrony arises when responses of multiple neurons are time-locked to a particular stimulus characteristic. This is the type of synchrony examined in the present study, as reflected in the phase-locking of neuronal ensemble responses to the periodic temporal envelope of harmonic complexes.

While multi-channel MUA recording offers the advantage of rapidly sampling synchronized activity of neural ensembles simultaneously across multiple cortical laminae, an important limitation of the technique is an inability to resolve individual cell types contributing to the overall response. It is likely that MUA recordings, particularly in the thalamorecipient zone, include contributions from thalamo-cortical axons and stellate cells, in addition to pyramidal cells. Since these input fibers and cell types have been reported to exhibit differential phase-locking capabilities (e.g., de Ribaupierre *et al.*, 1972; Creutzfeldt *et al.*, 1980), these methodological limitations must be considered in the interpretation of MUA results.

I. METHODS

Three adult male monkeys (*Macaca fascicularis*) were studied using methods previously reported (Steinschneider *et al.*, 1998). Animals were housed in our AAALAC-accredited Animal Institute under daily supervision by veterinary staff. All experiments were conducted in strict accordance with institutional and federal guidelines governing the ethical treatment of primates. Briefly, under general anesthesia and using aseptic techniques, small holes were made in the exposed skull to accommodate epidural matrices consisting of adjacently placed 18-gauge stainless steel tubes. Matrices were stereotaxically positioned to target A1 and were oriented at an angle of 30 degrees from normal to approximate the anterior–posterior tilt of the superior temporal plane. This orientation guided electrode penetrations roughly perpendicular to the cortical surface, thereby fulfilling one of the major technical requirements of one-dimensional CSD analysis (Vaughan and Arezzo, 1988). Matrices and plexiglass bars used for painless head immobilization during the recording sessions were held in place by a pedestal of dental acrylic fixed to the skull by inverted bone screws. Recordings began two weeks after surgery and were conducted in an electrically shielded, sound-attenuated chamber with the animals awake and comfortably restrained. An alert state was maintained by frequent visits into the recording chamber by the investigators at which times animals were given fruit juice reinforcements. Fluctuations in arousal were assessed on-line by monitoring the degree of slow-wave electroencephalographic activity. Intracortical recordings were obtained using linear-array multi-contact electrodes containing 14 recording contacts, evenly spaced at 150-μm intervals (Barna *et al.*, 1981). Individual contacts were constructed from 25-μm diam stainless steel wires, and had an impedance of about 200 kΩ that was checked prior to each recording session. An epidural stainless steel wire positioned over the occipital cortex served as a reference electrode. Field potentials were recorded using unity-gain headstage amplifiers and then amplified 5000 times by differential amplifiers with a frequency response down 3 dB at 3 Hz and 3 kHz. Signals which generated the evoked potentials were digitized at an A/D rate between 2 and 4 kHz (depending on the analysis time used) and averaged by computer (*Neuroscan* software and hardware, *Neurosoft, Inc.*) to yield AEPs. To derive MUA, signals were simultaneously high-pass filtered above 500 Hz, amplified an additional eight times, and full-wave rectified prior to digitization and averaging. Raw unfiltered data were simultaneously recorded on analog or digital tape for off-line analysis. Due to limitations of the acquisition computer, the sampling rates used were lower than the Nyquist frequency corresponding to the 3-kHz upper cutoff of the amplifiers. Empirical testing revealed, however, minimal signal distortion due to aliasing artifacts. This is attributed to the fact that most of the spectral energy in the MUA lies below 1 kHz. Using shorter analysis times, raw data redigitized at an A/D rate of 6 kHz, yielded nearly identical averaged waveforms as data sampled at the lower rate. MUA is a measure of the summed action potential activity of neuronal ensembles within a sphere of about 50–100 μm in diameter surrounding each recording contact (Arezzo *et al.*, 1986; Vaughan and Arezzo, 1988; Brosch *et al.*, 1997). The circumscribed nature of MUA is also demonstrated by the channel specificity of high-amplitude MUA (bicuculline-induced paroxysmal discharges) for electrode contacts separated by as little as 75 μm (Schroeder *et al.*, 1990). Using ensemble recording methods similar to those of the present study, Nelken *et al.* (1994) demonstrated the similarity of MUA to cluster activity and its superior response stability relative to cluster and single-unit activity.

One-dimensional CSD analyses were performed to characterize the laminar pattern of current sources and sinks within A1 generating the evoked potentials. CSD was calculated using a three-point algorithm that approximates the second spatial derivative of voltage recorded at each recording contact (Freeman and Nicholson, 1975; Nicholson and Freeman, 1975). Current sinks represent net inward transmembrane current flow associated with local depolarizing excitatory postsynaptic potentials or passive, circuit-completing transmembrane current associated with hyperpolarizing potentials at adjacent sites. Current sources reflect sites of net outward transmembrane currents associated either with active hyperpolarizations or with passive current return for adjacent depolarizing potentials. The corresponding MUA profile provides a basis for distinguishing these possibilities: current sinks associated with coincident increases in MUA likely reflect depolarizing processes, whereas current sources associated with concurrent reductions in MUA from baseline levels likely reflect hyperpolarizing processes rather than passive current return for adjacent depolarizing events.

Isointensity frequency response functions (FRFs) based on pure tone responses were used to characterize the frequency sensitivity of the cortical sites. Pure tone stimuli used

to generate the FRFs were typically separated by 100 Hz below 1 kHz, 200–300 Hz below 5 kHz, and 500 Hz below 15 kHz. For experiments involving one animal, pure tones ranging from 200 Hz to 12 kHz were generated at a sampling frequency of 44.1 kHz using *Turbosynth* and *SoundDesigner* sound synthesizing software (*Digidesign, Inc.*). For experiments involving the other two animals, pure tones ranging from 200 Hz to 15 kHz were produced by a waveform generator at a sampling frequency of 79.3 kHz (*Tucker-Davis Technologies, Inc.*). Pure tones were 175 ms in duration with rise and fall times of 10 ms. The interstimulus interval for pure tone presentation was 658 ms. All stimuli were monaurally delivered at 60 dB SPL via headphone to the ear contralateral to the recorded hemisphere. Sound generated by the headphone was channeled to the ear through a 3-in.-long, 60-cc plastic tube attached to the headphone. Sound intensity was measured with a *Bruel and Kjaer* sound level meter (*type 2236*) positioned at the opening of the plastic tube. The frequency response of the headphone was flattened (± 3 dB) from 0.2 to 17.0 kHz by a graphic equalizer (*Rane, Inc.*).

Harmonic complex tones, also generated using *Turbosynth* and *SoundDesigner* software, were composed of three equal-amplitude consecutive harmonics of fundamental frequencies (f_0s) ranging from 25 to 4000 Hz. Center frequencies of the complex tones corresponded to the best frequency (BF) of the cortical site. All harmonics were combined in sine phase. These complex stimuli are spectrally similar to AM tones with carrier frequencies corresponding to the center frequency and amplitude modulation rates corresponding to the f_0 (i.e., ΔF between components). The highest f_0 presented at a given cortical site was that for which the BF corresponded to the second harmonic. Complex tones were 450 ms in duration, with rise and fall times of 5 ms, and were presented at an interstimulus interval of 992 ms. The complex tone stimulus set invariably included f_0s of 25, 50, and 100 Hz, one f_0 between 50 and 100 Hz, at least one f_0 between 100 and 200 Hz, and at least one f_0 between 200 and 400 Hz. Since the complex tone components were harmonically related to the BF, the specific f_0s varied across cortical sites in relation to BF.

Electrodes were moved within the brain using a microdrive. Positioning of the electrode was guided by on-line examination of click-evoked potentials. Pure and complex tone stimuli were delivered when the electrode channels bracketed the inversion of early AEP components and the largest MUA, typically occurring during the first 50 ms within lamina IV (LIV) and lower lamina III (LLIII), was situated in the middle channels. Evoked responses to 75 presentations of the stimuli were averaged with an analysis time (including a 25-ms prestimulus baseline interval) of 300 ms for pure tones and 525 ms for complex tones. Complex tones and their response analysis windows were of longer duration in order to enhance the resolution of spectral analyses used to quantify phase-locked activity (see below). Stimuli were presented in pseudo-random order. In some electrode penetrations, several response averages for each complex tone stimulus were collected to evaluate response stability over time.

At the end of the recording period, animals were deeply anesthetized with sodium pentobarbital and transcardially perfused with 10% buffered formalin. Tissue was histologically examined using stains for acetylcholinesterase and Nissl substance to reconstruct the electrode tracks and to identify A1 according to previously published criteria (Wallace *et al.*, 1991a; Morel *et al.*, 1993). Field R was demarcated from A1 by a reversal in the best frequency gradient (Morel *et al.*, 1993). The earliest sink/source configuration was used to locate LIV (Steinschneider *et al.*, 1992). Other laminar locations were then determined by their relationship to LIV and the measured widths of laminae within A1 for each electrode penetration histologically identified.

The BF of the cortical site sampled in a given electrode penetration was defined as the pure tone frequency eliciting the largest peak amplitude MUA within LLIII during the first 50 ms following stimulus onset. This period encompasses the time of initial activation of thalamorecipient zone cells in LIV and LLIII (Steinschneider *et al.*, 1992, 1994). Use of peak amplitude initial MUA as a measure of BF yielded consistent anterior-lateral to posterior-medial topographic gradients of low- to high-frequency representation in all animals, in accordance with previous studies of single neurons and neuron clusters (Merzenich and Brugge, 1973; Morel *et al.*, 1993).

Phase-locked activity was examined as a function of f_0 and the BF of the location. Lamina-specific activity was examined by analysis of stimulus-evoked responses recorded from three different cortical depths corresponding to LLIII, upper lamina III (ULIII), and lamina II (LII). LLIII MUA and CSD are of interest because they reflect both initial cortical activation and activity at the location of cell bodies whose output is sent to other cortical areas potentially involved in further auditory processing (Galaburda and Pandya, 1983; Rouiller *et al.*, 1991; Pandya and Rosene, 1993). ULIII responses, on the other hand, may largely represent later polysynaptic activation of ULIII pyramidal cells by multiple interlaminar, intralaminar, and cortico-cortical inputs (Galaburda and Pandya, 1983; Mitani *et al.*, 1985; Matsubara and Phillips, 1988; Ojima *et al.*, 1991; Rouiller *et al.*, 1991; Wallace *et al.*, 1991b). Degree of phase-locking to the f_0 of the complex tones was quantified by spectral analysis of averaged responses using a fast Fourier transform (FFT) algorithm (*ProStat, Poly Software International*). The FFT was applied to the entire response analysis window. Results of spectral analyses were normalized using the following procedure. First, baseline power at the stimulus f_0 in the power spectrum of the complex tone response was estimated by averaging power over two groups of five consecutive frequency bins surrounding the bin corresponding to the f_0. One group was centered five bins above the f_0 and the other five bins below the f_0 (i.e., $f_0 \pm 9.6$ Hz) to ensure that the baseline estimate did not include power related to phase-locked activity. Baseline power was then subtracted from power at the f_0, thereby yielding the amount of power at the f_0 exceeding what would be expected for a response exhibiting no phase-locking. This normalization procedure is conceptually analogous to the linear interpolation method used by Kruse and Eckhorn (1996) to evaluate changes in MUA spectra. It is also similar to the method used by Srinivasan

et al. (1999) to derive signal-to-noise ratios of power at the stimulus frequency in neuromagnetic recordings. A complementary normalization procedure, wherein power at the complex tone f_0 in the spectrum of the response to a BF tone was subtracted from the power at the f_0 in the spectrum of the response to the complex tone, yielded virtually identical results.

The best f_0 (BF_0) of the cortical site was defined as the stimulus f_0 associated with the maximum normalized power at the f_0 in the response spectrum. The maximum f_0 (Max F_0) was defined as the highest stimulus f_0 capable of eliciting above-baseline phase-locked activity, as detected by spectral analysis. Power at the f_0 was regarded as present if its value was greater than two standard deviations above the mean estimated baseline power. Pearson correlation coefficients and associated one-tailed probabilities (values tabulated in Fisher and Yates, 1974) were computed to quantify the strength of the relationship between BF_0, Max F_0 and BF. Due to the linearity requirement for correlation analysis, data were logarithmically transformed prior to calculation of correlation coefficients in order to yield scatterplots amenable to description by linear regression lines. One-tailed probability values were considered because, for theoretical reasons (human psychoacoustics), the experimental hypothesis was directional—the null hypothesis being that the correlation coefficient is less than or equal to zero.

II. RESULTS

Results are based on 29 electrode penetrations into A1 of three monkeys. To satisfy the requirements of one-dimensional CSD analysis, only those penetrations histologically confirmed to be <20 degrees from perpendicular to the cortical surface are included in the results, as significant deviations from the major axis of current flow may introduce errors into the CSD computations (Freeman and Nicholson, 1975). Histological reconstruction of electrode tracks indicated that the majority of these penetrations were located in the central region of A1. BFs of the cortical sites sampled ranged from 0.3 to 10 kHz. Out of the 29 total penetrations, 2 failed to exhibit phase-locking at any of the f_0s presented. These penetrations were therefore not included in the statistical analyses of the present paper, although they were admitted into the analyses of the following companion paper (Fishman *et al.*, 2000).

A. Basic MUA and CSD response profiles

Figure 1(a) illustrates representative multi-electrode response profiles (CSD, left column, MUA, right column) evoked by a harmonic complex tone ($f_0=100$ Hz) centered at the BF (approximately 4 kHz). The BF corresponds to the peak in the LLIII MUA FRF of the site, as shown on the middle right in the figure. The MUA FRF (solid line) is based on the peak amplitude of LLIII MUA during the first 50 ms following stimulus onset. The corresponding FRF based on the peak amplitude of the LLIII current sink is represented by the broken line to illustrate concordance between the spectral sensitivity of MUA and that of CSD. Below-baseline portions of the CSD waveforms represent

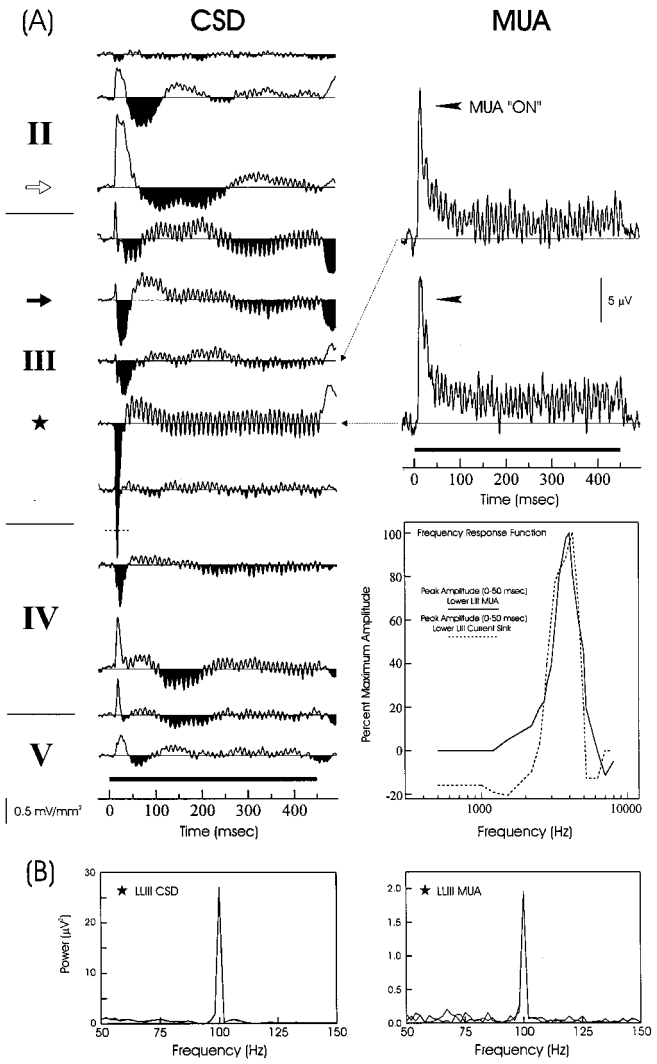

FIG. 1. (a) Representative examples of MUA (right column) and CSD (left column) response profiles evoked by a harmonic complex tone at a site in A1 with a BF of about 4 kHz (center frequency=4 kHz, $f_0=100$ Hz). Black bars directly above the time axes represent the duration of the stimulus. Approximate laminar boundaries are denoted on the far left of the figure. Black star, black arrow, and white arrow indicate LLIII, ULIII, and LII responses examined in the study. Note: due to the display gain of the waveforms, the initial current sink of the lower lamina III waveform extends through the waveform directly below it, obscuring a smaller sink occurring within the same timeframe. The peak of the occluded sink is indicated by the dashed horizontal line. FRFs based on peak amplitude LLIII MUA and CSD are shown on the middle-right of the figure (solid line, MUA; dashed line, CSD). (b) Power spectra corresponding to the LLIII responses shown in (a); MUA: right, CSD: left. See text for details.

current sinks, whereas above-baseline portions represent current sources. The earliest stimulus-evoked activity is represented by initial current sinks in the thalamorecipient zone (LIV and LLIII, black star; mean peak latency: 17.3 ms, standard deviation: 5.3 ms). These sinks are balanced by deeper sources in LIV and by sources in ULIII (initial positive deflections), primarily representing passive circuit-completing current flow. In conjunction with the underlying LLIII sinks, the ULIII current sources form a current dipole configuration characteristic of pyramidal cell activation.

Slightly later and more superficial evoked activity is manifested by current sinks located in mid- and ULIII (black

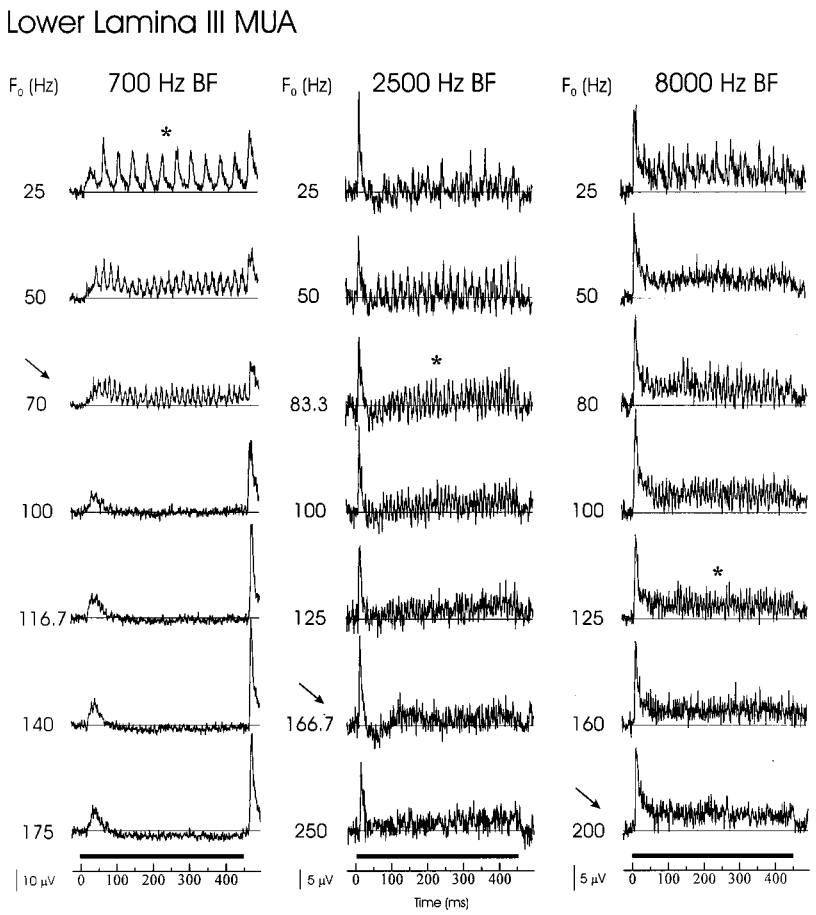

FIG. 2. LLIII MUA elicited by harmonic complex tones of varying f_0 at three different BF sites. Asterisks indicate responses exhibiting maximal phase-locking to the f_0 (BF_0). Black arrows indicate responses to stimuli with the highest f_0 capable of eliciting phase-locked activity (Max F_0). Both BF_0s and Max F_0s increase with BF. See text for details.

arrow; mean peak latency: 28.5 ms, standard deviation: 9.3 ms). These sinks are balanced by more superficial sources located in LII (white arrow; mean peak latency: 28.2 ms, standard deviation: 9.3 ms), thus forming a slightly later, more superficial current dipole indicative of pyramidal cell activity. Early sinks in LLIII and upper LIV are coincident with above-baseline peaks in MUA (''On'' response), indicating that they principally represent transmembrane current flow associated with depolarizing synaptic potentials. These basic response characteristics are consistently observed across A1 penetrations in the present study and in previous investigations using clicks, pure tones, and complex stimuli (Muller-Preuss and Mitzdorf, 1984; Steinschneider *et al.*, 1992, 1994, 1998; Fishman *et al.*, 1998a; Reser *et al.*, 2000).

Initial transient activation of neuronal ensembles in LIV and LLIII is followed by lower amplitude activity phase-locked to the f_0, as represented by the peaks at 100 Hz in the power spectra depicted in Fig. 1(b) (CSD: left, MUA: right). Spectra of two response averages recorded 30 min apart are shown superimposed to illustrate the high degree of response stability over time. Although most pronounced in the thalamorecipient zone, phase-locked activity is observed throughout CSD channels spanning several supra- and infragranular cortical laminae.

B. Relationship between BF of the site and BF_0, Max F_0

Figure 2 depicts LLIII MUA evoked by complex tones of varying f_0 from three cortical sites with different BFs. Peaks in MUA following the end of the stimulus represent ''off'' responses. Asterisks indicate responses displaying maximal phase-locking, as quantified by normalized spectral analyses. Black arrows indicate responses to the highest f_0 stimuli presented at each site capable of eliciting phase-locked activity, as detected by spectral analyses. The figure reveals two notable response features: (1) BF_0 increases with BF and (2) Max F_0 increases with BF. Figure 3 shows LLIII CSD correlates of the MUA data in Fig. 2. Similar to LLIII MUA, CSD BF_0 and Max F_0 also increases with BF. These response features are further illustrated in Fig. 4(a), which depicts power spectra of the responses shown in Figs. 2 and 3 (MUA: left column, CSD: right column). Spectra are overlaid to facilitate comparison. Prominent peaks in the spectra occur at frequencies corresponding to the f_0s of the complex stimuli. For both MUA and CSD, the highest peak corresponding to the BF_0 shifts towards higher f_0s with BF. Moreover, the highest frequency at which f_0 peaks are still apparent increases with BF. These trends are also evident in normalized results graphically depicted in Fig. 4(b) (MUA: left, CSD: right). Both peaks and falling edges of the curves shift towards higher f_0s with BF. BF_0s of these 700, 2500, and 8000 Hz BF sites are 25, 83.3, and 125 Hz for MUA and 25, 50, and 100 Hz for CSD, respectively. Max F_0s (values represented by black symbols in the graphs) are 70, 166.7, and 200 Hz, respectively, for both MUA and CSD. For the 2500 and 8000 Hz BF sites, CSD BF_0s are slightly lower

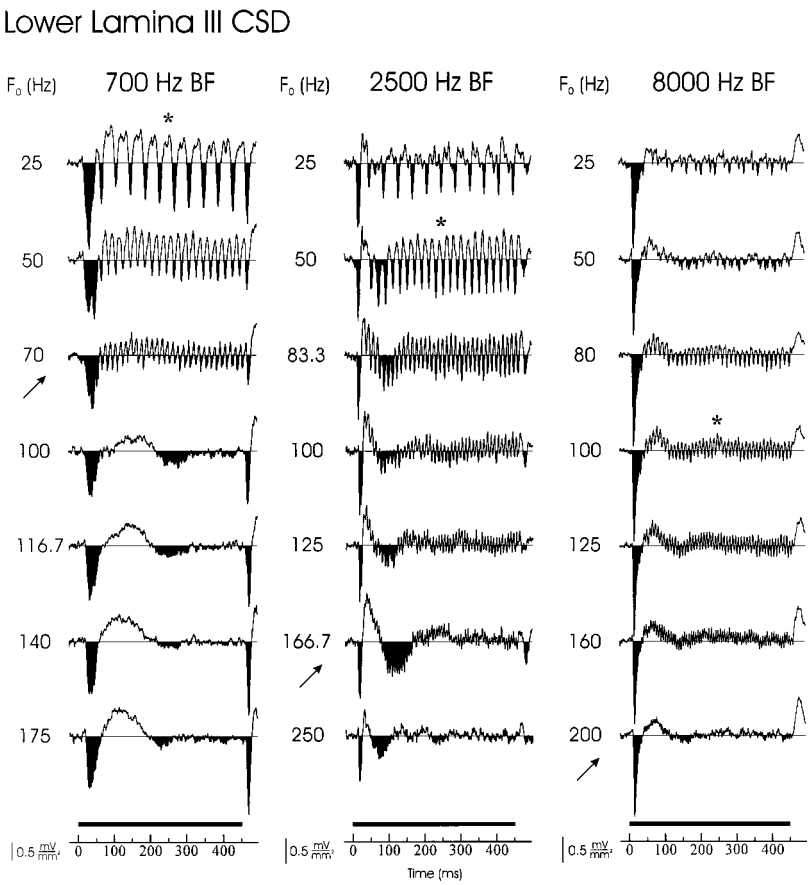

FIG. 3. LLIII CSD corresponding to the MUA data of Fig. 2. Same conventions as in Fig. 2. Both BF_0s and Max F_0s increase with BF.

than those observed for LLIII MUA. This discrepancy, wherein action potential responses ''do more'' than the CSD, suggests that LLIII MUA is not exclusively determined by synaptic activity represented by thalamorecipient zone CSD and may also reflect thalamo-cortical fiber contributions.

Figures 5(a) and 5(b) represent pooled results from the three animals based on responses recorded from LLIII [MUA: (a), CSD: (b)]. The white symbols represent BF_0s, while the black symbols represent Max F_0s. The number of symbol outlines denotes the number of points >1 represented. A power regression line is fitted to each set of data points (solid lines). For comparison with psychoacoustic data on roughness perception, power regression lines fitted to reported values corresponding to maximal roughness (lower broken line) and disappearance of roughness (upper broken line) for AM tones are included. Since these values differ somewhat between studies, the values used for the regressions are based upon averaged data from Terhardt (1968a,b, 1974a,b). The strength of the relationship between BF_0 and BF and between Max F_0 and BF is quantified by Pearson correlation analysis based on log-linearized data (see Sec. I). For both LLIII MUA and LLIII CSD, BF_0 is significantly correlated with BF ($r=0.55$, $p<0.005$ and $r=0.54$, $p<0.005$, respectively). The highest BF_0 observed for LLIII MUA is 130 Hz, whereas the highest for LLIII CSD is 100 Hz. Max F_0 for both LLIII MUA and CSD is also significantly correlated with BF ($r=0.67$, $p<0.0005$ and $r=0.68$, $p<0.0005$, respectively). The highest Max F_0 observed is 300 Hz for both LLIII MUA and CSD. It is important to note that the limited number of f_0s comprising the stimulus set in the present study precludes a precise determination of limiting phase-locking rates and thus provides only an estimate of these values. Physiological values fall roughly within the ranges described by psychoacoustic regression lines. Corresponding physiological regression lines exhibit similar slopes to those describing human psychoacoustic data, although they are systematically lower in height.

To determine whether similar relationships are exhibited for responses generated outside the thalamorecipient zone, additional analyses were performed for more superficial CSD channels corresponding to the ULIII current sink [Fig. 5(c)] and to the LII current source [Fig. 5(d)]. Both BF_0 and Max F_0 for ULIII CSD are correlated with BF, although less strongly than in the case of thalamorecipient zone responses (BF_0: $r=0.45$, $p<0.01$; Max F_0: $r=0.37$, $p<0.05$). For LII CSD, only Max F_0 displays a significant positive correlation with BF ($r=0.43$, $p<0.02$). The weaker correlations exhibited by these supragranular responses are accompanied by considerable deviations of physiologic values from those reported in the human psychoacoustic literature.

III. DISCUSSION

A. Summary of findings and relationship to roughness perception

If phase-locked responses in A1 represent physiological phenomena potentially relevant for the perception of roughness, then (1) best phase-locking rates and limiting phase-locking rates should increase with BF up to about 2–4 kHz (for narrow-band complex sounds with center frequencies

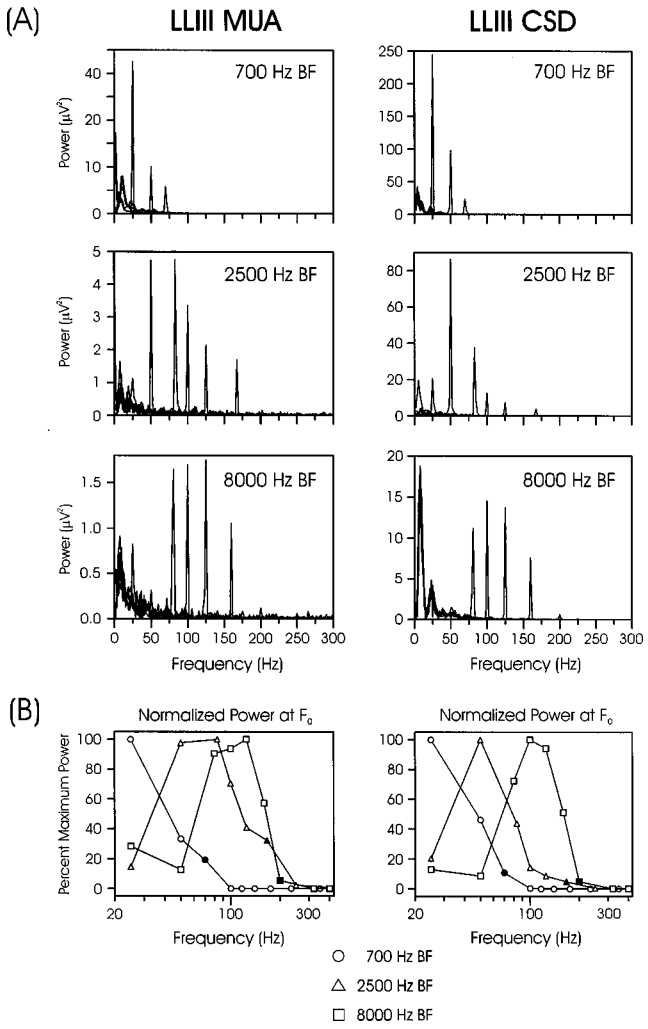

FIG. 4. (a) Spectra of responses shown in Figs. 2 and 3 (MUA: left, CSD: right). Spectra of responses to the different f_0 stimuli recorded at each BF site are overlaid to facilitate comparison. Major peaks correspond to the f_0s of the complex stimuli. The dc components and power at harmonics of the f_0s have been zeroed. Note the shift in the maximal peaks towards higher f_0s with BF. (b) Graphical representation of normalized results (MUA:left, CSD:right). Curve peaks denoting the BF_0s and Max F_0s (represented by the black symbols) shift towards higher f_0s with BF. See text for details.

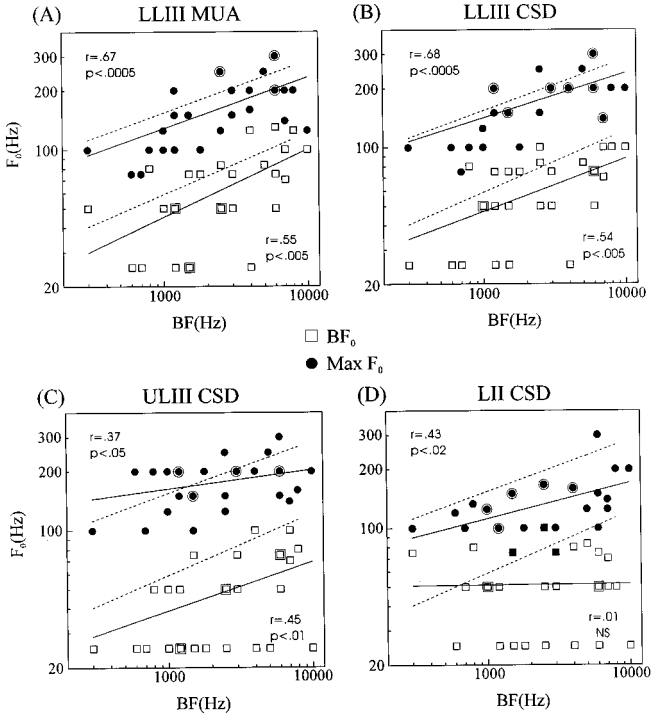

FIG. 5. Scatterplots of pooled results for (a) LIII MUA, (b) LLIII current sink, (c) ULIII current sink, and (d) LII current source. White symbols represent values of BF_0; black symbols, Max F_0. The number of symbol outlines indicates the number of points >1 represented. A power regression line is fitted to each set of data points (solid line). Broken lines represent power functions fitted to average psychoacoustic values corresponding to maximum roughness (lower) and disappearance of roughness (upper) from Terhardt (1968a,b, 1974a,b). Pearson correlation coefficients and associated one-tailed probability values are indicated in the top left (for Max F_0) and bottom right (for BF_0) of each graph. See text for details.

situated at the BF), and (2) best phase-locking rates and limiting phase-locking rates should encompass the range of waveform envelope fluctuation rates characteristic of maximal roughness (20–150 Hz) and roughness detection (20–300 Hz), respectively, as delineated in psychoacoustic experiments (Plomp and Steeneken, 1968; Terhardt, 1968a, 1974a,b).

In accordance with these requirements, we have shown that BF_0s and Max F_0s of neuronal ensembles in A1 of the awake monkey increase with BF of the cortical site and are comparable to ΔFs corresponding to maximal roughness and just noticeable roughness, respectively. Parallels between phase-locked activity and human psychoacoustic boundaries of roughness perception are most pronounced for responses generated in LLIII and diminish progressively with increasing supragranular distance from the thalamorecipient zone. The highest values of BF_0 observed in the present study are comparable to the highest ΔFs corresponding to maximal roughness reported in psychoacoustic studies using AM tones (75–125 Hz) and are slightly lower than those obtained in studies using two-tone stimuli (150 Hz). The source of the discrepancy between these values in the psychoacoustic literature is unclear, but may be due to differences in experimental methods and stimulus characteristics. Nonetheless, the consensus of these studies is that for stimulus center frequencies below 2–4 kHz, the ΔF corresponding to maximal roughness is governed by critical-band filtering. Above this range, the largest ΔF corresponding to just noticeable roughness (about 250–300 Hz for AM tones) is constrained by an inability to temporally encode higher rates of waveform envelope fluctuation (Plomp and Steeneken, 1968; Terhardt, 1968a,b, 1974a, 1978). The present results support both hypotheses: (1) Both BF_0 and Max F_0 increase with BF (critical-band filtering effect), and (2) the highest Max F_0 observed is 300 Hz, which corresponds to the upper boundary for roughness detection. The agreement between physiological and psychoacoustic data implies that higher-level perceptual judgments that partly depend upon the perception of roughness, such as the perception of dissonance for musical intervals, may involve similar temporal encoding mechanisms at the level of A1 (Plomp and Levelt, 1965; Kameoka and Kuriyagawa, 1969; Terhardt, 1974a,b). This is supported by preliminary evidence in A1 of the awake monkey showing that the perceived dissonance of musical intervals corre-

lates with the amount of activity phase-locked to the beat frequencies (Fishman *et al.*, 1998b).

There are discrepancies, however, between physiological values obtained in the present study and those delineating psychophysical boundaries of roughness for AM tones. While psychoacoustic regression lines and thalamorecipient zone regression lines of Fig. 5 are similar in slope, the latter are systematically lower in height. A number of possibilities can account for this departure. First, AM tones used in the psychoacoustic studies and the three-component complex tones used in the present study are not identical stimuli. Specifically, the latter have equal-amplitude spectral components, whereas the former are composed of a center component flanked by two lower-amplitude side-band frequencies. Thus, it is conceivable that the larger amplitude sidebands in our stimuli may have led to greater suppression of phase-locked responses than for AM tones. The fact that psychophysical boundaries of roughness for two-tone stimuli occur at somewhat higher modulation frequencies than those for AM tones is consistent with this possibility. Another consideration is that neural recordings were conducted under passive-listening conditions. Had the animals been trained to perform active discriminations, it is possible that physiological values would have approached psychoacoustic values more closely. Finally, as noted by Eggermont (1999), psychophysical boundaries may be based on the limits of processing capabilities that may be approached by only a few neurons, and not on the average behavior of auditory cortical cells. As evident in the present data, some of the sampled neuronal ensembles exhibited BF_0s and Max F_0s coinciding with psychophysical regression lines, while others displayed lower values. Thus, while the activity of only a small subpopulation of neurons may be sufficient to perform psychophysical discriminations at high modulation rates, the smaller proportion of neurons capable of phase-locking at these rates yields lower regression lines describing the average behavior of neuronal ensembles in A1.

It is unknown whether monkeys perceive roughness of complex sounds, since no psychophysical studies in monkeys have systematically examined the dependence of amplitude modulation detection on center frequency. However, an extrapolation of the present results to humans is reasonable in view of the similarity between macaque and human psychophysical amplitude modulation transfer functions, difference limens for AM stimuli, and two-tone masking critical band curves (Gourevitch, 1970; Pfingst, 1993; Moody, 1994). Specifically, macaque and human temporal modulation transfer functions and difference limens for detecting the presence and rate change of amplitude modulation, respectively, overlap considerably over a range of modulation frequencies relevant for roughness (20–200 Hz).

B. Relationship to other auditory physiological studies

The relationship between BMF and characteristic frequency (CF) was also examined in single- and multi-unit studies of several auditory cortical fields of the anesthetized cat (Schreiner and Urbas, 1986, 1988; Eggermont, 1998). In contrast to the results of the present study, these investigations did not find a correlation between BMF, limiting phase-locking rates, and CF in A1. On the other hand, a correlation between BMF and CF was consistently observed in the anterior auditory field (AAF) for AM tones (Schreiner and Urbas, 1986, 1988; Eggermont, 1998). However, the mean BMF and mean limiting rate (8.9 and 27.8 Hz, respectively, based on tMTFs) reported in Eggermont's (1998) study for AAF are below the range of rates characteristic of roughness perception and are more consistent with a temporal representation of rhythm at the cortical level. On the other hand, in the studies of Schreiner and Urbas (1986, 1988), BMFs in AAF as high as 100 Hz (mean 31.1 Hz) were observed, whereas in A1 BMFs only below about 50 Hz were seen. It is unclear whether the correlation between BMF and CF for AAF in the cat is relevant for roughness perception in humans, since the CF range over which correlation coefficients were computed extended up to 40 kHz, whereas human psychophysical curves describing roughness perception are defined only for center frequencies below 10 kHz.

Suppressive effects of anesthetics on neuronal phase-locking may be responsible for the generally low BMFs and limiting rates reported for A1 (Goldstein *et al.*, 1959; Makela *et al.*, 1990; Karmos *et al.*, 1993). Consistent with this possibility, other single- and multi-unit studies in unanesthetized animals have documented synchronization rates for responses to AM tones and click trains in A1 that are comparable to those observed in the present study. For example, Steinschneider *et al.* (1998) demonstrated neuronal ensemble phase-locking to click trains in A1 of the awake macaque at rates up to 200–300 Hz. Similarly, in A1 of the awake squirrel monkey, Bieser and Muller-Preuss (1996) observed multi-unit BMFs up to 128 Hz, thus implying limiting rates at least as high as 128 Hz (limiting rates were not indicated in their study). These findings corroborate the results of earlier studies reporting median limiting rates of 50–100 Hz for pyramidal cell phase-locking to click trains in A1 of unanesthetized cats (de Ribaupierre *et al.*, 1972). This contrasts with the mean limiting rate of 11.8 Hz for single-unit phase-locking to click trains in A1 of ketamine-anesthetized cats (Eggermont, 1998). Goldstein *et al.* (1959) demonstrated a 200-Hz limiting rate for phase-locking in the local field potential to click trains in A1 of the unanesthetized cat, which was reduced to below 100 Hz under barbiturate anesthesia. In combination, these findings suggest that the discrepancies among the results of these studies largely result from anesthesia-induced suppression of temporal processing at the cortical level.

Since LLIII receives direct thalamic inputs, however, it is likely that thalamo-cortical afferents contributed to the LLIII responses recorded in the present study. Thus, a more conservative conclusion is that at least thalamic input into A1 conveys a representation of roughness by phase-locked responses. Since the LII current source primarily represents passive current return for ULIII sinks, the absence of a correlation between LII BF_0 and BF implies that polysynaptic activity in LIII pyramidal cell elements does not reflect roughness by phase-locked responses. However, since the LLIII sink and ULIII sources (initial positive deflections in Fig. 1) form a current dipole configuration indicative of py-

ramidal cell activation, the fact that ULIII BF_0 did correlate with BF strongly suggests a cortical contribution to the LLIII responses, at least as reflected by postsynaptic potentials. The weaker correlations observed for ULIII CSD compared with LLIII CSD are consistent with the former representing both passive components of the LLIII current dipole, whose active sink in LLIII does display significant correlations, and active components of the ULIII current dipole, whose passive source in LII does not. The fact that ULIII Max F_0s are within the range of psychoacoustic values corresponding to just-noticeable roughness suggests that phase-locking limitations of auditory cortical neurons may define the upper boundary of roughness perception. In contrast, phase-locking to stimulus periodicities as high as 400 Hz are reported for some medial geniculate neurons and thalamo-cortical fibers (Rouiller *et al.*, 1979; Rouiller and de Ribaupierre, 1982; Steinschneider *et al.*, 1998). As this rate exceeds the upper perceptual boundary for roughness, degradation in the fidelity of temporal encoding at the cortical, rather than the thalamic level may be responsible for restricting limiting rates of phase-locking to those coinciding with the upper limits of roughness detection.

C. Relevance to temporal encoding of pitch

In addition to representing roughness, phase-locked responses in A1 may be associated with temporal encoding of pitch for complex tones composed of unresolved harmonics. Complex sounds comprised of harmonically related frequencies elicit the perception of a global pitch equal to the f_0, even in the absence of spectral energy at the fundamental—a phenomenon known as ''virtual pitch.'' While the physiologic basis of pitch perception remains controversial (see companion paper, Fishman *et al.*, 2000), psychoacoustic evidence suggests that the pitch of harmonic complexes composed of resolved components (whose ΔF exceeds the CBW) is determined by spectral pattern recognition mechanisms, while that of complexes composed of unresolved harmonics ($\Delta F <$ CBW) depends upon temporal encoding of waveform periodicity (Houtsma and Goldstein, 1972; Goldstein, 1973; Terhardt, 1974b; Burns and Viemeister, 1981; Pierce, 1991; Shackleton and Carlyon, 1994).

Using methods similar to those of the present study, Steinschneider *et al.* (1998) described click train-evoked response patterns in A1 of the awake macaque that parallel psychoacoustic boundaries of temporal pitch. As in the present study, phase-locked responses were detectable up to rates of 300 Hz, which is near the reported upper limit for the perception of temporal pitch for unresolved harmonics (Flanagan and Guttman, 1960; Guttman and Flanagan, 1964; Rosenberg, 1965; Burns and Viemeister, 1981; Pierce, 1991). As suggested by Schulze and Langner (1997), the possibility that both roughness and temporal pitch are represented by phase-locked responses in A1 may explain why the pitch of complex tones composed of unresolved harmonics has an additional buzz quality characteristic of roughness.

IV. SUMMARY AND CONCLUSIONS

Temporal representation of the f_0 of three-component harmonic complexes via phase-locked responses of neuronal ensembles in A1 was examined in order to clarify neural mechanisms associated with roughness perception. Center frequencies (middle harmonics) of the complex tones were situated at the BF of the cortical sites. F_0s of harmonic complexes eliciting maximal phase-locked responses increased with BF. The highest F_0s at which phase-locked responses were detected also increased with BF. These correlations were most pronounced for responses recorded in LLIII and diminished with increasing supragranular distance from the thalamorecipient zone. Phase-locked responses in A1 were observed up to f_0s of 300 Hz, and thus encompassed the range of rates characteristic of roughness. Synchronized phase-locked activity of neuronal populations in A1 may therefore be relevant for the physiological representation of roughness. Representation of other perceptual attributes of complex sounds, such as the pitch of complex tones comprised of unresolved components and sensory dissonance of musical intervals, may rely on similar temporal encoding mechanisms in A1.

ACKNOWLEDGMENTS

This research was supported by Grant Nos. DC00657 and HD01799, and the Institute for the Study of Music and Neurologic Function of Beth Abraham Hospital. We are grateful to Dr. Steven Walkley, May Huang, Linda O'Donnell, and Shirley Seto for providing excellent technical, secretarial, and histological assistance. We also thank Dr. Haftan Eckholdt for statistical advice and two anonymous reviewers for their helpful comments on a previous version of the manuscript. Submitted in partial fulfillment of the requirements for the degree of Doctor of Philosophy in the Sue Golding Graduate Division of Medical Sciences, Albert Einstein College of Medicine, New York.

Arezzo, J. C., Vaughan, Jr., H. G., Kraut, M. A., Steinschneider, M., and Legatt, A. D. (**1986**). ''Intracranial generators of event-related potentials in the monkey,'' in *Frontiers of Clinical Neuroscience, Vol. 3*, edited by R. Q. Cracco and I. Bodis-Wollner (Liss, New York), pp. 174–189.

Barna, J., Arezzo, J. C., and Vaughan, Jr., H. G. (**1981**). ''A new multicontact array for the simultaneous recording of field potentials and unit activity,'' Electroencephalogr. Clin. Neurophysiol. **52**, 494–496.

Beiser, A., and Muller-Preuss, P. (**1996**). ''Auditory responsive cortex in the squirrel monkey: neural responses to amplitude-modulated sounds,'' Exp. Brain Res. **108**, 273–284.

Brosch, M., Bauer, R., and Eckhorn, R. (**1997**). ''Stimulus-dependent modulations of correlated high-frequency oscillations in cat visual cortex,'' Cereb. Cortex **7**, 70–76.

Burns, E. M., and Viemeister, N. F. (**1981**). ''Played-again SAM: further observations on the pitch of amplitude-modulated noise,'' J. Acoust. Soc. Am. **70**, 1655–1660.

Creutzfeldt, O., Hellweg, F. C., and Schreiner, C. (**1980**). ''Thalamocortical transformation of responses to complex auditory stimuli,'' Exp. Brain Res. **39**, 87–104.

deCharms, R. C., and Merzenich, M. M. (**1996**). ''Cortical representation of sounds by the coordination of action potential firing,'' Nature (London) **381**, 610–613.

deRibaupierre, F., Goldstein, Jr., M. H., and Yeni-Komshian, G. (**1972**). ''Cortical coding of repetitive acoustic pulses,'' Brain Res. **48**, 205–225.

Eggermont, J. J. (**1994a**). ''Temporal modulation transfer functions for AM and FM stimuli in cat auditory cortex. Effects of carrier type, modulating waveform and intensity,'' Hear. Res. **74**, 51–66.

Eggermont, J. J. (**1994b**). ''Neural interaction in cat primary auditory cortex II. Effects of sound stimulation'' J. Neurophysiol. **71**(1), 246–270.
Eggermont, J. J. (**1998**). ''Representation of spectral and temporal sound features in three cortical fields of the cat. Similarities outweigh differences,'' J. Neurophysiol. **80**(5), 2743–2764.
Eggermont, J. J. (**1999**). ''Neural correlates of gap detection in three auditory cortical fields in the cat,'' J. Neurophysiol. **81**, 2570–2581.
Eggermont, J. J., and Smith, G. M. (**1995**). ''Synchrony between single-unit activity and local field potentials in relation to periodicity coding in primary auditory cortex,'' J. Neurophysiol. **73**(1), 227–245.
Fisher, R. A., and Yates, F. (**1974**). *Statistical Tables for Biological, Agricultural, and Medical Research*, 6th ed. (Longman, London).
Fishman, Y. I., Reser, D. H., Arezzo, J. C., and Steinschneider, M. (**1998a**). ''Pitch versus spectral encoding of harmonic complex tones in primary auditory cortex of the awake monkey,'' Brain Res. **786**, 18–30.
Fishman, Y. I., Reser, D. H., Arezzo, J. C., and Steinschneider, M. (**1998b**). ''Neural correlates of musical interval consonance and dissonance in primary auditory cortex (A1) of the awake monkey,'' Soc. Neurosci. Abstr. **24**, 401.
Fishman, Y. I., Reser, D. H., Arezzo, J. C., and Steinschneider, M. (**2000**). ''Complex tone processing in primary auditory cortex of the awake monkey. II. Pitch versus critical band representation,'' J. Acoust. Soc. Am. **108**, 247–262.
Flanagan, J. L., and Guttman, N. (**1960**). ''On the pitch of the periodic pulses,'' J. Acoust. Soc. Am. **32**, 1308–1319.
Freeman, J. A., and Nicholson, C. (**1975**). ''Experimental optimization of current source density technique for anuran cerebellum,'' J. Neurophysiol. **38**, 369–382.
Gaese, B. H., and Ostwald, J. (**1995**). ''Temporal coding of amplitude and frequency modulation in the rat auditory cortex,'' Eur. J. Neurosci. **7**, 438–450.
Galaburda, A. M., and Pandya, D. N. (**1983**). ''The intrinsic architectonic and connectional organization of the superior temporal region of the Rhesus monkey,'' J. Comp. Neurol. **221**, 169–184.
Galaburda, A., and Sanides, F. (**1980**). ''Cytoarchitectonic organization of the human auditory cortex,'' J. Comp. Neurol. **190**, 597–610.
Goldstein, J. L. (**1973**). ''An optimum processor theory for the central formation of the pitch of complex tones,'' J. Acoust. Soc. Am. **54**, 1494–1516.
Goldstein, Jr., M. H., Kiang, N. Y.-S., and Brown, R. M. (**1959**). ''Responses of the auditory cortex to repetitive acoustic stimuli,'' J. Acoust. Soc. Am. **31**, 356–364.
Gourevitch, G. (**1970**). ''Detectability of tones in quiet and in noise by rats and monkeys,'' in *Animal Psychophysics*, edited by W. C. Stebbins (Appleton-Century-Crofts, New York), pp. 67–97.
Guttman, N., and Flanagan, J. L. (**1964**). ''Pitch of high-pass-filtered pulse trains,'' J. Acoust. Soc. Am. **36**, 757–765.
Houtsma, A. J. M., and Goldstein, J. L. (**1972**). ''The central origin of the pitch of complex tones: evidence from musical interval recognition,'' J. Acoust. Soc. Am. **51**, 520–529.
Kameoka, A., and Kuriyagawa, M. (**1969**). ''Consonance theory part I: Consonance of dyads,'' J. Acoust. Soc. Am. **45**, 1451–1459.
Karmos, G., Makela, J. P., Ulbert, I., and Winkler, I. (**1993**). ''Evidence for intracortical generation of the auditory 40-Hz response in the cat,'' in *New Development in Event-Related Potentials*, edited by H. J. Heinze, T. F. Munte, and G. R. Mangun (Birkhauser, Boston), pp. 87–93.
Kruse, W., and Eckhorn, R. (**1996**). ''Inhibition of sustained gamma oscillations (35–80 Hz) by fast transient responses in cat visual cortex,'' Proc. Natl. Acad. Sci. USA **93**, 6112–6117.
Langner, G. (**1992**). ''Periodicity coding in the auditory system,'' Hear. Res. **60**, 115–142.
Lisman, J. E. (**1997**). ''Bursts as a unit of neural information: making unreliable synapses reliable,'' Trends Neurosci. **20**, 38–43.
Makela, J. P., Karmos, G., Molnar, M., Csepe, V., and Winkler, I. (**1990**). ''Steady-state responses from the cat auditory cortex,'' Hear. Res. **45**, 41–50.
Matsubara, J. A., and Phillips, D. P. (**1988**). ''Intracortical connections and their physiological correlates in the primary auditory cortex (A1) of the cat,'' J. Comp. Neurol. **268**, 38–48.
Merzenich, M. M., and Brugge, J. F. (**1973**). ''Representation of the cochlear partition on the superior temporal plane of the macaque monkey,'' Brain Res. **50**, 275–296.
Mitani, A., Shimokouchi, M., Itoh, K., Nomura, S., Kudo, M., and Mizuno, N. (**1985**). ''Morphology and laminar organization of electrophysiologically identified neurons in the primary auditory cortex in the cat,'' J. Comp. Neurol. **235**, 430–447.
Moody, D. B. (**1994**). ''Detection and discrimination of amplitude-modulated signals by macaque monkeys,'' J. Acoust. Soc. Am. **95**, 3499–3510.
Morel, A., Garraghty, P. E., and Kaas, J. H. (**1993**). ''Tonotopic organization, architechtonic fields and connections of auditory cortex in macaque monkeys,'' J. Comp. Neurol. **355**, 437–459.
Muller-Preuss, P., and Mitzdorf, U. (**1984**). ''Functional anatomy of the inferior colliculus and the auditory cortex: current source density analyses of click-evoked potentials,'' Hear. Res. **16**, 133–142.
Nelken, I., Prut, Y., Vaadia, E., and Abeles, M. (**1994**). ''Population responses to multifrequency sounds in the cat auditory cortex: one- and two-parameter families of sounds,'' Hear. Res. **72**, 206–222.
Nicholson, C., and Freeman, J. A. (**1975**). ''Theory of current source density analysis and determination of conductivity tensor for anuran cerebellum,'' J. Neurophysiol. **38**, 356–368.
Ojima, H., Honda, C. N., and Jones, E. G. (**1991**). ''Patterns of axon collateralization of identified supragranular pyramidal neurons in the cat auditory cortex,'' Cerebral Cortex **1**(1), 80–94.
Pandya, D. N., and Rosene, D. L. (**1993**). ''Laminary termination patterns of thalamic, callosal, and association afferents in the primary auditory area of the Rhesus monkey,'' Exp. Neurol. **119**, 220–234.
Pfingst, B. E. (**1993**). ''Comparison of spectral and nonspectral frequency difference limens for human and nonhuman primates,'' J. Acoust. Soc. Am. **93**, 2124–2129.
Phillips, D. P., Hall, S. E., and Hollett, J. L. (**1989**). ''Repetition rate and signal level effects on neuronal responses to brief tone pulses in cat auditory cortex,'' J. Acoust. Soc. Am. **85**, 2537–2549.
Pierce, J. R. (**1991**). ''Periodicity and pitch perception,'' J. Acoust. Soc. Am. **90**, 1889–1893.
Plomp, R. (**1964**). ''The ear as a frequency analyzer,'' J. Acoust. Soc. Am. **36**, 1628–1636.
Plomp, R., and Levelt, W. J. M. (**1964**). ''Tonal consonance and critical bandwidth,'' J. Acoust. Soc. Am. **38**, 548–560.
Plomp, R., and Mimpen, A. M. (**1968**). ''The ear as a frequency analyzer. II,'' J. Acoust. Soc. Am. **43**, 764–767.
Plomp, R., and Steeneken, H. J. M. (**1968**). ''Interference between two simple tones,'' J. Acoust. Soc. Am. **43**, 883–884.
Reser, D. H., Fishman, Y. I., Arezzo, J. C., and Steinschneider, M. (**2000**). ''Binaural interactions in primary auditory cortex of the awake macaque,'' Cereb. Cortex. (in press).
Rosenberg, A. E. (**1965**). ''Effect of masking on the pitch of periodic pulses,'' J. Acoust. Soc. Am. **38**, 747–758.
Rouiller, E. M., deRibaupierre, Y., and de Ribaupierre, F. (**1979**). ''Phase-locked responses to low frequency tones in the medial geniculate body,'' Hear. Res. **1**, 213–226.
Rouiller, E. M., and de Ribaupierre, F. (**1982**). ''Neurons sensitive to narrow ranges of repetitive acoustic transients in the medial geniculate body of the cat,'' Exp. Brain Res. **48**, 323–326.
Rouiller, E. M., Simm, G. M., Villa, A. E. P., de Ribaupierre, Y., and de Ribaupierre, F. (**1991**). ''Auditory cortico-cortical interconnections in the cat: evidence for parallel and hierarchical arrangement of the auditory cortical areas,'' Exp. Brain Res. **86**, 483–505.
Schreiner, C. E., and Urbas, J. V. (**1986**). ''Representation of amplitude modulation in the auditory cortex of the cat. I. The anterior auditory field (AAF),'' Hear. Res. **21**, 227–241.
Schreiner, C. E., and Urbas, J. V. (**1988**). ''Representation of amplitude modulation in the auditory cortex of the cat. II. Comparison between cortical fields,'' Hear. Res. **32**, 49–64.
Schroeder, C. E., Tenke, C. E., Givre, S. J., Arezzo, J. C., and Vaughan, Jr., H. G. (**1990**). ''Laminar analysis of bicuculline-induced epileptiform activity in area 17 of the awake macaque,'' Brain Res. **515**, 326–330.
Schulze, H., and Langner, G. (**1997**). ''Periodicity coding in the primary auditory cortex of the Mongolian gerbil (*Meriones unguiculatus*): two different coding strategies for pitch and rhythm?'' J. Comp. Physiol. A **181**, 651–663.
Shackleton, T. M., and Carlyon, R. P. (**1994**). ''Role of resolved and unresolved harmonics in pitch perception and frequency modulation discrimination,'' J. Acoust. Soc. Am. **95**, 3529–3540.
Srinivasan, R., Russell, D. P., Edelman, G. M., and Tononi, G. (**1999**). ''Increased synchronization of neuromagnetic responses during conscious perception,'' J. Neurosci. **19**(13), 5435–5448.
Steinschneider, M., Arezzo, J., and Vaughan, Jr., H. G. (**1980**). ''Phase-

locked cortical responses to a human speech sound and low-frequency tones in the monkey,'' Brain Res. **198**, 75–84.
Steinschneider, M., Reser, D., Fishman, F., and Arezzo, J. (**1998**). ''Click train encoding in primary auditory cortex of the awake monkey: evidence for two different mechanisms subserving pitch perception,'' J. Acoust. Soc. Am. **104**, 2935–2955.
Steinschneider, M., Schroeder, C. E., Arezzo, J. C., and Vaughan, Jr., H. G. (**1994**). ''Speech-evoked activity in primary auditory cortex: effects of voice onset time,'' Electroencephalogr. Clin. Neurophysiol. **92**, 30–43.
Steinschneider, M., Tenke, C. E., Schroeder, C. E., Javitt, D. C., Simpson, G. V., Arezzo, J. C., and Vaughan, Jr., H. G. (**1992**). ''Cellular generators of the cortical auditory evoked potential initial component,'' Electroencephalogr. Clin. Neurophysiol. **84**, 196–200.
Terhardt, E. (**1968a**). ''Uber akustische rauhigkeit und schwangkungsstarke,'' Acustica **20**, 215–224.
Terhardt, E. (**1968b**). ''Uber die durch amplitudenmodulierte sinustone hervorgerufene horempfindung,'' Acustica **20**, 210–214.
Terhardt, E. (**1974a**). ''On the perception of periodic sound fluctuations (roughness),'' Acustica **30**(3), 201–213.
Terhardt, E. (**1974b**). ''Pitch, consonance, and harmony,'' J. Acoust. Soc. Am. **55**, 1061–1069.
Terhardt, E. (**1977**). ''The two-component theory of musical consonance,'' in *Psychophysics and Physiology of Hearing* (Academic, New York), pp. 381–390.
Terhardt, E. (**1978**). ''Psychoacoustic evaluation of musical sounds,'' Percept. Psychophys. **23**(6), 483–492.
Vaughan, Jr., H. G., and Arezzo, J. C. (**1988**). ''The neural basis of event-related potentials,'' in *Human-Event Related Potentials, EEG Handbook (Revised Series, Vol. 3)*, edited by T. W. Picton (Elsevier, Amsterdam), pp. 45–96.
Wallace, M. N., Kitzes, L. M., and Jones, E. G. (**1991a**). ''Chemoarchitectonic organization of the cat primary auditory cortex,'' Exp. Brain Res. **86**, 518–526.
Wallace, M. N., Kitzes, L. M., and Jones, E. G. (**1991b**). ''Intrinsic inter- and intralaminar connections and their relationship to the tonotopic map in cat primary auditory cortex,'' Exp. Brain Res. **86**, 527–544.
Zurita, P., Villa, A. E. P., de Ribaupierre, Y., de Ribaupierre, F., and Rouiller, E. M. (**1994**). ''Changes of single unit activity in the cat's auditory thalamus and cortex associated to different anesthetic conditions,'' Neurosci. Res. **19**, 303–316.
Zwicker, E., Flottorp, G., and Stevens, S. S. (**1957**). ''Critical bandwidth in loudness summation,'' J. Acoust. Soc. Am. **29**, 548–557.

Complex tone processing in primary auditory cortex of the awake monkey. II. Pitch versus critical band representation

Yonatan I. Fishman[a)]
Department of Neuroscience, Albert Einstein College of Medicine, Rose F. Kennedy Center, Bronx, New York 10461

David H. Reser
Department of Neuroscience, Albert Einstein College of Medicine, Bronx, New York 10461

Joseph C. Arezzo and Mitchell Steinschneider
Departments of Neurology and Neuroscience, Albert Einstein College of Medicine, Bronx, New York 10461

(Received 20 September 1999; accepted for publication 20 April 2000)

Noninvasive neurophysiological studies in humans support the existence of an orthogonal spatial representation of pure tone frequency and complex tone pitch in auditory cortex [Langner *et al.*, J. Comp. Physiol. A **181**, 665–676 (1997)]. However, since this topographic organization is based on neuromagnetic responses evoked by wideband harmonic complexes (HCs) of variable fundamental frequency (f_0), and thus interharmonic frequency separation (ΔF), critical band filtering effects due to differential resolvability of harmonics may have contributed to shaping these responses. To test this hypothesis, the present study examined responses evoked by three-component HCs of variable f_0 in primary auditory cortex (A1) of the awake monkey. The center frequency of the HCs was fixed at the best frequency (BF) of the cortical site. Auditory evoked potential (AEP), multiunit activity, and current source density techniques were used to evaluate A1 responses as a function of f_0 ($=\Delta F$). Generally, amplitudes of nearly all response components increased with f_0, such that maximal responses were evoked by HCs comprised of low-order resolved harmonics. Statistically significant increases in response amplitude typically occurred at ΔFs between 10% and 20% of center frequency, suggestive of critical bandlike behavior. Complex tone response amplitudes also reflected nonlinear summation in that they could not be predicted by the pure tone frequency sensitivity curves of the cortical sites. A mechanism accounting for the observed results is proposed which involves mutual lateral inhibitory interactions between responses evoked by stimulus components lying within the same critical band. As intracortical AEP components likely to be propagated to the scalp were also strongly modulated by ΔF, these findings indicate that noninvasive recordings of responses to complex sounds may require a consideration of critical band effects in their interpretation. © *2000 Acoustical Society of America.* [S0001-4966(00)05407-2]

PACS numbers: 43.64.Qh, 43.64.Ri, 43.66.Hg [LHC]

INTRODUCTION

Harmonic complexes (HCs) comprise an important class of natural sounds commonly occurring in human speech, animal vocalizations, and music. A distinctive feature of such signals is that their frequency components are harmonics of a common fundamental frequency (f_0). When heard in isolation, each of these harmonics has a pitch related to its frequency. HCs, however, are usually perceived not as a collection of individual pitches, but as a single auditory object with a global pitch corresponding to the f_0. Importantly, this global pitch persists even when spectral energy at the f_0 is completely absent. This perceptual phenomenon, known as ''virtual pitch,'' suggests that the fundamental pitch of complex sounds is ultimately derived via a synthetic operation of the auditory system (Terhardt, 1974; Hartmann, 1996). In general, the global pitch of a complex tone and its virtual pitch are considered synonymous (Terhardt, 1974, 1978). Accordingly, virtual pitch has served as a foundation for theoretical models describing how the auditory system derives the pitch of complex sounds. Modern psychoacoustic theories postulate the existence of two complementary mechanisms of virtual pitch extraction (Houtsma and Smurzynski, 1990; Carlyon and Shackleton, 1994; Shackleton and Carlyon, 1994). The first essentially involves a pattern-recognition of resolved spectral components, i.e., whose frequency separation (ΔF) exceeds the width of an auditory filter, the so-called critical bandwidth (CBW). The perceived pitch is derived by matching the resolved spectral pattern to a ''harmonic template'' corresponding to the f_0 of which the components are integer multiples (e.g., Goldstein, 1973; Terhardt, 1974). The second mechanism relies on a temporal representation of the f_0 whereby pitch is extracted from the common temporal pattern of discharges (interspike intervals) corresponding to the period of the f_0 across the array of active frequency channels (e.g., Moore, 1989; Meddis and Hewitt, 1991; Meddis and O'Mard, 1997). Virtual pitch represents the product of an important auditory organizational process whereby harmonically related components of sound mixtures are fused together to form a single perceptual entity (Bregman, 1990;

[a)]Electronic mail: yfishman@aecom.yu.edu

Hartmann, 1996). Its biological importance is suggested by the demonstration of virtual pitch perception in multiple vertebrate species, including cats, birds, and monkeys (Heffner and Whitfield, 1976; Cynx and Shapiro, 1986; Tomlinson and Schwarz, 1988).

Lesion studies in animals and humans implicate primary auditory cortex (A1) and surrounding auditory cortical areas in encoding the pitch of complex sounds (Whitfield, 1980; Zatorre, 1988). Given this involvement, the question remains specifically how the pitch of complex sounds is represented at the cortical level. Regardless of whether pitch is based on spectral or temporal extraction methods, it is generally thought that the perceived pitch is ultimately represented at a relatively advanced level in the auditory system by a topographic map of stimulus f_0 (Licklider, 1951, 1956; Schreiner and Langner, 1988; Langner, 1997; Langner *et al.*, 1997; Schulze and Langner, 1997). Several studies in humans using magnetoencephalography (MEG) examined whether pure tones and complex tones of similar pitch are represented at the same topographic locations in A1 (Pantev *et al.*, 1989, 1996). This hypothesis was tested by comparing the locations of the derived equivalent current dipole (ECD) corresponding to the M100 component of the auditory evoked magnetic field (AEMF) elicited by a 250-Hz pure tone and by a complex tone composed of the third, fourth, and fifth harmonics of a missing 250-Hz f_0. The location of the M100 ECD evoked by the complex tone was similar to that evoked by the 250-Hz pure tone, whereas it was markedly different from that of the ECD evoked by a pure tone corresponding to a harmonic of the complex tone. These findings suggested that A1 organization reflects the perceived pitch of complex sounds rather than their spectral content. In contrast, single-unit and multi-unit investigations in monkeys provided evidence against corepresentation of complex tone and pure tone pitch along the tonotopic axis in A1, and instead supported the classical cochleotopic organization of A1 (Schwarz and Tomlinson, 1990; Fishman *et al.*, 1998). It is unclear whether the discrepancy between human and monkey findings is due to species differences, spatial resolution limitations of noninvasive recordings, or other technical features.

It is possible, however, that pitch is represented along some other spatial dimension in A1. Human MEG studies by Langner *et al.* (1997) suggest that the pitch of complex sounds may be spatially represented orthogonal to the tonotopic gradient (i.e., along the iso-frequency axis) in A1. These studies examined changes in the ECD locations of several components of the AEMF evoked by pure tones and by HCs with f_0s ranging from 50 to 400 Hz. The HCs were filtered between 400 (in some cases 800 Hz) and 5000 Hz, so that their overall spectral envelopes remained largely the same despite changes in f_0. While the ECD corresponding to the M100 component moved from posterior/superior to progressively anterior/inferior locations with increasing pure tone frequency, that evoked by the HCs moved roughly perpendicularly to the pure tone ECD trajectory with increasing f_0. Perpendicular pure tone and complex tone gradients were also reported for the ECD corresponding to the M60 component. These findings were interpreted as reflecting an orthogonal spatial representation of pure tone frequency and complex tone pitch in auditory cortex, i.e., complex sounds activate different regions along the iso-frequency axis depending upon their f_0. Importantly, unlike the organization proposed by Pantev *et al.* (1989, 1996), according to which pure tone pitch and complex tone pitch representations are colocalized, a consequence of the orthogonal model is that pure tones and complex tones *of the same pitch* are represented in *different* locations in A1.

MEG and other noninvasive techniques suffer from limitations that are particularly relevant to mapping of cortical representations. Specifically, components of the scalp-recorded auditory evoked potential (AEP) and AEMF neither reflect unitary cerebral processes nor uniquely determine their underlying generators (Wood and Wolpaw, 1982). Noninvasive and intracranial recordings in humans indicate that middle- (10–80 ms poststimulus onset) and long- ($>$80 ms) latency components of the scalp-recorded AEP and AEMF reflect contributions from multiple temporally overlapping but spatially distinct temporal lobe generators (Wolpaw and Penry, 1975; Wood and Wolpaw, 1982; Naatanen and Picton, 1987; Liegeois-Chauvel *et al.*, 1994; Halgren *et al.*, 1998; Steinschneider *et al.*, 1999; Howard *et al.*, 2000). To complicate matters further, intracranial recordings in monkeys support the existence of several auditory areas in the superior temporal gyrus that exhibit tonotopic organizations, some in mirror-image orientations (Morel *et al.*, 1993; Kosaki *et al.*, 1997; Kaas and Hackett, 1998). The single-dipole model of auditory cortical activation assumed in noninvasive studies is therefore highly problematic (see Lutkenhoner and Steinstrater, 1998; Schreiner, 1998) and calls into question whether the observed pattern genuinely reflects an underlying orthogonal organization of pure tone frequency and complex tone pitch. In view of these considerations, intracranial recordings in appropriate animal models can facilitate the validation of functional topographic maps proposed on the basis of noninvasive recordings.

The results of Langner *et al.* (1997) may be complicated also by the possibility that they reflect not complex tone pitch *per se*, but rather the result of critical band (CB) filtering. The concept of an auditory ''filter'' or CB has been invoked to explain a wide range of perceptual phenomena involving complex sounds. For example, tones and noise are effective in masking tonal signals only when their spectra lie within the same CB as the signal (Greenwood, 1961). Moreover, the perceived loudness and the ability to ''hear out'' individual components of complex sounds increases once the ΔF between components exceeds a critical bandwidth (CBW) (Zwicker *et al.*, 1957; Plomp, 1964; Plomp and Mimpen, 1968; Moore and Ohgushi, 1993). Virtual pitch is also most salient for HCs composed of low-order resolved harmonics, i.e., whose ΔF exceeds a CBW (Ritsma, 1962, 1967; Plomp, 1967; Fastl and Stoll, 1979; Houtsma and Smurzynski, 1990). Physiological correlates of CBW have been described in single-unit studies of A1 in cats and in several studies examining short- and middle-latency components of the surface-recorded AEP in humans. Specifically, Ehret and Schreiner (1997) reported an increase in tone-evoked responses of single A1 neurons once the width of a

noise masker was narrowed below the CBW, as psychophysically defined by other investigators using similar methods. Zerlin (1986) demonstrated an abrupt increase in the amplitude of wave V of the brainstem AEP evoked by two-tone complexes once the ΔF between the tones exceeded the CBW. Similarly, Burrows and Barry (1990) reported augmentation of the Na component of the middle-latency AEP once the ΔF between components of a two-tone complex exceeded the CBW. In combination, these findings suggest that a neural representation of CBW is present in A1, which can potentially be detected at the scalp by noninvasive recordings. Since the complex stimuli used by Langner *et al.* (1997) were wideband HCs filtered between 400 and 5000 Hz, changes in f_0 (and therefore interharmonic ΔF) would not only change the overall pitch, but would lead to changes in the relative resolvability of harmonics, depending on the CBW at their frequencies. For example, a harmonic centered at 2000 Hz would be resolved when the f_0 of the complex tone is 400 Hz, whereas it would be unresolved when the f_0 is 100 Hz. If auditory cortical responses are enhanced in tonotopic locations corresponding to spectrally resolved stimulus components, changing the relative resolvability of the components by varying stimulus f_0 could also lead to changes in the location of the ECD. Thus, it is possible that CB effects contributed to shaping the MEG responses recorded by Langner *et al.* (1997).

Given these considerations, the aim of the present study is to examine, using invasive recording techniques in awake macaques, whether neuronal ensemble responses in A1 support an orthogonal complex tone pitch representation, or rather reflect a representation of CBW. The present paper represents a continuation of the investigations described in the companion paper, in which we examined periodic aspects of responses in A1 to three-component HCs of varying f_0 as they relate to the encoding of roughness (Fishman *et al.*, 2000). Here we describe in the same animals and cortical sites changes in the amplitudes of transient response components evoked by HCs as a function of f_0. Old World monkeys are suitable animal models for investigating both pitch and CBW representation in A1, since they not only possess a similar primary auditory cortical anatomy to that of humans (Galaburda and Sanides, 1980; Galaburda and Pandya, 1983), but are capable of perceiving virtual pitch (Tomlinson and Schwarz, 1988), and display psychophysical CB curves that are nearly identical to those of humans (Gourevitch, 1970). The range of f_0s presented (25–4000 Hz) encompasses the existence region of virtual pitch (Ritsma, 1962; Plomp, 1967). These stimuli are therefore appropriate for investigating both pitch and CBW representations. Finally, the neuronal ensemble techniques utilized in the present study offer the advantage of bridging noninvasive recording techniques measuring synchronized activity of neuronal populations with more direct physiological approaches.

The specific pattern of neuronal ensemble responses to HCs of varying f_0 can provide a basis for distinguishing between pitch and CBW representation. An orthogonal organization of pure tone frequency and complex tone pitch in A1 implies that different sites within A1 of similar pure tone best frequency (BF) would display different ''best f_0s'' (i.e., stimulus f_0s associated with the largest responses), irrespective of the resolvability of the harmonics. Thus, given a sample of sites distributed along the tonotopic gradient, there should be no statistical correlation between best f_0 and BF, since sites with the same BF could have different best f_0s, and sites with different BFs could have the same best f_0. Alternatively, a representation of CBW would be supported if, on average, the smallest and largest responses are evoked by HCs composed of unresolved ($\Delta F <$ CBW) and resolved ($\Delta F >$ CBW) harmonics, respectively. For component frequencies above 500 Hz, CBW corresponds to 10%–20% of frequency (Zwicker *et al.*, 1957; Moore and Glasberg, 1983; Moore and Ohgushi, 1993; Zera *et al.*, 1993).

I. METHODS

Neuronal ensemble responses were recorded in A1 of three adult male monkeys (*Macaca fascicularis*). All procedures were approved by our institutional Animal Care and Use Committee. Surgical techniques, stimulus generation and delivery, recordings of AEPs, multiunit activity (MUA), and current source density (CSD), and histological procedures are identical to those described in the preceding companion paper (Fishman *et al.*, 2000). As in the companion study, linear array multi-contact electrodes (14 contacts; 150-μm intercontact spacing) were used to simultaneously record neuronal ensemble activity at multiple depths across the laminar extent of A1. The BF of the cortical site was defined as the pure tone frequency eliciting the largest peak amplitude MUA within lower lamina III (LLIII) during the first 50 ms following stimulus onset. This period includes the time of initial activation of thalamorecipient zone cells in lamina IV (LIV) and LLIII (Steinschneider *et al.*, 1992, 1994). Response amplitude versus pure tone frequency functions, or frequency response functions (FRFs), were generated for all cortical sites examined. Pure tones used to generate the FRFs ranged from 200 Hz to 15 kHz and were typically separated by 100 Hz below 1 kHz, 200–300 Hz below 5 kHz, and 500 Hz below 15 kHz. As in the companion paper, HCs were composed of three equal-amplitude consecutive harmonics of f_0s ranging from 25 to 4000 Hz. Center frequencies (f_cs) of the complex tones corresponded to the BF of the cortical site. All harmonics were combined in sine phase. The highest f_0 presented at a given cortical site was that for which the BF corresponded to the second harmonic. Thus, with the exception of the case in which the BF occupied the second harmonic position, all complex stimuli had ''missing'' f_0s. Complex tones were 450 ms in duration, with rise and fall times of 5 ms, and were presented at interstimulus intervals of 992 ms. All stimuli were presented at 60 dB SPL via headphone to the ear contralateral to the recorded hemisphere. The frequency response of the headphone was flattened (± 3 dB) by a graphic equalizer (*Rane, Inc.*) The complex tone stimulus set invariably included f_0s of 25, 50, and 100 Hz, one f_0 between 50 and 100 Hz, at least one f_0 between 100 and 200 Hz, and at least one f_0 between 200 and 400 Hz. Since the complex tones were

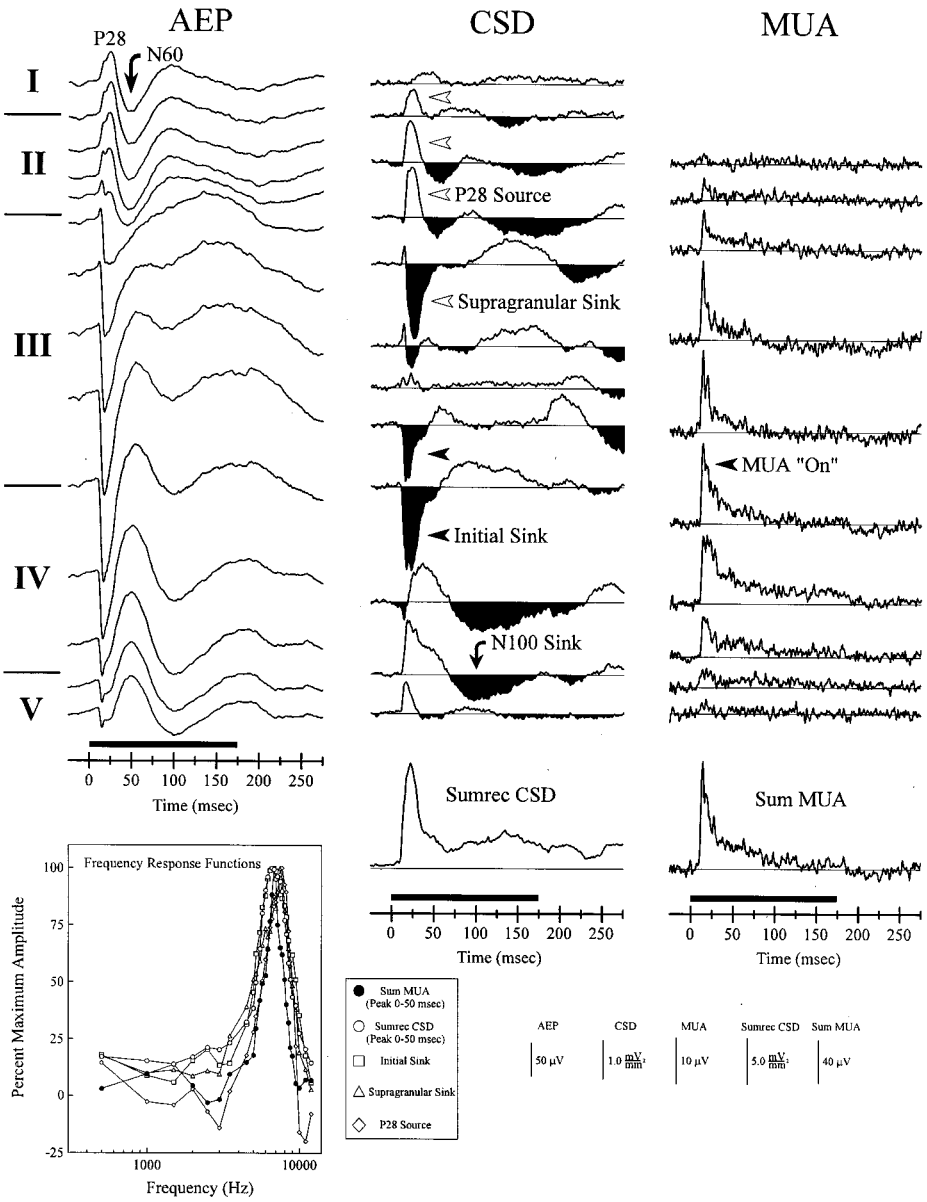

FIG. 1. Representative AEP, CSD, and MUA laminar response profiles evoked by a 60 dB SPL tone at the BF (7000 Hz). Arrows denote major response components examined in the study. Approximate laminar boundaries are shown at the far left of the figure. Black bars directly above the timelines represent the duration of the stimulus. Frequency response functions (FRFs) of the site, depicted at the bottom left, illustrate the correspondence in spectral sensitivity among the response components examined. Symbols representing individual components are identified in the legend. Summed rectified CSD (Sumrec CSD) and MUA summed across lamina III and IV channels (Sum MUA) representing more global measures of cortical activation are also examined in the study.

constructed from consecutive harmonics, the f_0 was always a subharmonic of the f_c and corresponded to the ΔF between components.

Peak amplitudes of AEP, MUA, and CSD response components evoked by the HCs were examined as a function of f_0, with the f_c of the HC fixed at the BF. The relationship between response amplitude and f_0 defined the complex tone response function (CTRF) of each response component at each cortical site. In order to combine results across electrode penetrations, CTRFs were normalized by expressing f_0 as a percentage of the f_c. Both parametric (analysis of variance) and nonparametric (chi-squared) statistical tests were performed to extract regularities in the CTRF across cortical sites.

II. RESULTS

Results are based on neuronal ensemble recordings from 29 orthogonal multi-contact electrode penetrations into A1. These penetrations are the same as those examined in the companion paper (Fishman *et al.*, 2000).

A. Basic A1 laminar response profiles

Figure 1 depicts a representative A1 BF tone response profile to illustrate the various response components analyzed in the study. AEPs are shown in the left column, derived CSD in the middle column, and MUA in the right column. Each waveform represents activity recorded simultaneously by the multi-contact electrode from the cortical tissue at 150-μm intervals. Approximate laminar boundaries

are denoted on the far-left of the figure. Response components examined in the study are indicated by arrows (white arrows, supragranular; black arrows, thalamorecipient zone and infragranular). The AEP elicited by the BF tone (in this case, 7.0 kHz) is characterized by a superficial positivity that peaks at about 28 ms (P28) followed by a negativity (N60), both of which invert in polarity across the lamina II/III border. These components are of interest since they may be homologous to the human surface-recorded AEP P50 and N100 components (see Arezzo *et al.*, 1986; Vaughan and Arezzo, 1988; Steinschneider *et al.*, 1994), the magnetic counterparts of which were examined by Langner *et al.* (1997) and reported to vary with stimulus f_0.

The derived CSD represents the laminar pattern of current sources (above-baseline deflections) and sinks (below-baseline deflections) giving rise to the AEP. BF tones trigger a stereotypical sequence of synaptic events in A1. The earliest current sinks (''Initial Sink'') occur within the thalamorecipient zone (LIV and LLIII: Steinschneider *et al.*, 1992; mean peak latency: 17.3 ms, standard deviation: 5.3 ms). Early sources in mid- and upper lamina III (initial positive deflections) partially balance the thalamorecipient zone sinks to form a current dipole configuration indicative of pyramidal cell activation. Thalamorecipient zone sinks are coincident with increases in MUA, indicating that they represent current flow associated with excitatory synaptic events. Early current sinks are followed by slightly later, more superficial sinks located in upper lamina III (''Supragranular Sink''; mean peak latency: 28.5 ms, standard deviation: 9.3 ms), which are balanced by current sources located in lamina II (''P28 Source''; mean peak latency: 28.2 ms, standard deviation: 9.3 ms). This sink-source configuration is consistent with polysynaptic activation of supragranular pyramidal cell elements. Lamina II current sources represent the predominant generators of the superficially recorded AEP P28 component. Since these sources largely reflect passive current return for supragranular sinks, they serve as potentially useful measures of polysynaptic cortical cell activation.

To provide a more global measure of cortical activation, the total stimulus-evoked net current flow during the first 50 ms was evaluated by full-wave rectifying and summing the CSD across channels (''Sumrec CSD''). Full-wave rectification and integration of the CSD profile results in the loss of information regarding both the depth and direction of stimulus-evoked current flow. Consequently, the Sumrec CSD measure incorporates both active and passive sinks and sources. Nonetheless, it is useful for comparing total transmembrane current flow across stimulus conditions and electrode penetrations.

MUA was evaluated by summing across lamina III and IV channels (''Sum MUA''), as these responses reflect activity associated with both the initial cortical sink located in LLIII and LIV, and the later sink located in more superficial regions of lamina III. Measures included peak amplitude of summed MUA during the first 50 ms (''MUA 'On'''') and area under summed MUA (''MUA Area'') from stimulus onset until the second zero-crossing of the supragranular sink. The rationale for this integration interval is based upon the observation (Steinschneider *et al.*, 1998) that early bursts of MUA following the initial ''On'' response coincide with the peak of the supragranular sink and therefore likely reflect intrinsically generated cortical activity. Area under MUA following this interval was not included in the analysis in order to avoid the problematic contribution of responses phase-locked to the waveform envelope of the lower f_0 stimuli. Thus, in combination, these MUA measures provide information regarding initial cortical activation as well as slightly later, presumably supragranularly driven activity. Representative FRFs of response components examined in the study are depicted in the lower left of the figure. Note the close correspondence in frequency sensitivity among components.

B. Modulation of response amplitudes by changes in f_0

Figure 2(a) depicts a representative example of responses evoked by HCs of varying f_0 (indicated on the far left of the figure). The f_c of the three-tone complex was set at 1000 Hz, the BF of this location. Summed middle-laminae MUA and corresponding summed rectified CSD waveforms are shown in the left and middle columns, respectively. Activity phase-locked to the f_0 is evident in the sustained portion of the responses evoked by the lower f_0 stimuli. The most noteworthy feature of this figure is the general increase in MUA and Sumrec CSD response amplitudes during the first 50 ms poststimulus onset with increases in stimulus f_0. In particular, the highest MUA and Sumrec CSD amplitudes are associated with f_0s ($=\Delta F$s) exceeding 125 Hz, in agreement with the traditional psychophysical value of CBW at 1000 Hz (Zwicker *et al.*, 1957). Superficially recorded intracortical AEPs and full CSD profiles evoked by the 500- and 100-Hz f_0 stimuli are shown superimposed in the right-hand column (thick and thin lines, respectively) to facilitate comparison between the largest and smallest amplitude responses. Approximate laminar boundaries are shown on the left of the CSD profiles. Relevant CSD components are indicated by arrows. The marked amplitude differences between corresponding CSD components across the entire laminar profile indicate that the effects of f_0 observed for the Sumrec CSD derive from the contribution of both supragranular and thalamorecipient zone synaptic events. Effects of stimulus f_0 are also manifested by dramatic differences between AEP P28 and N60 component amplitudes for these two stimuli, with the 500-Hz f_0 stimulus evoking P28 and N60 components that are more than twice the amplitude of those evoked by the 100-Hz f_0 stimulus.

These results are graphically represented in Fig. 2(b), showing complex tone response amplitudes as a function of the percent ΔF between harmonics (f_c=BF=1000 Hz). Note the general agreement among response components. The vertical dashed lines mark ΔFs corresponding to the CBW of Zwicker *et al.* (1957) (about 16% of f_c) and the equivalent rectangular auditory filter bandwidth (ERB) derived from notched-noise masking experiments (Moore and Glasberg, 1983; about 13% of f_c). The largest and smallest responses are thus associated with supra-CBW and sub-CBW harmonic separations, respectively.

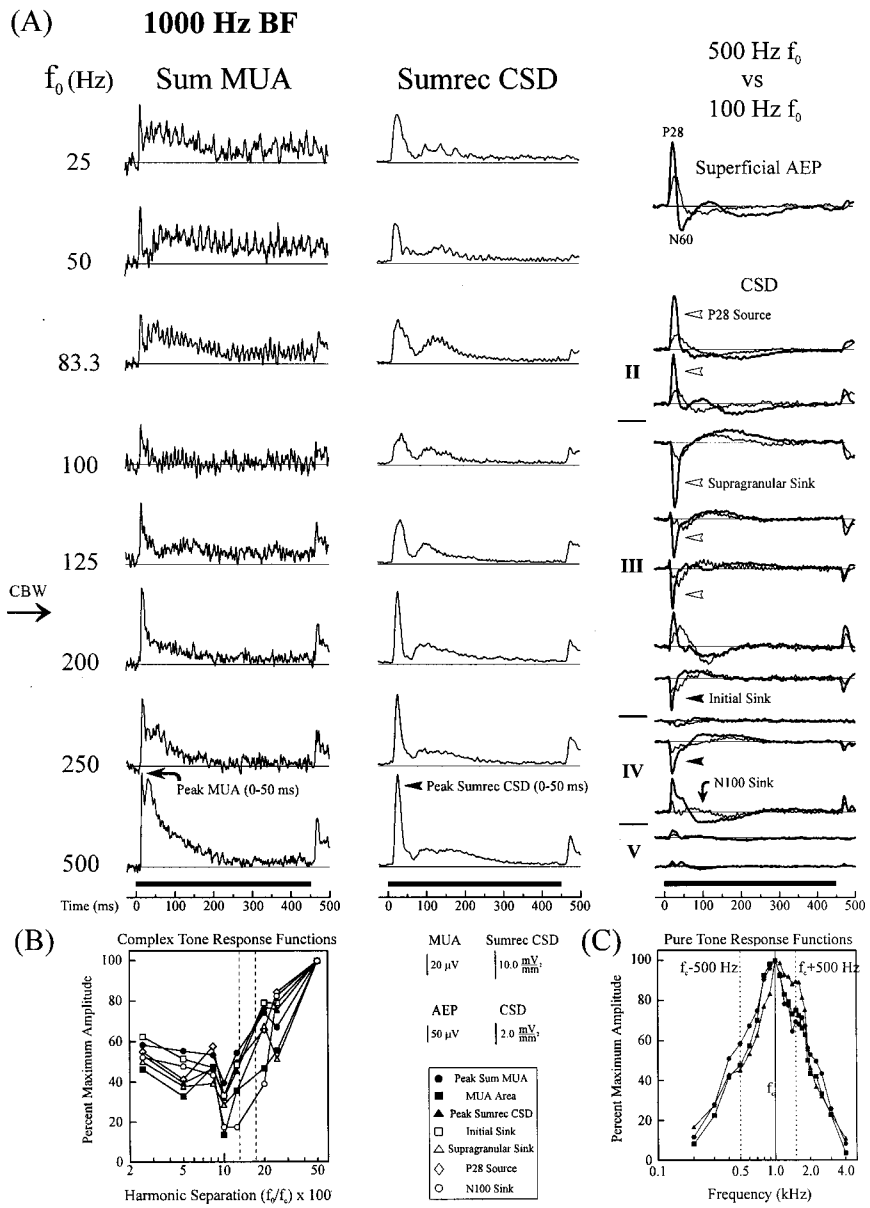

FIG. 2. (a) Illustrative examples of harmonic complex tone-evoked responses recorded from a site whose BF is 1000 Hz. The f_c (middle harmonic) was situated at the BF while the f_0 (denoted on the far left of the figure) was varied. Waveforms corresponding to summed MUA and summed rectified CSD are depicted in the left-hand and middle columns, respectively. Superficial intracortical AEPs and CSD profiles evoked by the 100 and 500 Hz f_0 complexes are shown superimposed in the right-hand column to facilitate comparison between responses evoked by sub- and supra-CBW complex stimuli. Approximate laminar boundaries are shown next to the CSD profiles. Major response components are indicated by black and white arrows. Note the multi-laminar extent of the differences between the two responses. (b) Complex tone response amplitude as a function of percent harmonic separation. Symbols representing individual response components are identified in the legend. The right and left vertical dashed lines denote harmonic separations corresponding to the classical CBW of Zwicker *et al.* (1957) and the equivalent rectangular bandwidth of the auditory filter of Moore and Glasberg (1983), respectively, at 1000 Hz. Response amplitudes are maximal for supra-CBW harmonic separations. (c) FRFs of the cortical site. The general decrease in pure tone response amplitudes with increasing spectral separation from the BF indicates that complex tone responses cannot be predicted on the basis of a simple summation of pure tone responses.

The general increase in response amplitudes with harmonic separation cannot be predicted on the basis of the site's pure tone FRFs. This feature is illustrated in Fig. 2(c), which depicts FRFs based on peak summed MUA, MUA area, and peak Sumrec CSD. The f_c of the HCs is indicated by the solid vertical line at 1000 Hz. Side-band frequencies of the 500-Hz f_0 stimulus (i.e., $f_c \pm 500$ Hz) are denoted by the dotted vertical lines. The falloff of response amplitudes with spectral distance from the f_c and the absence of peaks at the ± 500 Hz side-bands preclude an explanation for the augmented responses to the 500-Hz f_0 HC based on a simple summation of responses to individual frequency components of the complex tones.

Figure 3(a) illustrates similar results obtained from a higher BF location (6000 Hz) in A1. Phase-locked activity is again evident in the sustained portion of the responses evoked by the lowest f_0 stimuli. In this site, phase-locking is largely restricted to a single electrode channel located in LLIII, so oscillatory activity is diluted as a result of integrating middle laminae MUA responses. As in Fig. 2, the largest

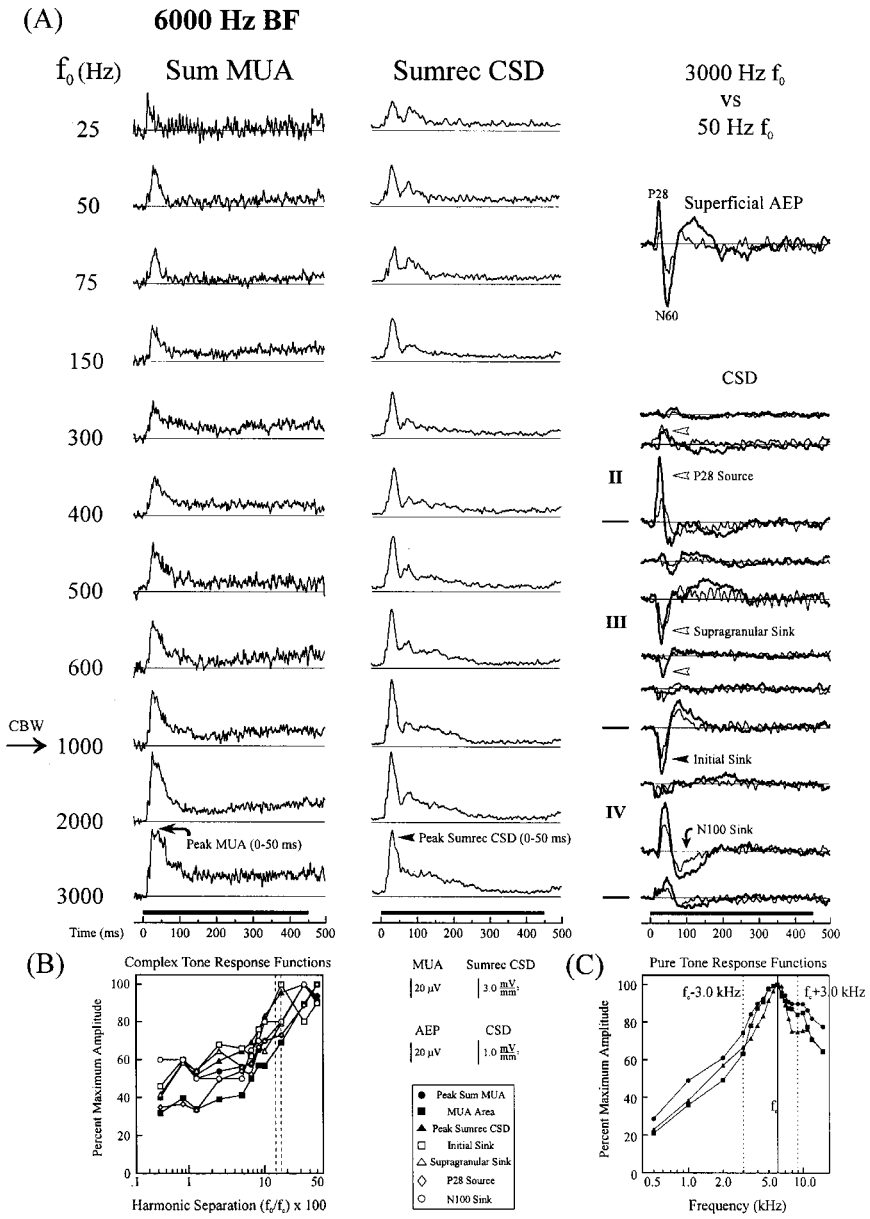

FIG. 3. (a) Harmonic complex tone-evoked responses recorded from a site whose BF is 6000 Hz. Same conventions as in Fig. 2. Intracortical superficial AEPs and CSD profiles evoked by the 50- and 3000-Hz f_0 stimuli are shown superimposed in the right-hand column, and again show the multi-laminar extent of differences between sub- and supra- CBW stimuli. (b) Complex tone response amplitude as a function of percent harmonic separation. The right and left vertical dashed lines denote harmonic separations corresponding to the classical CBW of Zwicker *et al.* (1957) and the equivalent rectangular bandwidth of the auditory filter of Moore and Glasberg (1983), respectively, at 6000 Hz. Response amplitudes are maximal for supra-CBW harmonic separations. (c) The FRFs of the cortical site. The general decrease in pure tone response amplitudes with increasing spectral separation from the BF indicates that complex tone responses cannot be predicted on the basis on a simple summation of pure tone responses.

and smallest responses are evoked by HCs with supra-CBW and sub-CBW f_0s, respectively. In this case, however, the general increase in complex tone response amplitudes is more gradual than for the site shown in Fig. 2. Superficial intracortical AEPs and full CSD profiles evoked by the 3000- and 50-Hz f_0 complexes are shown superimposed in the right column to facilitate comparison between responses elicited by these supra- and sub-CBW stimuli. There is a pronounced difference in amplitude between P28 and N60 components of the AEP as well as between CSD components located in both supragranular and thalamorecipient zone laminae. These results are graphically illustrated by the CTRFs shown in Fig. 3(b). Similarly to the results obtained for the lower BF site depicted in Fig. 2, there is a good agreement among response components, with the largest and smallest responses evoked by HCs with supra- and sub-CBW ΔFs, respectively. Furthermore, the general increase in complex tone response amplitude with ΔF cannot be predicted by the FRFs of the site [Fig. 3(c)], and again demonstrate the nonlinear nature of the complex tone responses. Specifically, since pure tone response amplitudes decrease with increasing spectral distance from the f_c, the enhanced responses to the higher f_0 HCs cannot be based on a simple summation of responses to the individual frequency components of the complex tones.

Figure 4 represents results pooled across animals and

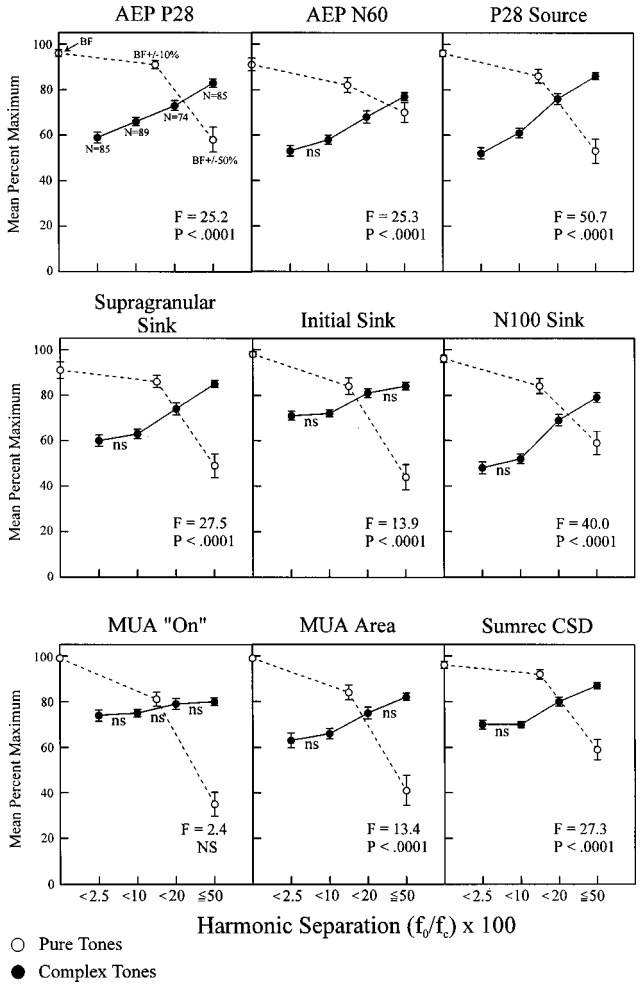

FIG. 4. Results pooled across animals and electrode penetrations for each of the response components examined in the study. Mean percent maximum amplitude of responses to complex tones (black symbols) is shown as a function of the percent separation between the complex tone harmonics, denoted by mutually exclusive categories on the *x* axis. Error bars represent SEM. Mean amplitudes of pure tone responses (white symbols) at the BF and at two spectral distances (±10% and ±50%) away from the BF are included to illustrate the nonlinear nature of the complex tone responses. ''N'' below each data point refers to the number of responses contributing to each mean value. ANOVA *F* and associated probability values are included in the bottom right of each graph. Complex tone response amplitudes tend to increase with increasing harmonic separation (and hence frequency separation of the side bands from the BF), whereas pure tone response amplitudes tend to diminish with increasing frequency separation from the BF. Nonsignificant ($p>0.05$) differences between means, as determined by *post hoc* analyses (Fisher LSD method), are indicated by ''ns.''

cortical sites for each of the response components examined. The graphs show mean percent maximum amplitudes as a function of the percent frequency separation between harmonics. Error bars indicate SEM. Complex tone responses are represented by black symbols. With the exception of the peak amplitude of the MUA ''On'' response, all response components exhibit general increases in amplitude with ΔF (by analysis of variance, $p<0.0001$; associated *F* values are shown in the bottom right corner of each graph). While not statistically significant, the MUA ''On'' response shows a similar increasing trend. Nonsignificant differences between means ($p>0.05$), as determined by *post hoc* analyses (Fisher LSD test), are indicated by ''ns.'' Most of the response components (AEP N60, supragranular sink, initial sink, N100 sink, MUA area, sumrec CSD) exhibit a pattern characterized by a ''plateau'' (i.e., nonsignificant differences in amplitude) for ΔFs below 10% and the first significant in-

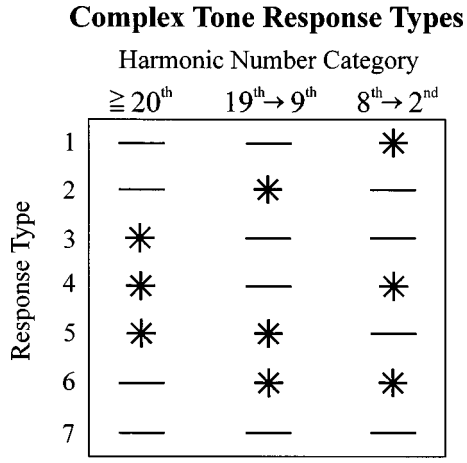

FIG. 5. Classification of complex tone response types identified in the study. Harmonic number categories refer to the harmonic number of the BF ($=f_c$) at which peaks in the CTRFs occurred (asterisks). Note that type 4, 5, and 6 responses were characterized by more than one peak, whereas type 7 responses contained no maxima.

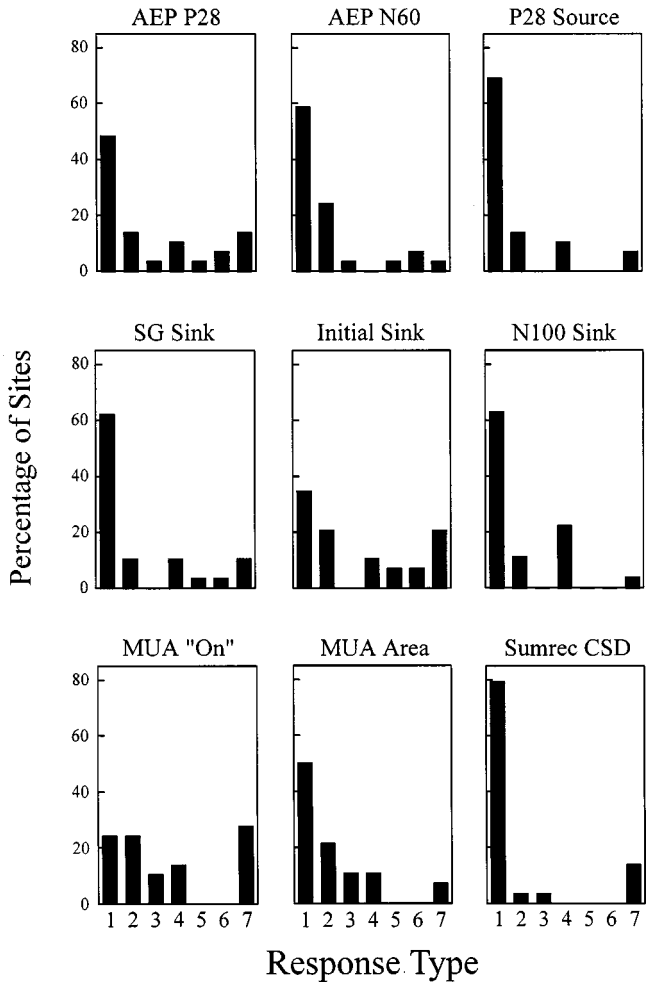

FIG. 6. Distributions of response types for each of the response components examined in the study. With the exception of MUA ''On,'' type 1 responses predominate.

creases in amplitude at ΔFs between 10% and 20%, suggestive of critical band-like behavior.

In order to examine whether the patterns observed for complex tone responses were due to general characteristics of the pure tone FRFs, mean pure tone response amplitudes were calculated at two different frequency separations away from the BF, 10% and 50%. Thus, for instance, in the case of a 5000-Hz BF site, responses to pure tones at BF+10% =5500 Hz and BF−10%=4500 Hz were averaged to yield a mean response amplitude corresponding to tones 10% away from the BF, while responses at BF+50%=7500 Hz and BF−50%=2500 Hz were averaged to yield a mean response amplitude corresponding to tones 50% away from the BF. Pure tone response amplitudes (white symbols) decrease with increasing ΔF from the BF, as would be expected for a roughly Gaussian-shaped FRF. Increases in f_0 entail increases in the ΔF between the BF and flanking harmonics. Consequently, if changes in complex tone response amplitudes with f_0 simply reflect pure tone tuning characteristics of the cortical sites, complex tone response amplitudes should, on average, decrease with ΔF. However, the opposite is the case. Strikingly, while pure tone response amplitudes generally decrease rapidly for frequencies separated from the BF by more than 10%, complex tone response amplitudes (for the majority of the response components) increase significantly when the harmonic sidebands are separated from the BF by more than 10%. Thus, complex tone responses exhibit nonlinear behavior in that they cannot be predicted on the basis of a simple summation of their constituent pure tone responses.

C. Complex tone response types

The general increase in response amplitudes with harmonic separation depicted in Fig. 4 represents the average behavior of response components across sites. However, a closer examination of individual CTRFs reveals that several different complex tone response patterns contribute to the average trend. The CTRFs were assigned to categories initially suggested by visual inspection of the data. Classification was based upon the harmonic number of the BF at which a peak occurred in the CTRF. A peak was defined as the ΔF associated with the largest amplitude response of all the complex tones presented in a given electrode penetration. In order to count as a peak, we used the criterion that the response amplitude at a given ΔF had to be at least 20% greater than the mean amplitude of the responses to all the complex tones presented. This is a conservative criterion, since repeated presentations of identical pure tone and complex tone stimuli in the present study yielded cortical response averages typically varying in amplitude by less than 10%. Similarly, a 20% elevation in spike rate was the criterion used by Ehret and Merzenich (1988) to define physiological CBWs in their studies of the inferior colliculus (IC). ΔFs corresponding to peaks in the CTRF were then expressed in terms of the harmonic number of the BF at which the peaks occurred. Figure 5 summarizes the classification scheme used in the study. Asterisks denote the harmonic number category within which a peak in the CTRF was observed. The category location of the peak thus defined the response type indicated on the left of the table. For example, if the amplitude of a given response component peaked when the harmonic number of the BF was less than or equal to 8, the component was classified as exhibiting type 1 behavior. The significance of the BF having a harmonic number of 8 is based on the fact that the lower side-band of the complex tone would have a harmonic number of 7, which is considered to be spectrally resolved in the psychoacoustic literature (Plomp, 1964; Plomp and Mimpen, 1968). In some cases, two peaks in the CTRF were identified, leading to classification as a type 4, 5, or 6 response, depending on the harmonic number category of the peaks. In cases where no peak was identified (i.e., no response greater than 20% of the mean of all responses) the response was classified as type 7.

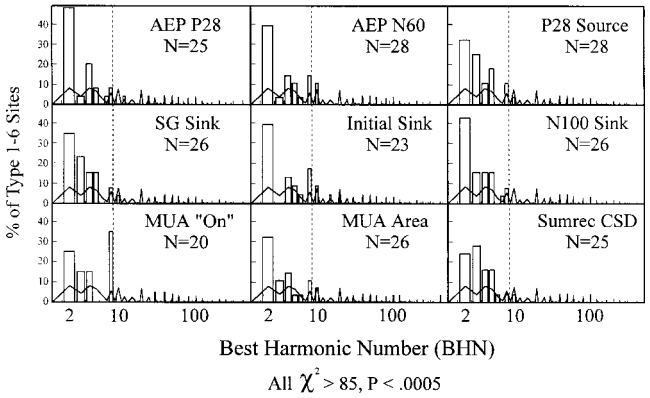

FIG. 7. Distributions of BHN for each of the response components examined in the study. Type 7 responses are not included in the distributions, since their CTRFs contain no maxima. The vertical dotted line separates the distributions into two regions corresponding to resolved and unresolved harmonic numbers, respectively (8 and below, 9 and above). The solid line passing through the bars indicates the distributions that would be expected by chance, based on harmonic numbers comprising the entire complex tone stimulus set. For all response components, differences between observed and expected distributions for resolved and unresolved harmonic numbers are statistically significant.

Figure 6 depicts the distribution of response types across cortical sites for each of the response components examined. Although there are differences in the distributions for the different components, with the exception of MUA ''On'' and the initial sink, type 1 was the dominant response pattern observed. In other words, for the majority of sites and response components, a peak in the CTRF occurred at f_0s for which the BF had a harmonic number less than or equal to 8. In contrast, MUA ''On'' and the initial sink exhibited many type 7 (no peak) response patterns, which accounts for their relative lack of sensitivity to ΔF evident in Fig. 4. For these components, fewer than 40% of the cortical sites sampled displayed type 1 response patterns.

Based upon the harmonic separation corresponding to peaks in the CTRFs, a ''best harmonic number'' (BHN) was identified for each response component at each cortical site. The distributions of BHN are shown in Fig. 7. Only type 1–6 responses are included, since type 7 response patterns have no peaks. For type 4, 5, and 6 responses, which exhibit two maxima in their CTRFs, the harmonic number corresponding only to the second peak (the one occurring at the higher f_0) is represented in the distributions. Using first peak values would not appreciably alter the overall results, since type 4,

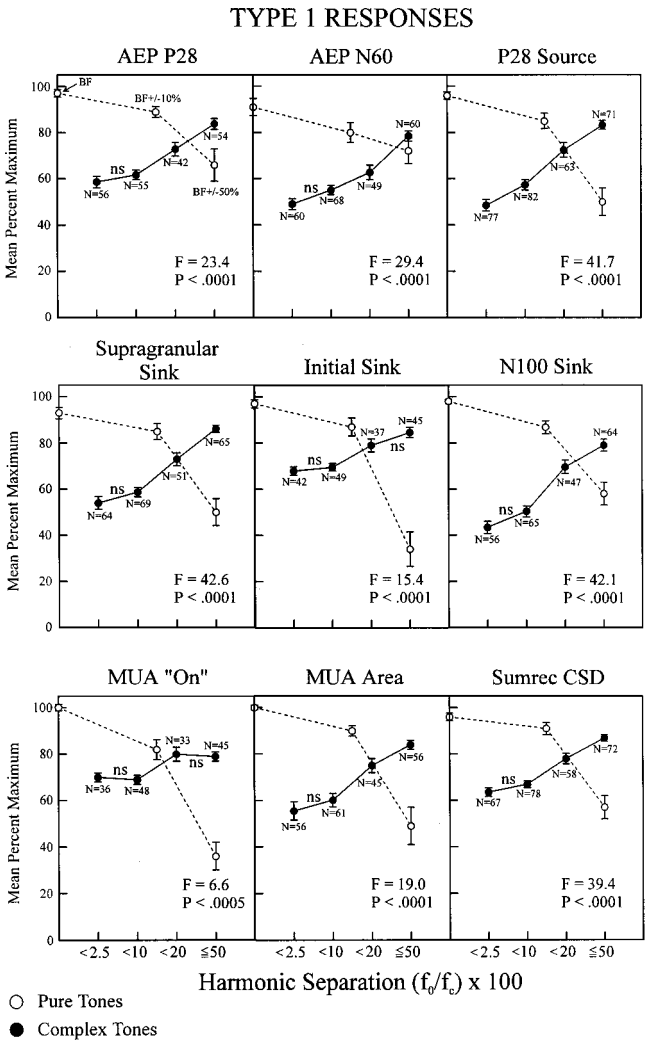

FIG. 8. Same graphs as in Fig. 4, but representing data for type 1 responses only. For all response components, differences between mean response amplitudes at the various harmonic separations are statistically significant. The ''inverse'' relationship between complex tone and pure tone response amplitudes demonstrates the nonlinear behavior of complex tone responses. For all response components, statistically significant increases in mean response amplitude occur at harmonic separations between 10% and 20%, whereas, with the exception of the P28 source, differences between mean amplitudes at separations of 2.5% and 10% are not statistically significant.

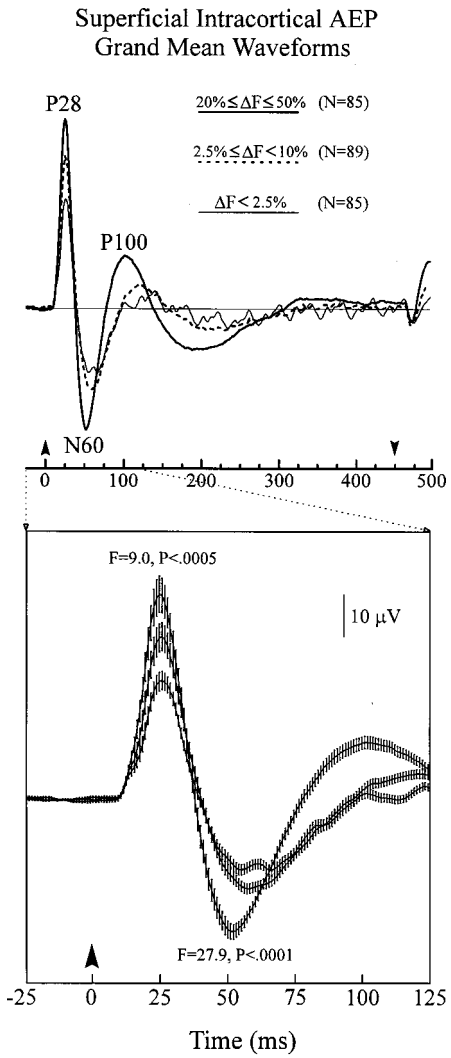

FIG. 9. Grand mean superficial intracortical AEPs recorded from the electrode contact directly above that corresponding to the CSD P28 current source under three different ΔF conditions. Major response components are indicated. Black arrowheads above the timeline bracket the duration of the stimulus. An expanded display of the first 125 ms of the waveform is shown in the bottom half of the figure. Lines above and below each waveform represent ±SEM, respectively. Differences among peak amplitudes of the P28 and N60 components under the three conditions are statistically significant.

5, and 6 responses are among the minority of response types observed. The vertical dotted lines divide the distributions into two regions corresponding to psychoacoustically resolved and unresolved harmonic numbers, 8 and below, 9 and above, respectively (Plomp, 1964; Plomp and Mimpen, 1968). Note that for all response components, the majority of BHNs lie within the region of resolved harmonics. The lines passing through the bars of the distributions indicate the relative proportions of the harmonic numbers corresponding to the f_c of all the stimuli presented in the study and thus represent the distributions that would be expected based on chance. Differences between the observed and expected distributions for resolved and unresolved harmonic numbers are statistically significant (chi-squared tests, $p<0.0005$). The BHNs were neither significantly related to BF region: <2 kHz/2–4 kHz/5–10 kHz (Kruskal-Wallis one-way analysis of variance, $p>0.05$), nor with the 6-dB-down bandwidth of the FRF based upon the peak amplitude of MUA ''On,'' the initial sink, and the supragranular sink (Spearman correlation analysis, $p>0.05$).

D. Complex tone responses and psychoacoustic CBWs

While the pooled and averaged data of Fig. 4 demonstrate a general augmentation of complex tone responses at large ΔFs, this feature by itself does not confirm the existence of a CBW representation, as CBW is traditionally conceived. Since the degree of masking depends on the amount of masker energy lying within the CB of the signal (Greenwood, 1961), the detection threshold for tonal signals is not a uniformly decreasing function of the ΔF between two flanking masker tones, but decreases abruptly at ΔFs corresponding to the CBW (Greenwood, 1961; Green, 1965; Rabinowitz *et al.*, 1980). Similarly, the loudness of complex sounds remains relatively invariant over stimulus bandwidths less

than a CBW and increases abruptly at bandwidths exceeding the CBW (Zwicker *et al.*, 1957). Analogously, complex tone response amplitudes should be relatively independent of ΔF for ΔFs below a CBW and should increase at ΔFs corresponding to the CBW. Averaged CTRFs of several of the response components did display such a pattern, as illustrated in Fig. 4 by the nonsignificant differences between mean response amplitudes for ΔFs below 10%, and the significant increases in amplitude at larger ΔFs. For other response components (namely, AEP P28, P28 source, and MUA ''On'') this pattern may have been obscured by the contribution of non-type 1 responses to the averaged data, as only type 1 responses would be expected to exhibit such CB-like behavior. Accordingly, when type 1 responses are considered in isolation (Fig. 8), *all* response components, including MUA ''On,'' exhibit statistically significant overall increases in response amplitude with ΔF. Moreover, with the exception of the P28 source, removal of non-type 1 responses reveals a CB-like CTRF characterized by a relative insensitivity to ΔF for ΔFs below 10%, and a significant increase in amplitude at ΔFs between 10% and 20%.

In combination, the present findings suggest that complex tone response amplitude patterns can be partly predicted by CB theory. In view of their possible relevance to MEG studies supporting a topographic representation of complex tone pitch in A1, it is important to show that a manifestation of a CBW representation generated intracortically can potentially be transmitted to the scalp and detected by noninvasive recordings. Figure 9 depicts grand mean waveforms derived from the superficial intracortical AEP recorded at the electrode contact 150 μm above that corresponding to the CSD P28 source. In the top half of the figure, three waveforms are superimposed, representing the mean HC-evoked AEP under three harmonic separation (ΔF) conditions (small, intermediate, and large, as indicated). *N* refers to the number of responses contributing to each mean waveform. Three major response components of the intracortical AEP are indicated (P28, N60, and P100). Amplitudes of these components increase with ΔF such that the largest responses are evoked by HCs with ΔFs greater than or equal to 20% of the f_c. Oscillations evident in the mean AEP evoked by HCs with small ΔFs ($<2.5\%$) reflect responses phase-locked to the waveform envelope of low f_0 HCs (see companion paper, Fishman *et al.*, 2000). The time window during which these response components occur is shown expanded in the lower half of Fig. 9. Vertical lines above and below the waveforms represent $\pm$SEM, respectively. Differences among the peak amplitudes of the P28 and N60 components are significant at the $p<0.0005$ and $p<0.0001$ level, respectively (analysis of variance). Since these mean responses are based on absolute rather than normalized amplitudes, they more accurately represent evoked activity that could potentially be detected at the scalp by noninvasive recordings.

III. DISCUSSION

A. Summary of rationale and findings

The present study examined whether amplitudes of auditory cortical responses to complex tones are modulated by ΔF in a manner that reflects CB filtering mechanisms. Such findings would potentially confound interpretations of human neuromagnetic recordings supporting an orthogonal topographic representation of complex tone pitch and pure tone frequency in auditory cortex (Langner *et al.*, 1997). To test this hypothesis, responses to three-component HCs of variable f_0 were recorded in A1 of the awake macaque monkey using neuronal ensemble techniques that bridge multiunit and noninvasive approaches, while overcoming the spatial resolution limitations of MEG recordings.

Amplitudes of intracortical AEP, MUA, and CSD components of responses to HCs centered at the BF in A1 can be partly explained by CB filtering mechanisms. Specifically, response amplitudes are generally maximal when the ΔF between harmonics is greater than 20% of the BF, in agreement with the nominal 10%–20% ΔF corresponding to the CBW (Zwicker *et al.*, 1957; Moore and Glasberg, 1983). Accordingly, the second harmonic was the most common BHN. Generally, amplitudes of the majority of response components were largely independent of ΔF for ΔFs below 10%, and increased significantly at harmonic separations of 10%–20%, indicative of CB-like behavior (see Fig. 4). Peak amplitudes of the AEP P28 component, the CSD P28 source, and MUA ''On,'' however, did not display this pattern, and either increased relatively uniformly or did not increase at all (MUA ''On'') with ΔF. Nonetheless, a uniform increase in amplitude is consistent with the proposal that auditory filters are not rectangular as traditionally assumed, but have a rounded exponential shape (see Patterson and Moore, 1986). Accordingly, psychoacoustic functions also do not always display an unambiguous break point at the CBW (e.g., Patterson, 1974; Glasberg *et al.*, 1984). It is important to note, however, that the curves depicted in Fig. 4 represent data averaged across electrode penetrations, irrespective of response type. Once type 1 responses were considered in isolation, a more ''classical'' CB-like pattern became evident for nearly all of the response components examined (Fig. 8).

That CB-like behavior was exhibited by both MUA and CSD components confirms an earlier report of a CBW representation in A1 based upon single unit responses (Ehret and Schreiner, 1997). A major cortical contribution to this representation is supported by the more pronounced effects of ΔF for MUA area, which incorporates neuronal firing extending beyond the initial cortical response, and for later CSD components than for early MUA and CSD components. The weaker sensitivity to ΔF seen for the initial sink and the peak of the MUA ''On'' response, which reflect thalamocortical input in addition to the activity of cortical cells, implies that subcortical representations of CBW may be amplified by processing mechanisms at the cortical level.

The increase in the absolute amplitude of both the P28 and N60 components of the superficial intracortical AEP with ΔF is consistent with a physiological representation of CBW suggested by human noninvasive evoked potential recordings (Burrows and Barry, 1990). These monkey AEP components are potentially homologous to the human AEP counterparts of the magnetic components, M60 and M100 (Arezzo *et al.*, 1986; Vaughan and Arezzo, 1988; Stein-

schneider *et al.*, 1994), whose ECD locations were reported by Langner *et al.* (1997) to depend on f_0. In combination, the present data suggest that a CBW representation generated within A1 can be propagated to the scalp and detected by noninvasive recording techniques such as MEG. Consequently, it is possible that CB effects significantly contributed to the neuromagnetic responses recorded by Langner *et al.* (1997).

It is important to emphasize that by a ''representation'' of CBW we do not mean to suggest that CBW is an organizational feature of A1, rather that neuronal ensemble responses to complex tones of the type used in the present study behave in accordance with the predictions of CB theory. Given this correspondence, the augmented responses to HCs comprised of low-numbered harmonics parallel the enhanced perceptual salience of spectrally resolved components of complex tones and the increased loudness of complex sounds with bandwidths exceeding a CBW (Zwicker *et al.*, 1957; Plomp, 1964).

It is unlikely that aural nonlinear distortion products were responsible for generating the present results. The two most prominent distortion products arising from the combination of two primary tones, $f1$ and $f2$ (with $f2>f1$), are $f2-f1$, and $2f1-f2$. The intensities of the individual complex tone components in this study (51 dB SPL) are well below threshold for detection of $f2-f1$ (about 50-dB sensation level, i.e., dB above hearing threshold, of the primary tones: Plomp, 1965; Goldstein, 1967). The detection threshold for $2f1-f2$, however, is considerably lower than that for $f2-f1$ (15-dB sensation level of the primary tones: Smoorenburg, 1972). Neural correlates of $2f1-f2$, as demonstrated by synchronization of auditory nerve fiber responses in the cat to cycles of the predicted combination tone, only begin to emerge when the primary tones are presented at about 50 dB SPL (Goldstein and Kiang, 1968). On average, similar thresholds were obtained by Smoorenburg *et al.* (1976) in the anterior cochlear nucleus of the cat. Importantly, since the frequencies of the primary tones in these physiological studies were chosen so as to produce combination tones overlapping the characteristic frequency (CF), and thus to maximize the probability of obtaining a response, these thresholds may actually overestimate the potential contribution of aural distortion products to the generation of responses recorded in the present study. Furthermore, the fact that neural and psychophysical detection thresholds for combination tones are, in general, significantly higher for large than for small ΔFs (Plomp, 1965; Smoorenburg *et al.*, 1976; Buunen and Rhode, 1978) is inconsistent with the observed augmentation of responses to HCs with increases in ΔF. Finally, using identical stimulation equipment, previous studies in our laboratory demonstrated absent responses to complex tones composed of the third, fourth, and fifth harmonics of a (missing) f_0 when the latter was situated at the BF (Fishman *et al.*, 1998). Distortion products generated in this situation would have corresponded to the f_0 and thus overlapped the BF. The fact that the levels of the individual harmonics were the same as those in the present study argues against the possibility that aural combination tones and distortion products generated by our acoustic stimulation equipment contributed significantly to the present results.

IV. PROPOSED MECHANISMS

Complex tone responses in A1 reflect nonlinear interactions between responses to individual frequency components in that they cannot be predicted by a simple summation of isolated pure tone responses used to define the spectral sensitivity of the cortical sites. Generally, complex tone response amplitudes changed in a direction *opposite* to that expected based upon the FRF (see Figs. 4 and 8). This finding indicates that such interactions must be considered for any explanation of complex sound processing at the cortical level. It is unclear at which level of the auditory pathway these nonlinearities originate to generate the observed CB-like response patterns. Demonstration of two-tone inhibition in the responses of auditory nerve fibers suggests the involvement of peripheral cochlear mechanisms (Sachs and Kiang, 1968). On the other hand, Pickles and Comis (1976) reported that effective bandwidths of auditory nerve fibers in the cat, determined by the noise band-expansion method, appreciably underestimated psychophysical CBWs in the same species and concluded that more central auditory structures are responsible for determining CBW. Accordingly, in the central nucleus of the IC of the anesthetized cat, neural CBWs, determined using noise band-narrowing and two-tone masking procedures, were more consistent with behavioral values (Ehret and Merzenich, 1985, 1988). Moreover, in agreement with our findings, CBWs could not be reliably predicted by pure tone excitatory tuning curve bandwidths in the IC, indicating that responses to complex sounds at the level of the midbrain are similarly shaped by nonlinear interactions. Single-unit studies in A1 of the anesthetized cat also revealed the lack of a simple correspondence between pure tone excitatory tuning curves and physiological CBWs (Ehret and Schreiner, 1997).

One possible mechanism underlying these cortical complex tone response patterns involves mutual lateral inhibitory interactions between responses evoked by frequency components lying within the same CB. In the present case, lateral suppression may be most effective when the harmonics are separated from one another by less than a CBW. Accordingly, the comparatively enhanced responses to complex tones with spectrally resolved harmonics may reflect a release from inhibition.

A lateral suppression mechanism which could potentially give rise to CB-like response patterns in A1 is supported by a number of physiological studies using two-tone stimuli. Responses to BF tones can be suppressed by simultaneously and nonsimultaneously presented tones lying within as well as outside the effective excitatory response area in A1 (e.g., Shamma and Symmes, 1985; Phillips and Hall, 1992; Shamma *et al.*, 1993; Nelken *et al.*, 1994; Calford and Semple, 1995; Brosch and Schreiner, 1997). Importantly, suppression of BF tone responses is generally maximal when the suppressor tone is at or near the BF and diminishes with increasing frequency separation between the tones. Moreover, consistent with the present results, in many of these studies (e.g., Shamma *et al.*, 1993; Calford and

Semple, 1995; Brosch and Schreiner, 1997) the frequency range within which two-tone suppression is maximal (for stimulus component intensities <60 dB SPL) commonly corresponds to about two CBWs surrounding the BF (combined range above and below the BF). Similarly, studies of A1 responses to stationary ripple stimuli (wideband complex sounds with a sinusoidal spectral profile) demonstrate a marked dependence of response amplitude on ripple density (number of ripples/octave): lower ripple densities generally lead to enhancement, whereas higher ripple densities (>2 ripples/octave) lead to suppression (Kowalski *et al.*, 1996, Calhoun and Schreiner, 1998). While these wideband stimuli are considerably more complex than the stimuli used in the present study, the results of these studies are consistent with the observed augmentation of responses with increases in interharmonic ΔF.

In combination, these studies provide strong evidence for ΔF-dependent lateral inhibitory interactions in A1, and support the proposal that inhibitory sidebands not revealed by isolated pure tone responses underlie the CB-like complex tone response patterns observed in the present study. Lateral suppression could arise from horizontal connections of pyramidal cell axon collaterals onto inhibitory interneurons of adjacent frequency regions (Ojima *et al.*, 1991, 1992; Kubota *et al.*, 1997). Consistent with this possibility, retrograde tracer experiments in A1 of the cat reveal prominent labeling of neurons with BFs different from that of neurons located at the tracer injection site, suggesting a considerable degree of connectivity between disparate iso-frequency bands (Matsubara and Phillips, 1988). Accordingly, inhibitory interactions across several different iso-frequency bands in A1 may modulate responses to sounds containing multiple frequency components. The anatomical bases and specific mechanisms underlying these interactions (e.g., active versus shunting inhibition) remain important questions for future investigations.

A. Implications for physiological representations of pitch

In supporting a representation of CBW in A1, the present findings urge a more cautious interpretation of MEG results suggesting an orthogonal spatial organization of pitch and frequency in A1. However, while the majority of sites and response components examined in the present study displayed CB-like behavior, the identification of other complex tone response patterns leaves open the possibility that subpopulations of neurons in A1 arranged along iso-frequency bands may represent additional perceptual features of complex sounds such as pitch. Thus, in the absence of a systematic spatial mapping along iso-frequency axes, our results cannot exclude the possibility that complex tone pitch is spatially represented orthogonal to the tonotopic map. Moreover, differences between the three-component HCs used in the present study and the wideband multi-component HCs used in the study by Langner *et al.* (1997) must be acknowledged. Since the latter were composed simultaneously of both resolved and unresolved harmonics, they may have engaged pitch mechanisms more effectively than our stimuli, in which harmonics were generally either resolved or unresolved, depending on the relationship between f_c and f_0.

An orthogonal organization of pitch and frequency in the auditory system is supported by studies demonstrating a topographic representation of the periodicity of amplitude-modulated (AM) tones orthogonal to the tonotopic gradient in the IC of the cat (Langner and Schreiner, 1988; Schreiner and Langner, 1988). This organization is presumably transmitted to higher auditory centers to form an analogous cortical representation (Langner, 1997). Accordingly, a topographic representation of stimulus periodicity was reported in the auditory cortex of the Mongolian gerbil (Schulze and Langner, 1997). In this latter case, however, the carrier frequencies of the AM tones used to define this organization were located outside of the neuron's receptive field, suggesting across-channel integration of subthreshold frequency information. The best modulation frequency (BMF), defined as the stimulus modulation frequency eliciting the highest spike rate, generally did not equal the BF, so these responses did not encode the ''missing fundamental'' in a manner corresponding to the tonotopic representation of pure tone frequency. Moreover, for a given single-unit, the BMF could change within a range of more than an octave depending upon the carrier frequency used. This finding is difficult to reconcile with the notion of a spatial representation of pitch according to which neurons are optimally responsive only to a narrow range of f_0s, irrespective of carrier frequency.

While providing a compelling physiological explanation for how complex signals with similar spectral envelopes can have different pitches depending on their f_0, the orthogonal model of pitch representation is unable to account for a key feature of pitch perception: that complex tones and pure tones with the same f_0 have the same pitch. Since the representations of pure tones and complex tones of the same f_0 occupy different spatial locations (Langner *et al.*, 1997), the orthogonal model does not explain how the pitches of these signals are perceived as similar. This correspondence might be achieved, however, in later processing stages by convergence of pure tone and complex tone-based f_0 information from A1 into surrounding nonprimary auditory cortical areas.

Alternatively, pitch may be based upon patterns of activity generated within networks of hierarchically organized auditory cortical fields. Anatomical tracer studies demonstrate extensive convergence of inputs originating from different frequency bands in A1 into surrounding auditory cortical areas (Ojima and He, 1997), as well as large-scale interconnectivity between A1 and surrounding ''belt'' areas (Rouiller *et al.*, 1991; Morel *et al.*, 1993; Jones *et al.*, 1995; Hackett *et al.*, 1998; Kaas and Hackett, 1998). Physiological investigations of nonprimary auditory cortical fields reveal functional connections with A1 (Rauschecker *et al.*, 1997; Howard *et al.*, 2000) and a general response preference for multi-component signals (Rauschecker *et al.*, 1995), consistent with spectral integration. Nonprimary auditory cortical fields receiving the output of A1 may therefore be well suited for extracting the pitch of complex sounds.

V. SUMMARY AND CONCLUSIONS

MUA, CSD, and AEP components of responses evoked by HCs with variable f_0s (and thus variable interharmonic ΔFs) were examined in A1 of the awake monkey. We investigated whether complex tone response amplitudes were consistent with a spatial representation of complex tone pitch orthogonal to the tonotopic gradient, or whether they could be explained by CB filtering mechanisms. Amplitudes of nearly all response components increased with f_0, such that maximal responses were evoked by HCs consisting of low-numbered resolved harmonics. While complex tone response amplitudes were largely invariant over ΔFs less than 10% of the center frequency, statistically significant increases in amplitude generally occurred at ΔFs between 10% and 20%, suggestive of CB-like behavior. Complex tone responses reflected nonlinear interactions between individual component responses, in that they could not be predicted on the basis of pure tone frequency tuning characteristics of the cortical sites. These findings based on neuronal ensemble responses corroborate results of both single-unit investigations of CB representation in A1 of the cat and human studies demonstrating CB-like increases in the amplitude of middle-latency components of the scalp-recorded AEP. Dependence of superficial intracortical AEP component amplitudes on ΔF suggests that CB effects would be evident in AEPs recorded from the scalp and that noninvasive recordings of responses to complex sounds may therefore require a consideration of these effects in their interpretation.

ACKNOWLEDGMENTS

This research was supported by Grant Nos. DC00657 and HD01799, and the Institute for the Study of Music and Neurologic Function of Beth Abraham Hospital. We are grateful to Dr. Steven Walkley, May Huang, Linda O'Donnell, and Shirley Seto for providing excellent technical, secretarial, and histological assistance. We also thank Dr. Haftan Eckholdt for statistical advice and two anonymous reviewers for their helpful comments on a previous version of the manuscript. Submitted in partial fulfillment of the requirements for the degree of Doctor of Philosophy in the Sue Golding Graduate Division of Medical Sciences, Albert Einstein College of Medicine, New York.

Arezzo, J. C., Vaughan, H. G., Jr., Kraut, M. A., Steinschneider, M., and Legatt, A. D. (**1986**). ''Intracranial generators of event-related potentials in the monkey,'' in *Frontiers of Clinical Neuroscience, Vol. 3*, edited by R. Q. Cracco and I. Bodis-Wollner (Liss, New York), pp. 174–189.

Bregman, A. S. (**1990**). *Auditory Scene Analysis: The Perceptual Organization of Sound* (MIT, Cambridge, MA).

Brosch, M., and Schreiner, C. E. (**1997**). ''Time course of forward masking tuning curves in cat primary auditory cortex,'' J. Neurophysiol. **77**, 923–943.

Burrows, D. L., and Barry, S. J. (**1990**). ''Electrophysiological evidence for the critical band in humans: middle-latency responses,'' J. Acoust. Soc. Am. **88**, 180–184.

Buunen, T. J. F., and Rhode, W. S. (**1978**). ''Responses of fibers in the cat's auditory nerve to the cubic difference tone,'' J. Acoust. Soc. Am. **64**, 772–781.

Calford, M. B., and Semple, M. N. (**1995**). ''Monaural inhibition in cat auditory cortex,'' J. Neurophysiol. **73**, 1876–1891.

Calhoun, B. M., and Schreiner, C. E. (**1998**). ''Spectral envelope coding in cat auditory cortex: linear and non-linear effects of stimulus characteristics,'' Eur. J. Neurosci. **10**, 926–940.

Carlyon, R. P., and Shackleton, T. M. (**1994**). ''Comparing the fundamental frequencies of resolved and unresolved harmonics: evidence for two pitch mechanisms?'' J. Acoust. Soc. Am. **95**, 3541–3554.

Cynx, J., and Shapiro, M. (**1986**). ''Perception of missing fundamental by a species of songbird (*Sturnus vulgaris)*,'' J. Comp. Psych. **100**(4), 356–360.

Ehret, G., and Merzenich, M. M. (**1985**). ''Auditory midbrain responses parallel spectral integration phenomena,'' Science **227**(4691), 1245–1247

Ehret, G., and Merzenich, M. M. (**1988**). ''Complex sound analysis (frequency resolution, filtering and spectral integration) by single units of the inferior colliculus of the cat,'' Brain Res. Rev. **13**, 139–163.

Ehret, G., and Schreiner, C. E. (**1997**). ''Frequency resolution and spectral integration (critical band analysis) in single units of the cat primary auditory cortex,'' J. Comp. Physiol. A **181**, 635–650.

Fastl, H., and Stoll, G. (**1979**). ''Scaling of pitch strength,'' Hear. Res. **1**, 293–301.

Fishman, Y. I., Reser, D. H., Arezzo, J. C., and Steinschneider, M. (**1998**). ''Pitch versus spectral encoding of harmonic complex tones in primary auditory cortex of the awake monkey,'' Brain Res. **786**, 18–30.

Fishman, Y. I., Reser, D. H., Arezzo, J. C., and Steinschneider, M. (**2000**). ''Compex tone processing in primary auditory cortex of the awake monkey. I. Neural ensemble correlates of roughness,'' J. Acoust. Soc. Am. **108**, 235–246.

Galaburda, A. M., and Sanides, F. (**1980**). ''Cytoarchitectronic organization of the human auditory cortex,'' J. Comp. Neurol. **190**, 597–610.

Galaburda, A. M., and Pandya, D. N. (**1983**). ''The intrinsic architectonic and connectional organization of the superior temporal region of the rhesus monkey,'' J. Comp. Neurol. **221**, 169–184.

Glasberg, B. R., Moore, B. C. J., and Nimmo-Smith, I. (**1984**). ''Comparison of auditory filter shapes derived with three different maskers,'' J. Acoust. Soc. Am. **75**, 536–544.

Goldstein, J. L. (**1967**). ''Auditory nonlinearity,'' J. Acoust. Soc. Am. **41**, 676–689.

Goldstein, J. L. (**1973**). ''An optimum processor theory for the central formation of the pitch of complex tones,'' J. Acoust. Soc. Am. **54**, 1496–1516.

Goldstein, J. L., and Kiang, N. Y. S. (**1968**). ''Neural correlates of the aural combination tone $2f1-f2$,'' Proc. IEEE **56**(6), 981–992.

Gourevitch, G. (**1970**). ''Detectability of tones in quiet and in noise by rats and monkeys,'' in *Animal Psychophysics*, edited by W. C. Stebbins (Appleton-Century-Crofts, New York), pp. 67–97.

Green, D. M. (**1965**). ''Masking with two tones,'' J. Acoust. Soc. Am. **37**, 802–813.

Greenwood, D. D. (**1961**). ''Auditory masking and the critical band,'' J. Acoust. Soc. Am. **33**, 484–502.

Hackett, T. A., Stepniewska, I., and Kaas, J. H. (**1998**). ''Subdivisions of auditory cortex and ipsilateral cortical connections of the parabelt auditory cortex in macaque monkeys,'' J. Comp. Neurol. **394**, 475–495.

Halgren, E., Marinkovic, K., and Chauvel, P. (**1998**). ''Generators of the late cognitive potentials in auditory and visual oddball tasks,'' Electroencephalogr. Clin. Neurophysiol. **106**, 156–164.

Hartmann, W. M. (**1996**). ''Pitch, periodicity, and auditory organization,'' J. Acoust. Soc. Am. **100**, 3491–3502.

Heffner, H., and Whitfield, I. C. (**1976**). ''Perception of the missing fundamental by cats,'' J. Acoust. Soc. Am. **59**, 915–919.

Houtsma, A. J. M., and Smurzynski, J. (**1990**). ''Pitch identification and discrimination for complex tones with many harmonics,'' J. Acoust. Soc. Am. **87**, 304–310.

Howard, M. A., Volkov, I. O., Mirsky, R., Garell, P. C., Noh, M. D., Granner, M., Damasio, H., Steinschneider, M., Reale, R. A., Hind, J. E., and Brugge, J. F. (**2000**). ''Auditory cortex on the human posterior superior temporal gyrus,'' J. Comp. Neurol. **416**, 79–92.

Jones, E. G., Dell'anna, M. E., Molinari, M., Rausell, E., and Hashikawa, T. (**1995**). ''Subdivisions of macaque monkey auditory cortex revealed by calcium-binding protein immunoreactivity,'' J. Comp. Neurol. **362**, 153–170.

Kaas, J. H., and Hackett, T. A. (**1998**). ''Subdivisions of auditory cortex and levels of processing in primates,'' Audiol. Neuro-Otol. **3**, 73–85.

Kosaki, H., Hashikawa, T., He, J., and Jones, E. G. (**1997**). ''Tonotopic organization of auditory cortical fields delineated by parvalbumin immunoreactivity in macaque monkeys,'' J. Comp. Neurol. **386**, 304–316.

Kowalski, N., Depireux, D. A., and Shamma, S. A. (**1996**). ''Analysis of dynamic spectra in ferret primary auditory cortex. I. Characteristics of single-unit responses to moving ripple spectra,'' J. Neurophysiol. **76**, 3503–3523.

Kubota, M., Sugimoto, S., Horikawa, J., Nasu, M., and Taniguchi, I. (**1997**). ''Optical imaging of dynamic horizontal spread of excitation in rat auditory cortex slices,'' Neurosci. Lett. **237**(2–3), 77–80.

Langner, G. (**1997**). ''Neural processing and the representation of periodicity pitch,'' Acta Otolaryngol. (Stockh) Suppl. **532**, 68–76.

Langner, G., Sams, M., Heil, P., and Schulze, H. (**1997**). ''Frequency and periodicity are represented in orthogonal maps in the human auditory cortex: evidence from magnetoencephalography,'' J. Comp. Physiol. A **181**, 665–676.

Langner, G., and Schreiner, C. E. (**1988**). ''Periodicity coding in the inferior colliculus of the cat. I. Neuronal Mechanisms,'' J. Neurophysiol. **60**(6), 1799–1822.

Licklider, J. C. R. (**1951**). ''A duplex theory of pitch perception,'' Experientia **7**, 128–134.

Licklider, J. C. R. (**1956**). ''Auditory frequency analysis,'' in *Information Theory*, edited by C. Cherry (Butterworth, London), pp. 253–269.

Liegeois-Chauvel, C., Musolino, A., Badier, J. M., Marquis, P., and Chauvel, P. (**1994**). ''Evoked potentials recorded from the auditory cortex in man: evaluation and topography of the middle latency components,'' Electroencephalogr. Clin. Neurophysiol. **92**, 204–214.

Lutkenhoner, B., and Steinstrater, O. (**1998**). ''High-precision neuromagnetic study of the functional organization of the human auditory cortex,'' Audiol. Neuro-Otol. **3**, 191–213.

Matsubara, J. A., and Phillips, D. P. (**1988**). ''Intracortical connections and their physiological correlates in the primary auditory cortex (AI) of the cat,'' J. Comp. Neurol. **268**, 38–48.

Meddis, R., and Hewitt, M. J. (**1991**). ''Virtual pitch and phase sensitivity of a computer model of the auditory periphery. I. Pitch identification,'' J. Acoust. Soc. Am. **89**, 2866–2882.

Meddis, R., and O'Mard, L. (**1997**). ''A unitory model of pitch perception,'' J. Acoust. Soc. Am. **102**, 1811–1820.

Moore, B. C. J. (**1989**). *An Introduction to the Psychology of Hearing*, 3rd ed. (Academic, London).

Moore, B. C. J., and Glasberg, B. R. (**1983**). ''Suggested formulas for calculating auditory-filter bandwidths and excitation patterns,'' J. Acoust. Soc. Am. **74**, 750–753.

Moore, B. C. J., and Ohgushi, K. (**1993**). ''Audibility of partials in inharmonic complex tones,'' J. Acoust. Soc. Am. **93**, 452–461.

Morel, A., Garraghty, P. E., and Kaas, J. H. (**1993**). ''Tonotopic organization, architechtonic fields and connections of auditory cortex in macaque monkeys,'' J. Comp. Neurol. **355**, 437–459.

Naatanen, R., and Picton, T. (**1987**). ''The N1 wave of the human electric and magnetic response to sound: a review and analysis of the component structure,'' Psychophysiology **24**(4), 375–425.

Nelken, I., Prut, Y., Vaadia, E., and Abeles, M. (**1994**). ''Population responses to multifrequency sounds in the cat auditory cortex: one- and two-parameter families of sounds,'' Hear. Res. **72**, 206–222.

Ojima, H., and He, J. F. (**1997**). ''Cortical convergence originating from domains representing different frequencies in the cat AI,'' Acta Otolaryngol. Suppl. (Stockh) **532**, 126–128.

Ojima, H., Honda, C. N., and Jones, E. G. (**1991**). ''Patterns of axon collateralization of identified supragranular pyramidal neurons in the cat auditory cortex,'' Cereb. Cortex **1**(1), 80–94.

Ojima, H., Honda, C. N., and Jones, E. G. (**1992**). ''Characteristics of intracellularly injected infragranular pyramidal neurons in cat primary auditory cortex,'' Cereb. Cortex **2**(3), 197–216.

Pantev, C., Hoke, M., Lutkenhoner, B., and Lehnertz, K. (**1989**). ''Tonotopic organization of the auditory cortex: pitch versus frequency representation,'' Science **246**, 486–488.

Pantev, C., Elbert, T., Ross, B., Eulitz, C., and Terhardt, E. (**1996**). ''Binaural fusion and the representation of virtual pitch in the human auditory cortex,'' Hear. Res. **100**, 164–170.

Patterson, R. D. (**1974**). ''Auditory filter shape,'' J. Acoust. Soc. Am. **55**, 802–809.

Patterson, R. D., and Moore, B. C. J. (**1986**). ''Auditory filters and excitation patterns as representations of frequency resolution,'' in *Frequency Selectivity in Hearing*, edited by B. C. J. Moore (Academic, London), pp. 123–177.

Phillips, D. P., and Hall, S. E. (**1992**). ''Multiplicity of inputs in the afferent path to cat auditory cortex neurons revealed by tone-on-tone masking,'' Cereb. Cortex **2**, 425–433.

Pickles, J. O., and Comis, S. D. (**1976**). ''Auditory nerve-filter bandwidths and critical bandwidths in the cat,'' J. Acoust. Soc. Am. **60**, 1151–1156.

Plomp, R. (**1964**). ''The ear as a frequency analyzer,'' J. Acoust. Soc. Am. **36**, 1628–1636.

Plomp, R. (**1965**). ''Detectability threshold for combination tones,'' J. Acoust. Soc. Am. **37**, 1110–1123.

Plomp, R. (**1967**). ''Pitch of complex tones,'' J. Acoust. Soc. Am. **41**, 1526–1533.

Plomp, R., and Mimpen, A. M. (**1968**). ''The ear as a frequency analyzer. II,'' J. Acoust. Soc. Am. **43**, 764–767.

Rabinowitz, W. M., Bilger, R. C., Trahiotis, C., and Nuetzel, J. (**1980**). ''Two-tone masking in normal hearing listeners,'' J. Acoust. Soc. Am. **68**, 1096–1106.

Rauschecker, J. P., Tian, B., and Hauser, M. (**1995**). ''Processing of complex sounds in the macaque nonprimary auditory cortex,'' Science **268**(5207), 111–114.

Rauschecker, J. P., Tian, B., Pons, T., and Mishkin, M. (**1997**). ''Serial and parallel processing in rhesus monkey auditory cortex,'' J. Comp. Neurol. **382**(1), 89–103.

Ritsma, R. J. (**1962**). ''Existence region of the tonal residue. I,'' J. Acoust. Soc. Am. **34**, 1224–1229.

Ritsma, R. J. (**1967**). ''Frequencies dominant in the perception of the pitch of complex sounds,'' J. Acoust. Soc. Am. **42**, 191–198.

Rouiller, E. M., Simm, G. M., Villa, A. E. P., de Ribaupierre, Y., and de Ribaupierre, F. (**1991**). ''Auditory cortico-cortical interconnections in the cat: evidence for parallel and hierarchical arrangement of the auditory cortical areas,'' Exp. Brain Res. **86**, 483–505.

Sachs, M. B., and Kiang, N. Y.-S. (**1968**). ''Two-tone inhibition in auditory-nerve fibers,'' J. Acoust. Soc. Am. **43**, 1120–1128.

Schreiner, C. E. (**1998**). ''Spatial distribution of responses to simple and complex sounds in the primary auditory cortex,'' Audiol. Neuro-Otol. **3**, 104–122.

Schreiner, C. E., and Langner, G. (**1988**). ''Periodicity coding in the inferior colliculus of the cat. II. Topographical organization,'' J. Neurophysiol. **60**(6), 1823–1840.

Schulze, H., and Langner, G. (**1997**). ''Periodicity coding in the primary auditory cortex of the Mongolian gerbil (*Meriones unguiculatus*): two different coding strategies for pitch and rhythm?'' J. Comp. Physiol. A **181**, 651–663.

Schwarz, D. W. F., and Tomlinson, R. W. W. (**1990**). ''Spectral response patterns of auditory cortex neurons to harmonic complex tones in alert monkey (*Macaca mulatta*),'' J. Neurophysiol. **64**, 282–298.

Shackleton, T. M., and Carlyon, R. P. (**1994**). ''Role of resolved and unresolved harmonics in pitch perception and frequency modulation discrimination,'' J. Acoust. Soc. Am. **95**, 3529–3540.

Shamma, S. A., and Symmes, D. (**1985**). ''Patterns of inhibition in auditory cortical cells in awake squirrel monkeys,'' Hear. Res. **19**, 1–13.

Shamma, S. A., Fleshman, J. W., Wiser, P. R., and Versnel, H. (**1993**). ''Organization of response areas in ferret primary auditory complex,'' J. Neurophysiol. **69**(2), 367–383.

Smoorenburg, G. F. (**1972**). ''Audibility region of combination tones,'' J. Acoust. Soc. Am. **52**, 603–614.

Smoorenburg, G. F., Gibson, M. M., Kitzes, L. M., Rose, J. E., and Hind, J. E. (**1976**). ''Correlates of combination tones observed in the response of neurons in the anteroventral cochlear nucleus of the cat,'' J. Acoust. Soc. Am. **59**, 945–962.

Steinschneider, M., Schroeder, C. E., Arezzo, J. C., and Vaughan, Jr., H. G. (**1994**). ''Speech-evoked activity in primary auditory cortex: effects of voice onset time,'' Electroencephalogr. Clin. Neurophysiol. **92**, 30–43.

Steinschneider, M., Reser, D. H., Fishman, Y. I., Schroeder, C. E., and Arezzo, J. C. (**1998**). ''Click train encoding in primary auditory cortex of the awake monkey: evidence for two mechanisms subserving pitch perception,'' J. Acoust. Soc. Am. **104**, 2935–2955.

Steinschneider, M., Volkov, I. O., Noh, M. D., Garell, P. C., and Howard, M. A. (**1999**). ''Temporal encoding of the voice onset time phonetic parameter by field potentials recorded directly from human auditory cortex,'' J. Neurophysiol. **82**(5), 2346–2357.

Steinschneider, M., Tenke, C. E., Schroeder, C. E., Javitt, D. C., Simpson, G. V., Arezzo, J. C., and Vaughan, Jr., H. G. (**1992**). ''Cellular generators of the cortical auditory evoked potential initial component,'' Electroencephalogr. Clin. Neurophysiol. **84**, 196–200.

Terhardt, E. (**1974**). ''Pitch, consonance, and harmony,'' J. Acoust. Soc. Am. **55**, 1061–1069.
Terhardt, E. (**1978**). ''Psychoacoustic evaluation of musical sounds,'' Percept. Psychophys. **23**(6), 483–492.
Tomlinson, R. W. W., and Schwarz, D. W. F. (**1988**). ''Perception of the missing fundamental in nonhuman primates,'' J. Acoust. Soc. Am. **84**, 560–565.
Vaughan, Jr., H. G., and Arezzo, J. C. (**1988**). ''The neural basis of event-related potentials,'' in *Human-Event Related Potentials, EEG Handbook (Revised Series, Vol. 3)*, edited by T. W. Picton (Elsevier, Amsterdam), pp. 45–96.
Whitfield, I. C. (**1980**). ''Auditory cortex and the pitch of complex tones,'' J. Acoust. Soc. Am. **67**, 644–647.
Wolpaw, J. R., and Penry, J. K. (**1975**). ''A temporal component of the auditory evoked response,'' Electroencephalogr. Clin. Neurophysiol. **39**, 609–620.
Wood, C. C., and Wolpaw, J. R. (**1982**). ''Scalp distribution of human auditory evoked potentials. II. Evidence for multiple sources and the involvement of auditory cortex,'' Electroencephalogr. Clin. Neurophysiol. **54**, 25–38.
Zatorre, R. J. (**1988**). ''Pitch perception of complex tones and human temporal-lobe function,'' J. Acoust. Soc. Am. **84**, 566–572.
Zera, J., Onsan, Z. A., Nguyen, Q. T., and Green, D. M. (**1993**). ''Auditory profile analysis of harmonic signals,'' J. Acoust. Soc. Am. **93**, 3431–3441.
Zerlin, S. (**1986**). ''Electrophysiological evidence for the critical band in humans,'' J. Acoust. Soc. Am. **79**, 1612–1616.
Zwicker, E., Flottorp, G., and Stevens, S. S. (**1957**). ''Critical bandwidth in loudness summation,'' J. Acoust. Soc. Am. **29**, 548–557.

Influence of peripheral resolvability on the perceptual segregation of harmonic complex tones differing in fundamental frequency

Nicolas Grimault
UMR CNRS 5020 Laboratoire ''Neurosciences and Systèmes Sensoriels,'' Hôpital E. Herriot-Pavillon U, 69437 Lyon Cedex 03, France and ENTENDRE Audioprothesists Group GIPA2, Pontchartrain, France

Christophe Micheyl
UMR CNRS 5020 Laboratoire ''Neurosciences and Systèmes Sensoriels,'' Hôpital E. Herriot-Pavillon U, 69437 Lyon Cedex 03, France

Robert P. Carlyon
MRC-Cognition and Brain Sciences Unit 15, Chaucer Road, Cambridge CB22EF, England

Patrick Arthaud
ENTENDRE Audioprothesists Group GIPA2, Pontchartrain, France

Lionel Collet
UMR CNRS 5020 Laboratoire ''Neurosciences and Systèmes Sensoriels,'' Hôpital E. Herriot-Pavillon U, 69437 Lyon Cedex 03, France

(Received 9 April 1999; revised 20 October 1999; accepted 31 March 2000)

Two experiments investigated the influence of resolvability on the perceptual organization of sequential harmonic complexes differing in fundamental frequency ($F0$). Using a constant-stimuli method, streaming scores for ABA-... sequences of harmonic complexes were measured as a function of the $F0$ difference between the A and B tones. In the first experiment, streaming scores were measured for harmonic complexes having two different nominal $F0$s (88 and 250 Hz) and filtered in three frequency regions (a LOW, a MID, and a HIGH region with corner frequencies of 125–625 Hz, 1375–1875 Hz, and 3900–5400 Hz, respectively). Some streaming was observed in the HIGH region (in which the harmonics were always unresolved) but streaming scores remained generally lower than in the LOW and MID regions. The second experiment verified that the streaming observed in the HIGH region was not due to the use of distortion products. Overall, the results indicated that although streaming can occur in the absence of spectral cues, the degree of resolvability of the harmonics has a significant influence. © *2000 Acoustical Society of America.* [S0001-4966(00)02807-1]

PACS numbers: 43.66.Ba, 43.66.Fe, 43.66.Hg, 43.66.Mk [SPB]

INTRODUCTION

An important phenomenon in the perceptual organization of sound sequences consists of stream segregation. This refers to the fact that, under certain conditions, sound sequences can give rise to the perception of two or more auditory streams (Miller and Heise, 1950; Bregman and Campbell, 1971; van Noorden, 1975; Anstis and Saida, 1985). It can be experienced each time one listens to music and follows a given instrument among the orchestral background. In laboratory conditions, it is traditionally investigated using simplified stimuli consisting of a repeating sequence of ''A'' and ''B'' tones (e.g., van Noorden, 1975); when the stimulus repetition rate is rapid enough, or the frequency separation between the ''A'' and ''B'' tones large enough, the sequence breaks down into two perceptual streams. The minimum frequency separation between ''A'' and ''B'' tones for which two streams can be heard when the listener is trying to attend to one or the other subset of elements has been dubbed the ''fission'' boundary (van Noorden, 1975).

To date, the mechanisms underlying this phenomenon remain largely unknown. While certain authors have suggested that streaming is a central phenomenon (Bregman, 1990), others have proposed that it is determined to a large extent by the functioning of peripheral mechanisms (Beauvois and Meddis, 1996). One question, in particular, concerns the role of peripheral auditory filtering in streaming. Hartmann and Johnson (1991) have proposed that beyond differences in the physical characteristics of the sounds, streaming is determined by parallel bandpass filtering, i.e., ''channeling'' of incoming sounds by the auditory periphery. Basically, sounds falling in different auditory channels are easily segregated, while sounds occupying successively the same auditory filters are less likely to be allocated to different auditory streams. This view is supported by the results of early experiments. Computer models based on this ''channeling'' principle can account successfully for a variety of experimental data on streaming (Beauvois and Meddis, 1996; McCabe and Denham, 1997). On the other hand, however, some experimental results demonstrate that signal features not related to channeling can affect stream segregation.

For example, it has been shown that differences in temporal envelope between sounds having the same frequency content can promote streaming (Iverson, 1995) and that the segregation boundary can be shifted by temporal envelope factors (Singh and Bregman, 1997). Therefore, at present, the extent to which streaming depends on peripheral filtering remains unclear.

The question of the influence of peripheral frequency resolution on streaming has been addressed recently by Rose and Moore (1997). Using repeating ABA sequences, these authors measured the fission boundary in normal-hearing and hearing-impaired subjects. Based on the notion that streaming depends on peripheral frequency selectivity (Hartmann and Johnson, 1991; Beauvois and Meddis, 1996) and that cochlear hearing impairment is associated with reduced frequency selectivity, one prediction was that the fission boundary would be larger in hearing-impaired than in normal-hearing subjects. The results in normal-hearing listeners indicated that the fission thresholds at different center frequencies were independent of the frequency difference between the A and B tones when expressed in terms of ERBs, a common measure of auditory-filter bandwidth; this argues for the hypothesis that streaming depends on frequency selectivity. However, the results in hearing-impaired subjects revealed a much less clear pattern, which did not allow this hypothesis to be confirmed.

One problem with the use of pure tones to study the role of peripheral frequency resolution on streaming comes from the fact that, for such tones, changes in frequency are strongly correlated with changes in pitch; consequently, these two factors cannot be disentangled. Complex tones, on the contrary, can vary by their fundamental frequency ($F0$, which largely determines virtual pitch) and/or their spectral locus, corresponding to the region in which the harmonics are filtered. Early experiments by van Noorden (1975) indicated that $F0$ played no significant role in streaming, in contrast to the spectral locus of the harmonics. In particular, it was shown that alternating complex tones that had the same $F0$ but that were composed of different sets of harmonics gave rise to two perceptual streams, one having a tinnier or brighter quality than the other. However, as pointed out by Bregman (1990), this experiment did not give $F0$ a ''fair chance'' as a potential factor of stream segregation given the known large influence of spectral differences. Later experiments concerned with the respective influence of $F0$ and spectral locus on streaming questioned this conclusion and suggested that these two factors both had a significant influence on streaming (Singh, 1987; Bregman *et al.*, 1990; Singh and Bregman, 1997). For example, Bregman and Levitan (cited in Bregman, 1990) and Bregman *et al.* (1990) found an effect of $F0$ on streaming in a study which measured streaming as a function of differences in $F0$ and peak position for harmonic complexes with a formantlike spectral envelope. However, as in the studies by Singh and by Bregman, they used resolved complexes, and so differences in $F0$ would have covaried with differences in the excitation patterns of the complexes.

This question of the influence of resolvability on the streaming of complex tones has recently become the object of increased interest. Very recently, Vliegen and Oxenham (1999) reported effects of $F0$ on streaming using complex tones consisting entirely of unresolved harmonics. They concluded that streaming can be mediated by $F0$ differences in the absence of excitation-pattern cues, and, indeed, reported that streaming was not reduced relative to a condition with resolved harmonics. This absence of an effect of resolvability is somewhat surprising because, as they pointed out, the virtual pitch percept produced by unresolved harmonics is considerably weaker than that obtained with resolved harmonics (Houtsma and Smurzynski, 1990; Shackleton and Carlyon, 1994). In a more recent study, Vliegen *et al.* (1999) showed that streaming induced by gross spectral differences, which were produced by filtering the harmonics in different frequency regions, was more potent than streaming induced by $F0$ differences in the absence of spectral cues. They suggested that the difference between these results and those obtained by Vliegen and Oxenham (1999) might be due to the fact that in that earlier study, stream segregation was advantageous (i.e., leading to better performance), whereas in the Vliegen *et al.* (1999) study it was detrimental. Unfortunately, the latter study did not include a condition in which the harmonics of the A and B complex tones were resolved *and* filtered in the same frequency region; therefore, the proposed explanation for the differences between the outcomes of the two studies may have been confounded by differences in the cues available to the listeners to perform the tasks (i.e., local spectral cues in the former study versus global spectrum or timbre cues in the latter).

Indirect evidence for the fact that harmonic resolvability influences streaming even when stream segregation is advantageous for the listeners has been provided in a study by Micheyl and Carlyon (1998), and recently confirmed by Gockel *et al.* (1999). These authors have shown that the $F0$ discrimination of target complex tones can be substantially impaired by preceding and following complex tones having a slightly different $F0$, and that this temporal interference effect is significantly larger when all complexes are made of unresolved harmonics than when they contain resolved harmonics. They paralleled this finding to the informal observation that in the unresolved condition, the listeners could not stream apart the target from the interfering complexes, whereas they could in the resolved conditions.

The present study investigated further the effect of resolvability on auditory stream segregation using a task and instructions which encouraged the use of a neutral criterion by the listeners—namely, whether the sequences sounded more like one or two streams. Stream segregation of complex tones was measured as a function both of $F0$ and of the frequency region into which the tones were filtered. The interaction between these two factors determined the extent to which the components in each complex were resolved by the peripheral auditory system in a way which has been measured in some detail (Shackleton and Carlyon, 1994), thereby allowing us to examine the effects of resolvability *per se*, independently of either frequency region or $F0$.

I. GENERAL METHODS

A. Procedure

Stream segregation was measured using a constant-stimuli procedure. Following a paradigm devised by van Noorden (1975), subjects were presented with repeating ABA tone sequences, where ''A'' and ''B'' represent tones of either the same or a different frequency. Subjects were instructed to indicate whether, at the end of the 4-s sequence, they heard either a single auditory stream with a galloping rhythm or two independent streams. Subjects indicated their response by pressing ''1'' or ''2'' on a computer keyboard. The program did not accept responses until completion of the whole sequence, and waited for the response before presenting the next sequence. Bregman (1978) has shown that streaming is a cumulative process, i.e., that it takes time for the listener to decide that there are two independent streams. He estimated the time constant of the process to be around 4 s. Over longer durations, spontaneous reversals in the percept have been shown to occur (Anstis and Saida, 1985). Accordingly, the stimulus duration was chosen in this study so that streaming was nearing its maximum at the end of the stimulus sequence, just as subjects had to indicate their response.

Overall, five or six different frequency separations between the A and B tones were presented, including a no-difference condition (control condition for false-alarm rate). These different stimulus conditions were presented ten times each, in random order. Tests began with a demonstration wherein the subjects could hear examples of sequences leading unambiguously to a single-stream or to a two-stream percept.

B. Material

Two testing systems were used. With the first, Tucker-Davis-Technologies-based system, signals were generated digitally in the time domain and output through a 16-bit digital-to-analog converter (TDT DA1) at a sampling rate of 44.1 kHz. A pink-noise background was generated digitally, recorded on CD, and played out continuously throughout the experiment (Sony CDP-XE300). The signals and background noise were low-pass filtered (TDT FT6-2 attenuation more than 60 dB at 1.15 times the corner frequency) at 15 kHz. They were then led to two separate programmable attenuators (TDT PA4). The outputs of the attenuators were summed (TDT SM3) and led to a Sennheiser HD465 headphone via a headphone buffer (TDT HBC). The subject was comfortably seated in a sound booth.

The second system consisted of an Interacoustics AC30 audiometer. The same sound files as used with the other testing system were used. The masker was produced using the same prerecorded CD, played from the computer CD-ROM drive. Signals were output via a 16-bit digital-to-analog converter. The masker and signals were then attenuated and added using the AC30 audiometer before being sent to one earpiece of Sennheiser HD465 headphones. Signal characteristics at the output of the two test systems were monitored using an HP3561A signal analyzer.

II. EXPERIMENT 1

A. Rationale

The aim of experiment 1 was to test systematically for the influence of resolvability on streaming elicited by $F0$ differences. To that end, differences in $F0$ were varied independently of differences in spectral regions. Three different frequency regions, defined by Shackleton and Carlyon (1994) and used in several subsequent studies (Carlyon and Shackleton, 1994; Carlyon, 1996a, b; Micheyl and Carlyon, 1998), were used here. A prediction inspired by the results of Micheyl and Carlyon (1998) was that streaming should decrease with decreasing resolvability.

B. Subjects

Seven subjects took part in the experiment. They ranged in age between 22 and 29 years (mean=25.7, s.d.=2.7). They all had normal hearing, i.e., absolute pure-tone thresholds at or below 15 dB HL at octave frequencies from 250 to 8000 Hz (ANSI, 1969). Four subjects were tested with the $F0$ of signal A set to 88 Hz; for the other three subjects, this $F0$ was set to 250 Hz.

C. Stimuli

The stimuli consisted of 4-s sequences of harmonic complex tones. Each sequence was formed by the repetition of three 100-ms complex tones (A-B-A) occurring immediately after each other. The three-tone sequences were separated by a 100-ms silent interval. The tones were gated with 20-ms raised-cosine ramps. The $F0$ of signal A was fixed at 88 or 250 Hz, whereas that of signal B varied between 88 and 352 Hz in half-octave steps. The signals were bandpass filtered digitally. The digital filter had a flat top and 48 dB/oct slopes. Depending on the condition, the filter lower and upper corner frequencies were set to 125 and 625 Hz, 1375 and 1875 Hz, or 3900 and 5400 Hz. These values correspond to the LOW, MID, and HIGH frequency regions of a previous study by Shackleton and Carlyon (1994). They showed that complexes with an $F0$ of 88 Hz were resolved in the LOW region and unresolved in the MID and HIGH regions, whereas those with $F0$s of 250 Hz were resolved in the LOW and MID regions and unresolved in the HIGH region. (Resolvability was defined as the number of harmonics falling within the 10-dB-down bandwidth of an auditory filter in the center of each region; this was lower than two for the resolved complexes and higher than 3.25 for the unresolved complexes. In addition, manipulating the phase of the unresolved but not of the resolved complexes could influence pitch). The signal level was set to 40 dB above the threshold in quiet measured using a sequence composed of signals filtered in the MID region, with $F0$s of 88 and 250 Hz for A and B, respectively. For convenience, this level will be referred to as 40 dB SL in the following.[1] All signals were presented in a pink-noise background. The level of this noise was set 10 dB above its absolute detection threshold, which was measured beforehand in each subject.

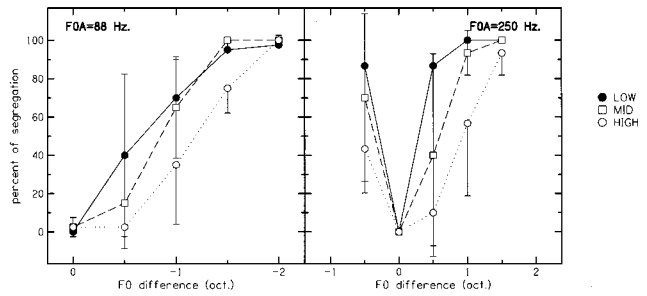

FIG. 1. Streaming scores as a function of $F0$ separation in the LOW, MID, and HIGH regions. Left-hand panel: data obtained with $F0_A = 88$ Hz. Right-hand panel: data obtained with $F0_A = 250$ Hz. The horizontal scale shows the distance in octaves between the $F0$s of A and B; negative values correspond to cases where the $F0$ of A was below that of B. The vertical scale represents streaming scores expressed in percent of ''two stream'' responses; the larger the score, the better the streaming performance. The parameter was the filtering region. Filled circles and continuous line correspond to data in the LOW region. Squares and dashed lines correspond to data in the MID region. Circles and dotted lines correspond to data in the HIGH region. The error bars show the standard error of the mean across subjects.

D. Results

The results of experiment 1 obtained when the $F0$ of the A tones was 88 and 250 Hz are shown in the left- and right-hand panels of Fig. 1, respectively. These results indicate at first sight that although differences in $F0$ are an important factor for streaming, there are other sources of variation. In particular, overall higher percents of segregation (corresponding to larger percentages of ''two streams'' responses) were observed in the LOW region than in the MID region, and in the MID region than in the HIGH region. Also, the way in which streaming scores varied as a function of the $F0$ separation between tones A and B appeared to be different across regions. In order to assess the significance of these observations, two-way repeated-measures ANOVAs were performed separately on the data obtained at each nominal $F0$.

The results revealed that at $F0_A = 88$ Hz there was, in addition to a significant effect of the $F0$ separation [$F(4,12) = 94.55$, $p < 0.001$], a significant effect of the frequency region in which the stimuli were filtered [$F(2,6) = 9.26$, $p < 0.05$]. There was no significant interaction between these two factors [$F(8,24) = 1.46$, $p = 0.22$]. At $F0_A = 250$ Hz, a significant effect of the frequency region [$F(2,4) = 6.98$, $p < 0.05$] and $F0$ separation [$F(4,8) = 14.24$, $p = 0.001$] was observed. In contrast to the results for $F0_A = 88$ Hz condition, a significant interaction between the frequency region and $F0$ separation [$F(8,16) = 4.21$, $p = 0.007$] was obtained.

In order to investigate the existence of quantitative relationships between the degree of resolvability of the stimuli and the streaming scores in the different conditions, we computed a ''combined resolvability index'' (CRI). This index, the mathematical details of which are given in the Appendix, depends on the interaction between auditory filter bandwidth (which covaries with the frequency region) and the $F0$s of the A and B sounds. It varies between 0 (fully unresolved) and 1 (fully resolved). Table I indicates the CRI and percent of ''two stream'' judgments for different combinations of $F0$s between the A and B tones, for cases where the $F0$ difference is constant and equal to half an octave. Note that both the CRI and segregation rates are greatest at high $F0$s and in low-frequency regions. A strong correlation was found between these two variables ($r = 0.95$, $p < 0.005$, $N = 6$), which does not appear to be due to either $F0$ or frequency region alone. For example, the CRI and segregation scores are both higher in the third than in the fourth row of Table I even though the stimuli are all filtered into the MID region; conversely, both scores are higher in the first than in the fifth row, even though the $F0$s of the stimuli are the same. This general pattern of results is consistent with the idea that resolvability, rather than $F0$ or frequency region *per se*, has an effect on streaming by $F0$ differences. Table II shows the CRI and percents of segregation for $F0$ separations of half an octave below and above 250 Hz in the different frequency regions. Here again, a strong correlation was obtained ($r = 0.93$, $p < 0.01$, $N = 6$).

TABLE I. CRI and experimental percent of segregation for $F0$ separations of -0.5 or $+0.5$ octave in the three different frequency regions tested in experiment 1.

$F0_A$	$F0_B$	Frequency region	CRI	Percent
250	176	LOW	0.8953	86.67
88	125	LOW	0.6426	40
250	176	MID	0.3527	40
88	125	MID	0.0155	15
250	176	HIGH	0.0007	10
88	125	HIGH	0	2.5

E. Discussion

The results of this experiment are in agreement with those of previous studies indicating that differences in $F0$ can be used to stream harmonic complexes (Singh, 1987; Bregman *et al.*, 1990; Singh and Bregman, 1997). In particular, the present finding that streaming can occur even when spectral cues are not available to the listeners (as in the HIGH frequency region) supports Vliegen and Oxenham's (1999) conclusion. However, our results differ from theirs in showing that streaming is enhanced when the components of each complex are resolvable by the peripheral auditory system.

Some other indirect evidence for an effect of resolvability on streaming is provided by the results of two recent

TABLE II. CRI and experimental percent of segregation for $F0$ separations of ± 0.5 octave around 250 Hz in the three different frequency regions tested in experiment 1.

$F0_A$	$F0_B$	Frequency region	CRI	Percent
250	352	LOW	0.9458	86.67
250	176	LOW	0.8953	86.67
250	352	MID	0.5912	70
250	176	MID	0.3527	40
250	352	HIGH	0.0265	43.33
250	176	HIGH	0.0007	10

studies (Micheyl and Carlyon, 1998; Gockel *et al.*, 1999), which revealed that, in the LOW and MID frequency regions, the $F0$ discrimination of a harmonic complex is impaired by preceding and succeeding complexes, i.e., temporal ''fringes,'' having a similar $F0$, but not by fringes having a widely different $F0$. In contrast, in the HIGH region, where all complexes were unresolved, interference effects occurred even between fringes and targets differing widely in $F0$. Informal observations made during the course of these studies indicated that the conditions in which interference effects occurred corresponded to those in which the fringe-target-fringe sequences could not be split into two streams; this was, in particular, the case when the fringes and targets were filtered in the same frequency region, were presented to the same ear, and had a similar $F0$. Thus, it was proposed that the $F0$ of the target could not be encoded independently of that of the fringes when it formed part of the same auditory stream. Consequently, the finding that interference effects in $F0$ discrimination occurred even for large target-fringe separations in the HIGH region was interpreted as indirect evidence for the fact that streaming was less easy in this HIGH region, unresolved condition. The present results support this interpretation.

A possible reason for the different outcomes of the present study and that of Vliegen and Oxenham (1999), which indicated no significant influence of resolvability on stream segregation, may come from the instructions given: Vliegen and Oxenham's listeners were told to ''try to hear out tone B separately from tone A,'' whereas our procedure encouraged a more ''neutral'' criterion (whether the sequence sounded more like one or two streams at the end). The task of trying to hear two streams is different from that of trying to hold on to a coherent percept (van Noorden, 1975; Bregman, 1990), which the neutral criterion used here may have encouraged the listeners to do. Also, the frequency separation at the temporal coherence boundary—where the listener is trying to hold on to the percept of a single stream—has been shown to be highly sensitive to the tone repetition rate (van Noorden, 1975). In fact, it has been suggested that the temporal coherence and the fission boundaries reflect different phenomena, the former indicating the point above which the auditory system is forced to segregation by automatic primitive processes, while the second indicates the limit of the attention-based component of streaming (Bregman, 1990). Consequently, it is conceivable that stimulus-related factors, like repetition rate and resolvability, have a larger influence on streaming when listeners are not trying to hear-out two streams. However, there is no evidence at present for the existence of an interaction between factors like repetition rate and resolvability.

Another possible reason for the apparent discrepancy between the results of Vliegen and Oxenham and those obtained here is that, in the present study and the preceding ones by Micheyl and Carlyon (1998) and Gockel *et al.* (1999), a larger $F0$ range was used (88 to 250 Hz) than in the study of Vliegen and Oxenham (100 to 189 Hz). We computed that while the minimum CRI in all studies is 0 (corresponding to a fully unresolved condition), the maximum CRI is 0.31 in Vliegen and Oxenham's study versus 0.94 in ours (given that 1 corresponds to a fully resolved condition). Thus, the use of more extreme resolved and unresolved harmonic conditions in the present study may have promoted the emergence of significant influences of resolvability.

Three interpretations can be invoked to explain the finding that although harmonic resolvability influences the streaming of complex tones differing in $F0$, streaming based on $F0$ differences can occur even when the harmonics are unresolved. According to a first interpretation, spectral cues are not absolutely necessary for streaming to occur, but they contribute to the phenomenon, together with other factors, namely, $F0$ differences. According to a second interpretation, streaming does not depend directly on spectral cues but on virtual pitch *per se*; the fact that streaming performances are larger for resolved than for unresolved harmonics can then be explained by the fact that the virtual pitch derived from resolved harmonics is generally more robust than that derived from unresolved harmonics (Houtsma and Smurzynski, 1990; Shackleton and Carlyon, 1994). These two interpretations are considered further in Sec. IV. According to a third interpretation, although the components in the physical stimulus could not be resolved by the peripheral auditory system, distortion products were generated by the ear; some of these combination tones were low enough in frequency to be resolved and may thus have provided spectral cues. This third interpretation was further tested in a second experiment, described in the next section.

III. EXPERIMENT 2

A. Rationale

The results of experiment 1 indicate that sequences of sounds differing by their $F0$ can still be split into different streams by the auditory system, even when the individual components of the sounds fall in the same frequency region and are unresolved. Nevertheless, although the physical components of the sounds were unresolved, one may not rule out the possibility that distortion products corresponding to subharmonics of these components were generated by the ear; these combination tones, falling in a region where the auditory filters were narrower, may have provided spectral cues as to the $F0$ differences between the A and B stimuli. This would, in particular, be the case if an internal component corresponding to the fundamental frequency of the high-frequency complex was generated by the ear. Recent results suggest that amplitude-modulated high-frequency components can give rise to a strong combination tone at the frequency of the modulation (Wiegrebe and Patterson, 1999). Earlier data in the literature indicate that combination tones produced by two-tone complexes are audible when the level of the primaries is between about 40 and 70 dB SL on average; however, there are large variations between subjects and some subjects can apparently detect combination tones at primary levels as low as 20 dB SL (Plomp, 1965). Similarly, combination tones corresponding to the missing fundamental of complexes composed of all harmonics between the second and the tenth can be detected when the level of the complex is on average 57 dB SL, but some subjects could detect it at

about 30 dB SL (Plomp, 1965). On the basis of these data, it cannot be completely excluded that some listeners can hear combination tones when presented with a 40 dB SL harmonic complex, as was the case in experiment 1.

In their recent article, Vliegen and Oxenham (1999) estimated that a pink-noise background with a spectrum level of 25 dB at 1 kHz ensured that the distortion products elicited by their harmonic complexes were masked. The overall level of their complexes being fixed at 70 dB SPL, the SPL per component in the passband varied between around 52 or 61, depending on the $F0$ and frequency region tested. Thus, at 1 kHz, the component level was between 27 and 36 dB above the level of the noise. In experiment 1 of the present study, the overall SPL of the stimuli in the MID region was estimated to be around 52 dB SPL and the SPL per component in the passband varied between about 44 and 49. The estimated spectrum level of the noise at 1 kHz was 9.71 dB. Thus at this frequency, the component level was between 35 and 39 dB above the noise level, and it cannot be concluded that distortion products were inaudible in that experiment.

Consequently, we performed a second experiment in which we first reduced the signal level by 10 dB, thereby making the signal-to-noise ratio 10 dB smaller than in experiment 1, and similar to that used by Vliegen and Oxenham (1999). Then, keeping this new signal-to-noise ratio, we ran a second condition in which we increased both the signal and noise levels by 20 dB, which were then comparable to those used in Vliegen and Oxenham (1999).

B. Subjects

Four subjects with normal hearing (thresholds less than 15 dB HL at conventional audiometric frequencies between 250 and 8000 Hz) who all had taken part in experiment 1 participated to experiment 2. They were aged between 22 and 29 years.

C. Stimuli

The stimuli were the same as those used in experiment 1 (open circles) in the HIGH frequency region condition with $F0_A = 88$, except for a change in level. Whereas in experiment 1 the signal and pink-noise background levels were 40 and 10 dB SL, respectively, in this experiment they were set either to 30 and 10 dB SL, or to 50 and 30 dB SL, respectively.

D. Results

The streaming scores obtained at the two test levels are shown in Fig. 2, along with the results from experiment 1 (HIGH region, $F0_A = 88$ Hz). The data in these three conditions—the two conditions of experiment 2 plus that of experiment 1—were analyzed using a two-way repeated-measures ANOVA. As in the previous experiment, a strong effect of $F0$ separation on streaming was observed [$F(4,12) = 73.32$, $p < 0.001$], but no statistically significant difference was found between the three conditions tested [$F(2,6) = 1.61$, $p = 0.28$]. No significant interaction between condition and $F0$ separation was noted either [$F(8,24) = 0.64$, $p = 0.74$].

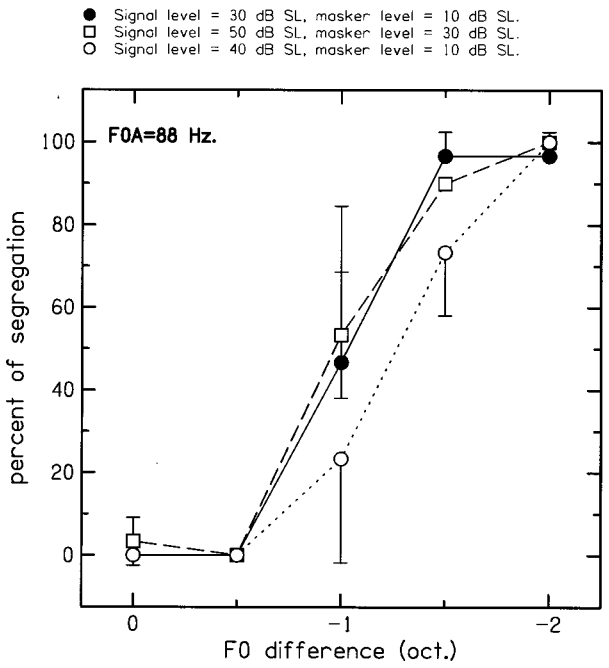

FIG. 2. Streaming scores as a function of $F0$ difference in three different level conditions in the HIGH region. The abscissa shows the distance in octave between the $F0$s of A and B. The ordinate represents the percent of segregation; the larger the score, the better the streaming performance. The parameter was the presentation level of the signal and noise. Filled circles and continuous line correspond to a 30 dB SL signal level and 10 dB SL masker level. Squares and dashed line correspond to a 50 dB SL signal level and 30 dB SL masker level (same signal-to-noise ratio). Circles and dotted line correspond to data from the first experiment (40 dB SL signal level and 10 dB SL masker level), replotted for comparison. The error bars show the standard error of the mean across subjects.

E. Discussion

The fact that the streaming scores for the HIGH frequency complex were not significantly reduced by a 10-dB decrease in signal-to-noise ratio even when the signal level was raised to 50 dB SL argues against the hypothesis that distortion products are necessary for the streaming of unresolved, high-frequency harmonics. This outcome is in broad agreement with the recent findings of Vliegen and Oxenham (1999). The agreement between their results and ours on this point is further supported by the fact that in the second condition of our experiment 2, the signal levels and signal-to-noise ratios were comparable to those used in their experiment 1a and, yet, streaming scores were not significantly different from those measured at the lower levels used in our experiments 1 and 2. In more general terms, the finding that a 20-dB increase in signal level with the same signal-to-noise ratio had no significant effect on streaming suggests that the signal level, independently of the signal-to-noise ratio, is not an important factor in the streaming of harmonic complexes, at least over the 30 to 50 dB SL range.

IV. SUMMARY AND CONCLUSION

Experiment 1 compared streaming in different resolvability conditions in the same, normal-hearing subjects. Streaming scores were found to decrease overall with increasing frequency region, being in some instances signifi-

cantly larger in the LOW and MID than in the HIGH frequency region. Furthermore, streaming scores appeared to be significantly correlated with a computed resolvability index taking into account the combined resolvability of the A and B tones forming the test sequences. However, the results of this experiment and those of experiment 2 also indicated that completely unresolved harmonic complexes could still give rise to two perceptual auditory streams, even in conditions where subjects were unlikely to use combination tones. These results confirm the recent demonstration by Vliegen and Oxenham (1999) that streaming of complex tones differing in $F0$ can occur on the sole basis of temporal cues. However, they differ from the results of these authors in showing that the degree of resolvability of the harmonics has a significant influence on streaming. This outcome is consistent with other recent results which suggest that streaming is substantially weaker for unresolved than for resolved harmonics (Micheyl and Carlyon, 1998; Gockel *et al.*, 1999). The present results further indicate that an effect of resolvability on stream segregation can be observed even if the task and instructions encourage the use of a neutral criterion by listeners. Therefore, the explanation proposed by Vliegen *et al.* (1999) to explain the difference between their conclusions and those reached by Vliegen and Oxenham (1999) may not be valid.

Overall, the results of the different experiments presented here suggest that although resolvability of the harmonics is not absolutely necessary for streaming, it significantly contributes to it. This contribution may be mediated either by spectral cues, which are associated to resolved harmonics, or by pitch strength, which is known to be larger for resolved than for unresolved harmonics. The aim of future experiments might consist of trying to disentangle the respective influence of these two factors by manipulating pitch strength independently of spectral cues. However, because of the strong relationship that exists between these factors, this aim may well prove difficult to achieve.

ACKNOWLEDGMENTS

This research was supported by the French National Center for Scientific Research (CNRS) and by the ENTENDRE hearing-aid dispensers group. The authors are grateful to Sid Bacon, Brian Roberts, and an anonymous reviewer for very helpful comments on earlier versions of the manuscript. Jean-Christophe Béra is gratefully acknowledged for his help with calibration.

APPENDIX

1. Apparatus interchangeability check

For practical reasons, not all subjects could be tested using the same apparatus; two testing systems had to be used. The preliminary experiment described below was performed in order to check that the streaming scores measured using these two systems were not different. To do this, we tested the same four subjects in the same conditions on the two systems. Furthermore, in order to investigate within-subject variability, the stimuli were presented 30 times at each $F0$ combination. The $F0$ of the A sound was maintained constant at 88 Hz; the $F0$ of B was varied between 88 and 352 Hz. The signal level was 40 dB SL and the noise level was 10 dB SL. The stimuli were filtered in the MID frequency region (1375–1875 Hz).

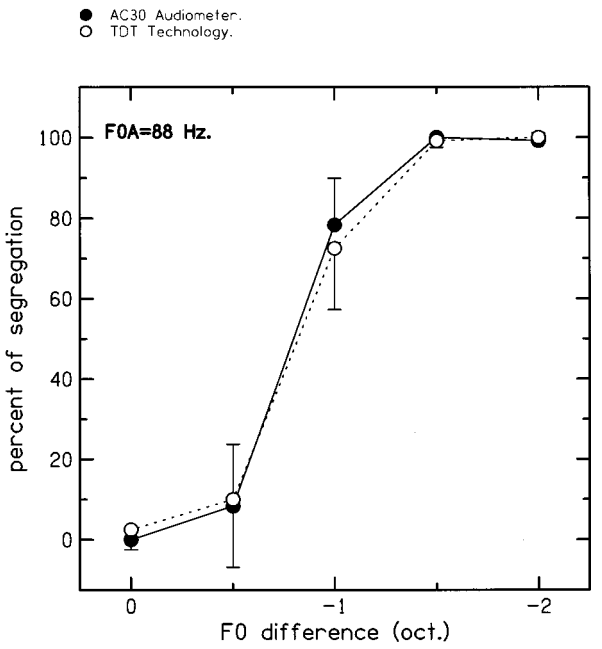

FIG. A1. Mean streaming scores on the two testing systems. Filled circles show the results obtained with the AC30-based system. Empty circles show results obtained using the Tucker-Davis-Technologies-based system.

Figure A1 shows the mean streaming scores of the four subjects on the two testing systems. The results obtained on the two testing systems are largely similar. A two-way

TABLE AI. CRI for different $F0$ separations ($F0_A = 88$ Hz) in the LOW (a), MID (b), and HIGH (c) region, ''y'' and ''n'' indicate that harmonics were or were not resolved according to Shackleton and Carlyon's (1994) definition.

	$F0_A = 88$ Hz	
$F0_B$	CRI	y/n
(a) LOW region		
62	0.4097	y
88	0.4097	y
125	0.6426	y
176	0.8	y
250	0.8953	y
352	0.9457	y
(b) MID region		
62	0.0002	n
88	0.0002	n
125	0.0155	?
176	0.1221	?
250	0.3527	y
352	0.5912	y
(c) HIGH region		
62	0	n
88	0	n
125	0	n
176	0	n
250	0.0007	n
352	0.0265	?

TABLE AII. CRI for different $F0$ separations ($F0_A = 250$ Hz) in the LOW (a), MID (b), and HIGH (c) regions. ''y'' and ''n'' indicate that harmonics were or were not resolved according to Shackleton and Carlyon's (1994) definition.

	$F0_A = 250$ Hz	
$F0_B$	CRI	y/n
(a) LOW region		
62	0.8953	y
88	0.8953	y
125	0.8953	y
176	0.8953	y
250	0.8953	y
352	0.9458	y
(b) MID region		
62	0.3527	y
88	0.3527	y
125	0.3527	y
176	0.3527	y
250	0.3527	y
352	0.5912	y
(c) HIGH region		
62	0.0007	n
88	0.0007	n
125	0.0007	n
176	0.0007	n
250	0.0007	n
352	0.0265	?

repeated-measure ANOVA indicated a significant effect of the $F0$ difference [$F(4,12) = 169.08$, $p < 0.001$] on streaming but no difference between the two systems [$F(1,3) = 0.03$, $p = 0.87$]. The results of this experiment also revealed that the streaming percentages estimated on the basis of 30 presentations were very close to those estimated on the basis of only ten presentations; using a Mann-Whitney pairwise comparison statistical test, the two were found not to be significantly different. In view of this small within-subject variability, we chose to restrict the number of presentations of each stimulus to ten in the actual experiments.

2. The combined resolvability index

This index was obtained by computing the average number of harmonics falling in the 10-dB auditory-filter bandwidth whose center frequencies fall within the corner frequencies of the considered frequency region (LOW, MID, HIGH). The resulting number was then transformed through a Gaussian function so that it was bounded between 0 (fully unresolved) and 1 (fully resolved). The formula used to compute the resolvability index is given below:

$$\mathrm{RI} = \exp\{-(\Sigma_{fl}^{fu}[1.8 \cdot \mathrm{ERB}(f)/F_0]/(fu - fl))^2/2\},$$

where *fu* and *fl* correspond to the upper and lower corner frequencies, respectively, of the considered frequency region, $F0$ corresponds to the $F0$ of the complex and ERB(f) is the equivalent rectangular bandwidth at the center frequency *f*, as defined in Glasberg and Moore (1990).

A complex was considered to be resolved if its resolvability index was greater than 0.135 and unresolved if its resolvability index was smaller than 0.005; these two values correspond respectively to mean numbers of harmonics falling in the auditory-filter bandwidth of 2 and 3.25 (Shackleton and Carlyon, 1994). Furthermore, because sequences comprising A and B tones having different $F0$s were used in this study, we computed a combined resolvability index (CRI). This index was computed as the maximum of the resolvability index of the A and B complexes comprising the sequence. The combined resolvability index of a sequence A-B-A is then given by

$$\mathrm{CRI} = \mathrm{MAX}\left[\exp\left\{-\left(\frac{\Sigma_{fl}^{fu}[1.8 \cdot \mathrm{ERB}(f)/F0_A]}{(fu - fl)}\right)^2 \Big/ 2\right\}; \exp\left\{\left(\frac{\Sigma_{fl}^{fu}[1.8 \cdot \mathrm{ERB}(f)/F0_B]}{(fu - fl)}\right)^2 \Big/ 2\right\}\right],$$

where all symbols are the same as in the previous formula.

Tables AI and AII show the CRI in each of the conditions tested in this study.

[1]All stimulus levels used in this study were specified in terms of SLs rather than SPLs. Nevertheless, some information regarding the SPLs used in the study could be obtained *a posteriori*. The Sennheiser HD465 headphones used in the study were calibrated using a Zwislocki coupler in combination with a 0.5-in. BK1433 condenser microphone and a BK2610 preamplifier feeding an HP35665A signal analyzer. Based on the measured absolute thresholds of one of the normal-hearing listeners who had taken part in the experiment, the level of the 40-dB SL signal was estimated to be approximately 52 dB SPL. The spectrum level of the 10-dB SL pink noise background was measured to be about 41 dB below the level per component of the harmonic at 1500 Hz in this listener.

ANSI (**1969**). ANSI S3.6-1969, *Specifications for Audiometers* (American National Standards Institute, New York).

Anstis, S., and Saida, S. (**1985**). ''Adaptation to auditory streaming of frequency-modulated tones,'' Percept. Psychophys. **11**, 257–271.

Beauvois, M. W., and Meddis, R. (**1996**). ''Computer simulation of auditory stream segregation in alternating-tone sequences,'' J. Acoust. Soc. Am. **99**, 2270–2280.

Bregman, A. S. (**1978**). ''Auditory streaming is cumulative,'' J. Exp. Psychol. **4**, 380–387.

Bregman, A. S. (**1990**). *Auditory Scene Analysis: The Perceptual Organization of Sound* (MIT, Cambridge, MA).

Bregman, A. S., and Campbell, J. (**1971**). ''Primary auditory stream segregation and the perception of order in rapid sequences of tones,'' J. Exp. Psychol. **89**, 244–249.

Bregman, A. S., Liao, C., and Levitan, R. (**1990**). ''Auditory grouping based on fundamental frequency and formant peak frequency,'' Can. J. Psychol. **44**, 400–413.

Carlyon, R. P. (**1996a**). ''Encoding the fundamental frequency of a complex tone in the presence of a spectrally overlapping masker,'' J. Acoust. Soc. Am. **99**, 517–524.

Carlyon, R. P. (**1996b**). ''Masker asynchrony impairs the fundamental-frequency discrimination of unresolved harmonics,'' J. Acoust. Soc. Am. **99**, 525–533.

Carlyon, R. P., and Shackleton, T. M. (**1994**). ''Comparing the fundamental frequencies of resolved and unresolved harmonics: Evidence for two pitch mechanisms?,'' J. Acoust. Soc. Am. **95**, 3541–3554.

Glasberg, B. R., and Moore, B. C. J. (**1990**). ''Derivation of auditory filter shapes from notched-noise data,'' Hear. Res. **47**, 103–198.

Gockel, H., Caryon, R. P., and Micheyl, C. (**1999**). ''Context dependence of fundamental frequency discrimination: Lateralized temporal fringes,'' J. Acoust. Soc. Am. **106**, 3553–3563.

Hartmann, W. M., and Johnson, D. (**1991**). ''Stream segregation and peripheral channeling,'' Mus. Perc. **9**, 155–184.

Houtsma, A. J. M., and Smurzynski, J. (**1990**). ''Pitch identification and discrimination for complex tones with many harmonics,'' J. Acoust. Soc. Am. **87**, 304–310.

Iverson, P. (**1995**). ''Auditory stream segregation by musical timbre: Effects of static and dynamic acoustic attributes,'' J. Exp. Psychol. **21**, 751–763.

McCabe, S. L., and Denham, M. J. (**1997**). ''A model of auditory streaming,'' J. Acoust. Soc. Am. **101**, 1611–1621.
Micheyl, C., and Carlyon, R. P. (**1998**). ''Effect of temporal fringes on fundamental-frequency discrimination,'' J. Acoust. Soc. Am. **104**, 3006–3018.
Miller, G. A., and Heise, G. A. (**1950**). ''The trill threshold,'' J. Acoust. Soc. Am. **22**, 637–638.
Plomp, R. (**1965**). ''Detectability threshold for combination tones,'' J. Acoust. Soc. Am. **37**, 1110–1123.
Rose, M. M., and Moore, B. C. J. (**1997**). ''Perceptual grouping of tone sequences by normally hearing and hearing-impaired listeners,'' J. Acoust. Soc. Am. **102**, 1768–1778.
Shackleton, T. M., and Carlyon, R. P. (**1994**). ''The role of resolved and unresolved harmonics in pitch perception and frequency modulation discrimination,'' J. Acoust. Soc. Am. **95**, 3529–3540.
Singh, P. G. (**1987**). ''Perceptual organization of complex-tones sequences: A tradeoff between pitch and timbre?'' J. Acoust. Soc. Am. **82**, 886–899.
Singh, P. G., and Bregman, A. (**1997**). ''The influence of different timbre attributes on the perceptual segregation of complex-tone sequences,'' J. Acoust. Soc. Am. **102**, 1943–1952.
van Noorden L. P. A. S. (**1975**). ''Temporal coherence in the perception of tone sequences,'' unpublished doctoral dissertation, Technische Hogeschool Eindhovern, Eindhoven, The Netherlands.
Vliegen, J., and Oxenham, A. J. (**1999**). ''Sequential stream segregation in the absence of spectral cues,'' J. Acoust. Soc. Am. **105**, 339–346.
Vliegen, J., Moore, B. C. J., and Oxenham, A. J. (**1999**). ''The role of spectral and periodicity cues in auditory stream segregation, measured using a temporal discrimination task,'' J. Acoust. Soc. Am. **106**, 938–945.
Wiegrebe, L., and Patterson, R. D. (**1999**). ''Quantifying the distortion products generated by amplitude-modulated noise,'' J. Acoust. Soc. Am. **106**, 2709–2718.

On the dichotic pitch of simultaneously presented interaurally delayed white noises. Implications for binaural theory

Frans A. Bilsen and Johan Raatgever
Applied Physics Department, Delft University of Technology, Lorentzweg 1, 2600 GA Delft, The Netherlands

(Received 16 June 1999; revised 8 December 1999; accepted 11 April 2000)

A dichotic pitch known as Fourcin Pitch (FP) is perceived when two independent interaurally delayed white noises are presented simultaneously. Experiments in the past mainly dealt with stimulus situations where one interaural delay was smaller than 4 ms and the other was in the range 0–10 ms. Here, experiments are reported showing a novel pitch percept that occurs when one noise is interaurally delayed at the left ear and the other noise is about equally delayed at the right ear, for delays in the range of 4–10 ms. It is shown that, for both the previously reported FP and the novel pitch, the Central Spectrum (CS) theory [Raatgever and Bilsen, J. Acoust. Soc. Am. **80**, 429–441 (1986)] provides a correct prediction of both the pitch value and the lateral position of the pitch image, where other current theories partly or completely fail. Further experiments indicate that the lateralized position of the pitch image is essentially not influenced by an interaural intensity difference (IID). This is also predicted by the CS model and leads to the generalized conclusion that interaural time and intensity differences are processed separately in the auditory system until, at least, the level where the dichotic pitch is generated. [S0001-4966(00)04407-6]

PACS numbers: 43.66.Ba, 43.66.Pn, 43.66.Rq, 43.66.Hg [DWG]

INTRODUCTION

Generally, dichotic pitches may arise when white noise is dichotically presented to both ears with a particular interaural phase relationship. The following dichotic pitches have been reported, in historical order: the Huggins Pitch (HP) for a dichotic noise with an interaural 2π-phase transition in a limited frequency range (Cramer and Huggins, 1958), the Fourcin Pitch (FP) for two or three uncorrelated dichotic noises each with a different interaural delay (Fourcin, 1962), the Dichotic Repetition Pitch (DRP) for one dichotic noise with an interaural delay (Bilsen, 1972), the Multiple Phase Shift (MPS) pitch for a dichotic noise with a series of interaural 2π-phase transitions equally spaced in frequency (in fact a multiple Huggins stimulus) (Bilsen, 1976), and the Binaural Edge Pitch (BEP) for a dichotic noise with an interaural π-phase transition in a limited frequency range (Klein and Hartmann, 1981). The pitch character and its salience are different for the different configurations: the HP has a pure tone character, the DRP, the FP, and the MPS have a ''low'' pitch (synonymously: residue pitch, periodicity pitch, virtual pitch) character (Bilsen, 1977), while the BEP was informally observed to have both a pure tone and a low pass (or high pass) noise band character (Frijns *et al.*, 1986). Informal listening lets one easily conclude that DRP is the most faint and MPS the most salient dichotic pitch.

In the course of studying dichotic pitch phenomena, we discovered that an essential attribute of dichotic pitches is their lateralizability. In other words: a dichotic pitch has a more or less well-defined binaural image, separated, in general, from the (diffuse) image of the generating dichotic noise itself. With the intrinsic exception of DRP (Bilsen, 1995), the lateral position of a dichotic pitch is dependent on the dichotic stimulus and can be manipulated by the addition of an extra interaural time delay (ITD) to the generating dichotic noise configuration. Systematic experiments were performed for HP, FP, and MPS (Raatgever and Bilsen, 1977, 1986). Further, experiments with HP and MPS (Raatgever, 1980a) indicated that the position of the dichotic pitch percept is only marginally influenced by an interaural intensity difference (IID), the trading ratio being significantly below the upper limit of 40 μs/dB as specified for ''time images'' (Blauert, 1997). It was hypothesized (Bilsen *et al.*, 1978) that a dichotic pitch image behaves like a ''time image'' as defined by Hafter and Jeffress (1968) and colleagues.

Under the supposition that dichotic pitches can be considered as not-unexpected epiphenomena of the processes of binaural interaction that underlie lateralization and binaural signal detection, the study of dichotic pitch phenomena is expected to provide extra information about these mechanisms (e.g., Stern and Trahiotis, 1995). Several models were developed in the past to deal with dichotic pitch phenomena in the context of lateralization and/or binaural signal detection (Durlach, 1962; Fourcin, 1962, 1970; Bilsen and Goldstein, 1974; Bilsen, 1977; Raatgever and Bilsen, 1977, 1986; Klein and Hartmann, 1981; Culling *et al.*, 1998a, b). In the present paper these models will be reconsidered in the light of old and new experiments with different FP configurations, keeping DRP in mind.

Reports on the existence of DRP came from Bilsen (1972, 1995), Bilsen and Goldstein (1974), Warren *et al.* (1981), and Culling (1996). It was not reported by Blodgett *et al.* (1956) although they studied the sidedness of interaurally delayed noise with relatively large interaural delays. Further, its existence was denied by Fourcin (1962, 1964, 1970) and disputed by Hartmann (1996). In contrast, a rather strong sensation of dichotic pitch is observed if two or three

independent interaurally delayed noises are presented simultaneously (Fourcin, 1962, 1964, 1970; Bilsen and Goldstein, 1974; Bilsen and Wesdorp, 1974; Bilsen, 1977).

Recently, we experienced that a special case of FP, i.e., with one noise interaurally delayed in one ear and the second (independent) noise interaurally delayed by about the same amount in the contralateral ear, delivered a very distinct pitch at a well-defined (lateralized) position. It occurred to us that this particular near-symmetric (to be called ''symmetric'') configuration would have special relevance for the ongoing discussion on DRP as well as for the discussion on the validity of different dichotic pitch theories in general. While results of informal listening by 14 subjects for a ''pitched quality'' in a strictly symmetric configuration (with continuously variable delays between 1 and 4 ms) were reported by Fourcin (1962), the novel pitch appeared to manifest itself most clearly for delays above 4 ms. Therefore, we decided to study the symmetric case (with both delays between 4 and 10 ms) and to repeat some measurements on the previously reported (''asymmetric'') case (with one delay smaller than 0.4 ms and the other delay larger than 4 ms) with similar procedures, taking special notice of the pitch value in relation to its lateral position. To this aim, in experiment 1 listening tests were organized such that, for each parameter setting, subjects had to determine in consecutive order both the pitch value by matching with a diotic pitch and the lateralized position of the pitch image by adjusting an ITD pointer (see also Raatgever *et al.*, 1998).

A second experiment was devoted to the question whether an interaural intensity difference (IID) would have a significant influence on the lateralized position of the novel pitch percept. As mentioned above, images of HP, (asymmetric) FP, and MPS were reported to behave as time images. Recent investigations by Grange and Trahiotis (1998) cast doubt on this result, at least for HP. Therefore, in experiment 2 the symmetric stimulus will be investigated for IID dependence using a similar ITD pointer paradigm as in the first experiment.

First, in the next section the DRP stimulus and the different FP configurations, especially the difference between ''symmetric'' and ''asymmetric,'' will be specified and clarified on the basis of the Central Spectrum model[1] (Raatgever and Bilsen, 1986). In the Discussion and the Appendix, the results of the present measurements and earlier results on other FP configurations as reported by Fourcin (1962, 1964, 1970) and Bilsen and Wesdorp (1974) will be summarized, and implications for current theories on dichotic pitch will be discussed.

I. SIGNALS AND THEIR CENTRAL SPECTRA

A successful theoretical concept to predict dichotic pitch values as well as their intracranial positions is the Central Spectrum model (Raatgever and Bilsen, 1986). In essence, based on cochlear frequency analysis and Jeffress' binaural cross correlation network (Jeffress, 1948; Colburn, 1973) it calculates a Central Activity Pattern (CAP) as a function of frequency and internal delay. A central pitch processor scans this CAP for a sharp isolated peak (giving rise to a pure tone like pitch) or a well modulated periodic spectral pattern at a particular internal delay (giving rise to a ''low'' pitch or synonymously: residue pitch, virtual pitch). This pattern selected, the ''Central Spectrum'' (CS) (compare Bilsen, 1977), is claimed to predict the value of the pitch, while the corresponding internal delay determines the perceived lateral position of the pitch image.

A crucial feature of the CS model is the absence of the need for long internal (compare: neural) delays to explain the low pitch values found. The longest internal delay needed depends only on the maximum ITD found in psychophysical experiments on lateralization with conventional signals, and with dichotic pitch images in particular. It is appealing, therefore, to limit the values of the internal delay parameter to the ecologically useful maximum value of about one millisecond for man depending on head size (see, e.g., Blauert, 1997), but also physiological data on neural delays measured could be indicative (see Sec. IV C).

Let it be recalled here that the CS model was devised for qualitative understanding rather than for exact quantitative prediction of central spectra. Detailed physiological and psychophysical knowledge of the peripheral hearing organ is not built in, although peripheral filtering is included formally in the original formulation of the model. Its elegance still is its mathematical simplicity, providing insight with a minimum of calculational effort. Because of its success in the past, and also for didactical reasons, the following calculations again are confined to the idealized case of infinitely sharp frequency analysis. Also temporal jitter in the cross correlation process is not included in detail. The consequences of limited frequency resolution will be addressed in the Discussion, together with the predictions made by other theories.

The selection mechanism for a Central Spectrum to be a serious candidate as predictor of low pitch was not mathematically specified in the original formulation of the model (Raatgever and Bilsen, 1986). The only essential criteria for the result of the scanning process, as described above, to be a CS candidate were (and still are) assumed to be:

(1) periodicity of the peak distance measured along the frequency axis, for one and the same internal delay, and
(2) a large modulation depth in the spectrum selected.

In the present paper, where we deal with the idealized case, the latter requirement will simply be fulfilled by claiming an *infinite peak-to-valley ratio* (or synonymously: an infinite level difference between peaks and valleys on a log scale).

Using Eq. (6) from Raatgever and Bilsen (1986), the Central Activity Pattern (CAP) of an FP stimulus consisting of three independent dichotic noises with interaural delays T_1, T_2, T_3 [a generalization of the special cases studied by Fourcin, 1962; see Figs. 1(a), 1(g), and 1(h)], can be written as

$$\begin{aligned}\mathrm{CAP}(f,\tau_i) = &\{1 \pm \cos(2\pi f T_1 + 2\pi f \tau_i)\} \\ &+ \{1 \pm \cos(2\pi f T_2 + 2\pi f \tau_i)\} \\ &+ \{1 \pm \cos(2\pi f T_3 + 2\pi f \tau_i)\}. \qquad (1)\end{aligned}$$

Note that the function $\mathrm{CAP}(f,\tau_i)$ results from the addition of

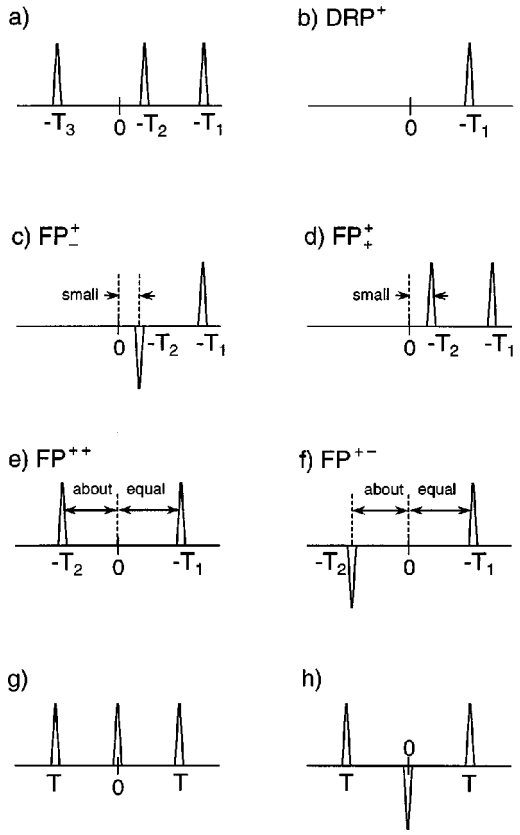

FIG. 1. Schematic wide-band cross-correlation functions indicating signal configurations relevant for dichotic pitch. Panel (a) represents the generalized case of three independent interaurally delayed white noises with delay times T_1, T_2, and T_3 respectively. Panel (b) indicates the specific stimulus (a single interaurally delayed white noise) for the Dichotic Repetition Pitch, symbolized by DRP^+. Panels (c) and (d) indicate the stimulus for the ''asymmetric'' ($T_1 \gg T_2$) Fourcin Pitch (aFP), symbolized by FP^+_- and FP^+_+, respectively. Panels (e) and (f) indicate the ''symmetric'' ($T_1 \approx -T_2$) Fourcin Pitch (sFP), symbolized by FP^{++} and FP^{+-}, respectively. Panels (g) and (h) represent special cases of (a) as originally explored by Fourcin (1962).

three power terms (within curly braces) for the three (uncorrelated) noises. The delays T_1, T_2, and T_3 are taken positive if the delay lines are positioned in the signal paths to the right ear. Similarly, the internal delay parameter τ_i is taken positive for a place in the CAP (compare perceived lateralized position) toward the right ear. The $\pm$ sign indicates addition $(+)$ in the case that a dichotic noise source is presented in-phase to both ears [as shown in Fig. 1(a)], and subtraction $(-)$ in case either the left or right ear is fed with the noise 180° phase reversed.

A. The DRP stimulus

In case we have only one noise source [see Fig. 1(b), for the in-phase case], Eq. (1) simplifies to

$$\mathrm{CAP}(f,\tau_i) = 1 \pm \cos(2\pi f T_1 + 2\pi f \tau_i). \tag{2}$$

This expression is relevant for the DRP stimulus, symbolized here by DRP^+ for the in-phase case and DRP^- for the phase-reversed case (not shown). Note that for each value of τ_i a well-modulated cosinusoidal function of frequency is found waxing and waning between 0 and 2, thus with a peak-to-valley ratio equal to infinity. A pitch equal to $\{1/T_1\}$ is predicted for $\tau_i = 0$, but other pitches equal to $\{1/(T_1+\tau_i)\}$ are expected at all possible values of τ_i in $\mathrm{CAP}(f,\tau_i)$.

This implies that no pitch at all would be predicted to be perceivable due to mutual competition of an infinite number of candidate spectra. The historical reports of only one faint pitch corresponding to $\{1/T_1\}$ in the in-phase case (or to two ambiguous pitches in the phase-reversed case) positioned in the center of the head ($\tau_i = 0$) are explained by the CS model only if strong prevalence for $\tau_i = 0$ would be assumed. Other data on dichotic pitch, but also on lateralization with conventional stimuli (e.g., Mossop and Culling, 1998) plead against such an assumption.

B. The asymmetric configuration and aFP

In case we have two instead of one noise source, the unlimited number of candidate cosine spectra with the DRP stimulus is reduced to only a few. For example, in the case of Fig. 1(c), Eq. (1) simplifies to

$$\mathrm{CAP}(f,\tau_i) = \{1+\cos(2\pi f T_1 + 2\pi f \tau_i)\} + \{1-\cos(2\pi f T_2 + 2\pi f \tau_i)\}. \tag{3}$$

For an arbitrary value of τ_i, Eq. (3) represents a complex function of frequency. Only for τ_i equal to $-T_2$ does a cosinusoidal function of frequency with an infinite peak-to-valley ratio result. Choosing a small, ecologically realistic value for T_2, a central spectrum follows as

$$\mathrm{CS}(f)_{\tau_i} = 1+\cos 2\pi f(T_1 - T_2), \quad \text{with} \quad \tau_i = -T_2. \tag{4}$$

This predicts a pitch corresponding to $\{1/(T_1-T_2)\}$ at a position lateralized to the left ear corresponding to $\{-T_2\}$. This pitch is known as the (classic) Fourcin Pitch. As $T_2 \ll T_1$, in general, we will call this an ''asymmetric'' FP configuration and we will symbolize its pitch by aFP, or more specifically by FP^+_-, to indicate the interaural phase. An illustration of the build-up of the CAP and CS for an asymmetric configuration by adding the second uncorrelated power term to the CAP of a DRP stimulus is given in Fig. 2, for the case $T_1 = 8$ ms and $T_2 = 0.2$ ms.

Likewise, for the case of Fig. 1(d) it follows

$$\mathrm{CAP}(f,\tau_i) = \{1+\cos(2\pi f T_1 + 2\pi f \tau_i)\} + \{1+\cos(2\pi f T_2 + 2\pi f \tau_i)\}. \tag{5}$$

Now, if $2\pi f(T_2+\tau_i) = \pm\pi$, and if f is given the value of 600 Hz being the center frequency of the dominant spectral region (Bilsen and Raatgever, 1973), then Eq. (5) generates two central spectra, well-modulated in the dominant region, given by

$$\mathrm{CS}(f)_{\tau_i} = 1+\cos 2\pi f(T_1 - T_2 \pm 0.8\times 10^{-3}), \quad \text{with} \quad \tau_i = -T_2 \pm 0.8\times 10^{-3}. \tag{6}$$

In this case, the pitch (FP^+_+) has two alternative values, one corresponding to $\{1/(T_1-T_2+0.8\times10^{-3})\}$ positioned at an internal delay equal to $\{-T_2+0.8\times10^{-3}\}$ and the other corresponding to $\{1/(T_1-T_2-0.8\times10^{-3})\}$ at $\{-T_2-0.8\times10^{-3}\}$.

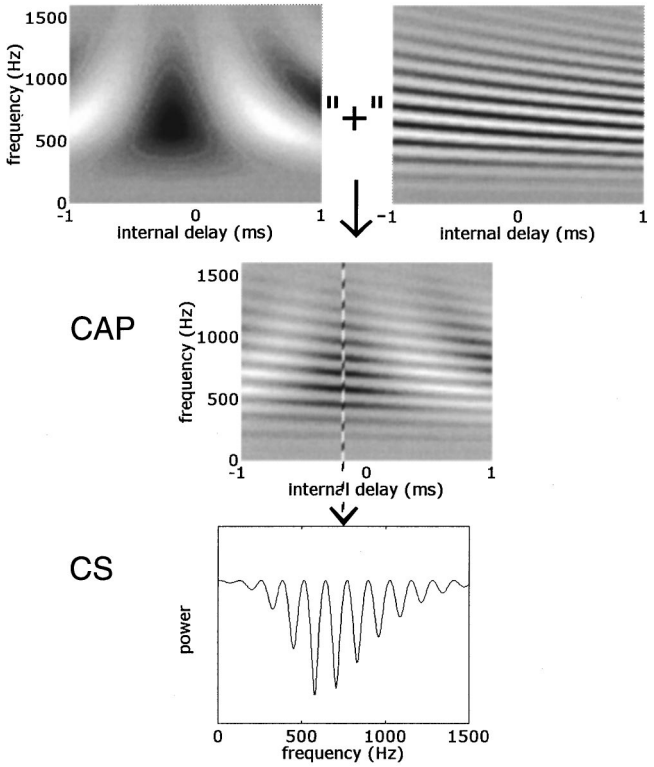

FIG. 2. Illustration of the build-up of the Central Activity Pattern, CAP (middle panel) and the first-candidate Central Spectrum, CS (lower panel) for an aFP stimulus following Fig. 1(c) by ''adding'' the CAP of a white noise with an interaural delay T_1 equal to 8 ms (upper right panel) and the CAP of an independent noise with an interaural delay T_2 equal to 0.2 ms (upper left panel). Power is translated into scales of gray, with white representing high power, and black low power. Frequency weighting (Raatgever, 1980b; Potter *et al.*, 1995) has been applied to the CAP and the CS to emphasize the dominant frequency region; further a logarithmic transformation has been applied in order to enhance differences in the modulation depth.

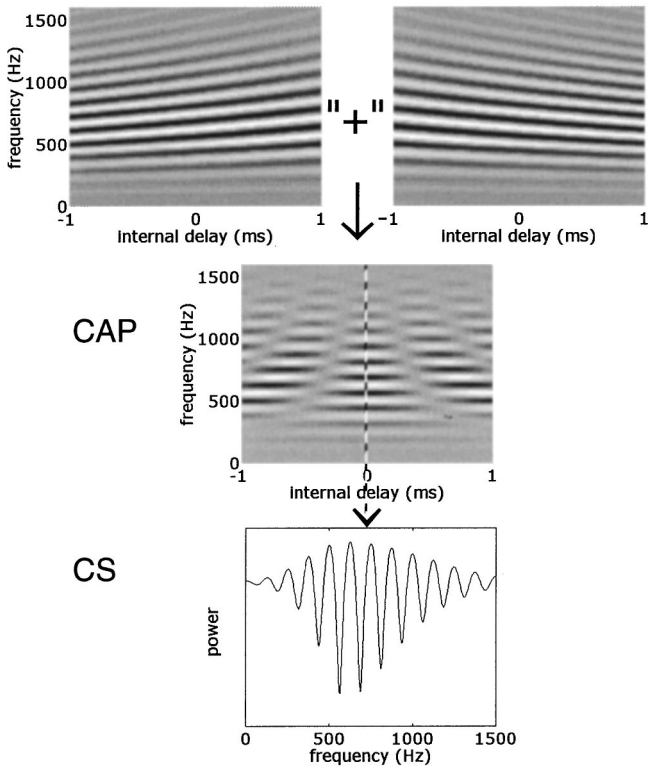

FIG. 3. Illustration of the build-up of the Central Activity Pattern, CAP (middle panel) and the first-candidate Central Spectrum, CS (lower panel) for a sFP stimulus following Fig. 1(e) by ''adding'' the CAP of a white noise with an interaural delay T_1 equal to 8 ms (upper right panel) and the CAP of an independent noise with an interaural delay T_2 equal to -8 ms (upper left panel). Further see legend of Fig. 2.

C. The symmetric configuration and sFP

Now, let us consider the case of Fig. 1(e), where contrary to cases *c* and *d*, the value of T_2 is chosen negative and, in absolute sense, about equal to the value of T_1, thus $T_2 \approx -T_1$. Because of its near-symmetry (i.e., nearly equal delays at opposite ears), we will call this the ''symmetric'' FP stimulus. Then, using the well-known geometric formulas, it makes sense (for reasons following soon) to rewrite Eq. (5) as follows

$$\mathrm{CAP}(f,\tau_i)=2+2\cos\left(2\pi f\frac{T_1+T_2}{2}+2\pi f\tau_i\right)\times\cos\left(2\pi f\frac{T_1-T_2}{2}\right). \tag{7}$$

Again searching for maximum modulation depth and periodicity along the frequency axis for a particular internal delay τ_i (i.e., ''scanning'' the CAP), a cosinusoidal spectrum with infinite peak-to-valley ratio is found if the first cosine term equals 1; thus for $T_1+T_2+2\tau_i=0$, as a first candidate we obtain

$$\mathrm{CS}(f)_{\tau_i}=2+2\cos 2\pi f\left(\frac{T_1-T_2}{2}\right),\quad \text{with}\quad \tau_i=-\frac{T_1+T_2}{2}. \tag{8}$$

Again τ_i should be small, i.e., within ecological limits. Basically, this appears to be the reason that it makes sense to consider the near-symmetry case with $T_2\approx -T_1$. Now, in order to mathematically visualize this near-symmetry, let us substitute $T_2=-(T_1+\Delta T)$ with ΔT small; then we obtain

$$\mathrm{CS}(f)_{\tau_i}=2+2\cos 2\pi f\left(T_1+\frac{\Delta T}{2}\right),\quad \text{with}\quad \tau_i=\frac{\Delta T}{2}. \tag{9}$$

This spectrum is expected to evoke a pitch, symbolized by sFP, or more specifically by FP^{++}, equal to the reciprocal value of $\{T_1+\Delta T/2\}$ at a lateralized position equal to $\{\Delta T/2\}$, i.e., a pitch lower than $\{1/T_1\}$ lateralized toward the right ear if ΔT is positive, or a pitch higher than $\{1/T_1\}$ lateralized toward the left ear if ΔT is negative. An illustration of the build-up of the CAP and CS for the symmetric configuration is given in Fig. 3 for the case of FF^{++} with $T_1=-T_2=8$ ms.

By adding $\pm 2\pi$ to the argument of the first cosine term of Eq. (7), second-candidate spectra are found for $T_1+T_2+2\tau_i\pm 2/f=0$. After substitution of $f=600$ Hz (dominant region) the corresponding pitches follow as $\{1/(T_1+\Delta T/2+0.8\times 10^{-3})\}$ with a lateral position $\{\Delta T/2+0.8\times 10^{-3}\}$ and $\{1/(T_1+\Delta T/2-0.8\times 10^{-3})\}$ at $\{\Delta T/2-0.8\times 10^{-3}\}$.

Similar expressions can be derived leading to different pitches at different positions, if one or both delayed noises are reversed in phase; e.g., for the case of Fig. 1(f) (symbolized by FF^{+-}) a sine spectrum instead of a cosine spectrum is found. Because of its intrinsic inharmonicity, ambiguity of pitch is expected following the ''best harmonic fit in the dominant region'' rule (Bilsen, 1977, Fig. 7; see also Hartmann, 1997, Fig. 15.4).[2] Thus for the case of Fig. 1(f), an ambiguous pitch equal to $\{1/(T_1+\Delta T/2-0.4\times10^{-3})\}$ or $\{1/(T_1+\Delta T/2+1.2\times10^{-3})\}$ is predicted at a lateral position given by $\{\Delta T/2-0.4\times10^{-3}\}$, and an ambiguous pitch of $\{1/(T_1+\Delta T/2+0.4\times10^{-3})\}$ or $\{1/(T_1+\Delta T/2-1.2\times10^{-3})\}$ at a position $\{\Delta T/2+0.4\times10^{-3}\}$.

Adding a third uncorrelated noise source generally has the effect of spoiling the infinite modulation depth of the spectra discussed above. Only in special cases where the delays T_1, T_2, and T_3 are given special values, is infinitely deep modulation or no modulation at all encountered. As an example, in the case of Fig. 1(g), $T_1=T$, $T_2=0$ and $T_3=-T$ [explored qualitatively by Fourcin (1962) for T between 1 and 4 ms], the spectrum found in the middle of the head [compare Eq. (1)] has a peak-to-valley ratio of $6/2=3$ instead of infinity. For the case of Fig. 1(h) an infinite peak-to-valley ratio again is found for $\tau_i=0$.

II. EXPERIMENT 1

To systematically investigate the symmetric Fourcin Pitch with regard to its pitch value and its pitch-image position, an experiment was devised such that subjects should match and report both the pitch value and the lateral position of the pitch image belonging to one and the same percept. We did not aim at exploring the existence region in detail, but the final sessions were performed for those parameter values only that delivered stimuli ''comfortably'' to match. A limited set of measurements only was devoted to the asymmetric Fourcin Pitch as a check, because such measurements have been reported already in the past.

A. Procedure

Continuous FP stimuli were processed in a digital signal processor (Loughborough DSP 96002) implemented in a host-PC configuration. A sample frequency of 20 kHz was used and a (program) code generated by SPW software (ALTA Comdisco) following the schematic of Fig. 1. The two uncorrelated noises were derived from two independent analog Gaussian noise sources, low pass filtered with a cutoff frequency of 5 kHz.

In order to match the perceived pitch, use was made of a diotic MRP stimulus, a stimulus consisting of noise plus its delayed replica fed to the same ear, and having similar pitch and timbre qualities as the pitches investigated; its pitch is given by $f_m=1/T_m$ with T_m being the delay time (e.g., Bilsen, 1977; see also Hartmann, 1997). In order to match the lateral position of a pitch image, use was made of a dichotic white-noise pointer with an interaural delay (ITD) τ_m (like τ_i, τ_m is taken positive for a lateralized position toward the right ear). Stimuli were presented by headphones Beyer DT 770 at a sensation level of 50 dB SL. Subjects were seated in a double-wall sound booth (Amplifon).

An experimental session was controlled by the host-PC and consisted of 25 trials of two matchings each. For the asymmetric FP stimulus, the basic parameter T_1 was given the values 4, 5, 6, 8, or 10 ms (or in terms of pitch: 250, 200, 167, 125, or 100 Hz equivalent), at random for each trial; for each T_1 value, T_2 was given the values -0.4, -0.2, 0, 0.2, or 0.4 ms, also at random. Likewise, for the symmetric FP stimulus, the parameter combination $\{T_1+\Delta T/2\}$ was given the values 4, 5, 6, 8, or 10 ms, at random for each trial; for each $\{T_1+\Delta T/2\}$ value, $\{\Delta T/2\}$ was given the values -0.4, -0.2, 0, 0.2, or 0.4 ms, also at random. The basic parameter values, T_1 and T_2, were chosen accordingly.

Subjects were instructed, for each parameter setting, to first match the lateral position of the pitch image by adjusting τ_m in steps of 0.05 ms, and then to match the pitch itself by adjusting $f_m(=1/T_m)$ in steps of 50, 10, or 1 Hz. They could switch at will between test and match stimuli. To help subjects find FPs that were not easily detected, they could temporarily change the pitch of the FP stimulus by 12% by pressing a key of the control keyboard. Further, subjects were allowed to skip performing a match in case they did not perceive a clear (comfortably to match) pitch. Each subject had to make two matches (pitch image position followed by pitch value) for the 25 different parameter settings in one session, but they were allowed to include a pause in a session at their own convenience. Each subject completed three sessions for FP_+^+, FP^{++}, and FP^{+-}, respectively. Three normal-hearing subjects (ages between 24 and 59) took part in this experiment, two experienced (the present authors) and one briefly trained.

B. Results

A limited set of measurements was performed as a check for aFP, because this pitch has been investigated and reported extensively in the past by the same authors (Bilsen and Goldstein, 1974; Bilsen and Wesdorp, 1974; Bilsen, 1977; Raatgever and Bilsen, 1977). As these former results were concerned with either the pitch value alone or the lateralization of the pitch image alone, with the present procedure we made sure that a matched pitch value and a matched pitch image position belonged together. Therefore, in Fig. 4 averaged pitch matchings for FP_+^+ by the two experienced subjects are given while the position of pitch images is marked by the data point symbols: circles for left images and squares for right images.

The straight solid lines drawn represent the prediction of the CS model as given by the text following Eq. (6). It can be seen that the measured pitch values are predicted correctly, although the fit for the left image is even better if we take 500 Hz (dashed line) instead of 600 Hz as the center frequency of the dominant spectral region. Also the laterality of the pitch image is correctly predicted. Only a few matches (crosses) seem to have laterality opposite to the prediction. This might easily be explained by a flaw in the execution of the procedure, where it cannot be avoided or registered if a subject is matching the image of one pitch and afterward

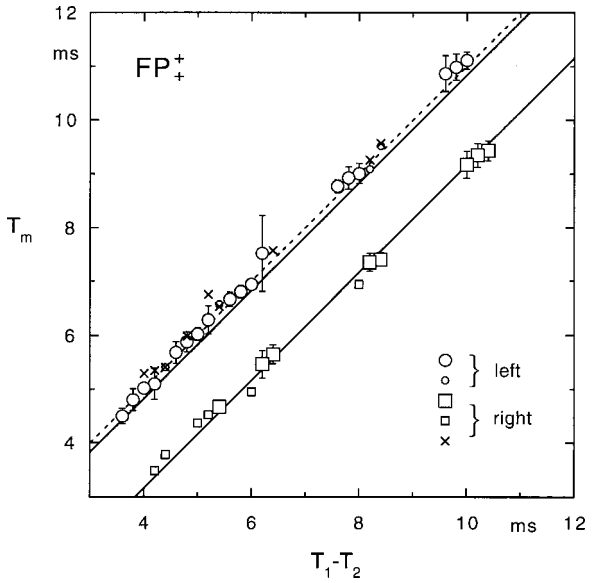

FIG. 4. Averaged pitch matchings of two subjects for the asymmetric Fourcin Pitch, FP^{+}_{+}. The delay time T_m (ms) of a diotic MRP match stimulus is plotted as a function of $\{T_1-T_2\}$. For each $\{T_1-T_2\}$-value maximally eight matches were obtained. Large symbols indicate three or more matches, small symbols two or less. Circles represent matches of a pitch localized toward the left ear, squares those of a pitch localized toward the right ear. Crosses represent ''wrong''-sided matches. Vertical bars represent the standard deviation. The straight lines represent CS predictions following Eq. (6). Likewise, the dashed line for a dominant region chosen at 500 Hz instead of 600 Hz.

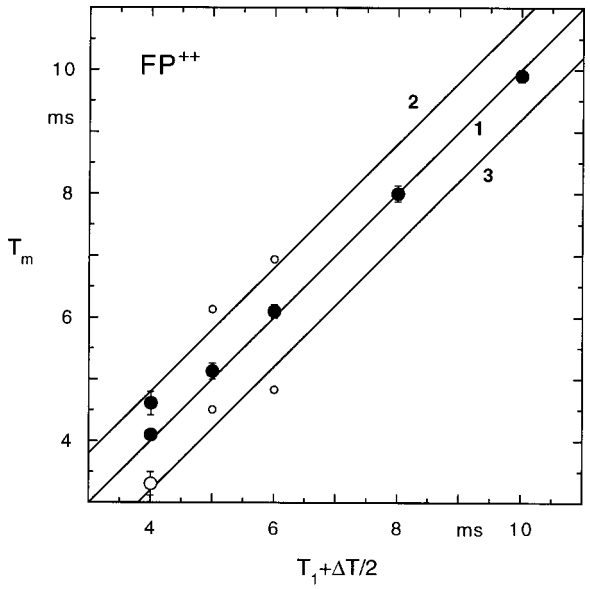

FIG. 6. Averaged pitch matchings of three subjects for the symmetric Fourcin Pitch, FP^{++}. The delay time T_m (ms) of a diotic MRP match stimulus is plotted as a function of $\{T_1+\Delta T/2\}$ (ms) [see text before Eq. (9)]. Closed circles represent more than 15 matches, open circles between 5 and 15, small circles less than 5 matches. Vertical bars represent the standard deviation. The straight line labeled ''1'' represents the CS prediction's first candidate following $\{T_1+\Delta T/2\}$; ''2'' and ''3'' represent secondary candidates following $\{T_1+\Delta T/2+0.8\}$ and $\{T_1+\Delta T/2-0.8\}$, respectively.

matching the value of another pitch, although he was instructed to adhere to the same percept. In conclusion, basically the former results in the literature are confirmed by the present results.

Results for sFP have been summarized in Figs. 5–8. Because the results of the three subjects appeared to agree in every respect, we have plotted their averaged results only. As we aimed at investigating in detail both the pitch value and the laterality of each pitch percept for this new stimulus, the results are plotted in separate figures. In Figs. 5 and 7, data are plotted as a function of $\{\Delta T/2\}$, where lateralization matches are combined for the five different values of $\{T_1$

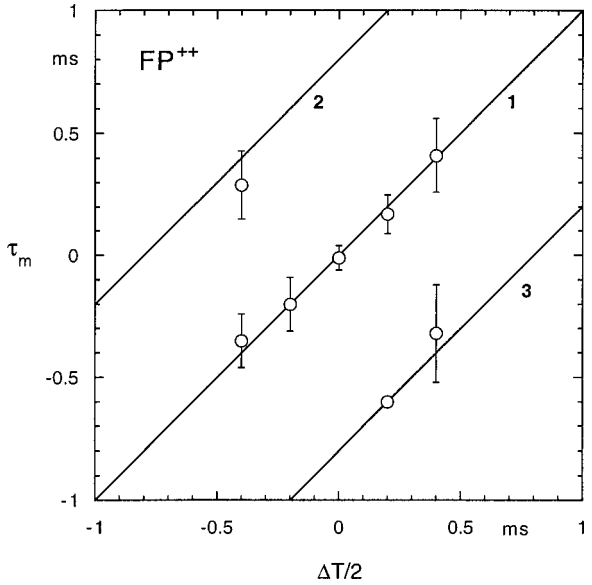

FIG. 5. Averaged pitch-image-position matchings of three subjects for the symmetric Fourcin Pitch, FP^{++}. The interaural delay time τ_m (ms) of a dichotic white noise pointer is plotted as a function of $\Delta T/2$ (ms) [see text before Eq. (9)]. Vertical bars represent the standard deviation. The straight line labeled ''1'' represents the CS prediction's first candidate following $\{\Delta T/2\}$; ''2'' and ''3'' represent secondary candidates following $\{\Delta T/2+0.8\}$ and $\{\Delta T/2-0.8\}$, respectively.

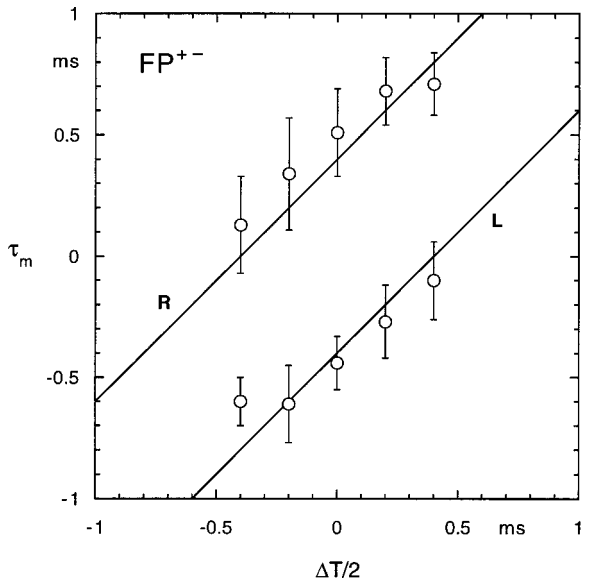

FIG. 7. Averaged pitch-image-position matchings of three subjects for the symmetric Fourcin Pitch, FP^{+-}. The interaural delay time τ_m (ms) of a dichotic white noise pointer is plotted as a function of $\Delta T/2$ (ms) [see text before Eq. (9)]. Vertical bars represent the standard deviation. The straight line labeled ''*R*'' represent the CS prediction's first candidate following $\{\Delta T/2+0.4\}$ for the right image; likewise, ''*L*'' represents $\{\Delta T/2-0.4\}$ for the left image.

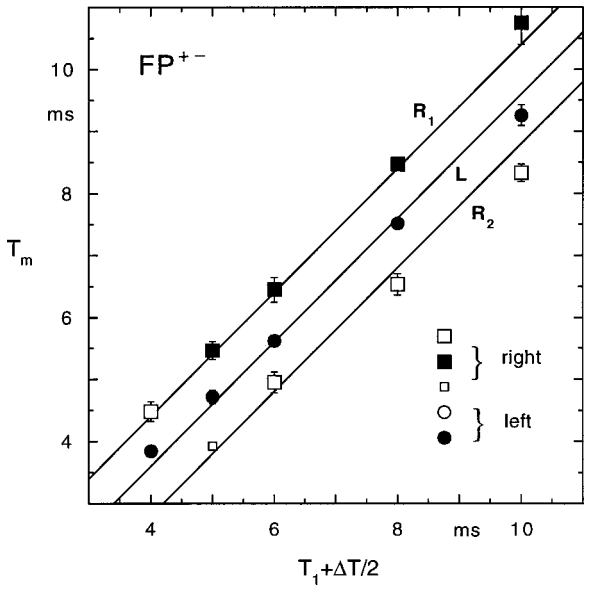

FIG. 8. Averaged pitch matchings of three subjects for the symmetric Fourcin Pitch, FP^{+-}. The delay time T_m (ms) of a diotic MRP match stimulus is plotted as a function of $\{T_1+\Delta T/2\}$ (ms) [see text before Eq. (9)]. Circles represent matches of a pitch percept lateralized towards the left ear; squares, matches towards the right ear. Closed symbols represent more than 15 matches, open symbols between 5 and 15, small symbols less than 5 matches. Vertical bars represent the standard deviation. The straight line labeled ''R_1'' represents the CS prediction's first candidate following $\{T_1+\Delta T/2+0.4\}$ for a pitch perceived at the right ear; likewise, ''R_2'' for the second candidate following $\{T_1+\Delta T/2-1.2\}$. The line labeled L represents the CS prediction's first-candidate pitch following $\{T_1+\Delta T/2-0.4\}$ lateralized at the left ear.

$+\Delta T/2\}$. Likewise, in Figs. 6 and 8, data are plotted as a function of $\{T_1+\Delta T/2\}$, where pitch matches are combined for the five different values of $\{\Delta T/2\}$. Given the procedural constraints the one, two or three data points in each figure belonging to each abscissa value are the result of 45 matches at maximum in total.

The results for FP^{++} are presented in Figs. 5 and 6. Figure 5 represents averaged pitch-image-position matchings expressed by the pointer ITD τ_m. The corresponding pitch values expressed by the MRP delay T_m are represented in Fig. 6. The straight lines labeled ''1,'' ''2,'' and ''3'' represent the prediction by the CS model following Eqs. (7)–(9) (see also figure legend). Both the measured pitch and position values appear to fit the theoretical predictions very closely. Further, notice that the majority of matches (closed circles in Fig. 6; see also figure legend) indeed belong to the first-candidate spectrum predicted by the theory.

The results for FP^{+-} are presented in Figs. 7 and 8. Figure 7 represents averaged pitch-image-position matchings expressed by the pointer ITD τ_m. The corresponding pitch values expressed by the MRP delay T_m are represented in Fig. 8. The straight lines labeled ''L,'' ''R,'' ''R_1,'' and ''R_2'' represent predictions by the CS model following the text after Eq. (9) (see also figure legends). Again the measured pitch and position values appear to fit the theoretical predictions very closely. Also the majority of matches (closed symbols in Fig. 8; see also figure legend) is found to comply with the first-candidate spectrum.

C. Interim discussion

A comparison between the results of experiment 1 and the data by Bilsen and Wesdorp (Bilsen, 1977, Fig. 5) for the in-phase configurations shows some noteworthy points. First, in both studies, no dichotic pitch higher than say 350 Hz (T_m smaller than 3 ms) was reported. Similarly, Bilsen and Goldstein (1974) did not report DRP for interaural delays smaller than 3 ms and the JND in pitch for DRP (Bilsen, 1995) shows a sharp increase below this value accordingly. Introspective listening leads us to believe that 350 Hz may be an upper limit to the frequency of the perceived low (residue) pitch produced by FP and DRP. Given the limited width of the binaural dominant region, the central spectrum apparently displays too few and too broad cosinusoidal peaks to be able to evoke the sensation of low pitch; rather ''colored noise'' is perceived then.

Second, although the Bilsen and Wesdorp experiments comprised parameter settings theoretically relevant for both the asymmetric and symmetric configurations, viz., $T_{1,2}=\pm 2$, ± 3, and ± 4 ms, the novel sFP was not reported. This is easily explained if one realize that on the one hand, in the present study, sFP appears to be comfortably perceivable if $T_{1,2}$ is chosen larger than 4 ms, and on the other hand, in the Bilsen and Wesdorp study, the delay T_2 was kept smaller than 4 ms because for larger values aFP became indistinguishable. In summary, $T_{1,2}=\pm 4$ ms seems to constitute a border between aFP and sFP, whereas introspective listening reveals that both pitch percepts (although faint) exist together at this very border.

With respect to the other extreme, it should be remarked that the value $T_{1,2}=\pm 10$ ms was arbitrarily chosen as a stop to the range of comfortably measurable pitches. It is expected that the lower border of the existence region of Fourcin Pitch will be reached for a larger value coinciding with a transition to Infrapitch (Warren *et al.*, 1981).

III. EXPERIMENT 2

As mentioned in the Introduction, dichotic pitch images have been reported to be sensitive to ITDs mainly. Only very small trading ratios of about 10 μs/dB were reported by Raatgever (1980a) for HP and FP. Accordingly, the CS model does not predict position shifts with IIDs. Only the salience of dichotic pitches is affected by IIDs. In Eq. (1) amplitude factors in one or more of the three power terms will only affect the modulation depth of the resulting central spectra. Recently, however, results of lateralization measurements with HP-like stimuli showing IID sensitivity were reported by Grange and Trahiotis (1996). Therefore, to explore the possible influence of IIDs on the new FP configurations an experiment was performed in which subjects had to match the lateral position of pitch images for stimuli similar to experiment 1, but also with an additional IID of 10 dB.

A. Procedure

Using the same experimental procedure as with experiment 1, subjects matched the (lateralized) position of a dichotic pitch image by adjusting a dichotic noise pointer with ITD equal to τ_m. The matching of the pitch for each stimu-

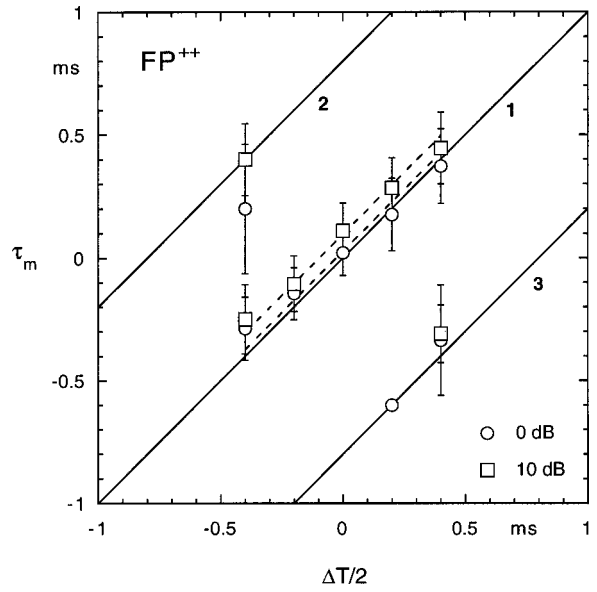

FIG. 9. Averaged pitch-image-position matchings of four subjects for the symmetric Fourcin Pitch, FP^{++}, given a fixed Interaural Intensity Difference (IID). The interaural delay time τ_m (ms) of a dichotic white noise pointer is plotted as a function of $\Delta T/2$ (ms) [see text before Eq. (9)]. Vertical bars represent the standard deviation. Circles represent data points for a 0 dB IID; squares represent a 10 dB IID. The straight line labeled ''1'' represents the CS prediction's first candidate following $\{\Delta T/2\}$; ''2'' and ''3'' represent secondary candidates (see also Fig. 5). The lower dashed line represents the best fit to the circles and the upper dashed line to the squares for a 45-deg straight line.

lus was skipped, as pilot experiments indicated no shift in pitch with IID. An IID of 10 or 0 dB (left ear attenuated), at random from trial to trial, was applied to all stimuli. Four subjects took part in this experiment, the three subjects of experiment 1 and one new briefly trained subject (age 27). Each subject took part in 3 sessions of 30 matchings, with 3 matches for each $\{T_1+\Delta T/2\}$ setting.

B. Results

The results of pitch-position matching for FP^{++} with a fixed IID of 10 dB, averaged over the four subjects, are given in Fig. 9 by open squares. Control measurements with an IID of 0 dB are represented by open circles. Each data point (or couple of data points for each $\{T_1+\Delta T/2\}$ setting) represents a maximum of 36 matches in total. Error bars indicate the standard deviation.

Curves drawn through the measured points represent best fits to a 45-deg straight line, i.e., shifted parallel to the theoretical $\tau_m=\Delta T/2$ curve. A position shift of 27 μs is found for 0 dB IID, and a position shift of 97 μs is found for 10 dB IID. Thus in terms of trading, a trading ratio of 7 μs/dB is obtained. The 0 dB data in Fig. 9 were collected under conditions identical to the data in Fig. 5. That is, the position shift for 0 dB seen in Fig. 5 appears to be approximately 0 μs, yielding a trading ratio of 9.7 μs/dB, very similar to that found by Raatgever (1980a) for asymmetric FP and HP. These are remarkably small values compared to values found in the literature for the time image (Blauert, 1997). In conclusion, an essentially negligable influence of IID is found.

IV. DISCUSSION

Given the existing data on DRP and aFP and the new data on sFP (experiment 1), the predictive power of older and current theories will be discussed. Concepts and models will be presented in historical order. Further, the results on the non-IID dependence of pitch images (experiment 2) will be discussed in the context of recent results in the literature.

A. Wide-band cross correlation

Adopting the spirit, if not the letter, of Licklider's Triplex Theory (Licklider, 1962), Fourcin (1962, 1970) tried to explain his original findings on FP with the wide-band interaural cross-correlation function. Especially the need for two cross-correlation peaks (i.e., a peak pair) to obtain a strong dichotic pitch prompted him to stress the importance of neural delay (cross correlation) and ''comparison patterning.''

With our present extended knowledge of the details of FP, however, the inadequacy of this concept has become manifest for a number of reasons. First, it is unclear how ambiguity of pitch should be predicted from one cross-correlation peak pair, the more so as the peaks have equal polarity. Second, it is not immediately clear how a negative peak [for example, for the stimulus of Fig. 1(c)] should predict a pitch image position corresponding to the image of a single interaurally delayed noise having a positive peak at the same external delay. Third, internal delays as long as 10 ms and longer would be needed to predict low-valued FPs, which is unrealistic from an ecological or physiological point of view. Finally, identical pitch values would be predicted for the symmetric and the asymmetric cases, which is in conflict with the data of the present paper.

Alternatively, one might consider the possible virtues of a ''Summary Cross Correlogram (SCCG),'' to be defined as the result of the ''addition'' of peripherally filtered cross correlation functions, very much in analogy with the Summary Auto Correlogram (SACG) as promoted by Patterson and colleagues (e.g., Yost *et al.*, 1996). As Yost repeatedly showed, the SACG resembles the wide-band autocorrelation function in its main features (e.g., position of first peak). The SCCG resembling the wide-band cross-correlation function likewise, should be expected to be unable to explain dichotic pitch behavior for reasons similar to those mentioned above.

B. The Equalization-Cancellation (EC) model

Using Durlach's Equalization-Cancellation model and his explanation of HP (Durlach, 1962, 1972), Bilsen and Goldstein (1974) calculated a ''central spectrum'' for DRP and gave a qualitative description for FP. They showed that the available DRP data (including ambiguity of pitch) are correctly predicted by the EC model in its addition mode. Also aFP is correctly predicted in addition mode, if the noise with the short delay is presented binaurally phase reversed. The model has to switch to subtraction mode, when the short delay noise is presented binaurally in-phase.

Indeed, Culling *et al.* (1998b) show that to explain the data by Bilsen and Wesdorp (1974) the EC model (coded rE-C or restricted E-C by Culling and his colleagues) requires different operations to predict different cases. How-

ever, they conclude that it is not clear how the model would select the appropriate operation each time. It may be added that the model is in more trouble if only one mode of operation would be allowed, i.e., interaural time delay for equalization and subtraction for cancellation, as in Durlach's (1972) final version of the model.

Regarding the lateralization of pitch images, the EC model does not provide any direct prediction. Only the interaural delay needed in the cancellation process could possibly be extracted as an indicator for pitch-image position. But given this possibility, we still are faced with the problem that multiple images are not predicted, because the EC model is intended to give only one unique solution for one stimulus configuration. Moreover, it can be shown that correct prediction of both pitch value and pitch-image position would always call for addition instead of substraction in the cancellation process.

Finally, the present results with the novel FP are not predicted by the EC model, simply because equalization by interaural delay always recovers the difference between the two delays (needed basically to predict aFP), but not the averaged value $\{T_1+\Delta T/2\}$ needed to predict sFP.

C. The Central Spectrum model

As shown in the results section of experiment 1, the CS model (Raatgever and Bilsen, 1986) following the present Eqs. (1)–(9) appears to predict correctly both the pitch values and pitch-image positions, for the sFP as well as the aFP conditions considered.

Culling *et al.* (1998b) performed calculations with three versions of the CS model: (1) with infinitely sharp frequency analysis, (2) with time and frequency weighting, and (3) with ROEX filtering, taking notice of central activity patterns generated within an internal delay of ± 1.5 ms. They also included a search algorithm to select central spectra with a large modulation depth. It is worth recalling that they found that the assumption of infinitely sharp frequency resolution [as used in the derivation of the present Eqs. (1)–(9)] seems to have only little influence on predictions of DRP and FP. However, to predict existence regions it will be necessary, of course, to include the properties of the peripheral auditory system as well as possible.

Culling *et al.* (1998b) considered five cases by including three configurations with delays 0 and 4 ms [compare Figs. 1(c) and 1(d)], and two configurations with delays -2 and 2 ms [compare Figs. 1(e) and 1(f)]. They compared their predictions with the data by Bilsen and Wesdorp (1974; see also, Bilsen, 1977, Fig. 5). The latter show the existence of aFPs for both the {0,4} and $\{-2,2\}$ cases. No sFP was reported for the latter case, apparently because its pitch value (500 Hz equivalent) would have been too high (see Sec. II C). Culling and his colleagues concluded that the pitches are predicted relatively well by their implementation of the CS model for the {0,4} cases, but not for the $\{-2,2\}$ cases.

A detailed discussion on these five cases can be found in the Appendix, where it is shown that the Bilsen and Wesdorp data are explainable by the present Eqs. (1)–(9), and where arguments are given to solve the disagreement with the predictions by Culling and colleagues. On the one hand, for the two $\{-2,2\}$ cases, pitches theoretically belonging to the new category (sFP) were predicted that had not been measured. On the other hand, for one {0,4} case, the pitch measured (aFP) was not considered predicted correctly, because its predictor along with two other competing candidate pitches had an internal delay outside the ecological range. As suggested in the Appendix, however, this range was chosen too narrow by Culling *et al.* (1998b).

It should be noted that in order to predict aFP for external delays as large as 4 ms in an otherwise symmetric stimulus configuration (Bilsen, 1977, Fig. 5; see also Sec. II C), the CS model following Eq. (6) needs internal delays as large as 3 ms (i.e., {4–0.8} ms), which are largely outside the ecological range. Let it be stressed that such large delays, although they are not essential to explain the stronger percepts, are allowed in the 1986 formulation of the CS model. In this context, it is striking that recent studies on spaciousness in room acoustics (Potter *et al.*, 1995) and on binaural detection (van der Heijden and Trahiotis, 1999) show the need for exactly the same rather large internal delay value of about 3 ms. It is even more striking that results from physiological studies in MSO and ICC of cat (Yin and Chan, 1990) show a distribution of coincidence cells (in majority EE-type) having characteristic delays within ± 1500 μs. With a head-diameter ratio between man and cat of about 2, we obtain physiological evidence for the 3 ms needed.

DRP data (Bilsen, 1972, 1995; Bilsen and Goldstein, 1974) reflect a faint dichotic pitch perceived in the middle of the head. At first sight, the value of the pitch and its position seem easily accounted for by the CS model, the central spectrum at internal delay 0 ms being the predictor. Nevertheless, there seems to be a problem for the CS model, because following Eq. (2) it predicts a continuum of pitches with varying internal delay (see also Bilsen, 1995). Such deviating pitches were never reported before and a possible prevalence for the center one is not easily explained. On the other hand, the predicted presence of a continuum of pitches might readily explain the low salience or the difficulty that some listeners have with matching DRP, although in an interval task they are able to observe a shift in ''color.'' Recently, Bilsen (2000; see also Hartmann *et al.*, 1998) using proper dynamic stimulus presentation succeeded in measuring different pitches at different lateralized positions, that appear to follow Eq. (2) closely.

D. A modified EC model

Culling *et al.* (1998b) proposed a modified Equalization-Cancellation (mE-C) model to account for dichotic pitches as illusions of binaural unmasking. Essentially, their model performs an equalization by adjustment of internal delay (and/or level) in each frequency channel (auditory filter) independently. Apparently, many different delays may be involved depending on the dichotic stimulus, instead of the same for all frequency channels as in Durlach's original concept. A mathematical analysis of the mE-C model leads Culling and colleagues to conclude that, for FP stimuli, ''the mE-C model always predicts that when one noise is inverted, a pitch will be heard whose period is equal to the difference in the interaural delays applied to the two noises, and that when

neither noise is inverted the pitch will be related to an odd-harmonic series, whose fundamental has a period which is half the difference between the two interaural delays'' (p. 3537).

For their testing of the mE-C model with the Fourcin Pitch, they considered and correctly predicted five cases, viz., external delays 0 and 4 ms with three combinations of interaural phase, and external delays ± 2 ms with two combinations of interaural phase (the same five cases the CS model was applied to). For these cases, the mE-C predictions of the pitch value appeared to be in agreement with the data by Bilsen and Wesdorp (1974). As mentioned in the foregoing section, these data reflect aFP as expressed by Eqs. (4) and (6). This result, of course, is in agreement with the working of their model as expressed by the above cited rule. However, note that the ± 2 ms cases can be considered representative for sFP as expressed by Eq. (9) also. Following the above cited rule, however, the mE-C model clearly does not (be it for small or large $T_{1,2}$) predict sFP, i.e., a pitch value corresponding to the average of the absolute values of the two interaural delays.

An indirect reason for this failure to predict sFP spectra along with aFP spectra is that the mE-C model, like the original EC model, allows only one unique way of operation, i.e., one ''recovered spectrum'' to arise as a result of optimal cancellation in the different frequency channels. Here the difference with the CS model becomes manifest, the latter allowing any well-modulated central spectrum to be found due to a shift of attention to different internal delays (with the delay chosen being identical for all frequency channels).

Let it be stressed here that the latter aspect, i.e., the experimental fact that a dichotic pitch has a distinct lateralized image, is not dealt with by the mE-C model. Because, unlike with the original EC model, the possibility to extract a single equalization delay as an indicator for laterality, seems essentially absent due to the property of independent equalization in each frequency channel.

For the DRP stimulus, the mE-C model does not produce any recovered spectrum at all. This nonprediction might be considered at odds with the possible existence of a continuum of pitches as predicted by Eq. (2) of the present paper (Bilsen, 2000). On the other hand, it might as well be considered indicative for the extremely low salience of DRP, or the difficulty that some listeners have to perceive or match DRP.

E. IID sensitivity

The data of experiment 2 clearly indicate that the lateral position of sFP is hardly influenced by an IID, the trading ratio found being less than 10 μs/dB. Similar results were found in the past for MPS, HP, and aFP (Bilsen *et al.*, 1978; Raatgever, 1980a). All of these results seem essentially in disagreement, though, with a recent conclusion by Grange and Trahiotis (1996) that, for an HP^+ stimulus and an $N_\pi N_0$ stimulus, the ''lateral position of dichotic pitches can be substantially affected by interaural intensitive differences.''

This disagreement might possibly be explained by differences in the experimental procedures. One difference, although hardly imaginable to be responsible for the disagreement, was the use of an IID pointer in the Grange and Trahiotis study instead of an ITD pointer. Probably more importantly, Grange and Trahiotis presented their stimuli in pulsed condition, i.e., the stimuli were 200 ms long including 20-ms $\cos^2$ ramps, while our present and past results were obtained with stimuli in continuous condition. In the present experiment 2, on purpose, the subject controlled the duration of the stimulus in order to be absolutely sure that he was perceiving the dichotic pitch and matching the position of the pitch image instead of the (different) noise image, the more as the latter being IID sensitive indeed. In the continuous stimulus condition, indeed, one of three subjects in the Grange and Trahiotis study also found that IIDs became virtually ineffective in moving the intracranial position of the dichotic pitch.

The results of experiment 2 confirm the notion that dichotic pitch images behave like time images (Hafter and Jeffress, 1968; Bilsen *et al.*, 1978), as they show hardly any IID sensitivity. In terms of general theory, this implies that percepts like dichotic pitches that arise at the output of the binaural interaction mechanism responsible for the mediation of temporal fine structure, essentially do not seem to be influenced by an IID. In contrast, the noise stimuli that are responsible for these percepts, substantially are affected by an IID. The CS theory is in agreement with this experimental fact: IIDs only affect the modulation depth of central spectra resulting in a decrease of the salience of the pitch, not its value nor its intracranial position.

As a final conclusion, it is tempting to hypothesize that the processing of ITDs and IIDs in general (thus also for ecological stimuli) takes place beyond the level at which dichotic pitches are generated (compare Raatgever, 1980b). Thereby, it seems essential that IIDs only affect the intracranial position of the percept of stimuli that have ''bi-monaural'' or ''bi-monotic'' existence, i.e., of which two near-copies exist at the level of the left and right cochlea. Such stimuli essentially can give rise to two near-identical monotic percepts also, if presented either at the left or right ear alone. A dichotic pitch is unique insofar that it has no near-copy, neither at the cochlear level nor somewhere else at the same level of processing. As a consequence its intracranial position is not essentially affected by IIDs.

V. CONCLUSIONS

A dichotic pitch, known as Fourcin Pitch (FP), is perceived when presenting the left and right ear simultaneously with two independent interaurally delayed white noises. Distinction can be made between the asymmetric Fourcin Pitch (aFP), occurring when one delay is smaller than about 4 ms and the other delay is in the range of 0–10 ms, and a novel pitch: the symmetric Fourcin Pitch (sFP) where both delays are about equal and larger than about 4 ms but at opposite ears. The aFP stimulus has the delays in the paths to either the same or opposite ears; its pitch is typically related to the difference between the two delays (see the literature and the present experiment 1). The sFP stimulus has one delay applied to one ear and the other delay applied to the opposite ear; its pitch is typically related to the average of the absolute values of both delays (experiment 1).

The FP image is perceived in the middle of the head or lateralized toward the left or right ear depending on the parameter condition. The aFP has a lateralized position of which the pointer delay typically relates to the smaller delay of the stimulus. The sFP has a pointer delay typically relating to half the difference between the absolute values of the two delays involved.

The Central Spectrum theory (Raatgever and Bilsen, 1986) is found able to correctly predict both the pitch values and the corresponding lateral positions of the pitch image for all the parameter conditions investigated. Other current theories on dichotic pitch fail to predict pitch values correctly for several parameter conditions, especially those of the symmetric case. Moreover, they do not provide predictions for the lateralized position of the pitch image.

The lateralized position of the perceived FP image is hardly affected by IIDs (experiment 2). The small position shift found is in the order of the trading ratio reported in the literature for the time image with conventional sounds. This result is in agreement with earlier findings on Huggins Pitch (HP) and Multiple Phase Shift pitch (MPS). It is tempting to generally conclude that the integrated processing of ITDs and IIDs takes place beyond the level at which dichotic pitches are generated.

ACKNOWLEDGMENTS

Experiment 1 was performed by Reshma Mungra in fulfillment of her master's degree. Experiment 2 was performed by Collin Franken in partial fulfillment of his master's degree. We are grateful to John Culling, Wesley Grantham, and two unknown reviewers for providing useful suggestions to improve the contents and the readability of the text.

APPENDIX: CASES OF (DIS)AGREEMENT

In this Appendix, it is investigated how well the data by Bilsen and Wesdorp (1974) are predicted by the Central Spectrum model following its implementation by Culling *et al.* (1998b) or the present Eqs. (1)–(9). Table AI summarizes measured and predicted pitches for the cases dealt with by Culling and his colleagues in their Figs. 5 and 6 and their Table I. These are compared with ''first-candidate'' aFP and sFP calculations following equations similar or identical to the present Eqs. (1)–(9) and the corresponding text. Pitch values are given in Hz with the internal delay of the corresponding central spectrum (across-frequency scan) in ms between brackets. Configurations are symbolized by $\{T_1[\pm], T_2[\pm]\}$ where $T_{1,2}$ (in ms) indicates the interaurally applied delay and $[\pm]$ the interaural phase of the noises. As sFPs have not been reported for the chosen configurations, sFP predictions are given in Table AI (between brackets) for as far they are theoretically relevant for explaining Culling's predictions.

One of the ''erroneous'' predictions that prompted Culling and colleagues to reject the CS model is the obvious prediction of a centralized 500 [0.0] pitch for the $\{-2[+], 2[+]\}$ case [compare Fig. 1(e)]. At the time they wrote their article, this pitch had not been measured, although Bilsen and Wesdorp (1974) included this particular parameter condition. At present, this prediction is easily explained by the novel sFP following Eq. (9). The obvious reason that it has not been measured, either by Bilsen and Wesdorp or by the present authors, is its high value of 500 Hz being well above the upper border of dichotic low (residue) pitch (350 Hz; see Sec. II C). The perceived pitches of 204 and 323 Hz instead are readily explained as aFPs of 208 [±2.8] and 312 [±1.2] following Eq. (6). Values comparable to 208 [±2.8] were not predicted by Culling *et al.* because they fell outside the scanning (internal delay) range (±1.5 ms), but there is no obvious reason for the nonprediction of the other values.

Culling's predictions of 302 [−0.3] and 417 [0.4] for the $\{-2[+], 2[-1]\}$ case seem in accordance with the sFP prediction of 312 [−0.4] and 417 [0.4]. However, these values have not been reported by Bilsen and Wesdorp (1974) and, thus they were considered erroneous by Culling and col-

TABLE AI. A compilation of measured and predicted FP data for the five cases studied by Culling *et al.* (1998b). Each configuration is symbolized by $\{T_1[\pm], T_2[\pm]\}$ where $T_{1,2}$ indicate the interaural delay (in ms) and $[\pm]$ the interaural phase of each noise. ''Pitch'' (in Hz) gives the measured FP following the experimental formulas by Bilsen and Wesdorp (1974). ''Culling'' represents predictins by Culling and colleagues following their implementation of the CS model. aFP and sFP follow from the present Eqs. (1)–(9). Each predicted pitch is given in Hz with its position in ms between brackets.

Configuration T_1, T_2 (ms)	Pitch (Hz)	aFP (Hz [ms])	Culling (Hz [ms])	sFP (Hz [ms])
{−2[+],2[+]}	204	208[±2.8]	396[±0.5]	
	323	312[±1.2]	500[0.0]	(500[0.0])
{−2[+],2[−]}		178[−2.8]	290[−0.65]	
	250	250[2.0]	302[−0.3]	(312[−0.4])
		250[−1.2]	417[0.4]	(417[0.4])
		250[−2.8]		
{0[+],4[+]}	204	208[0.8]	214[0.65]	
	323	312[−0.8]	297[−0.65]	
			336[−1.0]	
{0[+],4[−]}		178[0.8]	178[0.8]	
	250	250[±0.8]	248[−0.8]	
			290[−1.35]	
{0[−],4[+]}	250	250[0.0]	250[0,0]	
			346[−1.15]	

leagues. These sFP values were not perceived because they were border cases for the reasons mentioned in the second paragraph of Sec. II C. On the other hand, the perceived pitch of 250 Hz is not predicted by Culling *et al.* (1998b). However, aFP values 250 [−1.2], 250 [2.0], and 250 [−2.8], along with 178 [−2.8] are calculated. Apart from a possible prediction (not shown in their Fig. 6) at [−1.2] in their Fig. 5, such values fell outside the scanning range considered (±1.5 ms).

With the above cases, we should recall the general observation (made already in 1974, but not explicitly reported by Bilsen and Wesdorp) that some FP configurations give rise to ambiguously lateralized percepts having the same (unambiguous) pitch, which sometimes is perceived as a single percept with a broad fused image. Additionally, it should be reminded that ambiguous-pitch configurations in general (thus also monaural ones) not always allow every subject to detect each pitch expected. In the latter case, apparently the triple 250 Hz pitch dominated the single 178 Hz pitch, which was not probable anyway for its large lateralization. Finally, as said before, the Bilsen and Wesdorp experiments aimed at matching the most salient pitch percepts, not at determining the existence region of all possible Fourcin Pitches perceivable.

For the {0[+], 4[+]} and {0[−], 4[+]} case, Culling *et al.* (1998b) concluded the measured and predicted pitches to be in reasonable agreement. Only the {0[+], 4[−]} case was argued to give erroneous predictions. Although given a perceived pitch of 250 Hz (Bilsen and Wesdorp, 1974), they found no reason to prefer the 248 [−0.8] prediction above the others, the more as all scans lie outside the ecological range (taken at ±600 μs). However, without this (unreasonable) limitation, the 250 Hz pitch is readily explained as a double aFP of 250 [0.8] and 250 [−0.8], which appears to have dominated the single 178 [0.8] aFP (unnoticed in 1974). Further, Culling's finding of 178 [0.8] and 248 [−0.8] can be considered in agreement with the CS model.

Finally, inspecting the across-frequency scans extracted from the CAPs in Culling *et al.* (1998b, Fig. 6), it can be readily seen that some erroneous predictions are related to scans with shapes far from optimally resembling a central spectrum typical for low (residue) pitch. Residue-pitch spectra should (in analogy with the general monaural case) preferably show at least two or three equally spaced peaks with optimally equal height and modulation depth. For this reason, the 396 [±0.5] and 290 [−0.65] predictions for the {−2, 2} cases, and also the 290 [−1.35] and 346 [−1.15] predictions for the {0, 4} cases should be considered with some skepticism. Apparently the criterion to detect optimal peak-to-valley ratio worked out such for these scans that nearly singular peaks or irregularly shaped scans got too large a chance to be selected.

In conclusion, the disagreement proclaimed by Culling and colleagues to exist between the experimental data by Bilsen and Wesdorp (1974) and the CS model predictions is shown to be solvable. Thereby, the theoretical description of the novel pitch phenomenon (sFP) plays an important role. But also the existence of an upper border to dichotic (residue) pitch of about 350 Hz has to be taken into account. And, last but not least, for some individual predictions, Culling's scanning (compare: internal delay) range of ±1.5 ms should be broadened to ±2.0 (or ±2.8 ms); such values are still within the range of measurable physiological delays (Yin and Chan, 1990). Anyway, certainly no justification can be found for Culling and colleagues to restrict the range of realistic internal delays to an ecological range with such a small value of ±600 μs.

[1]The notion ''Central Spectrum'' (abbreviated CS) was introduced by Bilsen (1972; see also Bilsen and Goldstein, 1974), and it served as the name for the first version of the CS model (Bilsen, 1977). The notion ''Central Activity Pattern'' (abbreviated CAP) was introduced by Raatgever and Bilsen (1986) to help define the present version of the CS model, including the lateralization aspects. Although Culling *et al.* (1998b) refer to the present CS model as CAP model, we will for historical reasons continue to use the original name.

[2]An alternative way to extract pitch from a Central Spectrum would be based on temporal processing performed on the (resolved) peaks of the Central Spectrum. For example, for monaural MRP and IRN stimuli, Yost *et al.* (1996) have shown that the Summary Auto Correlogram of the (narrow band) autocorrelation functions belonging to the resolved ''harmonics'' reflects the correct pitch values also.

Bilsen, F. A. (**1972**). ''Pitch of dichotically delayed noise,'' in *Hearing Theory 1972*, edited by B. L. Cardozo (I.P.O., Eindhoven), pp. 5–8.

Bilsen, F. A. (**1976**). ''Pronounced binaural pitch phenomenon,'' J. Acoust. Soc. Am. **59**, 467–468.

Bilsen, F. A. (**1977**). ''Pitch of noise signals: evidence for a 'central spectrum,' '' J. Acoust. Soc. Am. **61**, 150–161.

Bilsen, F. A. (**1995**). ''What do dichotic pitch phenomena tell us about binaural hearing,'' in *Advances in Hearing Research*, edited by G. A. Manley, G. M. Klump, C. Köppl, and H. Fastl (World Scientific, Singapore), pp. 334–341.

Bilsen, F. A. (**2000**). ''The case of the missing central spectra,'' in *Common Issues in the Physiology and Psychophysics of Hearing*, edited by A. J. M. Houtsma, A. Kohlrausch, V. F. Prijs, and R. Schoonhoven (accepted).

Bilsen, F. A., and Goldstein, J. L. (**1974**). ''Pitch of dichotically delayed noise and its possible spectral basis,'' J. Acoust. Soc. Am. **55**, 292–296.

Bilsen, F. A., and Raatgever, J. (**1973**). ''Spectral dominance in binaural lateralization,'' Acustica **28**, 131–132.

Bilsen, F. A., and Wesdorp, C. (**1974**). ''Dichotic pitch phenomena and their common basis,'' Proc. 8th Int. Congr. Acoust., London, p. 165.

Bilsen, F. A., Cornelis, J. G., and Raatgever, J. (**1978**). ''On the 'time image' in lateralization,'' J. Acoust. Soc. Am. Suppl. 1 **64**, S36.

Blauert, J. (**1997**). *Spatial Hearing* (MIT Press, Cambridge, MA), pp. 169–172.

Blodgett, H. C., Wilbanks, W. A., and Jeffress, L. A. (**1956**). ''Effect of large interaural time differences upon the judgment of sidedness,'' J. Acoust. Soc. Am. **28**, 639–643.

Colburn, H. S. (**1973**). ''Theory of binaural interaction based on auditory-nerve data. I. General strategy and preliminary results on interaural discrimination,'' J. Acoust. Soc. Am. **54**, 1458–1470.

Culling, J. F. (**1996**). ''Dichotic pitches as illusions of binaural unmasking,'' J. Acoust. Soc. Am. **99**, 2515.

Culling, J. F., Summerfield, A. Q., and Marshall, D. H. (**1998a**). ''Dichotic pitches as illusions of binaural unmasking. I. Huggins' pitch and the binaural edge pitch,'' J. Acoust. Soc. Am. **103**, 3509–3526.

Culling, J. F., Marshall, D. H., and Summerfield, A. Q. (**1998b**). ''Dichotic pitches as illusions of binaural unmasking. II. The Fourcin pitch and the dichotic repetition pitch,'' J. Acoust. Soc. Am. **103**, 3527–3539.

Cramer, E. M., and Huggins, W. H. (**1958**). ''Creation of pitch through binaural interaction,'' J. Acoust. Soc. Am. **30**, 413–417.

Durlach, N. I. (**1962**). ''Note on the creation of pitch through binaural interaction,'' J. Acoust. Soc. Am. **34**, 1096–1099.

Durlach, N. I. (**1972**). ''Binaural signal detection: Equalization and Cancellation theory,'' in *Foundations of Modern Auditory Theory*, edited by J. V. Tobias (Academic, New York), Vol. II, pp. 369–462.

Fourcin, A. J. (**1962**). ''An aspect of the perception of pitch,'' Proc. 4th Int. Congr. Phonetic Sciences, Helsinki (Mouton & Co, The Hague), pp. 355–359.

Fourcin, A. J. (**1964**). ''Observations and measurements of central pitch phenomena,'' Proc. Symposium on Models for the Perception of Speech and Visual Form (Boston, MA), pp. 1–4.
Fourcin, A. J. (**1970**). ''Central pitch and auditory lateralization,'' in *Frequency Analysis and Periodicity Detection in Hearing*, edited by R. Plomp and G. F. Smoorenburg (A. W. Sijthoff, Leiden), pp. 319–328.
Frijns, J. H. M., Raatgever, J., and Bilsen, F. A. (**1986**). ''A central spectrum theory of binaural processing. The binaural edge pitch revisted,'' J. Acoust. Soc. Am. **80**, 442–451.
Grange, A. N., and Trahiotis, C. (**1996**). ''Lateral position of dichotic pitches can be substantially affected by interaural intensitive differences,'' J. Acoust. Soc. Am. **100**, 1901–1904.
Hafter, E. R., and Jeffress, L. A. (**1968**). ''Two image lateralization of tones and clicks,'' J. Acoust. Soc. Am. **44**, 563–569.
Hartmann, W. M. (**1996**). ''Almost dichotic repetition pitch,'' Michigan State Psychoacoustics Report **93**, pp. 1–6.
Hartmann, W. M. (**1997**). *Signals, Sound, and Sensation* (AIP Press, Woodbury, NY), pp. 361–376.
Hartmann, W. M., Bilsen, F. A., and Raatgever, J. (**1998**). ''Dichotic pitch. Minutes of the 1998 experiment session,'' Michigan State Psychoacoustics Report **104**, pp. 1–13.
van der Heijden, M., and Trahiotis, C. (**1999**). ''Masking with interaurally delayed stimuli: The use of ''internal'' delays in binaural detection,'' J. Acoust. Soc. Am. **105**, 388–399.
Jeffress, L. A. (**1948**). ''A place theory of sound localization,'' J. Comp. Physiol. Psychol. **61**, 468–486.
Klein, M. A., and Hartmann, W. M. (**1981**). ''Binaural edge pitch,'' J. Acoust. Soc. Am. **70**, 51–61.
Licklider, J. C. R. (**1962**). ''Periodicity pitch and related auditory process models,'' Internat. Audiol. **1**, 11–36.
Mossop, J. E., and Culling, J. F. (**1998**). ''Lateralization of large interaural delays,'' J. Acoust. Soc. Am. **104**, 1574–1579.
Potter, J. M., Raatgever, J., and Bilsen, F. A. (**1995**). ''Measures for spaciousness in room acoustics based on a binaural strategy,'' Acta Acustica **3**, 429–443.
Raatgever, J. (**1980a**). ''Binaural time processing and time-intensity trading,'' in *Psychophysical, Physiological and Behavioral Studies in Hearing*, edited by G. van den Brink and F. A. Bilsen (University Press, Delft), pp. 425–428.
Raatgever, J. (**1980b**). ''On the binaural processing of stimuli with different interaural phase relations,'' Doctoral Dissertation, Delft University of Technology.
Raatgever, J., and Bilsen, F. A. (**1977**). ''Lateralization and dichotic pitch as a result of spectral pattern recognition,'' in *Psychophysics and Physiology of Hearing*, edited by E. F. Evans and J. P. Wilson (Academic, London), pp. 443–453.
Raatgever, J., and Bilsen, F. A. (**1986**). ''A central spectrum theory of binaural processing. Evidence from dichotic pitch,'' J. Acoust. Soc. Am. **80**, 429–441.
Raatgever, J., Bilsen, F. A., and Mungra, R. (**1998**). ''New experiments beyond the traditional fourcin pitch range,'' J. Acoust. Soc. Am. **103**, 2767; Proc. 16th Int. Congr. Acoust., Seattle, Vol. 1, pp. 165–166.
Stern, R. M., and Trahiotis, C. (**1995**). ''Models of binaural interaction,'' in *Hearing*, edited by B. C. J. Moore (Academic, London), pp. 347–386.
Warren, R. M., Bashford, J. A., and Wrightson, J. M. (**1981**). ''Detection of long interaural delays for broadband noise,'' J. Acoust. Soc. Am. **69**, 1510–1514.
Yin, T. C. T., and Chan, J. C. K. (**1990**). ''Interaural time sensitivity in medial superior olive of Cat,'' J. Neurophysiol. **64**, 465–488.
Yost, W. A., Patterson, R., and Sheft, S. (**1996**). ''A time domain description for the pitch strength of iterated rippled noise,'' J. Acoust. Soc. Am. **99**, 1066–1078.

On the role of envelope fluctuation processing in spectral masking

Ralph P. Derleth and Torsten Dau[a)]
Carl-von-Ossietzky Universität Oldenburg, AG Medizinische Physik, Graduiertenkolleg Psychoakustik, D-26129 Oldenburg, Germany

(Received 23 August 1999; revised 15 December 1999; accepted 28 March 2000)

This study examines the role of temporal cues in spectral masking, such as beats and intrinsic envelope fluctuations. Predictions from the modulation-filterbank model developed by Dau *et al.* [J. Acoust. Soc. Am. **102**, 2906–2919 (1997)] are compared to average masking patterns from Moore *et al.* [J. Acoust. Soc. Am. **104**, 1023–1038 (1998)]. In these experiments, tones and narrow-band noises have been used as the signal and the masker, so that all four signal–masker combinations are considered. In addition, model predictions are compared with new experimental data in conditions of notched-noise masking, where the masker consisted of two narrow-band noises whose bandwidth and frequency separation were varied systematically. The model uses a peripheral filtering stage with linear and symmetric Gammatone filters, an adaptation stage that includes a static compressive nonlinearity for stationary input stumuli and a higher sensitivity for envelope fluctuation, and a modulation filterbank that analyzes the output for each peripheral channel. For low and medium masker levels, the model accounts very well for the masking patterns in all signal-masker conditions, as well as for the notched-noise conditions. In contrast, predictions from a version of the model that acts like an energy detector account for only some of the notched-noise data, and generally do not account for the shape of the masking patterns. For a high masker level, the simulations suggest the use of asymmetric filters, with a steeper high-frequency slope than is used in the linear model, consistent with results from previous studies. In addition, several nonlinear effects become apparent at this masker level, which cannot be accounted for by the current model.
 [S0001-4966(00)02707-7]

PACS numbers: 43.66.Ba, 43.66.Dc, 43.66.Mk [SPB]

INTRODUCTION

Spectral masking effects in the human auditory system have been investigated for a long time by many researchers using different psychoacoustic measurement paradigms. Spectral masking is generally used to quantify frequency selectivity in the auditory system. One typical experimental paradigm is the measurement of masking patterns. The amount of masking is plotted as a function of the signal frequency in the presence of a masker with fixed frequency and level. Masking patterns are often used as a tool for estimating the spread of excitation of the masker within the cochlea, where signal threshold is assumed to be directly related to the amount of excitation evoked by the masker at the place corresponding to the signal frequency (e.g., Wegel and Lane, 1924; Fletcher and Munson, 1937; Egan and Hake, 1950; Zwicker, 1956). However, masking patterns have also shown complex features that could not be explained in terms of spread of excitation (e.g., Buus, 1985; Richards, 1994; van der Heijden and Kohlrausch, 1995; Moore *et al.*, 1998). The present paper evaluates the extent to which the processing of temporal envelope fluctuations (i.e., modulations) in the auditory system contributes to spectral masking data.

Masking patterns obtained with sinusoidal or narrow-band noise maskers have been presented in several studies (e.g., Wegel and Lane, 1924; Fletcher and Munson, 1937; Egan and Hake, 1950; Zwicker, 1956; Ehmer, 1959; Greenwood, 1971; Buus, 1985; Mott and Feth, 1986; Zwicker and Fastl, 1990; Moore *et al.*, 1998). These studies show systematic differences between sinusoidal and narrow-band noise maskers. Generally, masking patterns obtained with narrow-band noise maskers are much more regular than those obtained with sinusoidal maskers. Masking patterns obtained with sinusoidal maskers often have nonmonotonicities, i.e., dips and peaks, above the masker frequency. For signals below or just above the masker frequency, masking is less for sinusoidal maskers than for the corresponding narrowband-noise maskers at the same presentation level. More masking is typically found for sinusoidal maskers than for noise maskers when the signal frequency is well above the masker frequency.

Masking patterns are influenced by a variety of complex factors. For example, thresholds may be influenced by the occurrence of combination tones or aural harmonics produced by a peripheral nonlinearity, by beats (envelope fluctuations), and by the ability of the auditory system to ''listen in the dips'' of the masker envelope (e.g., Buus, 1985; Moore and Glasberg, 1987; van der Heijden and Kohlrausch, 1995; Nelson and Schroder, 1996). Suppression, i.e., a reduction in response to the signal in the presence of the masker, may also have a big effect on masking patterns. For masker frequencies well below the signal frequency, it has been suggested that the masking is determined mainly by

[a)]Corresponding author. E-mail: torsten.dau@medi.physik.uni-oldenburg.de

suppression of the signal by the masker, rather than by spread of masker excitation (Kiang, 1974; Delgutte, 1990, 1996; Moore and Vickers, 1997; Oxenham and Plack, 1998; Hicks and Bacon, 1999).

Recently, Moore *et al.* (1998) made a comprehensive comparison among masking patterns obtained with tones and narrow-band (80-Hz wide) noises used as maskers and/or signals. All four masker-signal combinations were tested. The same subjects participated in the different experimental conditions, and the same experimental procedure was used in each condition. Several experiments explored the role of different cues which might influence the shape of the masking patterns. Despite a large interindividual variability in the data, Moore *et al.* (1998) found some general properties of the masking patterns. The shape of the patterns for signal frequencies above and below the masker frequency were determined mainly by the characteristics of the masker rather than the characteristics of the signal. They found that tone maskers produce less masking than noise maskers for frequency separations of 100–250 Hz between the signal and the masker, irrespective of the masker frequency. They also showed that beats between the signal and the masker contributed to the effect of less masking with tone maskers compared to noise maskers both below and above the masker frequency. When the signal frequency was equal to the masker frequency, thresholds were similar for all masker-signal combinations except for the tone masker and noise signal, which gave much lower thresholds. The authors attributed the latter effect to the availability of a within-channel, level-fluctuation cue, which has also been suggested in other studies (e.g., Hellman, 1972; Buus, 1985; Hall, 1997; Verhey *et al.*, 1999). Another major factor influencing the masking-pattern shape on the high-frequency side and at high masker levels has been shown to be the occurrence of combination tones (Greenwood, 1971).

One limitation of the study by Moore *et al.* (1998) is that it still remains unclear to what extent the temporal interactions between signal and masker contribute to the shape of the masking patterns. The present modeling attempts to separate the influence of temporal interactions between signal and masker, combination products, and the statistical properties of the stimuli on the shape of the masking patterns. Model predictions for the conditions measured by Moore *et al.* (1998) are presented on the basis of the processing model suggested by Dau *et al.* (1997a, b). This model has proven successful in predicting data from other experiments such as forward masking (Dau *et al.*, 1996a, b), modulation detection and modulation masking (Dau *et al.*, 1997a, b), and some conditions of comodulation masking release (CMR) (Verhey *et al.*, 1999). The model consists of several processing stages and an optimal detector as the decision device. The first processing stage is the linear Gammatone-filterbank model suggested by Patterson *et al.* (1987), which was originally developed to account for spectral masking data obtained with the notched-noise paradigm (Patterson, 1976). After peripheral filtering, the model includes half-wave rectification and low-pass filtering at 1 kHz (i.e., for high center frequencies only the envelope is processed). To establish an absolute threshold for an auditory signal, the minimal value of the basilar-membrane filtered signal is limited by a constant value (Dau *et al.*, 1996a). This can be interpreted as simulating ''physiological noise'' (Soderquist and Lindsay, 1972). To simulate the adaptive properties of the auditory periphery, the model contains a chain of five consecutive nonlinear feedback loops. Each feedback loop includes a static compressive nonlinearity and a higher sensitivity for fast fluctuations. For a stationary input stimulus, the overall compression within the model is close to logarithmic (for details, see Dau *et al.*, 1996a). With regard to the transformation of signal envelope variations, the adaptation stage transforms rapid input variations (as compared to the time constants of the low-pass filters within the five feedback loops) linearly. The stimuli at the output of the adaptation stage for each channel are then processed by a linear modulation filterbank (Dau *et al.*, 1997a, b). The frequency selectivity for modulation frequency is based on psychoacoustical data from modulation masking and modulation detection studies (Houtgast, 1989; Bacon and Grantham, 1989; Yost *et al.*, 1989; Dau *et al.*, 1997a, b), and motivated by physiological findings (Rees and Møller, 1983; Schreiner and Langner, 1988; Lorenzi *et al.*, 1995). The modulation filterbank stage allows the processing of envelope fluctuations with rates up to about 1 kHz, and enables the model to use beats (in this frequency region) as a detection cue. To model the limit on suprathreshold resolution, an internal noise with a constant variance is added to the output of each modulation filter. The variance of the internal noise was determined to satisfy the 1-dB criterion for level discrimination (Dau *et al.*, 1996a). The internal representation of the stimuli within the model has four dimensions: amplitude, time, modulation center frequency, and (audio) center frequency. The optimal detector calculates the correlation between the internal representation of the current stimulus and a template, which is a stored representation of a stimulus with a supra-threshold signal (Dau *et al.*, 1996a, 1997a).

Since the linear Gammatone filterbank (Patterson *et al.*, 1987) is used as the peripheral filtering stage, the model cannot account for effects associated with the cochlear active process, such as compression, suppression, level-dependent tuning, and combination tones (Yates, 1995). The predictions obtained with the model may therefore offer the possibility to separate the effects caused by beats (between the signal and the masker) and the detection of (intrinsic) envelope fluctuations, and those effects associated with peripheral nonlinearity. The predictions obtained with the modulation-filterbank model are compared with results obtained with a version of the model that acts like an energy-detector model. Energy-detector models have often been used in the literature (e.g., Fletcher, 1940; Patterson and Moore, 1986; Green and Swets, 1966) for describing masked thresholds.

To further explore the role of temporal cues in masking experiments, a second common spectral-masking condition was evaluated by comparing model predictions with new experimental data. Masking by notched-noise maskers consisting of two narrow-band noises was investigated by systematically varying the bandwidth and frequency separation of the noise bands.

I. MASKING PATTERNS FOR SINUSOIDAL AND NOISE MASKERS AND SINUSOIDAL AND NOISE SIGNALS

A. Method

1. Procedure and stimuli

Model predictions were obtained by simulating the measurement procedure described in Moore *et al.* (1998). An adaptive three-interval forced-choice (3IFC) procedure was used. The signal was gated on synchronously with the masker in one of the intervals, chosen randomly. The signal level decreased after three successive correct responses and increased after a single incorrect response (three-down, one-up algorithm). This procedure tracks the signal level corresponding to 79.4% correct. The initial step size was 8 dB. After each two reversals, the step size was halved until the minimal step size of 1 dB was reached. Eight further reversals were obtained, and the threshold was estimated as the mean of the signal levels at the final eight reversals. The mean value of several threshold estimates was used as the ''predicted threshold.'' The criterion to accept the predicted threshold as valid was a standard error of less than 2 dB. In conditions with a tone masker, two or three threshold estimates typically satisfied this criterion, while in conditions with a noise masker, three to five threshold estimates were typically needed.

All stimuli were digitally generated at a sampling frequency of 44.1 kHz with the aid of the signal processing software SI (developed at the University of Göttingen). The stimulus parameters were the same as those in Moore *et al.* (1998). Either a tone or an 80-Hz-wide Gaussian noise was used as the signal and the masker. Both were gated synchronously (10-ms raised-cosine rise/fall times) and had a steady-state duration of 200 ms. Simulated masking patterns for overall masker levels of 45, 65, and 85 dB SPL are shown in this study. The masker center frequency was 1 kHz. Signal frequencies of 0.25, 0.5, 0.75, 0.9, 1.0, 1.1, 1.25, 1.5, 2.0, 3.0, and 4.0 kHz were used. All four masker–signal combinations were tested (**nn**: noise-signal, noise-masker; **nt**: noise-signal, tone-masker; **tn**: tone-signal, noise-masker; **tt**: tone-signal, tone-masker). In the **tt**-condition, a 90-degree phase-shift between signal and masker was chosen while random onset phases were used in all other conditions. In the noise conditions, a noise sample was randomly chosen from a cyclic 1.5-s narrow-band noise for each stimulus presentation. The spectral shaping of the cyclic noise was performed in the frequency domain by setting all components outside the desired frequency range to zero. The generation of the noise bands was different from that in Moore *et al.* (1998), where sinusoids spaced at 5-Hz intervals were added with equal amplitudes, and phases were drawn randomly from a uniform distribution from 0 to 360 degrees. Equal-amplitude noise is somewhat less variable than Gaussian noise (Hartmann, 1987). On the other hand, a different randomly generated noise was used for every stimulus in the Moore *et al.* study, in contrast to the present study in which some correlation existed among the noise bursts because the cyclic noise had a period of only 7.5 times the stimulus duration. It is assumed here that the slight differences in the noise generation between the two studies do not affect the outcome of the simulations.

2. Simulations

Simulations were performed with the modulation-filterbank model by Dau *et al.* (1997a, b). The filter shapes of the Gammatone filters are symmetric on a linear frequency scale and the filter bandwidths are independent of stimulus level. The spacing of the filters was chosen in a way that the filter skirts cross at their −3-dB points. The parallel processing of stimulus information in different peripheral channels enables the model to integrate information across frequency. The use of multiple peripheral channels allows the model to account for effects of off-frequency listening. In the simulations of the present study, all peripheral channels in the range from half an octave below to one octave above the signal frequency are considered. These ranges were chosen to include the majority of the information useful in this task. As a modification of the original model, and as realized in the study of Verhey *et al.* (1999), the center frequency of the highest available modulation filter was restricted to one-quarter of the peripheral channel center frequency, but never exceeded 1 kHz. This is motivated by physiological studies by Langner and Scheiner (1988) who found best modulation frequencies (BMF) in this frequency region (in the inferior colliculus of the cat). In the simulations, the internal representations of the different peripheral channels are appended one after another in an array (see Dau *et al.*, 1997b). The template was calculated as the mean of eight supra-threshold signal representations. As explained in the Appendix, the signal level used to derive the template was determined with an iterative procedure, which ensured nearly optimal detection performance by the model.

It should be emphasized that the same parameter set was used for all model predictions throughout this paper. These model parameters (such as the time constants of the adaptation stage, the scaling of the modulation filter bandwidth, the variance of the internal noise) are the same as those determined in Dau *et al.* (1997a, b). Also, as in all previous simulations with this model, the absolute threshold within the model is assumed to be independent of frequency. For frequencies between 0.25 and 4 kHz (as considered in the present study) this is a good approximation for human thresholds. In the study of Moore *et al.* (1998), the mean absolute thresholds across subjects differed maximally by 10.5 dB across frequency (within 0.25 and 4 kHz). These data are certainly influenced by the characteristics of the earphones and depend on the exact measurement method. While the absolute threshold is of little importance in simultaneous-masking conditions, it plays a significant role if masking is expressed as the difference between the masked and the absolute threshold. This difference, reflecting the amount of masking, was used in the study of Moore *et al.* (1998) and is also used in the simulations of masking patterns in the present study.

Simulations were also run with a modified model, referred to as the ''modulation-low-pass model,'' which only processes the output of the lowest modulation filter in each

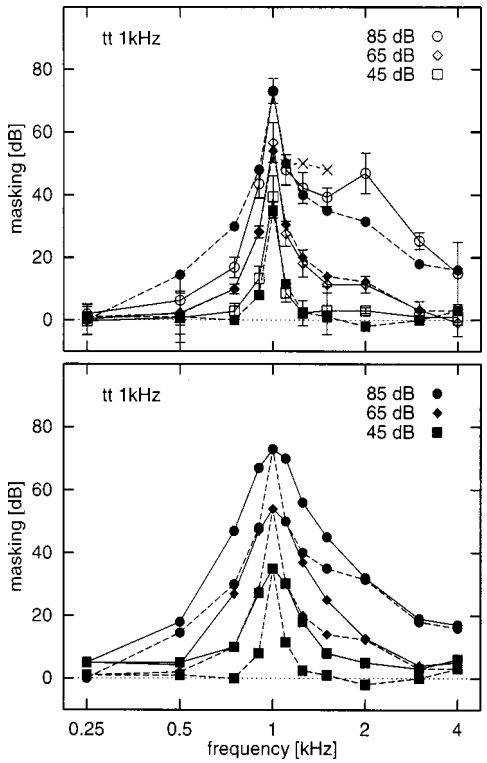

FIG. 1. Masking patterns for the tone-signal tone-masker (**tt**) condition, for masker levels of 85 (circles), 65 (diamonds), and 45 dB SPL (squares). The masker frequency was 1 kHz and the signal frequencies were 0.25, 0.5, 0.75, 0.9, 1.0, 1.1, 1.25, 1.5, 2.0, 3.0, and 4.0 kHz, respectively. The upper panel shows mean experimental data (solid curves with open symbols) for three normal-hearing listeners (replotted from Moore *et al.*, 1998) and predicted data (dashed curves with filled symbols) obtained with the modulation-filterbank model. The crosses show experimental results obtained using an extra low-pass noise to mask combination tones, replotted from Moore *et al.* (1998). The lower panel shows model predictions obtained with the modulation-low-pass model (solid curves with filled symbols). For direct comparison, the simulations from the left panel are replotted (dashed curves with filled symbols).

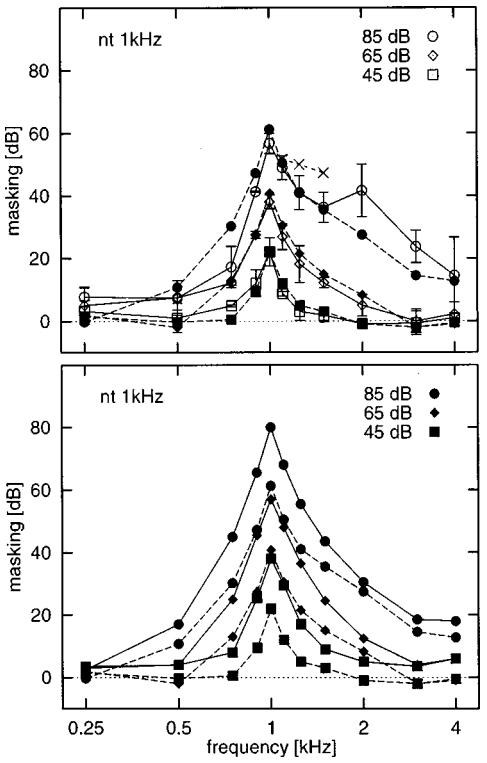

FIG. 2. As in Fig. 1, but for a noise signal and a tone masker (**nt**-condition).

peripheral channel. This modulation filter is a second-order low-pass filter with a cutoff frequency of 2.5 Hz. The output of the lowest modulation filter reflects primarily the overall level of the Gammatone-filtered stimulus, and contains little temporal information because it responds to fluctuations with durations equal to or longer than the stimulus duration. Thus, this processing strategy comes close to an energy-detector model (cf. Dau *et al.*, 1996a, b).

B. Results

Figures 1–4 show the masking patterns for the four signal-masker configurations tested. The masker level was 85 (circles), 65 (diamonds), and 45 dB SPL (squares), respectively. The ordinate represents masking, defined as the difference between masked threshold and absolute threshold at the specific signal frequency. The abscissa indicates signal frequency on a logarithmic scale. The left panels of Figs. 1–4 show mean data for three normal-hearing subjects [solid curves with open symbols, replotted from Moore *et al.* (1998)] together with model predictions (dashed curves with filled symbols) obtained with the modulation-filterbank model. The right panels of Figs. 1–4 show predictions obtained with the modulation-low-pass model (solid curves with filled symbols). For direct comparison, the simulations obtained with the filterbank model are replotted from the left panel (dashed curves with filled symbols).

1. Masking patterns obtained with a tone masker

Figure 1 shows masking patterns for the tone-signal tone-masker (**tt**) condition. The measured data (open sym-

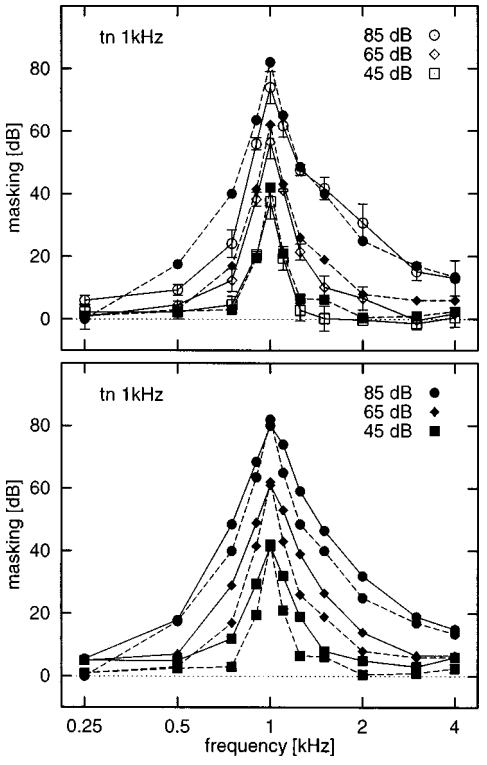

FIG. 3. As in the previous figures, but for a tone-signal and a noise-masker (**tn**-condition).

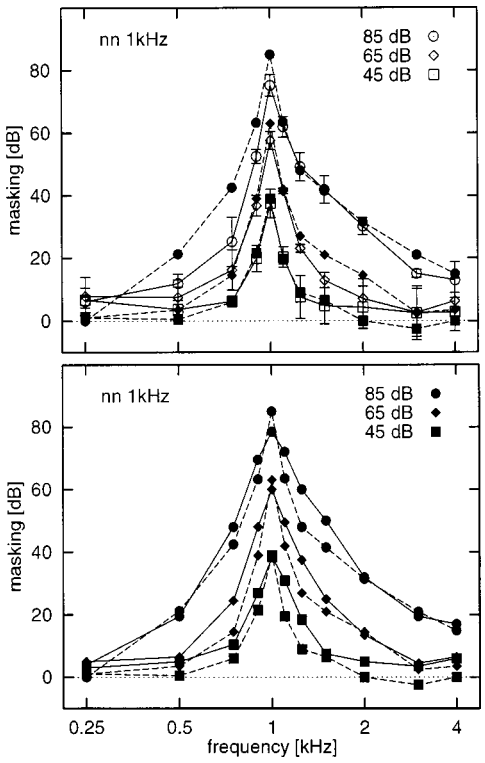

FIG. 4. As in the previous figures, but for a noise-signal and a noise-masker (**nn**-condition).

bols) show a sharp tuning around the masker frequency. Masking decreases with increasing signal-masker frequency separation, except for the signal frequency of 2 kHz at a masker level of 85 dB, where Moore *et al.*'s (1988) masking pattern shows a small peak. For masker levels of 45 and 65 dB, the simulations (filled symbols) agree very well with the experimental data for all signal frequencies tested. Threshold differences are smaller than 5 dB. In particular, the model accounts for the sharp tuning around the masker frequency. Discrepancies between data and simulations primarily occur at the highest masker level: On the low-frequency side, masking is overestimated by 9 and 13 dB at the signal frequencies 0.5 and 0.75 kHz, respectively. On the high-frequency side of the pattern, masking is underestimated by 15 and 8 dB at the signal frequencies 2 and 3 kHz, respectively. In particular, the model does not produce the peak in masking at 2 kHz for the 85-dB masker, which is seen in the experimental data.

The right panel of Fig. 1 shows the masking predicted on the basis of the modulation-low-pass model (solid curves). For equal signal and masker frequency, the amount of masking is the same in both models. No beats occur between signal and masker, only the increase in intensity can be used as a detection cue.[1] The masking predicted by the two models differs by as much as 20, 16, and 10 dB for signal-masker frequency separations of 100, 250, and 500 Hz, respectively, independent of the masker level. For separations $\geqslant$1 kHz the two models yield similar predictions. The masking patterns obtained with the modulation-low-pass model are much broader at all three masker levels than the patterns obtained with the modulation-filterbank model. This suggests that the processing of envelope fluctuations (beats) is most advantageous for signal-masker frequency separations up to 500 Hz. Moore *et al.* (1998) provided experimental evidence that beats play a role for separations up to 250 Hz, while for separations greater than 250 Hz, combination tones play a dominant role (see also Sec. III). Our observation that beats play a role for masker-signal frequency separations up to as much as 500 Hz is based on the differences between the predictions from the two versions of the model, and not on experimental evidence. We cannot exclude that the model overestimates the contribution of beats, at least at frequency separations larger than about 250 Hz (see also Sec. III).

Figure 2 shows results for the noise-signal tone-masker (**nt**) condition. Except for the 1-kHz signal frequency, the shape and absolute values of the listeners' masking patterns are very similar to those for the **tt**-condition (see Fig. 1). At 1 kHz, when the signal and the masker (center) frequencies are equal, the amount of masking is much lower for the noise signal than for the tone signal. Again, at masker levels of 45 and 65 dB, the simulations agree very well with the measured data for all signal frequencies tested. In particular, the model accounts for the reduction in masking (up to 18 dB) when the signal and the masker have the same frequency. A similar observation was made by Hall (1997). He presented evidence that when the signal bandwidth was greater than the masker bandwidth (as for the tone masker and noise signal from the present condition), detection was based on the temporal structure of the stimuli. Conversely, detection was based on the overall energy or level when the signal bandwidth was smaller than the masker bandwidth. As in the **tt**-condition, major differences between the model predictions and the data occur at the masker level of 85 dB SPL. Masking is overestimated by as much as 13 dB at a signal frequency of 0.75 kHz on the low-frequency side of the pattern, while it is underestimated by 14 and 10 dB at signal frequencies of 2 and 3 kHz on the high-frequency side, respectively. The peak in masking observed experimentally at 2 kHz is not produced by the model, similar to the **tt**-condition.

The right panel of Fig. 2 shows the corresponding patterns obtained with the modulation-low-pass model. Masking is increased at almost all signal frequencies compared to the results obtained with the modulation analysis, particularly at frequencies near the masker. For signal-masker separations $\leqslant$500 Hz, threshold differences between the two model predictions amount to 10–20 dB. Within the model, these differences can be attributed to beats between the signal and the masker components, and to the detection of the intrinsic fluctuations of the noise signal. The salience of the beat cue in the signal interval is probably somewhat *reduced* because modulation masking is also involved: All frequency components of the narrow-band noise can produce beats with the signal. Because the largest separation between the beat rates would be 80 Hz (corresponding to the noise-signal bandwidth), the fluctuations due to the beats between the signal and the masker components could mask one another to some extent. The considered temporal detection cues are exploited in the modulation-filterbank model but cannot be used in the modulation-low-pass model. The predictions given in Fig. 2

are comparable to those in the **tt**-condition. Note, however, that in the on-frequency situation of the **nt**-condition, the modulation-filterbank model correctly predicts the empirical threshold which is much lower than in the corresponding **tt**-condition. Within the model this is caused by the intrinsic envelope fluctuations of the noise signal that provide an additional detection cue in the signal interval. This cue is not accessible in the modulation-low-pass model. These intrinsic fluctuations are also the reason for the small threshold differences of 3–4 dB between the models for spectral separations >1 kHz.

2. Masking patterns obtained with a noise masker

Figure 3 shows results for the tone-signal noise-masker (**tn**) condition. The tuning width of the experimental masking patterns (open symbols) is broader than in the **tt**-condition (Fig. 1). For example, for a signal-masker frequency separation of 100 Hz, masking is about 10 dB higher in the **tn**- than in the **tt**-condition. This is the case for all masker levels. On the other hand, for the masker level of 85 dB SPL and signal frequencies $\geqslant$2 kHz, masking is *smaller* than in the **tt**-condition (see Moore *et al.*, 1998), which is also consistent with results from previous studies (e.g., Buus, 1985; van der Hejden and Kohlrausch, 1995). For the masker levels of 45 and 65 dB, the simulations agree very well with the measured data, except for the signal frequency of 1.5 kHz where the model overestimates masking by about 7 and 10 dB, respectively. For the high masker level of 85 dB, the simulations agree very well with the measured data for signal frequencies larger than 1 kHz. Too much masking is predicted on the low-frequency side of the pattern (similar to the results in the previous two conditions), as well as in the on-frequency condition.

The masking patterns obtained with the modulation-low-pass model (solid curves in the right panel of Fig. 3) are broader at all masker levels than the masking patterns obtained with the modulation-filterband model (dotted curves). The two curves differ by up to 12 dB for signal-masker frequency separations $\leqslant$250 Hz. For higher signal-masker frequency separations, the difference in predicted masking decreases with increasing signal frequency. In the on-frequency situation, the two models predict nearly the same masking. The processing of higher-frequency envelope fluctuations is not advantageous within the filterbank model in this condition, i.e., detection depends primarily on the dc-component of the modulation spectrum, which corresponds to the overall energy at the output of the peripheral channels.

Finally, Fig. 4 shows the results for the noise-signal noise-masker (**nn**) condition. The experimental masking patterns (open symbols) are very similar in shape and absolute values to those obtained in the **tn**-condition (Fig. 3). For the lowest masker level, the simulations (filled boxes in the left panel) agree very well with the experimental data at all signal frequencies. For the medium masker level, the agreement is good except for the signal frequencies 1.5 and 2 kHz. At these frequencies, the model overestimates masking by about 8 dB, similar to the **tn**-condition for 1.5-kHz signal frequency. For the high masker level, simulations agree very well for the high-frequency side of the pattern, while masking is overestimated for the low-frequency side of the pattern as well as in the on-frequency condition. The right panel of Fig. 4 shows the differences between the modulation-filterbank model and the modulation-low-pass model. These differences are similar to those found in the **tn**-condition (Fig. 3). In the on-frequency situation of the **nn**-condition, the two models predict the same masking for the lowest masker level. For the medium and high masker levels, the modulation-filterbank model predicts 4.5 and 6.5 dB more masking than the modulation-low-pass model, respectively. These differences result from the specific properties of the adaptation loops in response to stimulus onsets in combination with the model's high sensitivity for envelope fluctuations.[2]

C. Summary of results

In summary, the modulation-filterbank model accounts quantitatively for the sharp masking patterns observed in the **tt**-conditions. The model also accounts for the fact that on-frequency thresholds are similar for all masker-signal combinations except for the noise signal and tone masker (**nt**-condition) in which thresholds were much lower. This ''asymmetry'' of masking between a noise masker with a tone signal and vice versa has been reported previously, and has been explained by within-channel temporal envelope fluctuations introduced by the noise signal (Hellman, 1972; Hall, 1997; Moore *et al.*, 1998). Within the model, the lower thresholds are attributed to the availability of within-channel beats between the signal and the masker, and to the detection of intrinsic envelope fluctuations of the noise signal. Thus, the modulation-filterbank model accounts for both the conditions where detection is mainly based on a change in the overall energy as well as for conditions where temporal cues are used. The combination of the adaptation stage and the modulation filterbank allows for such a processing. The modulation-low-pass model fails in all conditions where temporal cues play a role. While the correspondence between predicted and experimental masking patterns is very good for low and medium masker levels, the model predicts too much masking on the low-frequency side of the pattern for the highest masker level in *all* signal–masker configurations. Also, the model fails to predict the peak on the high-frequency side of the masking pattern in the **tt**- and **nt**-conditions. Some of the differences between data and model predictions may result from nonlinear processing in the auditory periphery: compression and suppression have been proven to influence the shape of masking patterns (Delgutte, 1990; Moore and Vickers, 1997; Oxenham and Plack, 1998; Hicks and Bacon, 1999). Such effects are *not* incorporated within the present model, and will be further discussed in Sec. III.

II. NOTCHED-NOISE MASKING

A well-established method for estimating auditory-filter shape is based on measurement of the threshold of a sinusoidal signal in a notched-noise masker as a function of notch width (e.g., Patterson, 1976; Weber, 1977; Patterson and Nimmo-Smith, 1980; Moore and Glasberg, 1983; Glas-

berg and Moore, 1986, 1990; Dubno and Dirks, 1989; Rosen and Stock, 1989). Most studies used broad noise bands in the notched-noise masker to preclude cues away from the target frequency (e.g., caused by spread of excitation and/or the occurrence of distortion products). In contrast to the experiments from the previous part of this study, temporal cues in these conditions, such as beats between the signal and the spectral components of the masker, probably play a less dominant role since they are masked by the inherent envelope fluctuations of the passbands of the broadband noise. This might be different when the passbands of the noise are narrow. In the present study, experimental data were collected using broadband as well as narrow-band noises as the masker to reveal the role of envelope fluctuations in notched-noise masking conditions. The same model versions as in the previous experiments were used for predicting the data.

A. Method

1. Procedure and subjects

Masked thresholds were measured and simulated using a 3IFC procedure. The masker was presented in three consecutive intervals, separated by silent intervals of 500 ms. In one randomly chosen interval the signal was gated on synchronously with the masker. The subject's task was to specify the interval containing the signal. The threshold was adjusted by a two-down, one-up algorithm (Levitt, 1971), which converges at a signal level corresponding to a probability of being correct of 70.7%. A run was started with the signal level about 20 dB above the expected threshold value. The step size was 8 dB at the start of a run and was divided by 2 after every two reversals of the signal level until the step size reached a minimum of 1 dB, at which time it was fixed. Using the 1-dB step size, ten reversals were obtained and the median value of the signal levels at these ten reversals was used as the threshold value. The subjects received immediate feedback during the measurements. For each subject, the experimental run was repeated three times for each signal configuration. The mean of the threshold estimates was taken as threshold value. Three trained male normal-hearing subjects (audiometric thresholds within 10 dB HL) participated in the experiment, and were between 30 and 33 years old.

2. Apparatus and stimuli

All acoustic stimuli were generated digitally at a sampling frequency of 44.1 kHz. The on-board 16-bit D/A converters of a Silicon Graphics INDY work station were used to transform digital to analog stimuli, which were attenuated with the aid of a programmable amplifier and presented monaurally via headphones (Sennheiser HDA 200) in a single-walled soundproof booth (IAC). Stimulus generation and presentation of trials were controlled by a computer using the signal-processing software package SI. The subjects responded via a PC keyboard.

The masker used in this experiment was a Gaussian noise consisting of two noise bands, separated by a spectral notch that was linearly centered at 1 kHz. The notch width was 0, 100, 300, or 500 Hz in separate conditions. The bandwidth of each noise band was 640, 320, 160, 80, 40, and 20 Hz. Each noise interval had a steady-state duration of 100 ms, and was randomly cut out of a 3-s-long (cyclic) noise waveform to perform a running-noise experiment. Spectral shaping of the noise bands was achieved by setting all components outside the desired frequency range to zero. The signal was a 1-kHz sinusoid with the same duration as the masker. The starting phase of the signal was generated with a 90-degree shift relative to the 1-kHz frequency component of the masker (present only for the 0 notch-width case). Each stimulus was gated with 10-ms $\cos^2$-shaped ramps. The overall level of the masker was 68.5 dB SPL.

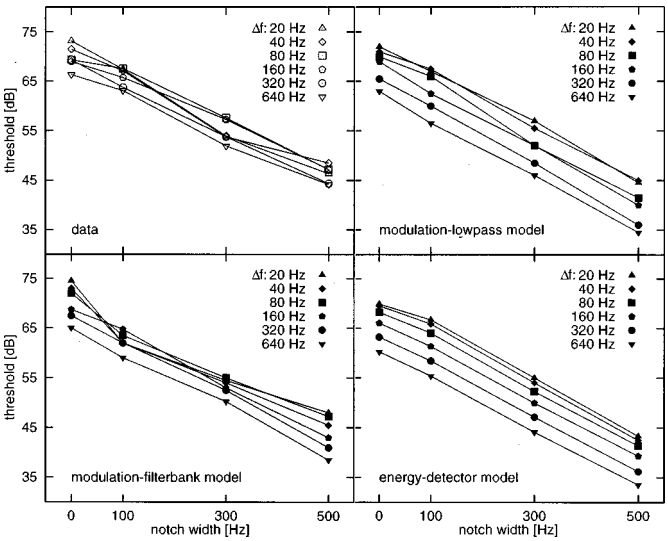

FIG. 5. The masked threshold, obtained with a notched-noise paradigm, is plotted as a function of the notch width. Upper left panel: Mean experimental data for three subjects. Upper right panel: Model predictions obtained with the modulation-filterbank model. Lower left panel: Predictions obtained with the modulation-low-pass model. Lower right panel: Predictions with the simple energy detection model. The bandwidth Δf of the masking noise bands are indicated by the different symbols.

3. Simulations

Simulations were carried out with the same model versions as used in the first experiment (modulation-filterbank model and modulation-low-pass model). As in the first experiment, all peripheral channels in the range from half an octave below to one octave above the signal frequency were considered. The same procedure for deriving the threshold as in the real experiment (two-down, one-up) was used. In addition, the simulations were compared with results obtained with an energy-detector model. This model approach simply calculates the masker energy which falls within the Gammatone filter tuned to the signal frequency.[3]

B. Results

The upper left panel of Fig. 5 shows mean experimental data for three subjects (open symbols). The other panels of Fig. 5 show model predictions (filled symbols) obtained with the modulation-filterbank model (upper right panel), the modulation-low-pass model (lower left panel), and the energy-detector model (lower right panel), respectively. Masked signal thresholds are plotted as a function of the notch width, with masker bandwidth Δf on either side of the notch as the parameter, indicated by the different symbols.

In all panels, thresholds decrease monotonically with increasing notch width. The rate of decrease is about 5 dB/100 Hz in the experimental data (upper left panel), independent of the noise bandwidth. This is consistent with corresponding notched-noise masking data by Patterson (1976) obtained with masker bandwidths larger than 640 Hz. The modulation-filterbank model (upper right panel) accounts well for the shape of the experimental threshold curves. This may not be surprising since the shape of the Gammatone filters was determined by Patterson and Moore (1986) in corresponding notched-noise masking experiments. The predicted thresholds on the basis of the modulation-low-pass model (lower left panel) and the energy-detector model (lower right panel) also decrease with increasing notch width at the same rate as the data. Thus, as assumed, the overall energy at the output of the Gammatone filter centered at the signal frequency accounts for the general shape of the threshold curve versus notch width for each noise bandwidth. Envelope fluctuations produced by beats between the signal and the masker, and the intrinsic fluctuations of the masker do not seem to play a dominant role for the notch-width effect.

However, distinct differences between the different model predictions can be observed for a fixed notch-width. Since the overall masker level was held constant in this experiment, the energy-detector model predicts a 3-dB decrease in threshold per doubling of the noise bandwidth when the frequency range of the noise extends beyond the bandwidth (about 130 Hz) of the Gammatone filter tuned to the signal frequency of 1 kHz. For noise bandwidths $\leqslant$80 Hz, the decrease is less than 3 dB, reflecting the skirt of the Gammatone filter. Very similar results are obtained with the modulation-low-pass model. In contrast to these predictions, the experimental data show an average decrease in threshold of only 1.5 dB per doubling of the noise bandwidth independent of the notch width. The modulation-filterbank model accounts for the less than 3-dB decrease for notch widths of 100 and 300 Hz. In these conditions, signal detection within the modulation-filterbank model is strongly influenced by the inherent masker fluctuations. For notch widths of 0 and 500 Hz, the two models lead to nearly the same predictions.

Overall, the differences across model predictions in this paradigm are much smaller than for the masking patterns described in the previous section. This may indicate that envelope fluctuations, such as beats between the signal and the masker, play a less dominant role in the notched-noise conditions than in the masking conditions with a single noise band.

III. DISCUSSION

The purpose of the present study was to examine the role of temporal cues in experiments commonly associated with spectral masking. Two ''classical'' masking conditions, masking patterns and notched-noise masking, were considered. Data obtained with these experimental paradigms are primarily considered as representing spectral effects explained in terms of the shape of auditory filters, i.e., on the basis of the excitation pattern produced on the basilar membrane. However, as discussed by other authors, the data for various combinations of noises and tones as maskers and signals show differences that cannot be explained solely on the basis of spectral properties (e.g., Gilkey, 1986; Kidd *et al.*, 1989; Richards, 1994; Hall, 1997; Moore *et al.*, 1998). Two model versions were used in the present study to evaluate the contribution of temporal cues in spectral masking: one of them allows the processing of envelope fluctuations by using a modulation filterbank for the output of each peripheral channel, while the other does not allow temporal envelope processing and therefore acts like an energy detector.

In the first part of the study, model predictions were compared with Moore *et al.*'s (1998) experimental masking patterns for sinusoidal and narrow-band noise maskers, and sinusoidal and narrow-band noise signals. For the low and medium masker level, the correspondence between predicted and experimental masking patterns was very good. For the highest masker level, the model predicted too much masking on the low-frequency side of the pattern in all signal–masker configurations. These results, obtained with the linear Gammatone filter whose high-frequency slope is apparently too shallow at high levels, are consistent with earlier findings (Moore and Glasberg, 1987; Glasberg and Moore, 1990; Moore, 1995; Patterson and Irino, 1998), and suggest a level-dependent high-frequency slope. The effects on the high-frequency side of the masking patterns are less clear. Experimental data are different for the noise- and tone-masker conditions which cannot be accounted for by the model on the basis of temporal effects.

The model in its present form does not contain peripheral nonlinearities, and may therefore be expected to be only very limited in its capabilities of predicting masking patterns. There are factors that likely play a significant role in masking, which are not considered by the model. Specifically, peripheral compression and suppression have been shown to influence the shape of masking patterns (Delgutte, 1990; Moore and Vickers, 1997; Oxenham and Plack, 1998; Hicks and Bacon, 1999; Plack and Oxenham, 2000). We might argue that this is not a significant limitation because suppression is not considered in either version of the model (energy detector or envelope processor). As the main goal of our study was to evaluate the relative role of temporal effects in masking, any difference in predictions by the two models can be attributed to temporal effects. However, this might not be the case for compression. Peripheral (and fast-acting) compression is likely to change the shape of the envelope of a fluctuating sound considerably, thus changing the modulation spectrum at the input of the modulation filterbank. The levels of 45 and 65 dB SPL are well within the compression range, so it is surprising that the model accounts so well for the data at these masker levels. Compression also affects the data obtained with a masker level of 85 dB SPL, and this is probably at least part of the reason why the model fails to provide good predictions at this level, particularly on the high-frequency side of the masking patterns.

Another possible explanation for the difference between the data and the model predictions on the high-frequency side of the masking patterns may be the occurrence of combination tones. One would assume that the influence of combination tones should be strongest in the **tt**-conditions (e.g.,

compared to the **nn**-condition), where only two primaries contribute to the (constant) signal power. Moore *et al.* (1998) argued that for masker–signal separations larger than 250 Hz, the dip in the masking pattern is continuous because of combination tones. This was supported by their data, which showed much higher thresholds obtained in the presence of low-pass-filtered noise (with a cutoff frequency of 800 Hz) used to mask the combination tones. The crosses in the left panels of Figs. 1 and 2 of the present study show the mean amount of masking observed by Moore *et al.* (1998) in the presence of the extra low-pass noise. Their experimental data seemed to indicate that the peak observed without the low-frequency noise masker likely results from the *inability* to use combination products $(2f1-f2)$ for larger masker–signal separations. The modulation-filterbank model predicts lower thresholds than the data, although the model does not take combination tones into consideration. However, it is possible that in such a condition, the intrinsic fluctuations of the additional noise interfere with the beats between the signal and the masker due to modulation detection interference (MDI) (e.g., Yost *et al.*, 1989; Dau and Verhey, 1999). This cannot be accounted for by the model since across-channel processing of amplitude modulation is not covered in the current version. One might argue that the increased masking found with the tone masker is due to the occurrence of aural harmonics. However, this appears to be unlikely since the data presented in Moore *et al.* (1998) for masker frequencies other than 1 kHz showed that the peaks in the masking patterns do not usually coincide with an integer multiple of the masker frequency. The interpretation of the high-frequency shape of the masking pattern for high-level tonal maskers remains unclear.

It might be argued that the observed differences between our predictions with the modulation-filterbank model and the modulation-low-pass model may not be used as a measure of the ''real'' contribution of temporal effects since peripheral nonlinearities are not taken into account. In principle, it is possible that human observes and the model obtain similar thresholds by using different detection cues. On the other hand, the linear Gammatone filters have been originally derived from notched-noise masking data at medium levels (Patterson and Moore, 1986). It must be assumed that peripheral nonlinearities also play a significant role in notched-noise masking. The derived filters may therefore be considered as ''effective'' filters which already reflect effects of peripheral nonlinearity on the filter bandwidth (at least for notched-noise stimuli). This might also be the reason why the filters are appropriate for describing the masking patterns from the present study for low and medium levels. The threshold of a signal in simultaneous masking might still be predicted reasonably well by modeling the auditory system as a system of linear filters at these levels.

It has been reported that the individual frequency selectivity of normal-hearing listeners can differ markedly. This variability across subjects was visible in the data by Moore *et al.* (1998). Also, the strength and salience of combination products may be different for the individual listeners because of the different fine-structure of the absolute threshold versus frequency curve (e.g., Long, 1984; Mauermann *et al.*, 1999). Thus, individual masking patterns are probably influenced more strongly by peripheral nonlinearities and the individual shape of the auditory filters than the averaged masking patterns. However, it can be assumed that the temporal information of envelope fluctuations is available to every listener in the same way. Since the Gammatone filters account only for the mean frequency selectivity of normal-hearing listeners, the simulations in the present study should only be compared with averaged data. The results indicate that for low and medium masker levels, detection cues produced by peripheral nonlinearities do not seem to be needed to account for these averaged masking patterns.

In the second part of the study, simulations were compared with new experimental data obtained for notched-noise masking for a variety of notch widths and masking-noise bandwidths. The same modulation-filterbank analysis which accounted for the masking patterns also described the notched-noise data very well. Differences between the modulation-filterbank model and modulation-low-pass model were much smaller than those observed in some of the masking patterns. Both models predicted the rate of decrease of signal threshold with increasing notch width very well. This indicates that an energy-based approach provides a good estimate for the shape of the derived filter, and that envelope fluctuations are a less effective cue than in the masking patterns. However, for a fixed notch width, the modeling results suggest that envelope fluctuations do have an influence. Thresholds obtained with the modulation-filterbank model showed the best agreement with the experimental thresholds, which decreased at a rate less than 3 dB per octave decrease of the noise bandwidth. It is possible that these observed changes in threshold may not be exclusively caused by changes in the fluctuation strength (as suggested by our modeling results). Suppression may also be involved when the noise bands fall beyond the critical band around the signal, and thus an increase of the noise bandwidth could result in more suppression of the signal.

The simulations from the present study showed that a spectro-temporal analysis, rather than a purely spectral analysis, can account for a large range of effects observed with the two measurement paradigms: masking patterns and notched-noise masking. The modulation-filterbank model quantitatively accounts for the sharp masking patterns, as well as for the notched-noise condition from which the peripheral model was derived. Future versions of the model should include a more realistic peripheral filtering stage that reflects level-dependent bandwidth and compression, which might account for the differences between the masking patterns obtained with a noise and tone masker at high levels.

IV. CONCLUSIONS

(i) The modulation-filterbank model suggested by Dau *et al.* (1997a, b) performs a combined spectro-temporal signal analysis, which appears necessary to predict the shape of masking patterns and the results of notched-noise masking. The model accounts for the differences between the masking effects observed with tone and noise maskers and tone and noise signals at low and medium masker levels.

(ii) Within the model, peripheral filtering by the Gammatone filterbank in combination with the processing of envelope fluctuations (such as intrinsic fluctuations and beats between signal and masker) can lead to sharply tuned masking patterns (such as in tone-on-tone masking conditions). The model essentially leads to predictions similar to those of an energy-detector model in conditions where envelope fluctuations are less effective (such as in noise-on-noise and notched-noise masking conditions).

(iii) For low and medium masker levels, the model accounts very well for the masking patterns obtained with narrow-band signals and maskers as well as for notched-noise masking data.

(iv) For high masker levels, an asymmetric peripheral filter with a steeper high-frequency slope than that of the Gammatone filters in the present model should be assumed to account for the shape of the masking patterns. In addition, peripheral nonlinearities that are not included in the current model appear to strongly influence the shape of the patterns obtained with a tone masker.

(v) Future model versions should incorporate more realistic peripheral filtering that includes level-dependent changes of filter bandwidth and compression. Such a model might account for the differences between the masking patterns obtained with a noise and tone masker at high levels.

ACKNOWLEDGMENTS

This work was supported by the Deutsche Forschungsgemeinschaft (DFG KO 942/12, ''Graduiertenkolleg Psychoakustik''). We would like to thank our colleagues of the research group ''AG Medizinische Physik'' and Michael Heinz for helpful comments on an earlier version of this paper. We want to thank Søren Buus and an anonymous reviewer for very constructive and helpful criticism.

APPENDIX: EFFECTS OF TEMPLATE LEVEL

The model version proposed by Dau *et al.* (1996a) derives the template for a threshold estimation at a clearly suprathreshold signal level. It was also pointed out that a more realistic implementation should recompute the template with a decreasing signal level. Such an implementation allows for changes in the detection cue with decreasing level. Subjects presumably would adapt to such changes. In the present study, an iteration procedure provided one possible implementation of such an ''adaptive'' template. Generally, the suprathreshold level for deriving the template was restricted to a range between 30 and 100 dB. Within this range, a suprathreshold level of the template was chosen well above the expected threshold value, which was taken as the measured threshold. Based on this template, a threshold estimate was computed as the first iteration step. For the second iteration step, the suprathreshold level of the template was chosen to be 10 dB above the predicted threshold obtained in the first iteration step. The predicted threshold obtained in the second iteration step was generally lower than the predicted threshold obtained in the first iteration step. Consequently, this iteration was continued until the predicted threshold remained constant, i.e., 10 dB below the template level. Alternatively, the iteration was stopped if the minimal level for deriving the template was reached.

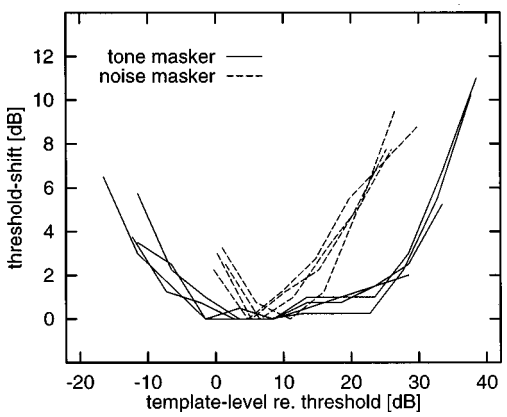

FIG. A1. Influence of the signal level for deriving the template (template level) on the predicted threshold, shown for the tone-masker condition (solid lines) and the noise-masker condition (dashed lines) and a signal (center) frequency of 900 Hz. The ordinate indicates the increase of the predicted threshold while the abscissa indicates the template level relative to the lowest predicted threshold. The different curves represent model predictions for all signal-masker combinations at masker levels of 65 and 85 dB (not indicated individually in the figure).

The adaptation of the template had to be used in the simulation of masking patterns because the predicted threshold depends on the suprathreshold level for deriving the template. This dependency was strongest for signal-masker frequency separations where modulations play an important role within the model. Figure A1 illustrates this dependency both for tone-masker (solid lines) and noise-masker conditions (dashed lines) for a signal frequency of 900 Hz (masker levels: 85 and 65 dB). The shift of the predicted threshold value is shown as a function of the suprathreshold level for deriving the template relative to the lowest predicted threshold.

The lowest threshold estimates are achieved if the level for deriving the template is 5 to 10 dB above the lowest predicted threshold for both noise-masker and tone-masker conditions. The range in which the threshold estimate is relatively independent of the template level is much broader for the tone masker (-5 to 20 dB) than for the noise masker (5 to 15 dB). Outside of these ranges thresholds increase at a rate of approximately 0.5 dB per 1-dB change in template level. The approximate center of this optimal range for both maskers is 10 dB. This value was therefore chosen as the target value of the iterative template adjustment procedure. Generally, the iterative procedure converges to within two to four iteration steps of this desired difference.

[1]A similar experimental condition (Dau *et al.*, 1996a, 1997a) has been chosen for adjusting the variance of the internal noise in the two model versions. The calibration of the model is based on the 1-dB criterion in intensity-discrimination tasks at medium stimulus levels. In the experimental conditions of the present study, the signal-to-masker ratio at threshold is about -7, -6, and -5 dB for the masker levels of 85, 65, and 45 dB SPL, respectively. This corresponds to predicted just noticeable differences

(jnd's) of 0.8, 1.0, and 1.2 dB according to the formula: $\text{jnd} = 10\log_{10}(1 + \Delta I/I)$.

[2]If two narrow-band noise stimuli (such as the signal and the masker in the **nn**-condition) of the same duration, center frequency, bandwidth, and with similar envelopes are added, very large amplitudes can occur at the output of the adaptation loops. In these specific situations, the large onset (as transient) also activates high-frequency modulation channels. For random stimuli, the internal representation of the stimulus is less correlated with the stored (mean) template representation than normal at this signal level, resulting in a higher threshold at the end of the experimental run. This ''artifact'' of the model is much weaker or absent for lower masker levels, and is not found for larger masker bandwidths (Verhey *et al.*, 1999).

[3]Note, in contrast to the simple single-channel energy detector model described here, the modulation-low-pass model (which is also basically an energy-detector model) performs a multi-channel analysis.

Bacon, S. P., and Grantham, D. W. (**1989**). ''Modulation masking: Effects of modulation frequency, depth, and phase,'' J. Acoust. Soc. Am. **85**, 2575–2580.

Buus, S. (**1985**). ''Release from masking caused by envelope fluctuations,'' J. Acoust. Soc. Am. **78**, 1958–1965.

Dau, T., and Verhey, J. (**1999**). ''Modeling across-frequency processing of amplitude modulation,'' in *Psychophysics, Physiology and Models of Hearing*, edited by T. Dau, V. Hohmann, and B. Kollmeier (World Scientific, Singapore), pp. 229–234.

Dau, T., Kollmeier, B., and Kohlrausch, A. (**1997a**). ''Modeling auditory processing of amplitude modulation: I. Detection and masking with narrowband carriers,'' J. Acoust. Soc. Am. **102**, 2892–2905.

Dau, T., Kollmeier, B., and Kohlrausch, A. (**1997b**). ''Modeling auditory processing of amplitude modulation: II. Spectral and temporal integration,'' J. Acoust. Soc. Am. **102**, 2906–2919.

Dau, T., Püschel, D., and Kohlrausch, A. (**1996a**). ''A quantitative model of the 'effective' signal processing in the auditory system. Model structure,'' J. Acoust. Soc. Am. **99**, 3615–3622.

Dau, T., Püschel, D., and Kohlrausch, A. (**1996b**). ''A quantitative model of the 'effective' signal processing in the auditory system. Simulations and measurements,'' J. Acoust. Soc. Am. **99**, 3623–3631.

Delgutte, B. (**1990**). ''Physiological mechanisms of psychophysical masking: Observations from auditory-nerve fibers,'' J. Acoust. Soc. Am. **87**, 791–809.

Delgutte, B. (**1996**). ''Physiological models for basic auditory percepts,'' in *Auditory Computation*, edited by H. L. Hawkins, T. A. McMullen, A. N. Popper, and R. R. Fay (Springer-Verlag, New York), pp. 157–220.

Dubno, J. R., and Dirks, D. D. (**1989**). ''Auditory filter characteristics and consonant recognition for hearing-impaired listeners,'' J. Acoust. Soc. Am. **85**, 1666–1675.

Egan, J. P., and Hake, H. W. (**1950**). ''On the masking pattern of a simple auditory stimulus,'' J. Acoust. Soc. Am. **22**, 622–630.

Ehmer, R. H. (**1959**). ''Masking patterns of tones,'' J. Acoust. Soc. Am. **31**, 1115–1120.

Fletcher, H. (**1940**). ''Auditory patterns,'' Rev. Mod. Phys. **12**, 47–65.

Fletcher, H., and Munson, W. A. (**1937**). ''Relation between loudness and masking,'' J. Acoust. Soc. Am. **9**, 1–10.

Gilkey, R. H., and Robinson, D. E. (**1986**). ''Models of auditory masking: A molecular psychophysical approach,'' J. Acoust. Soc. Am. **79**, 1499–1510.

Glasberg, B. R., and Moore, B. C. J. (**1986**). ''Auditory filter shapes in subjects with unilateral and bilateral cochlear impairments,'' J. Acoust. Soc. Am. **79**, 1029–1033.

Glasberg, B. R., and Moore, B. C. J. (**1990**). ''Derivation of auditory filter shapes from notched-noise data,'' Hear. Res. **47**, 103–138.

Green, D. M., and Swets, J. A. (**1966**). *Signal Detection Theory and Psychophysics* (Wiley, New York).

Greenwood, D. D. (**1971**). ''Aural combination tones and auditory masking,'' J. Acoust. Soc. Am. **50**, 502–543.

Hall, J. L. (**1997**). ''Asymmetry of masking revisited: Generalization of masker and probe bandwidth,'' J. Acoust. Soc. Am. **101**, 1023–1033.

Hartmann, W. M. (**1987**). ''Digital waveform generation by fractional addressing,'' J. Acoust. Soc. Am. **82**, 1883–1891.

Hellman, R. P. (**1972**). ''Asymmetry of masking between noise and tone,'' Percept. Psychophys. **11**, 241–246.

Hicks, M. L., and Bacon, S. P. (**1999**). ''Effects of aspirin on psychophysical measures of frequency selectivity, two-one suppression, and growth of masking,'' J. Acoust. Soc. Am. **106**, 1436–1451.

Houtgast, T. (**1989**). ''Frequency selectivity in amplitude-modulation detection,'' J. Acoust. Soc. Am. **85**, 1676–1680.

Kiang, N. Y.-S. (**1974**). ''Tails of tuning curves of auditory-nerve fibers,'' J. Acoust. Soc. Am. **55**, 620–630.

Kidd, G., Mason, C. R., Brentley, M. A., and Owen, G. A. (**1989**). ''Roving-level tone-in-noise detection,'' J. Acoust. Soc. Am. **86**, 1310–1317.

Langner, G., and Schreiner, C. (**1988**). ''Periodicity coding in the inferior colliculus of the cat. I. Neuronal mechanism,'' J. Neurophysiol. **60**, 1799–1822.

Levitt, H. (**1971**). ''Transformed up-down procedures in psychoacoustics,'' J. Acoust. Soc. Am. **49**, 467–477.

Long, G. R. (**1984**). ''The microstructure of quiet and masked thresholds,'' Hear. Res. **15**, 73–87.

Lorenzi, C., Micheyl, C., and Berthommier, F. (**1995**). ''Neuronal correlates of perceptual amplitude-modulation detection,'' Hear. Res. **90**, 219–227.

Mauermann, M., Uppenkamp, S., van Hengel, P., and Kollmeier, B. (**1999**). ''Evidence for the distortion product frequency place as source of DPOAE fine structure. I. Fine structure and higher order DPOAE in dependence on the frequency ratio $f2-f1$,'' J. Acoust. Soc. Am. **106**, 3473–3483.

Moore, B. C. J. (**1995**). *Perceptual Consequences of Cochlear Damage* (Oxford U. P., London).

Moore, B. C. J., and Glasberg, B. R. (**1983**). ''Suggested formulae for calculating auditory-filter bandwidths and excitation patterns,'' J. Acoust. Soc. Am. **74**, 750–753.

Moore, B. C. J., and Glasberg, B. R. (**1987**). ''Factors affecting thresholds for sinusoidal signals in narrow-band maskers with fluctuating envelopes.'' J. Acoust. Soc. Am. **82**, 69–79.

Moore, B. C. J., and Vickers, D. A. (**1997**). ''The role of spread of excitation and suppression in simultaneous masking,'' J. Acoust. Soc. Am. **102**, 2248–2290.

Moore, B. C. J., Alcántara, J. I., and Dau, T. (**1998**). ''Masking patterns for sinusoidal and narrowband noise maskers,'' J. Acoust. Soc. Am. **104**, 1023–1038.

Mott, J. B., and Feth, L. L. (**1986**). ''Effects of the temporal properties of a masker upon simultaneous masking patterns,'' in *Auditory Frequency Selectivity*, edited by B. C. J. Moore and R. D. Patterson (Plenum, New York).

Nelson, D. A., and Schroder, A. C. (**1996**). ''Release from upward spread of masking in regions of high-frequency hearing loss,'' J. Acoust. Soc. Am. **100**, 2266–2277.

Oxenham, A. J., and Plack, C. J. (**1998**). ''Suppression and upward spread of masking,'' J. Acoust. Soc. Am. **104**, 3500–3510.

Patterson, R. D. (**1976**). ''Auditory filter shapes derived with noise stimuli,'' J. Acoust. Soc. Am. **59**, 640–654.

Patterson, R. D., and Irino, T. (**1998**). ''Modeling temporal asymmetry in the auditory system,'' J. Acoust. Soc. Am. **104**, 2967–2979.

Patterson R. D., and Moore, B. C. J. (**1986**). ''Auditory filters and excitation patterns as representations of frequency resolution,'' in *Frequency Selectivity in Hearing*, edited by B. C. J. Moore (Academic, London), pp. 123–177.

Patterson, R. D., and Nimmo-Smith, I. (**1980**). ''Off-frequency listening and auditory-filter asymmetry,'' J. Acoust. Soc. Am. **67**, 229–245.

Patterson, R. D., Nimmo-Smith, I., Holdsworth, J., and Rice, P. (**1987**). ''An efficient auditory filterbank based on the gammatone function,'' paper presented at a meeting of the IOC Speech Group on Auditory Modelling at RSRE, 14–15 December 1987.

Plack, C. J., and Oxenham, A. J. (**2000**). ''Basilar-membrane nonlinearity estimated by pulsation,'' J. Acoust. Soc. Am. **107**, 501–507.

Rees, A., and Møller, A. R. (**1983**). ''Responses of neurons in the inferior colliculus of the rat to AM and FM tones,'' Hear. Res. **10**, 301–310.

Richards, V. M. (**1994**). ''Experiments related to the detection of a tone masked by another tone,'' J. Acoust. Soc. Am. **95**, 3481–3498.

Rosen, S., and Stock, D. (**1992**). ''Auditory filter bandwidth as a function of level at low frequencies (125 Hz–1 kHz),'' J. Acoust. Soc. Am. **92**, 773–781.

Schreiner, C., and Langner, G. (**1988**). ''Periodicity coding in the inferior colliculus of the cat. ii. topographical organization,'' J. Neurophysiol. **60**, 1823–1840.

Soderquist, D. R., and Lindsay, W. L. (**1972**). ''Physiological noise as a masker of low frequencies: The cardiac cycle,'' J. Acoust. Soc. Am. **52**, 1216–1220.

van der Heijden, M., and Kohlrausch, A. (**1995**). ''The role of envelope fluctuations in spectral masking,'' J. Acoust. Soc. Am. **97**, 1800–1807.

Verhey, L. J., Dau, T., and Kollmeier, B. (**1999**). ''Within-channel cues in comodulation masking release (CMR): Experiments and model predictions using a modulation-filterbank model,'' J. Acoust. Soc. Am. **106**, 2733–2745.
Weber, D. L. (**1977**). ''Growth of masking and the auditory filter,'' J. Acoust. Soc. Am. **62**, 424–429.
Wegel, R. L., and Lane, C. E. (**1924**). ''The auditory masking of one sound by another and its probable relation to the dynamics of the inner ear,'' Phys. Rev. **23**, 266–285.
Yates, G. K. (**1995**). ''Cochlear Structure and Function,'' in *Hearing*, edited by B. C. J. Moore (Academic Press, San Diego), pp. 41–74.
Yost, W. A., Sheft, S., and Opie, J. (**1989**). ''Modulation interference in detection and discrimination of amplitude modulation,'' J. Acoust. Soc. Am. **86**, 2138–2147.
Zwicker, E. (**1956**). ''Die elementaren Grundlagen zur Bestimmung der Informationskapazität des Gehörs,'' Acustica **6**, 356–381.
Zwicker, E., and Fastl, H. (**1990**). *Psychoacoustics—Facts and Models* (Springer-Verlag, Berlin).

Detection of whale calls in noise: Performance comparison between a beluga whale, human listeners, and a neural network

Christine Erbe[a)]
Institute of Ocean Sciences, Acoustical Oceanography, 9860 West Saanich Road, Sidney, British Columbia V8L 4B2, Canada

(Received 11 May 1999; accepted for publication 24 March 2000)

This article examines the masking by anthropogenic noise of beluga whale calls. Results from human masking experiments and a software backpropagation neural network are compared to the performance of a trained beluga whale. The goal was to find an accurate, reliable, and fast model to replace lengthy and expensive animal experiments. A beluga call was masked by three types of noise, an icebreaker's bubbler system and propeller noise, and ambient arctic ice-cracking noise. Both the human experiment and the neural network successfully modeled the beluga data in the sense that they classified the noises in the same order from strongest to weakest masking as the whale and with similar call-detection thresholds. The neural network slightly outperformed the humans. Both models were then used to predict the masking of a fourth type of noise, Gaussian white noise. Their prediction ability was judged by returning to the aquarium to measure masked-hearing thresholds of a beluga in white noise. Both models and the whale identified bubbler noise as the strongest masker, followed by ramming, then white noise. Natural ice-cracking noise masked the least. However, the humans and the neural network slightly overpredicted the amount of masking for white noise. This is neglecting individual variation in belugas, because only one animal could be trained. Comparing the human model to the neural network model, the latter has the advantage of objectivity, reproducibility of results, and efficiency, particularly if the interference of a large number of signals and noise is to be examined.
[S0001-4966(00)01007-9]

PACS numbers: 43.66.Dc, 43.66.Gf, 43.80.Lb [WA]

INTRODUCTION

Acoustic interference of noise with sound signals is an experience of our daily life. Noise obscures or masks signals, making it more difficult or even impossible to detect signals important to us. Masking is defined as the process or amount by which the threshold of audibility for one sound is raised by the presence of another sound.[1] Defining SL_0 as the detection threshold of a signal in the absence of noise (measured in dB) and SL_n as the detection threshold of the same signal in the presence of masking noise, then the masking M is expressed as the shift in threshold[2]

$$M = SL_n - SL_0 \ \text{[dB]}. \tag{1}$$

There are two types of masking: simultaneous masking (when signal and noise occur at the same time) and nonsimultaneous masking (backward masking and forward masking). The physiological processes responsible for masking are very complex and still not fully understood.[3,4] Masking is strongest when signal and noise contain the same or very similar frequencies. The frequency selectivity of the auditory system, i.e., the ability to resolve the sinusoidal components of a complex sound, plays an important role. The mammalian auditory system can generally be represented as a series of overlapping bandpass filters. The critical bandwidth is a measure of the width of the auditory filters;[5] Fletcher hypothesized that at detection threshold, the intensity of the signal equaled the intensity of the noise in the corresponding auditory filter (equal-power assumption).

Our understanding of masking is based on studies of the human auditory system, which have been carried out for many decades. Research on masking in marine mammals is fairly recent. In a few projects the signal and the noise were simple acoustic sounds, such as pure tones and white noise.[6–13] Erbe and Farmer[14] studied masking with underwater sounds as they occur in a marine mammal habitat. With a trained beluga whale, masked hearing data were collected in a go/no-go paradigm according to a titration (staircase) method. The signal was a typical beluga call, frequently used by the population in Maxwell Bay. The noise was icebreaker noise and natural ice-cracking noise. Figure 1 shows power-density spectrograms of the sounds. Bubbler noise was recorded from the bubbler system of the Canadian Coast Guard icebreaker HENRY LARSEN. This system blew high-pressure air into the water in order to push floating ice debris away. Ramming noise was propeller cavitation noise recorded from the same vessel during ice ramming, particularly when an ice ridge withstood the ship's force and stopped the ship despite the propeller still turning at full rpm. Sound of single ice-cracking events caused naturally by local temperature and pressure fluctuations was used for comparison. Results were that bubbler noise masked strongest. The call-detection threshold lay at a critical noise-to-signal ratio, NSR, of 15.4 dB (signal-to-noise ratio (SNR)-15.4 dB). The NSR was chosen over the SNR, because in the original experimental procedure, the noise was the variable and was increased re-

a)Electronic mail: erbec@pac.dfo-mpo.gc.ca

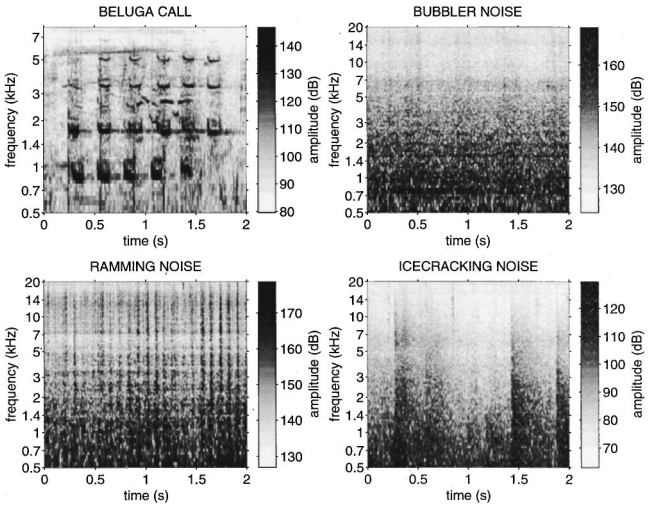

FIG. 1. Power density spectrogram of the beluga call, an icebreaker's bubbler and propeller (ramming) noise, and natural ice-cracking noise in dB *re* 1 μPa^2/Hz @ 1 m. A source level of 160 dB *re* 1 μPa @ 1 m was assumed for the beluga call. The source levels of the noises were respectively 194, 203, and 147 dB *re* 1 μPa @ 1 m.

flected in increasing NSR. Ramming noise followed with a critical NSR of 18.0 dB. Ambient ice-cracking noise masked the least with a critical NSR of 29.0 dB.

Controlled experiments with captive marine mammals are both time- and cost expensive. It would be far more efficient if a fast, ground-truthed model for masking experiments existed. The interference of a large variety of anthropogenic noise with signals used by animals could be studied more easily. The literature on the mathematics of signal detection in noise is vast. A few studies have applied standard techniques to the problem of finding whale calls in noise.[15–18] These studies compared techniques under the aspect of achieving the highest hit rate under the smallest false-alarm rate. Erbe *et al.*[19] compared techniques with respect to the order and level of the maskers as determined by masking experiments with a beluga whale in an earlier study.[14] Various implementations of matched filters, spectrogram cross-correlators, and an artificial neural network detected the same beluga call as the whale in the same three noises, Fig. 1. The neural network, trained with backpropagation,[20] modeled the beluga hearing data best, leading to the same order of masking noises and similar critical NSRs.

The fact that beluga calls and much of the noise in their habitat fall into the hearing range of humans poses the interesting question of whether human listening experiments could substitute for beluga experiments efficiently and with sufficient accuracy. In this article, I compare masked-hearing experiments with human subjects to the earlier beluga experiments[14] using the same signal and noise stimuli. The human results and the neural network developed previously[19] are then used to predict the degree of masking that a fourth type of noise, Gaussian white noise, would have on the beluga call. Performance is compared and rated by going back to the aquarium and measuring masked-hearing thresholds of the beluga whale in white noise.

I. METHODS AND RESULTS

A. Experiments with human subjects

The sounds used in this study were recorded digitally with 16-bit resolution and a sampling frequency of 44 kHz.[14] The beluga call chosen was about 2 s long. A sample of equal length was selected from each of the three noises, bubbler, ramming, and ice-cracking noise. In order to study the relative degree of masking, all four sounds were normalized by their root-mean-square (rms) pressure. Sounds were then digitally mixed by adding their time series according to

$$x[t]=s[t]+\alpha n[t]. \tag{2}$$

Here, $x[t]$ represents a 2-s time series of a mixed sound; $s[t]$ is the 2-s time series of the call; $n[t]$ is the time series of one of the three noises. The factor α denotes the noise-to-signal ratio (NSR). NSRs of 0, 6, 12, 18, 24, 30, and 36 dB were computed. The mixed sounds $x[t]$ were subsequently normalized by their rms pressure. Therefore, for increasing NSR, the noise in a mixed sound would get louder and the call quieter at the same time.

The sounds were digitally stored on a notebook computer. They were converted into analog form by an external soundcard (PORTABLE Sound Plus™ from Digispeech) and amplified by a 20-W audio amplifier (Realistic model MPA-30). Each human subject sat in a quiet room wearing headphones connected to the amplifier. First, the volume control was adjusted such that the normalized sound was comfortably loud. I then determined the call-detection threshold in the absence of noise for each subject using a titration (staircase) method[21] similar to the one described below for the masked-hearing study. This was to ensure that the signal content in mixed sounds with an NSR of 36 dB was at least 6 dB above the pure call-detection threshold. This way, masked-hearing thresholds would not be influenced by the call content dropping below audibility.

Masked-hearing data also were collected in a titration method. The subjects were asked to say ''yes'' when they detected a signal in the noise and ''no'' if they perceived only noise. Subjects received feedback after each trial about whether a signal had been present or absent. Starting with a high call content, mixed sounds were played at increasing NSR in steps of 6 dB as in the early beluga experiment.[14] The subjects were given 2 s to respond. If the subject missed a signal, I stepped back to the previous NSR. If the subject successfully detected a signal, the NSR was stepped down. This staircase method was continued until three consecutive lower reversal points had the same NSR or until the total number of trials exceeded 40. One such staircase was run for each of the three noises; all data were collected in one session. To reinforce the no response and to get information about the subject's response bias, one out of four signals was a catch trial (pure noise). According to the titration procedure, the masked-hearing threshold was calculated as the mean of all (upper and lower) reversal points[21] plus/minus one standard deviation. As is generally done, this ignores the fact that dB is a logarithmic ratio and thus does not give symmetric confidence intervals about the mean. With T_i

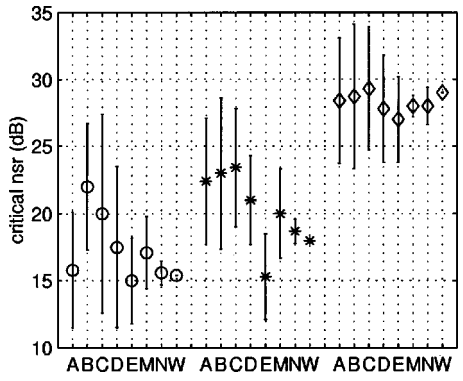

FIG. 2. Masked-hearing thresholds of five human listeners (A, B, C, D, and E) and their mean (M), compared to a neural network[19] (N) and the beluga whale Aurora[14] (W) for a beluga call buried in three types of noise: bubbler (○), ramming (*), and icecracking (◇).

$\pm\sigma_i$ being the threshold of one human subject, the average human threshold $\overline{T}$ was calculated as the weighted mean[22]

$$\overline{T}=\frac{\sum_{i=1}^{5}\frac{T_i}{\sigma_i^2}}{\sum_{i=1}^{5}\frac{1}{\sigma_i^2}}. \tag{3}$$

The standard deviation of the mean threshold was calculated as the average weighted variation of the individual thresholds around the mean[22]

$$\sigma_T=\sqrt{\frac{\sum_{i=1}^{5}\frac{1}{\sigma_i^2}(T_i-\overline{T})^2}{\sum_{i=1}^{5}\frac{1}{\sigma_i^2}}}. \tag{4}$$

Figure 2 summarizes the data for the human subjects and compares them to the neural network[19] and the beluga whale Aurora.[14] Results show that all five human subjects classified the three noises in the same order as the neural network and the whale: Bubbler noise was identified as the strongest masker, followed by ramming, then natural ice-cracking noise. Maximum deviation amongst the human listeners was 8.1 dB in the case of ramming noise. The probability of false alarms was very small for all human subjects. Subjects A and E gave no false alarms for any of the noises. Subject B had false-alarm rates of 0.25, 0, and 0.13 for bubbler, ramming, and ice-cracking noise, respectively. For Subject C, the corresponding values were 0.25, 0, and 0.14; for Subject D, 0.28, 0, and 0. With such ''conservative'' bias, calculated thresholds can be expected slightly shifted towards smaller NSRs than if the subjects had adopted a more ''liberal'' (risky) attitude.

With the exception of Subject B's bubbler threshold and Subject C's ramming threshold, the whale's thresholds lay within one standard deviation of the human thresholds. This indicates that, at least for these types of signal and noise, human experiments could substitute for beluga experiments. The mean plus/minus one standard deviation of the human responses correctly surrounded the beluga thresholds for bubbler and ramming noise. For ice-cracking noise, however, the beluga threshold fell just outside the interval. In fact, the beluga threshold lay at a higher NSR than the mean human threshold. This could indicate that beluga whales can detect their own calls in this type of ambient arctic noise better than the average human. This might point at a masked-hearing specialization of these animals living in a naturally noisy environment. On the other hand, the standard deviation for the mean human ice-cracking threshold was very small, smaller than the deviations for the other two noises. This occurred because of a smaller individual variation for ice-cracking noise. With only five human subjects, this might be coincidental, and testing of further human subjects could change the mean and deviation. Similarly, one would expect an individual variation amongst beluga whales and testing of further animals would allow more solid conclusions.

The neural network's thresholds approached the beluga's thresholds more closely than the human thresholds did. For examining the masking of a large variety of signals and noise, it is thus the more efficient technique. The neural network further poses the advantage of objectivity with its results being reproducible and independent of a potentially changing response bias.

During and after the experiment, all human subjects reported a ''frustration'' with the experimental procedure. The problem identified was that all sounds played had an equal length of 2 s and the call always happened at the same time in the noise. The initial reason for adding signal and noise this way was to fix a phase between them. With signal and noise exhibiting temporally varying spectral characteristics, masking was expected to depend on the time lag between signal and noise. Obviously, in the case of a pulsed signal and a pulsed noise, masking would be minimal if the pulses of the signal happened in between the pulses of the noise, and maximal if the pulses of signal and noise were in phase. Fixing the phase, however, meant that the subjects knew when to expect the signal. For large NSRs and occasionally for pure noise, subjects reported a frustration about the conflict between whether they thought they heard a signal only because their mind knew what it would sound like and when it would happen or whether they actually heard it. I therefore modified the experiment to include two more beluga calls with very different spectral characteristics.[23] Human subjects were asked not to simply say ''yes'' if any signal was detected but to identify which of the three signals was detected. The two subjects tested still had a problem with the procedure, because they perceived all three signals simultaneously at large NSRs or pure noise. It was then decided to modify the experiment such that noise would play continuously and the signal would be injected at random times so subjects did not receive any onset cues.

B. Modified human experiments

The experimental setup differed only slightly from the previous one. Two portable computers were used with the same soundcards. One computer stored 2-s sound files of the beluga call at varying sound-pressure levels. The other computer stored 15 min of pure noise. The analog outputs of the soundcards were connected to the two line-ins of the audio

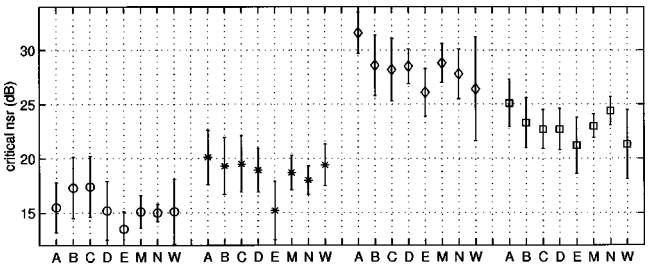

FIG. 3. Masked-hearing thresholds of five human listeners (A, B, C, D, and E) and their mean (M), compared to a neural network (N) and the beluga whale Aurora (W) for a beluga call buried in four types of noise: bubbler (○), ramming (*), icecracking (◇), and Gaussian (□). Modified experimental procedure.

amplifier, which mixed them at a volume ratio of 1:1 and sent a mixed sound to the headphones. Rather than taking a 15-min noise recording, the 15-min noise files were created by repeating the previous 2-s noise file 450 times. This way, no matter when the call happened in the noise, the NSR defined as the ratio of rms voltages was constant over the 2-s duration of the call. NSRs varied in steps of 3 dB, yielding a less coarse analysis than with the previous 6 dB. A fourth type of noise, Gaussian white noise, was created digitally and assigned the same bandwidth of 22 kHz as the other three noises. While the noise played continuously, beluga calls were inserted according to a titration method starting out with a loud volume and decreasing until the human missed a signal, then stepping up again, and so forth. The subjects received feedback after each trial. Every fourth trial was a signal-absent trial. A session (series of trials) ended after the lower reversal point had been constant three times in a row or if the total number of trials exceeded 40. If this took longer than 15 min, the noise playback was restarted after a brief 2-s break.

Results are summarized in Fig. 3. All five human subjects classified bubbler noise as the strongest masker, followed by ramming noise, then Gaussian white noise, then natural ice-cracking noise. Thresholds were slightly different from before. For all five subjects, the critical NSRs for bubbler and ramming noise decreased. For three out of five subjects, the critical NSR for ice-cracking noise decreased, while it increased for the other two. The mean ice-cracking threshold increased. These shifts, however, were small. A test of statistical significance was done on the difference of means, using 98 confidence intervals and student-*t* probabilities [Eq. (13.14a)[24]]. With the exception of Subject B's bubbler thresholds, all shifts in threshold were not statistically significant. Individual variation amongst the five humans was maximal with 5.5 dB in the case of ice-cracking noise and hence smaller than previously. An analysis of catch trials revealed a strongly conservative attitude in all subjects with a probability of false alarms close to zero throughout the experiment. In both human experiments, Subject E consistently provided thresholds at lower NSRs than other human subjects and also had the lowest false-alarm rate. Based on the conclusion from the previous experiment, that human listeners can successfully model beluga masking experiments at least with the signal chosen and bubbler, ramming, and ice-cracking noise, the human data predict a beluga masked hearing threshold of 23.0 ± 1.1 dB for white noise.

C. Modified beluga experiments

The experimental setup was identical to the previous beluga experiment.[14] At the Vancouver Aquarium, the beluga whale Aurora had been trained for a yes/no response according to a behavioral go/no-go paradigm. The instrumentation was the same as that used for the human experiments described in this article with the exception of an Argotec J9 underwater sound projector (with a bandwidth of 40 Hz–20 kHz) replacing the headphones. Noise played continuously for 15 min in the experiment pool. Aurora was asked to station against a stationing bar 1 m in front of the J9. At random times within 30 s after stationing, the beluga call was injected into the noise at a certain NSR according to a titration method with a step size of 3 dB. Aurora would break away from the stationing bar upon call detection. Otherwise, she would hold station and be recalled at the end of the 30-s period. She was given 2 s to respond on the signal-present trials; her reaction time was usually 1 s or less. Catch trials made up one- fourth of all trials. The animal received feedback after each trial, being rewarded for correct rejections and correct detections. Sessions were kept short, limited to 20 trials. About four sessions were run per noise.

Results are included in Fig. 3. Aurora's thresholds were similar to the ones from the previous experiment with the old critical NSRs falling into one standard deviation of the new NSRs. False-alarm rates were less than 0.1. Aurora classified the four noises in the same order, from strongest to weakest masking, as did the humans. Aurora's thresholds fell into one standard deviation of most of the individual human responses. For bubbler and ramming noise, Aurora's thresholds fell within one standard deviation of the average human threshold. For ice-cracking noise, however, the mean human threshold was previously smaller than and now larger than Aurora's threshold. As far as the predictability of the degree of masking of white noise is concerned, results of the human experiment slightly overestimate the beluga threshold. The discrepancy, on the other hand, can be considered small if one takes Aurora's standard deviations into account. In this case, the thresholds of Aurora and the humans overlap for all four noises.

Figure 4 illustrates masking as a shift in threshold. The *x* axis denotes frequency on a logarithmic scale; the *y* axis gives sound-pressure levels in dB *re* 1 μPa @ 1 m. The gray shaded area is the area underneath the beluga audiogram. Sound falling into this area is considered not audible to beluga whales. This audiogram is the mean of seven published beluga audiograms.[9,14,25,26] The top solid line is the spectrum of the noise as it was played continuously for 15 min in the experiment pool. Plotted are 12th-octave band levels corresponding to the width of the beluga critical bands in this frequency range, listed in Table I in Erbe *et al.*[19] All noises had a broadband noise level of $NL = 160$ dB *re* 1 μPa @ 1 m. The lower solid line represents 12th-octave band levels of the call at threshold in the absence of noise; the broadband signal level was[14] $SL_0 = 108$ dB *re* 1 μPa @ 1 m. The middle line gives band levels of the call at threshold in the presence

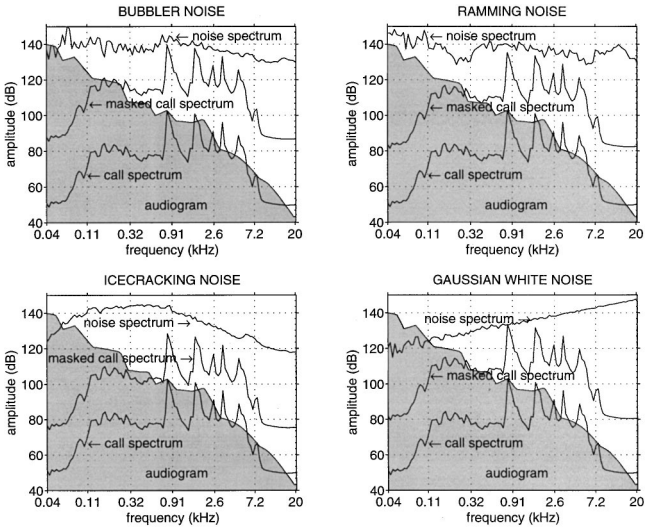

FIG. 4. Shift in threshold of the call from noise absence (call spectrum) to noise presence (masked call spectrum). Values for masking are 36.9 dB for bubbler, 32.6 dB for ramming, 25.6 dB for ice cracking, and 30.7 dB for white noise.

of noise. The amount of masking M can thus be read as the upwards shift of the masked call spectrum compared to the call spectrum. From Eq. (1), it can also be calculated as

$$M = SL_n - SL_0 = NL - \mathrm{NSR}_c - SL_0, \tag{5}$$

where NSR_c are the critical NSRs from Fig 3. In dB, the NSR is the noise level minus the signal level. The masking was 36.9 dB for bubbler noise, 32.6 dB for ramming noise, 25.6 dB for ice-cracking noise, and 30.7 dB for white noise.

There are a few important conclusions to be drawn from Fig. 4. First, in the absence of noise, the animal stopped responding ''yes'' to the call as soon as the low-frequency peaks dropped below audibility. The animal should, however, still have heard the call components at 3 and 5 kHz to much lower signal levels. I therefore like to call the call spectrum at threshold the ''call recognition level'' rather than the ''call detection level.'' This has important implications for masking in the wild. I hypothesize that an animal would be able to hear parts of a call over long ranges but recognize the call over shorter ranges.

In the presence of noise, for bubbler and ramming noise, the masked call spectrum was shifted upwards such that the three major peaks of the call just ''touched'' the noise spectrum. Spectrum levels plotted were means over the 2-s duration of the sounds. As can be seen from Fig. 1, the call consisted of six spectrally similar pulses (phonemes) which together occupied only about half of this time interval. In fact, the mean spectrum of the phonemes is about 6 dB higher than the mean over 2 s. Therefore, at the masked-hearing threshold, the power of the call equaled the power of the noise in the three critical bands surrounding the major peaks in the call. This corroborates Fletcher's equal-power assumption.[5] For Gaussian white noise, the two low-frequency peaks of the masked call spectrum just surpassed or equaled the noise power in the corresponding critical bands. This might indicate that the low-frequency components are more important than the high-frequency components for signal detection. For ice-cracking noise, the plot is misleading. This noise consisted of loud pulses occurring about twice a second. As concluded in an earlier study,[14] masking for ice-cracking noise was so low because the animal (and humans) could identify the call from the phonemes falling in between the pulses of the noise. It is this important temporal structure of the intermittent ice-cracking noise that is not represented in mean noise levels over 2 s. From Fig. 1, in between the pulses of nearby ice-cracking events, the spectrum levels of ambient ice-cracking noise drop at least 20 dB. From Fig. 4, for a phoneme falling in between two noise pulses, five out of the six call peaks would surpass or equal the noise power in the corresponding critical bands if one lowered the noise level by 20 dB.

D. Modified neural network

A backpropagation neural network was previously proven to successfully model beluga masked-hearing experiments.[19] The same neural net design was chosen to model the modified experiments with continuous noise. This neural network was a fully connected two-layer network with 400 input neurons, three hidden layer neurons, and one output neuron. It was trained to detect features of the beluga spectrogram in Fig. 1, buried in noise. As previously, random and sinusoidal noise was used during the training phase. The network gave an output close to 1 if it easily detected a signal and an output close to 0 if it failed to detect a signal. After training had been completed, the network was presented with spectrograms of the same mixed sounds as the beluga and the humans in this study. Critical NSRs were taken at an output of 0.5 resembling a 50% hit rate. As the time lag between the call and the noise was random in the modified experiment, thresholds of the humans and the whale represented means over all time lags encountered. Critical NSRs for the neural network were therefore averaged over 40 different time lags. This was done in the following way. While creating mixed sounds for the neural network, the time series of the noises were shifted against the time series of the call in steps of 40 ms. Figure 5 shows how the neural network's critical NSRs varied as a function of time lag between signal and noise. The plot can be wrapped around the x axis, i.e., the NSRs at the 41st time lag equal those at the first time lag. The maximum variation for bubbler and white noise was about 3 dB, which was small due to the fact that the spectral characteristics of these two noises didn't vary with time. Ramming noise exhibited a strong time dependence with sharp pulses occurring regularly every 90 ms. This time scale, however, was smaller than the time scale of the beluga call, where pulses occurred every 250 ms lasting for about 150 ms. The pulses (phonemes) of the beluga call therefore encountered the same amount of ramming noise relatively independent of the time lag. For ice-cracking noise the situation was different. Its pulses occurred irregularly and lasted a few hundred ms. Masking depended largely on the time lag between the noise pulses and the call phonemes. When they coincided, masking was greater; when they were out of phase, masking was less. Figure 5 shows six major maxima in the critical NSRs for icecracking noise. They are about 250 ms apart, as are the call phonemes.

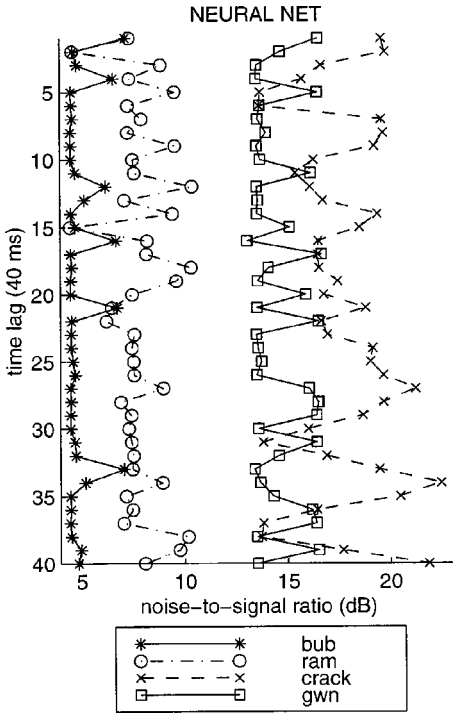

FIG. 5. Critical NSRs of the neural network for bubbler, ramming, ice cracking, and Gaussian white noise. The time lag between the call and the noises was changed in steps of 40 ms, indicating a strong dependence on when the call happened in the noise only for ice-cracking noise.

The mean critical NSRs over all time lags were 4.9, 7.9, 14.6, and 17.7 dB for bubbler, ramming, white, and ice-cracking noise, respectively. The standard deviations were 0.8, 1.3, 1.3, and 2.3 dB, respectively. As explained earlier,[19] the neural network (like other software techniques) required the setting of an offset. Otherwise, thresholds would only have relative meaning. Based on earlier results that this type of neural network can successfully model beluga masking experiments with bubbler, ramming, and ice-cracking noise,[19] I determined the offset using these three noises. Adding a constant 10.1 dB to the network's critical NSRs yielded Aurora's thresholds with a minimum sum-squared error. The neural network was then asked to predict the degree of masking of white noise. Results are printed in Fig. 3. The neural network slightly overestimated the degree of masking of white noise for beluga whales.

II. SUMMARY AND CONCLUSION

The purpose of this study was to find a model for beluga masked-hearing experiments which could accurately, reliably, and efficiently predict the degree of interference of anthropogenic noise with beluga communication signals. Masked-hearing thresholds of a beluga call in two types of icebreaker noise (bubbler system and propeller cavitation/ramming noise) and ambient arctic ice-cracking noise had previously been measured with a trained beluga whale.[14] A variety of software models had subsequently been developed identifying a backpropagation neural network as the most suitable model for beluga masking experiments.[19] Given that beluga calls and most of the noise in their habitat fall into the hearing range of humans, this article hypothesized that human listening experiments could estimate results of beluga experiments yielding data much faster without lengthy training. Five human subjects participated in this study. Their performance was compared to that of the whale[14] and the neural network.[19]

The humans, the whale, and the neural network classified the three noises in the same order, identifying bubbler noise as the strongest masker, followed by ramming, then natural ice-cracking noise. The mean plus/minus one standard deviation of the human responses correctly encompassed the beluga thresholds for bubbler and ramming noise, and were slightly lower than the beluga's threshold for ice-cracking noise. The beluga threshold fell within one standard deviation of the neural network results in the case of all three noises. The neural network therefore modeled the beluga data better than did the humans. The human subjects identified a psychoacoustic problem with the experiment procedure. All sounds played had an equal length of 2 s and the call always happened at the same time in the noise. Subjects therefore knew when to expect the call and had difficulty deciding whether they only imagined it at high NSRs.

I therefore changed the experiment procedure such that noise played continuously for 15 min and the call was injected at random times. Thresholds were not statistically significantly different compared to the previous experiment and were in fact within one standard deviation of the previous thresholds. Humans were then asked to detect the beluga call in a fourth type of noise, Gaussian white noise. The mean threshold was used to predict the masking of white noise in beluga whales. The human experiment predicted that masking of white noise would be stronger than that of ice-cracking noise but less than that of ramming noise.

I returned to the aquarium to measure beluga masked-hearing thresholds with the modified experimental procedure (continuous noise). The human experiment correctly predicted masking to lie in between that of ramming and ice-cracking noise. A comparison of spectrum levels of the masked call at threshold and the noise corroborated Fletcher's equal-power assumption[5] in that the call was just masked when the power in the critical bands surrounding the major call frequencies equaled the power of the noise. The animal attended strongly to the lower-frequency peaks of the call and stopped responding as soon as these were masked by noise or fell below the audiogram in the absence of noise. Higher-frequency peaks of the call were likely still audible. This fits in with the idea of call recognition rather than call detection.

The backpropagation neural network from an earlier study[19] was used to model the modified masking experiment with continuous noise. The network nicely illustrated how masking depended on the time lag between signal and noise. For ice-cracking noise, which had a temporal structure similar to the pulsed beluga call, masking was maximum when the call phonemes coincided with the noise pulses and minimum if the call phonemes fell in between. The neural network ordered the noises the same way as the human subjects and the whale. As with the human experiment, the neural network slightly overpredicted the amount of masking for white noise in beluga whales.

Unfortunately, due to time constraints at the Vancouver Aquarium, only one animal could be trained for the experiment. A variation between individuals in masked-hearing thresholds of a few dB can be expected. The testing of further animals would thus allow a better judgment of the ability of human and software models to estimate masking in beluga whales. Comparing the neural network model to the human model, the neural network has the advantage of being independent of subjectivity and of giving easily reproducible results.

ACKNOWLEDGMENTS

First of all, I wish to thank the Vancouver Aquarium for supporting this research by providing animals and trainers. Without the help, patience, good will, cheerful attitude, and commitment of Michelle Brown, Indy Canagaratnam, Dennis Christen, Joanne Cottrell, Jeremy Fitz-Gibbon, Christine Fritzsche, Kyle Jenkins, Sascha Melnechuck, Jane Osen, Christopher Porter, Alysoun Seacat, Todd Shannon, Brian Sheehan, Gwyneth Sheppard, Clint Wright, and Anne Young, the beluga experiments would simply not have taken place. The marine mammal staff miraculously squeezed my experiments into their already busy daily schedule. Thanks to Andrew, Kuan-Neng, Frank, Roblyn, and Chad for lending me their ears. Dr. Sue Cosens and Dr. Larry Dueck kindly gave me their recordings of beluga whale calls. Dr. Yunbo Xie recorded the icebreaker noise and ambient arctic noise. Last but not least, thanks to Patrice St-Pierre and the Canadian Coast Guard, Central and Arctic Region, for continued financial support.

[1] American Standards Association ''Acoustical Terminology S1, 1-1960'' (American Standards Association, New York, 1960).
[2] N. R. French and J. C. Steinberg, ''Factors governing the intelligibility of speech sounds,'' J. Acoust. Soc. Am. **19**, 90–119 (1947).
[3] J. O. Pickles, *An Introduction to the Physiology of Hearing* (Academic, San Diego, 1988).
[4] B. C. J. Moore, *An Introduction to the Psychology of Hearing*, 4th ed. (Academic, San Diego, 1997).
[5] H. Fletcher, ''Auditory patterns,'' Rev. Mod. Phys. **12**(1), 47–65 (1940).
[6] C. S. Johnson, ''Masked tonal thresholds in the bottlenosed porpoise,'' J. Acoust. Soc. Am. **44**, 965–967 (1968).
[7] C. S. Johnson, ''Auditory masking of one pure tone by another in the bottlenose porpoise,'' J. Acoust. Soc. Am. **49**, 1317–1318 (1971).
[8] V. I. Burdin, V. I. Markov, A. M. Reznik, V. M. Skornyakov, and A. G. Chupakov, ''Ability of *Tursiops truncatus* Ponticus Barabasch to distinguish a useful signal against a noise background,'' in *Morphology and Ecology of Marine Mammals*, edited by K. K. Chapskii and V. E. Sokolov (Wiley, New York, 1973), pp. 162–168.
[9] C. S. Johnson, M. W. McManus, and D. Skaar, ''Masked tonal hearing thresholds in the beluga whale,'' J. Acoust. Soc. Am. **85**, 2651–2654 (1989).
[10] W. W. L. Au and P. W. B. Moore, ''Critical ratio and critical bandwidth for the Atlantic bottlenose dolphin,'' J. Acoust. Soc. Am. **88**, 1635–1638 (1990).
[11] J. A. Thomas, J. L. Pawloski, and W. W. L. Au, ''Masked hearing abilities in a false killer whale (*Pseudorca crassidens*),'' in *Sensory Abilities of Cetaceans—Laboratory and Field Evidence*, edited by J. A. Thomas and R. A. Kastelein (Plenum, New York, 1990), pp. 395–404.
[12] A. Supin and V. Popov, ''Frequency-selectivity of the auditory system in the bottlenose dolphin, *Tursiops truncatus*,'' in *Sensory Abilities of Cetaceans—Laboratory and Field Evidence* (Ref. 11), pp. 385–393.
[13] A. Y. Supin, V. V. Popov, and V. O. Klishin, ''ABR frequency tuning curves in dolphins,'' J. Comp. Physiol. A **173**(5), 749–656 (1993).
[14] C. Erbe and D. M. Farmer, ''Masked hearing thresholds of a beluga whale (*Delphinapterus leucas*) in icebreaker noise,'' Deep-Sea Res., Part II **45**, 1373–1388 (1998).
[15] D. K. Mellinger, ''Handling time variability in bioacoustic transient detection,'' Oceans '93, Engineering in Harmony with the Ocean, Proceedings IEEE Vol. III, pp. 116–121 (1993).
[16] D. K. Mellinger and C. W. Clark, ''A method for filtering bioacoustic transients by spectrogram image convolution,'' Oceans '93, Engineering in Harmony with the Ocean, Proceedings IEEE Vol. III, pp. 122–127 (1993).
[17] J. R. Potter, D. K. Mellinger, and C. W. Clark, ''Marine mammal call discrimination using artificial neural networks,'' J. Acoust. Soc. Am. **96**, 1255–1262 (1994).
[18] D. K. Mellinger and C. W. Clark, ''Methods for automatic detection of mysticete sounds,'' Mar. Freshwater Behav. Physiol. **29**, 163–181 (1997).
[19] C. Erbe, A. R. King, M. Yedlin, and D. M. Farmer, ''Computer models for masked hearing experiments with beluga whales (*Delphinapterus leucas*),'' J. Acoust. Soc. Am. **105**, 2967–2978 (1999).
[20] D. E. Rumelhart, G. E. Hinton, and R. J. Williams, ''Learning internal representations by error propagation,'' in *Parallel Distributed Processing*, edited by D. E. Rumelhart and J. L. McClelland (MIT Press, Cambridge, MA, 1986), pp. 318–362.
[21] W. W. L. Au, *The Sonar of Dolphins* (Springer, New York, 1993).
[22] S. B. Richmond, *Statistical Analysis*, 2nd ed. (Ronald, New York, 1964).
[23] C. Erbe, ''The masking of beluga whale (*Delphinapterus leucas*) calls by icebreaker noise,'' Ph.D. thesis, Earth & Ocean Sciences, University of British Columbia, Canada (1997).
[24] R. L. Mason, R. F. Gunst, and J. L. Hess, *Statistical Design and Analysis of Experiments* (Wiley, New York, 1989).
[25] M. J. White, Jr., J. Norris, D. Ljungblad, K. Baron, and G. di Sciara, ''Auditory thresholds of two beluga whales (*Delphinapterus leucas*),'' Report by Hubbs/Sea World Research Institute for Naval Ocean System Center, Report 78-109 (San Diego, 1978).
[26] F. T. Awbrey, J. A. Thomas, and R. A. Kastelein, ''Low-frequency underwater hearing sensitivity in belugas (*Delphinapterus leucas*),'' J. Acoust. Soc. Am. **84**, 2273–2275 (1988).

The effect of modulation rate on the detection of frequency modulation and mistuning of complex tones

Robert P. Carlyon
MRC Cognition and Brain Sciences Unit, 15 Chaucer Road, Cambridge CB2 2EF, England

Brian C. J. Moore
University of Cambridge, Department of Experimental Psychology, Downing Street, Cambridge CB2 3EB, England

Christophe Micheyl
MRC Cognition and Brain Sciences Unit, 15 Chaucer Road, Cambridge CB2 2EF, England and University of Cambridge, Department of Experimental Psychology, Downing Street, Cambridge CB2 3EB, England

(Received 30 November 1999; revised 10 April 2000; accepted 21 April 2000)

Experiment 1 measured frequency modulation detection thresholds (FMTs) for harmonic complex tones as a function of modulation rate. Six complexes were used, with fundamental frequencies ($F0$s) of either 88 or 250 Hz, bandpass filtered into a LOW (125–625 Hz), MID (1375–1875 Hz) or HIGH (3900–5400 Hz) frequency region. The FMTs were about an order of magnitude greater for the three complexes whose harmonics were unresolved by the peripheral auditory system ($F0 = 88$ Hz in the MID region and both $F0$s in the HIGH region) than for the other three complexes, which contained some resolved harmonics. Thresholds increased with increases in FM rate above 2 Hz for all conditions. The increase was larger when the $F0$ was 88 Hz than when it was 250 Hz, and was also larger in the LOW than in the MID and HIGH regions. Experiment 2 measured thresholds for detecting mistuning produced by modulating the $F0$s of two simultaneously presented complexes out of phase by 180 degrees. The size of the resulting mistuning oscillates at a rate equal to the rate of FM applied to the two carriers. At low FM rates, thresholds were lowest when the harmonics were either resolved for both complexes or unresolved for both complexes, and highest when resolvability differed across complexes. For pairs of complexes with resolved harmonics, mistuning thresholds increased dramatically as the FM rate was increased above 2–5 Hz, in a way which could not be accounted for by the effect of modulation rate on the FMTs for the individual complexes. A third experiment, in which listeners detected constant (''static'') mistuning between pairs of frequency-modulated complexes, provided evidence that this deterioration was due the harmonics in one of the two ''resolved'' complexes becoming unresolved at high FM rates, when analyzed over some finite time window. It is concluded that the detection of time-varying mistuning between groups of harmonics is limited by factors that are not apparent in FM detection data.
 [S0001-4966(00)05207-3]

PACS numbers: 43.66.Fe, 43.66.Hg, 43.66.Mk [DWG]

INTRODUCTION

The fundamental frequency ($F0$) of a periodic sound is important both for the perception of pitch and for our ability to segregate that sound from interfering stimuli—such as the voice of someone we are trying to ignore (Brokx and Nooteboom, 1982; Scheffers, 1983; Assmann and Summerfield, 1990). Many of the periodic sounds that we encounter, including speech and music, have $F0$s that vary over time. However, most psychophysical studies investigating the encoding of $F0$ have focused on steady-state stimuli, and, conversely, the vast majority of psychophysical investigations into the perception of dynamic changes have used pure tones. Neither line of research directly examines the processing of dynamic changes in complex sounds, but both suggest that the ability of the auditory system to track fast changes in $F0$ may be limited. Experiments on the encoding of the $F0$ of steady-state complex tones has revealed that listeners are unable to ignore the $F0$ of immediately preceding and following tones, even when the duration of the ''target'' stimulus is as long as 100 or 200 ms (Carlyon, 1996b; Micheyl and Carlyon, 1998; Gockel *et al.*, 1999). Additionally, studies on the detection of frequency modulation (FM) imposed on sinusoids demonstrate that, at least for low carrier frequencies, performance deteriorates with increases in modulation rate up to at least 20 Hz (Demany and Semal, 1989; Sek and Moore, 1995; Moore and Sek, 1996). Both phenomena have been described using the term ''temporal sluggishness,'' although it is not clear that they are mediated by the same neural mechanism.

In this article we present three experiments which investigated the processing of frequency-modulated complex tones as a function of modulation rate. All experiments used bandpass-filtered harmonic complexes and independently varied their $F0$ and their frequency region (i.e., the filter cutoffs). A feature of the design was that it allowed us to manipulate the resolvability of the harmonics in each com-

plex tone independently of either $F0$ or frequency region alone. Half of the complexes contained at least some harmonics which were well resolved by the peripheral auditory system, and half contained only unresolved harmonics (Shackleton and Carlyon, 1994). Experiment 1 measured FM detection thresholds (''FMTs''), and extended earlier studies (Plack and Carlyon, 1994; Shackleton and Carlyon, 1994; Plack and Carlyon, 1995) to a range of FM rates. Of particular interest were the conditions involving complexes with unresolved harmonics, in which ''place of excitation'' cues were absent. These conditions provided an estimate of the sluggishness of a purely temporal form of processing. In addition, they allowed a further test of Sek and Moore's (1995) explanation for the finding that increasing modulation rate from 2.5 up to 20 Hz increases the FMT for low carrier frequencies, but reduces it for high carrier frequencies. They argued that, for low carrier frequencies, FM is detected via a phase-locking cue which is most effective at low modulation rates, whereas for higher carrier frequencies listeners detect modulations in the excitation pattern, this cue being most effective at higher rates. If this is the case then, because the excitation pattern does not encode the $F0$ of unresolved harmonics, FMTs for such stimuli should increase with increasing modulation rate, even when they are filtered into a high-frequency region.

A further aim of experiment 1 was to provide baseline data for experiment 2, which measured the detection of mistuning between simultaneous pairs of harmonic complexes. The mistuning was produced by modulating the $F0$s of the two complexes 180 degrees out of phase, resulting in an $F0$ difference ($\Delta F0$) which varied sinusoidally around zero at a rate equal to the FM rate. Carlyon (1991, 1992, 1994b) has shown that subjects are insensitive to the dynamic aspects of this ''FM incoherence,'' and detect the resulting mistuning, rather than using the Gestalt principle of common fate to segregate the components whose frequencies are moving in opposite directions. Experiment 2 revealed a limitation in listeners' ability to detect mistuning that changes quickly over time, *over and above* that which could be explained by the FMTs for the individual complexes. Finally, experiment 3 measured thresholds for detecting ''static'' mistuning between pairs of frequency-modulated complex tones, produced by increasing the $F0$ of one complex and decreasing the $F0$ of the other. Its aim was to investigate whether the limitation revealed in experiment 2 was related to listeners' ability to track differences in $F0$ over time, or whether it was caused by reduced resolvability of harmonics in complex tones with rapid modulation in $F0$.

I. EXPERIMENT 1: FM DETECTION

A. Method

1. Stimuli

The stimuli consisted of harmonic complexes which, in the standard interval of each two-interval, two-alternative forced-choice (2I-2AFC) trial, were unmodulated. In the signal interval, the logarithm of the $F0$ was sinusoidally modulated. We chose to modulate the logarithm of the $F0$ because pitch is scaled approximately logarithmically in the auditory system (Hermes and van Gestel, 1991), and, hence, with large frequency deviations, sinusoidal modulation on a linear scale might lead to a decrease in the mean pitch of the complex. We should note, however, that pilot experiments using modulation on a linear scale produced results similar to those presented here.

All stimuli were generated digitally in the time domain at a sampling frequency that was randomly varied, from presentation to presentation, over a 20% range centered on 40 kHz. They were then fed through an anti-aliasing filter (Kemo VBF25.01; attenuation rate 100 dB/oct) with a cutoff frequency of 17.2 kHz. The randomization of the sampling frequency meant that the mean frequency in the standard and signal intervals could differ. This was done to discourage listeners from adopting a strategy of, for the resolved harmonics, monitoring the average amount of excitation in an auditory filter adjacent to one of the components. The effectiveness of this deterrent will be considered in Sec. IV A, together with a discussion of a related strategy for unresolved complexes.

Each complex had a nominal $F0$ of either 88 or 250 Hz and was bandpass filtered (Kemo VBF25.03; attenuation outside the passband 48 dB/oct) into one of three different frequency regions: a LOW region (3-dB cutoff frequencies of 125 and 625 Hz), a MID region (1375–1875 Hz), or a HIGH region (3900–5400 Hz). Shackleton and Carlyon showed that, according to three criteria [size of the $F0$ difference limen ($F0$DL), the effect of phase on pitch, and number of components within an auditory filter bandwidth], the 88-Hz complex contained at least some resolved harmonics when filtered in the LOW region (but not when filtered in the MID and HIGH regions), and the 250-Hz complex contained at least some resolved harmonics in the LOW and MID regions (but not in the HIGH region). The level of each harmonic falling within the passband of the appropriate bandpass filter was 45 dB SPL. The ranks of the harmonics used to construct the complexes before filtering were chosen so as to ensure that enough components would be present in the unmodulated stimuli to fill the skirts of the filter passband down to a level of -6 dB SPL per component. These ranks were 1–21, 7–63, and 21–147 in the LOW, MID, and HIGH regions for an $F0$ of 88 Hz, and 1–8, 2–23, 7–51 for an $F0$ of 250 Hz. Even allowing for the frequency randomization and a zero-peak FM depth of 20% (roughly equal to the largest thresholds reported here), this meant that the skirts were filled down to a level of 10 dB SPL at all times. The modulation rates used were 1, 2, 5, 10, and 20 Hz, and the modulation started at a positive zero-crossing. All stimuli had a duration of 1 s, and were fed into one input of a headphone amplifier before being delivered via one earpiece of a Sennheiser HD414 headset. (In all experiments, this corresponded to the listeners' preferred ear, or, if they expressed no preference, their right ear.) The headphone amplifier mixed the complex tones with a continuous pink noise background, which had a spectrum level of 15 dB (*re* 20 μPa) at 1 kHz. The purpose of the noise was to reduce the detectability of any auditory distortion products and of energy in the extreme skirts of the filters, which were not always com-

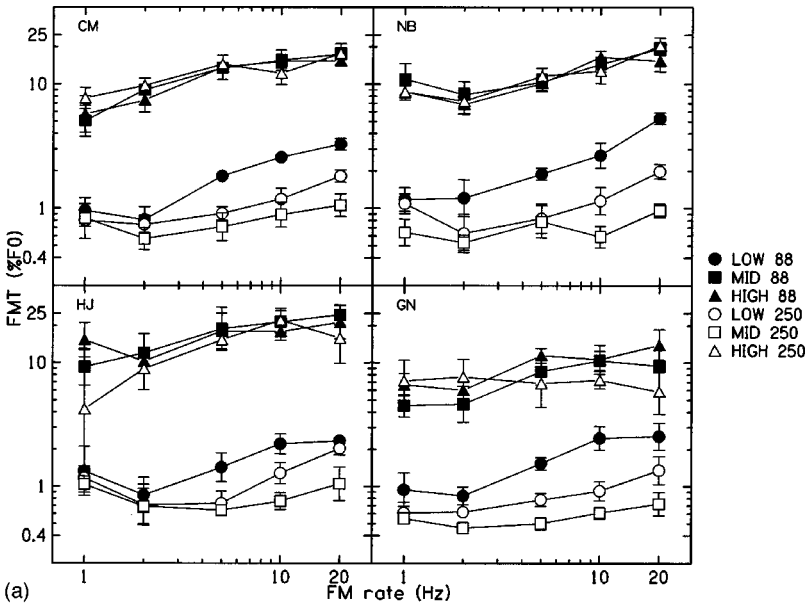

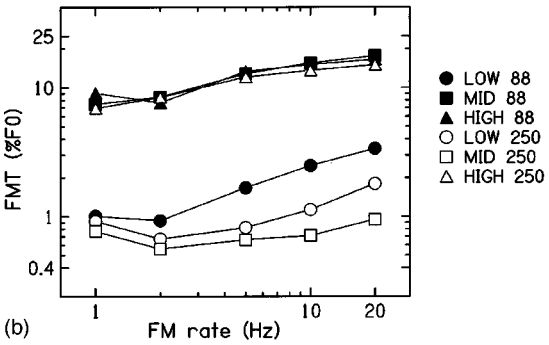

FIG. 1. The FMTs as a function of modulation rate in experiment 1 for (a) each of the four listeners individually, and (b) mean data. Filled symbols: $F0 = 88$ Hz, open symbols: $F0 = 250$ Hz. Stimuli were filtered in the LOW (circles), MID (squares), or HIGH (triangles) region.

pletely filled by the components of the complexes (see above).

2. Procedure and listeners

Frequency modulation detection thresholds (FMTs) were measured using a 2I-2AFC procedure with visual feedback. An adaptive, two-down, one-up tracking rule (Levitt, 1971) was used to estimate the 70.7% correct point on the psychometric function. The procedure stopped after 16 reversals. Threshold was estimated as the geometric mean modulation depth over the last 12 reversals. The initial zero-peak frequency modulation depth of the modulated stimulus was 40% of the nominal $F0$. The modulation depth was multiplied or divided by a factor of 2 until the fourth reversal, and by a factor of $\sqrt{2}$ thereafter. Thresholds were obtained from the geometric mean of four threshold estimates (three for listener HJ) in each condition, and were expressed as the zero-peak FM depth as a percentage of the $F0$. The various experimental conditions were tested in random order.

Four listeners, all with experience in psychoacoustic experiments, took part. Their age ranged from 25 to 56 years. They received at least 2 h of practice before data collection began. One was the third author. The others were paid an hourly wage for their service. All had hearing thresholds within normal limits at octave frequencies between 500 and 8000 Hz.

B. Results

The results of experiment 1 are shown for the individual listeners in Fig. 1(a). Although there were some differences across listeners, a number of common features are reflected in the mean data shown in Fig. 1(b). The significance of these features, discussed below, was assessed using a three-way ($F0 \times$ region $\times$ rate) repeated-measures ANOVA applied to the log FMTs for each listener. The Huynh–Feldt sphericity correction was used where appropriate, and the uncorrected degrees of freedom are reported.

1. Effect of F0 and frequency region on the overall size of the FMT

The FMTs for the three complexes containing only unresolved harmonics (88 Hz in the MID region and both $F0$s in the HIGH region) were similar to each other, and were substantially higher than FMTs for the three complexes containing at least some resolved harmonics. This finding, which replicates earlier results obtained at the single modulation rate of 5 Hz, was reflected by a significant interaction between $F0$ and frequency region [$F(2,6) = 178.5$, $p < 0.001$]. Of the three ''resolved'' complexes, two—those with a 250-Hz $F0$ filtered into the LOW and MID regions (open circles and squares)—showed only a small difference in FMTs, being slightly higher in the LOW than in the MID region. The largest difference between the resolved com-

TABLE I. Slopes of the best-fitting lines relating the log FMT to log FM rate. The lines were fitted using a least-squares method to the data for each listener, and the slopes were then averaged across listeners.

	*F*0		
Region	88	250	Mean
Low	0.55	0.42	0.48
Mid	0.42	0.25	0.34
High	0.35	0.18	0.26
Mean	**0.44**	**0.28**	**0.36**

plexes occurred with an 88-Hz $F0$ in the LOW region (filled circles), for which the FMTs were higher than for the other two resolved complexes, although lower than for the unresolved complexes. This difference was most marked at high modulation rates. Inspection of the data of previous studies (Shackleton and Carlyon, 1994; Micheyl and Carlyon, 1998; Gockel *et al.*, 1999) reveals that the ''static'' $F0$DL for the 88-Hz LOW-region complex is about a factor of 1.4 higher than the mean for the other two ''resolved'' stimuli. This difference is similar to that seen in experiment 1 at a modulation rate of 1 Hz, but is smaller than that observed with faster modulation rates.

2. Variation in FMT with modulation rate

Overall, the FMTs increased with increasing modulation rate, as confirmed by a highly significant main effect in the three-way ANOVA [$F(4,12)=55.8$, $p<0.001$]. However, thresholds were sometimes slightly higher at a 1-Hz FM rate than at 2 Hz. A similar, but more consistent, finding was observed for pure tones by Demany and Semal (1989). The effect of modulation rate interacted significantly both with $F0$ [$F(4,12)=6.55$, $p<0.01$] and with frequency region [$F(8,24)=4.90$, $p<0.05$]. A summary of the effects of FM rate on detection is provided in Table 1, which shows the slopes of the best-fitting lines relating log FMT to log FM rate in each condition, for FM rates from 2 to 20 Hz. The 1-Hz data were excluded from these linear fits because of the increase in FMTs at that rate for some conditions. The fits accounted for an average of 89% of the variance (as opposed to 63% when the 1-Hz data were included), and the slopes reflect some of the main effects that are apparent in the data shown in Fig. 1.

First, the effect of FM rate was greater when the $F0$ was 88 Hz than when it was 250 Hz, as reflected in the significant rate$\times F0$-interaction described earlier (obtained from an ANOVA on all the data, including those for an FM rate of 1 Hz). Separate two-way ANOVAs performed on the data in each frequency region revealed that this effect of $F0$ was significant only in the LOW and MID regions [LOW region: $F(4,12)=7.6$, $p<0.01$. MID region: $F(4,12)=6.44$, $p<0.05$; HIGH region: $F(4,12)=0.4$, n.s.]. Second, the effect of FM rate varied with frequency region, being generally greater in the LOW than in the MID or HIGH regions. This was reflected in the significant rate$\times$region interaction described earlier.

The functions relating FMTs for complex tones to modulation rate can be assessed with reference to Sek and Moore's (1995) interpretation of the analogous functions for pure-tone carriers, which revealed that increasing modulation rate increased FMTs at low carrier frequencies but decreased FMTs at high frequencies. They argued that this reflected a switch from phase-locking cues at low frequencies ($\leqslant$2000 Hz) to excitation-pattern cues at high frequencies ($\geqslant$4000 Hz). If this is so, then the FMTs for complexes with unresolved harmonics should increase with increasing modulation rate even for high-frequency regions, because excitation-pattern cues are unavailable. The data for our HIGH-region complexes confirm this prediction. This finding, combined with the fact that the $F0$s of such unresolved complexes are encoded by purely temporal mechanisms, lends support to the assertion that such mechanisms are to some extent sluggish, even when operating in high-frequency regions.

The effect of FM rate on the FMTs was not consistently larger for complexes with unresolved harmonics than for complexes with some resolved harmonics. At first sight this is surprising, because not only are FMTs much higher for unresolved than for resolved complexes, but this difference persists even when expressed relative to the difference limen ($F0$DL) for a long-duration version of the complex (Shackleton and Carlyon, 1994; Plack and Carlyon, 1995). This in turn might suggest that listeners have difficulty in tracking changes in the $F0$ of complexes with unresolved harmonics, and one might expect this difficulty to increase as the changes get faster. To evaluate whether this expectation is valid, it is necessary to examine in more detail the reasons why FMTs for unresolved harmonics are so high.

Plack and Carlyon (1995) have argued that the high FMTs for unresolved complexes are due to the relatively short time periods during which the modulated waveform is close to its frequency extremes, and to the fact that $F0$DLs for unresolved complexes increase markedly with decreases in duration. The combination of these two factors might also lead one to predict that FMTs would increase markedly with modulation rate. However, it may be that the large effect of duration on the $F0$DL of steady, unresolved complexes does not occur in other situations. For example, White and Plack (1998) have argued that listeners might integrate information over a long window for unresolved complexes which are steady, leading to a large effect of duration on $F0$DLs, but switch to a different strategy when the sound is either modulated or is interrupted. In support of this general idea, they showed that the $F0$DL for a 20-ms unresolved complex fell markedly when its duration was doubled, but dropped less when a second 20-ms sample was added after a brief (5–40 ms) gap. In the latter condition, the reduction in $F0$DL was similar for resolved and for unresolved complexes.[1] Thus, for modulated sounds, the effect of reducing the time spent at frequency extremes (by increasing the FM rate) may be similar for complexes with resolved and unresolved harmonics.

II. EXPERIMENT 2: TIME-VARYING MISTUNINGS

A. Rationale

Experiment 2 investigated whether there is any limitation in the detection of mistuning between two time-varying harmonic complexes, over and above that which would be expected from the FMTs for the individual complexes. Lis-

teners were required to discriminate between two simultaneous complexes whose $F0$s were modulated in phase and the same two complexes with the $F0$s modulated 180 degrees out of phase (''incoherent FM''). As described in the Introduction, the incoherent FM produced a mistuning which varied sinusoidally at a rate equal to that of the FM imposed on each complex, and between extremes proportional to the FM depth. Mistuning thresholds were measured by adaptively varying the FM depth for rates between 1 and 20 Hz. The results were compared to those predicted from the FM thresholds obtained for each complex alone in experiment 1. The predictions were derived from a simple detection-theory model similar to that described by Carlyon and Shackleton (1994) and described in detail in the Appendix. The main assumptions of the model are that information from each of the two complexes is combined optimally, and that d' is proportional to the square of the FM depth (Moore and Sek, 1992).

B. Method

1. Stimuli

The stimuli consisted of $F0$-modulated harmonic complexes. In each interval of a 2I-2AFC trial, two harmonic complexes were presented simultaneously; they had the same nominal $F0$ (88 or 250 Hz) but were filtered into different frequency regions. The two regions were either the LOW and MID or MID and HIGH regions as defined in experiment 1. In the standard interval, the $F0$s of both complexes were modulated with the same starting phase of 180 degrees, corresponding to a negative-going zero-crossing of the modulator. In the signal interval, the starting phase of the MID complex was also 180 degrees, but that of the other complex (LOW or HIGH, depending on the condition) was 0 degrees. This procedure meant that subjects could not perform the task by identifying the modulator phase in the MID region, which was the only region common to both conditions. In theory, however, they could have adopted a strategy of identifying the modulator phase in the ''other'' region, even though this was the HIGH region in some conditions and the LOW region in others. If they had done so, this would have allowed them to identify the signal without detecting mistuning *per se*. Evidence that they were not using such a strategy is provided by experiment 3, part of which replicates experiment 2's results with the paradigm modified to prevent them from doing so.

The design of the experiment was in other respects similar to that of experiment 1, except that the sampling rate was not randomized and that the $F0$ was modulated sinusoidally on a linear rather than a logarithmic scale. For example, at an FM depth of 10%, the lowest excursion in the instantaneous frequency was $100\% - 10\% = 90\%$ instead of $100\%/1.1 = 90.9\%$. This rather small difference was ignored when calculating the model predictions. The stimuli were 1 s, long, including 20-ms raised-cosine ramps.

2. Procedure and listeners

The minimum FM depth at which listeners could identify the mistuned (incoherently modulated) stimulus was measured using a 2IFC procedure with visual feedback. Modulation depth was varied adaptively as in experiment 1. Six runs were obtained in each condition, and thresholds from the six were geometrically averaged to obtain the final threshold values. The various experimental conditions were tested in random order. Three listeners took part, two of whom (CM and GN) had participated in experiment 1. All received at least 2 h of practice before data collection began, and had hearing thresholds within normal limits at octave frequencies between 500 and 8000 Hz

C. Results and discussion

The results of experiment 2 are shown for each of the three listeners in the left-hand column of Fig. 2(a), with the model predictions shown in the right-hand column. The predictions for listeners CM and GN were derived from their individual FMTs in experiment 1; those for listener GA, who had not participated in the earlier experiment, were derived from the mean data. Mean data and predictions are shown in Fig. 2(b). The data will be discussed with reference both to the model and to the results of Carlyon and Shackleton (1994), who compared the detection of ''static'' mistunings between the same pairs of complex tones as used here and the detectability of static $F0$ shifts on the individual complexes ($F0$DLs).

Perhaps the most striking effects of FM rate occur for the simultaneous comparisons between complexes in the LOW and MID region with a nominal $F0$ of 250 Hz (open circles). Both of these complexes contain resolved components according to Shackleton and Carlyon's (1994) criteria, and they produce thresholds which increase dramatically as the FM rate increases above 2–5 Hz, with the exact cutoff varying somewhat across listeners. This large deterioration cannot be accounted for by the slight increase in FMTs with increasing FM rate, as shown by the model predictions in the right-hand column. This indicates that there is a limitation in the ability of the auditory system to detect mistuning which varies over time at a rate greater than 2–5 Hz, and that this limitation is greater than predicted from the FMTs for the individual complexes. The nature of this limitation will be explored in experiment 3.

Some of the lowest thresholds overall are seen for simultaneous presentation of two complexes with a nominal $F0$ of 88 Hz in the MID and HIGH regions (filled triangles, left-hand column). This might seem surprising, given that both complexes contained unresolved harmonics and had high FMTs in experiment 1, leading to predicted thresholds (right-hand column) which, at low FM rates, are much higher than those actually observed. However, Carlyon and Shackleton (1994) demonstrated that, in this condition, listeners use an ''extra'' cue, termed ''pitch pulse asynchrony (PPA).'' In their experiment, this cue arose from the fact that, in the standard interval, the peaks in the waveforms of the two individual complexes occurred simultaneously, whereas the steady $F0$ difference in the signal interval caused the peaks to drift progressively out of synchrony. This led to a PPA which increased linearly throughout the stimulus, as shown by the diagonal line in Fig. 3. In the present paradigm, where the difference in $F0$ varies sinusoidally, the maximum dura-

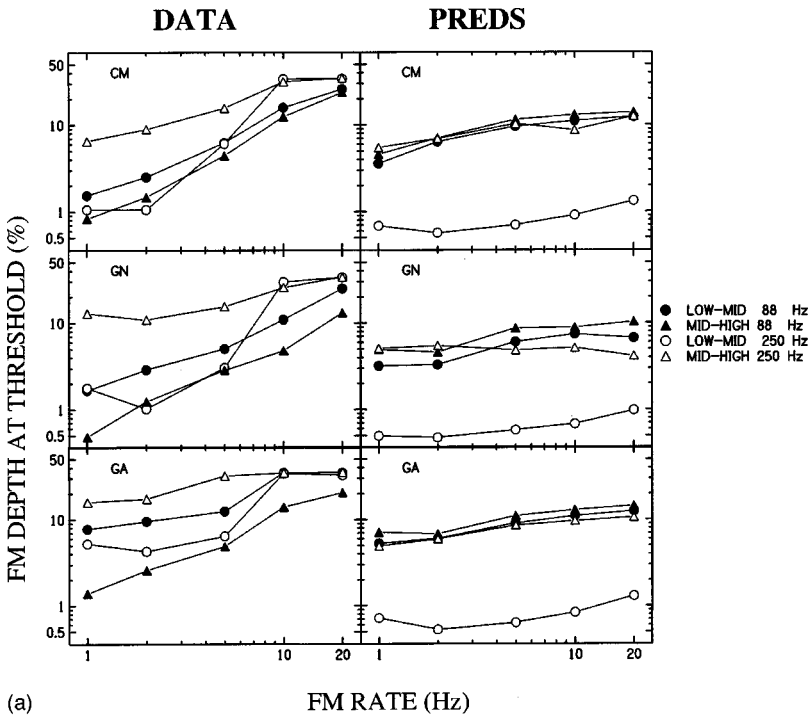

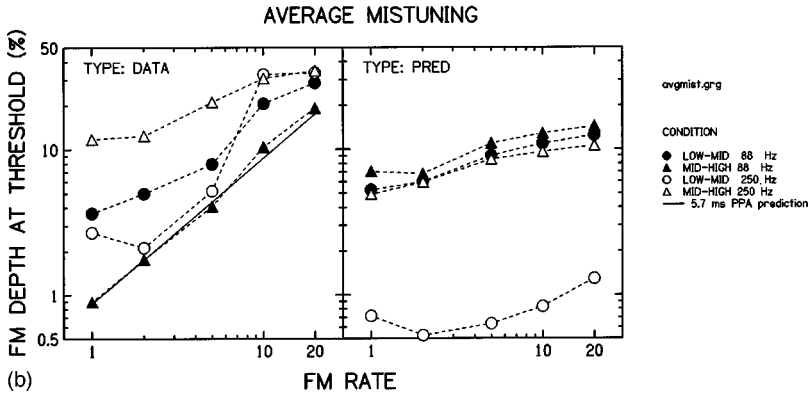

FIG. 2. Left-hand column: Mistuning thresholds as a function of modulation rate for stimuli having a mean $F0$ of 88 Hz (filled symbols) or 250 Hz (open symbols). The two complexes were filtered in the LOW and MID region (circles) or in the MID and HIGH region (triangles). Right-hand column: thresholds predicted from the FMTs for each individual complex (see the Appendix). Individual data are shown in part (a) and mean data in part (b). The solid line with no symbols in the left-hand column of part (b) shows thresholds that would be predicted if listeners could detect a pitch–pulse asynchrony of 5.7 ms (see text for details).

tion over which the PPA can ''build up'' is determined by the modulation rate, and is equal to one-half of the modulation period (after which the difference in $F0$ reverses sign, causing the pitch pulses in the previously ''lagging'' complex to catch up). The result is that, as shown by the other curves in Fig. 3, the PPA varies cyclically over time at a rate equal to the modulation rate; the *maximum* PPA (for a given FM depth) is inversely proportional to the FM rate. Hence, if the same maximum PPA is required for threshold at all modulation rates, thresholds should increase linearly with FM rate. This prediction is shown by the solid line with no symbols in Fig. 2(b), assuming that the maximum PPA required for threshold is equal to one-half of the period of the complex with $F0 = 88$ Hz (5.68 ms). It can be seen that the data for the 88-Hz MID–HIGH condition (filled triangles) follow the prediction very closely.

The remaining two conditions required subjects to compare pairs of complexes where one member of each pair contained some resolved harmonics and one contained only unresolved harmonics. For complexes with an $F0$ of 250 Hz filtered into the MID and HIGH regions (open triangles), thresholds at low FM rates are the highest of all four conditions, exceed the predictions shown in the right-hand column of Fig. 2, and increase gradually with increasing FM rate. The high overall thresholds in this condition are consistent with the thresholds measured by Carlyon and Shackleton

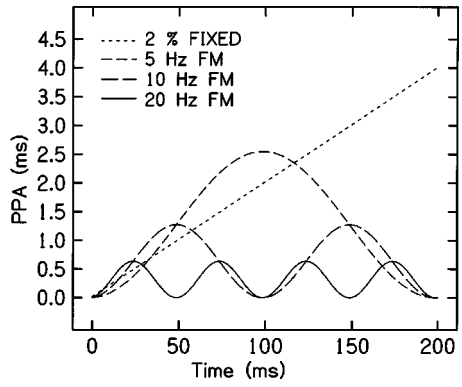

FIG. 3. The pitch–pulse asynchrony occurring during a 200-ms stimulus as a result of a static $F0$ difference of 2% (diagonal line) or an $F0$ difference caused by incoherently modulating the $F0$s of two complexes at rates of 5, 10, and 20 Hz (other lines) with a fixed FM depth. The baseline $F0$ was 100 Hz and, for the modulated stimuli, the zero-peak FM depth was 2%

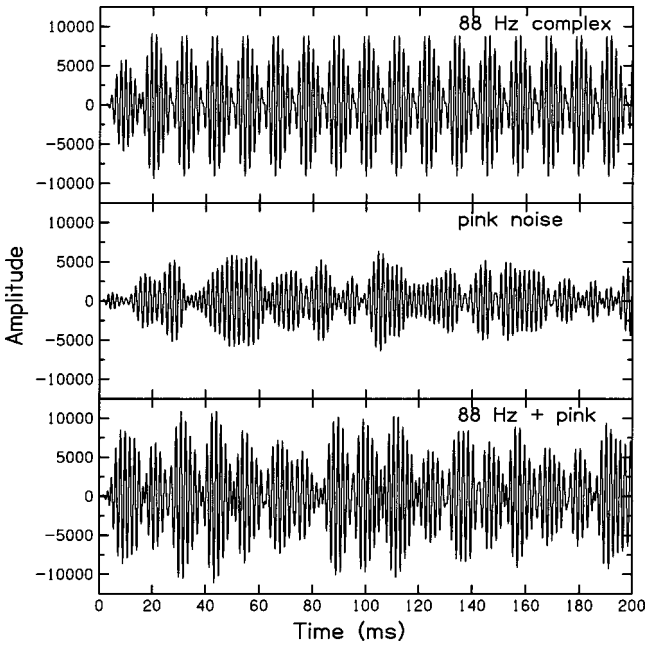

FIG. 4. Output of a fourth-order gammatone filter (Patterson *et al.*, 1988) having a center frequency of 570 Hz to (a) 88-Hz LOW-region complex, (b) pink noise, (c) 88-Hz LOW-region complex mixed with pink noise. The relative levels of the complex tone and the pink noise were the same as in the experiments.

(1994) for the detection of static differences in $F0$. These were also higher when listeners had to compare a complex with resolved harmonics and a complex with unresolved harmonics, than when the two complexes both contained resolved harmonics or both contained unresolved harmonics. Average thresholds in the other resolved–unresolved comparison (88 Hz, LOW versus MID regions, filled circles) are also higher than for the resolved–resolved (250-Hz LOW-MID, open circles) and unresolved–unresolved (88-Hz MID–HIGH, filled triangles) conditions, at least at low modulation rates, but are not as high as in the 250-Hz MID–HIGH condition (open triangles).

One possible reason for the relatively unimpaired performance in the 88-Hz LOW–MID condition is that, despite the 88-Hz LOW complex having been identified as ''resolved'' in previous studies, listeners may have been able to use residual PPA cues. That is, although some of the components were sufficiently well resolved to produce low static $F0$DLs and pitch estimates which were not affected by their relative phase (Shackleton and Carlyon, 1994), there may have been channels, tuned between adjacent harmonics or to the higher harmonics, whose output was sufficiently modulated for listeners to detect PPAs relative to the complex in the MID region. At the upper edge of the LOW region (625 Hz) the equivalent rectangular bandwidth of the auditory filter is about 92 Hz (Glasberg and Moore, 1990), which is greater than the 88-Hz $F0$, indicating that significant interaction would have occurred for the higher harmonics. This is supported by Fig. 4, the bottom part of which shows the response of a simulated auditory filter (fourth-order gammatone: Patterson *et al.*, 1988) centered on 570 Hz to an 88-Hz LOW-region complex mixed with pink noise. It can be seen that the modulations in the filter response to the stimulus presented in quiet (top panel) are still apparent when the noise is added (bottom panel).[2]

Further evidence in favor of this idea comes from the fact that, for the 88-Hz LOW–MID condition, thresholds at low FM rates for listeners CM and GN were lower than predicted from an optimum combination of independent observations (right-hand panel), and increased almost linearly with increasing FM rate. It is also worth pointing out that listeners would not have been able to detect such PPAs in the other resolved–unresolved comparison, for which the $F0$ was 250 Hz, because the maximum PPA that could occur at any $F0$ was equal to one-half of the period of the complex. For an $F0$ of 250 Hz this would be 2 ms. As discussed above, the data from the unresolved–unresolved comparison are consistent with detection occurring when the maximum PPA reaches 5.7 ms. Because the minimum detectable PPA is independent of $F0$ (Carlyon, 1994a), this means that, for an $F0$ of 250 Hz, half of one period (2 ms) would be too short to produce a detectable PPA.

III. EXPERIMENT 3: DETECTION OF STATIC MISTUNING BETWEEN MODULATED COMPLEXES

A. Rationale

One of the most intriguing findings to emerge from experiment 2 was the dramatic increase in mistuning thresholds for the 250-Hz LOW–MID comparison as FM rate increased above 2–5 Hz. One possible explanation for this finding is that, for these stimuli, there is a limit to the rate at which the auditory system can track time-varying differences in $F0$. However, another explanation derives from the idea that harmonics are less well resolved when $F0$ is modulated. If, at some stage auditory processing, the complexes are analyzed over a finite time window, then the internal representation of individual harmonics will become smeared by an amount that will increase with increases in the modulation rate (and also with increases in modulation depth). This might cause the harmonics of the complex filtered into the MID region to become unresolved. Given our argument that mistuning thresholds are highest when one complex is resolved and the other unresolved, this in turn could produce a marked increase in thresholds with increasing modulation rate.

To test the above idea, experiment 3 required listeners to discriminate between a standard stimulus consisting of a pair of simultaneous complex tones having the same $F0$ and modulated coherently, and a signal in which the $F0$s were still modulated coherently but differed by a small amount. In this experiment, then, the internal representation of individual harmonics would still be smeared as a result of the FM, but the $\Delta F0$ between the two complexes did not vary over time.

B. Method

The basic method was the same as in experiment 2, except that, in the ''static mistuning'' conditions, the $F0$s of all complexes were modulated with a starting phase of 0 degrees. In the signal interval of each trial, the $F0$ of one of the two simultaneous complexes was increased re: the nominal $F0$ by a factor of $\sqrt{(1+0.01x)}$, and that of the other com-

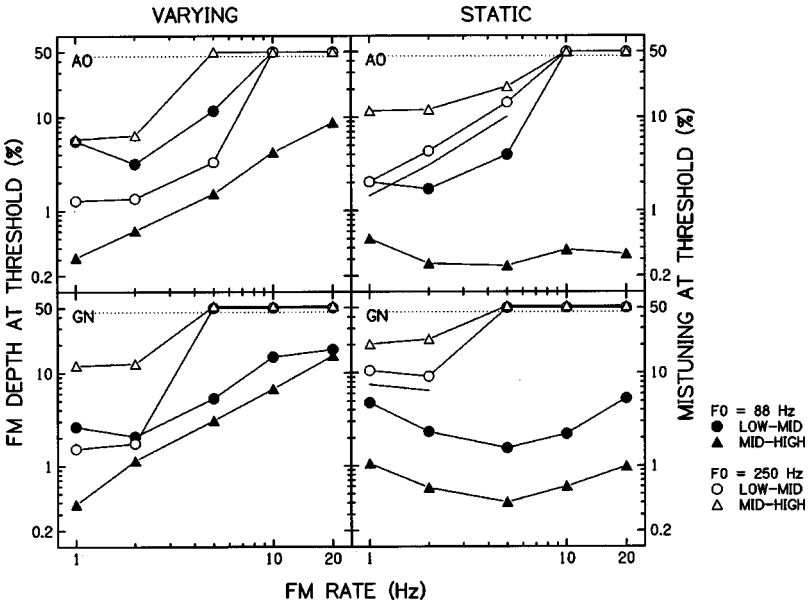

FIG. 5. Left-hand column: Thresholds in the varying mistuning condition of experiment 3 as a function of modulation rate for stimuli having a mean $F0$ of 88 Hz (filled symbols) or 250 Hz (open symbols). The two complexes were filtered in the LOW and MID region (circles) or in the MID and HIGH region (triangles). Thresholds are expressed with respect to the left-hand ordinate. Right-hand column: Thresholds in the static mistuning condition of experiment 3. Thresholds are expressed with respect to the right-hand ordinate. The solid line shows thresholds in the 250-Hz LOW–MID condition shifted down by a factor of $\sqrt{2}$. Symbols are the same as in the left-hand column. In both columns, symbols falling above the dashed line are for conditions where performance was so poor that an adaptive threshold of $\leqslant$40% could not be measured.

plex was reduced by the same factor, leading to a mistuning of x%. The choice of which complex had the higher $F0$ was made at random from trial to trial. In the standard interval, the two simultaneous complexes were randomly either both increased or both decreased by the same factor used in the signal interval. Hence, subjects could not use the $F0$ of either complex to identify the signal interval. As in experiment 2, all four combinations of nominal $F0$ and pairs of frequency region were tested, and modulation rates of 1, 2, 5, 10, and 20 Hz were used. The zero-peak FM depth was fixed at 33%, which was approximately equal to the mean threshold obtained in experiment 2 for the 250-Hz LOW–MID comparison and an FM rate of 10 Hz.

Experiment 3 also included a set of ''varying-mistuning'' conditions that were a replication of experiment 2. These were included for three reasons. First, the opportunity was taken to modify the paradigm so that the modulator phases for both complexes were selected at random (from 0 and 180 degrees) for each presentation, with the constraint that the phases for the two simultaneous complexes were always identical in the standard interval and different in the signal interval. This prevented listeners from identifying the signal interval from the modulation phase of one of the complexes, and forced them to compare the $F0$s of the two complexes. Second, experiment 3 was performed several months after experiment 2, and, as we wished to compare sensitivity to time-varying and static mistunings, it seemed wise to make both sets of measurements at approximately the same time. Third, one of the listeners in experiment 3 had not taken part in experiment 2, and so a fresh set of measures was needed in order to facilitate a comparison.

In both conditions, each adaptive run started with a mistuning or FM depth of 40%. Before the first four turnpoints of the adaptive procedure had been completed, this value was not exceeded, even if subjects made a series of errors that would have otherwise led to a larger value. If after the first four turnpoints, the adaptive procedure indicated a mistuning or FM depth of $>$40%, the run was terminated. The reported thresholds were obtained from the geometric means of four runs, except where one or more runs were terminated for that particular condition. Where only one run was terminated, thresholds were estimated from the remaining three runs. Where more than one run was terminated, thresholds were arbitrarily assigned a value of 50%.

Two listeners took part in this experiment. One, GN, had participated in experiments 1 and 2. The other, AO, was new to the study but had participated in numerous similar experiments. She received 8 h of practice before data collection began. The ''varying-mistuning'' conditions were completed before data collection for the ''fixed-mistuning'' conditions began.

C. Results

The results of the varying-mistuning conditions of experiment 3 are shown in the left-hand column of Fig. 5. Both the pattern of results and the overall level of performance are very similar to those obtained in experiment 2, indicating that performance was not affected by the minor procedural differences between the two experiments. The results of the static mistuning conditions are shown in the right-hand column, and reveal a number of interesting findings.

First, for the ''resolved–resolved'' comparison (250-Hz LOW–MID, open circles), thresholds increase with increasing FM rate and are at least as high as in the corresponding varying-mistuning condition. This is true even when the fixed-mistuning thresholds are reduced by a factor of $\sqrt{2}$ to allow for the fact that, in the varying-mistuning condition, the rms mistuning was equal to the FM depth multiplied by $\sqrt{2}$. (These corrected thresholds are shown by the solid lines with no symbols, for those points where a measurable threshold was obtained.) These results support the idea that the high thresholds, observed in experiment 2 for the 250-Hz LOW–MID comparison at high modulation rates, can be explained by the reduced resolvability of individual harmonics when $F0$ is modulated.

Second, and in contrast to the above finding, thresholds for the unresolved–unresolved comparison (88 Hz, MID–

HIGH, filled triangles) are lower when the mistuning is static than when it is varying, and, in the former case, do not increase with increasing FM rate. This is entirely consistent with our interpretation of the results of the corresponding condition in experiment 2, which we attributed to listeners detecting PPAs between the two unresolved complexes. In that experiment, and in the varying-mistuning condition of experiment 3, the maximum duration over which the PPA could ''build up'' was limited by the FM rate. No such limitation occurs when the modulation on the two complexes is in phase, and so thresholds remain low at all modulation rates. In fact, the thresholds obtained suggest that subjects could detect a somewhat smaller PPA when the mistuning was constant throughout the stimulus than when it varied sinusoidally: For example, both listeners showed threshold mistunings of $\leqslant$0.5%, which would lead to a PPA of about 1.15 ms at the end of the stimulus. This is considerably lower than the 5.68 ms ''maximum PPA'' used to fit the data of experiment 2 [Fig. 2(b)]. It is, however, roughly similar to the 1.4-ms threshold indicated by Carlyon and Shackleton's (1994) data for the detection of a constant PPA, produced by delaying one of two simultaneous complexes having the same $F0$.

The greater availability of PPA cues in the ''fixed mistuning'' paradigm may also explain why, for listener GN, thresholds for the 88-Hz LOW–MID comparison (filled circles) were lower than in the corresponding varying-mistuning condition, at least at high modulation rates. In Sec. II.C we suggested that thresholds for this 88-Hz LOW–MID comparison may have been mediated at least partly by the detection of PPAs. If so, we might expect thresholds to increase with increasing FM rate in the varying-mistuning condition, but not in the fixed-mistuning condition, because only in the former is the maximum PPA limited by the modulation rate. This was indeed observed. We should, however, note that listener AO's 88-Hz LOW–MID thresholds were also lower in the fixed-mistuning than in the varying-mistuning condition, but, as they also increased with increasing FM rate, are unlikely to have been mediated by the detection of PPAs.

IV. DISCUSSION

A. Factors affecting FM detection at large FM depths

The functions relating the FMTs to modulation rate, as determined in experiment 1, include some points where the FMT is very high ($\geqslant$20% zero-peak). This raises the question of whether listeners were genuinely following the pattern of frequency modulation in those conditions, or whether the very large FM depth gave rise to some other cue which they could use *in extremis*. As the large FMTs occurred exclusively for stimuli with unresolved harmonics, this in turn could complicate a comparison of listeners' ability to detect FM imposed on stimuli with resolved or unresolved harmonics.

One possible strategy would be to identify the modulated stimulus from the maximum or minimum $F0$ that was reached during *any* portion of the stimulus. For *resolved* complexes (or for pure tones) this could simply involve monitoring an auditory filter with a center frequency (CF) either just above or just below the carrier frequency of one component. To discourage listeners from doing this, the $F0$ of each complex was randomized by $\pm$10% of its nominal value from presentation to presentation. The $F0$ randomization prevented listeners from using the strategy for FM depths of about 5% or less (for derivations see Green, 1988; Plack and Carlyon, 1994), which was greater than any of the FMTs for resolved harmonics (with the exception of one point for listener NB).

For unresolved complexes, a strategy of monitoring the level at the output of one auditory filter would not have been useful, but listeners could have identified the signal as that stimulus which contained the highest (or lowest) instantaneous $F0$. The large FMTs for these conditions indicate that the $F0$ randomization was insufficient to rule out such a strategy. However, it is worth noting that such a strategy would require listeners to be able to ''pick out'' that portion of the stimulus at which the $F0$ was at a maximum or minimum. If the encoding of $F0$ were even more sluggish than the data in Fig. 1 suggest, its internal representation would presumably be smoothed over a long time window and that strategy would not be useful. It therefore appears that the data in Fig. 1 provide a reasonable measure of the ''sluggishness'' inherent in the processing of FM for unresolved complexes.

One final possibility arises from the fact that there was a modulation in overall level for the unresolved complexes. As the level per component was fixed, increasing the $F0$ meant that fewer harmonics fell within the passband of the hardware filter and of each auditory filter responding to the complex. For an FM depth of 20%, this level variation would have approached 1 dB. However, preliminary measures of the FMTs for an unresolved (62.5-Hz MID region) complex collected by S. Furukawa (personal communication) suggest that such a cue was probably not used. In one condition he applied a random-phase 62.5-Hz amplitude modulation (AM) in both the standard and signal intervals of each trial. At high modulation rates, where FMTs were highest (about 15%), thresholds were similar to those in a control condition with no AM.

B. Choice of dependent variable

The results of experiment 1 were plotted and analyzed with the dependent variable expressed as the logarithm of the FMT. Because the absolute size of the FMT differed markedly across conditions—being much larger for complexes with unresolved than with resolved harmonics—it is important to ensure that this logarithmic transformation was indeed appropriate. Specifically, if the slope of the underlying psychometric function differed markedly across conditions, it could be that a given proportional change in the FMT did not correspond to the same change in sensitivity in all conditions. We did not measure psychometric functions, and so cannot conclusively rule out this possibility. However, the following observations suggest that it is unlikely. First, it is known that the slopes of the psychometric functions for static differences in $F0$ do not differ between complexes with resolved and unresolved harmonics (Plack and Carlyon,

1995; Carlyon, 1996a). Second, the psychometric functions for the detection of FM imposed on the center frequencies of complex tones are also similar for complexes with resolved and unresolved harmonics (Lyzenga and Carlyon, 1999). Finally, the log standard deviations (calculated across subjects) observed here were roughly constant across conditions, as confirmed by a regression of the standard deviation of the log scores on the log FMT, which revealed a slope of only 0.016 and a modest correlation of 0.55.

C. Increase in mistuning thresholds at FM rates above 2–5 Hz

One of the most striking findings to emerge from this study is the fact that the low mistuning thresholds, observed at slow FM rates between two groups of resolved harmonics, increase dramatically once the modulation rate exceeds 2–5 Hz. Experiment 3 showed that thresholds at fast modulation rates are also high when a static mistuning is imposed on modulated complexes, indicating that the deterioration can probably be accounted for by reduced resolvability of harmonics in complexes with a modulated $F0$. It was argued in Sec. III C that this would have caused the harmonics of one of the two complexes to become unresolved at fast modulation rates, leading to the observed increase in thresholds.

Two conclusions can be drawn from the above finding. The first arises from the fact that, as shown in Fig. 2 and discussed in Sec.II C, the increase in the threshold for detecting mistuning with increasing modulation rate cannot be accounted for by the comparatively modest increase in the FMTs for the individual complexes. Hence the mistuning paradigm reveals a limitation in the processing of modulated sounds that is not revealed in a modulation detection task. In the latter paradigm, the harmonics in a given complex might be well resolved in the (unmodulated) standard interval of each trial, but, at high modulation rates, the harmonics in the signal interval might be unresolved. The reduced resolvability of the harmonics in the signal interval might lead to a less clear overall pitch, and this change in clarity would allow the listener to identify the signal interval without having to track the fast modulations in frequency *per se*.

Second, the increase in mistuning thresholds with increasing modulation rate underlines previous assertions that the *resolvability* of the complexes, rather than their $F0$ or frequency region alone, determines listeners' sensitivity to mistuning. As has been recently pointed out (Carlyon, 1999), at least one model of $F0$ processing (Meddis and O'Mard, 1997) predicts that the accuracy of encoding depends on the frequency region *per se*, rather than on the resolvability.[3] This prediction is not supported by the fact that increasing modulation rate can dramatically impair the detection of mistuning between two complex tones, without altering the frequency regions into which they are filtered.

D. FM-induced AM

In Sec. III C we described one cue—the reduced clarity of pitch resulting from reduced resolvability of harmonics in sounds with modulated $F0$—that could have been used in a FM detection task but which was unlikely to have influenced mistuning thresholds. Another cue that may fall into this category arises from the ''FM-induced AM'' that occurs in the outputs of auditory filters as frequency components sweep across their skirts. Plack and Carlyon (1994, 1995) performed simulations of the amount of FM-induced AM produced for complex tones with a 5-Hz modulation in $F0$ at a depth equal to threshold, and concluded that, for resolved harmonics, such modulations would indeed have been detectable. This cue may account for the fact that thresholds for detecting mistuning between pairs of complexes with resolved components ($F0 = 250$ Hz, LOW and MID regions) were higher than predicted from the FMTs on the basis of an optimum combination of independent observations. In this regard it is worth noting that the situation for static differences in $F0$ is different in that no AM cue is available for either sequential or simultaneous comparisons. Performance for simultaneous comparisons between two static resolved complexes in different frequency regions is at least as good as that predicted from the individual $F0$DLs (Carlyon and Shackleton, 1994).

V. SUMMARY AND CONCLUSIONS

(i) The FMTs for complex tones are larger when those tones contain only unresolved harmonics than when they contain at least some resolved harmonics.

(ii) The FMTs for all complexes increase with increases in modulation rate above 2 Hz. The size of this increase does not differ systematically between complexes with resolved and with unresolved components. It is larger overall when the $F0$ of the carrier is 88 Hz than when it is 250 Hz, and is greater for complexes filtered into the LOW- than into the MID- or HIGH-frequency regions.

(iii) Modulating the $F0$s of two simultaneous complexes out of phase by 180 degrees causes the difference in $F0$ to oscillate at a frequency equal to the FM rate. Thresholds for detecting this mistuning are greatest when one of the complexes is resolved and the other unresolved, and lowest when the two complexes are either both resolved or both unresolved.

(iv) When both complexes contain unresolved harmonics, the mistuning thresholds are consistent with the idea that the signal interval is identified using asynchronies between waveform peaks for the two complexes (pitch pulse asynchrony).

(v) When both complexes contain resolved harmonics, mistuning thresholds increase markedly as FM rate is increased above 2–5 Hz. This increase cannot be explained by the gradual increase that occurs in the FMTs for the individual complexes when the modulation rate is raised. It also occurs for the detection of a static $F0$ difference between two modulated complex tones. The increase may be attributed to reduced resolvability of harmonics resulting from the auditory system analyzing, over a finite time window, a stimulus having a fast rate of change. This finding demonstrates a limitation on temporal processing which is not revealed by FMTs and has not been identified in previous measures of mistuning detection, which have

generally used either steady sounds (e.g., Moore *et al.*, 1985) or a single modulation rate (Carlyon and Shackleton, 1994).

ACKNOWLEDGMENTS

This research was supported by a project grant (045965/Z/95/Z) from the Wellcome Trust. It was motivated by pilot data collected by Shigeto Furukawa, to whom we are grateful. We thank John Deeks for help with some of the figures and with data collection, and Hedwig Gockel, Laurent Demany, and Brian Roberts for helpful comments on a previous version of this paper.

APPENDIX

Here we describe a model for predicting the threshold for detecting a difference in $F0$ between two simultaneous complex tones, produced by incoherent FM. The model takes as its input the thresholds for detecting FM on each of the two complexes, and assumes that subjects detect FM on each complex by comparing the two extremes of the $F0$ excursion to each other (cf. Hartmann and Klein, 1980). We assume that listeners detect an $F0$ difference between two simultaneous complexes by comparing the maximum $F0$ reached by one complex with the minimum $F0$ reached by the other; because the modulations on the two complexes are 180 degrees out of phase in the signal interval, these maxima and minima occur at the same time.[4] For both the sequential and simultaneous comparisons, the $F0$ difference in the signal interval is equal to the peak-to-peak FM depth. Further assumptions made in the model are as follows.

(*i*) The psychometric function has the same form as for pure-tone carriers, namely $d' = kF^2$ (Moore and Sek, 1992), where F is the peak-to-peak FM depth.

(*ii*) Performance in any condition can be modeled by assuming

$$d' = \Delta / \sqrt{\{(\sigma_1^2 + \sigma_2^2)/2\}}, \tag{A1}$$

where Δ is the difference between the means of the distributions of the two internal representations of (instantaneous) $F0$ being compared, and σ_1 and σ_2 are the standard deviations of each distribution (When $\sigma_1^2 = \sigma_2^2$ this reduces to the more familiar $d' = \Delta/\sigma$.)

(*iii*) The relationship between Δ and the physical $F0$ difference is the same for all conditions, so that differences in sensitivity between conditions can be modeled solely by differences in σ. We assume that $\Delta = F^2$, so that σ is expressed in units of F^2, and is equal to $1/k$.

Before describing the details of the model, it is worth noting that variations in the above assumptions do not dramatically affect the predicted mistuning thresholds; to a first approximation, mistuning thresholds will always be limited by the larger of the two FMTs for the individual complexes.

For the detection of FM on a single complex, it is reasonable to assume that σ will be the same for the two sampling distributions (corresponding to the positive and negative $F0$ excursions). Substituting $\sigma_1^2 = \sigma_2^2$ into Eq. (A1),

$$D = \Delta/\sigma = F^2/\sigma. \tag{A2}$$

where D is the value of d' at which the adaptive procedure converges. The value of σ in, say, the LOW frequency region is then

$$\sigma_L = F_L^2/D. \tag{A3}$$

The aim now is to determine the FM depth for a simultaneous comparison at which the adaptive procedure converges on performance corresponding to the (fixed) value of $d' = D$. For a comparison between the LOW and MID regions, this FM depth will be termed F_{LM}. The model assumes that there is no additional internal noise in comparing $F0$s between two frequency regions (e.g., the LOW and the MID), over and above that involved in a sequential within-frequency comparison. The value of D for a *single* simultaneous comparison between the $F0$s of the two groups is

$$D = \frac{F_{LM}^2}{\sqrt{(\sigma_L^2 + \sigma_M^2)/2}}. \tag{A4}$$

However, for the simultaneous $\Delta F0$, listeners can make twice as many comparisons in each modulation period of the signal interval—once when the $F0$ in the LOW region is maximal and that in the MID region is minimal, and once when the converse is the case. This will increase sensitivity by a factor of $\sqrt{2}$. So, multiplying the right-hand side of (A4) by $\sqrt{2}$ and substituting (A3) into its denominator,

$$D = \frac{2DF_{LM}^2}{\sqrt{(F_L^4 + F_M^4)}} \tag{A5}$$

$$\Rightarrow F_{LM} = 0.71 \cdot \sqrt[4]{F_L^4 + F_M^4}. \tag{A6}$$

[1]One reason why listeners might use different strategies depending on the stimulus comes from the finding that, when estimating the pitch of steady unresolved complexes, they may rely at least partly on an analysis of the average number of periods in the entire stimulus (Carlyon, 1997; White and Plack, 1998). This metric would not differ between modulated and unmodulated sounds having the same mean $F0$, and so to detect FM listeners would again have to use a different form of analysis.

[2]Carlyon and Shackleton's (1994) data indicate that, for the detection of a static $\Delta F0$ measured using the method of constant stimuli, listeners could not use PPAs in the 88-Hz LOW–MID comparison. One factor which may have helped listeners CM and GN to do so in the present study is connected with the adaptive procedure used here. Each trial started with a modulation depth of 40%, which meant that the instantaneous $F0$ reached a minimum of 63 Hz. This low $F0$ would have increased the salience of the PPA cue, and may have helped those listeners to ''home in'' on that cue at the beginning of each adaptive trial, and to ''hold on'' to it as the FM depth was reduced. Alternatively, the different results in the two studies may simply reflect interlistener differences.

[3]Meddis and O'Mard discuss their model primarily in terms of pitch perception, rather than as a model of the detection of $F0$ differences between groups of components. However, Meddis and his colleagues *have* used an earlier version to model the processing of simultaneous across-frequency differences in $F0$ (Meddis and Hewitt, 1992).

[4]Recall that, in experiment 2, the complexes were modulated in both the standard and signal intervals. This forced listeners to compare the $F0$s of the two complexes, rather than detecting FM on each complex separately and then combining these two estimates optimally. Note also that the model assumes that, in both tasks, listeners compare two $F0$s within the signal interval, and ignore the standard interval. In fact, listeners may well have compared the $F0$ difference present in the signal interval to the (zero) difference present in the standard interval. Because the extra information provided in the standard interval would have been the same for the sequen-

tial and simultaneous comparisons, this would not have affected the relationship between the sensitivities in the two tasks.

Assmann, P., and Summerfield, Q. (**1990**). ''Modeling the perception of concurrent vowels: Vowels with different fundamental frequencies,'' J. Acoust. Soc. Am. **88**, 680–697.

Brokx, J. P. L., and Nooteboom, S. G. (**1982**). ''Intonation and the perceptual separation of simultaneous voices,'' J. Phonetics **10**, 23–36.

Carlyon, R. P. (**1991**). ''Discriminating between coherent and incoherent frequency modulation of complex tones,'' J. Acoust. Soc. Am. **89**, 329–340.

Carlyon, R. P. (**1992**). ''The psychophysics of concurrent sound segregation,'' Philos. Trans. R. Soc. London, Ser. B **336**, 347–355. Also in *Processing of Complex Sounds by the Auditory System*, edited by R. P. Carlyon, C. J. Darwin, and I. J. Russell (OUP, Oxford).

Carlyon, R. P. (**1994a**). ''Detecting pitch-pulse asynchronies and differences in fundamental frequency,'' J. Acoust. Soc. Am. **95**, 968–979.

Carlyon, R. P. (**1994b**). ''Further evidence against an across-frequency mechanism specific to the detection of FM incoherence between resolved frequency components,'' J. Acoust. Soc. Am. **95**, 949–961.

Carlyon, R. P. (**1996a**). ''Encoding the fundamental frequency of a complex tone in the presence of a spectrally overlapping masker,'' J. Acoust. Soc. Am. **99**, 517–524.

Carlyon, R. P. (**1996b**). ''Masker asynchrony impairs the fundamental-frequency discrimination of unresolved harmonics,'' J. Acoust. Soc. Am. **99**, 525–533.

Carlyon, R. P. (**1997**). ''The effects of two temporal cues on pitch judgments,'' J. Acoust. Soc. Am. **102**, 1097–1105.

Carlyon, R. P. (**1999**). ''Comments on 'A unitary model of pitch perception' [J. Acoust. Soc. Am. **102**, 1811–1820 (1997)],'' J. Acoust. Soc. Am. **104**, 1118–1121.

Carlyon, R. P., and Shackleton, T. M. (**1994**). ''Comparing the fundamental frequencies of resolved and unresolved harmonics: Evidence for two pitch mechanisms?'' J. Acoust. Soc. Am. **95**, 3541–3554.

Demany, L., and Semal, C. (**1989**). ''Detection thresholds for sinusoidal frequency modulation,'' J. Acoust. Soc. Am. **85**, 1295–1301.

Glasberg, B. R., and Moore, B. C. J. (**1990**). ''Derivation of auditory filter shapes from notched-noise data,'' Hear. Res. **47**, 103–138.

Gockel, H., Carlyon, R. P., and Micheyl, C. (**1999**). ''Context dependence of fundamental frequency discrimination: Lateralized temporal fringes,'' J. Acoust. Soc. Am. **106**, 3553–3563.

Green, D. M. (**1998**). *Profile Analysis* (Oxford U. P., New York).

Hartmann, W. M., and Klein, M. A. (**1980**). ''Theory of frequency modulation detection for low modulation frequencies,'' J. Acoust. Soc. Am. **67**, 935–946.

Hermes, D. J., and van Gestel, J. C. (**1991**). ''The frequency scale of speech intonation,'' J. Acoust. Soc. Am. **90**, 97–102.

Levitt, H. (**1971**). ''Transformed up-down methods in psychophysics,'' J. Acoust. Soc. Am. **49**, 467–477.

Lyzenga, J., and Carlyon, R. P. (**1999**). ''Center frequency modulation detection for harmonic complexes resembling vowel formants and its interference by off-frequency maskers,'' J. Acoust. Soc. Am. **105**, 2792–2806.

Meddis, R., and Hewitt, M. (**1992**). ''Modeling the identification of concurrent vowels with different fundamental frequencies,'' J. Acoust. Soc. Am. **91**, 233–245.

Meddis, R., and O'Mard, L. (**1997**). ''A unitary model of pitch perception,'' J. Acoust. Soc. Am. **102**, 1811–1820.

Micheyl, C., and Carlyon, R. P. (**1998**). ''Effects of temporal fringes on fundamental-frequency discrimination,'' J. Acoust. Soc. Am. **104**, 3006–3018.

Moore, B. C. J., and Sek, A. (**1992**). ''Detection of combined frequency and amplitude modulation,'' J. Acoust. Soc. Am. **92**, 3119–3131.

Moore, B. C. J., and Sek, A. (**1996**). ''Detection of frequency modulation at low modulation rates: Evidence for a mechanism based on phase locking,'' J. Acoust. Soc. Am. **100**, 2320–2331.

Moore, B. C. J., Glasberg, B. R., and Baer, T. (**1997**). ''A model for the prediction of thresholds, loudness and partial loudness,'' J. Audio Eng. Soc. **45**, 224–240.

Moore, B. C. J., Peters, R. W., and Glasberg, B. R. (**1985**). ''Thresholds for the detection of inharmonicity in complex tones,'' J. Acoust. Soc. Am. **77**, 1861–1867.

Patterson, R. D., Nimmo-Smith, I., Holdsworth, J., and Rice, P. (**1988**). ''Spiral Vos Final Report, Part A: The Auditory Filterbank,'' Applied Psychology Unit, Cambridge, England, Contract Report: APU 2341.

Plack, C. J., and Carlyon, R. P. (**1994**). ''The detection of differences in the depth of frequency modulation,'' J. Acoust. Soc. Am. **96**, 115–125.

Plack, C. J., and Carlyon, R. P. (**1995**). ''Differences in frequency modulation detection and fundamental frequency discrimination between complex tones consisting of resolved and unresolved harmonics,'' J. Acoust. Soc. Am. **98**, 1355–1364.

Robinson, D. W., and Dadson, R. S. (**1956**). ''A re-determination of the equal-loudness relations for pure tones,'' Br. J. Appl. Phys. **7**, 166–181.

Scheffers, M. T. M. (**1983**). ''Sifting vowels: auditory pitch analysis and sound segregation,'' Doctoral dissertation, Univ. Groningen, Netherlands.

Sek, A., and Moore, B. C. J. (**1995**). ''Frequency discrimination as a function of frequency, measured in several ways,'' J. Acoust. Soc. Am. **97**, 2479–2486.

Shackleton, T. M., and Carlyon, R. P. (**1994**). ''The role of resolved and unresolved harmonics in pitch perception and frequency modulation discrimination,'' J. Acoust. Soc. Am. **95**, 3529–3540.

White, L. J., and Plack, C. J. (**1998**). ''Temporal processing of the pitch of complex tones,'' J. Acoust. Soc. Am. **103**, 2051–2063.

The lateralization of simple dichotic pitches

Michael A. Akeroyd[a] and A. Quentin Summerfield
MRC Institute of Hearing Research, University Park, Nottingham NG7 2RD, United Kingdom

(Received 17 August 1999; revised 17 February 2000; accepted 7 March 2000)

A ''simple'' dichotic pitch arises when a single narrow band possesses a different interaural configuration from a surrounding broadband noise whose interaural configuration is uniform and correlated. Such pitches were created by interaurally decorrelating a narrow band (experiment 1) or by giving a narrow band a different interaural time difference from the noise (experiment 2). Using an adaptive forced-choice procedure, listeners adjusted the interaural intensity difference of ''pointers'' to match their lateralization to that of the dichotic pitches. The primary determinants of lateralization were the interaural configuration of the broadband noise (experiment 1), the center frequency of the narrow band (experiment 1), and its interaural configuration (experiment 2). The ability of two computational models to predict these results was evaluated. A version of the central-spectrum model [J. Raatgever and F. A. Bilsen, J. Acoust. Soc. Am. **80**, 429–441 (1986)] incorporating realistic frequency selectivity accounted for the main results of experiment 1 but not experiment 2. A new ''reconstruction–comparison'' model accounted for the main results of both experiments. To accommodate the variables shown to influence lateralization, this model segregates evidence of the dichotic pitch from the noise, reconstructs the cross-correlogram of the noise, and compares it with the cross-correlogram of the original stimulus. [S0001-4966(00)00107-7]

PACS numbers: 43.66.Pn, 43.66.Qp, 43.66.Ba [DWG]

INTRODUCTION

Dichotic pitches are sensations of pitch generated through binaural interaction. They are generally heard as faint tonal objects with specific lateralizations amidst a background noise. Because dichotic pitches are due entirely to binaural processing, their investigation may contribute to an understanding of the capacity of the binaural auditory system to locate signals in background noise.

This paper addresses the lateralization of ''simple'' dichotic pitches, of which the Huggins pitch (Cramer and Huggins, 1958) is an example. In Sec. A of this Introduction, the Huggins pitch is described and a definition of a simple dichotic pitch is given. In Sec. B two previous models of the perception of dichotic pitches are described. The first model—the central-spectrum model (e.g., Raatgever and Bilsen, 1986)—can explain the pitches evoked by some dichotic-pitch stimuli, but does not predict the pitch of others accurately. It does, however, provide the only account of the lateralization of dichotic pitches. The second model—the modified equalization–cancellation model (e.g., Culling *et al.*, 1998a, b)—can explain the pitches evoked by some of those dichotic-pitch stimuli for which the central-spectrum model fails, but it does not account for some others, nor does it purport to explain the lateralization of dichotic pitches.

The primary motivation for the experiments and modeling described in this paper was to evaluate the account of lateralization given by the central-spectrum model in relation to alternative accounts of the lateralization of simple dichotic pitches. The central-spectrum model was developed at a time when fast computational tools for auditory modeling were not readily available. A Fourier transform was used to perform an initial frequency analysis. This approach simulates unrealistically fine frequency resolution. Instead, we evaluated a ''modernized'' implementation of the central-spectrum model in which the Fourier analysis was replaced by a gammatone filterbank (Patterson *et al.*, 1995). This implementation is referred to as the ''gammatone central-spectrum'' model.

In Sec. C of this Introduction, a general rule for the lateralization of a simple dichotic pitch is described. An experimental test of the rule is reported in Sec. I. The results show that the rule is adequate as a gross predictor of the lateralization of a simple dichotic pitch. In Sec. II, computational implementations of four models of the lateralization of simple dichotic pitches are evaluated. These tests show that the gammatone central-spectrum model and a new model of lateralization—named the ''reconstruction–comparison'' model—both successfully explain the rule. An experimental dissociation of the predictions of these two models is reported in Sec. III. The results are more consistent with the reconstruction–comparison model than with the gammatone central-spectrum model.

The reconstruction–comparison model was designed to predict only the lateralization, not the pitch, of simple dichotic pitches. A comprehensive model of both the pitch and lateralization of simple dichotic pitches can be formed by combining the reconstruction–comparison model with the modified equalization–cancellation model. The ability of this combined model to account for the results of experiment 1 is confirmed in Sec. II B 4. Although the combined model has virtues that merit further study, two points require emphasis.

[a]Present address: Surgical Research Center, Department of Surgery (Otolaryngology) and Center for Neurological Sciences, University of Connecticut Health Center, Farmington, CT 06030. Electronic mail: michael@neuron.uchc.edu

First, we compared the combined model with a modernization of the central-spectrum model, not the original central-spectrum model. Second, the models were evaluated only with a restricted class of simple dichotic pitches.

A. The Huggins pitch

The first dichotic pitch was discovered by Huggins (Cramer and Huggins, 1958). The same white noise was presented over both channels of a headset, but with one channel filtered by an all-pass filter. The filter introduced a progressive shift in phase from 0° to 360° across a narrow range of frequencies centered on 600 Hz.[1] When either channel of the stimulus was presented monaurally, listeners heard the typical ''shshsh'' timbre of a noise, as expected because a phase-shifted white noise sounds the same as any other white noise. When the channels of the stimulus were presented binaurally, listeners heard a faint 600-Hz tone amidst the noise. For different listeners, the tone was lateralized to one or the other side of the head. The term ''dichotic pitch'' refers to the tone. In order to distinguish descriptions of this percept from descriptions of the stimulus, we use the term ''dichotic-pitch stimulus'' to refer to the entire stimulus.

The Huggins pitch is the prototypical ''simple dichotic'' pitch. The term simple refers to the fact that a single interaural manipulation, localized in frequency, creates the dichotic pitch against a broadband noise carrier of uniform interaural configuration. Because the single interaural manipulation is localized in frequency, the resulting pitch percept originates from a single frequency, in contrast to the situation with some other dichotic pitches in which interaural manipulations at multiple frequencies give rise to the perception of complex pitches. Two such examples are the multiple phase shift pitch (Bilsen, 1977; Raatgever and Bilsen, 1986) and the Fourcin pitch (Fourcin, 1970).

B. Two models of dichotic pitches

Bilsen, Raatgever, and their colleagues put forward the central-spectrum model as an account of both the pitch and lateralization of dichotic pitches (Bilsen, 1977; Raatgever and Bilsen, 1977, 1986; Frijns *et al.*, 1986; Raatgever *et al.*, 1998). Peripheral filtering of the left and right waveforms was simulated by a Fourier transform. Corresponding left and right Fourier components were vector summed as a function of an internal time delay applied to one component. The magnitude of the output vector was squared. The resulting three-dimensional plot of power versus internal time delay versus frequency was named the ''central activity pattern,'' and is equivalent to a cross-correlogram. Frequencies around 600 Hz and internal time delays near 0 μs were emphasized by applying weighting functions to the central activity pattern. Raatgever and Bilsen proposed that the central activity pattern was sliced into ''central spectra:'' profiles of power versus frequency for a fixed internal time delay. A selection mechanism searched for central spectra that contained well-defined peaks. The presence of a peak in a chosen spectrum determined that a dichotic pitch would be heard. The frequency of the peak determined the pitch and the internal delay of the chosen spectrum determined its lateralization.

Culling *et al.* (1998a, b) showed that this approach can give incorrect predictions of pitch when realistic frequency selectivity is simulated by a computational auditory filterbank instead of a Fourier transform. In particular, (1) for the binaural edge pitch (Klein and Hartmann, 1981), the model fails to predict that the pitch is salient at extremely narrow interaural-transition bandwidths, (2) for the Fourcin pitch (e.g., Fourcin, 1970), it predicts incorrect pitches for some combinations of the interaural phase and the interaural time delay (ITD) of the two noises used to generate the pitch, and (3) for the dichotic repetition pitch (Bilsen and Goldstein, 1974), it fails to predict that the pitch is not heard by many listeners who readily hear the other dichotic pitches.

Culling *et al.* (1998a, b) subsequently demonstrated that their modified equalization–cancellation model (Culling and Summerfield, 1995) could successfully explain cases (1) and (2). Peripheral frequency analysis of the left and right waveforms was simulated using a gammatone auditory filterbank (Patterson *et al.*, 1995) and a hair-cell model (Meddis, 1986, 1988). The model then performed equalization–cancellation (Durlach, 1960, 1972) independently in each frequency channel. In the equalization step, the outputs of corresponding left and right filters were equalized for level; in the subsequent cancellation step, one output was subtracted from the other as a function of an internal delay, with the remainder being temporally integrated by an exponential integrator of 50-ms time constant. The model next searched the set of such cancellation remainders across internal delay in order to find the smallest. It is termed the ''residual activation,'' and its value is approximately proportional to the interaural decorrelation in the frequency channel. The output of the model was a profile of residual activation versus frequency, termed the ''recovered spectrum.'' The frequency locations of peaks in recovered spectra account for the pitches of Huggins pitches, binaural edge pitches, and Fourcin pitches. The model does not explain the existence of the dichotic repetition pitch.

In summary, neither the central-spectrum model nor the modified equalization–cancellation model provides a comprehensive account of the pitch of all dichotic pitches. Culling *et al.* (1998a, b) suggested that the Huggins pitch, the binaural edge pitch, and the Fourcin pitch, which are all heard relatively easily by the majority of listeners, might arise through the processes described by the modified equalization–cancellation model, while the dichotic repetition pitch, which is heard by only a subset of listeners, might arise through the processes described in the central-spectrum model. A dilemma for this two-mechanism explanation is that only the central-spectrum model accounts for the lateralization of dichotic pitches: Culling *et al.* did not identify an extension to the modified equalization-cancellation model which predicts lateralization. This dilemma led us to investigate alternatives to the account of the lateralization of dichotic pitches given by the central-spectrum model.

C. The lateralization of a Huggins pitch

The lateralization of only one simple dichotic pitch—the Huggins pitch—has been studied quantitatively (Raatgever, 1980, a subset of whose results were reported by Raatgever

and Bilsen, 1986; Yost *et al.*, 1987; Grange and Trahiotis, 1996). Raatgever's results influenced the present study and are described next. Yost *et al.*'s and Grange and Trahiotis' results are described in Sec. IV B.[2]

Raatgever (1980) demonstrated that the lateralization of Huggins pitch depended upon the interaural configuration of the noise carrier. A Huggins pitch was created by a 6%-bandwidth phase change, centered on 600 Hz, imposed on either diotic ($N0$) or interaurally inverted ($N\pi$) noise carriers. Overall, the results showed that with the $N0$ carrier the Huggins pitch was lateralized to the left or right side of the head, but with the $N\pi$ carrier the Huggins pitch was lateralized near the midline. These results were obtained from experimental conditions in which listeners matched the lateralization of the Huggins pitch to the lateralization of a ''match stimulus.'' The match stimulus consisted of a broadband noise mixed with a 600-Hz pure tone that was just audible.[3] The ITD of the match stimulus was fixed within a condition, and varied across conditions. Listeners adjusted the ITD of the Huggins-pitch stimulus until its lateralization was the same as that of the match stimulus. Although there was considerable variability in the matches, they were compatible with the idea that there is a linear relationship between the ITD given to the match stimulus (ITD_M) and the adjusted ITD of the Huggins-pitch stimulus (ITD_{HP}), such that with the $N0$ carrier

$$ITD_{HP}=ITD_M+0.8\,\text{ms}\ \ (\text{for}\ \ ITD_M<0), \tag{1}$$

$$ITD_{HP}=ITD_M\pm0.8\,\text{ms}\ \ (\text{for}\ \ ITD_M=0), \tag{2}$$

$$ITD_{HP}=ITD_M-0.8\,\text{ms}\ \ (\text{for}\ \ ITD_M>0). \tag{3}$$

With the $N\pi$ carrier, the relationship was

$$ITD_{HP}=ITD_M\ \ (\text{for all}\ \ ITD_M). \tag{4}$$

Raatgever (1980) and Raatgever and Bilsen (1986) argued that these results were compatible with the central-spectrum model. For a 600-Hz Huggins pitch imposed on an $N0$ carrier, the selection mechanism would choose central spectra at internal delays of about -0.8 or $+0.8$ ms because in those central spectra the peak at 600 Hz was pronounced. For a 600-Hz Huggins pitch imposed on an $N\pi$ carrier, the selection mechanism would, for the same reason, choose a central spectrum close to 0 ms.

We hypothesized that the relationships defined by Eqs. (1)–(4) can be generalized in two respects. First, they apply to any simple dichotic pitch, including, but not limited to, the Huggins pitch. Second, they apply to simple dichotic pitches of any center frequency by specifying that the translation is not fixed at ±0.8 ms, but is plus-or-minus one-half the period of the center frequency of the dichotic pitch (which, for a 600-Hz Huggins pitch, is 0.833 ms). With these generalizations, the relationships define a ''half-period rule,'' as follows: *The lateralization of a simple dichotic pitch corresponds to the ITD of the noise carrier (measured at the center frequency f of the dichotic pitch) but translated by one-half of the period of f. The translation can be either to the left or to the right, with the dichotic pitch being heard in whichever final position is closer to the midline. If the two positions are equally close to the midline, then the dichotic pitch may be heard in either.*

The goal of the first experiment was to evaluate the generality of the half-period rule.

I. EXPERIMENT 1: EMPIRICAL TESTS OF THE HALF-PERIOD RULE

A. Rationale, conditions, and predictions

Given that the half-period rule had been derived from the lateralization of Huggins-pitch stimuli, it was desirable to use a new type of simple dichotic-pitch stimulus to test the generality of the rule. To meet this need, ''generic'' simple dichotic-pitch stimuli were created. These stimuli consisted of a broadband noise that was interaurally correlated at all frequencies except those defining a single narrow band. Within that band, the noise was decorrelated. The justification for this choice was twofold. First, informal listening suggested that, provided that the bandwidth of the decorrelated band was small, these stimuli sounded the same as a Huggins-pitch stimulus whose phase transition was centered on the same frequency as the center frequency of the decorrelated band. Second, such stimuli generate the same output from the modified equalization–cancellation model as Huggins-pitch stimuli. Accordingly, experiment 1 explored the generality of the half-period rule by evaluating its predictions for the lateralization of generic simple dichotic pitches at different frequencies with noise carriers of different interaural configurations.

The stimuli were created by inserting an interaurally decorrelated (Nu) band into an otherwise interaurally correlated noise carrier (Fig. 1). The band was 80 Hz wide and centered on either 400, 500, 600, 700, or 800 Hz.

In one set of dichotic-pitch stimuli (termed ''NR1''[4]), the noise carrier was given an ITD of $+833$ μs so that it was lateralized on the right side of the head [Fig. 1, panels (A) and (B)]. In Fig. 1, the vertical solid line represents the noise carrier. The hyperbolic dotted curves show the predictions of the half-period rule as a function of frequency. The rule predicts that the lateralizations of the 400, 500, 600, 700, and 800-Hz dichotic pitches would correspond to -417, -167, 0, $+119$, and $+208$ μs. In a second set of dichotic-pitch stimuli (termed ''NL1''), the left and right waveforms were swapped [Fig. 1, panels (C) and (D)]. The lateralizations of the NL1 dichotic pitches were expected to be the mirror images of the NR1 dichotic pitches, corresponding to $+417$, $+167$, 0, -119, and -208 μs. In a third set of dichotic-pitch stimuli (termed ''Nπ1'') the noise carrier was interaurally inverted [Fig. 1, panels (E) and (F)]. In these panels, the hyperbolic solid curves show the ITD of the noise carrier, whereas the predictions of the half-period rule are shown by the vertical dotted line. The rule predicts that the lateralization of the Nπ1 dichotic pitches would correspond to 0 μs for all frequencies.

In summary, the half-period rule predicts that lateralization depends on the center frequency of the dichotic pitch in the NR1 and NL1 conditions. It predicts that lateralization is fixed across frequency in the Nπ1 condition.

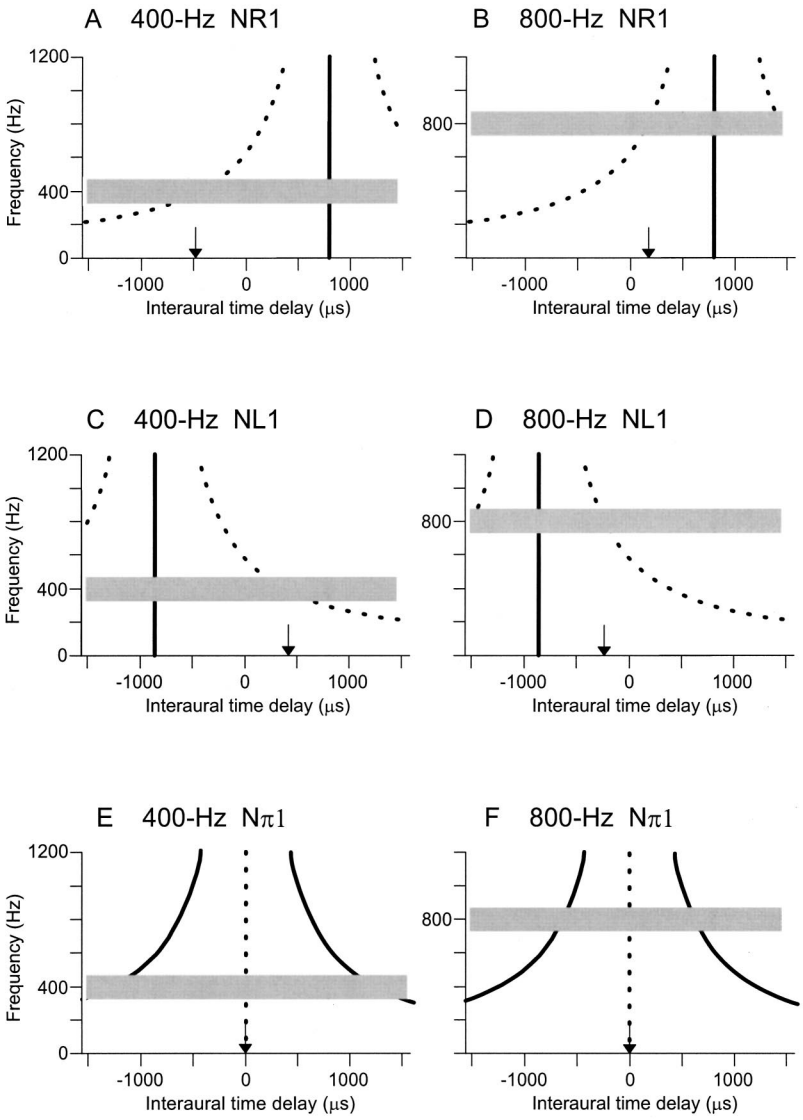

FIG. 1. Schematic plots of the dichotic-pitch stimuli used in experiment 1. The solid line shows the noise carrier. The dotted line shows the ITD corresponding to a translation of one-half period. The horizontal bar shows the interaurally decorrelated band. The arrow marks the ITD corresponding to the predicted lateralization of each dichotic pitch from the half-period rule.

B. Method

1. Stimuli and apparatus

The stimuli were generated digitally at a sampling rate of 20 000 samples per s with 16-bit amplitude quantization. They were created by modifying a digital, flat-spectrum noise constructed by summing together a sine and cosine component at each frequency from 2 to 1200 Hz (inclusive) in 2-Hz steps. The amplitude of each component was selected randomly from a Gaussian distribution.[5] Unless otherwise stated, the amplitude of any left-channel component was equal to the amplitude of the corresponding right-channel component. The components were summed to create the left-channel and right-channel waveforms, and then 20-ms raised-cosine ramps were applied to their onset and offset. The overall duration of each stimulus was 500 ms. Twenty independent tokens of each stimulus were created.

Interaurally decorrelated bands were made by selecting the amplitudes of the left-channel sine and cosine components independently of the corresponding right-channel sine and cosine components. This manipulation was restricted to an 80-Hz-wide band centered on either 400, 500, 600, 700, or 800 Hz. A bandwidth of 80 Hz was chosen because it is equal to the equivalent rectangular bandwidth (ERB) of the auditory filter centered on 500 Hz (Glasberg and Moore, 1990). The stimuli differed only in the interaural configuration of the remainder of the noise carrier. For the NR1 dichotic-pitch stimuli, the starting phase of each remaining component was set to give an ITD of $+833$ μs. For the NL1 dichotic-pitch stimuli, the starting phase was set to give an ITD of -833 μs by swapping the left and right waveforms of the NR1 stimuli. For the Nπ1 dichotic-pitch stimuli, the left waveform was inverted.

The procedure required listeners to compare the lateralizations of the dichotic pitches to those of known ''pointers.'' These pointers were created by synthesizing bandlimited diotic noises of 100-Hz bandwidth which were centered on either 400, 500, 600, 700, or 800 Hz. The design of the experiment required the lateralizations to be compared to the predictions. Consequently, lateralizations were also measured for a set of ''markers'' whose lateral position corresponded *exactly* to the predictions of the half-period rule. These markers were created by synthesizing bandlimited noises of 80-Hz bandwidth centered on either 400, 500, 600, 700, or 800 Hz. As a convenient method for achieving the

required interaural phases, the markers were constructed by giving each component an ITD of either $+833$ μs (NR1) or -833 μs (NL1) and then inverting one waveform. In Fig. 1, the markers are represented by the part of the dotted lines that falls behind the decorrelated noise that is represented by the gray bars.

The stimuli were converted to analog by a Loughborough Sound Images digital-to-analog converter (AM/D16DS). Each channel was passed separately through a custom-built attenuator, a custom-built headphone amplifier, and a further attenuator (Marconi Instruments type TF2612). They were then presented to listeners using a Sennheiser HD-480 headset at a spectrum level of 40 dB SPL. Listeners sat in a double-walled sound booth. The Marconi Instruments attenuators were set so that the difference between the left and right responses of the headset was less than 0.4 dB at 600 Hz. Over the 400–800-Hz range, the headset gave a near-flat response (± 1 dB) and near-identical left/right responses (± 1 dB). The levels were measured with a type 4153 Bruel & Kjaer artificial ear fitted with a type DB0843 flat-plate adapter, a type 4134 $\frac{1}{2}$-in. microphone, and a type 2636 measuring amplifier.

2. Procedures

A two-interval task was used to measure the lateralization of each dichotic pitch. In interval one a dichotic-pitch stimulus was presented. In interval two a pointer of the same center frequency was presented. Listeners indicated whether the pointer was lateralized to the left or to the right of the dichotic pitch. The lateralization of the pointer was then changed by varying its interaural intensity difference (IID). The IIDs were determined by an adaptive procedure, with trials from two such procedures randomly interleaved (Jesteadt, 1980). In one procedure the IID was increased by 4 dB in favor of the right ear following an ''on-the-left'' response, and was increased by 4 dB in favor of the left ear following two successive ''on-the-right'' responses. The procedure was continued until 14 reversals in the direction of change of IID had occurred. The threshold was estimated as the mean of the IIDs of the last ten reversals. The procedure converges on the IID for which the pointer is judged to be to the right of the dichotic pitch on 70.7% of presentations (Levitt, 1971), and so this threshold is the ''to-the-right'' threshold. In the second procedure the adaptive rule was reversed so that the ''to-the-left'' threshold was estimated. The lateralization in dB of the dichotic pitch was estimated as the mean of the to-the-left and to-the-right thresholds. The reported lateralizations are the means of five independent adaptive runs collected on separate days.

If no additional precautions are taken, the loudness of the pointer increases at nonzero IIDs. To prevent this, its loudness was kept constant by adjusting the intensities of the left and right channels together according to the rule defined by Hill and Darwin (1996, footnote 1). IIDs rather than ITDs were used to control the lateralization of the pointer because of concern that at large ITDs—approaching one-half of the period of the center frequency—the pointer would jump to the ''wrong'' side of the head, thereby confusing the listeners. The results thus measure lateralization on a scale of intensity. The half-period rule, however, predicts lateralization on a scale of time. The reason for measuring the lateralization of the marker stimuli was to permit the lateralization of the dichotic pitches to be compared with the predictions of the half-period rule. If the predictions are correct, then the lateralizations (in dB) of the marker stimuli and the dichotic-pitch stimuli should be the same. Marker stimuli were not included in the Nπ1 conditions because the predicted lateralization of 0 μs was assumed to correspond to an IID of 0 dB.

In each experimental session, listeners judged the lateralizations of an NR1 dichotic pitch, an NL1 dichotic pitch, an $N\pi 1$ dichotic pitch, an NR1 marker, and an NL1 marker, all with the same center frequency. This choice was made in order to minimize the error within each center frequency. The conditions were tested in a random order. Different center frequencies were tested in separate sessions.

3. Listeners

Three listeners participated, of whom Listener A was the first author. The remaining listeners were paid for their participation. All displayed hearing levels within normal limits at octave frequencies from 250 to 8000 Hz inclusive. At 500 Hz, the left/right asymmetries in thresholds were 0.3 dB (Listener A), 1.5 dB (B), and 1.8 dB (C), with the lower thresholds in the right ear (Listener A), the right ear (B), and the left ear (C). The listeners were those three from a pool of five with the lowest thresholds for detecting a simple dichotic pitch. These thresholds were measured by varying the level of an interaurally decorrelated band centered on 600 Hz in an $N0$ noise carrier.

4. Statistical analysis

The effect of center frequency on lateralization in the NR1, NL1, and Nπ1 conditions was analyzed using separate single-factor (center frequency) repeated-measures analyses of variance (ANOVAs). Comparisons between dichotic pitches and markers were analyzed using separate two-factor (stimulus type$\times$center frequency) repeated-measures ANOVAs. Comparisons between the NR1 and NL1 conditions were analyzed using the same two-factor design, but with the NL1 lateralizations multiplied by -1 to undo the effect of swapping the left and right waveforms.

C. Results

Figures 2, 3, and 4 show the lateralizations in dB for, respectively, the NR1, NL1, and Nπ1 conditions. In each figure both the individual and mean results are shown for the dichotic pitches (squares) and for the marker noises (asterisks). Error bars marking ± 1 standard deviation are plotted where they exceed the size of the symbols. The horizontal dashed line marks the 0-dB IID corresponding to the midline.

Figure 2 shows that the lateralization of the NR1 dichotic pitches depended upon frequency [$F(4,8)=7.7$, $p=0.008$]. At 400 Hz the dichotic pitch was heard on the left. As its frequency was increased to 600 Hz it moved towards the midline, but it did not reliably cross to the right at either

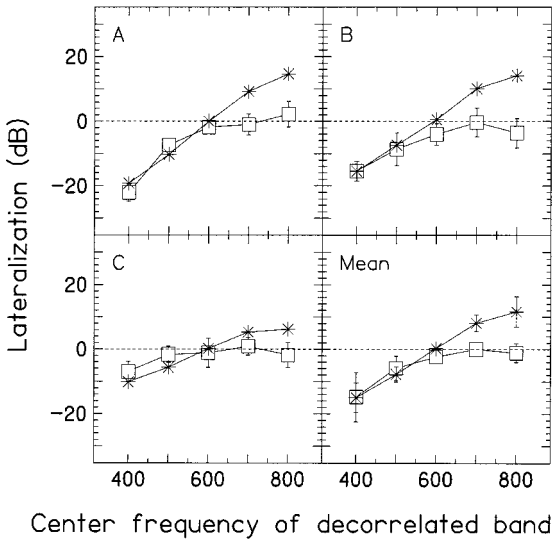

FIG. 2. Results of experiment 1 for the NR1 conditions. Squares: dichotic-pitch lateralizations; asterisks: marker lateralizations. Negative lateralizations correspond to the left side of the head, zero to the midline, and positive to the right.

700 or 800 Hz. The dichotic-pitch lateralizations differed from the marker lateralizations only at the higher frequencies. The difference ranged from 0.3 dB at 400 Hz to −12 dB at 800 Hz [main effect of stimulus type: $F(1,2)=7.3$, $p>0.1$; interaction of stimulus type with frequency: $F(4,8)=25.8$, $p<0.001$].

Figure 3 shows that the lateralization of the NL1 dichotic pitches also depended upon frequency [$F(4,8)=6.8$, $p=0.01$]. The dependence was the opposite of the NR1 stimuli. The dichotic-pitch lateralizations did not differ from the marker lateralizations [main effect of stimulus type: $F(1,2)=0.33$, $p>0.1$; interaction of stimulus type with frequency: $F(4,8)=1.5$, $p>0.1$].

Figure 4 shows that the lateralization of the Nπ1 dichotic pitches was independent of frequency [$F(4,8)=0.8$, $p=0.6$]. The mean lateralization, averaged across all conditions, was −3.0 dB, and so was biased towards the left side. The expected lateralization of 0 dB was outside the 95%-confidence interval (−4.3 to −1.7 dB; degrees of freedom =14).

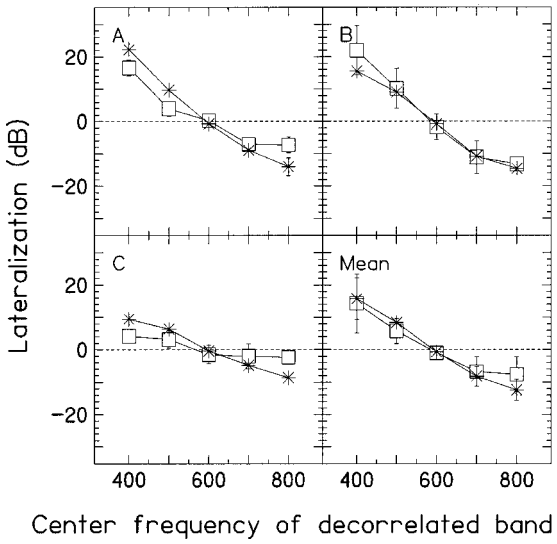

FIG. 3. Results of experiment 1 for the NL1 conditions, plotted in the same format as Fig. 2.

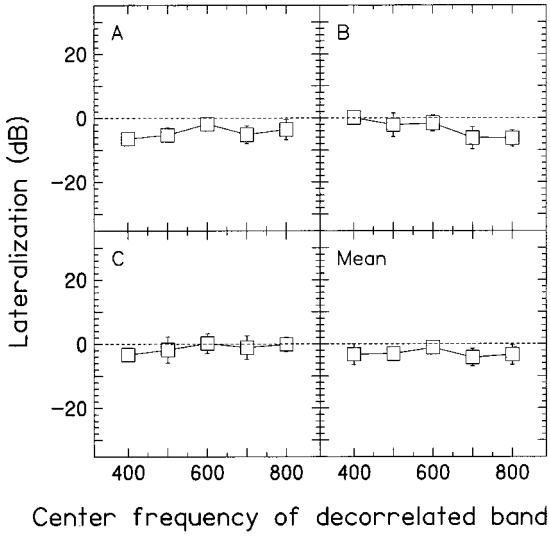

FIG. 4. Results of experiment 1 for the Nπ1 conditions, plotted in the same format as Fig. 2. Marker stimuli were not used in this condition and so no asterisks are plotted.

D. Discussion

The results of experiment 1 partially confirm the predictions of the half-period rule. The lateralization of the dichotic pitch shifted with frequency when it was predicted to do so (in the NR1 conditions, the mean lateralization shifted by 14 dB as the frequency was increased from 400 to 800 Hz and in the NL1 conditions it shifted by 22 dB). The lateralization did not shift with frequency when it was predicted not to do so (in the Nπ1 conditions, the mean lateralization shifted by only 0.1 dB). The data support the rule only partially because the lateralizations of the higher-frequency NR1 dichotic pitches were closer to the midline than predicted. Furthermore, the lateralizations of the Nπ1 dichotic pitches were biased towards the left side. In summary, the half-period rule predicts the gross pattern of lateralizations of a simple dichotic pitch, but does not account for the fine detail.

The goodness-of-fit of the half-period rule can be computed after the lateralizations are transformed to an ITD scale. The transformation was defined by fitting a quadratic curve to the lateralizations of the NR1 and NL1 *markers*, for which the actual ITD and the measured IID are known. The quadratics were then used to transform the dichotic-pitch lateralizations from dB to μs.[6] The results are shown in Fig. 5. The symbols plot the transformed lateralizations for each listener, and the solid lines plot the predictions of the half-period rule. The fit is best for the NL1 conditions. The rms errors of the predictions from the mean results were 127 μs (NR1), 23 μs (NL1), and 54 μs (Nπ1).

The only difference between the NR1 and NL1 stimuli was that the left and right waveforms were swapped before the digital-to-analog converter. The lateralizations of the NR1 dichotic pitches were therefore expected to be the exact opposites of the NL1 dichotic pitches. The observed asym-

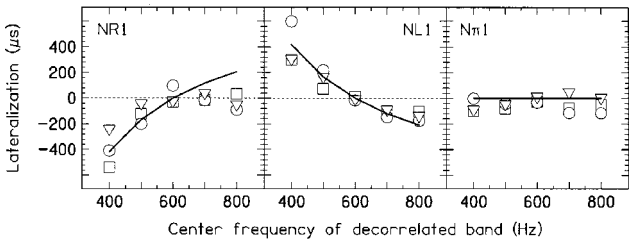

FIG. 5. Lateralizations in μs for the NR1 conditions (left panel), NL1 conditions (middle panel), and Nπ1 conditions (right panel). Squares: Listener A; circles: Listener B; triangles: Listener C. The solid lines mark the predictions of the half-period rule.

metry is surprising. It is unlikely to have arisen in the apparatus because the left and right channels were carefully balanced at the headset. The accuracy of the balancing is supported by the *symmetry* between the lateralizations of the NR1 and NL1 markers [main effect of stimulus type: $F(1,2)=0.06$; $p>0.1$; interaction of stimulus type with frequency: $F(4,8)=0.73$, $p>0.1$]. The dichotic-pitch asymmetry is more likely to have arisen in the auditory analysis. This idea is supported by two informal observations. First, the majority of our listeners perceived an $N0$-carrier Huggins pitch to be strongly lateralized to one side or the other, but not both sides, of the head. Second, the side remains the same even when the headset is reversed. It is possible that a similar asymmetry in the auditory analysis could account for the bias in the Nπ1 lateralizations. The source of the asymmetry is, however, not known.

Despite the asymmetry, the NR1, NL1, and Nπ1 dichotic pitches were lateralized systematically. The results demonstrate, therefore, that an important influence on the lateralization of a simple dichotic pitch is the configuration of the noise carrier. Although it is true that the perception of a dichotic pitch is due to the interaurally decorrelated band, if this band had been presented *alone* it would have had the diffuse lateralization typical of an interaurally decorrelated noise (Gabriel and Colburn, 1981; Grantham, 1995). Instead, when the band is presented amidst a noise carrier to form a simple dichotic pitch, it has a definite, systematic lateralization. Models of the lateralization of simple dichotic pitches should therefore take into account the interaural configurations of both the band and the noise carrier.

II. MODELS OF DICHOTIC-PITCH LATERALIZATION

The aim of the simulations reported next was to investigate the degree to which different computational models can accommodate the half-period rule and the results of experiment 1. Four accounts of the lateralization of a simple dichotic pitch were evaluated. The first account is our modernization of the central-spectrum model (e.g., Raatgever and Bilsen, 1986), which was described in the Introduction as the gammatone central-spectrum model. The second account is derived from the modified equalization–cancellation model (e.g., Culling *et al.*, 1998a, b). The third account is the reconstruction–comparison model. The fourth account combines the modified equalization–cancellation and reconstruction–comparison models. Each account was implemented as a computational model.

In order to highlight the key differences between the models, they were implemented within a common computational framework. In three models the lateralization of a dichotic pitch is determined from a cross-correlogram (e.g., Jeffress, 1948; Colburn, 1977; Shackleton *et al.*, 1992; Stern and Trahiotis, 1997). The calculation of the cross-correlogram is described in Sec. II A. The other account—the modified equalization–cancellation model—is based on cross-subtraction instead of cross-correlation. Cross-subtraction is described in Sec. II B 2. The central-spectrum and modified equalization–cancellation models were briefly described in Sec. B of the Introduction.

The ability of the models to account for the half-period rule and to predict the listeners' lateralizations in experiment 1 are reported separately in Secs. II B and II C. For the half-period rule the simulations are reported for just the NR1 and Nπ1 conditions. As both the rule and the computational models are left/right symmetric, the simulations for the NL1 conditions are the mirror images of the simulations for the NR1 conditions. The models were evaluated using the same digital stimuli used in experiment 1.

A. The computational framework and the binaural cross-correlogram

The calculation of a binaural cross-correlogram is illustrated schematically in Fig. 6. The digital representations of the left- and right channels of a stimulus are analyzed by a matched pair of gammatone filterbanks (Patterson *et al.*, 1995). Each filter has a bandwidth of 1 ERB (Glasberg and Moore, 1990). The filters span the range from 100 to 1200 Hz with a density of 5 filters per ERB, resulting in 68 filters in each filterbank.[7] The output of each filter is half-wave rectified and then logarithmically compressed.[8] These processes crudely simulate peripheral auditory frequency analysis and transduction by the inner-hair cells.

Next, the waveforms in corresponding frequency channels are cross-multiplied, sample-by-sample, as a function of an internal delay applied to one output. The internal delay ranges between -5000 and $+5000$ μs in steps of 50 μs. The cross-products at each internal delay are averaged across the duration of the stimulus. The result is the cross-correlogram: a three-dimensional plot of binaural cross-product versus frequency versus internal delay. Finally, a weighting function is applied in order to emphasize frequencies f (in Hz) around 600 Hz (Raatgever, 1980; Raatgever and Bilsen, 1986):

$$\text{frequency weight} = e^{-((f/300)-2)^2} \quad f < 600 \text{ Hz}, \tag{5}$$

$$\text{frequency weight} = e^{-((f/600)-1)^2} \quad f \geqslant 600 \text{ Hz}. \tag{6}$$

Raatgever and Bilsen (1986) used this weighting function in the central-spectrum model. It reflects the dominance of the 600-Hz region in percepts of complex dichotic pitches fashioned from multiple interaural phase transitions, although the function itself was derived from data describing the dominance of the 600-Hz region on the lateralization of a broadband noise (Raatgever, 1980). We included it to maintain compatibility with the central-spectrum model. We also did not include the filters that are often incorporated in computational auditory models to represent the transfer functions of

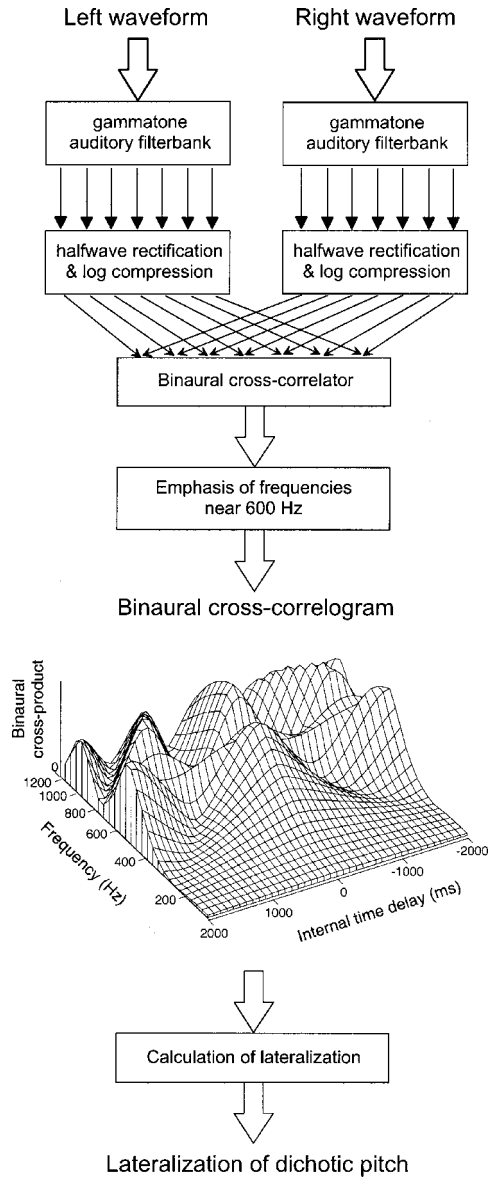

FIG. 6. Schematic illustration of the computational framework used in the simulations. The cross-correlogram is for a 600-Hz Huggins pitch on an $N0$ noise carrier.

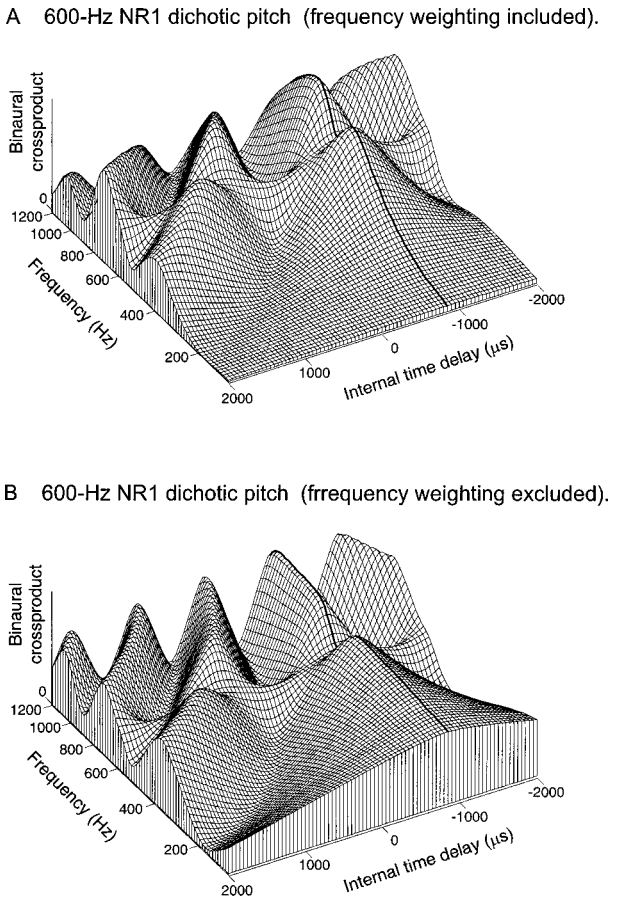

FIG. 7. Binaural cross-correlograms for a 600-Hz NR1 dichotic pitch. Panel (A) shows the result of the analysis with frequencies around 600 Hz emphasized. Panel (B) shows the result without any frequency emphasis. The bold lines mark the ridge due to the noise carrier. The illustrated resolution of frequency channels and internal time delays is the same as that used in all the simulations. The range of internal time delays illustrated is limited to ± 2000 μs although the simulations used ± 5000 μs.

the outer and middle ears, because they would further attenuate low and high frequencies relative to mid frequencies.

Two other omissions also deserve comment. First, the breakdown of neural phase locking at high frequencies was not simulated because the present stimuli did not contain any components above 1200 Hz. Second, many models of the lateralization of single, isolated sounds use a second weighting function to emphasize internal delays near 0 μs (e.g., Stern *et al.*, 1988; Shackleton *et al.*, 1992; Stern and Shear, 1996). The function also serves to remove additional peaks in the cross-correlogram that arise due to the relatively narrow bandwidth of the auditory filters. We did not incorporate this function because it prevents the modified equalization–cancellation model from detecting interaural decorrelation. Instead, we based our estimates of lateralization on the peak closest to an internal delay of 0 μs.

Panel (A) of Fig. 7 shows the binaural cross-correlogram of one of the 600-Hz NR1 dichotic-pitch stimuli from experiment 1. The noise carrier has an ITD of $+833$ μs and so gives rise to a ridge of peaks at an internal delay of -833 μs (marked by the bold line). Note that the numerical labeling of the internal-delay axis runs from positive values on the left to negative values on the right. This reversal facilitates the interpretation of the cross-correlogram because features heard on the right side of the head appear in the right half of the plot. The cross-correlation functions are sinusoidal in frequency channels distant from 600 Hz. This occurs because the channels are dominated by the noise carrier and so are interaurally correlated. The cross-correlation functions swing between values close to zero, at internal delays where the half-wave-rectified waveforms in the channels are out of phase, and high values, at internal delays where the waveforms are in phase. The cross-correlation functions are much flatter in channels near 600 Hz. This occurs because the channels are dominated by the interaurally decorrelated band creating the dichotic pitch. The half-wave-rectified waveforms in these channels are never perfectly out of phase, nor perfectly in phase, so the cross-correlation functions neither fall to zero nor do they reach high values. The effect of the frequency weighting [Eqs. (5) and (6)] can be gauged by comparing the two panels of Fig. 7, the lower panel of which

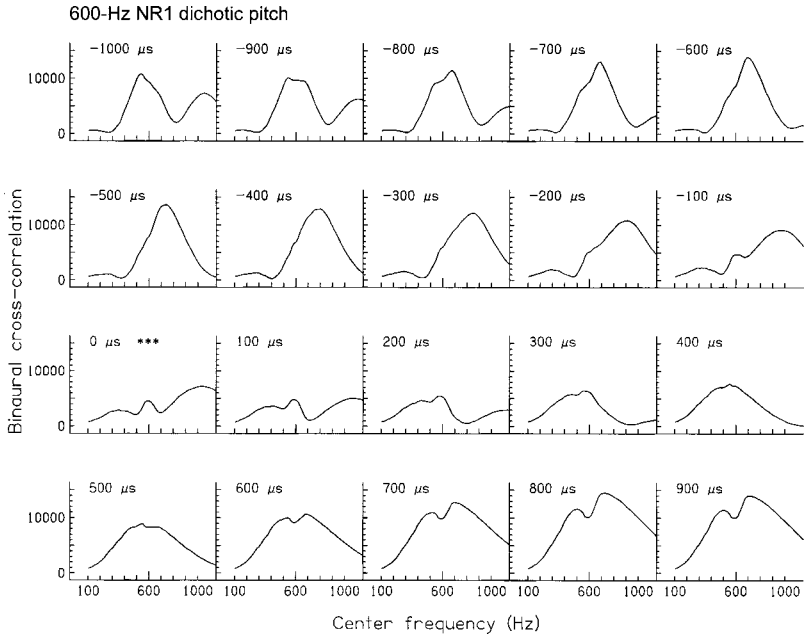

FIG. 8. Central spectra for a 600-Hz NR1 dichotic pitch generated by the gammatone central-spectrum model. The internal time delay of each spectrum is indicated on each panel. The 0-μs spectrum is marked by asterisks because the half-period rule predicts the lateralization of this dichotic pitch to correspond to 0 μs. In the simulations, central spectra were measured at 50-μs intervals instead of the 100-μs intervals illustrated.

contains the cross-correlogram of the same stimulus but with the frequency weighting excluded.

B. Modeling the half-period rule

1. The gammatone central-spectrum model

We implemented the central-spectrum model within the computational framework described in Sec. II A. The implementation is termed the ''gammatone central-spectrum model'' in order to emphasize that it differs from Raatgever and Bilsen's (1986) implementation by using a gammatone filterbank to simulate normal auditory frequency selectivity (e.g., Patterson and Moore, 1986; Moore, 1995) in place of a Fourier transform. The cross-correlogram shown in Fig. 7 (upper panel) is the central activity pattern generated by the gammatone central-spectrum model for a 600-Hz NR1 dichotic pitch. Figure 8 shows a set of central spectra for this stimulus. The interaurally decorrelated band creates the small peak at 600 Hz visible in some central spectra (e.g., at $+100$ μs) and the small valley at 600 Hz visible in others (e.g., at $+900$ μs). The majority of the activity in each central spectrum is due to the noise carrier. In some central spectra this activity is difficult to distinguish from the activity due to the interaurally decorrelated band (e.g., between -600 and -300 μs).

The central-spectrum model requires that the internal delay of the selected central spectrum corresponds to the lateralization of the dichotic pitch. The criteria for making the selection are therefore crucial for numerical predictions. Raatgever and Bilsen (1986) did not provide computationally rigorous criteria for selecting central spectra. They suggested that spectra are chosen using ''clues like harmonicity and depth of modulation or *a priori* knowledge of the spectral features'' (p. 431). They also commented that a peak defining a dichotic pitch should be ''pronounced'' (p. 432). Their suggestions were illustrated using a 600-Hz Huggins pitch (cf. Sec. C of the Introduction to this paper). With an $N0$ noise carrier, they argued that the selection mechanism would choose two central spectra: ''central spectra arise at ... ± 0.8 ms that have a pronounced peak at this very frequency [600 Hz]. In the center [0 ms] a broadband spectrum is found with a sharp dip. Both lateral spectra at ± 0.8 ms are characteristic for the pitch perceived. The model thus predicts the (ambiguous) lateralization of the pitch image at either lateral side'' (p. 432). With an $N\pi$ noise carrier, they argued that ''... only in the center [0 ms], a spectrum is found consisting of one peak at f_0 [600 Hz]. The predicted pitch will thus be centrally localized.'' (p. 432).

These qualitative criteria do not resolve the difficulty of distinguishing peaks due to the decorrelated band from peaks due to the correlated noise. Accordingly, to evaluate the gammatone central-spectrum model, we assumed that the frequency of the dichotic pitch is established by a separate process; this issue is addressed in Sec. II B 4. The only task of the model is to predict the lateralization of the dichotic pitch. Accordingly, the following rule was implemented: given a knowledge of the expected frequency of the dichotic pitch, the central spectrum with the most symmetric peak at that frequency is chosen, where a symmetric peak is one whose bounding valleys are equal in depth. Of the central spectra illustrated in Fig. 8, the one which meets this criterion is at 0 μs. The precise choice varied among the 20 exemplars of the set of 600-Hz NR1 stimuli used in experiment 1—due to the random fluctuations inherent to a noise—giving a mean internal delay of $+13$ μs. The gammatone central-spectrum model thus predicts that the lateralization of the 600-Hz NR1 dichotic pitch corresponds to an internal delay of $+13$ μs. The predicted lateralizations for all the NR1 and Nπ1 conditions are reported in Table I. They show that the gammatone central-spectrum model can accommodate the half-period rule. For the NR1 conditions the predictions increase monotonically in accordance with the rule. For the Nπ1 conditions the predictions fit the rule perfectly: the model consistently chose the 0-μs central spectrum because the activity due to the noise carrier is near zero in this central spectrum and so yields a highly symmetric peak (Fig. 9).

TABLE I. Predictions (ITDs in μs of the half-period rule and of four lateralization models for the NR1 conditions (upper panel) and the Nπ1 conditions (lower panel) of experiment 1. The rightmost column shows the rms error between the model predictions and the half-period rule. Because both the half-period rule and the computational models are left/right symmetric, the predictions for the NL1 conditions equal those for the NR1 conditions but with the sign reversed. For each model the mean and standard deviation (σ) of each lateralization are listed.

Model		Center frequency of decorrelated band (Hz)					rms error from half-period rule
		400	500	600	700	800	
Half-period rule (NR1 conditions)		**−417**	**−167**	**0**	**119**	**208**	···
Gammatone central spectrum	Mean	−285	−95	13	125	200	68
	σ	*24*	*22*	*22*	*34*	*0*	
Modified equalization–cancellation	Mean	93	233	−333	333	−23	355
	σ	*2350*	*2010*	*2920*	*1530*	*2070*	
Reconstruction–comparison	Mean	−365	−115	35	140	235	40
	σ	*78*	*54*	*37*	*35*	*24*	
Combined modified equalization–cancellation/reconstruction–comparison	Mean	−260	−98	30	135	210	78
	σ	*53*	*53*	*34*	*40*	*21*	
Half-period rule (Nπ1 conditions)		**0**	**0**	**0**	**0**	**0**	···
Gammatone central spectrum	Mean	0	0	0	0	0	0
	σ	*0*	*0*	*0*	*0*	*0*	
Modified equalization–cancellation	Mean	93	233	−333	333	−23	239
	σ	*2350*	*2010*	*2920*	*1530*	*2070*	
Reconstruction–comparison	Mean	−35	−75	125	−25	0	68
	σ	*67*	*44*	*36*	*26*	*0*	
Combined modified equalization–cancellation/reconstruction–comparison	Mean	−125	−75	125	−25	0	87
	σ	*36*	*34*	*32*	*26*	*0*	

2. The modified equalization–cancellation model

The modified equalization–cancellation model defined by Culling *et al.* (1998a, b) was designed to predict the pitch of dichotic pitches but not their lateralization. Nonetheless, it was evaluated here for two reasons: first, to demonstrate that a superficially attractive extension to the model also fails to predict lateralization; and second, to introduce the description of the ''combined model'' which is evaluated in Sec. II B 4.

The output of the modified equalization–cancellation model is a plot of residual activation versus frequency. Residual activation is the smallest time-integrated remainder after cancellation in each frequency channel. The value of the internal delay giving the residual activation is a possible source of information about lateralization. We tested the hypothesis that this ''best'' internal delay can predict the lateralization of a dichotic pitch. In order to accommodate the modified equalization–cancellation model within the computational framework described in Sec. II A, it was necessary to alter the model in two ways. First, half-wave rectification and logarithmic compression replaced the hair-cell model. Second, a 500-ms rectangular integrator replaced the 50-ms exponential integrator. The upper panel of Fig. 10 shows the recovered spectrum for a 600-Hz NR1 dichotic pitch. As expected, it contains a single peak, centered on 600 Hz, marking the perceived frequency of the dichotic pitch. The lower panels of Fig. 10 plot the relationship between the center frequency of the interaurally decorrelated band of the NR1 dichotic-pitch stimuli and the frequency of the single peak in the recovered spectrum (measured to a resolution of 1 frequency channel or 0.2 ERBs). The 1:1 correspondence between the two (lower-left panel) and the small standard deviation (lower-right panel) together demonstrate that our implementation of the modified equalization–cancellation model yields accurate estimates of the perceived pitches of simple dichotic pitches. In order to test the lateralization hypothesis, we measured the best delay in the single frequency channel closest to the center of the interaurally decorrelated band. For the 600-Hz NR1 dichotic pitches, this delay ranged from −5000 to +4850 μs. The predictions for the NR1 and Nπ1 conditions are similarly variable (Table I). Clearly, the best delay does not predict the lateralization of the dichotic pitch. The poor predictions arise because the random ITDs present in the interaurally decorrelated band mean that no single delay can be consistently best across a set of dichotic-pitch stimuli.

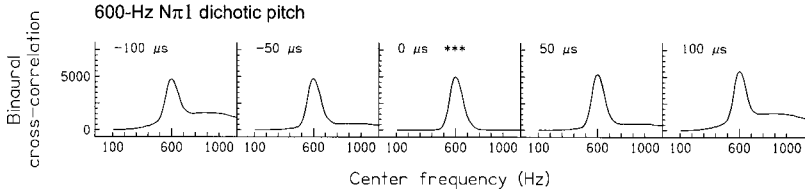

FIG. 9. Central spectra for a 600-Hz Nπ1 dichotic pitch. The activity due to the noise carrier is minimized in the central spectrum at 0 μs, and so this spectrum is chosen by the symmetric-peak criterion.

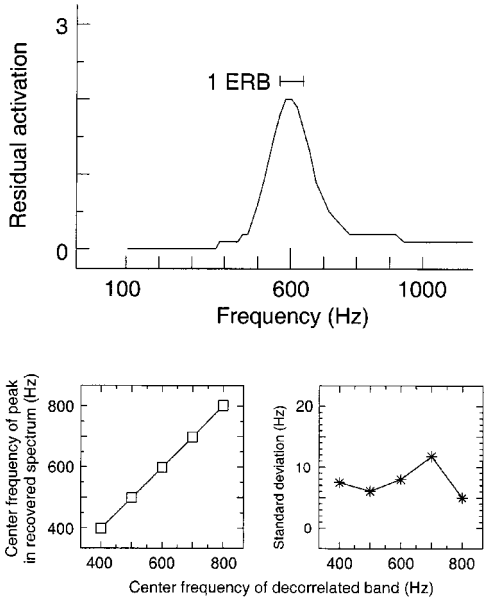

FIG. 10. Upper panel: recovered spectrum for a 600-Hz NR1 dichotic pitch generated by the implementation of the modified equalization–cancellation model. Lower-left panel: mean center frequency of peak in recovered spectrum for each NR1 dichotic pitch. Lower-right panel: standard deviation of those center frequencies.

In summary, the best-delay extension to the modified equalization–cancellation model cannot accommodate the half-period rule. Nevertheless, the model remains important because the recovered spectrum yields an accurate estimate of the center frequency of the dichotic pitch.

3. The reconstruction–comparison model

The ''reconstruction–comparison model'' is a new model designed specifically to account for the lateralization of a simple dichotic pitch. It is based on the idea that the binaural auditory scene is partitioned into two separate objects, one for the dichotic pitch and one for the background noise, *before* the lateralization of each object is computed. The model does not seek to estimate the frequency of the dichotic pitch. Instead, it assumes that its frequency is estimated by a separate process. This issue is addressed in Sec. II B 4. In overview, the model has five stages. First, it calculates the cross-correlogram of the dichotic-pitch stimulus (Fig. 11, row A). Second, it partitions the frequency channels into two groups, one for the dichotic pitch and the other for the background noise (Fig. 11, rows B and C). Third, it reconstructs the notch in the noise cross-correlogram resulting from the removal of the frequency channels carrying the dichotic pitch (Fig. 11, row D). Fourth, it subtracts the reconstructed noise cross-correlogram from the dichotic-pitch cross-correlogram. Fifth, it determines the lateralization of the dichotic pitch from the across-frequency average of the remainder after subtraction (Fig. 11, row E). Each stage will now be described in more detail.

Figure 11 shows the sequence of cross-correlograms for a 600-Hz NR1 dichotic pitch. In stage one the cross-correlogram of the dichotic-pitch stimulus is calculated using the peripheral model described in Sec. II A (Fig. 11, row A, left panel). In stage two the five frequency channels within ± 0.5 ERBs of the center frequency of the dichotic pitch are copied to the dichotic-pitch cross-correlogram (Fig. 11, row B, left panel). A band as narrow as 1 ERB is selected because a tonal object like a dichotic pitch should have a narrow bandwidth. The remaining cross-correlation functions are copied to the noise cross-correlogram (Fig. 11, row C, left panel). The model requires an independent estimate of the center frequency of the dichotic pitch. In this first evaluation, the estimate was given to the model as the frequency of the filter closest to the physical center frequency of the interaurally decorrelated band creating the dichotic pitch (see footnote 7). In stage three, the five-channel-wide notch in the noise cross-correlogram is reconstructed by linear interpolation (Fig. 11, row D, left panel)

$$b(n,\tau) = \frac{b(N+3,\tau) - b(N-3,\tau)}{6} n + b(N-3,\tau), \quad N-3 < n < N+3, \tag{7}$$

where $b(n,\tau)$ is the binaural activity in frequency channel n at internal delay τ and N is the frequency channel centered on the dichotic pitch. The interpolation is linear in frequency channel and therefore linear in ERBs; the parameters $N+3$, $N-3$, and 6 arise because the notch has a width of five frequency channels. The interpolation is performed independently at each internal delay. In stage four the dichotic-pitch cross-correlogram is compared with the reconstructed noise cross-correlogram by subtracting the latter from the former. Only positive remainders are retained (Fig. 11, row E, left panel). This remainder cross-correlogram is averaged across frequency (Fig. 11, row E, right panel; cf. Shackleton *et al.*, 1992). In stage five the peak in the average closest to an internal delay of 0 μs is found. Its delay is assumed to correspond to the lateralization of the dichotic pitch.

For the 600-Hz NR1 dichotic pitch shown in Fig. 11, this peak is at an internal delay of $+50$ μs. The mean value for the set of 600-Hz NR1 dichotic-pitch stimuli used in experiment 1 was $+35$ μs, with a standard deviation of 37 μs. Thus, the reconstruction–comparison model predicts that a 600-Hz NR1 dichotic pitch has a lateralization corresponding to $+35$ μs. The predictions for all the NR1 and Nπ1 conditions are reported in Table I. They show that the reconstruction–comparison model can account for the half-period rule. For the NR1 conditions, the predictions increase monotonically with center frequency in accordance with the rule. For the Nπ1 conditions the predictions are within 125 μs of the expected value of 0 μs, and do not vary systematically with frequency.

Only in the remainder cross-correlogram is there a peak near 0 μs for a 600-Hz NR1 dichotic pitch (marked by a bold line). Neither the cross-correlogram of the initial stimulus (Fig. 11, row A, right panel) nor the separated cross-correlogram of the dichotic pitch (Fig. 11, row B, right panel) show a peak near 0 μs. The peaks are instead near $+833$, μs corresponding to the lateralization of the noise carrier. Thus, the application of any model of the lateralization of single sounds (e.g., Stern *et al.*, 1988; Shackleton *et al.*, 1992) to the lateralization of dichotic pitches, without

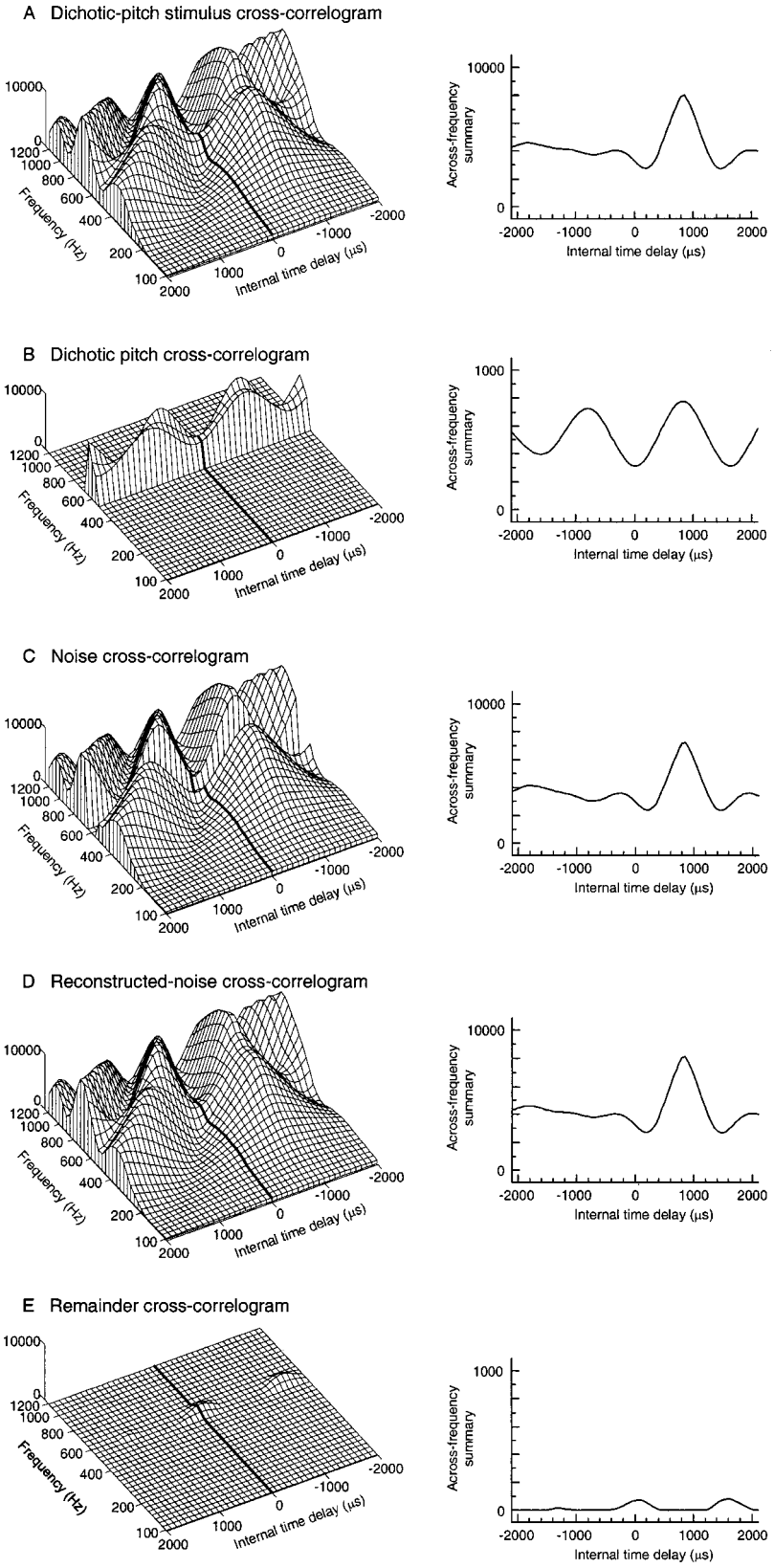

FIG. 11. Left column: the cross-correlograms for a 600-Hz NR1 dichotic pitch generated by the reconstruction–comparison model. For visual clarity the spacing of frequency channels is reduced to 2.5 per ERB, the resolution of internal time delay is reduced to 100 μs, and the span of internal delays is limited to $\pm$2000 μs. The bold lines mark the midline (0 μs). Right column: the across-frequency summaries of each cross-correlogram. Note that the vertical scale of the across-frequency summaries in rows B and E differs from the others.

a mechanism for separating the dichotic pitch from the noise, would predict only the lateralization of the noise. This separation is the foundation of the reconstruction–comparison model. The partitioning process achieves the required separation. The partitioning is not perfect, however, because channels offset from the center of the dichotic pitch contain frequency components of both the dichotic pitch and the noise carrier. Accordingly, the reconstruction and comparison processes are included to improve the partitioning. Reconstruction recreates the parts of the noise ''hidden'' by the dichotic pitch. Comparison removes them from the representation of the dichotic pitch.

4. Combined models

We have not addressed the question of how the gammatone central-spectrum model and the reconstruction–comparison model establish the frequency of a simple dichotic pitch. For example, considering the central spectra in Fig. 8, why is the 600-Hz peak chosen? There are peaks in numerous central spectra, but most of them are due to the noise carrier. For instance, the pronounced peak in the −600-μs central spectrum is *not* heard as a dichotic pitch. A method is required for distinguishing peaks that signal the dichotic pitch from peaks which belong to the noise carrier. The issue is equally problematic for the reconstruction–comparison model. In order for the initial cross-correlogram to be partitioned, the model must establish which frequency channels belong to the dichotic pitch.

A solution for both models is to employ the modified equalization–cancellation model as a ''front end'' to compute the center frequency of the dichotic pitch. To confirm the feasibility of this strategy, we assessed the accuracy with which the combination of the modified equalization–cancellation model with the reconstruction–comparison model accommodates the half-period rule. In the combined model, the center frequency of the dichotic pitch was estimated as the frequency of the single peak in the recovered spectrum (cf. Fig. 10). The predictions of the combined model are listed in Table I. The rms deviations of the predictions are greater than those of the reconstruction–comparison model alone, but only slightly; the mean rms errors increased by 38 μs for the NR1 conditions and by 19 μs for the Nπ1 conditions. The correspondence is due to the close relationship between the peak of the recovered spectrum and the physical center frequency of the interaurally decorrelated band defining the dichotic pitch (Fig. 10, bottom-left panel). The two differed for only a minority of the stimuli, and then only by ± 1 or ± 2 frequency channels. We conclude that the combination of the modified equalization–cancellation and reconstruction–comparison models can account for the half-period rule without requiring prior knowledge of the frequency of the dichotic pitch. A similar conclusion would hold for the combination of the modified equalization–cancellation model with the gammatone central–spectrum model, although this combined model was not evaluated explicitly.

5. Summary of modeling the half-period rule

Our implementation of the modified equalization–cancellation model cannot, on its own, account for the half-period rule and so is not considered further. Both the gammatone central-spectrum model and the reconstruction–comparison model can accommodate the rule, provided that they receive an independent estimate of the center frequency of the dichotic pitch. When given the true center frequency, the reconstruction–comparison model gives a better fit than the gammatone central-spectrum model for the NR1 conditions (rms errors of 40 μs versus 68 μs) but a poorer fit for the Nπ1 conditions (68 μs versus 0 μs). The modified equalization–cancellation model can provide the required independent estimate for both models, without serious detriment to the accuracy of predictions.

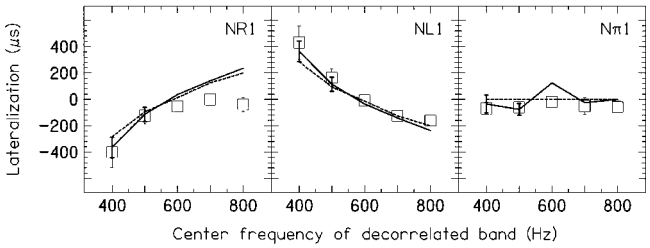

FIG. 12. Squares: mean lateralizations in μs for the conditions of experiment 1 (cf. Fig. 5). Dotted lines: predictions of the gammatone central-spectrum model. Solid lines: predictions of the reconstruction–comparison model.

C. Modeling the performance of listeners in experiment 1

Figure 12 shows the mean results of experiment 1 superimposed on the predictions of the gammatone central–spectrum model (dotted line) and the reconstruction–construction model (solid line). As expected from their ability to accommodate the half-period rule, the models achieve similar overall accuracy in predicting the lateralizations. The rms error for both models was 90 μs. Their predictions deviate from the listeners' data primarily in failing to predict the observed left/right asymmetry. The asymmetry is mysterious and we can offer no rigorous explanation for it.

III. EXPERIMENT 2: SYSTEMATIC DEVIATIONS FROM THE HALF-PERIOD RULE

A. Rationale and conditions

The goal of experiment 2 was to distinguish the predictions of the gammatone central-spectrum model from those of the reconstruction–comparison model. A simple dichotic pitch was created by giving a narrow band of noise a different ITD from the rest of a correlated noise carrier.[9] The perception of this dichotic pitch can be understood by reference to the modified equalization–cancellation model. The auditory filters centered at or near the narrow band pass components both of the carrier, with one ITD, and of the narrow band, with a different ITD. No single internal delay can compensate for both sets of components—i.e., no delay is ''best'' for both sets of components in the sense defined in Sec. II B 2—and so the recovered spectrum contains a peak centered on the ITD shift.

In one set of dichotic-pitch stimuli (termed ''NR2'') the noise carrier was a 1200-Hz low-pass noise with an ITD of +833 μs (Fig. 13, panels A and B). Frequency components between 480 and 520 Hz were given a different ITD: either −367, −267, −167, −67, or +33 μs, corresponding to relative shifts from the noise carrier of −1200, −1100, −1000 (one-half period of 500 Hz), −900, and −800 μs. The bandwidth of the ITD shift of 40 Hz was chosen to be half the equivalent-rectangular bandwidth of the 500-Hz auditory filter (Glasberg and Moore, 1990). In a second set of dichotic-

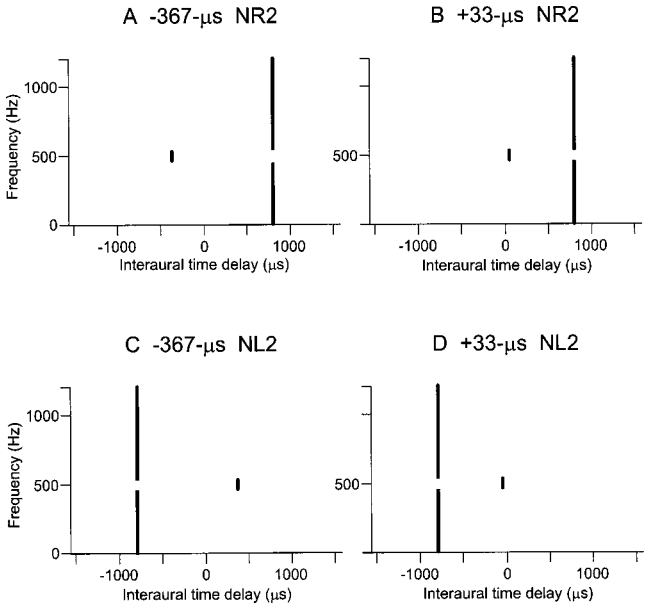

FIG. 13. Schematic frequency versus ITD plots of the stimuli used in experiment 2. (cf. Fig. 1.)

pitch stimuli (''NL2'') the left and right waveforms were swapped (Fig. 13, panels C and D).

B. Predictions of the models

There is a crucial difference between the stimuli for experiment 2 and those described previously for experiment 1. In experiment 1, the stimuli possessed no interaural structure in the region of the narrow band, because that band was given an interaural correlation of zero. In experiment 2, the stimuli possessed some interaural structure in the region of the narrow band, because that band was given a constant ITD. If the lateralization of a simple dichotic pitch is determined by the structure of the carrier noise alone, then lateralization will be fixed in experiment 2 and will not vary with the ITD. Alternatively, if the lateralization is determined by the structure of both the noise and the narrow band, then lateralization will vary with ITD. This difference is important because predictions of lateralization by the gammatone central-spectrum model depend only on the structure of the carrier noise, whereas predictions by the reconstruction–comparison model depend on the structure of both the carrier noise and the narrow band.

Figures 14 and 15 illustrate these points. Figure 14 shows central spectra from the gammatone central-spectrum model for a $+33$-μs NR2 dichotic pitch (upper row) and for a -367-μs NR2 dichotic pitch (lower row). The symmetric-peak criterion selects the central spectrum at -100 μs in both cases, despite the difference in the stimuli. More generally, the model predicts that the lateralization of the NR2 dichotic pitches corresponds to an ITD of -100 μs, independent of the value of the ITD in the 480–520-Hz band.

In contrast, the reconstruction–comparison model predicts that the lateralization of the NR2 dichotic pitches depends on the ITD of the 480–520-Hz band. Rows A and B of Fig. 15 show the dichotic-pitch and remainder cross-correlograms for a $+33$-μs NR2 dichotic pitch. The peak in the across-frequency summary of the remainder is at an internal delay of -50 μs. Rows C and D of Fig. 15 show corresponding cross-correlograms for a -367-μs NR2 dichotic pitch. The peak is at -250 μs. More generally, the reconstruction–comparison model predicts that lateralization is roughly proportional to the value of the ITD in the 480–520-Hz band.

The models make different predictions for the following reasons. Consider the gammatone central-spectrum model first. This model is, in essence, an implementation of the half-period rule. When a narrow band is interaurally decorrelated, by whatever means, in an otherwise correlated noise carrier, the cross-correlation function at the center of the band is flattened to at least some degree. Flattening increases the correlation at internal delays spanned by troughs in the cross-correlogram of the noise carrier. These increases produce peaks in central spectra at those delays. The most symmetric peak arises at the delay for which the cross-correlation of the carrier noise is most similar at frequencies above and below the narrow band. That delay is in the middle of the trough, and so is the delay specified by the half-period rule. Thus, the structure of the carrier noise determines which central spectrum is chosen. Accordingly, the model selects the same central spectrum independent of the way in which the narrow band is decorrelated.

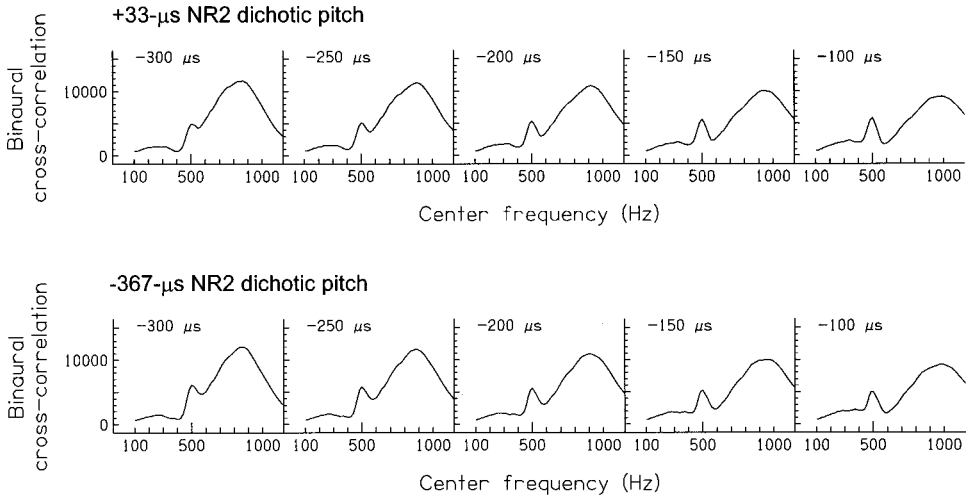

FIG. 14. Central spectra for (upper row) a $+33$-μs NR2 dichotic pitch and (bottom row) a -367-μs NR2 dichotic pitch as used in experiment 2. For both dichotic pitches the gammatone central-spectrum model chooses the central spectrum at -100 μs.

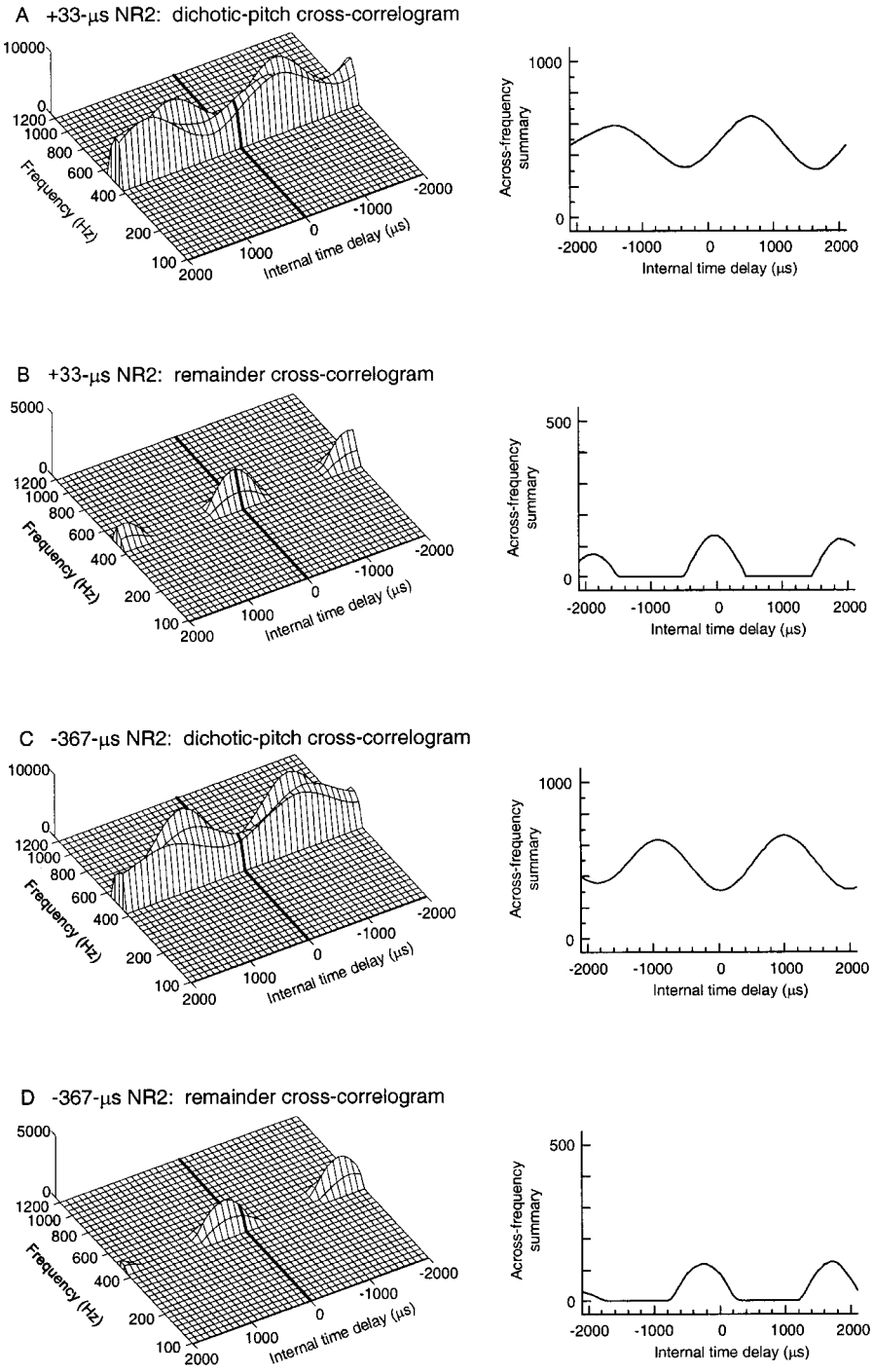

FIG. 15. The dichotic-pitch and remainder cross-correlograms generated by the reconstruction–comparison model for a +33-μs NR2 dichotic [panels (A) and (B)] and for a −367-μs NR2 dichotic pitch [panels (C) and (D)] (cf. Fig. 11.)

The reconstruction–comparison model is sensitive to the microstructure of the pattern of cross-correlation in the region of the narrow band. In the stimuli for experiment 2, the peak of the cross-correlation function at 500 Hz shifts from positive internal delays to negative internal delays as the ITD is changed from +33 to −367 μs. The shift is reflected in a change in position of the peak in the remainder cross-correlogram. This outcome occurs because the remainder cross-correlogram results from subtracting the model's estimate of the cross-correlogram of the noise from the cross-correlogram of the dichotic-pitch stimulus.

For these reasons, experiment 2 provides a critical test of the two models. If the lateralization of the dichotic pitch is independent of the ITD of the 480–520-Hz band, then the results would favor the gammatone central-spectrum model. Conversely, if the lateralization varies in proportion to the ITD, the results would favor the reconstruction–comparison model.

C. Method

The dichotic-pitch lateralizations were measured using the same method as in experiment 1 but with one important difference. In experiment 1 the markers were given the ITD corresponding to the lateralization predicted by the half-period rule. In experiment 2 the markers were given the actual ITD of the narrow band defining the dichotic pitch.

The stimuli were constructed digitally in a similar man-

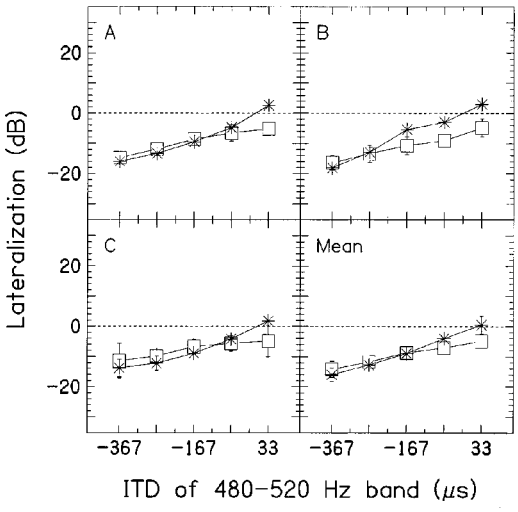

FIG. 16. Results of experiment 2 for the NR2 conditions. Squares: dichotic-pitch lateralizations; asterisks: marker lateralizations. Negative lateralizations correspond to the left side of the head, zero to the midline, and positive to the right.

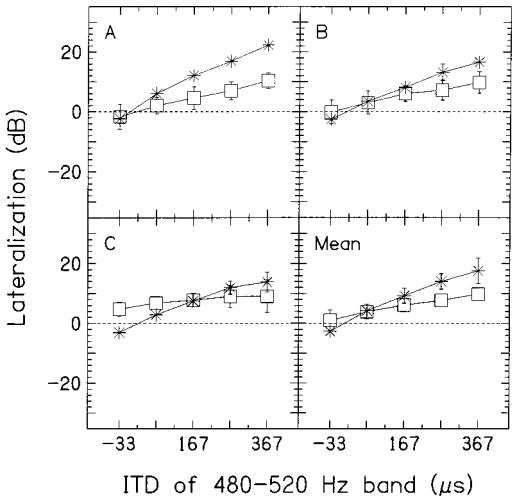

FIG. 17. Results of experiment 2 for the NL2 conditions, plotted in the same format as Fig. 16.

ner to experiment 1. The dichotic-pitch stimuli were created by modifying a 2–1200-Hz flat-spectrum noise. For the NR2 dichotic pitches the starting phases of components in a 40-Hz-wide band centered on 500 Hz were set to give an ITD of either −367, −267, −167, −67, or +33 μs. The starting phases of the remaining components were set to give an ITD of +833 μs. For the NL2 dichotic pitches the left and right waveforms of the NR dichotic pitches were swapped.

The markers had a bandwidth of 80 Hz centered on 500 Hz. For the NR2 markers, the starting phases of the components were set to give ITDs of −367, −267, −167, −67, or +33 μs. For the NL2 markers the left and right waveforms of the NR2 markers were swapped. The pointers were the same as in experiment 1.

The apparatus, statistical analysis, and listeners were the same as in experiment 1. In each experimental session, listeners judged the lateralizations of all the NR2 dichotic pitches, or all the NL2 dichotic pitches, or all the NR2 markers, or all the NL2 markers.

D. Results

Figures 16 and 17 show the results for the NR2 and NL2 conditions. In each figure both the individual and mean results are shown for the dichotic pitches (squares) and for the marker noises (asterisks). Where the standard deviations of each lateralization are larger than the symbol size, they are plotted as error bars. The horizontal dotted line marks the 0-dB IID corresponding to the midline.

Figure 16 shows that the lateralization of the NR2 dichotic pitches depended upon the ITD of the 480–520-Hz band [$F(4,8)=40.1$, $p<0.001$]. The dichotic pitch was always heard on the left side of the head, its lateralization decreasing from −14 to −4.9 dB as the ITD was increased from −367 to +33 μs. The dichotic-pitch lateralizations differed from the marker lateralizations at ITDs near 0 μs [main effect of stimulus type: $F(1,2)=5.3$, $p>0.1$; interaction of stimulus type with ITD: $F(4,8)=5.3$, $p=0.02$].

Figure 17 shows that the lateralization of the NL2 dichotic pitches also depended upon the ITD of the 480–520-Hz band [$F(4,8)=16.1$, $p<0.001$]. The lateralization increased from 1.0 to 9.8 dB as the ITD was increased from −33 to +367 μs. Again, the dichotic-pitch lateralizations differed from the marker lateralizations at ITDs near 0 μs [main effect of stimulus type: $F(1,2)=1.6$, $p>0.1$; interaction of stimulus type with ITD: $F(4,8)=94.1$, $p<0.001$].

E. Discussion

The results of experiment 2 show that the lateralization of both the NR2 and NL2 dichotic pitches depended systematically on the ITD of the 480–520-Hz band. These results are more compatible with the reconstruction–comparison model, which predicts a shift in lateralization with ITD, than with the gammatone central-spectrum model, which predicts no shift.

This conclusion is supported by a numerical comparison of the model predictions. As in experiment 1, the lateralizations were transformed from IIDs to ITDs. The results are shown in Fig. 18. The open symbols plot the transformed lateralizations for each listener. The dotted lines plot the predictions of the gammatone central-spectrum model and the solid lines plot the predictions of the reconstruction–comparison model. Table II lists the mean predictions and

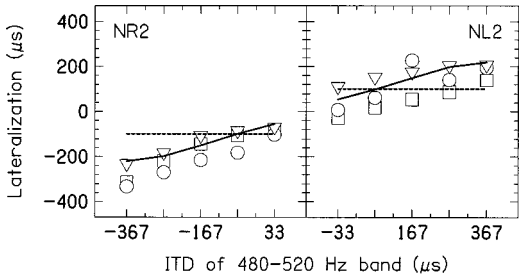

FIG. 18. Open symbols: lateralizations in μs for the three listeners in the conditions of experiment 2 (cf. Fig. 5). The assignment of symbols to subjects is: squares, Listener A; circles, Listener B; triangles, Listener C. Dotted lines: predictions of the gammatone central-spectrum model. Solid lines: predictions of the reconstruction–comparison model.

TABLE II. Experimental data (ITDs averaged over three listeners in μs) and predictions (ITDs in μs) of the reconstruction–comparison model and the gammatone central-spectrum model for the NR2 conditions (upper panel) and the NL2 conditions (lower panel) of experiment 2. The rightmost column lists the rms error between the model predictions and the experimental data.

Model		Absolute ITD of 500-Hz band (μs)					rms error from experimental data
		−367	−267	−167	−67	33	
Experimental data (NR2 conditions)		**−295**	**−227**	**−158**	**−127**	**−87**	···
Reconstruction–comparison	Mean	−220	−198	−150	−98	−55	42
Gammatone central-spectrum	Mean	−100	−100	−100	−100	−100	108
Experimental data (NL2 conditions)		**178**	**142**	**114**	**74**	**27**	···
Reconstruction–comparison	Mean	220	198	150	98	55	38
Gammatone central-spectrum	Mean	100	100	100	100	100	53

rms errors from the experimental data. For both the NR2 and NL2 conditions, the rms error was smaller for the reconstruction–comparison model than for the gammatone central-spectrum model (NR2 conditions: 42 μs versus 108 μs; NL2 conditions: 38 μs versus 53 μs).

The predictions from the gammatone central-spectrum model were based on the symmetric-peak criterion. This criterion failed to predict the experimental results accurately. While it is conceivable that an alternative criterion would succeed, it is not clear how it would be defined. Figure 14 illustrated the problem. It shows the central spectra for a +33-μs NR2 dichotic pitch (upper row) and for a −367-μs NR2 dichotic pitch (lower row). Corresponding spectra in the two rows are very similar, yet the observed lateralizations of the stimuli were different: respectively, −87 and −295 μs. We have been unable to find a computational strategy that chooses the appropriate central spectrum in each case, while rejecting the other central spectra.

The half-period rule also predicts that the lateralization of the dichotic pitches would be fixed. The fact that they were not fixed indicates that the lateralization is determined by the microstructure of the cross-correlogram rather than by its gross structure. The microstructure reflects characteristics of *both* the noise carrier and the narrow band defining the dichotic pitch. Thus, the half-period rule, in which the lateralization is determined by the characteristics of the noise carrier alone, makes only approximate predictions of the present results.

IV. GENERAL DISCUSSION

The primary motivation for investigating the lateralization of simple dichotic pitches was to compare the gammatone central-spectrum model with other models. The gammatone central-spectrum model accounted for major aspects of the lateralization of dichotic pitches created by decorrelating a narrow band in a correlated carrier noise (experiment 1), but not of dichotic pitches created by shifting the ITD of a narrow band (experiment 2). One alternative, the reconstruction–comparison model, accounted for the major aspects of the lateralization of both types of dichotic pitches. A second alternative was a development of the modified equalization–cancellation model, in which the lateralization of a simple dichotic pitch was predicted from the internal delay giving greatest cancellation at the center frequency of the pitch. This approach did not yield accurate predictions. However, the modified equalization–cancellation model can provide the estimate of the center frequency of dichotic pitches that is needed by the two more-successful models of lateralization.

A. The gammatone central-spectrum model

The gammatone central-spectrum model is a modernization of the central-spectrum model described by Raatgever and Bilsen (1986). It differs from the original model in three ways. First, it incorporates the realistic frequency selectivity provided by a computational auditory filterbank instead of that given by a Fourier transform. Second, it does not include a weighting function to emphasize internal delays near 0 μs. Third, it adopts a specific computational criterion for choosing a central spectrum, referred to as the ''most-symmetric-peak'' criterion. This change is the most important of the three modifications because the choice of central spectrum determines directly the lateralization of a dichotic pitch. The most-symmetric-peak criterion was based on just one of the qualitative criteria for selecting peaks put forward by Raatgever and Bilsen: that a peak should be ''pronounced.'' It is conceivable that one of their other criteria—depth of modulation (Raatgever and Bilsen, 1977; Raatgever *et al.*, 1998), harmonicity (Raatgever and Bilsen, 1977; Bilsen *et al.*, 1998), sharpness of peaks (Bilsen *et al.*, 1998) or spectral-pattern recognition (Raatgever and Bilsen, 1986)—could succeed where the most-symmetric-peak criterion fails. Experiment 2, however, demonstrated that stimuli which generate closely similar central spectra receive different lateralizations (Fig. 14). It is difficult to envisage how any criterion could accommodate this result within the framework of the gammatone central-spectrum model.

B. The reconstruction–comparison model

The reconstruction–comparison model implements the idea that the binaural auditory scene created by a simple dichotic-pitch stimulus is decomposed perceptually into two objects: a tonal pitch and a background noise. Only subsequent to this partitioning is the lateralization of each object calculated. In essence, the model determines which sound sources are present before it determines where those sound sources are located. This strategy is compatible with inde-

pendent perceptual data which suggest that the segregation of sources precedes the determination of their spatial positions (e.g., Woods and Colburn, 1992; Hill and Darwin, 1996; Darwin, 1997; Darwin and Hukin, 1999).

Akeroyd and Summerfield (2000) demonstrated that the model also accounts for major features of the lateralization of the Huggins pitch measured by Raatgever and Bilsen (1986) for $N0$ and $N\pi$ noise carriers. Further developments of the model, however, would be required to account for the individual differences between the listeners and for the variability in their judgments. Three additional sets of data will be relevant in establishing the generality of the model. First, Frijns *et al.* (1986) measured lateralizations of the binaural edge pitch (Klein and Hartmann, 1981). This dichotic pitch is created by synthesizing a broadband noise whose interaural configuration is $N0$ below a transition frequency f and $N\pi$ above it, or vice versa. Provided that f is below about 1500 Hz, listeners hear a dichotic pitch of frequency f amidst the background of a broadband noise. Frijns *et al.* observed a trimodal distribution of lateralizations (after pooling across listeners): a prominent central peak was located close to an internal delay of zero, and smaller side peaks were located at internal delays of, approximately, plus and minus one period of f.

The second relevant set of data was reported by Yost *et al.* (1987). They created simple dichotic pitches similar to those of experiment 2 but by applying an interaural-phase shift instead of an ITD shift to a narrow band. The dichotic pitch was lateralized to the ear leading in phase for phase shifts of up to 45°, but was described as being lateralized ambiguously to both ears for larger phase shifts. Initial investigations have shown that the model predicts that lateralization is approximately proportional to the value of the phase shift and towards the ear leading in phase until the phase shift approaches 180°, where the model predicts that the lateralization is ambiguous. Potentially, the introduction of internal noise into the model could result in predictions of ambiguous lateralizations for smaller phase shifts.

The third study was reported by Grange and Trahiotis (1996). They demonstrated that applying an interaural intensitive difference to a Huggins-pitch stimulus resulted in a shift in the perceived lateralization of the Huggins pitch. This result is outside the scope of the present version of the reconstruction–comparison model, because the model does not include an analysis of interaural intensitive differences. Potentially, the introduction of such an analysis could remedy this limitation.

Finally, we acknowledge that the calculations performed by the reconstruction–comparison model are subtle. The model compares its own *inference* of the spatial organization of the carrier noise with the evidence of spatial organization of the dichotic-pitch stimulus. It is implausible that the auditory machinery required to carry out these calculations would exist unless they served some more generally useful function than lateralizing dichotic pitches. For the model to justify its computational complexity, it needs to be demonstrated that it can account for the lateralization of signals that arise naturally in noise.

ACKNOWLEDGMENTS

We thank Trevor Shackleton and John Culling for useful discussions and, along with Katrin Krumbholz, Wes Grantham (associate editor), and three anonymous reviewers, for their insightful comments on previous versions of this paper. A preliminary version of the reconstruction–comparison model was described by Akeroyd and Summerfield (2000).

[1]Cramer and Huggins used a bandwidth of 10%, meaning that the bandwidth of the phase shift from 90° to 270° was 10% of the center frequency. This definition of bandwidth is usual if a Huggins pitch is generated using an analog all-pass filter.

[2]Cramer and Huggins did not report the lateral position of the Huggins pitch.

[3]Raatgever and Bilsen (1986, Fig. 7) report data from two of the three listeners tested by Raatgever (1980, Figs. V.3, V.4, and V.5). Raatgever (1980) mentions that the matching stimulus contained a ''weak'' pure tone together with the white noise.

[4]The abbreviation ''NR1'' summarizes ''*N*oise carrier lateralized on *R*ight, experiment *1*.'' The abbreviations for the other conditions were generated using a similar logic.

[5]The stimuli were created by modifying a digital, flat-spectrum, diotic noise constructed by summing together a sine and cosine component at each frequency from 2 to 1200 Hz (inclusive) in 2-Hz steps, so giving the left $L(t)$ and right $R(t)$ waveforms

$$L(t)=\sum_{f=2\ \mathrm{Hz}}^{f=1200\ \mathrm{Hz}}(A_{L,f}\sin(2\pi ft)+B_{L,f}\cos(2\pi ft)),$$

$$R(t)=\sum_{f=2\ \mathrm{Hz}}^{f=1200\ \mathrm{Hz}}(A_{R,f}\sin(2\pi ft)+B_{R,f}\cos(2\pi ft)),$$

where $A_{L,f}$, $A_{R,f}$, $B_{L,f}$, and $B_{R,f}$ are random variables chosen from a Gaussian distribution with a mean of zero and a standard deviation of 1. For all frequencies f other than those defining the decorrelated band, $A_{L,f}$ was equal to $A_{R,f}$ and $B_{L,f}$ was equal to $B_{R,f}$.

[6]For Listener B the quadratic fit failed to return an ITD for the 400-Hz NL1 dichotic pitch. The minimum IID (y) of the quadratic curve was −17.6 dB, at an ITD (x) of 599 μs. The experimental lateralization for the condition was −22.4 dB, and so was outside the range of IIDs that could be fitted by the quadratic curve. In the quantitative fits we therefore used a value of 599 μs for this condition, as it gave the closest IID to the one observed experimentally.

[7]The software puts filters at 1/5-ERB intervals above and below 500 Hz, thereby placing the lowest filter at 106 Hz and the highest filter at 1194 Hz. The closest filters to the center frequencies of the dichotic pitches were at 397.8, 500.0, 600.8, 695.3, and 800.7 Hz.

[8]All values of 1.0 or below were not log-compressed, but were transformed directly to 0.0.

[9]Dichotic pitches created in this manner have also been used by Dougherty *et al.* (1998).

Akeroyd, M. A., and Summerfield, A. Q. (**2000**). ''A computational auditory model of the lateralization of a Huggins pitch,'' in *Computational Models of Auditory Function*, edited by S. Greenberg and M. Slaney (IOS, Amsterdam).

Bilsen, F. A. (**1977**). ''Pitch of noise signals: Evidence for a 'central spectrum,' '' J. Acoust. Soc. Am. **61**, 150–161.

Bilsen, F. A., and Goldstein, J. L. (**1974**). ''Pitch of dichotically delayed noise and its possible spectral basis,'' J. Acoust. Soc. Am. **55**, 292–296.

Bilsen, F. A., van der Meulen, A. P., and Raatgever, J. (**1998**). ''Salience and jnd of pitch for dichotic noise stimuli with scattered harmonics: Grouping and the central spectrum theory,'' in *Psychophysical and Physiological Advances in Hearing*, edited by A. R. Palmer, A. Rees, A. Q. Summerfield, and R. Meddis (Whurr, London).

Colburn, H. S. (**1977**). ''Theory of binaural interaction based on auditory nerve data. II. Detection of tones in noise,'' J. Acoust. Soc. Am. **61**, 525–533.

Cramer, E. M., and Huggins, W. H. (**1958**). ''Creation of pitch through binaual interaction,'' J. Acoust. Soc. Am. **30**, 413–417.

Culling, J. F., and Summerfield, Q. (**1995**). ''Perceptual separation of concurrent speech sounds: Absence of across-frequency grouping by common interaural delay,'' J. Acoust. Soc. Am. **98**, 785–797.
Culling, J. F., Summerfield, A. Q., and Marshall, D. H. (**1998a**). ''Dichotic pitches as illusions of binaural unmasking. I. Huggins' pitch and the 'binaural edge pitch,''' J. Acoust. Soc. Am. **103**, 3509–3526.
Culling, J. F., Marshall, D. H., and Summerfield, A. Q. (**1998b**). ''Dichotic pitches as illusions of binaural unmasking. II. The Fourcin pitch and the dichotic repetition pitch,'' J. Acoust. Soc. Am. **103**, 3527–3539.
Darwin, C. J. (**1997**). ''Auditory grouping,'' Trends Cogn. Sci. **1**, 327–333.
Darwin, C. J., and Hukin, R. W. (**1999**). ''Auditory objects of attention: The role of interaural time differences in attention to speech,'' JEP: Hum. Percept. Perform. **25**, 617–629.
Dougherty, R. F., Cynader, M. S., Bjornson, B. H., Edgell, D., and Giaschi, D. E. (**1998**). ''Dichotic pitch: A new stimulus distinguishes normal and dyslexic auditory function,'' NeuroReport **9**, 3001–3005.
Durlach, N. I. (**1960**). ''Note on the equalization and cancellation theory of binaural masking-level differences,'' J. Acoust. Soc. Am. **32**, 1075–1076.
Durlach, N. I. (**1972**). ''Binaural signal detection: Equalization and cancellation theory,'' in *Foundations of Modern Auditory Theory*, edited by J. V. Tobias (Academic, New York), Vol. 2.
Fourcin, A. J. (**1970**). ''Central pitch and auditory lateralization,'' in *Frequency Analysis and Periodicity Detection in Hearing*, edited by R. Plomp and G. F. Smoorenburg (Sijthoff, Leiden).
Frijns, J. H. M., Raatgever, J., and Bilsen, F. A. (**1986**). ''A central spectrum theory of binaural processing. The binaural edge pitch revisited,'' J. Acoust. Soc. Am. **80**, 442–451.
Gabriel, K. J., and Colburn, H. S. (**1981**). ''Interaural correlation discrimination. I. Bandwidth and level dependence,'' J. Acoust. Soc. Am. **69**, 1394–1401.
Glasberg, B. R., and Moore, B. C. J. (**1990**). ''Derivation of auditory filter shapes from notched-noise data,'' Hear. Res. **47**, 103–138.
Grange, A. N., and Trahiotis, C. (**1996**). ''Lateral position of dichotic pitches can be substantially affected by interaural intensitive differences,'' J. Acoust. Soc. Am. **100**, 1901–1904.
Grantham, D. W. (**1995**). ''Spatial hearing and related phenomena,'' in *Hearing*, edited by B. C. J. Moore (Academic, London).
Hill, N. I., and Darwin, C. J. (**1996**). ''Lateralization of a perturbed harmonic: Effects of onset asynchrony and mistuning,'' J. Acoust. Soc. Am. **100**, 2352–2364.
Jeffress, L. A. (**1948**). ''A place theory of sound localization,'' J. Comp. Physiol. Psychol. **41**, 35–39.
Jesteadt, W. (**1980**). ''An adaptive procedure for subjective judgments,'' Percept. Psychophys. **28**, 85–88.
Klein, M. A., and Hartmann, W. M. (**1981**). ''Binaural edge pitch,'' J. Acoust. Soc. Am. **70**, 51–61.
Levitt, H. (**1971**). ''Transformed up–down methods in psychoacoustics,'' J. Acoust. Soc. Am. **49**, 467–477.
Meddis, R. (**1986**). ''Simulation of mechanical to neural transduction in the auditory receptor,'' J. Acoust. Soc. Am. **79**, 702–711.
Meddis, R. (**1988**). ''Simulation of auditory–neural transduction: Further studies,'' J. Acoust. Soc. Am. **83**, 1056–1063.
Moore, B. C. J. (**1995**). ''Frequency analysis and masking,'' in *Hearing*, edited by B. C. J. Moore (Academic, London).
Patterson, R. D., and Moore, B. C. J. (**1986**). ''Auditory filters and excitation patterns as representations of frequency resolution,'' in *Frequency Selectivity in Hearing*, edited by B. C. J. Moore (Academic, London).
Patterson, R. D., Allerhand, M. H., and Giguère, C. (**1995**). ''Time-domain modeling of peripheral auditory processing: A model architecture and a software platform,'' J. Acoust. Soc. Am. **98**, 1890–1894.
Raatgever, J. (**1980**). ''On the binaural processing of stimuli with different interaural phase relations,'' Doctoral dissertation (Delft University of Technology, Dutch Eff. Bureau, Pijnacker, The Netherlands).
Raatgever, J., and Bilsen, F. A. (**1977**). ''Lateralization and dichotic pitch as a result of spectral pattern recognition,'' in *Psychophysics and Physiology of Hearing*, edited by E. F. Evans and J. P. Wilson (Academic, London).
Raatgever, J., and Bilsen, F. A. (**1986**). ''A central spectrum theory of binaural processing. Evidence from dichotic pitch,'' J. Acoust. Soc. Am. **80**, 429–441.
Raatgever, J., Bilsen, F. A., and Mungra, R. (**1998**). ''New experiments beyond the traditional Fourcin pitch range,'' in *Proceedings of the 16th ICA and 135th ASA*, Volume 1, edited by P. K. Kuhl and L. A. Crum (Acoustical Society of America, Woodbury, NY).
Shackleton, T. M., Meddis, R., and Hewitt, M. J. (**1992**). ''Across frequency integration in a model of lateralization,'' J. Acoust. Soc. Am. **91**, 2276–2279.
Stern, R. M., and Shear, G. D. (**1996**). ''Lateralization and detection of low-frequency binaural stimuli: Effects of distribution of internal delay,'' J. Acoust. Soc. Am. **100**, 2278–2288.
Stern, R. M., and Trahiotis, C. (**1997**). ''Models of binaural perception,'' in *Binaural and Spatial Environments*, edited by R. H. Gilkey and T. R. Anderson (LEA, Mahwah, NJ).
Stern, R. M., Zeiberg, A. S., and Trahiotis, C. (**1988**). ''Lateralization of complex binaural stimuli: A weighted image model,'' J. Acoust. Soc. Am. **84**, 156–165.
Woods, W. S., and Colburn, H. S. (**1992**). ''Test of a model of auditory object formation using intensity and interaural time difference discrimination,'' J. Acoust. Soc. Am. **91**, 2894–2902.
Yost, W. A, Harder, P. J., and Dye, R. H. (**1987**). ''Complex spectral patterns with interaural differences: Dichotic pitch and the 'central spectrum,''' in *Auditory Processing of Complex Sounds*, edited by W. A. Yost and C. S. Watson (LEA, Hillsdale, NJ).

Effects of reverberation on spatial, prosodic, and vocal-tract size cues to selective attention

C. J. Darwin and R. W. Hukin
Experimental Psychology, University of Sussex, Brighton BN1 9QG, United Kingdom

(Received 29 June 1999; revised 31 January 2000; accepted 28 March 2000)

Three experiments explored the resistance to simulated reverberation of various cues for selective attention. Listeners decided which of two simultaneous target words belonged to an attended rather than to a simultaneous unattended sentence. Attended and unattended sentences were spatially separated using interaural time differences (ITDs) of 0, ±45, ±91 or ±181 μs. Experiment 1 used sentences resynthesized on a monotone, with sentence pairs having $F0$ differences of 0, 1, 2, or 4 semitones. Listeners' weak preference for the target word with the same monotonous $F0$ as the attended sentence was eliminated by reverberation. Experiment 1 also showed that listeners' ability to use ITD differences was seriously impaired by reverberation although some ability remained for the longest ITD tested. In experiment 2 the sentences were spoken with natural prosody, with sentence stress in different places in the attended and unattended sentences. The overall $F0$ of each sentence was shifted by a constant amount on a log scale to bring the $F0$ trajectories of the target words either closer together or further apart. These prosodic manipulations were generally more resistant to reverberation than were the ITD differences. In experiment 3, adding a large difference in vocal-tract size (±15%) to the prosodic cues produced a high level of performance which was very resistant to reverberation. The experiments show that the natural prosody and vocal-tract size differences between talkers that were used retain their efficacy in helping selective attention under conditions of reverberation better than do interaural time differences. [S0001-4966(00)02607-2]

PACS numbers: 43.66.Pn, 43.71.Es [RVS]

INTRODUCTION

This paper is concerned with some of the cues that listeners can use to attend to a particular sound source over time. It extends to conditions of reverberation from simulated room acoustics the findings of a recent article (Darwin and Hukin, 1999) and its companion article (Darwin and Hukin, 2000) on the effectiveness of spatial, prosodic, and vocal-tract size cues to auditory selective attention.

Reverberation has a variety of destructive influences on the intelligibility of speech, both for single sound sources (Moncur and Dirks, 1967; Nabelek and Robinson, 1982; Nabelek and Donahue, 1984; Nabelek and Dagenais, 1986; Nabelek, 1988) and when there are competing sounds (Plomp, 1976, 1977; Culling *et al.*, 1994). In this article we examine the effect that reverberation has on some of the cues that can potentially help listeners to attend to a particular talker across time.

Two types of cue that can potentially help a listener to maintain attention to a particular sound source have dominated discussions and were investigated in the companion article: localization and pitch. Both of these cues, however, are susceptible to adulteration by reverberation. Although single sounds with abrupt onsets are well localized in naturally reverberant or simulated reverberant environments due to the mechanism of the precedence effect (Hartmann, 1983; Culling *et al.*, 1994), localization of sounds that lack abrupt onsets is seriously impaired by reverberation (Hartmann, 1983), because of changes to both interaural time and intensity differences (Rakerd and Hartmann, 1985). When masking noise is present, the ability to localize speech (Abouchacra *et al.*, 1998) or click-trains (Good and Gilkey, 1996; Lorenzi *et al.*, 1999) is impaired at adverse signal-to-noise ratios in anechoic conditions; the influence of reverberation on this ability has not been studied systematically. However, even modest amounts of reverberation, which do not reduce listeners' ability to localize speech presented alone, can reduce listeners' ability to exploit localization cues in identifying a vowel target presented with spatially separated masking noise (Culling *et al.*, 1994).

If the $F0$ of a complex sound is steady, it should be little affected by reverberation, since the harmonic structure remains intact. However, the harmonic structure of frequency-modulated sounds is distorted by reverberation since each part of the reverberant sound, being delayed, will have a previous value of $F0$ rather than that of the current direct sound. Figure 1 shows spectrograms of the sentence ''Could you please write the word bead down now'' spoken with natural prosody for both the anechoic (upper panel) and reverberant (lower panel, $RT_{60}=0.4$ s) conditions used in the following experiments. Where the $F0$ contour is relatively flat, harmonic structure is still evident though with reduced clarity, but distortion of harmonicity is clearly visible where there are large changes in $F0$ (during the word ''now,'' for example).

The effect of this degradation has been shown in experiments on the recognition of double vowels (Culling *et al.*, 1994). For vowels with steady $F0$'s, the improved identification produced by putting the vowels on different $F0$'s survives reverberation. But for vowels with modulated $F0$'s it does not. These findings raise the question of whether more

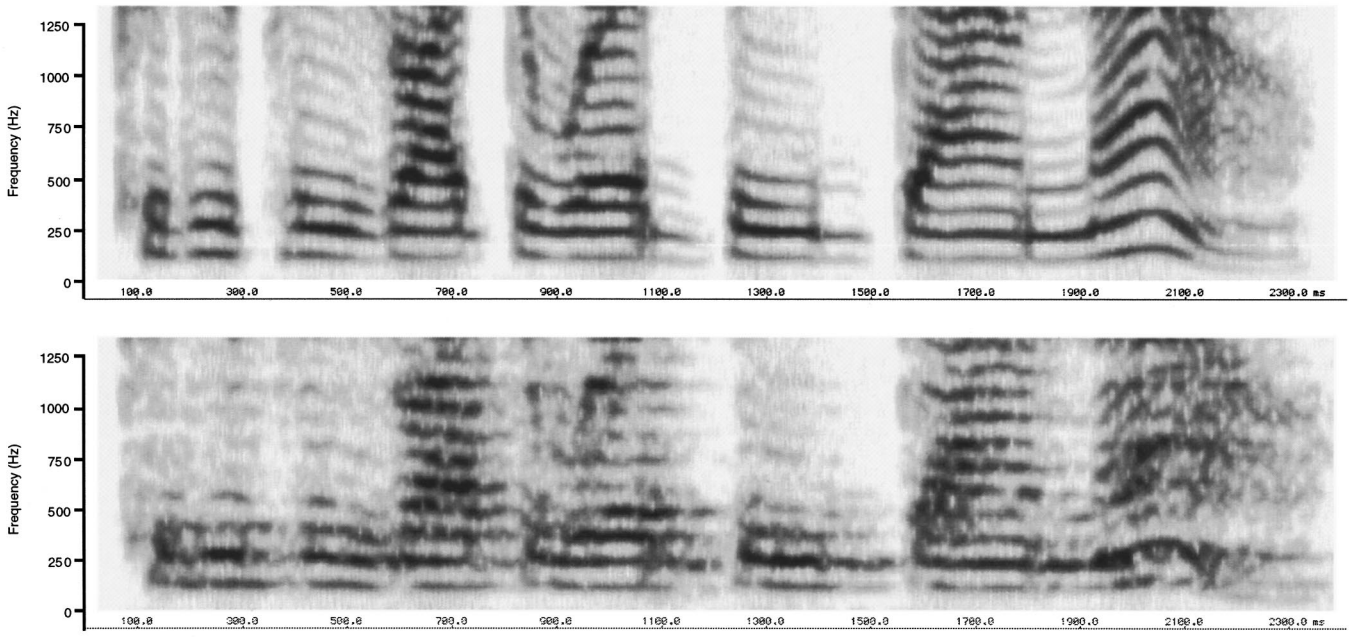

FIG. 1. Narrow-band spectrograms of the sentence ''Could you please write the word bead down now'' spoken with natural prosody for both anechoic (upper panel) and reverberant (lower panel, $RT_{60}=0.4$ s) conditions. The reverberation produces considerable smearing across time and distortion of harmonicity where there are rapid changes in $F0$ (during the word ''now,'' for example).

natural intonation contours are useful under reverberant conditions for selecting between alternative sound sources. Listeners might, for example, be able to attend more easily to an on-going natural contour than to artificial modulation, and so overcome the degrading effects of reverberation.

The experiments reported here use an established paradigm (Darwin and Hukin, 1999, 2000) to investigate the effects of reverberation on cues to speech source continuity. Subjects choose which of two simultaneous target words are part of an attended sentence rather than part of another simultaneous sentence. The paradigm has the advantage that it allows a rapid investigation of the effectiveness of localization and of prosodic and speaker cues in determining speech source continuity, although it does not measure the real-time allocation of attention. Since the two sentences and the target words remain the same throughout the experiment (apart from the manipulated cues), the intelligibility requirements of the task are minimal.

Our paradigm complements recent work by Assmann (1999b, a) which investigates how $F0$ and vocal-tract size differences contribute to the overall intelligibility of pairs of sentences. Assmann measures the total number of words recalled irrespective of which of the two sentences a particular word occurred in. Consequently, his work asks how various cues influence the intelligibility of individual words, but does not address the question of how listeners determine which words are part of the attended sentence. Our paradigm ignores the former question, and addresses the latter.

The first two experiments use a simulated room (Peterson, 1986) to explore the effects of reverberation on the usefulness of localization and prosodic cues to selective attention. The third experiment also varies the apparent vocal-tract size of the talker.

I. EXPERIMENT 1

This experiment repeats experiment 1 of Darwin and Hukin (1999) with simulated reverberation. The experiment examines the robustness to simulated reverberation of monotonous $F0$ differences and interaural time differences as cues for the selection of one of two simultaneous target words.

A. Stimuli

The recordings from the earlier article (Darwin and Hukin, 1999) were used in this experiment. The two sentences ''Could you please write the word bird down now'' and ''You will also hear the sound dog this time'' were spoken with a nearly flat intonation contour at around 125 Hz by a native speaker of British English (CJD). A short period of silence was added to the beginning of one sentence so that the two target words (''dog,'' ''bird'') began at the same time into their respective sound files.

The two sentences were resynthesised on a monotone using a PSOLA algorithm (Moulines and Charpentier, 1990) at fundamental frequencies of 100, 106, 112.3, and 125 Hz, corresponding to approximately 0, 1, 2, and 4 semitones above 100 Hz. This range of $F0$ differences is sufficient to produce substantial segregation both in speech identification tasks (Brokx and Nooteboom, 1982; Scheffers, 1983; Assmann and Summerfield, 1990; Culling and Darwin, 1993; Bird and Darwin, 1998) and in across-frequency integration of interaural time differences (ITDs) (Hill and Darwin, 1996).

In order to maintain the alignment of target word onsets, small adjustments were made to the silent closure interval before the target word in the different $F0$ conditions. These adjustments compensated for the PSOLA resynthesis round-

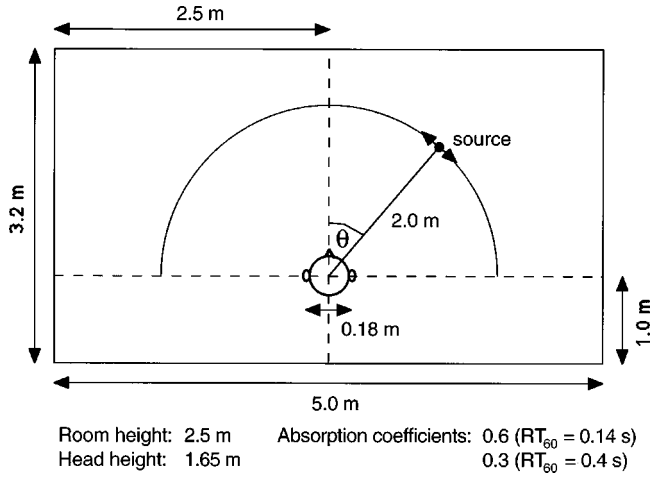

FIG. 2. Layout of simulated room for implementation of Peterson's ray-tracing method. The head was acoustically transparent, thus eliminating head-related interaural intensity differences (apart from those arising from the distance between the ears). Sources were positioned to give the nominal ITDs cited in the text when the absorption coefficient was unity.

ing durations to whole numbers of pitch periods.

This procedure produced sounds for the normal condition, where the $F0$'s of the target words ''dog'' and ''bird'' were the same as the sentence in which they occurred. To produce the swapped condition, these target words were digitally swapped round at stop-closure silences between various combinations of files so that the target word did not have the same $F0$ as its carrier sentence. The swapped condition allows us to separate spatial and prosodic contributions to attention.

The resynthesised sentences and their targets were then given simulated reverberation using Peterson's ray-tracing model (Peterson, 1986) previously used by Culling *et al.* (1994). The model room layout is illustrated in Fig. 2 and is identical to that used by Culling *et al.* The source was simulated to be 2 m from the head, which was placed in a slightly different position in the room from that used by Culling *et al.* Positions of the source were chosen to give a direct path-length difference at the two ears corresponding to the ITDs of 0, ±45, ±91, and ±181 μs used in the earlier experiment. The model calculated the waveform at each of the two ears represented as points in free space. Consequently, the model does not represent either interaural intensity differences (IID) arising from head shadow or pinna effects. The model does, however, incorporate intensity differences arising from different path lengths from the source to the two ears, though for a source 2 m away and opposite to one ear the IID is small (c. 0.7 dB). For convenience, and for ease of comparison of the results with those from our previous experiments, we will refer to the different source positions by their corresponding ITDs. Two absorption coefficients, 0.6 and 0.3, were used to give reverberation times (RT_{60} is defined as the time for the reverberant energy to drop by 60 dB) of 0.14 and 0.4 s, respectively. Our directly measured reverberation times differ slightly from those reported in Culling *et al.* (1994).

B. Procedure

The 13 listeners were native speakers of British English aged between 21 and 52 (including the two authors); all had pure-tone thresholds within the normal range at octave frequencies between 125 Hz and 8 kHz. They had all participated in experiment 1 of Darwin and Hukin (1999).

The procedure was identical to that of experiment 1 of Darwin and Hukin (1999) except that listeners were told that they should attend to the sentence ''Could you please write the word X down now,'' and to press the ''d'' or ''b'' key if it contained the target word ''dog'' or ''bird,'' respectively. One carrier sentence and one target word always had an $F0$ of 100 Hz, the other carrier sentence and the other target had an $F0$ that was either the same or 1, 2, or 4 semitones higher. The attended carrier sentence was thus separated from the other sentence by seven different intervals (−4, −2, −1, 0, 1, 2, or 4 semitones).

For the trials on which the ITD was zero, these seven conditions were combined with two conditions in which the target word that had the same $F0$ as the attended sentence was either ''dog'' or ''bird'' giving a total of 14 conditions (two of which are in fact identical, with zero ITD and zero difference in $F0$).

For the trials on which the ITD was not zero, there were three values of ITD combined with: $F0$ difference (seven values), whether the target with the same ITD was ''dog'' or ''bird'' (two values), whether the attended sentence had a positive or a negative ITD (two values), whether the target word with the same ITD as the carrier sentence also had the same $F0$ as the carrier sentence or not (normal versus swapped: two values). This combination gives a total of 168 conditions (some identical) which were presented five times each with each listener getting a different pseudo-random order. All these trials were presented in separate blocks of trials at the two reverberation times (0.1 and 0.4 s) in a counter-balanced order across subjects. The sentences when mixed at each headphone (Sennheiser 414) gave an average level of 68 dB SPL through a flat-plate coupler.

C. Results and discussion

Listeners' preferences for one or the other target word were subjected to analysis of variance with the following factors: ITD (±45, ±91, ±181 μs), $F0$ difference between the attended carrier sentence and the distractor ($\Delta F0 = -4$, −2, −1, 0, +1, +2, +4 semitones), correct target (''dog,'' ''bird''), correct target's $F0$ relation to attended carrier (same, different), and side of attended sentence (left, right). The reported significance levels have had the Greenhouse–Geisser correction for sphericity applied using SuperANOVA (Abacus Concepts).

1. Continuity of F0

When the two carrier sentences and target words have the same, zero ITD, the only cue to which target word belongs with the attended carrier is $F0$. Figure 3 shows the percentage of target words reported that had the same $F0$ as the attended sentence for both the reverberation conditions of this experiment, and also for the same 13 listeners for experi-

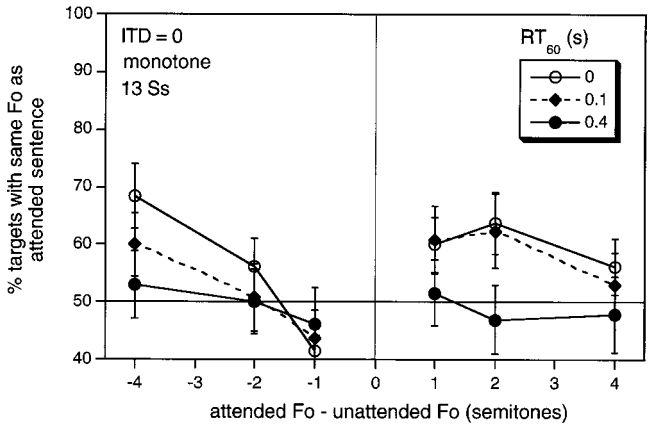

FIG. 3. Percent of target words reported that had the same $F0$ as the attended sentence for the conditions that had zero ITD in experiment 1 as a function of the $F0$ difference (attended-unattended) between sentences. The parameter is the reverberation time of the simulated room. Sound sources for both sentences were positioned directly ahead. Data for the $RT_{60}=0$ condition are for the same subjects from experiment 1 of Darwin and Hukin (1999). There is no data point at 0 semitones since the correct response is undefined.

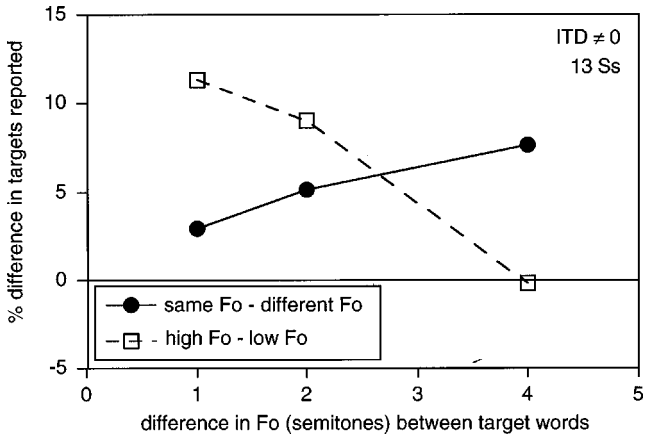

FIG. 4. The figure shows how strongly listeners in experiment 1 preferred the target word that had either the same (rather than different) $F0$ as the attended sentence (filled circles), or the target word that had the higher (rather than lower) $F0$ (open squares) as a function of the difference in $F0$ between target words (and so also between carrier sentences). Data are from trials where the ITDs were nonzero averaged across reverberation conditions.

ment 1 of Darwin and Hukin (1999) which used the same stimuli but without reverberation. The data are plotted as a function of the $F0$ difference between the attended and the carrier sentences.

Overall, the tendency for listeners to report the target with the same, monotonous $F0$ is rather weak, and is reduced by reverberation [$F(2,24)=15.8$, $p<0.0001$]. The reduction is rather slight for a RT_{60} of 0.1 s, but performance is at chance for a RT_{60} of 0.4 s. This result contrasts with Culling *et al.* (Exp. 3a, 1994), finding that a 0.4-s reverberation time did not reduce the substantial beneficial effect of a 1-semitone difference in $F0$ on the threshold level for identifying a steady-state vowel in the presence of a vowellike masker. Apart from the very different tasks used in the two experiments, possible factors responsible for the more substantial effect of reverberation time in the present experiment are the use of natural word targets embedded in a sentence context.

The below-chance performance for the two less reverberant conditions at an $F0$ difference of -1 semitone probably reflects a tendency for listeners to report the target word that has the higher $F0$ when there is only a small absolute difference in $F0$ between the two target words. This tendency is, in fact, a general one across the experiment. Figure 4 shows it for the rest of the experimental data (i.e., when there is also an ITD difference between the sentences). At small $F0$ differences, listeners tend to report the target word that has the higher $F0$, but at larger differences in $F0$ they tend to report the target word with the same $F0$ as the carrier sentence. Neither of these trends is large (maximally about 10%), but the interaction for the data in Fig. 4 is highly significant [$F(6,72)=40.4$, $p<0.0001$].

The tendency to prefer the higher of two different-pitched sounds has been noted previously. When two sentences are presented simultaneously with a pitch difference of 4 (but not at 1, 2, 6, or 8) semitones between them, the one with the higher $F0$ is more intelligible (Assmann, 1999a). Similarly, when listeners are asked to match the dominant pitch of two different vowels played simultaneously 2 or 4 semitones apart, listeners make matches which are closer to the higher than the lower pitch; when asked to match both pitches, matches tend to be made first and more accurately to the higher pitch (Assmann and Paschall, 1998). In a musical context, the higher of two polyphonic parts is easier to recognize than the lower (Gregory, 1990). However, extensive experiments on double-vowel recognition have failed to find any consistently better identification of the higher-pitched vowel (McKeown, 1992; de Cheveigné *et al.*, 1997; Paschall and Assmann, 1998). In our data, the preference for the higher-pitched target word weakens as the $F0$ difference increases from 1 to 4 semitones. This reduced preference for the higher-$F0$ target is probably due to an increased preference for the target with the same $F0$ as the attended sentence.

2. Continuity of ITD

When ITD is not zero, the spatial separation of the sentences provides an additional dimension for listeners to choose the target word. In the normal conditions spatial separation and $F0$ continuity work together whereas in the swapped conditions they are opposed. Since we have already shown that there is only a small tendency for listeners to report the target word with the same $F0$ as the attended carrier sentence, the data presented in Fig. 5 ignores the normal/swapped distinction. It shows the percentage of reported targets that had the same ITD as the attended sentence for the 13 Ss of experiment 1. The data in the left-hand panel of Fig. 5 are for the same subjects from experiment 1 of Darwin and Hukin (1999); they show that with no reverberation listeners show a strong tendency to report the target with the same ITD as the attended sentence.

The center and right-hand panels of Fig. 5 show that increasing reverberation time clearly reduces the ability of listeners to report the target that has the same ITD as the attended sentence [$F(2,24)=90.8$, $p<0.0001$]. The effect of

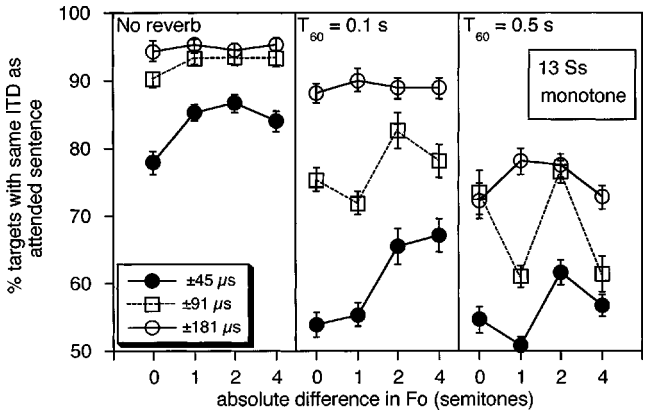

FIG. 5. Percent (±1 standard error) of target words reported that had the same ITD as the attended sentence for the 13 Ss of experiment 1. The $RT_{60}=0$ data are for these subjects from experiment 1 of Darwin and Hukin (1999).

reverberation is more marked for smaller ITDs [$F(4,48)=22.5$, $p<0.0001$], probably because of ceiling effects for the large ITD conditions. At the smallest ITD, ±45 μs, performance decreases markedly as reverberation time increases from 0 to 0.1 s, whereas for the largest ITD, listeners are still getting about 75% of the targets correct by ITD with a reverberation time of 0.4 s.

The data in Fig. 5 are shown plotted against the absolute difference in $F0$ between the two sentences; the generally small effects of the direction of $F0$ difference and of $F0$ continuity have been dealt with in the previous section. When there is no reverberation, subjects' ability to report the target with the same ITD as the attended sentence is somewhat lower when the two sentences have the same $F0$ than when there is a difference in $F0$. With increased reverberation, the effect of a difference in $F0$ becomes rather erratic, interacting with reverberation time and ITD [$F(24,288)=2.3$, $p<0.05$].

In summary, this experiment has shown that listeners' ability to use ITD to follow a particular target sentence is substantially disrupted when reverberation is introduced. In addition, the rather weak tendency to report the target that has the same $F0$ as the attended sentence, is also reduced by reverberation.

II. EXPERIMENT 2

The purpose of experiment 2 is to compare how resilient to reverberation are ITD and natural prosodic cues. The natural prosodic variation that we use here is more effective at maintaining a listener's attention than the monotone manipulations used in experiment 1 (Darwin and Hukin, 2000).

Reverberation impairs listeners' ability to use sinusoidally modulated $F0$'s to separate simultaneous vowellike sounds more than it impairs their ability to use monotonous $F0$'s (Culling *et al.*, 1994). Culling *et al.* attribute this impairment by reverberation to two causes: first, for small modulation depths reverberation blurs the harmonic structure of individual sounds; second, further impairment occurs when the modulation depth is comparable with the $F0$ separation of the two sounds so the blurred $F0$'s overlap. On the basis of this analysis we would expect reverberation to have more effect on the ability of listeners to use natural contours which are separated by an overall $F0$ difference which prevents the $F0$ of the reverberant sound becoming too close than on those with overlapping $F0$ contours.

A. Stimuli and procedure

The utterances used were those from experiment 1 of the companion article (Darwin and Hukin, 2000). In brief, two sentences with each of two target words (''Could you please write the word bead/globe down now'' and ''You'll also hear the sound bead/globe played here'') were spoken in two versions, one with the main sentence stress early in the sentence (on ''please'' or ''also''), and once with the stress late in the sentence (on ''now'' or ''here''). Sentences were paired so that a pair contained both carrier sentences, both target words, and both sentence stress positions. Three different resyntheses were then made for each sentence pair: *original*, in which the $F0$ values were unchanged; *together*, in which the two sentences, $F0$ contours were both shifted in order to make the values of $F0$ during the two target words similar; and *apart*, in which the two sentences, $F0$ contours were shifted the opposite way in order to make their values of $F0$ during the two target words more different. The $F0$ contours for a representative pair of sentences are shown in Fig. 1 of Darwin and Hukin (2000).

In order to measure the relative strengths of the ITD and prosodic cues, two different conditions were generated from these resynthesized sentence pairs: a normal condition, which retained the sentences as described in the previous paragraph, and a swapped condition in which the target words (with their prosodic attributes) were swapped between the two sentences of a pair. This swapping of target words was done before sentences were given different ITDs. A target word that had the same ITD as the target sentence would thus also have the same prosody in the normal condition, but different prosody in the swapped condition.

The simulated room used in experiment 1 with the same spatial positions and with $RT_{60}=0.4$ s then produced stereo sound files for presentation to listeners using the same procedure as in the previous experiment.

The experiment was taken by the 13 listeners who had taken the equivalent nonreverberant experiment—experiment 1 in the companion article (Darwin and Hukin, 2000). Half of the listeners were instructed to listen to one sentence throughout the experiment, and the others were instructed to listen to the other sentence.

B. Results and discussion

The percentage of targets reported that have the appropriate prosody for the attended sentence are shown in Fig. 6.

For the normal conditions, targets that have the appropriate prosody also have the same ITD as the attended sentence. Since both cues favor the same target word, performance is very high (about 90%) despite the reverberation both for the original condition where the $F0$ contours are unchanged, and for the apart condition where the $F0$ contours have been further separated by about 4 semitones. Performance goes down to about 70% in the together condition, where the two target words have very similar $F0$ contours.

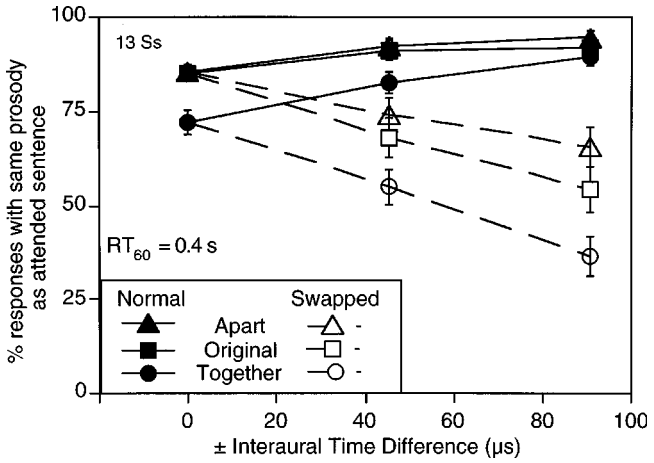

FIG. 6. Percent (±1 standard error) of target words reported that had the same prosody as the attended sentence as a function of the difference in ITD between the two sentences for the 13 Ss of experiment 2. Symbols joined by solid lines plot data from conditions where the target word with the same prosody as the attended sentence also had the same ITD. For those joined by dashed lines, the target word with the same prosody as the attended sentence had the same ITD as the unattended sentence.

Listeners are here mainly relying on other prosodic differences between the two words such as the level differences described in the companion article.

For the swapped conditions, the spatial cues are placed in opposition to the prosodic cues. As the nominal ITD increases, listeners report more of the targets that have the appropriate spatial cues and correspondingly fewer targets that have the correct prosody. In order to see more clearly the relative effect of reverberation on the two types of cue, Fig. 7 shows the size of the decrease, between the normal and the swapped conditions, in the percentage of reported targets that have the same ITD as the attended sentence. The more effective the prosodic cue, or the less effective ITD, the larger will be this change.

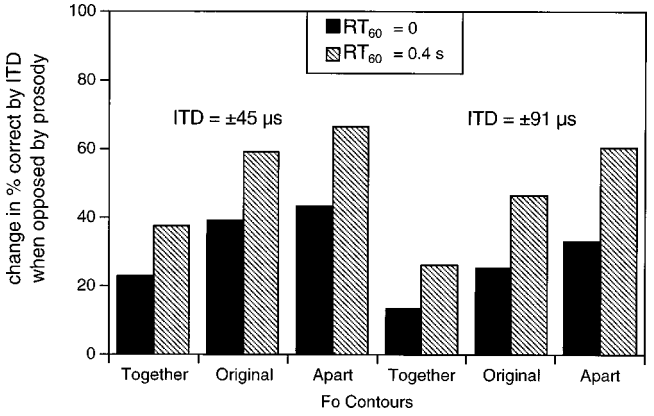

FIG. 7. Influence of reverberation on the relative effectiveness of ITD and prosody in experiment 2. The bars indicate the decrease in the percent of target words that had the same ITD as the attended sentence between the normal conditions (in which the target word shared both ITD and prosody with the attended sentence) and swapped conditions (where the target word had the same ITD but a different prosody). A large score indicates that prosodic cues are dominating over ITD. The scores are increased by increasing the $F0$ difference between the sentences (abscissa) and by reducing ITD. The increase with reverberation (shaded versus black bars) indicates that reverberation is degrading the ITD cue more than it is degrading the prosodic cue.

The solid bars of Fig. 7 show data from experiment 1 in the companion article, and their pattern simply shows that the *relative* effectiveness of the prosodic cues is increased by separating the $F0$ contours, and decreased by the larger ITD, as one would expect. The effect of reverberation (hatched bars) on this pattern is generally to favor the prosodic cues indicating that 0.4-s reverberation weakens the spatial cue more than it does the prosodic ones. That the $F0$ component of the prosody maintains its effectiveness compared with the spatial cue is shown by the fact that the hatched bars in Fig. 7 remain above the solid bars in the original and apart $F0$ conditions.

III. EXPERIMENT 3

The final experiment examines the effect of reverberation on listeners' ability to attend to a sentence which is spoken by a different apparent vocal-tract size from the unattended sentence. The experiment takes the original prosody conditions from experiment 2 and introduces a ±15% difference in spectral envelope between the attended and unattended sentences and also between the two target words.

A. Stimuli and procedure

The original sentences from experiment 2 were modified to produce two apparently different talkers by altering the spectral envelope without changing the $F0$ or duration. Sentences were resynthesised using PSOLA using a method described in detail in Darwin and Hukin (2000). Briefly sentences were globally reduced in duration and raised in $F0$ by 15%, resampled at 15% higher sampling frequency, and then played back at the original sample rate. This manipulation produced sentences that had the same durations and $F0$'s as the originals, but which had the spectral envelope lowered by 15% (effectively increasing the apparent vocal-tract size). Shorter vocal-tract voiced sentences were produced using opposite manipulations. A large difference in vocal-tract length was used since earlier work (Darwin and Hukin, 2000) had shown that such large differences were necessary to influence attention substantially. The vocal-tract was both lengthened and shortened by 15% (rather than being merely shortened by 30%) in order to maintain speech quality.

The sentences were paired as in experiment 2 with the additional constraint that each pair contained one long vocal-tract sentence and one short vocal-tract sentence. Target words could be swapped between the sentences of a pair before the sentences were allocated an ITD. In the swapped condition, the target word had the same ITD as the attended sentence, but the vocal-tract size and prosody of the unattended sentence.

Reverberation was added to the sentences in each pair using the same simulated room used in experiments 1 and 2, the same spatial positioning and with $RT_{60}=0.4$ s. The resultant stereo sound files were presented to the listeners using an identical procedure to the previous two experiments. Half of the listeners were instructed to listen to one sentence throughout the experiment, and the others were instructed to listen to the other sentence.

Of the 11 listeners who took the experiment, 8 had already taken part in the corresponding experiment in the com-

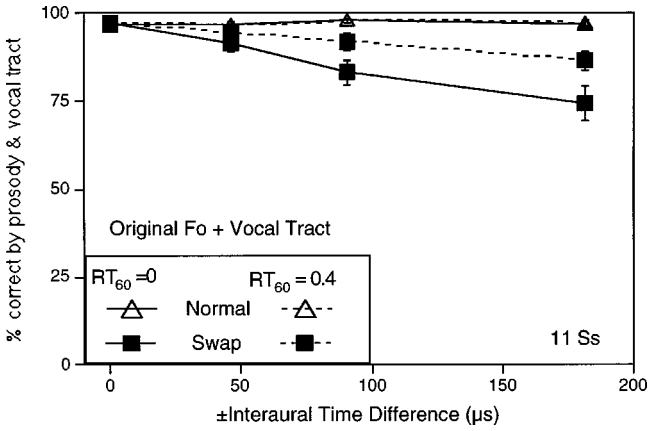

FIG. 8. Percent (±1 standard error) of target words reported that had the same prosody and vocal tract size as the attended sentence as a function of the difference in ITD between the two sentences for the 11 Ss of experiment 3. The open triangles plot data from conditions where the target word with the same prosody and vocal-tract size as the attended sentence also had the same ITD. The filled squares plot data from conditions where the target word with the same prosody and vocal-tract size as the attended sentence had the same ITD as the unattended sentence.

panion article with no reverberation. The remaining 3 subjects additionally took this experiment so that we had data from all 11 subjects both with and without reverberation.

B. Results and discussion

Introducing a difference in vocal-tract size between the attended and unattended sentences provides a cue which is extremely resistant to degradation by reverberation even when opposed by a substantial difference in ITD. Figure 8 shows the percent of target words reported that had the same prosody and vocal tract size as the attended sentence as a function of the difference in ITD between the two sentences. The notable feature of the figure is that in the swapped conditions, where the target that is correct by prosody and vocal-tract size has the wrong ITD, listeners very strongly prefer the target that has the correct prosody and vocal-tract size. This preference is still very substantial (87%) even when an ITD difference of ± 181 μs opposes these cues.

The substantial preference for the target word that had the same vocal-tract size as the carrier sentence contrasts with recent findings by Assmann (1999b) who found little consistent improvement in overall word intelligibility of simultaneously presented sentences with differences in vocal-tract size. Two differences between our experiments are probably responsible. First, we used a difference in vocal-tract length (-15% vs $+15\%$) that is almost twice that used by Assmann (0% vs $\pm 20\%$); smaller differences than our $\pm 15\%$ are less effective as cues (Darwin and Hukin, 2000). Second, as pointed out in the Introduction, while Assmann's experimental paradigm measures overall word intelligibility, but does not measure attention, our paradigm measures attention but does not measure word intelligibility.

IV. SUMMARY AND GENERAL DISCUSSION

The three experiments reported here have explored how resistant to simulated reverberation are various cues for selective attention. The listeners' task was to decide which of two simultaneous target words belonged to an attended rather than an unattended sentence. The experiments have shown the following.

(i) The weak preference of listeners for the target word with the same monotonous $F0$ as the attended sentence was eliminated by reverberation (experiment 1).
(ii) Listeners' ability to use ITD differences was seriously impaired by reverberation (experiment 1), although some ability remained for the longest ITD tested.
(iii) The prosodic manipulations (including $F0$ differences) used in experiment 2 were generally more resistant to reverberation than were the ITD differences.
(iv) Adding a difference in vocal-tract size to the prosodic cues produced a high level of performance which was very resistant to reverberation (experiment 3).

This paper has explored the effect of reverberation on one aspect of auditory attention: the ability of listeners to maintain attention to a particular sound source across time. We have used a paradigm that has minimal intelligibility requirements since listeners are always presented with the same two target words. The paradigm also minimizes local cues to sound-source continuity by presenting the two target words simultaneously and with silence (from stop closure) before and after. Although it might be argued that this latter constraint is somewhat artificial, it perhaps reflects the practicalities of attempting to assign to the appropriate sources, speech which is intermittently masked by other talkers.

The two main results of the paper are, first, that reverberation reduces the effectiveness of ITD as an attentional cue, and, second, that natural prosodic cues and large vocal-tract size differences between talkers provide additional cues that are generally more resistant to the effects of reverberation than is ITD.

Our previous work had shown that, in the absence of talker and $F0$ differences, listeners could use small differences in ITD to follow a particular sound source. The effectiveness of this cue (with monotone speech), however, is seriously reduced by reverberation despite the dynamic nature of the sentences and target sounds. Reverberation alters both the intensity and the phase of individual harmonics and also reduces their depth of amplitude modulation and so will make both the carrier sentence and the target harder to localize. Since the detrimental effect of reverberation persists even when there is a 4-semitone difference in $F0$ between sentences, it is unlikely that interference between the individual components of the two sentences is necessary for reverberation to have its effect.

Natural prosodic cues, although not particularly strong (at least in these experiments) in the absence of reverberation, are more resistant to reverberation than are the spatial cues used here. Both $F0$ differences and other prosodic cues (probably mainly amplitude differences) help listeners to select the appropriate target word, and their influence becomes relatively stronger than the spatial cue with increased reverberation. A large difference in vocal-tract size provides a more powerful continuity cue, and this too is very resistant to reverberation.

Although the paradigm used here allows sophisticated

stimulus manipulations to be made easily with natural stimuli, it does not allow us to determine to what extent the cues we are investigating are having their effect in real time, and to what extent they are (merely) influencing a listener's choice some time after the event. It is possible that spatial cues could be exploited more easily than prosody or vocal-tract size for directing of attention (Spence and Driver, 1994). If this were the case, then a task such as shadowing that is more sensitive to the real-time allocation of attention might be substantially disrupted by the erosion of spatial cues by reverberation even though prosodic and vocal-tract cues were also present.

ACKNOWLEDGMENTS

This research was supported by Grant No. G9801285 from the UK MRC to the first author. We are grateful to John Culling for help with the software implementation of the reverberation. Peter Assmann and Alain de Cheveigné made a number of helpful suggestions for improving the paper.

Abouchacra, K. S., Emanuel, D. C., Blood, I. M., and Letowski, T. R. (**1998**). ''Spatial perception of speech in various signal to noise ratios,'' Ear Hear. **19**, 298–309.

Assmann, P. F. (**1999a**). ''Fundamental frequency and the intelligibility of competing voices,'' 14th International Congress of Phonetic Sciences, San Francisco, 1–7 August 1999, pp. 179–182.

Assmann, P. F. (**1999b**). ''Vocal tract size and the perception of competing voices,'' J. Acoust. Soc. Am. **106**, 2272.

Assmann, P. F., and Paschall, D. D. (**1998**). ''Pitches of concurrent vowels,'' J. Acoust. Soc. Am. **103**, 1150–1160.

Assmann, P. F., and Summerfield, A. Q. (**1990**). ''Modelling the perception of concurrent vowels: Vowels with different fundamental frequencies,'' J. Acoust. Soc. Am. **88**, 680–697.

Bird, J., and Darwin, C. J. (**1998**). ''Effects of a difference in fundamental frequency in separating two sentences,'' in *Psychophysical and Physiological Advances in Hearing*, edited by A. R. Palmer, A. Rees, A. Q. Summerfield, and R. Meddis (Whurr, London), pp. 263–269.

Brokx, J. P. L., and Nooteboom, S. G. (**1982**). ''Intonation and the perceptual separation of simultaneous voices,'' J. Phonetics **10**, 23–36.

Culling, J. F., and Darwin, C. J. (**1993**). ''Perceptual separation of simultaneous vowels: Within and across-formant grouping by *F*0,'' J. Acoust. Soc. Am. **93**, 3454–3467.

Culling, J. F., Summerfield, A. Q., and Marshall, D. H. (**1994**). ''Effects of simulated reverberation on the use of binaural cues and fundamental-frequency differences for separating concurrent vowels,'' Speech Commun. **14**, 71–95.

Darwin, C. J., and Hukin, R. W. (**1999**). ''Auditory objects of attention: the role of interaural time-differences,'' J. Exp. Psychol. **25**, 617–629.

Darwin, C. J., and Hukin, R. W. (**2000**). ''Effectiveness of spatial cues, prosody and talker characteristics in selective attention,'' J. Acoust. Soc. Am. **107**, 970–977.

de Cheveigné, A., Kawahara, H., Tsuzaki, M., and Aikawa, K. (**1997**). ''Concurrent vowel identification. 1. Effects of relative amplitude and *F*-0 difference,'' J. Acoust. Soc. Am. **101**, 2839–2847.

Good, M., and Gilkey, R. (**1996**). ''Sound localization in noise: The effect of signal-to-noise ratio,'' J. Acoust. Soc. Am. **99**, 1108–1117.

Gregory, A. H. (**1990**). ''Listening to polyphonic music,'' Psychol. Music **18**, 163–170.

Hartmann, W. M. (**1983**). ''Localization of sound in rooms,'' J. Acoust. Soc. Am. **74**, 1380–1391.

Hill, N. I., and Darwin, C. J. (**1996**). ''Lateralisation of a perturbed harmonic: effects of onset asynchrony and mistuning,'' J. Acoust. Soc. Am. **100**, 2352–2364.

Lorenzi, C., Gatehouse, S., and Lever, C. (**1999**). ''Sound localization in noise in normal-hearing listeners,'' J. Acoust. Soc. Am. **105**, 1810–1820.

McKeown, J. D. (**1992**). ''Perception of concurrent vowels: the effect of varying their relative level,'' Speech Commun. **11**, 1–13.

Moncur, J., and Dirks, D. (**1967**). ''Binaural and monaural speech intelligibility in reverberation,'' J. Speech Hear. Res. **10**, 186–195.

Moulines, E., and Charpentier, F. (**1990**). ''Pitch synchronous waveform processing techniques for text-to-speech synthesis using diphones,'' Speech Commun. **9**, 453–467.

Nabelek, A. K. (**1988**). ''Identification of vowels in quiet, noise, and reverberation: relationships with age and hearing loss,'' J. Acoust. Soc. Am. **84**, 476–784.

Nabelek, A. K., and Dagenais, P. A. (**1986**). ''Vowel errors in noise and in reverberation by hearing-impaired listeners,'' J. Acoust. Soc. Am. **80**, 741–748.

Nabelek, A. K., and Donahue, A. M. (**1984**). ''Perception of consonants in reverberation by native and non-native listeners [letter],'' J. Acoust. Soc. Am. **75**, 632–634.

Nabelek, A. K., and Robinson, P. K. (**1982**). ''Monaural and binaural speech perception in reverberation for listeners of various ages,'' J. Acoust. Soc. Am. **71**, 1242–1248.

Paschall, D. D., and Assmann, P. F. (**1998**). ''Ranking the pitches of concurrent vowels,'' J. Acoust. Soc. Am. **103**, 2980.

Peterson, P. M. (**1986**). ''Simulating the response of multiple microphones to a single source in a reverberant room,'' J. Acoust. Soc. Am. **80**, 1527–1529.

Plomp, R. (**1976**). ''Binaural and monaural speech intelligibility of connected discourse in reverberation as a function of a single competing sound source (speech or noise),'' Acustica **34**, 200–211.

Plomp, R. (**1977**). ''Acoustical aspects of cocktail parties,'' Acustica **38**, 186–191.

Rakerd, B., and Hartmann, W. M. (**1985**). ''Localization of sound in rooms, II: The effects of a single reflecting surface,'' J. Acoust. Soc. Am. **78**, 524–533.

Scheffers, M. T. (**1983**). ''Sifting vowels: Auditory pitch analysis and sound segregation,'' Ph.D. dissertation, Groningen University, The Netherlands.

Spence, C. J., and Driver, J. (**1994**). ''Covert spatial orienting in audition: exogenous and endogenous mechanisms,'' J. Exp. Psychol. **20**, 555–574.

Acoustic modeling of American English /r/

Carol Y. Espy-Wilson[a)]
Electrical and Computer Engineering Department, Boston University, Boston, Massachusetts 02215 and Research Laboratory of Electronics, Massachusetts Institute of Technology, Cambridge, Massachusetts 02139

Suzanne E. Boyce
Department of Communication Sciences and Disorders, University of Cincinnati, Cincinnati, Ohio 45267 and Electrical and Computer Engineering Department, Boston University, Boston, Massachusetts 02215

Michel Jackson
Electrical and Computer Engineering Department, Boston University, Boston, Massachusetts 02215

Shrikanth Narayanan
AT&T Labs, Florham Park, New Jersey 07932

Abeer Alwan
Department of Electrical Engineering, University of California at Los Angeles, Los Angeles, California 90024

(Received 29 December 1998; accepted for publication 22 March 2000)

Recent advances in physiological data collection methods have made it possible to test the accuracy of predictions against speaker-specific vocal tracts and acoustic patterns. Vocal tract dimensions for /r/ derived via magnetic-resonance imaging (MRI) for two speakers of American English [Alwan, Narayanan, and Haker, J. Acoust. Soc. Am. **101**, 1078–1089 (1997)] were used to construct models of the acoustics of /r/. Because previous models have not sufficiently accounted for the very low $F3$ characteristic of /r/, the aim was to match formant frequencies predicted by the models to the full range of formant frequency values produced by the speakers in recordings of real words containing /r/. In one set of experiments, area functions derived from MRI data were used to argue that the Perturbation Theory of tube acoustics cannot adequately account for /r/, primarily because predicted locations did not match speakers' actual constriction locations. Different models of the acoustics of /r/ were tested using the Maeda computer simulation program [Maeda, Speech Commun. **1**, 199–299 (1982)]; the supralingual vocal-tract dimensions reported in Alwan *et al.* were found to be adequate at predicting only the highest of attested $F3$ values. By using (1) a recently developed adaptation of the Maeda model that incorporates the sublingual space as a side branch from the front cavity, and by including (2) the sublingual space as an increment to the dimensions of the front cavity, the mid-to-low values of the speakers' $F3$ range were matched. Finally, a simple tube model with dimensions derived from MRI data was developed to account for cavity affiliations. This confirmed $F3$ as a front cavity resonance, and variations in $F1$, $F2$, and $F4$ as arising from mid- and back-cavity geometries. Possible trading relations for $F3$ lowering based on different acoustic mechanisms for extending the front cavity are also proposed. [S0001-4966(00)00407-0]

PACS numbers: 43.70.Fq [AL]

INTRODUCTION

Historically, models for the more articulatorily complex liquids have been less well developed than models for vowels and obstruent consonants (Chiba and Kajiyama, 1941; Fant, 1960, 1980; Stevens, 1999; Rubin, Baer, and Mermelstein, 1981; Harshman, Ladefoged, and Goldstein, 1977; Maeda, 1982). Recently, however, several researchers have proposed models of the acoustics of American English /r/ (Stevens, 1999; Alwan *et al.*, 1997; Hagiwara, 1995; Veatch, 1990; Ohala, 1985) and similar rhotic sonorants (McGowan, 1994; Narayanan *et al.*, 1999). Several aspects of /r/ make this a complicated and interesting task. First, /r/ is characterized by a particularly stable acoustic pattern of $F3$ lowering close to the value of $F2$ (Boyce and Espy-Wilson, 1997; Guenther *et al.*, 1999). However, the acoustic means by which $F3$ is lowered has not been clear. Second, speakers of ''rhotic'' varieties of American English use a multitude of articulatory configurations (Westbury *et al.*, 1999; Delattre and Freeman, 1968; Zawadaski and Kuehn, 1980; Alwan *et al.*, 1997; Ong and Stone, 1998). These configurations may involve substantially different tongue shapes and different parts of the tongue as primary articulators, but researchers so far have failed to link patterns of acoustic variability in formant values with the different articulatory configurations. For instance, Delattre and Freeman's (1968) ground-

a)Electronic mail: espy@bu.edu

breaking x-ray study of articulatory configuration types across speakers failed to identify consistent acoustic differences associated with different types. Similarly, studies by Westbury *et al.* (1999) and Guenther *et al.* (1999) have found that different types of articulatory configurations could not easily be correlated with specific patterns of formant values. The conclusion has been that different configurations produce essentially equivalent acoustical profiles (Delattre and Freeman, 1968; Westbury *et al.*, 1999). As such, American English /r/ is often cited as an example of a many-to-one articulatory–acoustic relationship. Third, acoustic models of /r/ must deal with three constrictions along the vocal tract, and the dimensions of the cavities thus formed were not known from physiological data until recently (Moore, 1992; Alwan *et al.*, 1997; Ong and Stone, 1998). This is particularly true of the sublingual space, which is not easily estimated using surface point-tracking systems such as x-ray microbeam or palatography (but see Sundberg *et al.*, 1992, for an alternative method).

Because of the difficulty in obtaining precise physiological data for vocal tract dimensions during a segment of interest, investigators developing acoustic models have for the most part been forced to make plausibility the criterion for assumptions about physical vocal tract features, such as constriction size, cavity volume, etc. In addition, the criteria for a successful match between predicted and actual acoustic patterns have been in terms of ability to capture general patterns of phonemic difference across multiple speakers. Recently, however, advances in physiological data collection methods have made it possible to test the accuracy of predictions against speaker-specific vocal tracts and acoustic patterns. This advance enables model makers to use a more demanding set of criteria; namely, a successful match between predicted and actual patterns for a given speaker's vocal tract. For instance, Story *et al.* (1996) used MRI-derived vocal-tract area functions from a single speaker to obtain simulated formant frequencies for vowels that were almost always within 10% of those measured from natural speech. In a similar study, Yang and Kasuya (1994) obtained vowel formant frequencies from a model using MRI-derived area functions that were within 5% of those measured from natural speech.

In this paper, we use recently available magnetic resonance imaging (MRI) data for American English /r/ (Alwan *et al.*, 1997) to examine various current theoretical models of the acoustics of /r/ in greater detail and with narrower criteria than has previously been possible. These data, and modifications thereof, are used to supply vocal-tract dimensions for VTCALCS, Maeda's vocal-tract computer modeling software (1982). Our major aim is to understand the acoustic mechanism responsible for the distinctive characteristics of /r/, in particular, its unusually low $F3$.

A. Acoustics of /r/

American English /r/ occurs both as a syllable nucleus and in consonantal position, where it is classified as a sonorant liquid.[1] The characteristic formant pattern for both involves an $F1-F2$ pattern similar to that of a canonical central, rounded vowel (Espy-Wilson, 1992), together with a very low $F3$. A typical example of intervocalic /r/, illustrating the severe dip in $F3$, is shown spectrographically in Fig. 1. As in this case, $F3$ is often low enough to approach and/or merge with $F2$ (Stevens, 1999). $F1$ and $F2$ values are predictable from the general articulatory shape of /r/, and accordingly overlap with those of vowels with similar place and height features. The $F3$ of such vowels is around 2500 Hz or above for most speakers (cf. Hagiwara, 1995). Consequently, the major problem in modeling the acoustics of American English /r/ is accounting for the very low third formant. Although formant values for /r/ vary somewhat from speaker to speaker and across prosodic conditions such as initial vs final word position, syllabic vs consonantal function, etc., $F3$ remains low relative to other segments. In a study of male–female and subject-to-subject variability in formant frequencies for /r/, Hagiwara (1995) used $F3$ in the neutral vowel to normalize between-speaker formant frequencies. He then determined that $F3$ for any one subject falls between 60% and 80% below the $F3$ value in the neutral vowel. For most speakers, this puts $F3$ below 2000 Hz. The range of actual values reported in the literature (across sex, syllabic vs consonantal prosodic position, etc.) is approximately 250–550 Hz for $F1$, 900–1500 Hz for $F2$, and 1300–1950 Hz for $F3$ (Delattre and Freeman, 1968; Lehiste, 1962; Zawadaski and Kuehn, 1980; Nolan, 1983; Espy-Wilson, 1992; Westbury *et al.*, 1999; but see Hagiwara, 1995, for outliers).

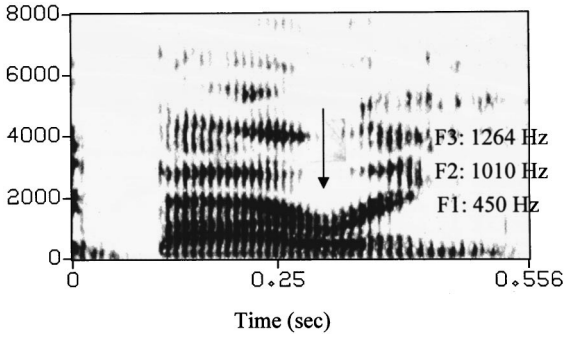

FIG. 1. Spectrogram of the word ''barring'' spoken by a male speaker.

B. Articulation of /r/

Overall, articulatory configurations for /r/ involve three constrictions: in the pharynx, along the palatal vault, and at the lips. The configurations differ most by what happens in the palatal region, i.e., by whether the effective constriction occurs (1) at the alveolar ridge and is made solely by the tongue tip, (2) in the palatovelar region and is made solely by the tongue dorsum with a lowered tongue tip, or (3) in both alveolar and palatovelar regions, and is made by the simultaneous raising of the tongue tip and tongue dorsum. Traditionally, these configurations have been divided into contrasting categories of ''retroflex'' (in which the tongue tip is raised and the tongue dorsum is lowered) versus ''bunched'' (in which the tongue dorsum is raised and the tongue tip lowered) (Delattre and Freeman, 1968; Shriberg and Kent, 1982; Kent, 1998). However, as a number of re-

searchers have pointed out, these two categories are only the extremes in a continuum that includes many incremental variants (Zawadaski and Kuehn, 1980; Delattre and Freeman, 1968; Westbury *et al.*, 1999; Alwan *et al.*, 1997; Guenther *et al.*, 1999; Ong and Stone, 1998). Further, the variant in which both tongue tip and tongue dorsum are raised does not easily fit into the traditional dichotomy of retroflexed versus bunched. In this paper, therefore, the major types of configurations will be categorized as (1) tip-up retroflex /r/, (2) tip-up bunched /r/, and (3) tip-down bunched /r/. It is worth noting that these different configurations occur both within and across speakers; that is, while some speakers may use one type of configuration exclusively, other speakers switch between two or three different types of configurations for /r/ in different phonetic contexts (Delattre and Freeman, 1968; Guenther *et al.*, 1999), and according to prosodic variables such as word position, syllabic versus consonantal function, etc. (Delattre and Freeman, 1968; Zawadaski and Kuehn, 1980).

C. Modeling /ɹ/: Acoustic sources of *F*3

Proposed models of the acoustics of American English /r/ divide into two types: (1) the Perturbation Theory account, which has been promulgated primarily through teaching and laboratory demonstrations,[2] but is described in Johnson (1997) and Ohala (1985), and (2) decoupling accounts, exemplified by the model of Stevens (1999) and modified versions by Alwan *et al.* (1997) and Narayanan *et al.* (1999). The Perturbation Theory account of /r/ is based on a general principle of tube acoustics; namely, that for a relatively open tube, constrictions at points where standing waves have maximum volume velocity have the effect of lowering the natural resonances of the resonating tube (Chiba and Kajiyama, 1941; Heinz, 1967; Schroeder, 1967). Such points of sensitivity to constriction are commonly invoked to explain the formant-lowering effect of lip-aperture narrowing and to predict the effect of certain articulatory changes on vowel acoustics (Stevens, 1999, p. 284; also Mrayati, Carré, and Guérin, 1988). It happens that when the vocal tract is modeled as a quarter-wavelength tube, maximum volume velocity points for *F*3 occur in the pharyngeal, palatal, and labial regions. Because the common denominator across various types of /r/ is the presence of constrictions in these three regions, some investigators have suggested that the lowering effects of all three combine to produce the low *F*3 typical of /r/ (Hagiwara, 1995; Veatch, 1990; Ohala, 1985). Indeed, modeling trials where realistic constrictions are inserted at points of maximum velocity produce *F*3 values in the appropriate range for /r/ (Espy-Wilson *et al.*, 1997). The usefulness of this approach for modeling speech sounds in general is controversial (Boe and Perrier, 1990); with regard to /r/ this is primarily because the perturbation effect applies only to cases where constrictions are mild.[3] Another prediction of the Perturbation Theory account is that speakers place their actual constrictions for /r/ at extremely specific points along the vocal tract, i.e., the points of maximum volume velocity. Thus, a finding that speakers place constrictions at other points along the vocal tract would be evidence against this model of /r/ acoustics.

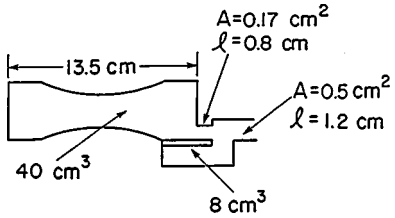

FIG. 2. Stevens' simple tube model for a tip-up retroflex /r/. The symbol ''*A*'' stands for area and the symbol ''*l*'' stands for length. The orientation of this model is such that the glottis is at the left edge and the lips are at the right edge. (Reprinted with permission from K. Stevens, *Acoustic Phonetics*, MIT Press.)

In contrast to the Perturbation Theory account, decoupling accounts, such as Fant (1960), Stevens (1999), Alwan *et al.* (1997), and Narayanan *et al.* (1999), assume that the vocal tract is divided into several different tubes, of differing areas and lengths, and that different formants have their origin as resonating frequencies of different tubes. Thus, a major issue for decoupling accounts is the question of boundary conditions for the particular shapes, lengths, and proportions of tubes in the vocal tract. If a constriction at one end of a cavity is narrow enough, for instance, the cavity is modeled as a tube with a closed end. If a constriction is wide enough, cavities on either side of the constriction are no longer decoupled. If both ends of a cavity have narrow constrictions, and the cavity-to-constriction ratio is high enough, the cavity and the constriction anterior to it can be modeled as a Helmholtz resonator. If, on the other hand, the constriction posterior to the cavity is narrow and the constriction anterior to the cavity is wide, the cavity and the anterior constriction can be modeled as a quarter-wavelength tube. The choice of such boundary conditions determines the appropriate equations for estimating formant frequencies and, conversely, determines which of many possible combinations can match a particular set of formant frequencies. Until recently, the dimensions of cavities and constrictions in the vocal tract had to be estimated, based on what seemed anatomically likely and what worked to produce formant frequencies approximately in the correct range. As we show in this paper (see Sec. II E, simulation experiment 5), availability of directly observed, segment-specific physiological data allows the boundary conditions for modeling to be determined substantially more accurately.

The most detailed model of the acoustics of /r/ can be found in Stevens (1999), which was primarily designed for articulatory configurations found in tip-up /r/'s where the tongue dorsum is lowered. A sketch of this model is shown in Fig. 2. Note that this model assumes a sizable difference between the area of the back cavity (about 3 cm^2) and the area of the front cavity (0.5 cm^2). Also, Stevens included a substantial sublingual space with a volume of 8 cm^3. Similar models are given in Fant (1960), Alwan *et al.* (1997), and Narayanan *et al.* (1999). In Stevens' model, the palatal constriction is assumed to be narrow enough, and the lip constriction narrow enough, that the cavity behind the lips (i.e.,

the ''front'' cavity) and the lip cavity can be modeled together as a quarter-wavelength tube that is closed at the palatal end and open at the lip end. $F3$ is assumed to be the lowest resonance of this quarter-wavelength tube.[4] Given this assumption, the front cavity must be 5 cm long to produce a resonance at 1750 Hz—a value in the middle of the typical $F3$ range for English speakers. It must be correspondingly longer in order to produce a resonance in the lower portion of the typical range, e.g., 1300–1600 Hz. This model may also be modified in such a way that, if the lip constriction is narrow enough, the front part of the vocal tract may resemble a Helmholtz resonator. That is, it may consist of a relatively large cavity with an anterior constriction (due to either lip rounding or natural tapering by the teeth and lips). In this case, a high volume-to-constriction degree ratio is required in order to produce an $F3$ within the typical range.

I. METHOD

A. Magnetic resonance imaging data

The data used for this study were collected by Alwan *et al.* (1997). They used magnetic resonance imaging (MRI) to collect data from four phonetically trained native American English speakers who produced sustained /r/'s in two different production conditions, as described below. Subjects sustained each sound for 13–16 s in a supine position, enabling four or five image slices to be recorded in that time period (about 3.2 s per image). Recordings were made in sagittal, axial, and coronal planes. Subjects repeated each sound six to nine times, with a pause of 3 to 10 s between repetitions, to enable the entire vocal tract to be scanned. Further details of the MRI recording, data acquisition, and analysis methodologies are provided in Alwan *et al.* (1997) and Narayanan *et al.* (1997).

Production conditions for Subject PK consisted of instructions to produce a retroflex and a bunched /r/. Tracings of the midsagittal profiles for these productions are shown in the left and right lower panels of Fig. 3. Note that the production labeled as tip-up bunched /r/ in Fig. 3 came from the retroflex condition, and the production labeled as tip-down bunched /r/ came from the bunched condition.[5] In other words, for the retroflex condition, the speaker produced an /r/ with both dorsum and tongue tip raised. This was somewhat of a surprise, as the traditional image of a retroflex /r/ involves a lowered tongue dorsum (Delattre and Freeman, 1968; Kent, 1998). Production conditions for Subject MI consisted of intentional production of /r/'s as they would occur in word-initial position and syllabically. These are again shown in the left and right upper panels of Fig. 3. Notably, Subject MI also produced /r/'s with raised, or bunched tongue dorsum; his tongue tip is slightly raised in his ''word-initial'' /r/. Altogether, we consider four sets of vocal-tract dimensions from two speakers, corresponding to the four vocal-tract profiles in Fig. 3. All fit the category of bunched, i.e., the tongue dorsum is up.

MRI data consisted of cross-sectional images, from which vocal-tract area functions were calculated. Area functions were measured separately for the sublingual space

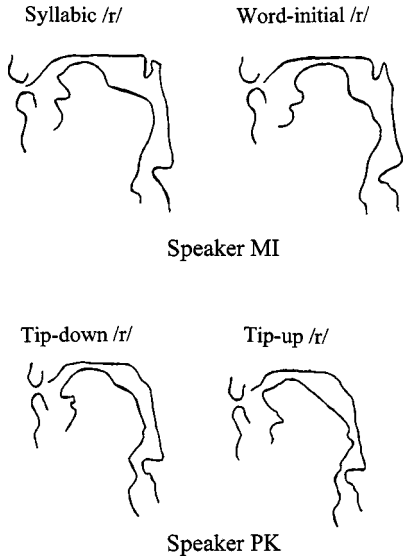

FIG. 3. Vocal-tract profiles for /r/ in midsagittal plane (adapted from Alwan *et al.*, 1997).

(when appropriate) and for the continuous supralingual space running from the lips to the glottis. Figure 4 shows the area functions for the supralingual space for each of the four data sets. The data are positioned such that the glottis is to the left, at 0 cm, while the lip opening is on the right. Larger areas under the curve indicate vocal-tract cavities; constrictions occur where the distance between the data curve and the abscissa are small. These area functions served as input for the Maeda (1982) vocal-tract model VTCALCS, a computer program using standard acoustical tube assumptions to predict formant frequencies from vocal-tract dimensions. We used a MATLAB version of the original VTCALCS program developed by Dr. Ronan Scaife (personal communication). For Subject PK this involved a model vocal tract of 15.3 cm, divided into 51 sections of 0.3-cm length. For Subject MI, this involved a model vocal tract of 18 cm, divided into 60 sections of 0.3-cm length.

The cross-sectional areas of the sublingual space measured from MRI data for each subject and production condition are listed in Table I. Note that sub- and supralingual space was measured from coronal sections in the superior–inferior plane; thus, the sublingual space is defined as any space bounded vertically by the tongue and buccal floor. For PK, the sublingual space was measured as being three sections (i.e., 0.9 cm) long for both her tip-up and tip-down production conditions. Sublingual space lengths were measured as four sections (i.e., 1.5 cm) long in the case of MI's word-initial /r/ and four sections (1.2 cm) in the case of MI's syllabic /r/. The sublingual cavity started at 3 cm from the lips for both of MI's productions, and at 2.1 cm from the lips in both of PK's production conditions.[6]

B. Audio recording

Due to noise in the experimental chamber, it was not possible to record speakers' acoustic output during the MRI sessions. However, each subject recorded four repetitions of nine (PK), or ten (MI) real words containing consonantal /r/ or syllabic /r/. A list of the words is given in the Appendix.

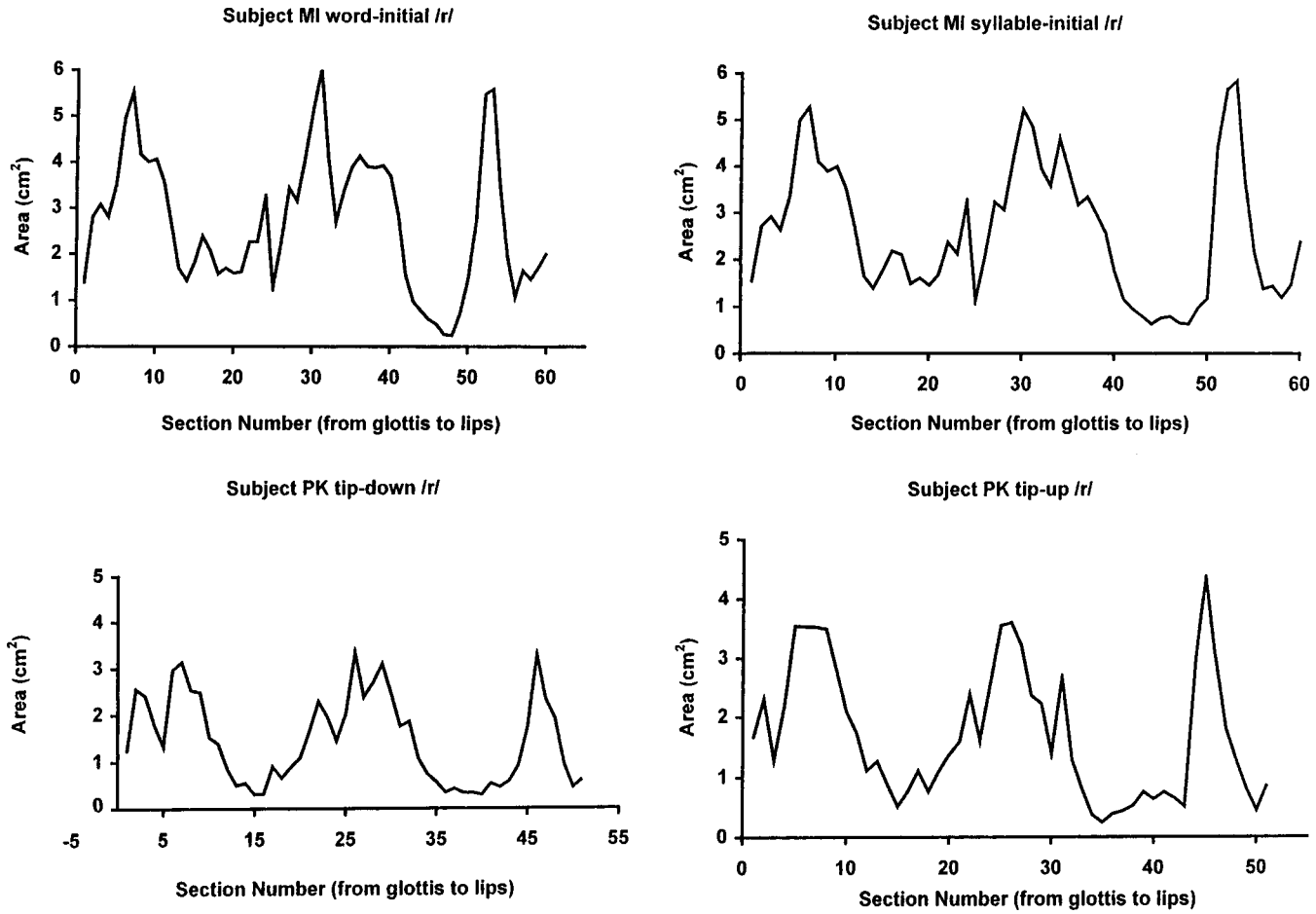

FIG. 4. MRI-derived supralingual area functions for the /r/'s produced by PK and MI.

These words were embedded in the carrier phrase ''Say ___ again.'' The speech data were recorded in a soundproof facility at 44.1 kHz directly onto a Sun workstation and were later downsampled to 11.025 kHz. An omnidirectional microphone (Beyerdynamic M101) with a flat frequency response (within 4 dB) between 40–20 000 Hz was placed at approximately 22 cm from the subject's mouth at about a 15° angle off the midline. The Entropic Signal Processing Systems (ESPS) Waves environment was used to display spectrograms of each utterance and automatically track the first four formants. Measurement of the formants was made at the lowest point of $F3$. In a few utterances (one for PK and three for MI), it was not possible to get the frequency of $F4$ when $F3$ was at its lowest point. The energy above $F3$ was very weak, so $F4$ was not visible in the spectrogram and was not properly tracked. Thus, these values of $F4$ were not considered in our analysis.

TABLE I. MRI-derived areas of sublingual space (in cm^2). Each section is of length 0.3 cm, resulting in a sublingual cavity of 0.9 cm for PK, 1.5 cm for MI's word-initial /r/ and 1.2 cm for MI's syllabic /r/. The sublingual cavity starts 3 cm from the lips in the case of MI, and 2.1 cm from the lips in the case of PK.

PK tip up	2.707	0.897	0.594		
PK tip down	1.025	0.984	0.465		
MI initial	1.833	0.865	0.542	0.419	0.156
MI syllabic	2.88	1.251	0.659	0.306	

C. Vocal-tract acoustic model

Vocal-tract modeling in this study is based on the VTCALCS program developed by Maeda (1982). This time-domain simulation of the vocal tract assumes one-dimensional wave propagation and includes acoustic losses due to yielding walls, fluid viscosity, and radiation effects from the mouth. VTCALCS as originally written allows for a side branch corresponding to the nasal cavity in the velar region, but this option is not suitable for modeling the sublingual space. To model the sublingual space, we modified the original VTCALCS program (in its MATLAB version) to allow for a parallel side branch in the palatal region (Jackson *et al.*, submitted). This modeling procedure is discussed in detail in Sec. III D.

II. SIMULATION EXPERIMENTS

An ideal model of the acoustics of /r/ will account for the full range of variability in formant values exhibited by all speakers of American English. However, since the MRI data from our speakers may not match all speakers' vocal tracts, our aim was to match the range of variability in formant values for our particular speakers, as shown in their real word productions. All experimental simulations in this paper used as their base the vocal-tract area functions reported in Alwan *et al.* (1997) and here in Fig. 4 and Table I. Table II contains the $F1-F4$ data measured from the subjects' pro-

TABLE II. Real word formant frequencies (in Hz). For Subject PK, $N=36$; for Subject MI, $N=40$.

	Subject PK			Subject MI		
	Mean	Range	s.d.	Mean	Range	s.d.
$F1$	349.5	202–517	98.0	388.0	234–489	78.3
$F2$	1355.4	989–1698	147.7	1383.8	989–1586	153.7
$F3$	1833.8	1479–2157	137.7	1664.9	1400–1946	127.4
$F4$	4110.8	3898–4483	134.8	3113.7	2742–3483	139.3

duction of real words containing /r/. These data, including the full range of $F3$ values produced by the speakers, are the standard against which we measure the success or failure of a particular modeling schema. Given the difficulty of accounting for very low $F3$ in current models, we particularly focus on accounting for the full range of $F3$.

In experiment 1, we use these data to estimate whether the location of actual constrictions seen in MRI data match the locations predicted by the Perturbation Theory. In experiment 2, we present estimates of formant values produced when the supralingual vocal-tract area functions of Fig. 4 are input to the VTCALCS program, and compare the results to those from real words. In experiments 3 and 4, we present estimates of the formant values when the sublingual area functions are taken into account. Finally, in experiment 5, we develop a simple tube model that accurately predicts $F1$ through $F4$ while accounting for formant cavity affiliations across different articulatory configurations for /r/.

A. Experiment 1: Locations predicted by perturbation theory

As noted above, the Perturbation Theory approach to /r/ assumes that subjects' constriction locations will coincide with the points of maximum volume velocity predicted by the Perturbation Theory.

To determine the predicted locations for our speakers, we calculated points of maximum volume velocity (where constriction decreases $F3$), and maximal pressure (where constriction increases $F3$), for the vocal-tract lengths 15.3 cm (for PK) and 18 cm (for MI). Table III shows how these predicted constriction locations compare with the constriction locations found in the MRI data. Because the MRI data constriction locations extended over several sections, these are expressed as ranges across which the constriction was maximal. The criterion for constriction beginning and end was set at area$=1.0$ cm^2 for PK and at area$=2.4$ cm^2 for MI. Wide ranges indicate stretches for which constriction met criterion.

TABLE III. Real versus predicted constriction locations.

	Actual palate	Predicted palate	Actual pharynx	Predicted pharynx
PK tip up	10.2–13.3	9.6	4.3–6.2	3.1
PK tip down	10.5–13.6	9.6	4.3–5.9	3.1
MI initial	12.6–15.0	10.8	3.9–6.9	3.6
MI syllabic	12.0–15.0	10.8	3.9–6.3	3.6

TABLE IV. $F1-F4$ values predicted by VTCALCS from supralingual MRI data.

	PK tip up	PK tip down	MI initial	MI syllabic
$F1$ (Hz)	367.5	373.8	310.9	340.2
$F2$ (Hz)	1336.4	1175.7	1173.4	1210.2
$F3$ (Hz)	1938.9	2167.5	1921.0	1883.5
$F4$ (Hz)	4369.2	4132.2	3068.0	3275.9

It is clear that for both speakers, real palatal constrictions are long, and appear to cover an area considerably forward of the location predicted by the Perturbation Theory to have the maximal lowering effect on $F3$ (see Table III). Indeed, for both subjects, palatal constrictions center over areas predicted by the Perturbation Theory to correspond with maximal pressure, making constrictions in these areas more likely to raise $F3$ than to lower it. For PK, the pharyngeal constriction ranges forward of the predicted point. For MI, the pharyngeal constriction apparently covers an area that may be conducive to $F3$ lowering, but is longer than necessary. Thus, neither the pharyngeal nor the palatal constriction is located as would be predicted by the Perturbation Theory. In particular, the palatal constrictions here cover areas that should affect $F3$ in the wrong direction. This is true regardless of the type of /r/; for instance, PK's ''tip-down'' /r/ and ''tip-up'' /r/ have slightly different constriction lengths but similarly forward constriction locations and similar constriction degrees. We conclude that subjects are not taking advantage of points of maximum volume velocity along the vocal tract to lower $F3$ in any obvious way.

B. Experiment 2: Formant frequencies from MRI-derived supralingual area functions

As a first approximation to modeling the acoustics of /r/ from MRI data, the supralingual area functions from the four MRI data sets were used as input to VTCALCS. The resulting estimates of $F1-F4$ values are shown in Table IV.

These estimated formant values are within the general range of $F1$, $F2$, and $F3$ reported across different studies using different speakers of American English (see the Introduction, Sec. A above). Further, the estimates for $F1$ and $F2$ compare favorably with the subjects' real word data, being squarely within their respective ranges and not far from the average frequency values. In contrast, the estimates of $F3$, at 1938.9 and 2167.5 for PK and 1921 and 1883.5 for MI, are in the very high portion of the reported range across studies, and 2–3 standard deviations higher than the average $F3$ formant frequency values reported for speakers of American English. Further, these $F3$ values match only the highest values in each speaker's range. Thus, the shape of the supralingual vocal tract for these subjects (as measured by MRI) is apparently enough to specify $F1$ and $F2$, but is not enough to specify the most notable mid-to-lower values of $F3$.

There are several possible explanations for this result. First, because the MRI data were collected with the subject in a supine position, differences in the effect of gravity might account for the high $F3$ values. However, previous studies contrasting vowel formant frequencies produced in supine

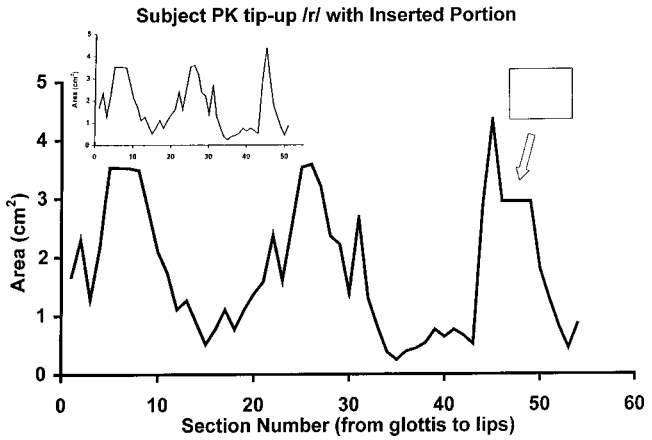

FIG. 5. MRI-derived area function for PK's tip-up /r/ with a uniform tube (the length of PK's sublingual space with area equal to the maximum cross-sectional area of the sublingual space) inserted into the front cavity at the measured location of the opening into the sublingual space.

versus upright position have found very minor effects (Shiller, Ostry, and Gribble, 1999; Tiede *et al.*, 1997; Tiede, personal communication). Second, because the MRI and audio data were collected at different times, it is possible that during MRI data collection the subject was producing the very high $F3$ values we see here. A more powerful explanation, however, comes from looking at the dimensions of the supralingual MRI vocal-tract data. According to Fant (1960), $F3$ is a front cavity resonance. As noted above, when modeled as a quarter-wavelength tube, the front cavity must be around 5 cm long to produce a resonance in the midrange of $F3$. The length of the front cavity in our supralingual MRI data is less than 2 cm. Thus, given the proportions of the MRI supralingual vocal tract, additional length, or alternative acoustic models, are needed to account for the mid-to-low $F3$ values produced by these speakers.

C. Experiment 3: Formant frequency estimates from extending the front cavity

Stevens (1999) and Alwan *et al.* (1997) suggest that the sublingual space adds to the volume of the front cavity and thereby lowers the front cavity resonance ($F3$). Thus, in our first attempt to model the sublingual space, we increased the volume of the front cavity by inserting a uniform tube into the front cavity portion of the MRI-derived area function plots, at the measured location of the opening into the sublingual space. The cross-sectional area of the uniform tube corresponded to the largest area of the sublingual space. The length corresponded to the measured length of the sublingual space. An example of this type of modification is shown in Fig. 5.

Table V shows the $F1-F4$ values predicted from the extended front cavity. A comparison of these data with those of Table IV shows that the added volume to the front cavity lowers $F3$ by 200 Hz to 300 Hz.

Alternatively, the volume of the front cavity can be increased by adding the area of the sublingual space.

TABLE V. $F1-F4$ values predicted by VTCALCS with extended front cavity.

		PK tip up	PK tip down	MI initial	MI syllabic
Length of front cavity increased	$F1$ (Hz)	360.8	360.6	295.7	337.7
	$F2$ (Hz)	1284.6	1162.8	1156.2	1180.0
	$F3$ (Hz)	1650.2	1949.9	1637.4	1616.3
	$F4$ (Hz)	4287.5	4079.6	3051.8	3255.1
Area of front cavity increased	$F1$ (Hz)	368.2	375.1	313.6	349.9
	$F2$ (Hz)	1317.8	1173.2	1170.8	1201.9
	$F3$ (Hz)	1766.2	1996.1	1793.7	1751.0
	$F4$ (Hz)	4357.3	4126.5	30568.2	3272.5

D. Experiment 4: Formant frequency estimates using side branch

In this part of the study, we modeled the sublingual cavity as a side branch. To do so, the MATLAB version of Maeda's VTCALCS program was revised to allow a side branch, as shown in Fig. 6. Sublingual MRI-derived area functions, measured as noted above, were used as input to the model. (See Table I for the data.) Each section of the side branch is modeled in the same way as the sections in the main tube, and the side branch terminates in an open circuit to model the effects of a hard wall (infinite impedance). Since the volume element of this side branch and the volume element of the front cavity are in parallel, they effectively add for the purposes of calculating the front cavity resonances. In addition, the model assumes that the sublingual space, acting as a side branch, generates an antiresonance that is proportional to its length. Given the 3–5-section length of the measured sublingual space, this antiresonance can be expected to fall in the range of 5–6 kHz. Details of the side-branch model are reported in Jackson *et al.* (submitted).

The formant values obtained are given in Table VI. As

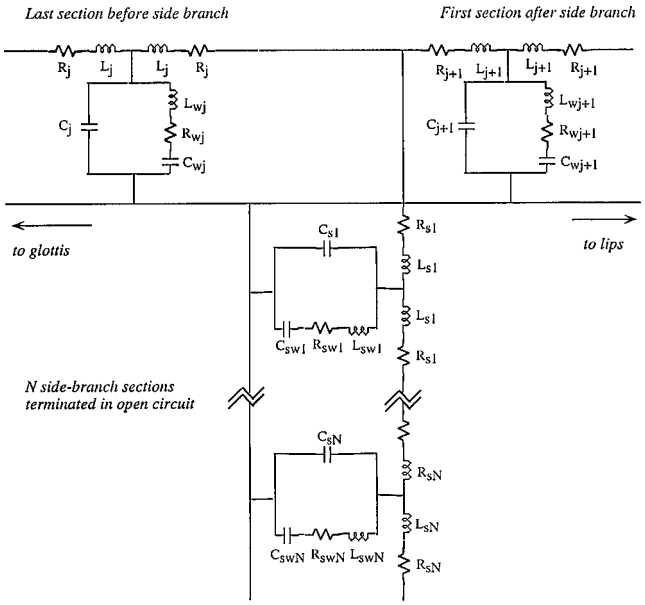

FIG. 6. A diagram representing how Maeda's vocal-tract model was modified to include a side branch. The side branch is terminated in an open circuit to model the effects of a hard wall (infinite impedance). R_w, L_w, and C_w model the impedance of the vocal-tract walls.

TABLE VI. $F1-F4$ values predicted by VTCALCS with sublingual cavity modeled from MRI data as a side branch.

	PK tip up	PK tip down	MI initial	MI syllabic
$F1$ (Hz)	366.6	373.3	310.5	348.4
$F2$ (Hz)	1302.4	1170.4	1167.2	1194.0
$F3$ (Hz)	1692.5	1947.6	1719.8	1682.5
$F4$ (Hz)	4334.9	4124.7	3064.1	3269.9

can be seen, taking the sublingual space into account does not change the frequencies of $F1$ and $F2$ very much, but it does lower $F3$ by about 200 Hz. These results are very close to those obtained for the manipulation of experiment 3 (see Table V), where the sublingual space was accounted for by increasing the volume of the front cavity by a simple extension. For the purpose of producing $F3$ values, these two different ways of accounting for the sublingual space are essentially equivalent. These results suggest that the sublingual space acts primarily to increase the volume of the front cavity, at least for the purpose of producing appropriate formant values. (Note that these different methods of accounting for the sublingual space make different predictions regarding other variables such as existence of an antiresonance, changes in formant bandwidth, etc. that are outside the scope of this paper.) Note also that the methods of experiments 3 and 4 may not necessarily be equivalent for articulatory configurations involving longer sublingual space dimensions, such as might be found in true tip-up retroflex /r/'s. However, both sets of results show a definite positive advance on previous modeling attempts, as we have achieved $F3$ values that match (approximately) the average $F3$ produced by our speakers (see Table II, real data).

E. Experiment 5: Formant frequency calculations using a simple tube model for /ɹ/

1. Simple tube models

In this section, we consider simple tube models for /r/, to determine which cavities contribute to which formants. We consider first the sources of formants $F1$, $F2$, and $F4$ as being the easier to predict, and then consider the source of $F3$. Overall, we attempt to build a single model with the potential to account for data-derived variations in constriction type, constriction degree, and cavity dimensions. For this analysis, we assume plane wave propagation and no acoustic losses. To be consistent with Maeda's vocal-tract modeling program, the value used for the speed of sound, c, in all calculations was 35 000 cm/s.

Stevens (1999) provides a simple acoustic tube model, complete with approximate dimensions, for the tip-up retroflex type of /r/ configuration as shown in Fig. 2. To account for the fact that our MRI-derived area functions show slightly different cavity and constriction dimensions and describe bunched /r/'s (some with the tongue tip up), we adapted Stevens' simple tube model to the generic version shown in Fig. 7. Differences between our model and that of Stevens include the following: (1) Stevens model assumed a relatively small supralingual front cavity with dimensions equal to the area of the lip opening. Because the MRI data show both a considerably larger oral cavity and tapering of the front part of the mouth around the teeth and lips, our model consists of two tubes, a larger one representing the front cavity and a narrower one representing the lip constriction. (2) Because the physiological data represents bunched /r/'s (both tip up and tip down), the palatal constriction in our model is considerably longer than that proposed by Stevens. As a result, the total length of each cavity between the palatal constriction and the glottis is shortened. (3) As Stevens did, we take into account the sublingual space in the acoustic modeling of /r/. However, Stevens assumes a considerably longer sublingual space than we found to exist in the MRI-derived data. Accordingly, in our model the sublingual space is shorter. (4) Finally, in Stevens' model the pharyngeal constriction is modeled as a slight narrowing of the tube rather than as a tight constriction. In our data, there was a qualitative difference between subjects' data in degree of pharyngeal constriction. To account for this, we allow for a variant of the simple tube model, in which the pharyngeal constriction is modeled as a separate tube rather than as a perturbation of a larger tube. For purposes of precision in terminology, we refer to the cavity between the lips and the palatal constriction as the ''front'' cavity, the cavity between the palatal and pharyngeal constrictions as the ''mid'' cavity, and the cavity behind the pharyngeal constriction as the ''back'' cavity. Based on data presented here, and elsewhere (Espy-Wilson *et al.*, 1997; Stevens, 1999; Narayanan *et al.*, 1999), we assume that $F3$ is a front cavity resonance.

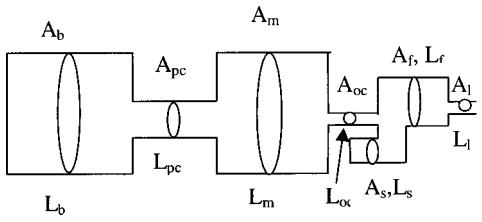

FIG. 7. Our simple tube model for the bunched /r/'s produced by PK and MI. A_b and L_b correspond to the area and length of the back cavity; A_{pc} and L_{pc} correspond to the area and length of the pharyngeal constriction; A_m and L_m correspond to the area and length of the midcavity between the pharyngeal constriction and the oral constriction; A_{oc} and L_{oc} correspond to the area and length of the oral (palatal) constriction; A_f and L_f correspond to the area and length of the front cavity between the oral constriction and the lip constriction; and A_l and L_l correspond to the area and length of the lip constriction.

Our simple tube model, although based on MRI-derived dimensions, is considerably simplified compared to the real dimensions. In what follows, we describe the series of tests we ran to determine how well our estimates of formant frequency values based on simple tube dimensions match estimates based on actual dimensions. To simplify comparisons, we compared formant frequency patterns calculated from the supralingual portion of our model (i.e., without reference to sublingual space effects) to formant frequencies estimated by the VTCALCS program from MRI supralingual dimensions. The supralingual portion of the model includes all the dimensions listed in Table VII, except those related to the augmented front cavity (A_f' and L_f') and the augmented back cavity (A_b' and L_b'), which refer to sublingual dimensions.

A sketch of the simple tube model, modified to reflect only supralingual data, is given in Fig. 8. Speaker-specific

TABLE VII. Dimensions for simple tube model estimated from the MRI-derived area functions in Fig. 4. A_l and L_l refer, respectively, to the area and length of the lip constriction, A_f and L_f refer to the area and the length of the cavity between the lip constriction and the palatal constriction, A_f' and L_f' refer to the area and length computed by combining the sublingual cavity with the cavity between the lip constriction and the palatal constriction, A_{oc} and L_{oc} refer to the area and length of the palatal (oral) constriction, A_m and L_m refer to the area and length of the cavity between the oral constriction and the pharyngeal constriction, A_{pc} and L_{pc} refer to the area and length of the pharyngeal constriction, A_b and L_b refer to the area and length of the cavity posterior to the pharyngeal constriction, and A_b' and L_b' refer to the area and length of the cavity between the palatal constriction and the glottis.

	PK tip up	PK tip down	MI initial	MI syllabic
A_l (cm^2)	0.71	0.67	1.58	1.62
L_l (cm)	0.90	0.90	1.50	1.50
A_f (cm^2)	2.66	2.03	3.84	4.47
L_f (cm)	1.5	1.5	1.5	1.5
A_f' (cm^2)	2.19	1.58	2.57	3.05
L_f' (cm)	2.40	2.40	3.00	2.70
A_{oc} (cm^2)	0.53	0.45	0.78	0.87
L_{oc} (cm)	3.00	3.00	2.70	3.00
A_m (cm^2)	2.18	2.07	3.88	3.70
L_m (cm)	4.20	4.20	4.50	4.20
A_{pc} (cm^2)	0.94	0.62	1.94	1.93
L_{pc} (cm)	2.40	2.40	4.20	4.20
A_b (cm^2)	2.56	2.12	3.53	3.56
L_b (cm)	3.30	3.30	3.60	3.60
A_b' (cm^2)	2.29	1.74	3.12	3.25
L_b' (cm)	9.9	9.9	12.3	12

dimensions of the different tubes were derived by averaging the areas of the sections appropriate to a particular tube, and summing the corresponding section lengths. In the case of PK, areas less than 1 cm^2 were taken as part of a constriction and areas larger than 1.5 cm^2 were taken as part of one of the larger cavities. The inflection point (i.e., the largest first difference) in the transition region was taken as the boundary between the constriction and the larger cavity. In the case of MI, areas less than 1.5 cm^2 in the lip area and in the palatal region were taken as part of the constriction. Areas larger than 2.0 cm^2 were taken as part of a larger cavity. The region behind the palatal constriction was divided into several cavities where the areas greater than 2.6 cm^2 formed the larger mid- and back cavities and areas less than this formed the smaller cavity in the pharyngeal region. Table VII shows the

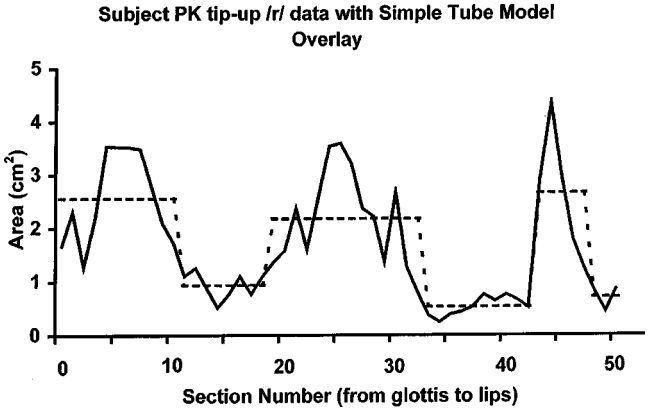

FIG. 8. MRI-derived area function for PK's tip-up bunched /r/ with the corresponding simple tube model from Table VIII superimposed.

TABLE VIII. Formant frequencies estimated from VTCALCS using supralingual simple tube model dimensions as input.

	PK tip up	PK tip down	MI initial	MI syllabic
$F1$	377.1	389.4	349.9	358.3
$F2$	1360.6	1282.5	1207.0	1229.3
$F3$	1892.4	2253.6	2020.1	1923.6
$F4$	3798.9	3905.2	3108.4	3156.8

tube dimensions derived for our model for each speaker. For purposes of comparison, Fig. 8 shows the supralingual simple tube model for PK's tip-up /r/ superimposed on PK's MRI-derived supralingual area function from Fig. 7.

The supralingual vocal-tract dimensions of the simple tube model were put into VTCALCS, and the resulting formant frequencies are given in Table IX. Compare these results with those of Table V, which were obtained via VTCALCS with the actual MRI-derived supralingual dimensions. As can be seen, differences between $F1-F3$ values in Tables V vs IX are no greater than 110 Hz in any case. In fact, for many comparison pairs the correspondence is much closer; for example, the $F1$ values for PK's tip-up /r/ differ by 10.4 Hz while her $F3$ values differ by 46.5 Hz. Given the simplifications inherent in any simple tube model, these result suggest that our supralingual model is equivalent to the actual MRI-derived dimensions, in terms of its accuracy in predicting our speakers' real formant frequencies.

2. F1, F2, and F4 calculation (resonances from behind the palatal constriction)

In this section, we dissect the cavity origins of $F1$, $F2$, and $F4$. Both Stevens (1999) and Alwan *et al.* (1997) assume these formants come from a cavity that either involves the palatal constriction or is posterior to it. Stevens (1999) models $F1$ and $F2$ of a tip-up retroflex /r/ configuration (see Fig. 3) as follows: (1) $F1$ is a Helmholtz resonance formed by the large back cavity (extending from the palatal constriction to the glottis) and the palatal and labial constrictions (see footnote 3), and (2) $F2$ is a half-wavelength resonance of the back cavity behind the palatal constriction. Alwan *et al.* (1997) propose a similar model, with the difference that $F1$ is considered to be a Helmholtz resonance formed by the palatal constriction and the back cavity behind it. In contrast to Stevens' approach, the Alwan *et al.* paper did not take lip constriction into account. They added the observation that $F2$ may be a Helmholtz resonance between the pharyngeal constriction and the cavity posterior to it if the pharyngeal constriction is narrow enough.

In this context, our data are particularly interesting, because the /r/ productions of the two speakers PK and MI show very different degrees of pharyngeal constriction. This can be seen in Table VIII, for instance, by comparing the narrow pharyngeal constriction value (A_{pc}) of 0.94 cm^2 for PK's tip-up /r/ (and similar value for tip-down /r/ against the wider constriction of 1.94 cm^2 for MI's word-initial /r/ (and similar value for syllabic /r/). As Alwan *et al.* (1987) note, if the pharyngeal constriction is narrow enough, separate large resonating cavities are formed in front and behind. This may be the case for speaker PK. On the other hand, if the pha-

TABLE IX. $F1$ calculated as a Helmholtz resonance and $F2$ calculated as a half-wavelength resonance.

	PK tip up	PK tip down	MI initial	MI syllabic
$F1$	418	453	406.5	406.9
$F2$	1767	1767	1422	1458

ryngeal constriction is wide enough, the area behind the palatal constriction may act as a single resonator. We call the latter variant of the simple tube model the long *back cavity* model, and the former variant the *additional cavity* model. To determine which model best predicts the different subjects' data, we ran separate calculations for these two variants of the simple tube model, for each speaker and speaking condition.

In the *long back cavity* variant of the simple tube model, $F1$ is a Helmholtz resonance formed by the palatal constriction and a back cavity posterior to it (extending from the palatal constriction to the glottis, with dimensions A_b' and L_b' in Table VII). Accordingly, $F1$ is calculated by summing the admittances of the back cavity $[-j(A_b'/\rho c)\tan \omega L_b'/c]$ and the palatal constriction $[-j(A_c/\rho c)\cot \omega L_c/c]$ and finding the frequency of the first zero crossing. $F2$ is calculated as a half-wavelength resonance of the back cavity $(c/2l_b')$. $F4$ is calculated as the second half-wavelength resonance of the back cavity $(2*c/2l_b')$. The frequencies of $F1$, $F2$, and $F4$ resulting from this method are given in Tables IX and XI. Note that in this simple tube calculation, as in Stevens' model, the pharyngeal constriction is not accounted for. Our data show, however, that it occurs at a point along the tube where a perturbation would be expected to lower the formants by 100–200 Hz.

In the *additional cavity* method, we model the back part of the vocal tract with a separate tube for the pharyngeal constriction. In this case, the palatal constriction and the cavities posterior to it form a double-Helmholtz (coupled) resonator. To estimate formant frequencies from this complicated configuration, we had three options for simplifying the calculation of $F1$ and $F2$ values at this point; (1) by assuming decoupling in a distributed system, (2) by assuming decoupling but using a lumped approximation, and (3) by using a double-Helmholz lumped equation. In option (1), we decoupled the double-Helmholtz resonator into two single-Helmholtz resonators. $F1$ was calculated by summing the admittances of the midcavity $[j(A_m/\rho c)\tan \omega L_m/c]$ and the palatal constriction $[-j(A_c/\rho c)\cot \omega L_c/c]$ and finding the frequency of the first zero crossing. Similarly, $F2$ was calculated by summing the admittances of the back cavity $[j(A_b/\rho c)\tan \omega L_b/c]$ and the pharyngeal constriction $[-j(A_{pc}/\rho c)\cot \omega L_{pc}/c]$ and finding the frequency of the first zero crossing. For option (2) we again assumed decoupled Helmholtz resonators but used lumped approximation to obtain values for $F1$ $[c/2\pi(A_{oc}/L_{oc}A_mL_m)^{1/2}]$ and $F2$ $[c/2\pi(A_{pc}/L_{pc}A_bL_b)^{1/2}]$. Finally, we computed the frequencies for $F1$ and $F2$ by using Fant's double-Helmholz lumped equation (Fant, 1960) to account for the interconnection between the two Helmholtz cavities. These values of $F1$ and $F2$ are given in Table X. Note that one consequence of using the lumped-coupled model is that, relative to the lumped-decoupled values, $F1$ is shifted down by the proportion that $F2$ is shifted up. To calculate $F4$, we decoupled all of the tubes making up the double-Helmholtz resonator. $F4$ was then calculated as the half-wavelength resonance of the longest cavity. For all the subjects and conditions, this meant that $F4$ was the half-wavelength resonance of the midcavity $(c/21_m)$. (Note that in the case of MI's syllabic /r/, the lengths of the tube formed by the pharyngeal constriction and the midcavity are the same.) Again, the $F4$ frequencies by this method are given in Table XI.

TABLE X. $F1$ and $F2$ calculated from a double-Helmholtz model. The decoupled values of $F1$ and $F2$ are computed by disconnecting the two Helmholtz resonators and using the appropriate admittance functions. The decoupled and lumped values are computed again with the Helmholtz resonators disconnected, and with the lumped approximation used. The coupled and lumped values are calculated from the double-Helmholtz lumped formula (Fant, 1960, p. 286).

	PK tip up	PK tip down	MI initial	MI syllabic
$F1$ (decoupled)	715.8	682.1	668.0	705.6
$F1$ (decoupled–lumped)	774.2	732.1	716.9	761.3
$F1$ (coupled–lumped)	528.3	511.9	513.2	525.5
$F2$ (decoupled)	1072.4	976.9	912.2	907.6
$F2$ (decoupled–lumped)	1200.0	1071.0	1062.5	1055.3
$F2$ (coupled–lumped)	1756.6	1530.1	1482.8	1527.4

Whether the *long back cavity* or the *additional cavity* variant of the model works best can be seen for each speaker by comparing the $F1$, $F2$, and $F4$ values in Tables IX and XI. Remember that speaker MI had relatively wide pharyngeal constrictions, while speaker PK had relatively narrow pharyngeal constrictions. A comparison of the values in Tables IX and X shows that modeling the back part of the vocal tract as a single long cavity gives reasonable values for MI's /r/ productions. For instance, the values for MI's $F2$ in Table IX are 1422 and 1458 Hz.[7] These frequencies compare well with those from the real data (see Table II) which range from 989–1556 Hz. However, as Table X shows, the additional cavity model also produces reasonable $F2$ values, from 912.2 and 907.6 Hz for the decoupled calculation to 1482.8 and 1527.4 Hz for the coupled-lumped calculation. For PK, on the other hand, modeling the pharyngeal constriction as an additional cavity produces better $F2$ values. For instance, in the case of PK's (tip-down) bunched /r/, modeling the back part of the vocal tract as a double-Helmholtz resonator results in an $F2$ frequency of 1530 Hz (see Table X, coupled-lumped option). This is much lower than the 1767-Hz value obtained when the *long back cavity model* is used (see Table IX). It should be noted that calculations us-

TABLE XI. $F4$ calculated as the second resonance of a half-wavelength tube model for the back cavity (between the palatal constriction and the glottis) and the lowest resonance of the midcavity (between the palatal and pharyngeal constrictions) from the double-Helmholtz model.

	PK tip up	PK tip down	MI initial	MI syllabic
$F4$ (half-wavelength tube model)	3535.4	3535.4	2845.5	2916.7
$F4$ (double-Helmholtz model)	4166.7	4166.7	3888.9	4166.7

ing a lumped approximation tend to overshoot the true value by 100–200 Hz. A demonstration of this general tendency can be seen in Table X by comparing the lumped and distributed estimates of $F2$ for a decoupled system. Thus, we expect that the true value of $F2$ (relative to the coupled-lumped method) for PK's tip-down /r/ is closer to 1350 Hz, while the likely true value for her tip-up /r/ is closer to 1550 Hz. Similarly, we expect MI's true $F2$ value to be in the region of 1250 Hz. The difference between predictions of the *additional cavity* simple tube model for PK's tip-up and tip-down /r/ are likely due to the larger area ratios (A_m/A_{pc} and A_b/A_{pc}) between cavities (see Table VII).

Looking at the $F4$ calculations, we see that for PK the values of 4166.7 Hz obtained from the additional cavity model (see Table XI) are within range of the 4110.8-Hz average $F4$ frequencies observed in her real data (see Table II). At the same time, the $F4$ frequencies predicted by the *long back cavity* model, at 3535.4 Hz, are too low. On the other hand, the $F4$ values calculated by the *additional cavity* model for MI are too high at 3888.9 and 4166.7 Hz, compared to the average $F4$ value of 3113.7 Hz in his real data (see Table II). In contrast, the values calculated by the *long back cavity* model, at 2845.5 and 2916.7 Hz are appropriately near the real data average of 3113.7 Hz.[8]

3. F3 calculation

Stevens (1999) and Alwan *et al.* (1997) assume that $F3$ results from the front cavity represented by a large volume, including the sublingual cavity, and by a narrowed lip opening. Both assume that for tip-up /r/'s the volume of the front cavity may not be large enough to account for $F3$ unless the sublingual space is included. For tip-down /r/'s, both assume the front cavity is large enough to account for $F3$ as a front cavity resonance. Because the contribution of the sublingual space to the volume of the front cavity is reduced as the tongue tip moves down, Alwan *et al.* note the possibility of a trading relation between sublingual space volume (for tip-up /r/'s) and a relatively more posterior palatal constriction for tip-down /r/'s. In other words, front cavity volume, and consequent low $F3$, may be maintained by either increasing the sublingual space or by moving the palatal constriction back and thereby increasing the length of the front cavity. Although neither paper specifically suggests a mechanism whereby the increase in volume would lower $F3$, there are two possibilities: (1) that the sublingual space acts to increase the length of the front cavity, thereby lowering its full set of resonant frequencies, or (2) that the sublingual space, by increasing the front cavity volume-to-lip constriction ratio, contributes to the formation of a front cavity with the shape of a Helmholtz resonator.

To calculate $F3$, we assume that the front cavity can be decoupled from the palatal constriction. Further, the results of experiment 3 suggest that the sublingual space acts to increase the volume of the front cavity and thereby lower the frequency of $F3$. Thus, to calculate $F3$, we combined the front cavity and the sublingual space into one uniform tube. The lengths of the oral cavity and the sublingual cavity were added and the average of the areas involved was taken as an estimate of the uniform area. $F3$ was calculated by summing the admittance of the combined oral and sublingual cavity $[-j(A_f'/\rho c)\tan \omega L_f'/c]$ and the admittance of the lip constriction $[-j(A_l/\rho c)\cot \omega L_l/c]$ and determining the first zero crossing. This value for $F3$ is given in Table XII. Two further effects cancel each other out: if we take into account the radiation impedance of the mouth opening, then the value of $F3$ is lowered by about 200 Hz, while if we take into account the effect of the acoustic mass that results from the palatal constriction, $F3$ is raised by about 200 Hz (Guenther *et al.*, 1999).

TABLE XII. $F3$ calculated from the cavity anterior to the palatal constriction including the sublingual space.

	PK tip up	PK tip down	MI initial	MI syllabic
$F3$	1874.3	2064.5	1675.9	1698.7

III. DISCUSSION

In this paper, we consider several issues important to the development of an acoustic model for American English /r/. First, we show that the Perturbation Theory does not make appropriate predictions of constriction location for /r/'s of the type produced by our speakers. It is likely that this difficulty extends to /r/'s of similar articulatory configuration reported in Guenther *et al.* (1999), Westbury *et al.* (1999), Zawadaski and Kuehn (1980), Lindau (1985), Kent (1998), Delattre and Freeman (1968), and additional speakers reported in Alwan *et al.* (1997), among others.

In experiments 1, 2, and 3, we use MRI-derived dimensions and the Maeda computer simulation program to present evidence from several sources that $F3$ is a front cavity resonance. In experiment 1, we show that the effects of eliminating the pharyngeal constriction on $F3$ are minimal. In experiments 2 and 3, we further demonstrate that in fact the addition of the sublingual space is crucial for achieving $F3$ values that match the full range of speakers' values. By comparing the results of experiments 3 and 4, we further show that the sublingual space acts to extend the front cavity. Furthermore, for articulatory configurations with limited sublingual area, such as the ones reported in this study, the branch cavity antiresonance is well above the region of $F3$ (>5000 Hz) so that it is not a factor in predicted $F3$ for /r/. [Note that, in a tip-up retroflex /r/ where the tongue dorsum is lowered (Stevens, 1999; Narayanan *et al.*, 1999), the sublingual cavity may be considerably longer so that the antiresonance may occur in a region close to $F3$ or $F4$.] In experiment 5, we developed a simple tube model based on the MRI-derived dimensions, and show that $F3$ can be derived by positing (1) a lip constriction formed by the tapering gradient of the teeth and lips (with or without rounding), and (2) a large-volume cavity behind it and anterior to the palatal constriction. The larger volume in turn results from a combination of the front cavity proper together with the volume of the sublingual space. Narayanan *et al.* (1999) discuss a similar role for the front cavity in Tamil retroflex liquids. For these retroflex liquids, however, a tongue tip-up articulatory configuration with less-pronounced lip constriction and a

long sublingual space allowed application of Stevens' model (1999) of the front cavity as a quarter-wavelength resonator.

An interesting aspect of the difference between the Stevens (1999) model and our own model is the contrast between the role of the lip constriction and the sublingual space. If the lip constriction and tapering produce a front cavity of a Helmholtz shape, adjustments to lower $F3$ must have the effect of adding to the volume of the cavity. As noted above, this effect may be produced either by the addition of a sublingual space, or by more posterior placement of the palatal constriction. We may imagine here a trading relation between the placement of the palatal constriction and the existence of a sublingual space, such that each contributes to increasing the volume of the cavity. On the other hand, if the lip constriction is wide enough that the front cavity is best modeled as a quarter-wavelength resonator, the dimension that matters most for lowering $F3$ is an increase in the length of the front cavity. Again, we may imagine a trading relation between increases to the length of the front cavity and the narrowing of the lip constriction, in essence, a trading relation between a Helmholtz-type and quarter-wavelength model of the front cavity acoustics. These putative trading relations are slightly different, but complementary to, the trading relations between measures of palatal constriction location, degree, and length discussed in Guenther *et al.* (1999). In addition, the formation of a separate lip protrusion channel has a lowering effect on $F3$. Because the MRI-derived configurations of speakers PK and MI describe bunched configurations, it might be tempting to assume that the Helmholtz shape is typical of bunched configurations, while the quarter-wavelength shape characterizes retroflex configurations such as those in Narayanan *et al.* (1999). Please note, however, that lip constriction dimensions are not available for the retroflex /r/ of Ong and Stone (1998), or for any other American English tip-up retroflex /r/. [The dimensions in Fant (1960) are based on a Russian trilled /r/.] Thus, although we can posit a general trading relation, we cannot relate it to the classical contrast between retroflex and bunched /r/'s in any detail.

In this paper, we have discussed the sublingual space only in the context of how it helps to lower $F3$. However, the sublingual space also functions as a side branch (that can itself be modeled as a quarter-wavelength tube), introducing an antiresonance in the spectrum of /r/. For the articulatory configurations considered in this paper, the side branch is no more than 1.5 cm long, producing an antiresonance between 5–6 kHz. Note that configurations exist where the sublingual space is considerably longer, as in the Tamil /r/ described by Narayanan *et al.* (1999) and the retroflex /r/ assumed by Stevens (1999). In such cases, the antiresonance is between 3–4 kHz. An antiresonance in this region of the spectrum may have a considerable effect on the distinctive acoustic profile of /r/.

Another interesting result of the modeling involves the role of the pharyngeal constriction. In the case of PK, the pharyngeal constriction is narrow enough so that the back part of the vocal tract behind the palatal constriction is best modeled as a double-Helmholtz resonator. On the other hand, for MI, the pharyngeal constriction is wider so that this portion of the vocal tract is best modeled as a half-wavelength resonator. These different models result in very different values of $F4$ for PK and MI. In both cases, $F4$ is a half-wavelength resonance. However, in the case of PK, the length of the cavity is only about 4 cm long, resulting in a frequency for $F4$ around 4200 Hz. On the other hand, for MI, the length of the half-wavelength resonator is around 12 cm, resulting in an $F4$ frequency around 2900 Hz.

IV. CONCLUSION

Our primary aim in this paper was to examine and modify existing acoustic models of American English /r/, using recently obtained MRI-derived vocal-tract dimensions. A second aim was to model the full range of formant frequencies, and in particular $F3$, produced by our speakers. We first considered the Perturbation Theory account of /r/ acoustics, and found that the placement of constrictions in the MRI-derived data did not match predicted locations. We then proceeded by using MRI-derived vocal-tract dimensions as input to the Maeda VTCALCS program. Comparing these results to the range of actual formant frequencies produced by our speakers, we found that even in the case of tip-down bunched /r/, the addition of the sublingual space to the front cavity was necessary to achieve $F3$ frequencies that match speakers' mid- and low-range $F3$ values. We then developed a simple tube model whose output formant frequencies match those derived via the Maeda computer simulation model and actual MRI-derived dimensions. As such, it adequately accounts for the cavity affiliations and frequencies of $F1$, $F2$, $F3$, and $F4$. In this model, $F3$ is a front cavity resonance where the front cavity includes a lip constriction formed by the tapering gradient of the teeth and lips (with or without rounding) and a large volume cavity behind it that includes the sublingual space. The sublingual space acts to increase the volume of the cavity and thereby lower $F3$. The results also suggest that $F1$, $F2$, and $F4$ arise from the palatal constriction and/or the cavities posterior to it.

Although to this point we have largely succeeded in modeling the mid-to-low range of $F3$, we have not yet fully accounted for the lowest $F3$ values. This may stem from the fact that the MRI-derived dimensions and the real words were recorded at different time points; in other words, during the MRI experiment the speakers may actually have been producing /r/'s with $F3$'s in their own midrange. Also, the nature of the MRI technique, and the orientation of the magnetic coil, means that peripheral structures such as lips and glottis are imaged with less accuracy. The error in imaging the lip area may be as much as 1 cm; an increase or decrease of this magnitude in lip protrusion or narrowing would have a major effect on $F3$. In addition, other acoustic mechanisms that we have not considered may be at work. Recent work, Story, Titze, and Hoffman (1998) and Dang and Honda (1997), for instance, document the role of the piriform sinuses in lowering formant frequencies. We hope to explore these issues further in future research.

ACKNOWLEDGMENTS

We thank Ken Stevens for his help and comments, Shinji Maeda for the VTCALCS program, and Ronan Scaife for the MATLAB version of VTCALCS. This work was supported by an NIDCD Grant No. IR03-C2576-01 to Suzanne Boyce and NSF Grant No. IRI-9310518 and NIH Grant No. 1 K02 DC00149-01A1 to Carol Espy-Wilson. We also thank Maureen Stone for furnishing her MIT data.

APPENDIX: LIST OF REAL WORDS SPOKEN BY PK AND MI

(1) beaker;
(2) beeper;
(3) beater;
(4) kirk;
(5) perk;
(6) reed;
(7) rod;
(8) rude;
(9) turd;
(10) turk (MI only).

[1]Phoneticians typically classify American English /r/ into a syllabic, or vocalic, allophone and a consonantal allophone /r/. Because modeling issues are the same for all such allophones, we have chosen to treat /r/ in this paper as a single entity. Thus, we have maximized the challenge to our modeling results by including data from all allophonic types of /r/ in our discussions of formant values typical of /r/, including discussion of ranges of formant values.

[2]The currency of the perturbation model for /r/ among teachers of speech acoustics has been confirmed in conversations with, among others, John Ohala, Pat Keating, Louis Goldstein, Mary Beckman, Keith Johnson, and Peter Ladefoged. It is the basis of the discussion of American /r/ acoustics in Johnson (1997).

[3]Conditions under which a constriction is narrow enough that cavities on either side are best modeled as separate resonators, rather than as coupled areas separated by a perturbation, have been a matter of empirical investigation. In general, Mrayati *et al.* (1988) estimate that the cross-over point for ''one-tract-mode'' (OTM) resonance vs ''two-tract-mode'' (TTM) resonance is a 0.8 cm^2 constriction in a 5-cm^2 tube, or a 0.65-cm^2 constriction in a 4-cm^2 tube—essentially a 6-to-1 ratio. On this logic, a vocal tract with less extreme constrictions might plausibly be modeled as resonating in OTM (perturbation) mode. In the case of /r/, modeling trials have established that when tapering palatal, pharyngeal, and lip constrictions of 0.8 cm^2 are inserted in a tube of uniform 4-cm^2 area and 15.3-cm length (essentially a 5-to-1 ratio), $F1$ is at 480 Hz, $F2$ at 1274 Hz, and $F3$ at 1728 Hz. These numbers are securely in the range of attested $F3$ values for /r/. Thus, an idealized vocal tract configured as predicted by the Perturbation Theory does in fact produce acceptable formant values for /r/. [It should be noted that $F3$ decreases further as constriction size decreases at these points. This may be an instance of what Mrayati *et al.* (1988) term ''observations that... the relation predicted by 'small' perturbation theory continues to hold even if 'large' variations are introduced.''] However, the actual constrictions measured from the MRI data for our subjects in Fig. 4 are typically much smaller—with palatal constrictions typically less than 0.65 cm^2 and as low as 0.25 cm^2. These data on constriction size suggest that Perturbation Theory may not be the appropriate model for /r/ as produced by our subjects.

[4]At low frequencies, the impedance of the palatal constriction and the impedance of the lip constriction are in series, since the impedance of the front cavity (which consists of an acoustic compliance) can be ignored. For more details, see Stevens (1999).

[5]In Alwan *et al.* (1997), PK's vocal-tract profiles are labeled according to production condition, i.e., as ''retroflex'' and ''bunched.''

[6]The sublingual areas used in this study differ from those reported in Alwan *et al.* (1997). The sublingual areas given in Table II of Alwan *et al.* (1997) were measured directly from raw coronal images of the oral cavity and included only the airspace areas that appeared directly below the tongue surface. The sublingual areas reported in this paper are based on an improved and more realistic specification of the sublingual cavity: (1) The contiguous raw coronal image scans were used to obtain a 3D reconstruction of the oral cavity that included the sublingual cavity and any airspace along the sides of the tongue. (2) Cross sections of the supra- and sublingual cavities were then obtained from resectioning these cavities along planes perpendicular to their midlines. Specifically, note that the ''improved'' sublingual areas also included some contributions from air space along the sides of the front tongue.

[7]As noted above, if we model the pharyngeal narrowing as a perturbation in MI's *long back cavity* model, its position is such that it would lower the frequencies of $F2$ (1422 and 1458 Hz) by 100–200 Hz.

[8]Again, if we model the pharyngeal narrowing as a perturbation in MI's long back cavity model, we would expect it to raise $F4$ by 100–200 Hz, bringing the values of 2845.5 and 2916.7 Hz even closer to the real data average of 3113.7.

Alwan, A., Narayanan, S., and Haker, K. (**1997**). ''Toward articulatory–acoustic models for liquid approximants based on MRI and EPG data. II. The rhotics,'' J. Acoust. Soc. Am. **101**, 1078–1089.

Boe, L., and Perrier, P. (**1990**). ''Comments on Distinctive regions and modes: A new theory of speech production,'' Speech Commun. **7**, 217–230.

Boyce, S., and Espy-Wilson, C. (**1997**). ''Coarticulatory stability in American English /r/,'' J. Acoust. Soc. Am. **101**, 3741–3753.

Chiba, T., and Kajiyama, M. (**1941**). *The Vowel: Its Nature and Structure* (Kaiseikan, Tokyo).

Dang, J., and Honda, K. (**1997**). ''Acoustic characteristics of the piriform fossa in models and humans,'' J. Acoust. Soc. Am. **101**, 456–465.

Delattre, P., and Freeman, D. (**1968**). ''A dialect study of American Rs by x-ray motion picture,'' Language **44**, 29–68.

Espy-Wilson, C. (**1992**). ''Acoustic measures for linguistic features distinguishing the semivowels in American English,'' J. Acoust. Soc. Am. **92**, 736–757.

Espy-Wilson C. Y., Narayanan, S., Boyce, S. E., and Alwan, A. (**1997**). ''Acoustical modeling of American English /r/,'' Proceedings of Eurospeech '97, September, Patras, Greece.

Fant, G. (**1960**). *Acoustic Theory of Speech Production* (Mouton, Gravenhage).

Fant, G. (**1980**). ''The relations between area functions and the acoustic signal,'' Phonetica **37**, 55–86.

Guenther, F. H., Espy-Wilson, C. Y., Boyce, S. E., Matthies, M. L., Zandipour, M., and Perkell, J. S. (**1999**). ''Articulatory tradeoffs reduce acoustic variability during American English /r/ production,'' J. Acoust. Soc. Am. **105**, 2854–2865.

Hagiwara, R. (**1995**). ''Acoustic realizations of American /r/ as produced by women and men,'' UCLA Phonetics Laboratory Working Papers, 90.

Harshman, R., Ladefoged, P., and Goldstein, L. (**1977**). ''Factor analysis of tongue shapes,'' J. Acoust. Soc. Am. **62**, 693–707.

Heinz, J. M. (**1967**). ''Perturbation functions for the determination of vocal-tract area functions from vocal-tract eigenvalues,'' STL-QPSR 1/1967, pp. 1–14.

Jackson, M., Espy-Wilson, C., and Boyce, S. (**1999**). ''Verifying a vocal tract model with a closed side branch,'' J. Acoust. Soc. Am. (submitted).

Johnson, K. (**1997**). *Acoustic and Auditory Phonetics* (Blackwell, Cambridge).

Kent, R. (**1998**). ''Normal aspects of articulation,'' in *Articulation and Phonological Disorders*, edited by J. Bernthal and N. Bankson (Allyn and Bacon, Boston).

Lehiste, I. (**1962**). ''Acoustical characteristics of selected English consonants,'' University of Michigan Communication Sciences Laboratory Report #9.

Lindau, M. (**1985**). ''The Story of /r/,'' in *Phonetic Linguistics: Essays in Honor of Peter Ladefoged*, edited by V. A. Fromkin (Academic, Orlando), pp. 157–168.

Maeda, S. (**1982**). ''Digital simulation method of the vocal tract system,'' Speech Commun. **1**, 199–299.

McGowan, R. S. (**1992**). ''Tongue-tip trills and vocal-tract wall compliance,'' J. Acoust. Soc. Am. **91**, 2903–2910.

Moore, C. (**1992**). ''The correspondence of vocal tract resonance with volumes obtained from magnetic resonance images,'' J. Speech Hear. Res. **35**, 1009–1023.

Mrayati, M., Carré, R., and Guérin, B. (**1988**). ''Distinctive regions and modes: A new theory of speech production,'' Speech Commun. **7**, 257–286.
Narayanan, S., Alwan, A., and Haker, K. (**1997**). ''Toward articulatory–acoustic models for liquid approximants based on MRI and EPG data. I. The laterals,'' J. Acoust. Soc. Am. **101**, 1064–1077.
Narayanan, S., Byrd, D., and Kaun, A. (**1999**). ''Geometry, kinematics, and acoustics of Tamil liquid consonants,'' J. Acoust. Soc. Am. **106**, 1993–2007.
Nolan, F. (**1983**). *The Phonetic Bases of Speaker Recognition* (Cambridge University Press, Cambridge, England).
Ohala, J. (**1985**). ''Around flat,'' in *Phonetic Linguistics: Essays in Honor of Peter Ladefoged*, edited by V. A. Fromkin (Academic, Orlando), pp. 223–241.
Ong, D., and Stone, M. (**1998**). ''Reconstruction of vocal tract shape from magnetic resonance images during production of [r] and [l],'' Phonoscope **1**, 1–14.
Rubin, P., Baer, T., and Mermelstein, P. (**1981**). ''An articulatory synthesizer for perceptual research,'' J. Acoust. Soc. Am. **70**, 321–328.
Scaife, R. (**1997**). Personal communication.
Schroeder, M. R. (**1967**). ''Determination of the geometry of the human vocal tract by acoustic measurements,'' J. Acoust. Soc. Am. **41**, 1002–1010.
Shiller, D., Ostry, D., and Gribble, P. (**1999**). ''Effects of gravitational load on jaw movement in speech,'' J. Neurosci. **19**, 9073–9080.
Shriberg, L., and Kent, R. (**1982**). *Clinical Phonetics* (Macmillan, New York).
Stevens, K. N. (**1999**). *Acoustic Phonetics* (MIT Press, Cambridge, MA).
Story, B. H., Titze, I. R., and Hoffman, E. A. (**1998**). ''Vocal tract area functions for an adult female speaker based on volumetric imaging,'' J. Acoust. Soc. Am. **104**, 471–487.
Sundberg, J., Lindblom, B., and Liljencrants, J. (**1992**). ''Formant frequency estimates for abruptly changing area functions: A comparison between calculations and measurements,'' J. Acoust. Soc. Am. **91**, 3478–3482.
Tiede, M. (**1999**). Personal communication.
Tiede, M., Masaki, S., Wakumoto, W., and Vatikiotis-Bateson, E. (**1997**). ''Magnetometer observation of articulation in sitting and supine conditions,'' J. Acoust. Soc. Am. **102**, 3166.
Veatch, T. C. (**1991**). ''English vowels: Their surface phonology and phonetic implementation in vernacular dialects,'' University of Pennsylvania Ph.D. dissertation.
Westbury, J. R., Hashi, M., and Lindstrom, M. J. (**1999**). ''Differences among speakers in lingual articulation of American English /r/,'' Speech Commun. **26**, 203–226.
Yang, C. S., and Kasuya, H. (**1994**). ''Accurate measurement of vocal tract shapes from magnetic resonance images of child, female, and male subjects,'' in Proceedings of the International Conference on Spoken Language Processing, Yokohama, Japan, pp. 623–626 (unpublished).
Zawadaski, P., and Kuehn, D. (**1980**). ''A cineradiographic study of static and dynamic aspects of American English /r/,'' Phonetica **37**, 253–266.

Reconstruction of bowing point friction force in a bowed string

J. Woodhouse[a)]
Department of Engineering, Cambridge University, Trumpington Street, Cambridge CB2 1PZ, United Kingdom

R. T. Schumacher[b)] and S. Garoff
Department of Physics, Carnegie Mellon University, Pittsburgh, Pennsylvania

(Received 25 August 1999; accepted for publication 28 March 2000)

A method is presented for reconstructing the friction force and the velocity at the bowing point of a string excited by a rosined bow sliding transverse to the string. Two versions of the method of reconstruction are presented, each approximate in different ways, but both capable of sufficient accuracy to allow useful application to problems of understanding frictional interactions in this dynamical system. The method is illustrated with simulated data to verify its accuracy, and results are shown for two contrasting cases of observed stick-slip string motion. As has been found in other investigations, the friction force during sliding is not determined by the instantaneous sliding speed. The results seem to be compatible with a thermally based model of rosin friction. © *2000 Acoustical Society of America.* [S0001-4966(00)01507-1]

PACS numbers: 43.75.De, 43.40.Cw, 43.60.Pt [WJS]

INTRODUCTION

The excitation of autonomous oscillations in a stretched string by drawing a bow transversely across it is thought to have originated no later than the 10th century.[1] The historical reference to the earliest use in Islamic societies is accompanied by the remark that the ''string'' of the bow, i.e., the horsehair, has been rubbed with ''pitch or resin.'' The bow has been used for musical purposes ever since, most familiarly in the instruments of the violin family. To achieve the characteristic slip-stick oscillations whose nature was first identified by Helmholtz[2] it is necessary to use a substance as an intermediary between string and bow that adheres sufficiently strongly to the string during the sticking part of the motion, and that ''softens'' so as to encourage steady oscillations when the string dynamics breaks the adhesive bond and slipping occurs.

The intermediary substance has conventionally been rosin, a solid distillate obtained from the pitch of coniferous trees. Rosin has extraordinary frictional properties which make it ideal for this purpose. A physically plausible theoretical model for the motion of a bowed string must obviously include a constitutive model for rosin friction. Experimental techniques and theoretical modeling developed for this purpose may have applications in other areas involving stick-slip friction.

The behavior of frictional force and velocity at the contact region of a simple dynamical system excited into stick-slip vibration has been reported by Smith[3] and Smith and Woodhouse.[4] Their system was a version of the prototypical autonomous oscillator system of a system of a single mass on a spring with continuous excitation by a rosin-coated rod moving at constant velocity. Because this system is so simple, it is straightforward to infer the frictional force from observations of the motion of the vibrating mass. The results showed clearly that the frictional force could not be explained with a simple functional relation between the force and velocity, as had been assumed in all previous discussions of rosin-mediated slip-stick motion. An improved constitutive law governing rosin friction is obviously needed. Based on their observations, Smith and Woodhouse[4] proposed models in which friction depends not on sliding speed but on contact temperature.

The oscillator used by Smith and Woodhouse in their measurements necessarily had properties quite different from those of a stretched string. To reconstruct the frictional force and the velocity of a real string at the bowing point from observations of the string's motion is less easy, but a method of doing this was first described by Schumacher.[5,6] We report here a further development of that method, backed by more extensive experimental results. With care, the velocity of a string at the bowed point can be observed directly and noninvasively by the use of a laser-Doppler vibrometer, but there is no corresponding direct method of measuring frictional force. The reconstruction method overcomes the difficulties of direct observation by using the signals from force transducers that serve as the fixed terminations of the string. Both the frictional force and the string velocity at the bow can be deduced from these transducer signals. The approach has the advantage of not disturbing the motion of the string or interfering with the physical properties in the vicinity of the friction contact.

We present first the governing equations, then describe two alternative methods for reconstructing the force and motion at the bowing point. One of the methods allows reconstruction for all motions of the string, including particularly the nonperiodic motions that occur during the initial transient part of the motion. In its present implementation this method is limited by a requirement that the string terminations be effectively rigid. The dispersive effects of propagation along the string are included by a time-domain approach based on

[a)]Electronic mail: jw12@eng.cam.ac.uk
[b)]Electronic mail: rts@andrew.cmu.edu

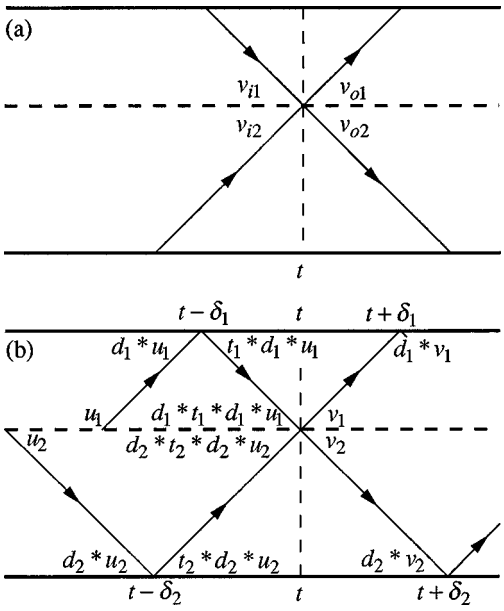

FIG. 1. Space–time diagrams of traveling velocity waves on the string which interact at the bowed point at a particular instant. Horizontal axis: time; vertical axis: distance along the string; horizontal dashed line: bow position; vertical dashed line: required time t. Labeling of trajectories is described in the text.

FIR digital filters. The second method could more readily be applied if the terminations were not rigid, so that their dynamics have an effect on the string's motion. However, this method can only be applied to periodic motions of the string since the crucial stage of the analysis is carried out in the frequency domain. Both methods are limited to excitation by a bow whose dynamics can be neglected. To achieve this in the laboratory we use as a ''bow'' a rosin-coated glass rod rigidly attached to a massive sled that is computer controlled to move in a precisely-defined way.

To illustrate the reconstruction methods, they are applied to measured signals from the experimental system. Some typical results are shown, and their significance discussed. To assess the accuracy of the approach we also apply them to simulated signals, obtained using a model of rosin friction proposed by Smith and Woodhouse[4] and embodying a reasonably accurate representation of the transverse and torsional dynamics of the string used in the experimental tests. In this case the correct velocity and force at the bowed point are known from the simulation, so that a direct assessment of the accuracy of the method is possible.

I. THEORY

Figure 1 shows two space–time (or characteristic) diagrams relating to the trajectories of propagating transverse waves on the string that are relevant to events at the bow (horizontal dashed line) at time t. Time runs horizontally, and position along the string runs vertically. In Fig. 1(a) are shown the two incoming and two outgoing waves, denoted v_{i1}, v_{o1}, v_{i2}, v_{o2}. For an ideal string with tension T and mass per unit length m, these quantities suffice to determine the velocity v and the force f at the bow. The velocity follows by continuity, in the two alternative expressions

$$v = v_{i1} + v_{o1} = v_{i2} + v_{o2}. \tag{1}$$

Corresponding expressions for the force are given by the following argument. In the absence of a force applied at the bow, the two incoming waves would simply carry on unchanged as the outgoing waves. The effect of the applied force is to generate an additional velocity wave which radiates equally in both directions outwards from the bow, thus modifying both outgoing waves relative to the incoming waves. For an ideal string the additional outgoing velocity wave has magnitude $f/2Z$, where

$$Z = \sqrt{Tm} \tag{2}$$

is the wave impedance of the string. It follows that

$$f = 2Z(v_{o1} - v_{i2}) = 2Z(v_{o2} - v_{i1}). \tag{3}$$

Equality of these two expressions is readily shown to be equivalent to equality of the expressions in Eq. (1).

The strategy now is to express the incoming and outgoing velocities at the bow in terms of the forces on the terminations at earlier and later times determined by the propagation times from the terminations to the string. For this we need a larger portion of the characteristic diagram, shown in Fig. 1(b). Following one segment of trajectory some notation can be defined. Consider a velocity wave leaving the bow, denoted u_1 in Fig. 1(b). By the time this wave returns to the bow it has been modified by various linear processes. First, the wave propagates to the end of the string, during which journey some dispersion and dissipation take place. This is represented by convolution with a function d_1, the convolution operator being denoted ''$*$.'' The wave now reflects from the string termination, a process represented by convolution with a function r_1. Finally, the wave propagates back to the bow, represented by a second convolution with d_1. These stages are all labeled in the figure, together with similar sequences for the other initial velocity waves denoted v_1, u_2, v_2. The time delays denoted δ_1, δ_2 are assumed to be incorporated within the definitions of the transmission functions d_1 and d_2.

The forces exerted by the terminations on the string are now

$$f_1(t-\delta_1) = Z(r_1*d_1*u_1 - d_1*u_1), \tag{4a}$$

$$f_1(t+\delta_1) = Z(r_1*d_1*v_1 - d_1*v_1), \tag{4b}$$

$$f_2(t-\delta_2) = Z(r_2*d_2*u_2 - d_2*u_2), \tag{4c}$$

$$f_2(t+\delta_2) = Z(r_2*d_2*v_2 - d_2*v_2). \tag{4d}$$

If the terminations are rigid, these reduce to simpler forms because the reflection process becomes a simple multiplication by -1. Then,

$$f_1(t-\delta_1) = -2Zd_1*u_1, \tag{5a}$$

$$f_1(t+\delta_1) = -2Zd_1*v_1, \tag{5b}$$

$$f_2(t-\delta_2) = -2Zd_2*u_2, \tag{5c}$$

$$f_2(t+\delta_2) = -2Zd_2*v_2, \tag{5d}$$

so that the (measured) force waveforms are equal (apart from a scalar multiplication by $2Z$) to the velocity waveforms sent out from the terminations towards the bow.

Equations (4), or (5) if appropriate, can be used to provide the needed velocities v_{i1}, v_{o1}, v_{i2}, v_{o2} if they can be deconvolved, that is, if they can be solved for the velocities in terms of the measured termination forces. There are two approaches to the problem of eliminating the velocities in favor of the termination forces, depending on whether one works in the time domain or the frequency domain. If the termination is rigid and the dissipation during one transit of a wave between bow and termination is small, then a simple time-domain approach is possible which uses digital filters to effect the solution. In the absence of dissipation on the string, the functions d_1 and d_2 are all-pass filters representing the dispersive propagation on the string. These functions can be represented as FIR digital filters, by virtue of an explicit expression for the propagation of an impulse along a stretched string with nonzero bending stiffness due to Scott, described by Woodhouse.[7] The velocity at position x after time t is given approximately by

$$v(x,t) \approx \frac{3^{1/6}(k_p^2+1)^{2/3}}{2^{2/3}(2k_p^2+3)^{1/2}\bar{t}^{1/3}} \mathrm{Ai}\left[-\left(\frac{3\bar{t}}{2} \right)^{2/3} \frac{k_P^2}{(k_P^2+1)^{1/3}} \right], \tag{6}$$

where Ai is the Airy function, k_p is a stationary-phase wave number satisfying

$$k_P^2 = \frac{1-4\tau^2+(1+8\tau^2)^{1/2}}{8\tau^2}, \tag{7}$$

and

$$\bar{t} = t\frac{T}{\sqrt{Bm}}, \quad \bar{x} = x\sqrt{\frac{T}{B}} \tag{8}$$

are nondimensional time and distance, with $\tau = \tilde{t}/\bar{x}$ and where B is the bending stiffness of the string. In practice, it is necessary to apply an antialiasing low-pass filter to this function, as illustrated by Woodhouse.[7]

Now it is a property of any such all-pass digital filter that its inverse may be obtained simply by time reversal. This reversal is an anticausal filter, which advances the signal in time while ''de-dispersing'' it. This is precisely what we need to obtain the outgoing velocity wave v_1 from the velocity wave at the termination, $d_1 * v_1$, and similarly for v_2 and $d_2 * v_2$. Denote these inverse filters d_1^{-1}, d_2^{-1}. The four velocity waves needed to reconstruct the force and velocity according to Eqs. (1) and (3) are then given by

$$v_{i1} = d_1 * f_1/(2Z), \tag{9a}$$

$$v_{01} = -d_1^{-1} * f_1/(2Z), \tag{9b}$$

$$v_{i2} = d_2 * f_2/(2Z), \tag{9c}$$

$$v_{02} = -d_2^{-1} * f_2/(2Z). \tag{9d}$$

Provided the assumptions of this model are satisfied, these equations give a way to find the velocity and force under the bow from arbitrary waveforms f_1 and f_2, including initial transients. If the assumptions are not satisfied, in particular if the string terminations are sufficiently nonrigid to influence the dynamics of the vibration, then things become more difficult. In principle it might still be possible to design an inverse digital filter to deconvolve the effects of reflections at the terminations, but this is likely to be difficult in practice. If this problem must be grappled with, it is easier to work in the frequency domain, where the operations of convolution and deconvolution are replaced by algebraic operations with transfer functions. The price of this approach is that it can only be implemented robustly when the measured signals f_1 and f_2 are periodic to reasonable accuracy.

For deconvolution in the frequency domain, the data must first be made digitally periodic by resampling it into a form that has an integral number of samples per period over at least a few periods, so that the data excerpt which will be processed is cyclic. Now Eqs. (4) can be Fourier transformed: transforms of each quantity are denoted by corresponding upper-case letters:

$$U_1 = \frac{F_1^{\mathrm{del}}}{ZD_1(R_1-1)}, \tag{10a}$$

$$V_1 = \frac{F_1^{\mathrm{adv}}}{ZD_1(R_1-1)}, \tag{10b}$$

$$U_2 = \frac{F_2^{\mathrm{del}}}{ZD_2(R_2-1)}, \tag{10c}$$

$$V_2 = \frac{F_2^{\mathrm{adv}}}{ZD_2(R_2-1)}. \tag{10d}$$

The superscripts ''del'' and ''adv'' refer to the transforms of $f_j(t-\delta_j)$ and $f_j(t+\delta_j)$, respectively. These expressions are then used in Eqs. (1) and (3) to obtain the expressions for bow force and velocity transforms, which are finally inverse transformed to the time domain.

The limitation on the reflection functions is no longer required, but the reflection functions must nevertheless be known. We will describe in the next section how the transmission functions are obtained from a combination of theory and fitting to plucked data. For our particular apparatus, it was not necessary to determine reflection functions since the terminations were sufficiently rigid to allow reasonable reconstructions assuming perfect delta-function reflection behavior. However, if it were desired to apply the method to bowed strings attached to a real violin body, an additional procedure would be necessary to identify the reflection function. The simplest way to obtain a first approximation to this would be to measure the input admittance at the instrument bridge, and then use a theoretical expression given by Woodhouse [Ref. 7, Eq. (6)]. It should be pointed out that, of course, the frequency-domain method can equally well be applied to rigid-termination data, as is needed by the time-domain method described above, subject to the limitation that a suitably periodic region of the bowed data set can be found.

II. PLUCK TESTS

To accomplish the reconstruction of the events at the bowing point, one needs, in addition to the termination force waveforms, the gains of the two input channels of the force transducers, and accurate values for the time delays from the bowed point to the two terminations. In addition, one needs to know the string's wave impedance, and information about wave dispersion, which is to be expected as a result of the string's bending stiffness. Good estimates of these quantities can be obtained from a calibrated pluck of the string, achieved by breaking a fine wire at the bowing point and recording the subsequent termination signals. The wire we use is 44 gauge copper magnet wire, for which independent measurements have determined that the breaking strength when looped around the string is 1 N, with an uncertainty of about 3%. The string that will provide the illustrations used in this paper is a violin E string, constructed of plain steel wire with no wrappings. In our experiments the string length $L=0.314\,\mathrm{m}$. For a fundamental frequency of 660 Hz, the tension of this string is 72.5 N and the wave impedance is $Z=0.175\,\mathrm{Ns/m}$.

The solid lines in Figs. 2(a) and 2(b) show the measured force signals from a pluck at a distance from the nearest termination of βL where $\beta=0.3$. The growing oscillations that precede each step in the signals show the effect of dispersion. It is easy to compute the theoretical form of such pluck responses, if it is assumed that the wave propagation behavior on each section of the string is governed by transmission functions d_1 and d_2 which are (suitably filtered) versions of the theoretical expression equation (6). The two time delays, the gain factors for the transducers and their amplifiers, and the bending stiffness can all be determined by best-fitting the simulated responses to the measured ones: the result is shown as the dashed lines superimposed on the measurements in Fig. 2. The fit between theory and measurement is generally excellent, giving some confidence in the use of these transmission functions for the deconvolution process. The value of the bending stiffness B was found to be $4.7\times10^{-5}\,\mathrm{N\,m^2}$. This value is in good agreement with expectation: for a circular wire of radius a, the theoretical value is

$$B=\pi E a^4/4, \tag{11}$$

and with $E=210\,\mathrm{GPa}$ and a measured radius $a=0.13\,\mathrm{mm}$, this gives the same result within the measurement uncertainty.

The most obvious area where the signals do not quite agree is just after the first force step in Fig. 2(a) or 2(b): the theory predicts constant force whereas the measurement shows some variation. This is probably evidence of nonrigidity of the termination, so that resonances of the support structure are excited by the step in force. Having determined the transmission functions d_1 and d_2 as above, it might be possible in principle to use the pluck response data to find the reflection functions r_1 and r_2 needed to describe this nonrigidity, by attributing to them the disparity between the theoretical and measured step responses. If the reflection functions are short compared to the reflection times on the string, extraction might be relatively straightforward. However, if the reflection functions involve long reverberation (as they would if the string were mounted on a real violin), the extraction process could be expected to be very tricky. For this initial study the terminations will be assumed to be rigid.

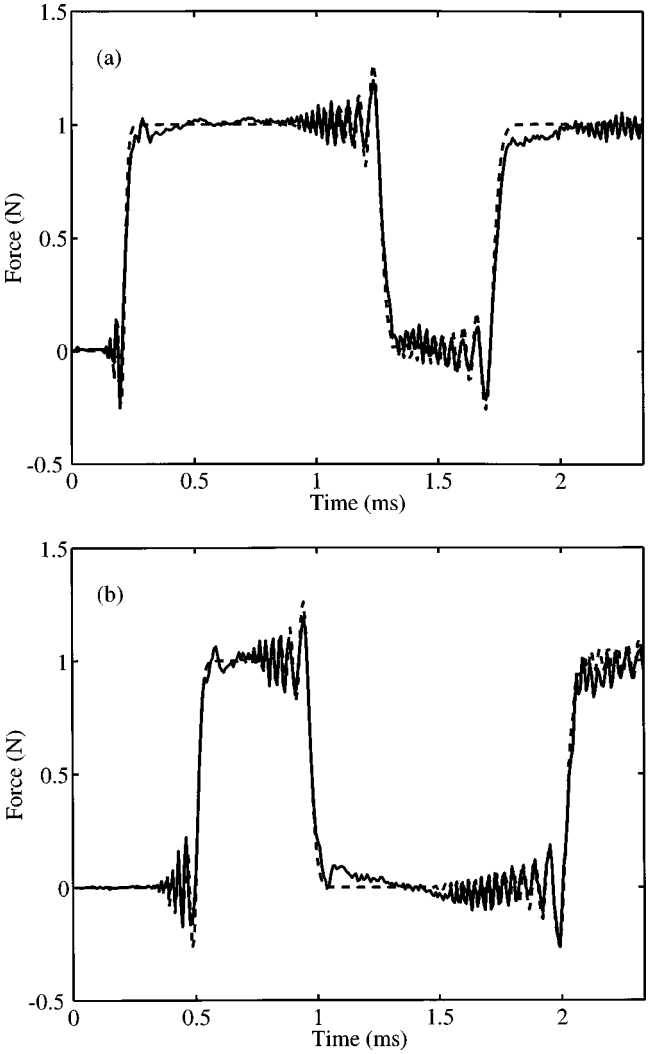

FIG. 2. Measured (solid) and theoretical (dashed) waveforms of force at the string's terminations following a pluck: (a) end nearer to pluck position and (b) end remote from pluck position.

Each time a run is made on the apparatus, a corresponding pluck test is also made. The fitting procedure just described is then used to determine the correct time delays to the ends of the string, and the gain factors for the transducers. This takes into account any variations in string tension, position of bowing point, and transducer performance. The bending stiffness is kept constant at the value stated above, since there is no reason to expect this to vary from day to day with a given steel string.

III. RECONSTRUCTION OF VELOCITY AND FORCE

A. Time-domain reconstruction

Having analyzed the pluck response to obtain the time delays and so on, the time-domain reconstruction of a bowed signal is now straightforward to carry out. Example results will be shown from a run with the bowing point at $\beta=0.3$ as appropriate to the pluck results already shown, with a normal force between rod and string of 0.3 N. The rod was of glass,

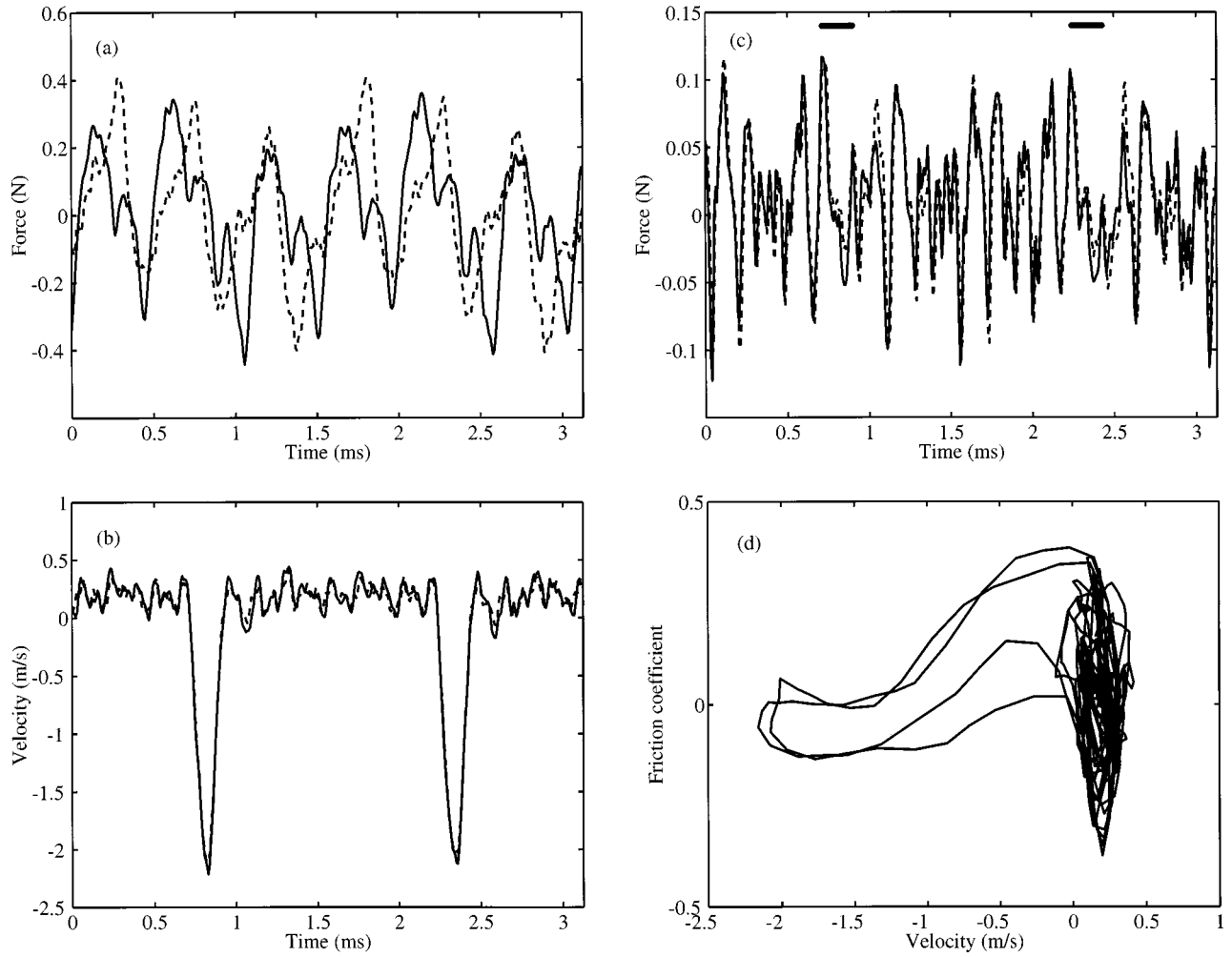

FIG. 3. Results for nearly periodic motion from a typical experimental run with the glass bow: (a) measured forces at the string's terminations; (b) waveforms of the deduced bowing-point velocity from Eqs. (1); (c) waveforms of the deduced bowing-point friction force from Eqs. (3); and (d) velocity/force trajectory of the data shown in (b) and (c). In (c), the segments of heavy horizontal line indicate the times of slipping deduced from (b).

with a diameter of 6 mm and a surface finish smooth to within 5 μm. It was coated not with ordinary violin rosin, which contains unknown chemical impurities, but with technical grade abietic acid, the principal constituent of rosin. The abietic acid was dissolved in ethanol, and the rod was drawn vertically from a container of this solution so that a uniform layer was deposited when the solvent evaporated.

To excite the string into vibration, the rod was driven at a ''bowing'' speed of 0.2 m/s. After a transient, the string settled into a reasonably periodic oscillation regime. A typical portion of the two measured force signals at the terminations is shown in Fig. 3(a). These signals have been digitized at a rate of 128 kHz, with 16-bit resolution. As is not surprising at this very large value of β, the string has not chosen to oscillate in the ''Helmholtz motion'' which violinists usually require.[2] This would involve a single ''corner'' or velocity jump moving on the string, and would result in a sawtooth wave for both termination force signals. Instead, a more complicated regime is established, one of the ''higher types'' analyzed by Raman.[8]

The two versions of the reconstructed velocity signal under the bow, given by Eq. (1), are shown in Fig. 3(b). To produce the best possible versions of these, the calibration results from the pluck test have been fine-tuned: the two time delays and the relative gain of the two sensors have been slightly adjusted by searching in the vicinity of the initial estimates in order to minimize a measure the difference between the two estimates of the velocity. These adjustments are extremely small, within the limits of uncertainty of the calibration procedure using the pluck data, but nevertheless result in a perceptible improvement in the quality of the results.

It is satisfying to see that the two waveforms are very similar, so that the reconstruction process is at least self-consistent. The waveform shows approximately constant velocity, oscillating around the bow speed, for most of each cycle, followed by a short spell of high negative velocity. This may be tentatively interpreted as a stick-slip oscillation, with a single slip per cycle. The measured velocity, which is the transverse velocity of the string's center, is not exactly equal to the bow speed during sticking, due mainly to torsional motion of the string.[9–11] We return to this issue in some detail in Sec. IV. It is possible to check the reconstruction of the string-center velocity waveform by a direct measurement. A small magnet can be positioned close beneath the string at the bowed point. As the (metal) string vibrates,

a voltage is induced across its ends which is proportional to the velocity through the magnetic field.[9] After suitable amplification, this signal can be displayed and compared with the reconstruction. The resolution of this method is limited by noise and by spatial spread of the magnetic field, but within the measurement accuracy the results are indistinguishable from the reconstructed velocity waveform.

The corresponding reconstructed force signal is shown in Fig. 3(c). Again, two versions are shown, corresponding to the two expressions in Eq. (3). Comparing Eqs. (1) and (3), the difference between the two estimates of reconstructed force is the same as the difference of the two reconstructed velocities (apart from a factor $2Z$). Because the variation of force is much less than that of velocity, this difference shows up more clearly in the force plot. Even so, the two curves are very similar, differing only in local details rather than in major features. Note that the amplifiers for the force sensors are ac-coupled, so that the force signal as computed here has a zero dc level. In practice, there must be a nonzero mean friction force opposing the direction of mean sliding—this would give the force a positive dc value in Fig. 3(c). A value for the missing dc level will be estimated shortly. This issue did not arise with the velocity signals, because for a periodic motion the velocity waveform cannot have a nonzero dc value, otherwise the string would have a net displacement after one cycle.

The time range of Fig. 3(c) is identical to that in Fig. 3(b), and it is interesting to note that the intervals of slipping do not stand out to the eye in the force waveform—these intervals are indicated by the heavy lines at the top of the plot. Comparing carefully, it can be seen that the force is high at the start of slipping, and reduces during the period of slipping. This has a striking consequence if the results are plotted in a different way. Until now, virtually all modeling of bowed-string motion has assumed that the friction force is determined by the sliding speed. If we test this idea by plotting force against sliding speed, as in Fig. 3(d), we see that the traditional assumption is not valid: instead of a single curve, the results show a hysteresis loop in a counterclockwise sense. (To produce this plot, the average of the two versions of the reconstructed force and the average of the two velocity reconstructions have been used.) Similar hysteresis loops have been seen in other measurements of rosin friction.[4] It has been suggested that the variable which governs the friction force is not in fact sliding speed, but the rosin temperature in the contact region. Since the contacting bodies have some thermal inertia, changes in temperature lag behind changes in sliding speed, producing a hysteresis loop in the sense observed here.

Figure 3(d) allows us to make a guess at the unknown dc level of the friction force. Since the shape revealed here is very reminiscent of those found in other experiments using rosin,[4] one might expect the absolute level of the coefficient of friction to be comparable. This would be achieved by adding approximately 0.5 to the coefficient of friction, so that it ranges from about 0.4 to 0.9 in the hysteresis loop. That in turn corresponds to adding a dc force of the order of 0.15 N in Fig. 3(c).

The time-domain reconstruction method should work

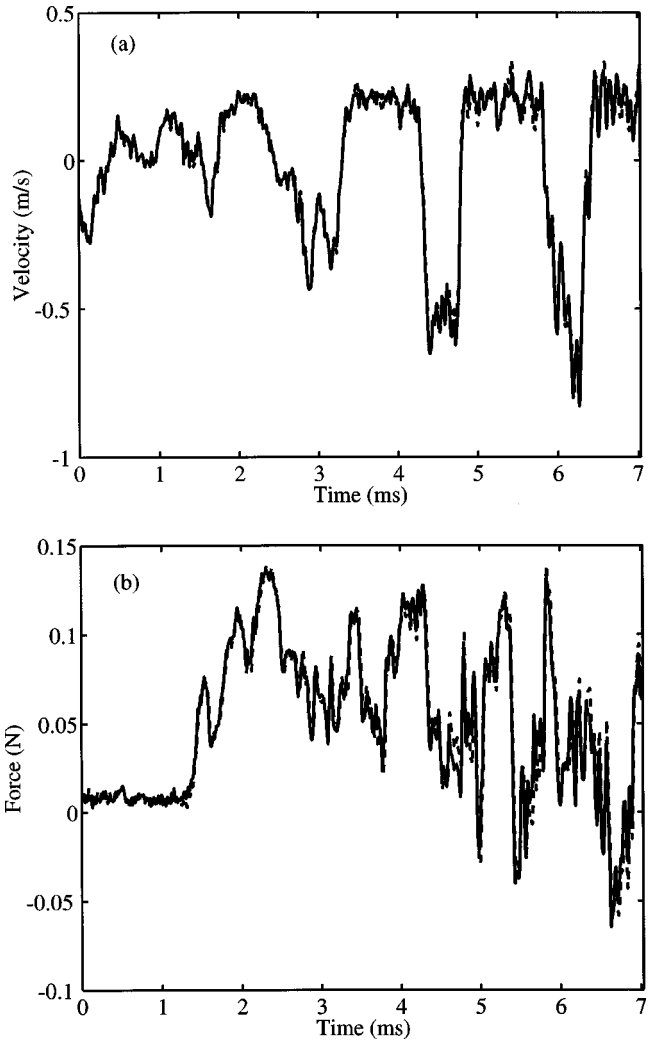

FIG. 4. Results from the initial transient of the experimental run shown in Fig. 3: (a) deduced bowing-point velocity and (b) deduced bowing-point friction force.

equally well during nonperiodic portions of the signal. As an illustration, Fig. 4 shows the reconstructed velocity and force signals from the same experimental run, around the time in the initial transient when the first stick-slip events occur. Again, both versions of the velocity and of the force are shown superimposed. Again, the agreement between the pairs is very good. In this initial stick-slip motion, something closer to the Helmholtz motion is seen: the right-hand half of Fig. 4(a) shows proportions of sticking time to slipping time roughly in the ratio $(1-\beta):\beta$, which is the Helmholtz characteristic. In the nearly periodic data shown in Fig. 3(b), slipping occupied a much smaller fraction of the period. This tendency of Helmholtz motion to be unstable to regimes with shorter slip times, when bowing with large β, has been noted by previous authors.[12,13] This is one reason why in conventional violin playing, β is usually kept rather small except when special effects are wanted.

B. Frequency-domain reconstruction

We now turn to the alternative reconstruction algorithm, operating in the frequency domain. The procedure can be illustrated using the same measured data as shown in Fig. 3.

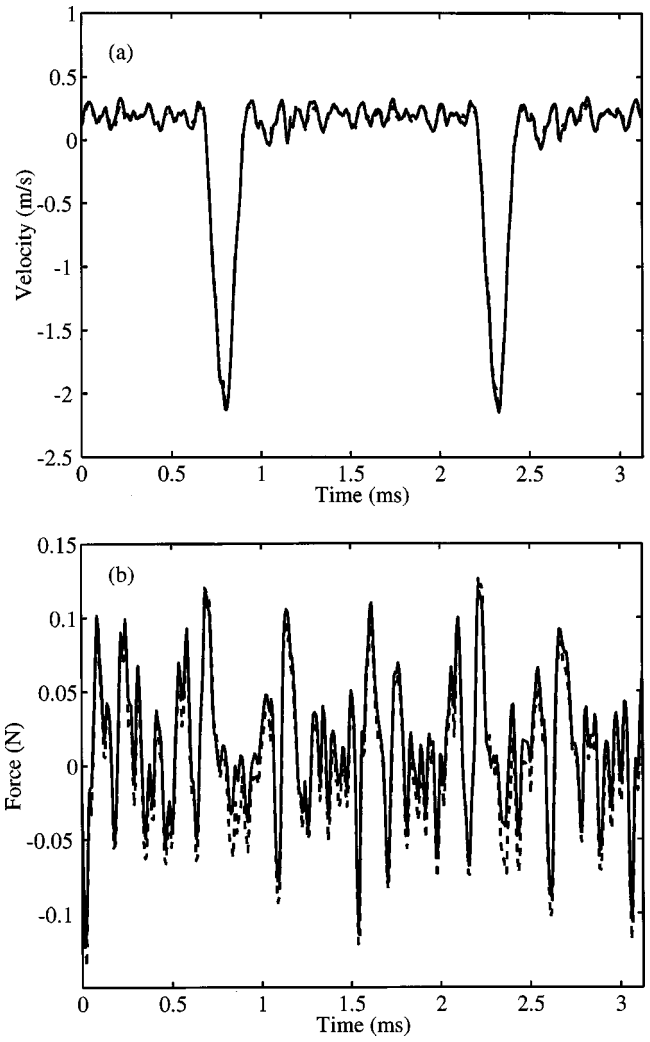

FIG. 5. Comparison of time-domain and frequency-domain reconstruction: (a) deduced bowing-point velocity and (b) deduced bowing-point friction force. Solid lines: time-domain results; dashed lines: frequency-domain results.

As a first stage, the data is resampled so as to produce an integral number of samples per period. For a string adjusted to 660 Hz, the number of samples per period for our sampling rate of 128 kHz is 193.94. A region is selected of about seven periods of the bowed data showing good periodicity. This region is resampled to 200 samples per period, and from that six contiguous periods are selected. Thus the transforms, direct and inverse, are 1200 samples long. The resampling is done by Fourier interpolation. The reconstruction now requires the evaluation of the data at delayed and advanced times. These are not in general integer numbers of samples, so an interpolation scheme is used. Good estimates of the delay times have already been found by analysis of the pluck response. As in the time-domain approach, these can be fine-tuned by a local search during the reconstruction process, to minimize the difference between the two estimates of force (or velocity).

The reconstruction is now carried out using the equations given in Sec. I. Figure 5 shows a comparison between the reconstruction of the bowing force and velocity using the time-domain and frequency-domain methods, for the same section of data shown in Fig. 3. It is very reassuring to see that the two methods give answers which differ from one another by about the same amount as the differences seen in either method separately between the alternative estimates of force and velocity. It seems that whichever way the detailed computation is done, the results are consistent within the bounds shown by Figs. 3 and 5.

C. Reconstruction of simulated data

The next step in assessing the accuracy of the method is to use it to reconstruct signals where the correct answer is known by independent means. The only way to do this at present is to use simulated data. A bowing simulation has been constructed which is reasonably close to the behavior of the physical apparatus as used to generate the results of Figs. 3–5. The general approach to such simulations has been described in detail in previous papers.[14,15] The correct properties were used for the tension, impedance, length, and bending stiffness of the string. Approximately correct Q-factors for transverse modes of the string were included, using a ''constant-Q reflection function'' described in a previous paper.[16] The measured Q-factors for the experimental string were in the range 500–1000 up to 6 kHz, rising to 1000–2000 above that. The model was able to achieve Q-factors around 1000 up 5 kHz, falling gently at higher frequencies to about 600 by 10 kHz because of the filter applied to the stiff-string response, Eq. (6). The bowing speed, normal force and position were matched to the experiment, as was the sampling rate. A plausible model for the torsional behavior of the string was used, with a torsional-to-transverse wave speed ratio of 7, a torsional-to-transverse impedance speed ratio of 3.5, and torsional Q-factors set to a constant value 15 using another version of the constant-Q reflection function.

Finally, the frictional behavior of the rosin was represented by a thermal model described by Smith and Woodhouse.[4] Friction force is regarded as arising from plastic yielding of a thin layer of rosin in the contact region, with a yield strength which varies with temperature in a manner deduced from steady-sliding experiments in a different apparatus.[4] The estimates of the contact size and layer thickness will be discussed in the next section, when the physical evidence of the track left in the rosin surface on the glass rod will be examined. The other thermal properties of rosin were as described in the earlier work. The thermal conductivity of the metal string was assigned a value which was the geometric mean of the values for rosin and steel, to model in a crude way the fact that a layer of rosin is transferred to the string very quickly, and this layer shields the high-conductivity metal from the rapid temperature variations in the thin layer of deforming rosin. This modified value was found to give more realistic results than using the conductivity of steel unmodified.

When this simulation was run, it produced a transient, leading after a while to accurately periodic motion of the string. The transverse forces exerted on the two terminations of the string were stored in the same format as the raw data gathered during the experiments. The simulation program was also used to generate corresponding results of a simu-

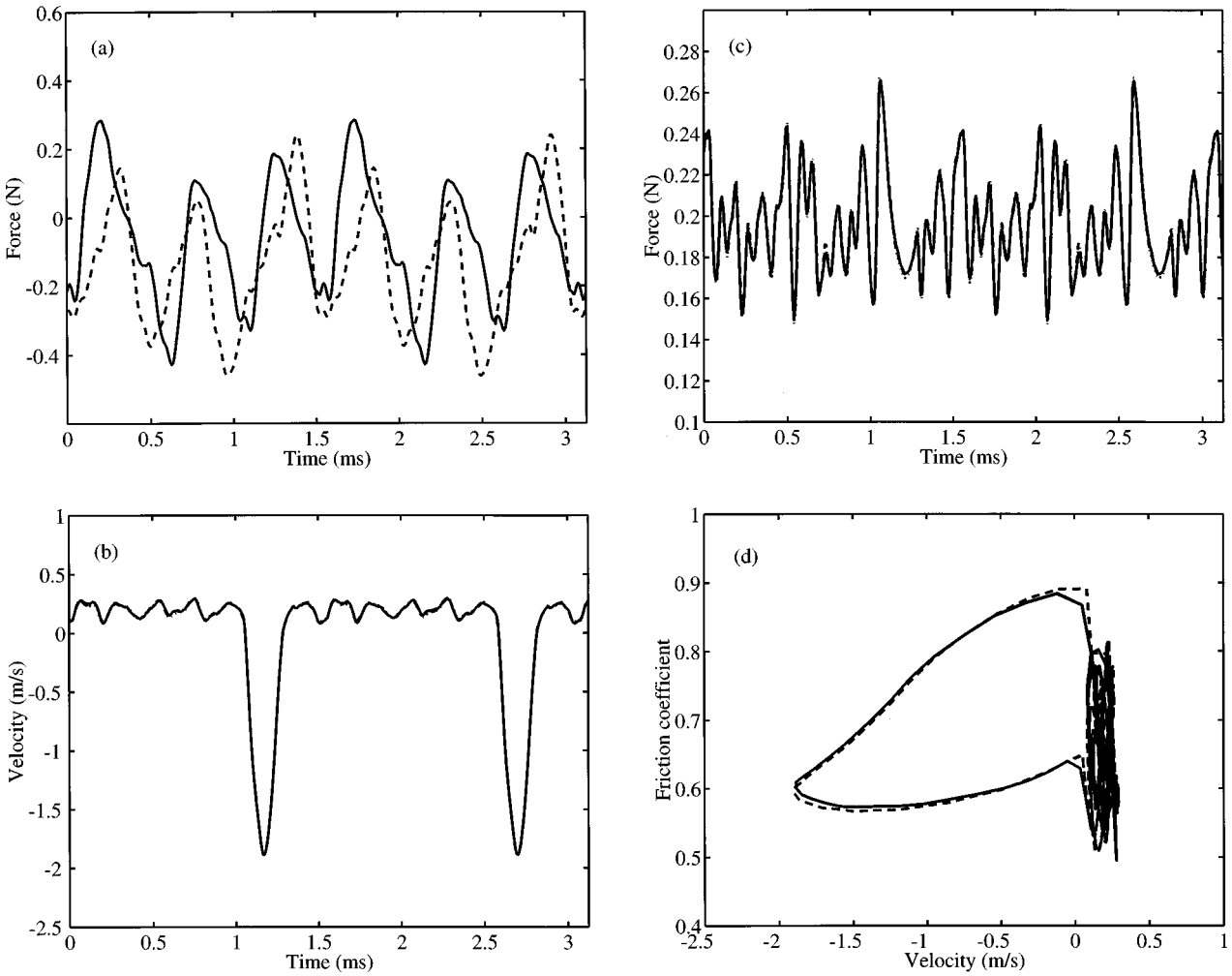

FIG. 6. Results of analysis using simulated bowing-string motion as described in the text, presented in the same form as Fig. 3: (a) forces at the string's terminations; (b) waveforms of the deduced bowing-point velocity from Eqs. (1); (c) waveforms of the deduced bowing-point friction force from Eqs. (3); and (d) velocity/force trajectory of the data shown in (b) and (c). In (b) and (c) the two versions of the deduced waveforms are plotted with solid and dashed lines, while the correct waveforms from the simulation are plotted dotted. In (d) the correct trajectory obtained from the simulation is shown dashed, while the deduced trajectory is shown solid.

lated pluck test. The procedure for time-domain reconstruction of experimental results was then applied, exactly as it was used with experimental data. Results pertaining to the periodic part of the response are shown in Fig. 6, in the same format as those of Fig. 3, with the same axis scalings.

Although it does not particularly matter for the purpose of checking the accuracy of the reconstruction procedure, it is encouraging to see that the simulation has resulted in very similar waveforms to those seen in the experiment. The same regime of oscillation has been chosen by the model string, from among the many which are possible in principle. The ''termination force'' signals, shown in Fig. 6(a), are of similar magnitude and form to those of Fig. 3(a). The reconstructed velocity waveforms, in Fig. 6(b), show stick-slip motion very similar to Fig. 3(b). In the case of the simulation, there is no doubt that the motion really does involve sticking, and that the oscillatory velocity signal seen during the sticking intervals is exactly compensated by torsional motion. Whether this is entirely true for the experimental string will be considered in the next section. The precise form and frequency content of the oscillations during sticking are somewhat different from those in the simulation, which may arise from errors in the assumed friction model or from incorrect values for the torsional properties of the string, especially the frequency-dependent torsional damping, since there is no reliable published measurement of this quantity for any violin E string.

The two versions of the reconstructed velocity waveform from Eqs. (1), shown as solid and dashed lines, also compare well with the exact answer, which was stored during the simulation and is superimposed here as a dotted line. The same is true of the force waveforms, shown with the same plotting conventions in Fig. 6(c). In the simulation, the termination forces have the correct dc level, so that the reconstructed force has a dc level which is missing from Fig. 3(c). Apart from this, the magnitude of the oscillating component of the force is rather bigger for the measured data. However, a careful comparison of Figs. 3(c) and 6(c) shows a very good correspondence of the pattern of major features. In both cases the largest positive value of the frictional force occurs at the onset of slipping, exactly as one would expect

since it is presumably the occurrence of a high force which causes slipping to occur.

As shown by Fig. 6(d), when the reconstructed results are plotted in the force/velocity plane a hysteresis loop is seen, similar to that generated by the measured signals, and circulating in the same counterclockwise sense. The ''correct'' answer from the simulation is shown dashed. This matches the reconstructed version quite accurately. Note that this comparison draws attention to fine details of the force and velocity waveforms during the intervals of slipping only. During sticking, the force fluctuates while the transverse velocity of the string stays approximately constant, resulting in the patch of ''scribble'' to the right of the figure. If the surface velocity, rather than the center velocity, had been used for the horizontal axis, this patch would have appeared as a single vertical line.

These results can be combined with those from the previous section to give a good idea of the overall accuracy of the reconstruction process. A quantitative discussion of this issue requires comparisons between waveforms which are very similar to the eye, so that a numerical measure of difference is required. Various measures are possible, leading to similar conclusions: the following discussion is couched in terms of a normalized rms value of the difference of force waveforms:

$$\Delta = \left[\frac{\Sigma_j (f_j^{(1)} - f_j^{(2)})^2}{\Sigma_j f_j^{(1)^2} + \Sigma_j f_j^{(2)^2}} \right]^{1/2}, \tag{12}$$

where $f_j^{(1)}$ and $f_j^{(2)}$ $(j=1,\ldots,N)$ are the sampled values of the two waveforms being compared. Both waveforms are zero-meaned before this computation. This normalization produces the value unity for uncorrelated signals. Force rather than velocity is chosen because differences are shown more conspicuously, and because the determination of force is the main objective of this study.

By this measure the rms difference between the two versions of the force waveform shown in Fig. 6(c) is $\Delta = 0.07$. When the mean of these two waveforms is compared to the true force from the simulation, the difference is $\Delta = 0.042$. Numbers of this order set a limit to the accuracy which can be expected from the reconstruction method in its current form—the simulated data has no measurement noise, and the underlying dynamical model matches the assumption of the theory used here, so that the differences found here are due to the processing alone. It is, of course, possible that the details of the processing could be improved to reduce these errors further.

The calculated difference of the two force waveforms shown in Fig. 3(c) is $\Delta = 0.20$. It is not surprising to get a bigger difference than for the simulated results, since the experimental results have several additional sources of error: measurement noise, possible misalignment of the two force sensors with respect to the plane of motion, incorrect representation of the transmission function $d(t)$ and its inverse, neglect of the reflection function $r(t)$, and so on. However, one would tentatively conclude from the magnitude of the difference that the mean of the two force estimates might be within 10% or so of the true force. When the comparison is made of the two versions of the force waveform reconstructed by the frequency-domain method, used in Fig. 5, the result is $\Delta = 0.29$. The difference is somewhat bigger than that found with the time-domain method, suggesting that additional errors arise in this approach, probably from noise introduced in frequency ranges where the expressions in the denominators of Eqs. (10) have small magnitude. The time-domain method, in which deconvolution is achieved by the time-reversal trick, does not involve any comparable mechanism of amplifying noise.

IV. RECONSTRUCTION OF TORSIONAL MOTION

The underlying purpose of these experiments is to elucidate the physical mechanisms and behavior of friction at the rod–string contact. It has been shown that the method is capable of giving reasonably convincing versions of the waveforms of friction force and string transverse velocity. However, for a detailed discussion of the micromechanics of friction, the relative motion of the two surfaces is needed. This is somewhat obscured by torsional motion of the string, which cannot be directly observed by the method described here. It would be useful to obtain at least an estimate of the torsional motion.

We can do this by combining the friction force already determined with a theoretical model of torsional response. It is straightforward to convert part of the simulation program used to generate the data of Fig. 6 to this purpose. The average of the two versions of the friction force computed by the time-domain method is taken as the best available estimate of force throughout the transient, and this used as input to a linear model of torsional response. The model operates in the time domain, using constant-Q reflection functions.[16] It should be emphasized at the outset that there is no direct experimental support for this particular form of reflection function for a solid steel string. The most relevant data on torsional behavior of musical strings came from studies of cello strings, which all had a core+wrapping construction. For these strings it was shown that the first few torsional modes were harmonically spaced to reasonable accuracy, and had approximately constant Q-factors.[16] Constant-Q reflection functions give the simplest way to reproduce this behavior.

The model requires as input parameters the torsional wave speed, impedance, and damping. We have reasonable first estimates for the first two of these quantities, based on the standard elastic properties of steel wires. The damping can only be guessed: a number of the order of tens would be consistent with existing data. All these values can be adjusted by searching in the vicinity of the initial estimates, with the aim of minimizing the fluctuation of aggregate velocity, transverse plus torsional, during a typical interval of sticking. If the model were perfect and the string were truly sticking to the rod during these intervals, it should be possible to reduce these fluctuations to zero.

Not surprisingly, it is not possible to achieve this perfect match, but encouraging results can be obtained. The most striking illustration comes from a different experimental run from the one examined so far. When the bowing point was close to $\beta = \frac{1}{4}$, data was obtained which led to a recon-

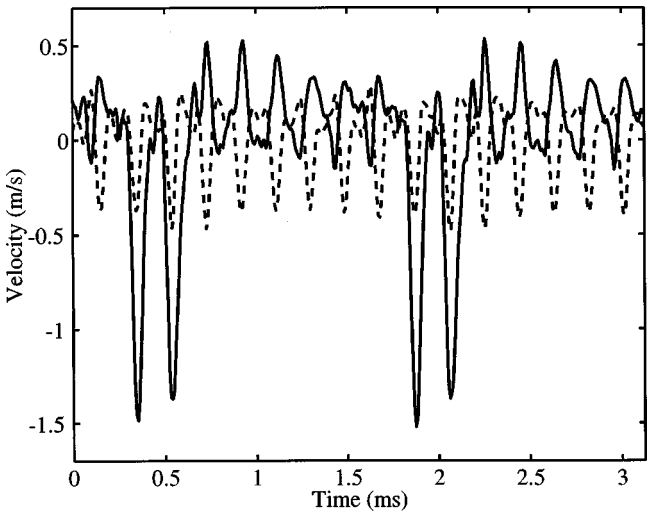

FIG. 7. Reconstructed bowing-point velocity (solid line) and reconstructed surface velocity due to string rotation (dashed line) as described in the text.

structed string-center velocity waveform with unusually large fluctuations of velocity during sticking. A typical portion, where the motion was almost periodic, is shown as the solid line in Fig. 7. The dashed line superimposed on this figure shows the best estimate of the reconstructed torsional motion—it is clear that the waveform is rather close to a mirror image of the transverse velocity during sticking, so that the sum of the two has much smaller fluctuations. In this case, it is easy to believe that at least the majority of the observed velocity fluctuation is caused by torsional motion. The best-fitting torsional wave speed in this case was close to eight times the transverse wave speed, which accounts for the large amplitude of torsional motion. With $\beta=\frac{1}{4}$ the second harmonic of the frequency of ''Schelleng ripples'' [9–11] is approximately in resonance with the fundamental torsional mode. The fitted estimate of torsional speed is consistent with the expected result based on typical handbook values for the density and shear modulus of steel, bearing in mind that the precise values of these quantities are not available for the (unknown) particular steel of this E string.

This procedure for estimating torsional motion using the reconstructed force waveform has been applied to other cases as well. In all cases, the magnitude of the velocity fluctuations during sticking is predicted well, and the detailed motion is matched reasonably well. Also, the best fit is always obtained when the torsional wave speed is around eight times the transverse wave speed, suggesting that this admittedly indirect observation of torsional speed is indeed approximately correct. However, the estimated waveform of torsional velocity should not be regarded as accurate in all details. It is based on a theoretical model, involving the constant-Q reflection functions, for which there is only relatively sketchy validation, and the resonant nature of the torsional waves on the string makes the fine details very sensitive to errors in the friction force waveform. A similar reconstruction can be made for the transverse motion, using the inferred friction force waveform and the corresponding theoretical model for transverse motion. In this case the results can be compared with the known answer, and they turn

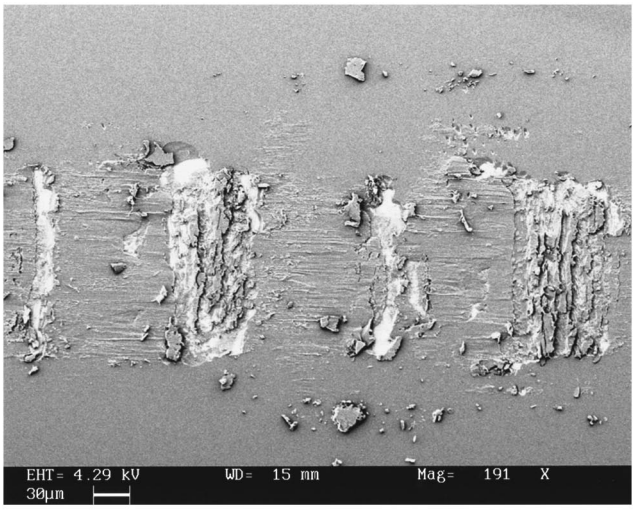

(a)

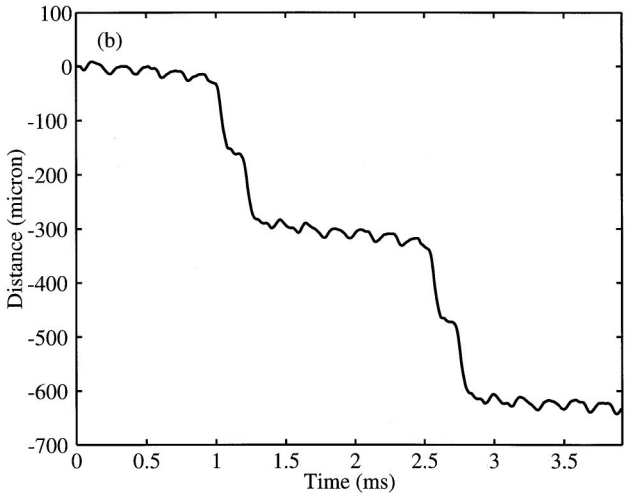

FIG. 8. (a) Scanning electron micrograph of part of the track left in the rosin surface after the bowing run used to compute Fig. 7. (b) Waveform of distance along the glass rod moved by the center of the string during this run, deduced by integration of the solid curve in Fig. 7.

out to be rather poor, presumably because the transverse reverberation time is much longer. It should be noted that the accuracy of the frictional force in this example is probably significantly lower than was the case for the results shown in Fig. 3. When the difference of the two versions of the force is computed the result is $\Delta=0.36$, much larger than the previous case.

We can obtain some further information about the motion in this case by looking at the track left in the rosin surface after the experiment. As has been shown previously,[17] stick-slip events leave tell-tale marks in the rosin. In this case, a section of the rod from the test was coated with a thin layer of gold and examined in a scanning electron microscope. A typical portion of the friction track is shown in Fig. 8(a). The details should be compared with the time history of relative displacement between string and rod, shown in Fig. 8(b), obtained by integration of the difference between the velocity waveform shown in Fig. 7 and the known rod speed. The motion has two slips per cycle, with approximately equal slip distances. These are separated by intervals of sticking which have left conspicuous scars in the

rosin surface. One of the intervals of sticking is very short, leaving a narrow mark each time. The longer interval of sticking involves, as we have just seen, large amplitudes of torsional motion. This has resulted in relatively large scars on the rosin surface, where the material has been churned up. Figure 8(b) also shows that some ''creep'' has occurred during these long intervals of ''sticking:'' the torsional oscillations are superimposed on a nonzero steady velocity difference. The slips show in the picture as relatively smooth surface marked by lines parallel to the slip direction. These are evidence of large deformation in a thin surface layer of the rosin, qualitatively compatible with the theory advanced by Smith and Woodhouse involving shearing of a layer of rosin, generating significant heating in the process.[4]

Much might be learned about the physical mechanisms underlying the friction force deduced by the reconstruction process by examining the details of such friction tracks. Examples can be found of brittle fracture, ductile failure, and delamination failure at, or close to, the rosin/glass interface. Information can be gleaned about the thickness of the rosin layer and of the actively deforming layer during slipping, and about the interaction of torsional motion, heating of the rosin, and creep deformation. These are all topics for later stages of this continuing investigation. For the moment, it is sufficient to deduce from this figure that the reconstructed velocity waveform matches very well, both qualitatively and quantitatively, the pattern of physical traces left in the rosin surface.

V. CONCLUSIONS

A method has been presented for reconstructing the waveforms of friction force and string velocity on a bowed string, at the point of bowing. The method uses measurements of the transverse forces at the two terminations of the string, together with calibration data from the results of a controlled pluck of the string. It has been shown to perform well on simulated signals, where the answer is known in advance. It also performs well, so far as can be established, on real data obtained from a laboratory rig in which a violin E string is bowed with a rosin-coated glass rod. The velocity waveforms obtained by this procedure can be checked by independent methods, and always seem to be reliable. The friction force at the contact point cannot be measured directly, so this procedure provides a totally new source of data to check and refine theoretical models of the process of vibration excitation by friction.

The key feature of the reconstruction method is that the measured force signals must be propagated both forwards and backwards in time and space to establish what happens at the bowed point. Working forwards in time involves convolution with a suitable function to describe the dispersive propagation characteristics of waves on the string. Working backwards involves deconvolution with this function, potentially a more difficult undertaking. Two approaches have been illustrated. The first operates in the time domain and achieves the deconvolution using the fact that if we are only dealing with dispersion and not dissipation, the effect of propagation is represented by an all-pass filter, whose inverse can be obtained by simple time reversal. The second method, which in principle could allow for dissipation and more complicated reflection processes, is carried out in the frequency domain and so is restricted to data which is fairly accurately periodic. Both methods have been shown to work well, and to give consistent answers when both are applicable. For the particular system used in the measurements, the time-domain approach is more versatile.

The results are in good qualitative agreement with measurements of the frictional characteristics of rosin from a different stick-slip oscillator.[4] They show very clearly that the friction force cannot be expressed as a function of the instantaneous relative sliding velocity, a model which has been used almost universally in earlier studies of the motion of a bowed string. When force is plotted against sliding velocity, a hysteresis loop is obtained rather than a single-valued function—an example is shown in Fig. 3(d). It has been suggested[4] that a better model of rosin friction involves the temperature at the contact point. Thermal inertia of the material around the contact results in a time lag between temperature and sliding velocity, which, it is argued, is responsible for the observed hysteresis. Simulation of stick-slip motion using a model based on this idea, together with parameter values appropriate to the experimental rig, produces encouraging qualitative agreement with the measured results (see Fig. 6).

This idea is supported by another aspect of the measurements reported here. After it has been used, once only, in the bowing rig, the glass rod can be examined in the scanning electron microscope. A track is left in the rosin surface which contains a great deal of information about the history of deformation and friction in the rosin layer. An example is shown in Fig. 7(a). Each interval of sticking leaves a conspicuous scar on the rosin surface. During slipping a thin layer of highly-deformed material is visible, as expected from the thermal model. The history of relative displacement between string and rod, revealed by the track, is in good quantitative agreement with that deduced from the velocity waveform.

With this technique we expect to be able to correlate the friction force and the string velocity with position along the friction track and thus correlate the morphology of the interfaces of the wear track with the forces and velocities associated with those events. We will be able to vary both the substrates and the intermediate material—rosin here—to probe how material properties control stick-slip oscillations in this system. This work will lead to a better understanding of the interaction of autonomous dynamical systems and the frictional forces that drive them. We should ultimately be able to provide information which will lead to a more accurate and reproducible production of rosin for bowed-string musical instruments.

ACKNOWLEDGMENTS

The authors thank Claire Barlow and Alan Heaver for their invaluable help with the technology and interpretation of the scanning electron micrograph.

[1] W. Bachmann, *The Origins of Bowing and the Development of Bowed Instruments up to the 13th Century* (Oxford U. P., New York, 1969).

[2] H. Helmholtz, *On the Sensations of Tone* (Dover, New York, 1954).
[3] J. H. Smith, ''Stick-slip vibration and its constitutive laws,'' Dissertation, University of Cambridge, 1990.
[4] J. H. Smith and J. Woodhouse, ''The tribology of rosin,'' J. Mech. Phys. Solids **48**, 1633–1681.
[5] R. T. Schumacher, ''Measurement of bow force,'' Proceeding of the Institute of Acoustics **19**(5), 43–48 (1997).
[6] R. T. Schumacher, ''Studies in bowing-point friction in bowed strings,'' J. Acoust. Soc. Am. **103**, 2915(A) (1998).
[7] J. Woodhouse, ''On the playability of violins. Part I: reflection functions,'' Acustica **78**, 125–136 (1993).
[8] C. V. Raman, ''On the mechanical theory of vibrations of bowed strings,'' Indian Assoc. Cult. Sci., Bull. **15**, 1–158 (1918).
[9] J. C. Schelleng, ''The bowed string and the player,'' J. Acoust. Soc. Am. **53**, 26–41 (1973).
[10] L. Cremer, *The Physics of the Violin* (MIT, Cambridge, MA, 1985).
[11] M. E. McIntyre, R. T. Schumacher, and J. Woodhouse, ''Aperiodicity in bowed-string motion,'' Acustica **49**, 13–32 (1981).
[12] G. Weinreich and R. Caussé, ''Elementary stability considerations for bowed-string motion,'' J. Acoust. Soc. Am. **89**, 887–895 (1991).
[13] J. Woodhouse, ''On the stability of bowed string motion,'' Acustica **80**, 58–72 (1994).
[14] M. E. McIntyre, R. T. Schumacher, and J. Woodhouse, ''On the oscillations of musical instruments,'' J. Acoust. Soc. Am. **74**, 1325–1345 (1983).
[15] R. T. Schumacher and J. Woodhouse, ''The transient behaviour of models of bowed-string motion,'' Chaos **5**, 509–523 (1995).
[16] J. Woodhouse and A. R. Loach, ''Torsional behaviour of cello strings,'' Acustica—Acta Acustica (in press).
[17] R. T. Schumacher and S. Garoff, ''Bowing with a glass bow,'' J. Catgut Acoust. Soc. **3**(2), 9–17 (1996).

Evolution of the vibrational behavior of a guitar soundboard along successive construction phases by means of the modal analysis technique

M. J. Elejabarrieta[a)]
Departamento de Física Aplicada II, Universidad del País Vasco, Apdo. 644-48080 Bilbao, Spain

A. Ezcurra
Departamento de Física, Universidad Pública de Navarra, 31006 Pamplona, Spain

C. Santamaría
Departamento de Física Aplicada II, Universidad del País Vasco, Apdo. 644-48080 Bilbao, Spain

(Received 15 November 1999; accepted for publication 20 March 2000)

The crucial piece of a craft guitar is the soundboard since it determines the quality of the sound given by the instrument. From the initial phase (the gross plate with no hole) until the last construction phase (the plate with the full structure) several stages are followed to modify the dynamic behavior of the structure and hence the acoustic response of the final guitar. The aim of this work is to analyze the effect of each modification on the vibrational response of the plate. With this in mind, an experimental modal analysis of all the construction phases has been performed in the low frequency range under free conditions. The response of the plate in each stage is defined by vibration patterns, resonance frequencies, quality factors, and admittance curves. © *2000 Acoustical Society of America.* [S0001-4966(00)00307-6]

PACS numbers: 43.75.Gh [WJS]

INTRODUCTION

String instruments have attracted the interest of researchers for centuries and much work has been dedicated to the study of different aspects of these acoustic systems from the selection of materials to the radiation of the sound. One of the main difficulties in studying the performance of these instruments derives from the fact that they are the result of a craft industry which is quite often not very systematic and fixed. It is well known that small changes in the craft manufacture may cause big changes in the resulting instrument,[1] which gives endless trouble to researchers. Hence, the importance of a good knowledge of the contribution of each modification to the final vibrational behavior of the instrument.

Several experimental and computational techniques have been applied in this field, to study the mechanical vibrational properties. Among these techniques, modal analysis provides quantitative results that can be compared with those obtained by other procedures, such as finite element methods. The aim of the present work is to investigate in depth the dynamic behavior of the guitar soundboard under free conditions. It should be pointed out that several qualitative studies have been carried out, using holographic techniques, for example,[2,3] but not quantitative results are found for guitar plates under free conditions.

This study is part of a more extensive work involving the whole resonance box and box-fluid coupling. Furthermore, we try to determine the outcome, from a physical point of view, of all the different stages followed by the luthier in the construction of the soundboard, which is the element of the guitar that to a large extent determines its musical-acoustic quality. Therefore, it is of great interest to understand how the construction process influences the dynamic behavior of the guitar. Although the soundboard does not work freely when it is part of a guitar, it is made separately by the luthier and it was interesting to know the influence of every step of the whole manufacturing process on the eventual guitar. For this reason we have tried to follow the real process that takes place when a guitar is being made.

I. CONSTRUCTION PHASES OF THE SOUNDBOARD

The construction of the soundboard of a high quality classical guitar consists of several stages. First, the choice of the wood is very important for the acoustic quality of the instrument. After a previous dynamic study of the materials most commonly used for plates,[4] we decided to employ cedar, and our luthier chose a good piece of Canadian Cedar. This species is characterized by having a low density (342 Kgm^{-3}) and a high flexibility. As a guarantee of the quality of the plate (and subsequently of the whole instrument) the following requirements were accomplished:

- the grain was parallel to the longitudinal axis of the plate, preserving the symmetry;
- the grain was as fine as possible, to gain homogeneity; and
- the wood was old enough to have stable physical properties.

The main construction stages, as decided by the luthier, are described below. A modal and dynamic analysis was carried out at each stage in order to evaluate the effect of each transformation. The most relevant physical characteristics at the end of each stage are summarized in Table I.

[a)]Present address: Departamento de Mecánica, Mondragon Unibertsitatea, 20500 Mondragon, Guipuzcoa, Spain.

TABLE I. Construction stages of a craft soundboard.

Stages	Thickness (mm)	Mass (g)	Characteristics
$s1$	3.50	166.5	• Unsmoothed wood. • No orifice. • Approximated contour.
$s2$	2.85	143.5	• Smoothed wood. • Preliminary orifice: diameter=10 mm. • Definite contour.
$s3$	2.70	130.0	• Definitive mouth: diameter=85 mm. • Zuncho.
$s4$	2.70–2.00	123.0	• Variable thickness.
		149.0	• Two transverse bars.
$s5$	···	$b_1=14.0$ $b_2=12.0$	
		170.0	• Fan:
		$r_1=3.2$	Seven rods in rough state.
$s6$	···	$r_2,r_3=6.4$ $r_4,r_5=6.0$ $r_6,r_7=5.4$	Symmetrical distribution: Torres.
		165.2	• Definitive fan:
$s7$	···	$r_8,r_9=0.8$	Two additional rods. Well shaped rods.

After choosing the wood, the joining of the two halves, parallel to the grain, was considered as the first stage ($s1$). The contour was nearly equal to the definitive one, but 1 cm larger. The two wooden halves forming the plate must come from contiguous cuttings of the trunk, ensuring that the plate will be symmetric with respect to the grain distribution. At this point the wood was not smoothed and so the thickness of the plate was not uniform.

Next, the plate was smoothed and the contour given the final form ($s2$). This implied a uniform loss of mass over the whole surface of the plate. Also an initial orifice (10.0 mm diameter) was made through the plate in this phase, that caused a very small mass decrease (0.33%) in comparison with the total diminution of mass in this stage. The orifice was located at the central position of the future mouth.

In the third stage ($s3$) the mouth of diameter 85.0 mm was cut out. To avoid a split in the direction of the grain, a hoop (''*zuncho*'') was placed around the mouth. This zuncho is made of polychromatic woods, and, apart from its mechanical function, is decorative. The contour was not modified with respect to the previous phase, but the thickness was reduced by 5%. In this phase, the variation in mass with respect to ($s2$) is due to the definitive size of the mouth (45%) and to the decrease in thickness.

In the following construction stage ($s4$) the thickness was varied from point to point. The performance of this phase depends on the luthier and sometimes is not essential. As can be observed in Fig. 1, the upper part of the plate, above the mouth, maintains the thickness of the previous stage, but in the lower part the thickness of the plate is progressively reduced toward the edge. The thickness was measured on the 115 response points with a dial indicator (accuracy 0.01 mm). The plate was pressed slightly on a flat and smooth surface to measure the correct thickness, avoiding the casting.

Afterward stage ($s5$) took place. Some additional structures were provided to the plate. In particular, two bars were placed perpendicular to the grain, respectively, over and below the mouth. These bars were of spruce (density 460 Kgm^{-3}). The upper bar ($b1$) had a constant rectangular cross section. The low bar ($b2$) had also a rectangular section, but its height was reduced linearly from the two ends to the center of the bar. The form and dimensions of these two structures are shown in Figs. 2(a) and 2(b). The grain of the bars was parallel to the longitudinal axis and so perpendicular to the grain of the plate. These bars implied a mass in-

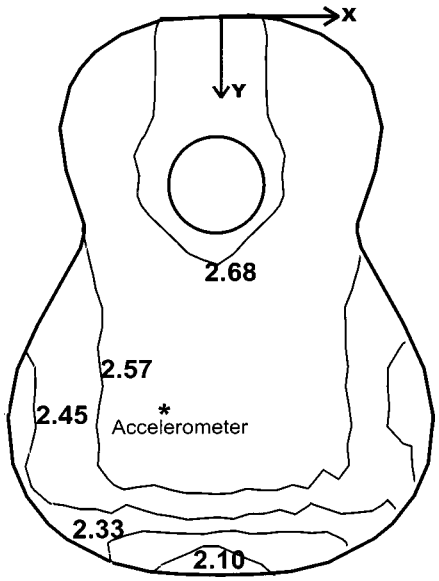

FIG. 1. Variable thickness (mm) in stage ($s4$). The position of the accelerometer and the coordinate axes are indicated.

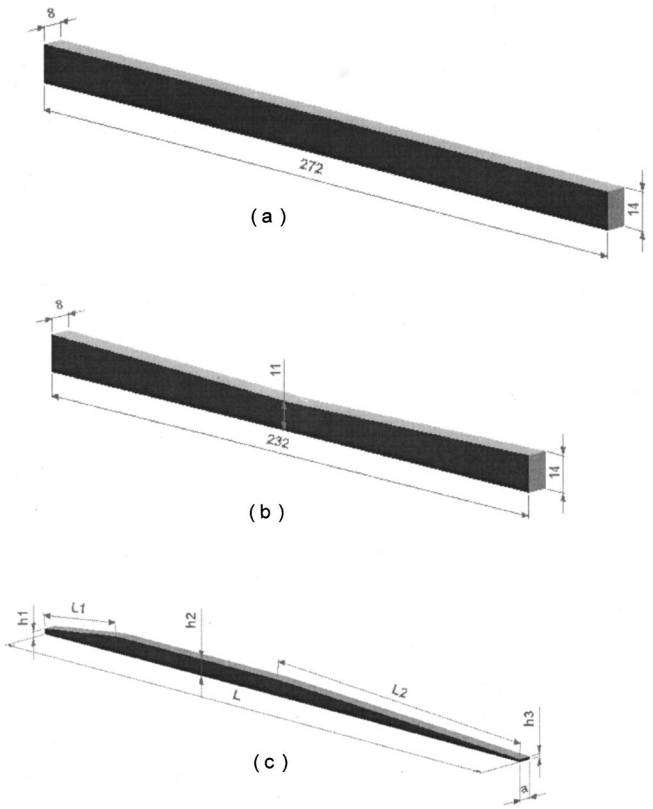

FIG. 2. Shape and size (mm) of: (a) upper bar; (b) lower bar; (c) rod.

TABLE II. Rod sizes (mm) at ($s7$) stage. The symbols are described in Fig. 2(c).

	r_1	r_2	r_3	r_4	r_5	r_6	r_7	r_8	r_9
a	5	5	5	5	5	5	5	3	3
h_1	2	2	2	2	2	2	2	6	6
h_2	6	6	4	4	4	4	4	6	6
h_3	1	1	1	1	1	1	1	6	6
L_1	35	30	30	30	30	30	30	⋯	⋯
L_2	120	115	115	110	110	85	85	⋯	⋯
L	235	233	233	218	218	198	198	106	106

crease of 22% with respect to the mass of the plate.

In the next stage ($s6$) seven of the nine rods of the fan were placed on the plate. The rods were arranged in the classic way, according to the *Torres* distribution. At this step, the rods had a constant section and their length was the final one. However, they had not been given the correct shape yet, but still offered a rough aspect. All the rods had identical section, but had different lengths [see Fig. 2(c) and Table II] and were made of the same type of wood as the bars (spruce). The distribution of the rods was symmetric in relation to the central longitudinal axis of the plate, increasing the slope angle with respect to it. Figure 3 shows these positions and the angles.

In the last stage ($s7$) of the construction of the soundboard two symmetrical rods were placed ($r9$), on the lower part of the plate. Their section was rectangular and uniform and their positions and slopes can be seen in Fig. 3. Also, in this phase the other rods were given the definitive profile. Their sizes are shown in Table II. The seven rods forming the fan had a similar shape, but each pair of symmetrical rods were of different size. The final mass of the soundboard with all the internal structures was 165.2 g, which means that, despite the addition of the last two rods, the weight of the plate was reduced by 2% with respect to the previous phase.

Finally it must be noted that the bridge has not been included in this study, although it is an essential part of the guitar top, because our craftsman is used to glue it after the box is assembled.

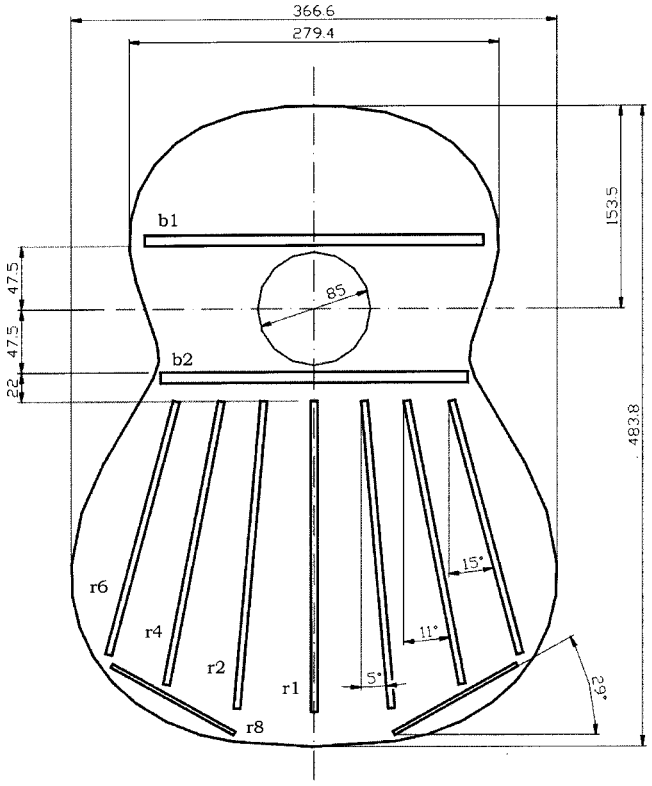

FIG. 3. Definitive shape and size (mm) of the guitar soundboard including the position of the internal structures, according to the *Torres* distribution.

II. EXPERIMENTAL SETUP

The experimental method used in this work was the Modal Analysis technique.[5–7] Among the available applications the Frequency Response Function (FRF) was chosen. The structure was put into vibration by a transducer hammer acting on successive points, and the response was recorded at one fixed point (the so-called Roving Hammer Method) through an accelerometer. The accelerometer was attached to the structure by a thin wax layer. This type of joint avoids relative movements between the structure and the transducer and optimizes the range of use of the accelerometer since its resonance frequency remains constant.

A Brüel & Kjaer type 4500 accelerometer (frequency range: 3 Hz to 16 kHz, sensitivity: 0.3 pC/ms^{-2}, weight: 3.5 g) was used, as these characteristics as well as its resolution were the most suitable for the system. The miniature transducer hammer was a Brüel & Kjaer model 8203 [sensitivity: 3.47 pC/N, weight (tip): 3.2 g] compatible with the accelerometer. The hammer signal was obtained by making it act on the woods and was flat over the frequency band of interest.

The FFT analyzer was a two-channel Brüel & Kjaer mod. 2148 (0.7 Hz–25.6 kHz, resolution $=0.1$ dB). The accelerometer and the hammer were connected directly to the two channels. In the case of the hammer, a power unit was not necessary, for the analyzer had an integrated power circuit. The two channels took measurements simultaneously.

The frequencies studied were in the 0 to 800 Hz range in all cases, although an estimation of the modal parameters was carried out in more reduced bands whose ranges were determined by the different structures and situations analyzed, whereas the resolution was 1 Hz.

An analysis of the measurements was performed by means of specific software for experimental modal analysis, CADA-PC (LMS, Leuven Measurement System). As the graphic performance of this software was rather poor, Micro CalOrigin software was used for graphic representations. Admittance curves (and related parameters), vibration patterns, natural frequencies, and quality factors were obtained by

means of LSCE (Least Square Complex Exponential) and LSFD (Least Squares Frequency Domain) techniques.[8] Once the modal parameters had been obtained, they were validated with the aid of several techniques such as the reverse synthesis of FRFs, the MAC (Modal Assurance Criterion), the MP (Modal Participation), and the MPC (Modal Phase Colinearity).

The system under study was a guitar soundboard in the successive stages of its construction, whose boundaries were supposed to be free. Theoretically, with free boundary conditions the six rigid solid modes should have an associated frequency of 0 Hz. Nevertheless, in practice it is not possible to work with a structure of utterly free boundaries because it needs to be hung in some way. In order to obtain approximately free experimental boundary conditions, very flexible bands were used so that the first six modes had frequencies very low with respect to the structure frequency. Four rubber bands were used and the resulting resonance frequencies were around 1–2 Hz. All these bands were identical and equally stretched. They were attached to the edge of the soundboard, on the upper part of the longitudinal axis. It was found that any changes in the stress of the bands or in the support points of the soundboard did not alter significantly the response of the structure. The support point minimized the influence of this suspensions, since it was located on the nodal line of the shear modes, and many transverse flexural modes also had coincident central nodal line. A preliminary test was carried out to compare the responses with those obtained when fixing the opposite point in the lower zone. The results were indistinguishable, except for points very close to the fixed one in each case. Finally, we chose the upper point because that zone of the plate becomes more rigid when other structures are added and, consequently, it is not so interesting from a dynamic point of view.

Both the excitation and the response were perpendicular to the plate, the most important direction regarding vibration and acoustic radiation of the final instrument. The response point was located at the position of the bridge, next to the bass bar coordinates (-6 cm, 34 cm), and 115 excitation points were distributed over the plate. Keeping the accelerometer fixed, the mass distribution was constant throughout the analysis. The admittance curves were obtained at a lateral point with coordinates (12 cm, 42 cm). This point was selected because it did not coincide with any nodal line, at least in the first stages of construction. [Note: the *y*-axis is the symmetry axis, and the point (0,0) is at the upper edge.]

The number and location of the selected measurement points (maximum distance 5.85 cm; minimum distance 2.82 cm) covered the frequency range as well as the number of expected modes, each node being connected with its neighbors (eight connections for each interior node). Prior to the experimental analysis, a finite element analysis was carried out to validate the boundary conditions and the suitability of the excitation and response points.

Finally, it was experimentally determined that the system met the Maxwell's reciprocity principle by interchanging the accelerometer and hammer positions. This allowed us to consider that we had one excitation point (at the accelerometer position) and multiple response points (the 115 impacts). Then the system could be described as having one input and multiple outputs.

III. RESULTS AND DISCUSSION

The modes were named as (m,n), m being the number of transverse half-waves and n the number of longitudinal half-waves on the plate.[9] In the latter case, in patterns with only one line, the modes were designated with a plus sign $(+)$ above the mouth and a minus $(-)$ below the mouth, depending on their situation.

A. Dynamic behavior of the plate without any added structure

Now the evolution of the dynamic behavior of the soundboard is to be described accounting for the vibration modes, the natural frequencies, the quality factors, and the cross admittance of the harmonic plate in the first construction stages of a crafted guitar. This section evaluates the contribution of each transformation, prior to the addition of the structures, from the vibrational point of view.

The estimation of the modal parameters was global, since each modal analysis was made up of the 115 response functions. Therefore, the reported natural frequencies, the vibration modes, and the quality factors do not depend on the particular response point.

The vibration modes obtained had a normal character, since their MPC was between 91% and 99%. This index indicates that the imaginary part of the pattern is practically negligible compared to the real part, and so the relative phase for the 115 degrees of freedom was 0 or 180 degrees. Consequently, the modes can be considered as normal, with proportional viscous damping.

1. Vibrational patterns, natural frequencies, and quality factors

In the first four construction phases the harmonic plate is subjected to a decrease in thickness and so a decrease in mass. Taking into account the decrease in each natural frequency it can be concluded that the decrease in thickness affects the stiffness more than the mass of the structure.

The natural frequencies of the eight vibrational patterns undergo changes through stages $(s1)$ to $(s4)$ and because of this we limited the number of modes instead of the frequency band to be analyzed. Furthermore, the patterns were ordered as in the first phase of construction, overlooking the particular frequency value in the successive construction phases. In this way, the evolution of the modal patterns along the construction process can be clearly seen.

In Fig. 4 the eight lower vibration modes are shown in phases $(s1)$ and $(s4)$, rough state and final outline with varying thickness, respectively. It can be seen that the form of the patterns is practically equal in both phases. This indicates that the mouth and the decrease in thickness do not imply any change in the form of the vibration modes, although the nodal lines are much more defined after the last modification in phase $(s4)$. This can be explained by considering that in the initial phase the plate is not smoothed and so the structure is more imperfect. The vibrational amplitude

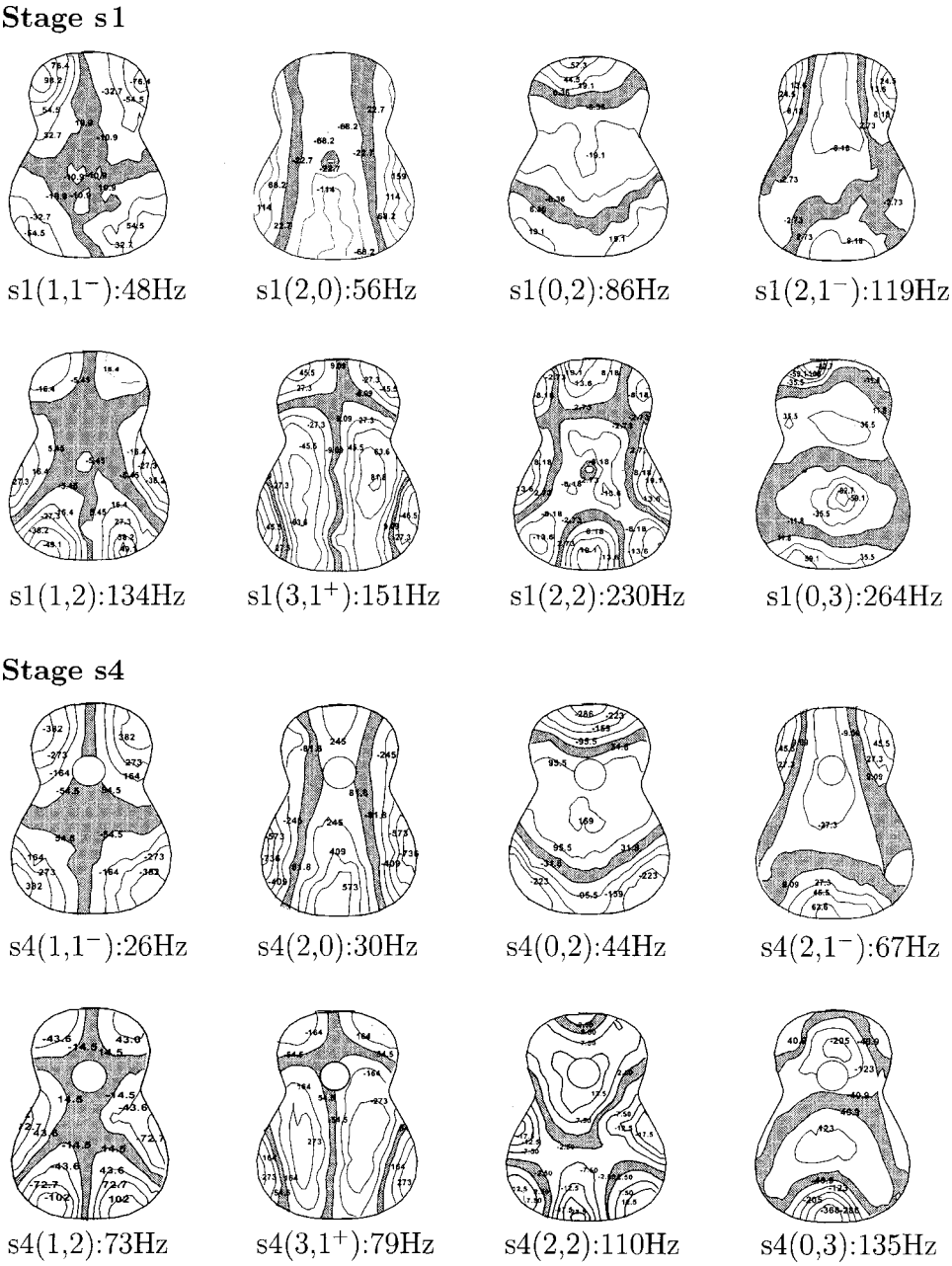

FIG. 4. Vibrational modes and natural frequencies in stages ($s1$) and ($s4$). Equal displacement lines are showed; the gray areas represent nodal zones. The vibrational amplitude of the modes could not be compared one another, since each pattern was normalized to unit modal mass.

of the modes could not be compared to one another, since each pattern was normalized to unit modal mass. Accordingly, an increase in the level line density from phase ($s1$) to phase ($s4$) can be seen in the lower zone for almost all the modes. This is due mainly to the varying thicknesses in the upper and central zones, and in the lower one, the latter showing greater mobility.

The normal modes in these first four construction phases are independent since the relationship among the different patterns has a MAC lower than 15%. This MAC index is an indicator of the influence of one pattern on another. Thus the shear mode (1,2) is more influenced by the transverse flexural patterns than by those of longitudinal flexion, owing to the slope of the transverse nodal lines at the lower part, and this will be reflected in the MAC indices. In the case of the transverse flexural modes, two groups can be distinguished, depending on their reciprocal influence: on the one hand, those presenting a longitudinal central nodal line and, on the other, those which do not present such a line. Thus a mode such as (2,0) is not affected by the (3,1+) mode, but it is affected by the (4,0) mode.

Taking into account that all the modal analyses were performed with the same reference point, located next to the position of the bass string, it is possible to establish, by means of the modal participation index, the dominant modes for that position. For the four stages analyzed, the dominant mode is (2,0). The other modes have similar contributions, except for modes (2,1−) and (2,2), whose modal participation is negligible due to the particular excitation point.

It should be noted that the construction of the mouth, in phase ($s3$), affects the form of modes presenting a notable vibration in their zone, mainly (0,2) and (0,3). In Fig. 4 it can be observed that modes with a central nodal line [(1,1−), (1,2), and (3,1+)] preserve the slope of the nodal lines. On the other hand, the rest of the patterns modify the bending

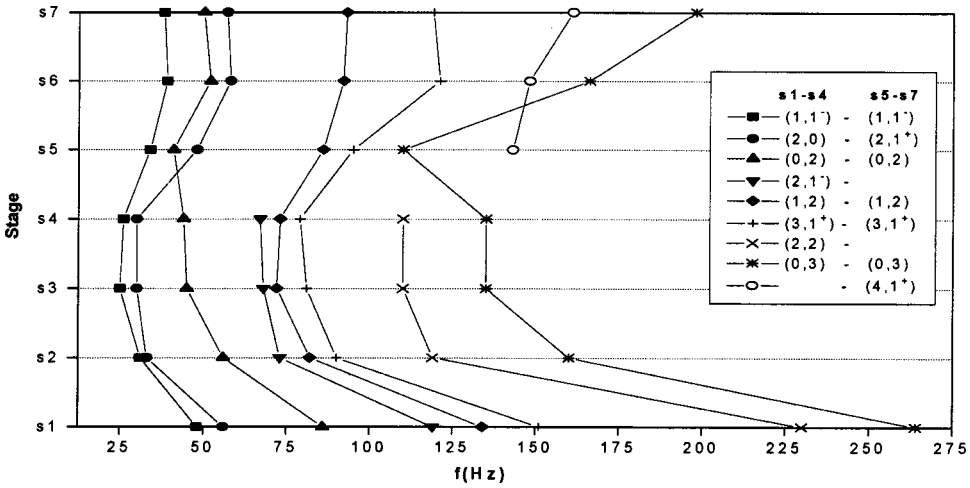

FIG. 5. Natural frequencies (Hz) corresponding to the eight lower modes in stages ($s1$) to ($s7$).

and the position of the nodal lines when the mouth is cut out in phase ($s3$).

Figure 5 shows the evolution of the natural frequencies corresponding to the eight lower vibration modes. The decrease in thickness elicits a decrease in the frequencies, mainly from the stage ($s1$) to the stage ($s2$), when mass decreases by 14% uniformly, apart from the preliminary hole. This decrease causes another decrease in frequencies of between 35% and 48%, being greater in the highest modes. Thus the decrease in thickness decreases the stiffness more than the mass. In phases ($s2$) and ($s3$) the decrease in mass is localized in the mouth zone, and this affects some of the frequencies, mainly those of longitudinal flexion, (0,2) and (0,3), and to a greater extent lower frequency modes. The relative frequency changes were between 7% and 20%. Finally, the decrease in thickness on the lower contour does not affect the frequencies between the variations obtained are smaller than the experimental precision. It was observed that modes with higher frequencies than those presented in this work were affected and tended to decrease.

Like natural frequencies, quality factors decreased substantially between stages ($s1$) and ($s4$) (see Fig. 6). The effect on the quality factors due to varying thickness—phase ($s4$), (-40%)—is remarkable, in spite of the invariability of the natural frequencies. Taking the quality factors in free boundary conditions as a quality standard,[10] it may be concluded that the plate decreases in quality over these four stages.

2. Admittance curves

Figure 7(a) shows the evolution of the cross admittance curves for the selected point (see Sec. I) from phase ($s2$) to ($s4$). A similar behavior can be observed in these admittance curves. From stage ($s3$) to ($s4$) the peaks broaden out, so the quality factors decrease in this step. Furthermore, admittance increases over the band, mainly at the high frequencies, and, moreover, the six lowest modes have a similar level, this level being higher than the one corresponding to higher modes in the three stages.

B. Dynamic behavior of the soundboard with structures

The dynamic behavior of the soundboard was substantially modified when the bars and the internal rods were added. These structures cause an increase in the stiffness of the plate without limiting its mobility. The actual position of the structures maintains the symmetry of the plate with respect to its central longitudinal axis.

In previous phases, the plate itself was transformed by the change in thickness or by removing the material of the mouth, but in phase ($s5$) the plate behavior was modified due to the addition of supplementary structures. The initial

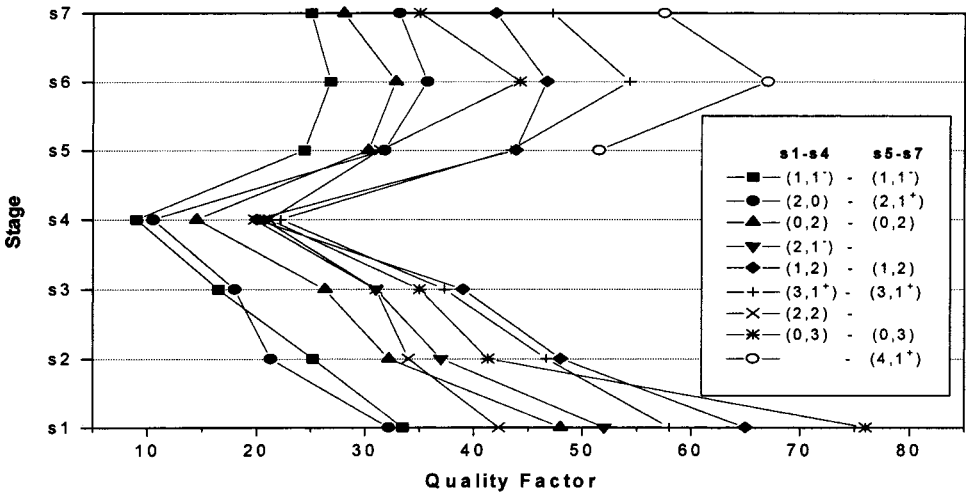

FIG. 6. Quality factors in stages ($s1$) to ($s7$).

phases imply a nearly uniform decrease in mass over the whole surface of the plate, except for phase ($s4$), when a decline in thickness was made in the lower area. Afterward, the plate recovered the previously eliminated mass, although now in a specifically located way, and, as a result, the dynamic behavior should be different from that in the initial stages.

The additional structures, from phase ($s5$) to ($s7$), consist of two parts, each one with a different function, the two transverse bars and the fan. The bars, above and under the mouth, strengthen the upper part of the plate, to endure the neck. Therefore, this zone becomes more rigid. In the lower zone, i.e., under the mouth, the emplacement of the fan and later of the bridge help the fragile plate to support the tension exerted by the strings. The literature on the subject report many fan distributions, craftsmen say, in order to improve the acoustic properties, but this literature does not offer any objective criteria on rod quantity and positions.

As already mentioned, dynamic and modal analyses were carried out during all the remaining construction phases. The results of these analyses are given below.

1. Vibrational patterns, natural frequencies, and quality factors

The results displayed have been recorded as functions of the quantity of modes, with no limit for the frequency band, because this band increases in length up to the final stage. The order is the same as that of the first stage ($s1$), as previously explained. Mode (4,1+) has also been included, for it presents a frequency lower than mode (0,3) in stages ($s6$) and ($s7$).

Figure 8 shows the first seven vibrating patterns in stages ($s5$) and ($s7$). These two stages were selected for the following reasons, respectively, phase ($s5$) to appreciate the effect implied by the emplacement of the two transverse bars, and phase ($s7$) because it is the last construction stage before the piece is assembled to form the resonance box. As can be seen, the vibration patterns change their forms when the transverse bars and the rods are added, in contrast to the first construction stages.

The first remarkable point in stage ($s5$) was the disappearance of two vibration patterns, (2,1−) and (2,2). These two modes did not reappear in the subsequent stages. When comparing the modes corresponding to stages ($s4$) and ($s5$) some changes can be seen in position and curvature for the nodal lines. As a general rule, emplacement of the transverse bars hinders the vibration in the upper zone, at least for the analyzed modes.

There are not any notable changes in the form of the patterns corresponding to longitudinal flexion, (0,2) and (0,3). The change in curvature of the (0,3) mode nodal lines should be noted, these lines becoming parallel to the transverse bars. In these longitudinal flexural modes the vibration amplitudes were similar all over the whole surface of the plate. This did not occur in previous stages, since the intermediate zone remained practically fixed.

Although the patterns are independent, some relationship (lower than 15% in the MAC matrix coefficients) between modes with the same vibrational character is still present. This is the case of the transverse flexural modes, (2,1+) and (4,1+). The emplacement of the two bars minimizes the vibration in the upper zone for both modes and gives rise to a new nodal line in the former (2,0) mode.

It should be emphasized that the mode (1,2), in addition to its previous relationship with the (1,1−) mode, is influenced by the (2,1+) mode in the phase ($s5$). This can be explained in terms of the immobility of the upper zone and its transverse flexural character in the lower zone of the plate (the level lines are practically parallel to the grain and not perpendicular, as would correspond to the second shear mode of an isotropic plate). The shape of the nodal lines of the (1,2) mode would suggest calling it (3,1+), but according to a finite element analysis it originated as the (1,2) mode.

The emplacement of the rods in stages ($s6$) and ($s7$) caused a practically equal mass distribution between the upper and the lower zones, and the total mass in phase ($s7$) was almost equal as that of the initial stage ($s1$). The rods permit the upper zone to vibrate again, as can be seen in Fig. 8.

No changes occurred in the pattern shapes in stages ($s6$) and ($s7$) in comparison with ($s5$), except for the curvature change of the (0,2) mode in the lower zone of the soundboard. The vibration modes remained normal, since the imaginary part of the 115 response functions is negligible in comparison to the real part, as in the previous phases. From phase ($s5$) to ($s7$), a MPC between 91% and 100% was obtained for the seven studied modes.

In phase ($s5$), the modal participation of the present modes was quite similar. However, after the addition of the ribs, the modal participation of the longitudinal flexural patterns diminished. This can be explained by taking into account the curvature change in the nodal line on the lower zone of the soundboard. This line is close to the position of the bass string and, because of this, these modes present a low modal participation factor. Thus after emplacing the rods, the modes that most contribute in the band from 20 Hz to 200 Hz are the transverse flexural and shear modes.

Figure 5 shows the evolution of the natural frequencies of the modes analyzed from phase ($s4$) to ($s7$). The emplacement of the two transverse bars in the upper zone of the plate had a different effect depending on the vibrational character of the modes. Thus it produced an increase in the stiffness of the shear and transverse flexural modes, due to the rise of the equivalent Young modulus $E2$ (perpendicular to the grain) of the whole structure and these modes notably increased their frequencies in a consistent manner. In the case of the longitudinal flexural modes, (0,2) and (0,3), the emplacement of the two bars in the upper zone had a mass-increasing effect, and so their natural vibration frequency diminished.

The emplacement of the seven rods in the rough state at phase ($s6$) increased the stiffness of the structure in the band analyzed. This effect became greater on the longitudinal flexural modes, since the fan implies an increase on the equivalent Young modulus $E1$ (parallel to the grain), the main agent responsible of the natural frequency in those modes. Finally, concerning the natural frequencies, the

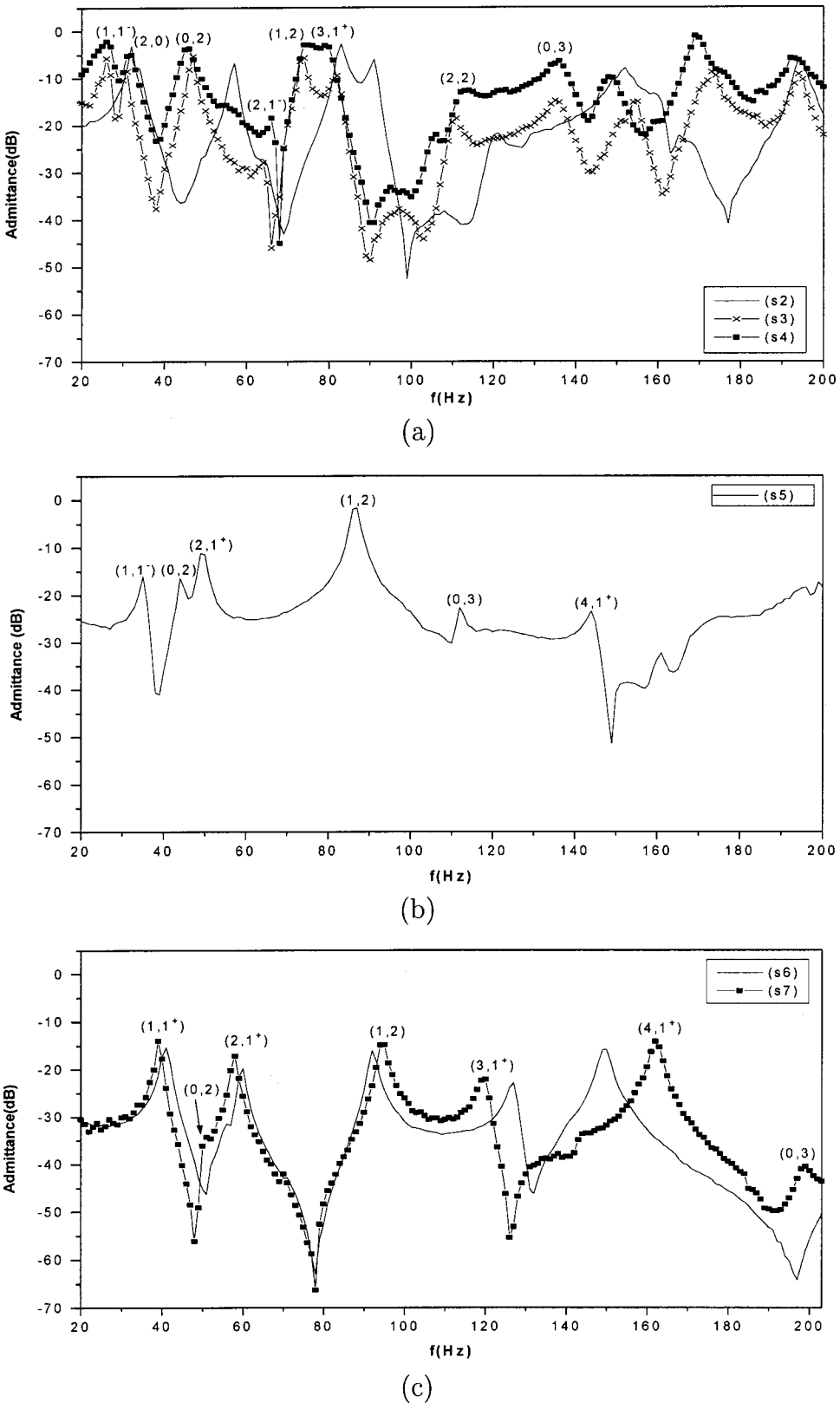

FIG. 7. Cross admittance curves (dB): (a) In stages (*s*2), (*s*3), and (*s*4); modes are labeled for stage (*s*4). (b) In stage (*s*5). (c) In stages (*s*6) and (*s*7); modes are labeled for stage (*s*7).

emplacement of the two rods in the lower zone and the perfection of the previously attached rods only affected the two highest modes. The frequencies of the five lowest modes remained unchanged, within the 1 Hz experimental resolution. In the case of the two highest modes, the phase (*s*7) involved an increase in their natural frequencies, this effect being stronger in the (0,3) mode.

Figure 6 shows the quality factors. The emplacement of the internal structures involves an increase in the quality factors for the seven modes analyzed. The increase in mass (21%) due to the two transverse bars elicited an increase in the quality factors of at least 50%. The least affected modes in this stage were those of longitudinal flexion, especially the (0,3) mode. The emplacement of the seven rods in phase

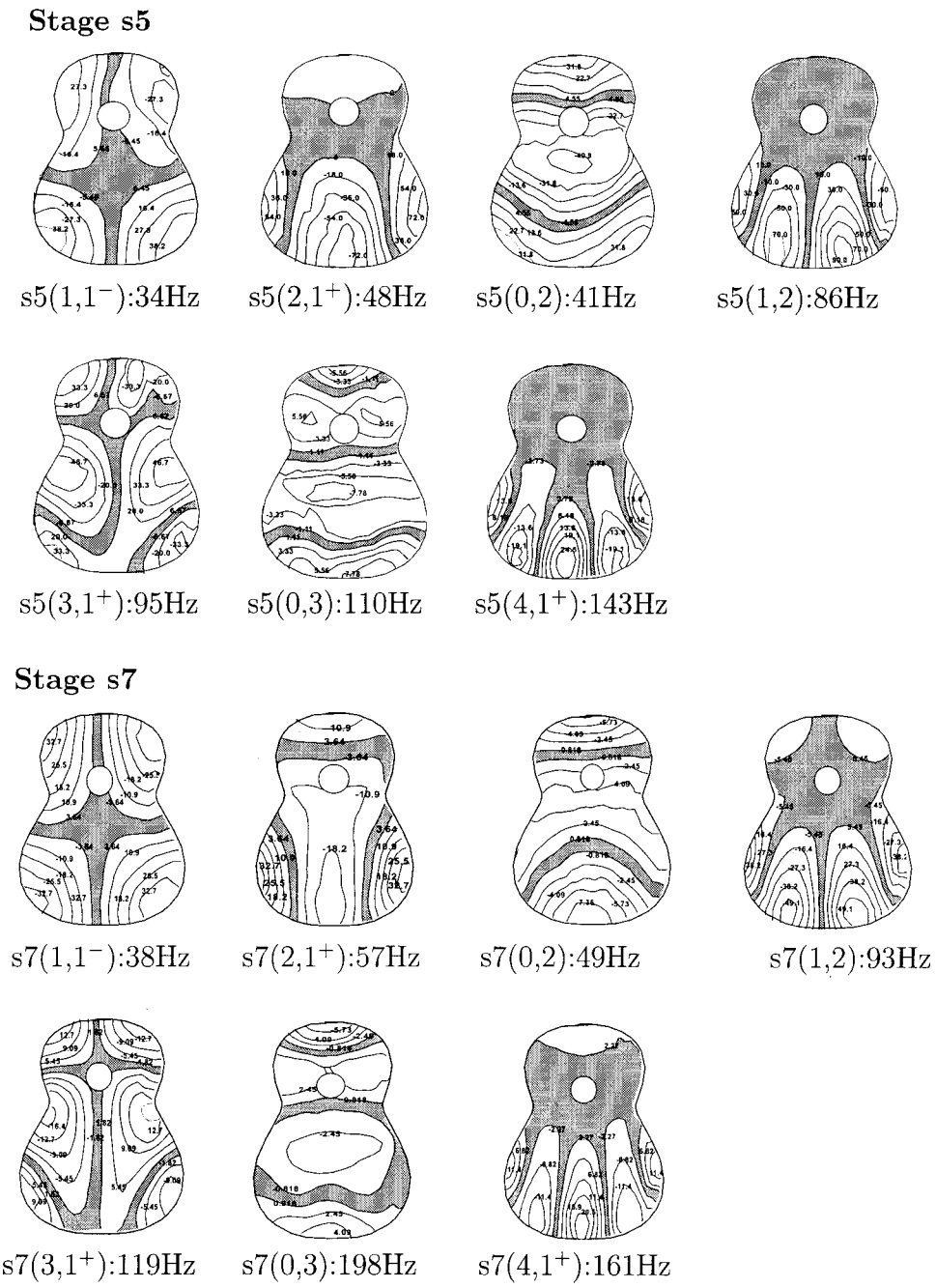

FIG. 8. Vibrational modes and natural frequencies in stages ($s5$) and ($s7$) (see Fig. 4 caption).

($s6$) implied a mass increase of 14% with respect to ($s5$) and a stiffness increase on the lower zone of the plate in the direction of the grain. This change in stiffness and mass elicited an increase higher than 25% in the quality factor for the highest three modes. Also, it can be observed that the longitudinal flexural modes were those most affected by the fan, just as for the natural frequencies; for example, mode (0,3) increased its quality factor by 40% with respect to ($s5$).

In the phase ($s7$), in spite of the two new rods in the lower zone, the mass of the whole plate was reduced [3% less than in stage ($s6$)] due to the good shaping of the fan. This decrease became apparent as a decline in the quality factors of the modes analyzed. As can be seen in the figure, phase ($s7$) had the opposite effect to that of phase ($s6$), and, as a result, the quality factors at ($s7$) were similar to those of ($s5$) for the four lowest modes. In the case of the three highest modes, although these were more affected by the shaping, the increase in the quality factor in stage ($s6$) was not compensated.

2. Admittance curves

Figures 7(b) and 7(c) show, respectively, the curves of cross admittance corresponding to the aforementioned point in phases ($s5$), ($s6$), and ($s7$).

In Fig. 7(b), the response level in the band from 20 Hz to 200 Hz is shown, the (1,2) mode featuring the maximum admittance. Likewise, mode (3,1+) is not detected since the response point coincides with one of its nodal lines. In comparison to ($s4$), the emplacement of the bars prevented mobility of the soundboard, since the admittance curve was in general reduced by more than 10 dB, this decrease being

more visible at high frequencies. It is also possible to appreciate a narrowing of the peak bandwidths with respect to the plate without structures. This was clearly seen in the increase in the quality factors.

Figure 7(c) shows the effect of the rods in the rough state and in the well-shaped state [phases $(s6)$ and $(s7)$] on cross admittance. Besides, in phase $(s5)$ the modes were more equidistant and the level of admittance was uniform throughout the frequency range. Also, it can be appreciated that the longitudinal flexural modes were not detected in phase $(s6)$ in the response point selected and showed a low amplitude in phase $(s7)$. This is due to the curvature change of its form in the lower zone, the response point being close to the lowest nodal line. Finally, in phases $(s6)$ and $(s7)$ a slight increase occurred in the admittance level for all the modes studied.

IV. CONCLUSIONS

A detailed study of the vibrational behavior during the construction stages of a guitar soundboard has been made, before setting up the resonance box. In this sense, the vibrational modes, natural frequencies, and quality factors, as well as the admittance curves, have been determined at each stage, and their evolutions along the process in relation to the modifications have been discussed.

As a natural sequel of this work, we are interested in a similar study, considering the soundboard with its actual boundary conditions. It is hoped that such a study, together with the present one, will help us to influence and to improve the construction process of a guitar.

ACKNOWLEDGMENTS

The authors are grateful to S. A. Keller for their important collaboration, and very much obliged to Alberto Atxotegi, the craftsman, for his careful work.

[1] B. E. Richardson, Catgut Acoust. Soc. J. **2** (5, Series II), 1–10 (1994).
[2] E. V. Jansson, Acustica **25**, 95–100 (1970).
[3] B. E. Richardson, Catgut Acoust. Soc. Newsletter **40**, 13–17 (1983).
[4] M. J. Elejabarrieta and A. Ezcurra, Proc. Institute of Acoustics **19**, 143–148 (1997).
[5] D. J. Ewins, *Modal Testing: Theory and Practice* (Research Studies Press Ltd., England, 1984).
[6] K. D. Marshall, Catgut Acoust. Soc. J. **46**, 7–17 (1986).
[7] K. D. Marshall, J. Acoust. Soc. Am. **77**, 695–709 (1985).
[8] CADA Modal Analysis User Manual, Rev. 2.3, LMS-International, Leuven.
[9] B. E. Richardson and G. W. Roberts, SMAC'83, Vol. II (Publication of the Royal Swedish Academy of Music, No. 46:2), pp. 285–302 (1985).
[10] F. Orduña-Bustamante, Catgut Acoust. Soc. J. **2** (1, Series II), 20–23 (1992).

Measurements and efficient simulations of bowed bars

Georg Essl[a)]
Computer Science Department, Princeton University, Princeton, New Jersey 08544

Perry R. Cook[b)]
Computer Science Department and Music Department, Princeton University, Princeton, New Jersey 08544

(Received 20 December 1999; accepted for publication 4 April 2000)

Bowing bar percussion instruments is an increasing part of the repertoire of modern composition and performance. Yet the system has not been studied systematically. In this paper experimental measurements of bars of bar percussion instruments bowed by a double bass bow and by a bowing machine are presented. They examine the relationships between performance parameters and perceptional parameters which are relevant for musical performance. In addition, a new efficient simulation method using a time-domain approach has been developed and the measured results are compared to the simulation. Most measurement results are in good qualitative agreement with the known results of the bowed string. The spectrum of the bowed bar is observed to be harmonic, independent of the harmonicity or inharmonicity of the eigenfrequencies of the bar. Important distinctions from the known results of the bowed string are the weakness or independence of bowing force and velocity on the fundamental frequency and the spectral content of the produced sound. Simulations show qualitative agreement with the measurements. © *2000 Acoustical Society of America.* [S0001-4966(00)03507-4]

PACS numbers: 43.75.Kk [WJS]

INTRODUCTION

Bowed bar percussion instruments have found increasing interest and application in musical composition and performance in recent years. However, the excitation of a sustained oscillation of a bar by means of a rosined bow for musical purposes has not yet been studied systematically.

So far research on bar percussion instruments has focused on the issue of tuning by removing material at various locations along the bar,[1–4] the influence of the resonators on the vibrating bar and the radiated sound,[2,5] and the effect of striking excitation using mallets.[6] Material properties have also been studied.[7,8] Numerical simulations use either finite difference[2,6,5] or finite element methods.[1,4,9] Summaries and reviews of the research on bar percussion instruments are available.[10–12] When the sound of bar percussion instruments is synthesized for real-time performance using electronic sound generation, the above-mentioned finite difference and element methods lack the necessary efficiency on current hardware to be appropriate. Hence, current techniques only model the modes of the system, using modal filters[13,14] or additive sinusoidal synthesis[15,16] ignoring the modal shapes. Hence the notion of physical shape and interaction is lost, and a direct way to use these approaches for bow interactions is not possible. In essence, the spatial dynamics is removed by replacing the actual physical system by an equivalent mass-spring system which models the same modal response. However, the dynamics (in particular the propagation of disturbances) of the original system is lost. Hence it cannot, in general, be expected that nonlinear interactions are captured by the simplified mass-spring model. If the modal shapes are known, the spatial information can be maintained and bowing interactions remain meaningful. This approach has not yet been tried for bars of musical instruments, but was used to study the stick-slip interaction.[17] To use this method, the modal shapes have to be known *a priori*. These are difficult to get analytically because the undercutting of tuned bars make the equations nonlinear and experimental measurement is much more costly than simple frequency analysis.

This paper describes a new simulation method for the purpose of preserving a notion of spatial shape while achieving real-time performance. An *a priori* knowledge of modal shapes is not necessary. A preliminary version of this method and results have been previously published by the authors.[18] It will be described in this paper in more detail and compared to physical experiments in Sec. II.

The action of the bow has only been studied extensively when exciting strings.[19,20] Numerical simulations typically use an efficient time-domain approach which follows from the constant phase delay characteristic of the ideal string equation[21] and this approach has been refined for synthesis purposes.[22,23] The string has also been studied using a finite difference approach.[24–26] The action of the bow on solids is known to be able to excite a sustained oscillation and is especially famous in the creation of Chladni figures.[27] However, a study of the dynamics and kinematics of this system is lacking as is a study of parameters which are relevant for musical performance. The violin bow has also been used to study the excitation of glass harmonica glasses.[28]

The paper is structured in the following way. First, Sec. I contains the description of the measurements. In Sec. I A measurements performed by hand bowing are presented followed by measurements using a bowing machine in Sec. I B. In Sec. II simulations are discussed. In Sec. II A details of the new simulation method are described and in Sec. II B simulation results using this method are presented. Finally in Sec. III we present discussions and conclusions.

[a)]Electronic mail: gessl@cs.princeton.edu
[b)]Electronic mail: prc@cs.princeton.edu

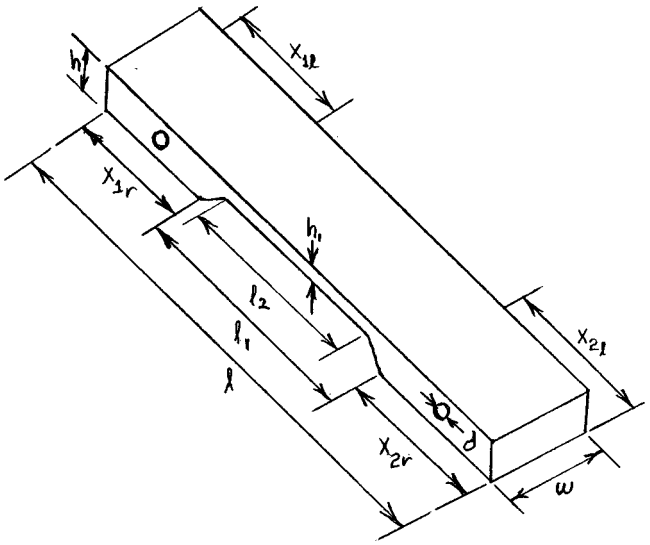

FIG. 1. Sketch of shape and dimensions of a bar.

I. MEASUREMENTS

The primary goal of the experiment was the measurement of parameters which are of importance for musical performance when bowing bar percussion instruments. The parameters in control of the performer are primarily bowing velocity and bowing force. Parameters like angle, type of bow, and amount of rosin were not considered in detail in these experiments. The performance parameters of interest were assumed to be loudness, temporal responsiveness, pitch, timbre, and brightness. Other interesting parameters like ease of performance and ''feel'' of the bowing action were not investigated directly. From the measured parameters the region of oscillation is derived, but effects like the ease of locking to higher modes were not considered at all.

Loudness was measured by calculating the energy of the signal. Temporal responsiveness was measured as the time it took from starting the bowing action to reaching a maximum amplitude self-sustained oscillation. This time will be referred to as onset time. Pitch was measured by finding the fundamental in spectra taken from the measured signals. Timbre and brightness was measured by calculating the spectral centroid of the spectra of the measured signals.

Two distinct measurement setups were used. First, a number of bars of different size, shape, and material were bowed by hand using a double bass bow. These measurements were performed to get a qualitative result of most of the described quantities.

In order to get more quantitative and reproducible measurements, a bowing machine was built and one bar was systematically studied for quantitative relationships between input (bow) velocity and force to output amplitude, energy, fundamental frequency, spectral content, and onset time. These results will be described in Sec. I B.

TABLE I. Dimensions and material constants of measured bars.

	l (cm)	w (cm)	h (cm)	l_1 (cm)	l_2 (cm)	h_1 (cm)	E (GPa)	ρ (km/m^3)
Uniform wood	38.1	4.05	1.95	N/A	N/A	N/A	10	640
$C_4^\#$ wood	30.7	3.5	1.6	17.3	7.0	0.5	16	740
Uniform aluminum	17.8	3.8	0.3	N/A	N/A	N/A	70	2710
$F_4^\#$ aluminum	29	3.9	1.8	11.95	5.3	0.6	70	2710
$F_3^\#$ aluminum	36.4	5.1	1.8	16.4	9.3	0.5	70	2710

TABLE II. Positions and diameter of cord holes in bars.

	x_{1r} (cm)	x_{1l} (cm)	x_{2r} (cm)	x_{2l} (cm)	d (cm)
Uniform wood	3.9	3.9	3.9	3.9	0.7
$C_4^\#$ wood	5.8	5.8	6	5.6	0.5
Uniform aluminum[a]	4	4	4	4	N/A
$F_4^\#$ aluminum	5.7	5.8	5.6	6.2	0.6
$F_3^\#$ aluminum	7.3	7.4	7.5	6.8	0.6

[a]The aluminum bar had no cord holes. Instead it was held in place by rubber bands on thin plastic rods which were wrapped with felt at the given positions.

A. Measurements by hand bowing

1. Experimental setup

For hand bowing, two different types of bars were used. One set of bars consisted of bars taken from real musical instruments. These bars are undercut to tune the upper partials to be close to harmonic. In this set, a bar representing the xylophone and marimba family and bars for vibraphones were used. Xylophone and marimba bars are made of wood (typically rosewood) whereas vibraphone bars are metal (typically aluminum).

The second set of bars consisted of wood and aluminum bars of uniform cross section. These have inharmonic partials. The measurement of bars of uniform thickness has two purposes. For one it serves as comparison to the behavior measured for undercut bars. Second, the Euler–Bernoulli equation for constant cross-section and homogeneous material is a linear fourth-order partial differential equation which lends itself to analytical treatment, which is otherwise not easily possible.

A sketch of the typical shape of a bar can be found in Fig. 1. Table I shows the dimensions of the measured bars and Table II shows the position and size of the cord holes. The material constants (Young's modulus and the mass den-

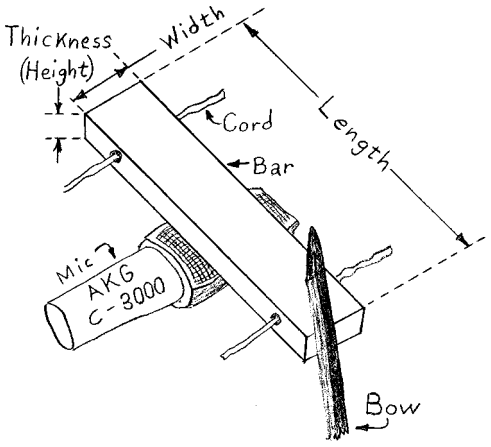

FIG. 2. Experimental setup for hand bowing measurements of bars.

TABLE III. Spectral frequencies of dominant partials of measured bars and theoretical values given as $f_n:f_1$. The left side of the table contains the theoretical prediction for uniform bars and the actually measured ratios of the two measured bars. The right side contains the usual tuning and the measured ratio for tuned bars. The first row contains the actual fundamental frequency f_1 of the bars.

n	Theory	Wooden (uniform)	Aluminum (uniform)	Usual tuning	$C_4^\#$ xylo	$F_3^\#$ vibra	$F_4^\#$ vibra
f_1		693.9	487		280.6	187.3	373.6
2	2.756	2.572	2.756	4	3.932	3.984	3.997
3	5.404	4.644	5.423	10	9.538	10.668	9.469
4	8.933	6.984	8.988		16.688	17.979	15.566
5	13.346	9.723	13.448		24.566	23.679	20.863
6	18.6408		18.680		31.147	33.642	29.440

sity) were taken from a standard reference (see Table 19.1, p. 625 in Ref. 12) and were not measured for the experimental bars.

The bar to be measured was suspended using two stiff cords under tension between two vices. The microphone was placed underneath the middle of the bar. The typical bowing point when bowing xylophone or vibraphone bars in a complete instrument is on the narrow end, as this is the only side which can be conveniently reached with a bow by the performer. Hence our measurements concentrate on bowing positions on the end of the bar. In some bowing strokes, especially when high bowing forces are applied, the oscillation of the mass spring system of the cords and the bar had to be damped by placing one hand on one of the cords and pulling down. The typical setup is depicted in Fig. 2. A rosined double bass bow was used for all measurements.

2. Measurement results

First, the response of the measured bars to impulsive excitation was measured using both a force hammer and a hard plastic glockenspiel mallet. Table III shows the frequencies of the dominant partials of each test bar along with the theoretical values for uniform bars as well as the usual tuning frequencies for undercut bars. As can be seen, the uniform aluminum bar is very close to the values predicted by the Euler–Bernoulli theory. The uniform wooden bar deviates substantially from the theoretical values, for two likely reasons. One is that the bar is not perfectly uniform due to its holes drilled 3.95 cm from both ends with a diameter of 0.75 cm. Second, the thickness is comparable to the width of the bar, in which case the application of the Timoshenko theory is more appropriate, which lowers the frequency of the upper partials.[12]

The bowed bar exhibits a harmonic spectrum, though often weaker partials at the possibly inharmonic eigenfrequencies can be seen. This behavior can also be seen when bowing at positions other than one of the free ends. Bowing at the side is easily possible only with sufficient distance to the suspension holes. When bowing in the middle, the fundamental of the bar can also be excited. For the $F_1^\#$ vibraphone bar bowing in the middle will often lock to the second eigenfrequency of the bar, which lies two octaves above its fundamental eigenfrequency. This tendency to lock to the higher mode can usually only be overcome with increasing friction by tilting the bow or by other means. Another possible way of excitation is to contact the top surface of the bar. By bowing with little bowing force a proper regime of oscillation can be excited.

Using hand bowing, a qualitative relationship between bowing velocity and amplitude as well as between bowing force and amplitude was investigated. It should be noted that constancy of velocity and force within each measurement as well as across measurements (when applicable) were not possible as they are highly dependent on the subjective perception and the skill of the performer. As will be seen in the quantitative measurements using a bowing machine, the lack of constancy of bowing force is likely not a problem as the amplitude appears to be independent of the bowing force.

Figures 3 and 4 show the time domain envelopes of bowing strokes with increasing velocity and increasing force. From the length of the bow and the stroke time, which can be

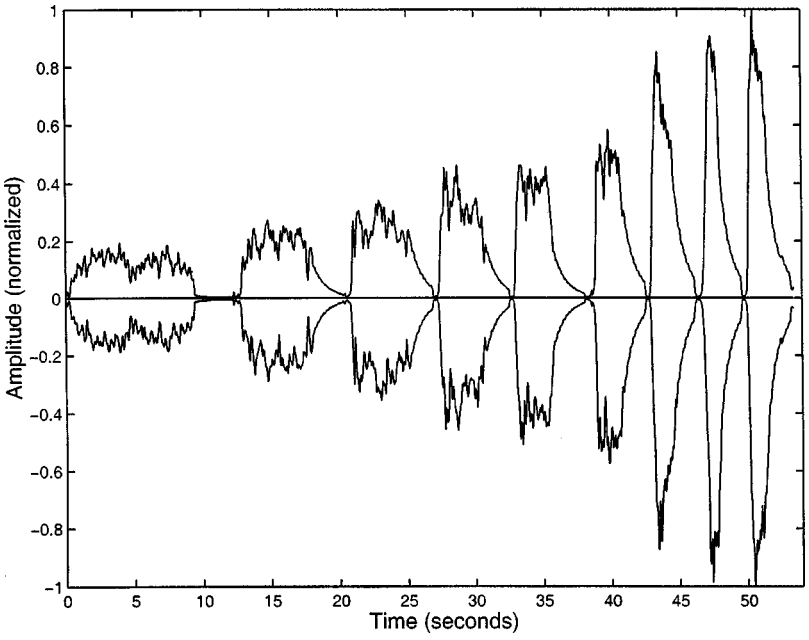

FIG. 3. Time-domain amplitude envelope of hand strokes with increasing velocity and force held approximately constant.

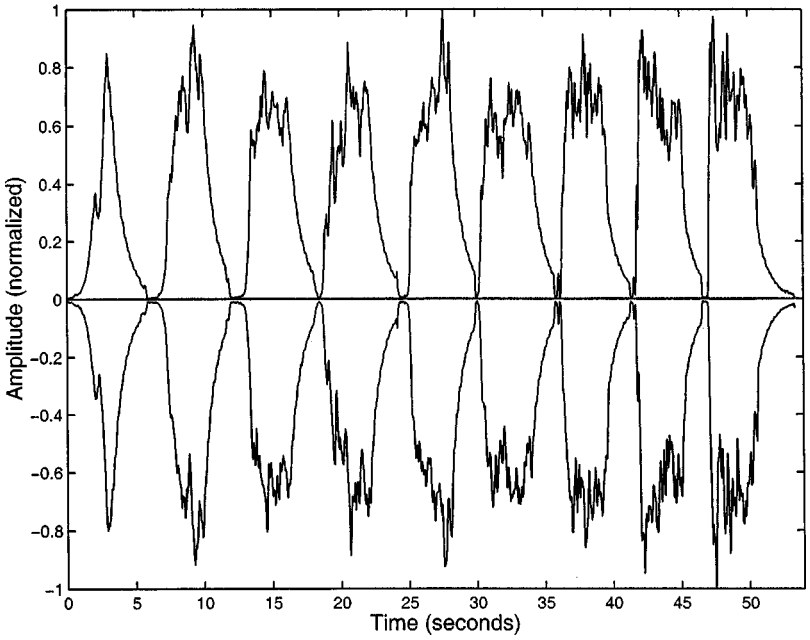

FIG. 4. Time-domain amplitude envelope of hand strokes with increasing force and velocity held approximately constant.

retrieved from the time-domain plot, an average input velocity can be deduced. Setting this velocity in relationship to the amplitude of the signal shows an approximately linear increase of amplitude with increasing velocity. Force was held nearly constant in the velocity measurement. The force measurement shows no clear influence on the amplitude. This finding was later validated by the bowing machine measurements. The time-domain shapes of the force-amplitude relation also hint at a decrease of onset time with increasing force. This result was also quantified using bowing machine measurements, as described in the next section.

B. Measurements using the bowing machine

1. Experimental setup

The $F_3^{\#}$ aluminum vibraphone bar under investigation (see Table I) was suspended in a rigid bar holder. The holder has two effects. First, it removes the cord modes or other movements which are not of interest while keeping the important degrees of freedom. Second, it allows very high bowing forces to be applied by the bowing machine. As shown in Fig. 5, angled screws were screwed into a wooden base at the positions of the cord holes of the bar. Rubber tips were placed between the metallic holder and the bar to minimize the friction noise and keep a flexible interface. The wooden base was shaped to allow bowing at the narrow side and at the wide side at positions between the suspension holes. In the bowing machine measurement, the bar was pulled towards the bowing machine (which will be described in the next section) by means of a cord which was tied to a hook on one narrow side of the bar holder. When the applied force was measured, the cord was replaced by a spring scale with a scale range of 0 to 2000 g. The microphone position for these measurements was above the middle of the bar as the bar holder did not leave enough space underneath the bar.

2. Bowing machine

The bowing machine consisted of a standard variable speed power drill, a cylindrical drum of hard rubber with a 2.6-cm radius and width of 3.75 cm around which a band of horse hair was wound and glued together at the open ends using super-glue to form a loop. The typical loop width and thickness were comparable to the width of the double bass bow. The horse hair was then rosined. In order to calibrate bowing speed, a bicycle speedometer was added to the drill. The magnet was placed on the rotating part and the pickup sensor was glued to the nonrotating casing of the drill reaching over the magnet. In measurement, the bowing drill was held in place by a vice and the bar was pulled against it. The noise of the drill was damped from the recording by placing

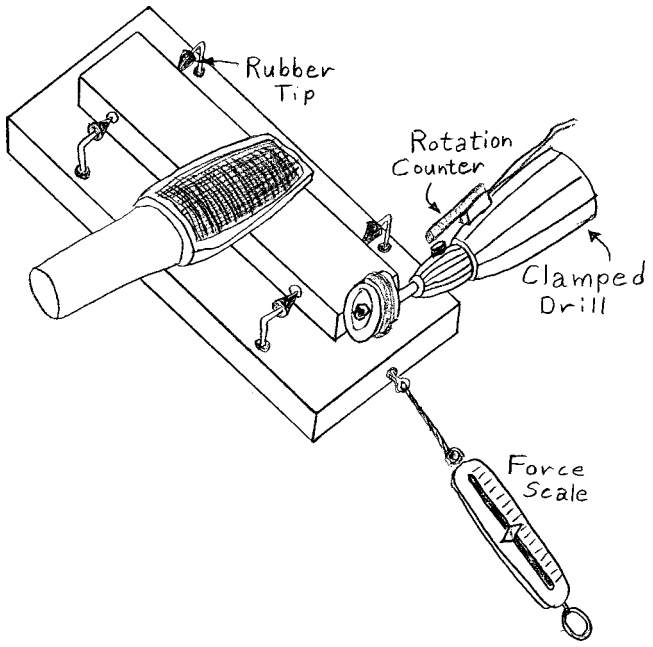

FIG. 5. Experimental setup for bowing machine measurements of bars.

sound-absorbing foam between the drill and the microphone. Also, the microphone position was generally facing away from the drill and towards the primary sound radiation direction of the bar, enhancing the signal-to-noise ratio. The microphone position was adjusted to maximize the signal from the bar while avoiding saturation.

3. Measurement procedure

Two series of measurements were performed using the bowing machine described in the previous section. Before each series the bowing drum had to be rehaired and new rosin was applied. Hence it should be noted that direct quantitative comparisons between these two series are not easily possible. The reason for the need to rehair the bowing machine stems from the fact that the high force measurements at the end of each series resulted in breaking of the hair loop and hence rendered the loop useless for more measurements. There is another reason why the measurements should not be compared between measurement series. The microphone was moved and recalibrated between the series and hence the attenuation of output levels between series should be expected to be different.

The unevenness and change of stiffness of the hair loop at the glue joint yielded an overlap of impulsive excitations over the total bowing excitation. This effect can be expected to influence some of the behavior measured. The impulses overlaying the overall sound were used as an independent measure of velocity because of the occurrence of one impulse per revolution. Later this measurement was correlated with the independent velocity measurement using a speedometer to get an error estimate.

The first series consisted of nine runs starting at a particular bowing speed in gradually increasing forces between 0 and 14 N (or 0 and 2000 g spring scale readings with a relative force contribution of $\sqrt{2}$ due to an angle of 45 degrees). Forces were taken at the following spring scale readings if oscillations occurred: 125, 250, 500, 1000, 1250, 1500, 1750, and 2000 g. In this measurement series, the oscillation was not damped out and restarted at each measurement point, but the force was steadily increased with the bowing machine continuously in contact. The setting of the drill speed was not adjusted, which resulted in a decrease of the actual bowing speed due to the reduced drill speed from the increased force load. All taken measurement points can be seen in Fig. 6. As can be seen, the velocity of each run decreases as a function of input force. The velocity was derived from the recording as described before. The last run (run 9) did not result in oscillation and hence indicates points lying beyond the upper velocity limit.

These measurements were aimed towards finding the regions of oscillation as a function of velocity and force. In addition relative energy as a function of velocity and force was calculated from the recorded sounds and the change in spectral content was characterized using the spectral centroid, which is the center of gravity of the spectrum. The spectral centroid correlates roughly with brightness. Finally, the fundamental frequency of the recorded sounds was also measured. The results will be discussed in subsequent sections.

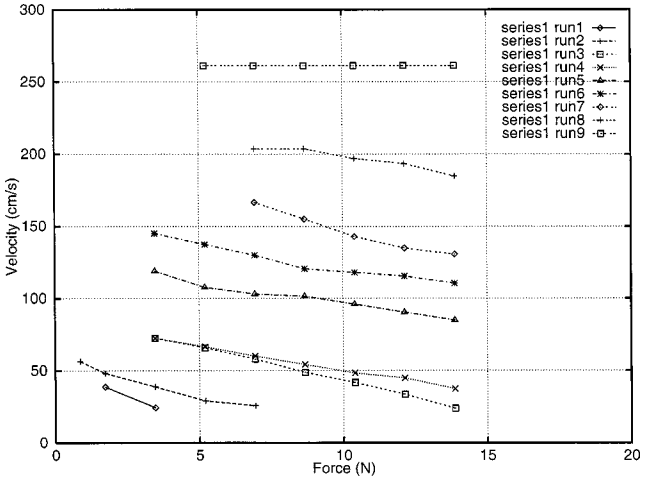

FIG. 6. Bowing machine measurement series 1. Measured input parameters: force and velocity.

The second series consisted of three runs again starting at a particular bowing speed. This time the oscillation was damped out after recording for each measurement point and, using the attached speedometer, the input velocity was adjusted in the attempt to keep the actual bowing speed roughly constant. If a measurement point yielded oscillation, the recording was taken long enough to measure the full oscillation buildup until the maximum and a significant part of the steady state oscillation. Hence, in addition to all the measures derived from series 1, the onset transient time until maximum oscillation was reached was measured in this series. The force range was extended for the first two runs of this series to a maximum force of about 20 N (or a spring scale reading of 2000 g at 0 degree angle).

All measurement points of this series can be found in Fig. 7. The velocities were measured both using the measure of the speedometer and from the recording. A correlation between the two independently measured velocity values shows the average error to be 2.21 cm/s (or 1.2%) with a standard deviation of 2.06 cm/s (or 1.1%). As can be seen, the error is very low. This has to do with the high number of

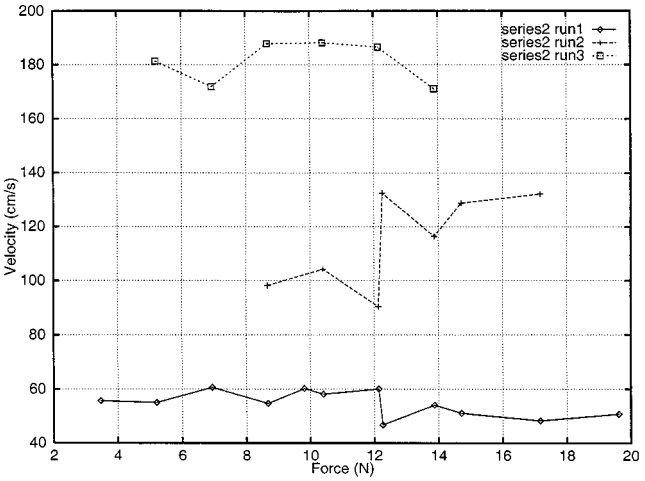

FIG. 7. Bowing machine measurement series 2. Measured input parameters: force and velocity.

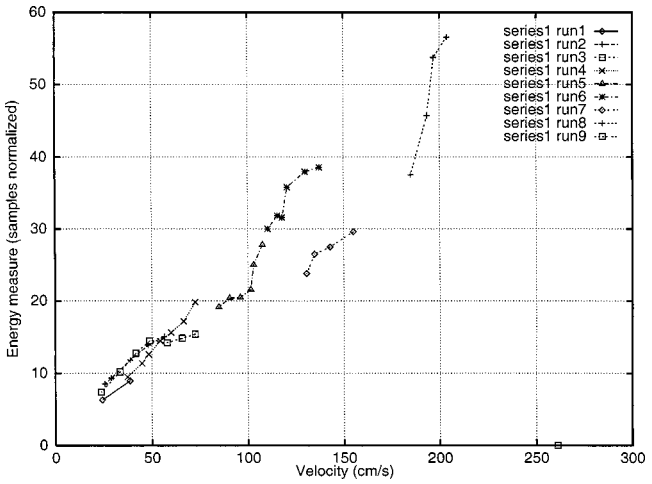

FIG. 8. Bowing machine measurement series 1. Recorded radiation energy as a function of bowing velocity.

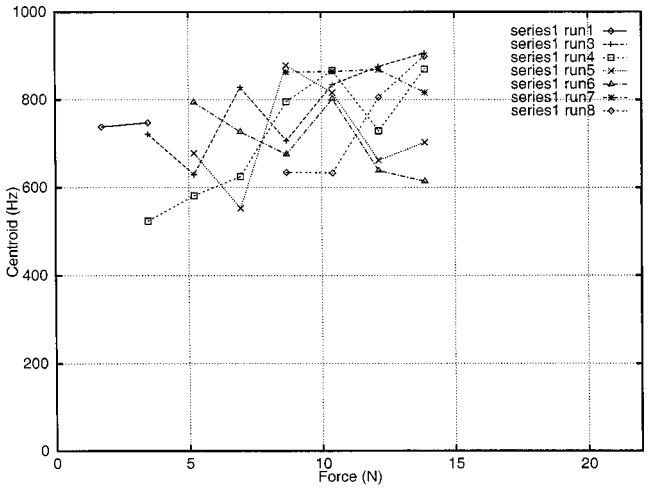

FIG. 10. Bowing machine measurement series 1. Spectral centroid as a function of bowing force. Only measurement points with a clear steady-state oscillation are shown.

revolutions measured in both cases yielding a good resolution.

C. Results of bowing machine measurements

1. Region of oscillation

As can be clearly seen from Fig. 6, the minimum bowing force increases as a function of velocity. A maximum bowing force could only be found for the first two runs of series 1, which are at velocities below 50 cm/s. At higher bowing speeds an upper force limit could not be found within the measurement range. The minimum speed at which steady oscillation was found was 23.83 cm/s with a force of 13.87 N. It should be noted that using the undamped measurement approach of series 1, very low velocities can be achieved even for high forces (as can be seen from run 3 in Fig. 6). (This point is the highest measured force point in this run.) The maximum bowing speed from series 1 is found to be above 203.72 cm/s and below 261.14 cm/s.

2. Energy and power, spectral content, fundamental frequency, and onset times

Both measurement series show that the energy of the fully developed steady state oscillation increases as a function of velocity and the relationship seems to be approximately linear (the measurements of the first series can be seen in Fig. 8). Taking this linear velocity dependency into account, the energy radiation seems to be independent of the input bowing force. (This effect can be seen more clearly in series 2, where the force-energy relationship as depicted in Fig. 9 correlates closely with the force-velocity relationship as depicted in Fig. 7.)

The spectral centroid of series 1 seems uncorrelated with the input force and velocity. No clear upward trend was observed with increasing force (see Fig. 10) in contrast to known behavior of the bowed string. Series 2 verifies this result.

The measurements of the fundamental frequency as a function of velocity and force result in minor fluctuations without a clear trend. In series 1, the mean frequency was 186.67 Hz with a standard deviation of 0.26 Hz (33 data

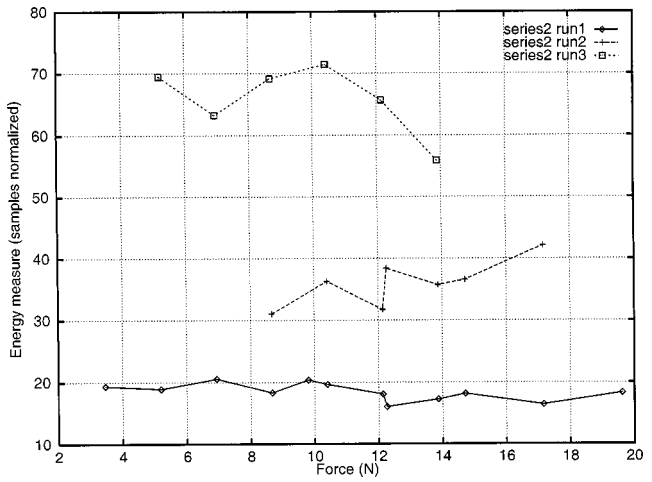

FIG. 9. Bowing machine measurement series 2. Recorded radiation energy as a function of bowing force.

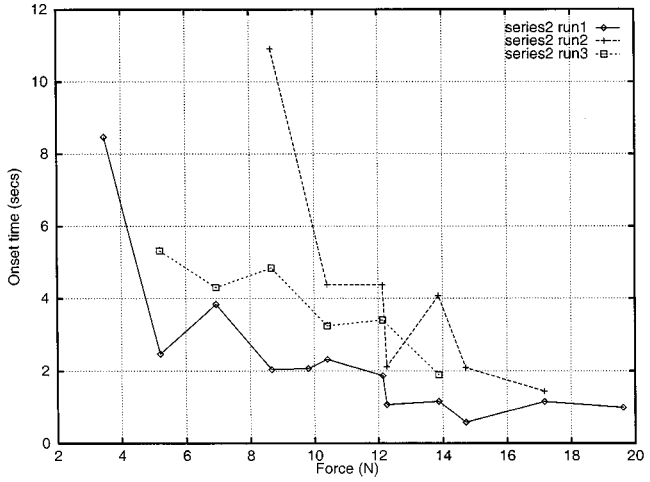

FIG. 11. Bowing machine measurement series 2. Onset time as a function of bowing force.

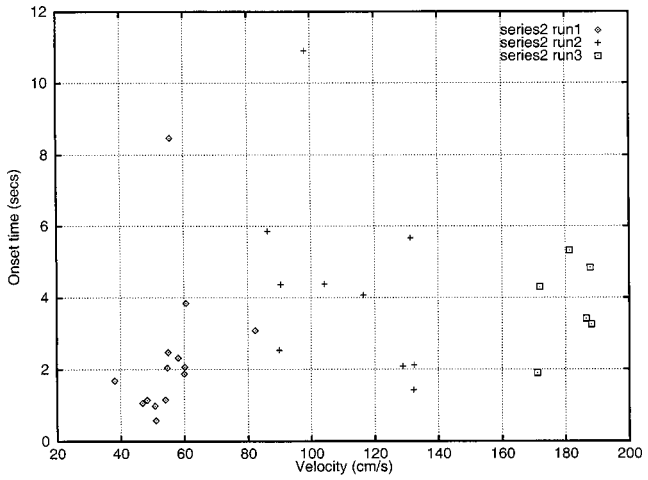

FIG. 12. Bowing machine measurement series 2. Onset time as a function of bowing velocity.

points) and in series 2, the mean frequency was 186.73 Hz with a standard deviation of 0.27 Hz (25 data points). The measurements as a function of velocity seem to indicate a trend towards flattening with increasing velocity, whereas there is no trend observable in dependency of force. In any case, the effect is very small (less than 10 cents) even over the full range. High velocities should be difficult to achieve by hand bowing and hence within the usual bowing domain, the dependency of the fundamental on the bowing parameters is negligible.

Onset time as a function of velocity and force was measured in series 2 only. As was already noted from the time-domain shapes of hand-bowed measurements, there is a clear decrease of the onset times with increasing bowing force (see Fig. 11). The onset time appears uncorrelated with the input bowing velocity (see Fig. 12).

II. SIMULATIONS

A. Simulation method

Taking the finite difference method approach to simulate the model equations can result in remarkably good simulations, but it has the disadvantage of being time consuming to run.[6] The method requires a running time of the order of N calculations, where N is the number of spatial subdivisions. In asymptotic notation this is usually written as $O(N)$. In order to be able to study the qualitative behavior of the system more efficiently and also in order to find a real-time synthesis method for musical performance, a new approach was found. The new method has the advantage of being $O(1)$, that is, independent of the number of spatial sampling points. While modal simulations are also $O(1)$ they either remove the spatial information by ignoring the modal shapes[13–16] or require *a priori* knowledge of the modal shapes.[17] The method to be introduced here will model the spatial information approximately while not requiring the explicit knowledge of modal shapes.

The simulation can be understood in a variety of ways. The derivation presented here is close to the one used to originally derive it. Additional conceptual ways of understanding the methods will be described later.

McIntyre, Schumacher, and Woodhouse's time-domain modeling technique[21] has proven to be very useful in simulating musical instruments with a resonant system which is well approximated by the one-dimensional wave equation. The propagation speed in the resonant part of the instrument (string, pipe) is roughly constant and the computational task involves a convolution with a rather narrow reflection function which contains effects which deviate from the ideal d'Alembert response like weak dispersion due to the weak bending stiffness of the string and dissipation.[29] Smith[22] introduced extensions to the idea taken from scattering filter theory and coined the term *waveguide* for simulations based on this one-dimensional technique.

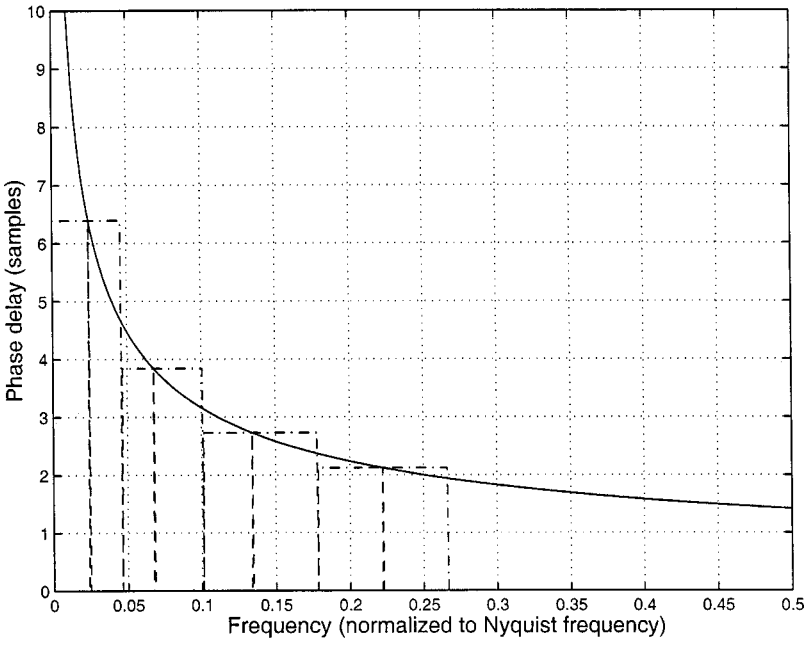

FIG. 13. Discretization of the phase delay in a banded waveguide simulation.

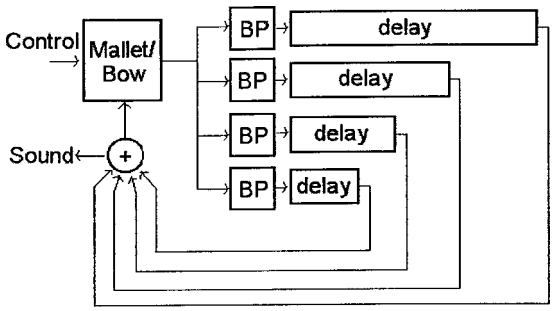

FIG. 14. Flow diagram of the banded waveguide simulation showing excitation and propagation parts.

An attempt to incorporate this idea directly for the Euler–Bernoulli bar equation fails, because the propagation speed is not close to constant but strongly dependent on frequency (see Fig. 13). This makes the direct implementation of the waveguide idea inefficient because the reflection function is not narrow anymore. The nonzero region to be computed by convolution integral becomes large and hence the advantage over implementing a finite difference simulation is removed.

The idea which leads to the banded waveguide simulation is the following. Efficient time-domain simulation is possible if the propagation speed of disturbances in the medium is to a good approximation constant. Instead of trying to implement the propagation speeds at all frequencies correctly, the propagation speeds around the eigenmodes of the systems are modeled correctly and the neighboring frequencies are modeled with the constant propagation speed of the system at the eigenfrequency under consideration. This adds an additional approximation to the system, but it makes the simulation feasible. Another view of this approach is that the wavetrain closures of the system are modeled exactly (within numerical precision) and the approximation gets worse away from the eigenmode. However, the system shows severe damping away from the mode and hence the error is made in the strength of the damping. In the neighborhood of the mode, the error is small. The modal frequencies are modeled accurately to within the numerical resolution.

An illustration of the idea of the approximation is depicted in Fig. 13 assuming the propagation delay of disturbances in a uniform bar, which is a function of the square-root of the frequency in case of the propagating terms in the solution of the Euler–Bernoulli equation for a uniform bar. The assumed constancy of the phase delay within a frequency band can be interpreted as a second quantization of the system in the frequency domain.

In the case of bowing on the narrow side of the bar, disturbances leave only in one direction and only this propagation has to be modeled. The system implemented for simulation can be seen in Fig. 14. As can be seen, this picture follows the general McIntyre, Schumacher, and Woodhouse idea of excitation-resonator decomposition. In the case of a banded waveguide simulation, the resonant part models the propagation of different frequency bands separately.

It should be noted that this approach does not model the spatial shape correctly. There are two ways to illustrate this. First, if only the known propagation speed is modeled, then the near-field oscillations are neglected. Second, if the wavetrain-closure frequencies containing the near-field terms are modeled, then their contribution to the frequency is modeled as propagating waves and not as standing waves.

However, the propagation delay of a physical disturbance is modeled properly. The physical quantity will arrive back at the bowing point after the appropriate time and hence the bow bar interaction is working with reasonable response values.

Another important remark about undercutting should be made. If the undercutting is not too deep, the physics of the bar can be expected to be close to the behavior of the uniform bar and this method is appropriate. The wavetrain closures change with the undercutting and the banded waveguides have to be tuned to the changed frequencies. However, it is important to observe that for severe undercutting, reflections at the points of changing impedance have to

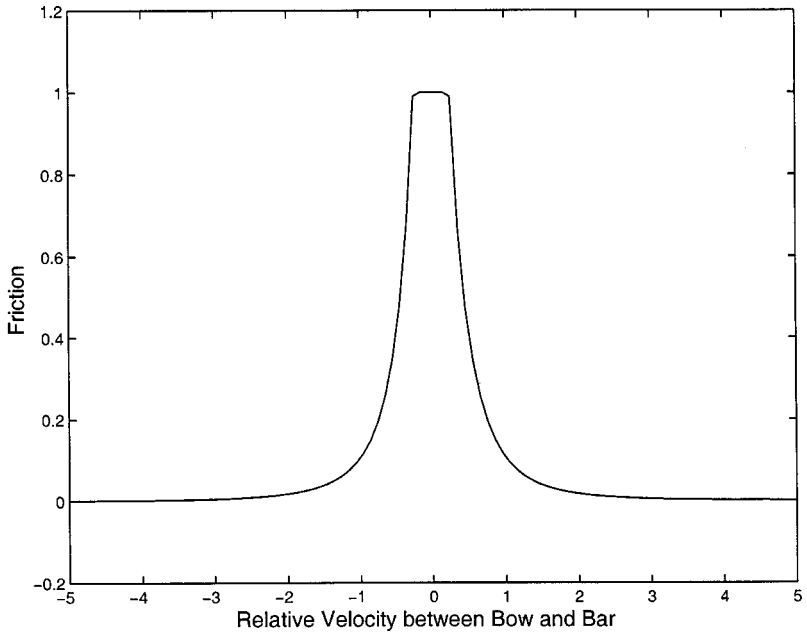

FIG. 15. Friction characteristic used in the banded waveguide simulation. For a relative velocity around zero, the bow exerts a nearly constant strong static friction on the bow whereas when exceeding the relative break-away velocity, the characteristics drops quickly to low dynamic friction.

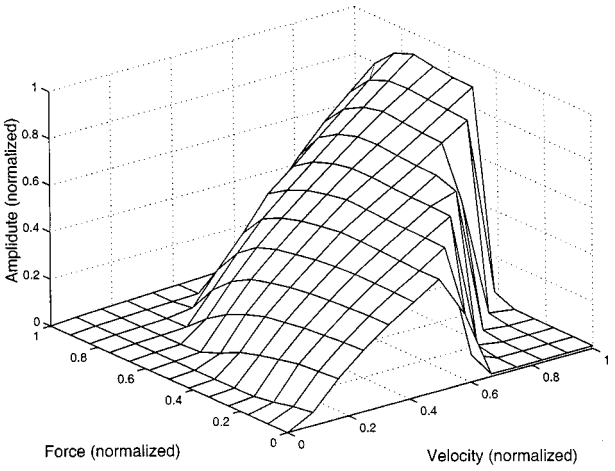

FIG. 16. Amplitude as a function of input force and velocity in a bowed bar simulation using the banded waveguide method.

be expected that are not captured in a straightforward way in an unmodified banded waveguide.

In the implementation used for simulations for this publication, Smith's method of applying the bow nonlinearity to a waveguide simulation[22] was used. This simplified approach simulates the behavior of sticking and sliding friction. During sticking the friction coefficient is independent of the input velocity, but once the differental velocity exceeds a certain value, the friction characteristics drops off rapidly to a weak sliding friction. Figure 15 depicts the actual functional shape used. This model does not contain the hysteresis effect which arises in a slightly more detailed model.[21] Yet the model used seemed to capture the measured phenomena and an extension to incorporate the hysteresis rule has not been found to be necessary. Only the wavetrain closures of the lowest four modes were modeled by banded waveguides. This is reasonable considering the stretching of the partials in a bar. Hence higher modes quickly fall outside the audible range. In addition, higher frequency modes are severely damped. For higher accuracy additional modes could easily be added for low computational cost.

B. Simulation results

Simulations using banded waveguides were performed in 12 steps between normalized input parameters of velocity and force yielding 144 data points. At each point, the amplitude, onset time, fundamental, and spectral centroid (as measure of spectral content) were extracted from the data.

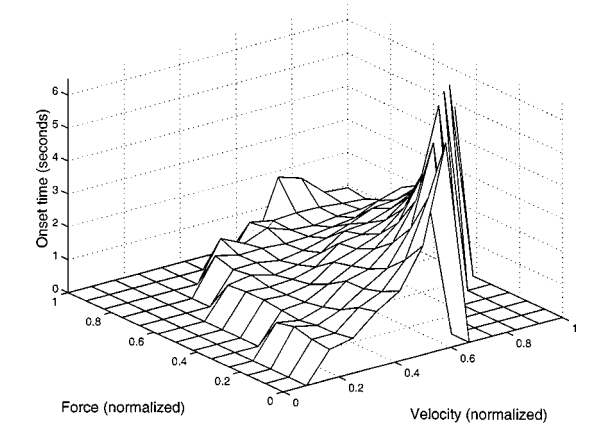

FIG. 17. Onset time as a function of input force in a bowed bar simulation using the banded waveguide method.

The simulations show qualitative similarity with the measured parameters. The output amplitude is very nearly linearly dependent on the velocity and largely independent of the force (Fig. 16). A separation of regions of oscillations and nonoscillation can also be seen in this figure. The onset time decreases with increasing force (Fig. 17 is at a normalized input velocity of 0.75). However, the surface plot reveals a more complicated dependency of the onset time with force and velocity which goes beyond the measurements made. Unfortunately, there are too few velocities measured to make a clear comparison of this result with measurement and its interpretation remains open. The fundamental frequency is independent of both force and velocity. The observed spectrum is harmonic. The simulations show that the spectral centroid is independent of both force and velocity, as found in the measurements.

III. CONCLUSIONS

The measurements conducted give evidence that for a set of physical quantities of interest for musical performance, the behavior of the bowed bar is in good qualitative agreement with known behavior of the bowed string while another set of physical quantities shows different behavior. In particular, the increase of output amplitude with increasing velocity and the independence on bowing force is observed in both the bowed string and the bowed bar. Similarly the onset time shows a dependency on the bowing force in both cases. Whereas the simulation of the bar shows also a dependency on bowing velocity as known for the bowed string,[19] this could not be seen from the measurements. The observed modes of the bowed bar are in analogy to the string also harmonic. It should be noted that the action of the bow on solids has often been used to study the modal shape of the solid. However, it seems questionable that the underlying assumption that the oscillation is essentially free and the observed shapes correspond to the eigenmodes of the system. The assumption that the oscillation of the bowed string can be described as a free oscillation has been made early but is known to be flawed.[19] In the case of the bowing of an idealized string, the eigenmodes and the partial frequencies of the nonlinearly excited string coincide, which makes the free oscillation assumption possible and allowed it to yield useful interpretations. As can be seen from the measurements, the eigenmodes of a bar and the partial frequencies of the bowed bar do not coincide and the hope to interpret the system from a free oscillation perspective should be considered inappropriate.

A clear effect of the bowing force and velocity on the fundamental could not be observed in the bar. The same is true for the spectral content. These two parameters show a clear dependency on the input force in the bowed string case. For the bowed string, both effects find intuitive explanation in the interplay between the corner rounding of the string due to stiffness and frequency-dependent dissipation and corner sharpening due to the action of the bow. This intuition does

not lend itself well to the bowed bar, because the kinematics cannot be assumed to be of Helmholtz type.

In the research work on the bowed string, knowing the kinematic motion of the string has led to intuitive explanations for many of the known effects. The vibrational shape of the bowed bar remains unknown and it seems suggestive that knowing the kinematics might help interpret the bowed bar results as well as allowing for a more detailed exploration of the similarities and differences to the bowed string. The authors made an attempt to measure the vibrational shape of the bowed bar using a high-speed CCD camera. Unfortunately the magnification was too weak to yield a clear picture of the vibration. All that could be deduced from the measurements was an upper limit of the maximum mid-point amplitude at medium bowing force at the narrow end of 100 μm which corresponded to a one pixel displacement. This result already has interesting implications on the stick-slip dynamics of bowed bars, because it sets an upper limit to the sticking time at average bowing speed. An average bowing speed of 0.2 m/s yields a maximum sticking time of 500 μs, which is only a short fraction of the total fundamental oscillation of the measured bar, with a fundamental frequency of 186.5 Hz or a period of 5.4 ms. Whereas in the bowed string case the sticking phase is a large part of the oscillatory cycle, this is obviously not the case for the bowed bar.

Simulations using the banded waveguide approach are in qualitative agreement with measurement. Hence the simulation approach seems a reasonable tool for qualitative investigation of the bowed bar phenomenon as well as an attractive efficient simulation method for musical performance.

ACKNOWLEDGMENTS

The authors are thankful for discussions about bowed string and bowed bar performance with Dan Trueman and Virgil Moorefield. Robert Schumacher and Chris Chafe provided helpful comments on bowing machine design. We greatly appreciated input by Antoine Chaigne and Davide Rocchesso on numerical simulation methods and filter design. The authors are grateful for the support of Peter Barker of the Applied Physics Group at Princeton University for assistance in conducting high-speed video measurements using the group's high-speed camera equipment. The authors are grateful for insightful remarks by two anonymous reviewers, which helped clarify some points and improve the paper. Georg Essl would like to acknowledge partial financial support by the Austrian Federal Ministry for Science and Traffic. The authors would like to thank Intel, Interval Research, and Arial Foundation for financial support.

[1] F. Orduña Bustamante, ''Nonuniform beams with harmonically related overtones for use in percussion instruments,'' J. Acoust. Soc. Am. **90**, 2935–2941 (1991); Erratum: J. Acoust. Soc. Am. **91**, 3582–3583 (1992).
[2] I. Bork, ''Practical tuning of xylophone bars and resonators,'' Appl. Acoust. **46**, 103–127 (1995).
[3] J. Petrolito and K. A. Legge, ''Optimal undercuts for the tuning of percussion beams,'' J. Acoust. Soc. Am. **102**, 2432–2437 (1997).
[4] J. Bretos, C. Santamaría, and J. A. Moral, ''Finite element analysis and experimental measurements of natural eigenmodes and random responses of wooden bars used in musical instruments,'' Appl. Acoust. **56**, 141–156 (1999).
[5] V. Doutaut, D. Matignon, and A. Chaigne, ''Numerical simulations of xylophones. II. Time-domain modeling of the resonator and of the radiated sound pressure,'' J. Acoust. Soc. Am. **104**, 1633–1647 (1998).
[6] A. Chaigne and V. Doutaut, ''Numerical simulations of xylophones. I. Time-domain modeling of the vibrating bars,'' J. Acoust. Soc. Am. **101**, 539–557 (1997).
[7] V. Bucur, *Acoustics of Wood* (CRC, Boca Raton, FL, 1995).
[8] D. Holz, ''Acoustically important properties of xylophone-bar materials: Can tropical woods be replaced by European species?,'' Acust. Acta Acust. **82**, 878–884 (1996).
[9] I. Bork, A. Chaigne, L.-C. Trebuchet, M. Kosfelder, and D. Pillot, ''Comparison between modal analysis and finite element modelling of a marimba Bar,'' Acust. Acta Acust. **85**, 258–266 (1999).
[10] J. L. Moore, ''Acoustics of Bar Percussion Instruments,'' Ph.D. thesis, Ohio State University, Columbus, 1970.
[11] T. D. Rossing, ''Acoustics of percussion instruments—Part I,'' Phys. Teach. **14**, 546–556 (1976).
[12] N. H. Fletcher and T. D. Rossing, *The Physics of Musical Instruments*, 2nd ed. (Springer Verlag, New York, 1998).
[13] J. Wawrzynek, ''VLSI Models for Sound Synthesis,'' in *Current Directions in Computer Music Research*, edited by M. Mathews and J. Pierce (MIT, Cambridge, 1989), Chap. 10, pp. 113–148.
[14] P. R. Cook, ''Physically informed sonic modeling (PhISM): Synthesis of percussive sounds,'' Comput. Music J. **21**, 38–49 (1997).
[15] X. Serra, ''A Computer Model for Bar Percussion Instruments,'' in *Proceedings of the International Computer Music Conference (ICMC)* (International Computer Music Association (ICMA), The Hague, 1986), pp. 257–262.
[16] K. van den Doel and D. Pai, ''The Sound of Physical Shapes,'' Tech. Rep., Dept. of Computer Science, University of British Columbia, Canada, Vancouver (1996).
[17] J. H. Smith, ''Stick-Slip Vibration and its Constitutive Laws,'' Ph.D. thesis, University of Cambridge, March 1990.
[18] G. Essl and P. R. Cook, ''Banded Waveguides: Towards Physical Modeling of Bowed Bar Percussion Instruments,'' in *Proceedings of the International Computer Music Conference (ICMC)* (International Computer Music Association (ICMA), Beijing, China, 1999), pp. 321–324.
[19] L. Cremer, *The Physics of the Violin* (MIT, Cambridge, 1984).
[20] C. Hutchins and V. Benade, eds., *Research Papers in Violin Acoustics 1975–1993* (Acoustical Society of America, Woodbury, NY, 1997).
[21] M. E. McIntyre, R. T. Schumacher, and J. Woodhouse, ''On the oscillation of musical instruments,'' J. Acoust. Soc. Am. **74**, 1325–1344 (1983).
[22] J. O. Smith, ''Efficient Simulation of the Reed-Bore and Bow-String Mechanisms,'' in *Proceedings of the International Computer Music Conference (ICMC)* (International Computer Music Association (ICMA), The Hague, 1986), pp. 275–280.
[23] S. Serafin, C. Vergez, and X. Rodet, ''Friction and Application to Real-time Physical Modeling of a Violin,'' in *Proceedings of the International Computer Music Conference (ICMC)* (International Computer Music Association (ICMA), Beijing, China, 1999), pp. 216–219.
[24] A. Chaigne and A. Askenfelt, ''Numerical simulations of piano strings. I. A physical model for a struck string using finite difference methods,'' J. Acoust. Soc. Am. **95**, 1112–1118 (1994).
[25] A. Chaigne and A. Askenfelt, ''Numerical simulations of piano strings. II. Comparisons with measurements and systematic exploration of some hammer-string parameters,'' J. Acoust. Soc. Am. **95**, 1631–1640 (1994).
[26] M. Palumbi and L. Seno, ''Physical modeling by directly solving wave PDE,'' in *Proceedings of the International Computer Music Conference (ICMC)* (International Computer Music Association (ICMA), Beijing, China, 1999), pp. 325–328.
[27] M. D. Waller, *Chladni Figures—A Study in Symmetry* (Bell, London, 1961).
[28] T. D. Rossing, ''Acoustics of the glass harmonica,'' J. Acoust. Soc. Am. **95**, 1106–1111 (1994).
[29] J. Woodhouse, ''On the playability of violins. Part I: Reflection functions,'' Acustica **78**, 125–136 (1993).

Constancy of loudness of pipe organ sounds at different locations in an auditorium

J. M. Harrison
Department of Psychology and Hearing Research Center, College of Engineering, Boston University, 64 Cummington Street, Boston, Massachusetts 02215

N. Thompson-Allen
Yale School of Music, Stoeckel Hall, 96 Wall Street, New Haven, Connecticut 06511

(Received 10 November 1999; accepted for publication 28 March 2000)

Pipe organ sounds, as judged by ear, tend to remain constant across different locations in an auditorium, yet the SPL of line spectra may vary by a maximum of 26 dB (mean 8.98 dB, s.d. 2.5), and the overall level may vary, typically, 10 to 12 dB from location to location. However, organs are designed, listened to, and regulated using the psychophysical units of loudness and timbre, and it is possible that the heard sound constancy exists at the psychophysical level. The present work recorded the sound of the C's and G's of pipe organ stops at three different locations in a church. The sound pressure levels were transformed to loudness. Similarity of loudness across the locations was measured two ways. First, the bass to treble distribution of loudness across the compass was measured using cross-correlation functions across pairs of locations. Second, the degree of similarity of loudness at the different locations was quantified by calculating ratios of loudness between the different locations. By these measures, the bass to treble loudness distribution and absolute loudness of the reeds were found to be nearly identical at the three locations. Two psychophysical processes were shown to be responsible for the loudness constancy. The first depended upon the power summation of harmonics within each third octave band above band 9 which contain two or more harmonics. The power summation of these harmonics greatly reduced the effect of SPL variability of the line spectra contained within these higher numbered bands. The second depended upon interharmonic loudness summation and upward masking of the first six harmonics. Greater loudness variability at the different locations was found after transforming the SPL measurements of two 8-ft diapasons to loudness compared with the reeds. The larger loudness variability was due to the smaller number of harmonics above the third of the diapasons compared with the reeds. The psychoacoustic measures indicate what a listener will hear as he/she moves among the locations. [S0001-4966(00)01407-7]

PACS numbers: 43.75.Np [WJS]

INTRODUCTION

Lottermoser (1950) noted that if one moves around an auditorium, an organ maintains its characteristic sound to the ear. However, when he measured the sounds at several positions 10 m from the original position he reported that ''a maximum reduction of an harmonic was 20% of the maximum measured value.'' Fletcher *et al.* (1963) measured the SPLs of the harmonics of G2 of an organ reed from different microphone locations, about 10 ft apart, in the nave of a church, and found that the SPL of the harmonics varied up to a maximum of about 15 dB. The amplitude changes found in both studies were randomly different for different harmonic numbers at each location, and no case was found where all the harmonics dropped to a low value at the same location. Stepanek and Otcenasek (1994) measured the variation of sine wave signals in a church using multiple microphone locations and reported variations over 20 dB. Investigations made on the present organ showed harmonic variations up to a maximum of 26 dB, with a mean variation of 8.98 dB. Lottermoser (1950) attributed the constancy of the sound to the ear to the fact that the amplitudes of all the harmonics never changed together, and for this reason he used only a single microphone at one location in the auditorium in the majority of his acoustical investigations (Lottermoser, 1940, 1948, 1950, 1952, 1953, 1968). Later investigators have also reported measurements at a single location in the auditorium (Pollard, 1988; Pollard and Jansson, 1982a, b; Churcher, 1962; Hall, 1993; Harrison and Thompson-Allen, 1996, 1998). Plomp and de Laat (1984) used factor analysis of data collected by Lottermoser (1950) and Lottermoser and Meyer (1960) (using a single microphone) to tonally differentiate 14 organs. None of these studies investigated the differential effects of microphone location upon the sound of the instruments. Pollard (1978a, b) measured four organs using several microphone positions, and two different microphones, but did not report differences across the locations or microphones.

Organ builders judge the sound of an instrument by the psychophysical standards of loudness and timbre, not by its measurement in physical units, and organs are also ''finished'' and ''regulated'' (bass to treble distribution of loudness) at installation using judgments based on the same psychophysical units. This suggests that one reason for the tendency to heard sound constancy may reside in the transformations performed by the cochlea, and auditory neural

centers on the physical signals of the organ sound, and that the physical units should be transformed to psychophysical units. Pollard (1978a, b, 1988), Pollard and Jansson (1982a, b), and Churcher (1962) used psychophysical analysis in their studies of loudness and timbre of organ tone so that the properties of hearing would be incorporated in the measurements. Miskiewicz and Rakowski (1994) also used loudness transformations to study other musical instruments.

Three major points need investigation:

First, physical units do not appear to show sufficient constancy from location to location to explain the degree of heard sound constancy between different locations. Does their transformation into psychophysical units lead to the necessary constancy?

Second, if psychophysical measures give more constant results across different locations, what kinds of mechanisms change large variations of physical units to small variations of psychophysical units?

Third, methods need to be selected to quantify both the distribution of loudness across the compass and the absolute loudness at different locations in the auditorium.

The present work examined these problem areas with respect to the regulation of bass to treble loudness distribution of steady-state sounds across the keyboard compass and the absolute loudness at each location. The study of variation of timbre (spectral envelope) at different locations will be discussed elsewhere.

I. GENERAL METHOD

A. The organ

The three manual and pedal mechanical action organ used in the present study was built by the Noack Organ Company, Opus #111, in 1989. The instrument is located at the east end (chancel) of The Church of the Redeemer, Chestnut Hill, MA. This is a large stone church with a reverberation time of approximately 2.2 s (extrapolated to -60 dB). The console is located in the choir, with the choir organ immediately behind it. The great is located in the chancel, over the console. The swell and pedal are located in a chamber behind the great, and project to the body of the church through a large opening. The ambient noise level in the church was 53 dBC, measured using a GenRad sound level meter, 1565-D. The temperature was 79 °F at the start of measurement and dropped to 78 °F by the end.

The purpose of the present work, and that of the other investigators quoted above, is to study the sound of the organ as heard by listeners (i.e., as produced by the transfer function of the church). It is not the purpose to study either the transfer function of the church or the sound of the pipes in a free field (i.e., independently of the transfer function). To include the transfer function of a church, Lottermoser (1948, 1968), for example, located the microphone about 25 m from the organ at a normal listening position in the nave. In only one study (Lottermoser, 1940) was the microphone placed only 1 m from the labia of the pipes, in this case, with the idea of excluding the transfer function of the church. Many investigators have studied the sound of organ pipes independently of the transfer function of a hall. Boner (1938), for example, mounted voiced pipes at the top of a high pole in the middle of a field, and mounted the microphone about 2 m from the pipe. Ingerslev and Frobenius (1947) excluded echoes and standing waves by using a room, with some echoes, but with the microphone mounted close to the pipes so as to exclude interference.

B. Bandwidth and amplitude response of the measuring system

The system was designed to measure frequencies from 15 Hz to 10 kHz. This span covers the range from the fundamental frequency of a 32-ft stop to the top note of a 2-ft stop. The lower notes of some 32-, 16-, and 8-ft stops may have fundamentals which are below absolute threshold in some locations [less than 76 dBC for a 32-ft stop, 55 dBC for a 16-ft stop, and 35 dBC for an 8-ft stop (Robinson and Dadson, 1956; Jackson *et al.*, 1999)] and it is necessary to show that the measured absence of a fundamental is not an artifact due to an inadequate frequency response at the low end of the measuring system. The pitch, if below about 1 kHz, is unchanged if the fundamental is missing [periodicity pitch, Houtsma and Goldstein (1972); Terhardt *et al.* (1982); Fletcher (1928); Licklider (1951, 1956)].

Two Bruel and Kjaer 1-in. condenser microphones (#4132) were used. These have a random field response from 15 Hz to 5 kHz which is flat within 0.75 dB. The response from 5 to 10 kHz varied about 1.0 dB. The sensitivity of the microphones was matched to within 0.2 dB. The output of each microphone was passed through a 20-dB amplifier prior to further processing (Coulbourn, S79-01). These amplifiers have a dc to 50-kHz (within ± 1 dB) pass band.

A digital audio tape recorder (DAT, Sony DTC790) was used to record the sounds. The frequency response of the DAT was measured and found to be flat within 0.7 dB from 15 Hz to 18 kHz. A sampling rate of 48 kHz was used. The DAT is equipped with an internal low-pass filter to prevent aliasing above about 19 kHz.

A Tahiti sound card (Turtle Beach) was used. This is listed as having a response from dc to 20 kHz, ∓ 0.2 dB. The frequency response of the sound card in conjunction with the sound analysis software (Spectraplus, Pioneer Hill) was measured using sine wave signals. The amplitude of the single spectral line was flat with a maximum of 0.8 dB over the range 15 Hz to 10 kHz. During analysis, a sampling rate of 44.1 kHz was used at 16-bits amplitude resolution, and the fast Fourier transform (FFT) size was 65 536 points, giving a line resolution of 0.673 Hz. These settings give a harmonic analysis starting at about 1 Hz, well below the fundamental of a 32-ft stop.

Signals with a peak above 99 dB SPL overloaded the system. The strongest peak signal encountered in the present set of measurements was about 85 dB SPL, well below the distortion level of the system.

The rms level of the system was calibrated to dB SPL (reference 20 μPa) using a Bruel and Kjaer pistonphone #4220.

Overall SPL (dB) measurements were made directly from the DAT recordings using a Tektronix digital multimeter (DM502A).

C. Microphone placement and procedure

(1) Both microphones were placed in the nave. Microphone 1(M1) was 17 m from the organ and microphone M2, in its first position (M2p1), was 20 m from the instrument, and 1.7 m to the left side. These distances are typical of those used in investigations of organ tone. Bottom C, bottom G, the remainder of the C's, and top G of the great 8-ft diapason were recorded twice on the two channels of the DAT in quick succession. Comparison of the two takes will indicate the stability of the recording system in the absence of any changes in the organ or the church.
(2) Bottom C, bottom G, the remainder of the C's, and top G's of the two 8-ft manual Diapason stops and the three manual 8-ft reed stops were then recorded using the two microphones connected to the two channels of the DAT.
(3) M2 was then moved forward to its second position, 14 m from the organ (M2p2). The same stops were then recorded again from M1 (position not changed) and microphone 2 (in the new position, M2p2) using the two channels of the DAT. Comparison of the two records taken from M1 (fixed position) will indicate any changes (such as temperature) which occurred over the time necessary to make the first measurements. The record obtained from the shifted microphone M2p2 will give data at a third microphone location.

Each record consisted of 10 s of silence, 10 s of the note, followed by 10 s of silence.

D. Analysis of the data

A $\frac{1}{3}$-octave band spectrum, using the nominal frequencies of the bands according to ISO 532 B [see Patterson (1980), p. 118, for details, and the actual frequencies of the standard bands] of each note was prepared. Loudness was calculated from these bands using the methods of Zwicker and Fastl (1999), Zwicker *et al.* (1984), and Fastl *et al.* (1990). Similar procedures were used by Pollard and Jansson (1982a, 1982b), Pollard (1978a), and Lottermoser (1969) to calculate loudness using standard $\frac{1}{3}$-octave bands. The present results are thus comparable with this previous work.

Pollard (1978b) also used standard $\frac{1}{3}$-octave bands and showed that the location of harmonics within each band was different for each note (his Fig. 1). Pollard (1978b) did not consider these differences to affect seriously computed values and used the standard bands for all note frequencies. The loudness calculating routines (Zwicker *et al.*, 1984; Moore and Glasberg, 1996; Moore *et al.*, 1997) contain large look-up tables for converting, for example, standard $\frac{1}{3}$-octave bands to equivalent Bark bands. Shifting the frequency of the third octave bands to equalize the position of harmonics of different notes in the bands would require that a set of look-up tables be constructed for each note, and each tuning temprement. The psychophysical data necessary to construct each tables may not be available.

Pollard (1978b) also considered that the incorporation of wider bandwidths for the lower frequencies used by Zwicker (1961) had little effect on the loudness calculations, and used the standard bands for notes of all frequencies [as Zwicker *et al.* (1984) did in their later system].

Pollard and Jansson (1982a) also used Stevens Mark VII procedure (which is also based on the standard $\frac{1}{3}$-octave band frequencies) which gave correlated results (Stevens, 1971). We have also used Stevens Mark VI (Stevens, 1961) and Churcher's (1962) modification of Stevens' (1961) method for harmonic sounds with similar results.

Stevens Mark VI and Mark VII (1961, 1971) procedures measure the pressure level (in dB) of the sound using standard third octave (or octave) bands. These data are converted to loudness for each band. It is assumed that the overall loudness will not be less than the third octave band of greatest loudness. The loudness of this band is then added to a fraction (Steven's F) of the sum of the loudnesses of the remaining bands. The value of F is determined by the width of the band ($\frac{1}{3}$ or 1 octave).

Zwicker (1961), Zwicker *et al.* (1984), and Zwicker and Fastl (1999) improved the treatment of interaction between the bands (represented by Stevens's F). They transformed $\frac{1}{3}$-octave band data to the ''specific'' loudness of modified Bark bands, and summed the ''specific'' loudnesses to obtain overall loudness. Unlike third octave bands, the Bark bands have a concave skirt on the high-frequency side, which may overlap (and mask) up to two or more adjacent bands. The interaction between bands due to the concave skirt can be seen in Zwicker diagrams [Pollard and Jansson (1982a), their Fig. 5, and Fig. 1 of Zwicker *et al.* (1984), for example]. It is the concave shape of the upper frequency side of these bands which determines whether masking will occur in each particular case.

There is a difference in loudness of a given signal in a free field compared with the diffuse field of an auditorium. In their method, Zwicker *et al.* (1984) calculate loudness for a free or diffuse field. The difference varies with frequency [see their Fig. 8.2, in Zwicker and Fastl (1999), for details of the diffuse/free field loudness difference]. Diffuse field calculations were used in the present work.

The first six harmonics of the line spectra of the C's are contained in third octave band numbers 1, 4, 6, 7, 8, and 9, the fundamental always falling into the first band (Pollard, 1978b). Two or more harmonics occupied higher band numbers. The SPLs of each of the several harmonics in each of these higher number bands were combined on a power basis (Pollard, 1978a). For the G's, only the first five harmonics fall with separate bands (1, 4, 6, 7, and 8). It is necessary to take this difference into account when calculating loudness since the harmonics included in the power summations will differ for different notes of the scale.

The overall SPL (dB) of each note was also recorded to obtain a measure of the variation between the records from the different microphones.

E. Loudness

Loudness is a prothetic (ratio) scale (Stevens, 1951, 1966; Zwicker and Fastl, 1999, p. 233; Stevens and Davis (1938), p. 112 ff.), so differences in loudness in the present work are expressed in terms of ratios of the loudness coefficients.

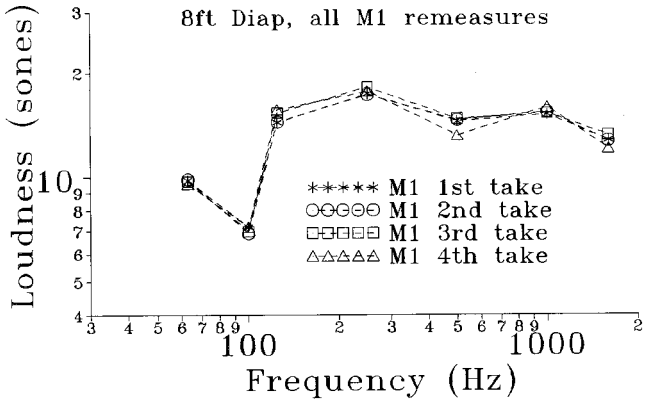

FIG. 1. Four measurements of the loudness of the 8-ft great diapason at the M1 microphone location. Each point indicates the loudness of the notes (C2, G2, etc.). Take 1 was the first measurement of the day, and take 4 the last, after the whole organ was measured. The loudness measurements were virtually identical. M1=position of microphone 1.

To accommodate the ratio characteristics of loudness and facilitate the reading of data plots, loudness has been plotted on the ordinate using a log scale so that equal vertical distances indicate equal loudness ratios. Frequency is also plotted on a log scale. In these plots a given rate of decrease (or increase) in loudness per octave is represented by the slope of a straight line. Scale lines showing the ratio of sones (always the smaller number over the larger number of sones) across an octave have been fitted, by eye, to the plots to aid in estimating this variable. A horizontal line indicates no change in loudness across an octave.

II. RESULTS AND DISCUSSION

A. Remeasurements

The four measurements of the overall loudness of the 8-ft diapason (Gt) made at the M1 location are shown in Fig. 1. The first and second measurements were taken immediately after each other. The results were identical. The third measurements was taken about 10 min after the second. The fourth measurement was made after the completion of the first measurement of the instrument (about 2 h). These measurements were also essentially identical. The constancy of these data show that any observed differences between the different locations were not due to changes in the organ or church, but in the properties of the locations.

B. Loudness of reeds at the three locations

The diffuse loudness of the three 8-ft manual reeds at each of the locations is shown in Fig. 2. Each point represents the loudness of the sound produced by pressing the designated key (C2, G2, etc.). Straight (dashed) lines of various slopes were fitted, by eye, to the plots to indicate the ratios of loudness change over an octave.

The degree of similarity, at the three locations, of the distribution of loudness across the compass of each stop was quantified by measuring the cross correlations of loudness distribution (distribution envelope) across pairs of different locations (Table I). All the zero lag correlations were significant at, or better than, the 0.01 confidence level. The correlations are very high, indicating a near identity of the envelopes of loudness distribution across the compass at the different locations.

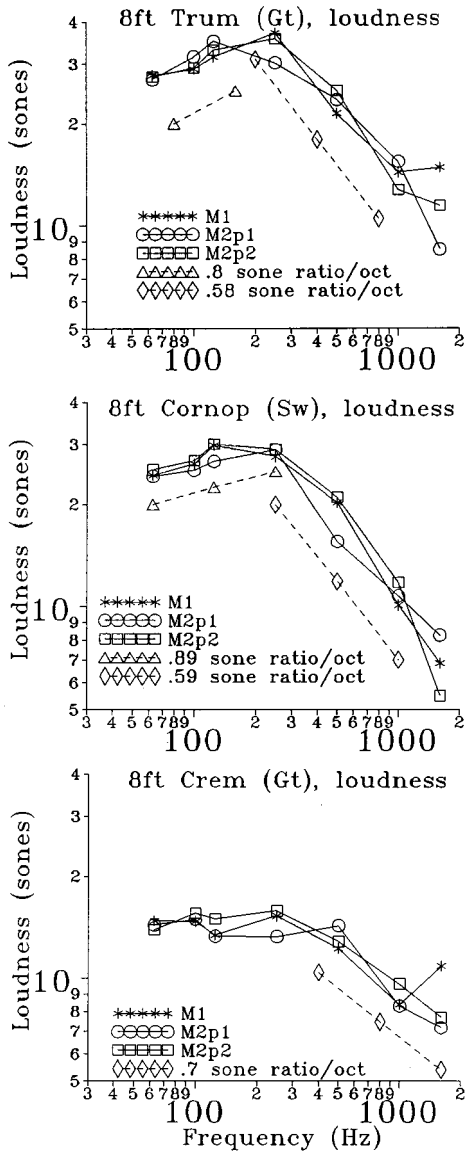

FIG. 2. The overall loudness of the three manual reeds. Each point shows the loudness of that note (C2, G2, etc.) at one of the three microphone positions. The envelope of the solid lines joining the points shows the distribution of loudness across the scale from C2 or G6, at each of the three microphone positions as indicated by the asterisk, circle, and square symbols. Scale lines (dashed) were fitted by eye to show the ratio of loudness (sone ratio) over an octave. M1, M2p1, and M2p2 indicate the different positions of the two microphones, M1 and M2. Trump=trumpet, Cornop=Cornopean, Crem=Cremona, Gt=great, Sw=swell, Ch=choir.

The correlation table can be viewed as one measure of the bass to treble ''regulation'' of the organ. ''Regulation'' is one of the last operations carried out by the builder before handing the instrument over to the owner. This may be done at several locations because of possible differences in loudness distribution at different sites. ''Regulating'' consists of playing each note and setting its loudness to achieve as near to the desired level as is possible by spreading the energy evenly enough among the many harmonics that the effects investigated below help make the loudness more uniform.

TABLE I. Cross correlation (lag 0) of loudness across the compass.

Stop	Microphone locations		
	M1:M2p1	M1:M2p2	M2p1:M2p2
Trump (Gt)[a]	0.889	0.973	0.945
Corn (Sw)[b]	0.965	0.995	0.965
Crem (Ch)[c]	0.895	0.882	0.910

[a]Trump=8-ft trumpet; GT=great.
[b]Corn=8-ft Cornopean, Sw=swell.
[c]Crem=8-ft Cremona, Ch=choir.

The degree of success in equalizing the shape of the loudness distribution (i.e., the envelope) at different places in the auditorium is shown by the size of the correlations of Table I, unity indicating no difference between the locations.

The cross correlations quantify similarity of the shape of (envelope of) the distribution across the compass, but not the absolute loudness of each distribution. The degree of similarity of loudness of each note at the different locations was quantified by taking the ratio of loudness for each pair of sites (Table II). The ratios approached unity, except for G6. The relatively large ratio variations at G6 are due to the small number of harmonics at this top note (see analysis later in this article).

It is assumed here that a ratio of about 0.9 represents a working differential threshold, and that two sounds having loudness ratios of 0.9 (or 1.11) and above (or below) are not readily distinguishable. This number was obtained from listening to and measuring the loudness of records of pipes slightly off speech and variable in loudness. The majority of the ratios from C2 to C5 are near unity, indicating that the loudnesses of the notes at different locations are not readily distinguishable. Above C5, the ratios become variable, as can be seen at G6, most being below 0.9.

The constancy of the loudness of the sound as one moves around the auditorium is apparent in the loudness data (Fig. 2 and Table II) and was compelling to the ear. The high cross correlations of the loudness data together with the loudness ratios across locations imply that three listeners at the different locations will describe the loudness of each note in essentially the same way, or that the same person will hear essentially the same loudness at the different locations.

C. Psychophysical mechanisms underlying loudness constancy

There are two psychophysical processes that favor loudness constancy across different locations. The first is the interaction within critical bands of the higher numbered harmonics, and the second is the interharmonic loudness summation and masking across critical bands of the first six harmonics which compresses variation from the second to the sixth harmonic.

1. Reduction of $\frac{1}{3}$-octave band SPL variations by power summing

For the C's harmonics one through six are contained in separate third octave bands 1, 4, 6, 7, 8, and 9 (which may therefore be treated as line spectra). Beyond band 9, the third octave bands contain a progressively increasing number of harmonics per band. The location of harmonics in third octave bands was made by marking the frequency of each harmonic, then converting to third octave bands. The markers appeared at the same frequency on the third octave display, allowing their location within bands to be determined. The amplitude of the harmonics was obtained directly from the software. The SPL of the higher numbered bands was calculated by summing the power of the contained harmonics (Pollard, 1978a). Since these multiple harmonics in each band are separated by less than a third of an octave (nominal critical band), their loudnesses will not sum within the band. In summary, harmonics of organ sounds fall into two distinct classes, the first five or six in which loudness summation occurs, and the remainder which are distributed two or more to a band, within which there is no loudness summation.

TABLE II. Ratio of loudness across the three positions: reeds.

Stop	Note	Microphone positions		
		M1;M2p1	M1;M2p2	M2p1;M2p2
Trump[a]	C2	1.0	1.01	1.01
	G2	0.92	0.99	1.08
	C3	0.90	0.95	1.06
	C4	1.22	1.04	0.85
	C5	0.91	0.86	0.94
	C6	0.93	1.13	1.21
	G6	1.78	1.25	0.71
Cornop[b]	C2	1.01	0.96	0.96
	G2	1.04	0.98	0.94
	C3	1.12	0.99	0.89
	C4	0.96	0.95	1.00
	C5	1.30	0.97	0.74
	C6	0.94	0.86	0.91
	G6	0.83	1.24	1.50
Crem[c]	C2	1.01	1.05	1.03
	G2	1.02	0.98	0.96
	C3	1.00	0.89	0.89
	C4	1.05	0.88	0.84
	C5	0.91	0.96	1.05
	C6	1.02	0.88	0.87
	G6	1.42	1.32	0.93

[a]Trump=trumpet.
[b]Cornop=Cornopean.
[c]Crem=Cremona.

The effect of power summing of multiple harmonics within a band is to reduce the effect of the difference (dB) between the amplitudes of the harmonics at different locations. This is shown by using C2 of the trumpet as an example (Table III). Comparison between two locations (M1 and M2pl) was used in this example. Similar results were obtained from analysis of the Cornopean (Sw) and Cremona (Ch).

Harmonic numbers above 6 are shown in the first column of Table III. The next two columns (recorded from M2pl and M1, respectively) show the levels (dB SPL) of the harmonics at the M2pl and M1 locations. The fourth column shows the difference (dB) between the harmonics. The fifth column shows the third octave band numbers. Columns 6 and 7 show the pressure level of the bands at the two locations obtained by power summing of the contained harmonics. The difference between the bands is shown in the last

TABLE III. Reduction of difference between harmonics due to energy summation: Trum C2.[a]

Harmonic no.	M2p1	M1	Difference (dB)	Band no.	M2p1	M1	Difference (dB)
7	65	67	2)				
8	60[b]	67[b]	7)	10	66[b]	70[b]	4
9	68	65	3)				
10	54	61	7)	11	68	66	2
11	52	48	4)				
12	55	52	3)				
13	61	60	1)	12	62	60	2
14	59	57	2)				
15	59	62	3)				
16	65	52	13)				
17	53	42	11)	13	66	63	3
18	56	56	0)				
19	59	55	4)				
20	51	40	11)				
21	50	59	9)	14	62	62	0
22	46	34	12)				
23	42	31	11)				
24	44	49	5)				
25	41	41	0)				
26	40	38	2)	15	50	50	0

[a]Trum=trumpet.
[b]dB (SPL).

column. For example, harmonics 7 and 8 differed across the sites by 2 and 7 dB. Band 10, however, differed by only 3.82 dB across the two sites. Similar reductions can be seen for the other bands. It is the SPL of these bands which is used to calculate loudness, the small SPL variations favoring loudness constancy across locations. This analysis holds from C2 to about C5. Above C5, the number of high-numbered harmonics declined, and by G6, only three to five harmonics remained.

2. Compression effects of loudness summation and masking of the first six harmonics

Two mechanisms have been suggested as responsible for the small variation of loudness from location to location. Cumulative loudness plots were prepared to display the actual number of possible mechanisms responsible for the reduction of loudness variability. These plots (Figs. 3–5) were produced by calculating loudness using only the first band,

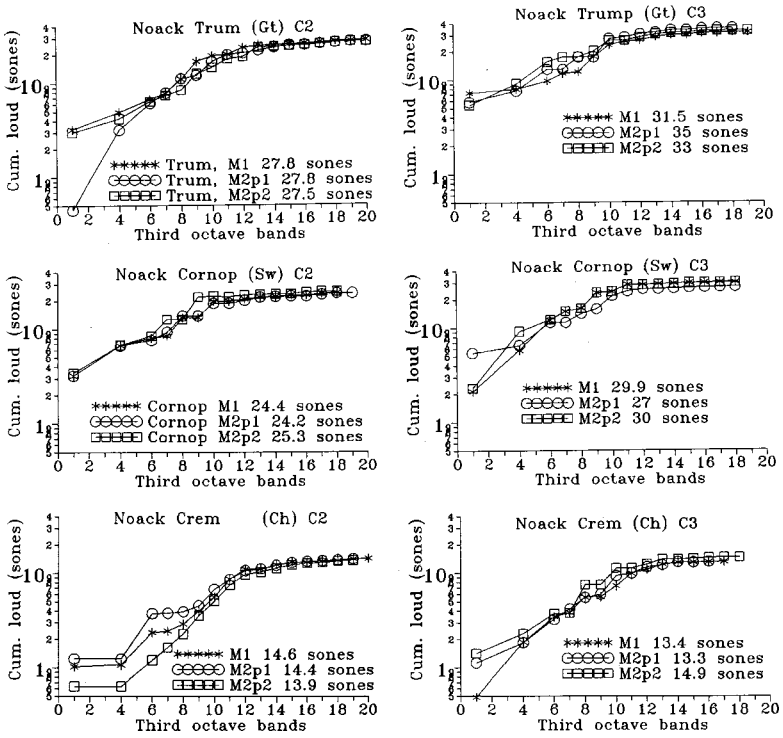

FIG. 3. Cumulative loudness (see text for the method) of C2 and C3 of the three manual reeds. Note the two components of each plot: (*i*) a smooth loudness increase from about the tenth to the top band and (*ii*) a variable segment from bands 1 to 9. The number of sones shown for each microphone position in the legend refers to the overall loudness of C2 and C3 as plotted in Fig. 2. M1, M2p1, and M2p2 indicate the three microphone positions. Note the large variability of the first harmonic. Trump=Trumpet, Cornop=Carnopean, Crem=Cremona, Gt=Great, Sw=Swell, M1, M2p1, M2p2 =Microphone positions.

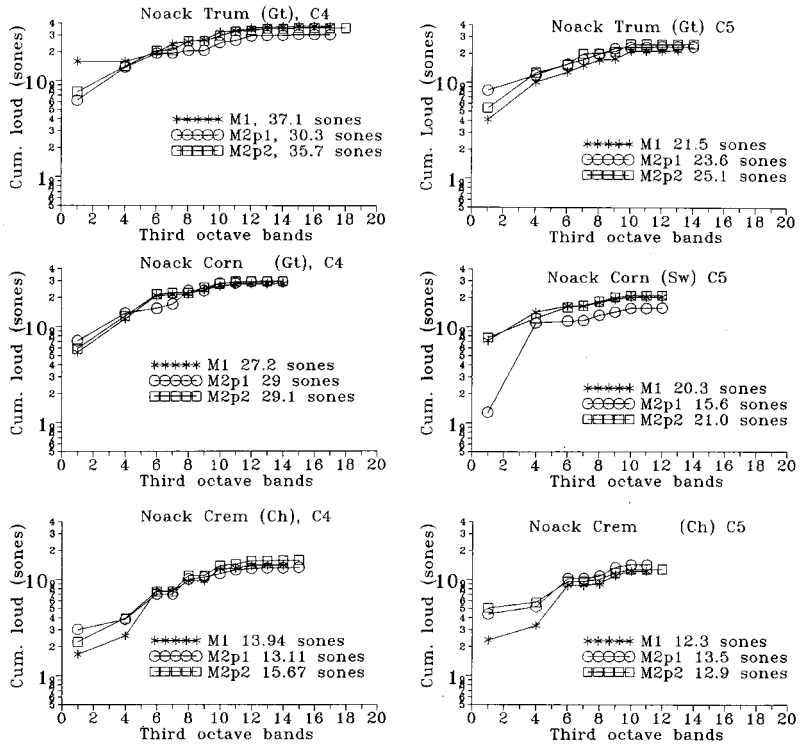

FIG. 4. Cumulative loudness (see text for the method) of C4 and C5 of the three manual reeds. The component starting at band 10 dwindles as the number of bands decline. M1, M2p1, and M2p2 indicate the three microphone positions. The numbers of sones shown in the legend refer to the overall loudness of the plotted points of C4 and C5 shown in Fig. 2. Trump=trumpet, Cornop =Cornopean, Crem=Cremona, Gt=great, Sw=swell, Ch=choir.

then bands 1 and 4, then bands 1, 4, and 6, and so on. The cumulative loudness plot of G2 was similar to the plots of C2 and C3, so is not shown here.

The plot of C2 (top of left column of Fig. 3), for example, appears to have two sections. From about band 10 up, there is a steady and smooth increase in loudness to the top band. This section of the plot shows the small loudness variability due to the effect of power summation. The section of the plot from band 1 to band 9 shows two characteristics; one a random variability of loudness of the first two or three harmonics (bands 1, 4, and 6), and two, a reduction of this random variability as the sixth harmonic (band 9) is approached. The cumulative loudness plots show a clear difference between the roles in reduction of loudness variability of bands 1, 4, 6, 7, 8, and 9 (first six harmonics) and the higher number bands containing two or more harmonics. The first band of the Cremona varies equally randomly, but the compressive effect looks different because of the weak second

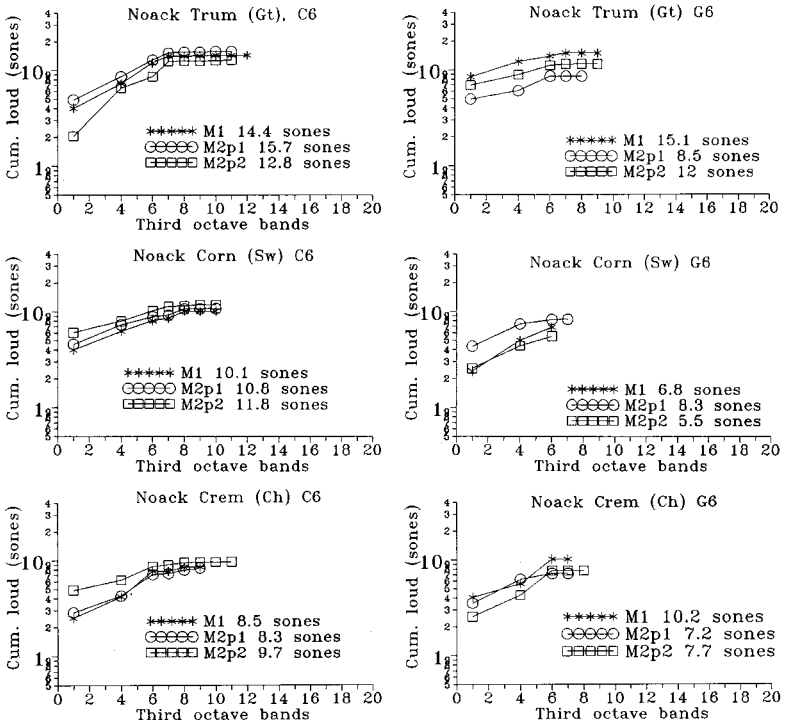

FIG. 5. Cumulative loudness records of C6 and G6 of the three reeds. M1, M2p1, and M2p2 indicate the three microphone positions. The numbers of sones shown in the legends are the overall loudness of C6 and G6 of Fig. 2. Note the absence of the upper (above band 9) loudness system. At G6, there is an insufficient number of harmonics to support even the lower harmonic number constancy system. Trump=trumpet, Cornop =Cornopean, Crem=Cremona, Gt=greats, Sw=swell, Ch=choir.

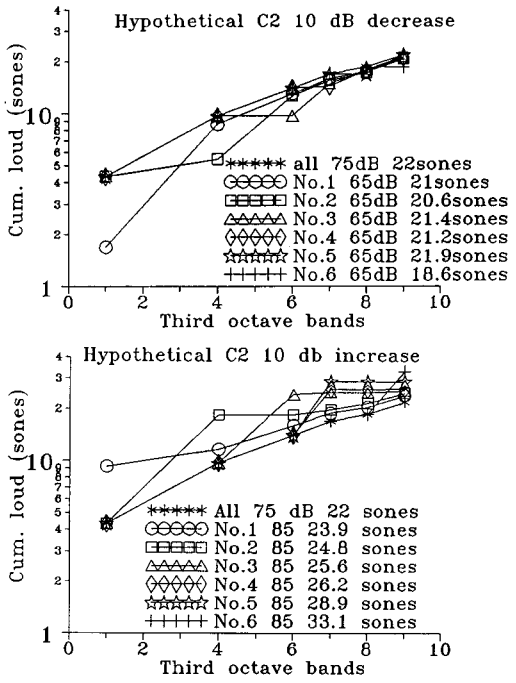

FIG. 6. The first six harmonics (all 75 dB) of a hypothetical reed, together with a reduction by 10 dB of each harmonic in succession (top panel). The 10-dB reductions had little effect on the overall loudness as shown by the sone numbers in the figure legends. The lower panel shows the effect of increasing each harmonic by 10 dB. There is still a trend to the same overall loudness, but the effect is smaller.

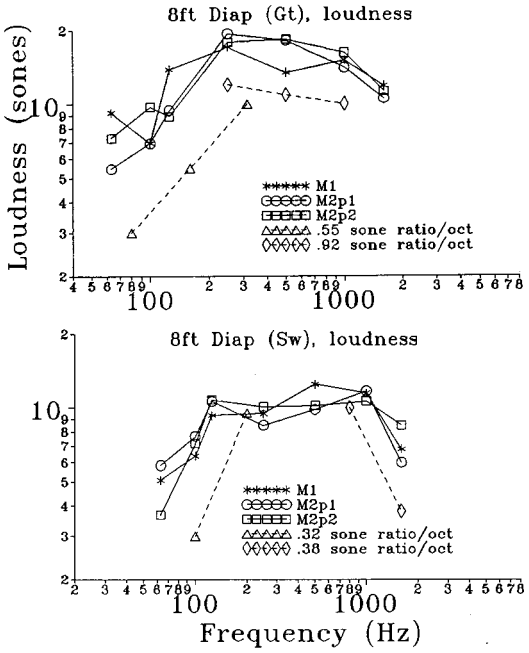

FIG. 7. Overall loudness of the two 8-ft manual diapasons. Each point (solid lines) represents the loudness of C2, G2, etc. The dashed scale lines, fitted by eye, show the ratio of loudness over an octave range (small no./large no.). M1, M2p1, and M2p2 indicate the three microphone positions. Diap=diapason, Gt=great, Sw=swell.

harmonic seen at C2, C4, and C5 of this clarinet sounding stop. At C3 of this stop, the second harmonic was relatively strong at the three microphone positions.

By C4 (left column of Fig. 4) the plots are beginning to change because of the decreasing number of bands above 9. From C5 to C6 the number of bands above 9 decreases, reaching near zero by C6 (left column of Fig. 5). By C6 only the first six harmonic system is available to reduce variability. By G6 (right column of Fig. 5) only bands 1, 4, and 6 (harmonics 1, 2, and 3) are available for reduction of variability in loudness, and only a small reduction was found.

The reduction of variability found in the first six harmonics appears to be due to interharmonic loudness summation and upward masking. The number of octaves between adjacent harmonics decreases with harmonic number. Harmonics one and two are separated by one octave (three nominal critical bands), two and three by about two critical bands, and so on. The degree of loudness summation of line spectra is a function of their octave separation, summation decreasing with narrowing of the octave separation (Zwicker and Fastl, 1999; Zwicker, 1961; Zwicker *et al.*, 1957). Harmonics four and five are separated by approximately 0.3 octaves and are the last pair for which there will be a significant summation of loudness.

Upward masking of each harmonic by the one below it increases with decreases in octave separation of the spectra. There is little downward masking below about 2 kHz. (Fletcher, 1928). Zwicker and Fastl (1999) accommodate masking by giving the critical bands a sloping skirt on the high-frequency side.

The first harmonic has unique properties. It has virtually no masking, exerts the least masking on the second harmonic because of the whole octave separation, and the maximum addition of loudness to the loudness of the second harmonic because of the large octave separation (one octave). Thus the loudness and the SPL of the first harmonic is free to vary randomly with the standing wave patterns at different locations. The large random variations of the first harmonic across different locations can be seen in the cumulative loudness plots (particularly in Figs. 3 and 4).

To illustrate more clearly the effect of loudness summation and upward masking, the first six harmonics of two hypothetical reeds were plotted. Both hypothetical reeds contain six harmonics (bands 1, 4, 6, 7, 8, and 9) of equal amplitude (75 dB). Such a distribution is typical of many reed stops.

In one of the hypothetical reeds (top panel of Fig. 6), the first harmonic was reduced to 65 dB, the remainder remaining at 75 dB. The second component was then reduced to 65 dB, the rest returning at 75 dB. This was continued for all six harmonics. The cumulative loudness plot is shown in Fig. 6, top panel. The total loudness after each harmonic shift is shown in the legend of the figure. Wherever the 10-dB re-

TABLE IV. Cross correlation (lag 0) of loudness across compass.

Stop	Microphone positions		
	M1:M2p1	M1:M2p2	M2p1:M2p2
8-ft Diap[a] (Gt)[b]	0.820	0.714	0.965
8-ft Diap[a] (Sw)[c]	0.852	0.832	0.798

[a]Diap=diapason.
[b]Gt=great.
[c]Sw=swell.

TABLE V. Ratio of loudness across the three sites: 8-ft diapasons.

Stop	Note	Microphone positions M1;M2p1	M1;M2p2	M2p1;M2p2
Diap,[a] Gt[b]	C2	1.81	1.36	0.75
	G2	1.00	0.78	0.78
	C3	1.67	1.69	1.01
	C4	0.96	1.02	1.06
	C5	0.97	1.30	1.35
	C6	1.05	0.90	0.86
	G6	1.14	1.09	0.96
Diap. Sw[c]	C2	0.88	1.38	1.57
	G2	0.84	0.89	1.06
	C3	0.88	0.85	0.96
	C4	1.12	0.94	0.84
	C5	1.26	1.23	0.97
	C6	0.98	1.07	1.09
	G6	1.13	0.80	0.71

[a]Diap=diapason.
[b]Gt=great.
[c]Sw=swell.

duction occurred, the loudness at the ninth band (sixth harmonic) was the same as that with no shifts within a ratio of 0.96, except when the shift occurred at the sixth harmonic, where the ratio was 0.85. The loudness at the ninth band (sixth harmonic) is shown in the legend of the figure. The large variation of the harmonics had very little effect on the total loudness.

The effect of increasing each band by 10 dB is shown in the lower panel of Fig. 7. The compressing effect was less than found when each harmonic was decreased by 10 dB. The ratios for the first five harmonics varied from 0.92 to 0.76. The ratio for the sixth harmonic was 0.66.

D. Loudness of two 8-ft diapasons at the three locations

1. Loudness (sones) of the 8-ft diapasons

The loudnesses of the 8-ft great and swell diapasons of the organ are shown in Fig. 7, and the cross-correlation functions are shown in Table IV. Each point (of the solid line plots) shows the loudness of a note (C2, G2, etc.) at one of the locations. The cross correlations of Table IV are, generally, lower than those seen for the reeds (Table I). The lower correlations do not indicate poor ''finishing,'' but are due to the fact that the diapasons have fewer harmonics than the reeds so that there is less opportunity for the two psychophysical processes, discussed in the reed section, to reduce variability.

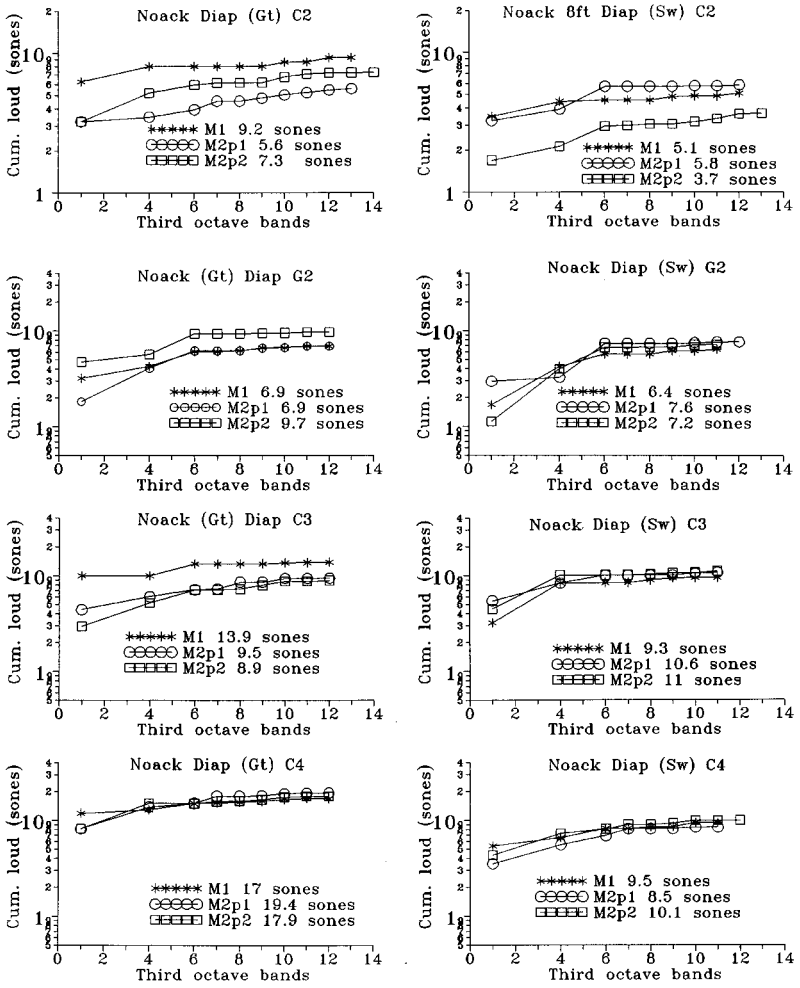

FIG. 8. Cumulative loudness (see text for method) of C2 to C4 of the two 8-ft diapasons. M1, M2p1, and M2p2 indicate the three microphone positions. The overall loudness of each of the notes at each microphone position is shown in the figure legends. Diap =diapason, Gt=great, sw=swell.

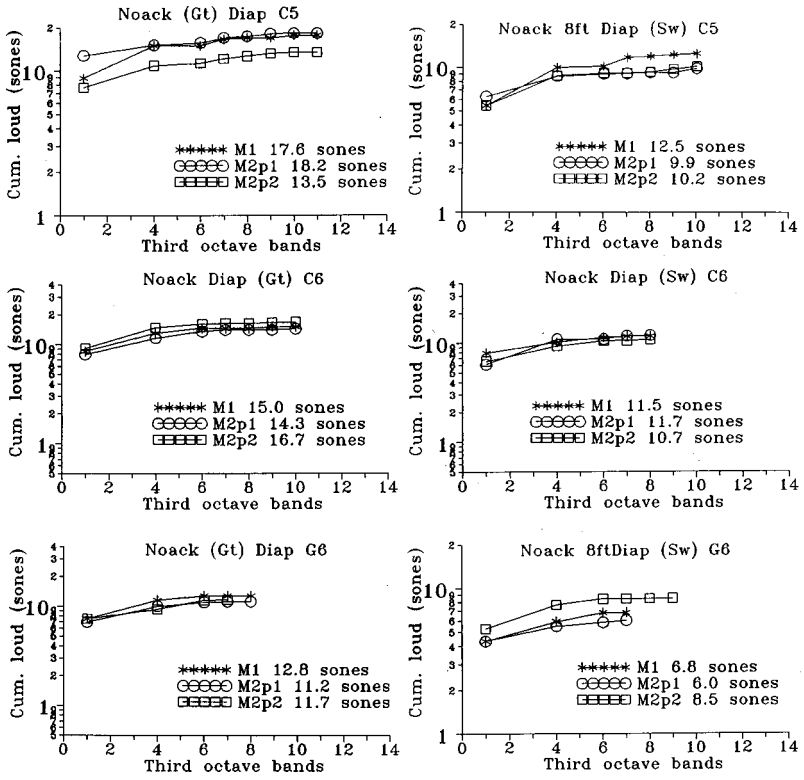

FIG. 9. Cumulative plots (see text for method) of C5 to G6 of the two 8-ft diapasons. The overall loudness of each of the notes at each microphone position is shown in the figure legends. M1, M2p1, and M2p2 indicate the three microphone positions. Diap=diapason, Gt=great, Sw=swell.

The degree of similarity of loudness at different locations for the two 8-ft diapasons was quantified by taking the ratios of overall loudness numbers at pairs of locations (Table V). These numbers are more variable than the corresponding values for the reeds (Table II). Most of the numbers fell below the working assumption of 0.9 (or above 1.11) ratio indicating no essential differences in loudness. According to these data, as a listener moves about, loudness will be different (by the amount in Table IV) at the different locations.

2. Cumulative loudness

The cumulative loudness plots of the 8-ft diapasons are shown in Figs. 8 and 9. The plots show that the largest random variation of loudness (from C2 to C5) is most likely to occur at the first harmonic. Similar large random loudness variation of #1 harmonic was shown in the cumulative loudness plots of the reeds (Figs. 3–5). In general, the first three to four harmonics dominated the spectra of the diapasons, the remainder being small, and not always sufficient in number (compared with the reeds) to eliminate variability above the sixth harmonic.

III. CONCLUSIONS

(1) The present work has shown that there are two psychophysical mechanisms that favor constancy of the loudness of the sound of pipe organs in auditoria. The first depends upon the power summation of harmonics (above the sixth) within each $\frac{1}{3}$ octave band above band #9. The second depends upon interharmonic loudness summation and upward masking of the first six harmonics. These two mechanisms reduce the effects of variations of the SPL of the sound caused by standing waves and other forms of interference with the sound on the measured loudness.

(2) The degree of the compressive effect of the two psychophysical processes on effects of variation of SPL at different locations in an auditorium depends on there being strong harmonics over a wide range. This means that greater constancy is likely to be found for chorus reed stops, compared with diapasons.

(3) The degree of compressive effect of the psychophysical processes on loudness was such that a listener will hear little, if any, change in loudness of reed stops from place to place in the auditorium. The data indicate that noticeable differences in loudness of diapasons are likely to be heard at different locations.

(4) The present work confirmed Pollard's (1988) ideas on the necessity of using psychophysical transformations (''feature analysis'') of the data in the study of organ sounds. Organs are designed and listened to in terms of the various facets of timbre and loudness, rather than physical units, suggesting that analysis of the sound should also be at the psychophysical level.

(5) The magnitude of the cross correlations of the envelopes of the lines joining the loudnesses of notes across the compass of the instrument at different locations is one measure of the finishing of the loudness aspects of the organ.

(6) The present methods provide data indicating the loudness of notes that a listener will hear at different locations in an auditorium.

ACKNOWLEDGMENTS

We thank the Director of the Church of the Redeemer, The Rev. Richard Downes, and the organist, Elizabeth Gray,

for permission to make the acoustical measurements. We thank Fritz Noack, the Noack Organ Co, Georgetown, MA, for information on the organ. We thank Dr. Laurel Carney, Biomedical Engineering, Boston University, for comments on an earlier version of this manuscript.

Boner, C. P. (**1938**). ''Acoustic spectra of organ pipes,'' J. Acoust. Soc. Am. **10**, 32–40.

Churcher, B. G. (**1962**). ''Calculation of loudness levels for musical sounds,'' J. Acoust. Soc. Am. **34**, 1634–1639.

Fastl, H., Jaroszewski, A., Schorer, E., and Zwicker, E. (**1990**). ''Equal loudness contours between 100 and 1000 Hz for 30, 50, and 70 phons,'' Acustica **70**, 197–201.

Fletcher, H. (**1928**). *Speech and Hearing* (Macmillan, London), p. 169 ff.

Fletcher, H., Blackham, E. D., and Christensen, D. A. (**1963**). ''Quality of organ tones,'' J. Acoust. Soc. Am. **35**, 314–323.

Hall, D. E. (**1993**). ''Musical dynamic levels of pipe organ sounds,'' Music Percep. **10**, 417–434.

Harrison, J. M., and Thompson-Allen, N. (**1996**). ''Loudness level survey of the Newbury Memorial organ, Yale University,'' J. Acoust. Soc. Am. **100**, 3909–3916

Harrison, J. M., and Thompson-Allen, N. (**1998**). ''Steady-state spectra of diapason class stops of the Newberry Memorial organ, Yale University,'' J. Acoust. Soc. Am. **103**, 626–629.

Houtsma, A. J. M., and Goldstein, J. A. (**1972**). ''The central origin of the pitch of complex tones from musical interval recognition,'' J. Acoust. Soc. Am. **51**, 520–429.

Ingerslev, F., and Frobenius, W. (**1947**). ''Some measurements of the end corrections and acoustic spectra of cylindrical open flue pipes,'' Trans. Danish. Acad. Tech. Sci. **1**, 7–44.

Jackson, L. L., Heffner, R. S., and Heffner, H. E. (**1999**). ''Free-field audiogram of the Japanese macaque (*Macaca fuscata*),'' J. Acoust. Soc. Am. **106**, 3017–3023.

Licklider, J. C. R. (**1951**). ''Basic correlates of the auditory stimulus,'' in *Handbook of Experimental Psychology*, edited by S. S. Stevens (Wiley, New York).

Licklider, J. C. R. (**1956**). ''Auditory frequency analysis,'' in *Information Theory*, edited by C. Cherry (Butterworth Scientific, London), pp. 253–268.

Lottermoser, V. (**1940**). ''Klangspektren einer Silbermannorgel,'' Akust. Z. **5**, 324–330.

Lottermoser, W. (**1948**). ''Elektroakustische Messungen an beruhmten Barockorgeln Oberschwabens. I. Schalldruckaufnahmen,'' Z. Naturforsch. A **3A**, 3/13–13/13.

Lottermoser, W. (**1950**). ''Elektroakustische Messungen an beruhmten Barockorgeln Oberschawbens II. Klanganalytische Untersuchungen,'' Z. Naturforsch. A **5A**, 3/12–12/12.

Lottermoser, V. (**1952**). ''Warum akustische Messungen an Barockorgeln?'' Arch. Mugikwissensch. **2**, 148–158.

Lottermoser, V. (**1953**). ''Vergleichende Untersuchungen an Orgeln,'' Acustica **3**, 129–138.

Lottermoser, V. (**1968**). ''Klanganalytische Untersuchungem an der G. Silbermann-Orgel in Reinhardtsgrimma,'' Das Musikinstr. **17**, 172–175.

Lottermoser, V. (**1969**). ''Orgelgutachten auf Grund akustischer Messungen (Schnitger-Orgel von Hollern/Stade),'' Das Musikinstr. **18**, 185–191.

Lottermoser, V., and Meyer, J. (**1960**). *Orgelakustik in Einzeldarstellungen* (Verlag Das Musikinstrument, Frankfurt am Main).

Miskiewicz, A., and Rakowski, A. (**1994**). ''Loudness level versus sound pressure level; a comparison of musical instruments,'' J. Acoust. Soc. Am. **96**, 3375–3397.

Moore, B. C. J., and Glasberg, B. R. (**1996**). ''A revision of Zwicker's loudness model,'' Acustica **82**, 335–345.

Moore, B. C. J., Glasberg, B. R., and Baer, T. (**1997**). ''A model for the prediction of thresholds, loudness, and partial loudness,'' J. Audio Eng. Soc. **45**, 224–239.

Paterson, A. P. G. (**1980**). *Handbook of Noise Measurement* (Genrad, Concord, MA), p. 118.

Plomp, R., and de Laat, J. A. P. M. (**1984**). ''Comparison of organs in a spectrum space,'' Acustica **55**, 193–194.

Pollard, H. F. (**1978a**). ''Loudness of pipe organ sounds I. Plenum combinations,'' Acustica **41**, 66–74.

Pollard, H. F. (**1978b**). ''Loudness of pipe organ sounds II. Single notes,'' Acustica **41**, 75–85.

Pollard, H. F. (**1988**). ''Feature analysis of musical sounds,'' Acustica **65**, 232–243.

Pollard, H. F., and Jansson, E. V. (**1982a**) ''A tristimulus method for the specification of musical timbre,'' Acustica **51**, 162–171.

Pollard, H. F., and Jansson, E. V. (**1982b**). ''Analysis and assessment of musical starting transients,'' Acustica **51**, 250–261.

Robinson, D. W., and Dadson, R. S. (**1956**). ''A redetermination of the equal loudness relations for pure tones,'' Br. J. Appl. Phys. **7**, 166–181.

Stepanek, J., and Otcenasek, Z. (**1994**). ''Acoustic documentation of 12 pipe organs and analysis of their plena,'' J. Phys. IV **4**, C5-645–C5-648.

Stevens, S. S. (**1951**). ''Mathematics, measurement, and psychophysics,'' in *Handbook of Experimental Psychology*, edited by S. S. Stevens (Wiley, New York), pp. 1–49.

Stevens, S. S. (**1961**). ''Procedure for calculating loudness: Mark VI,'' J. Acoust. Soc. Am. **33**, 1577–1585.

Stevens, S. S. (**1966**). ''Matching between loudness and ten other continua,'' Percept. Psychophys. **1**, 5–8.

Stevens, S. S. (**1971**). ''Perceived level of noise by Mark VII and decibels (E).'' J. Acoust. Soc. Am. **51**, 575–601.

Stevens, S. S., and Davis, H. (**1938**). *Hearing* (Wiley, New York), pp. 112–123.

Terhardt, E., Stoll, G., and Seewann, M. (**1982**). ''Pitch of complex signals according to virtual pitch theory; tests, examples and deductions,'' J. Acoust. Soc. Am. **71**, 671–678.

Zwicker, E. (**1961**). ''Subdivisions of the audible frequency range in criticial bands (Frequenzgruppen),'' J. Acoust. Soc. Am. **33**, 248.

Zwicker, E., and Fastl, H. (**1999**). *Psycho-acoustics. Facts and Models* (Springer, Berlin).

Zwicker, E., Fastl, H., and Dallmayr, C. (**1984**). ''Basic program for calculating the loudness of sounds from their third octave band spectra, according to ISO522B,'' Acustica **55**, 63–67.

Zwicker, E., Flottorp, G., and Stevens, S. S. (**1957**). ''Critical bandwidth in loudness summation,'' J. Acoust. Soc. Am. **29**, 548–557.

Oscillating reed valves—An experimental study

A. Z. Tarnopolsky, N. H. Fletcher,[a] and J. C. S. Lai
School of Aerospace and Mechanical Engineering, Australian Defence Force Academy, Canberra 2600, Australia

(Received 8 November 1999; accepted for publication 7 April 2000)

The results of experiments on the threshold behavior and large-amplitude oscillation of ''outward-swinging door'' vibrating flap valves in an air environment are reported and compared with the predictions of a simple nonlinear theory that parametrizes aerodynamic effects by means of a simple damping coefficient together with a contraction coefficient for the flow. The agreement is acceptably good for the threshold blowing pressure for valve oscillation, the large-signal vibration amplitude, the pressure jump in the transition from threshold to large-signal behavior, and the variation in vibration frequency, all as functions of reservoir volume. The calculated pressure waveform in the reservoir has the observed phase and magnitude but fails to reproduce finer details. It is concluded that the simple theory provides an adequate account of the behavior of such valves. There are just two parameters in the theory, describing jet contraction and aerodynamic damping, respectively. Since these may depend significantly upon the detailed geometry, valves with different shapes may behave in quantitatively different ways.
[S0001-4966(00)04107-2]

PACS numbers: 43.75.Pq [WJS]

INTRODUCTION

Pressure-controlled vibrating valves are important in many contexts. They provide the sound-generating mechanism for the vocal utterances of birds, humans, and many other animals, and also for musical instruments of the brass and reed–woodwind families.

The geometric and dynamic complexity of many of these systems is great, since the vibrating element has many possible modes of deformation, but it has proved helpful to consider three simplified situations in which the motion of the valve can be described by a single displacement parameter x measuring the valve opening. We can then specify the behavior of the valve by a two-element parameter (σ_1,σ_2) in which $\sigma_1=+1$ if a steady positive pressure applied to the upstream or inlet port of the valve tends to increase the valve opening x, and $\sigma_1=-1$ if this pressure tends to close the valve. The second parameter σ_2 is defined similarly for a pressure applied to the downstream or exit port of the valve. For convenience, the configuration of a valve will be described simply by $(+,-)$, for example, rather than giving the complete symbol $(+1,-1)$.

We can recognize three distinct types of valves within this simple classification. Valves of type $(-,+)$, which can be pictured as inward-swinging doors or doors that are blown closed, are found in the reed mechanisms of woodwind instruments such as clarinets or oboes. Valves of type $(+,-)$ are like outward-swinging doors or doors that are blown open, and describe the motion of a trumpet player's lips over at least part of the range of the instrument. Valves of configuration $(+,+)$ are like sliding doors or doors that are blown sideways, and represent another possible motion of a trumpet player's lips. This ambiguity in the case of brass-instrument playing arises because description of the motion of the soft tissue of the lip really requires at least two displacement parameters,[1] and ideally a continuum description.[2] The same is true of human vocal folds and the syringeal membranes of birds, both of which could be approximated by $(+,-)$ or $(+,+)$ but are really more complex than this.[3,4]

The remaining valve type, described by $(-,-)$, does not appear to occur naturally or in any musical instruments, or to have any practical utility. This is perhaps because of its tendency to simply blow closed for any applied pressure.

There have been many studies of the behavior of $(-,+)$ valves in woodwind instruments, particularly clarinets, following early work by Backus,[5] but here the air column of the instrument is a dominant influence. A more general study of the acoustics of valves of both $(-,+)$ and $(+,-)$ types was carried out by Fletcher *et al.*,[6,7] while lip valves in brass instruments have been investigated by Elliott and Bowsher,[8] Yoshikawa,[9] Copley and Strong,[10] and others. The behavior of free reeds, as in harmoniums, has been studied by St. Hilaire *et al.*,[11] and more recently by Johnston,[12] Koopman, Cottingham *et al.*,[13,14] and particularly by Bahnson *et al.*[15] A summary of most of this work has been given by Fletcher and Rossing.[16]

The threshold for self-excited oscillation of the three simple valve classes in the absence of an attached resonator has been examined theoretically in another paper by one of the present authors.[17] In that paper it is shown that, if the acoustic impedance presented to the inlet of the valve is $Z_1=R_1+jX_1$ and that presented to the outlet is $Z_2=R_2+jX_2$, then a necessary condition for the initiation of self oscillation is that

$$\sigma_1 X_1-\sigma_2 X_2<0. \tag{1}$$

This condition (1) is, however, not sufficient. In addition, there is a condition on the blowing pressure (or, more gen-

[a]Permanent address: Research School of Physical Sciences and Engineering, Australian National University, Canberra 0200, Australia. Electronic mail: Neville.Fletcher@anu.edu.au

erally, the pressure difference across the valve) that depends in detail upon valve geometry and internal damping.

In the case of valves of configuration $(+,-)$, which are considered in the present paper, the requirement $X_1+X_2<0$ can be achieved by supplying the valve from a reservoir of fixed volume V, in which case $X_1=-\rho c^2/V\omega$ (where ρ is the density of air, c the speed of sound, and ω the frequency of the oscillation), and allowing the valve to exhaust to the open air so that $X_2=0$. It is then found[17] that there is a preferred volume for the supply reservoir at which self-oscillation can be maintained at low blowing pressure; for larger or smaller reservoir volumes a greater threshold blowing pressure is required. The first part of our experimental study investigates these predictions.

The small oscillations of a valve are, however, generally unstable, and tend to grow rapidly to large amplitude. This transition, and the limiting state achieved by the large-amplitude oscillations, form another major part of the study. In contrast to the threshold determination, which can be described by linearizing the equations of flow and motion,[17] a description of this large-amplitude behavior necessarily involves proper treatment of the many nonlinearities involved.

I. BACKGROUND THEORY

The theoretical background that the experiments are designed to check has been given before.[17] We repeat here only its elements, and give details of a few refinements required to bring its assumptions closer to the realities of the experiment. The valve flap is taken to be a flexing plate of length L, width W, and effective mass m, clamped across one end. In the original theory, air was assumed to issue through the valve only across its tip, where the height of the opening is $x(t)$. To bring this treatment closer to the realities of experiment, we must allow for an additional escape of air through the opening of average width $a(x)$ along the sides of the valve, and through clearance gaps of width b between the valve tongue and the base plate. The total exit area of the valve is thus approximately

$$F(x)=W[x^2+b^2]^{1/2}+2L[a(x)^2+b^2]^{1/2}. \tag{2}$$

As already discussed, the valve is assumed to be fed from a reservoir of volume V, which is supplied with a steady volume flow U_0 from a high impedance source, and to exhaust to free air so that the downstream impedance is zero. The volume flow $U(t)$ through the valve is given by Bernoulli's equation, modified by a flow-contraction coefficient C, often written C_c in the literature, which has the value $C=0.61$ for flow through a sharp-edged slit.[18,19] The pressure must also be supplemented by a small term to represent the inertia of the air in the channel of length δ at the tip of the flap. The resulting equation for the pressure $p(t)$ in the reservoir is then

$$p=\frac{\rho U^2}{2C^2F(x)^2}+\frac{\partial}{\partial t}\left[\frac{\rho U\delta}{CF(x)}\right], \tag{3}$$

where ρ is the density of air. While the opening x is a linear variable for small oscillations of the valve tongue, it has a more complex form when the valve tongue enters the aperture of the backing plate or ultimately protrudes through its rear face. This is easily taken into account when the equations are solved numerically for large-amplitude oscillations.

The vibration of the valve flap is that of a simple cantilever, assumed to have natural frequency ω_0 and quality factor Q, so that, in the absence of air flow, its damping factor is $k=\omega_0/2Q$. This damping is provided largely by viscous losses in the surrounding air and, in some of our experiments, by added mechanical damping material near the root of the valve flap. As shown in the Appendix, the equation of motion of the flap, expressed in terms of its tip opening x, is

$$\frac{d^2x}{dt^2}+2k\frac{dx}{dt}+\omega_0^2(x-x_0)=\frac{1.5WLp}{m}, \tag{4}$$

where x_0 is the static opening of the valve flap with no applied pressure and m is the effective moving mass of the valve flap, as derived in the Appendix. For the experimental arrangement used, the valve tongue is initially flat and is raised a distance x_0 above the base plate. It then follows, as also shown in the Appendix, that

$$a(x)\approx 0.6x_0+0.4x. \tag{5}$$

In Eq. (4) we might expect the damping coefficient k to be a constant, determined by the combination of internal losses in the valve flap material and viscous damping in the surrounding air. The value of k should thus be determinable from the quality factor Q of the free oscillation damping of the valve flap by the relation $k=\omega_0/2Q$. Schlieren images of the oscillating valve, to be reported elsewhere, show however that a vortex develops downstream during the closing part of the valve cycle, and it would be surprising if this did not contribute damping to the mechanical oscillation of the valve. To allow for this possibility, we introduce an additional damping proportional to the change in momentum flux caused by the motion of the valve flap. Since the change in flow direction is presumably proportional to $(1/v)dx/dt$, where v is the air jet velocity as determined by Bernoulli's principle, it is a reasonable assumption that the extra damping is proportional to $\rho v x_0\, dx/dt$ per unit vibrating length of edge of the valve flap. We can then write

$$k=\frac{\omega_0}{2Q}+\beta\frac{\rho v(W+0.8L)x_0}{m}, \tag{6}$$

where β is a numerical coefficient which we expect to be approximately unity. In the calculations to follow, it is assumed that $\beta=1$, and the resulting aerodynamic damping is then small enough that its precise value is not important.

A third and final equation relates the pressure in the reservoir to the steady inflow U_0, the outflow $U(t)$ through the valve, and the change in reservoir volume caused by the valve vibration. This leads to

$$\frac{dp}{dt}=\frac{\rho c^2}{V}\left(U_0-U-0.4WL\frac{dx}{dt}\right). \tag{7}$$

The quantity $0.4WLx'$ is approximately the volume displaced by a cantilever strip of width W and length L when its tip is displaced from equilibrium by an amount x'.

A. Small-signal approximation

A simpler form of these three equations, linearized for the case of small oscillations, $x \ll x_0$, by writing U, x, and p in the form $U = U_0 + \tilde{U} \sin \omega t$ etc., formed the basis of the earlier analysis of oscillation threshold,[17] though in the examples computed there the flow-contraction effect, the flow inertia in the valve gap, the contribution of valve displacement to reservoir pressure, the flow through the sides of the valve, and the additional aerodynamic damping, were all omitted. For the particular values of the physical parameters of the valve used in the present experiment, in which both blowing pressure and frequency are rather low, it turns out that the contributions of flow inertia, and to a large extent aerodynamic damping, can indeed be neglected, but side flow and the flow-contraction correction must both be taken into account.

In the present paper, linearized versions of the full equations are used for threshold calculations, and the complete equations are solved numerically to predict the large-amplitude behavior. The linearized threshold equations are derived in the same way as before.[17] Neglecting the air-inertia term, the equation for the threshold pressure is now

$$-\frac{(2\bar{p}\rho)^{1/2} WLX_1[2\bar{p}C(W+0.8L)+0.4\omega_0 WLX_1 CF(\bar{x})]}{2\bar{p}\rho + C^2 F(\bar{x})^2 X_1^2} > \tfrac{4}{3} k\omega_0 m, \tag{8}$$

where $\bar{p}$ is the average reservoir pressure, $\bar{x} = x_0 + 1.5\bar{p}WL/m\omega_0^2$ is the equilibrium opening of the valve under this pressure, $F(x)$ is given by (2), and $X_1 = -\rho c^2/V\omega$ is the imaginary part of the acoustic impedance of the reservoir cavity. The principal modifications to the corresponding result derived in the original treatment are insertion of numerical factors of order unity, derived from the replacement of $W\bar{x}$ by $F(\bar{x})$ to account for air flow from the sides of the valve and through the clearance leaks and from the inclusion of the flow-contraction coefficient C, and insertion of the second term in the numerator, which is derived from the displacement of air by the valve motion. Note that the threshold, and indeed all the behavior later calculated for the valve, depends upon the profile of the valve tongue, if it is not flat, through the form of $F(x)$.

Another consequence of change in reservoir volume, in the case of a swinging-door $(+,-)$ valve, is an increase in vibration frequency with decreasing reservoir volume, because of the acoustic stiffness of the enclosed air. A simple linear treatment suggests that the valve oscillation frequency ω is given by

$$\omega^2 \approx \omega_0^2 + \frac{0.6\rho c^2 W^2 L^2}{mV}. \tag{9}$$

While the general trend of this result is correct, it ignores the effect of flow through the valve and overestimates the frequency shift. To obtain a reliable estimate of the frequency shift, Eqs. (3), (4), and (7) must be integrated numerically and the oscillation frequency determined directly.

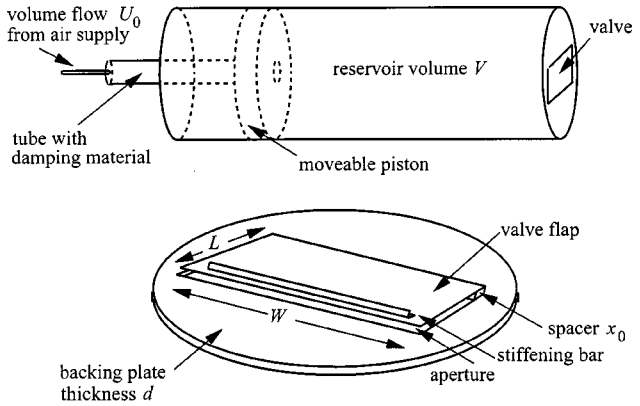

FIG. 1. The experimental setup. The upper part of the figure shows a general view, and the lower part a detailed view of the valve itself.

II. EXPERIMENTS

Figure 1 gives details of the experimental arrangement used. The valve flap was cut from flat brass sheet of either 0.33- or 0.15-mm thickness and was 28 mm in length and 52 mm in width. The relatively large width was chosen in order to give a good approximation to two-dimensional flow through the valve for associated experiments in flow visualization. The valve flap was stiffened by a thin aluminum bar of mass about 0.8 g, glued parallel to the tip to prevent lateral oscillations, which could be observed stroboscopically in the absence of such stiffening. The aperture under the valve was a little larger than the valve flap in both length and width, giving a clearance b of about 0.5 mm on all three sides, so that the valve was ''free'' rather than striking against the plate. A free rather than a striking valve tongue was chosen for study because of its greater simplicity—the exact course of any strike impact has a significant effect on the vibrational behavior of a striking valve flap.

The thickness of the aperture plate was 4 mm, so that the valve flap penetrated to its opposite side during very large-amplitude oscillation. The distance x_0 between the stationary valve flap and the plate could be varied by inserting a thin shim sheet, and was normally fixed at either 0.5 or 1.0 mm. The natural frequency of the valve oscillation was in the range 100 to 300 Hz, corresponding to the lowest natural frequency of the flexing cantilever, the actual frequency depending upon the sheet thickness and the added load, if any. The Q value, which was measured by the free decay behavior, was about 55 for the bare valve and could be reduced to as little as 10 by applying adhesive tape to the flap near its clamped end.

The upstream reservoir was constructed from heavy PVC pipe of inside diameter 101 mm, closed with a solid piston, the position of which could be changed to alter the reservoir volume. Air was supplied to the reservoir through a long, narrow tube terminating in a short coaxial pipe of 20-mm diameter filled with acoustically absorbent wool, as shown in Fig. 1. This arrangement minimized turbulence in the reservoir while adequately defining its volume. The isolation effectiveness of the absorbing material was checked by using, in one experiment, a much narrower tube. The air supply itself was drawn from a high-pressure source through

a reducing valve, and therefore constituted a high-impedance constant-flow source, as assumed in the theoretical treatment.

The instrumentation for the measurement of all the important physical parameters included: a rotameter for the steady volume flow U_0, a water manometer for the average reservoir pressure p_0, a pressure transducer for the varying reservoir pressure $p(t)$, an accelerometer for the motion of the valve flap $x(t)$, a condenser microphone for the radiated sound waveform or alternatively for the reservoir pressure, and a fast Fourier transform (FFT) analyzer for the waveform and spectrum of the quantities involved.

A. Oscillation threshold

One of the major predictions of the linearized threshold theory[17] is that valves of configuration $(+,-)$ should be able to begin autonomous oscillation when fed at an adequate pressure from a closed reservoir, which is itself fed from a constant-flow source. The theory predicts that the threshold pressure for oscillation should depend upon the volume of the reservoir, there being in each case an optimal volume, determined by the physical parameters of the valve flap, near which the threshold pressure is lowest.

Most of the physical parameters of the valve were easily measured directly, but its resonance frequency and damping behavior required experimental determination. This was done by flicking the valve in a controlled manner and capturing the decay transient of its oscillation using a microphone and storage oscilloscope. The bare brass valve flap had little intrinsic damping, so that for many of the experiments the mechanical damping was augmented by adding strips of adhesive tape to both sides of the flap close to the clamped edge. In the same way, the resonance frequency of the valve flap could be changed by gluing strip masses near the tip of the valve flap. In all cases an adjustment was required in the calculations to allow for the mass added to the vibrating valve flap.

Figure 2(a) shows the measured pressure threshold for oscillation of the valve, as a function of reservoir volume, for various values of the mechanical Q factor. It is clear that there is indeed a volume-dependent threshold behavior of the type predicted by theory, and that the threshold pressure rises as the valve damping is increased. In Fig. 2(b) the threshold curves calculated from the theory leading to Eq. (8) are shown. There are no adjustable parameters in the theory, and the agreement with experiment is moderately satisfactory, given the approximate nature of the theory, and indeed of the experiment, since the threshold behavior may well depend upon subtleties of air flow.

Figure 3(a) shows similar curves with resonance frequency as the parameter. The resonance frequency was changed by adding mass to the valve tongue near its tip, and the effective mass of the tongue was evaluated from the shift in resonance frequency. The theoretical curves are shown in Fig. 3(b), and again there is broad agreement between theory and experiment. The agreement can be improved considerably by increasing the value of the aerodynamic damping coefficient β, but there is no immediate justification for this.

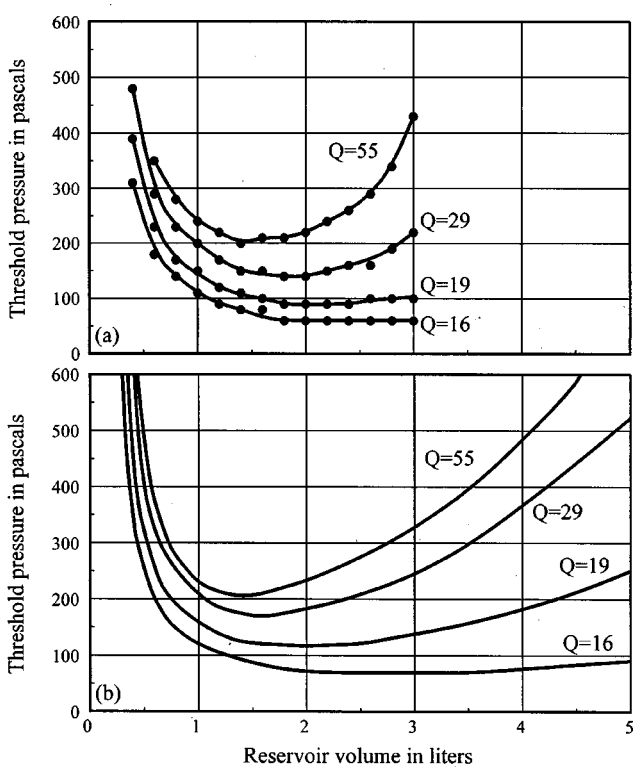

FIG. 2. (a) Measured threshold oscillation pressure of the experimental valve as a function of reservoir volume, with the Q value of the free valve flap as a parameter. For this valve the sheet thickness was 0.15 mm and the free resonance was 105 Hz. (b) Oscillation threshold as calculated from the theory.

B. Large-amplitude behavior

As already noted, the threshold vibration of the system is unstable, and rapidly grows to a limit cycle with a large amplitude and with an increased reservoir pressure. In the course of the experiments, this large-amplitude motion of the valve flap was monitored through a telemicroscope using stroboscopic illumination, and was also measured by twice integrating the output of a subminiature accelerometer attached to the flap near its fixed end. Once oscillation begins, the valve oscillation amplitude increases sharply, as does the reservoir pressure, until a limit cycle is reached in which the valve closes into the aperture plate for a time approaching half of each cycle. For very large oscillation amplitudes (exceeding about 5 mm in the case of our experiments) the valve flap emerges at the back of the aperture plate and allows secondary air flow during this part of the cycle. There is hysteresis in this behavior so that, once oscillation has begun, the air flow into the reservoir, and thus the reservoir pressure, can be reduced without the vibration stopping. The behavior of oscillation amplitude as a function of reservoir pressure is illustrated for the case of a valve with static opening $x_0 = 1$ mm and several different reservoir volumes in Fig. 4(a). In Fig. 4(b) the behavior calculated by integrating Eqs. (3)–(7) numerically is shown, assuming an initial displacement of the valve flap that is analogous to flicking it with a finger. Agreement between theory and experiment is again satisfactory, and the hysteresis can be understood from the fact that an oscillating valve of $(+,-)$ configuration presents a rather high, steady flow impedance because the res-

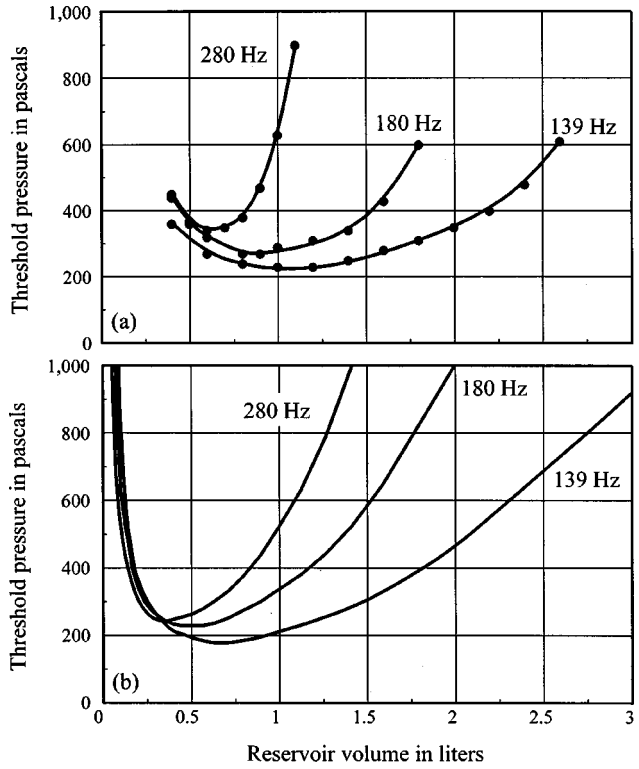

FIG. 3. (a) Measured threshold oscillation pressure of the experimental valve as a function of reservoir volume, with mass-loaded frequency as a parameter. The valve sheet thickness in this case was 0.33 mm and no stiffening bar was required. Measured Q values ranged between 44 and 52. (b) Oscillation threshold as calculated from the theory. The effective mass of the valve flap was scaled as (frequency)$^{-2}$.

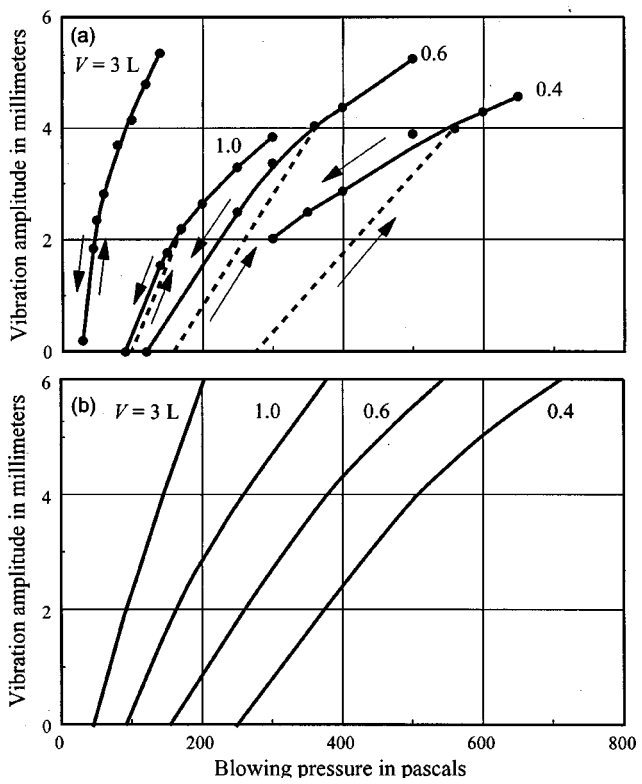

FIG. 4. (a) Measured oscillation amplitude, as a function of mean reservoir pressure, for four different reservoir volumes given in liters as a parameter, for a valve with flap thickness 0.15 mm and free resonance frequency 106 Hz. The arrowed curves show the hysteresis observed. (b) Calculated behavior omitting hysteresis effects.

ervoir pressure generated by its motion is such as to decrease the pressure, and thus the flow, when the valve is open.

The magnitude of the pressure jump when the oscillation increases from threshold to its limit-cycle value is another interesting experimental quantity, which is plotted in Fig. 5. The effect is greater for a small reservoir than for a large one, as might be expected. The pressure jump can be calculated from Eqs. (3)–(7) of the theory, essentially by performing numerical experiments for progressively increasing flow rates until oscillation begins. The calculated jump, shown as a full curve in Fig. 5, is in good agreement with the measurements, which are shown as data points.

It is also interesting to examine the dependence of the oscillation frequency of the valve on reservoir volume. The experimental results are shown as data points in Fig. 6 and the results computed from the large-signal theory as a full curve. The agreement is again acceptably good, the large-signal frequency shift being very much smaller than that predicted from small-signal theory in Eq. (9), which is shown as a broken curve in the figure. The frequency variation is neither predicted nor found to depend significantly upon blowing pressure or valve damping.

Another measurement was of the time-varying pressure within the reservoir, which was measured with either the pressure transducer or a 1/8-in. condenser microphone. The waveform of the pressure oscillation is a distorted sinusoid, as shown in Fig. 7(a), and its phase is very nearly 180° behind that of the valve opening displacement, shown in Fig. 7(b), which confirms that the major contribution to the pressure variation comes from the volume displacement of the moving flap. The motion of the valve flap, as monitored by the twice-integrated output of the accelerometer, is very closely sinusoidal, as is to be expected since it is operating very close to its natural resonance frequency. Integration of Eqs. (3)–(7) gives the form of the reservoir pressure variation shown in Fig. 7(c). The agreement with experiment is good in relation to amplitude and phase, and moderately good in relation to waveform, though clearly some of the details are not captured by the theory. The variation of the

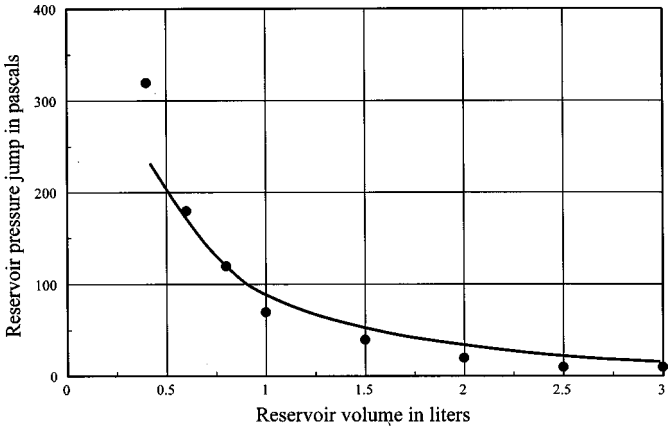

FIG. 5. Measured pressure increase as a threshold oscillation is allowed to grow to its steady state, as a function of reservoir volume (data points) for the valve of Fig. 4. The full curve shows the calculated pressure jump.

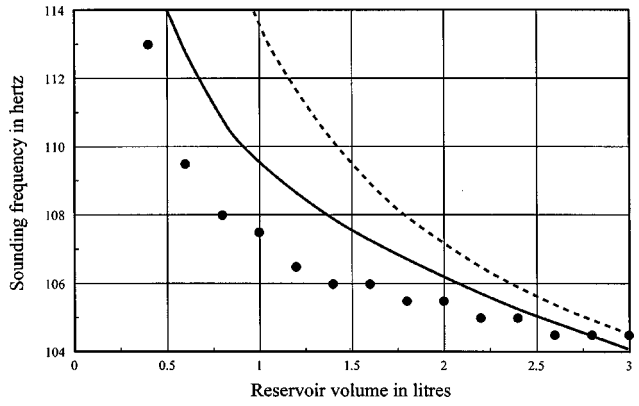

FIG. 6. Measured frequency of oscillation of the valve of Fig. 4 as a function of reservoir volume (data points). The full curve shows the theoretical prediction from numerical integration of the equations, while the broken curve shows the prediction of the simple equation (9). The vibration frequency is insensitive to blowing pressure over a large range.

pressure waveform when the valve is nearly fully open may perhaps be associated with the development of a downstream vortex in the flow, as observed in Schlieren photographs.

The radiated sound spectrum can, in principle, be derived from a knowledge of the total flow waveform $U(t) + 0.4WL\, dx/dt$, which includes both flow through the valve aperture and displacement flow. This is not reported upon here, however, since details of the spectral envelope depend upon rather fine aspects of the valve construction and reservoir geometry.

C. Striking valves

In this study a nonstriking valve was used because of difficulty in specifying precisely the nature of the striking contact. A brief subsidiary study of striking valves was, however, undertaken. To make the behavior as reproducible as possible, the valve flap was made a little larger than the plate aperture in all dimensions; the flap was clamped to the plate without an intervening spacer, and the valve flap was bent slightly to give a tip aperture of about 1 mm. When the valve closed, it did so around its whole periphery.

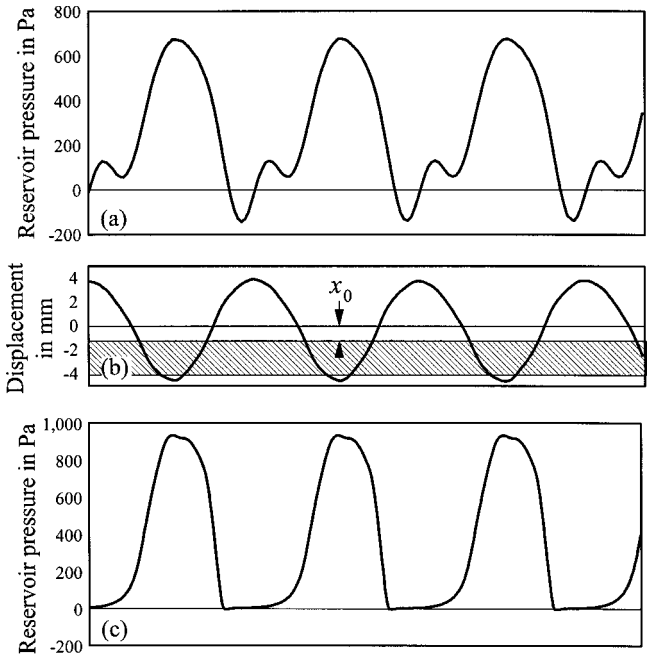

FIG. 7. (a) Measured waveform of the reservoir pressure for reservoir volume 0.8 L and an average reservoir pressure of 350 Pa. (b) Measured displacement of the valve flap (as an indication of relative phase). The shaded region shows the portion of the cycle during which the tip of the flap is within the base-plate aperture. (c) Calculated reservoir pressure waveform.

The experiments followed very much the same lines as those reported in detail above. The main difference observed was that the limit-cycle valve oscillation was of a much smaller amplitude, indeed less that than 2 mm, than for a free valve, presumably because the valve flap loses a great deal of energy during the impact. Stroboscopic study of the valve oscillation revealed complex behavior and the presence of higher cantilever modes, the amplitude of which depended upon the precise geometry of the striking contact. This fact is well-known to the voicers of organ reed pipes, since reed curvature must be properly adjusted to achieve satisfactory sounding behavior, although in that case the reed configuration is $(-,+)$. Much the same thing happens for striking $(+,-)$ valves and, because of this complication, the matter was not pursued further here.

III. CONCLUSIONS

This experimental study of an oscillating-flap valve of the outward-swinging door $(+,-)$ type shows that its behavior is well accounted for by a simple theory, without invoking any adjustable parameters or aerodynamic complications. The agreement between theory and experiment is not exact, but is as good as could reasonably be expected, bearing in mind the subtleties of reed adjustment that are involved in the sounding behavior of reed-driven musical instruments. A reasonable explanation of this sensitivity to flow conditions is the fact that the contraction coefficient C can actually vary between 0.5 and 1.0 depending upon the precise geometry of the flow aperture.[19] There is also the possibility that the aerodynamic damping coefficient β might be similarly affected.

In the course of the experiments certain interesting aerodynamic phenomena were in fact observed, particularly the formation of a downstream vortex during the closing phase of the oscillation of the valve. The behavior of this vortex will be reported on elsewhere, for its own intrinsic interest, since the present study suggests that it does not have a major effect on the behavior of the valve.

Finally, we note that only the $(+,-)$ outward-swinging door type of valve has been studied here. The fact that the simple theory,[17] with the refinements introduced above, gives a good account of the behavior of valves of this type, however, leads us to expect that it should be able to give a similarly accurate description of valves of $(+,+)$ and $(-,+)$ configuration, which were also included in its formulation.

ACKNOWLEDGMENT

This work is part of a program supported by a grant from the Australian Research Council.

APPENDIX

Let $\xi(s,t)$ be the form of the displacement of the valve flap, with s measuring distance from its clamped root. The equation of motion of the flap then has the form

$$[\rho_v Wh + m'\delta(s-s')]\frac{\partial^2\xi}{\partial t^2} + R\frac{\partial\xi}{\partial t} + K\frac{\partial^4\xi}{\partial s^4} = Wp(t), \tag{A1}$$

where ρ_v is the material density, W the width, h the thickness and K the bending stiffness of the valve flap, and R is its damping coefficient. It is also allowed that there is a further mass m', representing the stiffening bar, fixed to the valve at a distance s' from its root.

Since we are concerned with oscillation near the fundamental cantilever mode of the flap at frequency ω_0, we can write $\xi(s,t)=[x(t)-x_0]\psi(s)$ where $\psi(s)$ is the form of the mode function,[20] normalized so that $\psi(L)=1$. Multiplying both sides of (A1) by $\psi(s)$ and integrating over the flap length L then gives

$$\frac{d^2x}{dt^2} + 2k\frac{dx}{dt} + \omega_0^2(x-x_0) = \frac{\gamma WLp}{m}, \tag{A2}$$

where k is a new damping coefficient given by (6), m is the effective mass of the valve flap as given by

$$m = \rho_v WLh + \frac{m'L\psi(s')^2}{\int_0^L \psi(s)^2 ds} \approx \rho_v WLh + 4m', \tag{A3}$$

and

$$\gamma = \frac{\int_0^L \psi(s)ds}{\int_0^L \psi(s)^2 ds} \approx 1.5. \tag{A4}$$

The approximate result in (A3) derives from the form of $\psi(s)$ and from the fact that $s'\approx L$ for the stiffening bar. Since $s'\ll L$ for the damping material added near the clamped edge of the flap, the contribution of its mass to m is negligibly small.

From a knowledge of the form of $\psi(s)$, we can also evaluate the area of the vertical component of the side opening beneath the valve when its tip opening is x. For the case of a planar valve flap, as in the experiment,

$$a(x) = x_0 + (x-x_0)\int_0^L \psi(s)ds \approx 0.6x_0 + 0.4x. \tag{A5}$$

If the flap is curved, as in many free-reed musical instruments, then the form of $a(x)$ may differ considerably from this. The form (A5) is, of course, valid only if the flap does not enter the aperture block. If this happens, then a more complicated expression must be used.

[1] S. Adachi and M. Sato, ''Trumpet sound simulation using a two-dimensional lip vibration model,'' J. Acoust. Soc. Am. **99**, 1200–1209 (1996).
[2] R. D. Ayers, ''New perspectives on the brass instruments,'' in *Proceedings of the International Symposium of Musical Acoustics, Leavenworth, 1998* (Acoustical Society of America, New York, 1998), pp. 129–134.
[3] K. Ishizaka and J. L. Flanagan, ''Synthesis of voiced sounds using a two-mass model of the vocal cords,'' Bell Syst. Tech. J. **51**, 1233–1268 (1972).
[4] N. H. Fletcher, *Acoustic Systems in Biology* (Oxford University Press, New York, 1992), Chap. 14.
[5] J. Backus, ''Vibrations of the reed and air column in the clarinet,'' J. Acoust. Soc. Am. **33**, 800–809 (1961).
[6] N. H. Fletcher, ''Excitation mechanisms in woodwind and brass instruments,'' Acustica **43**, 63–72 (1979); **50**, 155–159 (1982).
[7] N. H. Fletcher, R. K. Silk, and L. M. Douglas, ''Acoustic admittance of air-driven reed generators,'' Acustica **50**, 155–159 (1982).
[8] S. J. Elliott and J. M. Bowsher, ''Regeneration in brass wind instruments,'' J. Sound Vib. **83**, 181–217 (1982).
[9] S. Yoshikawa, ''Acoustical behavior of brass player's lips,'' J. Acoust. Soc. Am. **97**, 1929–1939 (1995).
[10] D. C. Copley and W. J. Strong, ''A stroboscopic study of lip vibrations in a trombone,'' J. Acoust. Soc. Am. **99**, 1219–1226 (1996).
[11] A. O. St. Hilaire, T. A. Wilson, and G. S. Beavers, ''Aerodynamic excitation of the harmonium reed,'' J. Fluid Mech. **49**, 803–816 (1971).
[12] R. B. Johnston, ''Pitch control in harmonica playing,'' Acoust. Austral. **15**, 69–75 (1987).
[13] P. D. Koopman and J. P. Cottingham, ''Acoustical properties of free reeds,'' Quarterly Reed Organ Soc. **15**(3–4), 17–23 (1996).
[14] J. P. Cottingham, C. J. Lilly, and C. H. Reed, ''The motion of air-driven free reeds,'' J. Acoust. Soc. Am. **105**, 940(A) (1999).
[15] H. T. Bahnson, J. F. Antaki, and Q. C. Beery, ''Acoustical and physical dynamics of the diatonic harmonica,'' J. Acoust. Soc. Am. **103**, 2134–2144 (1998).
[16] N. H. Fletcher and T. D. Rossing, *The Physics of Musical Instruments*, 2nd ed. (Springer, New York, 1998), Chaps. 13–15.
[17] N. H. Fletcher, ''Autonomous vibration of simple pressure-controlled valves in gas flows,'' J. Acoust. Soc. Am. **93**, 2172–2180 (1993).
[18] D. Gilbarg, ''Jets and cavities,'' in *Handbuch der Physik*, edited by S. Flügge, Fluid Dynamics III, Vol. 9 (Springer, Berlin, 1960), pp. 311–445.
[19] B. R. Munson, D. F. Young, and T. H. Okiishi, *Fundamentals of Fluid Mechanics*, 3rd ed. (Wiley, New York, 1998), p. 123.
[20] P. M. Morse, *Vibration and Sound* (McGraw-Hill, New York, 1948), p. 160.

Synthesis and modification of the whistles of the bottlenose dolphin, *Tursiops truncatus*

John R. Buck
Department of Electrical and Computer Engineering and Center for Marine Science and Technology, University of Massachusetts Dartmouth, 285 Old Westport Road, North Dartmouth, Massachusetts 02747-2300 and Biology Department, Woods Hole Oceanographic Institution, Woods Hole, Massachusetts 02543

Hugh B. Morgenbesser
EECS Department, MIT, Cambridge, Massachusetts 02139

Peter L. Tyack
Biology Department, Woods Hole Oceanographic Institution, Woods Hole, Massachusetts 02543

(Received 20 October 1999; accepted for publication 24 March 2000)

A signal-processing algorithm was developed to analyze harmonic frequency-modulated sounds, to modify the parameters of the analyzed signal, and to synthesize a new analytically specified signal that resembles the original signal in specified features. This algorithm was used with dolphin whistles, a frequency-modulated harmonic signal that has typically been described in terms of its contour, or pattern of modulation of the fundamental frequency. In order to test whether other features may also be salient to dolphins, the whistle analysis calculates the energies at the harmonics as well as the fundamental frequency of the whistle. The modification part of the algorithm can set all of these energies to a constant, can shift the whistle frequency, and can expand or compress the time base or the frequency of the whistle. The synthesis part of the algorithm then synthesizes a waveform based upon the energies and frequencies of the fundamental and first two harmonics. These synthetic whistles will be useful for evaluating what acoustic features dolphins use in discriminating different whistles. © *2000 Acoustical Society of America.*
[S0001-4966(00)01107-3]

PACS numbers: 43.80.Lb, 43.80.Jz [WA]

INTRODUCTION

This paper presents a simple signal-processing algorithm to analyze, modify, and synthesize frequency-modulated tonal signals. Many animals make this kind of signal, and it has been difficult to test the precise features these animals use to discriminate between different natural signals. The algorithm presented here was developed in order to provide a tool for designing stimuli for use in discrimination tests or naturalistic playback experiments.

While visual models are relatively easy to create, it has taken much longer to develop methods to create well-specified acoustic models of natural sounds. Mammals and birds have ears that perform a frequency analysis of sound as well as detect temporal patterns, and many species produce sounds with complex patterns in time and frequency. In the case of human speech, however, considerable effort has been devoted to analyzing which acoustic features are used to discriminate between phonemes. The ability to generate synthetic speech stimuli with a graded series of values for specific acoustic parameters has been critical for testing these analyses, which can be performed with preverbal infants[1] and animals.[2] Similar techniques have been developed to analyze and synthesize natural vocalizations of animals.[3]

The question of how dolphins perceive, categorize, and discriminate between whistles has become increasingly important as different investigators have proposed different methods for categorizing whistles. These different categorizations have led in some cases to very different interpretations about the functions of dolphin whistles. One of the dominant interpretations for dolphin whistles has been the signature whistle hypothesis (SWH). The SWH[4,5] posits that dolphins can recognize another individual when they hear its individually distinctive signature whistle. The SWH proposes that each bottlenose dolphin produces whistles with a distinctive time–frequency contour whose shape identifies the specific dolphin. Other features of signature whistles such as duration or number of repetitions may vary; the original paper on the SWH suggests that ''These variable units are potentially capable of conveying much information ... The basic information transmitted, however, would be the identity of the animal doing the whistling.''[4] The SWH originated in the 1965 observations of Melba and David Caldwell[4] that many of the whistles emitted by each of five freshly captured bottlenose dolphins had a stereotypical time–frequency contour that was distinctive to that animal in a broad variety of behavioral contexts: ''On the basis of these observations we do not intend to state arbitrarily that a single animal has a vocabulary of a single somewhat variable whistle contour. However, this distinctive whistle occupied much more than 90 percent of the total whistle vocabulary of any one animal during this three-week period following capture.''[4] In other data sets, the Caldwells and others have reported lower percentages of signature whistles, but they often make up a majority of whistles.[5]

McCowan[6] used a new method to categorize whistles of captive dolphins and McCowan and Reiss[7,8] used these results to challenge the SWH. They recorded whistles from small social groups of captive dolphins, using bubblestreams to identify which dolphin produced which whistle. McCowan and Reiss[7,8] reported a large repertoire of whistles within small groups of captive dolphins, sharing of whistle types across social groups, and they found one common whistle type. They argue that this pattern of whistle usage is not consistent with the SWH.

Initial analyses of dolphin whistles relied upon visual inspection of spectrograms.[4,9,5,10,11] However, in the past decade, many researchers have applied signal-processing techniques to identify or classify the whistles of *T. truncatus*,[6,7,12–20] using a variety of models and assumptions. Many of these techniques succeed impressively at distinguishing and classifying *Tursiops* whistles under favorable recording conditions. The quantitative measures computed by some of these algorithms discriminate amongst the whistles of individual dolphins as successfully as earlier behavioral studies using subjective comparisons of spectrograms by human observers.[21,10] However, none of these studies gives any indications which acoustic features are perceptually relevant to the dolphins themselves for discrimination. Rather, the studies indicate there are several workable alternatives for distinguishing individual animals based on their whistles.

Janik[22] compared categorizations performed by humans and three different computer techniques including that used by McCowan.[6] All of these different categorization methods were tested on one data set of whistles recorded from captive dolphins (more information on the whistle sample is provided in Janik and Slater[23]). The categorization of whistles in Ref. 23 was validated by the dolphins' usage of whistles, as follows. Janik and Slater[23] used the traditional method of categorizing whistles by visual examination of spectrograms, and whistles were categorized before they analyzed whistle usage. They found four very stereotyped whistles, along with a variety of other whistle types. Each stereotyped whistle showed individual specific usage: it was used almost exclusively by only one individual dolphin and only when that individual was isolated. Since each of these whistles was used by a different individual when isolated, Janik and Slater categorized these as signature whistles. This validation of signature whistles allowed Janik[22] to test how well the different categorization methods can identify these whistle types. The classic manual categorization was replicated with five humans visually categorizing spectrograms of the whistle sample, presented in random order. No information on context was presented to the judges. All five humans agreed on a classification of whistles that matched the individual usage of signature whistles by the dolphins. Three different automated methods for classifying whistle were tested. These included the method described by McCowan,[6] a comparison of the average difference in frequency across two whistle contours, and a comparison of cross-correlation coefficients. However, none of the three computer methods was capable of identifying signature whistles reliably.

Results from discrimination tasks show that captive dolphins can be trained to categorize signature whistles from the same individual as similar, and signature whistles from different individuals as different, even if these are novel whistles from dolphins with which they have not interacted. A captive male bottlenose dolphin was able to discriminate signature whistles from two different males, in a design which used a large sample of whistles from both individuals.[9] This study also showed that dolphins can identify and categorize signature whistles to an individual, even if they hear as little as 0.5 s of the whistle. Playback experiments with wild dolphins show that dolphins respond more strongly to the signature whistles of animals with whom they have shared a strong bond.[24] These studies clearly demonstrate that whistles carry the information required for individual recognition for the dolphins.

The following three techniques have yielded considerable progress in validating classification of signature whistles:

(1) Patterns of whistle usage, as in Ref. 23;
(2) Monitoring untrained responses to playback of recorded whistles in settings as natural as possible;
(3) Conditioning dolphins to discriminate natural whistles.

However, these techniques cannot elucidate which acoustic features dolphins use to identify signature whistles, nor can they easily be used to study more general properties of whistle perception and categorization. The critical missing element for future work to resolve these questions is a tool to analyze natural whistles, modify specific acoustic features of the whistle, and resynthesize an analytic signal with total control of the acoustic properties of the stimulus. These can then be used either in naturalistic playbacks or in conditional discrimination studies.

Experimental playback of whistles designed to test how the dolphins perceive identity have been difficult to design and execute because of the near impossibility of controlling the acoustic stimulus presented to the animals such that only one parameter under investigation is varied in a known and controlled fashion. This paper presents an algorithm for generating synthetic *T. truncatus* whistles with complete quantitative control of the acoustic features of the whistle.

The synthetic whistle algorithm produces a signal consisting of a weighted superposition of harmonically related sinusoids. Most descriptions of dolphin whistles have described them as frequency-modulated tonal calls, and our representation of whistles as harmonically related sinusoids embodies this assumption. Specifically, the signal is of the form

$$s[n]=\sum_{r=1}^{R} a_r[n]\sin(2\pi\phi_r[n]), \tag{1}$$

where the $a_r[n]$ and $\phi_r[n]$ are the amplitudes and phases of the rth harmonic at the nth sample of the signal, respectively. The phase $\phi_r[n]$ is related to the frequency of the harmonic component in a manner described in detail in Sec. I C. The synthetic signal will have R harmonics. The frequency and amplitude contours of the harmonics can be completely, precisely, and quantitatively modified by experimenters to con-

struct a suite of acoustic stimuli for experimental playback to dolphins. This algorithm will allow investigation of which acoustic features may be used for individual recognition and which may contain information about the whistler's emotional state, social context, etc.

The synthesis algorithm described below applies common signal-processing techniques to the problem of synthesizing a signal with the structure of a dolphin whistle. We later discovered, and must credit, the work of McAulay and Quatieri[25,26] who had proposed an extremely similar algorithm for representing human speech. It may be that their approaches and that of Almeida and Silva[27] produce better solutions to some of the issues we encountered in developing our algorithm. The presentation in Sec. I will be based on our original derivation and not on these earlier ones, although they indisputedly may claim precedence over our formulation. Beeman[28] also describes a conceptually similar approach for analyzing, modifying, and synthesizing frequency-modulated tonal calls of animals. However, Beeman presumes that the amplitude and frequency contours of the desired synthetic signal are available as continuous-time functions $a(t)$ and $f(t)$. Consequently, he does not examine several of the detailed issues involved in synthesizing these stimuli in discrete time as we discuss in Sec. I C. Future work on synthetic dolphin whistles should compare the approaches in Refs. 25–28 to ours to determine which are best suited to this problem.

Section II presents several examples using the algorithm first to synthesize a recorded dolphin whistle without modification, then to demonstrate how the acoustic features of the whistle can be manipulated by the algorithm. Spectrograms are included for all of the example signals synthesized, and .wav files of the synthesized signals may be downloaded over the Worldwide Web from http://www.ece.umassd.edu/Faculty/Faculty&Staff/jbuck/synthwh.htm

I. ALGORITHM DESCRIPTION

This section describes each component of the algorithm used to synthesize whistles: analysis, modification, and synthesis. The analysis portion is not strictly necessary—whistles can be synthesized from fictitious contours not based on the whistles of real dolphins. However, in many playback experiments it will be desirable to begin with a synthetic whistle that resembles the whistle of one of the subject's associates as closely as possible. The modification step is also not mandatory. The whistle may be synthesized without any changes to the contour, but even this step will modify the signal by representing it as the sum of R sinusoids [Eq. (1)]. Specifically, any part of the whistle or noise energy not occurring at one of the R selected harmonic frequencies for the current segment will be removed from the signal. Consequently, the synthetic whistles generally have little or no background noise.

A. Contour extraction

The problem of extracting the frequency contour of a narrow-band whistle has been the subject of several studies. The algorithm used here is based on one described in detail in Ref. 18. This algorithm works well for recordings made of individual animals in high signal-to-noise ratio environments. The whistles used for the initial development of the synthesis algorithm fit in this category. Other algorithms have been proposed for the more challenging problem of extracting whistle contours in continuous recordings of several dolphins.[14,15]

The analysis algorithm is essentially a peak-picking contour extractor. The original continuous-time whistle $s(t)$ is assumed to have been sampled to yield a discrete-time signal $s[n]=s(nT)$, where $1/T$ is the sampling frequency. The discrete-time signal is broken into short blocks of L samples each, where the signal is expected to be relatively constant in amplitude and frequency over L samples. These blocks are indexed on m, and $s[n]$ is assumed to have M such blocks. Let $X_m[k]$ be the L-point Hamming-windowed fast Fourier transform (FFT) for the mth such block.[29] The fundamental frequency of the signal for block m, $f_1[m]$, is initially chosen to be the strongest frequency peak, i.e., $f_1[m] = \arg\max_k |X_m[k]|$. The only exception to this choice occurs when the strongest peak appears to be the second harmonic, as is often observed for segments at the beginning or end of dolphin whistles. Thus, if there is a strong peak at half the frequency of the strongest peak, this lower frequency is chosen for the fundamental. To be considered a suitably strong peak, the peak at half the frequency of the strongest peak must satisfy two criteria. First, the peak must be at least three times as strong as the noise floor of the current FFT block. Second, the peak must be within a factor of 5 of the strongest peak in that FFT block, i.e., no more than 14 dB below the strongest peak in the current block. These thresholds were empirically determined from whistles in Ref. 18. If these criteria are met, the initial estimate of the strongest peak is discarded, and the contour frequency for this block is set to be half the frequency of the strongest peak.

Once the fundamental has been chosen, the R desired harmonics are assigned to be integer multiples of the fundamental in that block, i.e., $f_r[m]=rf_1[m]$ for $2\leqslant r\leqslant R$. The energies of the harmonics $e_r[m]$ are computed from the FFT of the mth block as $e_r[m]=|X_m[f_r[m]]|^2$. Any blocks whose total energy $\Sigma_r e_r[m]$ falls below a certain threshold are chosen to be silent periods in a multiloop whistle. This threshold is determined by the quality of the recording, and usually is a fixed number of dB below the strongest energies in the signal. The energy contours of all harmonics are set to be zero during any of these interloop silence intervals. This prevents the algorithm from synthesizing the noise observed during these silence intervals.

As noted above, the specific contour extraction algorithm used is not of critical importance. We present ours as one possibility that is relatively simple to implement. What is important is that the output of whatever contour extractor is used provide a list of the frequencies $f_r[m]$ and associated energies $e_r[m]$ for each short block of the original signal. The complete set of these frequencies and energies for all blocks will be used, possibly after modifications, to synthesize the whistle of the form in Eq. (1). The precise algorithm

for obtaining the values of the amplitudes $a_r[n]$ from the block energies $e_r[m]$ and the phases $\phi_r[n]$ from the block frequencies $f_r[m]$ will be described in Sec. I C. The next section describes typical modifications of the contours prior to synthesis, and how they are implemented using the frequency and energy contours $f_r[m]$ and $e_r[m]$.

B. Modification

This section describes several potential modifications of dolphin whistles and outlines how synthetic whistles can be modified by editing the frequencies $f_r[m]$ and energies $e_r[m]$ for the blocks. These modifications will be illustrated in Sec. II using spectrograms of the original and modified whistles.

The first modification would be to remove all the harmonics of the whistle, leaving only the fundamental. Playback experiments with these signals could be used to investigate whether the fundamental contains sufficient information to identify an individual. This modification can be accomplished by setting $e_r[m]=0$ for $2\leqslant r\leqslant R$ and $1\leqslant m\leqslant M$: the energy in all components above $r=1$ will be zero for all blocks.

Removing the harmonics is not a sufficiently discriminatory test to test whether the recognition is based on the contour of frequency against time, or the overall signal energy against time. We can determine the relative salience of these factors by setting the energy of the signal to be constant over time. This is accomplished by making $e_1[m]=E$ (a constant) for all m. Synthesized signals where $f_r[m]$ is unmodified, $e_1[m]=E$, and $e_r[m]=0$ for $2\leqslant r\leqslant R$, should be capable of testing whether individual recognition can be achieved using synthetic whistles containing the original contour of frequency against time, but lacking all information in the energy envelope and harmonics.

Another interesting question is whether translating the contour in frequency changes the dolphins' perception of the whistler's identity. This modification is implemented by setting $f_r[m]=f_r[m]+r\Delta f$, where Δf is the desired frequency offset for the fundamental. Note that the harmonics must be moved by $r\Delta f$, not simply Δf, to insure that the frequencies are still harmonically related.

The modifications can also be used to produce a signal whose average frequency is unchanged but which is dilated in frequency. Let

$$f_0=(1/M)\sum_{m=1}^{M} f_1[m]$$

be the average frequency of the fundamental. We may expand or contract the frequency contour of the signal by changing the fundamental contour $f_1[m]$ to be $f_0+a(f_1[m]-f_0)$. When $a>1$ this will expand the contour about its mean frequency, and when $a<1$ it will be contracted. The remaining harmonic frequencies $f_r[m]$ are then set to be $rf_1[m]$.

The signal may be modified by time dilation as well. The frequency and energy contours can both be modified using standard sampling rate conversion operations (decimation and interpolation) as described in Oppenheim and Schafer[29] to obtain time dilation by any amount desired. It is also possible to segment the whistle in time and dilate each segment by different amounts. For example, the first half of the whistle could be sped up by 50% while the second half is slowed by the same amount. This is particularly straightforward to implement on separate loops of a multiloop whistle.

C. Synthesis

The method described in this section computes the appropriate signals for the amplitude $a_r[n]$ and phase $\phi_r[n]$ of the rth harmonic in the model in Eq. (1) from the corresponding frequency contour $f_r[m]$ and energy contour $e_r[m]$ for that harmonic. Each harmonic is processed independently, and then the resulting time-domain signals are summed to yield the synthetic whistle $s[n]$. Each of the M samples in $f_r[m]$ and $e_r[m]$ represents a block of L data points, so the synthesis must reconstruct or expand each sample in $f_r[m]$ to get L points of $\phi_r[n]$, and likewise each point in $e_r[m]$ must be used to obtain L points of $a_r[n]$. The key assumption used to do this is that the block length L used to extract the contours $f_r[m]$ and $e_r[m]$ was short enough that the energy and frequency of each harmonic changed slowly between adjacent blocks, i.e., the signal is quasistationary over blocks of length L.

1. Energy-to-amplitude interpolation

The amplitude signal $a_r[n]$ is obtained by letting the first sample of each block $a_r[mL]=2\sqrt{e_r[m]}/L$, then using bandlimited interpolation (Sec. 4.6 of Ref. 29) at π/L to fill in the remaining $L-1$ points of the block, as is standard when upsampling by a factor of L. The square root is needed to convert the energy measurement back to an amplitude. Strictly speaking, the normalization by $1/L$ is necessary because the upsampling is by a factor of L and the factor of 2 is required because the value of $e_r[m]$ obtained from the FFT only accounts for one of the two complex exponentials used in Euler's Identity[30,31] to construct the real sinusoid $a_r[n]\sin(2\pi\phi_r[n])$. Realistically, these factors are a constant gain on the signal. Any convenient choice for this gain may be used so long as the same gain is applied to each harmonic and $a_r[mL]$ is proportional to $\sqrt{e_r[m]}$. The bandlimited interpolation filter used for the amplitudes was a Parks–McClellan low-pass filter of length $20\times256+1=5121$ with cutoff frequency of π/L.[29]

2. Frequency-to-phase conversion

The instantaneous frequency $f(t)$ for a continuous-time signal $s(t)=\cos(2\pi\phi(t))$ is defined to be $f(t)=d\phi(t)/dt$.[31] Note that for a constant frequency sinusoid $\cos(2\pi f_0 t)$, this yields $f(t)=f_0$, an intuitively reassuring result. The synthesis process starts with samples $f_r[m]=f(mLT)$ and must reconstruct $\phi_r[n]=\phi(nT)$. This process occurs in two steps, and exploits the assumption that the FFT blocks are short enough that the frequency changes only slightly between adjacent blocks. In precise terms, this assumption means that the block length is short enough that $1/LT$ is above the Nyquist rate for the modulation rate of the frequency contour $f(t)$.[31] Based on this assumption, the signal

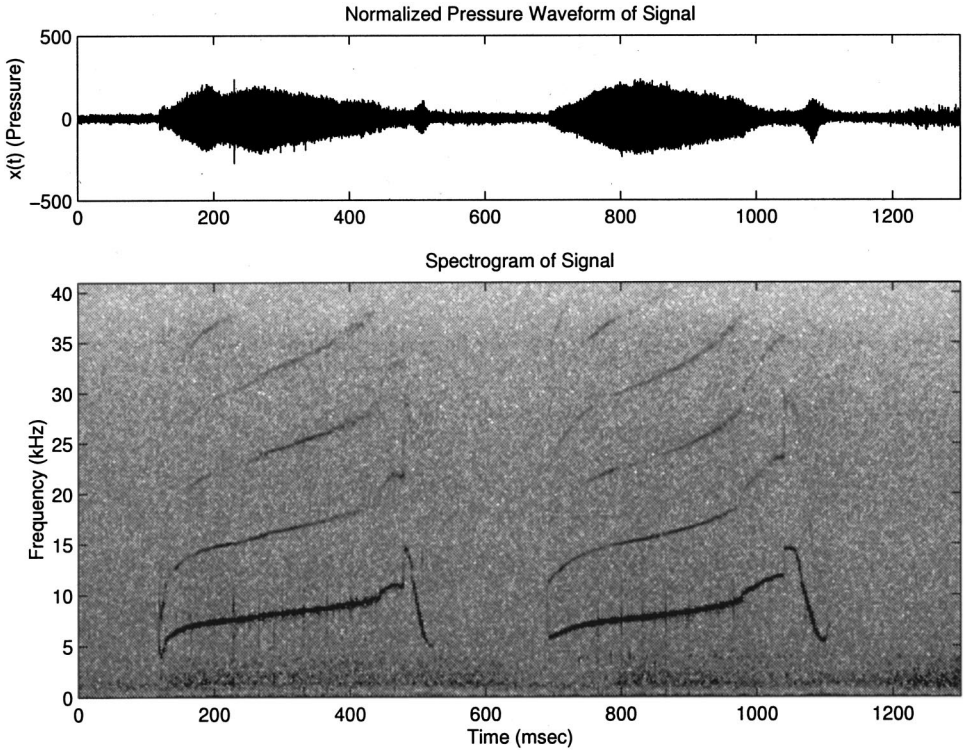

FIG. 1. Waveform and spectrogram of recording of original *T. truncatus* call used as basis for all subsequent synthetic whistles.

$f_r[n]=f_r(nT)$ is reconstructed by upsampling by L and interpolating as described for the amplitude signals.[29] The synthesis algorithm then numerically integrates the interpolated frequency contour $f_r[n]$ to obtain $\phi_r[n]$. The integration of a discrete-time signal is not mathematically well-defined. Rather, the algorithm is computing samples of the integral of the bandlimited interpolation of $f_r[n]$. This is approximated using the trapezoidal method for numerical integration.[30] This is not the most sophisticated numerical integration technique available, but it is sufficiently accurate given that the sampling rate $1/T$ used to satisfy the Nyquist criteria for the original signal $s(t)$ usually highly oversamples the frequency contours $f_r(t)$.

After computing $a_r[n]$ and $\phi_r[n]$ using the methods described here, it is straightforward to compute $s[n]$ using Eq. (1).

II. EXAMPLES

This section presents several examples demonstrating typical whistles which can be generated using the synthetic whistle algorithm. All the examples presented in this section are based on the recorded signal whose spectrogram is shown in Fig. 1. This whistle was made by a 9-year-old female free-ranging *Tursiops truncatus* in the population studied off Sarasota by Wells *et al.*[33] The recording was made using a suction cup hydrophone, and a Panasonic AG-6400 stereo hi-fi VCR on standard VHS tapes. The measured frequency response of this system was 20–20 000 Hz. The signal was subsequently digitized on a Kay Elemetrics Corp. model 5500 digital signal-processing system at 81 920 Hz. The contours used for the modification and synthesis algorithm were extracted using 512-point Hamming-windowed FFTs with 256 points of overlap between adjacent blocks. Due to this overlap, the effective L for the frequency and energy contour extractors was 256. The signal used for this example suffered recording defects, or dropouts, during two FFT blocks. The amplitude and frequency contours were repaired for these values of m by manually specifying values which fit smoothly with those in the blocks on either side. Figure 2 shows the contours $f_1[m]$, $f_2[m]$, and $f_3[m]$ with appropriate normalization to convert the block index m to the original time axis.

Figure 3 shows the spectrogram of the unmodified synthetic whistle. The most obvious difference between the original whistle in Fig. 1 and the synthetic whistle in Fig. 3 is the absence of the background noise in the synthetic whistle. Another difference audible in quarter-speed playbacks is that the synthetic whistles sound very clean, lacking the roughness heard in the original signal.

Figure 4 displays the spectrogram of the synthetic whistle resulting when all harmonics have been removed from the signal. This stimulus synthesizes what most earlier analyses of whistles assume is the dominant feature perceived by the dolphin—the fundamental contour. As noted earlier, other features of the whistle may be varied to test the animals' sensitivity to these features. Figure 5 plots the spectrogram of a synthetic whistle where the energy in each harmonic is held constant over time at the average value of the total energy of that harmonic. Synthetic whistles such as the one shown in Fig. 6 can be used to evaluate the salience to dolphins of the relative energies of the various harmonics. The synthetic whistle shown in this figure has the same energy in each harmonic at any given time, although the total energy in the signal varies with time.

Figure 7 shows the spectrogram of a synthetic whistle where the fundamental contour has been shifted up in frequency by 3 kHz. Modified synthetic whistles of this nature

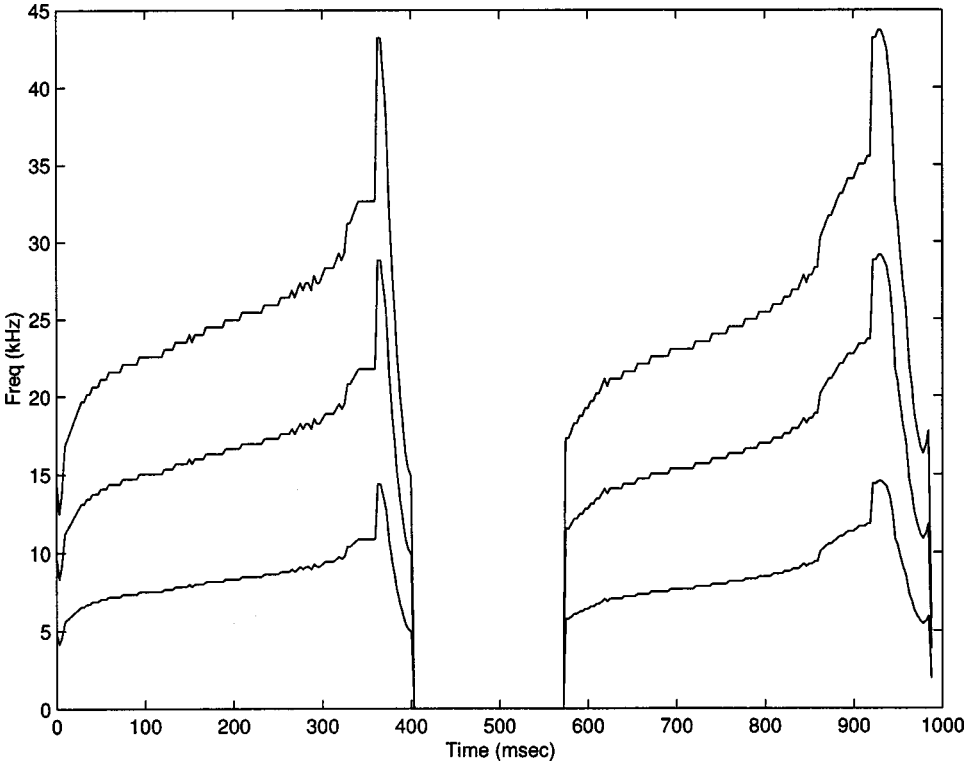

FIG. 2. Frequency contours extracted from original spectrogram in Fig. 1.

could be used to determine whether absolute frequency is salient to the dolphin. Figure 8 demonstrates another possible test for changing the frequencies in a contour while preserving the overall shape of the contour. The fundamental contour of this synthetic whistle has the same mean frequency as that of the original signal, but all excursions away from this mean have been scaled by 1.25. The result is that the spectrogram appears stretched vertically while staying centered at the same location. Synthetic whistles such as those illustrated in Figs. 7 and 8 could test the hypothesis proposed by McCowan and Reiss[7] that the specific frequencies used in the contours are not used when dolphins categorize whistles.

Figure 9 demonstrates one possible use of time dilation on synthetic whistles. For this whistle, the first loop is sped up to be 2/3 the duration of its original length, while the second loop is slowed down to be 3/2 of its original duration. Synthetic whistles of this nature could evaluate the extent to which dolphins tolerate temporal variations in the whistle

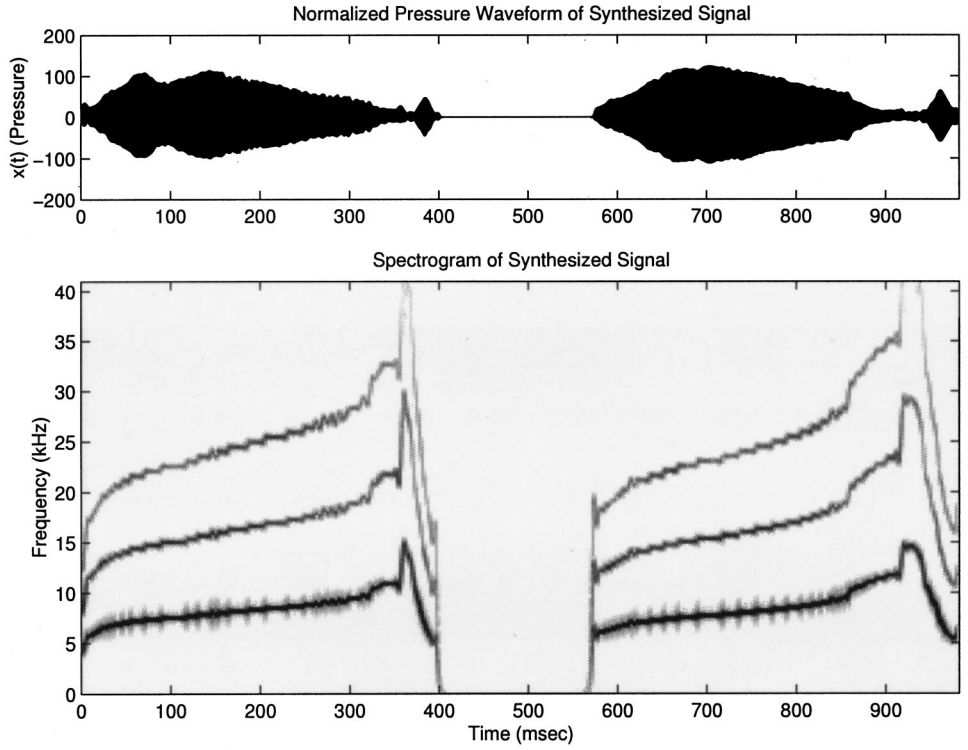

FIG. 3. Waveform and spectrogram of unmodified synthetic whistle.

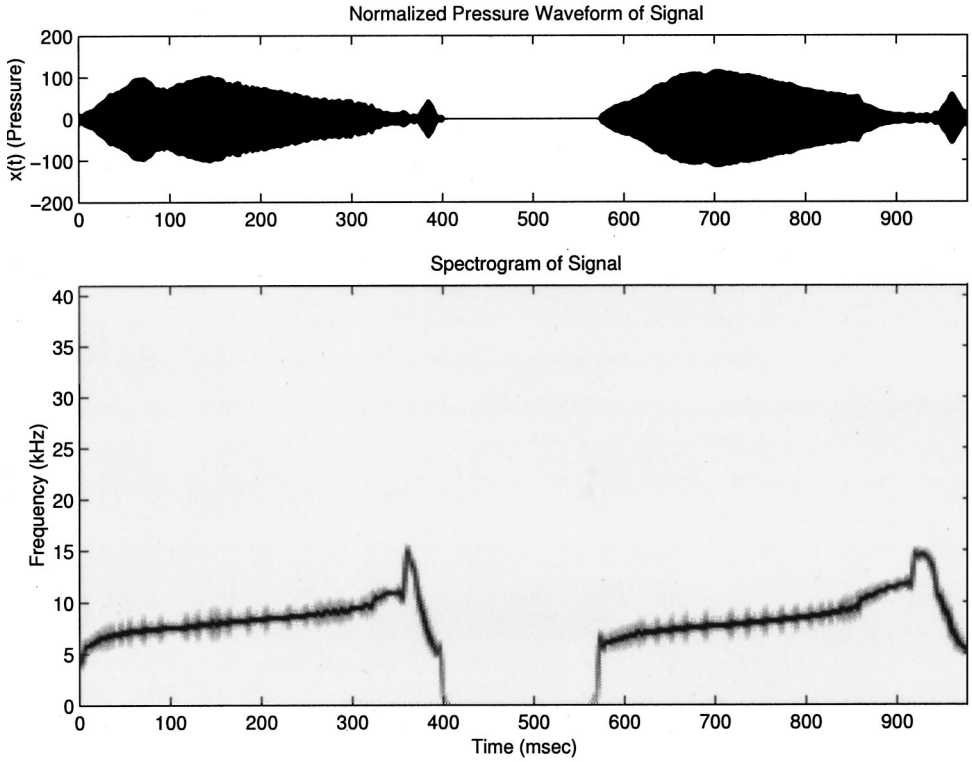

FIG. 4. Waveform and spectrogram of synthetic whistle containing only fundamental contour.

contours. Most automatic recognition algorithms presume that the animals tolerate some amount of temporal variability, and compensate for this variability with differing techniques including uniform dilation to a standard length[7] and nonuniform time dilation.[18] Nonuniform time dilations allow for the possibility that the animals may vary speeds within the same whistle, speeding some parts up, slowing others down, and leaving others unchanged. Behavioral experiments using synthetic whistles of this sort can test how important such time dilations are to the animals.

III. CONCLUSION AND DISCUSSION

An algorithm has been presented for synthesizing frequency-modulated tonal signals. It has been developed to gain analytic control over stimuli based upon the natural

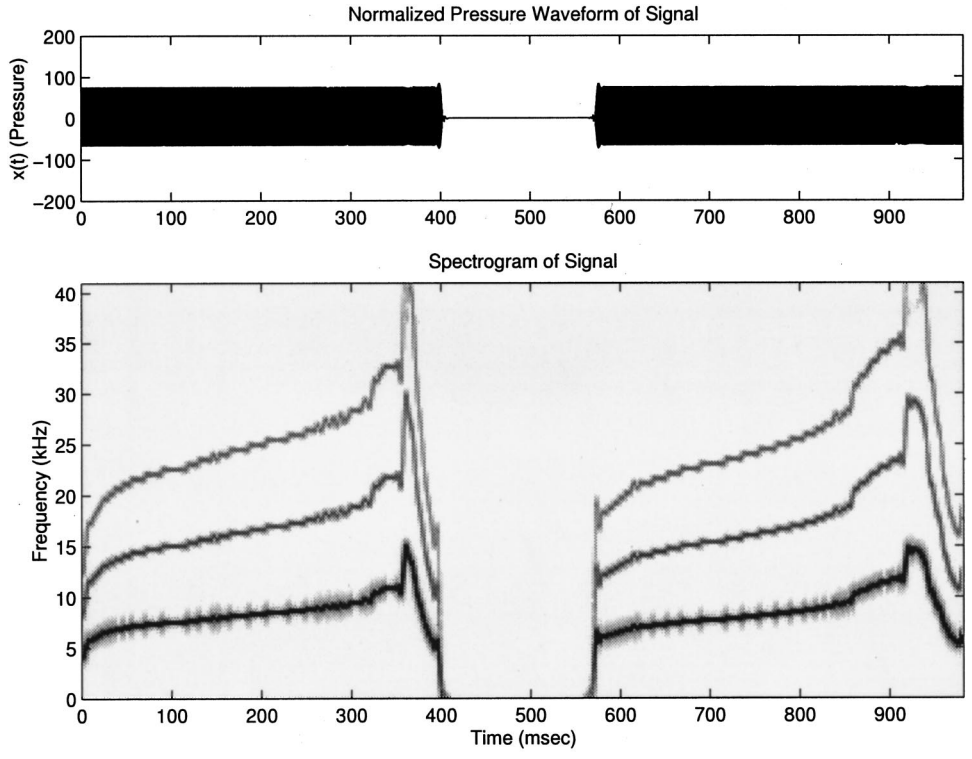

FIG. 5. Waveform and spectrogram of synthetic whistle with constant energy at any given time.

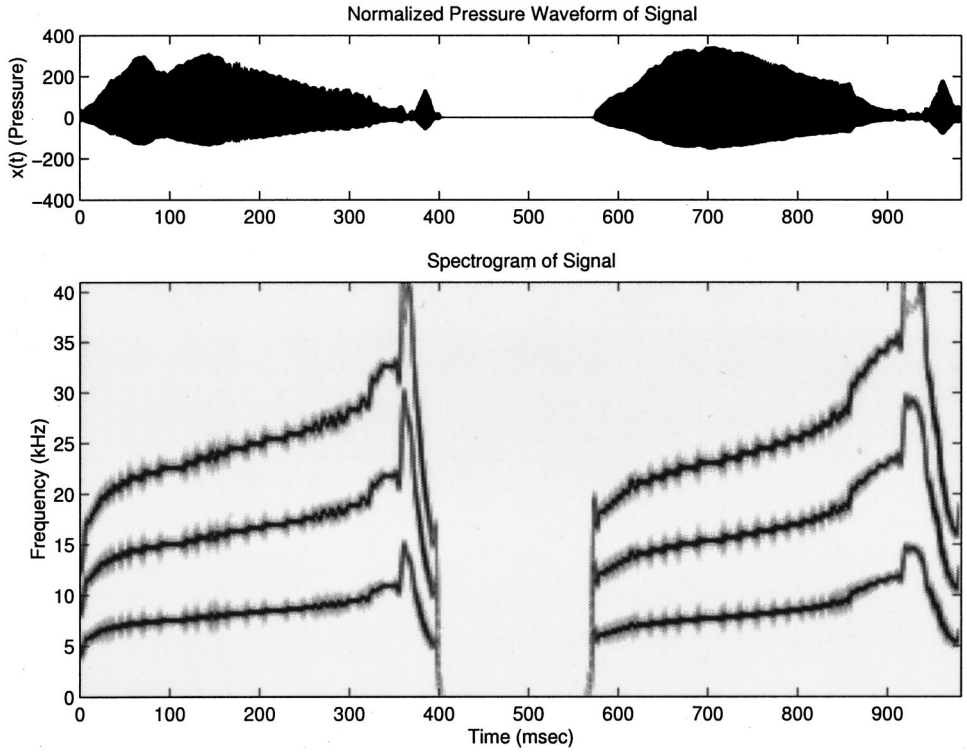

FIG. 6. Waveform and spectrogram of synthetic whistle with equal energy in all harmonics.

acoustic signals of animals. The application described here involved the whistles of bottlenose dolphins, *Tursiops truncatus*. This algorithm allows the construction of suites of signals whose features vary in a quantitatively controlled manner for use in playback experiments. Such signals can be used in a manner not currently possible to test the SWH and other hypotheses about which acoustic features are used by dolphins for categorization and discrimination of whistles.

The first step in any such program of experiments would have to be an evaluation of the quality of the unmodified synthetic whistles. If the dolphins indicate that the unmodified synthetic whistles are perceptually equivalent to playbacks of unprocessed recordings of the same animals, further experiments could proceed. If not, the synthesis algorithm must be improved to capture the features important to dolphins not adequately reproduced in the synthetic whistles. In quarter-speed in-air playbacks using the current algorithm, human listeners can consistently distinguish between original

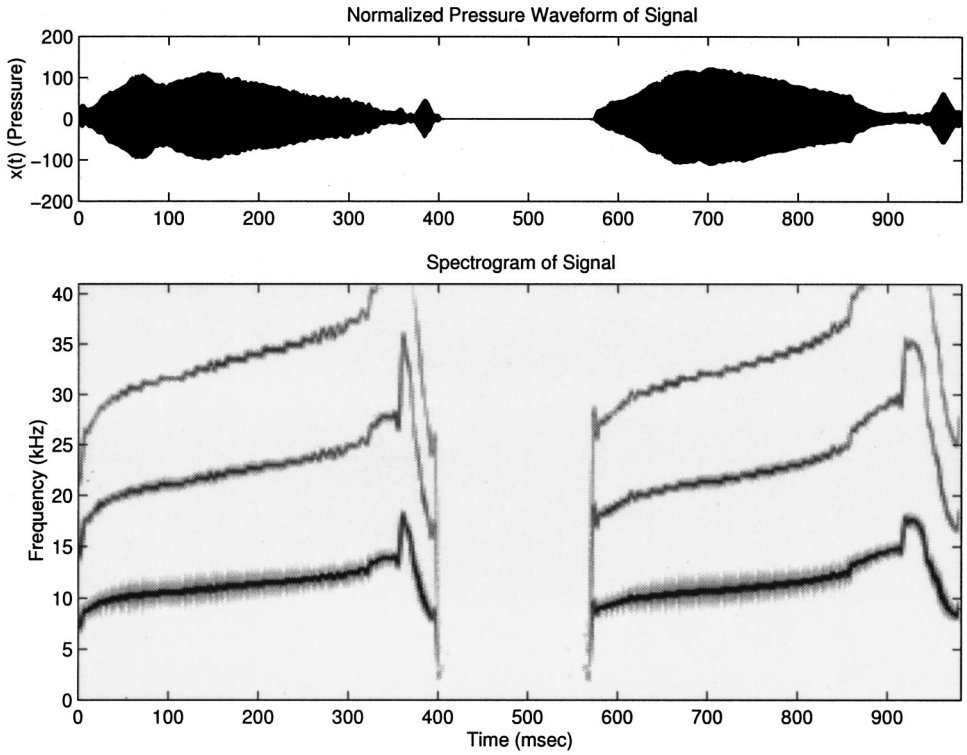

FIG. 7. Waveform and spectrogram of synthetic whistle with fundamental contour shifted up by 3 kHz.

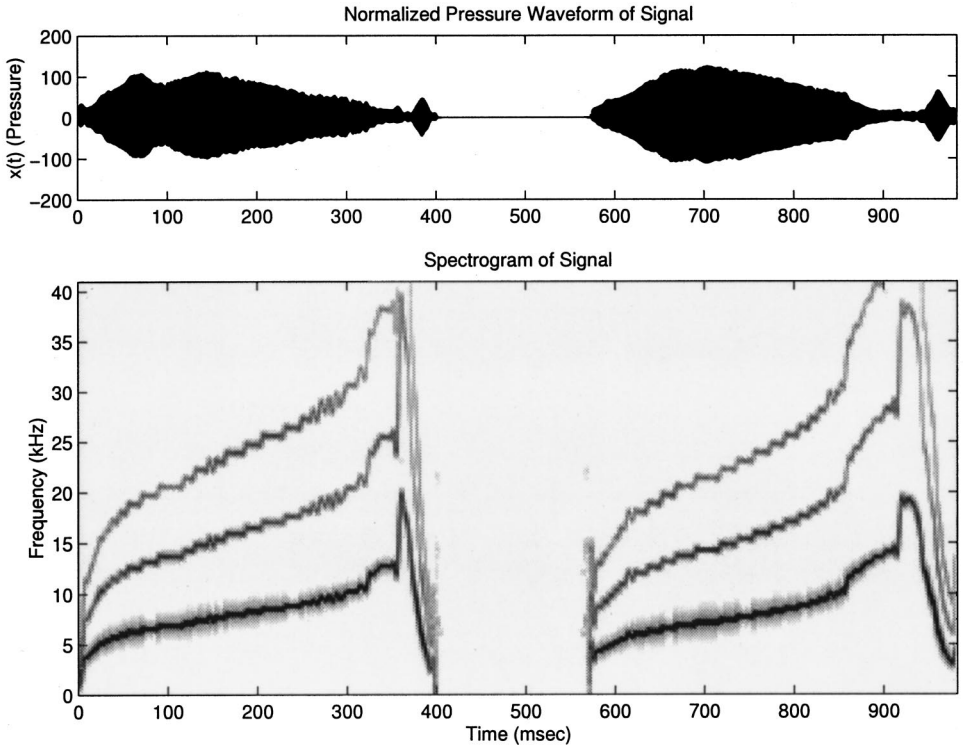

FIG. 8. Waveform and spectrogram of synthetic whistle with same mean fundamental frequency, but scaled in frequency by 1.25.

recordings and synthetic whistles. It is possible that dolphin whistles are not simple tonal signals, but may have a more complex short-term structure.[32] The features cited by the listeners as distinctive to the synthetic whistles, such as ''clean sounding'' and ''not enough noise'' may not be as apparent in ambient noise conditions in underwater trials after propagation through the marine environment. However, it is unclear whether the noise and higher harmonics the synthesis algorithm removes will be perceptually relevant to the animals.

Although it was not demonstrated here, the modification and synthesis algorithm could easily create a range of intermediate stimuli varying specific acoustics parameters between two natural signals. Previous studies[1,2] found such suites of stimuli very helpful for studying the categorical perception of natural signals.

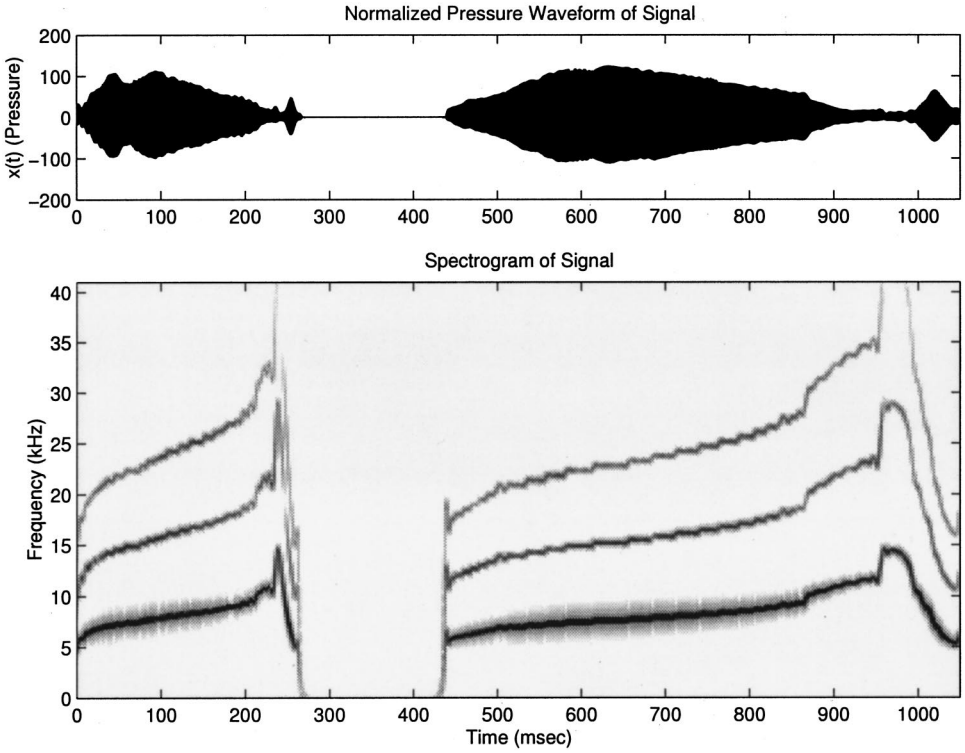

FIG. 9. Waveform and spectrogram of synthetic whistle with the length of the first loop decreased by 33% and the length of the second loop increased by 50%.

ACKNOWLEDGMENTS

J.R.B. gratefully acknowledges the support of NSF Ocean Sciences CAREER Award No. 9733391. This research was supported in part by the U.S. Air Force Office of Scientific Research under Grant No. AFOSR-F49620-96-1-0072. P.L.T. acknowledges the support of the Office of Naval Research Grant No. N00014-87-K-0236 and NIH Grant No. 5 R29 NS25290 for supporting the collection of the data used in this study. This is Contribution Number 990901 from the UMass Dartmouth Center for Marine Science and Technology and Contribution Number 10039 from the Woods Hole Oceanographic Institution. We wish to thank the anonymous reviewers for helpful suggestions which we incorporated into the paper.

[1] P. D. Eimas, E. R. Siqueland, P. Jusczyk, and J. Vigorito, ''Speech perception in infants,'' Science **171**, 303–306 (1971).
[2] P. Kuhl, ''Discrimination of speech by nonhuman animals: Basic auditory sensitivities conducive to the perception of speech-sound categories,'' J. Acoust. Soc. Am. **70**, 340–349 (1981).
[3] K. K. Ohlemiller, J. S. Kanwal, J. A. Butman, and N. Suga, ''Stimulus design for auditory neuroethology: Synthesis and manipulation of complex communication sounds,'' Aud. Neurosci. **1**, 19–37 (1994).
[4] M. C. Caldwell and D. K. Caldwell, ''Individualized whistle contours in bottle-nosed dolphins (*Tursiops truncatus*),'' Nature (London) **207**, 434–435 (1965).
[5] M. C. Caldwell, D. K. Caldwell, and P. L. Tyack, ''Review of the signature-whistle hypothesis for the atlantic bottlenose dolphin,'' in *The Bottlenose Dolphin* (Academic, New York, 1990), Chap. 10, pp. 199–234.
[6] B. McCowan, ''A new quantitative technique for categorizing whistles using simulated signals and whistles from captive bottlenose dolphins (Delphinidae, *Tursiops truncatus*),'' Ethology **100**, 177–193 (1995).
[7] B. McCowan and D. Reiss, ''Quantitative comparison of whistle repertoires from captive adult bottlenose dolphins (Delphinidae, *Tursiops truncatus*): A re-evaluation of the signature whistle hypothesis,'' Ethology **100**, 194–209 (1995).
[8] B. McCowan and D. Reiss, ''Vocal learning in captive bottlenose dolphins: A comparison with humans and nonhuman animals,'' in *Social Influences on Vocal Development*, edited by C. T. Snowdon and M. Hausberger (Cambridge University Press, Cambridge, 1997), pp. 178–207.
[9] M. C. Caldwell, D. K. Caldwell, and N. R. Hall, ''An experimental demonstration of the ability of an atlantic bottlenosed dolphin to discriminate between whistles of other individuals of the same species,'' Technical Report 6, Los Angeles County Museum of Natural History Foundation, 1969.
[10] L. S. Sayigh, P. L. Tyack, R. S. Wells, and M. D. Scott, ''Signature whistles of free-ranging bottlenose dolphins *Tursiops truncatus*: Stability and mother–offspring comparison,'' Behav. Ecol. Sociobiol. **26**, 247–260 (1990).
[11] L. S. Sayigh, P. L. Tyack, R. S. Wells, M. D. Scott, and A. B. Irvine, ''Signature difference in signature whistle production of free-ranging bottlenose dolphins *Tursiops truncatus*,'' Behav. Ecol. Sociobiol. **36**, 171–177 (1995).
[12] C. W. Clark, P. Marler, and K. Beeman, ''Quantitative analysis of animal vocal phonology: an application to swamp sparrow song,'' Ethology **76**, 101–115 (1987).
[13] K. G. Christian. ''Generic Compression and Recall of Signals with Application to Dolphin Whistles,'' Ph.D. thesis, MIT, Dept. of EECS, June 1993.
[14] C. Sturtivant and S. Datta, ''Techniques to isolate dolphin whistles and other tonal sounds from background noise,'' Acoust. Lett. **18**, 189–193 (1995).
[15] C. Sturtivant and S. Datta, ''The isolation from background noise and characterization of bottlenose dolphin (*Tursiops truncatus*) whistles,'' Journal of the Acoustical Society of India, Proceedings of Silver Jubilee NSA-95, 23 (4), The Acoustical Society of India, National Symposium on Acoustics 95, New Delhi, India, December 1995, pp. 199–204.
[16] J. R. Potter, D. K. Mellinger, and C. W. Clark, ''Marine mammal call discrimination using artificial neural networks,'' J. Acoust. Soc. Am. **96**, 1229–1254 (1994).
[17] D. K. Mellinger and C. W. Clark, ''Bioacoustic transient detection by image convolution,'' J. Acoust. Soc. Am. **93**, 2358 (1993).
[18] J. R. Buck and P. L. Tyack, ''A quantitative measure of similarity for *Tursiops truncatus* signature whistles,'' J. Acoust. Soc. Am. **94**, 2497–2506 (1993).
[19] K. M. Fristrup and W. A. Watkins, ''Characterizing acoustic features of marine animal sounds,'' Technical Report 92-04, Woods Hole Oceanographic Institution, Woods Hole, MA, 1992.
[20] K. M. Fristrup and W. A. Watkins, ''Marine animal sound classification,'' Technical Report 94-13, Woods Hole Oceanographic Institution, Woods Hole, MA, 1994.
[21] P. Tyack, ''Whistle repertoires of two bottlenosed dolphins, *Tursiops truncatus*: Mimicry of signature whistles?'' Behav. Ecol. Sociobiol. **18**, 251–257 (1986).
[22] V. M. Janik, ''Pitfalls in the categorization of behavior: A comparison of dolphin whistle categorization methods,'' Anim. Behav. **57**, 133–143 (1999).
[23] V. M. Janik and P. J. B. Slater, ''Context-specific use suggests that bottlenose dolphin signature whistles are cohesion calls,'' Anim. Behav. **56**, 829–838 (1998).
[24] L. S. Sayigh, P. L. Tyack, R. S. Wells, A. Solow, M. D. Scott, and A. B. Irvine, ''Individual recognition in wild bottlenose dolphins: A field test using playback experiments,'' Anim. Behav. **57**, 41–50 (1999).
[25] R. J. McAulay and T. F. Quatieri, ''Speech analysis/synthesis based on a sinusoidal representation,'' IEEE Trans. Acoust., Speech, Signal Process. **34**, 744–754 (1986).
[26] T. F. Quatieri and R. J. McAulay, ''Speech transformations based on a sinusoidal representation,'' IEEE Trans. Acoust., Speech, Signal Process. **34**, 1449–1464 (1986).
[27] L. B. Almeida and F. M. Silva, ''Variable-frequency synthesis: An improved harmonic coding scheme,'' in Proceedings Int. Conference on Acoustics, Speech, Signal Processing, page 27.5.1, IEEE Press, 1984.
[28] K. Beeman, ''Digital signal analysis, editing, and synthesis,'' in *Animal Acoustic Communication*, edited by S. L. Hopp, M. J. Owren, and C. S. Evans (Springer, Berlin, 1998), pp. 59–103.
[29] Alan V. Oppenheim and Ronald W. Schafer with John R. Buck, *Discrete-time Signal Processing*, Prentice-Hall Signal Processing Series, 2nd ed. (Prentice-Hall, Englewood Cliffs, NJ, 1999).
[30] G. B. Thomas, Jr. and R. L. Finney, *Calculus and Analytic Geometry*, 16th ed. (Addison-Wesley, Reading, MA, 1984).
[31] A. V. Oppenheim and A. S. Willsky with H. Nawab, *Signals and Systems*, Prentice-Hall Signal Processing Series, 2nd ed. (Prentice-Hall, Englewood Cliffs, NJ, 1997).
[32] P. L. Tyack, W. J. Williams, and G. Cunningham, ''Time-frequency fine structure of dolphin whistles,'' in Proceedings of the IEEE-SP Symposium on Time-frequency and Time-scale Analysis, IEEE Press, 1992.
[33] R. S. Wells, M. D. Scott, and A. B. Irvine, ''The social structure of free-ranging bottlenose dolphins,'' in *Current Mammalogy*, edited by H. Genoways (Plenum, New York, 1987), Vol. 1.

Auditory and behavioral responses of bottlenose dolphins (*Tursiops truncatus*) and a beluga whale (*Delphinapterus leucas*) to impulsive sounds resembling distant signatures of underwater explosions

James J. Finneran[a)]
Space and Naval Warfare Systems Center D351, 49620 Beluga Road, Room 204, San Diego, California 92152-6266

Carolyn E. Schlundt
Science Applications International Corporation, Maritime Services Division, 3990 Old Town Avenue, Suite 105A, San Diego, California 92110

Donald A. Carder
Space and Naval Warfare Systems Center D351, 49620 Beluga Road, Room 204, San Diego, California 92152-6266

Joseph A. Clark and Jane A. Young
Naval Surface Warfare Center, Carderock Division, Bethesda, Maryland 20084

Joel B. Gaspin
Naval Surface Warfare Center, Indian Head Division, Indian Head, Maryland 20903

Sam H. Ridgway
Space and Naval Warfare Systems Center D3503, 49620 Beluga Road, Room 204, San Diego, California 92152-6266

(Received 1 December 1999; accepted for publication 14 April 2000)

A behavioral response paradigm was used to measure masked underwater hearing thresholds in two bottlenose dolphins and one beluga whale before and after exposure to impulsive underwater sounds with waveforms resembling distant signatures of underwater explosions. An array of piezoelectric transducers was used to generate impulsive sounds with waveforms approximating those predicted from 5 or 500 kg HBX-1 charges at ranges from 1.5 to 55.6 km. At the conclusion of the study, no temporary shifts in masked-hearing thresholds (MTTSs), defined as a 6-dB or larger increase in threshold over pre-exposure levels, had been observed at the highest impulse level generated (500 kg at 1.7 km, peak pressure 70 kPa); however, disruptions of the animals' trained behaviors began to occur at exposures corresponding to 5 kg at 9.3 km and 5 kg at 1.5 km for the dolphins and 500 kg at 1.9 km for the beluga whale. These data are the first direct information regarding the effects of distant underwater explosion signatures on the hearing abilities of odontocetes.
[S0001-4966(00)04807-4]

PACS numbers: 43.80.Nd, 43.80.Lb [WA]

INTRODUCTION

It is becoming increasingly clear that intense anthropogenic (human-generated) underwater sound may adversely affect the hearing and behavior of many marine mammals. Cetaceans, which spend their entire lives in water, may be particularly vulnerable because of their relatively high auditory sensitivity, wide frequency bandwidth, and their reliance on acoustic stimuli to navigate, forage, and communicate (Ridgway, 1997). Unfortunately, there are few direct data regarding the effects of intense sound on cetaceans, making it extremely difficult to predict safe exposure levels for these mammals.

Exposure to intense sound may produce an elevated hearing threshold, also known as a threshold shift (TS). If the threshold returns to the pre-exposure level after a period of time, the TS is known as a temporary threshold shift (TTS); if the threshold does not return to the pre-exposure level, the TS is called a permanent threshold shift (PTS). Studies of PTS and TTS were instrumental in establishing noise-exposure limits in humans; however, there are no data on PTS and few data on TTS in cetaceans. There have been to date only two studies of TTS in cetaceans: Au *et al.* (1999) measured TTS in a single bottlenose dolphin exposed to 50 min of octave-band noise centered at 7.5 kHz; Schlundt *et al.* (2000) measured temporary shifts of masked-hearing thresholds (MTTS) in bottlenose dolphins and white whales exposed to 1-s pure tones at frequencies of 0.4, 3, 10, 20, and 75 kHz. These data included and expanded on the original pure-tone MTTS data for bottlenose dolphins described in a technical report by Ridgway *et al.* (1997).

Although pure-tone stimuli are fair representations of many military and commercial sonars, many anthropogenic

[a)]Electronic mail: finneran@spawar.navy.mil

TABLE I. Animal subjects used in this study.

Species	Animal identification	Gender	Weight (kg)	Length (cm)	Age (yrs)
Tursiops truncatus	BEN	M	250	270	35
Tursiops truncatus	NEM	M	250	280	33
Delphinapterus leucas	MUK	F	550	350	31

sources of intense sound produce impulsive signals, i.e., transient signals with rapid rise times and high peak levels. Impulsive sources include seismic air guns and underwater explosions. Peak sound-pressure levels (SPLs) of underwater explosions may exceed 250–260 dB *re*: 1 μPa at 1 m (1 μPa-m) (Richardson *et al.*, 1995). Air guns used in geophysical surveys are routinely operated at peak source levels exceeding 210 dB *re*: 1 μPa-m (Richardson *et al.*, 1995). TTS data obtained with pure-tone stimuli may suggest the effects of impulsive sounds; however, the relationship between hearing loss and the fundamental parameters of sound such as peak frequency, duration, rise time, peak pressure, and total energy are unknown; thus, TTS measurements with impulsive stimuli are still needed for direct predictions.

This report presents the results of a study designed to measure TTS in bottlenose dolphins (*Tursiops truncatus*) and beluga whales (*Delphinapterus leucas*) exposed to impulsive sounds with pressure waveforms resembling those produced by underwater explosions (HBX-1, charge weight 5 or 500 kg) at ranges of 1.5 to 55.6 km. A behavioral response paradigm was used to measure hearing thresholds before and after exposure to the impulsive sounds. The test site in San Diego Bay featured a relatively high and variable ambient noise background dominated by shipping as well as biological sources such as snapping shrimp and other animals housed at the facility. Bandlimited white noise (masking noise) was therefore introduced to create a floor effect and keep thresholds consistent despite fluctuations in the ambient noise level. The presence of masking noise has been shown to decrease the amount of TTS observed in humans (e.g., Parker *et al.*, 1976; Humes, 1980) and the amount of PTS in terrestrial mammals (Ades *et al.*, 1974). To indicate that the thresholds presented here were measured in the presence of masking noise, we use the term MTTS to identify these data. The effects of the masking noise on the measured thresholds are discussed as well.

I. METHODS

A. Experimental animals

Cetacean species potentially usable in a study of TTS are currently limited to those animals under human care at research facilities and oceanaria. This limitation excludes the study of baleen whales and allows only the study of smaller odontocetes such as dolphins and porpoises. Table I lists the experimental animals used in this study: two bottlenose dolphins and one beluga whale. A fourth subject (beluga whale, male, age 22 years) was rejected during the course of the study after being diagnosed with a systemic fungal infection. No substantial TSs (i.e., at or above 6 dB) were observed in this subject during any of the tests in which he participated.

The remaining three subjects were healthy and were not known to have any hearing deficits at the frequencies at which they were tested. Animals were housed in floating net enclosures (10×10 m to 13×25 m) located in San Diego Bay. All animals were under constant veterinary supervision in accordance with applicable federal regulations. The study followed a protocol approved by the Institutional Animal Care and Use Committee under guidelines of the Association for the Accreditation of Laboratory Animal Care.

Behavioral audiograms measured for *Delphinapterus leucas* (White *et al.*, 1978; Awbrey *et al.*, 1988; Johnson *et al.*, 1989) and *Tursiops truncatus* (Johnson, 1967) show these species to have hearing ranges and sensitivities equivalent to or better than many marine mammals (see Fay, 1988; Richardson *et al.*, 1995). *Delphinapterus and Tursiops* may thus be considered representative of many marine mammals that have broad auditory bandwidth and high sensitivity. These mammals also are widely distributed across the globe: *Tursiops* has an around-the-world distribution in temperate and tropical waters (Wells and Scott, 1998) and *Delphinapterus* has a wide distribution in arctic and subarctic waters (Brodie, 1989), as far south as the St. Lawrence River mouth in the Atlantic (rarely as far south as New Jersey) and Sakhalin Island in the Pacific. Their wide distribution and keen hearing give these animals the potential to be impacted by a variety of acoustic devices.

B. Experimental apparatus

1. Underwater stations

Figure 1(a) illustrates the test apparatus. This 8×8-m floating net enclosure featured two underwater listening stations, designated ''S1'' and ''S2.'' The S1 station was the site for presentation of the ''start'' tone for the animal to begin hearing tests, as well as the impulsive stimulus. The actual hearing tests were conducted at the S2 station. Each station consisted of a polyvinyl chloride (PVC) frame with a plastic biteplate on which the subject was trained to station. The S1 and S2 biteplates were located at depths of approximately 4 and 2 m, respectively. Each station contained an underwater video camera which was used to observe each subject on the biteplate. A third video camera was located in-air with a view of the entire test enclosure.

The S1 station [Fig. 1(b)] contained a single sound projector (ITC 1042) that was used to emit a 1-s tone as the start signal for the subject to begin hearing tests. These start tones, or ''S1 tones,'' were at a frequency of 20 kHz and an SPL of approximately 140 dB *re*: 1μPa. The S1 start tones were produced using a programmable function generator (Wavetek 178), filtered (Ithaco 4302), and amplified (BGW PS4) before being input to the S1 sound projector.

The S2 station [Fig. 1(c)] contained two sound projectors: one (ITC 1001) mounted 1.5 m below the animal's ears and used to project hearing test tones, or ''S2 tones,'' and one (NRL J9) located 1.5 m in front of the animal and used to project masking noise. Masking noise was generated on a dedicated computer running custom software (Finneran *et al.*, 1999). This system allowed for the continuous generation of masking noise whose frequency spectrum was com-

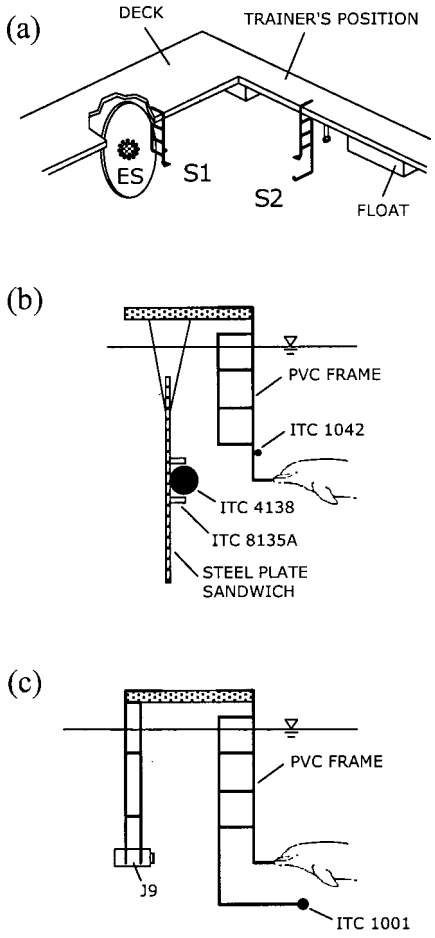

FIG. 1. (a) Schematic of the test apparatus showing the locations of the S1 and S2 underwater listening stations. The deck is shown cut-away to reveal the explosion simulator (ES). (b) Horizontal detail view showing the ES and the S1 station. (c) Horizontal detail showing the S2 station.

pensated to eliminate the effects of projector frequency-dependent transmission characteristics and acoustic standing waves. The projected masking noise had a spectral density level of 95 dB *re*: 1 μPa^2/Hz and frequency bandwidth of 0.8–3 kHz; the noise spectral density was flat within ± 2 dB over this range. The S2 tones were 250 ms in duration including 50-ms rise and fall times. S2 tones were generated using a digital computer and multifunction board (National Instruments PCI-MIO-16E-1), filtered (Ithaco 4302), and amplified (BGW PS4) before being input to the ITC 1001 projector.

Threshold estimates obtained with a behavioral response paradigm using animal subjects are generally time consuming; thus, the number of S2 frequencies that could be tested was limited. Hearing tests were originally performed at two S2 frequencies: 1.2 and 1.8 kHz; these frequencies were selected because they corresponded to the approximate peak frequency of the impulses (see Sec. I B 2 and Fig. 3 below) and a frequency 1/2 octave above the peak frequency, respectively. At high levels of exposure, TTS has been shown to occur at frequencies above the exposure stimulus frequency, often at a frequencies 1/2 octave to one octave above (Yost, 1994). A third frequency (2.4 kHz) was added shortly after the start of the test sequence, to help insure that shifts occurring at frequencies one octave above the impulse spectral peak would be detected. The order in which the S2 frequencies were tested was counterbalanced between sessions and days.

The acoustic pressure during each S2 tone presentation was measured using a B&K 8103 hydrophone (mounted to the S2 PVC frame) and a B&K 2635 charge amplifier, digitized using the PCI-MIO-16E-1 multifunction board, and stored on a personal computer. The pressure during the S1 start-tone presentation was also measured using a B&K 8103 hydrophone (mounted to the S1 PVC frame), amplified and filtered (B&K 2635), and digitized (PCI-MIO-16E-1). The computer was also used to record the time each S1 and S2 tone was produced.

2. Explosion simulator

For ''high'' explosives like TNT and its derivatives (including HBX-1), the velocity of detonation is extremely fast and a spherically symmetric shock wave is produced along with an oscillating globular mass of gaseous materials (Weston, 1960; Urick, 1967). At close range the pressure signature of an underwater detonation of HBX-1 therefore consists of the shock wave followed by a number of bubble pulses (Urick, 1967). At longer ranges, the signature is complicated by surface and bottom reflections, attenuation, and refraction effects. Pressure signatures of underwater explosions at large distances therefore cannot simply be produced by smaller charges at close range.

In this study, impulsive sounds were generated by a piezoelectric transducer array specifically designed to replicate pressure waveforms produced by distant underwater explosions. This system, referred to here as the explosion simulator (ES), is described in Clark *et al.* (1999); only the salient features are repeated here. The ES consisted of a backplate and an array of projectors. The backplate was constructed out of two 3-m diameter, 0.6-cm-thick stainless-steel plates with a 0.6-cm viscous rubber layer sandwiched between. A 50-cm-diameter piezoelectric sphere (ITC 4138) was located on the backplate at the center. Twelve cylindrical piezoelectric projectors (ITC 8135A) were also mounted on the backplate around the sphere in a 60-cm-radius circle. The ES was suspended from the test enclosure at a depth of 4.3 m, with the backplate vertical in the water column and the projectors facing the S1 biteplate, as shown in Fig. 1(b). The ES was located at a horizontal distance of approximately 1.5 m from the subjects' ears. For stimulus levels 1–8, the S1 biteplate was 0.6 m above the depth of the ES center. For levels 9 and 10, the S1 biteplate and the ES were at the same depth.

Calibration of the ES was a two-step process. First, a system identification was performed *in situ* (using a swept sine wave) to determine the system impulse response relating acoustic pressure to source input voltage. The system impulse response was then used to derive the input voltage waveforms for the spherical and cylindrical projectors required to generate the desired pressure waveform.

Table II shows the test matrix. Each impulse was assigned a nominal stimulus level, from 1 to 10, in order of increasing peak pressure. Simulated explosions ranged from a 5-kg charge at 55.6 km (level 1) to 500 kg at 1.7 km (level 10). Pressure signatures were based on predictions from the

TABLE II. Specifications for the ten impulse levels used in this study.

Level	Equiv. HBX-1 charge weight [kg (lb)]	Equiv. range [km (naut. mi.)]	$SPL_{p\text{-}p}$ (dB *re*: 1 μPa)	p_p [kPa (psi)]	U_T [dB *re*: 1 J/m^2 (1 μPa^2 s)]	τ (ms)
1	5 (11)	55.6 (30)	170	0.17 (0.025)	−52 (130)	5.4
2	5 (11)	37 (20)	179	0.45 (0.065)	−43 (139)	7.6
3	5 (11)	18.5 (10)	189	1.5 (0.22)	−33 (149)	6.9
4	5 (11)	9.3 (5)	196	3.8 (0.55)	−26 (156)	6.4
5	500 (1100)	27.8 (15)	196	3.9 (0.57)	−25 (157)	8.2
6	5 (11)	3.7 (2)	200	6.0 (0.87)	−20 (162)	13
7	5 (11)	1.5 (0.8)	209	16 (2.3)	−13 (169)	8.7
8	500 (1100)	3.7 (2)	213	27 (3.8)	−10 (172)	11
9	500 (1100)	1.9 (1)	220	56 (8.2)	−5 (177)	5.1
10	500 (1100)	1.7 (0.9)	221	70 (10)	−3 (179)	9.5

U.S. Navy's REFMS numerical modeling program (e.g., Britt, 1987; Britt *et al.*, 1991) for mid-depth in 24 m of water at a typical test site in the Baltic Sea (the Baltic was chosen because of test requirements of the German Navy and the University of Kiel, who furnished support for developing the ES). The data in Table II are the mean values from calibration measurements conducted prior to testing each day and include the peak-to-peak SPL ($SPL_{p\text{-}p}$), peak pressure (p_p), duration (τ), and total energy flux (U_T). Individual pressure signatures were measured using a B&K 8105 hydrophone located at a position estimated to lie approximately between the subjects' ears. The hydrophone output was filtered from 2 Hz–200 kHz and amplified (B&K 2635), then digitized (256 kSamples/s), using an HP3561A digital signal analyzer. The digitized waveforms were transferred to a digital computer and analyzed using custom software to calculate $SPL_{p\text{-}p}$, p_p, τ, and U_T.

The peak pressures in Table II were based on the absolute values of the measured waveforms (i.e., the maximum negative or positive peak). The duration of each impulse was defined using the first and last time values at which the absolute value of the waveform reached an amplitude of −20 dB relative to the maximum amplitude. The energy flux spectral density $E(m)$ was calculated as outlined by Fricke *et al.* (1985) and Johnston *et al.* (1988)

$$E(m)=\frac{1}{\rho c}|P(m)|^2, \quad m=0,1,...,N-1, \tag{1}$$

where ρ is the medium density, c is the sound speed,

$$P(m)=\Delta t\sum_{n=0}^{N-1} p(n)e^{-j2\pi mn/N}, \quad m=0,1,...,N-1, \tag{2}$$

$p(n)$ is the digitized time series (the measured pressure waveform), $P(m)$ is the discrete Fourier transform of $p(n)$, N is the number of samples in the time series, Δt is the sampling interval, and $j=(-1)^{1/2}$. Fourier analysis of each signal was based on a 20-ms time window, regardless of the calculated duration. Note that Eq. (1) implicitly assumes plane waves or far-field conditions away from any reflective surfaces, such that the acoustic particle velocity magnitude $v=p/(\rho c)$. The medium characteristic impedance ρc is often removed from Eq. (1) so that the energy flux spectral density may be expressed in units of μPa^2 s/Hz, rather than J m^{-2} Hz^{-1} (0 dB *re*: 1 J m^{-2} Hz$^{-1}\approx$182 dB *re*: 1 μPa^2 s/Hz, for seawater with nominal values of $\rho=1026$ kg/m^3 and $c=1500$ m/s). The total energy flux U_T was calculated using

$$U_T=\Delta f\sum_{k=0}^{N-1} E(k), \tag{3}$$

where $\Delta f=1/(N\Delta t)$. The energy flux is sometimes expressed in μPa^2 s, rather than J/m^{-2} (0 dB *re*: 1 J/m^2 $\approx$182 dB *re*: 1 μPa^2 s, for seawater with $\rho=1026$ kg/m^3 and $c=1500$ m/s).

Figure 2 shows representative pressure waveforms and energy flux spectral densities measured for each of the ten impulse levels. The fidelity of each measured ES waveform to the corresponding REFMS prediction was evaluated by comparing features such as peak pressure, 1/3-octave spectra, and major peaks in the time histories. The measured (synthesized) waveforms were in good agreement with the predicted waveforms, with the exception of the frequency range below approximately 1 kHz, where the ES was incapable of producing sufficient amplitudes to match the predictions (see Clark *et al.*, 1999).

At large distances from any real source, the relationship between acoustic pressure and particle velocity magnitude approaches the plane wave relationship $v=p/(\rho c)$. As the distance (relative to the acoustic wavelength) from any real source decreases, a larger acoustic particle velocity is associated with a given pressure amplitude. Distant signatures from underwater explosions would be expected to obey the plane wave relationship; however, the proximity of the ES to the test subjects compelled measurement of the acoustic particle velocity to insure that it was not substantially elevated from the plane wave value. The acoustic particle velocity was therefore estimated from pressure gradient measurements (using a two-hydrophone technique) at the location of the test subjects. These data did not show any substantial increase in the particle velocity (compared to the plane wave value) at frequencies above 1 kHz, where the bulk of the energy of the impulses used in this study existed.

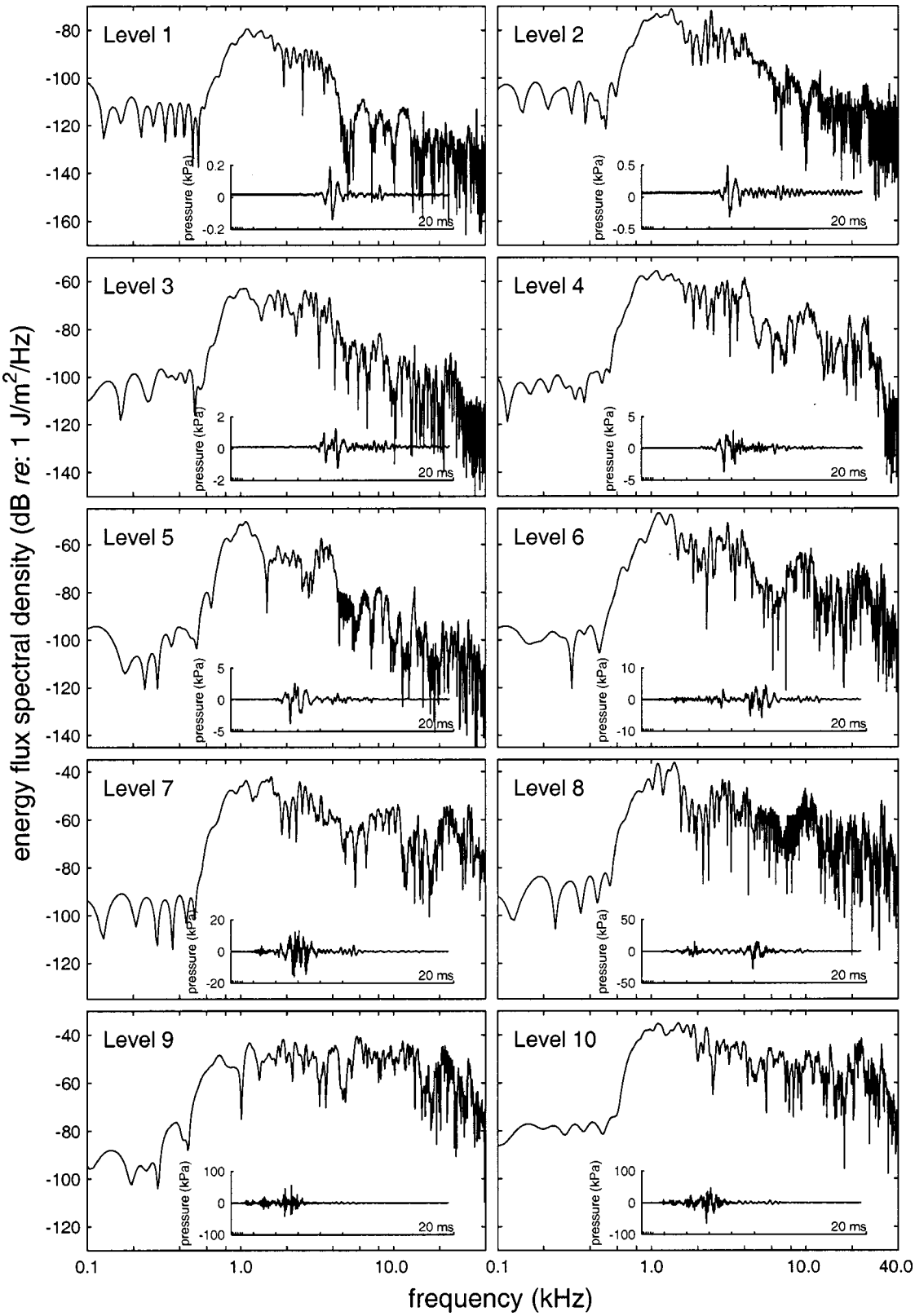

FIG. 2. Representative pressure signatures and energy flux spectral densities for the ten impulse levels. The analysis frequency bandwidth was 6.1 Hz.

C. Procedure

The experimental procedure consisted of the following steps: (1) measure the subject's pre-exposure hearing thresholds at each S2 frequency; (2) expose the subject to an impulse generated by the ES; (3) immediately measure the subject's hearing thresholds at each S2 frequency (postexposure thresholds); (4) measure the subject's hearing thresholds at each S2 frequency approximately 1–1.5 h after exposure (first recovery thresholds); and (5) measure the subject's hearing thresholds at each S2 frequency approximately 2–3

h after exposure (second recovery thresholds). Subjects were tested at each condition shown in Table II. Testing began with each animal at level 1. The impulse level for each animal was incremented by one each test day as long as no MTTS (see Sec. I C 5) had been observed.

Each test day was divided into four sessions: (1) pre-exposure, (2) post-exposure, (3) first recovery, and (4) second recovery. During each session, hearing thresholds were measured at several frequencies. The order in which the frequencies were tested was counterbalanced between sessions and days. Each threshold measurement consisted of several ''dives'' and multiple S2 hearing-test tones were presented during each dive. Sessions, dives, and the hearing-test procedure are described in more detail next, within the context of a pre-exposure session. Post exposure and recovery sessions are then described.

1. Pre-exposure sessions

Pre-exposure sessions consisted of individual hearing threshold measurements conducted at each of the S2 frequencies. The hearing-test procedure was based on the method of free response, or MFR (Egan *et al.*, 1961). Each subject was presented with a number of S2 tones during a relatively long observation period, designated here as a ''dive.'' Each threshold measurement required approximately 1–4 dives. Multiple dives were required to allow the subjects to periodically surface for air. Each dive began with the trainer directing the animal (with a hand signal) to the S1 station. The subject was trained to remain on the S1 station until presented with the S1 start tone. Upon hearing the S1 start tone, the subject proceeded directly to the S2 station for hearing tests.

Once the animal was positioned at the S2 station, S2 tones were presented. The time interval between tones (the interstimulus interval, or ISI) was randomized and the subject did not know when the next tone would occur. Subjects were trained to whistle if they heard a tone and to remain quiet otherwise (see Ridgway and Carder, 1997). The amplitudes of the S2 tones were adjusted using a modified staircase procedure (e.g., Cornsweet, 1962; Rosenberger, 1970): the amplitude was decreased 4 dB following each hit (a whistle response to a tone) and increased 2 dB following each miss (no whistle response to a tone). After a variable number of tones, the trainer sounded an underwater buzzer which signaled the animal to leave the S2 station and return to the surface for a fish reward. The next dive was then begun, if necessary.

Hearing thresholds were defined as the mean SPL of the first ten hit–miss/miss–hit reversal points. The first three tones were presented at suprathreshold levels (as warm-up tones) and were not included in the threshold determination. A subject's threshold at any given frequency could usually be estimated after presenting 15 to 30 tones.

The time period between 0.05 and 2.05 s immediately following each tone start was designated as a ''hit interval.'' Only whistle responses occurring within a hit interval following a tone onset were recorded as hits. Any whistle response by a subject not occurring within a hit interval was recorded as a false alarm. The ISI (defined from the start of one tone to the start of the next tone) was randomly varied between 5–8 s; thus, the majority of time spent on the S2 station was outside any hit intervals and functioned as a ''catch trial'' period. Time catch trials (Ljungblad *et al.*, 1982), or no-tone periods, with durations of between 10–60 s, were also randomly introduced while the animal was on the S2 station.

It has been demonstrated that variations in a measured sensory threshold may result from changes in a subject's response bias, rather than an actual change in sensitivity *per se* (Schusterman, 1980). False-alarm rates provide some insight into a subject's response bias from session to session. For this study, the false-alarm rate r was defined as the number of false alarms, N_{FA}, divided by the total amount of time during which the subject was on the S2 station with no hit interval present. To obtain a dimensionless quantity, r is multiplied by the hit interval duration T_1

$$rT_1 = \frac{N_{\mathrm{FA}}}{T - N_{\mathrm{S2}} T_1} T_1, \tag{4}$$

where T is the total amount of time the animal spent on the S2 station and N_{S2} is the number of S2 tones presented. For the MFR, rT_1 values calculated using Eq. (4) are analogous to false-alarm rates obtained from a single interval experiment (Miller, 1969). This study employed a modified version of the MFR: the distribution of S2 tones did not follow a Poisson distribution because of the 5–8-s ISI (i.e., the ISI was not open-ended). The rT_1 values calculated here are therefore not strictly analogous to those obtained with the MFR or to false-alarm rates obtained from a single interval experiment; however, we still computed rT_1 values in order to assess a subject's response bias from session to session. The use of rT_1 was a method of normalizing the number of false alarms with respect to the number of tones presented and the total time that the subject was on the S2 station.

2. Postexposure sessions

Postexposure sessions were identical to pre-exposure sessions with the following exception: a single impulse was produced by the ES 30 ms after the start of the first S1 start tone cuing the animal to the S2 station. The postexposure threshold at the first S2 frequency tested was generally obtained within 2–3 min following exposure to the impulse. Thresholds at the remaining S2 frequencies were normally obtained within 5–15 min following the impulse. After all S2 frequencies had been tested, threshold measurements were repeated at the first S2 frequency tested after exposure. In some circumstances (e.g., if the first postexposure threshold at a frequency suggested a potential shift) testing was also repeated at one or more of the other S2 frequencies.

3. First recovery sessions

Threshold measurements were also repeated at approximately 1–1.5 h following the postexposure session; these test sessions were designated as ''first recovery sessions.'' During first recovery sessions, thresholds were again measured at all S2 frequencies; these sessions were conducted in a manner identical to that of pre-exposure sessions.

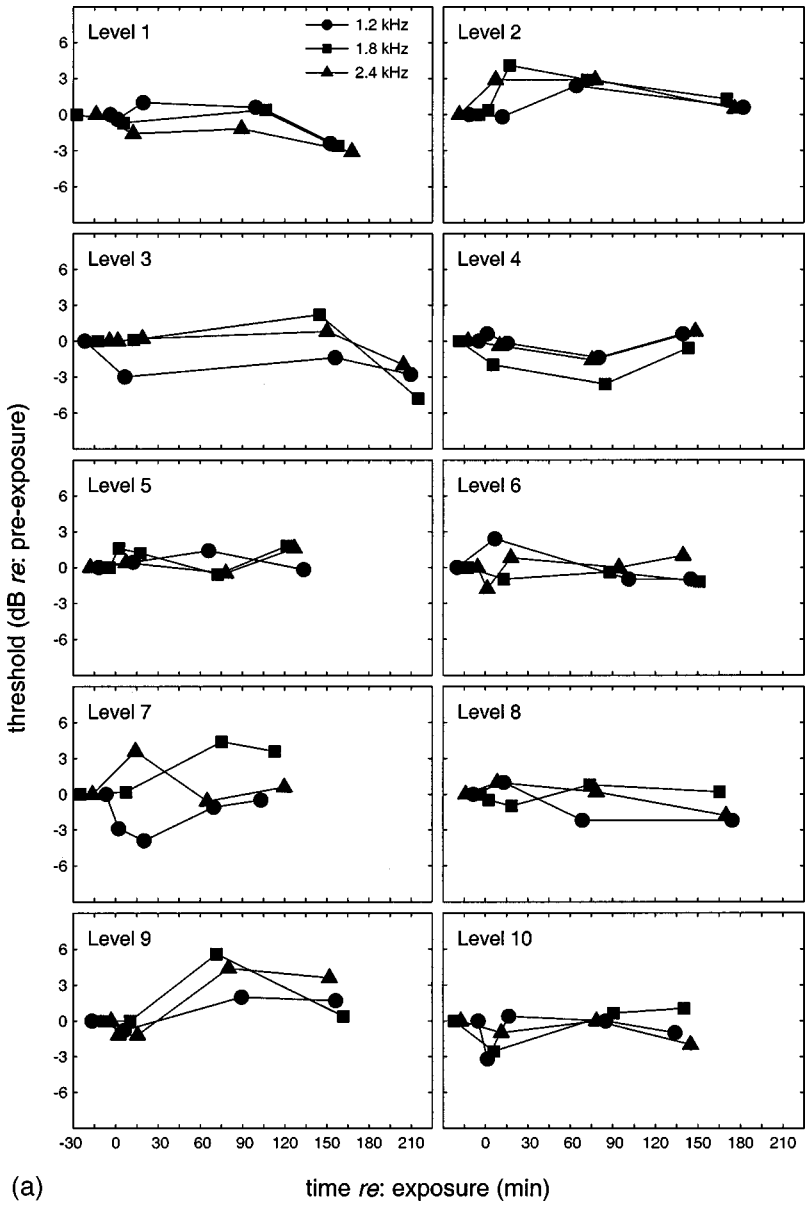

FIG. 3. Pre-exposure, postexposure, and recovery thresholds for subjects (a) BEN, (b) NEM, (c) MUK as functions of the time relative to exposure, for each of the ten impulse levels.

4. Second recovery sessions

The ''second recovery session'' consisted of threshold measurements conducted at approximately 2–3 h following the postexposure session. The second recovery sessions were conducted identically to pre-exposure sessions and thresholds were again measured at all S2 frequencies.

5. MTTS criterion

Postexposure and recovery hearing thresholds were compared to pre-exposure thresholds to determine if a subject experienced MTTS, defined as a 6-dB or larger increase in threshold over the pre-exposure threshold at that frequency. This 6-dB criterion was based on a substantial amount of threshold data for these animals obtained at several frequencies over a period of several years (e.g., Ridgway and Carder, 1997; Ridgway *et al.*, 1997; Schlundt *et al.*, 2000) and was considered to be the minimum shift that was clearly larger than any day-to-day or session-to-session variations in the subjects' masked-hearing thresholds. Studies of TTS in terrestrial mammals have shown that TTSs larger than 40 dB may be fully recovered without a PTS or the loss of sensory hair cells (e.g., Ahroon *et al.*, 1996); therefore, the 6-dB criterion was also considered well below levels capable of causing a PTS.

II. RESULTS

Table III presents the means and standard deviations for the pre-exposure thresholds measured for each subject, at each S2 frequency, for the ten impulse levels. These data confirm that there were no significant differences between

TABLE III. Mean values for the pre-exposure masked hearing thresholds (dB *re*: 1 μPa) and standard deviations (s.d.) measured for the three test subjects. $n=10$ for all categories, except: NEM at 2.4 kHz ($n=7$) and MUK at 2.4 kHz ($n=8$).

Subject	1.2 kHz	1.8 kHz	2.4 kHz
BEN	123 (s.d. 1.6)	120 (s.d. 1.6)	119 (s.d.1.2)
NEM	122 (s.d. 1.6)	116 (s.d. 2.2)	117 (s.d.1.8)
MUK	121 (s.d. 2.6)	119 (s.d. 2.7)	123 (s.d.0.73)

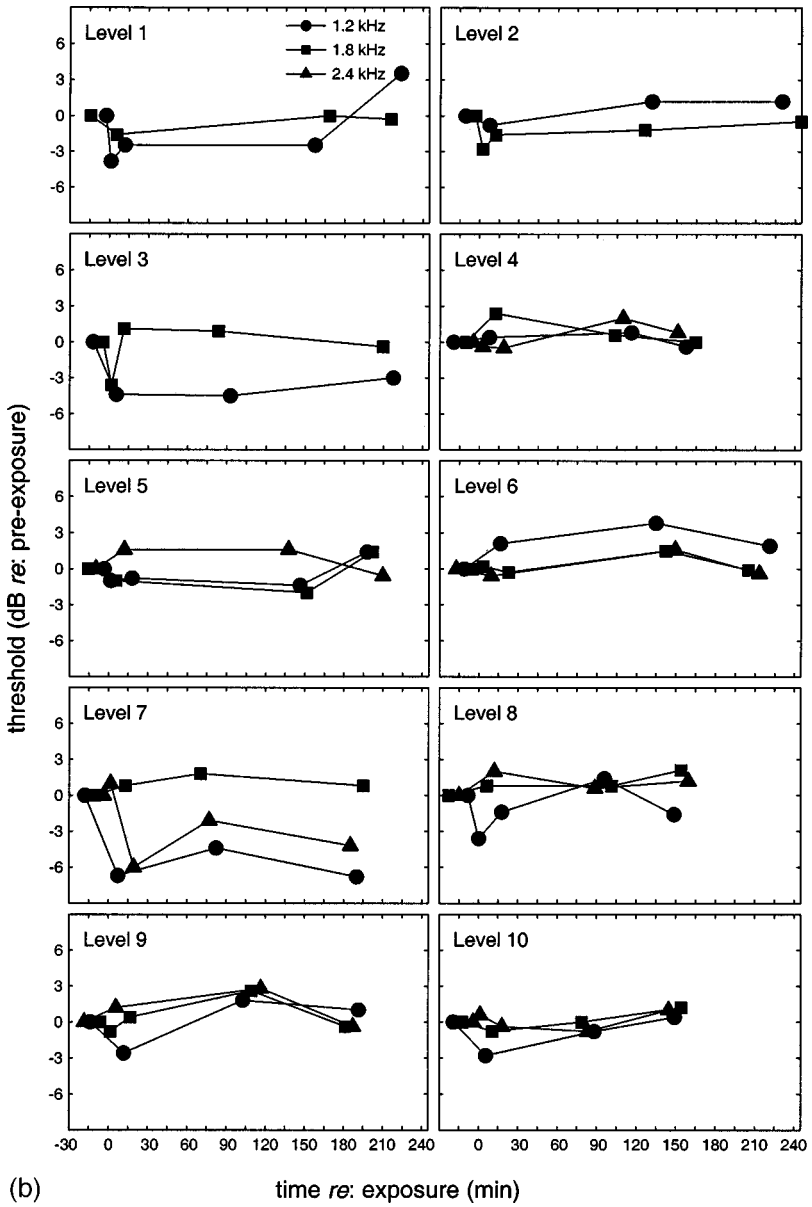

FIG. 3. (*Continued.*)

pre-exposure thresholds measured during the 4-month period of this study and that there were no PTSs produced from any cumulative effects of the exposures.

Figure 3 shows the pre-exposure, postexposure, and recovery thresholds measured for subjects (a) BEN, (b) NEM, and (c) MUK for each of the ten impulse levels. The abscissa is time relative to the time of the impulse; the time for each threshold measurement was defined as the mean time between the first and last S2 tone presentations at that frequency. The ordinate is the measured threshold, expressed in dB relative to the pre-exposure threshold for that frequency measured that day. The circles, squares, and triangles represent the thresholds measured at 1.2, 1.8, and 2.4 kHz, respectively. Thresholds at negative times (i.e., before the impulse) correspond to pre-exposure thresholds and have normalized amplitudes of 0 dB. The cluster of thresholds just after time zero are postexposure thresholds. The first and second recovery thresholds are visible as two separate data clusters at approximately 60–90 min and 120–240 min, respectively, after the impulse. Technical difficulties prevented recovery thresholds from being measured for MUK at level 1.

For the ten impulse levels, there were no substantial MTTSs (i.e., 6-dB or larger increases) in any of the subjects tested. The majority of the postexposure and recovery thresholds (264/280, 94.3%) was within 4 dB of the pre-exposure values. There were some (9/280, 3.2%) small (4–5.6 dB), yet statistically significant, threshold increases [e.g., the dolphin BEN at level 9 (5.6 dB at 1.8 kHz, $t=8.73$, $p<0.01$; 4.4 dB at 2.4 kHz, $t=4.64$, $p<0.01$) and the whale MUK at level 10 (4.0 dB at 2.4 kHz, $t=5.61$, $p<0.01$)], which may suggest that the impulses were approaching levels sufficient to induce an MTTS according to our 6-dB criterion. For the dolphin BEN, these small threshold increases all occurred during the first recovery sessions; five out of six of the (4–5.6-dB) threshold shifts observed in the whale MUK occurred during the second recovery sessions. It is difficult to state whether these small shifts seen during recovery sessions (approximately 180 min postexposure) were caused by exposure to the impulses or were behavioral artifacts caused by subject

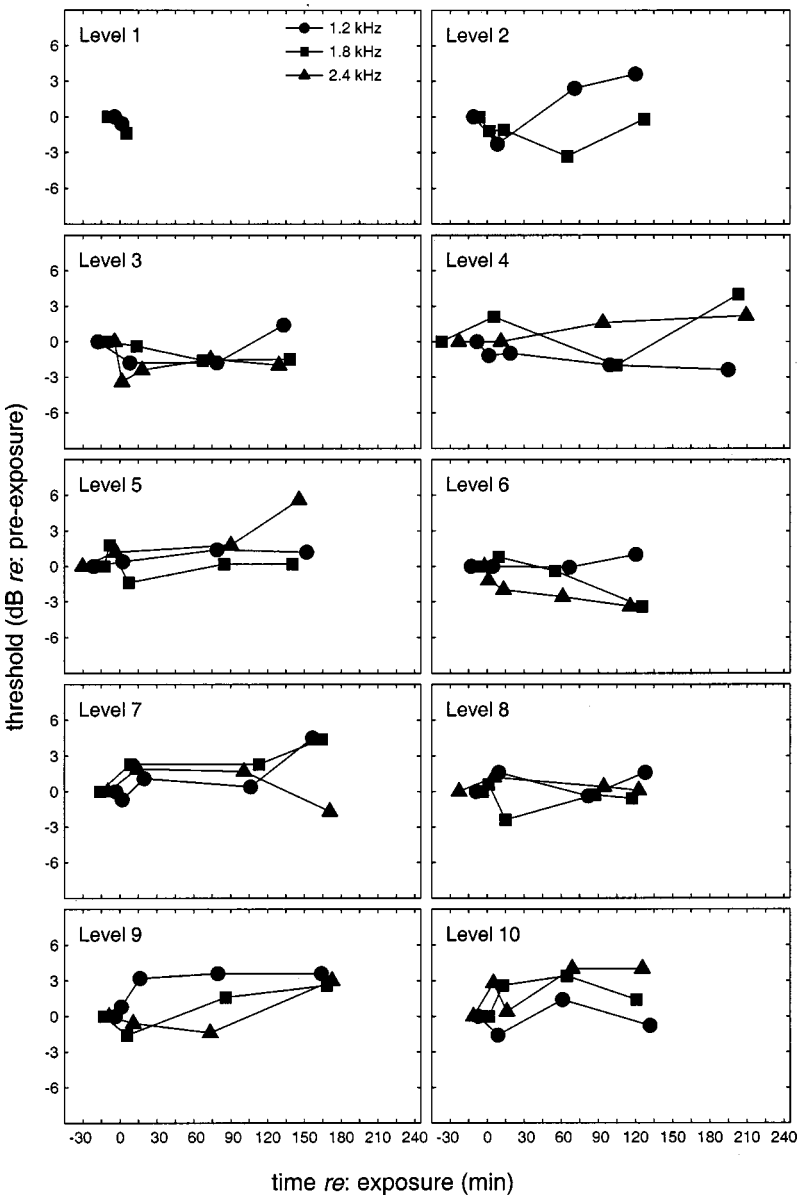

FIG. 3. (*Continued*.)

fatigue, or declining food motivation coincident with testing later in the day.

In some cases (7/280, 2.5%), thresholds decreased following exposure [e.g., BEN at level 7 (−3.9 at 1.2 kHz)]. It has been suggested that hypersensitivity such as this may occur at levels approaching those sufficient to induce a TTS (Silbiger, 1965; Hodge and McCommons, 1966; Schlundt *et al.*, 2000). If negative TTSs are real and occur at levels preceding actual TTS, they may provide some predictive effect.

Figure 4 presents the rT_1 values for subjects (a) BEN, (b) NEM, and (c) MUK for each frequency at each of the ten levels. These data are presented in a manner analogous to Fig. 3 (i.e., each symbol in Fig. 4 corresponds to a hearing threshold in Fig. 3) and may be used to determine if any changes in the subjects' response bias occurred. For example, the dolphin NEM at level 7, 1.2 kHz had significantly lower postexposure, first recovery, and second recovery thresholds (−6.7, −4.4, −6.8 dB, respectively); however, these were accompanied by an rT_1 increase from 0.023 (pre-exposure) to 0.096, 0.059, and 0.052 for postexposure, first recovery, and second recovery thresholds, respectively.

Figure 5 presents histograms of the rT_1 values (pooled regardless of frequency or impulse level) for (a) BEN, (b) NEM, and (c) MUK. Using Fig. 5, the subjects' response criteria were categorized according to rT_1:$rT_1 \leqslant 0.01$ was considered conservative, $0.01 < rT_1 \leqslant 0.05$ was considered moderate, and $rT_1 > 0.05$ was considered liberal. The beluga whale MUK was generally conservative and rarely committed false alarms; the dolphins were more liberal, but still in the range of conservative to moderate. A multiple regression analysis with dummy coding (Pedhazur, 1982) was used to compare postexposure and recovery rT_1 values to those obtained during pre-exposure sessions. The results of the regression were significant for the dolphins NEM ($F_{3,115} = 4.14$, $p < 0.01$) and BEN ($F_{3,126} = 2.94$, $p < 0.05$). For NEM, there was a statistically significant increase in postexposure rT_1 values compared to pre-exposure values ($t = 2.50$, $p < 0.05$). The mean values for rT_1 were 0.020 and 0.037 for pre- and postexposure sessions, respectively. A

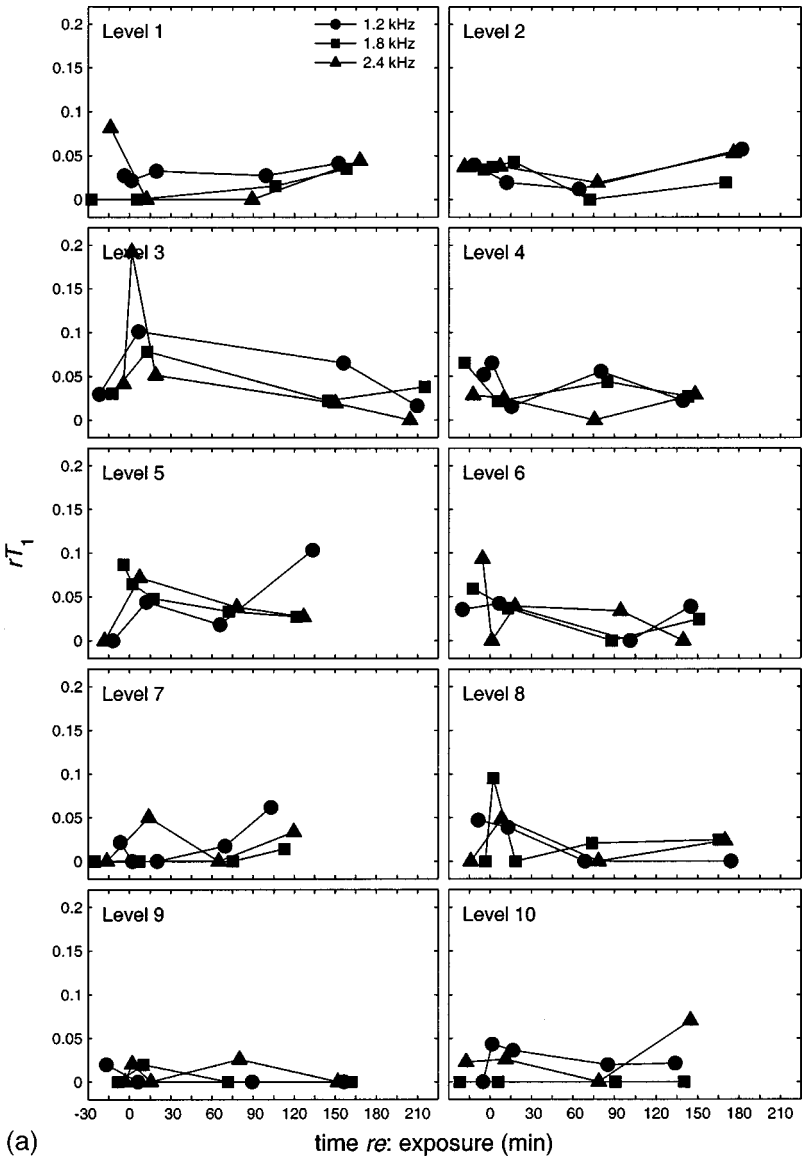

FIG. 4. Values of rT_1 measured during pre-exposure, postexposure, and recovery sessions for subjects (a) BEN, (b) NEM, (c) MUK, plotted as functions of the time relative to exposure, for each of the ten impulse levels.

similar increase in false-alarm rates was also observed in pinnipeds by Kastak *et al.* (1999). For the subject BEN, the mean values for rT_1 were 0.027 and 0.016 for the pre-exposure and the first recovery sessions, respectively; however, this difference was not significant. No significant differences in rT_1 were found for the beluga whale MUK between pre-exposure and the postexposure and recovery sessions.

As in previous studies of TTS in marine mammals (Ridgway *et al.*, 1997; Kastak *et al.*, 1999; Schlundt *et al.*, 2000), the animals began to exhibit alterations in their trained behaviors as the intensity of the fatiguing stimulus increased. These behaviors included remaining on the S1 station after being presented with an impulse until a second S1 tone was presented (i.e., not recognizing the S1 tone as the start signal), swimming around the enclosure before proceeding to the S2 station, refusing to return to the S1 station on subsequent dives (in which case the subject was cued directly to the S2 station for hearing tests), and vocalizing after exposure to the impulse. Behavioral alterations began at levels 4 (5 kg at 9.3 km) and 7 (5 kg at 1.5 km) for the dolphins NEM and BEN, respectively, and at level 9 (500 kg at 1.9 km) for the whale MUK. Behavioral alterations continued for each animal at the higher test levels as well; however, the impulses were presented in increasing intensity from level 1 to level 10; thus, this pattern could have been an order effect. As noted by Schlundt *et al.* (2000), the beluga whale MUK appeared to be more tolerant of intense sounds than were either of the dolphins.

III. DISCUSSION

This study used a modified version of the MFR where the ISI was randomized between 5–8 s and was not open-ended. The minimum ISI was limited by the time required to digitize and write to disk the acoustic pressure measured during each hit interval (the S2 tone as well as the subject's whistle response, if present). The maximum ISI was restricted to 8 s to insure that thresholds could be collected quickly. The modified MFR used in this study allowed behavioral thresholds to be measured very quickly (see Fig. 3) following exposure to the impulse; the first threshold esti-

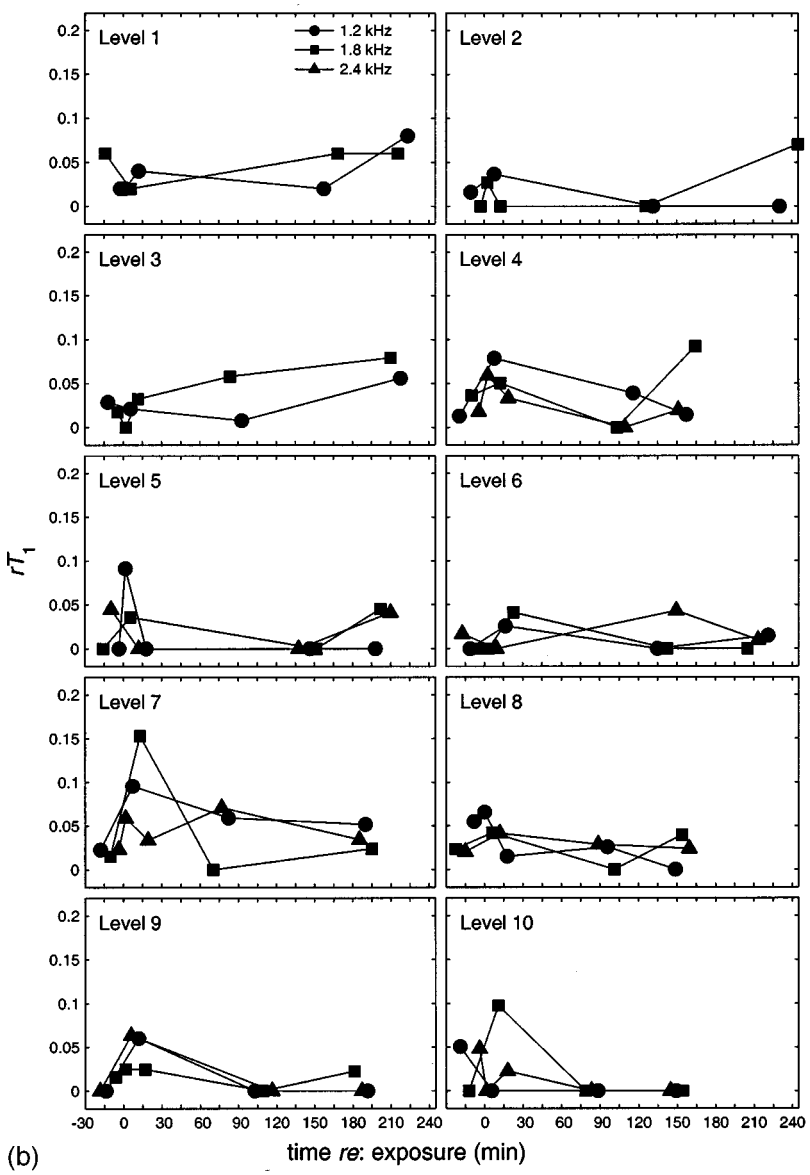

FIG. 4. (*Continued.*)

mate, based on ten reversals, was normally obtained within 2–3 min. A high level of computer control also allowed the precise times of the S1 start signals and S2 tones to be recorded.

Although no 6-dB or larger MTTSs were actually observed, the results of this study are still valuable because they are the first direct measurements of the effects of distant signatures of underwater explosions on the hearing abilities of odontocetes. There are some indications that the maximum impulse levels obtained may have been approaching those sufficient to induce MTTS. These include apparent hypersensitivity in some cases as well as some smaller (4–5.6 dB), yet statistically significant increases in threshold measured in recovery sessions.

A. Impulsive stimuli

The time waveforms and 1/3-octave energy spectra of the synthesized impulses were in close agreement with those predicted using the REFMS numerical modeling program, with the exception of the frequency range below 1 kHz, where the ES could not produce sufficient pressure to match the predicted waveforms. It is important to note the differences between these waveforms (and distant signatures of underwater explosions in general) compared to near-blast pressure signatures which are dominated by a single shock wave with a very large peak pressure and very fast rise time. Most studies of the auditory effects of impulsive sounds in terrestrial mammals have dealt with subjects exposed to aerial gunfire or similar sounds at relatively close range. These sources *do* produce pressure signatures consisting of a single high-peak pressure with a rapid rise time, followed by smaller oscillations, similar to the Friedlander wave with a finite rise time (Hamernik and Hsueh, 1991). The differences between these aerial waveforms and those found at even modest ranges from an underwater source must be considered when extrapolating data from impulsive tests on terrestrial mammals to predict the effects of underwater impulsive sounds on marine mammals, unless the mammals are very close to the source, in which case a TTS would be of minor importance compared to near-blast trauma.

As stated previously, the ES could not produce sufficient

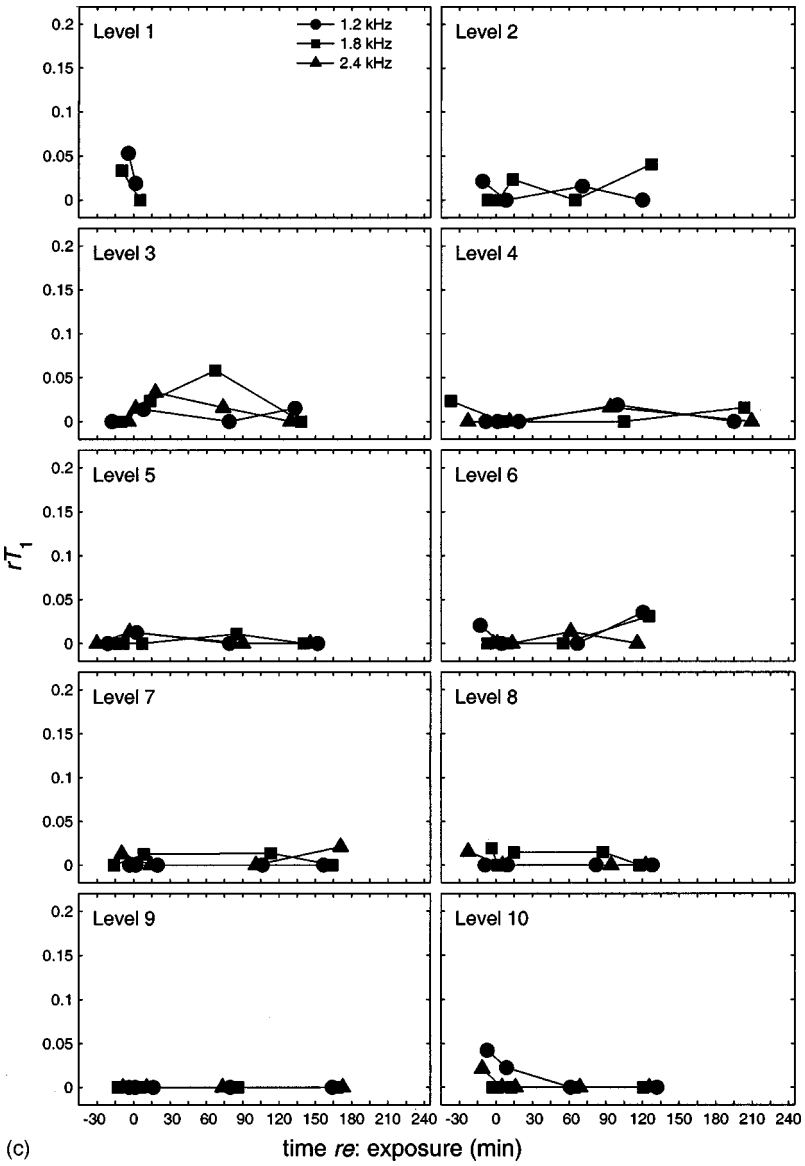

FIG. 4. (*Continued.*)

pressures at frequencies below 1 kHz to match the REFMS predictions. The effects of the pressure signature low-frequency energy deficit is uncertain. Distant signatures from actual explosions would be expected to contain more energy at frequencies below 1 kHz and as a result more total energy as well. *Tursiops* and *Delphinapterus* have relatively poor hearing sensitivity at frequencies below 1 kHz; however, it is not certain if the effects of low-frequency sound are reduced as a result. Some PTS studies in terrestrial mammals suggest that the effects of lower-frequency sounds are mitigated by properties of the outer and middle ear and that the higher frequencies cause the bulk of the damage (e.g., Price, 1974); however, these data are based on exposure to stimuli that create large amounts of PTS and it is not clear whether the odontocete middle ear or other adaptations are suited to perform a similar function underwater. It is clear that caution should be exercised in the interpretation of the results of the current study; those extrapolating these data to other impulsive waveforms must keep in mind that the results presented here are valid only for comparable waveforms and may have been influenced by the relative lack of low-frequency energy.

B. Masking-noise effects

Studies of TTS in humans (Parker *et al.*, 1976; Humes, 1980) have shown that the presence of masking noise results in elevated hearing thresholds (effectively simulating a pre-exposure loss in hearing sensitivity) and decreases the amount of TTS observed. Ades *et al.* (1974) also observed smaller amounts of PTS in chinchillas when thresholds were measured in the presence of masking noise compared to those PTSs observed when thresholds were measured in quiet. There are currently no conclusive data for the relationship between masking noise and TTS in odontocetes. We employed masking noise out of necessity because the test site (San Diego Bay) had a relatively high (and variable) ambient noise level. The masking noise employed was at the lowest level (above ambient) at which we could maintain uniform frequency content between 0.8 and 3 kHz. Subjects' pre-exposure hearing thresholds (Table III) were approximately 20 dB above published absolute thresholds for *Tursiops* and *Delphinapterus*; thus, we must acknowledge the possibility that larger TSs may have been observed without the

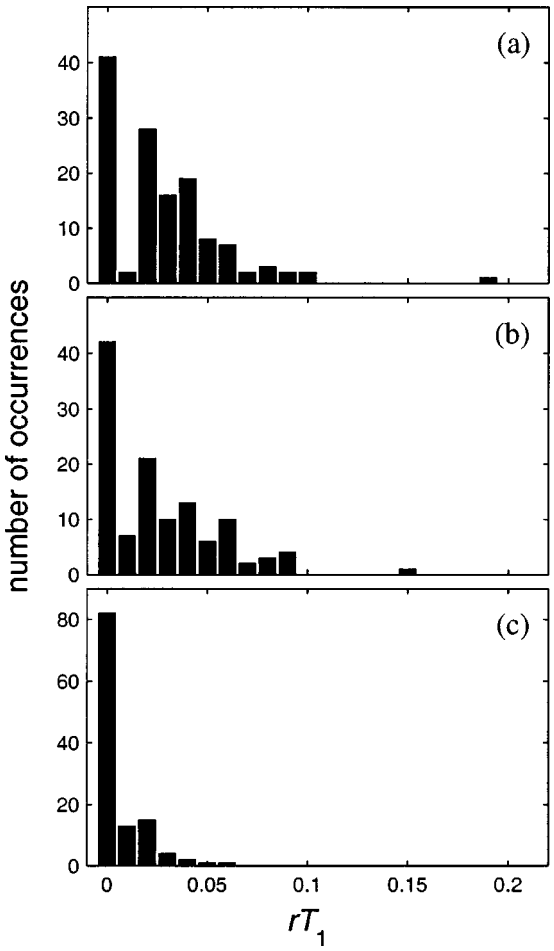

FIG. 5. Histograms of the pooled rT_1 values for subjects (a) BEN, (b) NEM, and (c) MUK.

masking noise. Humes (1990) presented data for humans showing that exposure to broadband masking noise sufficient to raise pre-exposure thresholds 20 dB resulted in TTSs that were approximately 5 dB lower than those obtained without masking noise.

C. Damage risk criteria

The long-term goal of projects such as the current study is the identification of underwater sound parameters that affect hearing loss in marine mammals and the establishment of effective damage risk criteria (DRC) for these animals. At relatively low pressure and sufficiently long exposure duration, the total acoustic energy determines the amount and type of TS; DRC for impulsive sounds are often modified to take into account the peak pressure and/or rise time because impulses may have a very high peak pressure and yet low energy if the duration is very short (Glorig, 1988). One of the chief difficulties lies in establishing where along a continuum of exposure regimes, from relatively long exposure to steady-state signals to brief exposure to a single shock wave, a particular exposure condition (i.e., pressure waveform and duration) exists.

Figure 6 compares the data from the present study to the marine mammal TTS studies of Schlundt *et al.* (2000), Au *et al.* (1999), and Kastak *et al.* (1999). Schlundt *et al.* (2000) measured MTTS (6-dB or larger shifts) in dolphins and beluga whales exposed to 1-s pure tones at frequencies between 3 and 75 kHz (no MTTS was observed at 0.4 kHz at the highest level obtained). Au *et al.* (1999) observed 12–18-dB TTSs in a bottlenose dolphin exposed to 50 min of octave-band noise centered at 7.5 kHz. Kastak *et al.* (1999) measured mean TTSs of 4.6–4.9 dB in pinnipeds exposed to bandlimited noise with center frequencies between 100 and 2000 Hz and a bandwidth of one octave. Figure 6(a) plots the peak SPL versus the fatiguing stimulus duration from each study. The rectangles represent TTS-inducing stimulus levels from Schlundt *et al.* (2000) (3–20 kHz only), Au *et al.* (1999), and Kastak *et al.* (1999). Peak SPL values from Kastak *et al.* (1999) and Au *et al.* (1999) were approximated as the octave band (rms) level +3 dB. The open circles represent the data from the current study. Figure 6(a) also includes lines with slopes of 3-dB (solid line) and 5-dB (dashed line) per doubling of time fit to the mean values of the fatiguing stimuli used by Schlundt *et al.* (2000) and Au *et al.* (1999). The 3-dB per doubling of time slope, also called a 3-dB exchange rate (NIOSH, 1998), is equivalent to an equal energy criterion for relating SPL and permissible exposure duration (for continuous-type sounds). The 5-dB exchange rate was originally proposed to account for interruptions in the noise exposure that frequently occur during the workday (NIOSH, 1998). NIOSH previously endorsed the 5-dB exchange rate but has recently proposed the more conservative 3-dB exchange rate; however, at this time OSHA still uses the 5-dB exchange rate (OSHA, 1995; NIOSH, 1998). These exchange rates were developed for relatively long exposures and/or multiple impulses; however, NIOSH (as well as the ISO) currently recommends calculating exposure levels by integrating both impulsive and continuous-type noise over the duration of the measurement and applying the equal-energy criterion (NIOSH, 1998).

To a first approximation, exposure characteristics (i.e., peak SPL and duration) within the upper right of Fig. 6(a) are likely to produce a TS in pinnipeds and odontocetes, while those in the lower left are not likely to produce a TS. Figure 6(a) suggests that the impulses used in this study, because they model distant explosion signatures and include the effects of multipath propagation and refraction, are fairly close in their effects to the continuous signals used in the other two studies; that is, these signatures do not appear to have short-enough rise times and/or high-enough peak pressures to produce TTSs at energy levels below those of the longer duration, steady-state sounds used by Schlundt *et al.* (2000), Au *et al.* (1999), and Kastak *et al.* (1999). Figure 6(a) also suggests that for odontocetes exposed to these particular stimuli, the 3-dB exchange rate may be a more appropriate predictor than the 5-dB exchange rate.

Figure 6(b) shows the total energy flux for the fatiguing stimuli in each study plotted versus the stimulus duration. Again, the rectangles represent stimulus levels from Schlundt *et al.* (2000) (3–20 kHz only), Au *et al.* (1999), and Kastak *et al.* (1999); the open symbols represent the data from the current study. Total energy fluxes for the stimuli used by Schlundt *et al.* (2000) and Kastak *et al.* (1999) were estimated using

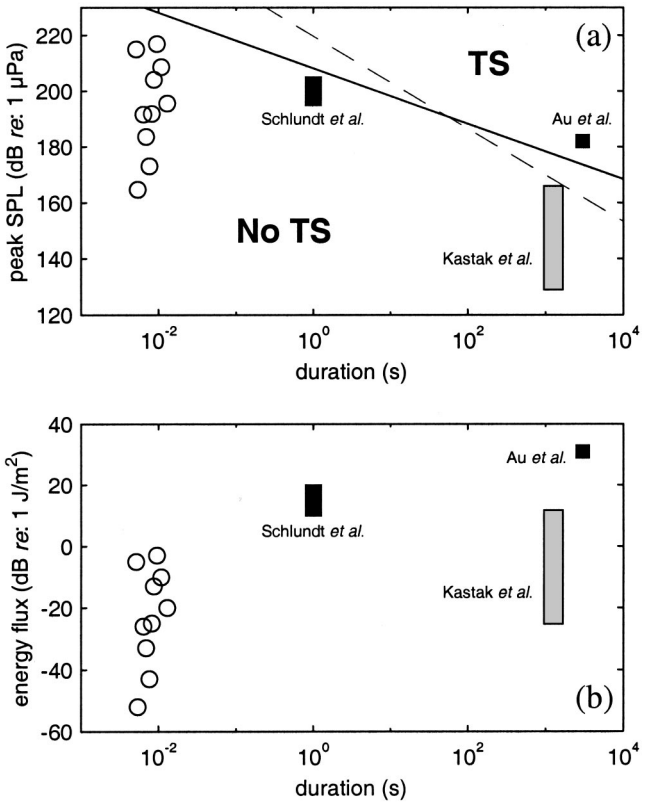

FIG. 6. Existing underwater TTS data for marine mammals plotted as (a) peak SPL versus fatiguing stimulus duration and (b) total energy flux versus duration. Open circles: present study; dashed line: 5-dB exchange rate; solid line: 3-dB exchange rate.

$$U_T = \mathrm{SPL}_{\mathrm{rms}} + 10\log_{10}\tau - 182, \tag{5}$$

where U_T has units of dB re:1 J/m^2, $\mathrm{SPL}_{\mathrm{rms}}$ is the (octave band) rms SPL (dB re:1 μPa), and τ is the exposure duration (s). The factor of 182 dB was used to convert from dB re:1 μPa^2 s to dB re:1 J/m^2, assuming seawater with nominal values of $\rho = 1026$ kg/m^3 and $c = 1500$ m/s.

Figure 6 is presented here as an attempt to demonstrate how, given enough data, similar graphic aids could potentially be constructed to aid those establishing safe exposure guidelines for anthropogenic sources of underwater sound. Plots such as Fig. 6 may also be used to guide future studies of marine mammal TTS in the choice of fatiguing stimuli. Additional data using different combinations of peak SPL, energy flux, duration, and number of exposures may enable crude relationships to be established as a foundation for the establishment of a DRC for marine mammals.

A final note is in order regarding the difficulty experienced in this study (also see Ridgway *et al.*, 1997; Schlundt *et al.*, 2000) in generating sufficiently intense sounds to actually cause a reliable TTS in the dolphins and beluga whale(s) studied. Although the presence of masking noise may have reduced the TTSs observed in these studies, the extremely high pressures required imply a large dynamic range and high resilience for the odontocete auditory system. These factors make TTS studies employing impulsive waveforms resembling distant explosion signatures very challenging—it is difficult to generate sufficient source levels to produce a threshold shift in odontocetes using very short duration sounds without resorting to actual impulsive sources located fairly close to the test subject.

IV. CONCLUSIONS

A behavioral response paradigm was used to measure masked underwater hearing thresholds in two bottlenose dolphins and one beluga whale before and after exposure to impulsive underwater sounds with waveforms resembling distant signatures of underwater explosions. An array of piezoelectric transducers was used to generate impulsive sounds with waveforms approximating those predicted from HBX-1 charges of weight 5 or 500 kg at ranges from 1.5 to 55.6 km. At the conclusion of the study, no MTTS, defined as a 6-dB or larger increase in threshold over pre-exposure levels, had been observed; however, alterations in the animals' trained behavior began to occur at levels 4 (5 kg at 9.3 km) and 7 (5 kg at 1.5 km) for the dolphins and at level 9 (500 kg at 1.9 km) for the beluga whale. These data are the first information on the effects of distant underwater explosion signatures on the hearing abilities of odontocetes.

ACKNOWLEDGMENTS

The explosion simulator was developed and maintained by Joseph Clark, Jane Young, and Joel Gaspin. Tricia Kamolnick, Jennifer Carr, Randy Dear, Scott Peluso, Josh Rosenberg, Mark Todd, and Michelle Reddy provided animal training and/or other technical assistance. Software for computer control of stimuli and recording of animal responses was developed by Wesley Elsberry. Software for computer recognition of the animal whistle responses was developed by Diane Blackwood. We thank Robert Gisiner, Frank Stone, Tim McBride, and Paul Towner, as well as Uwe Vogel, Ursula Siebert, Klaus Lucke, and their German colleagues for encouragement. We also thank John Sigurdson for helpful comments. Funding was provided by the Office of Naval Research. James Finneran was supported by a National Research Council Research Associateship.

Au, W. W. L., Nachtigall, P. E., and Pawloski, J. L. (**1999**). ''Temporary threshold shift in hearing induced by an octave band of continuous noise in the bottlenose dolphin,'' J. Acoust. Soc. Am. **106**, 2251(A).

Ades, H. W., Trahiotis, C., Kokko-Cunningham, A., and Averbuch, A. (**1974**). ''Comparison of hearing thresholds and morphological changes in the chinchilla after exposure to 4 kHz tones,'' Acta Oto-Laryngol. **78**, 192–206.

Ahroon, W. A., Hamernik, R. P., and Lei, S.-F. (**1996**). ''The effects of reverberant blast waves on the auditory system,'' J. Acoust. Soc. Am. **100**, 2247–2257.

Awbrey, F. T., Thomas, J. A., and Kastelein, R. A. (**1988**). ''Low-frequency underwater hearing sensitivity in belugas, *Delphinapterus leucas*,'' J. Acoust. Soc. Am. **84**, 2273–2275.

Britt, J. R. (**1987**). ''Shock wave reflection and refraction in multi-layered ocean/ocean bottoms with shear wave effects. A user's manual for the REFMS code,'' NSWC TR 87-312, Naval Surface Warfare Center, November 1987.

Britt, J. R., Eubanks, R. J., and Lumsden, M. G. (**1991**). *Underwater Shock Wave Reflection and Refraction in Deep and Shallow Water: Volume I—A User's Manual for the* REFMS *Code (Version 4.0)* (Science Applications International Corporation, St. Joseph, LA).

Brodie, P. F. (**1989**). ''The white whale *Delphinapterus leucas* (Pallas, 1776),'' in *Handbook of Marine Mammals: River Dolphins and the Larger Toothed Whales*, edited by S. H. Ridgway and R. Harrison (Academic, London), Vol. 4, pp. 119–144.
Clark, J. A., Young, J. A., and Gaspin, J. B. (**1999**). ''Validation of a system for synthesizing distant signatures of underwater explosions for sea mammal hearing studies,'' Proceedings of the Joint EAA/ASA meeting, Berlin, Germany, 14–19 March 1999.
Cornsweet, T. N. (**1962**). ''The staircase method in psychophysics,'' Am. J. Psychol. **75**, 485–491.
Egan, J. P., Greenberg, G. Z., and Schulman, A. I. (**1961**). ''Operating characteristics, signal detectability, and the method of free response,'' J. Acoust. Soc. Am. **33**, 993–1007.
Fay, R. R. (**1988**). *Hearing in Vertebrates: A Psychophysics Databook* (Hill-Fay, Winnetka, IL).
Finneran, J. J., Carder, D. A., Ridgway, S. H., and Schlundt, C. E. (**1999**). ''Technique for the generation and frequency compensation of bandlimited white noise and its application in studies of masked hearing thresholds,'' J. Acoust. Soc. Am. **106**, 2130(A).
Fricke, J. R., Davis, J. M., and Reed, D. H. (**1985**). ''A standard quantitative calibration procedure for marine seismic sources,'' Geophysics **50**, 1525–1532.
Glorig, A. (**1988**). ''Damage-risk criteria for hearing,'' in *Noise and Vibration Control*, edited by L. L. Beranek (INCE, Washington, DC), pp. 537–553.
Hamernik, R. P., and Hsueh, K. D. (**1991**). ''Impulse noise: Some definitions, physical acoustics and other considerations,'' J. Acoust. Soc. Am. **90**, 189–196.
Hodge, D. C., and McCommons, R. B. (**1966**). ''Reliability of TTS from impulse-noise exposure,'' J. Acoust. Soc. Am. **40**, 839–846.
Humes, L. E. (**1980**). ''Temporary threshold shift for masked pure tones,'' Audiology **19**, 335–345.
Johnson, C. S. (**1967**). ''Sound detection thresholds in marine mammals,'' in *Marine Bio-Acoustics*, edited by W. N. Tavolga (Pergamon, New York), Vol. 2, pp. 247–260.
Johnson, C. S., McManus, M. W., and Skaar, D. (**1989**). ''Masked tonal hearing thresholds in the beluga whale,'' J. Acoust. Soc. Am. **85**, 2651–2654.
Johnston, R. C., Reed, D. H., and Desler, J. F. (**1988**). ''Special report of the SEG technical standards committee, SEG standards for specifying marine seismic energy sources,'' Geophysics **53**, 566–575.
Kastak, D., Schusterman, R. J., Southall, B. L., and Reichmuth, C. J. (**1999**). ''Underwater temporary threshold shift induced by octave-band noise in three species of pinniped,'' J. Acoust. Soc. Am. **106**, 1142–1148.
Ljungblad, D. K., Scoggins, P. D., and Gilmartin, W. G. (**1982**). ''Auditory thresholds of a captive Eastern Pacific bottle-nosed dolphin, *Tursiops* spp.,'' J. Acoust. Soc. Am. **72**, 1726–1729.
Miller, H. (**1969**). ''The FROC curve: a representation of the observer's performance for the method of free response,'' J. Acoust. Soc. Am. **46**, 1473–1476.
NIOSH (**1998**). *Criteria for a Recommended Standard: Occupational Noise Exposure, Revised Criteria 1998*, DHHS (NIOSH) Publication No. 98–126 (NIOSH, Cincinnati, OH).
OSHA (**1996**). ''Occupational Noise Exposure,'' in OSHA Safety and Health Standards 29 CFR 1910.95, Fed. Regist. 61, 9227, 7 March 1996.
Parker, D. E., Tubbs, R. L., Johnston, P. A., and Johnston, L. S. (**1976**). ''Influence of auditory fatigue on masked pure-tone thresholds,'' J. Acoust. Soc. Am. **60**, 881–885.
Pedhazur, E. J. (**1982**). *Multiple Regression in Behavioral Research*, 2nd ed. (Harcourt Brace Jovanovich, Fort Worth, TX), pp. 271–333.
Price, G. R. (**1974**). ''Upper limit to stapes displacement: Implications for hearing loss,'' J. Acoust. Soc. Am. **56**, 195–197.
Richardson, W. J., Greene, Jr., C. R., Malme, C. I., and Thomson, D. H. (**1995**). *Marine Mammals and Noise* (Academic, San Diego).
Ridgway, S. H., and Carder, D. A. (**1997**). ''Hearing deficits measured in some *Tursiops truncatus*, and discovery of a deaf/mute dolphin,'' J. Acoust. Soc. Am. **101**, 590–594.
Ridgway, S. H., Carder, D. A., Smith, R. R., Kamolnick, T., Schlundt, C. E., and Elsberry, W. R. (**1997**). ''Behavioral responses and temporary shift in masked hearing thresholds of bottlenose dolphins, *Tursiops truncatus*, to 1-second tones of 141–201 dB re 1 μPa,'' Technical Report 1751, Naval Command, Control, and Ocean Surveillance Center, RDT&E Division, San Diego.
Ridgway, S. H. (**1997**). ''Who are the whales?'' Bioacoustics **8**, 3–20.
Rosenberger, P. B. (**1970**). ''Response-adjusting stimulus intensity,'' in *Animal Psychophysics: The Design and Conduct of Sensory Experiments*, edited by W. C. Stebbins (Appleton-Century-Crofts, New York), pp. 161–184.
Schlundt, C. E., Finneran, J. J., Carder, D. A., and Ridgway, S. H. (**2000**). ''Temporary shift in masked hearing thresholds (MTTS) of bottlenose dolphins, *Tursiops truncatus*, and white whales, *Delphinapterus leucas*, after exposure to intense tones,'' J. Acoust. Soc. Am. **107**, 3496–3508.
Schusterman, R. J. (**1980**). ''Behavioral methodology in echolocation by marine mammals,'' in *Animal Sonar Systems*, edited by R. G. Busnel and J. F. Fish (Plenum, New York), pp. 11–41.
Silbiger, H. R. (**1965**). ''Temporary threshold shifts due to single clicks,'' J. Acoust. Soc. Am. **38**, 937–938.
Urick, R. J. (**1967**). *Principles of Underwater Sound for Engineers* (McGraw-Hill, New York).
Wells, R. S., and Scott, M. D. (**1998**). ''Bottlenose dolphin *Tursiops truncatus*'' (Montagu, 1821) in *Handbook of Marine Mammals: The Second Book of Dolphins and the Porpoises*, edited by S. H. Ridgway and R. J. Harrison (Academic, London), Vol. 6, pp. 137–182.
Weston, D. E. (**1960**). ''Underwater explosions as acoustic sources,'' Proc. Phys. Soc. London **LXXVI**, 233–249.
White, Jr., M. J., Norris, J., Ljungblad, D., Baron, K., and di Sciara, G. (**1978**). ''Auditory thresholds of two beluga whales (*Delphinapterus leucas*),'' Hubbs/Sea World Research Institute Tech. Rep. 78–108.
Yost, W. A. (**1994**). *Fundamentals of Hearing*, 3rd ed. (Academic, San Diego).

Modeling of high-intensity focused ultrasound-induced lesions in the presence of cavitation bubbles

F. Chavrier and J. Y. Chapelon[a)]
INSERM Unité 281, 151 Cours Albert Thomas, 69424 Lyon Cedex 03, France

A. Gelet
Edouard Herriot Hospital, Urology Department, Lyon, France

D. Cathignol
INSERM Unité 281, 151 Cours Albert Thomas, 69424 Lyon Cedex 03, France

(Received 8 November 1999; accepted for publication 27 March 2000)

The classical ''Bio Heat Transfer Equation (BHTE)'' model is adapted to take into account the effects of oscillating microbubbles that occur naturally in the tissue during high-intensity focused ultrasound (HIFU) treatment. First, the Gilmore–Akulichev model is used to quantify the acoustic pressure scattered by microbubbles submitted to HIFU. Because this scattered pressure is not monochromatic, the concept of harmonic attenuation is introduced and a global attenuation coefficient is estimated for bubble-filled tissues. The first results show that this global attenuation coefficient varies significantly with respect to several parameters such as the frequency and the density of microbubbles in the medium, but also with respect to the incident acoustic pressure which thus becomes a transcendental function. Under these conditions, a layer-by-layer modeling, in the direction of propagation, is proposed to calculate the ultrasonic beam. Finally, the BHTE is solved and the HIFU-induced lesions are estimated by the calculation of the thermal dose. Using this model, it can be observed first that, when the firing power increases, the lesion develops clearly in the direction of the transducer, with a shape agreeing with *in vivo* experimentation. Next, it is observed that the lesion can be significantly modified in size and position, if an interface (skin or inner wall) is simulated as a zone with multiple cavitation nuclei. With a firing power increase, it is also shown how a secondary lesion can appear at the interface and how, beyond a certain threshold, this lesion develops at the main lesion expense. Finally, a better in-depth homogeneity of lesions is observed when the acoustic frequency of HIFU is increased. [S0001-4966(00)01307-2]

PACS numbers: 43.80.Sh, 43.80.Gx, 43.25.Yw [FD]

INTRODUCTION

In the context of a project where high-intensity focused ultrasound (HIFU) is used in the ablation of prostatic cancer tissue,[1,2] the question of exactly where and how the lesions develop in tissue was considered. In order to reduce the number of *in vivo* experiments, a model was designed to predict the shape and the position of HIFU-induced lesions. The use of HIFU for the noninvasive ablation of cancerous tissue is the subject of many research studies and has already found its way into clinical applications.[1–8] However, the mechanism of lesion growth remains poorly understood. Indeed, the currently available experimental results show that neither the shape nor the position of the lesions obeys some purely thermal process. Several hypotheses have been put forward to explain these results. First, the variation of the attenuation coefficient with temperature[9] and/or structural modification during necrosis[10] has been introduced in a lesion modeling. Unfortunately, these corrections are insufficient to support the experimental results. Another hypothesis has been proposed by Le Floch *et al.*,[11] who developed a model based on sound velocity variation in heated areas that act as thermal lenses for the ultrasonic beam. Although this model is very interesting regarding lesion distortion, it is not adapted to reveal secondary effects such as alteration of lesions by skin or tissue interfaces. The same remark can be made concerning the work presented by Wojcik *et al.*,[12] who proposed a model taking into account the nonlinear propagation and the presence of a reflecting bubble at the focus. In addition, Watkin *et al.*[13] demonstrated that nonlinear effects are only of minor importance at the intensity level used in HIFU and that, above all, they do not account for the ''tadpole-shaped'' lesions. In the same paper,[13] these authors then discussed the hypothesis that bubble formation increases attenuation, through acoustic cavitation and/or tissue boiling. Several reasons make us believe that we should go in this direction. Indeed, the presence of cavitation bubbles is confirmed by the analysis of post-treatment ultrasound images,[14,15] which show a hyperechoic pattern in the prefocal area. Furthermore, increased heating efficiency in the presence of a contrast agent such as Albunex® was observed in hyperthermia.[16] In the same way, Wu[17] studied the temperature increase of cardiac tissue when diagnostic ultrasound is used in the presence of Albunex®. He showed that micro-

a)Electronic mail: chapelon@lyon151.inserm.fr

spheres, exposed to an acoustic beam, alter the absorption of the medium by emitting harmonic and subharmonic components of the fundamental frequency.

Given these findings, the problem of modeling HIFU lesions, when microbubbles are present in the targeted tissue, was reconsidered. In Sec. I of the paper, the theoretical aspects are discussed. Starting from the classical Bio Heat Transfer Equation (BHTE),[18] the volumetric heat rate generated by the HIFU is estimated when oscillating microbubbles are present in tissues. For this, the behavior of these microbubbles is studied, especially by quantifying the time and spectral components of the scattered pressure. Then, by using a concept close to the harmonic absorption of finite amplitude ultrasound in tissues, defined by Carstensen *et al.*,[19] a global attenuation coefficient for bubble-filled tissues is evaluated. The interdependence of the acoustic pressure and the global attenuation coefficient led us to reconsider the modeling of the acoustic beam according to an approach close to that proposed by Tavakkoli *et al.*[20] In this approach, the attenuated field is calculated layer by layer in the direction of propagation. Finally, the BHTE is solved and the thermal dose corresponding to the temperature increases is estimated. In Sec. II, it is first shown how the global attenuation coefficient varies according to the acoustic pressure, the density of the microbubbles, and the frequency. Then, the modeling is applied to simulate HIFU-induced lesions for different shot conditions and with different bubble distributions. Section III includes discussions of the model limitations and of the potential of this new tool to explain typical lesion shapes observed in practice.

I. THEORY

The formation of HIFU-induced lesions is based on the ability of biological tissues to absorb part of the acoustic energy. When transformed into heat, the absorbed energy creates a localized temperature increase that leads to a nearly total ablation of tissue cells. Mathematically, the thermal response of perfused biological tissues can be calculated by solving the BHTE, defined by Pennes[18] in 1948 in the form

$$\rho_t c_t \frac{\partial \theta_P}{\partial t} = \nabla \cdot (k_t \nabla \theta_P) + \omega_b c_b (\theta_a - \theta_P) + Q_P, \tag{1}$$

where θ_P is the temperature at point P, ρ_t is the tissue density, c_t is the tissue-specific heat, k_t is the tissue thermal conductivity, ω_b is the volumetric blood perfusion rate, c_b is the specific heat of blood, and θ_a is the arterial blood temperature. Here, Q_P represents the volumetric heat rate generated at point P by the HIFU.

To solve Eq. (1), we use the finite difference method, which is well described by Chato *et al.*,[21] with a three-dimensional field in Cartesian coordinates.

The determination of Q_P in Eq. (1) is a fundamental point. In general, the amount of heat $Q_P \Delta^3$, generated in a volume Δ^3, is equal to the acoustic energy lost by HIFU in passing through it. Thus, one has

$$Q_P \Delta^3 = \beta (E_{a0} - E_a), \tag{2}$$

where E_{a0} and E_a correspond, respectively, to the acoustic energy entering and leaving Δ^3. The coefficient, $\beta \leqslant 1$, expresses the fact that the acoustic attenuation is not just a result of the absorption phenomenon.

It is usually assumed, in the case of a single-frequency and low-intensity (I_{a0}) plane wave, that the attenuation remains constant, and Q_P is written as

$$Q_P = \beta \frac{(I_{a0} - I_a)}{\Delta}, \quad \text{with } I_a = I_{a0} e^{-2A\Delta}. \tag{3}$$

In biological tissue, the attenuation coefficient A varies with the frequency[22] and is expressed in terms of the frequency f_a as $A = \alpha f_a$, where α is the usual attenuation coefficient. For prostatic tissue, *in vivo* measurements[23] in the range 1–10 MHz give a value of the coefficient α of about 9 Np/MHz/m. We note that the analysis of the experimental data supplied by Damianou *et al.*[9] shows that β can be estimated to be 0.85.

When the acoustic pressure rises (above several tens of kPascal for a frequency of 3.0 MHz), Church[24] showed that, in the biomedical frequency range of 1–10 MHz, some cavitation nuclei may take ''stable'' oscillatory motions. The literature pertaining to bubble dynamics[25,26] describes in detail these motions called stable and/or repetitive transient cavitation. In terms of attenuation, one aspect of this phenomenon is particularly remarkable: the microbubbles capture a part of the ultrasound energy which is then redistributed as spherical waves, with a spectral content different from that of the incident beam. Since the absorption of the tissue varies with frequency, Eq. (3) is not valid and Q_p must be calculated by a different approach.

Assuming that the gaseous cavities in the tissues during treatment are air microbubbles immersed in a liquid, this approach consists of quantitatively evaluating the pressure scattered by oscillating bubbles. For this, we calculate by numerical integration (fourth-order Runge–Kutta) the Gilmore[25–27] second-order differential equation, which governs the dynamic response of spherical cavities, immersed in a compressible liquid and filled with a perfect gas undergoing adiabatic transformations. This equation has the form

$$\ddot{R} = -\frac{3}{2}\frac{\dot{R}^2}{R}\frac{1 - \dot{R}/3C_L}{1 - \dot{R}/C_L} + \frac{1}{R}\frac{1 + \dot{R}/C_L}{1 - \dot{R}/C_L} H + \frac{1}{C_L}\frac{dH}{dt}, \tag{4}$$

where R is the time-dependent radius of the bubble, $\dot{R} = dR/dt$, and $\ddot{R} = d^2R/dt^2$ are, respectively, the speed and acceleration of the bubble wall, H is the time-dependent mass enthalpy of the liquid between the bubble wall and infinity, and C_L is the speed of sound at the bubble wall. One has

$$H = \int_{P_L|_{r=\infty}}^{P_L|_{r=R}} \frac{1}{\rho_L} dp_L \quad \text{and} \quad C_L^2 = \left.\frac{\partial p_L}{\partial p_L}\right|_{r=R}, \tag{5}$$

where p_L is the time-varying pressure of the liquid, ρ_L is the time-varying density of the liquid, and r is the distance from the center of the bubble. For the same reasons as those discussed by Church,[27] p_L is determined using the modified Tait equation of state for the liquid. Then, Eq. (5) yields

$$H=\frac{n_T}{n_T-1}\frac{A_T^{1/n_T}}{\rho_{L0}}[(p_b+B_T)^{(n_T-1)/n_T}-(p_a+p_0+B_T)^{(n_T-1)/n_T}],$$
$$C_L=[C_0+(n_T-1)H]^{1/2}. \tag{6}$$

In Eqs. (6), C_0 is the speed of sound in the liquid at rest, ρ_{L0} is the density of the liquid at rest, p_0 is the ambient pressure of the surrounding liquid, $n_T=7$, $A_T=C_0^2\rho_{L0}/n_T$, $B_T=A_T-p_0$, p_a is the incident acoustic pressure, and p_b is the pressure at the bubble wall, which is given by

$$p_b=p_g-\frac{2\sigma}{R}-\frac{4\upsilon\dot{R}^2}{R},\quad \text{with } p_g=\left(P_0+\frac{2\sigma}{R_0}\right)\left(\frac{R_0}{R}\right)^{3\eta}, \tag{7}$$

where σ is the surface tension, υ is the coefficient of shear viscosity, p_g is the pressure of the gas inside the bubble, R_0 is the initial radius of the bubble, and η is the polytropic exponent of the gas. Note that the vapor pressure is ignored here. Gas-rectified diffusion across the bubble wall, which could be introduced using the diffusion equation described by Eller and Flynn,[28] is also ignored.

Finally, the time-varying scattered pressure, $P_S|_{r,R_0,P_a}$, given at a distance r from the center of a bubble with an initial radius R_0 and subjected to an acoustic pressure $p_a=P_a\sin(2\pi f_a t)$, is calculated according to the method described by Akulichev.[27] One has

$$P_S|_{r,R_0,P_a}=A_T\left[\frac{2}{n_T+1}+\frac{n_T-1}{n_T+1}\left(1+\left(\frac{n_T+1}{rC_L^2}\right)\times\left(H+\frac{\dot{R}^2}{2}\right)R\right)^{1/2}\right]^{2nT/(n_T-1)}. \tag{8}$$

The energy $E_S|_{R_0,P_a}$ scattered by the bubble is given by

$$E_S|_{R_0,P_a}=S_S|_{R_0,P_a}I_a, \tag{9}$$

where I_a is the incident intensity and $S_S|_{R_0,P_a}$ is the scattering cross section of the bubble, defined by

$$S_S|_{R_0,P_a}=\frac{4\pi r^2 I_S|_{r,R_0,P_a}}{I_a}=\frac{4\pi r^2\,(1/T)\int_{t_0}^{t_0+T}|P_S|_{r,R_0,P_a}|^2dt}{P_a^2/2}, \tag{10}$$

where T is the largest period of the bubble oscillation. In an elementary absorbing volume, Δ^3, containing N bubbles/m^3, the total energy E_{b0} absorbed by the bubbles is then approximately equal to

$$E_{b0}\cong N\cdot\Delta^3\cdot S_S|_{R_0,P_{a0}}I_{a0}e^{-2A(\Delta/2)}, \tag{11}$$

where it is assumed that all the bubbles of the volume Δ^3 have the same initial radius R_0 and the same behavior as a bubble located at the center of Δ^3.

This hypothesis is justified to the extent that after a first shot (of several seconds), cavitation nuclei present in the tissue have either disappeared by dissolution or have reached an equilibrium radius which is pressure dependent.[24,26] If the following shots are sufficiently close (in space and/or in time), the bubbles are still present and very rapidly reach their new equilibrium radius. Thus, in a small-volume Δ^3, where the acoustic pressure varies little, all the bubbles may be considered homogeneous in size throughout the whole shot duration.

The resonance of the bubbles being a nonlinear process, the attenuation of the scattered energy (E_{b0}) can be calculated by following a method similar to that used by Carsensten *et al.*[19] to determine the harmonic attenuation of shock waves in tissues. For that, the scattered intensity, $I_S|_{R_{\max},R_0,P_a}$, is expressed as a Fourier series of harmonic spectral components of the form

$$I_S|_{R_{\max},R_0,P_a}\cong\frac{2}{\rho_{L0}C_0}\sum_{m=0}^{+\infty}|c_m|_{R_{\max},R_0,P_a}|^2, \tag{12}$$

where c_m are the Fourier coefficients of the scattered pressure P_S [Eq. (8)] and $R_{\max}$ is the maximum radius reached by the oscillating bubble.

At a distance r_w from the bubble wall, i.e., at r from its center, the scattered intensity in an absorbing medium is attenuated according to the equation

$$I_S|_{r,R_0,P_a}\cong\left(\frac{R_{\max}}{r}\right)^2\frac{2}{\rho_{L0}C_0}\sum_{m=0}^{+\infty}|c_m|_{R_{\max},R_0,P_a}|^2e^{-2A_m\cdot r_w}, \tag{13}$$

where A_m is the attenuation corresponding to the mode of order m. Here, we postulate that each harmonic generated by a bubble is absorbed in a purely classical manner at a rate determined by the coefficient A_m at the appropriate frequency. The attenuation of the acoustic intensity along the axis r_w is written as

$$\frac{-\partial I_S}{\partial r_w}\frac{1}{2I_S}=\frac{1}{r}+\frac{\Sigma_{m=0}^{+\infty}A_m|c_m|_{R_{\max},R_0,P_a}|^2e^{-2A_m r_w}}{\Sigma_{m=0}^{+\infty}|c_m|_{R_{\max},R_0,P_a}|^2e^{-2A_m r_w}}=\frac{1}{r}+A_{\text{Harm}}|_{r_w,R_0,P_a}, \tag{14}$$

where A_{Harm} is the harmonic attenuation. It can be noted that for the given values of R_0 and P_a, A_{Harm} is a function of r_w, expressing the fact that the spectral decomposition of the scattered wave is modified as it propagates. In the case of r_w being fixed and large with respect to $R_{\max}$, i.e., $r\cong r_w$, the scattered intensity at a distance r can be calculated by integrating Eq. (14). The result is

$$I_S|_{r,R_0,P_a}=\left(\frac{R_{\max}}{r}\right)^2I_S|_{R_{\max},R_0,P_a}e^{-2rA_{\text{Harm}}|_{r,R_0,P_a}}. \tag{15}$$

Thus, for a density of N bubbles/m^3, one has

$$E_b\cong E_{b0}\cdot e^{-2rA_{\text{Harm}}|_{r,R_0,P_a}}. \tag{16}$$

By choosing a sufficiently large value for Δ with respect to the bubble radius, in order to limit the bubble heat contribution to its containing volume alone, and choosing r so that $\Delta^3\cong 4\pi r^3/3$, Q_P can be calculated as follows:

$$Q_P\Delta V\cong\beta[E_{a0}-[(E_{a0}-E_{b0})e^{-2A\Delta}+E_{b0}e^{-2rA_{\text{Harm}}|_{r,R_0,P_a}}]]. \tag{17}$$

By using Eq. (11), it follows from Eq. (17) that

$$Q_P \cong \beta \frac{Ia_0}{\Delta}[1-(1-N\Delta Sc|_{R_0,P_a}e^{-A\Delta})e^{-2A\Delta} - N\Delta Sc|_{R_0,P_a}e^{-A\Delta}e^{-2rA_{\mathrm{Harm}}|_{r,R_0,P_a}}]. \quad (18)$$

As Q_P depends on the acoustic pressure, the final stage of the study is to calculate the ultrasound field in the tissue. By taking Eq. (17) and considering that all the nonabsorbed energy is transmitted to the ultrasound beam, the transmitted acoustic intensity can be written in the form

$$I_a \cong [(1-N\Delta S_S|_{R_0,P_a}e^{-A\Delta})e^{-2A\Delta} + N\Delta S_S|_{R_0,P_a}e^{-A\Delta}e^{-2rA_{\mathrm{Harm}}|_{r,R_0,P_a}}]I_{a0}. \quad (19)$$

If we define the quantity

$$A^*|_{N,R_0,P_a} = \frac{-1}{2\Delta}\ln[(1-N\Delta S_S|_{R_0,P_a}e^{-A\Delta})e^{-2A\Delta} + N\Delta S_S|_{R_0,P_a}e^{-A\Delta}e^{-2rA_{\mathrm{Harm}}|_{r,R_0,P_a}}], \quad (20)$$

the attenuation of the acoustic pressure takes the form

$$P_a \cong P_{a0}\cdot e^{-A^*|_{N,R_0,P_a}\cdot\Delta}. \quad (21)$$

Note that for the given values of Δ, R_0, and P_a, then A^*, corresponding to a global attenuation coefficient, is a function of N with $A^*=A$ when $N=0$. For values where $N\neq 0$, it must be seen that Eq. (19) has a physical meaning only when

$$N \leqslant \frac{e^{-2A\Delta}}{\Delta S_S|_{R_0,P_a}e^{-A\Delta}(e^{-2A\Delta}-e^{-2rA_{\mathrm{Harm}}|_{r,R_0,P_a}})} = N_{\max}|_{R_0,P_a}. \quad (22)$$

Note that the global attenuation coefficient, $A^*|_{N,R_0,P_a}$, must be used within a very small volume insofar as it depends itself on the acoustic pressure. It is however possible to approach the problem by considering that Eq. (21) is applicable to each elementary volume if Δ is not too large and N is small enough with respect to $N_{\max}|_{R_0,P_a}$. In these conditions, the pressure field can be calculated by using the classical Rayleigh surface integral.[29] As the acoustic pressure depends on the global attenuation coefficient and vice versa the pressure field must be constructed step by step. This approach is close to that proposed by Tavakkoli *et al.*[20] for the propagation of shock waves in a dissipative medium. First, the acoustic pressure field, $P_a(x,y,z_0)$, is calculated at the water–tissue interface. Second, each global attenuation coefficient $A^*(x,y,z_0)$ corresponding to each Δ^3 volume included in the first tissue layer of thickness Δz is calculated from Eq. (20). Third, using these coefficients the attenuated field $P_a(x,y,z_0+\Delta)$ is calculated. Then, these three stages are iterated, layer by layer, in the direction of the ultrasound propagation, to construct the whole attenuated pressure field and the corresponding distribution of global attenuation coefficients.

From Eq. (18), the BHTE can be solved, the temperature field calculated, and finally the lesions induced by temperature increases in biological tissue evaluated. The solution is obtained by using the concept of thermal doses defined by Sapareto and Dewey.[30] A numerical integration is used to calculate the time that would yield biological effects equivalent to those obtained by an exposure to a constant reference temperature (43 °C). So, if θ_t is the average temperature during Δt, the thermal dose is given by

$$D_{43\,^\circ\mathrm{C}} = \sum_{t=0}^{t=\mathrm{final}} \mathcal{R}^{(43-\theta_t)}\Delta t, \quad (23)$$

where $\mathcal{R}$ is 0.25 for temperatures lower than 43 °C and 0.5 for temperature higher than 43 °C.

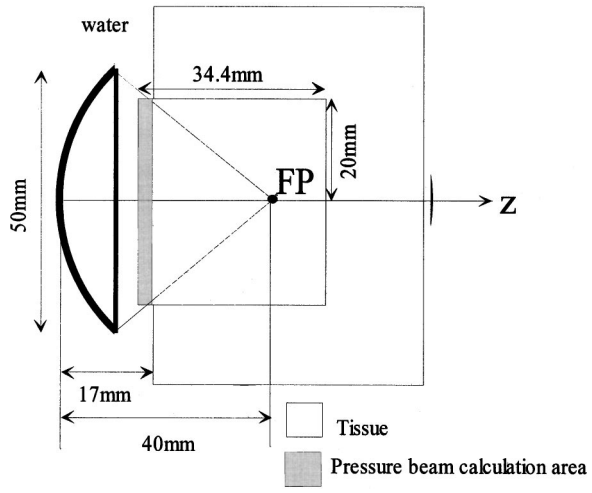

FIG. 1. Schematic representation of the simulation conditions.

II. RESULTS

The developed model is applied to a spherically curved transducer of 50-mm diameter and 40-mm focal length, working at a nominal frequency f_a of either 2.25 or 3.0 MHz. We consider that the transducer is set in water, 17 mm from a sample of prostate tissue (Fig. 1). The temperature of the water-sample model is initially set at 37 °C and the value of Δ fixed at 0.8 mm. The choice of Δ is based on a compromise between the restrictions arising from the method, and the calculation time limit for the pressure field.

Before solving the BHTE, we evaluate the variations of the scattering cross section $S_S|_{R_0,P_a}$ [Eq. (10)] and the harmonic attenuation $A_{\mathrm{Harm}}|_{r,R_0,P_a}$ [Eq. (14)] with respect to the initial microbubble radius, R_0, and the amplitude, P_a, of the acoustic pressure. These two quantities have been evaluated, on the basis of conclusions given by Leighton[26] concerning the works of Church, Lewin, ter Haar, Daniels, Crum, and Hansel, for a series, S1, of microbubbles, with initial radii ranging from 1 to 3 μm in 0.1-μm steps. The calculations have been carried out at the two acoustic frequencies (2.25 and 3.0 MHz) for an air bubble immersed in water ($\rho_{L0}=10^3$ kg/m^3, $C_0=1500$ m/s, $p_0=1.01\times10^5$ Pascal, $\eta=1.4$, $\sigma=0.07$ N/m, $\upsilon=1.08\times10^{-3}$ Ns/m^2).

A. Scattering cross section

Figure 2 shows the variation in the cross-section radius, $R_S=\sqrt{S_S/4\pi}$, calculated from Eq. (10). Without going into the details relative to the various resonance phenomena observed at the beginning of the curves, the increase in the

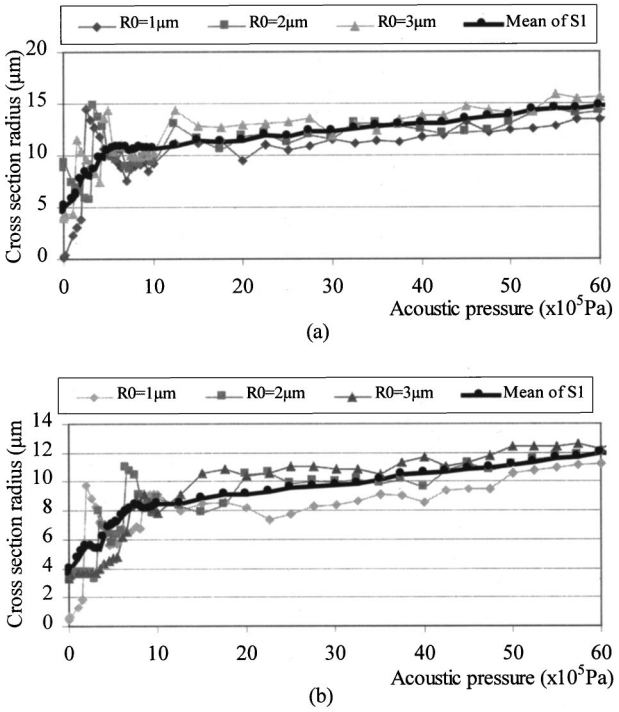

FIG. 2. Variation of scattering cross-section radius versus acoustic pressure: (a) Frequency=2.25 MHz; (b) frequency=3 MHz.

cross-section radius can be considered globally as logarithmic above a certain threshold of pressure, which is distinct for each bubble size.

In order to simplify the setup of the model, the dependence of the scattering cross section on the acoustic pressure has been approximated via an analytical function close to the mean curve obtained from the series S1

$$S_S|_{Pa}=\begin{cases}4\pi(R_1\ln(P_{\mathrm{Th1}}/P_{\mathrm{Scale}})+R_2)^2 & \text{if } P_a\leqslant P_{\mathrm{Th1}},\\ 4\pi(R_1\ln(P_a/P_{\mathrm{Scale}})+R_2)^2 & \text{if } P_a\geqslant P_{\mathrm{Th1}}.\end{cases} \tag{24}$$

Figure 3 shows these curves obtained at 2.25 and 3 MHz, with $R_1=1.89\,\mu$m, $R_2=6.4\,\mu$m, $P_{\mathrm{Th1}}=0.5\times10^5$ Pascal (correlation coefficient=0.984) and $R_1=1.77\,\mu$m, $R_2=4.16\,\mu$m, $P_{\mathrm{Th1}}=0.9\times10^5$ Pascal (correlation coefficient =0.989), respectively ($P_{\mathrm{Scale}}=10^5$ Pascal).

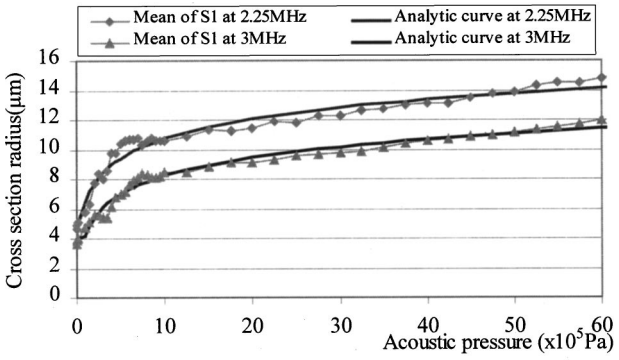

FIG. 3. Analytical curves of scattering cross-section radius versus acoustic pressure.

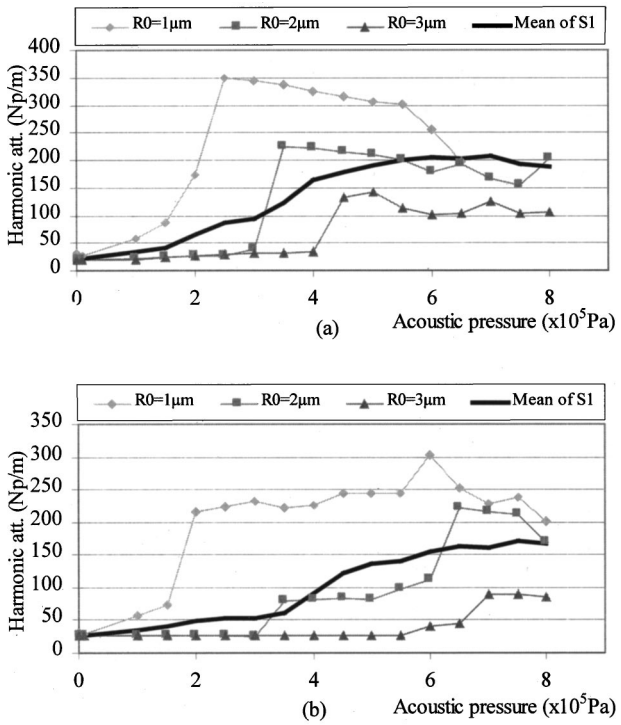

FIG. 4. Variation of harmonic attenuation versus acoustic pressure: (a) Frequency=2.25 MHz; (b) frequency=3 MHz.

B. Harmonic attenuation

The harmonic attenuation was calculated from Eq. (14) by sampling the scattered pressure with $M=2^{22}$ samples and using the coefficient A_m such as $A_m=\alpha(m/T)$ with $\alpha=9$ Np/MHz/m, $m=0,...,M/2$ and $T=kT_a$, where T_a is the acoustic period. For each time waveform $P_S|_{R_{\max},R_0,P_a}$, the value k was optimized in order to obtain the maximum spectral information from the signal. This implies that, with 2^{22} samples, the harmonic attenuation could not be reliably calculated above 8×10^5 Pascal. Figure 4 shows the variation of the harmonic attenuation as a function of the pressure. As was done previously for the estimate of the scattering cross section, the harmonic attenuation is approximated via an analytical function close to the mean curve obtained from the series S1

$$A_{\mathrm{Harm}}|_{P_a}=\begin{cases}A_0+A_1e^{\chi Pa/P_{\mathrm{Scale}}} & \text{if } P_a\leqslant P_{\mathrm{Th2}},\\ A_0+(A_2-A_1e^{\chi(2P_{\mathrm{Th2}}-P_a)/P_{\mathrm{Scale}}}) & \\ \quad\text{if } P_a\geqslant P_{\mathrm{Th2}}.\end{cases} \tag{25}$$

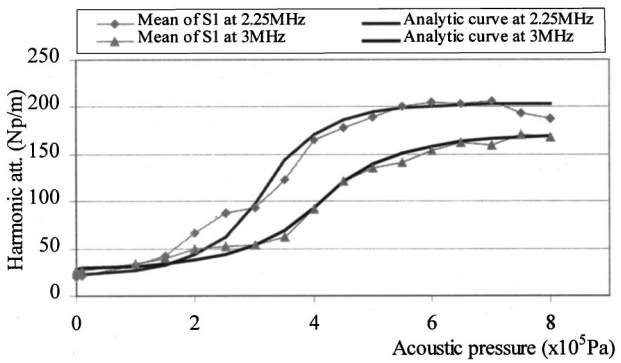

FIG. 5. Analytical curves of harmonic attenuation versus acoustic pressure.

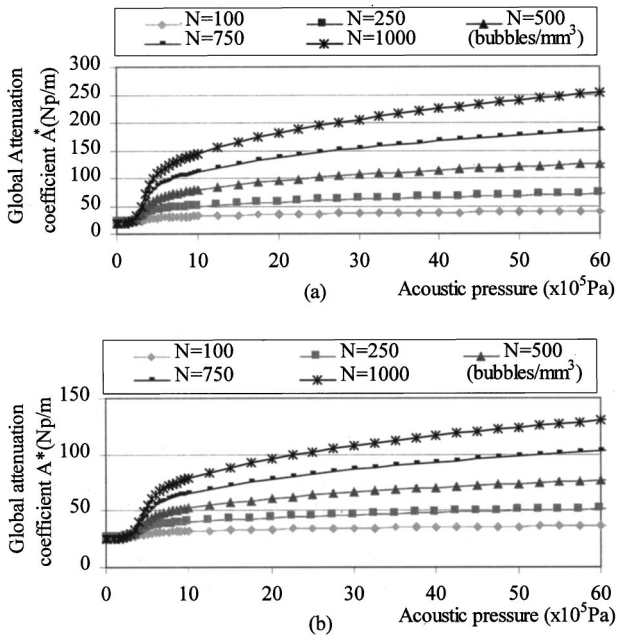

FIG. 6. Global attenuation coefficient A^* versus acoustic pressure for different bubble densities: (a) Frequency=2.25 MHz; (b) frequency=3.0 MHz.

Figure 5 shows these curves obtained at 2.25 and 3 MHz, with $A_0=20.25$ Np/m, $A_1=2.1$ Np/m, $A_2=184$ Np/m, $\chi=1.2$, $P_{Th2}=3.15\times10^5$ Pascal (correlation coefficient $=0.991$) and $A_0=27$ Np/m, $A_1=1.8$ Np/m, $A_2=145$ Np/m, $\chi=0.9$, $P_{Th2}=4.12\times10^5$ Pascal (correlation coefficient $=0.997$), respectively ($P_{Scale}=10^5$ Pascal).

C. Global attenuation coefficient

Using Eqs. (24) and (25), several curves (Fig. 6) of the global attenuation coefficient $A^*|_{N,P_a}$ were calculated from Eq. (20). As no precise data are available on the density of microbubbles naturally present in biological tissues, these calculations have been carried out for different values of N. Six values have been taken: $N=0$, 100, 250, 500, 750, and 1000 bubbles/mm^3. All these values satisfy the condition $N \leqslant N_{\max}|_{P_a}/3$ (Fig. 7), where this condition is imposed, in order to be consistent with all the assumptions used in the evaluation of Eq. (11).

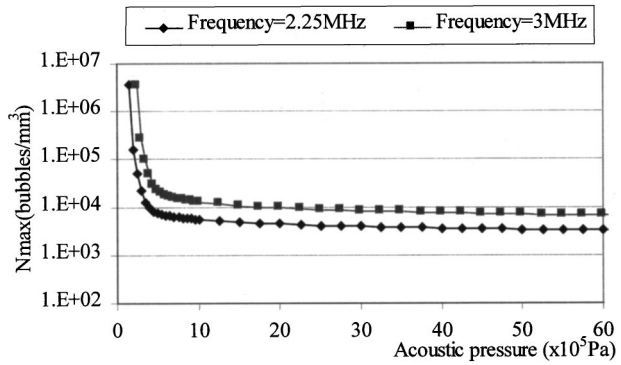

FIG. 7. Bubble maximum density versus acoustic pressure for two frequencies.

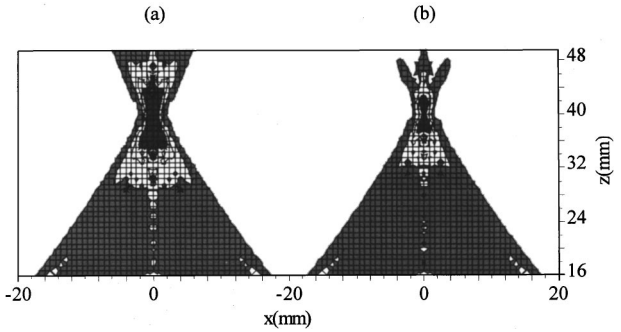

FIG. 8. Pressure field calculated for one shot with power $\mathbf{P}=2.45\,\mathbf{P}_{ref}$ ($\mathbf{P}_{ref}=1700$ W/cm^2 in water at the focal point) and for a frequency of 2.25 MHz: (a) $N=0$; (b) $N=750$ bubbles/mm^3.

D. Pressure field

The pressure field was calculated in the volume defined in Fig. 1 for the different values of N and different levels of the acoustic power $\mathbf{P}$. Figure 8 shows an example of fields calculated at 2.25 MHz, for $\mathbf{P}=2.54\,\mathbf{P}_{ref}$ and for values of $N=0$ and 750 bubbles/mm^3. The reference value, $\mathbf{P}_{ref}$, corresponds to an acoustic intensity, I_{SPTA}, of 1700 W/cm^2, calculated at the focal point in a nonabsorbing medium.

E. Temperature field

Assuming that the pressure field is constant for the duration of a shot (4.5 s), and ignoring the case of the first shot, where the cavitation field has not been established, we calculate the temperature field by resolving the BHTE [Eq. (1)] with values of Q_P calculated from Eq. (18) with a coefficient $\beta=1$. All the calculation parameters are listed in Table I. Figure 9 shows the temperature levels reached after a 4.5-s shot is performed in condition identical to those of Fig. 8. For this result and all the following results, the temperature in the tissues is limited to 100 °C, the approximate temperature above which the intracellular liquid vaporizes.

F. Elementary lesion

Starting from the temperature field, calculation of the thermal dose received by the tissues makes it possible to evaluate the shape and position of the HIFU-induced lesions. Each elementary lesion is estimated after a shot lasting 4.5 s followed by a resting time of 20 s. The results given in Figs. 10 and 11 show that the lesions develop well in front of the focal point like the ''tadpole-shaped'' lesions described by Watkin.[13] The analysis of the results also shows that these displacement and deformation effects are only sensitive above the limit of 500 bubbles per mm^3 and are more impor-

TABLE I. Parameters used for the resolution of BHTE.

	Water	Tissue	Blood
Thickness (mm)	17	23	
Initial temperature (°C)	37	37	37
thermal condutivity (W/m/°C)	0.627	0.495	0.54
Density (kg/m^3)	1000	1060	1060
Specific heat (J/kg/°C)	4188	3700	3770
Volumetric perfusion rate (kg/m^3/s)		30	1160

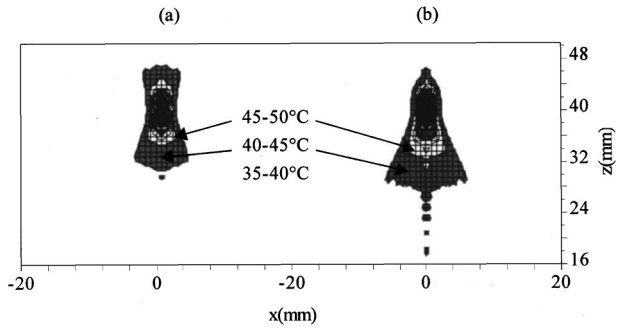

FIG. 9. Temperature field calculated for one shot with power $\mathbf{P}=2.45\,\mathbf{P}_{\text{ref}}$ ($\mathbf{P}_{\text{ref}}=1700\ \text{W/cm}^2$ in water at the focal point) and for a frequency of 2.25 MHz (a) $N=0$; (b) $N=750$ bubbles/mm^3.

tant at 2.25 MHz than at 3.0 MHz. In order to simplify the analysis of the following results, the density is arbitrarily set at $N=N_t=750$ bubbles per mm^3.

G. Multiple shot sequence

The analysis of the temperature field in Fig. 9 shows that the presence of microbubbles considerably increases the heated zone in the prefocal area. In the case of a multiple shot sequence, such as that for an HIFU treatment of the prostate, the consequences of this phenomenon may be quite important. Figures 12(a) and 12(b) show the lesion modeling achieved after a sequence of eight shots, without and with cavitation effects, $N=0$ and $N=N_t$, respectively. For $N=0$ the lesion is 8 mm long, centered at 39.2 mm, whereas for $N=N_t$ the lesion length reaches 12.8 mm with a shift of 3.2 mm in front of the transducer focus.

H. Interface lesion

Figure 7 shows that in low acoustic pressure zones (below $5\cdot10^5$ Pascal), the microbubble density may be greatly increased, even within the reliability conditions of the model given by Eq. (22). The hypothesis of a greatly increased microbubble density at a tissue interface[31] can thus be modeled. Figure 12(c) shows the result of such a simulation obtained at $\mathbf{P}=1.94\,\mathbf{P}_{\text{ref}}$, assuming a microbubble density of $N_{if}=20\,N_t$ at the water–tissue interface. In these conditions, the modeled lesion is thus considerably increased (17.6 mm) by the presence of the interface. Its center is located at 35.2 mm, i.e., 4.8 mm in front of the transducer focus. The results of this simulation are close to those found in clinical experimentation. Indeed, histology data obtained after radical prostatectomy in a patient treated with the same HIFU parameters, show a 18-mm-long lesion shifted by 5 mm in front of the theoretical transducer focus.[14]

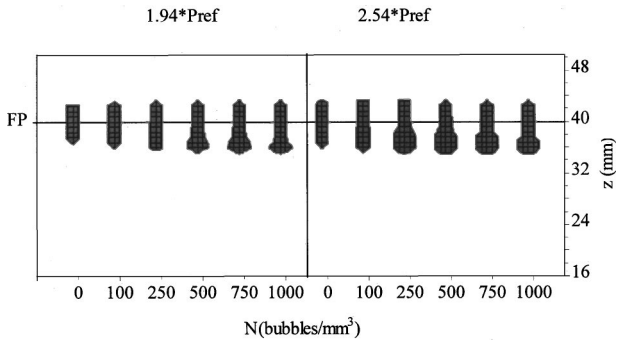

FIG. 10. Variation of the shape and position of elementary lesions according to the microbubble density and the acoustic power when frequency=2.25 MHz ($D_{43\,^\circ\text{C}}=600$ s; $\mathbf{P}_{\text{ref}}=1700\ \text{W/cm}^2$ in water at the focal point; PF =focal plane).

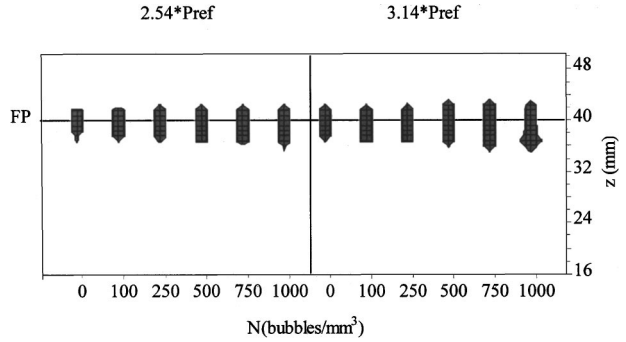

FIG. 11. Variation of the shape and position of elementary lesions according to the microbubble density and the acoustic power when frequency=3.0 MHz ($D_{43\,^\circ\text{C}}=600$ s; $\mathbf{P}_{\text{ref}}=1700\ \text{W/cm}^2$ in water at the focal point; PF =focal plane).

The thermal dose analysis at the interface after a sequence of eight shots shows that an interface lesion develops when the power is gradually increased [Figs. 13(a) and 13(b)]. During *in vivo* treatment of the prostatic tissue, this kind of lesion has been clinically observed on the rectal wall, necessitating the use of a cooling system.[14] It can be noted that interface lesions are not limited to the water–tissue interface (skin or rectal wall), but may occur in all areas potentially rich in cavitation nuclei even at a distance from the transducer focus. Indeed, such an interface lesion has been observed between two lobes in the rabbit liver during *in vivo* HIFU experimental treatment.

Figure 14(c) shows how, at a certain level of the transmitted power, the interface lesion merges with the internal lesion to form a ''diabolo-shaped'' lesion. It should be noted that it is imperative to avoid this situation, particularly in postate HIFU treatment where it would cause a uretro–rectal fistula. Finally, Fig. 14(d) shows how at very high power

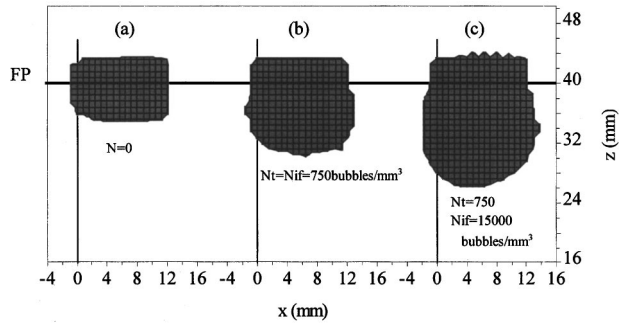

FIG. 12. Lesions created by an eight-shot sequence: frequency=2.25 MHz, acoustic power=1.94 $\mathbf{P}_{\text{ref}}$, shot duration=4.5 s, time between shots=5 s, space between shots=1.6 mm for: (a) $N=0$; (b) a microbubble density identical in tissue and at the interface, i.e., $N_t=N_{if}=750$ bubbles/mm^3; (c) a density at the interface 20 times greater than density in tissue, i.e., $N_{if}=20\,N_t$ with $N_t=750$ bubbles/mm^3 ($D_{43\,^\circ\text{C}}=600$ s; $\mathbf{P}_{\text{ref}}=1700\ \text{W/cm}^2$ in water at the focal point).

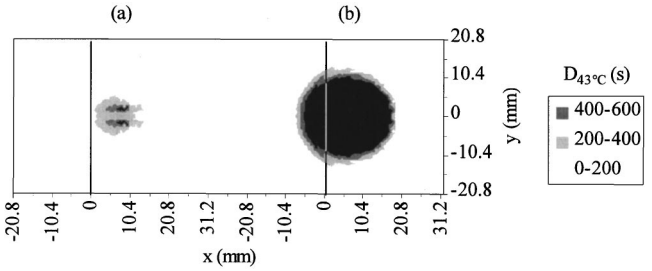

FIG. 13. Thermal dose, $D_{43\,^\circ C}$(s), calculated at the water–tissue interface in a sequence of eight shots: frequency=2.25 MHz, shot duration=4.5 s, time between shots=5 s, distance between shots=1.6 mm for a microbubble density at the interface 20 times greater than the density in tissue, i.e., $N_{if}=20\,N_t$ with $N_t=750$ bubbles/mm^3: (a) acoustic power=2.54 $\mathbf{P}_{\text{ref}}$; (b) acoustic power=3.14 $\mathbf{P}_{\text{ref}}$ ($\mathbf{P}_{\text{ref}}=1700$ W/cm^2 in water at the focal point).

levels, conditions at the interface block the in-depth penetration of the ultrasound.

III. DISCUSSION

Before starting the discussion, one must remember that the present model is only a first approach to a highly complex process and should therefore be considered in this context. At present, the bubble dynamic behavior in a medium other than liquid, the bubble content, the conditions of equilibrium controlling the bubble behavior in stable or repetitive transient cavitation, are not fully understood, and the bubble density in the tissues is not known. The same comments can be made for the attenuation process in biological tissues at high acoustic frequencies. The modeling of the ultrasound beam may also be questioned, because the diffusion effect of the bubbles has been neglected. In particular, when the bubble density at the interface is high, it would be wise to quantify the backscattered energy, and perhaps even to consider the whole collection of pinpoint sources as a pseudo ''circular piston,'' since these quantities may considerably alter the focusing conditions and thus the in-depth penetration of the ultrasound waves. Last, for the sake of simplicity, the model does not take into account the assumptions mentioned in the Introduction (nonlinear effects, temperature dependence of the ultrasonic attenuation, thermal lens effect, etc.,...), which certainly also play an important role in the formation of HIFU-induced lesion.

However, without claiming to quantify the exact phenomenology of tissue ablation by HIFU, this first rough simulation already provides a better comprehension of the mechanism of lesion development. It confirms that cavitation plays a major role in HIFU-induced lesion formation. In the absence of tools to quantify its effects, cavitation was generally considered to be a harmful phenomenon which should be avoided wherever possible. This is the reason why different solutions were proposed such as lowering the acoustic intensity below the cavitation threshold or taking precautions regarding the spacing of elementary lesions and the cooling time between two shots.[10,13,32] These rigorous constraints result in prohibitive treatment times, which are incompatible with a clinical application. Fortunately, experimental data achieved so far show that it is possible in one way or another to master the cavitation effects by a judicious choice of the firing sequence parameters.[8] Therefore, it is expected that the present modeling will help us to optimize treatment parameters without having to sacrifice animals, which is currently necessary to validate different treatment configurations. The simulation results given here have already provided partial answers to some nagging questions. In particular, they help us better understand how an increase in the transmitted power and/or a high bubble density at the interface significantly shift the center of the lesion in front of the transducer focus. Moreover, when the interface is close to the focal point, the results show how unwanted lesions can appear very rapidly with a power increase, and how this occurs at the expense of the desired lesion in the target volume. It can be shown that, at constant power, the process is identical when the shot duration is increased. The cooling time between two shots may be studied, knowing that it must be short enough to reduce the treatment duration and long enough to avoid heat accumulation in the prefocal area and at the interface. The same study may be performed for the geometric spacing between two elementary lesions.

Last but not least, we can study the influence of the acoustic frequency. It is current practice to consider that the attenuation coefficient of tissue is directly proportional to the frequency. Consequently, a 2.25-MHz frequency was initially defined as the most appropriate one to ablate prostate tissue transrectally.[14] However, Fig. 6 shows that the global attenuation coefficient A^* verifies this law only at low pressure (about 20 and 27 Np/m at 2.25 and 3.0 MHz, respectively) and that the proportionality is reversed for $P_a>5\times10^5$ Pascal (for example, when $P_a=10^6$ Pascal and $N=750$ bubbles per mm^3: $A^*=111$ Np/m at 2.25 MHz and only 65 Np/m at 3.0 MHz). Therefore, for a given transmitted power, the effective *in situ* focal intensity becomes higher at 3.0 MHz than at 2.25 MHz (Fig. 15). This confirms that the cavitation is less important when frequency increases, the consequences being that there is less energy dispersion in the prefocal area and that the displacement, the lengthening, and the deformation of the HIFU-induced lesions are less important (Figs. 10 and 11). The energy concentration being greater in the target area, this ensures a higher ''quality'' of necrosis, explaining the greater homogeneity of HIFU-induced lesions observed at 3.0 MHz for prostate treatment.[7]

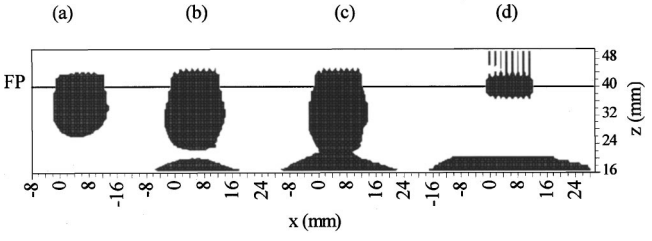

FIG. 14. Lesions created by an eight-shot sequence: frequency=2.25 MHz, shot duration=4.5 s, time between shots=5 s, distance between shots=1.6 mm, for a microbubble density at the interface 20 times as large as the density in tissue, i.e., $N_{if}=20\,N_t$ with $N_t=750$ bubbles/mm^3, with an acoustic power equal to: (a) 1.94 $\mathbf{P}_{\text{ref}}$; (b) 3.14 $\mathbf{P}_{\text{ref}}$; (c) 3.74 $\mathbf{P}_{\text{ref}}$; and (d) 6.72 $\mathbf{P}_{\text{ref}}$ ($D_{43\,^\circ C}=600$ s; $\mathbf{P}_{\text{ref}}=1700$ W/cm^2 in water at the focal point).

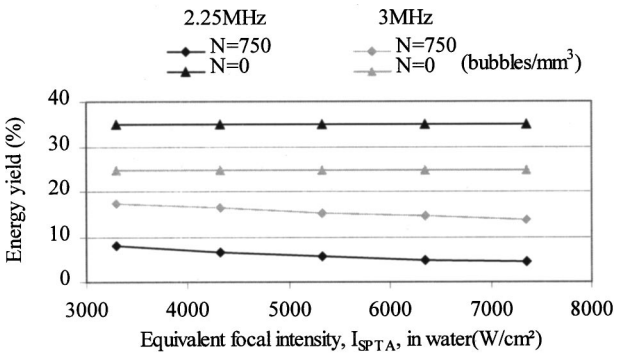

FIG. 15. Variation of the energy yield at 2.25 and 3.0 MHz when $N=0$ and $N=750$ bubbles/mm^3. The energy yield is calculated as the ratio of the focal intensity in tissue to the equivalent focal intensity in water.

IV. CONCLUSION

The analysis of our results demonstrates that, in taking into account the presence of oscillating microbubbles in tissue, it is possible to model HIFU-induced lesions where the shape and the position are in better agreement with clinical experiments. This first series of simulation allows us to explain why, with lower cavitation effects, the treated volume diminishes and vice versa. It confirms that with an increase in the incident power the lesion does not develop around the focal point, but always in front of it, thus shifting the center of the lesion by several millimeters. Above all, this approach can be used to simulate interface lesions. And, finally it justifies the present choice of the acoustic frequency, set at 3.0 MHz in the Ablatherm™ project. Indeed, at this frequency a better concentration of energy in the target volume is achieved, which ensures a greater homogeneity in lesions, less displacement in front of the focal point, and lower risks of superficial lesions.

As a conclusion, it can be said that this approach to the problem yields simulation results closer to reality with regard to the size, shape, and position of lesions. It suggests the possibility of further improvements of the firing sessions in terms of power, geometric spacing, duration, and shot frequency.

[1] A. Gelet, J. Y. Chapelon, R. Bouvier, C. Pangaud, and Y. Lasne, ''Local control of prostate cancer by transrectal high intensity focused ultrasound therapy: Preliminary results,'' J. Urol. (Baltimore) **161**, 156–162 (1999).

[2] J. Y. Chapelon, M. Ribault, A. Birer, F. Vernier, R. Souchon, and A. Gelet, ''Treatment of localised prostate cancer with transrectal high intensity focused ultrasound,'' Eur. J. Ultrasound **9**, 31–38 (1999).

[3] F. L. Lizzi, D. J. Coleman, J. Driller, M. Ostromogilsky, S. Chang, and P. Greenall, ''Ultrasonic hyperthermia for ophthalmic surgery,'' IEEE Trans. Sonics Ultrason. **31**, 473–480 (1984).

[4] G. Vallancien, M. Harouni, B. Veillon, A. Mombet, D. Prapotnich, J. Bisset, and J. Bouragan, ''Focused extracorporeal pyrotherapy: Feasibility study in man,'' J. Endourol. **6**(2), 173–180 (1992).

[5] C. Delon-Martin, C. Vogt, E. Chigner, C. Guers, J. Y. Chapelon, and D. Cathignol, ''Venous thrombosis generation by means of high-intensity focused ultrasound,'' Ultrasound Med. Biol. **21**, 113–119 (1995).

[6] G. ter Haar, ''Ultrasound focal beam surgery,'' Ultrasound Med. Biol. **21**(9), 1089–1100 (1995).

[7] K. Hynynen, *Interventional Magnetic Resonance Imaging*, edited by J. F. Debatin and G. Adam (Springer, Berlin, 1998), pp. 187–194.

[8] N. T. Sanghvi, F. J. Fry, R. Bihrle, R. S. Foster, M. H. Phillips, J. Syrus, A. V. Zaitsev, and C. W. Henninge, ''Non-invasive surgery of prostate tissue by high-intensity ultrasound,'' IEEE Trans. Ultrason. Ferroelectr. Freq. Control **43**, 1099–1110 (1996).

[9] C. A. Damianou, N. T. Sanghvi, F. J. Fry, and R. Maass-Moreno, ''Dependence of ultrasonic attenuation and absorption in dog soft tissues on temperature and thermal dose,'' J. Acoust. Soc. Am. **102**, 628–634 (1997).

[10] L. Chen, G. ter Haar, and C. R. Hill, ''Influence of ablated tissue on the formation of high-intensity focused ultrasound lesions,'' Ultrasound Med. Biol. **23**(6), 921–931 (1997).

[11] C. Le Floch and M. Fink, ''Ultrasonic Mapping of Temperature in Hyperthermia: The Thermal Lens Effect,'' in Proceedings of the 1997 IEEE Ultrasonics Symposium (Toronto) Vol. 2, pp. 1301–1304 (1997) (unpublished).

[12] G. Wojcik, J. Mould, J. F. Lizzi, N. Abboud, M. Ostromogilsky, and D. Vaughan, ''Nonlinear modeling of therapeutic ultrasound,'' IEEE Ultrasonics Symposium, Vol. 2, pp. 1617–1622 (1995) (unpublished).

[13] N. A. Watkin, G. R. ter Haar, and I. Rivens, ''The intensity dependence of the site of maximal energy deposition in focused ultrasound surgery,'' Ultrasound Med. Biol. **22**(4), 483–491 (1996).

[14] A. Gelet, J. Y. Chapelon, R. Bouvier, R. Souchon, C. Pangaud, A. F. Abderlrahim, D. Cathignol, and J. M. Dubernard, ''Treatment of prostate cancer with transrectal focused ultrasound: Early clinical experience,'' Eur. Urol. **29**, 174–183 (1996).

[15] N. T. Sanghvi, J. F. Fry, R. Bihrle, R. S. Foster, M. H. Phillips, J. Syrus, A. V. Zaitsev, and C. W. Hennige, ''Noninvasive surgery of prostate tissue by high-intensity focused ultrasound,'' IEEE Trans. Ultrason. Ferroelectr. Freq. Control **43**(6), 1099–1110 (1996).

[16] S. Fujishiro, M. Mitsumori, Y. Nishimura, Y. Okuno, Y. Nagata, M. Hiraoka, T. Sano, T. Marume, and N. Takayama, ''Increased heating efficiency of hyperthermia using an ultrasound contrast agent: A phantom study,'' Int. J. Hyperthermia **14**(5), 495–502 (1998).

[17] J. Wu, ''Temperature rise generated by ultrasound in the presence of contrast agent,'' Ultrasound Med. Biol. **24**(2), 267–274 (1998).

[18] H. H. Pennes, ''Analysis of tissue and arterial blood temperatures in the resting human forearm,'' J. Appl. Physiol. **1**(2), 93–122 (1948).

[19] E. L. Carstensen, N. D. McKay, D. Dalecki, and T. G. Muir, ''Absorption of finite amplitude ultrasound in tissues,'' Acustica **51**(2), 116–123 (1982).

[20] J. Tavakkoli, D. Cathignol, R. Souchon, and O. Sapozhnilov, ''Modeling of pulsed finite-amplitude focused sound beams in time domain,'' J. Acoust. Soc. Am. **104**, 2061–2072 (1998).

[21] J. C. Chato, ''Fundamentals of Bioheat Transfer'' in *Thermal Dosimetry and Treatment Planning*, edited by M. Gautherie (Springler-Verlag, Heidelberg, 1990), pp. 1–56.

[22] H. J. Huisman and J. M. Thijssen, ''Precision and accuracy of acoustospectrographic parameters,'' Ultrasound Med. Biol. **22**, 855–871 (1996).

[23] M. Ribault, J. Y. Chapelon, D. Cathignol, and A. Gelet, ''Differential attenuation imaging for the characterisation of high intensity focused ultrasound lesions,'' Ultrason. Imaging **20**, 160–177 (1998).

[24] C. C. Church, ''Prediction of rectified diffusion during nonlinear bubble pulsations at biomedical frequencies,'' J. Acoust. Soc. Am. **83**, 2210–2217 (1988).

[25] F. R. Young, *Cavitation* (McGraw-Hill, London, 1989).

[26] T. G. Leighton, *The Acoustic Bubble* (Academic, New York, 1994).

[27] C. C. Church, ''A theoretical study of cavitation generated by an extracorporeal shock wave lithotripter,'' J. Acoust. Soc. Am. **86**, 215–227 (1989).

[28] A. Eller and H. G. Flynn, ''Rectified diffusion during nonlinear pulsations of cavitation bubbles,'' J. Acoust. Soc. Am. **37**, 493–503 (1965).

[29] J. W. S. Rayleigh, *The Theory of Sound* (Dover, New York, 1945), Vol. II, p. 107.

[30] S. A. Sapareto and W. C. Dewey, ''Thermal dose determination in cancer therapy,'' Int. J. Radiat. Oncol., Biol., Phys. **10**, 787–800 (1984).

[31] F. J. Fry, G. Kossof, R. C. Eggleton, and F. Dunn, ''Threshold ultrasonic dosages for structural changes in the mammalian brain,'' J. Acoust. Soc. Am. **48**, 1413–1417 (1970).

[32] K. Hynynen, ''The threshold for thermally significant cavitation in dog's thigh muscle *in vivo*,'' Ultrasound Med. Biol. **17**, 157–169 (1991).

Field characterization of therapeutic ultrasound phased arrays through forward and backward planar projection

G. T. Clement and Kullervo Hynynen
Brigham & Women's Hospital, Harvard Medical School, 75 Francis Street, Boston, Massachusetts 02115

(Received 30 August 1999; accepted for publication 27 March 2000)

Spatial planar projection techniques propagate field measurements from a single plane in front of a transmitter to arbitrary new planes closer to or further away from the source. A linear wave vector frequency-domain projection algorithm is applied to the acoustic fields measured from several focused transducer arrays designed for ultrasound therapy. A polyvinylidene difluoride hydrophone is first scanned in a water tank over a plane using a three-dimensional positioning system to measure the complex pressure field as a function of position. The field is then projected to a series of new planes using the algorithm. Results of the projected fields are compared with direct measurements taken at corresponding distances. Excellent correlation is found between the projected and measured data. The method is shown to be accurate for use with phase-controlled field patterns, providing a rapid and accurate method for obtaining field information over a large spatial volume. This method can significantly simplify the characterization procedure required for phased-array application used for therapy. Most significantly, the wavefront propagated back to a phased array can be used to predict the field produced by different phase and amplitude settings of the array elements. A field back-projected to the source could be used as an improved source function in acoustic modeling. [S0001-4966(00)01207-8]

PACS numbers: 43.80.Vj, 43.35.Yb [FD]

INTRODUCTION

Measurement of a radiating field across an appreciable spatial volume can require an exhaustive amount of physical measurement. However, knowledge of the field over these volumes may be necessary when the source involves complicated amplitude and phase shading, since the field resulting from the response of a physical transducer can be difficult to predict. Spatial planar propagation methods[1] greatly reduce the data required for global reconstruction of a linear field. These methods allow the acoustic pressure in a single plane in front of a source to be rapidly propagated to arbitrary new planes. This ability is particularly appealing for the case of therapeutic ultrasound arrays,[2–4] which use areas of high pressure to necrose cells through elevated temperature[5] or cavitation.[6] A full knowledge of the spatial field obtained from projected data could provide an accurate mapping of a focal region as well as identify unexpected intense sidelobes and other regions of high acoustic intensity away from the area of ultrasound treatment. Additionally, a pressure field projected to a plane near the transducer surface could provide information for precise field modeling.[7–9] Phased arrays consisting of a large number of elements could use the projected information to adjust the amplitude and phase of individual driving signals and improve radiated signals.

A variety of harmonic and transient planar propagation algorithms has been described. These algorithms generally relate the fields of two planes in terms of a transfer function in either the wave vector-frequency[10] domain or the wave vector-time domain.[11] Experimental harmonic[12,13] and transient[10] fields for a number of transducer geometries have been propagated using these approaches. The present study examines the use of forward and backward projection for the characterization and analysis of the fields produced by therapeutic phased arrays. We utilize the 2D angular spectrum method[1] for projecting harmonic waves. The algorithm is valid in a boundless, lossless region. Basic theory is outlined in Sec. I for the case of a linear, freely propagating field. In this limit, the field may be propagated to any plane that does not intersect with the source. Spherically concave transducers considered here may be propagated backward to the plane tangent to the edge of the transducer.

To evaluate the method for the case of phased arrays, phase-controlled field patterns described in Sec. II are produced by three transducer arrays with varying geometric configurations. Each of these transducers and their corresponding field patterns are designed for use in a variety of therapeutic applications. A single planar scan is performed using a stepping motor-controlled positioning system to scan a polyvinylidene difluoride (PVDF) hydrophone over an arbitrary plane situated normal to the acoustic axis of propagation. The fast Fourier transform (FFT)-based algorithm then propagates the field to a series of new planes, both in the acoustic near field and far field. In Sec. III, the projections are compared with experimental measurements of the planes corresponding to the experimental distances. Results indicate that the projected fields correlate closely with directly measured fields.

I. THEORY

The projection algorithm assumes that the acoustic field satisfies the linearized acoustic wave equation. While therapeutic arrays generally operate at high powers, the linear approximation is found to be appropriate for evaluating transducers.[14] For a time-harmonic field, the temporal depen-

dence can be separated so that the pressure is expressed as $P(r,t)=\tilde{P}(r)e^{i\omega t}$, and the wave equation becomes

$$\left(\nabla^2+\frac{\omega^2}{c^2}\right)\tilde{P}(r)=0, \tag{1}$$

where c is the speed of sound and ω is the angular frequency. A Helmholtz equation in Cartesian coordinates is obtained through the substitution of the 2D Fourier integral

$$\tilde{P}(x,y,z)=\frac{1}{2\pi}\int\int \tilde{p}(k,k,z)e^{i\omega t}e^{ik_x x}e^{ik_y y}\,dk_x\,dk_y \tag{2}$$

into Eq. (1) yielding

$$\frac{\partial\tilde{p}(k_x,k_y,z)}{\partial z}+\left(\frac{\omega^2}{c^2}-k_x^2-k_y^2\right)\tilde{p}(k_x,k_y,z)=0. \tag{3}$$

To propagate the field in a plane at a distance z_0 in front of a source to a new plane z, the advanced solution of Eq. (3) is used

$$\tilde{p}(k_x,k_y,z)=\tilde{p}(k_x,k_y,z_0)e^{i(z-z_0)\sqrt{(\omega^2/c^2)-k_x^2-k_z^2}}. \tag{4}$$

In wave vector space, the field recorded in a plane z_0 is thus related to the field at any other plane z by a simple transfer function given in the right-hand side of Eq. (4). The pressure field in space at z may be obtained by taking the inverse Fourier transform of Eq. (4).

Backward projection to the source could serve as an source function for more realistic acoustic modeling. The source function can also be numerically adjusted to predict the field for additional field patterns.[15] This process is demonstrated in a simple example where a field is backward projected toward the source and numerically modified with a synthetic phase pattern. The adjusted field is then projected away from the source. This projected field is found to closely correlate with hydrophone measurements when the transducer is driven with the new phase pattern.

II. MATERIALS AND METHODS

A. Apparatus

All experiments were performed in a water tank, depicted in Fig. 1. The inner walls of the tank were covered with rubber to prevent reflection and standing wave interference. A transducer (T) was rigidly mounted with its axes of propagation parallel with the long axis of the tank. A Precision Acoustics 0.5-mm PVDF hydrophone (H) was attached to a Parker 3D stepping motor-guided positioning system and scanned over the plane perpendicular to the acoustic axis. The hydrophone signal was amplified by a Precision Acoustics submersible preamplifier (PA) and recorded by a Tektronix TDS 380 oscilloscope (O). The hydrophone position and data acquisition were both computer controlled (C).

Three transducers, described in detail below, were used for the experiments. Each of the arrays consisted of fully isolated air-backed PZT elements. Each array in the study was powered by a phased-array driving system (DS) manufactured in-house, and equipped with power and phase feedback for increased control.[16] Individual channels of the arrays were equipped with impedance matching circuitry,

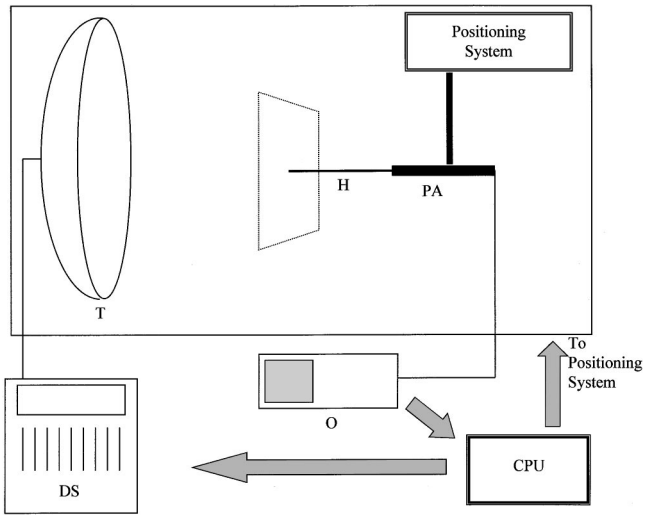

FIG. 1. Experimental setup for driving phased arrays and measuring the acoustic signal.

matching the channel to electrical resonance at 50 Ω, to assure maximum power output to the transducer. To accommodate the hydrophone in the focal region, all experiments were performed at low power, with total electrical inputs not exceeding 1 W.

In each experiment the hydrophone was scanned over a plane 10×10 mm^2 at steps of 0.4 mm and resulting in a sampling resolution of 2.5 pts/mm^2. While the hydrophone is not omnidirectional, the directivity of the hydrophone is nearly constant over the measured planes. A sensitivity drop of no less than -0.7 dB is expected for the frequencies and angles encountered in the planar measurements. For each sampled position, the time trace recorded by the oscilloscope was downloaded to a PC and Fourier transformed to obtain the amplitude and phase at the driving frequency of the transducer. Fields were measured in the planes at the geometric focus and 10 mm in front and behind the focus so that they could be compared with projected data. Additionally, a line scan was performed along the axis of propagation using the Parker positioning system. Data from the focal plane were then entered into the projection algorithm based on the relation described in Eq. (4) and propagated. The algorithm typically took less than 5 s to complete the projection using a 250-MHz Pentium processor with 128 MB of RAM.

A quantitative comparison of the measured and projected planes is performed using a rms measurement calculated for the difference in the amplitudes

$$R=\left[\frac{\Sigma_{i,j}^{M,N}(P_{ij}-P'_{ij})^2}{\Sigma_{i,j}^{M,N}(P_{ij})^2}\right]^{1/2}, \tag{5}$$

where P_{ij} is a measured amplitude point over an $M\times N$ matrix and P'_{ij} is an element of the projection.

B. Transducers

The first transducer considered is a 1.5-MHz 14-element concentric ring array[17] with both a diameter and radius of curvature of 100 mm, as shown in Fig. 2(a). The rings are all equal in width as measured perpendicular to the radial axis. The ultrasound focus is steered away from the geometric

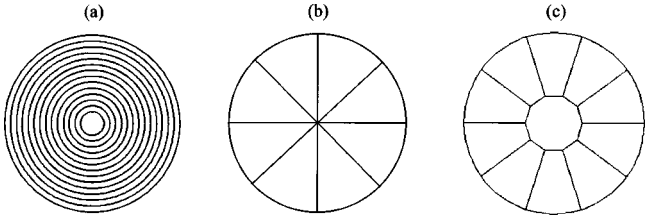

FIG. 2. Overhead view of focused phased arrays used in the study. (a) 14-element concentric ring array. (b) Eight-element sector vortex array. (c) A ten-sided center element with adjacent outer elements.

point of convergence by setting the contribution of individual elements in phase at the desired focal point. The transducer was operated with the focus shifted from 100 to 90 mm. Power to the elements was adjusted according to the ring surface area so that the intensity is uniform across the transducer.

The second array is an eight-element sector vortex array,[18] 1.1-MHz array with diameter of 100 mm and an 80-mm radius of curvature, depicted in Fig. 2(b). A sector vortex array consists of N symmetrical elements such that N is an even power of 2. The array can be driven to produce $N/2$ different acoustic field patterns by phase shifting. The phases for the elements of a sector vortex array are calculated as follows:

$$\theta_n = m \cdot n\left(\frac{2\pi}{N}\right), \tag{6}$$

where θ_n is the phase of element $n=0,1,...,N-1$, and $m \leqslant N/2$ is the mode of phase revolution. For the experiment the array was powered in modes zero and four.

The third array is an 11-element 0.67-MHz transducer with a diameter of 100 mm and a radius of curvature equal to 80 mm. The geometric configuration of the elements is shown in Fig. 2(c). Each of the elements in this array is driven in phase; however, the resulting field pattern presented differ from that of a uniform transducer due to uneven displacement across the elements.

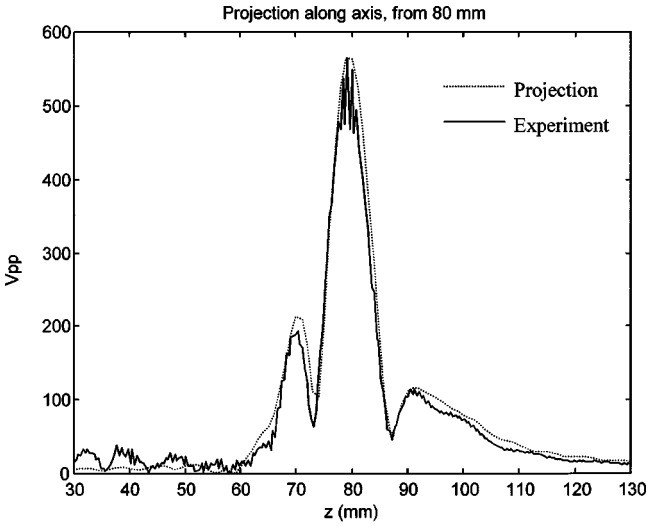

FIG. 4. The measured (solid) and projected (dotted) signals along the axis of propagation due to the sector vortex array driven in mode 0. Projections are from the plane at $z=80$ mm.

III. RESULTS

The sector vortex transducer in mode 0 was scanned over planes at distances of 65, 80, and 90 mm from the transducer face as shown in Fig. 3(a). Data along the plane at 80 mm [Fig. 3(a 2)] was entered into the projection algorithm and propagated to distances corresponding to the three measured planes, as displayed in Fig. 3(b). The 80-mm data in Fig. 3(b 1) simply represent a projected distance of 0 mm and serve to check the algorithm. Next, a line along the axis of propagation was measured between 30 and 130 mm from the transducer. The 80-mm planar data set was then projected over this line. The measured and projected data are displayed

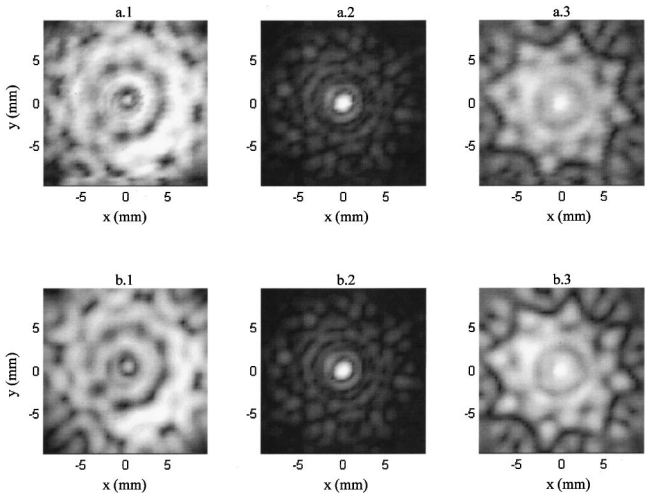

FIG. 3. (a) Radial measurements of the sector vortex array in mode 0, and (b) their corresponding projections. Image intensity is linearly scaled with the acoustic pressure amplitude. Fields are measured at distances of (a 1) 70 mm, (a 2) 80 mm, and (a 3) 90 mm form the source. Projection from $z=80$ mm to distances of (b 1) 70 mm, (b 2) 80 mm, and (b 3) 90 mm.

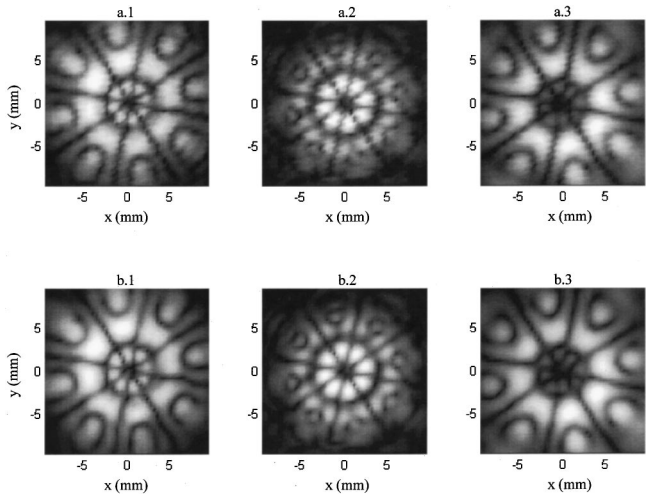

FIG. 5. (a) Radial measurements of the sector vortex array in mode 4, and (b) their corresponding projections. Image intensity is linearly scaled with the acoustic pressure amplitude. Fields are measured at distances of (a 1) 70 mm, (a 2) 80 mm, and (a 3) 90 mm from the source. Projection from $z=80$ mm to distances of (b 1) 70 mm, (b 2) 80 mm, and (b 3) 90 mm.

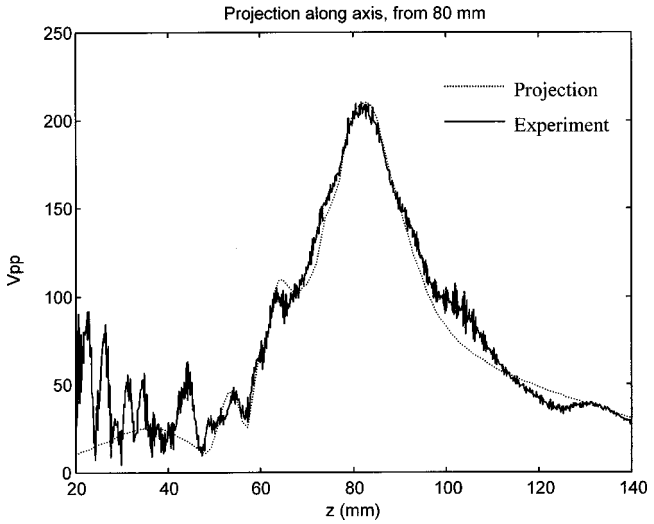

FIG. 6. The measured (solid) and projected (dotted) signals along the axis of propagation due to the concentric ring array focused at 80 mm. Projections are from the plane at $z=90$ mm.

in Fig. 4. The mean deviation across the line is 3% of the signal peak, with a maximum deviation of 20% occurring in the region close to the transducer.

The rms comparison given in Eq. (5) yielded values of 5.0% at 65 mm, 0.3% at 80 mm, and 0.6% at 90 mm. Next, the sector vortex transducer was operated in mode 4 and measurements were made in planes similar to those scanned in mode 0. Experimental results displayed in Fig. 5(a) may be compared with the projections shown in Fig. 5(b). The mode 4 projection produced rms difference values of 2.4% at 65 mm, 0.4% at 80 mm, and 2.2% at 90 mm.

Planar scans of the concentric ring array were performed at distances of 70, 80, and 90 mm from the transducer. Projections were calculated with data from 90 mm. Discrepancies of 1.0%, 1.4%, and 0.2% were calculated using Eq. (5). As with the concentric ring array, axial measurements were acquired and compared with a projection using the 90-mm data. The result is shown in Fig. 6. A mean deviation 5% of

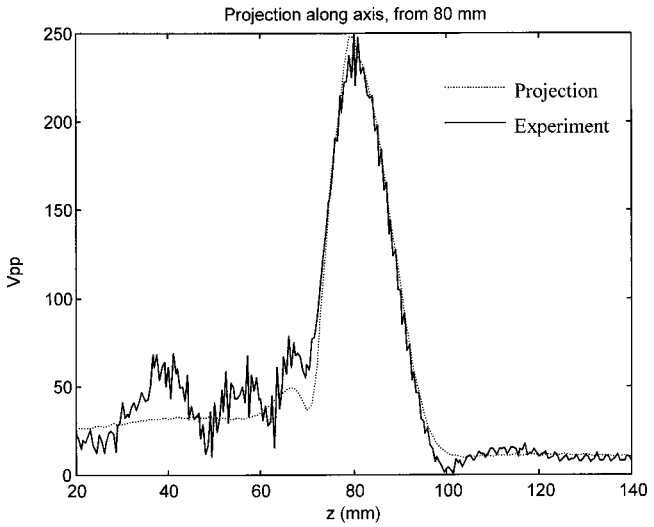

FIG. 7. The measured (solid) and projected (dotted) signals along the axis of propagation due to the 11-element array with all elements driven in phase. Projections are from the plane at $z=80$ mm.

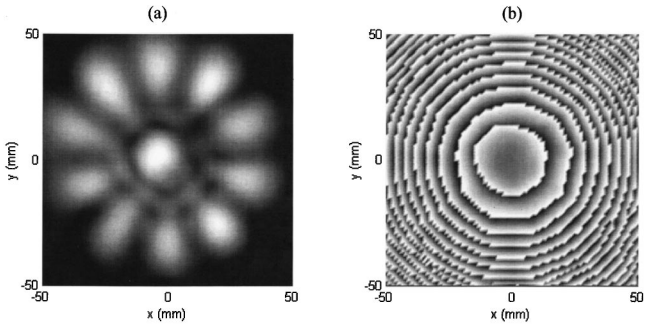

FIG. 8. Projection of the 11-element array's signal from 80 mm to the transducer. (a) A linear intensity plot of the acoustic pressure amplitude, and (b) the phase of the acoustic pressure.

the signal peak is found across the axis, with a maximum deviation of 30%.

The 11-element array was measured at 70, 80, and 90 mm. The associated rms discrepancies were 0.3%, 5%, and 0.6%, respectively. As with the sector vortex transducer, data from the 80-mm plane were projected. Results of the line scan are presented in Fig. 7, indicating a mean deviation of 4% of the maximum amplitude with a maximum deviation of 18%.

To illustrate the ability of the method to project toward the source, the acoustic field of the 11-element array is propagated close to the transducer face. In Fig. 8 the projection from 80 to 20 mm indicates that field information at the focus is sufficient to identify the radiation of the individual elements. The amplitude plot in Fig. 8(a) of this planar scan illustrates a lack of uniformity in amplitude across individual elements, while the phase plot in Fig 8(b) shows the expected radial phase shifting across the array. The sector vortex transducer driven in mode 4 was projected toward the transducer face, showing amplitude variation in Fig. 9(a) and phase variation in Fig. 9(b). For the case of large phased arrays, projections could be used to determine amplitude and phase corrections for each element, improving the overall ultrasound field.

Fields projected backward to the transducer could also provide computer models with more realistic source functions. This is demonstrated in the following: (i) The sector vortex field in mode 0 was measured near its focus [Fig. 3(a 2)]. (ii) The data were projected backward to the transducer ($z=17.6$ mm). (iii) A synthetic mode 4 planar phase

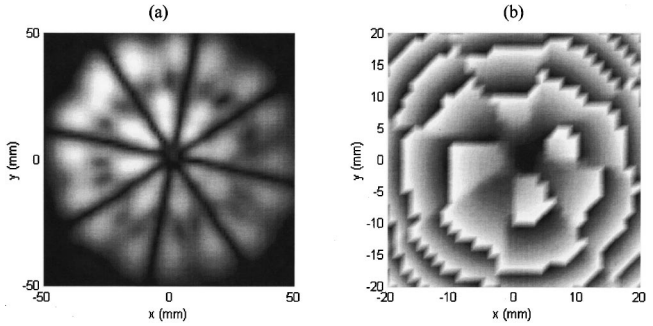

FIG. 9. Projection of the sector vortex mode 4 signal from 80 mm to the transducer. (a) A linear intensity plot of the acoustic pressure amplitude, and (b) the phase of the acoustic pressure.

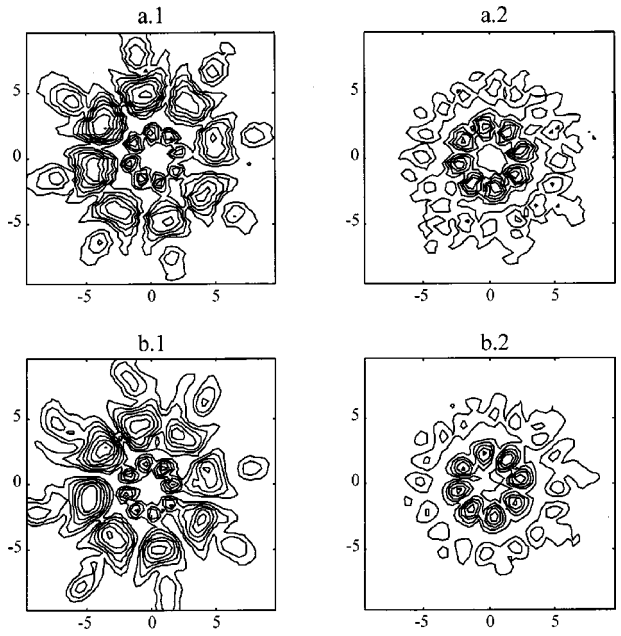

FIG. 10. Modeled mode 4 sector vortex field using mode 0 data projected from 80 mm to the transducer face, where a synthetic phase file is introduced. (a 1) Contour of the measured mode 4 field at 70 mm. (a 2) Contour of the measured mode 4 field at 80 mm. (b 1) The modeled field at 70 mm. (a 2) The modeled field at 80 mm. Contours lines are at 10% intervals of the signal amplitude.

file was generated and combined with the projected data. (iv) The new file was projected forward to 70 mm, resulting in the simulated field shown in Fig. 10(b 1). The field may be compared with the direct mode 4 measurement of Fig. 10(a 1). Similarly, the direct measurement and the corresponding modeled field at 80 mm are shown in Figs. 10(a 2) and 10(b 2).

IV. DISCUSSION

Projected fields presented in the previous section demonstrate excellent agreement with experimental measurement. An example of the algorithm's ability to reconstruct detailed lobe structure is seen in the amplitude values of the sector vortex mode 4 scan illustrated in Fig. 5(a). Looking along the radial direction, local maxima occurring before and after the signal peaks are found to be successfully reconstructed. Another feature apparent from comparing the experimental plots [Figs. 3(a) and 5(a)] with their projections [Figs. 3(b) and 5(b)] is the capacity of the algorithm to identify asymmetries in the field. The primary limitation to reconstruction of small features is the bandwidth of the spatial frequency. If required, the bandwidth could be increased by using a smaller hydrophone and increasing the sampling rate. It is stressed that the method assumes linear propagation through a homogeneous fluid and is limited to cases where this assumption holds.

A significant advantage of planar projection methods is their ability to identify asymmetries throughout the field from a single cross section of the field. Unexpected bias of the amplitude toward the fourth quadrant of the plane in Fig. 3(a 1) is also predicted by the backward projection of Fig. 3(b 1). Likewise, a peak in the second quadrant is predicted in the forward projection from 80 to 90 mm, Fig. 3(b 3), which also appears in the direct measurement, Fig. 3(a 3).

Planar projection allows fields to be calculated in areas that are normally difficult to measure, such as the high-intensity regions of a focused beam and at a distance close to the source where the hydrophone directionality can affect measurements. Although low-intensity ultrasound was used for the present experiment, the backward projection of the concentric ring array field into the focus could be performed for higher intensities, as long as the linear wave approximation is valid. Thus, a hydrophone designed for lower pressure fields could be used to predict a high-intensity focus. Discrepancy between the transducer and the hydrophone close to the source is observed in the axial scans shown in Figs. 6 and 7. The oscillations observed in the measured data may result from standing waves between the transducer and the hydrophone holder.

Projection of the field backward to the transducer could serve as a source function for a wide variety of modeling problems. Once propagated near the source, the original plane measured in a homogeneous medium can now be used as an accurate starting point in models that calculate fields through tissue and other heterogeneous layers. Further, from a single measurement the phase and amplitude of each element's response can be numerically adjusted to predict the field for additional field designs used for beam steering as well as multiple foci patterns.[15] This could be particularly useful in the case of arrays containing a large number of elements. The numeric phase shift presented in Fig. 10 demonstrates feasibility of numeric modification of the source function. In practice, large arrays may require several field patterns to be measured and projected to the surface in order to correctly adjust for element coupling.

V. SUMMARY

A linear planar projection algorithm was applied toward the projection of fields generated by focused phased arrays in water designed for therapeutic ultrasound. The algorithm provides a rapid and accurate method for characterizing a pressure field. Projection of a planar measurement to an arbitrary new plane takes under 5 s on a 250-MHz Pentium processor. Excellent correlation was observed between the projected data and direct measurements. The rms difference between the two planes was 5% or less for all distances considered. Further, the algorithm successfully identified peaks in the pressure amplitudes along the projected planes.

Several features of the algorithm are particularly appealing for use with focused therapeutic arrays. Direct measurements of the field in front of the transducer normally subject to interference can be projected backward from data near the focus where a much smaller area may be scanned. Field information near the face may be used for correction of the transducer driving signals. This information may also be used as a source function in conjunction with field modeling to be used for field control in heterogeneous tissues. In the case of high-intensity ultrasound, the focus of the transducer could be measured in a lower-intensity plane safe for a PVDF hydrophone and then projected into the converging

region. Finally, fast projection times allow asymmetries in the field or possible transducer defects to be quickly identified.

ACKNOWLEDGMENT

This work was supported by Grant No. CA 46627 from the National Institutes of Health.

[1] P. R. Stepanishen and K. C. Benjamin, ''Forward and backward projection of acoustic fields using FFT methods,'' J. Acoust. Soc. Am. **71**, 803–812 (1982).
[2] L. A. Frizzell, P. J. Benkeser, K. B. Ocheltree, and C. A. Cain, ''Ultrasound phased arrays for hyperthermia treatment,'' IEEE Ultrasonics Symp. **2**, 931–935 (1985).
[3] E. S. Ebbini and C. A. Cain, ''A spherical-section ultrasound phased array applicator for deep localized hyperthermia,'' IEEE Trans. Biomed. Eng. **38**(7), 634–643 (1991).
[4] D. R. Daum and K. Hynynen, ''Spherical phased array design optimized for ultrasound surgery,'' 1997 IEEE Ultrasonics Symposium Proceedings—An International Symposium, 1315 (1997).
[5] G. ter Haar, ''Therapeutic ultrasound,'' Eur. J. Ultrasound **9**(1), 3–9 (1999).
[6] F. J. Fry, N. T. Sanghvi, R. S. Foster, R. Bihrle, and C. Hennige, ''Ultrasound and microbubbles: their generation, detection and potential utilization in tissue and organ therapy—experimental,'' Ultrasound Med. Biol. **21**(9), 1227–1237 (1995)
[7] C. J. Vecchio and P. A. Lewin, ''Finite amplitude acoustic propagation modeling using the extended angular spectrum method,'' J. Acoust. Soc. Am. **95**, 2399–2408 (1994).
[8] X. Fan, E. Moros, and W. L. Straube, ''Acoustic field prediction for a single continuous-wave source using an equivalent phased array method,'' J. Acoust. Soc. Am. **102**, 2734–2741 (1997).
[9] X. Fan, E. Moros, and W. L. Straube, ''A concentric-ring equivalent phased array method to model fields of large axisymmetric ultrasound transducers,'' IEEE Trans. Ultrason. Ferroelectr. Freq. Control **46**(4), 830–841 (1999).
[10] G. T. Clement, R. Liu, S. V. Letcher, and P. R. Stepanishen ''Forward projection of transient signals obtained from a fiber-optic pressure sensor,'' J. Acoust. Soc. Am. **104**, 1266–1273 (1998).
[11] M. Forbes, S. V. Letcher, and P. R. Stepanishen, ''A wave vector, time-domain method of forward projecting time-dependent pressure fields,'' J. Acoust. Soc. Am. **90**, 2782–2793 (1991).
[12] R. Reibold and F. Holzer, ''Complete mapping of ultrasonic fields without the wavelength limit,'' Acustica **58**, 11–16 (1985).
[13] M. E. Schafer and P. A. Lewin, ''Transducer characterization using the angular spectrum approach,'' J. Acoust. Soc. Am. **85**, 2202–2214 (1989).
[14] K. Hynynen, ''The role of nonlinear ultrasound propagation during hyperthermia treatments,'' Med. Phys. **18**(6), 1156–1163 (1991).
[15] D. R. Daum and K. Hynynen, ''Theoretical design of a spherically sectioned phased array for ultrasound surgery of the liver,'' Eur. J. Ultrasound **9**(1), 61–69 (1999).
[16] D. R. Daum, M. T. Buchanan, T. Fjield, and K. Hynynen, ''Design and evaluation of a feedback based phased array system for ultrasound surgery,'' IEEE Trans. Ultrason. Ferroelectr. Freq. Control **45**(2), 431 (1998).
[17] T. Fjield, X. Fan, and K. Hynynen, ''A parametric study of the concentric-ring transducer design for MRI guided ultrasound surgery,'' J. Acoust. Soc. Am. **100**, 1220–1230 (1996).
[18] C. A. Cain and S. A. Umemura, ''Concentric-ring and sector vortex phased array applicators for ultrasound hyperthermia therapy,'' IEEE Trans. Microwave Theory Tech. **MTT-34**, 542–551 (1986).

LETTERS TO THE EDITOR

This Letters section is for publishing (a) brief acoustical research or applied acoustical reports, (b) comments on articles or letters previously published in this Journal, and (c) a reply by the article author to criticism by the Letter author in (b). Extensive reports should be submitted as articles, not in a letter series. Letters are peer-reviewed on the same basis as articles, but usually require less review time before acceptance. Letters cannot exceed four printed pages (approximately 3000–4000 words) including figures, tables, references, and a required abstract of about 100 words.

Near-field–far-field measurement of loudspeaker response

John L. Butler and Charles H. Sherman
Image Acoustics, Inc., 97 Elm Street, Cohasset, Massachusetts 02025

(Received 22 February 2000; accepted for publication 4 April 2000)

An improved method of determining the low-frequency far-field response of a loudspeaker, or other transducer, from near-field measurements is presented. The method is based on modeling the transducer as a thin disk vibrating uniformly on one side. © *2000 Acoustical Society of America.* [S0001-4966(00)02407-3]

PACS numbers: 43.58.Vb, 43.38.Dv [SLE]

We derive a new numerical factor that relates the near field measured at the center of a transducer to the far field on the axis of the transducer. In 1974 Keele[1] used the well-known field on the axis of a uniformly vibrating baffled piston (case 1) to derive such a relationship. His result for the pressure in the far field at distance z, when the piston radius is small compared to the wavelength, can be expressed as

$$p_1(z)=[a/(2z)]e^{ikz}p_1(0), \tag{1}$$

where a is the radius of the piston, k is the wave number, and $p_1(0)$ is the pressure on the surface of the piston at the center. The numerical factor $[a/(2z)]$ relating the measured near-field magnitude to the desired far-field magnitude has often been used for loudspeaker measurements, although the baffled piston is clearly not a good model for most loudspeakers.

In 1994 Struck and Temme[2] pointed out that a better model would be an unbaffled piston vibrating on one side (case 2), where $p_2(z)$ would be related to $p_2(0)$ in the same way as Eq. (1) except for an additional factor of $\frac{1}{2}$ on the right-hand side. D'Appolito[3] includes this additional factor of $\frac{1}{2}$ in his book on testing loudspeakers. The factor $\frac{1}{2}$ is the correct difference between cases 1 and 2 in the far field, but it is not correct in the near field. The relation valid at all distances, obtained from superposition of boundary conditions, is

$$p_2(z)=\tfrac{1}{2}[p_1(z)+p_3(z)], \tag{2}$$

where $p_3(z)$ is the pressure for the unbaffled piston vibrating as a rigid body (case 3). Since case 3 is a dipole source, which has a negligible far field compared to cases 1 and 2 when $ka\ll 1$, $p_2(z)\approx\frac{1}{2}p_1(z)$ in the far field. However, $p_3(z)$ is not negligible in the near field, and the factor $\frac{1}{2}$ does not convert Eq. (1) from case 1 to case 2.

The correct factor can be found by use of Silbiger's[4] calculation for case 3 (which he calls the free piston) for which the pressure on the surface at the center for $ka\ll 1$ is

$$p_3(0)=\rho cV(-i2ka/\pi), \tag{3}$$

where ρ and c are the density and sound speed of the medium and V is the velocity of the piston. The pressure on the surface at the center for case 1 is

$$p_1(0)=\rho cV(-ika), \tag{4}$$

and from Eq. (2)

$$p_2(0)=\rho cV(-ika)\left[\frac{1}{\pi}+\frac{1}{2}\right]=p_1(0)\left[\frac{1}{\pi}+\frac{1}{2}\right]. \tag{5}$$

Since $p_2(z)\approx\frac{1}{2}p_1(z)$ in the far field, use of Eqs. (1) and (5) now gives

$$p_2(z)\approx[a/(2z)][\pi/(2+\pi)]e^{ikz}p_2(0). \tag{6}$$

Thus the correct factor for converting Eq. (1) to the model of an unbaffled piston vibrating on one side is $\pi/(2+\pi)=0.611$, rather than the Struck and Temme factor of 0.5.

We summarize using terminology similar to D'Appolito's:

$$\text{far-field response}=\text{near-field response}-20\log(fz/a)\ \text{dB}, \tag{7}$$

which gives the far-field response at distance z of a speaker with effective diaphragm radius a where the factor f is:

Keele: $f=2$, for a source in an infinite baffle radiating into 2 π space;

Struck and Temme: $f=4$, first approximation for an unbaffled source radiating into 4 π space;

this paper: $f=2[(2+\pi)/\pi]=3.27$, for a thin back-enclosed source radiating into 4 π space.

The difference in the last two cases of 1.74 dB may often be significant when near-field measurements are used to evaluate the far-field low-frequency response of loudspeakers or other piston-type transducers in air or water.

[1] D. B. Keele, Jr., ''Low-frequency loudspeaker assessment by near-field sound pressure measurements,'' J. Audio Eng. Soc. **22**, 154–162 (1974).

[2] C. J. Struck and S. F. Temme, ''Simulated free field measurements,'' J. Audio Eng. Soc. **42**, 467–482 (1994).

[3] J. A. D'Appolito, *Testing Loudspeakers* (Audio Amateur, Peterborough, NH, 1998), pp. 61–62.

[4] A. Silbiger, ''Radiation from circular pistons of elliptical profile,'' J. Acoust. Soc. Am. **33**, 1515–1522 (1961).

A comparative study of transforms for use in digital audio data compression

B. E. Rulon
Lexmark International, Inc., Lexington, Kentucky 40550

M. F. Shaw and K. D. Donohue[a)]
Department of Electrical Engineering, University of Kentucky, Lexington, Kentucky 40506-0046

(Received 18 March 1999; accepted for publication 6 April 2000)

This paper provides a subjective quality analysis of transforms used in audio compression algorithms for a class of music signals. A 34-subject listener test compares three transforms in conjunction with an MPEG I layer 1 compression scheme. One test compares the performances of the discrete wavelet packet transform (DWPT) and the modified discrete cosine transform (MDCT) used in MPEG. Another test compares the performances of a DWPT eight-level nonuniform critical-band split and a DWPT five-level uniform subband split. Results indicate that the critical-band split provides significantly better quality than the uniform subband split for sounds with tonal and strong low-frequency content, while the DWPT outperforms the MDCT with significant improvement for nontonal sounds. © *2000 Acoustical Society of America.* [S0001-4966(00)03907-2]

PACS numbers: 43.60.Gk, 43.58.Ta [JCB]

INTRODUCTION

This paper evaluates three audio compression schemes, where the basic shell is the industry standard MPEG Audio Layer I,[1] which is shown in Fig. 1. The compression schemes analyzed in this paper differ only in their transform filter bank, which is either a discrete wavelet packet transform (DWPT) with uniform subbands, a DWPT with nonuniform subbands (which more closely resembles the psychoacoustic critical-band model of human hearing), or a conventional modified discrete cosine transform (MDCT). This study differs from others that have compared coding schemes with different transforms,[2–5] in that this work directly examines the performance enhancement from the various filter bank transforms by keeping the rest of the encoder the same. Performance is evaluated over a class of music signals at different compression levels by identifying the highest compression level at which no distortion could be detected using a large-scale subjective listening test. The purpose for this approach is to understand the performance contribution of the transform to the compression scheme.

The issue concerning performance enhancement resulting from a critical-band split versus a uniform subband split has been addressed in the literature,[4–8] where opinions vary on whether or not the benefits of the additional compression gain from a critical-band split outweigh the additional complexity. This work contributes to the discussion by considering the significance of the performance gain over a class of musical signals using a computationally efficient DWPT.[3]

Figure 1 shows how each transform fits in with the compression scheme. The encoder consists of a filter bank, psychoacoustic model, bit allocation scheme, and bitstream formatting. The input signal passes through the filter bank and psychoacoustic model simultaneously. The filter bank (wavelet or MDCT) transforms the signal into coefficients that are quantized for transmission or storage. The bit allocation incorporates a psychoacoustic model to quantize each coefficient such that the quantization error is the least audible. The bitstream formatting arranges the bits for transmission or storage. Details of the MPEG coding scheme and the psychoacoustic model can be found elsewhere in the literature.[1,9,10]

I. TRANSFORM PROPERTIES

Wavelet transforms use basis functions that are not necessarily continuous, and in some cases, vanish outside compact intervals. Cosine transforms, on the other hand, use sinusoidal basis functions, which are continuous, smooth, and infinitely supported in time. Tonal sounds (local concentration of energy in the frequency domain) are produced by instruments like the clarinet and strings, and are efficiently represented by frequency-localized functions like the sinusoid, while transient sounds (local concentration of energy in the time domain) are produced by instruments like the drums or castanets, and are better represented with time localized functions, such as wavelets.

Both the uniform subband and critical-band wavelet decompositions used in this paper to obtain the transform coefficients consisted of a 40-coefficient Daubechies wavelet filter bank, as suggested by Sinha and Tewfik.[4] The transforms for both the MDCT and DWPT were implement using MATLAB,[11] in conjunction with WAVELAB.[12] Detailed properties of the wavelets used in this work are provided by Daubechies.[13]

The critical-band split for the filter bank more closely models how the human ear responds to different frequencies, which has higher frequency resolution in the lower frequency range. The dyadic nature by which the wavelet

[a)]Author to whom correspondence should be addressed; electronic mail: donohue@engr.uky.edu

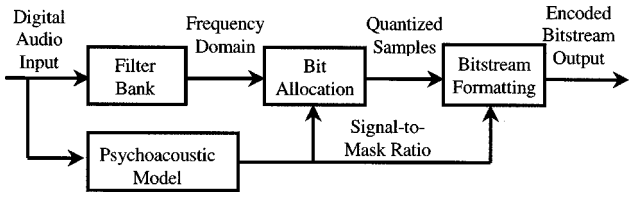

FIG. 1. Block diagram of the MPEG I audio layer 1 encoder.

packet filter bank divides the frequency range limits flexibility in band selection. Therefore, critical bands were approximated with the natural dyadic division corresponding to the DWPT. Table I shows the 29 frequency bands used in the DWPT critical-band split. A fixed tree for the DWPT was used primarily to model the critical-band and uniform band splits. However, more efficient decompositions may be obtained with wavelet packets using adaptive trees or a best-basis approach, with additional complexity added to the overall compression scheme.[2]

The critical-band split requires that the DWPT decompose the signal down to eight levels in the lower frequency range. While an eight-level uniform subband decomposition (over the whole frequency range) would have 256 frequency bands, such resolution would escalate the time required in the quantization loop and decomposition stage of the decoder. As it stands, the critical-band split keeps the number of frequency bands comparable to the subband split (29 to 32, respectively), while providing a distribution of time–frequency resolution similar to that of the human ear.

Due to the different time–frequency localization characteristics of the basis functions used in each transform, it is expected that the MDCT would perform better on the tonal clips and that the DWPT would do better with the transient clips. This is illustrated in Figs. 2–4. Examples of frames (used in the compression algorithms) containing a signal produced by strings and castanets are shown in Figs. 2(a) and 2(b), respectively. These signals were sampled at 44.1 kHz and each segment contained 2048 samples.

The squared transform coefficients for the strings signal are shown in Fig. 3. Notice that the squared amplitude for the

TABLE I. Critical bands used in the wavelet packet decomposition.

Frequency band	Lower cutoff (Hz)	Upper cutoff (Hz)	Frequency band	Lower cutoff (Hz)	Upper cutoff (Hz)
1	0	90	16	2800	3 100
2	90	170	17	3100	3 400
3	170	260	18	3400	4 100
4	260	340	19	4100	4 800
5	340	430	20	4800	5 500
6	430	520	21	5500	6 200
7	520	690	22	6200	6 900
8	690	860	23	6900	8 300
9	860	1030	24	8300	9 600
10	1030	1200	25	9600	11 000
11	1200	1400	26	11000	13 800
12	1400	1700	27	13800	16 500
13	1700	2100	28	16500	19 300
14	2100	2400	29	19300	22 000
15	2400	2800	⋯	⋯	⋯

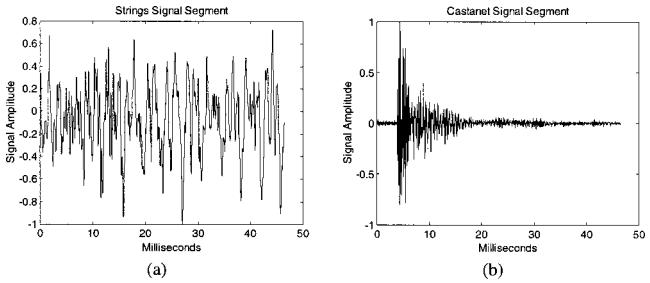

FIG. 2. (a) Example frame from a strings sound. (b) Example frame from a castanets sound.

largest DCT coefficient is about three times greater than the largest coefficients for wavelet transforms. This implies that the basis functions for the DCT capture the dominant dynamics of the signal more efficiently (since total energy for all transforms of the signal is equal, a higher amplitude coefficient implies more energy captured in fewer coefficients). The distribution curves in Fig. 3(d) illustrate the efficiency of the transforms more directly. Each curve results from applying a series of increasing thresholds (abscissa of the plot) to the coefficient amplitudes and computing the percentage of energy in the coefficients exceeding the threshold. More energy stored in fewer coefficients implies a more efficient representation of the signal, and thus the potential for better compression capabilities.

Notice from Fig. 3(d) that for a broad range of thresholds the DCT coefficients contain about 30% more energy than the uniform subband DWPT coefficients (and an even greater margin for the critical-band DWPT coefficients). Relative to the entire strings signal clip, the signal segment shown in Fig. 3 is an example of a median efficiency frame segment (i.e., 50% of the segments had better efficiency and 50% had worse). For some segments, the wavelet coefficients were actually more efficient; however, this occurred in less than 5% of the cases and was typically in segments

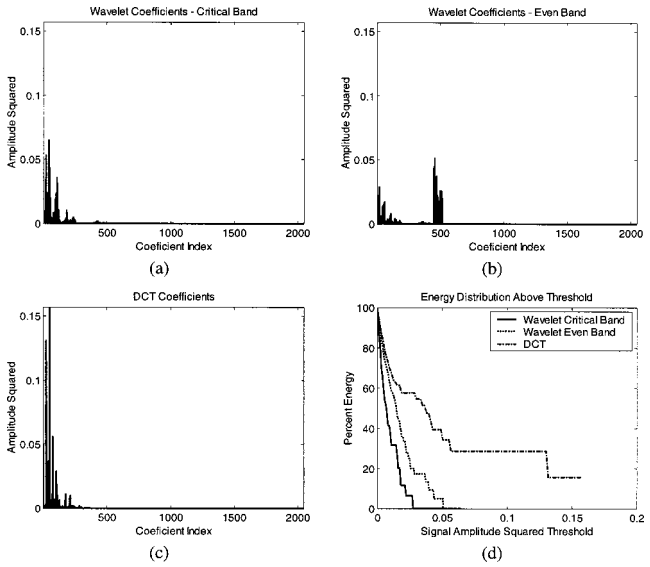

FIG. 3. Example string's frame transform coefficients squared for (a) critical-band DWPT, (b) uniform subband DWPT, and (c) DCT. (d) Percent energy in coefficients as a function of an applied threshold.

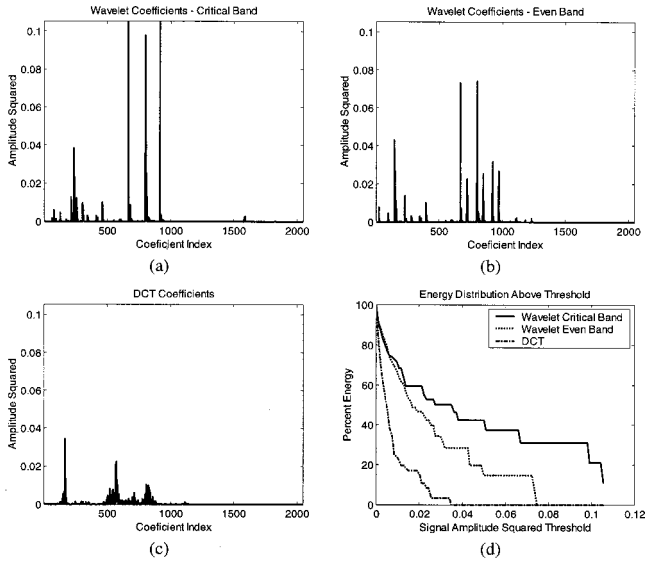

FIG. 4. Example transforms coefficients for castanets' frame for (a) critical-band DWPT, (b) uniform subband DWPT, and (c) DCT. (d) Percent energy in coefficients as a function of an applied threshold.

containing a transition from one note to the next, or a rapid amplitude change.

Figure 4 shows the efficiency of the transform coefficients for the castanets, analogous to what is shown for the strings in Fig. 3. In this case, Fig. 4(d) indicates that the critical-band wavelet coefficients contain about 20% more energy than the uniform subband wavelet coefficients for most of the thresholds and about 40% more energy than the DCT coefficients. The effects of increased efficiency for transient signals using the critical-band wavelet coefficients will be observed in the listen tests discussed in Sec. III. Other sound clips were also examined with this efficiency analysis. For most frames (more than 75%), the DCT was the better basis. This advantage, however, was not observed in the listening test results, as will be seen in Sec. III.

II. THE LISTENING TEST

The sound clips used for the subband-versus-critical-band test were taken from a CD recording of bongos, clarinet, piano, strings, vocals, and orchestra. For the DWPT-versus-MDCT comparisons, sound clips were taken from recordings of bongos, castanets, a clarinet playing a single note (clarinet 1), a clarinet playing two different notes (clarinet 2), drums, a piano playing a chord (piano 1), a piano playing several distinct notes (piano 2), and an orchestra. The clips were selected to give examples of tonal, transient, and mixed signals. Tonal sounds produced by the clarinet or strings exhibit highly localized spectral energy, while transient sounds produced by the castanets or bongos exhibit localized energy in the time domain. The mixed sounds of the piano clips show characteristics of both.

Once the music was recorded, it was converted into a raw data file for use in the compression algorithms. All of the coding and decoding was done directly in a MATLAB using the WAVELAB subroutines.[12] The window size for the transforms used in compression was 2048 points (46 ms), with 50% overlap for each frame.

TABLE II. Average compression rates from listening test with 95%-confidence limits and significance of performance difference for the DWPT uniform subband transform versus critical-band transform comparison.

Instrument	Uniform subband Average kbit/s	Critical-band average kbit/s	Percent significance of the difference
Bongos	112±5.0	112±4.6	0
Clarinet 1	155±8.8	140±8.2	99.5
Piano 1	126±4.4	83±7.8	99.5
Strings	172±9.2	166±11.4	72.5
Vocals	151±4.4	129±0.8	99.9
Orchestra	159±7.7	155±7.8	52.4

The subjects for the listening tests were recruited from the University of Kentucky's Department of Electrical Engineering. This group included professors and students with a wide range of musical skills and listening habits. An initial group of 40 listeners was subjected to a screening test to reject outliers. A hearing spectrum test and a corrupted tone test, as presented by Houtsma *et al.*,[14] was used to reject six of the listeners whose hearing characteristics differed significantly from the rest of the listeners. Thus, the results of the compression algorithm evaluations were taken from a group of 34 people.

The compression level of a signal for each method was increased in increments of 32 kbits/s until the listener was able to correctly identify a loss in signal quality relative to the original uncompressed sound. The clips were presented in pairs of compressed and uncompressed files starting with the lowest compression factor, and the listener was asked to pick out the compressed sound. If the listener could not do this, the next higher compression factor was used. The compression factor was increased until the listener could consistently identify the compressed clip. A response was considered consistent if a correct selection was given three times in a row. Also, before each instrument type was administered, the original was played twice along with a severely compressed clip to demonstrate how the distortion may sound. The participants were allowed to hear each pair up to two times and could listen to the original clip at any time as a frame of reference.

III. PERFORMANCE RESULTS

Tables II and III present results in terms of the average rate for the compressed signal computed over the 34 listen-

TABLE III. Average compression rates from listening test with 95%-confidence limits and significance of performance difference for the DWPT uniform subband transform versus MDCT comparison.

Instrument	DWPT average kbit/s	MDCT average kbit/s	Percent significance of the difference
Bongos	151±7.0	212±8.3	99.9
Castanets	186±6.4	267±13.4	99.9
Clarinet 1	116±3.0	116±2.8	16.9
Clarinet 2	116±2.6	117±2.9	69.6
Drums	132±4.8	180±15.1	99.9
Piano 1	76±3.1	76±3.8	8.65
Piano 2	124±3.4	184±15.1	99.9
Orchestra	148±7.3	150±7.6	51.2

ers. The 95%-confidence limits are also given, along with the significance of the rate difference based on a *t*-test. Similar music clips were played for each comparison test; however, the clip length was longer (5 to 11 s) for the comparisons of Table II. For Table III results, the clips were 2- to 4-s long, which resulted in an improved ability for the listener to compare two sounds and detect distortion at lower compression rates. This difference is not critical for the comparative results of this work. However, as seen in the differences between the DWPT rates for both tables with similar music clips, absolute performance numbers can vary significantly depending on the nature of the listening test.

The results of the critical-band versus uniform subband split, given in Table II, show that the critical-band split consistently outperforms the uniform subband split for all signals used in the test. Significant improvement was noted for three music clips (clarinet, piano, and vocals). The critical-band split performed much better for the piano, vocal, and clarinet pieces because of the dominant low-frequency content in these signals and the higher frequency resolution provided by the critical-band split in the lower frequency range. The higher frequency resolution at low frequencies results in spreading the quantization error in the lower bands more evenly throughout the lower frequency bands.

The relative performance gain of the critical-band split over the uniform subband decreases for signals with significant energy in the higher frequency range or more transient in nature as seen in the case of the bongos, strings, and orchestra. Since the decomposition doesn't exceed the fifth level for frequencies higher than 6.9 kHz, the energy in higher frequency bands is assigned fewer quantization bits than in the even-band encoder causing more distortion in the higher frequencies. The relative performance decrease in this case is due to the increased number of significant coefficients in the higher frequency bands for these signals. Table II, however, indicates that these effects did not degrade the performance of the critical-band encoder below that of the uniform subband encoder.

Table III presents the results for the MDCT versus the uniform subband DWPT test. These results used shorter music clips (2 to 4 s) than the tests in Table II, which enabled the listener to better remember the dynamics of a previously played clip and detect distortion at a lower compression level. (This is observed in comparing the bongos clip result for the equal subband in both Tables II and III.) In general, improvement is more significant for the MDCT versus DWPT test than for the uniform subband versus critical-band test. As shown in the previous section, the MDCT provides a more efficient characterization for tonal signals than the DWPT. Therefore, it was expected that the MDCT would do better with tonal signals. However, the MDCT never performed significantly better than the DWPT for the tonal sounds. This result was unexpected since the efficiency of the MDCT basis function is much better in these cases.

The superior results for the DWPT in these tests indicates a psychoacoustic effect, where listeners' ability to perceived distortions due to quantization error is more enhanced for transient dynamics over tonal. The wavelet transforms showed more efficiency than the DCT for frames corresponding to the transient dynamics, and thus less quantization error was associated with these frames for the DWPT. The test results suggest the listeners were more sensitive to errors associated with a transient signal, since for the tonal components, the DWPT yields more quantization error, and yet no significant preference was given to the MDCT in these cases.

IV. CONCLUSION

It has been demonstrated that the critical-band split outperforms or matches the uniform subband split for compressing signals with strong low-frequency content. In the best case (piano playing chords), and additional 43 kbits/s compression was accomplished using the critical-band split. It has also been shown that the DWPT outperforms the MDCT for compressing signals containing transients with varying attack and decay properties. In the extreme case of castanets, a difference of about 80 kbits/s was obtained at a 99.9%-significance level. It has also been shown that compressing music with strong tonal qualities does not show significant differences between the MDCT and DWPT.

Additional improvement in quality for the DCT transform may be obtained by choosing a smaller time window for processing frames, resulting in more time localization. This would improve the ability of both DCT and wavelet transforms for compressing frames containing transient signals. However, a smaller frame would also reduce the low-frequency resolution, which was critical in providing an advantage for the critical-band split over the equal subband split. From the results of this study, no clear conclusion can be drawn on how changes in the frame size would affect total performance.

[1] ISO/IEC 11172-3, ''Information technology—Coding of moving pictures and associated audio for digital storage media at up to about 1.5 Mbits/s (Part 3: Audio),'' August 1993.

[2] P. Srinivasan and L. H. Jamieson, ''High-quality Audio Compression Using an Adaptive Wavelet Packet Decomposition and Psychoacoustic Modeling,'' IEEE Trans. Signal Process. **46**(4), 1085–1093 (1998).

[3] R. A. Wannamaker and E. R. Vrscay, ''Fractal Wavelet Compression of Audio Signals,'' J. Audio Eng. Soc. **45**, 540–553 (1997).

[4] D. Sinha and A. H. Tewfik, ''Low Bit Rate of Audio Compression using Adapted Wavelets,'' IEEE Trans. Signal Process. **41**(12), 3463–3479 (1993).

[5] J. D. Johnston, ''Transform Coding of Audio Signals Using Perceptual Noise Criteria,'' IEEE J. Sel. Areas Commun. **6**(2), 314–323 (1988).

[6] J. Watkins, *Compression in Audio and Video* (Focal, Oxford, 1995).

[7] Y. Sung and J. Yang, ''An Audio Compression System Using Modified Transform Coding and Dynamic Bit Allocation,'' IEEE Trans. Broadcasting **40**(4), 255–259 (1993).

[8] Y. Mahieux and J. P. Petit, ''High Quality Audio Transform Coding at 64 kbps,'' IEEE Trans. Commun. **42**(11), 3010–3019 (1994).

[9] E. Zwicker and E. Feldtkeller, *Psychoacoustics, Facts and Models* (Masson, Paris, 1981).

[10] Barron E. Rullon, ''A Comparative Study of Transforms For Use in Digital Audio Data Compression,'' Masters thesis, University of Kentucky, May 1997.

[11] MATLAB©, Version 4.2c, The MathWorks, Inc., Natick, MA, Nov. 1994.

[12] D. Donoho, X. Huo, and T. P.-Y. Yu, WAVELAB, Software routine, Stanford University, Standford, CA, 1997.

[13] I. Daubechies, ''Orthonormal Bases of Compactly Supported Wavelets,'' Commun. Pure Appl. Math. **41**(7), 909–996 (1988).

[14] A. J. M. Houtsma, T. D. Rossing, and W. M. Wagenaars (Acoustical Society of America), Audio Demonstrations IPO NIU ASA, West Germany: Philips, 1 September 1987.

The role of magnesium in the susceptibility of soldiers to noise-induced hearing loss

Brian E. Walden[a] and Lynn W. Henselman
Army Audiology and Speech Center, Walter Reed Army Medical Center, Washington, D.C. 20307-5001

Elena R. Morris
Department of Clinical Investigation, Walter Reed Army Medical Center, Washington, D.C. 20307-5001

(Received 2 February 1999; revised 19 January 2000; accepted 28 March 2000)

A number of studies have demonstrated that magnesium, administered prophylactically, can reduce the amount of hearing loss resulting from noise exposure. This study explored the possible role of naturally occurring body magnesium concentration in susceptibility of soldiers to noise-induced hearing loss. Participants were 68 adult males who had received extensive noise exposure over several years as a result of training with weapon systems. Each participant provided a pure-tone audiogram, blood sample, and noise-exposure history. A variety of pure-tone indices was correlated with serum magnesium levels as determined by atomic absorption spectroscopy. No significant correlations were observed between any audiometric index and body magnesium. The results of this study, therefore, do not support the hypothesis that there is a strong association between naturally occurring body magnesium and susceptibility to noise-induced hearing loss.
[S0001-4966(00)02507-8]

PACS numbers: 43.66.Sr, 43.64.Gz [SPB]

INTRODUCTION

It is well known that prolonged exposure to intense noise can cause hearing loss. The amount of hearing loss and cochlear damage resulting from noise exposure depends upon the intensity, spectral composition, and duration of the exposure. However, the amount of hearing loss that results from a given exposure varies considerably across individuals. The underlying determinants of individual susceptibility to noise-induced hearing loss (NIHL) are unknown, although a number of biological determinants have been suggested as contributing factors (Salvi *et al.*, 1998). Magnesium (Mg) is a common element of the body essential to regulating cell membrane permeability and energy consumption. It has been hypothesized that low levels of body Mg may increase susceptibility to NIHL by increasing cochlear hair-cell energy consumption under conditions of extreme exposure (Attias *et al.*, 1994).

Most of the Mg in the body is contained in the bone and soft tissue. Although only about 1% of body Mg is in the blood cells and plasma, the most frequently used clinical method for characterizing body magnesium level is to measure its concentration in the extracellular serum (SMg), using atomic absorption spectroscopy. In a normal population, SMg follows a Gaussian distribution within a fairly narrow range (approximately 0.60 to 1.1 mmol/L) (Danielson *et al.*, 1979; Djurhuus *et al.*, 1995).

Several aspects of Mg metabolism should influence the potential clinical value of naturally occurring body Mg as a predictor of individual susceptibility to NIHL. First, SMg varies considerably across the normal range with dietary intake of Mg. As a result, SMg level can fluctuate significantly within an individual during a 24-h period (Szyszka *et al.*, 1992). Second, in order for a predictive relationship to exist, relative Mg levels for a group of individuals must remain stable over the many years that are typically necessary to acquire a significant NIHL. Similarly, intersubject variations in naturally occurring Mg levels must be significantly greater than intrasubject variations. Although there is not complete agreement on these latter two issues, it appears that body Mg level does not vary systematically with age (Danielson *et al.*, 1979; Lowenstein and Stanton, 1986; Yang *et al.*, 1990; however, see Duncanson and Worth, 1990) and that the normal variations observed within a single individual are typically smaller than those observed across individuals (Djurhuus *et al.*, 1995).

Several reports suggest that the amount of hearing loss resulting from noise exposure can be manipulated by altering Mg levels, both in animals (Ising *et al.*, 1982; Joachims *et al.*, 1983; Boyev *et al.*, 1997; Scheibe and Haupt, 1998) and in humans (Attias *et al.*, 1994). In these studies, body Mg levels were controlled through diet or injections, and influenced the amount of NIHL that resulted from noise exposure. Although these reports suggest that either elevating or lowering Mg levels outside the normal range can influence the amount of NIHL that results from a relatively brief period of intense noise exposure (e.g., a few hours or days), these findings are not directly applicable to more typical cases of NIHL in which Mg levels are maintained within the normal range and the hearing loss accumulates from exposures over a period of many years.

In apparently the only study of its kind reported to date, Joachims *et al.* (1987) explored the relationship between naturally occurring levels of body Mg and NIHL in a group of 24 Israeli Air Force pilots who had been ''frequently exposed to noise levels above 90 dB(A)'' (Joachims *et al.*, 1987, p. 130). The ages ranged from 21 to 47 years ($M = 32.5$).[1] The authors did not report the number of years of

[a]Author to whom correspondence should be addressed.

exposure, although it was likely to have varied widely because of the age range included. Similarly, whether the participants had routinely used hearing protection was not reported. Pure-tone thresholds were obtained in the frequency range from 0.25–8 kHz. Thresholds at 3, 4, and 6 kHz were averaged and age-corrected to provide a measure of NIHL for each participant. The age-corrected pure-tone average (PTA_{AC}) ranged from 2–39 dB HL ($M=21.3$). A blood sample was taken, and serum magnesium (SMg) was measured for each participant via atomic absorption spectroscopy (AAS). A correlation coefficient of $r=-0.61$ ($p<0.0001$)was observed between the PTA_{AC} and SMg levels across the 24 participants.

The results of Joachims *et al.* (1987) are quite remarkable in that more than a third of the variance in NIHL observed among their subjects was attributable to normal variations in SMg. Given the wide range of ages among these pilots (26 years) and length of military service, the total exposure to hazardous noise undoubtedly varied considerably across the 24 subjects. Presumably, differences in noise exposure should account for much of the variance in NIHL across these pilots. The results of Joachims *et al.*, therefore, suggest that normal variations in SMg levels may be a highly significant factor in determining susceptibility to NIHL. This study sought to replicate the Joachims *et al.* (1987) results in a larger sample of U.S. Army soldiers who had significant long-term exposure to weapon systems and who were more homogeneous in age and total noise exposure than the pilots studied by Joachims *et al.* (1987).

I. METHOD

A. Subjects

The subjects of this study were 68 male soldiers, recruited from the U.S. Army John F. Kennedy Special Warfare Center and School, Ft. Bragg, N.C. Participants were 26–37 years old ($M=31.7$) and had 8–18 years ($M=12.3$) of military service that involved frequent exposure to high-level weapon noise. As part of the Army's hearing conservation program, participants typically used personal hearing protection when exposed to hazardous noise.

Variations in noise exposure history and other potential intervening variables were controlled experimentally through subject selection. Participants were recruited from a single combat unit and had routinely been exposed to similar high-level weapon noise over a number of years. Compared to the pilots in the Joachims *et al.* (1987) study, the soldiers included in this investigation were relatively similar in age, length of service, and noise exposure history. A written survey was administered to each participant that provided a detailed chronology of their noise exposure history. These questionnaires were reviewed to assure that all soldiers enrolled in the study had a similar history of frequent exposure to weapon systems over a number of years.

Potential participants were screened for medical problems such as diabetes mellitus, renal disorders, thyroid disease, parathyroid disease, chronic gastrointestinal disease, adrenal gland disorder, and other disorders requiring use of diuretic therapy. All of these conditions are known to affect Mg metabolism and precluded participation in the study. Additionally, alcohol ingestion, antacid ingestion, magnesium or mineral supplements, diarrhea, starvation, excessive sweating, or dehydration can alter SMg. Consequently, participants were screened for these conditions as well.

B. Procedures

1. Pure-tone audiogram

Pure-tone air-conduction thresholds were measured at 0.25, 0.5, 1, 1.5, 2, 3, 4, 6, and 8 kHz bilaterally by means of the Carhart and Jerger (1959) modification of the Hughson–Westlake ascending technique. If a threshold exceeded 15 dB HL (ANSI, 1989) at 0.25, 0.5, 1, 1.5, 2, 3, or 4 kHz, bone-conduction thresholds were measured to rule out a conductive component. If an air–bone gap of 15 dB or greater was observed for a potential participant at any frequency from 0.5 to 4 kHz, he was excluded from the study. Threshold tests were conducted in a sound-treated audiometric test suite with ambient noise levels meeting the tolerances of ANSI S3.1 (1977).

2. Blood samples

In order to limit temporary variations in Mg level due to dietary intake, participants fasted (with the exception of tap water) for a minimum of 6 h, but not more than 12 h, prior to specimen collection. All blood samples were collected in the morning and shipped within 12 h via express delivery from Ft. Bragg to the Flow Cytometry Laboratory, Department of Clinical Investigation, Walter Reed Army Medical Center for analysis. Specimens received less than 48 h from the time of collection were analyzed via atomic absorption spectroscopy to determine SMg. Standard methods of specimen collection, shipping, and analysis were used, the details of which are available from the authors.

II. RESULTS AND DISCUSSION

Consistent with the purpose of this investigation, the primary analysis consisted of correlations computed between audiometric and body Mg measures, across the sample of 68 soldiers. Based on Joachims *et al.* (1987), the initial audiometric index evaluated was the PTA_{AC} (3, 4, and 6 kHz, bilaterally), age-corrected by 1 dB (25–29 years), 4 dB (30–34 years), or 7 dB (35–39 years). However, a variety of other audiometric threshold indices was correlated with the Mg measures including thresholds without age corrections, averages of other audiometric frequencies, thresholds at various single test frequencies, thresholds in the poorer ear only, and thresholds in the better ear only.

The PTA_{AC} ranged from -4.5 to 41.8 dB HL ($M=4.7$). A scatter plot relating the PTA_{AC} to SMg is shown in Fig. 1. The correlation of $r=-0.07$ did not approach statistical significance. Nonsignificant correlations of similar magnitude were obtained for the other audiometric indices derived from the pure-tone thresholds. This study, therefore, failed to replicate the results of Joachims *et al.* (1987).

There are a number of possible explanations for why significant correlations were not observed between naturally occurring body Mg levels and NIHL. The results of

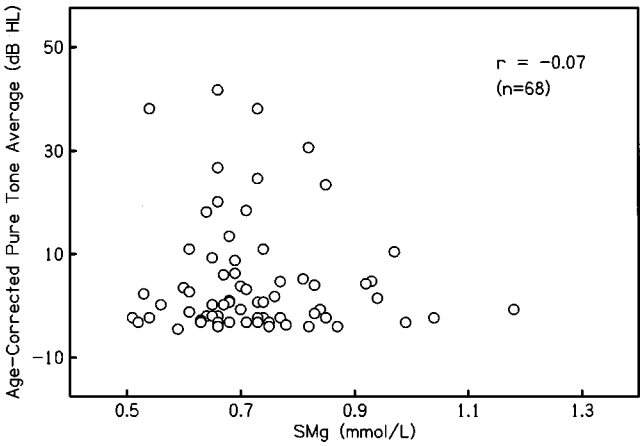

FIG. 1. Scatter plot of the age-corrected pure-tone average (3, 4, 6 kHz, bilaterally) versus serum magnesium level for 68 noise-exposed soldiers.

Joachims *et al.* (1987) notwithstanding, such a relationship may not exist. Because serum magnesium in healthy adults is typically maintained within a relatively narrow range, it is possible that normal variations in body Mg levels are not sufficient to alter susceptibility to NIHL. Alternatively, the influence of body Mg on susceptibility to NIHL may be such a small effect that it is masked by the inevitable differences in noise exposure that will exist among a group of soldiers, even those who have had comparable training and job assignments over a relatively similar period of time, such as the participants of this study. Because the soldiers who participated in this study were all selected from the same combat unit, they had relatively similar noise exposure histories. However, the questionnaire revealed some differences in the frequency and duration of exposure to various weapon systems, as well as some differences in the use of hearing protection. These inevitable intersubject differences in noise exposure may have made it impossible for small effects due to normal variations in Mg levels to emerge. In an effort to test this possibility, the correlation analysis was repeated with a subset of 23 subjects[2] who were more homogeneous in length of military service and, presumably, in noise exposure. Years of military service for the 23 subjects ranged from 13.5–18.0 years ($M=15.1$). The correlation between PTA_{AC} and SMg was $r=0.04$. Again, this did not approach statistical significance.

Although the present study included more subjects than were studied in Joachims *et al.* (1987), the subjects of this study, on average, had substantially less hearing loss. Many, in fact, had PTA_{AC} within normal limits. The correlation analysis was repeated for the 25 soldiers with the greatest PTA_{AC}. The PTA_{AC} of this subgroup of soldiers ranged from 3.5–41.8 dB HL ($M=15.5$), representing a broad range of hearing abilities, comparable to the 24 pilots in the Joachims *et al.* study (2–39 dB HL). The correlation between the PTA_{AC} and SMg was $r=-0.27$. Although the magnitude of this correlation was somewhat higher than that for all 68 subjects ($r=-0.07$), it did not achieve statistical significance and was substantially smaller than the correlation of -0.61 observed by Joachims *et al.* between SMg and PTA_{AC}.

In summary, although there have been a number of reports (primarily using animal models) which suggest that susceptibility to NIHL can be altered by manipulating body Mg levels outside of the normal range, the findings of this study and those of Joachims *et al.* (1987), are not in agreement regarding whether normal variations in body Mg levels may be a significant factor in determining susceptibility to NIHL. Definitive research to resolve this issue is difficult to conduct with human subjects because of the multiple factors that may determine NIHL.

ACKNOWLEDGMENTS

This work received support from the Department of Clinical Investigation, Walter Reed Army Medical Center, Washington, D.C., under Work Unit #2551. All soldiers included in this study volunteered to participate and provided informed consent. The authors wish to acknowledge the technical and administrative contributions of Mary Cord, John Leu, Bradley Pickett, Maria Sjogren, Kalman Salata, and Maged Abdelrahim, as well as Richard Salvi for his helpful suggestions regarding an earlier draft of the manuscript. The opinions and assertions presented are the private views of the authors and are not to be construed as official or as reflecting the views of the Department of the Army, or the Department of Defense.

[1]The age of two subjects was not reported. Therefore, these descriptive statistics are based on a sample size of 22.

[2]The median years of military service for all 68 subjects was 13 years. All subjects who had more than 13 years of military service were included in the subsample ($n=23$).

ANSI (**1977**). ANSI 3.1-1977 (R1986), ''Criteria for Permissible Ambient Noise During Audiometric Testing'' (American National Standards Institute, New York).

ANSI (**1989**). ANSI S3.6-1989, ''American National Standard Specification for Audiometers'' (American National Standards Institute, New York).

Attias, J., Weisz, G., Almog, S., Shahar, A., Wiener, M., Joachims, Z., Netzer, A., Ising, H., Rebentisch, E., and Guenther, T. (**1994**). ''Oral magnesium intake reduces permanent hearing loss induced by noise exposure,'' Am. J. Otolaryngol. **15**, 26–32.

Boyev, K. P., Jastreboff, M. M., Hu, S., and Jastreboff, P. J. (**1997**). ''Magnesium supplement decreases sound induced hearing loss in pigmented rats,'' paper presented at the Midwinter Meeting of the Association for Research in Otolaryngology, St. Petersburg, FL.

Carhart, R., and Jerger, J. F. (**1959**). ''Preferred method for clinical determination of pure-tone thresholds,'' J. Speech Hear. Disord. **24**, 330–345.

Danielson, B. G., Johansson, G., and Ljunghall, S. (**1979**). ''Magnesium metabolism in healthy subjects,'' Scand. J. Urol. and Nephrol. Suppl. **51**, 49–73.

Djurhuus, M. S., Gram, J., Petersen, P. H., Klitgaard, N. A. H., Bollerslev, J., and Beck-Nielsen, H. (**1995**). ''Biological variation of serum and urinary magnesium in apparently healthy males,'' Scand. J. Clin. Lab. Invest. **55**, 549–558.

Duncanson, G. O., and Worth, H. G. J. (**1990**). ''Determination of reference intervals for serum magnesium,'' Clin. Chem. **36**, 756–758.

Ising, H., Handrock, M., Gunther, T., Fischer, R., and Dombrowski, M. (**1982**). ''Increased noise trauma in guinea pigs through magnesium defi-

ciency,'' Arch. Otorhinolarygol. **236**, 139–146.
Joachims, Z., Babisch, W., and Ising, H. (**1983**). ''Dependence of noise-induced hearing loss upon perilymph magnesium concentration,'' J. Acoust. Soc. Am. **74**, 104–108.
Joachims, Z., Ising, H., and Gunther, T. (**1987**). ''Noise-induced hearing loss in humans as a function of serum Mg concentration,'' Magnesium Bull. **9**, 130–131.
Lowenstein, F. W., and Stanton, M. F. (**1986**). ''Serum magnesium levels in the United States, 1971–1974,'' J. Am. Coll. Nutrition **5**, 399–414.
Salvi, R. J., Shulman, A., Stracher, A., Ding, D., and Wang, J. (**1998**). ''Protecting the inner ear from acoustic trauma,'' Int. Tinnitius J. **4**, 11–15.
Scheibe, F., and Haupt, H. (**1998**). ''Protective effects of magnesium on noise-induced hearing loss: Animal studies,'' J. Acoust. Soc. Am. **103**, 3054(A).
Szyszka, A., Brocki, Z., Mrozikiewicz, A., and Paradowski, S. (**1992**). ''Circadian changes in levels of magnesium in serum of healthy individuals,'' Pol. Tyg. Lek. **47**, 1078–1079.
Yang, X. Y., Hosseini, J. M., Ruddel, M. E., and Elin, R. J. (**1990**). ''Blood magnesium parameters do not differ with age,'' J. Am. Coll. Nutrition **9**, 308–313.

Line spectral frequencies are poles and zeros of the glottal driving-point impedance of a discrete matched-impedance vocal tract model

Mark Hasegawa-Johnson[a)]
Department of Electrical and Computer Engineering, University of Illinois at Urbana–Champaign, Urbana, Illinois 61801

(Received 20 July 1999; revised 14 November 1999; accepted 14 March 2000)

This correspondence demonstrates that the line spectral frequencies (LSFs) are the pole and zero frequencies of the glottal driving-point impedance of a discrete matched-impedance vocal-tract model. Several well-known characteristics of the LSFs, including the interlacing of pole and zero frequencies, are shown to follow naturally from this proof. © *2000 Acoustical Society of America.* [S0001-4966(00)02307-9]

PACS numbers: 43.72.Ar, 43.72.Ct [DOS]

INTRODUCTION

Linear prediction analysis is often used to calculate the cross-sectional areas of a particular discrete, linear, matched-impedance vocal-tract model. The discrete matched-impedance model (DMI model) is a concatenated tube model, of a length specified by the experimenter, in which all terminations are lossless except for a single matched-impedance termination at the glottis (Furui, 1989). The DMI model is useful primarily because, given an all-pole estimate of the vocal-tract transfer function, the cross-sectional areas in the DMI model are unique, and may be calculated using an efficient algorithm. The model is often used in speech coding, synthesis, and recognition systems whose designers wish to simulate speech production without the cost of calculating a more accurate area function.

The purpose of this letter is to demonstrate that the line spectral frequencies (LSFs) are the poles and zeros of the glottal driving-point impedance of the DMI model. This new definition of the LSFs is more concise than the standard definition, according to which the LSFs are the resonances of two variants of the DMI model (Furui, 1989). The new definition also allows one to think about the LSFs using a type of physical reasoning not previously applicable. For example, many acousticians are aware of Foster's reactance theorem, which states that the poles and zeros of a driving-point reactance alternate in frequency (Foster, 1924). Section III uses Foster's reactance theorem to demonstrate a concise alternative proof of the well-known and useful interlacing property of the LSFs (Sugamura and Itakura, 1981; Soong and Juang, 1984).

I. BACKGROUND

During the production of oral vowels and glides, the vocal tract may be modeled as a one-dimensional acoustic resonator excited by a high-impedance volume velocity source located at the glottis. The shape of the one-dimensional vocal-tract resonator is commonly approximated using a series of concatenated cylindrical tubes, each of length l, and with varying cross-sectional areas Φ_n, as shown in Fig. 1 (the derivations in this article will assume an arbitrary number of tube sections; for convenience, Fig. 1 shows only five tubes). Let $\tilde{U}_n^+(s)$ denote the forward-going volume velocity wave at the left end of the nth such tube, and let $-\tilde{U}_n^-(s)$ denote the backward-going wave at the right end of the same tube, where $s=\sigma+j\Omega$ is the complex frequency variable. The volume velocity and pressure at the left end of the nth such tube are

$$\tilde{U}(-nl,s)=\tilde{U}_n^+(s)-e^{-sl/c}\tilde{U}_n^-(s), \tag{1}$$

$$\tilde{P}(-nl,s)=Z_n[\tilde{U}_n^+(s)+e^{-sl/c}\tilde{U}_n^-(s)], \quad Z_n\equiv\frac{\rho c}{\Phi_n}, \tag{2}$$

where ρ is the density of air, c is the speed of sound, and Z_n is called the characteristic impedance of the nth tube section. By applying pressure and volume velocity continuity constraints at the boundary between tubes n and $n+1$, it is possible to define a constant reflection coefficient k_n such that

$$\tilde{U}_n^+(s)=e^{-sl/c}[(1-k_n)\tilde{U}_{n+1}^+(s)-k_n\tilde{U}_n^-(s)], \tag{3}$$

$$\tilde{U}_{n+1}^-(s)=e^{-sl/c}[(1+k_n)\tilde{U}_n^-(s)+k_n\tilde{U}_{n+1}^+(s)], \tag{4}$$

where

$$k_n=\frac{Z_n-Z_{n+1}}{Z_n+Z_{n+1}}. \tag{5}$$

The vocal-tract model is terminated at the glottis by a massless, frictionless piston driven by signal $\tilde{E}(s)$, in parallel with a passive termination element with impedance Z_g. If Z_g is independent of frequency, the termination can be written using a constant reflection coefficient k_g

$$\tilde{U}_N^+(s)=\tilde{E}(s)-k_g\tilde{U}_N^-(s)e^{-sl/c}, \tag{6}$$

where N is the number of tube sections (e.g., Fig. 1 shows the case in which $N=5$). The vocal tract is terminated at the lips by radiation impedance Z_0, which yields reflection coefficient k_0

$$\tilde{U}_1^-(s)=k_0\tilde{U}_1^+(s)e^{-sl/c}. \tag{7}$$

Inspection of Eqs. (3) through (7) reveals that, in an undriven system, $\tilde{U}_n^+(s)$ and $\tilde{U}_n^-(s)$ are periodic in s

a)Electronic mail: jhasegaw@uiuc.edu; telephone: +1-217-333-0925.

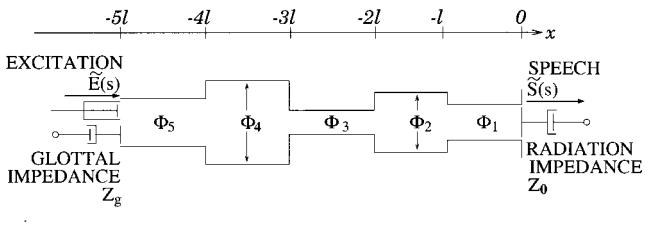

FIG. 1. Concatenated tube model of the vocal tract.

$$\tilde{U}_n^+(s)=\tilde{U}_n^+(s\pm j2\pi mF_s),\quad F_s\equiv\frac{c}{2l},\quad m=1,2,\ldots, \tag{8}$$

and the same relation holds for $\tilde{U}_n^-(s)$. Without loss of information, we may therefore define discrete-time transform quantities $U_n^+(z)$, $U_n^-(z)$, $P(n,z)$, and $U(n,z)$. Furui (1989) describes a number of different discrete-time implementations of Fig. 1; one of the most common implementations is the lattice filter structure shown in Fig. 2. The discrete-time quantities in Fig. 2 include a constant delay and a constant scaling factor; thus,

$$U_n^+(z)=\tilde{G}_n(s)\tilde{U}_n^+(s)\big|_{s=F_s\log z}, \tag{9}$$

$$U_n^-(z)=e^{-s/2F_s}\tilde{G}_n(s)\tilde{U}_n^-(s)\big|_{s=F_s\log z}, \tag{10}$$

$$U(n,z)=\tilde{G}_n(s)\tilde{U}(-nl,s)\big|_{s=F_s\log z}, \tag{11}$$

where

$$\tilde{G}_n(s)\equiv e^{-ns/2F_s}\prod_{i=1}^{n-1}(1-k_i). \tag{12}$$

The ''speech signal'' may be conveniently defined to be the volume velocity which passes through Z_0, i.e.,

$$\tilde{S}(s)=(1-k_0)\tilde{U}_1^+(s)e^{-sl/c}. \tag{13}$$

The transfer function of the vocal tract is the ratio of $\tilde{S}(s)$ to $\tilde{E}(s)$. During oral vowels and glides, the transfer function is an all-pole function, with the form

$$\tilde{T}(s)=\frac{\tilde{S}(s)}{\tilde{E}(s)}=\frac{1}{\tilde{A}(s)}=\prod_{m=1}^{\infty}\frac{s_m s_m^*}{(s-s_m)(s-s_m^*)}. \tag{14}$$

The discrete-time transfer function is likewise defined to be

$$T(z)=\frac{S(z)}{E(z)}=\frac{1}{A(z)}. \tag{15}$$

The roots of $\tilde{A}(s)$, $s_m=\pi B_m+j2\pi F_m$, are the resonant frequencies of the vocal tract; the roots of $A(z)$ are $z_m=e^{s_m/F_s}$. This section considers two standard methods for calculating the resonant frequencies: the series impedance method, and the Levinson–Durbin recursion.

One of the most general methods for calculating s_m requires cutting the vocal-tract resonator in half at some coordinate $x_n=-nl$, creating two half-resonators called the back cavity ($x<x_n$) and the front cavity ($x>x_n$). The geometry of the back cavity dictates a relationship between pressure and flow, and the geometry of the front cavity dictates a second relationship. If these relationships are linear, they may be expressed as a back-cavity impedance and a front-cavity impedance

$$P(n,z)=-Z_b(n,z)U(n,z), \tag{16}$$

$$P(n,z)=Z_f(n,z)U(n,z). \tag{17}$$

$U(n,z)$ can only be nonzero at frequencies for which

$$Z_b(n,z)+Z_f(n,z)=0, \tag{18}$$

while $P(n,z)$ can only be nonzero at frequencies for which

$$Y_b(n,z)+Y_f(n,z)=0, \tag{19}$$

where $Y_b=1/Z_b$ and $Y_f=1/Z_f$. Barring any pole-zero cancellations, it can be shown that the solutions to both Eqs. (18) and (19) are given by the resonant frequencies z_m. Equation (18) is sometimes called the ''series impedance'' method of calculating resonant frequencies, and Eq. (22) is called the ''parallel admittance'' method.

The Levinson–Durbin recursion is more computationally efficient than the series impedance method, but it has only been shown to be useful for two particular distributions of losses. Specifically, the Levinson–Durbin recursion assumes that all vocal-tract boundaries are lossless except for a single matched-impedance termination, which may be placed at either the lips or the glottis (Furui, 1989). For convenience, this article uses the term ''DMI model'' to mean a vocal-tract model in which

$$Z_0=0,\quad Z_g=Z_N, \tag{20}$$

The corresponding reflection coefficients are

$$k_0=-1,\quad k_g=0. \tag{21}$$

With this matched-impedance termination, the energy lost by the vocal tract is

$$\text{loss spectrum}=\tfrac{1}{2}Z_g|B(z)|^2, \tag{22}$$

where

$$B(z)\equiv U_N^-(z)=z^{-N}A(z^{-1})S(z). \tag{23}$$

The line spectral frequencies (LSFs) are typically defined as the resonant frequencies of two variants of the DMI model. Both modified models are created by first calculating the cross-sectional areas Φ_n of the DMI model using the Levinson–Durbin recursion, and then creating a new model which has the same Φ_n, and the same lossless termination at the lips, but a different glottal termination.

In the first modified model, which we may call the ''Q model,'' the glottal impedance is set to $Z_g=0$, thus $k_g=1$, and the forward-going wave at the left end of the Nth tube is

$$U_N^+(z)=E(z)-B(z)=Q(z)S(z), \tag{24}$$

$$Q(z)\equiv A(z)-z^{-N}A(z^{-1}). \tag{25}$$

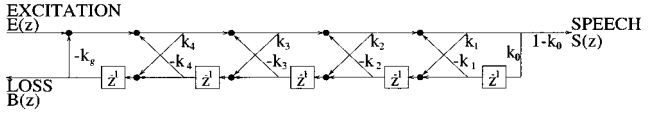

FIG. 2. Discrete-time implementation of a concatenated tube model of the vocal tract.

The resonances of this system are the frequencies at which $Q(e^{jq_i})=0$. $Q(z)$ can be factored as

$$Q(z)=\prod_{i=0}^{N-1}(1-e^{jq_i}z^{-1}), \tag{26}$$

where the frequencies q_i are real numbers, $0\leqslant q_i<2\pi$, and satisfy the following symmetry condition:

$$q_i=\begin{cases}0 & i=0\\ 2\pi-q(N-i) & 1\leqslant i\leqslant N-1.\end{cases} \tag{27}$$

In the second modified model, which we may call the ''*R* model,'' the glottal impedance is set to $Z_g=\infty$, thus,

$$U_N^+(z)=E(z)+B(z)=R(z)S(z), \tag{28}$$

$$R(z)\equiv A(z)+z^{-N}A(z^{-1}). \tag{29}$$

$R(z)$ can be factored as

$$R(z)=\prod_{i=0}^{N-1}(1-e^{jr_i}z^{-1}), \tag{30}$$

$$r_i=2\pi-r_{(N-1-i)}, \quad 0\leqslant i\leqslant N-1. \tag{31}$$

The line spectral frequencies q_i and r_i are a unique and invertible representation of the polynomial $A(z)$. They are real, and, if and only if $1/A(z)$ is stable, they are ordered according to the interlacing property (Sugamura and Itakura, 1981; Soong and Juang, 1984)

$$0=q_0<r_0<q_1<\cdots<q_{N-1}<r_{N-1}<2\pi. \tag{32}$$

The interlacing property of the LSFs is useful in speech coding and speech synthesis. A speech-synthesis filter constructed from quantized LSFs (in speech coding), or from LSFs linearly interpolated between two phoneme targets (in speech synthesis), is guaranteed to be stable if and only if the quantized LSFs obey Eq. (32).

II. FORM OF THE GLOTTAL DRIVING-POINT IMPEDANCE

The purpose of this letter is to prove the following theorem.

A. Theorem

The glottal driving-point impedance of the discrete matched-impedance vocal-tract model is given by

$$Z_{dp,g}(z)=-H\frac{Q(z)}{R(z)}, \tag{33}$$

where $Q(z)$ and $R(z)$ are the LSF polynomials given in Eqs. (25) and (29), and H is a real constant.

This section proves that the driving-point impedance is the ratio of two polynomials in z^{-1}, and that the roots of the numerator and denominator alternate. Section III proves that the numerator polynomial is $Q(z)$ and the denominator polynomial is $R(z)$.

Consider applying the series impedance method [Eq. (18)] to the DMI model at the position $x_N=-Nl$ (the left end of the *N*th tube section). The ''back cavity'' (the cavity to the left of x_N) has zero length, but it has a finite, real-valued impedance

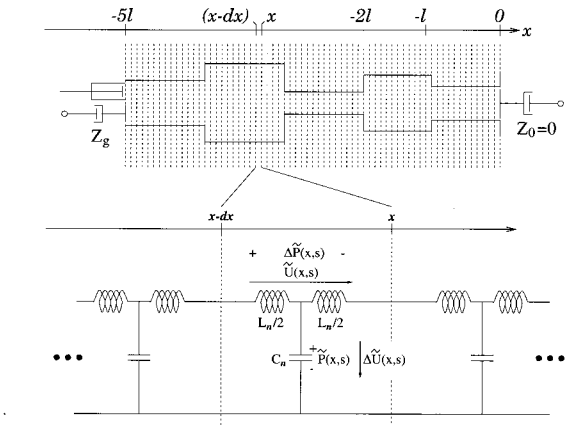

FIG. 3. A continuous hard-walled one-dimensional acoustic resonator, such as the DMI model, may be approximated to arbitrary precision using a discrete ladder network as shown here. $\tilde{U}(x,s)$ is the average of the flow through the two $L_n/2$ elements.

$$Z_b(N,z)=Z_g\,. \tag{34}$$

The front cavity (the cavity to the right of x_N) consists of the entire vocal tract except the glottal termination, so $Z_f(N,z)$ is appropriately called the glottal driving-point impedance

$$Z_{dp,g}(z)=Z_f(N,z). \tag{35}$$

In the DMI model, all boundaries to the right of the glottis are lossless, so the glottal driving-point impedance is a pure reactance with zero-bandwidth poles and zeros.

B. Foster's reactance theorem (1924)

The most general form of the driving-point impedance of any finite network of positive-valued lossless inductors and capacitors is

$$\tilde{Z}_{dp,M}(j\Omega)=j\tilde{H}\frac{(\Omega^2-\Omega_0^2)(\Omega^2-\Omega_2^2)\cdots(\Omega^2-\Omega_{2M-2}^2)}{\Omega(\Omega^2-\Omega_1^2)(\Omega^2-\Omega_3^2)\cdots(\Omega^2-\Omega_{2M-3}^2)}, \tag{36}$$

where $\tilde{H}$ and M are real constants determined by the problem, and

$$0\leqslant\Omega_0<\Omega_1<\Omega_2<\cdots<\Omega_{2M-2}<\infty. \tag{37}$$

Consider dividing each of the tubes in the DMI model into many smaller tubes, each of length *dx*, as shown in Fig. 3. Each of the tiny tube sections may be approximated using the discrete ladder section shown in Fig. 3. As the number of ladder sections approaches infinity, the constitutive equations of the ladder network approach the acoustic constitutive equations of the DMI model. Guillemin (1935) shows that the driving-point impedance of the network shown in Fig. 3 is of the form given in Eq. (36), with M equal to the number of ladder sections, and $\Omega_0=0$. The driving-point impedance of the DMI model is therefore

$$\tilde{Z}_{dp,g}(j\Omega)=\lim_{M\to\infty}\tilde{Z}_{dp,M}(j\Omega), \quad \Omega_0=0. \tag{38}$$

Recall that, because the DMI model is constructed from a discrete number of length-l tubes,

$$\tilde{Z}_{dp,g}(j\Omega)=\tilde{Z}_{dp,g}(j\Omega\pm j2\pi kF_s),\quad k=1,2,\ldots. \tag{39}$$

Equation (39) requires that Ω_{2i} is a zero of $\tilde{Z}_{dp,g}(j\Omega)$ if and only if $\Omega_{2i}\pm 2\pi kF_s$ is also a zero. As M approaches infinity, therefore, the poles and zeros of $\tilde{Z}_{dp,M}(j\Omega)$ must approach the periodic repetition of a finite set of ''base-band'' poles and zeros; thus,

$$\lim_{M\to\infty}\tilde{Z}_{dp,M}(j\Omega)=j\tilde{H}\prod_{k=-\infty}^{\infty}\prod_{i=0}^{N-1}\frac{\Omega-\Omega_{2i}+2\pi kF_s}{\Omega-\Omega_{2i+1}+2\pi kF_s}, \tag{40}$$

where the pole and zero frequencies satisfy

$$0=\Omega_0<\Omega_1<\Omega_2<\cdots<\Omega_{2N-1}<2\pi F_s, \tag{41}$$

$$\Omega_m=2\pi F_s-\Omega_{2N-m},\quad 1\leqslant m\leqslant 2N-1. \tag{42}$$

Equation (40) may be simplified by applying the infinite product expansion of a sine, yielding

$$\tilde{Z}_{dp,g}(j\Omega)=j\tilde{H}\prod_{i=0}^{N-1}\frac{\sin\left(\frac{\Omega-\Omega_{2i}}{2F_s}\right)}{\sin\left(\frac{\Omega-\Omega_{2i+1}}{2F_s}\right)}. \tag{43}$$

Replacing sine functions by complex exponentials and noting that $z=e^{j\Omega/F_s}$ yields the discrete-time impedance

$$Z_{dp,g}(z)\equiv\tilde{Z}_{dp,g}(j\Omega)=-H\prod_{i=0}^{N-1}\frac{1-z^{-1}e^{j\Omega_{2i}/F_s}}{1-z^{-1}e^{j\Omega_{2i+1}/F_s}}, \tag{44}$$

where, by making use of Eq. (42) H is shown to be

$$H=-j\tilde{H}\exp\left(\frac{j}{2F_s}\sum_{i=0}^{N-1}(\Omega_{2i+1}-\Omega_{2i})\right)=\tilde{H}. \tag{45}$$

III. POLES AND ZEROS OF THE GLOTTAL DRIVING-POINT IMPEDANCE

Remember that, by applying the series impedance method to the DMI model at $x_N=-Nl$, one obtains a front cavity whose impedance is $Z_{dp,g}(z)$, and a back cavity whose impedance is

$$Z_b(N,z)=Z_g. \tag{46}$$

The frequencies of the poles and zeros of $Z_{dp,g}(z)$ can be calculated by constructing modified vocal-tract models in which $Z_b(N,z)$ is replaced by values which happen to be more convenient for the problem at hand. Notice, for example, that the zeros of $Z_{dp,g}(z)$ are the roots of the equation

$$0+Z_{dp,g}(z)=0. \tag{47}$$

Comparing Eqs. (47) and (18), we discover that the zeros of $Z_{dp,g}(z)$ are also the resonances of a modified vocal-tract model in which

$$Z_f(N,z)=Z_{dp,g}(z),\quad Z_b(N,z)=0. \tag{48}$$

Equation (48) is satisfied by the Q model introduced in Sec. I. The zeros of $Z_{dp,g}(z)$ are therefore the resonances of the Q model, which are given by

$$\Omega_{2i}/F_s=q_i, \tag{49}$$

In a similar manner, the poles of $Z_{dp,g}(z)$ are also the roots of the equation

$$0+Y_{dp,g}(z)=0, \tag{50}$$

where $Y_{dp,g}(z)=1/Z_{dp,g}(z)$.

Equation (50) is satisfied by the R model introduced in Sec. I. The poles of $Z_{dp,g}(z)$ are therefore

$$\Omega_{2i+1}/F_s=r_i, \tag{51}$$

By combining Eqs. (44), (49), and (51), we obtain

$$Z_{dp,g}(z)=-H\prod_{i=0}^{N-1}\frac{1-e^{jq_i}z^{-1}}{1-e^{jr_i}z^{-1}}=-H\frac{Q(z)}{R(z)}, \tag{52}$$

which proves the theorem given in Eq. (33).

Notice that Eq. (40) dictates that the poles and zeros of $Z_{dp,g}(z)$ must alternate. Guillemin's analysis (1935) of Foster's reactance theorem shows that the poles and zeros of the driving-point impedance fail to alternate if and only if the circuit contains at least one negative inductor ($L_n<0$) and at least one negative capacitor ($C_n<0$). Negative-valued reactances cannot be realized using passive physical elements—in particular, in Fig. 3, negative-valued reactances correspond to negative cross-sectional areas in the DMI model. Negative reactances can be modeled in a digital simulation, but since the DMI model contains a single positive resistance (the glottal resistance), negative reactances are a sufficient and necessary condition for instability of the circuit. Thus, the well-known interlacing property of the LSFs may be restated as a corollary of Eq. (33).

A. Corollary (interlacing property of the LSFs)

The following conditions are equivalent:

(a) The LSFs are interlaced.
(b) The cross-sectional areas Φ_n in the DMI model are everywhere positive.
(c) The transfer function $T(z)=1/A(z)$ is stable.

IV. CONCLUSIONS

This letter demonstrates that the glottal driving-point impedance of the standard DMI model is proportional to $Q(z)/R(z)$, where $Q(z)$ and $R(z)$ are the standard LSF polynomials. In this way, a new definition of the LSFs is proposed: the LSFs are the poles and zeros of the glottal driving-point impedance of a discrete matched-impedance vocal-tract model.

Foster, R. M. (**1924**). ''A reactance theorem,'' Bell Syst. Tech. J. **3**, 259–267.

Furui, S. **(1989)**. *Digital Speech Processing, Synthesis, and Recognition* (Dekker, New York).

Guillemin, E. A. **(1935)**. *Communication Networks* (Wiley, New York), Vol. II.

Soong, F., and Juang, B.-H. **(1984)**. ''Line spectral pair (LSP) and speech data compression,'' in Proceedings of the ICASSP, pp. 1.10.1–1.10.4 (IEEE, New York).

Sugamura, N., and Itakura, F. (**1981**). ''Speech data compression by LSP speech analysis–synthesis technique,'' Trans. Inst. Electron. Commun. Eng. Jpn. **64-A**(8), 599–606 (in Japanese).